JOURNAL OF THE ELECTROCHEMICAL SOCIETY

LECTROCHEMICAL
CIENCE AND TECHNOLOGY

OLID-STATE
CIENCE AND TECHNOLOGY

EVIEWS AND NEWS
Spring Meeting Program
Call for Papers—
Denver, Colorado, Meeting

VOL. 128, NO. 3 MARCH 1981

JESOAN 128 (3) 491-718, 47C-154C

FUTURE MEETINGS

MINNEAPOLIS, MINNESOTA—MAY 10-15, 1981—HEADQUARTERS AT THE LEAMINGTON HOTEL

Final program published in the March 1981 issue of **This Journal.** If you would like a copy of the advance program booklet and other information pertaining to this meeting, please write: Minneapolis Meeting, The Electrochemical Society, Inc., 10 South Main Street, Pennington, NJ 08534.

DENVER, COLORADO—OCTOBER 11-16, 1981—HEADQUARTERS AT THE DENVER HILTON

The detailed Call for Papers published in the December 1980-May 1981 issues of **This Journal.** Final program published in the August 1981 issue of **This Journal.**

Planned symposia for the Denver Meeting include the following Divisions, Group, Subcommittee, and subjects: **Battery**—Accelerated Testing of Batteries, Environmental Safety and Recycling of Batteries, The Nickel Electrode, Thermal Analysis in Battery Design, General Session; **Battery/Corrosion/Electrothermics and Metallurgy/Energy Technology**—Corrosion in Batteries and Fuel Cells; **Battery/Energy Technology**—Acid Fuel Cell Technology: An Update, Metal-Air Batteries; **Corrosion**—Impedance and Pulse Methods for Investigation of Corrosion Processes, Corrosion in Metal Matrix Composites, H. H. Uhlig Seventy-Fifth Birthday Symposium, General Session; **Corrosion/Energy Technology**—Corrosion in Solar Energy Systems; **Dielectrics and Insulation/Electronics**—Cleaning Processes and Contamination Control in the Semiconductor Industry, Organic Insulators, Third Symposium on Plasma Processing; **Electrodeposition**—Engineering Topics in Electrodeposition, General Session; **Electronics**—Ion Implantation in Compound Semiconductors, Materials for Optical Recording, Surface and Thin Film Analysis of Semiconductor Materials; **Electronics/Dielectrics and Insulation**—Dielectric Materials and Processing for Multilevel Metal Technology, Silicon Dioxide and Other Insulators for VLSI, General Session, Recent News Papers Session; **Electrothermics and Metallurgy**—Amorphous Materials, Processes, and Applications, High Temperature Materials Chemistry; **Electrothermics and Metallurgy/Dielectrics and Insulation/Energy Technology**—Silicon Purification; **Energy Technology**—Measurement Techniques for Photoelectrochemical Solar Cells, General Session; **Energy Technology/All Divisions**—Electrochemistry in Our Future: The Year 2000 Symposium; **Industrial Electrolytic**—General Session; **Industrial Electrolytic/Electrodeposition/Energy Technology/New Technology Subcommittee**—Chemical and Electrochemical Methods for Deposition of Semiconductors; **Physical Electrochemistry**—Photoelectrochemical Processes, General Session; **Physical Electrochemistry/Battery**—New Techniques for the Study of Electrode Processes; and **New Technology Subcommittee/Battery/Dielectrics and Insulation**—Ion-Conducting Polymers.

MONTREAL, CANADA—MAY 9-14, 1982—HEADQUARTERS AT THE QUEEN ELIZABETH

The detailed Call for Papers published in the July-November 1981 issues of **This Journal.** Final program published in the March 1982 issue of **This Journal.**

Planned symposia for the Montreal Meeting include the following Divisions, Group, Subcommittee, and subjects: **Corrosion**—General Session; **Corrosion/Energy Technology/Dielectrics and Insulation/Electrothermics and Metallurgy**—Corrosion Problems in Nuclear and Fusion Technology; **Dielectrics and Insulation/Corrosion/Electronics/Electrothermics and Metallurgy/Energy Technology**—New Concepts in Photovoltaic Devices; **Dielectrics and Insulation**—Glass Applications in Semiconductors; **Electronics**—Micromachining and Micromechanics, General Luminescence, Luminescence in Amorphous Materials, Phosphor Depreciation, Phosphor Screening; **Electronics/Dielectrics and Insulation**—Growth of Single Crystals on Amorphous Substrates, Materials and Processes for Integrated Optics, Tutorial on Semiconductor Technology, General Session, Recent News Papers Session; **Electrothermics and Metallurgy**—Alternative Processes for Pollution Abatement, Electrochemistry of Pyrometallurgical Processes, Transport Phenomena in Metals; **Electrothermics and Metallurgy/Corrosion**—Electrochemical Techniques for High Temperature Corrosion Studies; **Electrothermics and Metallurgy/Dielectrics and Insulation/Electronics**—Tenth International Conference on Electron and Ion Beam Science and Technology; **Energy Technology**—Ion Insertion Phenomena, Photobiological Energy Conversion, General Session; **Energy Technology/Battery**—Efficient Utilization of and Alternatives to Platinum, Electrocatalytic Behavior of Amorphous Materials, Energy Systems for Developing Countries; **Energy Technology/Battery/Corrosion**—Advanced Aqueous Electrolytes for Energy Systems, Molten Carbonate Fuel Cell Technology; **Energy Technology/Corrosion/Industrial Electrolytic**—Energy Conservation in Electrochemical Processes; **Industrial Electrolytic**—General Session; **Physical Electrochemistry**—Double Layer Phenomena, General Session; **Physical Electrochemistry/Battery/Energy Technology**—Solid Electrolytes; **New Technology Subcommittee/Dielectrics and Insulation/Electronics**—Inorganic Resists; and **New Technology Subcommittee/Physical Electrochemistry**—Alternative Electrical Contacts.

DETROIT, MICHIGAN—OCTOBER 17-22, 1982—HEADQUARTERS AT THE DETROIT PLAZA

The detailed Call for Papers published in the December 1981-May 1982 issues of **This Journal.** Final program published in the August 1982 issue of **This Journal.**

Planned symposia for the Detroit Meeting include the following Divisions, Group, Subcommittee, and subjects: **Battery**—Economic and Trade Off Consideration on Batteries for Electric Vehicles, Long Term Batteries, Near Term Batteries, Thin Film Batteries, General Session; **Corrosion**—Automotive Corrosion, General Session; **Dielectrics and Insulation/Electronics**—Reliability of Components for Automotive Applications; **Electrodeposition**—Electrodeposition in Automotive Applications, General Session; **Electronics**—Automotive Microelectronics; **Electronics/Dielectrics and Insulation**—VLSI Technology, General Session, Recent News Papers Session; **Electrothermics and Metallurgy**—Arc Furnace Materials and Technologies, Emission Control, Materials Aspects of Turbine Technologies, High Temperature Oxidation, Thermal Management of Batteries, **Energy Technology**—Electrical Methods for Synfuel Production, Extraction of Minerals from the Ocean, Novel Techniques in Electrochemical Techniques, Photoelectrochemical Synthetic Routes, Redox Energy Storage Systems, Surface Charge, Measurement Control, and Modification for Industrial Processes, General Session; **Energy Technology/Corrosion**—Corrosion in Fossil Fuel Systems; **Energy Technology/Physical Electrochemistry**—Intercalation Electrodes, Photoelectrochemical Energy Conversion; **Physical Electrochemistry**—General Session; **Physical Electrochemistry/Battery/Corrosion**—Reactions in High Temperature Batteries; **New Technology Subcommittee**—Reindustrialization of America; and **New Technology Subcommittee/Energy Technology**—Electrochemistry and Electronics in the Automotive Industry.

THE ELECTROCHEMICAL SOCIETY
BOOKS IN PRINT

Society Proceedings Series

The following softbound proceedings volumes are sponsored and published by The Electrochemical Society, Inc., 10 South Main Street, Pennington, N.J. 08534. Orders filled at the list price given, subject to availability. Enclose payment with order.

Electron and Ion Beam Science and Technology, Fourth International Conference. R. Bakish, Editor. A 1970 symposium. 680 pages, **$7.50.**

Fundamentals of Electrochemical Machining. C. L. Faust. Editor. A 1970 symposium. 365 pages, **$4.50.**

Electron and Ion Beam Science and Technology, Fifth International Conference. R. Bakish, Editor. A 1972 symposium. 420 pages, **$5.50.**

Electrochemical Contributions to Environmental Protection. T. R. Beck, O. B. Cecil, C. G. Enke, J. McCallum, and S. T. Wlodek, Editors. A 1972 symposium. 173 pages, **$4.00.**

Oxide-Electrolyte Interfaces. R. S. Alwitt, Editor. A 1972 symposium. 312 pages, **$9.00.**

Electrochemical Bioscience and Bioengineering. H. T. Silverman, I. F. Miller, and A. J. Salkind, Editors. A 1973 symposium. 268 pages, **$8.00.**

Chlorine Bicentennial Symposium. T. C. Jeffery, P. A. Danna, and H. S. Holden, Editors. A 1974 symposium. 404 pages, **$11.00.**

Properties of Electrodeposits—Their Measurement and Significance. R. Sard, H. Leidheiser, Jr., and F. Ogburn, Editors. A 1974 symposium. 430 pages, **$13.00.**

Metal-Slag-Gas Reactions and Processes. Z. A. Foroulis and W. W. Smeltzer, Editors. A 1975 symposium. 1032 pages, **$20.00.**

Chemistry and Physics of Aqueous Gas Solutions. W. A. Adams, G. Greer, J. E. Desnoyers, G. Atkinson, G. S. Kell, K. B. Oldham, and J. Walkley, Editors. A 1975 symposium. 522 pages, **$11.00.**

Thermal and Photostimulated Currents in Insulators. D. M. Smyth, Editor. A 1975 symposium. 215 pages, **$7.00.**

Electron and Ion Beam Science and Technology, Seventh International Conference. R. Bakish, Editor. A 1976 symposium. 632 pages, **$18.00.**

International Symposium on Molten Salts. J. P. Pemsler, J. Braunstein, K. Nobe, D. R. Morris, and N. E. Richards, Editors. A 1976 symposium. 632 pages, **$16.00.**

Properties of High Temperature Alloys. Z. A. Foroulls and F. S. Pettit, Editors. A 1976 symposium. 851 pages, **$12.00.**

Semiconductor Silicon 1977. H. R. Huff and E. Sirtl, Edltors. A 1977 symposium. 1100 pages, **$15.00.**

A History of The Electrochemical Society. The first 75 years. R. M. Burns with E. G. Enck. 160 pages, **$5.00.**

Semiconductor-Liquid Junction Solar Cells. A. Heller, Edltor. A 1977 symposium. 340 pages, **$7.00.**

3/81

Load-Leveling. N. P. Yao and J. R. Selman, Editors. A 1977 symposium. 412 pages, **$13.00.**

Chemical Vapor Deposition, Sixth International Conference. L. F. Donaghey, P. Rai-Choudhury, and R. N. Tauber, Editors. A 1977 symposium. 596 pages, **$14.00.**

High Temperature Metal Halide Chemistry. D. L. Hildenbrand and D. D. Cubicciotti, Editors. A 1977 symposium. 678 pages, **$17.00.**

Thin Film Phenomena—Interfaces and Interactions. J. E. E. Baglin and J. M. Poate, Editors. A 1977 symposium. 525 pages, **$14.00.**

Semiconductor Characterization Techniques. P. A. Barnes and G. A. Rozgonyi, Editors. A 1978 symposium. 532 pages, **$16.00.**

Industrial Water Electrolysis. S. Srinivasan, F. J. Salzano, and A. R. Landgrebe, Editors. A 1978 symposium. 297 pages, **$12.00.**

Selected Topics in the History of Electrochemistry. George Dubpernell and J. H. Westbrook, Editors. A 1977 symposium. 523 pages, **$11.00.**

Battery Design and Optimization. S. Gross, Editor. A 1978 symposium. 486 pages, **$14.00.**

The Electrocatalysis of Fuel Cell Reactions. W. E. O'Grady, S. Srinivasan, and R. F. Dudley, Editors. A 1978 workshop sponsored by the Division of Fossil Fuel Utilization, United States Department of Energy. 228 pages, **$8.00.**

Chemical Vapor Deposition, Seventh International Conference. T. O. Sedgwick and H. Lydtin, Editors. A 1979 symposium. 658 pages, **$16.00.**

Laser and Electron Beam Processing of Electronic Materials. C. L. Anderson, G. K. Celler, and G. A. Rozgonyi, Editors. A 1979 symposium. 560 pages, **$13.00.**

Thin Film Interfaces and Interactions, J. E. E. Baglin and J. M. Poate, Editors. A 1979 symposium. 536 pages, **$16.00.**

Electrode Processes, S. Bruckenstein, J. D. E. McIntyre, B. Miller, and E. Yeager, Editors. A 1979 symposium. 500 pages, **$21.00.**

Power Sources for Biomedical Implantable Applications and Ambient Temperature Lithium Batteries. B. B. Owens and N. Margalit, Editors. A 1979 symposium. 652 pages, **$18.00.**

Electronic and Optical Properties of Polycrystalline or Impure Semiconductors and Novel Silicon Growth Methods. K. V. Ravi and B. O'Mara, Editors. A 1980 symposium. 280 pages, **$15.00.**

Electron and Ion Beam Science and Technology, Ninth International Conference. R. Bakish, Editor, A 1980 symposium. 672 pages, **$28.00.**

EDITOR
Norman Hackerman
Jackie Bourne, **Assistant to the Editor**

DIVISIONAL AND GROUP EDITORS

BATTERY
R. J. Brodd — Boone B. Owens
Elton J. Cairns — C. Joseph Venuto
G. F. Nordblom — J. L. Weininger

CORROSION
J. R. Ambrose — Florian Mansfeld
J. W. Faust, Jr. — E. McCafferty
R. P. Frankenthal — Ken Nobe
Jerome Kruger — W. H. Smyrl
D. D. MacDonald

DIELECTRICS AND INSULATION
Robert S. Alwitt — T. W. Hickmott
Rudolf G. Frieser — George L. Schnable
Dennis Hess

ELECTRODEPOSITION
Ugo Bertocci — Y. Okinaka
Huk Y. Cheh — Mordechay Schlesinger

ELECTRONICS
Ephraim Banks — Ernest Paskell
D. M. Brown — Bertram Schwartz
Ted F. Ciszek — Frederic N Schwettmann
George R. Cronin — Thomas O. Sedgwick
John A. DeLuca — Melvin Tecotzky
Murray Gershenzon — C. C. Wang
James S. Harris — P. Wang
Simon Larach — J. M. Woodall
David L. Nelson

ELECTROTHERMICS AND METALLURGY
William A. Adams — R. A. Rapp
Joan B. Berkowitz — David A. Shores
Lee P. Hunt — Gene F. Wakefield
V. K. Kapur — Jack H. Westbrook

High Temperature Science and Technology
Leo Brewer — E. D. Cater
Daniel Cubicciotti

ENERGY TECHNOLOGY GROUP
S. Srinivasan

INDUSTRIAL ELECTROLYTIC
Richard C. Alkire — Scott Lynn

ORGANIC AND BIOLOGICAL ELECTROCHEMISTRY
Martin Blank — Stanley Wawzonek
M. Dale Hawley

PHYSICAL ELECTROCHEMISTRY
M. J. Dignam — Robert A. Osteryoung
Gregory C. Farrington — David K. Roe
David S. Ginley — C. W. Tobias
Gleb Mamantov — F. G. Will
Barry Miller — Ronald H. Wilson
Keith B. Oldham — M. S. Wrighton

News Editor—Jack H. Westbrook

Book Review Editor—Julius Kleror

JOURNAL OF THE ELECTROCHEMICAL SOCIETY
(USPS 284-140)

The JOURNAL OF THE ELECTROCHEMICAL SOCIETY (USPS 284-140) is published monthly by The Electrochemical Society, Inc. at 215 Canal St., Manchester, N.H. 03108. The address for the Executive Offices, Editorial and Advertising Office, and Circulation Department of The Electrochemical Society, Inc., is 10 South Main St., Pennington, N.J. 08534. Subscription to members as part of membership service; subscription to nonmembers $80.00 plus $5.00 for postage outside U.S. and Canada. Single copies $4.00 to members, $7.00 to nonmembers. © Copyright 1981 by The Electrochemical Society, Inc. Second Class Postage paid at Pennington, New Jersey and at additional mailing offices.

POSTMASTER: Send address changes to THE ELECTROCHEMICAL SOCIETY, INC., 10 South Main St., Pennington, N.J. 08534.

March 1981

ELECTROCHEMICAL SCIENCE AND TECHNOLOGY

TECHNICAL PAPERS

R. Pollard, J. Newman . . . 491 — Mathematical Modeling of the Lithium-Aluminum, Iron Sulfide Battery I. Galvanostatic Discharge Behavior

R. Pollard, J. Newman . . . 503 — Mathematical Modeling of the Lithium-Aluminum Iron Sulfide Battery II. The Influence of Relaxation Time on the Charging Characteristics

S. Dallek, S. D. James, W. P. Kilroy . . . 508 — Exothermic Reactions among Components of Lithium-Sulfur Dioxide and Lithium-Thionyl Chloride Cells

F. B. Tudron . . . 516 — Dynamic Microcalorimetry: Thermal Effects of Miniature Alkaline Cells under Load

U. Bertocci . . . 520 — Separation Between Deterministic Response and Random Fluctuations by Means of the Cross-Power Spectrum in the Study of Electrochemical Noise

M. C. H. McKubre, D. D. Macdonald . . . 524 — The Dissolution and Passivation of Zinc in Concentrated Aqueous Hydroxide

J. Perriere, J. Siejka, M. Croset . . . 530 — Anodization of Metals Through Thin Solid Electrolyte Films of Calcia Stabilized Zirconia

C. Ogden, D. Tench . . . 539 — On the Mechanism of Electrodeposition in the Dimercaptothiadiazole/Copper Pyrophosphate System

K. Colbow, D. J. Harrison, B. L. Funt . . . 547 — Energy Dependence of the Quantum Efficiency of CdSe Photoelectrochemical Cells

Z. Harzion, N. Croitoru, S. Gottesfeld . . . 551 — The Measurement of Fast Transients in the CdSe/$S^{=}$, S° Photoelectrochemical Cells

TECHNICAL NOTE

R. C. McCune, C. J. Russo . . . 555 — The Use of Rutherford Backscattering Spectroscopy for Characterization of Surface Films Produced by Aluminum/Water Reactions

SOLID-STATE SCIENCE AND TECHNOLOGY

TECHNICAL PAPERS

J. R. Shealy, B. J. Baliga, R. J. Field, S. K. Ghandi . . . 558 — Preparation and Properties of Zinc Oxide Films Growth by the Oxidation of Diethylzinc

R. S. Nowicki, J. F. Moulder . . . 562 — Comparison of the Properties of Molybdenum Silicide Films Deposited by D-C Magnetron and RF Diode Co-Deposition

W. Hartmann . . . 568 — Fluorescent Screens for High-Resolution Real-Time X-Ray Topography

K. Okumura . . . 571 — Degradation of Bonding Strength (Al Wire-Au Film) by Kirkendall Voids

ELECTROCHEMICAL SOCIETY

Vol. 128 • No. 3

H. R. Maxwell, Jr.
W. R. Knolle
. . . 576 — Densification of SIPOS

S. Hamar-Thibault
J. Trilhe
. . . 581 — Transmission Electron Observations of the Early Stage of Epitaxial Growth of Silicon on Sapphire

A. Yamamoto
S. Shinoyama
C. Uemura
. . . 585 — Silicon Contamination of InP Synthesized under High Phosphorus Pressure

D. E. Aspnes
G. P. Schwartz
G. J. Gualtieri
A. A. Studna
B. Schwartz
. . . 590 — Optical Properties of GaAs and Its Electrochemically Grown Anodic Oxide from 1.5 to 6.0 eV

T. R. Anthony
. . . 597 — The Electromigration Directions of Liquid Au-Ag Alloy Droplets in Single Crystals of Si

L. C. Linares
S. S. Li
. . . 601 — An Improved Model for Analyzing Hole Mobility and Resistivity in p-Type Silicon Doped with Boron, Gallium, and Indium

K. H. Nicholas
I. J. Stemp
H. E. Brockman
. . . 609 — Measurement and Identication of Distortion, Alignment, and Mask Errors in IC Processing

Y. Misawa
H. Hachino
S. Hara
T. Ogawa
H. Yagi
. . . 614 — Surface Charges in a Zinc-Borosilicate Glass/Silicon System

J. Götzlich
H. Ryssel
. . . 617 — Tapered Windows in SiO_2, Si_3N_4, and Polysilicon Layers by Ion Implantation

L. E. Katz
P. F. Schmidt
C. W. Pearce
. . . 620 — Neutron Activation Study of a Gettering Treatment for Czochralski Silicon Substrates

H. H. Madden
. . . 625 — AES Investigation of the Chemical Structure of Plasma-Deposited Silicon Nitride

P. F. Schmidt
C. W. Pearce
. . . 630 — A Neutron Activation Analysis Study of the Sources of Transition Group Metal Contamination in the Silicon Device Manufacturing Process

T. Shibata
T. W. Sigmon
J. L. Regolini
J. F. Gibbons
. . . 637 — Metal Silicon Reactions Induced by CW Scanned Laser and Electron Beams

Y. Tamaki
S. Isomae
S. Mizuo
H. Higuchi
. . . 644 — Evaluation of Dislocation Generation at Si_3N_4 Film Edges on Silicon Substrates by Selective Oxidation

G. W. B. Ashwell
R. Heckingbottom
. . . 649 — Interdiffusion of Titanium and Gold: A Comparison of Thin Films Deposited in Technical Vacuum and Ultrahigh Vacuum

J. A. Mroczkowski
H. R. Vydyanath
. . . 655 — Liquid Phase Epitaxial Growth of $(Hg_{1-x}Cd_x)Te$ from Tellurium-Rich Solutions Using a Closed Tube Tipping Machine

DIVISION AND GROUP OFFICERS

Battery Division
John Pierson, Chairman
Theodore Katan, Vice-Chairman
Gene Gagnon, Secretary-Treasurer
General Motors Corp.
Research Laboratories, Dept. 37
12 Mile and Mounds Rds.
Warren, Mich. 48090

Corrosion Division
Robert P. Frankenthal, Chairman
Florian Mansfeld, Vice-Chairman
Robert A. Rapp, Secretary-Treasurer
Dept. of Metallurgical Engineering
Ohio State University
116 West 19th Ave.
Columbus, Oh. 43210

Dielectrics and Insulation Division
James A. Amick, Chairman
Werner Kern, Vice-Chairman
John L. Mauer IV, Treasurer
John S. Judge, Secretary
Raytheon Equipment Division
528 Boston Post Road
Sudbury, Mass. 01776

Electrodeposition Division
Richard Sard, Chairman
Thomas Franklin, Vice-Chairman
Lubomyr Romankiw, Secretary-Treasurer
IBM T. J. Watson Research Center
P.O. Box 218
Yorktown Heights, N.Y. 10598

Electronics Division
Arnold Reisman, Chairman
Don W. Shaw, Vice-Chairman (Semiconductors)
Frederick M. Ryan, Vice-Chairman (Luminescence)
Ronald E. Enstrom, Vice-Chairman (New Electronic Technologies)
William A. McAllister, Treasurer
Edward H. Nicollian, Secretary
Bell Laboratories
Murray Hill, N.J. 07974

Electrothermics and Metallurgy Division
William A. Adams, Jr., Chairman
Lee P. Hunt, Senior Vice-Chairman
Wayne Worrell, Junior Vice-Chairman
Frederick S. Pettit, Secretary-Treasurer
Pratt and Whitney Aircraft
Materials Engineering and Research Laboratory
Middletown, Conn. 06457

Energy Technology Group
Sigurd Wagner, Chairman
James McBreen, Vice-Chairman
A. J. Appleby, Treasurer
Arthur J. Nozik, Secretary
Solar Energy Research Institute
Golden, Colo. 80401

Industrial Electrolytic Division
Leonard Nanis, Chairman
Morris Grotheer, Vice-Chairman
Robert Karpiuk, Secretary-Treasurer
Dow Chemical Co.
Functional Products and Systems
2020 Dow Center
Midland, Mich. 48640

Organic and Biological Electrochemistry Division
Larry L. Miller, Chairman
John H. Wagenknecht, Vice-Chairman
Martin Blank, Secretary-Treasurer
Dept. of Physiology
Columbia University
630 W. 168th St.
New York, N.Y. 10032

Physical Electrochemistry Division
Fritz G. Will, Chairman
Elton J. Cairns, Vice-Chairman
Robert A. Osteryoung, Secretary-Treasurer
Dept. of Chemistry
State University of New York
Buffalo, N.Y. 14214

SOCIETY OFFICERS AND STAFF

Erik M. Pell, President
Xerox Corp.
Xerox Square—W105
Rochester, N.Y. 14644

Ralph J. Brodd, Vice-President
INCO Electro Energy
5 Penn Center Plaza
Philadelphia, Pa. 19103

Frederick J. Strieter, Vice-President
Texas Instruments, Inc.
7814 Fallmeadow Lane
Dallas, Texas 75240

J. Bruce Wagner, Vice-President
Center for Solid State Science
Arizona State University
Tempe, Ariz. 85281

Forrest A. Trumbore, Secretary
Bell Laboratories
Room 1E-208
Murray Hill, N.J. 07974

John L. Griffin, Treasurer
Research Laboratories
General Motors Corporation
General Motors Technical Center
Warren, Mich. 48090

V. H. Branneky, Executive Secretary
The Electrochemical Society, Inc.
10 South Main Street
Pennington, N.J. 08534

Donna Kimberlin, Administrative Assistant
The Electrochemical Society, Inc.
10 South Main Street
Pennington, N.J. 08534

PUBLICATION STAFF

Sarah A. Kilfoyle, **Publication Editor**
Annette R. Van Deusen, **Assistant Publication Editor**

PUBLICATION COMMITTEE

Paul C. Milner, **Chairman**
Newton Schwartz
Forrest A. Trumbore
Norman Hackerman
Glenn W. Cullen
Rudolf Keller
Lawrence Young
Halina S. Wroblowa
Robert P. Frankenthal

Manuscripts submitted to the JOURNAL should be sent in triplicate to the Editorial Office at 10 South Main Street, Pennington, N.J. 08534. They should conform to the revised "Instructions to Authors" available from Society Headquarters. Manuscripts so submitted, as well as papers presented before a Society technical meeting, become the property of the Society and may not be published elsewhere in whole or in part without written permission of the Society. Address such requests to the Editor.

The Electrochemical Society does not maintain a supply of reprints of papers appearing in its JOURNAL. A photoprint copy of any particular paper may be obtained from University Microfilms, Inc., 300 N. Zeeb St., Ann Arbor, Mich. 48106.

Inquiries regarding positive microfilm copies of issues should be addressed to University Microfilms, Inc., 300 N. Zeeb St., Ann Arbor, Mich. 48106.

Walter J. Johnson, Inc., 355 Chestnut St., Norwood, N.J. 07648, have reprint rights to out-of-print volumes of the JOURNAL, and also have available for sale back volumes and single issues with the exception of the last two calendar years.

The JOURNAL OF THE ELECTROCHEMICAL SOCIETY combines the JOURNAL and TRANSACTIONS OF THE ELECTROCHEMICAL SOCIETY. Statements and opinions given in articles and papers in the JOURNAL OF THE ELECTROCHEMICAL SOCIETY are those of the contributors, and The Electrochemical Society, Inc. assumes no responsibility for them.

Claims for a missing issue should be reported within 60 days of normal delivery date to the Circulation Dept., The Electrochemical Society, Inc., 10 South Main Street, Pennington, N.J. 08534.

Notice of a change in address should be sent to the Circulation Dept., The Electrochemical Society, Inc., 10 South Main Street, Pennington, N.J. 08534. Include the mailing label or the number from the mailing label from your previous issue of the JOURNAL to ensure proper identification.

SOLID-STATE SCIENCE (Cont.)

A. K. Chin
W. C. King
T. J. Leonard
R. J. Roedel
C. L. Zipfel
V. G. Keramidas
F. Ermanis
. . . 661
Stress-Induced Dark Line Defect Formation in GaAlAs:Si LED's

K. Graff
H. Pieper
. . . 669
The Properties of Iron in Silicon

R. L. Guldi
R. E. Fontana, Jr.
D. C. Bullock
. . . 675
Effects of Multiple Slice Epitaxy and Front End Processing on Generation Threshold Current in Bubble Memory Devices

D. L. Flamm
D. D. Bacon
E. Kinsbron
A. T. English
. . . 679
Chemical Reaction of Sulfur Dioxide at High Humidity and Temperature: Implications for Accelerated Testing

H. Ogawa
A. Abe
M. Nishikawa
S. Hayakawa
. . . 685
Preparation of Tin Oxide Films from Ultrafine Particles

W. A. Tiller
. . . 689
On the Kinetics of the Thermal Oxidation of Silicon III. Coupling with Other Key Phenomena

TECHNICAL NOTES

L. Jastrzebski
J. Lagowski
H. C. Gatos
. . . 697
Formation of Recombination Centers in Epitaxial GaAs due to Rapid Changes of the Growth Velocity

D. Y. Lou
. . . 699
The Archival Stability of Tellurium Films for Optical Information Storage

B. T. Reagor
J. D. Sinclair
. . . 701
Tarnishing of Silver by Sulfur Vapor: Film Characteristics and Humidity Effects

ACCELERATED BRIEF COMMUNICATIONS

M. S. Whittingham
G. H. Newman
. . . 706
Niobium Triselenide in a Lithium Dioxolane Cell

I. Szendro
E. Marton
. . . 708
Low Pressure Deposition of Silicon Nitride by $SiCl_4$ and NH_3 Reacton

S. Takahashi
N. Koura
. . . 710
Al/FeS_2 Secondary Cells Using Organic Electrolytes

M. A. Butler
D. S. Ginley
. . . 712
Surface Treatment Induced Sub Bandgap Photoresponse of GaP Photoelectrodes

R. Dupon
D. H. Whitmore
D. F. Shriver
. . . 715
Transference Number Measurements for the Polymer Electrolyte Poly(ethylene oxide) · NaSCN

REVIEWS AND NEWS

PROGRAM
. . . 51C

NEWS
. . . 138C

JOURNAL OF THE ELECTROCHEMICAL SOCIETY

ELECTROCHEMICAL SCIENCE AND TECHNOLOGY

MARCH 1981

Mathematical Modeling of the Lithium-Aluminum, Iron Sulfide Battery

I. Galvanostatic Discharge Behavior

Richard Pollard*,[1] and John Newman*

Materials and Molecular Research Division, Lawrence Berkeley Laboratory and Department of Chemical Engineering, University of California, Berkeley, California 94720

ABSTRACT

A mathematical model of the LiAl/LiCl, KCl/FeS high temperature battery is presented. The model considers a whole prismatic cell which consists of negative electrode, separator, electrolyte reservoir, and positive electrode. Physical phenomena described are ohmic potential drop and diffusion potential in the electrolyte, changes in porosity and electrolyte composition due to electrochemical reactions, local reaction rates, and diffusion, convection, and migration of electrolyte. In addition, the analysis includes finite matrix conductivities, variable physical properties, and the possibility of specific simultaneous reactions in the positive electrode. The theoretical results show many of the trends in behavior observed experimentally. The effects of state of charge, initial electrolyte composition, cell temperature, and current density are presented, and factors that can limit cell performance are identified.

The LiAl/LiCl, KCl/FeS_z high temperature battery is a candidate for off-peak electrical energy storage and for electric vehicle propulsion. A mathematical model is needed to predict the operational characteristics of the system and to assess the influence of changes in design parameters on the cell performance.

Many models have been proposed to describe the behavior of flooded porous electrodes, and current and reaction distributions in a direction perpendicular to the separator have been considered in great detail (1). The electrode can be regarded as a homogeneous mixture of matrix and electrolyte (2) or as a single pore, provided that proper averages are taken over a cross section (3, 4).

The macrohomogeneous model has been applied to several specific battery electrodes. An analysis of the constant current discharge behavior of electrodes with sparingly soluble reactants, such as the Ag-AgCl and Cd-$Cd(OH)_2$ couples, has elucidated the relative importance of different failure modes in these systems (3). Transient and failure analyses have also been made of the zinc electrode (5) and the lead dioxide electrode (6, 7). An assessment of steady-state composition profiles in lithium/sulfur battery analogues has been made, but the results are restricted to nonporous systems (8).

Far less effort has been directed toward modeling complete cells and, up until now, only the lead acid cell has been considered in detail (9-12). In this paper, a one-dimensional model is presented for the LiAl/FeS system, which is currently being developed at the Argonne National Laboratory (13). A whole prismatic cell is considered, consisting of negative electrode, separator, electrolyte reservoir, and positive electrode (see Fig. 1). The model can be used to identify system limitations and to help guide experimental research.

* Electrochemical Society Active Member.
[1] Present address: Department of Chemical Engineering, University of Houston, Houston, Texas 77004.
Key words: porous electrodes, molten salt electrolyte, cell performance.

Model Development

The analysis is based on the macroscopic theory of porous electrodes in which the solution and matrix phases are treated as superposed continua without regard for the actual geometric details of the pores (2). With this approach, one can obtain a consistent framework for the description of isothermal transport processes in the molten salt electrolyte (14).

A material balance for species i is given by

$$\frac{\partial(\epsilon c_i)}{\partial t} = a j_{in} - \nabla \cdot \mathbf{N}_i \qquad [1]$$

where $\mathbf{N}_i$ is the flux of species i in the pore solution averaged over the cross-sectional area of the electrode and where aj_{in} represents the transfer rate of species i from the solid phases to the pore solution per unit electrode volume. In addition, the superficial current density in the pore solution is due to the movement of the charged species

$$\mathbf{i}_2 = \mathbf{F}\sum_i z_i \mathbf{N}_i \qquad [2]$$

and, as a consequence of the condition of electrical neutrality, the divergence of the total current density is zero

$$\nabla \cdot \mathbf{i}_1 + \nabla \cdot \mathbf{i}_2 = 0 \qquad [3]$$

For j simultaneous reactions of the form

$$\sum_i s_{ij} M_i^{z_i} \rightarrow n_j e^- \qquad [4]$$

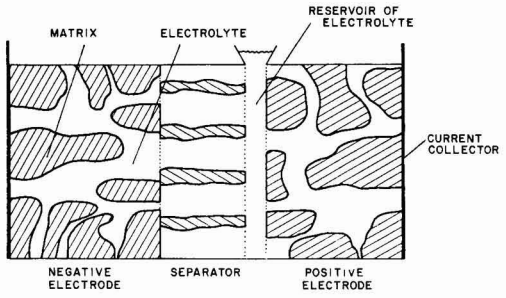

Fig. 1. Schematic diagram of LiAl/FeS cell

Faraday's law can be expressed as

$$aj_{in} = -\sum_j \frac{s_{ij}}{n_j \mathbf{F}} ai_{nj} - \frac{1}{\tilde{V}_k} \frac{\partial \epsilon_{pk}}{\partial t} \quad [5]$$

provided that double layer charging can be ignored. The last term on the right side of Eq. [5] represents the removal of species i from the electrolyte as a result of precipitation of salt k. The transfer current per unit electrode volume $\nabla \cdot \mathbf{i}_2$ is related to the individual average transfer current densities by

$$\nabla \cdot \mathbf{i}_2 = \sum_j (ai_n)_j \quad [6]$$

A material balance on the solid phases indicates how the electrode porosity changes with the extent of reaction at each location within the electrode

$$\frac{\partial(\epsilon + \epsilon_p)}{\partial t} = \sum_j \sum_{\substack{\text{solid} \\ \text{phases}}} \frac{s_{ij}\tilde{V}_i}{n_j \mathbf{F}} (ai_n)_j \quad [7]$$

where $\epsilon_p = \sum_k \epsilon_{pk}$.

The flux of mobile species in the electrolyte can be attributed to the combined effects of diffusion, migration, and convection. For the LiCl-KCl electrolyte, the fluxes of lithium and potassium ions are given by (14)

$$\mathbf{N}_1 = -\frac{\epsilon D}{\tilde{V}} \nabla x_A + \frac{t\star_1 \mathbf{i}_2}{\mathbf{F}} + x_A(c_A + c_B)v\star \quad [8]$$

$$\mathbf{N}_2 = -\frac{\epsilon D}{\tilde{V}} \nabla x_B + \frac{t\star_2 \mathbf{i}_2}{\mathbf{F}} + x_B(c_A + c_B)v\star \quad [9]$$

These relationships can be substituted into Eq. [1] to give, respectively

$$\frac{\partial(\epsilon x_A/\tilde{V})}{\partial t} + \nabla \cdot \left[x_A \mathbf{g} + (x_B t\star_1 - x_A t\star_2)\frac{\mathbf{i}_2}{\mathbf{F}} - \frac{\epsilon D}{\tilde{V}} \nabla x_A\right] = aj_{1n} \quad [10]$$

$$\frac{\partial(\epsilon x_B/\tilde{V})}{\partial t} + \nabla \cdot \left[x_B \mathbf{g} + (x_A t\star_2 - x_B t\star_1)\frac{\mathbf{i}_2}{\mathbf{F}} - \frac{\epsilon D}{\tilde{V}} \nabla x_B\right] = aj_{2n} \quad [11]$$

where

$$\mathbf{g} = \frac{\mathbf{v}\star}{\tilde{V}} + (t\star_1 + t\star_2)\frac{\mathbf{i}_2}{\mathbf{F}} \quad [12]$$

For the special case where $t\star_1 = x_A/2$ and $t\star_2 = x_B/2$, the direct dependence of Eq. [10] and [11] on current density is removed. The molar average velocity has been chosen as the reference frame because physical data for LiCl-KCl mixtures are often correlated with the mole fraction (see Appendix).

The movement of electrons in the matrix phase is governed by Ohm's law

$$\mathbf{i}_1 = -\sigma \nabla \phi_1 \quad [13]$$

where σ is the effective conductivity of the matrix. In the electrolyte, the variation in solution potential is given by (14)

$$\frac{\mathbf{i}_2}{\kappa} = -\nabla \Phi_2 - \frac{1}{\mathbf{F}}\left[\left(\frac{s_1}{n} + t^c_1\right)\frac{1}{x_B} - \frac{s_3 x_A}{n x_B}\right] \nabla \mu_A \quad [14]$$

where Φ_2 is measured with a reference electrode that has stoichiometric coefficients s_i and number n of electrons transferred, and μ_A is the chemical potential of LiCl (see Appendix). Equations [13] and [14] may be combined to obtain variations in the overpotential $\eta = \Phi_1 - \Phi_2$ directly.

Polarization equations are needed to express the dependence of the local rate of each reaction on the various concentrations and on the potential difference driving force at the reaction interface. Electrode kinetics do not follow fundamental laws that can be expressed as reliably as Ohm's law or the law of conservation of matter. Consequently, the polarization relationships will be subject to further refinement, as one tries to account not only for the mechanism of the charge transfer process but also for the morphology of the electrode, the formation of covering layers, and the transport of species to and from the reaction site.

It is common to begin with a polarization equation of the form

$$i_{nj} = i_{oj}\left[e^{\alpha_{aj}\mathbf{F}\eta_{sj}/RT} - e^{-\alpha_{cj}\mathbf{F}\eta_{sj}/RT}\right] \quad [15]$$

where η_{sj} is the local value of the surface overpotential, $\eta_{sj} = \eta - U_{j,o}$, and where the exchange current density can be written as

$$i_{oj} = i_{oj,ref} \prod_i \left(\frac{c_{j,o}}{c_{i,ref}}\right)^{\gamma_i} \prod_k a_k^{\gamma_k} \quad [16]$$

The theoretical open-circuit cell potential for reaction j is given by

$$U_{j,o} = U_j^\theta - U_{re}^\theta + \frac{RT}{n_{re}\mathbf{F}} \sum_i s_{i,re} \ln a_{i,re} - \frac{RT}{n_j \mathbf{F}} \sum_i s_{i,j} \ln a_{i,o} \quad [17]$$

The discharge reaction in the negative electrode is

$$\mathrm{LiAl} \rightarrow \mathrm{Li}^+ + \mathrm{Al} + e^- \quad [\mathrm{I}]$$

In the fully charged state, it is assumed that the negative matrix consists of nonporous, spherical particles of β-LiAl. On discharge, the outermost region of a particle reacts first and a layer of α-Al is established which thickens gradually, at the expense of β-LiAl, as the reaction proceeds. The Butler-Volmer Eq. [15] should be modified to include the diffusional overpotential for mass transport of lithium across the α-phase to the solid-electrolyte interface.

The parameter

$$S = \frac{3.87(1-\epsilon)I}{n\mathbf{F}\tilde{c}_{Li^\beta} \mathrm{La}^2 D_\alpha} \quad [18]$$

can be used as a criterion to assess the importance of solid-state diffusion within an LiAl particle (16). Small values of S indicate that the time required for diffusion is much shorter than the time needed for complete utilization of the particle. Even though $S \sim 0(0.1)$ for this system, the influence of solid-state diffusion may be appreciable at high current densities or with low specific interfacial areas, particularly toward the end of discharge. However, for $S < 1$, it is reasonable to invoke the pseudo-steady state approximation to evaluate the composition profile within the α-phase. With this assumption, and with unit activity coefficients, the surface concentration of lithium can be written as (17)

$$\frac{(c_{Li^\alpha})_o}{(c_{Li^\alpha})_{sat}} = 1 - \frac{\nabla \cdot \mathbf{i}_2}{(\nabla \cdot \mathbf{i}_2)_{lim}} \quad [19]$$

The diffusion-limited transfer current is given by

$$(\nabla \cdot \mathbf{i}_2)_{lim} = \frac{4\pi N \mathbf{F} D_\alpha (c_{Li^\alpha})_{sat}}{(1 - \bar{x}_{Li^\alpha})\left(\frac{1}{r_\beta} - \frac{1}{r_\alpha}\right)} \quad [20]$$

where r_α and r_β can be related to the state of charge (17). Combination of Eq. [6], [15], [19], and [20] gives

$$\nabla \cdot \mathbf{i}_2 = \frac{e^{\alpha_a \mathbf{F}\eta/RT} - e^{-\alpha_c \mathbf{F}\eta/RT}}{\dfrac{1}{4\pi N r_\alpha^2 i_{o,ref}\left(\dfrac{x_A}{x_{A,ref}}\right)^{\gamma_{Li^+}}} + \dfrac{e^{\alpha \mathbf{F}_a \eta/RT}}{(\nabla \cdot \mathbf{i}_2)_{lim}}} \quad [21]$$

where η is measured with a reference electrode of the same kind as the working electrode, but with a fixed lithium activity corresponding to saturated β-phase (see Table I). Implicit in Eq. [21] are the assumptions that there is no more reaction after the β-LiAl is completely transformed to α-Al and that there are no variations in electrolyte composition between the center of a pore and the ajdacent solid surface.

The complicated discharge processes in the positive electrode are represented by two simultaneous reactions

$$2FeS + 2Li^+ + 2e^- \rightarrow Li_2FeS_2 + Fe \quad [IIA]$$

$$Li_2FeS_2 + 2Li^+ + 2e^- \rightarrow 2Li_2S + Fe \quad [IIB]$$

Equation [15] is used to describe the rate of each reaction, and the reference electrode is taken to be the same kind as reaction [IIB] (see Table I). More sophisticated models for the positive electrode kinetics could include additional intermediate reactions, diffusion of reactants and products to and from reaction sites, and crystallization overpotentials for the formation of solid products. However, the detailed mechanism of the reactions and the juxtaposition of the different phases have not yet been formally established and are the subject of a separate study (18). At the high operating temperatures of the lithium/iron sulfide system, and with the relatively high concentration of lithium ions in the electrolyte, the rate of reaction is expected to be high and, therefore, the simplified kinetic analysis may be adequate.

The governing differential equations for the lithium-aluminum/iron sulfide system are subject to the following boundary conditions (see Fig. 1):

(*i*) at the current collectors

$$(a)\ \mathbf{N}_i = 0$$
$$(b)\ \mathbf{g} = 0 \quad [22]$$
$$(c)\ \mathbf{i}_2 = 0$$

(*ii*) at the negative electrode/separator interface

$$(a)\ \mathbf{i}_2 = I$$
$$(b)\ x_A, \mathbf{v}\bigstar \text{ continuous} \quad [23]$$
$$(c)\ \left(\epsilon D \frac{\partial x_A}{\partial y}\right)_s = \left(\epsilon D \frac{\partial x_A}{\partial y}\right)_e$$

(*iii*) at the positive electrode/reservoir interface

$$(a)\ \mathbf{i}_2 = I$$
$$(b)\ x_A \text{ continuous} \quad [24]$$
$$(c)\ \frac{V_R}{A}\frac{\partial x_{AR}}{\partial t} = \left(\epsilon D \frac{\partial x_A}{\partial y}\right)_e - \left(\epsilon D \frac{\partial x_A}{\partial y}\right)_s$$

where V_R/A can be estimated from

$$\frac{\partial (V_R/A)}{\partial t} = \mathbf{v}\bigstar_s - \mathbf{v}\bigstar_e + \frac{V_R}{A}\frac{d \ln \tilde{V}}{dx_A}\frac{\partial x_A}{\partial t} \quad [25]$$

The electrolyte composition is assumed to be uniform across the reservoir. It should also be noted that alternative formulations can be used for the boundary conditions at the front of the electrodes. These choose control volumes for the material balances that avoid the need for separate evaluation of the composition gradients at the interfaces (17). In the separator, the governing equations can be simplified in accordance with

$$(a)\ \mathbf{i}_2 = I$$
$$(b)\ \nabla \cdot \mathbf{i}_2 = 0 \quad [26]$$
$$(c)\ \epsilon = \epsilon_s$$

The initial conditions are taken as

(*i*) $x_A = x_A^o$

(*ii*) $\epsilon_e = \epsilon_e^o$ [27]

$$(iii)\ \nabla \cdot (\tilde{\nabla}\mathbf{g}) = \bar{V}_A a j_{1n} + \bar{V}_B a j_{2n} - \frac{\partial \epsilon}{\partial t} + \frac{\epsilon}{\bar{V}}\frac{\partial \tilde{V}}{\partial T}\frac{\partial T}{\partial t} + \tilde{V}\nabla \cdot \left(\frac{\epsilon D}{\bar{V}}\nabla x_A\right)$$

where Eq. [27(*iii*)] is derived from Eq. [10] and [11].

During discharge the temperature is assumed to be uniform throughout the cell sandwich, but it can change with time in response to reversible heat effects, Joule heating, overpotentials associated with electrode reactions, and precipitation or dissolution of electrolyte. The first law of thermodynamics gives

$$\frac{m\hat{C}_p}{2A}\frac{dT}{dt} = \left[U_o - V - T_o\frac{\partial \hat{U}_o}{\partial T}\right]I - h_o(T - T_A) + \sum_k \frac{L_k}{\bar{V}_k}\int_0^{L_T}\frac{\partial \epsilon_{pk}}{\partial t}dy \quad [28]$$

where the heat transfer coefficient h_o is based on estimated heat losses for a battery module. The total cell potential V is obtained by integration of local matrix and electrolyte potential gradients in the electrodes and separator, in accordance with Eq. [13] and [14], respectively. Kirchhoff's voltage law requires inclusion of the surface overpotentials (with appropriate signs) at the front of each electrode as well as the difference in potential between the two types of reference electrode at one location. Resistances of the electrolyte reservoir and current-collector grid can also be included.

The LiAl/LiCl, KCl/FeS system can be described by the local variables x_A, ϵ, $\mathbf{i}_2$, $\mathbf{g}$, and η, and by the governing Eq. [7], [10], [11], [14], and [15], subject to the specified boundary conditions. These relationships constitute a set of coupled, ordinary, nonlinear differential equations at each time step which are cast into finite

Table I. Kinetic parameters used in model

Negative electrode		Positive electrode	
Parameter	Value	Value	Parameter
$\alpha_a = \alpha_c$	0.5	1.0	$\alpha_{aj} = \alpha_{cj}$
n	1.0	2.0	n_j
s_1	−1.0	−2.0	$s_{1,j}$
s_3	0.0	0.0	$s_{3,j}$
$(x_A)_{ref}$	0.58	1.0	$(x_A)_{ref}$
γ_{Li^+}	0.5	1.0	γ_{Li^+}
i_o (A/cm²)	2.8	2.0×10^3	$(ai_o)_j$ (A/cm³)
D_α (cm²/sec)	4.0×10^{-10}	0.0326	$U_{IIA,o}$ (V)
$\bar{x}_{Li^\alpha}^{(30)}$	0.05	0.0	$U_{IIB,o}$ (V)

difference form accurate to $0(h^2)$, and solved simultaneously by a numerical technique (19). Each nonlinear equation is linearized properly to assure convergence, and each time-dependent equation is programmed symmetrically between the old time step and the present one, in order to attain stability.

Results and Discussion

Electrolyte composition.—Figure 2 shows composition profiles across the cell sandwich for several times during a constant current discharge of 41.6 mA/cm². A lithium-rich electrolyte is used, and the dimensions and capacities of the fully charged electrodes correspond to those of the Argonne National Laboratory, Mark 1A cell (13). When the discharge is started, lithium ions are introduced into the electrolyte at the negative electrode and transported across the porous separator to the positive electrode, where they can react cathodically to form Fe and Li_2FeS_2 or Li_2S. Since the transference number of Li^+ is not unity, a concentration profile develops, and diffusion aids migration in the transport of lithium ions. An almost constant composition gradient is established across the separator that corresponds to the flux of lithium ions needed for the specified current density. The presence of the reservoir attenuates composition changes at the front of the positive but, within the electrode, the composition variations are accentuated by local porosity changes.

The details of the composition variations can be attributed to the combined effects of diffusion, migration, convection, and electrochemical reaction. The contribution of convection, which arises primarily from the influx or squeezing out of electrolyte as the porosity alters, is expected to be small for this system ($\mathbf{v}\star \sim 0(10^{-5})$ cm/sec). However, convection is included in the analysis to ensure that the accuracy of the electrolyte material balances is retained.

The importance of $\mathbf{v}\star$ was tested by repeating the simulation in Fig. 2, with the temperature dependence of the electrolyte molar volume included in a manner that caused oscillation in $\mathbf{v}\star$, without adversely affecting the material balances. The results differed by less than 0.2%, except in the region with KCl precipitation, where the largest error in ϵ_p was 5%. The sensitivity of precipitation to temperature and composition indicates that a significant proportion of this error should be associated with changes in $\tilde{V}$, rather than $\mathbf{v}\star$.

If the cell temperature remains constant, the model predicts that the electrolyte composition in the negative electrode would cross the solubility limit for LiCl (indicated by the dashed line) after 1.5 hr. However, the average temperature rises by approximately 15°C during this period, and therefore precipitation of LiCl is avoided. Nevertheless, at about 54% depth of discharge, the composition has fallen markedly in the positive electrode and precipitation of KCl is predicted. This is illustrated in Fig. 3, which shows the variations in maximum and minimum electrolyte concentrations during the discharge, in comparison with the saturation compositions. The prediction of large variations in electrolyte composition during discharge emphasizes the need for inclusion of variable physical properties in the theoretical analysis.

The fraction of active material utilized within the negative electrode is shown in Fig. 4, at several discharge times. The large electrode surface area and the high operating temperature help to create fast reaction kinetics. As a result, a highly nonuniform reaction distribution, dominated by ohmic effects, is obtained. Initially, the sharp reaction front is restricted to the electrode/separator interface because an infinite matrix conductivity has been assumed for the simulation (2, 20). This reaction zone gradually moves through the electrode as active material is consumed and the potential required for the reaction becomes more positive. At the back of the electrode, the transfer current rises gradually in response to the composition-dependent term in the Ohm's law relationship for the electrolyte. This effect is more pronounced at high current densities and, as a result, the reaction front at a given state of charge is less sharp at higher discharge rates.

The complementary reaction distributions for the positive electrode are presented in Fig. 5. Reaction [IIA] starts first, and after 2 hr it has proceeded about two-thirds of the way through the electrode. The FeS is fully converted to Li_2FeS_2 behind this reaction front, which is itself relatively narrow. Subsequently, a front for reaction [IIB] begins to move through the electrode, and its influence on the composition can be seen in Fig. 2 at 2.5 hr.

The distance that the first reaction penetrates the electrode before onset of the second front is dependent on the operating conditions. Table II indicates that the

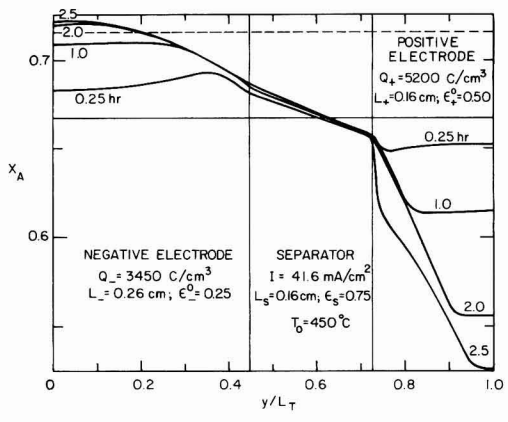

Fig. 2. Position dependence of mole fraction of LiCl at different discharge times. Dashed line represents saturation limit for LiCl at 450°C, Simulation parameters: $N = 1.1 \times 10^8$ cm^{-3}; Tables I and III.

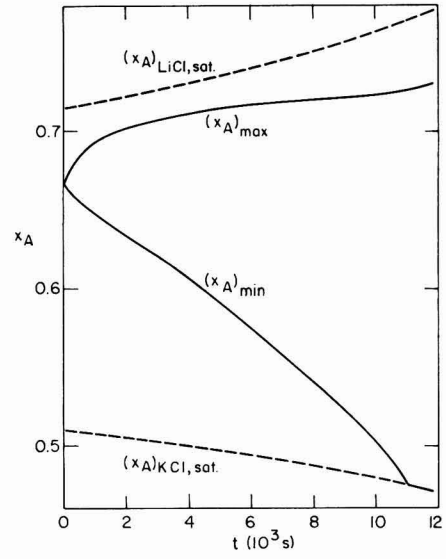

Fig. 3. Comparison of variations in saturation limits for LiCl and KCl and maximum and minimum electrolyte concentrations. Parameters as in Fig. 2.

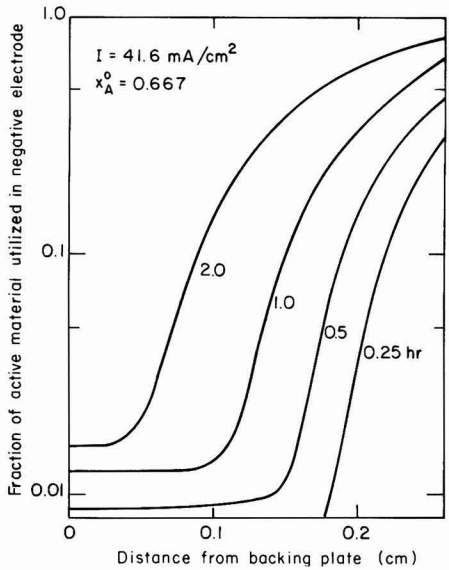

Fig. 4. Fraction of active material utilized in negative electrode at different discharge times. Parameters as in Fig. 2.

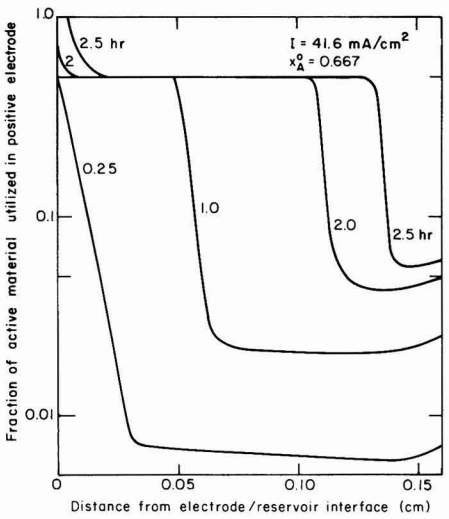

Fig. 5. Fraction of active material utilized in positive electrode at different discharge times. Parameters as in Fig. 2.

distance between the fronts is smaller, and hence the reactions are less distinct, with higher current densities or with lower initial electrolyte compositions.

The microstructure in the positive shortly after the second reaction has begun is shown in Fig. 6. In this example, the initial composition is that of the eutectic, 58 mole percent LiCl, and precipitation of KCl occurs at a relatively low depth of discharge. Precipitation is responsible for the extremely small value of the porosity ϵ at a distance of about 0.075 cm which effectively blocks off the back portion of the electrode. In this isolated region, self-discharge reactions can take place as a result of composition variations in the electrolyte and potential gradients in the matrix. The diagram shows that, in the depth of the electrode, reaction [IIA] has occurred to some extent, producing a certain volume fraction ϵ_X of Li_2FeS_2 and slightly decreasing the porosity from its initial value of 0.5. Behind the central reaction front, there is a plateau for the values of ϵ_X, ϵ, and ϵ_{Fe} that corresponds to completion of reaction [IIA]. At distances less than 0.01 cm from the reservoir, the consequence of reaction [IIB] can be seen; Li_2FeS_2 is consumed, Li_2S is produced, and the porosity drops to a small value.

As the first reaction front moves back through the positive electrode, the precipitated region does so also, and it remains as a sharp spike located in the region of highest transfer current. The progression of the second reaction is accelerated by the isolation of the back of the electrode, and the region of precipitation can spread rapidly to affect a larger part of the electrode. The local reductions in porosity that result from the large molar volume of the Li_2S and the precipitation

Table II. Characteristics of reaction fronts in positive electrode

	x_A°			
	0.58		0.667	
I (A/cm²)	0.0416	0.1	0.0416	0.1
L_{gap}/L_+	0.40	0.18	0.63	0.30
$100t_{t2}/t_t$	22.7	12.2	33.6	17.7

Table III. Physical parameters used in analysis

Parameter	Value
U_o (V)	1.34
$\partial U_o/\partial T$ (V/K)	-1.55×10^{-4}
C_p (kJ/kg · K)	1.03
h_o (W/m² · K)	4.13×10^{-2}
T_A (K)	298.15
$\tilde{V}_{LiCl}$ (cm³/mole)	20.50
$\tilde{V}_{KCl}$ (cm³/mole)	37.58
$\tilde{V}_{FeS}$ (cm³/mole)	18.55
$\tilde{V}_{Fe}$ (cm³/mole)	7.11
$\tilde{V}_X$ (cm³/mole)	46.23
$\tilde{V}_{Li_2S}$ (cm³/mole)	27.677
σ_{Fe} (Ω^{-1} cm^{-1})	8.23×10^4
σ_{FeS} (42) (Ω^{-1} cm^{-1})	1.90×10^3
σ_X (Ω^{-1} cm^{-1})	5.00×10^2
ρ_α (g/cm³)	2.70
ρ_β (g/cm³)	1.75
V_R°/A (cm)	0.03

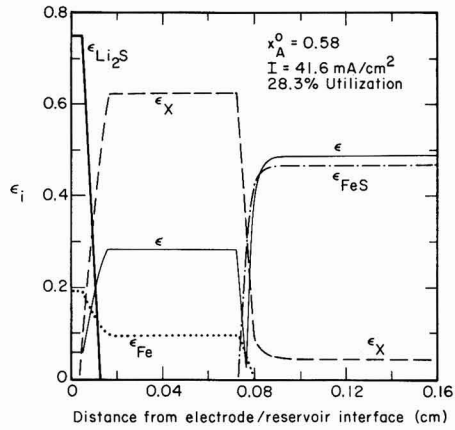

Fig. 6. Volume fractions of solid phases and electrolyte in positive electrode. Parameters as in Fig. 2, except as indicated.

of KCl lead to a reduction in local electrolyte conductivity in accordance with Eq. [A-2]. Consequently, a significant potential drop can develop across the low porosity region, and this may severely limit utilization of the electrode. The plugging of porous electrodes has been cited as a possible cause of failure in other electrodes (5, 21). In the zinc electrode, for example, a large volume fraction of ZnO can be produced at the front face early in a discharge, particularly if the reaction distribution is highly nonuniform.

Initial electrolyte composition.—An important consideration in the development of the LiAl/LiCl, KCl/FeS battery is the choice of initial electrolyte composition, x_A^o. The dependence of composition changes on x_A^o is illustrated in Fig. 7, at two different depths of discharge. The difference between the maximum and minimum electrolyte compositions is larger for smaller x_A^o, and this effect becomes magnified as the discharge proceeds. The composition changes have a direct influence on the extent of precipitation and on the Nernst relationship for the cell potential.

With pure LiCl, there is no concentration polarization, but the minimum operating temperature would be 609°C. For molten salt mixtures with Li^+ as a common ion, the composition changes in the Li/FeS cell are expected to be small. The transport theory developed in Ref. (14) can be applied directly to binary electrolytes such as LiCl-LiF. It also applies to more complicated mixtures, such as LiCl-LiF-LiBr, provided that it is reasonable to assume that, from a mass transport standpoint, the anions can be lumped together to give only a single independent composition variable.

If the anions do not participate in the electrode reactions, the production term in the material balance equation is given by (14)

$$R_A = \tilde{V} a j_{3n} \left(\frac{c_2 t_1^r}{\nu_2^B \nu_3^A} - \frac{c_1 t_2^r}{\nu_1^A \nu_3^B} \right) \qquad [29]$$

For electrolytes with unit stoichiometric coefficients, and for transference numbers that are directly proportional to concentration, Eq. [29] reduces to $R_A = 0$ and, therefore, the electrolyte composition is constant.

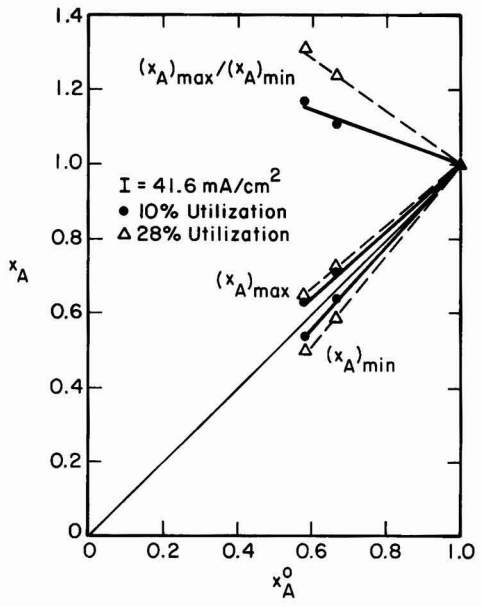

Fig. 7. Dependence of composition variables on initial electrolyte concentration. Parameters as in Fig. 2, except as indicated.

In practice, R_A is still expected to be small even with transference numbers not exactly proportional to concentration, and successful cell operation may be possible at temperatures much closer to the melting point than are permissible with the LiCl-KCl electrolyte.

Discharge curves.—An important capability of the model is to predict the dependence of total cell voltage on state of charge. Discharge curves for the Argonne Mark 1A cells are presented in Fig. 8 for several different operating conditions. The upper curves are for a current density of 41.6 mA/cm², and the highest of these is for a lithium-rich electrolyte, which has a larger bulk electrolyte conductivity than the eutectic mixture. Two curves are shown for the eutectic, which is the composition actually used in the Mark 1A cell design. Curve A takes account of precipitation of either component of the electrolyte, whereas curve B does not. For all three curves, the sharp reduction in cell voltage can be attributed to the localized porosity reductions in the fully reacted region of the positive electrode. Precipitation reduces the porosity still further, and the decline in voltage is correspondingly more acute. In practice, the porosity changes may not be quite so dramatic because it is possible for the electrodes to swell. Expansion may occur by compaction of the separator and displacement of the can walls during the formation cycles of the cell, or by motion of the electrodes relative to one another during a particular charge or discharge. The extent to which swelling can take place will depend on the stresses generated within the cell and the physical restraints on the container.

At the high current density, the initial cell voltage is considerably reduced as a result of the finite grid resistance (see Appendix). Also, the cell voltage declines more rapidly since there is less time available for diffusional processes to take place, and because the reaction distribution in the positive electrode is less uniform (see Table II).

The triangles in Fig. 8 indicate the onset of precipitation of KCl. They show that, at lower I or higher x_A^o, precipitation is delayed. The exact time when precipitation begins is largely dependent on the details of the heat balance used to estimate the average cell temperature, Eq. [28]. Small changes in the rate of heat loss from the battery module, or slight differences in initial cell temperature, could have a significant impact on the extent of precipitation and, possibly, on the cell performance. In the examples shown, precipitation of LiCl is not predicted, even though the maximum composition is close to the solubility limit (see Fig. 3).

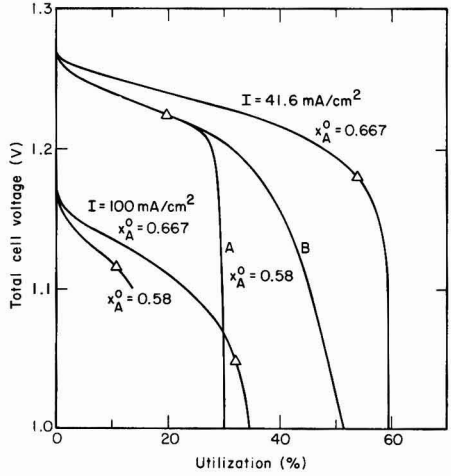

Fig. 8. Theoretical discharge curves for Argonne National Laboratory Mark 1A cells. Parameters as in Fig. 2, except as indicated.

Careful consideration of precipitation is needed for several additional reasons. The rate of mass transport from the electrolyte in the bulk of the pores to the matrix surface may influence the rate at which precipitation takes place. This has been included in previous studies of electrodes with sparingly soluble reactants (22-24), but the effects may not be so important in molten salt systems because the salt concentrations are generally much higher. The morphology of the precipitate may be important, particularly if it forms as a passivating layer over the active material. Furthermore, local thermal effects may influence the extent and nature of precipitation; heat generated as precipitate forms will tend to retard the precipitation process.

In Fig. 9, an experimental discharge curve is compared with theoretical predictions obtained at a similar current density. The experiment was done with a bicell (2 negative electrodes with a central positive plate) that was built with electrodes designed for the Mark 1A battery program (25). The computer simulation is based on the electrode capacities specified in Fig. 8, but it is assumed that the positive and negative electrodes have expanded 12.5% and 23%, respectively. It is also assumed that the heat transfer coefficient h_0 is twice as large as the value assumed for the Mark 1A battery model. The ambient temperature used in the model remains at 25°C, whereas it may be closer to 450°C in the experiments.

Theoretical curves A and B in Fig. 9 indicate the influence of initial cell temperature on the predicted system behavior. The cell temperatures rise by 18° and 26°C during the discharge, for low and high T_0, respectively. Even with high operating temperatures and swollen electrodes, the maximum predicted utilization is still considerably below the experimental observations. Two possible reasons for this discrepancy are: (*a*) Larger local porosities in the positive electrode at a given stage of charge due to: (*i*) additional expansion, (*ii*) solid phase intermediates with relatively low molar volumes that are not included in the present model, and (*iii*) more uniform distribution of reactions. (*b*) Reduction in amount of KCl precipitation due to: (*i*) smaller composition variations as a result of larger porosities or free convection, (*ii*) high local temperatures, (*iii*) mass transport limitations, and (*iv*) modification of the equilibrium solubility limit by the presence of sparingly soluble species in the electrolyte or due to supersaturation.

Curve C in Fig. 9 represents the same simulation as curve B, except that precipitation of electrolyte is not taken into account. The relatively good agreement with the experimental data, although possibly fortuitous, gives some support to the reduced precipitation concept and provides an incentive for a more detailed examination of the possible causes enumerated above. In particular, a force balance on the electrolyte in a direction parallel to the separator, together with Darcy's law, indicates that free convection is even less important than forced convection in vertical LiAl/FeS cells.

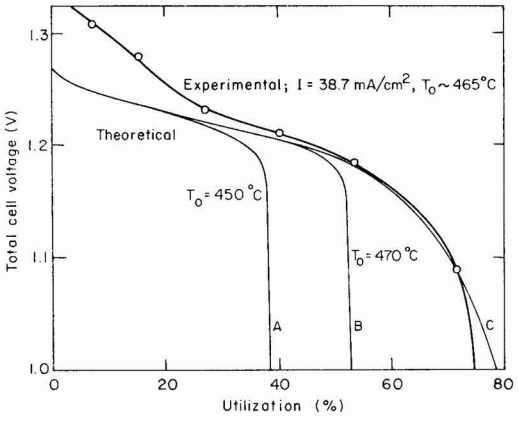

Fig. 9. Comparison of theoretical and experimental (25) discharge curves. Simulation parameters: Q_- = 2800 C/cm³, Q_+ = 4630 C/cm³, L_- = 0.32 cm, L_s = 0.16 cm, L_+ = 0.18 cm, ϵ_-° = 0.39, ϵ_s° = 0.75, ϵ_+° = 0.555, x_A° = 0.58, I = 41.6 mA/cm², $N = 5.5 \times 10^7$ cm^{-3}, $h_0 = 8.25 \times 10^{-2}$ W/m² · K.

In addition, at the end of the simulation depicted by curve C in Fig. 9, $(x_A)_{min}$ = 0.220, whereas $(x_A)_{sat}$ = 0.437. If local temperature effects dominated, the temperature in the positive electrode would need to be 155 K above the average cell temperature; temperature differentials of this magnitude are not expected to be observed in these cells because the electrodes are thin and the materials have relatively high thermal conductivities. Furthermore, large degrees of supersaturation would not be expected in the heterogeneous electrode medium. A separate study may be needed to monitor cell temperature and to investigate local variations in electrolyte composition, under closely controlled experimental conditions.

One can also speculate on the reasons for the differences between experiment and theory shown in Fig. 9, at low utilizations. The experimental curve rises more sharply than the model predictions at depths of discharge below approximately 25%. This can be attributed, at least in part, to the presence of about 15% Cu_2S in the positive electrode. Copper sulfide was added to the Mark 1A electrodes to minimize the formation of an intermediate sulfide, $LiK_6Fe_{24}S_{26}Cl$ (J-phase), which can adversely affect cell performance (26). There is now evidence to suggest that J-phase can also be suppressed by the use of lithium-rich electrolytes and increased operating temperatures (27). Elimination of Cu_2S from the positive would be advantageous because gross movement of Cu_2S to the separator, with subsequent cell shorting, can take place (28).

Small quantities of lithium are sometimes added to the negative to augment the electrode capacity. As with Cu_2S, addition of lithium tends to raise the total cell voltage. However, the lithium activity is increased, and this may cause operational difficulties, such as displacement of potassium from the electrolyte, reaction with the separator material, dendrite formation, shift of charge range in cycling, or failure to achieve full charge.

An alternative explanation for the differences at low utilizations resides in the higher potentials present during the preceding charge half-cycle, which persist for a while after discharge is begun. These would not be present in the computer simulation.

The small discrepancy between experiment and theory at approximately 30% utilization could result, among other reasons, from uncertainty in the estimation of the current collector and terminal resistance (see Appendix). The finite conductance of the grid will also lead to nonuniform current and potential distributions across the face of an electrode, which are not included explicitly in the one-dimensional cell model. A separate study has been made of ohmic drop in current collectors in order to help provide a rational basis for scale-up of cells (29).

An analysis of local variations in potential across the cell sandwich can provide additional insight into the behavior of the individual electrodes. Figure 10 shows potentials at different positions across the cell described in Fig. 9, relative to a saturated β-LiAl/LiCl, KCl reference electrode placed at the front face of the negative. The separator potential Φ_s is almost unchanged throughout the discharge, in keeping with the constancy of the composition profile across the separator (see Fig. 2). The open-circuit potential difference $(\Phi_s)_{I=0}$, that would be measured by a reference electrode at the front face of the positive electrode, indicates the influence of concentration polarization, which

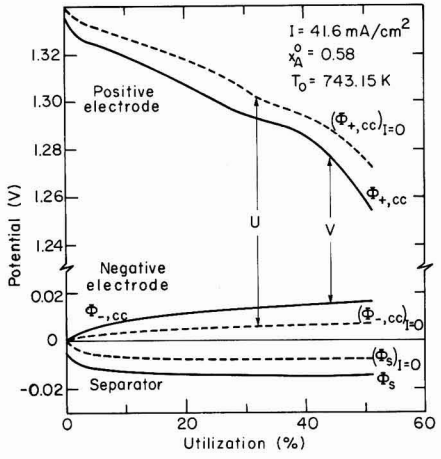

Fig. 10. Theoretical potential variations at different locations across the cell sandwich. Parameters as in Fig. 9. Dashed lines represent open-circuit potentials.

is characterized by the composition dependent term in Ohm's law, Eq. [14]. The curves marked $\Phi_{+,cc}$ and $\Phi_{-,cc}$ represent the potentials of the positive and negative current collectors, respectively. The difference between these potentials and their open-circuit counterparts can be regarded as the resistances of the individual electrodes. In the negative electrode, there is assumed to be no potential difference in the matrix phase, and, in the positive electrode, the matrix potential difference is too small to be discernable in Fig. 10 because the effective matrix conductivity calculated with Eq. [A-10] is large [$\sigma \sim 0(10^4)\ \Omega^{-1}\ cm^{-1}$], throughout the discharge.

The components of the potential for the experimental cell depicted in Fig. 9 are presented in Fig. 11 (25). Both experimental and theoretical results indicate that changes in total cell voltage are largely dependent on the variations in apparent open-circuit cell potential U,

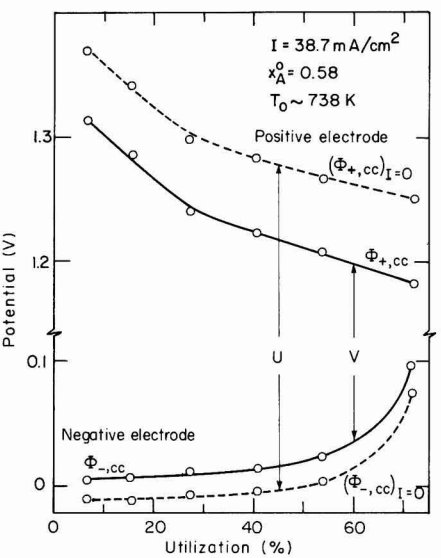

Fig. 11. Potentials at different locations across a cell sandwich measured with a reference electrode placed at the edge of the separator (25). Dashed lines represent open-circuit potentials, 15 sec after current interruption.

and that changes in electrode resistances are relatively small. The experimental results show that the positive is polarized more strongly than the negative electrode, but that the negative electrode potential rises more sharply toward the end of discharge. This could be interpreted as a negative electrode "limitation," although this term has not been carefully defined. In this context, it is not possible to distinguish between limitations caused by inherent electrochemical factors or by changes in the usable capacity of an electrode over a number of cycles. It might be expected that, with a sufficient increase in excess capacity in the negative electrode, the positive would limit cell performance on both charge and discharge.

For both electrodes, the model predicts resistances that are smaller than the observed values. This could be caused by overestimation of electrochemically active interfacial areas, exchange current densities, or matrix conductivities. Contact resistance or partial loss of electrical connectivity between electrode particles can lead to conductivities below those calculated from Eq. [A-10], which is based on the concept of parallel conduction paths. Separate experiments may be needed to establish the conductivity of each electrode matrix as a function of stage of charge. Contact resistances are not expected to be significant in the positive electrode during discharge because the large volume of solid products tends to increase the internal electrode pressure. Furthermore, the presence of Li_2S at the front of the positive electrode may not influence cell behavior markedly, since all the current will be carried in the electrolyte across the fully reacted region. However, the formation of a poorly conducting layer adjacent to the current collector could have a more profound effect on the predicted potential distribution.

Despite the underestimates for the electrode resistances, the model still gives voltages that lie below the experimental results in Fig. 9. This is directly associated with the estimated value of the current collector resistance R_g, which is included in the model only to improve the accuracy of the heat balance. The estimate of R_g could be refined with more precise experimental data for the polarization conductance Y of a cell element. This parameter (Y) could be obtained directly in a small, open test cell with current collectors large enough to ensure insignificant current and potential variations across the face of a plate and with voltage taps placed in direct contact with the current collectors.

Additional experiments may also be needed to elucidate the reasons for the observed rise in potential of the negative electrode toward the end of discharge (see Fig. 11). The theoretical calculations indicate that the increase in porosity as the discharge proceeds more than compensates for the additional distance the current must penetrate the electrode and that the current collector potential approaches a constant (see Fig. 10). The discrepancy between theory and experiment may result from: (*a*) reduction in negative electrode porosity caused by expansion of the positive, (*b*) gross morphology changes in the negative electrode, (*c*) reduction in the available electrode capacity and uncertainty in the state of charge caused by (*i*) segregation of active material from the bulk and (*ii*) cumulative coulombic losses, and (*d*) nonuniform initial distribution of reactants.

Agglomeration would reduce the electrochemically active interfacial area and increase the diffusion overpotential for transport of lithium atoms across the α-Al. A computer simulation with the initial particle size r_o^o increased by a factor of 4.5 shows an increased electrode resistance at a particular depth of discharge but, contrary to observations, the open-circuit potential $(\Phi_{-,cc})_{I=0}$ does not alter appreciably. The influence of the initial variation in state of charge across the negative electrode could be investigated by comparing potential distributions obtained

during two experiments; one where a considerable time interval was introduced between the discharge of interest and the previous charge, and the other where the discharge followed the charge immediately, but the overall initial state of charge matched the first experiment.

It should also be noted that a considerable quantity of lithium can be retained in the α-Al after the β-phase has been completely utilized. For the example B in Fig. 9, the characteristics of particles at the front of the electrode when the cutoff voltage is reached are: $r_\beta = 0.474 \times 10^{-3}$ cm, $r_\alpha = 1.115 \times 10^{-3}$ cm, and $(c_{Li^\alpha})_o/(c_{Li^\alpha})_{sat} = 0.78$. This indicates that the reaction is not limited by diffusion of lithium across the α-Al and that a minimum of approximately 7.8% of the total theoretical capacity could be stored in the α-Al when no β-LiAl remains. Consequently, the available capacity in the negative electrode may be significantly lower than the theoretical estimate, and this could contribute to the apparent limitation observed in this electrode.

Polarization characteristics.—In many applications it is important to know the effect of discharge rate and depth of discharge on the usable capacity of the cell. Figure 12 shows polarization curves that represent a voltage sweep of a cell that has been discharged at a specified constant current density for a given period of time. It should be emphasized that this is not simply a cross-plot of a number of constant current discharges. Before discharge begins, there is a single current-potential curve, but the polarization characteristics will change during the discharge in a manner that depends on the total applied current. In general, polarization is greater at larger depths of discharge and for higher current densities at a given depth of discharge.

An important feature of the curves in Fig. 12 is that they are substantially straight, and there is little error in approximating them by the equation

$$I = Y(U - \Phi_+ + \Phi_-) \qquad [30]$$

where Y is the polarization conductance, given by the reciprocal of the slope of the lines, and U is the apparent open-circuit cell potential, given by the ordinate intercept. In this way, the polarization characteristics of the LiAl/FeS cell can be summarized by the dependence of U and Y on the operating conditions.

Figure 13 shows the dependence of electrochemical resistance on state of charge for several different current densities. Each curve shows that, in an overall sense, the resistance increases as more active material is consumed. However, for $I = 0.1$ A/cm^2, there is an almost discontinuous reduction in $1/Y$ at a time that corresponds to the onset of reaction [IIB] ($X + 2Li^+ + 2e^- \rightarrow 2Li_2S + Fe$) at the front of the positive electrode. At lower current densities the drop in resistance is neither as marked nor as abrupt, and it occurs later in the discharge (see Table II). At each current density, the resistance rises again as porosity variations in the positive electrode lower the effective electrolyte conductivity. In practice, there is much less distinction between the intermediate reaction steps in the positive electrode. Consequently, it is not expected that the sharp changes in resistance predicted with the model will be observed experimentally. It should also be emphasized that the model does not include the possibility for reaction of additives such as Cu_2S or CoS_2, or for additional intermediates such as J-phase in the conversion of FeS to Li_2S and Fe.

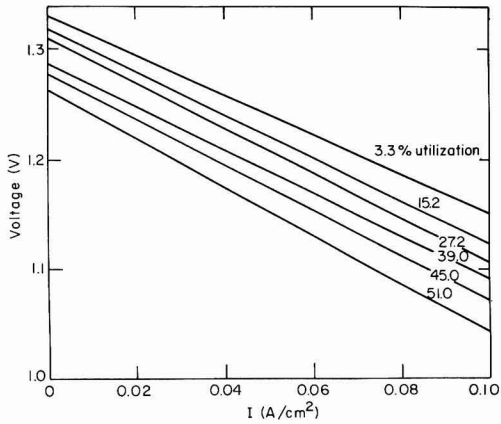

Fig. 12. Effect of state of charge on theoretical cell polarization behavior. Simulation parameters as in Fig. 9, $T_o = 470$°C.

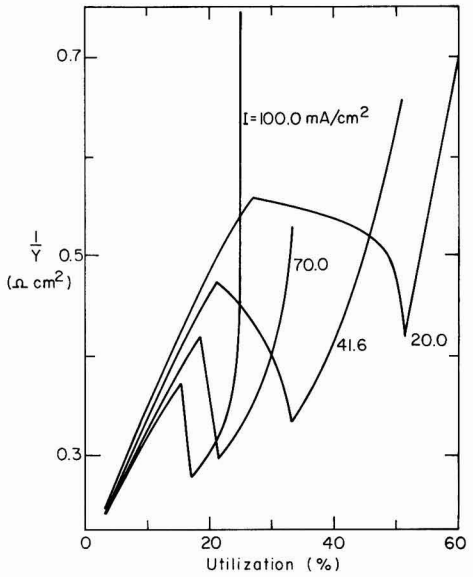

Fig. 13. Predicted dependence of polarization resistance on utilization at different discharge rates. Parameters as in Fig. 9, $T_o = 470$°C.

The dependence of the apparent open-current cell potential on state of charge and discharge current density is presented in Fig. 14 and 15, for theory and experiment, respectively. In both cases, the value of U drops markedly during the discharge. The experimental results lie above the model predictions as a consequence of the presence of additives, such as Cu_2S, which raise the equilibrium open-circuit cell potential. For less than about 30% utilization, the experimental curves show no systematic dependence on current density. At greater depths of discharge, U changes more markedly at higher I, as predicted in Fig. 14.

The reduction in U during the discharge can be associated with concentration polarization caused by nonuniform utilization of active material. In the negative, lithium is preferentially removed from the front of the electrode first, as illustrated in Fig. 4, and a maximum in electrolyte composition can develop part of the way through the electrode. At open circuit, the region with highest electrolyte composition becomes cathodic with respect to the rest of the electrode, and local concentration cells are set up which act in a manner that tends to reduce the composition variations. These variations can be more substantial at higher discharge rates, for a given state of charge, and, consequently, the open-circuit resistance can be higher in the negative electrode, leading to smaller values for U.

In the positive electrode, the situation is complicated by the possibility of simultaneous reactions. Before re-

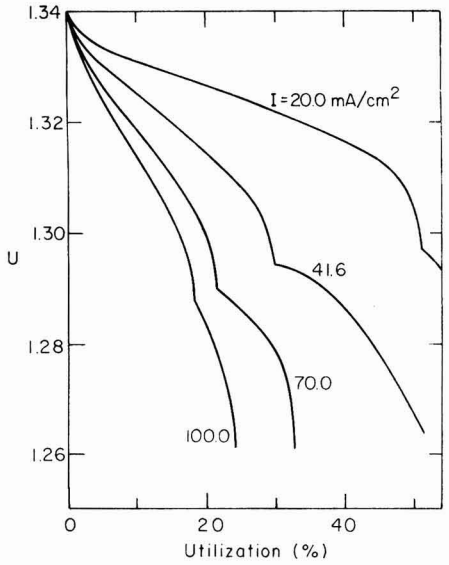

Fig. 14. Effect of discharge rate and state of charge on the theoretical apparent open-circuit cell potential. Parameters as in Fig. 9, $T_o = 470°C$.

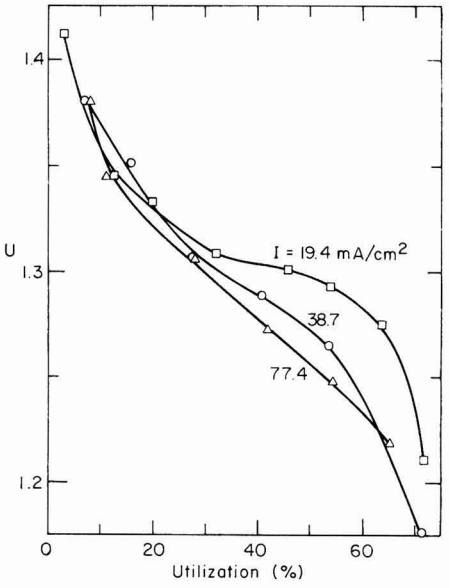

Fig. 15. Variation in experimental apparent open-circuit cell potential with discharge current density and utilization. Measurements taken 15 sec after current investigation (25).

action [IIB] begins, $(\Phi_{+,cc})_{I=0}$ is controlled by local concentration cells that result from electrolyte composition variations, in much the same way as described for the negative electrode. When reactions [IIA] and [IIB] both occur, a corrosion potential can be established on open circuit, which corresponds to cathodic formation of Li_2FeS_2 in the back of the electrode and anodic formation of Li_2FeS_2 toward the front. These reactions would be observed on current interruption, even in the absence of a composition gradient in the electrolyte. As the second reaction, [IIB], progresses, the mixed corrosion potential shifts toward the equilibrium potential $U_{[IIB],o}$.

The positive electrode behavior is the major factor that leads to the predicted reduction in U. At higher current densities, reaction [IIB] begins earlier in the discharge and therefore U declines more rapidly. The less marked dependence of U on current density observed experimentally is further evidence to suggest that there is less distinction between the positive electrode reactions in practice.

Conclusions

A mathematical model has been developed that can describe the time-dependent and position-dependent behavior of a complete LiAl/LiCl,KCl/FeS cell. Composition and reaction distributions can be predicted, as well as variations in volume fractions of individual phases and electric potential within the electrodes. The results of the theoretical analysis show many of the general trends in discharge behavior that are observed experimentally. The model predicts that high internal resistance can develop in the positive electrode as a result of low local porosities which are, in turn, caused by large volume reaction products or precipitated KCl. This implies that, with the electrode capacities currently being considered for electric vehicle applications, swelling may be a prerequisite for successful operation and thermal management of battery modules may also be important. Furthermore, an investigation of the potential distribution across the cell sandwich indicates that, before porosity reductions become critical, variations in total cell voltage are controlled more by changes in apparent open-circuit cell potential than by changes in resistance across the individual electrodes.

Acknowledgment

The authors are extremely grateful to the members of the Chemical Engineering Division at the Argonne National Laboratory for many useful discussions and valuable suggestions. This work was supported by the Division of Solar, Geothermal, Electric and Storage Systems, Office of the Assistant Secretary of Energy Technology, U.S. Department of Energy under Contract No. W-7405-Eng-48.

Manuscript submitted Feb. 22, 1980; revised manuscript received *ca* Aug. 27, 1980.

Any discussion of this paper will appear in a Discussion Section to be published in the December 1981 JOURNAL. All discussions for the December 1981 Discussion Section should be submitted by Aug. 1, 1981.

Publication costs of this article were assisted by the University of California.

APPENDIX

Physical Properties of the LiAl/LiCl,KCl/FeS System

Electrolyte conductivity.—The dependence of bulk electrolyte conductivity on composition and temperature is described by

$$\kappa_\infty = (ax_A^2 + bx_A + c)e^{-E/T} \qquad [A\text{-}1]$$

where: $a = 18.9803$; $b = -5.0170$; $c = 9.0903$; $E = 1425.76$ K (31, 32). The effective conductivity in the porous medium is estimated from

$$\kappa = \epsilon\kappa_\infty/\zeta^2 \qquad [A\text{-}2]$$

where the tortuosity factor ζ is directly related to porosity by

$$\zeta = \epsilon^{(1-q)/2} \qquad [A\text{-}3]$$

and the constant q is taken as 1.5.

Transference number.—Measurements of transference numbers in binary nitrate melts show that deviations from the relation $t_i^c = x_i$ are often relatively small (34). Experiments in LiCl-KCl melts (35) also tend to substantiate the use of this assumption which, for the molar average velocity reference frame, gives: $t_1\star = x_A/2$; $t_2\star = (1 - x_A)/2$.

Activity coefficient.—If dissociation of electrolyte is disregarded (36), the gradient of chemical potential of LiCl in the LiCl-KCl mixture can be written as

$$\nabla\mu_A = RT\left(1 + \frac{d\ln\gamma_A}{d\ln x_A}\right)\nabla\ln x_A \qquad [A\text{-}4]$$

Information from the LiCl-KCl phase diagram can be used to obtain the composition and temperature dependence of the activity coefficient (37-39). A relationship of the form (40)

$$\ln\gamma_A = \frac{b}{T}\tanh\left(\frac{a(1-x_A)^n}{bx_A}\right) \qquad [A\text{-}5]$$

with $a = -1023.84$, $b = -1555.11$, and $n = 3$, has been chosen to represent the data.

Molar volume of electrolyte.—The molar volume of electrolyte is defined as $\tilde{V} = \sum_k M_k x_k/\rho$ where the density ρ is given by $\rho = 1.735 - 0.15x_A$.

Diffusion coefficient.—For the special case where the diffusion coefficients for binary interactions are all equal, it may be shown that

$$D_\infty = \frac{\kappa_\infty RT\tilde{V}}{2F^2}\left(1 + \frac{d\ln\gamma_A}{d\ln x_A}\right) \qquad [A\text{-}6]$$

On this basis, it is assumed that

$$D_\infty = 2.442 \times 10^{-4}\, e^{-E/T}(x_A + 0.4) \qquad [A\text{-}7]$$

over the composition and temperature range of interest. The molecular diffusion coefficient in the porous media can be characterized by

$$D = D_\infty/\zeta^2 \qquad [A\text{-}8]$$

together with Eq. [A-3].

LiCl-KCl phase diagram.—The equilibrium compositions that characterize the onset of precipitation of LiCl and KCl are approximated by (41)

$$(x_A)_{\mathrm{LiCl,sat}} = 0.34080 - 4.773 \times 10^{-4}T + 1.376 \times 10^{-6}T^2 \qquad [A\text{-}9]$$

$$(x_A)_{\mathrm{KCl,sat}} = 0.14615 + 1.9117 \times 10^{-3}T - 1.948 \times 10^{-6}T^2$$

Matrix conductivity.—In general, the matrix conductivity can be influenced by the volume fraction of the conducting phases, the inherent conductivity of each solid phase, and the manner in which the particles of conducting phases are interconnected. As a first approximation, it has been assumed that parallel conduction pathways exist in the positive electrode so that

$$\sigma = \sum_i \sigma_i\epsilon_i^q \qquad [A\text{-}10]$$

and q is taken to be 1.5. In the negative electrode, the conductivities of the active materials and the supporting grid are each very high ($\sigma_{Li} \cong 1.0 \times 10^5\ \Omega^{-1}\ cm^{-1}$; $\sigma_{Al} \cong 2.2 \times 10^5\ \Omega^{-1}\ cm^{-1}$; $\sigma_{Fe} \cong 2.34 \times 10^4\ \Omega^{-1}\ cm^{-1}$, at $T = 450°C$) and consequently the matrix conductivity is assumed to be infinite.

Current collector resistance.—The combined resistance R_g of the grid and terminal is obtained from a preliminary estimate of the polarization conductance, as defined by Eq. [30]. The resistance R_b of a bicell can be separated into electrochemical and current collector contributions, according to

$$R_b = \frac{1}{2A}\left(\frac{1}{Y} + R_g\right) \qquad [A\text{-}11]$$

In the calculations, it is assumed that $R_b = 4\ m\Omega$, $Y = 1.013\ \Omega^{-1}\ cm^{-2}$ (29), and $A = 316\ cm^2$. This yields $R_g = 1.55\ \Omega\ cm^2$.

LIST OF SYMBOLS

a interfacial area per unit electrode volume (cm^{-1})
a_k relative activity of species k
A cross-sectional area of electrode (cm^2)
c_i concentration of species i (mole/cm^3)
$\hat{C}_p$ specific heat (J/g·K)
D diffusion coefficient (cm^2/sec)
$\mathbf{F}$ Faraday's constant (96,487 C/equiv.)
$\mathbf{g}$ variable defined by Eq. [12]
h mesh size (cm)
h_o heat transfer coefficient ($W/m^2\cdot K$)
i_o exchange current density (A/cm^2)
$\mathbf{i}_1$ superficial current density in matrix phase (A/cm^2)
$\mathbf{i}_2$ superficial current density in pore phase (A/cm^2)
i_{nj} local current density due to reaction j (A/cm^2)
I superficial current density to an electrode (A/cm^2)
j $= \nabla\cdot\mathbf{i}_2$, transfer current per unit electrode volume (A/cm^3)
j_{in} pore wall flux of species i (mole/cm^2·sec)
L electrode thickness (cm)
L_k latent heat of fusion of salt k
L_T width of cell sandwich (cm)
m mass of cell (kg)
$\mathbf{M}_i$ symbol for the chemical formula of species i
M_i molecular weight of species i (g/mole)
n_j number of electrons transferred in electrode reaction j
N number of LiAl particles per unit electrode volume (cm^{-3})
$\mathbf{N}_i$ superficial flux of species i (mole/cm^2·sec)
r_i radius of β-LiAl in LiAl pellet (cm)
r_o radius of LiAl pellet (cm)
R universal gas constant (8.3143 J/mole·K)
R_A parameter defined by Eq. [29]
R_g grid resistance ($\Omega\ cm^2$)
s_{ij} stoichiometric coefficient of species i in electrode reaction j
S parameter defined by Eq. [18]
t time (sec)
t_f final time (sec)
t_{f2} time between start of discharge and onset of reaction [IIB] in positive electrode (sec)
t_i^r transference number of species i with respect to reference frame, r
T absolute temperature (K)
T_A temperature of surroundings (K)
T_o initial temperature (K)
U apparent open-circuit cell potential (V)
$U_{j,o}$ theoretical open-circuit potential for reaction j at the composition prevailing locally at the electrode surface, relative to a reference electrode of a given kind (V)
U_j^θ standard electrode potential for reaction j (V)
U_o open-circuit cell potential (V)
$\mathbf{v}_3$ velocity of common ion in molten salt mixture (cm/sec)
$\mathbf{v}^\star$ molar average velocity (cm/sec)
$\tilde{V}$ molar volume (cm^3/mole)
$\overline{V}_k$ partial molar volume of salt k (cm^3/mole)
V_R reservoir volume (cm^3)
w reservoir width (cm)
x_k mole fraction of salt k
Y polarization conductance ($\Omega^{-1}\ cm^{-2}$)
z_i valence or charge number of species i

Greek Letters

α_a transfer coefficient in anodic direction
α_c transfer coefficient in cathodic direction
γ mean molal activity coefficient
γ_i exponent in Eq. [16]
γ_k activity coefficient of salt k
ϵ porosity or void volume fraction
ϵ_i volume fraction of species i
ϵ_p total volume fraction of precipitate
ϵ_{pk} volume fraction of precipitate of salt k
ζ tortuosity defined by Eq. [A-3]
η $\Phi_1 - \Phi_2$
κ effective solution conductivity (mho/cm)
μ_k chemical potential of salt k (J/mole)
ν_i^k number of ions of species i produced by dissociation of a mole of salt k
ρ density (g/cm^3)
σ effective matrix conductivity (mho/cm)
Φ_1 electric potential in the matrix (V)
Φ_2 electric potential in the solution (V)

Subscripts

A salt A, *e.g.*, lithium chloride

B salt B, *e.g.*, potassium chloride
cc current collector
e electrode
j reaction j
k salt A or B
lim limiting value
o at the electrode surface
ref reference electrode
s separator
sat saturation value
α α-Al
β β-LiAl
+ positive electrode
− negative electrode
∞ bulk solution property

Superscripts

A salt A, *e.g.*, LiCl
B salt B, *e.g.*, KCl
o initial value
α α-Al
β β-LiAl
★ relative to molar average reference velocity

REFERENCES

1. J. Newman and W. Tiedemann, *AIChE J.*, **21,** 25 (1975).
2. J. Newman and C. W. Tobias, *This Journal*, **109,** 1183 (1962).
3. J. S. Dunning, Dissertation, University of California, Los Angeles (1971).
4. A. Winsel, *Z. Elektrochem.*, **66,** 287 (1962).
5. W. G. Sunu, Dissertation, University of California, Los Angeles (1978).
6. W. Stein, Ph.D. thesis, Rheinisch-Westfalischen Techn. Hochschule, Aachen (1959).
7. K. Micka and I. Rousar, *Electrochim. Acta*, **18,** 629 (1973); *ibid.*, **19,** 499 (1974).
8. C. E. Vallet and J. Braunstein, *This Journal*, **125,** 1193 (1978).
9. K. Micka and I. Rousar, *Electrochim. Acta.*, **21,** 599 (1976).
10. W. Tiedemann, J. Newman, and F. De Sua, *Power Sources*, **6,** 15 (1977).
11. W. Tiedemann and J. Newman, in "Battery Design and Optimization," S. Gross, Editor, p. 23, The Electrochemical Society Softbound Proceedings Series, Princeton, N.J. (1979).
12. W. Tiedemann and J. Newman, *ibid.*, p. 39.
13. P. A. Nelson *et al.*, Progress Report for the period 11/78-3/79, ANL 79-39, Argonne National Laboratory (May 1979).
14. R. Pollard and J. Newman, *This Journal*, **126,** 1713 (1979).
15. R. White, Dissertation, University of California, Berkeley (1977).
16. W. Tiedemann and J. Newman, *This Journal*, **122,** 1482 (1975).
17. R. Pollard, Dissertation, University of California, Berkeley (1979).
18. R. Pollard and J. Newman, Unpublished work.
19. J. Newman, "Electrochemical Systems," Prentice-Hall, Englewood Cliffs, N.J. (1973).
20. R. Pollard and J. Newman *Electrochim. Acta*, **25,** 315 (1980).
21. D. Gidaspow and B. S. Baker, *This Journal*, **120,** 1005 (1973).
22. J. S. Dunning, D. N. Bennion, and J. Newman, *ibid.*, **118,** 1251 (1971).
23. J. S. Dunning, D. N. Bennion, and J. Newman, *ibid.*, **120,** 906 (1973).
24. H. Gu, D. N. Bennion, and J. Newman, *ibid.*, **123,** 1364 (1976).
25. L. Redey and D. R. Vissers, Personal communication.
26. D. R. Vissers, K. E. Anderson, C. K. Ho, and H. Shimotake, in "Battery Design and Optimization," S. Gross, Editor, p. 416, The Electrochemical Society Softbound Proceedings Series, Princeton, N.J. (1979).
27. M. L. Saboungi and A. E. Martin, Abstract 339, p. 919, The Electrochemical Society Extended Abstracts, Pittsburgh, Pennsylvania, Oct. 15-20, 1978.
28. N. C. Otto and J. E. Battles, in Progress Report for the period 11/78-3/79, ANL 79-39, p. 50, Argonne National Laboratory (May 1979).
29. J. Newman and R. Pollard, in Progress Report for the period 10/78-9/79, ANL 79-94, p. 109, Argonne National Laboratory (March 1980).
30. C. A. Melendres, *This Journal*, **124,** 650 (1977).
31. S. V. Karpachev, A. G. Stromberg, and V. N. Podchainova, *Zh. Obshchei Khim.*, **5,** 1517 (1935).
32. E. R. van Artsdalen and I. S. Yaffe, *J. Phys. Chem.*, **59,** 118 (1955).
33. J. Newman and W. Tiedemann, "Advances in Electrochemistry and Electrochemical Engineering," Vol. 11, H. Gerischer and C. W. Tobias, Editors, Wiley-Interscience (1977).
34. J. Richter, U. Gasseling, and R. Conradt, *Electrochim. Acta*, **23,** 1165 (1978).
35. C. T. Moynihan and R. W. Laity, *J. Phys. Chem.*, **68,** 3312 (1964).
36. M. Blander, in "Molten Salt Chemistry," M. Blander, Editor, pp. 127-238, Interscience, New York (1964).
37. E. Aukrust, B. Bjorge, H. Flood, and T. Førland, *Ann. N. Y. Acad. Sci.*, **79,** 830 (1960).
38. B. Chu and J. J. Egan, *ibid.*, **79,** 908 (1960).
39. J. Lumsden, "Thermodynamics of Molten Salt Mixtures," Academic Press, New York (1966).
40. T. J. Edwards, J. Newman, and J. M. Prausnitz, *Ind. Eng. Chem. Fundam.*, **17,** 264 (1978).
41. M. Hansen, "Constitution of Binary Alloys," Metallurgy and Metallurgical Engng. Series, 2nd ed., McGraw-Hill, New York (1958).
42. J. P. Suchet, "Crystal Chemistry and Semiconduction in Transition Metal Binary Compounds," Academic Press, New York (1971).

Mathematical Modeling of the Lithium-Aluminum, Iron Sulfide Battery

II. The Influence of Relaxation Time on the Charging Characteristics

Richard Pollard[*,1] **and John Newman**[*]

Materials and Molecular Research Division, Lawrence Berkeley Laboratory and Department of Chemical Engineering, University of California, Berkeley, California 94720

ABSTRACT

A mathematical model of the LiAl/LiCl, KCl/FeS cell has been used to study the behavior of the system during relaxation and charging. The effects of state of charge, cell temperature, and current density are presented, and the influence of a period of relaxation on the subsequent charging operation is investigated. In addition, factors that can have a significant impact on the charging characteristics are identified.

The mathematical model of the LiAl/LiCl, KCl/FeS cell (1) can also be used to investigate the behavior of the system during relaxation and charging. The changes that take place under these conditions could influence the dependence of cell performance on the number of completed cycles.

In the laboratory, current interruption techniques can be used to assess the resistance within the electrodes, separator, and grids. Furthermore, in some experiments, such as post-mortem cell examinations, a period of relaxation may be needed before the temperature is low enough to begin the analyses. Current interruption may also be important in modules for electric vehicle propulsion, where it is anticipated that there will be significant periods when the battery is not in use. Cell behavior on charge can control the overall energy efficiency of the system and may also directly affect the nature of the subsequent cell discharge (2, 3). For these reasons, it is necessary to identify the factors that can limit the system during the relaxation and charging modes of operation.

The governing differential equations presented previously (1) can be used directly in the analysis, and it is only necessary to replace the initial conditions, $x_A = x_A^o$ and $\epsilon = \epsilon^o$, with the appropriate composition and porosity distributions and to modify the model for negative electrode kinetics. At any point in the electrode, it is assumed that an outer layer of β-LiAl forms as soon as charging begins and that the electrochemical reaction is restricted to the solid-electrolyte interface. The analysis of diffusion of lithium through the β-phase and the gradual reduction in thickness of the α-Al region parallels the model for discharge (1, 4), but the limiting transfer current becomes

$$(\nabla \cdot \mathbf{i}_2)_{\lim} = \frac{4\pi N F D_\beta (c_{Li^\beta})_{sat}}{(1 - \bar{x}_{Li^\beta})\left(\frac{1}{r_o} - \frac{1}{r_1}\right)} \qquad [1]$$

and the reference concentration $(c_{Li^\alpha})_{sat}$ should be replaced by $(c_{Li^\beta})_{sat}$.

Results and Discussion

Relaxation.—Figure 1 shows composition profiles across the cell sandwich for several times after interruption of the current at the end of a discharge with $I = 41.6$ mA/cm^2. The concentration variations diminish in both electrodes and, after 2 hr, the electrolyte composition is practically uniform. In the negative, the region with highest x_A, at the back of the electrode, becomes cathodic with respect to the front portions. Local concentration cells, with the reaction

$$LiAl \rightleftharpoons Li^+ + Al + e^- \qquad [I]$$

are established that reduce the initial composition variations. However, there is no driving force for equalization of the local state of charge within the α-Al, β-LiAl alloy, and the reactions that take place to give a uniform electrolyte composition accentuate the nonuniform utilization of reactants. The magnitude of this effect is dependent on the composition profile and the depth of discharge before current interruption.

In the positive electrode, the situation is complicated by the possibility of simultaneous reactions and by precipitation of electrolyte. Initially, the electrolyte concentration is almost uniform across the majority of the electrode due to precipitation of KCl as two spikes adjacent to the reaction fronts and self-discharge reactions in the isolated regions behind the spikes. Adjacent to the current collector, FeS reacts with lithium ions according to

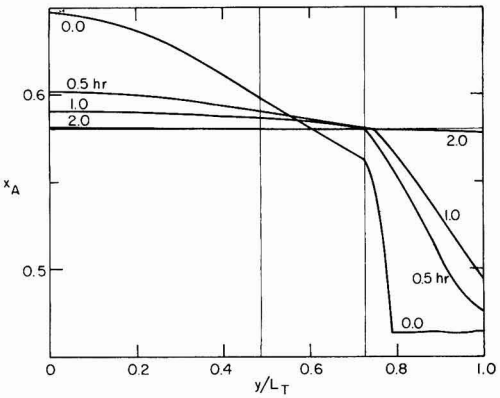

Fig. 1. Position dependence of mole fraction of LiCl at different times after current interruption. Simulation parameters: $Q_- = 2800$ C/cm^3, $Q_+ = 4630$ C/cm^3, $L_- = 0.32$ cm, $L_S = 0.16$ cm, $L_+ = 0.18$ cm, $N = 5.5 \times 10^7$ cm^{-3}, $h_o = 8.25 \times 10^{-2}$ W/m^2 · K, $R_g = 1.55\ \Omega$ cm^2, $h = 0.004$ cm, $w = 0$, $-c_{Li^\beta}/(c_{Li^\beta})_{sat} = 1.0$, $D_\beta = 4 \times 10^{-8}$ cm^2/sec. Parameters at start of previous discharge: $\epsilon_-^\circ = 0.39$, $\epsilon_S = 0.75$, $\epsilon_+^\circ = 0.555$, $T_o = 470$°C, $I = 41.6$ mA/cm^2, $x_A^\circ = 0.58$. Initial stage of charge, $\lambda(t = 0) = 47.9\%$. Additional parameters specified in Tables I and III of Ref. (1).

[*] Electrochemical Society Active Member.
[1] Present address: Department of Chemical Engineering, University of Houston, Houston, Texas 77004.
Key words: porous electrodes, molten salt electrolyte, cell performance.

$$2FeS + 2Li^+ + 2e^- \rightleftharpoons Li_2FeS_2 + Fe \qquad [IIA]$$

whereas, near the front of the electrode, Li_2S reacts anodically with iron, thus

$$2Li_2S + Fe \rightleftharpoons Li_2FeS_2 + 2Li^+ + 2e^- \qquad [IIB]$$

The transformation of Li_2S and FeS to the intermediate sulfide reduces the local variations in state of charge although, once all the FeS has been removed, it is not possible for the remainder of the Li_2S to react further. Consequently after approximately 1 hr, there are no more reactions in the positive, and the composition now relaxes under the influence of diffusion alone.

Characteristic times for other relaxation processes can also be identified from the composition profiles. In Fig. 1, the electrolyte concentration changes by less than 1% across the separator after 1.3 hr, whereas the 1% condition is achieved in the negative electrode after only 0.8 hr. This reflects, to some extent, the influence of the electrochemical reaction on the relaxation time (5). However, the 1% criterion is rather arbitrary and, even though the composition is fairly uniform at 0.8 hr, the concentration in the negative still needs to drop by another 2.5%, as diffusion takes place across the separator. In the positive, an additional characteristic time can be distinguished. Self-discharge reactions take place in the region where Li_2FeS_2 is only partially converted to Li_2S. Here, the portion closest to the front of the electrode becomes preferentially cathodic and, after approximately 4 min, a sharp reaction front for the second reaction has been formed.

Heat is not generated in the cell during relaxation, and the temperature falls in accordance with the specified rate of heat transfer to the surroundings. As a result, the saturation concentration for KCl can rise faster than the minimum electrolyte concentration and, under these circumstances, the total volume of precipitate becomes greater than the value at current interruption. However, the reduction in minimum composition soon dominates and, in this example, all the KCl has dissolved after 1500 sec.

Figure 2 shows the variations in total cell voltage that take place after the current is switched off, for simulations A and B described in Fig. 9 of Ref. (1). Curve A is for the example that had a temperature of 450°C at the start of discharge and that achieved 39.2% utilization before the cutoff voltage was reached. The second example had a higher initial temperature (470°C), and a greater utilization was attained before the termination of discharge. In both cases, there is an initial instantaneous rise in cell voltage. The magnitude of this step change can, in principle, be used as a basis for estimation of cell resistance. However, the numerical predictions cannot be used directly because the effects of double layer capacity are not included in the model, and because the final total cell voltage, prior to interruption, can be much lower than expected in practice, due to the acute nature of the predicted failure mechanism. Therefore, separate calculations are necessary to estimate the interrupter resistance.

At the instant of interruption, there is no change in the composition profile. The potential profile retains the same shape within the negative electrode, and the potential difference $\Phi_1 - \Phi_2$ in the positive is constrained to maintain the same value because of the double layer capacity. Consequently, at any point in the system, Ohm's law gives

$$\frac{\mathbf{i}_1}{\sigma} - \frac{\mathbf{i}_2}{\kappa} = -\nabla\eta = \frac{\mathbf{i}_1^o}{\sigma} - \frac{\mathbf{i}_2^o}{\kappa} \qquad [2]$$

where the superscript refers to conditions just before interruption. Since $\mathbf{i}_1 + \mathbf{i}_2 = 0$ and $\mathbf{i}_1^o + \mathbf{i}_2^o = I$, one may write

$$\mathbf{i}_1 - \mathbf{i}_1^o = -\frac{I\sigma}{\sigma + \kappa} \qquad [3]$$

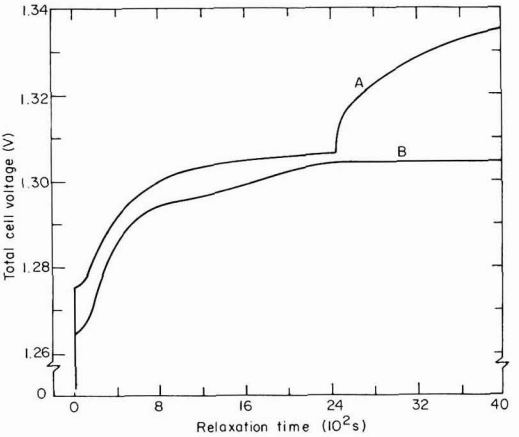

Fig. 2. Dependence of total cell voltage on relaxation time. Simulation parameters as in Fig. 1, except as indicated. Curve A: $\lambda(t = 0) = 60.8\%$, $R_I = 0.15\ \Omega\ cm^2$, $T(t = 0) = 468.2°C$, T_o (at start of previous discharge) $= 450.0°C$. Curve B: $\lambda(t = 0) = 47.9\%$, $R_I = 0.14\ \Omega\ cm^2$, $T(t = 0) = 496.2°C$, T_o (at start of previous discharge) $= 470°C$.

which indicates that the resistance of matrix and solution are effectively in parallel, even though each segment of the electrode is in series. Combination of Eq. [3] and Ohm's law for the matrix phase gives the change in cell voltage, $\Delta(V - V^o)$, as

$$\frac{\Delta(V - V^o)}{I} = \int_o^{L_T} \frac{dy}{\sigma + \kappa} \qquad [4]$$

where the left side represents the interrupter resistance, R_I. In the computer calculations, R_I is dominated by the resistance across the separator because the matrix conductivity is assumed to be infinite in the negative and high in the positive electrode. The separator resistance changes only slightly during operation of the cell, in response to variations in electrolyte conductivity.

It should be emphasized that the theoretical models for the LiAl/FeS cell (6) do not include double layer effects since they are not generally regarded as being significant in the normal operation of a cell. Therefore, for the purpose of measuring the cell polarization characteristics, one may prefer the resistance to be measured after charging of the electric double layer has been completed. For this system, the double layer relaxation time, from point to point within an electrode, is estimated as approximately 50 msec (6), whereas relaxation of concentration profiles by diffusion and reaction is on the order of 3000 sec (see above).

After interruption, the voltage gradually approaches the equilibrium open-circuit cell potential. The shape of the curves is determined by the details of the reactions that occur in the individual electrodes. In particular, a corrosion potential is established in the positive by reactions [IIA] and [IIB]. In example A, all the Li_2S has been converted to Li_2FeS_2 after approximately 2450 sec, and the voltage rises sharply to the open-circuit value, $U_o = 1.34V$. Curve B does not show this effect because some Li_2S still remains when reactions [IIA] and [IIB] are completed. In this case, the voltage slowly approaches the open-circuit potential, $U_o - U_{[IIA],o} = 1.3074V$, as the electrolyte composition becomes more uniform. It should also be noted that the small initial rate of rise of cell voltage shown in the examples is atypical, and it results from potential drop across the sharp spike of precipitate that was responsible for the rapid decline in cell volt-

age before current interruption. Both theoretical and experimental results indicate that the initial voltage rise is more rapid when the current is interrupted before the cutoff voltage is reached (7).

Charging.—Figure 3 shows simulated composition profiles at different stages of a constant current charge. A relaxation time of 2 hr was included between the initial discharge and the start of the charging process. The parameter λ represents the overall state of charge; when the cutoff voltage of 1.65V is reached, 89.3% of the total theoretical capacity is available for the next discharge.

In contrast to discharge, lithium ions are now introduced into the electrolyte at the positive electrode and transported across the separator to the negative electrode, where they are incorporated into the LiAl alloy. The composition profiles represent the combined effects of diffusion, migration, and electrochemical reaction. An almost constant composition gradient is established across the separator, but the electrolyte concentration in the reservoir rises significantly during the charge. The model predicts that the electrolyte composition is almost uniform behind each reaction front.

The variations in electrolyte concentration in Fig. 3 can be compared with those in Fig. 4, for the same cell, but without relaxation between discharge and charge. At $\lambda = 77.6$, the profiles are very similar in the two cases, and there is little trace of the composition profile before the charge was started.

The average cell temperature in Fig. 3 falls from 753.5 to 740.0 K during the charge, as a result of reversible heat effects and heat transfer to the surroundings. Consequently, the saturation limit for KCl rises, and precipitation begins at the reaction front in the negative electrode when $\lambda = 85.9$. The temperature of the cell in Fig. 4 also falls, but over the range 769.4 to 751.6 K, and precipitation is delayed until $\lambda = 91.1$. For this reason, 93.7% of the theoretical capacity can be recovered before the resistance across the precipitated region becomes excessive and the cutoff voltage is reached.

The difference in charging behavior caused by the temperature drop during relaxation emphasizes the need for careful thermal management of battery modules. At lower charging current densities the temperature falls even more dramatically, but the maximum and minimum concentrations are smaller at a given state of charge, and precipitation of KCl no longer controls the final value of λ. For the cell characteristics used in the simulations, a current density of -70 mA/cm^2 is needed to keep the average cell temperature reasonably constant.

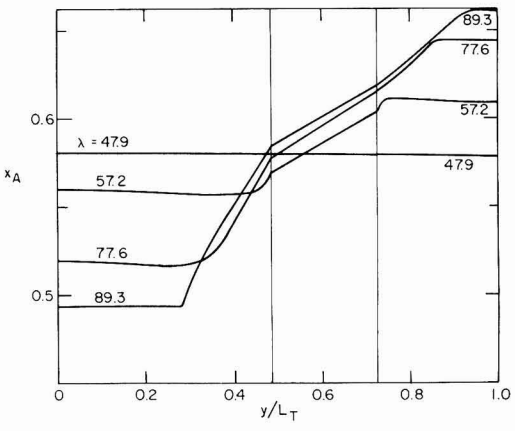

Fig. 3. Position dependence of mole fraction of LiCl at different states of charge for a constant current charge of -41.6 mA/cm^2. A relaxation time of 2 hr is included between the end of the previous discharge and the beginning of the charging process. Simulation parameters: $T(t = 0) = 480.4$°C, see also Fig. 1.

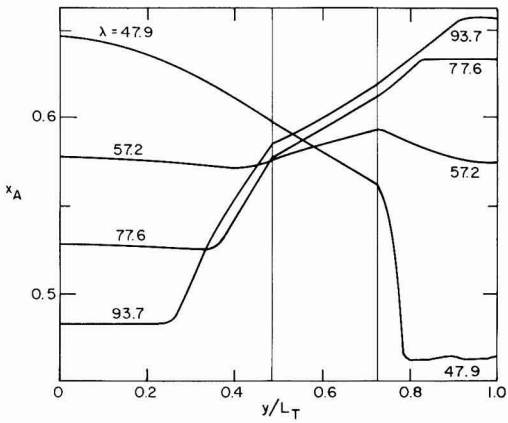

Fig. 4. Position dependence of mole fraction of LiCl at different states of charge for a constant current charge of -41.6 mA/cm^2. No relaxation between the end of the previous discharge and the start of the charging process. Simulation parameters: $T(t = 0) = 496.2$°C, see also Fig. 1.

Figures 5 and 6 show the fraction of active material utilized within the negative electrode, at several overall states of charge, for the examples in Fig. 3 and 4, respectively. A comparison of the curves at $\lambda = 47.9$ ($t = 0$) shows the increase in nonuniform utilization of reactants that results from relaxation of the electrolyte composition. The general charging mechanism is similar in two cases: the region closest to the electrode/separator interface is recharged first, and the reaction front moves back through the electrode as the alloy is completely reconverted to β-LiAl. Further reaction of the β-LiAl is not included in the model because the necessary increase in overpotential of al-

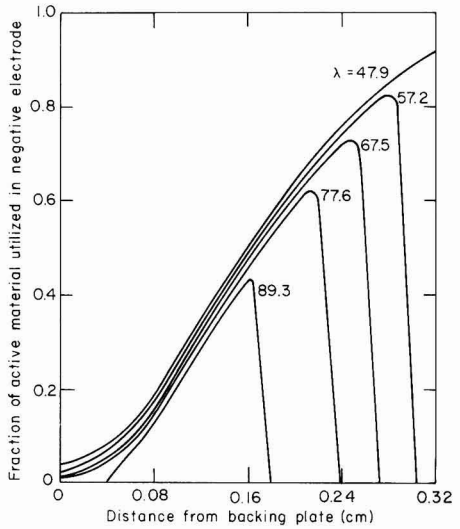

Fig. 5. Fraction of active material utilized in negative electrode at different overall states of charge during a constant current charge of -41.6 mA/cm^2. A relaxation time of 2 hr is included between the end of the previous discharge and the beginning of the charging process. Simulation parameters are as in Fig. 1.

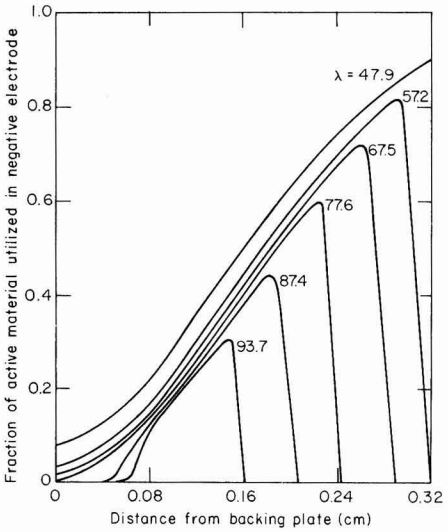

Fig. 6. Fraction of active material utilized in negative electrode at different overall states of charge during a constant current charge of −41.6 mA/cm². No relaxation between the end of the previous discharge and the start of the charging process. Simulation parameters are as in Fig. 1.

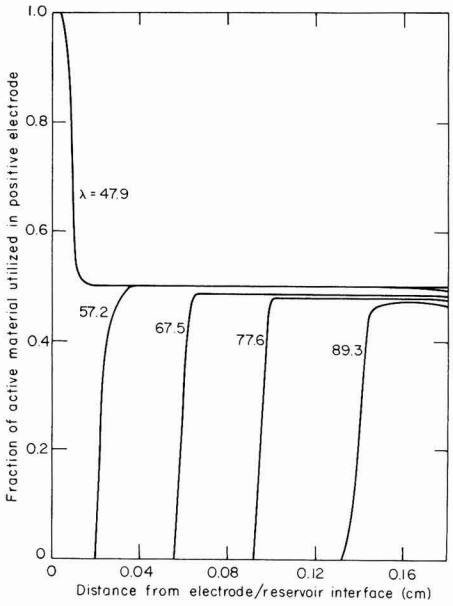

Fig. 7. Fraction of active material utilized in positive electrode at different overall states of charge during a constant current charge of −41.6 mA/cm². A relaxation time of 2 hr is included between the end of the previous discharge and the beginning of the charging process. Simulation parameters as in Fig. 1.

most 0.3V (8) cannot be obtained with the specified cutoff voltage. However, recent evidence (9) suggests that the change in overpotential when a particle becomes completely converted to β-LiAl may not be as dramatic as reported previously (8). Consequently, reaction may be possible at the surface of particles where no α-Al remains. In general, diffusion of lithium in the β-phase is considerably faster than in α-Al (10), and only very small concentration differences are predicted across the outer β-LiAl layer.

The complementary reaction distributions for the positive electrode are presented in Fig. 7 and 8. The results at $\lambda = 47.9$ show explicitly the equalization in local state of charge that takes place during relaxation. Figure 7 shows that reaction [IIA] occurs preferentially at the front of the electrode, adjacent to the reservoir, and that a sharp reaction front moves through the electrode as Li_2FeS_2 is consumed. This mechanism also predominates in Fig. 8, although the final distribution of unreacted material is shifted from the back of the electrode. Figure 8 also indicates that, early in the charge and at a distance of approximately 0.14 cm, FeS reacts cathodically to form X-phase, in accordance with reaction [IIA]. This self-discharge process corresponds, in part, to the charge equalization predicted during relaxation. The effect is more pronounced at lower current densities.

The variations in total cell voltage for several constant current charges are presented in Fig. 9. In each case, there is a relatively sharp rise in electrode potential when reaction [IIB] is completed in the positive electrode because the corrosion potential can no longer be maintained. Also, precipitation of KCl in the negative electrode is predicted, and the local reduction in electrolyte conductivity that results causes a sharp increase in resistance at the higher current densities. At $I = -20$ mA/cm², charging is completed before precipitation effects dominate. The time for onset of precipitation is sensitive to the cell temperature, and this is largely responsible for the lower final states of charge that are predicted when a period of relaxation is included in the operating cycle.

Experiments on the charging behavior of LiAl/FeS cells (7) show that the positive electrode current collector potential, measured relative to a reference electrode placed adjacent to the separator, can rise sharply toward the end of charge. The rate of change of this potential can be larger than that of the negative elec-

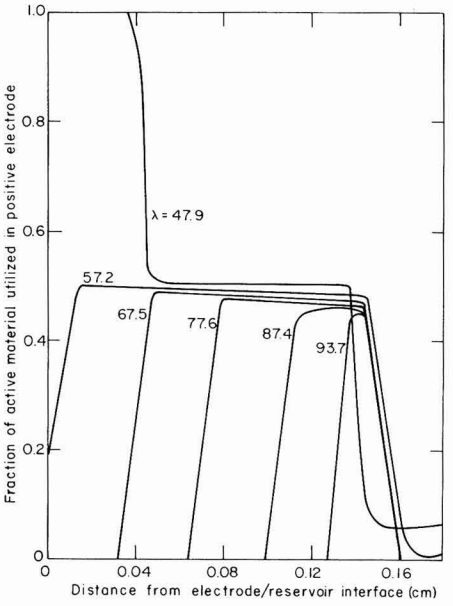

Fig. 8. Fraction of active material utilized in positive electrode at different overall states of charge during a constant current charge of −41.6 mA/cm². No relaxation between the end of the previous discharge and the start of the charging process. Simulation parameters as in Fig. 1.

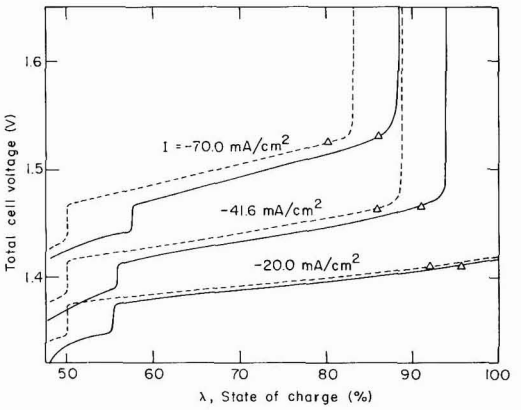

Fig. 9. Dependence of total cell voltage on state of charge during constant current charges. Simulation parameters as in Fig. 1 and $\lambda(t = 0) = 47.9\%$. ———: Charge begins immediately after discharge, $T(t = 0) = 480.4°C$; - - -: 2 hr relaxation between discharge and charge, $T(t = 0) = 496.2°C$; △: onset of precipitation of KCl in negative electrode.

trode current collector, and this might be interpreted as a positive electrode limitation on charging. There are several possible reasons for this apparent discrepancy between experiment and theory: (*i*) reduction in positive electrode porosity caused by expansion of the negative, (*ii*) reduction in available electrode capacity and uncertainty in state of charge, and (*iii*) development of high matrix resistance in the positive electrode due to poor electrical connectivity of the phases or large contact resistances.

Additional experiments may be needed to obtain a clearer picture of the factors that limit the charging behavior and to assess the validity of the numerical predictions. The nature of overcharge reactions, and the potentials at which they become thermodynamically feasible, may also need to be investigated.

Conclusions

A mathematical model of the LiAl/FeS cell has been used to investigate the influence of relaxation on the charging characteristics of the system. The analysis indicates that composition variations become less pronounced during relaxation, but the local state of charge within the electrodes can become more nonuniform. The concentration changes induced on charging mask the effects of current interruption, and the effect of relaxation on cell temperature can be more important. The model shows that precipitation of KCl in the negative electrode can cause a rapid rise in applied potential toward the end of charge, but that the effect is not critical at low current densities. The results obtained are sensitive to the details of the heat balance used in the calculation, and this reflects a need for precise thermal management of LiAl/FeS battery modules.

Acknowledgment

The authors are extremely grateful to the members of the Chemical Engineering Division at the Argonne National Laboratory for many useful discussions and valuable suggestions. This work was supported by the Division of Solar, Geothermal, Electric and Storage Systems, Office of the Assistant Secretary of Energy Technology, U.S. Department of Energy, under Contract No. W-7405-Eng-48.

Manuscript submitted Feb. 22, 1980; revised manuscript received *ca.* Aug. 27, 1980.

Any discussion of this paper will appear in a Discussion Section to be published in the December 1981 JOURNAL. All discussions for the December 1981 Discussion Section should be submitted by Aug. 1, 1981.

Publication costs of this article were assisted by The University of California.

LIST OF SYMBOLS

c_i	concentration of species i (mole/cm³)
D	diffusion coefficient (cm²/sec)
$\mathbf{F}$	Faraday's constant (96,487 C/equiv.)
h	mesh size (cm)
h_o	heat transfer coefficient (W/m²·K)
$\mathbf{i}_1$	superficial current density in matrix phase (A/cm²)
$\mathbf{i}_2$	superficial current density in pore phase (A/cm²)
I	superficial current density to an electrode (A/cm²)
L	thickness of electrode or separator (cm)
L_T	width of cell sandwich (cm)
N	number of LiAl particles per unit electrode volume (cm⁻³)
r_i	inner radius of outer region of β-LiAl in spherical pellet
r_o	radius of particle at solid/electrolyte interface
R_g	grid resistance (Ω cm²)
R_I	interrupter resistance (Ω cm²)
T_o	initial temperature (K)
$U_{j,o}$	theoretical open-circuit potential for reaction j, relative to a reference electrode of a given kind (V)
V	cell voltage (V)
w	reservoir width (cm)
x_A	mole fraction of LiCl

Greek letters

ϵ	porosity
η	$\Phi_1 - \Phi_2$
κ	effective solution conductivity (mho/cm)
λ	state of charge (%)
σ	effective matrix conductivity (mho/cm)
Φ_1	electric potential in the matrix (V)
Φ_2	electric potential in the electrolyte (V)

Subscripts

lim	limiting value
s	separator
sat	saturation value
β	β-LiAl
+	positive electrode
−	negative electrode

Superscripts

°	initial value
β	β-LiAl
—	average value

REFERENCES

1. R. Pollard and J. Newman, *This Journal*, **128**, 491 (1981).
2. J. S. Dunning, D. N. Bennion, and J. Newman, *ibid.*, **120**, 1005 (1973).
3. H. Gu, D. N. Bennion, and J. Newman, *ibid.*, **123**, 1364 (1976).
4. R. Pollard, Dissertation, University of California, Berkeley (1979).
5. K. Nisancioglu and J. Newman, *This Journal*, **120**, 1339 (1973).
6. J. Newman and R. Pollard, in Progress Report for the Period 10/78-9/79, ANL 79-94, Argonne National Laboratory (March 1980).
7. L. Redey and D. R. Vissers, Personal communication.
8. J. R. Selman, D. K. DeNuccio, C. J. Sy, and R. K. Steuneberg, *This Journal*, **124**, 1160 (1977).
9. C. J. Wen, B. A. Boukamp, R. A. Huggins, and W. Weppner, *ibid.*, **126**, 2258 (1979).
10. C. A. Melendres, *ibid.*, **124**, 650 (1977).

Exothermic Reactions among Components of Lithium-Sulfur Dioxide and Lithium-Thionyl Chloride Cells

S. Dallek,* S. D. James,* and W. P. Kilroy*

Naval Surface Weapons Center, Electrochemistry Branch, White Oak Laboratory, Silver Spring, Maryland 20910

ABSTRACT

Differential scanning calorimetry measurements were made on various components of Li-SO_2 and Li-$SOCl_2$ cells to identify those combinations that react exothermically and might cause batteries to explode. The passivation of Li by SO_2 in acetonitrile (AN) was characterized over a wide range of SO_2 concentration (0.1-14M). In the absence of SO_2, trace additions of water greatly lower the exothermicity of the Li-AN reaction. The Li-$SOCl_2$-$LiAlCl_4$ mixture is inert over a wide range of temperature well above the melting point of Li. However, adding carbon black converts this inert mixture into one which is highly and consistently reactive. The addition of copper powder enhances carbon's catalytic effect on the reactivity of the Li-$SOCl_2$-$LiAlCl_4$ mixture while trace additions of water have the opposite effect.

Batteries based on the Li/SO_2 and Li/$SOCl_2$ electrochemical couples have shown great promise for use in military applications requiring high energy density power sources. However, hazards associated with these batteries may delay their use in future military devices. The incidents involving explosions of these cells under various conditions may be attributable to exothermic chemical reactions among initial cell constituents and/or discharge products.

A thermal analysis study was undertaken to determine the reactivity of various combinations of cell components which could cause thermal runaways resulting in cell explosions. Recent work in this area has been conducted on the Li/SO_2 (1-3) and on the Li/$SOCl_2$ (4, 5) systems. The present work involved the use of hermetically-sealed high pressure sample containers to extend our previous studies (1, 2) of Li/SO_2 cell components to include volatile substances. Another objective was to perform a similar study of the Li/$SOCl_2$ system using the high-pressure sample containers to obviate the problems associated with pressure bursts of sample containers encountered in other Li/$SOCl_2$ DTA studies (4, 5). Finally, the reactivity of the lithium-boron alloy was studied for comparison with that of lithium in combination with Li/SO_2 and Li/$SOCl_2$ cell components. This alloy has shown great promise for use as an anode material in molten salt batteries (6-8).

Experimental

Apparatus.—A du Pont Model 990 differential scanning calorimeter (DSC) was employed to measure the reaction initiation temperatures and the relative reactivity of various combinations of Li/SO_2 and Li/$SOCl_2$ cell constituents. In our DSC curves, since the ordinate corresponds to a rate of heat generation and the abscissa is proportional to time, a measure of the relative reactivity is accomplished by a comparison of peak areas and from the masses of the reactants. We sometimes mention the "temperature excursion" (not illustrated) noted for a particular reaction. This does not refer to a deflection of the DSC curves in the ordinate direction (which measures a rate of heat generation). This term refers to excursions of the actual reaction temperature above the programmed temperature. Most DSC curves were recorded at an ordinate sensitivity of 20 mcal/sec · in. (20×). A sensitivity of 5 mcal/sec · in. (5×) is four times as responsive to enthalpy changes as is a setting of 20×. The sensitivity selection is included in the illustrations to allow comparison of the endothermic (endo) and exothermic (exo) areas. We deliberately used an insensitive recorder setting of 20× since we were mostly interested in comparing relatively vigorous reactions. Thus any reactions that involved relatively small amounts of heat change escaped our attention. The termination temperature on any DSC analysis is referred to in the test as the "cutoff" temperature.

All DSC measurements were made under a flowing atmosphere of dry argon at a programmed heating rate of 10°C/min. The DSC instrument was calibrated with pure metals melting over the temperature range studied (In, 156.6°C; Li, 180.5°C; Sn, 231.9°C; Zn, 419.4°C).

Thermal analysis of solids was performed in crimp-sealed du Pont-type Armco iron crucibles. Armco iron is inert to lithium and offers the advantage of excellent thermal response.

Mixtures containing volatile liquids were studied using high-pressure, corrosion-resistant Ni-Cr alloy (Nimonic) 500 μl crucibles purchased from Mettler Instrument Corporation, Princeton, New Jersey. Hermetic seals, capable of withstanding 100 atm of pressure, were achieved when an open-ended screw cap was tightened onto a gold diaphragm placed between the cap and the crucible. The hermeticity was confirmed by observing no loss of mass on reweighing the sample after the DSC run.

A comparison of the two types of sample cups is illustrated in Fig. 1. There is a large mass difference between the Armco cup (200 mg) and the Nimonic cup (2500 mg). The large size of the Nimonic cups necessitated modification of the DSC analytical procedure. Since the DSC chamber could not accommodate a second Nimonic cup for a reference, a stainless steel rod of similar mass was used as a reference and the instrument was then recalibrated. This disparity of sample cup and reference gives rise to a slightly sloping base line.

Sample preparation.—Lithium-boron alloy, containing 72 weight percent (w/o) lithium, was prepared as previously described (8). All solid mixtures containing either lithium-boron alloy or lithium (99.9% Foote Mineral) were prepared by sandwiching the other solid components into a single piece of the alloy or the lithium. The Li or Li-B fragment was pressed into a thin film and then the other solid powder was

* Electrochemical Society Active Member.

Key words: battery, carbon, discharge, catalysis.

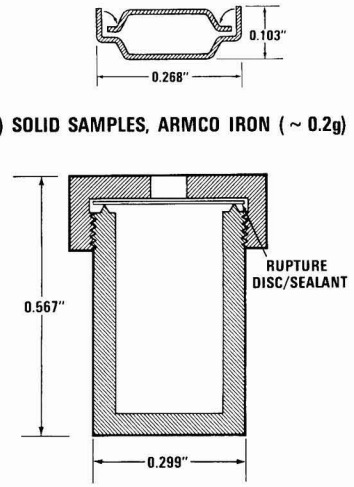

Fig. 1. DSC sample cups

pressed into this Li surface thus ensuring intimate contact. All samples were weighed, mixed, and sealed in a Dry Room maintained at 0.25% relative humidity. All salts, carbon, etc. were vacuum dried at appropriate temperatures. Lithium hexafluoroarsenate was obtained from U.S. Steel Corporation. The lithium tetrachloroaluminate was Matheson-Coleman-Bell "polaroquality" and was used as received. Lithium thiosulfate (Pfaltz and Bauer) was washed in carbon disulfide then in carbon tetrachloride. With the exception of the lithium bromide (Fisher) and the anhydrous lithium sulfide (Ventron), all the other salts used were anhydrous, Reagent-Grade chemicals. Methyl isocyanate (Aldrich) and thionyl bromide (Alfa) were used as received.

The "active" and "reserve" battery electrolytes (~14M in SO_2) were provided by Honeywell Power Sources Incorporated. The active battery electrolyte was approximately 70, 22, and 8 w/o in SO_2, CH_3CN, and LiBr, respectively. The reserve electrolyte was 72.6, 18.4, and 8.9 w/o in SO_2, CH_3CN, and $LiAsF_6$, respectively. The reserve electrolyte was developed for reserve, Li-SO_2 batteries where exceptional long-term stability of the electrolyte is needed.

Acetonitrile was doubly distilled, first over sodium hydride then over phosphorus pentoxide. Only the middle fractions were collected. Dilute solutions of SO_2 in acetonitrile were prepared by bubbling 99.9% SO_2 into the doubly distilled acetonitrile. The dilute solutions (0.1M) of SO_2 were analyzed by adding a known volume of the solution to an excess of standard iodine in acid buffer. The unreacted iodine was titrated with standard thiosulfate solution. The more concentrated solutions (1.7M) were analyzed by weighing the CH_3CN before and after absorption of the SO_2.

Thionyl chloride was refluxed with lithium for approximately 20 hr under an argon atmosphere followed by distillation under argon. Only the palest portion of the middle fraction was collected for use in the DSC studies. All other liquid chemicals were used as received.

A stock solution of 1.6M $LiAlCl_4$ was prepared in $SOCl_2$. A saturated solution of SO_2 in this electrolyte was prepared by bubbling the SO_2 into the $LiAlCl_4$-$SOCl_2$ solution cooled in powdered Dry Ice. This solution was allowed to equilibrate at room temperature and 1 atm pressure.

Discharge products were obtained by constant current discharge of a pressurized laboratory cell containing 30 ml of Li/SO_2 reserve battery electrolyte. Precaution was taken to insure that the carbon-Teflon current collector was very dry and that only clean-surfaced lithium was used. The cell was assembled under helium and discharged at approximately 2-3 mA/cm² current density at ambient temperature. The discharged cell was pumped dry overnight and disassembled in the Dry Room. The products were separated, washed with doubly distilled acetonitrile, and vacuum dried.

Results and Discussion

Sulfur Dioxide System

Table I summarizes the DSC data obtained in this system. The table is arranged in the order of increasing mixture complexity. Mixtures containing the Li-B alloy are segregated at the bottom. Figures 2B and 2C compare the thermal response of the relatively heavy, high-pressure Nimonic sample cups (2.5g) with that of the much lighter Armco iron containers (0.2g). For this purpose we chose the (Li + $Li_2S_2O_3$) reaction which is known to be very exothermic (2). The figure illustrates the generally greater sensitivity of the lighter Armco iron cups. The difference between Fig. 2B and 2C in exotherm initiation temperatures should not be attributed to the mass differences of the sample containers since heterogeneous sample mixtures can often generate irreproducible thermal data. In this connection we note that the curve of Fig. 2B differs slightly from that obtained previously (2). Most of the DSC runs reported herein were performed in duplicate, some in triplicate, to check for reproducibility. Generally, simple mixtures of solid components gave very reproducible results, whereas the initiation temperatures and enthalpic changes of more complicated mixtures, especially those containing liquids, were sometimes less reproducible.

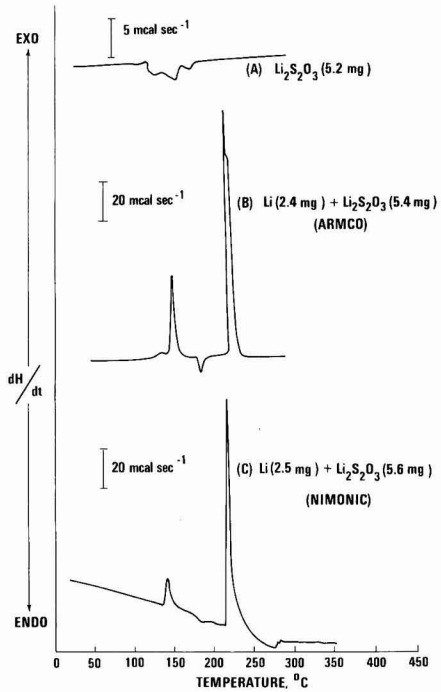

Fig. 2. Reactivity of lithium thiosulfate

Table I. Summary of DSC data for the Li/SO_2 system

Reaction	Reactants	Cutoff temperature (°C)*	Transition temperatures (°C)*** Endothermic	Exothermic
1	Li	—	180	—
2	S	—	113, 118	—
3	AN**	284	—	241
4	$LiAsF_6$	300	258	—
5	$Na_2S_2O_4$	260	—	190
6	Products of reaction 5	495	281, 365	440
7	$Li_2S_2O_3$	305	132	—
8	Li + LiBr	300	181	142
9	Li + $LiAsF_6$	400	—	187(210)
10	Li + AN	300	180	40(5)
11	Li + S	242	180	127(100)
12	Li + $Na_2S_2O_4$	353	180	190, 256
13	Li + $Li_2S_2O_3$ (ARMCO)	290	181	147(5), 222(145)
14	Li + $Li_2S_2O_3$ (NIMONIC)	343	180	137(5), 209(20)
15	Li + Li_3N	391	181	—
16	Li + Li_2SO_4	400	181	—
17	Li + $SOBr_2$	229	179	—
18	Li + CH_3NCO	408	—	152
19	Active electrolyte†	340	177	—
20	Li + anode discharge product	416	181	—
21	Li + cathode discharge product	452	181	251(5)
22	Li + [AN-H_2O (0.2%)]‡	426	180	20 (minor)
23	Li + AN + LiBr	295	—	—
24	Li + [AN-LiBr (satd.)]	400	—	35 (minor)
25	Li + AN + $LiAsF_6$	300	—	50(5), 181
26	[AN-SO_2 (0.1M)] + $LiAsF_6$	268	—	266(15)
27	Li + [AN-SO_2 (0.1M)]	305	—	142(30)
28	Li + [AN-SO_2 (1.7M)]	400	186	122
29	Li + S + S_2Cl_2	265	180	261
30	Li + active electrolyte	343	—	156(5), 180
31	Li + reserve electrolyte§	387	—	180(5)
32	Li + [AN-LiBr (satd.)] + C	408	181	—
33	Li + [AN-SO_2 (0.1M) — LiBr (satd.)]	429	179	86(17)
34	Li + [AN-SO_2 (1.7M)] + LiBr	408	180	122, 181
35	Li + [AN-SO_2 (0.1M)] + $LiAsF_6$	295	—	115(10), 209
36	Li + [AN-SO_2 (1.7M)] + $LiAsF_6$	400	181	142, 189, 217
37	Li + [AN-SO_2 (0.1M)-H_2O (0.07%)] + $LiAsF_6$	276	180	98, 202
38	Li + C + [AN-SO_2 (1.7M) — LiBr (satd.)]	266	180	35
39	Li + C + reserve electrolyte	324	181	142
40	Li + PC** + active electrolyte	348	172	174, 222
41	Li-B alloy + AN	372	180	50(5)
42	Li-B alloy + S	300	180	127(80)
43	Li-B alloy + $Li_2S_2O_3$	324	181	147(5), 245(10)
44	Li-B alloy + active electrolyte	338	—	167
45	Li-B alloy + cathode discharge product	452	181	253(5)

* Temperature at which the DSC linearly programmed temperature scan was terminated.
** AN = acetonitrile; PC = propylene carbonate.
*** Figure in parenthesis represents the increase in the sample temperature above the linearly programmed temperature.
† Active electrolyte: 70, 22, 8% w/w in SO_2, AN, and LiBr (~14 M SO_2).
‡ Ingredients within the square brackets are a homogeneous solution.
§ Reserve electrolyte: 72.6, 18.4, 8.9% w/w in SO_2, AN, and $LiAsF_6$ (~14M SO_2).

Lithium thiosulfate and sodium dithionite.—Figure 2A reveals that $Li_2S_2O_3$ begins to decompose endothermically at about 132°C. This indicates that the first exotherms in Fig. 2B and 2C are associated with the reaction of Li with these thiosulfate decomposition products. In agreement with the literature (9, 10), Fig. 3A shows rapid exothermic decomposition at 190°C for a sample of sodium dithionite ($Na_2S_2O_4$) containing 7.5% sodium sulfite and 2.5% sodium thiosulfate as impurities. This is as chemically similar as we could get to the commercially unavailable lithium dithionite which appears to be the primary product in discharged Li/SO_2 cells (18). Figure 3A agrees with previously published data (3). A repeated DSC run on the decomposed salt of Fig. 3A is shown in Fig. 3B. Contrary to a previous report (3) no evidence is seen for sulfur having been formed in Fig. 3A.

Cell discharge products.—Figure 4 shows thermal analysis of mixtures of Li with discharge products taken from an Li-SO_2 cell. This cell contained the "reserve" electrolyte (SO_2-AN-$LiAsF_6$) and was discharged at a constant current density of 2-3 mA · cm^{-2} to a 0.2V cutoff voltage. A grayish-colored spongy product was scraped off the Li anode surface, mixed with Li, and analyzed as in Fig. 4A to a 400°C cutoff. In this range the trace is thermally featureless except for the 180°C endotherm for melting of Li. The discharged cathode was washed with pure acetonitrile to remove SO_2 and salt, dried by evacuation, and then a fragment of it was mixed with Li and thermally analyzed to give Fig. 4B. The sharp exotherm at 251°C appears to be due to the reaction of Li with decomposition products of $Li_2S_2O_4$. DSC curves of discharged cathodes in the absence of Li (not shown) reveal a minor exotherm due to decomposition of $Li_2S_2O_4$ with initiation temperatures from approximately 185° to 230°C. A small exotherm is also visible in Fig. 4B. The exotherm is minor because of the very small

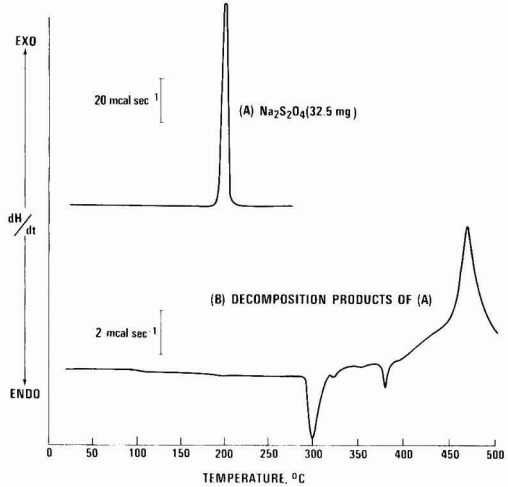

Fig. 3. Thermal decomposition of sodium dithionite

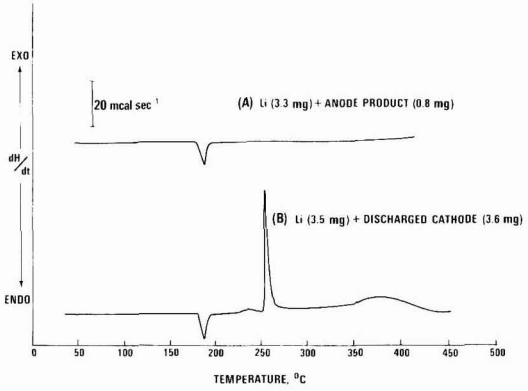

Fig. 4. Lithium reactivity with discharge products of Li-AN-SO_2-$LiAsF_6$ cell.

quantity of $Li_2S_2O_4$ (0.2-0.3 mg) imbedded in the (3.0-4.0 mg) of current collector. The variation in the initiation temperature is a function of the heterogeneous distribution of $Li_2S_2O_4$ in the carbon-Teflon collector. It is reasonable to speculate that under certain abusive conditions of battery discharge, $Li_2S_2O_4$ may undergo decomposition similar to the $Na_2S_2O_4$, thereby generating large temperature increases. The low broad exotherm at about 350°C is associated with the reaction between Li and Teflon binder from the cathode structure. This reaction was characterized thermally both previously (2) and in the present work.

Lithium-acetonitrile reaction.—Lithium and acetonitrile (AN) are unstable at ambient temperatures; a reaction starts slowly then accelerates and generates large amounts of heat. It is generally agreed that the heat and flammable gas generated in this reaction are a possible source of the explosions which have marred the generally good safety record of the Li-SO_2 battery. A typical DSC curve shown in Fig. 5A reveals a characteristic broad exotherm starting at about 40°C. Reaction rate is affected by purity both of Li and AN. Addition of 0.2% w/w of water to the AN greatly suppresses the exothermicity of the reaction (Fig. 5B). A similiar suppression of Li-AN exothermicity is seen when the AN is saturated with LiBr (Fig. 5C). Lithium bromide additions were found to consistently mimic the effect of added water, whether or not excess solid LiBr was present. We presume this is indeed due to the presence of moisture in the very deliquescent LiBr. Even in a 0.2% relative humidity Dry Room, LiBr picks up water quite rapidly. DSC analysis of an (Li + LiBr) mixture gives an exotherm at 140°C despite starting with a vacuum-dried sample and working in a Dry Room (1, 3). This is apparently due to an Li-H_2O reaction. If an easily dried salt like $LiAsF_6$ is substituted for LiBr (Fig. 5D), the low temperature, Li-AN exotherm is again evident. The high temperature exotherm at the melting point of Li appears to involve the $LiAsF_6$, but is also in agreement with the previously recorded DSC curve (1) for Li plus the tetrasolvated salt, $Li(AN)_4AsF_6$ (11).

The effect of SO_2 concentration on the thermal behavior of the Li-AN system was studied in the presence of both the "active" (LiBr) and "reserve" ($LiAsF_6$) salts. Table II makes evident that the initiation temperature of the Li-AN reaction generally rises with increasing SO_2 concentrations. In the absence of SO_2 there is a slow, low temperature reaction as illustrated in Fig. 5A. At a level of 0.1M SO_2 (simulating that present in a discharged, SO_2-depleted Li-SO_2 cell) initiation temperature increases substantially. However, the delayed reaction is both more rapid and more exothermic (Fig. 6A, D, and E). At the 1.7M SO_2 level

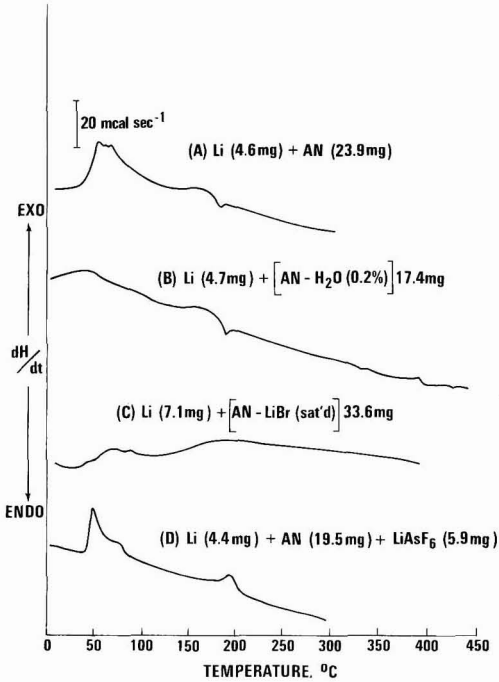

Fig. 5. Li-acetonitrile reactivity in absence of SO_2

(not illustrated) two exotherms were present corresponding to the Li-AN reaction and to one occurring at or near the melting point of Li. Finally, at concentrations of SO_2 found in the actual battery (about 14M), exothermic behavior occurs at higher temperatures (Fig. 6B and C). The heat liberated in the Li-AN reaction is similar to that noted in the absence of SO_2 and the dual peak behavior observed in 1.7M SO_2 is much less evident at these high SO_2 concentrations.

The quenching effect of water evident in Fig. 5 is no longer apparent in Fig. 6 when SO_2 is now present. Figure 6, curves D and E show big, sharp exotherms despite the addition of water. Perhaps the hydrolysis reaction between H_2O and SO_2 removes water from the system rendering it unable to quench the Li-AN reaction. The high temperature exotherm in Fig. 6D appears to result from the Li-$LiAsF_6$ reaction. This exotherm is regularly seen in the presence of $LiAsF_6$, but not in its absence (Fig. 6A).

Addition of propylene carbonate to a mixture of Li with the "active" battery electrolyte [AN-SO_2 (14M), LiBr] revealed that the Li-AN reaction is effectively quenched up to the vicinity of the melting point of Li (Table I, reaction 40).

Methyl isocyanate.—Rapid discharge caused by internal shorting has been reported to lead to the formation of methyl isocyanate (CH_3NCO) in the electrolyte

Table II. Effect of SO_2 concentration on initiation temperature for the Li-acetonitrile exotherm

SO_2 concentration (moles/liter)	Initiation temperature (°C)		
	No salt	LiBr	$LiAsF_6$
0	40	35	50
0.1	142	86	115
~1.7	122	122	142
~14*	—	156	180

* Battery electrolyte.

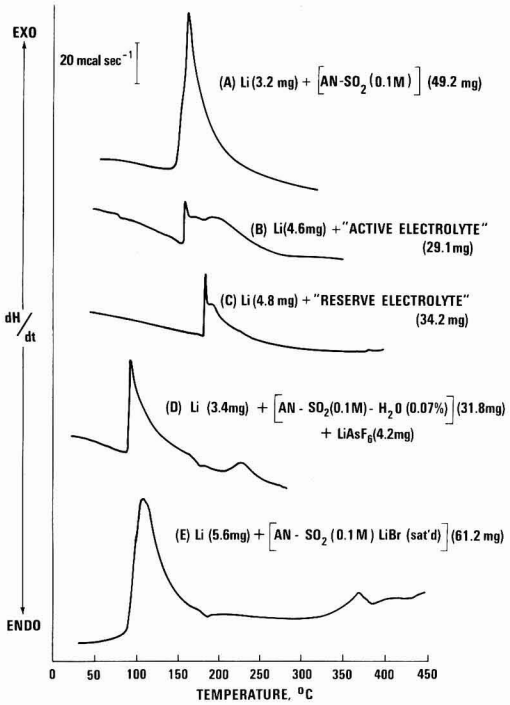

Fig. 6. Li-acetonitrile reactivity in presence of SO_2

of Li-SO_2 cells (12). The DSC curve for the reaction of Li with CH_3NCO is presented in Fig. 7. The reaction is slower than some of the explosive reactions reported here and elsewhere in this system (2). However it begins at 152° (below the melting point of Li) and generates substantial amounts of heat.

Thionyl Chloride System

Table III summarizes the data. The only previous thermal analysis work in this system is that of Dey *et al.* (5). Their work was limited to relatively low temperatures by the use of sealed glass ampuls as sample cups. In Li-containing mixtures, runs were usually terminated at little over 200°C by destructive reaction of molten Li with the glass container. Mixtures containing $SOCl_2$ developed high pressures which burst the cup at temperatures from 76° to 270°C. Cups used in the present work were normally hermetic up to at least 500°C.

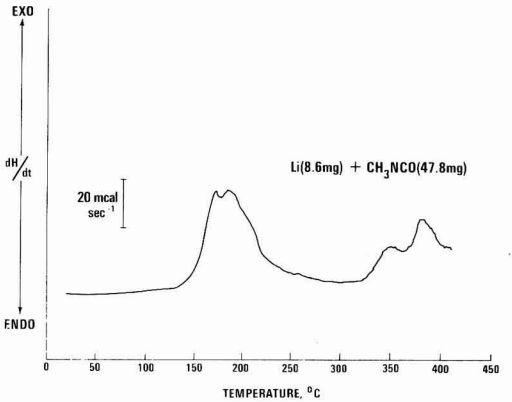

Fig. 7. Reactivity of lithium with methyl isocyanate

Initial components.—Figure 8E shows that the active materials of the Li-$SOCl_2$ battery display no reactivity together up to 335°C cutoff at which the DSC temperature scan was automatically terminated. The chloroluminate by itself melts at about 143°C (Fig. 8A) in agreement with the literature. Mixed with Li in Fig. 8B, the salt rapidly and exothermically reacts near its melting point. Thionyl chloride alone (Fig. 8C) began breaking up (into $SO_2 + S_2Cl_2 + Cl_2$) at about 212°C, but the thermal effects are small. In Fig. 8D we see essentially the same thing with Li unreactive up to at least 345°C. Finally Fig. 8E brings together conductive salt and both active materials. This combination suppresses both the Li-$LiAlCl_4$ reaction of Fig. 8B and the $SOCl_2$ decomposition evident in Fig. 8C and D. Thus, the initially present components of an undischarged battery seem quite unreactive over a wide temperature range even after the lithium has melted.

Possible discharge products.—Under this heading we include products of the direct electrode reactions and also secondary products resulting from further reaction (*e.g.* direct product S further reacts giving secondary product Li_2S).

Sulfur.—Figure 9 shows DSC curves for combinations containing elemental sulfur. In combination with Li (Fig. 9A) the usual violent reaction at sulfur's melting point was observed. This Li-S reaction is noticeably absent from Fig. 9B where no exotherm appears at all until 400°C. In Fig. 9B's mixture, if all the S dissolved in the electrolyte, its concentration would be about 9M. The solubility of S in the electrolyte rises with temperature and is about 1.5M at 50°C (16). So in this run, above the melting point of S, both molten S and high concentrations of dissolved S should be present. Presumably the $SOCl_2$ protects Li from reacting with both molten and dissolved S by virtue of a passivating film of LiCl as in the battery. The 400°C exotherm may be a belated Li-S reaction occurring 300°C higher than usual. Thus we have confirmed a previous find of the beneficial effect of $SOCl_2$ (5) and extended it to 400°C. Figure 9C shows the in-

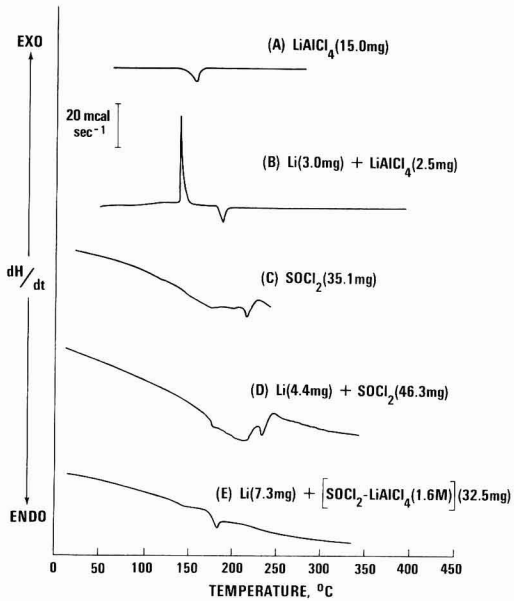

Fig. 8. Reactivity of the major initial components of the Li-$SOCl_2$ battery.

Table III. Summary of DSC results for Li/$SOCl_2$ system

Reaction	Reactants	Cutoff temperature (°C)†	Transition temperature (°C)‡ Endothermic	Exothermic
1	$SOCl_2$	241	212	214
2	$LiAlCl_4$	271	143	—
3	Li + $SOCl_2$	338	176	217, 231
4	Li + $LiAlCl_4$	410	181	137(5)
5	Li + Li_2SO_4	400	181	—
6	Li + S_2Cl_2	343	172	—
7	$SOCl_2$ + Li_3N	346	—	196(70)
8	$SOCl_2$ + Li_2S	276	—	—
9	$SOCl_2$ + C	241	—	—
10	Li + [$SOCl_2$-$LiAlCl_4$]*	329	177	—
11	[$SOCl_2$-$LiAlCl_4$] + S	391	236	—
12	[$SOCl_2$-$LiAlCl_4$] + Li_3N	367	—	132(150)
13	[$SOCl_2$-$LiAlCl_4$] + Li_2S	367	—	—
14	Li + $SOCl_2$ + C	343	169	—
15	Li + $LiAlCl_4$ + C	362	179	137(5)
16	Li + [$SOCl_2$-$LiAlCl_4$] + C	350	—	54, 326(25)
17	Li + [$SOCl_2$-$LiAlCl_4$] + C	302	167	169, 204
18	Li + [$SOCl_2$-$LiAlCl_4$] + C	362	181	85
19	Li + [$SOCl_2$-$LiAlCl_4$] + Cu	408	186	—
20	Li + [$SOCl_2$-$LiAlCl_4$] + S	414	184	395(15)
21	[$SOCl_2$-$LiAlCl_4$] + C + S	384	—	—
22	[$SOCl_2$-$LiAlCl_4$] + C + Cu	408	—	—
23	Li + $SOCl_2$ + LiCl + C	362	187	—
24	Li + $SOCl_2$ + Li_2SO_4 + C	362	181	—
25	Li + [$SOCl_2$-$LiAlCl_4$-1% H_2O + C]	455	180	378
26	Li + [$SOCl_2$-$LiAlCl_4$-SO_2] (satd.) + S	414	189	—
27	Li + [$SOCl_2$-$LiAlCl_4$] + C + Cu	417	177	83(30), 348(25)
28	Li + [$SOCl_2$-$LiAlCl_4$-SO_2 (satd.)] + C + S	408	181	88, 181(75)
29	Li-B alloy + $LiAlCl_4$	369	181	137
30	Li-B alloy + $SOCl_2$	343	192	231, 249
31	Li-B alloy + [$SOCl_2$-$LiAlCl_4$]	343	172	—
32	B + [$SOCl_2$-$LiAlCl_4$]	395	—	—
33	Li-B alloy + [$SOCl_2$-$LiAlCl_4$] + C	391	172	59(20), 322(75)

* Ingredients within the square brackets are a homogeneous solution.
† Temperature at which the DSC linearly programmed temperature scan was terminated.
‡ Figures in parenthesis are the increase in the sample temperature above the linearly programmed temperature.

ertness of S with the electrolyte. The addition of carbon black to the ingredients of Fig. 9C also gave an inert mixture (reaction 21, Table III). The DSC trace is not illustrated; it was thermally featureless in the range studied (up to 384°C). We have found carbon to catalyze the reaction of $SOCl_2$ with Li (see below) but evidently it has no effect on the (S + $SOCl_2$) reaction. The small endotherms in Fig. 9B and C at about 250°C may be associated with the reaction

$$3S + 2SOCl_2 \rightarrow 2S_2Cl_2 + SO_2 \qquad [1]$$

Calculation indicates this to be an endothermic reaction (14). Furthermore we always observed a clear, boiling liquid (presumably SO_2 solution) when cups initially containing (S + $SOCl_2$) were unsealed at room temperature at the end of the run.

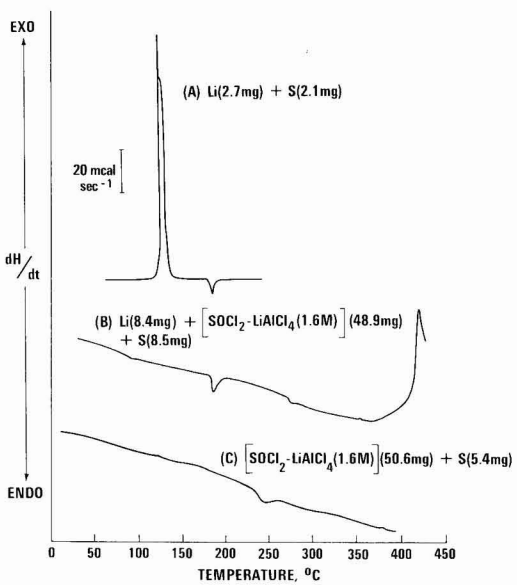

Fig. 9. Reactivity of mixtures containing elemental sulfur

Lithium sulfide.—Some workers have reported (5, 13) that anhydrous Li_2S reacts violently with $SOCl_2$ generating considerable heat and gas while others (14) found this combination to be inert. The present work has shown that Li_2S is essentially unreactive with $SOCl_2$ up to a 276°C cutoff and with $SOCl_2$-1.6M $LiAlCl_4$ up to a 367°C cutoff. The DSC curves were basically featureless and they are not illustrated. (See Table III, reactions 8 and 13.)

Sulfur dioxide.—This is generally accepted as one of the main products of the battery discharge reaction. We showed above that SO_2 retards the Li-AN reaction. We now wished to determine if SO_2 could deactivate the most reactive mixtures in the $SOCl_2$ system. Accordingly, we saturated a portion of the 1.6M $LiAlCl_4$-$SOCl_2$ electrolyte with SO_2 at 1 atm and room temperature. The SO_2 concentration was 3-4M (16). A DSC curve recorded to 414°C for this solution with added Li and S (reaction 26, Table III) showed no significant change in reactivity *vs.* the SO_2-free solution illustrated in Fig. 9B. Furthermore, Fig. 10D shows that the catalytic effect of carbon on the Li-$SOCl_2$-$LiAlCl_4$ mixture (discussed below) proceeded unimpeded, by the presence of SO_2. Thus for these combinations, at least, SO_2 has no passivating effect in the $SOCl_2$ system.

Lithium sulfate, lithium chloride, sulfur monochloride.—Both sulfate and sulfite have been reported as low temperature discharge products of the thionyl chloride battery (14). Lithium sulfite has been previously studied (2, 5) with conflicting results, though the preponderance of evidence favors its nonreactivity. The present work has found lithium sulfate to be quite unreactive to Li up to a 400°C cutoff (reaction 5, Table III). It was also inert in combination with Li, C, and $SOCl_2$-$LiAlCl_4$. Sulfur monochloride, S_2Cl_2, is known to result from the thermal decomposition of $SOCl_2$ especially in the presence of trace catalysts like $FeCl_3$ (14) as described above. Thus we tested its reactivity with Li (reaction 6, Table III). It was quite inert over

the range studied, up to 346°C. Dey (5) had reported a strong exotherm at 302°C for (Li + S + S_2Cl_2). Lithium chloride, one of the main discharge products formed in the cathode appears quite inert (to a 362°C cutoff) in combination with Li, C, and $SOCl_2$ (reaction 23, Table III). If $LiAlCl_4$ is substituted for LiCl, the mixture becomes extremely and consistently reactive; see discussion below of the effect of carbon in catalyzing reactions in this system (Fig. 10).

Catalysis of reactions by carbon black.—We invariably found that whenever an Li/C mixture was contacted with the 1.6M $LiAlCl_4$-$SOCl_2$ electrolyte, a reactive mixture was produced. In these experiments the Shawinigan carbon black was pressed into both sides of a piece of flattened Li and the electrolyte dripped onto this sandwich. The mixture always warmed up the Nimonic cups to about 40°-50°C. Occasionally the reaction was so vigorous that the $SOCl_2$ boiled dry and more was added before the cup was sealed. Accordingly we began precooling cups in Dry Ice (−80°C) before adding electrolyte so as to postpone reaction and record it on the DSC trace. Figure 10 shows four DSC curves of mixtures involving Li-C-$SOCl_2$-$LiAlCl_4$. The addition of carbon black transformed the inert Li-$SOCl_2$-$LiAlCl_4$ mixture into a consistently reactive one. However the data were unpredictable both as to peak height and even peak position. We include Fig. 10C, which actually contained Li-B alloy rather than Li, as the present work has shown the alloy behaves essentially the same as Li. The mixture of Fig. 10D contained S and SO_2 in addition to Li, C, $SOCl_2$, and $LiAlCl_4$. However, we believe that the reactivity of this mixture is due to the presence of carbon rather than to that of S and/or SO_2. This is supported by the fact that the mixture (Li + $SOCl_2$ + $LiAlCl_4$ + S + SO_2) was quite inert up to its 414°C cutoff (reaction 26, Table III). We should point out that the mixture referred to in Fig. 10D contains virtually all of the most reactive ingredients thought to be present in a partly-discharged thionyl chloride battery.

Of the four possible mixtures employing ternary combinations of the ingredients Li, C, $SOCl_2$, and $LiAlCl_4$, none approached the reactivity of the quaternary mixture (Li + $SOCl_2$ + $LiAlCl_4$ was inert, see Fig. 8E; Li + C + $SOCl_2$ was inert to a 343°C cutoff, see reaction 14; Li + C + $LiAlCl_4$ was no more reactive than Li + $LiAlCl_4$, see reaction 15; C + $SOCl_2$ + $LiAlCl_4$ was inert, even with added S to a 384°C cutoff, see reaction 21). Consistent strong reactivity was observed only when all four ingredients were together. This is understandable if we assume that a local cell is formed which activates the Li-$SOCl_2$ reaction. Carbon's function is to provide a catalytically active surface at which $SOCl_2$ can be cathodically reduced at high rates by electrons emanating from anodically dissolving lithium. Essentially we regard each carbon particle stuck in the Li surface as forming a tiny, short-circuited Li-$SOCl_2$ battery.

This is supported by the fact that the corrosion of a variety of metals in the $LiAlCl_4$-$SOCl_2$ electrolyte is greatly accelerated if they are electrically contacted with carbon, probably due to the local cell effect (4). So the only function of $LiAlCl_4$ is to render the $SOCl_2$ highly conductive so as to complete the ionic part of the local cell circuit. Accordingly we tried to replace it with other conductive, nonreactive Li salts. We tried Li_2SO_4 and LiCl separately in mixtures with (Li + C + $SOCl_2$). However DSC curves of these two mixtures showed them to be inert up to their 362°C cutoff (Table III, reactions 23 and 24). Apparently these salts did not impart the necessary ionic conductivity, probably due to a limited solubility in $SOCl_2$.

The local cell idea is of course not new; it is very old and by now obvious to skilled electrochemists. However it is useful to point out the obvious if its important implications for battery safety have been previously overlooked. The above experiments are very suggestive in this connection. Cathode failure in one out of a chain of cells will cause Li to be plated out onto the carbon of the failed cathode. Indeed, complete reversal of cell voltage is not needed. Whenever cathode voltage falls below about 1V *vs.* Li, this potentially dangerous mixture may form by undervoltage deposition of Li into carbon (20). Recent work in our laboratories has shown that the situation may involve more than a simple Li-C mixture. ESCA(XPS) studies indicate that compound formation occurs in intimate mixtures of elemental Li and C.

Effect of copper.—In view of the use of powdered copper metal in the cathodes of some Li-$SOCl_2$ batteries (17) we studied the effect of added Cu on reactivity in this system. Figure 11 shows the effect of adding 99.9% pure Cu powder to the (Li + C + $SOCl_2$-$LiAlCl_4$) mixture. Reactivity seems to be enhanced *vs.* Fig. 10, not so much in terms of a more rapid reaction with high peak temperatures, but rather in terms of a larger total amount of heat liberated. The low temperature exotherm starting at about 80°C is much

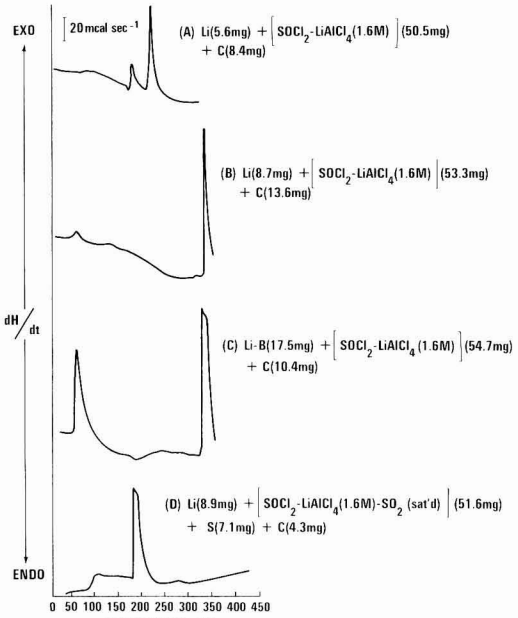

Fig. 10. Catalysis by carbon black of Li-$SOCl_2$-$LiAlCl_4$ reactivity

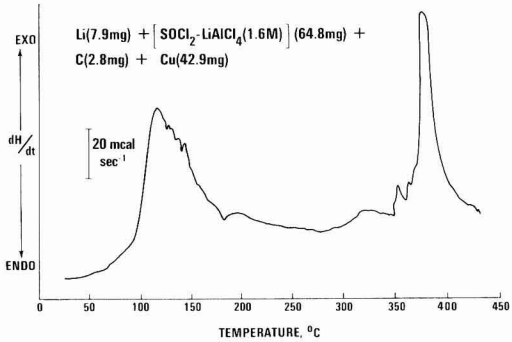

Fig. 11. Enhancement by copper of the carbon-catalysis of Li-$SOCl_2$-$LiAlCl_4$ reactivity.

more pronounced than in the absence of Cu. Reactions 19 and 22 where first C then Li was omitted from the ingredients of Fig. 11 were quite inert up to 410°C. Thus both Li and C are necessary for reactivity. It appears that the basic reactivity of the system is accelerated by the highly conductive Cu.

Carbon catalysis in the SO_2-acetonitrile-electrolyte?—Preliminary work has produced evidence that carbon black is catalytically active also in this electrolyte. In an acetonitrile solution which was saturated with LiBr and 1.7M in SO_2, the Li-AN reaction initiation temperature was 122°C. However in the presence of carbon the reaction began at about 35°C (see reactions 34 and 38, Table I). On the other hand, in a solution that was identical except that it contained no SO_2, added carbon had no clear effect on the reactivity (reactions 24 and 32, Table I). More work is needed to better characterize carbon's effect in the SO_2 battery electrolyte.

Impurities.—Lithium nitride.—Li_3N is a very reactive material. When mixed with water it catches fire and burns violently with great heat. It was recently reported (14) to react violently with $SOCl_2$, but only if it was finely divided and if mixing were done in a normally humid atmosphere. In an argon atmosphere containing 1 ppm water, no reaction occurred. This applied both to the commercially obtained powder and to nodules of reaction product removed from air-reacted Li foil. The reaction with $SOCl_2$ could be hazardous if Li_3N forms on the Li anode during cell assembly or during the disassembly of discharged cells. In the present work no reaction was noted on mixing Li_3N with $SOCl_2$ in our Dry Room at 0.25% R.H. (81 ppm water). Figure 12A shows that Li and Li_3N commercial powder are quite inert together up to the 390°C cut-off, whereas 12B and 12C show that Li_3N undergoes violent exotherms with $SOCl_2$ and with $SOCl_2$-$LiAlCl_4$. At about 130°C, the exotherm shown in Fig. 12C was associated with the biggest temperature excursion (150°C) observed in the present work (see reaction 12, Table III).

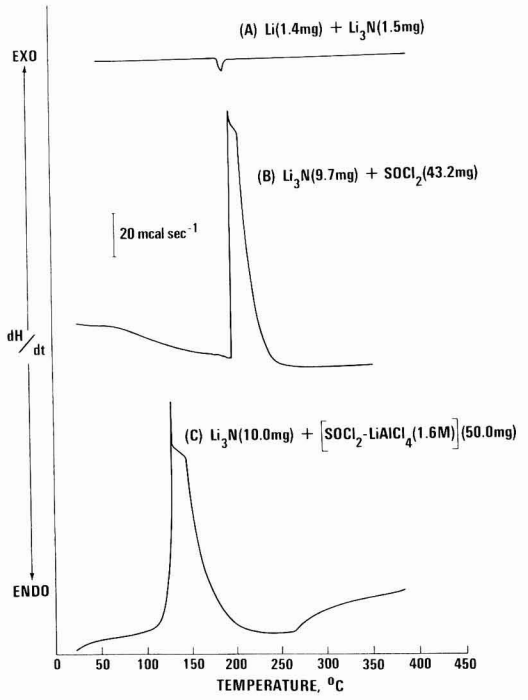

Fig. 12. Reactivity of lithium nitride

Water.—It is of interest to study the effect of added water on reactivities since this material is a ubiquitous contaminant which is very strongly absorbed by most battery active-materials. We added water only to the most consistently reactive combination, namely (Li + C + $SOCl_2$ + $LiAlCl_4$). Water added to the electrolyte to the extent of 1% by weight gave an immediate white precipitate. We homogenized the electrolyte before adding it to the Li/C sandwich so as to include some of this precipitate in the reaction mixture. This work is presently at an early stage, but it appears that this trace amount of water does exert some quenching effect on exothermicity in this system, at least in the lower half of the temperature range of Fig. 10. This contrasts with Dey's finding (5) that moisture enhances the reactivity of $SOCl_2$ with Li_2S, with Li_2O and with LiOH.

Relative Reactivities of Pure Lithium vs. Lithium-Boron Alloy

The Li-B alloy is a refractory Li-B solid compound permeated with fine pores filled with elemental Li. Because of its high temperature rigidity and the presence of the relatively inert boron, the alloy was considered as potentially safer than pure Li as a battery anode. In preparing reaction mixtures for DSC runs we used twice the mass of Li-B *vs.* that of pure Li. Since elemental Li forms 51% w/w of our alloy composition this provides for a just comparison of exothermicity. The results showed with two exceptions, no significant difference in reactivity between the alloy and pure lithium. Reaction initiation temperatures and temperature excursions shown in Tables I and III are quite similar for the two materials.

In only one case was Li-B clearly less reactive than Li. This occurred with $Li_2S_2O_3$, where temperature excursions for the major (~230°C) of the two exotherms were fifteen times greater for pure Li (150° *vs.* 10°, see reactions 13 and 43, Table I). The second difference with pure Li was in the C-$SOCl_2$-$LiAlCl_4$ system. Here the catalytic effect of carbon on this system's reactivity was somewhat greater with the alloy. This is illustrated in Fig. 10C.

Conclusions

1. For Li-SO_2-$LiAsF_6$ cell discharge products, the discharged cathode gave a significant exotherm with Li while films formed on the anode were inert to Li.

2. Trace additions of water greatly lower the exothermicity of the Li-acetonitrile (AN) reaction. Water entering the electrolyte via the extremely hygroscopic LiBr electrolyte-salt had the same effect.

3. The addition of SO_2 delays initiation of the Li-AN reaction to higher temperatures. An SO_2 concentration of 0.1M is sufficient to realize most of the rise in initiation temperature. The delayed, higher temperature reaction occurs more rapidly. The quenching effect of water on Li-AN reaction is no longer observed when SO_2 is present.

4. Addition of propylene carbonate to Li-AN-SO_2-LiBr delays the Li-AN reaction to the vicinity of the melting point of Li.

5. The Li-$SOCl_2$-$LiAlCl_4$ mixture is quite unreactive over a wide range of temperature, well above the melting point of Li.

6. The presence of carbon black converts the inert, Li-$SOCl_2$-$LiAlCl_4$ mixture into one which is highly and consistently reactive. This may affect battery safety because cathode failure in one out of a chain of cells will cause Li to be plated out onto the carbon of the failed cathode. Indeed complete reversal of cell voltage is not needed. Whenever the cathode voltage falls below about one volt *vs.* Li, this potentially dangerous mixture may form by undervoltage deposition of Li into carbon (20).

7. Some evidence was obtained for carbon catalysis also in the Li-SO_2 system.

8. The addition of copper powder enhanced carbon's catalytic effect on the reactivity of Li-$SOCl_2$-$LiAlCl_4$. Trace additions of water, on the other hand, had a counteracting effect on the carbon-catalyzed reactivity.

9. The presence of $SOCl_2$ delays the very exothermic Li-S reaction by at least 300°C.

10. We confirmed the nonreactivity of $SOCl_2$ with Li_2S.

11. Sulfur dioxide seems to have no retarding effect on reactions in the $SOCl_2$ system (in contrast to its suppression of the Li-AN reaction).

12. We confirmed the violent reactivity of Li_3N with $SOCl_2$.

13. We found no significant difference in chemical reactivity between lithium-boron alloy and pure lithium.

Acknowledgments

The authors thank the Independent Research Program of the Naval Surface Weapons Center and the Naval Sea Systems Command (PMS407) for financial support of this work.

Manuscript submitted June 3, 1980; revised manuscript received Oct. 20, 1980.

Any discussion of this paper will appear in a Discussion Section to be published in the December 1981 JOURNAL. All discussions for the December 1981 Discussion Section should be submitted by Aug. 1, 1981.

Publication costs of this article were assisted by the Naval Surface Weapons Center.

REFERENCES

1. W. P. Kilroy and S. Dallek, NSWC/WOL TR 78-156 (Nov. 13, 1978).
2. W. P. Kilroy and S. Dallek, *J. Power Sources*, **3**, 291 (1978).
3. A. N. Dey and R. W. Holmes, *This Journal*, **126**, 1637 (1979).
4. A. N. Dey, Final Report ERADCOM, DELET-TR-74-0109-F, P. R. Mallory and Co. Inc. (July 1978).
5. A. N. Dey, in Proceedings of the 28th Power Sources Symposium, Atlantic City, N.J., June 1978.
6. S. D. James and L. E. DeVries, *This Journal*, **123**, 321 (1976); **126**, 993 (1979).
7. B. F. Larrick, S. D. James, and R. Szwarc, in Proceedings of the 28th Power Sources Symposium, Atlantic City, N.J., June 1978.
8. S. Dallek, D. W. Ernst, and B. F. Larrick, *This Journal*, **126**, 866 (1979).
9. D. Lyons and G. Nickless, in "Inorganic Sulfur Chemistry," G. Nickless, Editor, p. 521, Elsevier Publishing Co., Netherlands (1968).
10. O. Dienes and G. Elstner, *Z. Anorg. Allg. Chem.*, **191**, 340 (1930).
11. W. P. Kilroy, *J. Solution Chem.*, **6**, 487 (1977).
12. G. Reinhard and A. R. Jones, Eastern Airlines Engineering Labs (MIAEL) Report, April 8, 1975, to Chromalloy Corp., Hollywood, Florida.
13. G. L. Holleck, M. J. Turchan, and D. R. Cogley, ECOM-74-0030-7 (January 1975).
14. C. R. Schlaikjer, F. Goebel, R. Staniewicz, and K. Klinedinst, Final Report on Contract No. N00014-76-C-0524 (1-76 to 10-78) (January 1979).
15. C. R. Schlaikjer, F. Goebel, and N. Marincic, *This Journal*, **126**, 513 (1979).
16. K. A. Klinedinst and M. L. McLaughlin, *J. Chem. Eng. Data*, **24**, 203 (1979).
17. L. R. Giattino, U.S. Pat. 4,167,608 (1979).
18. W. P. Kilroy, Unpublished data.
19. P. M. Shah and W. J. Eppley, in Proceedings of the 28th Power Sources Symposium, Atlantic City, N.J., June 1978.
20. J. O. Besenhard and H. P. Fritz, *J. Electroanal. Chem. Interfacial Electrochem.*, **53**, 329 (1974).

Dynamic Microcalorimetry: Thermal Effects of Miniature Alkaline Cells under Load

Frank B. Tudron*

Union Carbide Corporation, Battery Products Division, Parma, Ohio 44130

ABSTRACT

A nonrigorous thermodynamic calculation is performed yielding an expression which relates the rate of heat evolution by a miniature battery under load to the current flowing through the cell. At small values of I, the expression predicts a linear plot of $-dQ/dt$ *vs.* I. To demonstrate this behavior, thermal effects of an Ag_2O-Zn cell are measured under various conditions of constant load. The heat evolution data vary linearly with I over the range 0.300 μA, with a slope of 74.3 mV and an intercept of 2.1 μW. The slope gives a value of -0.175 mV/K for $(\partial E/\partial T)_p$, corresponding to the formation of inactive ZnO as a discharge product at the anode. Additional data obtained for HgO-Zn and MnO_2-Zn cells with alkaline electrolytes are present. The heat release data do not vary linearly with current. Analysis of the discharge mechanism for the HgO system is possible. The discharge mechanism for the HgO cathode can be represented by a simple reduction to elemental mercury with formation of inactive ZnO as the discharge product at the anode.

Recently, the area of battery thermodynamics has shown significant activity (1-4). This activity is in part explained by the commercial availability of very sensitive differential calorimeters designed to accept miniature sized batteries. The utility of these so-called microcalorimeters has been demonstrated in a number of applications. One application is the evaluation of self-discharge processes in small batteries (1, 9). These processes will, of course, determine the shelf-life of the cell and will also be important in determining the cell's operating life. Other processes, however, also contribute to the observed thermal effects. As they may not be related to capacity loss, a straightforward calculation of shelf-life from raw microcalorimeter data is often quite misleading. A second application is in the area of cell discharge mechanisms. Since the thermal effects measured are sensitive to the reaction path, mechanistic information can be obtained by comparing the results of the microcalorimeter experiment

* Electrochemical Society Active Member.

Key words: battery thermodynamics, silver oxide-zinc cells, mercuric oxide-zinc cells.

to predictions based on various models of the cell discharge (3, 4).

The purpose of the paper is twofold. The first goal is the derivation of an equation describing the dependence of the rate of heat release from a battery on the current flowing through the cell. The second goal is to present microcalorimeter data obtained for miniature alkaline cells of the types Ag_2O-Zn, HgO-Zn, and MnO_2-Zn and to analyze these data by means of the equation presented, thereby relating the results to the discharge mechanism.

Theory

The dependence of the rate of heat release in a galvanic cell on current flowing in the cell has been previously derived in a rigorous fashion (5-8). This exercise will be performed here in a totally nonrigorous way merely to establish notation.

The first law of thermodynamics may be written $\Delta U = Q - W$, whereby the increase of the internal energy (ΔU) of the system (battery) is given by the heat flowing into the system less the work done by the system in the surroundings. What is measured by the microcalorimeter is the rate of heat flow out of the system (battery), *i.e.*

$$\frac{d}{dt}(-Q) = \frac{d}{dt}(-\Delta U - W)$$

Now $\Delta U = \Delta H - p\Delta V = \Delta H_f + \Delta H_{nf}$ where $p\Delta V$ term vanishes, the battery being a constant volume, sealed system.[1] Also, $\Delta H_f = \Delta G_f + T\Delta S_f$ and $\Delta H_{nf} = \Sigma_i \Delta H_i n_i$ where the sum is over all non-Faradaic processes. Thus

$$\frac{d}{dt}(-Q) = \frac{d}{dt}[-\Delta G_f - T\Delta S_f - \Sigma_i \Delta H_i \nu_i - I^2Rt]$$

$$= \frac{d}{dt}\left[nFE_o - Tn\mathbf{F}\left(\frac{\partial E}{\partial T}\right)_p - \Sigma_i \Delta H_i \nu_i - I^2 R_L t \right]$$

where R_L is the load resistance. Faraday's law may be written $It = n\mathbf{F}$. Consequently, for the Faradaic process $dn/dt = I/\mathbf{F}$. For the non-Faradaic processes, $d\nu_i/dt = v_i$ where v_i is the rate of the ith process. The equation can now be written

$$\frac{d}{dt}(-Q) = IE_o - IT\left(\frac{\partial E}{\partial T}\right)_p - \Sigma_i \Delta H_i v_i - I^2R$$

Now IR is the terminal potential and $E_o - IR$ is the polarization, η. Thus

$$\frac{d}{dt}(-Q) = \left[\eta - T\left(\frac{\partial E}{\partial T}\right)_p\right] I - \Sigma_i \Delta H_i v_i \quad [1]$$

which is the desired expression.

The shape of the curve obtained by plotting the calorimeter output *vs.* the current flowing through the battery will be determined by a number of factors. In the region of small polarization (*i.e.*, for small I), the curve will be essentially linear. As the current increases, η becomes larger and a divergence from linearity is observed. This is magnified by the fact that the rates of certain parasitic processes, v_i, are dependent on the concentration of certain species in solution, and a current dependence arises due to the last term in the equation. What we have is a limiting expression: as I approaches zero, linear behavior is observed.

Experimental

The microcalorimeter used in the present study is the Tronac Model 351 RA battery calorimeter. This device has been described extensively in the literature (1). The batteries used in the study are "Eveready" miniature alkaline cells. Pertinent data concerning cell specifications are given in Table I.

[1] The subscript "f" refers to Faradaic process, "nf" refers to non-Faradaic processes.

Table I. Specifications of batteries used in experiments

Cell type	UCC designation	Diameter (in.)	Height (in.)	Rated capacity (mA-hr)	Voltage (V)
Ag_2O-Zn	386	0.455	0.165	120	1.60
HgO-Zn	354	0.455	0.165	150	1.35
MnO_2-Zn	186	0.455	0.165	80	1.60*
HgO-Zn	E41	0.455	0.165	160	1.35

* Sloping discharge. Value reported is open-circuit voltage.

The value of the rate of heat release under open-circuit conditions was measured as follows. These cells were placed in an equilibration chamber immersed in the calorimeter water bath for 8-12 hr. The cells were then introduced into one of the microcalorimeter chambers designated as the sample chamber. The rate of heat release generally increased dramatically, but settled to a steady-state value within about 2 hr. This steady-state value minus the baseline value divided by the number of cells in the chamber is taken as the average rate of heat release.

Attempts to calculate shelf-life of a practical system from open-circuit microcalorimeter data are attended by many difficulties. As has been pointed out previously, many processes not associated with a decrease in capacity give rise to open-circuit heat production. As always, actual experimental determination of capacity following shelf storage is the most reliable indication of capacity maintenance.

To determine the rate of heat release under load, it was necessary to spot weld No. 25 AWG wires to both the cathode can and the anode cup of the cell. After equilibration, the cell was introduced into the sample chamber with the wires leading out to the surroundings. Here voltage measurements were obtained and resistors were attached. The wire was kept in good thermal contact with the aluminum calorimeter block to prevent spurious thermal effects.

To check the effectiveness of this technique, a 1 MΩ precision resistor was connected to two wires just as the cell was. Following equilibration, the resistor was placed in the sample chamber and the wires were connected to a Keithley Model 225 Current source. Figure 1 shows the result of successive applications of 1, 2, and 3 μA currents. The output power recorded agrees with that expected on the basis of heat dissipation due to I^2R loss. The wires exiting the chamber do not constitute a measurable heat leak.

All measurements were made at 25°C.

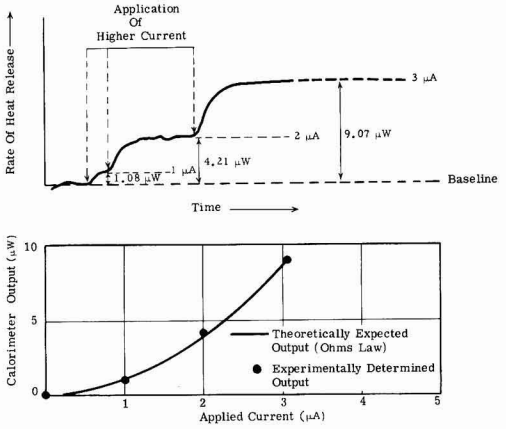

Fig. 1. Calibration of Tronac microcalorimeter by resistive technique.

Results and Discussion

The results of successive application of increasing loads to the cells, specified in Table I, are summarized along with polarization data and calculated values of current in Table II. The systems will be discussed individually.

Ag_2O-Zn.—Table II gives the values of the thermal effect along with the terminal voltage, load, polarization, and calculated current. As can be seen, the thermal output responds as would be expected: a smaller load results in a larger current and consequently, a larger thermal effect. The thermal effect is measured, as always, when the signal attains a steady-state value. Figure 2 is a plot of the rate of heat release (dQ/dt) *vs.* current (I). The discrete points are the experimental data. The data are linear over the region considered with intercept 2.1 μW and slope 74.3 mV. The solid curves are calculated using Eq. [1] with values of $(\partial E/\partial T)_p$ corresponding to formation of the oxidized forms of Zn indicated. The lower curve, that corresponding to the reaction

$$Zn + Ag_2O \rightarrow ZnO + 2Ag^\circ$$

fits the experimental values quite well. As is pointed out by Bode *et al.* (10), the thermal coefficient for the Ag_2O-Zn cell depends on the form in which the oxidized zinc deposits on the anode. Even if the electrolyte solution is not saturated with zincate, a thin film (oxide or hydroxide) is formed on the anode. It is this film that determines the anode thermodynamics, *i.e.*, the zinc electrode is an electrode of the second kind. If the film is inactive ZnO, the temperature coefficient for the cell is -0.177 mV/deg; if it is ϵ-$Zn(OH)_{2+}$ the temperature coefficient is -0.337 mV/deg. Using Eq. [1] and the experimental slope (74.3 mV) yields an experimental value of $(\partial E/\partial T)_p$ of -0.175 mV/K. This analysis of the microcalorimeter data indicates that the discharge product is inactive ZnO.

HgO-Zn.—The No. 354 HgO-Zn cell attains steady-state values of heat release much as does the No. 386 Ag_2O-Zn. Table II summarizes the data. In an attempt to analyze the data using Eq. [1], the plots depicted in Fig. 3 were made. Two cell reactions were considered

Table II. Microcalorimetry data for miniature alkaline cells under load

R_{Load} (kΩ)	V_{op} (V)	η(mV)	I (μA)	$\frac{dQ}{dt}$ (μW)
		No. 386 Cell		
60	1.612	5	26.9	4.43
30	1.607	10	53.6	6.31
10	1.588	29	158.8	13.5
7	1.582	35	226.0	19.8
5	1.581	36	316.4	26.3
O.C.	1.617	—	—	2.03
		No. 354 Cell		
30	1.344	12	44.8	1.17
10	1.332	24	131.7	2.90
5	1.320	36	257.6	7.22
2	1.303	53	625.5	24.8
O.C.	1.356	—	—	0.93
		No. E41 Cell		
10	1.4655-1.4536	18.2-30.1	146-145	5.59-7.92 (2 hr)
7	1.4417-1.4348	42.0-48.9	206-205	12.82-14.45 (1 hr)
5	1.4215-1.4098	62.2-73.9	284-282	Not measured
O.C.	1.4837	—	—	3.26
		No. 186 Cell		
10	1.5685	6.9	156.9	6.06
7	1.5539	21.5	222.0	9.32
5	1.5423	33.1	308.5	13.51-14.91 (1 hr)
O.C.	1.5754	—	—	2.33

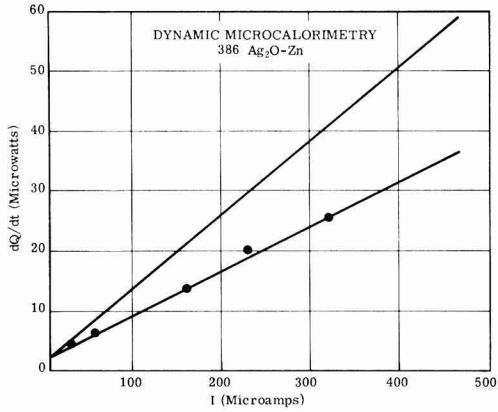

Fig. 2. Current dependence of the thermal effect for a No. 386 Ag_2O-Zn cell. The solid lines are calculated from theory based on $Zn(OH)_2$ (upper curve) and on ZnO (lower curve). The discrete points are experimental data.

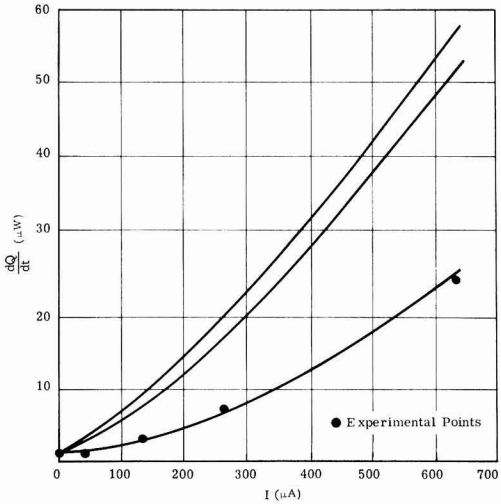

Fig. 3. Current dependence of the thermal effect for a No. 354 HgO-Zn cell. The solid lines are calculated from theory based on a two-electron reduction with $Zn(OH)_2$ formation (top curve), a two-electron reduction with ZnO formation (bottom curve), and a one-electron reduction with ZnO formation (middle curve).

$$Zn + HgO \rightarrow Hg + ZnO$$

$$\left(\frac{\partial E}{\partial T}\right)_p = 0.040 \text{ mV/K}$$

$$Zn + HgO + H_2O \rightarrow Hg + Zn(OH)_2$$

$$\left(\frac{\partial E}{\partial T}\right)_p = -0.128 \text{ mV/K}$$

As shown in the figure, the first reaction represents the experimental data well. Just as in the case of an Ag_2O-Zn cell, the discharge product at the anode is ZnO instead of $Zn(OH)_2$. That this is the case in these systems can be attributed to the small amount of water present in these limited electrolyte cells.

One other possibility which must be considered seriously is an alternate discharge mechanism proposed by Yosizawa *et al.* (11). According to this model, mercuric oxide is reduced to an intermediate product

which then disproportionates to elemental mercury and mercuric oxide

$$HgO + 1/2\,H_2O + e^- = (Hg_2O)_{1/2} + OH^-$$

$$2(Hg_2O)_{1/2} = HgO + Hg$$

Using an estimated value of $S°$ for Hg_2O (12) of 30 eu gives $(\partial E/\partial T)_p = -0.09$ mV/K. The resulting curve is also shown in Fig. 3. Clearly, it does not fit the data. Mercurous species are not part of the mechanism.

The behavior of the No. E41 cell is remarkably different from that of the No. 354 cell (see Fig. 4). The rate of heat release does not come to a steady-state value, but rather increases linearly with time. The difference between this cell and the No. 354 is the presence of MnO_2 in the cathode. The rate at which dQ/dt increases with time is a function of the current flowing through the cell, increasing with increasing current. Figure 4 shows the result of allowing the cell to remain on a 10 kΩ load. Increase of the thermal effect is observed for 17.5 hr. This corresponds to 91% of the MnO_2 contained in the cell, assuming a one-electron reduction. It should be noted that such an effect will not be seen in Ag_2O cells (*e.g.*, No. 386) since the MnO_2 potential is lower than Ag_2O. The first material to discharge in an Ag_2O cell is Ag_2O.

The behavior of the cells is explained by recalling the sigmoid nature of the MnO_2 discharge curve. After a load is applied to the cell, the voltage, and consequently the current, continues to decrease for a rather long time. The basic microcalorimetry equation must be written

$$\frac{dQ}{dt} = \left[\, \eta(t) - T\left(\frac{\partial E}{\partial T}\right)_p \,\right] I(t) - \Sigma_{nf}\Delta H_{nf}\upsilon_{nf}$$

The variation of the voltage of a No. E41 cell is shown in Fig. 5. If this data is inserted into the above equation, the experimental data (represented by the symbol ⊙) can be fit assuming a value of $(\partial E/\partial T)_p = -49$ μV/K (see Fig. 6).

MnO_2-Zn.—The fact that MnO_2 is responsible for the unique behavior of fresh E41 cells is corroborated by microcalorimetry experiments on the No. 186 MnO_2-Zn cells. Figure 7 shows the data obtained by applying various loads to the cell. The same linear variation of thermal effect with time is observed indicating that MnO_2 is the material responsible for the unique behavior of the E41 cell. Reaction products cannot be determined by this method for systems with cathodes exhibiting such variations of operating potential with time.

Conclusions

It has been shown that microcalorimetry is an effective tool for the generation of mechanistic information for practical battery systems. An expression for the dependence of the rate of heat release on current has been derived. This expression has been used to analyze data obtained for an Ag_2O-Zn and for an HgO-Zn cell. In both cases it is found that ZnO is formed rather than $Zn(OH)_2$ upon discharge. The effect of time variation of the cell polarization on the thermal effect has been observed in certain cells containing MnO_2. This effect is attributed to the sigmoid nature of the MnO_2

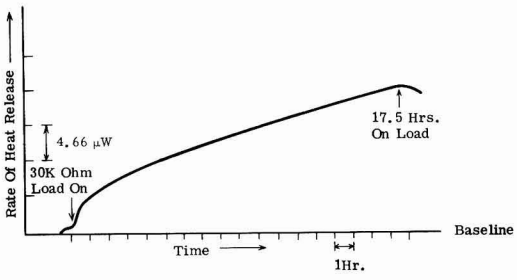

Fig. 4. Response of a No. E41 HgO-Zn cell to the application of a 30 kΩ resistive load.

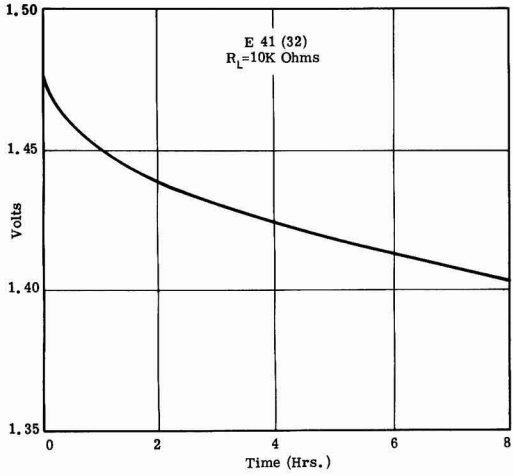

Fig. 5. Variation of the operating voltage of a No. E41 HgO-Zn cell under 10 kΩ resistive load.

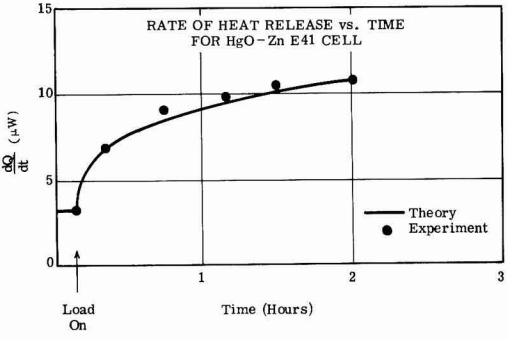

Fig. 6. Calculated response of a No. E41 HgO-Zn cell to a 10 kΩ resistive load. The procedure is described in the text.

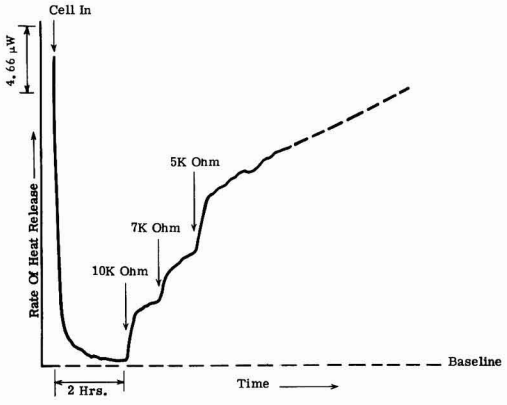

Fig. 7. Response of a No. 186 MnO_2-Zn cell to the application of various resistive loads.

discharge, and thus, ultimately, to the mechanism of MnO_2 reduction.

Acknowledgment

The authors would like to thank S. J. Cieszewski for her able assistance in performing the microcalorimeter experiments and in organizing the data.

Manuscript submitted Oct. 31, 1979; revised manuscript received Oct. 10, 1980. This was Paper 167 presented at the Los Angeles, California, Meeting of the Society, Oct. 14-19, 1979.

Any discussion of this paper will appear in a Discussion Section to be published in the December 1981 JOURNAL. All discussions for the December 1981 Discussion Section should be submitted by Aug. 1, 1981.

Publication costs of this article were assisted by Union Carbide Corporation.

REFERENCES

1. L. D. Hansen and R. M. Hart, *This Journal*, **125**, 842 (1978).
2. a. D. F. Untereker and B. B. Owens, Paper 13 presented at the 33rd Annual Calorimetry Conference, Utah State University, Logan, Utah, July 26-28, 1978; b. D. F. Untereker and B. B. Owens, Paper 24 presented at The Electrochemical Society Meeting, Atlanta, Georgia, Oct. 9-14, 1977.
3. P. Bro, *This Journal*, **125**, 674 (1978).
4. H. Frank Gibbard and C. C. Chen, Paper 12 presented at the 33rd Annual Calorimetry Conference, Utah State University, Logan, Utah, July 26-28, 1978.
5. J. M. Sherfey and A. Brenner, *This Journal*, **105**, 665 (1958).
6. S. Gross, *Energy Conversion*, **9**, 55 (1969).
7. T. Jacobsen and G. H. J. Broers, *This Journal*, **124**, 210 (1977).
8. H. F. Gibbard, *ibid.*, **125**, 353 (1978).
9. H. A. Cataldi, in Proceedings of the 27th Power Sources Symposium, Atlantic City, N.J., June 21-24, 1976.
10. H. H. Bode with V. A. Oliapuram, D. Berndt, and P. Ness, in "Zinc-Silver Oxide Batteries," A. Fleischer and J. J. Lander, Editors, John Wiley & Sons, Inc., New York (1971).
11. S. Yosizawa, Z. Takehara, and Y. Namba, *J. Electrochem. Soc., Jpn.*, **30**, 185 (1962) and references therein.
12. J. P. Coughlin, U.S. Bureau of Mines, Bulletin 542, p. 30.

Separation Between Deterministic Response and Random Fluctuations by Means of the Cross-Power Spectrum in the Study of Electrochemical Noise

Ugo Bertocci*

National Bureau of Standards, Chemical Stability and Corrosion Division, Washington, D.C. 20234

ABSTRACT

It is shown that by calculating the cross-power spectrum between the input (the electrode potential) and the output (the cell current) of an electrochemical system under potentiostatic conditions, it is possible to identify which part of the cell current is the response to the input voltage and which part is caused by random fluctuations of the parameters characterizing the electrode. The noise introduced by the amplifiers can be measured separately and then subtracted from the signal. As an example, the current noise of an aluminum electrode below and at the pitting potential is examined. Both electrode impedance and spectral power density of the random fluctuations are obtained. It is shown that below the pitting potential random fluctuations are below the minimum detectable value of 10^{-23} A^2/cm^4 Hz.

In the analysis of electrochemical noise, an important problem is that of knowing which part of the output signal is caused by the input (*i.e.*, the deterministic response to the input) and which is caused by random fluctuations of the parameters characterizing the electrochemical system under study. Both parts can give important information, as long as they can be properly identified. The analysis is further complicated by the noise introduced by the amplifiers necessary to detect the generally small signals.

Digital signal processing equipment can be used, with the aid of the Fast Fourier Transform algorithm, to transform the signal received into the frequency domain, which simplifies the task of analyzing and manipulating the results. A two-channel spectrum analyzer can receive a signal which is the difference between reference electrode and working electrode as well as a second signal proportional to the current flowing into a three-electrode, potentiostatted cell, and calculate the cross-power spectrum between the two signals. The purpose of this note is to show that the cross-power spectrum can be employed for separating the various components of the output signal.

* Electrochemical Society Active Member.

Key words: aluminum, cross-power spectrum, electrochemical noise, electrode impedance, pitting.

Statement of the Problem and Mathematical Treatment

In electrochemical studies it is expedient in general to maintain the working electrode at constant potential by means of a potentiostat, and to observe and analyze the current output of the cell. Such a current output can be the deterministic response of the system to the input signal provided by the potentiostat or can be caused by internal fluctuations of the characteristics of the electrode, such as changes in surface area, crystal orientation of the surface, and film coverage, or processes such as passive film breakdown and repair, pitting, or other localized corrosion processes.

The internally generated noise, therefore, can give information relative to the magnitude and relaxation times of the electrode processes (1). It has been used, for instance, for the detection of the onset of pitting (2), to monitor the effect of corrosion inhibitors (3), and to study electrocrystallization (4), and anodic dissolution (5).

The experimental problem consists in detecting the signal, that is, amplifying it to a level sufficient for processing, and distinguishing which part of the signal is deterministic, random, or caused by the instrumentation.

The circuit with its sources of signal can be schematized as shown in Fig. 1. The potentiostat delivers a control voltage, the input to the electrochemical cell, which consists of a constant (d-c) voltage and of broad-band noise caused by the instability of such a d-c level. To this a signal may be added, produced by a signal generator. This additional signal can be a constant amplitude sinusoid, a swept frequency signal ranging between two predetermined frequencies, or white noise. The symbol X represents here the a-c part of the input signal, expressed as a function of frequency, $X = X(\nu)$. Such a signal can be quite small, ranging in amplitude between 10^{-4} and 10^{-8}V. An amplifying stage is therefore necessary for its detection and processing, adding noise with spectrum $N_I(\nu)$ to the signal. The output of the first channel of the spectrum analyzer is therefore $A = X + N_I$.

The input signal generates a current in the cell. H represents the cell transfer function so that the output $Y(\nu)$ in the frequency domain is $Y = HX$. For an electrochemical cell H is the admittance, which is in general complex and frequency dependent. Random fluctuations of the electrode characteristics generate an additional noise current $N(\nu)$. The total current is transformed in an appropriate current-to-voltage converter (schematically indicated in Fig. 1) from which the signal emerges with noise $N_O(\nu)$ added at the output of the amplifying stage. The output of the second channel of the spectrum analyzer is therefore $B = Y + N + N_O$.

The auto- and cross-power spectra are, respectively

$$P_{AA} = (X + N_I)(X + N_I)^* = P_{XX} + P_{II} \quad [1]$$

$$P_{BB} = (HX + N + N_O)(HX + N + N_O)^* = |H|^2 P_{XX} + P_{NN} + P_{OO} \quad [2]$$

$$P_{BA} = (HX + N + N_O)(X + N_I)^* = HP_{XX} \quad [3]$$

The terms marked with an asterisk are the complex conjugates of those without asterisk. In deriving [1], [2], and [3] it is assumed that all noise signals are uncorrelated with the input and with one another, so that the average values of the cross-products are zero

$$XN_I^* = N_I X^* = XN^* = NX^* = XN_O^* = N_O X^* = 0 \quad [4]$$

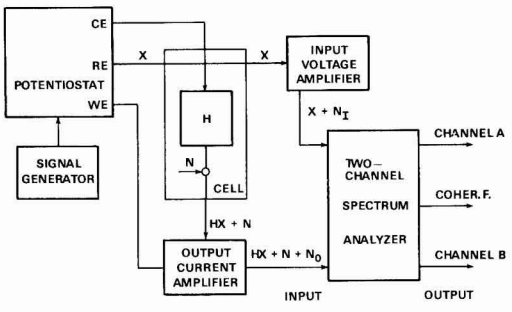

Fig. 1. Schematic representation of the measurement system with noise sources and spectrum analyzer outputs identified.

It should be remembered also that experimentally the spectrum analyzer averages out a large number of time records of the signals, so that, at least asymptotically, [4] is valid.

Taking [4] into account, Eq. [1], [2], and [3] contain five unknowns. It is therefore necessary to determine experimentally two of the unknowns in an independent way. This can be accomplished in the following manner: when the input of the amplifier of the voltage signal is short-circuited, X is effectively zero and therefore

$$(P_{AA})_{X=0} = P_{II} \quad [5]$$

the auto-power spectrum of the amplifier noise. This spectrum can be measured and stored in an appropriate memory. For the measurement of the current amplifier noise N_O it is sufficient to substitute the electrochemical cell with a resistor. Increasing the value of such a resistor decreases the current signal Y until the output of channel B becomes independent of the value of the resistance. In these conditions

$$(P_{BB})_{Y=0} = P_{OO} \quad [6]$$

Since a resistor has been substituted for the cell, no random fluctuations occur and therefore $N = 0$. The auto-power spectrum P_{OO} is also recorded and stored. Once P_{II} and P_{OO} are subtracted from P_{AA} and P_{BB}, it is easy to solve the system of equations so that H and N can be obtained.

Experimental Procedure

The measurements described here were taken with an experimental setup similar to that reported previously (6), which is a practical implementation of Fig. 1. The potentiostat employed, especially built for its low noise, has been described elsewhere (7). The analyzing instrument was a digital two-channel spectrum analyzer which provided the auto-power spectra of the two channels as well as the coherence function γ^2, which is defined as

$$\gamma^2 \equiv \frac{|P_{BA}|^2}{P_{AA}, P_{BB}} \quad [7]$$

and from which, therefore, the cross-power spectrum can be obtained. As it is well known, the coherence function γ^2 ranges from 1, when the output signal is entirely deterministic, to 0 when there is no casual relationship between P_{AA} and P_{BB}.

The electrochemical system investigated was aluminum in borate buffer (pH = 7.5), to which 0.01 mole/liter of NaCl was added. At potentials more positive than −650 mV *vs.* SCE this electrode undergoes pitting [8], whereupon the noise pattern of the current changes drastically (9). The measurements were carried out at −700 and at −650 mV *vs.* SCE. In some runs white noise of the order of a few $\mu V/\sqrt{Hz}$ were added to the control voltage of the potentiostat. The spectrum analyzer, which has a frequency resolution of 1/256 of the range, was set for a 51.2 Hz range, so that the resolution was 0.2 Hz.

The results reported here were obtained manually; the spectra and the coherence function were recorded on an X-Y recorder and the calculations were done for only a few of the 256 points available. Such an experimental procedure is slow and tedious, but it was used to test the capability of the method. However, the spectrum analyzer can be interfaced to a computer so that acquisition, storage, and subtraction of the instrumental noise spectra P_{II} and P_{OO}, as well as all necessary calculations, can be carried out under software control with minimum time delay.

Experimental Results

The auto-power spectra of the noise N_I ofthe amplifier operating on the input signal (the electrode potential) and that of the noise N_O of the output amplifier operating on the cell current were measured over a

wide frequency range, and are shown in Fig. 2. Since P_{OO}, the power spectrum of the current amplifier, is added to the current signal, it is given in current units, A^2/Hz. These spectra are averages over a number of repeat measurements, ranging from 512 at high frequency to 64 at low frequency, where the total acquisition times are of the order of 1 hr.

Results obtained on the Al electrode below (−700 mV *vs.* SCE) and at the pitting potential (−650 mV) in the absence of an external signal in the control voltage are shown in Fig. 3 and 4. The auto-power spectrum of the voltage is that of channel A and it is given in V^2/Hz. Channel B shows the current power spectrum in A^2/Hz. In order to facilitate comparisons the current spectra are not given in units of current density (P_{OO} is independent of surface area), but they can be easily and quite precisely transformed into A^2/cm^4Hz by dividing by 10, since the electrode surface area in all experiments was 3.17 cm^2. The figures show also the coherence function *vs.* frequency. Figure 5 shows power spectra and coherence function for an electrode at the pitting potential when white noise of 2 $\mu V/\sqrt{Hz}$ was applied as an external signal.

From these data, according to the calculation method described earlier, the auto-power spectrum of the random fluctuations P_{NN} and the absolute value of the electrode impedance $|Z| = 1/|H|$ were obtained. They are shown in Fig. 6 and 7, respectively.

Discussion

The results presented here show a number of interesting features and illustrate the usefulness of quanti-

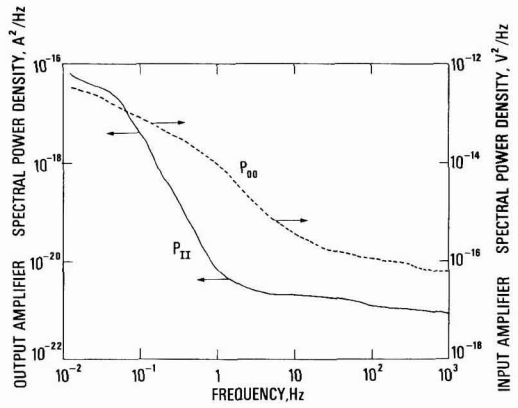

Fig. 2. Auto-power spectra of the instrumental noise of the input amplifier P_{II} (electrode potential) and output amplifier P_{OO} (cell current).

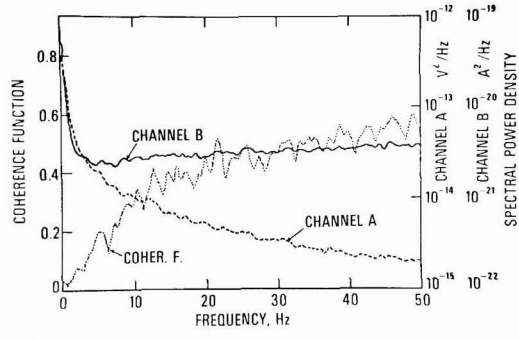

Fig. 3. Auto-power spectra and coherence function for Al in borate buffer + 0.01 mole/liter NaCl at −700 mV *vs.* SCE. Surface area = 3.17 cm^2.

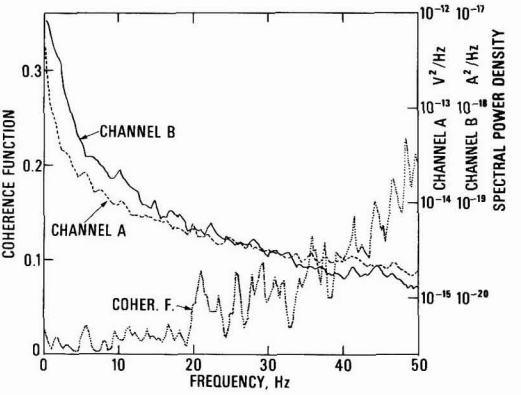

Fig. 4. Auto-power spectra and coherence function for Al in borate buffer + 0.01 mole/liter NaCl at −650 mV *vs.* SCE. Surface area = 3.17 cm^2.

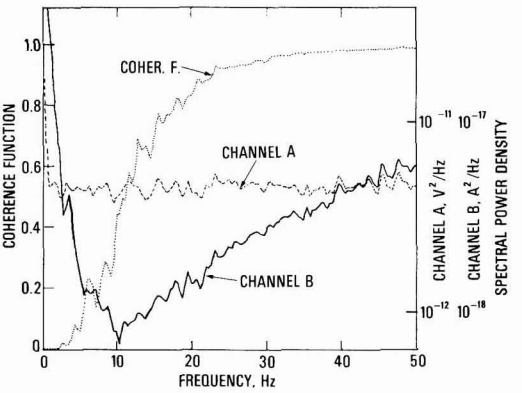

Fig. 5. Auto-power spectra and coherence function for Al in borate buffer + 0.01 mole/liter NaCl at −650 mV *vs.* SCE. Surface area = 3.17 cm^2. White noise 2 $\mu V/\sqrt{Hz}$ added to input signal.

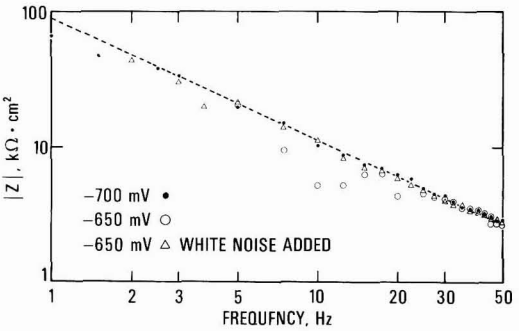

Fig. 6. Absolute value of the electrode impedance |Z| per unit surface area derived from data of Fig. 3, 4, and 5. Squares: −700 mV. Circles: −650 mV. Triangles: −650 mV, white noise added to input.

tative criteria for identifying the sources of noise. For instance, although the voltage spectra in Fig. 3 and 4 are virtually identical, the current spectrum is much larger at −650 mV (Fig. 4), confirming that the noise level increases considerably when pitting begins (9). However, the coherence function in Fig. 3 indicates that a substantial part of the signal in channel B is not

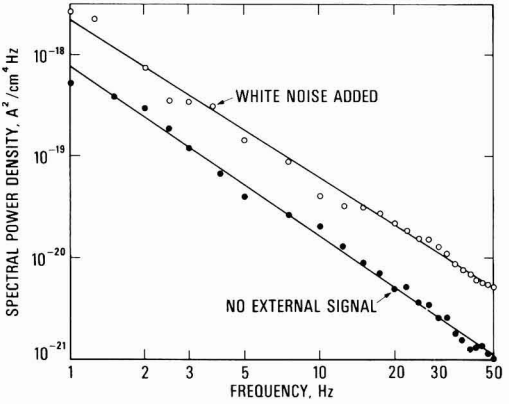

Fig. 7. Auto-power spectra P_{NN} of the random noise derived from data of Fig. 4 and 5 at −650 mV. Squares: no external input signal. Circles: white noise added to input.

causally related to the input, but such a noise may either be instrumental or may mark the beginning of the breakdown of the protective oxide film. However, when the separation of the noise sources is carried out, it is found that P_{NN} at −700 mV is practically zero over the whole frequency range studied. An upper value can be set for P_{NN} at about $10^{-22}A^2/Hz$ (or $10^{-23}A^2/cm^4Hz$), which is of the order of one-tenth of the instrumental noise as indicated by P_{OO}. The difference between the value of the coherence function in Fig. 3 and unity can be accounted for entirely by the instrumental noise.

The impedance, shown in Fig. 6, corresponds essentially to the behavior of a capacitor of about 1.5 $\mu F/cm^2$. The corrosion resistance cannot be determined with assurance because of the limited frequency range studied, but is larger than 60 $k\Omega \cdot cm^2$. Here the advantage of adding white noise to the input signal is shown by the data in Fig. 5, from which the deterministic response can be recovered in spite of the random fluctuations, while no reliable value of $|Z|$ can be calculated from Fig. 4 below 30 Hz because γ^2 is too close to zero.

In conclusion, with the aid of an instrument capable of processing voltage and current signals simultaneously and of calculating the cross-power spectrum, random noise can be separated from the deterministic response. Sensitivity is also enhanced, and noise about one-tenth of the instrumental noise can still be detected. However, it is evident that the noise level of the amplifier operating on the cell current is the main factor limiting the detectability of the random fluctuations of the electrode characteristics, and that its reduction would improve considerably the performance of the whole system.

As far as the pitting of Al is concerned, these rather limited results give nevertheless some interesting information. First of all, the impedance data of Fig. 6 show that, although pitting causes large current fluctuations, the deterministic behavior below and at the pitting potential is substantially the same. The random noise spectra of Fig. 7 show that reproducibility is only fair, as to be expected since number and size of the pits tend to vary from experiment to experiment. The major point seems to be that the amplitude of the fluctuations decays approximately as the reciprocal of the frequency, like the "flicker" noise observed in electronic devices (10). The decay with frequency also indicates that the capacitance of the electrode undergoes smaller fluctuations than the resistance during the pitting process (9).

Finally, the results have shown that the degree of random fluctuations below the pitting potential is so low that the picture of the protective film on aluminum as being in a state of dynamic equilibrium with continuous breakdown and repair does not seem to be supported by the experimental evidence.

Acknowledgment

The author wishes to thank Mr. S. Simms of the Hewlett-Packard Corporation for graciously lending part of the equipment used in this work.

Manuscript submitted May 5, 1980; revised manuscript received Oct. 15, 1980.

Any discussion of this paper will appear in a Discussion Section to be published in the December 1981 JOURNAL. All discussions for the December 1981 Discussion Section should be submitted by Aug. 1, 1981.

Publication costs of this article were assisted by the National Bureau of Standards.

REFERENCES

1. G. Blanc, I. Epelboin, C. Gabrielli, and M. Keddam, *J. Electroanal. Chem. Interfacial Electrochem.*, **62**, 59 (1975).
2. U. Bertocci, Seventh International Congress on Metallic Corrosion, p. 2010, Rio de Janeiro 1978, ABRACO (1979).
3. W. P. Iverson, *This Journal*, **115**, 617 (1968).
4. C. Gabrielli, M. Ksouri, and R. Wiart, *J. Electroanal. Chem. Interfacial Electrochem.*, **86**, 233 (1978).
5. G. Blanc, I. Epelboin, C. Gabrielli, and M. Keddam, *ibid.*, **75**, 97 (1977).
6. U. Bertocci, *This Journal*, **127**, 1931 (1980).
7. U. Bertocci and R. W. Shideler, *Nat. Bur. Stand. J. Res.*, **85**, 211 (1980).
8. J. R. Galvele and S. M. de DeMicheli, *Corros. Sci.*, **10**, 795 (1970); K. Nisancioglu and H. Holtan, *ibid.*, **18**, 835 (1978).
9. U. Bertocci and J. Kruger, "Proceedings of the International Conference on Non-Traditional Approaches to the Study of the Solid-Electrolyte Interface," Snowmass, CO (1979), in press.
10. D. K. C. MacDonald, "Noise and Fluctuations," p. 90, J. Wiley, New York (1962); A. van der Ziel, "Noise," p. 106, Prentice Hall, Englewood Cliffs, NJ (1970); A. H. W. Beck, "Statistical Mechanics, Fluctuations and Noise," p. 176, J. Wiley, New York (1976).

The Dissolution and Passivation of Zinc in Concentrated Aqueous Hydroxide

M. C. H. McKubre* and D. D. Macdonald*,[1]

SRI International, Materials Research Laboratory, Menlo Park, California 94025

ABSTRACT

The rotating ring-disk electrode has been applied in this study to the related phenomena of dissolution, current oscillation, and passivation of zinc in concentrated aqueous NaOH. The results of potentiostatic and potentiodynamic experiments are compared with those of previous workers, and a physical model is proposed to describe the anodic behavior of zinc in four successive potential regions: active dissolution, prepassivation, pseudopassivation, and true passivation.

The requirements for high specific energy, high specific power, and low cost make zinc an attractive negative electrode material for aqueous alkaline batteries in electric vehicular applications (1). However, a number of specific limitations await satisfactory resolution. Recent studies have been concerned with the limitations of cycle life associated with dendritic (2-5) and nonadherent (6-9) zinc deposition during charging, and with the problems of electrode shape change with cycling (1, 2, 10). The shelf life and cycle life of zinc battery electrodes is also limited by the corrosion of zinc in concentrated alkali (11-13).

In the present study we focus on the related processes of anodic dissolution and passivation. Rapid discharge of the zinc electrode is associated largely with the high solubility of Zn(II) as a zincate ion (14, 15) in alkaline solutions. At high currents, however, zinc discharge is often inhibited by the formation of a passivating zinc oxide or hydroxide layer by a dissolution-precipitation mechanism (16-28). Before the onset of passivation, the discharge of zinc is generally agreed (21) to proceed via the formation of complex hydroxyl zincate anion. The nature of this anion has been the subject of considerable thermodynamic (14, 29-31) and spectroscopic (15, 32-34) investigation, and is thought to have the form $Zn(OH)_4^{2+}$ in strongly alkaline solutions. However, the spectroscopic investigations of Jackovitz and Langer (32) suggest that "only a small fraction, about one-sixth of the anodically dissolved zinc, was converted to $Zn(OH)_4^{2-}$."

Experimental Procedure

Experiments were performed using a rotating ring-disk electrode (RRDE). The importance of adequate hydrodynamic control in studies of zinc dissolution and passivation phenomena has been stressed by several authors (20, 26, 35, 36).

The RRDE was constructed using a vitreous carbon[2] ring with a 99.999% purity zinc disk, as shown in Fig. 1. Vitreous carbon constitutes a nearly ideal, nonporous, inert ring material for current collection at large cathodic potentials. The radius ratios r_3/r_2 and r_2/r_1 exceed those tabulated by Albery *et al.* (37) and Pleskov (38), and the electrode collection efficiency was determined experimentally in 0.1M $K_3Fe(CN)_6$ with 1.0M NaOH supporting electrolyte. This calibration procedure has been described previously (39). At 20°C the measured collection efficiency was 70.9 ± 0.2%. Details of the rotating ring-disk electrode construction are shown in Fig. 1.

Experiments were conducted in an all Teflon cell shown in Fig. 2, situated in a water-ethylene glycol bath controlled to within ± 0.1 K. Potentiodynamic control of the disk and *IR* compensation were accomplished using a PAR Model 173 potentiostat and Model 175 potential programmer. The disk current and charge were recorded using a PAR model 179 digital coulometer. Potentiostatic control of the ring electrode was achieved using a purpose-built, high-speed potentiostat electrically isolated from the disk control circuit.

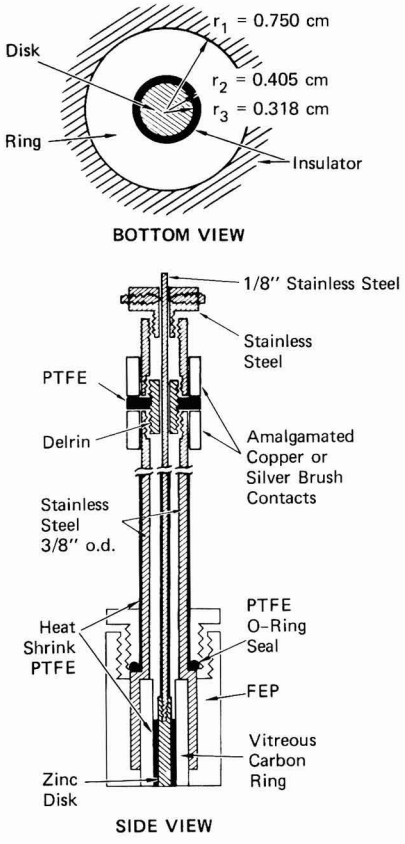

Fig. 1. Schematic diagram of RRDE construction and contact assembly.

* Electrochemical Society Active Member.

[1] Present address: The Fontana Corrosion Center, Department of Metallurgical Engineering, The Ohio State University, Columbus, Ohio 43210.

Key words: electrolyte, electrode, charge, dissolution, passivity.

[2] Vitreous carbon was generously supplied by Dr. A. Norris, Fluorocarbon Corporation, Anaheim, California.

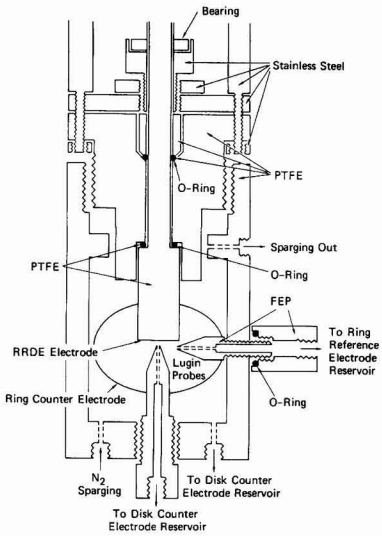

Fig. 2. RRDE cell construction

Details of the ring potentiostat, and six electrode cell geometry have been described previously (39, 40).

RRDE studies were performed in 9.78m [28 weight percent (w/o)] NaOH, prepared using analytical grade NaOH and water doubly distilled from deionized stock. The second distillation was under high purity nitrogen to exclude atmospheric CO_2, and the cell was continuously sparged with N_2 except during periods of measurement.

The RRDE electrode was polished with varying grades of carborundum paper, the final grade having 25 micron particle size. The electrode assembly was degreased with hot ethanol in an ultrasonic bath, then rinsed with distilled water immediately prior to use.

Results

Figure 3 shows schematically the general features observed during a slow anodic potentiodynamic sweep covering the zinc discharge region in initially zincate-free NaOH. The region "b" is characterized by an exponential dependence of the dissolution current on applied potential (31, 36, 41). The current increases in a nearly linear fashion with potential (25, 36) between "b" and "c" reaching a maximum at "d" and attaining a plateau value "e" before passivation. Two peaks in the region "cf" have been observed at very low potential sweep rates (< 1 mV sec^{-1}) by other workers (21, 26, 42). The peaks were interpreted by Powers and Breiter (21) in terms of growth of two surface oxide films. The features shown in Fig. 3 represent the limiting low rate potentiodynamic sweep behavior, and we have observed no evidence for a second peak under controlled hydrodynamic conditions.

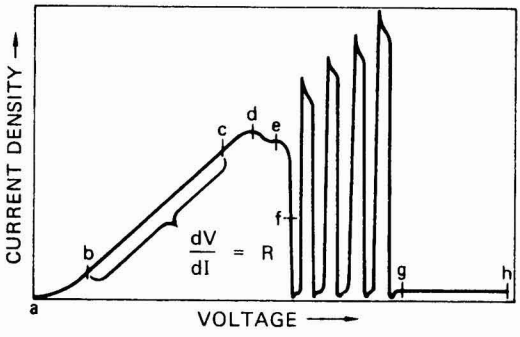

Fig. 3. Anodic potentiodynamic sweep of zinc in aqueous NaOH

Active dissolution.—We observed that the form of the repetitive sweep voltammogram depends critically on both electrode rotation speed and electrolyte temperature. Figure 4 shows the influence of rotation speed and Fig. 5 shows the influence of temperature on the zinc voltammogram. It is immediately apparent from Fig. 4 that the peak and plateau currents, as well as the slope in the linear I-V region, are strongly influenced by electrolyte convection at low sweep rates, suggesting that these are controlled not by factors at the zinc/electrolyte interface, but by processes within the diffusion layer.

The data in the region "bc" were analyzed as a function of temperature and rotation speed and the results are presented in Table I. The linearity of this portion of the current voltage curve is reflected in the near-unity values of the regression coefficients shown for an equation of the form

$$V = V_o + IR$$

It is clear from the values in Table I that V_o is effectively independent of ω, while R decreases monotonically with ω and T.

The linear dependence of the dissolution current on applied potential indicates that electrode discharge in

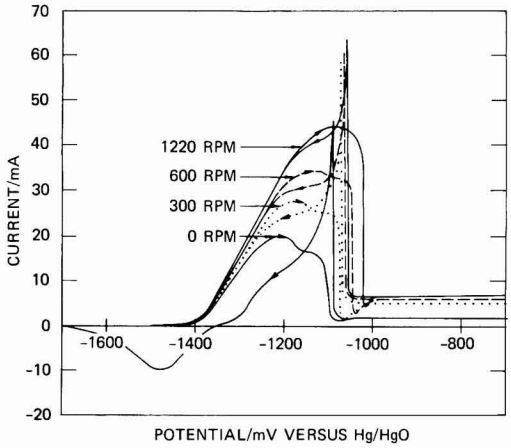

Fig. 4. The influence of electrode rotation speed on the zinc cycle voltammogram: 28 w/o NaOH, 0°C, sweep rate 5 mV sec^{-1}.

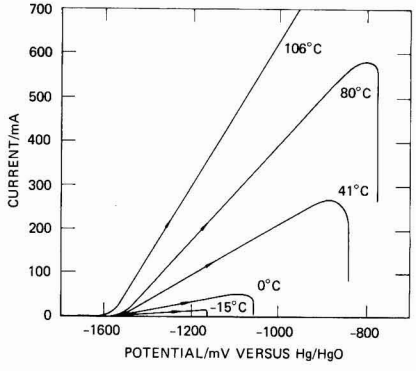

Fig. 5. The influence of temperature on the potentiodynamic discharge of zinc: 28 w/o NaOH, 1200 rpm, sweep rate 5 mV sec^{-1}.

Table I. Linear regression of current vs. applied potential for the potentiodynamic discharge of Zn at 5 mV sec^{-1}

T (°C)	ω (rpm)	V_o/mV	R/Ω	r^2
−15	1160	−1405	13.75	0.998
−15	600	−1406	15.00	0.999
−15	300	−1406	15.54	0.999
−15	0	−1403	15.88	1.000
−15		$\bar{V}_o = -1405 \pm 1$		
0	1220	−1387	5.44	0.999
0	600	−1389	5.89	0.998
0	300	−1389	6.23	1.000
0	0	−1393	7.43	0.999
0		$\bar{V}_o = -1390 \pm 3$		
41	1200	−1379	1.93	1.000
41	600	−1381	2.18	1.000
41	300	−1379	2.48	1.000
41	0	−1379	2.48	1.000
41		$\bar{V}_o = -1379 \pm 2$		
80	1200	−1360	0.925	0.999
80	600	−1360	1.118	0.999
80	300	−1358	1.501	0.995
80	0	−1358	1.501	0.995
80		$\bar{V}_o = -1359 \pm 1$		
106	1200	−1385	0.597	0.999
106	600	−1384	0.656	0.998
106	300	−1383	0.716	1.000
106	0	−1378	1.077	0.995
106		$\bar{V}_o = -1383 \pm 3$		

Note: potentials are with respect to Hg/HgO. r^2 is the regression coefficient.

this region is not determined by ionic diffusion of OH^- to, or product from the interface. Sanghi and Fleischmann (42) discounted mass transport limitation by OH^- ions, observing that the maximum dissolution rate is only a fraction of the limiting diffusion current of hydroxyl ions at bulk concentration greater than 0.01M. However, resistive (migration) limitation, which is functionally dependent on the rate of electrolyte convection, suggests that the process that determines the Zn electrode discharge rate occurs either within the diffusion layer or within a surface film, the thickness of which is determined by ablation or dissolution to the bulk electrolyte.

As expected for a process occurring within the diffusion layer, the dissolution resistance values presented in Table I are approximately linear with the inverse square root of electrode rotation speed

$$T = -15°C, \quad R = 12.17 + 60.74\,\omega^{-1/2}, \quad r^2 = 0.992$$
$$T = 0°C, \quad R = 4.74 + 26.38\,\omega^{-1/2}, \quad r^2 = 0.968$$
$$T = 41°C, \quad R = 1.39 + 19.09\,\omega^{-1/2}, \quad r^2 = 0.997$$
$$T = 80°C, \quad R = 0.33 + 20.13\,\omega^{-1/2}, \quad r^2 = 0.992$$
$$T = 106°C, \quad R = 0.48 + 4.08\,\omega^{-1/2}, \quad r^2 = 0.991$$

Powers and Breiter (21) observed for Zn in KOH that, although faceting of the single crystal surfaces occurs in the linear-I-V region, there is no direct evidence of film formation until very near the potential at which the current density is a maximum, *i.e.*, near "d." In a subsequent publication, Breiter (25) suggested that the linear region may result from the initial formation and spreading of a compact film across the surface. This proposal appears to conflict with their previous observation (21), and is clearly inconsistent with the rotation speed dependence of R observed in the present study. Armstrong *et al.* (36, 41) ascribe an observed I^{-1} *vs.* $\omega^{-1/2}$ linearity for the initial dissolution of Zn in NaOH to a Zn $\rightleftarrows$ $Zn(OH)_4^{2-}$ equilibrium process in which current limitation is imposed by the diffusion of zincate to the bulk. This model has been extended (34) to predict an exponential dependence of I_∞, the current extrapolated to the limit of high rotation speed, on the applied overvoltage, $V - V^o$. Figure 6 shows plots of I_∞ and ln I_∞ *vs.* applied potential. Values of I_∞ were calculated by the linear regression of I^{-1} *vs.* $\omega^{-1/2}$ data, extrapolated to $\omega^{-1/2} = 0$, for varying temperatures and voltages in the region "bc," during a slow (5 mV sec^{-1}) anodic potentiodynamic sweep. While the data in Fig. 6(a) may be construed as straight lines in accordance with Armstrong's model (36, 41), a significantly better fit to the data is shown in Fig. 6(b). The vectors shown are regression lines for all data presented in Fig. 6(a).

To elucidate further the mechanisms of Zn dissolution, we determined the fraction of the dissolved zinc species that was reducible at the vitreous carbon ring. Three striking results immediately were apparent from the study.

1. Under all conditions, the fraction of dissolved zinc detected at the ring was less than that predicted by the calibrated collection efficiency.

2. The fraction at the dissolved zinc that was collected was a function at the electrode rotation speed.

3. When corrected for the increasing background current, the percentage of collected material increased with an increasing concentration of dissolved zinc in the bulk electrolyte.

Figure 7 shows the influence of rotation speed on disk and ring currents in initially zincate-free solution. The collection percentages shown at each rotation speed are determined from the current peaks for i_d and i_r, appropriately corrected for background currents, expressed as a percentage of the calibrated collection

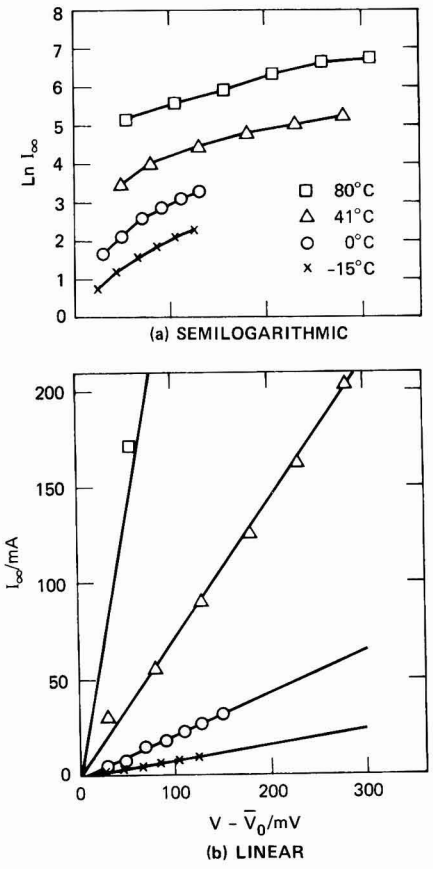

Fig. 6. The current extrapolated to infinite rotation speed vs. applied potential: 28 w/o NaOH, sweep rate 5 mV sec^{-1}.

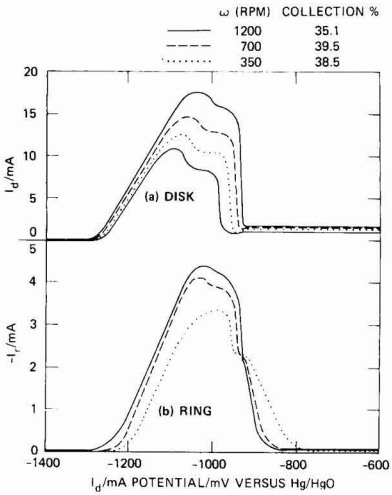

Fig. 7. RRDE study of zinc during anodic potentiodynamic sweep at 5 mV sec^{-1}: 28 w/o NaOH, 15°C.

efficiency. The concentration of dissolved zinc was then increased by controlled coulombic electrochemical dissolution of an auxiliary zinc electrode within the cell. Collection percentages determined at the peak are plotted *vs.* rotation speed in Fig. 8, together with data obtained at a single potential in initially zincate-free NaOH.

It is apparent from Fig. 8 that the percentage of dissolved zinc species that is reducible declines at high rotation speed, but increases with dissolved zinc concentration. The apparent small decreases in collection at very low rotation speeds seems to be an artifact of the ring disk system. A decrease in collection percentage at high rotation speed has been observed previously (17) and may be interpreted as follows. The

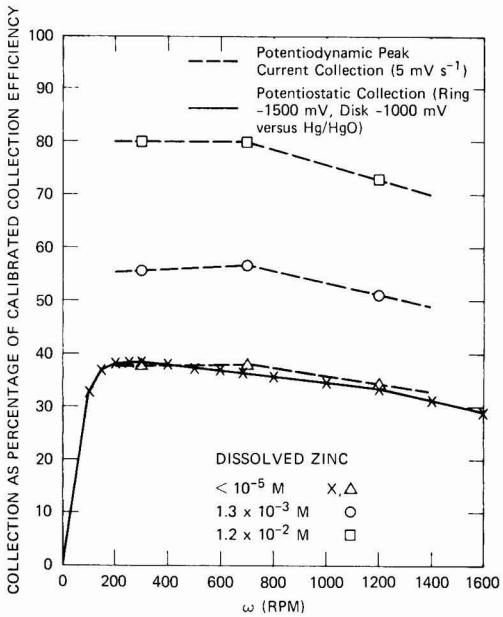

Fig. 8. Collection percentage *vs.* electrode rotation speed as a function of dissolved zinc concentration: 28 w/o NaOH, −15°C.

anodic charge transfer process produces an inactive intermediate, which transforms in time to the electrochemically active products by chemical dissolution. It is this final product that is reducible on the ring. Using laser Raman techniques, Kato and co-workers (17) suggested that this product is $Zn(OH)_4^{2-}$. If we assume that the intermediate is a dissolved Zn(II) species, then the model for dissolution is consistent with that originally proposed by Gerischer (43) and provides a mechanism for subsequent passivation

$$Zn + nOH^- \rightleftarrows Zn(OH)_n^{2-n} + 2e^-$$

$$Zn(OH)_n^{2-n} + (4 - n)OH^- \rightarrow Zn(OH)_4^{2-}$$

where

$$0 \leq n \leq 3$$

This second reaction proceeds at a moderate rate. At high rotation speeds the intermediate species has insufficient time to transform to the reducible zincate ion, and the amount of species collected at the ring is less.

Passivation.—It is helpful to divide the passivation of Zn in concentrated aqueous hydroxide into three separate regions of applied potential: prepassive, pseudopassive or unstable, and true passive regions. The potentiokinetic current behavior within these regions is shown schematically in Fig. 3.

Prepassive region.—At potentials more positive than "d," a white flocculent film is observed (21) to be deposited on the electrode. This has been associated (21, 24, 25) with the precipitation of $Zn(OH)_2$ from a near-surface solution supersaturated with $Zn(OH)_4^{2-}$. The dissolution current is reduced by the three-dimensional porous film, possibly as a consequence of the reduced effective surface area. A well-defined current plateau, "e" with current $\alpha\omega^{1/2}$, is seen at low temperatures. It is apparent from the work of Breiter (21, 25) that passivation is not caused by the porous $Zn(OH)_2$ film, but by a thin, compact, adherent film that forms directly on the zinc surface. We will adopt the nomenclature of Powers and Breiter (21), and refer to these films as types I and II, respectively. While the type I film is not passivating, we believe that its existence is required for the formation of a passivating type II film.

Unstable region.—The onset of passivation is rapid but not irreversible. Under potentiostatic or slow potentiodynamic sweep conditions, we have observed zinc electrodes to undergo an oscillatory activation/passivation process within a defined potential region "fg." Current and potential oscillations have been observed previously (44-50) for a variety of systems including Zn in aqueous hydroxide (50, 51). Hampson *et al.* (18) observed that a passivated zinc electrode becomes dispassivated after it is "rested for a few minutes," and that depassivation becomes more rapid as the electrolyte temperature and concentration are increased. Breiter *et al.* ascribed fluctuations (21) and current oscillations (25) under potentiodynamic sweep conditions to buckling and tearing of the compact type II film. A close examination of this phenomenon provides a considerable insight into the mechanisms of passivation.

Figure 9 shows the broad potential region of current instability observable at elevated temperatures under single anodic potentiodynamic sweep conditions. The envelope of current peaks extends the region of current-voltage linearity discussed in the previous section. Thus, the current upon reactivation appears initially to be determined by the same diffusion layer resistance we believe is associated with active zinc dissolution.

Onset potentials for passivation are shown in Fig. 10, superimposed upon the reversible potential profiles calculated (52) for pertinent redox reactions in 9.7m NaOH. Under the conditions of our experiments, passivation occurs well into the potential regions of ZnO

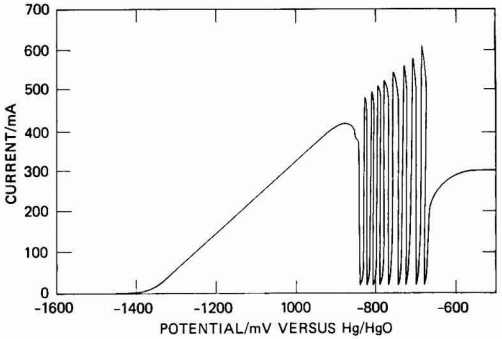

Fig. 9. Current oscillations of zinc during anodic potentiodynamic sweep at 5 mV sec^{-1}: 28 w/o NaOH, 80°C, 600 rpm.

and $Zn(OH)_2$ stability, and there is little correlation between initial passivation and the reversible potentials calculated for the formation of latently passivating oxide species. Under potentiodynamic conditions the passivation potential increases approximately linearly with temperature, with a slope that increases with increasing rotation speed.

Further information regarding current instability can be obtained by using the vitreous carbon ring to monitor the concentration of reducible Zn species adjacent to the electrode. Figure 11 shows the results of RRDE potentiostatic step experiments at 22.5°C and at 300 rpm. Under these conditions oscillation is confined to a ± 25 mV region. On the time scale shown, passivation and reactivation occur virtually instantaneously. By using a Biomation Model 805 Wave Form Recorder in the pre-trigger mode, we ascertained that reactivation occurs in tens of milliseconds, and passivation somewhat less quickly. The nearly sinusoidal ring current perturbation reflects the concentration wave of

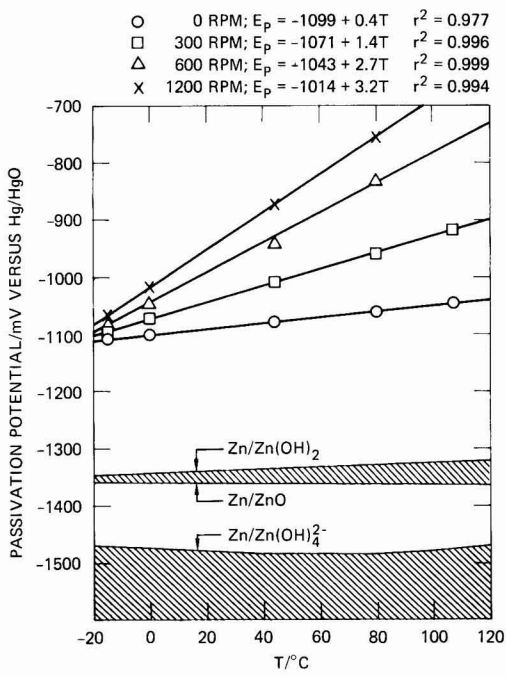

Fig. 10. Measured passivation onset potentials and calculated reversible potentials vs. temperature, for zinc in 28 w/o NaOH.

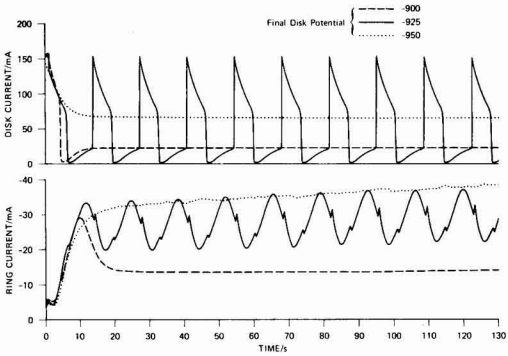

Fig. 11. RRDE potential step experiment for zinc in 28 w/o NaOH at 22.5°C. Ring potential and initial disk potential —1500 mV vs. Hg/HgO.

reducible zinc ions that propagates through the electrolyte as a result of intermittent disk dissolution. The glitches appearing on the ring current sinusoid result from coupling of the ring and disk currents (40, 53) and are artifacts of the RRDE system.

Under controlled hydrodynamic conditions, oscillations appear to be sustainable indefinitely. However, both amplitude and period are markedly influenced by step potential, temperature, and rotation speed. Below room temperature, oscillation is observed at $\omega \leq 300$ rpm. At 41°C, oscillation occurs for $\omega \leq 600$ rpm, and above 80°C it may be sustained at all rotation speeds accessible to us (up to 1200 rpm). Figure 12 shows the limits of potential over which oscillation occurs in a quiescent system as a function of temperature.

Discussion

In the preceding sections we described the chronology of Zn anodization under controlled potential conditions, comparing our experimental results with the conclusions of previous authors, as a first step in the development of a self-consistent picture of the passivation of zinc. The sequence of important processes that require explanation may be summarized as follows.

1. Following an initial Tafel region, the zinc dissolution current increases linearly with applied potential, the resistance being proportional to the diffusion layer thickness.

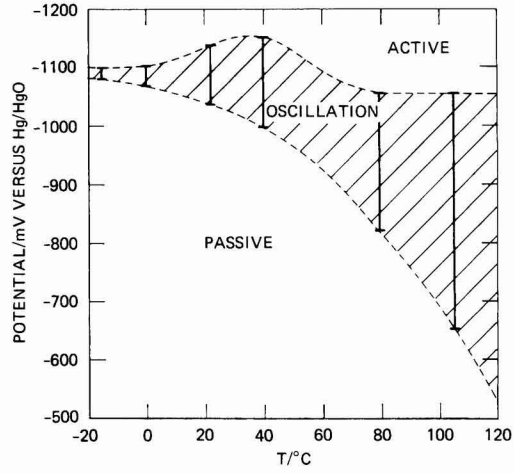

Fig. 12. Region of current instability for zinc in 28 w/o NaOH under quiescent conditions.

2. Zinc dissolves electrochemically via an intermediate species to a final product believed to be $Zn(OH)_4^{2-}$.

3. $Zn(OH)_2$ precipitates on the electrode in a prepassive region, producing a loose flocculent film denoted as type I (21, 25).

4. The temperature and convection dependence of passivation are consistent with a dissolution-precipitation mechanism, but the electrode is passivated by the formation of a compact, adherent (type II) film directly on the Zn electrode surfaces (21, 25).

5. Rapid reactivation may occur within a defined region of potential, the current initially attaining a value equivalent to the extrapolation of the linear *I-V* active dissolution region.

6. Current oscillations may effectively be sustained indefinitely and result in a near sinusoidal reducible Zn concentration wave in the electrolyte. The potential region of instability is strongly influenced by electrolyte temperature and convection, but is not correlated with known thermodynamic processes.

7. At sufficiently large anodic potentials, true passivation occurs, which results in a passive dissolution current independent of potential and time.

These observations are consistent with the following model. Initial dissolution proceeds according to the overall Eq. [1]

$$Zn + 4(OH)^- \rightleftarrows Zn(OH)_4^{2-} + 2e^- \quad [1]$$

At a potential roughly corresponding to the onset of linear current-voltage behavior, the Zn/ZnO reversible potential is exceeded (51, 52) and the predominant electrode reaction becomes

$$Zn + 2\,OH^- \rightleftarrows ZnO + H_2O + 2e^- \quad [2]$$

Because hydroxide ions are the reactant in Eq. [2], there is no supporting electrolyte. Under these conditions an impedance term must be included to account for the migration resistance (54-58). We propose that at moderate current densities the resistance due to the migration of OH^- ions becomes rate limiting.

ZnO forms on the electrode and then dissolves by reaction with further hydroxide to form the zincate ion

$$ZnO + H_2O + 2\,OH^- \rightleftarrows Zn(OH)_4^{2-} \quad [3]$$

When the electrolyte in the immediate vicinity of the electrode becomes supersaturated with zincate, $Zn(OH)_2$ precipitates on the electrode forming a porous (type I) film. Dissolution proceeds according to reaction [3] until the *p*H within the porous film is reduced to the extent that ZnO is insoluble (24). At this stage the electrode passivates due to the surface formation of a thin compact ZnO (type II) layer. With the reduced dissolution current, the zincate concentration declines and the *p*H increases, redissolving the $Zn(OH)_2$ (type I) and ZnO (type II) films. This mechanism is consistent with the observation (59) that Zn can be reactivated in a thin layer cell by the addition of very small amounts of fresh hydroxide. In the absence of the type I film, reactivation results initially in a current limited only by the hydroxide migration resistance. The next cycle is initiated with the precipitation of a new $Zn(OH)_2$ film. The passivation onset potential and the period of oscillation are determined by the difference between the active dissolution current and rate of mass transport (diffusion plus convection) from the electrode surface.

To explain the true passive behavior of the Zn electrode, it is necessary to postulate that the pseudopassivating film undergoes a phase change to form a species that is relatively insoluble at high pH.

The model presented above can be used, at least qualitatively, to explain our experimental observations and those of other workers. However, it should not be regarded as definitive and requires substantive verification. A more detailed and quantitative study is currently under way in our laboratory.

Acknowledgment

Funding was provided by the Department of Energy under Contract EM-78-C-01-5159. The authors wish to thank Dr. S. Ruby and Dr. F. R. McLarnon of DOE for their continued interest in this study.

Manuscript submitted July 14, 1980; revised manuscript received Sept. 23, 1980.

Any discussion of this paper will appear in a Discussion Section to be published in the December 1981 JOURNAL. All discussions for the December 1981 Discussion Section should be submitted by Aug. 1, 1981.

Publication costs of this article were assisted by SRI International.

REFERENCES

1. E. J. Cairns, General Motors Research Publication GMR-2170 (1976).
2. J. McBreen, *This Journal*, **119**, 1620 (1972).
3. G. A. Dalin, in "Power Systems for Electric Vehicles," U.S. Department of Health, Education and Welfare, Cincinnati (1967).
4. P. Bauer, Batteries for Space Power Systems, NASA, Washington, D.C. (1968).
5. M. Eisenberg, in "Power Systems for Electric Vehicles," U.S. Department of Health, Education and Welfare, Cincinnati (1967).
6. I. Epelboin, M. Ksouri, and R. Wiart, *J. Electroanal. Chem. Interfacial Electrochem.*, **75**, 115 (1977).
7. H. G. Oswin and K. F. Blurton, in "Zinc-Silver Oxide Batteries," A. Fleischer, Editor, John Wiley, New York (1971).
8. H. K. Varmary and W. A. Smith, in "Batteries," D. H. Collins, Editor, Pergamon Press, New York (1963).
9. I. Epelboin, M. Ksouri, and R. Wiart, *This Journal*, **122**, 1206 (1975); *J. Less-Common Metals*, **43**, 235 (1975); I. Epelboin, M. Ksouri, E. Lejay, and R. Wiart, *Electrochim. Acta*, **20**, 603 (1975).
10. S. P. Poa and C. H. Wu, *J. Appl. Electrochem.*, **8**, 427 (1978).
11. P. Ruetschi, *This Journal*, **114**, 301 (1967).
12. L. Z. Vorkapic, D. M. Drazic, and A. R. Despic, *ibid.*, **121**, 1385 (1974).
13. V. S. Muralidharan and K. S. Rajagopalan, *J. Electroanal. Chem. Interfacial Electrochem.*, **94**, 21 (1978).
14. T. P. Dirkse, in "Zinc-Silver Oxide Batteries," A. Fleischer, Editor, John Wiley, New York (1971).
15. N. A. Hampson, in "Zinc-Silver Oxide Batteries," A. Fleischer, Editor, John Wiley, New York (1971).
16. R. D. Armstrong and G. M. Bulman, *J. Electroanal. Chem. Interfacial Electrochem.*, **25**, 121 (1970).
17. H. Kato, T. Yoshaimura, and M. Yamashita, *Nippon Kagaku Kaishu*, **12**, 1811 (1977).
18. N. A. Hampson, M. J. Tarbox, and J. T. Lilley, *J. Electrochem. Technol.*, **2**, 309 (1964).
19. T. I. Popova, V. S. Bagotskii, and B. N. Kabanov, *Russ. J. Phys. Chem.*, **36**, 766 (1962).
20. M. A. V. Devanathan and S. Lakshamanan, *Electrochim. Acta*, **13**, 667 (1968).
21. R. W. Powers and M. W. Breiter, *This Journal*, **116**, 719 (1969).
22. J. O'M. Bockris, Z. Nagy, and A. Damjanovic, *ibid.*, **119**, 285 (1972).
23. T. P. Dirkse, in "Power Sources 3," D. H. Collins, Editor, Oriel Press, Newcastle-upon-Tyne (1971).
24. P. B. Mathur and K. R. Murti, *J. Ind. Chem. Soc.*, **44**, 407 (1967).
25. M. Breiter, *Electrochim. Acta*, **15**, 1297 (1970).
26. T. P. Dirkse and N. A. Hampson, *ibid.*, **17**, 387 (1972).
27. M. Yamashita, T. Yoshimura, Y. Imanaka, and H. Furuta, *Doshisha Daigaku Rikogaku Kenkyu Hokuku*, **18**, 204 (1977).
28. F. Jolas, *Electrochim. Acta*, **13**, 2207 (1968).
29. T. P. Dirkse, *This Journal*, **101**, 328 (1954).
30. H. H. Bode, V. A. Oliapuran, D. Berndt, and P. Ness, in "Zinc-Silver Oxide Batteries," A. Fleischer, Editor, John Wiley, New York (1971).
31. N. A. Hampson, G. A. Herdman, and R. Taylor, *J. Electroanal. Chem. Interfacial Electrochem.*, **25**, 9 (1970).

32. J. F. Jackovitz and A. Langer, in "Zinc-Silver Oxide Batteries," A. Fleischer, Editor, John Wiley, New York (1971).
33. J. S. Fordyce and R. L. Baum, *J. Chem. Phys.*, **43**, 843 (1965).
34. G. H. Newman and G. E. Blomgren, *ibid.*, **43**, 4393 (1965).
35. M. Eisenberg, H. F. Bauman, and D. M. Brettner, *This Journal*, **108**, 909 (1961).
36. R. D. Armstrong and G. M. Bulman, *J. Electroanal. Chem. Interfacial Electrochem.*, **25**, 121 (1970).
37. W. J. Albery and M. L. Hitchman, "Ring-Disc Electrodes," Clarendon Press, Oxford (1971).
38. Y. V. Pleskov and V. Y. Filinovskii, "The Rotating Disk Electrode," Consultants Bureau, New York (1971).
39. M. C. H. McKubre and D. D. Macdonald, "The Temperature Limitations of Primary and Secondary Battery Electrodes. Part I. Kinetics," SRI International, Final Report to the Department of Energy under Contract EM-78-C-01-5159 (1979).
40. M. C. H. McKubre and D. D. Macdonald, Submitted to *This Journal*.
41. R. D. Armstrong and M. F. Bell, *J. Electroanal. Chem. Interfacial Electrochem.*, **55**, 201 (1974).
42. I. Sanghi and M. Fleischmann, *Electrochim. Acta*, **1**, 161 (1959).
43. H. Gerischer, *Z. Phys. Chem.*, **202**, 302 (1953).
44. K. J. Vetter, "Electrochemical Kinetics," Academic Press, New York (1967).
45. J. Wojtowicz, in "Modern Aspects of Electrochemistry," Vol. 8, J. O'M. Bockris and B. E. Conway, Editors, p. 47, Butterworth, London (1937).
46. J. J. Podesta. R. C. V. Piatti, and A. J. Arvia, *This Journal*, **126**, 1363 (1979).
47. A. Y. Gokhshtein, *Dokl. Akad. Nauk. SSR*, **140**, 761 (1961).
48. A. Y. Gokhshtein and A. N. Frumkin, *ibid.*, **144**, 727 (1962).
49. C. Gabrielli, "Regulation et analyse des Systemes a Etats Stationnaires Multiples," Thesis, Paris (1973); I. Epelboin, C. Gabrielli, M. Keddam, J. Lestrade, and H. Takenouti, *This Journal*, **119**, 1632 (1972).
50. M. N. Hull, J. E. Ellison, and J. E. Toni, *This Journal*, **117**, 192 (1970).
51. U. F. Franck, *Z. Electrochem.*, **62**, 649 (1958).
52. D. D. Macdonald and M. C. H. McKubre, "The Temperature Limitations of Primary and Secondary Battery Electrodes. Part II. Thermodynamics," SRI International, Final Report to the Department of Energy under Contract EM-78-C-01-5159 (1979).
53. M. Shabrang and S. Bruckenstein, *This Journal*, **121**, 1439 (1974).
54. H. Chang and G. Jaffe, *J. Chem. Phys.*, **20**, 1071 (1952).
55. E. Levart and D. Schumann, *J. Electroanal. Chem. Interfacial Electrochem.*, **24**, 41 (1970).
56. E. Levart and D. Schuhmann, *ibid.*, **53**, 77 (1974).
57. J. R. Macdonald and D. R. Franceschetti, *ibid.*, **99**, 283 (1979).
58. D. R. Franceschetti and J. R. Macdonald, *ibid.*, **100**, 583 (1979).
59. T. Katan, J. R. Savory, and J. Perkins, *This Journal*, **126**, 1835 (1979).

Anodization of Metals Through Thin Solid Electrolyte Films of Calcia Stabilized Zirconia

J. Perriere and J. Siejka*

Groupe de Physique des Solides de l'Ecole Normale Supérieure,

Université Paris VII, 75221 Paris Cedex 05, France

and M. Croset*

Laboratoire Central de Recherches, Thomson-CSF, Corbeville 91401 Orsay, France

ABSTRACT

This paper shows that anodic oxidation of the metals Nb, Ta, and Al through thin solid electrolyte films of calcia stabilized zirconia (CSZ) is possible. The metal oxides grown are stoichiometric and the CSZ behaves like pure anodic oxide, since the electric field in CSZ in the 0.1-10 mA cm^{-2} current density range is comparable with those in anodic oxides. Anodization of Nb|Ta|CSZ or Al|CSZ|Nb|Ta systems shows that only oxygen movements take place in CSZ during oxide growth (*i.e.*, transport number of cations $t^+ = 0$), while both oxygen and cations take part in ionic current in the metal oxides underlying and overlying the CSZ layer (*i.e.*, $t^+ \neq 0$). Thus the transport number of cations can be considered as an intrinsic property of an oxide layer, independent of the nature and of the position of the other layers. Possible microscopic transport mechanisms for oxygen and cations through superimposed oxide films are discussed.

Ionic transport under high electric field through oxide films is generally explained by the thermally activated motion, over discrete energy barriers, of charged point defects (1). It is generally assumed that these defects are injected in the oxide at one of the interfaces (2). For films sufficiently thick ($d > \simeq$ 100Å) the anodization process is believed to be controlled by the migration in the bulk (1). The applied electric field E lowers the energy barrier W, leading to an exponential type relationship between ionic current i and electric field E: $i \simeq A \exp -(W - BE/Kt)$. This expression is obtained with the assumption of a sole migration specie, over a well-defined activation energy barrier. This is generally not the case for the anodization of valve metals, however in a first approach, this convenient theoretical expression has been generally used to describe anodic oxidation of valve metals [for example see Ref. (1-3) and references cited].

A number of works have been devoted to the study of cation or/and anion transport during anodic growth

* Electrochemical Society Active Member.
Key words: solid electrolyte, metals, oxidation, migration, nuclear reactions.

of oxide films. It has been clearly evidenced that the two species, oxygen and metal, may take part in the total ionic current during anodization (4-6), their motion obeying a neighbor-to-neighbor jump process (7, 8). It has been shown that the transport numbers of cations and of oxygen for several oxides (Al_2O_3, Nb_2O_5, and Ta_2O_5) have comparable values (5, 6, 9), although it seems unlikely that cation and oxygen defect species have similar activation energy of motion under a wide range of experimental conditions. Note however that during anodization of Zr only oxygen movements have been observed (10). Following Dignam (2) the microscopic mechanism of ionic movement during anodic oxidation of Ta or Al could be different from that of Zr: network defects (AlO^+ or AlO_2^- for example) in the first case, and oxygen point defects (vacancy or interstitialcy) in the second case.

The study of ionic movements during the anodization of superimposed metallic layers showed that it is possible to anodize a metal M_1 covered with a thin oxide film of a metal M_2 (11) even when their respective transport number for cations (t^+) are different; for example Nb can be anodized through thin Al_2O_3 films (12), or Zr through thin Ta_2O_5 films. In the last case the physical nature of moving defects in ZrO_2 and in Ta_2O_5 can also be different (2). Moreover a strong correlation has been evidenced between oxygen and cation jump probabilities during anodization of superimposed layers (13).

All these results did not allow one to construct an unambiguous model for the microscopic mechanism of ionic movements under high electric field. This is due to the fact that the nature of moving defects which are responsible for ion transport in Al_2O_3, Ta_2O_5 as well as in ZrO_2 is unknown. A possible way to overcome this difficulty is to study ionic movements under high electric field through thin layers of solid electrolyte in which the thermally activated microscopic movements and the nature of moving defects are well known (14). This is the case for calcia stabilized zirconia (CSZ) which is a pure oxygen ion conductor via a vacancy-type mechanism (14). In fact, it has been recently shown (15) that dense and stoichiometric films of CaO doped zirconia of the fluorite-type structure can be obtained by rf sputtering. The conductivity and the activation energy of conduction (Ec) of these films were near to those found for oxygen conduction in bulk material of the same composition, *i.e.*, 3×10^{-7} $(\Omega \cdot cm)^{-1}$ at 300°C and $Ec = 1.2$ eV for $(ZrO_2)_{0.88}(CaO)_{0.12}$. The study of Ni-NiO|CSZ|Pt-O_2 electrochemical cells (16, 17) allowed the authors to conclude that the oxygen transport number in rf sputtered thin CSZ films is near unity (0.99).

The aim of the present work was twofold: to study the ionic movements and the current field relationship in thin CSZ layers under high electric field, and to study cationic movements during anodic oxidation of various metallic substrates covered with superimposed thin CSZ and metallic films, *i.e.*, anodization of metal|CSZ or metal|CSZ|metal systems.

The aim of our study of the current-field relationship in CSZ thin films during the anodization of metal/CSZ systems was to answer the following question: can the convenient theoretical expression

$$i = 2anvq \exp - \frac{W - qaE}{KT} \qquad [1]$$

be used to describe the high field ionic transport in CSZ thin films? Let us notice that the CSZ represents the best case to apply this theoretical expression, since in CSZ a sole moving specie (oxygen vacancy) exists, the concentration of which is well known, while in the other classical cases, such as Ta, due to the presence of two migrating species, the theoretical expression has not been proven experimentally. Moreover all terms except the field are known in this expression for $(ZrO_2)_{0.88}(CaO)_{0.12}$ [*i.e.*, $a = 1.27 \times 10^{-8}$ cm, $n = 3.14 \times 10^{21}$ cm^{-3}, $q = 2 \times 1.6 \times 10^{-19}$ C, $\nu = 10^{13}$ s^{-1}, $W = Ec = 1.2$ eV (17)], a theoretical electric field value can be calculated from the relationship [1], for each current density and so can be compared to the value experimentally determined. Thus, in principle, the concept of thermally activated point defects moving under the influence of electric field may be studied in the particular case of the high field ionic conduction in CSZ.

The study of cationic movements during the anodization of metallic substrates covered with thin films of CSZ was carried out in order to check the role played by interfaces in the injection of defects. Moreover in order to establish whether or not cation movements take place in the underlying oxides, anodization of Nb|Ta|CSZ or Nb|Al|CSZ systems were carried out since we have shown (11, 12) that the anodization of Nb|Ta and Nb|Al systems leads to a partial inversion of the order of cations due to cationic movements. In a similar way, we have studied the anodization of Al|CSZ|Nb|Ta systems in order to see if cationic movements exist in the metal oxides superimposed on the CSZ layer. All these experiments may permit us to elucidate the following problem: in the case of various superimposed oxide layers does a sole transport number of metal characteristic of the whole system exist? As the hypothesis of ionic movements in oxide films taking place by injection of point defects at one of the interfaces (metal-oxide or oxide-solution) implies the preservation of the cationic transport number (2), these experiments can give insights on the microscopic transport mechanism of cations.

This work is part of a general program devoted to the study of oxidation mechanisms of duplex layers and to their applications (18), and to thermal, anodic, and plasma treatments of solid surfaces covered with thin films of solid electrolytes acting as selective membranes (19).

Experimental

Sample preparation.—The metallic and CSZ thin films were deposited on silicon or aluminum substrates. The silicon samples were single crystal, [100] oriented with an n-type bulk resistivity of 10^{-2} Ωcm. Prior to deposition they were cleaned by successive dipping in HF, deionized water, and acetone. Niobium and tantalum films were deposited either by electron gun evaporation in high vacuum (less than 10^{-8} Torr during deposition) or by d-c triode sputtering in an argon plasma at a 0.13 Pa pressure. Ta and Nb sputtering targets were supplied by Kawecki Berylco Industries with a 99.98% purity for Ta and 99.9% for Nb. In the same way, Al films were obtained by d-c triode sputtering of an Al cathode in an argon plasma. CSZ films were made by rf sputtering of a sintered CSZ cathode supplied by LCC-France; the technique used is described in detail elsewhere (15).

Anodic oxidations were carried out at constant current density and temperature either in ammonium citrate solutions (0.5 or 2% by weight) or in ammonium borate solutions (0.5% by weight, pH kept at 9 by ammonium hydroxide additions). Exactly the same results were obtained whatever the solutions, thus in what follows, the electrolytes used will not be specified. Anodizations were performed using an anode assembly described elsewhere (20), in which a 1 cm^2 surface is delimited by a pressed Teflon O-ring. In the case of M_1|CSZ and M_1|M_2|CSZ structures, an ohmic contact was made with a conducting Ag paste on the back side of the Al or Si substrate. When metallic layers were deposited on top of CSZ films (Si|M_1|CSZ|M_2 structures), in order to anodize these metallic layers, we established outside the area in contact with the electrolyte an electrical contact (with Ag conducting paste) between the substrate and the metallic layers. Let us notice that it was not possible to anodize the metallic

layers on top of CSZ without the short circuit between these layers and the substrate. Hence we can exclude the presence of defects in CSZ layer which allowed the deposited metal layers to contact the substrate, so the CSZ takes part in the subsequent anodization. Due to possible roughness effects at the CSZ-M_2 interface, we cannot ascertain that all the deposited layer on top of CSZ was anodized without leaving unanodized metal islands. However, the same results were obtained for $Si|M_1|CSZ|M_2$ as well as for $M_1|CSZ|M_2$ structures, while the roughness effects must be more important in the last case. Thus we can reasonably assume that unanodized metal islands, if existing, are of very small dimensions (< 5 nm) and do not modify the anodization of the substrate.

Analysis of samples.—Nuclear microanalysis by the direct observation of nuclear reactions and of backscattering particles was used to study the samples before and after anodization. The experiments were carried out using the 2 MeV Van de Graaff accelerator of the Ecole Normale Supérieure.

The ^{16}O content of the films was measured using the $^{16}O(d,p)^{17}O^*$ nuclear reaction as described in detail by Amsel *et al.* (21). Absolute values were obtained by comparison with a reference target known to within ±3% (22).

Rutherford backscattering techniques were used to analyze the depth distribution of cations in the films and in their anodic oxides; lateral homogeneity was assumed for the interpretation of the spectra. The basic concepts and equations pertaining to Rutherford backscattering spectra interpretation can be found in Ref. (23) and will not be presented here; the application to the case of superimposed layers is described in detail in Ref. (11). In all analyses, $^4He^+$ ion beams were used and the backscattered particles were detected at 165° angle by means of a surface barrier detector (21). The energy resolution being about 14 keV, it was possible to evaluate the depth distribution for Nb, Ta, Al, or Zr atoms in the oxide films with a depth resolution of about 20 nm.

Absolute amounts of Nb, Ta, Al, or Zr expressed in atoms/cm² were obtained (assuming the validity of the Rutherford law) by comparison with a Ta film taken as a standard (24). The film thicknesses will be given in nanometers, the equivalence atoms/cm² — nanometer being obtained by assuming, respectively, a density of 4.74 for Nb_2O_5 (25), 8.04 for Ta_2O_5 (25), 3.17 for Al_2O_3 (26), and 5.32 for CSZ [deduced from Ref. (17)].

Results and Interpretation

In order to describe our results on ionic movements under high electric field in terms of microscopic transport mechanisms, we use the concepts of oxygen and cationic transport events [see for details p. 1551, Ref. (11)]. By the term of cationic (or oxygen) transport events, one means the sequence of elementary jumps of one or more cations (or oxygen) which results in a transport of charges from their creation point to that of their recombination.

During the anodization of metals covered with a thin CSZ film some stresses can be developed at the metal oxide-CSZ interface, due to the increase of volume of the underlying metal oxide (Pilling-Bedworth ratio equal to 1.6 or 2.5 for Al or Ta for example). The ductility of anodic oxides is known to be very high (27); this should make easier the displacement of the CSZ layer located on the top of growing metal oxide. But this last phenomenon is not associated with an ionic migration and so will not be taken into consideration in what follows.

Relationships between oxidation potential V and time t: $V = f(t)$.—Figure 1 shows some typical curves obtained by recording oxidation potential as a function of time during the anodization of Ta substrates covered

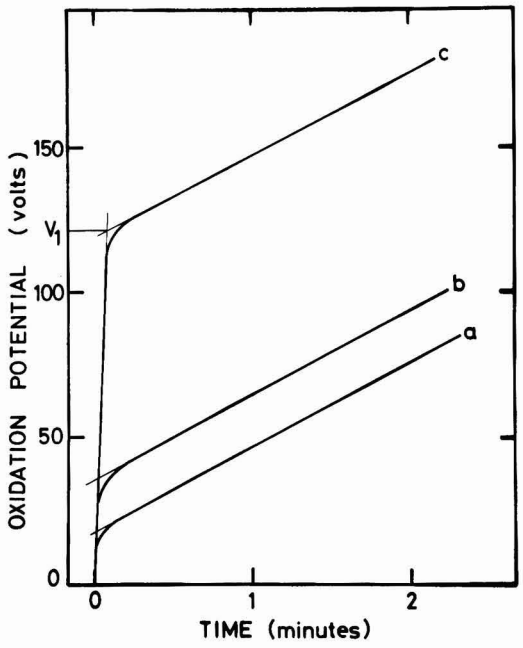

Fig. 1. Oxidation potential V as a function of time during anodization at ≃1.3 mA/cm² current density at a 23°C temperature for Ta substrates covered with thin CSZ films of various thicknesses: (a) 40 nm, (b) 80 nm, (c) 270 nm.

with CSZ thin films. The three curves of Fig. 1 were obtained for various thicknesses of the CSZ layer; these experiments were carried out at 23°C temperature with a current density of ~1.3 mA/cm².

Two linear regions can be distinguished on the three curves; the first region corresponds to a rapid potential increase, while the slope observed at high potential is the same as the one measured in the case of pure Ta_2O_5 growth. The nonabrupt transition between these two regions may be due to the roughness of the Ta-CSZ interface. As a slight thermal oxidation of the Ta substrate was observed (17) during CSZ film deposit, we cannot exclude some lateral inhomogeneity of the tantalum oxide thickness which could increase the roughness of the CSZ|Ta interface; let us notice that for Al|CSZ samples this transition region practically disappears.

The intercept of the two straight lines determines an oxidation potential V_1 which was taken as a measure of the potential drop in the CSZ layer. Since the thickness d of the CSZ films is determined by backscattering measurements (see experimental), we can evaluate the mean field E_{exp} in the CSZ layer by $E_{exp} = V_1/d$. The linear increase of the potential drop V_1 as a function of the thickness of the CSZ layer excludes any artifacts due to the possible presence of pores in the deposit.

The same values of V_1 were obtained during the anodization of Al or Nb substrates covered with thin CSZ layers of the same thicknesses. This shows that no appreciable influence of the substrate has been evidenced in these experiments.

In Table I. we present the values of the electric field E_{exp} in the CSZ layers at various current densities and for a temperature of 23°C. These values are mean values obtained by more than ten measurements performed either on Ta|CSZ or Al|CSZ systems. The values of the theoretical electric field E_{th} obtained from the expression

Table I. Values of the electric field E_{exp} in CSZ layers and in pure ZrO_2 as a function of current density; E_{th} calculated following Eq. [1]

Current density	$E_{exp} \times 10^6$ V/cm in CSZ	$E_{th} \times 10^6$ V/cm	$E_{exp} \times 10^6$ V/cm in ZrO_2
0.1 mA/cm²	3.5 ± 0.3	19.12	3.6
1 mA/cm²	4.3 ± 0.4	21.39	4
10 mA/cm²	5.5 ± 0.5	23.65	4.3

$$i = 2anvq \exp - \frac{W - qaE_{th}}{KT} \qquad [1]$$

as described in the introduction are presented in Table I. The values of the electric field during anodization of zirconium, *i.e.*, in pure anodic ZrO_2, for the same experimental conditions, are also given for comparison (28).

Table I shows that E_{exp} in CSZ, which increases when i increases is always much lower than E_{th}. The difference between E_{exp} and E_{th} cannot be explained by our experimental uncertainties on E_{exp} which are of the order of 10%. These uncertainties preclude a precise determination of the $E_{exp} = f(\log i)$ relationship. However, it seems that E_{exp} in CSZ does not increase linearly with $\log i$. Such an effect is also observed in pure anodic ZrO_2 (28) for high current densities. The values of the electric field in CSZ and in ZrO_2 are similar for current densities of 0.1 and 1 mA/cm² and are different for 10 mA/cm². As most of the results presented in this work were obtained at current densities of about 1 mA/cm², in what follows we shall consider CSZ films like zirconia anodic oxides, *i.e.*, with $t^+ \simeq 0$ (10).

Note that this assumption (*i.e.*, CSZ behaves like ZrO_2 anodic oxide) has been checked by experiments on oxygen movement which evidenced a partial inversion of the oxygen atom order in CSZ layers (29) during anodization of underlying metallic layers, like for pure zirconium anodization (28).

Anodization of Metal|CSZ systems.—Figures 2 and 3 represent, respectively, typical backscattering spectra for Ta|CSZ and Al|CSZ samples before and after anodization. In Fig. 2 the Zr spectrum is shaded, and the area of this spectrum does not change after anodization. This means that no dissolution from the CSZ layer occurs. In Fig. 3, the Zr, Hf, and Ca spectra which are clearly separated and isolated from Al background, are exactly the same before and after anodization. Thus it may be concluded that there is no dissolution of any cationic constituents of the CSZ layer.

Two plateaus are observed on the Ta spectrum after anodization (see Fig. 2); plateau 1 corresponds to Ta atoms in the Ta oxide layer while plateau 2 corresponds to unoxidized Ta atoms. As the ratio of plateau heights is the same as the one obtained in the case of pure Ta anodization, it can be assumed that pure Ta_2O_5 is formed during the anodization of Ta|CSZ systems. Similar conclusions for Al are obtained from the analysis of the Al spectrum in Fig. 3. Hence, the anodic oxidation of metal|CSZ systems leads to the formation of stoichiometric metal oxides.

The width of the front edge of the Ta (or Al) spectrum after anodization in Fig. 2 (or 3) is practically the same as the corresponding width before anodization. Note that the arrows in all figures indicate the position of elements on the surface of samples. This result demonstrates that metallic atoms did not enter the CSZ layer during anodization within our experimental resolution (about 20 mn). Let us notice, however, that we do not exclude a slight mixing between the metallic layers and CSZ during the deposit of the latter; the magnitude of such a mixing may be a function of the deposition conditions (17). The interpretation of these results, based on the necessary assump-

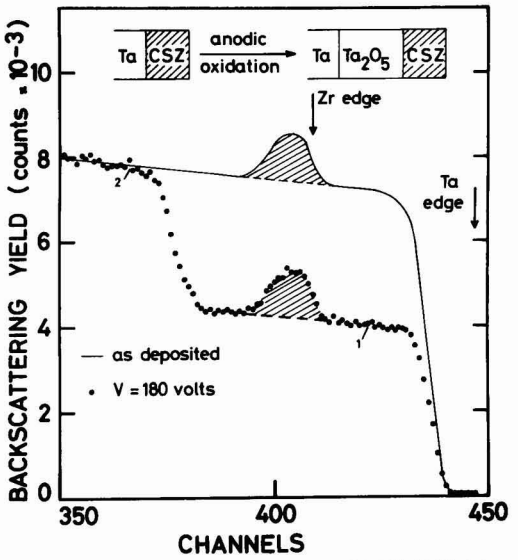

Fig. 2. Rutherford backscattering spectra of 1.6 MeV $^4He^+$ ions (3.2 keV/channel) for a CSZ film (48 nm) deposited on Ta substrate: before anodization (solid line) and after anodization (·) at $V = 180V$ and $i = 1$ mA/cm². The arrows indicate the position of elements at the surface of the sample.

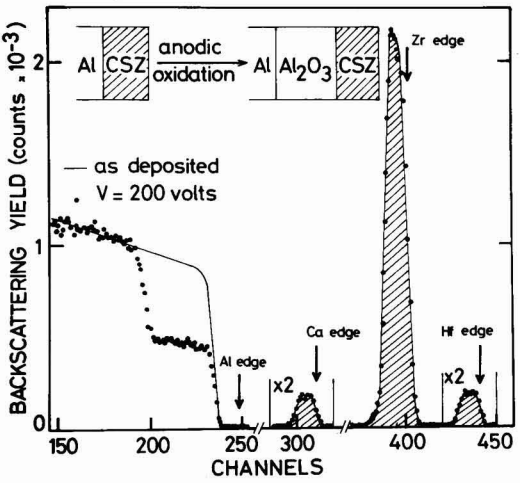

Fig. 3. Rutherford backscattering spectra of 1.8 Mev $^4He^+$ ions (3.3 keV/channel) for a CSZ film (53 nm) deposited on Al substrate: before anodization (solid line) and after anodization (·) at $V = 200V$ and $i = 1$ mA/cm². For arrows see Fig. 2.

tion of current continuity can be sought in the frame of one of the two following assumptions:

(1) The transport number of cations (t^+) is the same in each layer, *i.e.*, in the CSZ layer and in the underlying metal oxide, the value of t^+ being determined by the mechanism of injection of transport events at the interfaces (oxide-solution or metal-oxide interface). This hypothesis means that the fluxes of anionic and cationic transport events are preserved through all the film (*i.e.*, in the CSZ layer and in the metal oxide).

(2) The value of t^+ is different in the CSZ layer and in the underlying metal oxide. This hypothesis means that t^+ may be an intrinsic property of each layer, which does not depend on the other layers nor on the

position of the layer. In this case the t^+ values should be equal to 0.25 and 0.4 in Ta_2O_5 and in Al_2O_3 layers (6, 9), respectively, and to zero in CSZ layer.

The results presented on Fig. 2 and 3 can be explained by both assumptions. Let us now analyze the mechanisms of ionic movement involved in these two cases.

Two different mechanisms may be considered for the first hypothesis:

(a) The injection of point defects is determined by the nature of the oxide-solution interface. In the case of CSZ-solution interface, due to the properties of CSZ ($t^+ = 0$), it is logical to assume that only oxygen transport events are injected, *i.e.*, the cationic current J_c is thus equal to zero in CSZ and in the underlying metal oxide (Fig. 4a). Following this mechanism (a) the anodization of Ta or Al substrates covered with a thin CSZ layer involves only oxygen movement.

(b) The injection of point defects is determined by the nature of the metal-oxide interface. In the case of $Al|Al_2O_3$ or $Ta|Ta_2O_5$ interfaces, both oxygen and cation transport events are observed ($t^+ \neq 0$) (6, 9) during the anodization of pure metals. According to this fact, in the frame of this mechanism (b) oxygen and cation movements must be preserved through the whole oxide, *i.e.*, in the underlying metal oxide and in the CSZ layer (Fig. 4b). Thus cations move in the metal oxide and in the CSZ layer. As no broadening of the oxide-CSZ interface is observed, this cationic movement, if it takes place, must lead to the conservation of the order of cations. This is possible with some assumptions on the various jump probabilities of cations like those developed for Ta and Nb in a previous paper (11). In fact, to obtain the conservation or the order of cations, we must assume that the jump probability of Ta or Al cations (P_{Ta} or P_{Al}) are lower than that of Zr (P_{Zr}), Ca (P_{Ca}), and Hf (P_{Hf}). Moreover, since no relative movement of Zr, Ca, and Hf occurs (the cation distribution in CSZ film does not change after anodization, see Fig. 3), we must assume that $P_{Zr} = P_{Ca} = P_{Hf}$. Owing to the properties of CSZ previously defined, and to the fact that Zr cations do not seem to take part in the ionic current during Zr anodization (10), this mechanism (b) appears questionable.

The mechanism of ionic movement involved by hypothesis (2) is schematically presented on Fig. 5. In this case, cationic and anionic movements exist in the underlying metal oxide ($J_C \neq 0$ and $t^+ \neq 0$) while there is only oxygen movement in the CSZ layer ($J_C = 0$ and $t^+ = 0$). With this hypothesis metallic atoms do not enter the CSZ layer and thus this means that metal oxide must be formed partially at the oxide-CSZ interface.

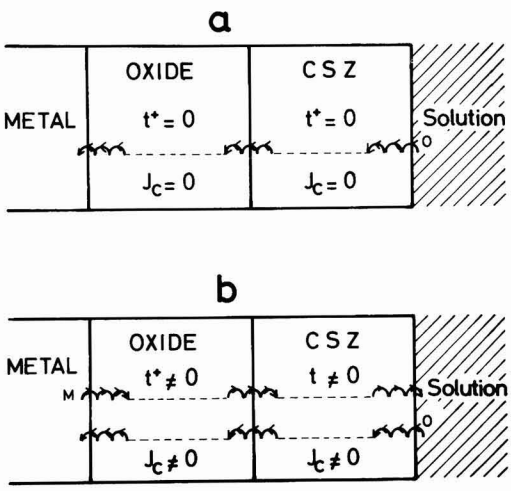

Fig. 4. Schematic representation of ionic movements during the anodization of Metal | CSZ systems with the same value of the transport number of cations t^+ in the whole oxide. (a) $t^+ = 0$, (b) $t^+ \neq 0$.

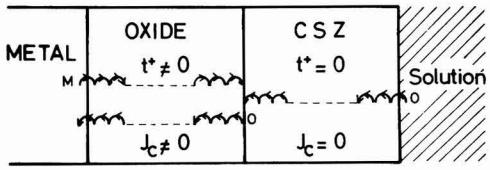

Fig. 5. Schematic representation of ionic movements during the anodization of Metal | CSZ systems with different values of t^+ in each layer.

Anodization of $M_1|M_2|CSZ$ systems.—To establish whether cationic movements take place in the underlying metal oxide, anodization of Nb|Ta|CSZ systems was carried out. Figure 6 represents backscattering spectra obtained on such systems before and after anodization. As a result of the preceding experiments, these spectra were analyzed assuming that no dissolution of Zr occurs during oxide growth; therefore the

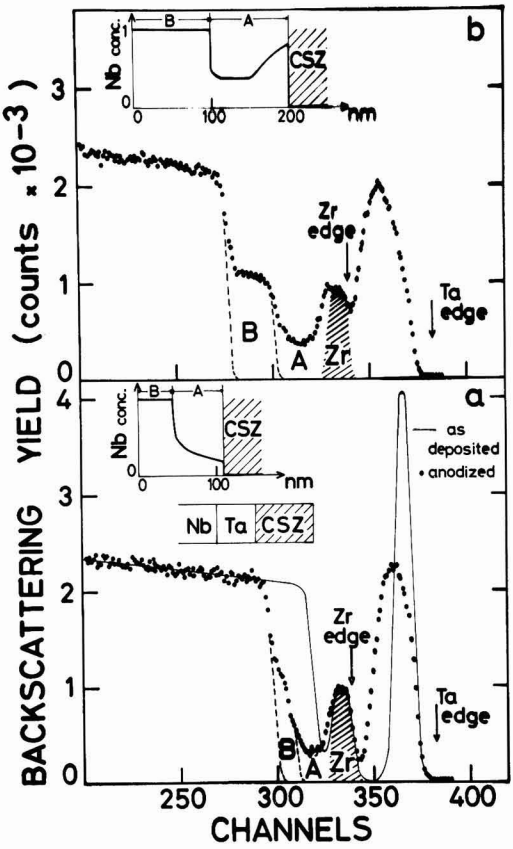

Fig. 6. Rutherford backscattering spectra of 1.8 Mev $^4He^+$ ions (3.2 keV/channel) for a CSZ layer (47 nm) superimposed on a Ta film (21 nm) deposited on Nb substrate before and after anodization at two potentials: (a) $V = 80V$, (b) $V = 120V$, $i = 1$ mA/cm^2. The inserts represent the corresponding schematic Nb depth profiles in the oxide. For arrows, see Fig. 2.

Zr spectrum is shaded with a constant overall area on each figure. The front edge of the Ta peak before and after oxidation on Fig. 6a is located at the same energy, lower than for Ta atoms located at the surface of the sample (shown by the arrow Ta edge). This shift is due to the presence of the CSZ layer and means that Ta atoms did not enter the CSZ layer. On Fig. 6a two regions A and B can be defined in the Nb spectrum after anodization. Region A corresponds to Nb atoms which have entered the Ta oxide and thus have formed a Ta and Nb oxide mixture, while region B corresponds to the remaining oxidized Nb atoms [see Ref. (11) for details]. The corresponding Nb depth distribution in the oxide is schematically presented in the insert of the figure and it shows that Nb atoms have crossed the inner edge of the Ta atom distribution. This fact is evidence for cationic movements in the metal oxide underlying the CSZ layer. The behavior of Nb and Ta cations during oxidation of Nb|Ta|CSZ systems appears qualitatively similar to that observed during Nb|Ta anodization (11).

Figure 6b is obtained at a higher oxidation potential. The area of region A of the Nb spectrum increases when the potential increases. This means that more and more Nb cations penetrate into the Ta oxide layer as anodization is pursued. This is checked by the fact that the front edge of the Ta peak is broadened when the potential increases. It was already observed for Nb|Ta anodization (11). Moreover the Ta peak is not shifted toward high energies, this means that the Ta atoms do not enter the CSZ layer. Hence the broadening of the front edge of the Ta peak (Fig. 6b) is only due to the increase in Nb concentration at the metal oxide-CSZ interface. Penetration of Nb cations into the CSZ layer cannot be detected on the Zr or Nb spectrum, but the analysis of the Ta spectrum (shift of the peak to lower energies and broadening of the front edge) indicates that this Nb penetration, if it occurs, must be so weak that we cannot detect it within our experimental sensitivity. In what follows, we shall thus assume that Nb cations, like Ta or Al cations, do not enter into the CSZ layer during anodization.

The Nb depth distribution in the oxide is schematically represented in the insert on Fig. 6b. The various parts of the oxide film are hence: (*i*) a pure Nb_2O_5 layer at the metal-oxide interface (region B); and (*ii*) a region containing both Nb and Ta cations (region A). In this latter region the Nb concentration is maximum at the oxide-CSZ interface and then drops in the bulk down to a value which remains constant until region B is reached. These results demonstrate that cationic movements exist in the underlying metal oxide, and are consistent with the idea that Nb atoms do not cross the oxide-CSZ interface. Moreover, although no precise measurement of the fraction of the oxidized Nb atoms located in region A [*i.e.*, F_t in Ref. (11)], was carried out, the results obtained on this system are similar to those observed on Nb|Ta samples.

These results allow us to eliminate the first mechanism of hypothesis (1) (only oxygen movement through all the film), since oxygen movement cannot lead to a cation mixing. Let us notice that they can be explained by the second mechanism of hypothesis (1), if we assume that the jump probabilities of Nb and Ta cations (P_{Nb} and P_{Ta}) are lower than that of Zr (P_{Zr}) so that Nb or Ta cations do not significantly penetrate in the CSZ layer. On the other hand the results are in good agreement with hypothesis (2), *i.e.*, the transport number of cations is an intrinsic property of each layer.

Anodization of $M|CSZ|M_1|M_2$ systems.—In order to establish whether cationic movements take place in metal oxides located above a CSZ layer, *i.e.*, at the oxide-solution interface, and in the underlying CSZ layer, the anodization of Al|CSZ|Nb|Ta systems was studied.

Figure 7 represents backscattering spectra after anodization at various potentials of an Al substrate covered with a CSZ layer (30 nm), itself covered with a 55 nm thick Nb layer on which a Ta film (22 nm) was deposited. On each figure, the Zr spectrum is shaded with a constant overall area. Figure 7a corresponds to an oxidation potential equal to 160V for which the Ta and Nb layers are fully oxidized, the potential drop in CSZ is established and the Al substrate just begins to be anodized. Due to the cationic movements during the anodization of Nb and Ta layers, Nb atoms have crossed the inner edge of the Ta atoms distribution, and thus have formed an Nb and Ta oxide mixture. These Nb atoms correspond to region A of the Nb spectrum, while region B corresponds to the remaining oxidized Nb atoms. The insert in the figure represents schematically the Nb depth profile in the near surface region of the film, as deduced from the spectrum.

On Figure 7b and c, the backscattering spectra correspond to the anodization of the Al substrate at higher

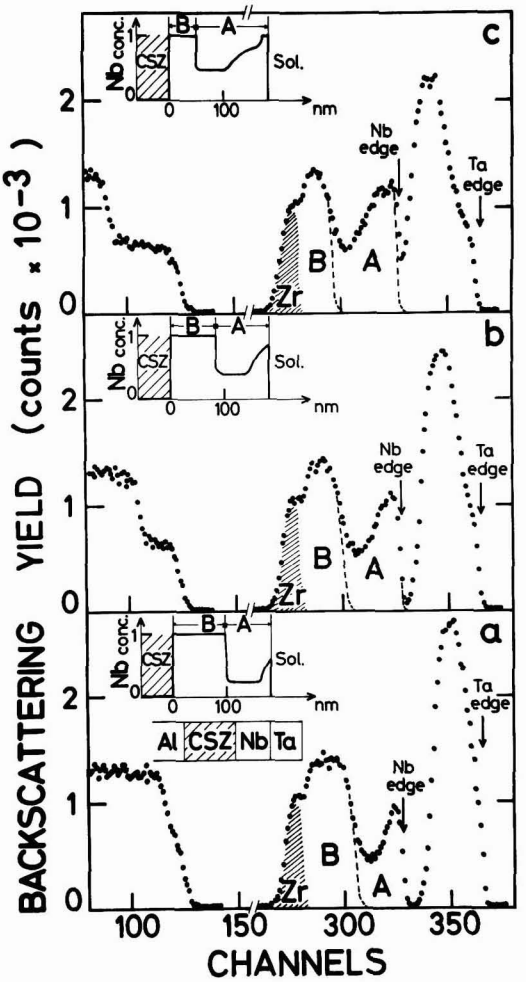

Fig. 7. Rutherford backscattering spectra of 1.8 Mev $^4He^+$ ions (3.5 keV/channel) for multi superimposed layers on Al substrate: Al | CSZ(30 nm) | Nb(55 nm) | Ta(22 nm) anodized at $i = 1$ mA/cm^2 and at various oxidation potentials: (a) $V = 160$V, (b) $V = 210$V, (c) $V = 270$V. The inserts represent the corresponding schematic Nb depth profiles in the oxides. For arrows, see Fig. 2.

potentials. The comparison of these two figures with Fig. 7a shows that the area of region A of the Nb spectrum increases with oxidation potential. This demonstrates that Nb cations go on entering the Ta oxide layer whatever the potential. At the same time, the Al substrate is oxidized and Al_2O_3 is formed as the corresponding plateau can be observed in the Al spectrum. These results evidence cationic movements in the Nb and Ta oxide region, located above the CSZ layer, during the anodization of the Al substrate. It must be emphasized that cationic movements occur while the Nb and Ta oxide mixture is separated from the Al substrate by the CSZ layer.

The analysis of the spectra shown on Fig. 7 is consistent with the idea that Zr atoms (of the CSZ layer) have not entered the Nb oxide layer, and thus inserts in Fig. 7b and c represent schematically the Nb depth profile in the oxide with a sharp boundary at the interface with the CSZ layer.

The assumption of no penetration of Zr cations in the metal oxide was checked by experiments carried on Nb|CSZ|Ta samples. After anodization, the Ta_2O_5 layer at the oxide-solution interface and the Nb_2O_5 layer at the metal-oxide interface were separated by the CSZ layer without penetration of Zr cations into the Ta_2O_5 layer.

Another point to notice about Fig. 7 is that the front edge of the Al spectrum is wider than that observed on Fig. 3; however, as the oxidation potential increases, no further broadening occurs. This probably means that during the deposit of the CSZ layer some mixing with the Al substrate occurred, but during the anodization process no Al atoms entered the CSZ layer. On the three spectra the areas of the Nb and of the Ta components are constant; thus there is no appreciable dissolution of Nb or Ta during anodic oxidation.

These results allow us to eliminate mechanism (b). In fact in the frame of this mechanism, the cation movements evidenced in the Nb and Ta oxide mixture must be preserved in the whole oxide. In order to explain the preservation of the order of cations between the CSZ layer and the Nb and Ta oxide mixture, one must assume that P_{Ta} and P_{Nb} are higher than P_{Zr}. A contradiction appears, since in the frame of mechanism (b) the preceding results (anodization of Nb|Ta|CSZ systems) have been explained assuming P_{Ta} and $P_{Nb} < P_{Zr}$. As the mechanism (a) was eliminated previously, it appears that the hypothesis (1) [assuming the preservation of transport events through the whole oxide] is in contradiction with our experimental results and must be eliminated. It means that the cation constituents of CSZ layer (Zr, Ca, and Hf) do not move during anodization while cationic movements take place in the metal oxide layers located either on the top or under the CSZ layer. These results are in good agreement with hypothesis (2) which assumes that the transport number t^+ is an intrinsic property of each layer.

The results of this last experiment can be compared to those obtained during the anodization of Al|Nb|Ta systems (30) in which during the oxidation of the Al substrate, the Nb and Ta cation distribution, in the oxide mixture, goes on changing as the oxidation potential increases. These results were interpreted (31) assuming that cation transport events, coming from the underlying pure Al_2O_3 layer are preserved in the whole oxide, *i.e.*, move through the mixed Ta and Nb oxide by a neighbor-to-neighbor type propagation process. Since the same results are obtained on Al|CSZ|Nb|Ta systems, we can conclude that the presence of the CSZ layer, in which only oxygen moves, does not eliminate cationic movements by a neighbor-to-neighbor jump in the Ta and Nb oxide mixture at the oxide solution interface.

Very similar results were obtained during the anodization of Al|CSZ|Nb|Al system, *i.e.*, the cation distribution in the oxide in the near surface region of the film undergoes strong changes whereas the Al substrate is oxidized as it is observed for the Al|Nb|Al system (29). In this case also, no penetration of Zr cations in the mixed oxide was evidenced.

Figure 8 represents schematically the main conclusion drawn from these experiments: the transport number of cations t^+ changes from one part of the film to another. t^+ is equal to zero in the CSZ layer, while there is cationic movement ($t^+ \neq 0$) in the metal oxide at the oxide-solution interface. Hence ionic current is transported by cation and oxygen in the outer part of the film while there is only oxygen movement in the CSZ layer.

Anodization of $M_1|M_2|CSZ|M'_1|M'_2$ systems.—All the preceding experimental results are in good agreement with hypothesis (2). In order to further confirm the validity of this hypothesis, we have studied the cation distribution in oxides formed by anodization of Nb|Al|CSZ|Nb|Ta systems. It was expected that cationic movements had to take place in metal oxides above and below the CSZ layer, while in the CSZ layer only oxygen movements have to take place.

Figure 9 represents backscattering spectra from Nb|Al (20 nm)|CSZ (85 nm)|Nb (36 nm)|Ta (14 nm) systems oxidized at two oxidation potentials. On the two figures, the Zr and Ta contributions are shaded while the two Nb parts corresponding to the Nb layer above the CSZ and to the Nb substrate are labelled Nb(1) and Nb(2). Figure 9a corresponds to an oxidation potential equal to 100V, for which the Ta and Nb layers are fully oxidized, part of the potential drop in the CSZ layer is established while the Al layer and the Nb substrate are not oxidized. As a result of cationic movements during the anodization of Ta and Nb layers, Nb atoms have crossed the inner edge of the Ta atom distribution and thus have formed the Ta and Nb oxide mixture at the oxide-solution interface. These Nb atoms correspond to region A of Nb(1), while region B of Nb(1) corresponds to the remaining oxidized Nb atoms. The insert in the figure shows schematically the Nb depth profile in the near surface region of the oxide.

Figure 9b corresponds to a potential equal to 200V for which the Al layer and the Nb substrate underlying the CSZ layer are oxidized. This figure shows that the area of part A of Nb(1) has increased; this indicates that Nb atoms have entered the Ta oxide layer during the anodic oxidation of metallic layers underlying the CSZ film. This result is identical to that obtained in the preceding experiments and can be interpreted by the fact that cationic movements take place in the oxide near the oxide-solution interface whereas the substrate is oxidized. Two regions (A′ and B′) can be distinguished on Nb(2) spectrum. Region B′ represents Nb atoms in a pure Nb_2O_5 layer at the metal-oxide interface, while region A′ corresponds to Nb atoms which have crossed the inner edge of the Al atoms distribution and thus have formed an Nb and Al oxide mixture. This result is similar to that obtained during the anodic oxidation of the Nb|Al system (12). The insert on the figure schematically represents the Nb depth profile in the film. The two Nb distributions (under and above the CSZ layer) are shown with sharp boundaries with the CSZ layer, *i.e.*, assuming, as above, no penetration of Zr cations in the Nb and Ta oxide mixture superimposed on the CSZ layer, and

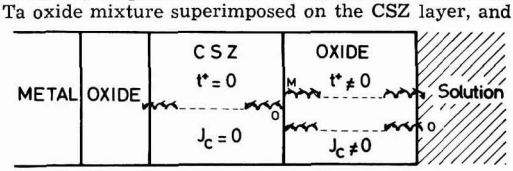

Fig. 8. Schematic representation of ionic movements during the anodization of Metal | CSZ | Metal systems with different values of t^+ in CSZ and in the metal oxide at the oxide solution interface.

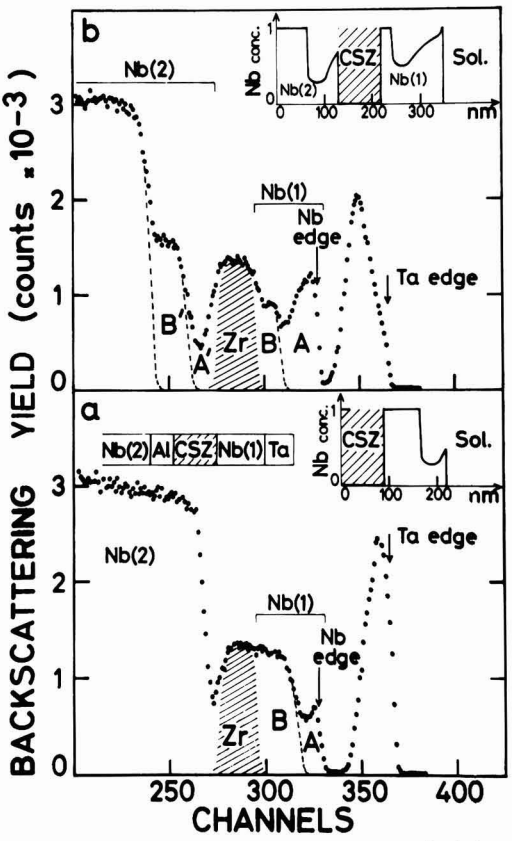

Fig. 9. Rutherford backscattering spectra of 1.8 Mev $^4He^+$ ions (3.5 keV/channel) for multi superimposed layers on Nb substrate: Nb | Al(20 nm) | CSZ(85 nm) | Nb(36 nm) | Ta(14 nm) anodized at $i = 1$ mA/cm^2 at different potentials: (a) $V = 100$V, (b) $V = 200$V. The inserts represent the corresponding schematic Nb depth profiles in the oxides. For arrows, see Fig. 2.

without penetration of Nb coming from the underlying layer into the CSZ layer.

These results fully confirm the preceding results and are in agreement with hypothesis (2): cationic movements take place both under and above the CSZ layer during the anodization of the substrate. Figure 10 schematically represents this conclusion: the transport number of cations t^+ depends on the nature of each layer while cations move in the metal oxide located above and below the CSZ layer. Note that the confirmation of hypothesis (2) needs the knowledge of the values of t^+ in metal oxides overlying or underlying the CSZ layer. Our experimental conditions do not allow us to measure precise values of F_t, *i.e.*, the transport number of cations in the Nb and Ta oxides located over and under the CSZ layer (11). Thus, at the present time, it is not possible to quantitatively compare these F_t values to that measured during pure Nb|Ta anodization. However, work is in progress to check hypothesis (2), since we have realized a computing calculation of backscattering spectra which allow us to precisely determine the cation distribution in the oxide films. Results of this study will be published in a later paper.

Discussion and Conclusions

In this work we have shown that it is possible to anodize metallic substrates (Nb, Ta, or Al) covered

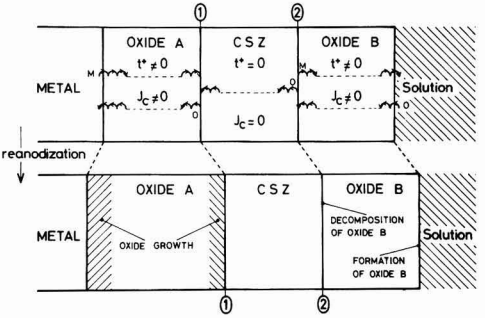

Fig. 10. Schematic representation of ionic movements during the anodization of Metal | CSZ | Metal systems with different values of t^+ in each layer, leading to oxide A growth while thicknesses of the CSZ layer and of oxide B are preserved.

with CSZ thin films. The growth rates of oxide on metallic substrates in metal|CSZ systems are similar to those observed for pure metals, and the current field relationship in CSZ appears similar to the one observed during pure Zr anodization. The anodization of $M_1|M_2|CSZ$ or $M_1|M_2|CSZ|M'_1|M'_2$ systems gives the experimental proof that cation movements take place in metal oxides located above and below the CSZ layer. Moreover, all these results are consistent with the idea that only oxygen atoms move through CSZ films, *i.e.*, the cationic constituents of CSZ do not take part in ionic current. These results seem to indicate that the mechanism of high field conduction in CSZ film is similar to that of pure anodic ZrO_2 in which the transport number of oxygen is above 0.95 (10). This means that the introduction of 12 atomic percent of Ca to stabilize the fluorite structure of ZrO_2 does not notably affect the high field ionic conduction in zirconia oxide. Two possibilities appear in order to explain this last point: (*i*) anodization of Zr leads to the formation of a highly conducting phase, similar to the one obtained by inclusion of CaO in ZrO_2. In this case, according to the presence in CSZ of a high oxygen vacancy concentration, oxygen ion movement takes place by a vacancy-type mechanism; (*ii*) oxygen ion movement does not take place by vacancy-type mechanism, neither in pure ZrO_2 film nor in CSZ film, in spite of the presence in CSZ of a high oxygen vacancy concentration with a low activation energy of movement (1.2 eV).

In hypothesis (*i*), one must explain the disagreement between E_{th} and E_{exp} (Table I). This disagreement seems to disappear if we use an effective field E_{eff} instead of the one of Maxwell, *i.e.*, the experimental field ($E_{Maxw} = E_{exp}$), in the relationship [1]. In fact in ionic cubic crystals (32) (and the oxygen sublattice is of cubic symmetry), the following relationship is valid

$$E_{eff} \leq E_{Maxw} + \frac{\epsilon - 1}{3} E_{Maxw}$$

where ϵ is the static dielectric constant, *i.e.*, $\epsilon = 25$ for CSZ thin films (17). This means that $E_{eff} \leq 9\ E_{Maxw}$, *i.e.*, $E_{eff} \leq 3.9 \times 10^7$ V/cm for $i = 1$ mA/cm^2. A question arises whether E_{eff} or E_{Maxw} (*i.e.*, E_{exp}) must be used in relationship [1]. Dignam has analyzed this question (2) and concludes that the Maxwell field must be used; however this problem has given rise recently to contradictory discussions (33) which indicate that Dignam's approach is not fully accepted.

The second possibility (*ii*) based on the fact that oxygen movement does not take place by a vacancy-type mechanism, implies that one must consider a new mechanism. Some essential features of such mechanism seem to be the following: injection of oxygen

charged species at the oxide-solution interface, which migrate by a neighbor-to-neighbor jump process, the activation energy of movement being lower than 1.2 eV. Works of Dignam (2), Fromhold (34), and Ortega (28) are attempts to provide at least partial informations on these migration mechanisms.

The second purpose of this work was devoted to study the mechanism of ionic movement through various superimposed layers having different values of cationic transport numbers. The essential results of this study are presented in Fig. 10. This figure shows schematically the presence of oxygen and cation transport events in metal oxides below and above the CSZ layer [respectively labelled (A) and (B)], and only of oxygen events in the CSZ film; at steady-state conditions the total ionic current (the electronic current can be neglected) must be preserved through the whole oxide, this means that $J_o(A) + J_c(A) = J_o(CSZ) = J_o(B) + J_c(B)$.

From the macroscopic standpoint, this figure indicates on the one hand the formation of oxide at the metal-oxide(A) and at the oxide(A)-CSZ interfaces, and on the other hand the decomposition of oxide(B) at the CSZ-oxide(B) interface, associated with the formation of the same quantity of oxide(B) at the oxide(B)-solution interface (see Fig. 10). In this way, the overall quantity of oxide(B) is preserved during anodization of the substrate as experimentally observed. It can be noticed that according to the fact that oxide(A) and (B) can have different values of cationic transport number, the quantity of oxide formed and eliminated at the interfaces of the CSZ layer are not necessarily equal. Thus, the role played by these interfaces appears to be very important. However it should be emphasized that the phenomena occurring at these interfaces (injection of charged species and oxide decomposition) are not the rate-determining steps of anodic growth since we have shown that the growth rates of oxide on metallic substrates (Ta or Al for example) covered with CSZ films are similar to those observed for pure metal anodization.

From the microscopic standpoint, the results summarized in Fig. 10 can be discussed by using the concept of oxygen and cationic transport events (see below).

Two extreme assumptions may be made to explain ionic movements in such superimposed layers. First, it could be assumed that oxygen and cation transport events are not distinct. There would be only one transport event implying the simultaneous movement of cations and anions. Thus, at a molecular scale, both cations and oxygen move in a ratio equal to the transport number which is a measure, at the macroscopic scale, of this movement and which appears as an intrinsic property of each oxide. In this frame, the results could be interpreted by assuming that each oxide layer preserves its own transport number. The microscopic jump process which can sustain this proposition could be searched in a similar way as that suggested by Fromhold (34), *i.e.*, some sort of place exchange mechanism.

At the interface between the crystalline CSZ and the amorphous metal oxide, some rearrangement of the structure has to occur. This can be obtained by taking into consideration the property of plasticity (25) of anodic oxides related to their amorphous nature. It is, however, difficult to explain with such a mechanism the absence of noticeable mixing at the two interfaces of CSZ.

The other extreme assumption is that the oxygen and cation transport events are distinct (note that this does not mean that we consider these two charge transport events as independant since we have shown that a strong correlation exists (13) between oxygen and cation jump probability during anodic oxide growth. It appears, in this frame, that the role played by interface 2 is fundamental. In fact, at this CSZ-oxide(B) interface, the following processes must occur: injection of oxygen charged species in the CSZ layer, and simultaneous generation of cationic transport events in the oxide(B). At the interface 1, the total current is due to oxygen injection in a way similar to the one taking place at an oxide-liquid electrolyte interface, CSZ acting thus as a solid electrolyte. Oxygen transport events have to exist in the whole oxide, but the associated charge q^- can be different in the CSZ layer and in metal oxide. For example at interface 2, oxygen transport events may be in the form of interstitialcy O^- in oxide(B) and in the form O^{2-} in CSZ layer. The current continuity, and the continuity of oxygen fluxes imply that a cationic charge M^+ has to be created at this interface. Here enough plasticity of anodic oxides must be assumed to explain the necessary rearrangement of the structure at the interface. In this assumption, the transport number in metal oxide(B) will be determined by the nature of the CSZ-metal oxide(B) interface. In the future work, we will try to answer this question.

Acknowledgments

The authors wish to express their thanks to G. Amsel, C. Ortega, and G. Velasco for helpful discussions. The technical assistance of MM. J. P. Enard, M. Guyery, and A. Laurent was much appreciated. This work was supported by the Centre National de la Recherche Scientifique (R.C.P. No. 157), by the D.G.R.S.T. and the D.R.E.T.

Manuscript submitted Feb. 20, 1980; revised manuscript received Sept. 12, 1980. This was Paper 189 presented at the Seattle, Washington, Meeting of the Society, May 21-26, 1978.

Any discussion of this paper will appear in a Discussion Section to be published in the December 1981 JOURNAL. All discussions for the December 1981 Discussion Section should be submitted by Aug. 1, 1981.

Publication costs of this article were assisted by the Laboratoire Central de Recherches Thomson—C.S.F.

REFERENCES

1. L. Young, "Anodic Oxide Films," Academic Press, New York (1961).
2. M. J. Dignam, in "Oxides and Oxide Films," Vol. 1, J. W. Diggle, Editor, Marcel Dekker, Inc., New York (1973).
3. C. J. Dell'Oca, D. L. Pulfrey, and L. Young, *Phys. Thin Films*, **6**, 1 (1971).
4. J. A. Davies, J. P. S. Pringle, R. L. Graham, and F. Brown, *This Journal*, **109**, 999 (1962).
5. J. A. Davies, B. Domeij, J. P. S. Pringle, and F. Brown, *ibid.*, **112**, 675 (1965).
6. J. P. S. Pringle, *ibid.*, **121**, 865 (1974).
7. G. Amsel and D. Samuel, *J. Phys. Chem. Solids*, **21**, 1707 (1962).
8. J. P. S. Pringle, *This Journal*, **120**, 1391 (1973).
9. F. Brown and W. D. Mackintosh, *ibid.*, **120**, 1096 (1973).
10. J. L. Whitton, *ibid.*, **115**, 58 (1968).
11. J. Perriere, S. Rigo, and J. Siejka, *ibid.*, **125**, 1549 (1978).
12. J. Perriere, S. Rigo, and J. Siejka, Abstract 194, p. 462, The Electrochemical Society Extended Abstracts, Seattle, Washington, May 21-26, 1978.
13. J. Perriere, S. Rigo, and J. Siejka, Abstract 196, p. 468, The Electrochemical Society Extended Abstracts, Seattle, Washington, May 21-26, 1978.
14. T. H. Etsell and S. N. Flengas, *Chem. Rev.*, **70**, 339 (1970).
15. M. Croset, J. P. Schnell, G. Velasco, and J. Siejka, *J. Appl. Phys.*, **48**, 775 (1977).
16. M. Croset, J. P. Schnell, G. Velasco, and J. Siejka, *J. Vac. Sci. Tech.*, **14**, 777 (1977).
17. J. P. Schnell, Thesis, Université Paris VI, Paris (1977).
18. S. Rigo and J. Siejka, French Pat. "Anvar No. 7193."
19. M. Croset and G. Velasco, French Pat. No. 77.27.470.
20. G. Amsel, J. P. Nadai, C. Ortega, and J. Siejka, *Nucl. Instr. Meth.*, **149**, 713 (1978).
21. G. Amsel, J. P. Nadai, E. D'Artemare, D. David, E. Girard, and J. Moulin, *ibid.*, **92**, 481 (1971).
22. G. Amsel, J. P. Nadai, C. Ortega, S. Rigo, and J.

Siejka, *ibid.*, **149**, 705 (1978).
23. W. K. Chu, J. W. Mayer, A. Nicolet, T. M. Buck, G. Amsel, and F. Eisen, *Thin Solid Films*, **17**, 1 (1973).
24. S. Rigo, C. Cohen, A. L'Hoir, and E. Backelandt, *Nucl. Instr. Meth.*, **149**, 721 (1978).
25. A. J. Schrijner and A. Middlehoek, *This Journal*, **111**, 1167 (1964).
26. W. J. Bernard and J. W. Cook, *ibid.*, **106**, 643 (1959).
27. M. Propp and L. Young, Abstract 184, p. 438, The Electrochemical Society Extended Abstracts, Seattle, Washington, May 21-26, 1978.
28. C. Ortega, Ph.D. Thesis, University Paris 7, Paris (1981).
29. J. Perriere, J. Siejka, and M. Croset, Abstract 189, p. 448, The Electrochemical Society Extended Abstracts, Seattle, Washington, May 21-26, 1978.
30. J. Perriere, S. Rigo, and J. Siejka, Abstract 129, p. 294, The Electrochemical Society Extended Abstracts, Toronto, Canada, May 11-16, 1975.
31. J. Perriere, Thesis, Université Paris VII, Paris (1974).
32. J. Tessman, A. Kahn, and W. Shockley, *Phys. Rev.*, **92**, 890 (1953).
33. Panel discussion at The Electrochemical Society Meeting, Seattle, Washington, May 21-26, 1978.
34. A. T. Fromhold, Jr., *This Journal*, **127**, 411 (1980).

On the Mechanism of Electrodeposition in the Dimercaptothiadiazole/Copper Pyrophosphate System

Cameron Ogden* and Dennis Tench*

Rockwell International, Electronics Research Center, Thousand Oaks, California 91360

ABSTRACT

Cyclic voltammetric stripping results are presented which show that a dynamic equilibrium exists in the dimercaptothiadiazole (DMTD)/copper pyrophosphate system involving a species which accelerates the copper deposition rate, a decelerating species, Cu^{+2} ions, and other bath constituents. The experimental data are well explained by assuming that the accelerator is the copper-complexed DMTD monomer species, whereas deceleration is produced by the DMTD dimer. A model is presented which explains the additive effects in terms of a critical balance between the nucleation of new growth centers by the accelerating additive species and copper ammine complexes, and the limitations on growth imposed by the decelerating additive species which functions by blocking growth sites. Based on this model, which is supported by a-c impedance data and morphological studies, the important deposit properties can be understood and predicted.

Copper pyrophosphate electroplating baths containing dimercaptothiadiazole leveling additives (1, 2) are widely used in applications for which throwing power, tensile strength, and ductility are important considerations, as in electroforming and the plating of through-hole interconnections in high reliability circuit boards. Our previous work (3) has shown that additives of this class function in a complex way, decelerating the copper deposition rate at higher concentrations while exerting an accelerating effect at lower levels. Such dual decelerating/accelerating behavior results in enhanced leveling power, but also underlies a strong dependence of the deposit uniformity (4) and tensile properties (5) on the additive concentration. Control of this system is rendered more difficult by the slow additive activation required to produce decelerated deposition (3). In the present paper, the additive species present in copper pyrophosphate baths and the mechanisms by which they affect copper deposition are discussed.

Experimental Details

System description.—Unless otherwise noted, all measurements were made in air-saturated copper pyrophosphate baths at 55°C containing 22.5 g/liter Cu^{+2}, 175 g/liter $P_2O_7^{4-}$, 2.25 g/liter NH_3, and up to 50 μmoles/liter of the organic additive 2,5-dimercapto-1,3,4-thiadiazole (Aldrich Chemical Company). This pure compound was used as the additive since it is easier to control and has been shown (3-5) to yield results comparable to those for the proprietary formulation PY61-H (M & T Chemicals, Incorporated). Baths were prepared from concentrates C10XB and C11XB (M & T Chemicals, Incorporated) and were operated at a pH of 8.3.

The cell was Pyrex glass with a Teflon top and had a volume of 150 ml. Temperature was maintained constant within ±1°C by water circulated through a cell jacket from a Haake FT circulator-controller. The Pt-40% Rh counterelectrode and commercial SCE reference were dipped directly in the bath.

Cyclic voltammetric stripping studies.—The cyclic voltammetric stripping (CVS) method (3) was used extensively in these studies to measure changes in the copper electrodeposition rate produced by additive species. In this method, the potential of an inert Pt electrode is cycled in copper pyrophosphate baths at 50 mV/sec between −0.700 and 1.000V *vs.* SCE so that a small amount of copper is alternately deposited on the Pt surface and stripped off by anodic dissolution. The charge required to oxidize the copper deposit is proportional to the average deposition rate for that cycle and is found to be related to the concentration of additive in the bath when adequate solution mass transport is provided. The latter is attained by mounting the Pt electrode in the standard disk configuration (6) and rotating it at 2500 rpm. The rotating Pt disk electrode used for the present studies and its pretreatment are described elsewhere (3).

The effects of other bath species which affect the electrodeposition rate are to some extent cancelled by using the internal standard provided by the static electrode in the same bath. When the electrode rotation is stopped, those additive species which are present in very small concentrations compared to other bath constituents become depleted at the electrode surface as they are destroyed by reduction and inclusion in the

* Electrochemical Society Active Member.

Key words: electroplating, copper pyrophosphate, additive effects, molecular dynamics.

deposit. Thus, the stripping peak area approaches that which would be obtained in the same bath without low-level additive species present. The ratio of the stripping peak area with rotation (A_r) to that for the static electrode in the same solution (A_s) yields a relative rate parameter which reflects only the effect of such additive species on the electrodeposition rate.

Measurements of A_r/A_s were made under complete computer control using a Hewlett-Packard Model 9825 minicomputer in conjunction with a PAR Model 173 Potentiostat/Galvanostat and a PAR Model 179 Digital Coulometer. A Hewlett-Packard Model 6940B Multiprogrammer and a Model 98033A BCD were used as computer interfaces. Steady state for each measurement was assured by establishing a convergence limit of 4% for successive peak integrations.

A-C impedance analysis.—Measurements of the a-c impedance of the electrode during copper electrodeposition at constant potential were made from 0.1 Hz to 10 kHz using a Solartron Model 1174 Frequency Response Analyzer in conjunction with the PAR Models 173 and 179 instruments. Electrodes were rotated at 2500 rpm and comparable steady-state results were obtained with Pt (0.13 cm^2) and Cu (0.30 cm^2) substrates.

Results and Discussion

Additive activation studies.—A plot of A_r/A_s *vs.* the additive concentration for baths at operating temperature is shown in Fig. 1. Good sensitivity to the additive, which is the basis for use of this method as an analytical technique, is evident. It is also apparent that the additive accelerates the deposition rate at low concentrations ($A_r/A_s > 1$) but exerts a decelerating effect at higher levels ($A_r/A_s < 1$). The dependence of A_r/A_s on concentration is linear in the decelerating region and extrapolates to an A_r/A_s value of unity at zero concentration. This indicates that two additive species are involved, an accelerator and a decelerator, which act independently to affect the deposition rate. The presence of two species is also indicated by the observation that an activation period is required to produce deceleration on addition of the additive to the bath, whereas accelerated deposition is rapidly attained. The data in Fig. 1 were obtained after the baths were allowed to equilibrate for 16 hr at 55°C.

Plots of A_r/A_s as a function of time after addition of the additive to the bath at operating temperature are shown in Fig. 2. It is evident that the accelerating species is formed almost immediately (A_r/A_s rapidly increases to a steady value), whereas the decelerator forms more gradually, at a rate which increases with initial concentration. The minima observed at the higher concentrations are discussed below.

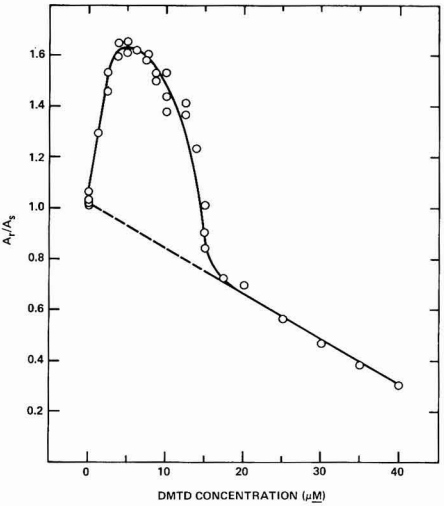

Fig. 1. Relative rate parameter (A_r/A_s) *vs.* additive concentration for copper pyrophosphate baths at 55°C (after 16 hr).

Analog additive studies.—A_r/A_s ratios were measured at room temperature in baths containing molecular analogs of 2,5-dimercapto-1,3,4-thiadiazole for which amino (-NH_2) or methyl (-CH_3) groups were substituted for one or both of the mercapto (-SH) groups. To ensure equilibration, baths were heated at 55°C for 16 hr before measurements were made. Data are given in Fig. 3. Both acceleration and deceleration were produced by 2-amino-5-mercapto-1,3,4-thiadiazole, but this analog was less effective than the dimercapto compound. The 2-methyl-5-mercapto-1,3,4-thiadiazole and 2-mercaptothiazoline analogs produced only deceleration, whereas 2,5-dimethyl-1,3,4-thiadiazole had no effect on the deposition rate. These results indicate that acceleration requires two groups which can complex with Cu^{+2} (*i.e.*, -SH or -NH_2), whereas one such group can produce deceleration (after activation). It should be noted that other compounds that are not direct analogs of the dimercaptothiadiazoles but contain the —S—C=N— group, like trithiocyanuric acid and sodium thiocyanate, also produce accelerated deposition. All of the accelerating species studied are capable of forming a ligand bridge between two copper ions which permits interaction via a conjugated framework.

Additive equilibria.—The simplest additive equilibrium scheme consistent with the available data is illustrated in Fig. 4. It should be borne in mind that the bath copper ions are highly complexed so that the concentration of free Cu^{+2} is extremely small (6) and may limit the rate of Cu^{+2} reactions. In aqueous solutions, the dimercaptothiadiazole (DMTD) additive (a) is expected (8-10) to exist predominately in the thiol-thione monoanion form (b) which readily complexes with Cu^{+2} ions. Since the analog additive studies showed that two donor groups capable of coordinating Cu^{+2} are required to produce acceleration, the accelerating species is presumably the copper-complexed monomer species (c and d). Since mercaptans also oxidatively dimerize (11), a DMTD dimer species (e) is also expected to form, although more slowly since the additive concentration is small and the oxidation reaction is bimolecular. That the DMTD dimer (e) and its complexed form (f) are the decelerating species is supported by the observation that increasing the Cu^{+2} concentration in the bath suppresses formation of the decelerator, presumably by tying up the DMTD monomer (b) required for dimerization. This is evident from the data in Table I which show that both the final A_r/A_s value and the time required for activation increase approximately linearly with Cu^{+2} concentration. As the additive level is decreased, the effect of increasing Cu^{+2} concentration saturates at progressively lower Cu^{+2} concentrations, as would be expected.

To corroborate the identity of the decelerator, the DMTD dimer (e) was synthesized (by oxidation of the monomer with iodine in acetonitrile/ethanol solution) and was found to be almost immediately active as a decelerator in copper pyrophosphate baths. Although the

Table I. Effect of Cu^{+2} concentration on the final A_r/A_s ratio and the time required for A_r/A_s to reach a plateau value for copper pyrophosphate baths containing 30 μmole DMTD additive

Cu^{+2} concentration (g/liter)	Final A_r/A_s	Time (hr)
20.0	0.36	0.3
22.5	0.65	1.2
24.8	0.80	2.2

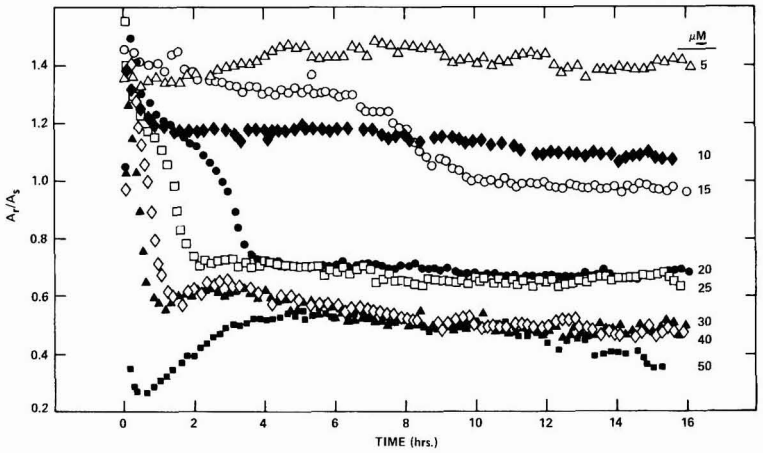

Fig. 2. Relative rate parameter (A_r/A_s) as a function of time after addition of various amounts of additive to copper pyrophosphate baths at 55°C.

dimer produces deceleration even at room temperature, its effectiveness increases with heating at bath operating temperature, which suggests that its copper complexes are more effective decelerators [(f) in Fig. 4 is the expected di-copper species]. Typical activation plots are shown in Fig. 5. At low dimer concentrations, there is a short induction period of several minutes, while low A_r/A_s values are obtained almost immediately at higher concentrations. This also suggests that the dimer must complex with Cu^{+2} in solution before it is active. A_r/A_s increases at longer times for low dimer concentrations (12.5 μmoles in Fig. 5) and accelerating baths are produced when low concentrations of dimer are allowed to equilibrate, indicating that a monomer/dimer equilibrium is established.

Additional strong support for a monomer/dimer equilibrium is found in the experimental verification that the initial monomer concentration must be double that of the dimer to produce approximately the same A_r/A_s value at equilibrium. Thus, a monomer concentration of 25 μmoles results in an A_r/A_s value of about 0.65 (Fig. 2) and the activation curve (Fig. 5) for 12.5 μmoles dimer approaches this value with time. An exact equivalence is difficult to obtain because of the difficulties involved in synthesizing and purifying the dimer and holding the bath composition (particularly the ammonia level) constant for the long times required to reach equilibrium. Also, the dimerization/dissociation is a redox process which must involve other solution redox species (*e.g.*, dissolved oxygen or Cu^+ species) that may be present in small concentrations.

The minimum in A_r/A_s observed early in the activation of higher concentrations of both the dimer and monomer and the peak observed at longer times (Fig. 2 and 5) presumably reflect the presence of appreciable amounts of intermediate species having varied activities. For example, the uncomplexed monomer species [(a) and (b) in Fig. 4] may be decelerating (unlike their Cu^{+2} complexes) so that the presence of significant amounts of these species in the early stages of the monomer and dimer activations could initially suppress A_r/A_s. A_r/A_s would then rise as most of the monomer was complexed with copper to form the accelerating species. The peak would be produced as A_r/A_s again decreased because of formation of di-copper dimer complex [(f) in Fig. 4] which is presumably much more effective as a decelerator than the mono-copper dimer species (not shown in Fig. 4).

It should be mentioned that, although this simple monomer/dimer scheme explains the data well, the situation is probably somewhat more complex. For

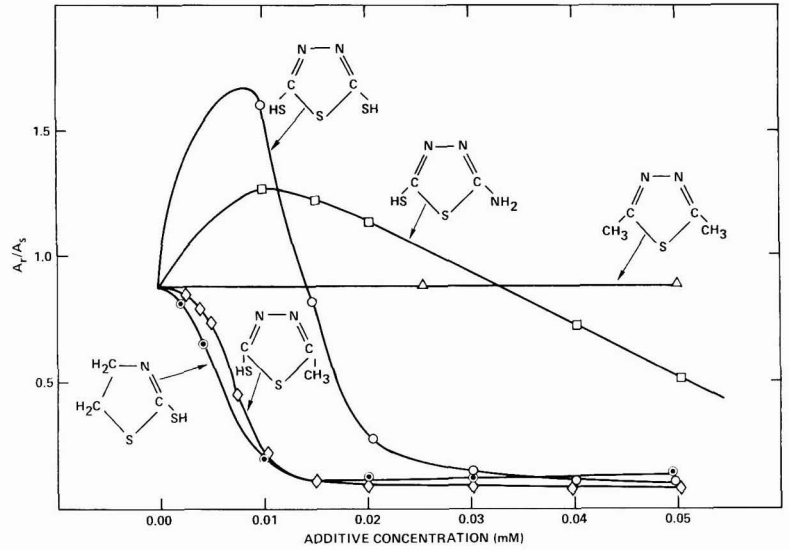

Fig. 3. Relative rate parameter (A_r/A_s) vs. the concentration of various additive analoas. Baths were heated at 55°C for 16 hr, then quenched to room temperature before the measurements.

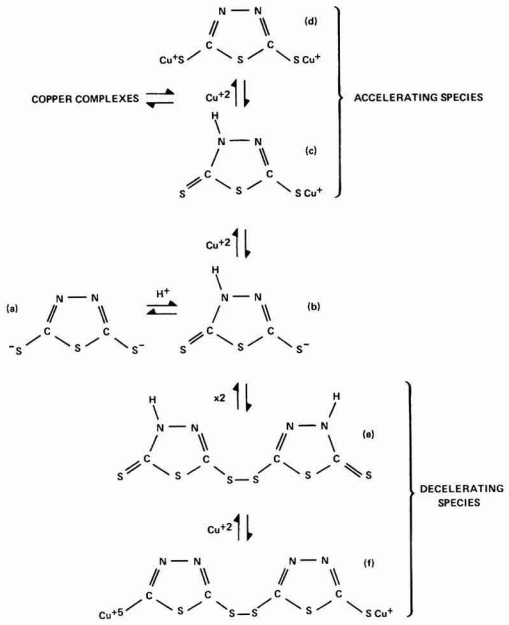

Fig. 4. Proposed equilibria involving the dimercaptothiadiazole additive in copper pyrophosphate baths.

example, in aqueous solutions, DMTD can exist as a monoanion or a dianion, and has several tautomeric forms which can coordinate with Cu^{+2} via mercapto groups, thione groups, an N-S chelate, or the diazo nitrogens of the ring system (9, 10). Large three-dimensional polymeric complexes with DMTD as the sole ligand have also been reported (8).

Considerable insight into the position of the accelerator/decelerator equilibrium and the relative effects of these two types of additive species on the deposition rate can be gained by plotting the A_r and A_s values from Fig. 1 separately *vs.* the overall additive concentration. Such a plot is shown in Fig. 6. These data indicate that the accelerator concentration is higher at equilibrium, but the decelerator produces the larger effect on the deposition rate (per molecule). Thus, A_s increases slowly with additive concentration

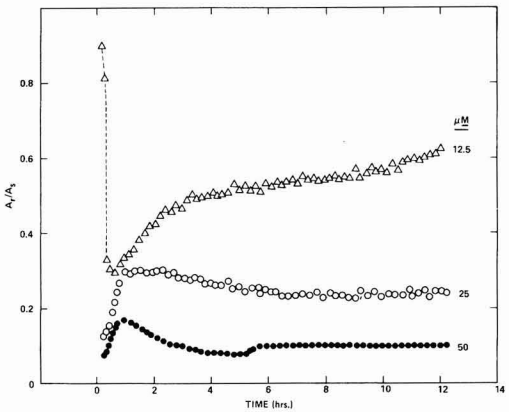

Fig. 5. Relative rate parameter (A_r/A_s) as a function of time after addition of various amounts of DMTD dimer to copper pyrophosphate baths at 55°C.

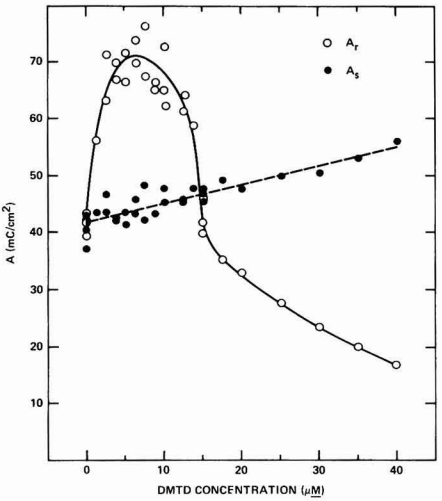

Fig. 6. Rate parameters (A_r and A_s) *vs.* additive concentration for copper pyrophosphate baths at 55°C (after 16 hr).

since in the absence of effective mass transport (electrode rotation), the decelerator concentration is exhaustively depleted at the electrode surface. With electrode rotation, the decelerator effect predominates at the higher concentrations for which sufficient decelerator is formed, so that A_r goes through a maximum then decreases sharply with additive concentration.

The analogous A_s plot is also expected to be linear. Consider the dimerization

$$2M \rightleftharpoons D \qquad [1]$$

for which the equilibrium constant is given by

$$K = C_D/C_M^2 \qquad [2]$$

where C_D is the dimer concentration and C_M is the monomer concentration. When monomer is added to the bath, the initial concentration (C_o) is always given by

$$C_o = C_M + 2C_D \qquad [3]$$

so that

$$C_o = C_M + 2KC_M^2 \qquad [4]$$

Thus, if the effect of monomer on the deposition rate is directly proportional to its concentration, which will be shown to be a reasonable assumption, A_s should be linear in C_o at equilibrium unless K is extremely large so that $2KC_M^2$ is not negligible.

It should be mentioned that ammonia in the bath also affects the copper deposition rate. This is not surprising since copper forms a series of ammine complexes, *e.g.*, $[Cu(NH_3)_4]^{+2}$ and $[Cu(NH_3)_2]^{+}$, which have stability constants comparable to those of the copper pyrophosphate species (7), *i.e.*, in the 10^{12} range. Mixed ammine/pyrophosphate copper complexes would also be expected. Since ammonia is an uncharged ligand, its copper complexes are less negatively charged than the pure pyrophosphate complexes so that copper discharge from the ammine complexes more readily occurs (12) and ammonia would thus be expected to accelerate deposition from copper pyrophosphate baths. As expected, the final A_r/A_s values after activation of copper pyrophosphate baths increase linearly with ammonia concentration. This is illustrated by the data in Table II. The time required for activation of the additive is not significantly affected by the presence of ammonia, indicating that ammonia does not play a major role in the activation process.

Mechanistic/a-c impedance studies.—In order to discuss the mechanism by which the additive species

Table II. Effect of NH_3 concentration on the final A_r/A_s value for copper pyrophosphate baths at 55°C

NH_3 concentration (g/liter)	Final A_r/A_s	
	15 μmoles DMTD	30 μmoles DMTD
0	0.52	0.24
1.13	0.77	0.38
2.25	1.0	0.62

affect the copper electrodeposition rate, some additional data must be considered. First of all, we have observed by scanning electron microscopy that copper deposited from pyrophosphate baths in the absence of additives is large grained, whereas deposits from accelerating baths are nodular and those from decelerating baths are fine grained (4). Such dramatic differences in deposit morphology would be expected only if significant changes occurred in the deposition mechanism or rate-determining step. These additive-induced mechanistic changes can be investigated by determination of the charge transfer resistance and double layer capacitance from a-c impedance measurements. The double layer capacitance is particularly important since it reflects the surface concentration of copper adions, which are intermediates in the overall deposition process (13).

The principle of a-c impedance analysis is illustrated in Fig. 7. If we assume that the cathodic half-cell can be represented by the simple electrical network shown at the top of the figure, the electrode impedance can be calculated as a function of frequency (ω) in the complex plane as illustrated at the bottom of the figure (where R_s is the solution resistance, C_{DL} is the double layer capacitance, R_{CT} is the charge transfer resistance, and W is the Warburg impedance). The semicircle obtained is characteristic of a given combination of C_{DL} and R_{CT}, and the linear response at low frequencies is associated with the Warburg (diffusional) impedance.

Impedance diagrams determined during electrodeposition from copper pyrophosphate baths at −0.70 *vs.* SCE are shown in Fig. 8. Behavior is practically ideal for the additive-free and accelerated baths. The diagram for the decelerating bath approximates the ideal

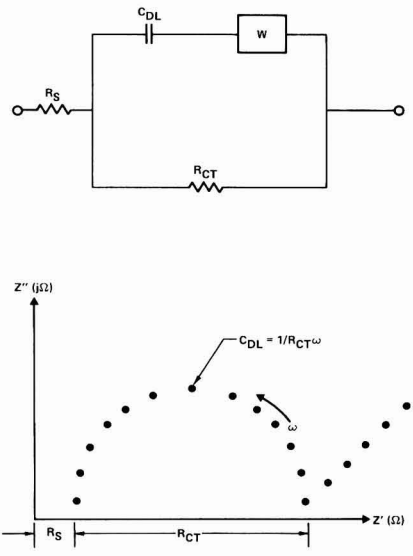

Fig. 7. Simple equivalent circuit for an electrode (top) and the expected a-c response in the complex plane (bottom).

semicircle and should provide semiquantitative information. Data derived from these impedance diagrams are given in Table III. As expected, R_{CT} is slightly smaller for the accelerating bath compared to the additive-free system, and considerably larger for the decelerating bath. The value of 11 μF/cm² for C_{DL} is only slightly smaller in the accelerating system, but is a factor of 24 larger in the decelerating case. This may be interpreted as a significant increase in the copper adion concentration during additive-decelerated deposition since adions reside within the Helmholtz plane and thus reduce the overall extent of charge separation so that C_{DL} increases when the adion concentration increases.

Mechanism of additive effects.—These results provide the basis for understanding the mechanism by which the accelerating and decelerating additive species affect copper electrodeposition. First, consider the overall electrodeposition process in the absence of additives (13) which is illustrated in Fig. 9. Solvated/complexed Cu^{+2} ions in the electrolyte are discharged on surface planes to form partially solvated/complexed Cu^{+1} adions which surface diffuse over lattice planes and along steps to kink sites where they are discharged to Cu^0 and incorporated into the lattice. It is generally accepted that the rate-determining step at moderate current densities for acid copper sulfate baths is discharge of Cu^{+2} solution species to form adions (13) which has also been shown to apply to pyrophosphate copper deposition in the absence of additives (12). In this case, incorporation of adions into the lattice is fast and the adion surface concentration remains low; growth is orderly and deposits are large grained.

The situation for decelerated deposition is depicted in Fig. 10. In this case, the dimerized additive species adsorbed on the electrode surface interfere with surface diffusion of adions and block lattice growth at kink sites. This necessitates frequent renucleation to sustain a constant deposition rate which is reflected in the increased overvoltage, higher overall charge transfer resistance, and fine-grained deposit morphology. At sufficiently cathodic potentials, lattice incorporation, *i.e.*, growth at kink sites, becomes the rate-determining step and the surface adion concentration increases sharply raising the measured C_{DL}. This change in rate-determining step from adion discharge to lattice incorporation is evident at an overpotential of 250 mV in the C_{DL}-overpotential plot shown in Fig. 11. It should be mentioned that the increased overvoltage may also affect the structure of the double layer electrostatically, especially since pyrophosphate anions are known to desorb at potentials more cathodic than −0.75V *vs.* SCE (14, 15). Such effects were probably minimal in our studies since the electrode potential was always held below this value.

The situation for accelerated deposition is illustrated in Fig. 12. The accelerating additive species apparently lowers the overpotential and overall charge transfer resistance by assisting in the nucleation of new growth centers on surface planes, which ultimately grow to form the almost spherical nodules observed by scanning electron microscopy. As also observed, C_{DL} would be expected to decrease slightly because of the reduction in adion concentration resulting from the shorter average surface diffusional path to the more numerous growth sites.

Table III. Charge transfer resistance (R_{CT}) and double layer capacitance (C_{DL}) during electrodeposition from copper pyrophosphate baths

Additive concentration (μmoles)	A_r/A_s	R_{CT} (Ω)	C_{DL} (μF/cm)²
0 (additive-free)	0.98	29	11
6 (accelerating)	1.55	24	10
25 (decelerating)	0.31	57	260

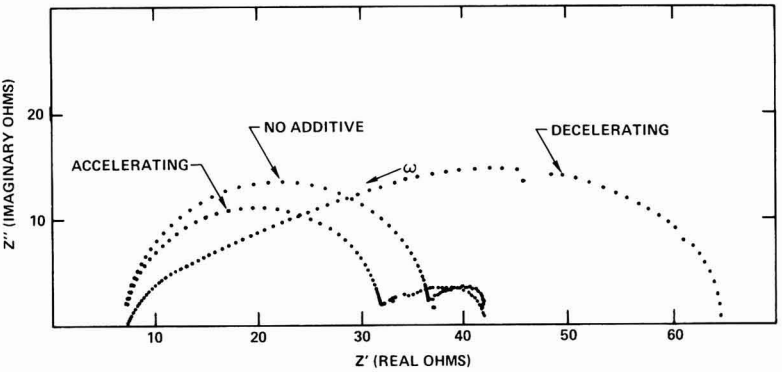

Fig. 8. Complex impedance data obtained during electrodeposition at —0.70V vs. SCE from copper pyrophosphate baths at 55°C.

The way in which the accelerator might assist in nucleation of new growth centers on electrode surface planes can be visualized as follows. For the purposes of discussion, we will assume that the accelerator is the copper-complexed thiol-thione tautomer [(c) in Fig. 4], although the situation for the di-copper monomer species [Fig. 4 (d)] would be equivalent after the initial electron transfer. The accelerating species would be expected to adsorb on the electrode surface with the thiadiazole ring sulfur, which has a lone pair of exoelectrons, serving as the attachment site. As the complexed Cu^{+2} is reduced to Cu^{+}, and ultimately Cu^{o}, to initiate the nucleation process, the charge would be redistributed via the ring structure to form the thiol-thione tautomer which is the mirror image of the original species. The thiol group thus generated would then be available to complex another Cu^{+2} from solution and the reduction process would be repeated. Thus, Cu^{+2} acquisition/Cu^{o} deposition would alternate between the thiol sites which would explain why two Cu^{+2} complexing groups are apparently required for accelerated deposition. If the thiadiazole sulfur-metal interaction is not too strong, the additive could move (via desorption/readsorption) along the surface of the growing nucleus, and the deposition of many Cu atoms could be facilitated before the additive was included in the deposit. The onset of spherical diffusion as the growing nuclei become three-dimensional would also enhance the deposition rate and result in nodular deposits.

Quantitative treatment.—A more quantitative view of the effects of the accelerating species on the electrodeposition rate can be obtained by assuming that the accelerator and decelerator act more or less independently. As mentioned above, this appears to be a good assumption since the plot of the relative rate parameter (A_r/A_s) *vs.* additive concentration in Fig. 1 is linear at higher concentrations and extrapolates to unity for the additive-free system. Thus, we can subtract the decelerating effect of the dimer species according to the linear dashed line in Fig. 1 to obtain the plot shown in Fig. 13 of the accelerator effect on A_r/A_s. Based on the data in Fig. 6, we have assumed that the accelerator concentration is equivalent to the overall additive concentration in this concentration range.

Let us now assume that the monomer acceleration effect can be described in terms of birth and death of nodules so that the relative rate parameter after subtraction of the decelerator effect is given by

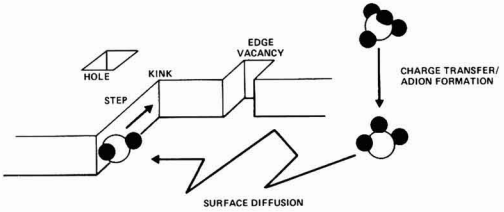

Fig. 9. Representation of copper electrodeposition in the absence of additives at moderate current densities.

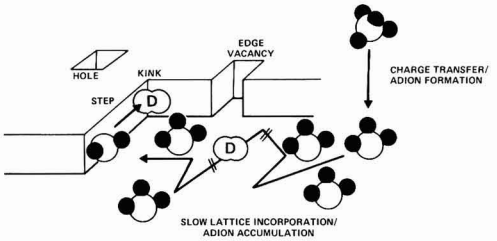

Fig. 10. Representation of additive-decelerated electrodeposition from copper pyrophosphate baths.

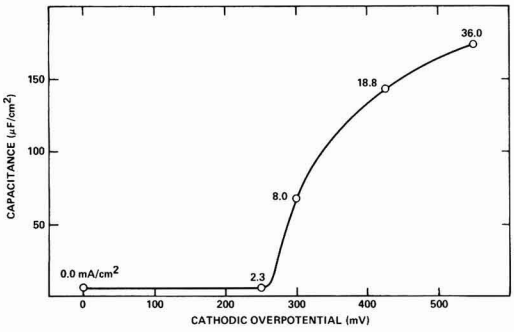

Fig. 11. Double layer capacitance *vs.* overpotential for additive-decelerated electrodeposition of copper from pyrophosphate baths at 55°C.

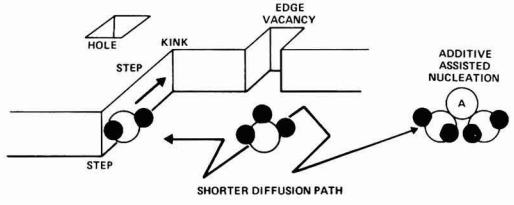

Fig. 12. Representation of additive-accelerated electrodeposition of copper from pyrophosphate baths.

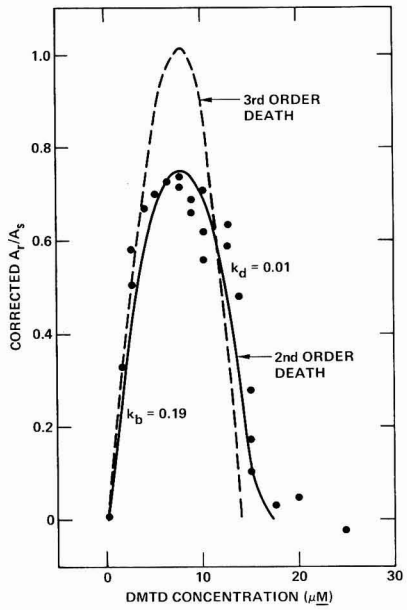

Fig. 13. Plot of A_r/A_s vs. additive concentration after subtraction of the decelerating effect of the dimer species.

$$A_r/A_s = 1 + k_bC_M - k_dC_M^x \quad [5]$$

where $(k_bC_M - k_dC_M^x)$ can only be positive. The assumptions concerning birth are that each nodule exerts an equivalent effect on the deposition rate and that the number of nodules formed is proportional to the monomer concentration. In this case, the accelerating effect on A_r/A_s is given by k_bC_M, where k_b is the proportionality constant. The death process which causes individual nodules to cease growing so that they no longer contribute to accelerated deposition is assumed to be collision with other nodules. Note that collision in this context means that the nodules interact at a small separation distance to stop growth. The collision frequency is assumed to increase with the number of nodules, which is in turn proportional to the monomer concentration so that the net decelerating effect of nodular death is $-k_dC_M^x$, where x is the number of collisions required to produce death and k_d is the death proportionality constant.

In order to test this model, we need to determine k_b and k_d. Assuming that death is unimportant when the density of nodules is low, k_b is obtained from the slope of the corrected A_r/A_s plot (Fig. 13) in the linear region at low additive concentrations. The value of k_d is determined by differentiating Eq. [5] and setting the differential equal to zero at the peak in the corrected A_r/A_s plot. For second-order death, $k_d = k_b/2C_M' = 0.01$, where C_M' is the additive concentration corresponding to the peak in the corrected A_r/A_s plot. The nodule death process seems to be second order as indicated by the excellent fit (solid line in Fig. 13) to the corrected A_r/A_s data. This implies that nodule death involves interruption of growth at specific sites, so that spherical diffusion of copper ions alone would not account for the accelerated deposition and nodular deposits. A plot for third-order death (dashed line) is included for comparison.

A unified model.—The results presented above show that there are two important additive species present in copper pyrophosphate baths. One of these suppresses (decelerates) deposition by blocking growth sites, whereas the other enhances (accelerates) deposition by assisting in the nucleation of new growth centers. Ammonia also enhances deposition, presumably by forming complexes from which copper can be discharged at lower overpotentials to nucleate new growth centers. Nucleation via copper ammine complexes is supported by the observation of nodular deposits at high bath ammonia levels (12).

We propose here that the maintenance of the proper balance between the decelerating and accelerating bath species is critical to the attainment of acceptable pyrophosphate copper deposits. Consider deposition at a high overall additive concentration in the absence of ammonia in the bath. In this case, the limited number of growth sites are quickly blocked by the predominant decelerating dimer species and provisions for generating new sites are inadequate so that appreciable deposition can only occur at high cathodic overvoltages. Under these circumstances, nucleation occurs preferentially at surface microprotrusions where the electric field strength is highest and, once initiated, growth is extremely rapid and disorderly for the short time before it is blocked by adsorption of a new decelerating additive species. The resulting deposits are burnt and powdery with extremely poor crystallinity and mechanical properties.

To obtain acceptable deposits at reasonable current densities, provisions must be made for nucleation of a sufficient number of growth centers at low overvoltages where orderly deposition occurs and deposits are highly crystalline. This can be accomplished by lowering the additive concentration to attain a better balance between the accelerating and decelerating additive species, and by adding ammonia to the bath. On the other hand, sufficient decelerator must always be present to limit the extent to which individual nuclei are permitted to grow. Otherwise, as the nuclei expand in three dimensions, spherical diffusion enhances mass transport and consequently the growth rate, so that growth again becomes disorderly and nodular deposits are obtained. Within this model, it is readily apparent why ammonia is a critical constituent of copper pyrophosphate baths (1) and its concentration must be increased for plating at higher additive levels (16).

Practical implications.—In most applications for which copper pyrophosphate baths are used, the deposit tensile properties are of paramount importance. For example, to avoid cracking problems, plated through-hole deposits in multilayer circuit boards must be highly ductile to relieve stress generated by the excess thermal expansion of the laminant during soldering and must be sufficiently strong to resist fatigue failure upon thermal cycling (17). In addition, deposits must generally be uniform and adherent. Our previous work has shown that both the tensile properties and uniformity of pyrophosphate copper deposits depend strongly on the overall additive concentration and correlate well with cyclic voltammetric stripping data and morphological studies (3-5). Specifically, nodular deposits resulting from additive accelerated deposition were found to have poor tensile properties, and the nonuniform deposition within through-holes known as "foldback" was shown to be a consequence of the dual accelerating/decelerating nature of the additive.

The model presented here, which involves a critical balance between nucleation (initiated by the accelerating additive species and copper ammine complexes) and growth (limited by the decelerating additive species), provides a basis for improving control of copper pyrophosphate plating. First of all, since the three principal species (decelerator, accelerator, and ammonia) which affect the deposition rate (and consequently the deposit properties) vary in activity and concentration, it is clear that the bath additive and ammonia levels must be considered as interdependent variables. Control is therefore rendered considerably less difficult if the additive system is maintained near

equilibrium where the concentrations of additive species are fixed relative to one another. This also ensures that the concentration of monomer which must be balanced by dimer is minimal, so that the total amount of organic material included in the deposit is minimized. An excess of such included material can lead to deposit brittleness. Thus, the additive should be added in such a way as to ensure activation to the dimer form. This implies that, in some cases, making batch additions may be preferable to continuously feeding the additive. Of course, the optimum situation would involve approaching the equilibrium from the other direction by adding dimer directly, if this procedure can be shown to yield deposits with comparable mechanical properties.

Since the three species affecting the deposition rate vary in concentration and relative effectiveness, it might be expected that the effects of changes in bath agitation would be difficult to predict. Fortunately, the decelerator appears to be relatively low in concentration, but highly effective, so that changes in electrolyte mass transport primarily affect the magnitude of the decelerating effect. Thus, if the ammonia concentration is held constant and the additive system is close to equilibrium, variations in agitation can be countered by changes in the overall additive level. Nonetheless, caution should be exercised in making extrapolations for mass transport differences.

It should also be mentioned that the relative rate parameter (A_r/A_s) measured by cyclic voltammetric stripping (3) reflects primarily the concentration of the decelerating additive species in copper pyrophosphate baths. Thus, if the additive system is maintained near equilibrium and the bath ammonia level is held constant, this method provides excellent control of pyrophosphate copper plating.

Summary

The dimercaptothiadiazole/copper pyrophosphate system involves two additive species in dynamic equilibrium. One appears to be the copper complexed DMTD monomeric species which assists nucleation of new growth sites on crystal planes and can lead to nodular deposits. In this case, the electrodeposition rate is accelerated, presumably by some combination of additive-assisted growth randomly over the surface of the nodules, and the onset of spherical diffusion to the new isolated growth sites. The other additive species is apparently the DMTD dimer which decelerates the electrodeposition rate by blocking growth sites. Additive-accelerated deposition can be quantitatively described in terms of birth and death of nodules, where the birth rate is proportional to the accelerator concentration and death results from second-order collision of growing nodules.

Deposition in the dimercaptothiadiazole/copper pyrophosphate system can be understood by assuming that a balance must be maintained between suppression of growth by the decelerating additive species and nucleation of new growth centers via the accelerating additive species and copper ammine complexes. This model could prove to be general for electrodeposition from highly complexed systems.

Acknowledgments

The authors gratefully acknowledge support of a portion of this work by the United States Air Force Materials Laboratory under contract No. F33615-79-C-5079. The authors are also indebted to Drs. D. O. Raleigh and L. F. Warren for many useful comments on the manuscript.

Manuscript submitted June 18, 1980; revised manuscript received *ca.* Sept. 22, 1980.

Any discussion of this paper will appear in a Discussion Section to be published in the December 1981 JOURNAL. All discussions for the December 1981 Discussion Section should be submitted by Aug. 1, 1981.

Publication costs of this article were assisted by Rockwell International.

REFERENCES

1. J. W. Dini, in "Modern Electroplating," 3rd Ed., F. A. Lowenheim, Editor, p. 205, Wiley-Interscience, New York (1974).
2. F. H. Wells and D. M. Lyde, Brit. Pat. 939,997 (1960).
3. D. Tench and C. Ogden, *This Journal*, **125,** 194 (1978); U.S. Pat. 4,132,605 (1979).
4. D. Tench and C. Ogden, *This Journal*, **125,** 1218 (1978).
5. C. Ogden and D. Tench, *Plating Surf. Finishing*, **66,** 30 (1979).
6. V. G. Levich, "Physicochemical Hydrodynamics," Prentice-Hall, Englewood Cliffs, N.J. (1962).
7. A. J. Bard, "Chemical Equilibria," p. 192, Harper and Row, London (1966).
8. M. R. Gajendragad and U. Agarwala, *Z. Anorg. Allg. Chem.*, **415,** 84 (1975).
9. S. Zaidi and D. Varshney, *J. Inorg. Nucl. Chem.*, **37,** 1804 (1975).
10. M. R. Gajendragad and U. Agarwala, *Indian J. Chem.*, **13,** 697 (1975).
11. D. Cram and G. Hammond, "Organic Chemistry," p. 440, McGraw-Hill, New York (1959).
12. O. Radovici, C. Vass, and I. Solacoln, *Electrodep. Surf. Treat.*, **2,** 263 (1973).
13. J. O'M. Bockris and A. K. N. Reddy, "Modern Electrochemistry," Vol. 2, Plenum Press, New York (1970).
14. H. Konno and M. Nagayama, *Electrochim. Acta*, **22,** 353 (1977).
15. H. Konno and M. Nagayama, *ibid.*, **23,** 1001 (1978).
16. D. E. Sherlin and L. K. Bjelland, *Circuit World*, **4,** 22 (1977).
17. J. K. Hagge, Proc. Printed Circuit World Expo '80, Pasadena, California, May 1980.

Energy Dependence of the Quantum Efficiency of CdSe Photoelectrochemical Cells

K. Colbow, D. J. Harrison, and B. L. Funt*

Departments of Physics and Chemisty, Simon Fraser University, Burnaby, Vancouver, B.C., V5A 1S6 Canada

ABSTRACT

Polycrystalline CdSe electroplated on nickel and titanium substrates was used as photoanode in electrochemical cells with S^{2-}/S_n^{2-} as a redox couple. When compared to a single crystal photoanode, the quantum efficiency is found to be larger for photon energies below the bandedge and smaller for those above the bandedge. The single crystal efficiency dependence on photon energy near the bandedge is well described by the Butler equation and dominated by variation of the absorption coefficient and the depletion layer width and less sensitive to the minority carrier diffusion length for the crystal under study. The electroplated samples may be assigned a bandgap of about 1.70 eV compared to 1.72 eV for the single crystal. Information about impurity content may be obtained from the photoresponse for energies below the bandedge.

The aim of this research was to understand the performance of electroplated and single crystal n-type CdSe as solar cells in terms of their fundamental semiconductor parameters, such as absorption coefficient (α), impurity concentration (N_D), depletion layer width (W), flatband potential V_{FB}, energy gap (E_g), hole diffusion length (L_p), and hole diffusion coefficient (D_p). To this end we studied the short-circuit photocurrent efficiency (η) as a function of wavelength in an aqueous electrolyte consisting of 1.0M NaOH, 1.0M Na_2S, and 1.0M S. Photoanodic dissolution does not occur under these conditions (1) and the electrode reactions are the oxidation of S_n^{2-} at the photoanode and the reduction of S_n^{2-} at the platinum dark electrode. We compared the data to the simple Butler equation (2)

$$\eta = \frac{I}{qA\phi_0} = 1 - \frac{e^{-\alpha W}}{1 + \alpha L_p} \qquad [1]$$

where I is the short-circuit current, q the electronic charge, A the cell area, and ϕ the incident light flux. The depletion layer width is given by

$$W = \left\{ \frac{2\epsilon_0 \kappa}{qN_D} (V - V_{FB}) \right\}^{1/2} \qquad [2]$$

$\epsilon_0 = 8.85 \times 10^{-12} C^2 n^{-1} m^{-2}$ is the permittivity of free space, $q = 1.60 \times 10^{-19}$C the electron charge, and V the measured or applied potential. The dielectric constant $\kappa = 10$ for CdSe (3).

For the flatband potential of CdSe with an S^{2-}/S_n^{2-} redox couple Gerischer and Gobrecht (4) obtained a value of -1.27V *vs.* NHE (normal hydrogen electrode) from capacitance measurements for CdSe single crystal whose surface had been converted to CdS. This corresponds to -1.51V *vs.* SCE (standard calomel electrode). Ellis *et al.* (1) obtained a flatband potential of -1.45V *vs.* SCE for single crystal CdSe from capacitance or open-circuit voltage at high light intensity and -1.40V from the less accurate onset of photocurrent at high light intensity. Noufi *et al.* (5) obtained -1.34V *vs.* SCE for pressed powder pellets and -1.30V for vacuum-deposited films of CdSe using the onset of photocurrent. We shall choose a value of -1.50V *vs.* SCE. Using a value of -0.72V for platinum in a polysulfide electrolyte *vs.* SCE (6, 7), we obtain $V_{FB} = -0.78$V *vs.* platinum electrode in S^{2-}/S_n^{2-}, which was used in our experiments.

Experimental

Monochromatic excitation was obtained using a 1000W quartz iodine tungsten lamp and a Jarrel-Ash grating monochromator with a 100Å bandpass. Infrared radiation was filtered out by passing the light through 2 in. of water, second-order grating effects were eliminated with a Corning 3.71 filter. The monochromatic beam was expanded by lenses to provide full sample illumination and a reasonably parallel beam.

Polycrystalline samples were prepared by an electrodeposition technique which evolved as an extension of a method reported previously (8, 9). Controlled electrodeposition was performed at -0.72V *vs.* SCE for 15 min on a titanium or nickel substrate, which had been etched, cleaned meticulously, and cathodized for 15 sec in an acidic oxidizing medium. The deposition bath consisted of 1M NH_4Cl, 0.5M $CdSO_4$, and 0.01M SeO_2. Electrodeposition at -0.76V and -0.64V *vs.* SCE was also performed in order to obtain electrodes lacking stoichiometry, being rich in Cd and Se, respectively. The plated photoelectrodes were about 1 μm thick and were subsequently heated under 100 Torr N_2 at 400°C for 15 min. The counterelectrode was platinum.

The single crystal CdSe was obtained from Cleveland Crystal Incorporated, its c-axis was perpendicular to the front surface. Electrical contact at the back side was made with a GaIn eutectic, and a copper wire was attached to this with Ag epoxy. This was then sealed with epoxy and mounted on a Teflon rod. The quartz cell had a flat window, allowing a 2-3 mm optical path length through the electrolyte. The cells were flushed with nitrogen gas prior to and after introduction of the electrolyte and then sealed from the atmosphere.

In order to test the polycrystalline electrodes under equilibrium conditions, the cells were left overnight in the electrolyte, and the open-circuit voltage V_{oc} was monitored to determine if a steady state had been reached. Steady open-circuit voltage always correlated with steady short-circuit current I_{sc} in the dark.

The "short-circuit" current was measured after the cells had equilibrated by determining the voltage drop across a 10Ω resistor in series with the photocell. The voltage in the dark and under illumination was measured and the difference was reported as the photocurrent.

Results and Discussion

Figure 1 shows the experimental points (□) for the quantum efficiency as a function of wavelength of the incident light. The data was obtained for a single crystal under low light intensity and corrected for light absorption by the solution. The curves represent Eq. [1] with the absorption coefficient α as function of wavelength taken from Parsons *et al.* (10) for light polarized perpendicular to the c-axis of the crystal.

* Electrochemical Society Active Member.
Key words: electroplating, photoanode, crystals.

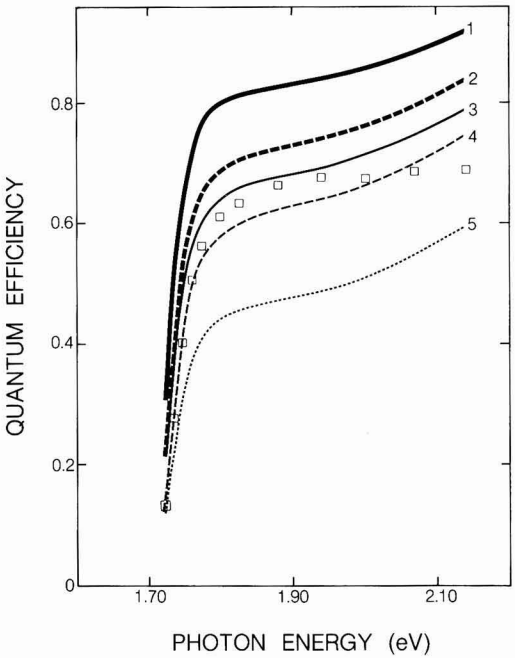

Fig. 1. Quantum efficiency vs. photon energy for a single crystal of CdSe (experiment: □), and theoretical curves for W, L_p values of curve 1, 0.2, 0.1; curve 2, 0.2, 0; curve 3, 0.1, 0.1; curve 4, 0.15, 0, and curve 5, 0.1, 0 μm.

For W and L_p various values were chosen in order to demonstrate the sensitivity of the Butler equation to changes in these parameters. Curve 4 is a least squares fit to the experimental data. Using in Eq. [2] a dielectric constant $\kappa = 10$, and a flatband potential $V_{FB} = -0.78$V, a depletion layer width of $W = 0.15$ μm corresponds to an impurity concentration of $N_D = 4 \times 10^{16}$ cm^{-3}, which appears reasonable. The fact that Eq. [1] provides a reasonable fit to the data with negligible value of L_p merely suggests that $\alpha L_p < 1$ and thus most of the variation of efficiency comes through W.

To obtain a better fit between theory and experiment, one may consider that the most important neglect in the Butler equation is the assumption of no surface recombination. Analogous to Wilson's (11) treatment this may be rectified in the simplest way by multiplying the right-hand side of Eq. [1] by the ratio $S_t/(S_t + S_r)$, where S_t and S_r are the relative probabilities of surface transfer (S_t) and nonproductive surface recombination (S_r) of light-generated charge carriers at the semiconductor-electrolyte interface. This introduces one new parameter, namely the ratio of S_t/S_r. A more detailed theoretical treatment will be presented separately. Reiss' (12) more elaborate theory of photoelectrochemical cells also neglects surface recombination and gives a behavior similar to Butler's equation. A further complication to Eq. [1] arises for samples of thickness comparable to the inverse of the absorption coefficient (≈1 μm). This is a factor for our thin electroplated samples (≈1 μm thickness), but not for the single crystal (≈10^3 μm thickness) measurements.

Considering absorption coefficients such that $\alpha L_p << 1$ and $\alpha W << 1$, expansion of Eq. [1] yields

$$\eta \approx \alpha(W + L_p) \qquad [3]$$

For $L_p \approx W \approx 0.1$ μm this approximation is thus good for $\alpha << 10^5$ cm^{-1}.

The absorption coefficient α has different functional dependencies on photon energy $h\nu$, depending on the nature of the transition (13). For a direct gap material like CdSe near the absorption edge the absorption coefficient is described by

$$\alpha = \frac{A}{h\nu}(h\nu - E_g)^{1/2} \qquad [4]$$

Combining Eq. [3] and [4], a plot of $(\eta h\nu)^2$ *vs.* $h\nu$ should give a straight line with intercept on the x-axis equal to the energy bandgap. This plot is shown in Fig. 2, curve 1, for the single crystal of CdSe.

For comparison we also show plots of $(\eta h\nu)^{1/2}$ *vs.* $h\nu$ (curve 2) and $(\eta h\nu)^{2/3}$ *vs.* $h\nu$ (curve 3), whose straight line sections extrapolate to the energy gap in the cases of an indirect semiconductor and a forbidden (phonon assisted) transition in a direct semiconductor, respectively (13). In curve 1 the full line extrapolates to an energy gap for CdSe of $E_g = 1.72$ eV. This compares with a quoted room temperature literature value of 1.74 eV (14-16). Curves 2 and 3, which should not apply, extrapolate to energy gaps of 1.68 and 1.69 eV, respectively. Figure 3 shows an expansion of the efficiency scale for photon energies below the bandedge for the single crystal of CdSe. The data indicates the typical Urbach exponential tail below the bandedge (above 1.60 eV) and what we interpret as impurity absorption below 1.60 eV. The peak at 1.50 eV we believe is due to defect absorption. The peak is 0.240 eV below the bandedge and in analogy to CdS may represent energy absorption by electrons bound to deep acceptors, possibly cadmium vacancies (17).

Figure 4 compares the wavelength dependence of the quantum efficiency for a single crystal of CdSe with electroplated samples of about 1 μm thickness. The latter were plated at −0.72V *vs.* SCE and subsequently heat-treated for improved response, as described earlier. Titanium substrates gave consistently higher efficiencies than nickel substrates, however, both had

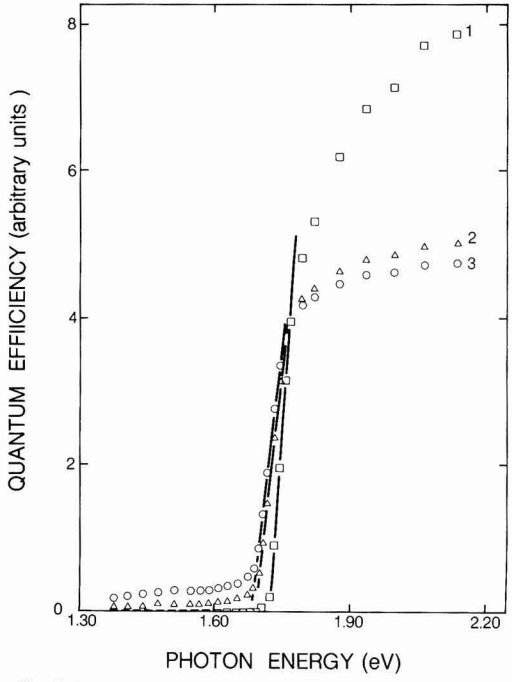

Fig. 2. Bandgap determination. Various fits of the single crystal quantum efficiency data for different functional forms of absorption coefficient *vs.* photon energy: 1, $(\eta h\nu)^2$, 2, $(\eta h\nu)^{1/2}$, 3, $(\eta h\nu)^{2/3}$.

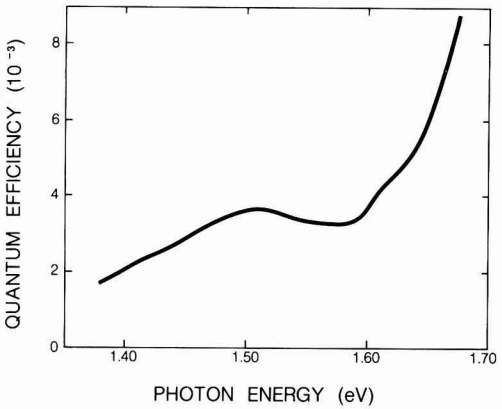

Fig. 3. Expansion of the experimental quantum efficiency (from Fig. 1) below the bandedge for single crystal CdSe.

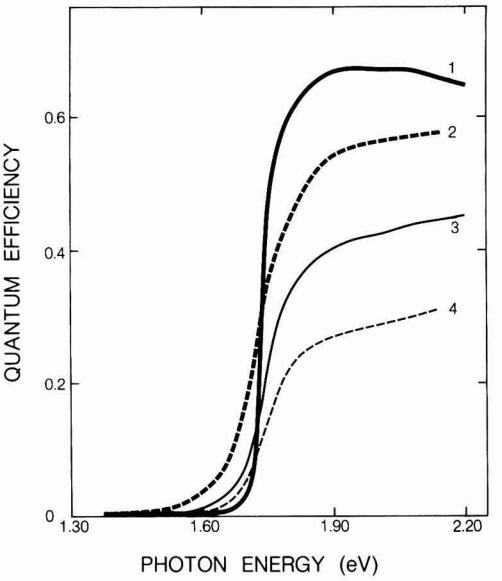

Fig. 4. Experimental quantum efficiency *vs.* photon energy of curve 1, CdSe single crystals; curve 2, electroplated samples on titanium substrate; curves 3 and 4, on nickel substrate.

a lower efficiency for photon energies above the bandedge and higher efficiencies for lower energy photons. Curves 3 and 4 show measurement on two different samples, which were prepared on different days under supposedly identical conditions to illustrate the reproducibility of sample preparation. Figure 5 shows a plot of $(\eta h\nu)^2$ *vs.* photon energy for two samples each, electroplated on nickel and titanium substrates. The straight line intercepts with the x-axis should give the energy bandgap of the CdSe (13). The samples on titanium substrate (curves 1 and 2) extrapolate to E_g = 1.69 eV and the samples on nickel substrate to 1.71 eV compared to our single crystal value of 1.72 eV.

Figure 6 compares electrodes plated at slightly lower (−0.76V) and higher potential (−0.64V) than the plating potential (−0.72V *vs.* SCE) that produces the most efficient electrodes (curve 1), corresponding to best stoichiometry. Plating at lower or higher potential probably produces electrodes rich in cadmium or selenium, respectively, which show a reduced efficiency

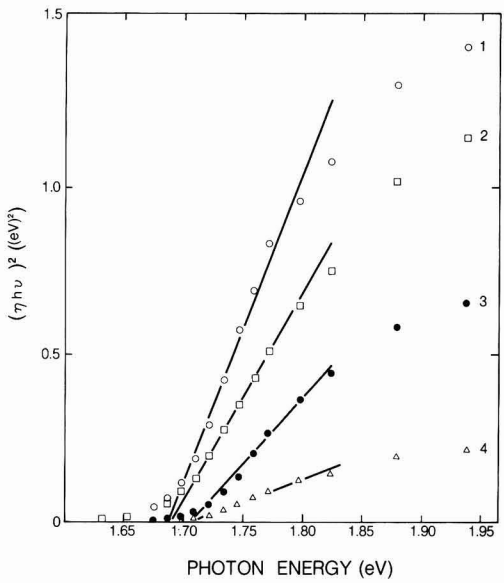

Fig. 5. Bandgap determination. $(\eta h\nu)^2$ *vs.* photon energy for electroplated CdSe on titanium (○, □) and nickel (●, △) substrates.

at all wavelengths. In contrast to the samples in Fig. 4, those in Fig. 6 did not undergo heat-treatment after plating.

Figure 7 shows on an expanded efficiency scale the photoresponse of electroplated CdSe below the band-

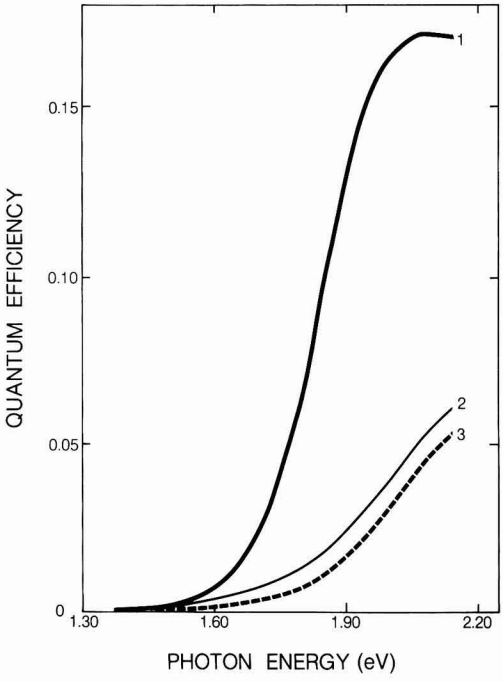

Fig. 6. Quantum efficiency *vs.* photon energy for CdSe electroplated on nickel substrates at plating potentials *vs.* SCE of curve 1, −0.72V, curve 2, −0.76V, and curve 3, −0.64V.

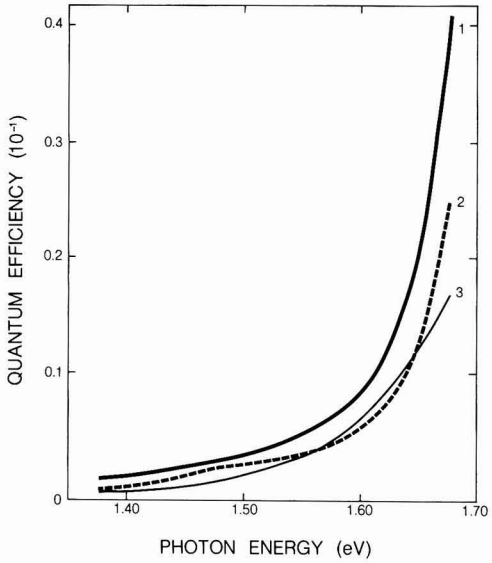

Fig. 7. Quantum efficiency *vs.* photon energy below the bandedge for CdSe electroplated on nickel substrate at −0.72V *vs.* SCE. Samples for curves 1 and 2 were heat-treated but that for curve 3 was not heat-treated.

edge. While the response is large when compared to the single crystal data (Fig. 3), a 1.50 eV peak is not always as well defined, and no clear spectral differences due to heat-treatment were observable.

Conclusions

The Butler equation accounts reasonably well for the wavelength dependence of the quantum efficiency in single crystal CdSe for photons near the bandedge. The efficiency is controlled by the absorption coefficient and the depletion layer width, rather than the minority carrier diffusion length.

For photon energies below the bandedge a small photocurrent is observable in single crystal CdSe due to well-defined defect or impurity absorption.

In electroplated polycrystalline CdSe the efficiency above the bandedge is reduced by about a factor of two for 1 μm thick samples on nickel substrate and by half that for samples on titanium substrate, when compared to thick single crystal of CdSe. The efficiency below the bandedge is increased in electroplated samples. The "impurity absorption" is much broader in the electroplated samples.

However, it appears that one still has a well-defined energy gap, which is only 20-30 meV smaller than our single crystal gap.

Preliminary experiments show that the electroplated CdSe efficiency can be enhanced with proper surface treatment.

Acknowledgments

This work was supported by a Strategic Grant from the National Science and Engineering Research Council of Canada.

Manuscript submitted July 17, 1980; revised manuscript received *ca.* Oct. 20, 1980.

Any discussion of this paper will appear in a Discussion Section to be published in the December 1981 JOURNAL. All discussions for the December 1981 Discussion Section should be submitted by Aug. 1, 1981.

Publication costs of this article were assisted by Simon Fraser University.

REFERENCES

1. A. B. Ellis, S. W. Kaiser, J. M. Bolt, and M. S. Wrighton, *J. Am. Chem. Soc.*, **99**, 2839 (1977).
2. M. A. Butler, *J. Appl. Phys.*, **48**, 1914 (1977).
3. S. M. Sze, "Physics of Semiconductor Devices," Wiley-Interscience, New York (1969).
4. H. Gerischer and J. Gobrecht, *Ber. Bunsenges. Phys. Chem.*, **80**, 327 (1976).
5. R. N. Noufi, P. A. Kohl, and A. J. Bard, *This Journal*, **125**, 375 (1978).
6. P. L. Allen and A. Hickling, *Trans. Faraday Soc.*, **53**, 1626 (1957).
7. W. M. Latimer, "The Oxidation States of the Elements and Their Potentials in Aqueous Solutions," Prentice Hall Inc., New York (1952).
8. J. Manassen, G. Hodes, and D. Cahan, *This Journal*, **124**, 931 (1977).
9. B. L. Funt, M. Leban, and A. Sherwood, *Am. Chem. Soc. Symp. Series No. 90*, **242** (1979).
10. R. B. Parsons, W. Wardzynski, and A. D. Yoffe, *Proc. Roy. Soc. A*, **262**, 120 (1961).
11. R. H. Wilson, *J. Appl. Phys.*, **48**, 4292 (1977).
12. H. Reiss, *This Journal*, **125**, 937 (1978).
13. R. H. Bube, "Photoconductivity of Solids," p. 211, John Wiley, New York (1960).
14. A. R. Hutson, "Semiconductors," N. B. Hannay, Editor, p. 541, Reinhold Publishing Corp., New York (1959).
15. R. H. Bube, *Proc. IRE*, **43**, 1836 (1955).
16. R. C. Weast, Editor, "Handbook of Chemistry and Physics," 59th ed., CRC Press (1978-79).
17. K. Colbow, *Phys. Rev.*, **141**, 742 (1966).

The Measurement of Fast Transients in the CdSe/$S^{=}$, S° Photoelectrochemical Cell

Z. Harzion

Department of Chemistry, University of Tel-Aviv, Ramat-Aviv, Israel

N. Croitoru

Department of Electronics, University of Tel-Aviv, Ramat-Aviv, Israel

and S. Gottesfeld*

Department of Chemistry, University of Tel-Aviv, Ramat-Aviv, Israel

ABSTRACT

Fast photocurrent transients were recorded in a CdSe/$S^{=}$, S° cell employing a spark-gap lamp as a source of illumination. From the measured dependence of the decay time on the value of the load resistor it is shown that photocurrent decay is controlled by an R-C time constant which is determined by the properties of the cell. The form of the decay is sensitive to the state of the photoelectrode surface, as shown by the pronounced effect of chemical etching which enhances the amplitude and reduces the decay time of the transients. The damaged surface layer produced by mechanical polishing increases the effective series resistance of the cell and decreases the photocharge obtained (per flash) through the external load.

The importance of kinetic parameters in the determination of the efficiency and stability of semiconductor (SC) photoelectrodes has been stressed by many authors (1). Transient techniques have served as an important tool for the evaluation of kinetic parameters in both electrochemical (2) and solid-state solar cells (3-10). The use of such techniques in photoelectrochemical cells has been introduced very recently (11-18). We present in this contribution results of fast transient measurements in the CdSe/$S^{=}$, S° photoelectrochemical system, and their analysis in terms of elements of an equivalent circuit.

Experimental

A block diagram of the experimental system for measuring fast transients in photoelectrochemical cells (PEC) is given in Fig. 1. A well-shielded spark-gap lamp served as a white light source, generating pulses of 10 nsec width and 50 Hz repetition rate. The peak power was 10^5W and the spectrum was continuous, peaking around 330 nm. These light pulses were directed at the surface of a single crystal CdSe electrode immersed in a 4.5M NaOH, 0.2M S, 0.2M Na_2S solution.

The hexagonal n-type CdSe single crystals (Cleveland Crystals, Incorporated) were 1-2 mm thick, had a resistivity of 12.2 Ω cm, and a surface perpendicular to the C-axis. The ohmic contact to the crystal was prepared with an In/Ga eutectic, and the crystal was then attached to a copper foil with silver epoxy. The copper foil was coated by a layer of epoxy so that only a single surface of the CdSe crystal was in contact with the electrolyte. The exposed area varied from sample to sample in the range of 0.1-0.2 cm^2. Polishing was performed by 0.3 μm alumina and etching was carried out in 4:1 HCl:HNO_3. The duration of etching was 30 sec, followed by washing in alkaline polysulfide solution and rinsing in distilled water.

The PEC was completed by a load resistor and a reversible brass counterelectrode (19) of large area immersed in the same solution. The brass counterelectrode was wrapped by glass microfiber paper to avoid contamination of the solution by ZnS or CuS particles. The very short wires used to connect the electrodes to the load resistor, as well as the large areas of the CdSe copper foil support and of the brass counterelectrode minimized the inductance of the total circuit. The PEC itself was well shielded electrically.

The high frequency photovoltaic signals were monitored using FET probes, (Type P6045 or plug-in unit 7A11, Tektronix). Photocurrents were measured under conditions close to external short circuit with a current-probe (P6022, Tektronix), and amplified when required by the current-probe amplifier (Type 134, Tektronix). To overcome problems due to lamp jitter and due to the initial delay of the boxcar unit, a compensated delay line was employed. The gate output of the scope (7904, Tektronix) was used to synchronize the scan delay generator (Brookdeal, 425A) while the amplified signal was applied through the delay-line to the linear-gate (Brookdeal, 415). The output signal from the boxcar was displayed on an X-Y recorder.

Results

Figure 2 demonstrates the pronounced effect of surface treatment on the amplitude and the decay time of the measured photocurrent transients: chemical etching of a mechanically polished CdSe electrode resulted in higher photocurrent peaks, in a larger charge per pulse, and in shorter decay times. The pronounced effect of surface treatment on the amplitude and decay time could be reproducibly repeated, while keeping the cell composition and electrode configuration con-

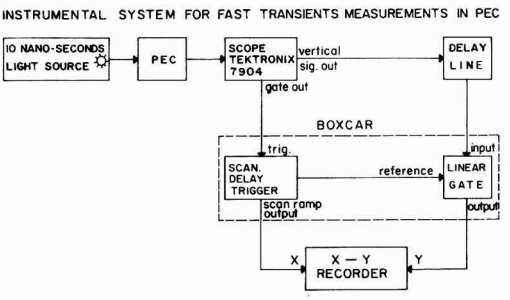

Fig. 1. The instrumental system for fast transient measurements in PEC.

* Electrochemical Society Active Member.
Key words: photocurrent, illumination, cell.

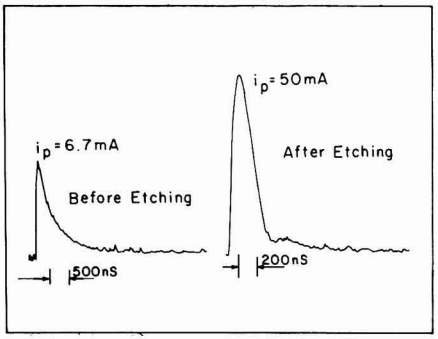

Fig. 2. Photocurrent transients for a mechanically polished (left) and for an etched (right) CdSe crystal, $R_L = 1\Omega$ in both cases. Semiconductor surface area = 0.2 cm².

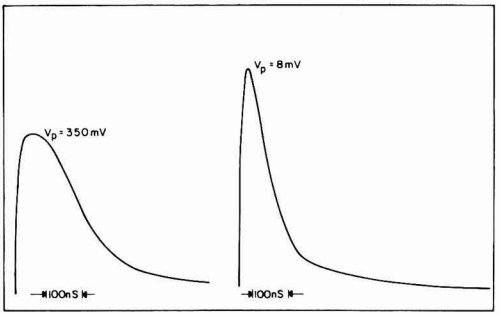

Fig. 4. Form of transients obtained for an etched electrode under saturation conditions at full light intensity (left), and with illumination attenuated by the use of neutral density filters (right). $R_L = 8.3\Omega$ in both cases. Semiconductor surface area = 0.1 cm².

stant. This proved conclusively that interfacial effects were not masked in this mode of measurement by other possible contributions to the time constant of the complete circuit. Figure 3 shows the steady-state photocurrent-voltage curves obtained for the same mechanically polished CdSe electrode prior to and after etching. It is clear that large changes in the steady-state performance of the cell are brought about by the same surface treatment which causes the modification of the transients.

In an attempt to evaluate quantitatively the measured photocurrent decay curves, the dependence of the decay time τ on the value of the load resistor, R_L, was recorded under conditions of small potential perturbations, so as to keep the interfacial parameters practically constant. To ensure such conditions, the light intensity was attenuated by a neutral filter so that the total drop across the load would not exceed 25 mV. The quasipotentiostatic conditions and low intensities employed resulted in simple exponential decay with a single time-constant τ. Figure 4 demonstrates the difference in the shape of decay curves obtained under small and large perturbations. Such differences were pronounced especially for etched electrodes, for which saturation conditions due to bands flattening were reached at full lamp intensity. A τ *vs.* R_L plot recorded at small perturbations is presented in Fig. 5 (the same attenuating filter was employed for all values of R_L). It can be seen that for small values of R_L the curve is linear, but the slope becomes smaller at higher values of R_L. In the same measurement, τ was found to approach an almost constant level for load resistors higher than 5 KΩ. The effect of etching on the τ *vs.* R_L plot is demonstrated in Fig. 6. (Again, small perturbations were employed.) The insert in Fig. 6 is an enlargement of the linear sections (small R_L regions) of the plots obtained before and after etching. These linear sections were evaluated by a linear regression analysis for slope and intercept (correlation function better than 0.99 for both lines). It can be seen that the intercept of the plot has become lower as a result of etching, while the slope has become somewhat smaller.

Discussion

The decay of the photocurrent in solar cells following an illumination pulse may be controlled, in principle, by the following factors (3): (*i*) the diffusion time of minority carriers towards the junction; (*ii*) the transit time through the junction; (*iii*) the Maxwell relaxation time; (*iv*) the lifetime of minority nonequilibrium carriers; and (*v*) a combined cell-circuit *R-C* time constant. Since CdSe is a direct band-gap semiconductor (20), most of the light is absorbed in the space-charge region and factor (*i*) should be insignificant. Strong band bending, imposed by keeping the CdSe electrode close to the potential of the $S^=/S^\circ$ couple, makes factor (*ii*) unimportant. Factor (*iii*) is not expected to play an important role thanks to the low resistivity of both the SC and the electrolyte employed. The most important factors to be considered are thus (*iv*) and (*v*). *In situ* photoluminescence decay-time measurements, conducted for the same photoelectrode by employing a dye laser of 2 nsec

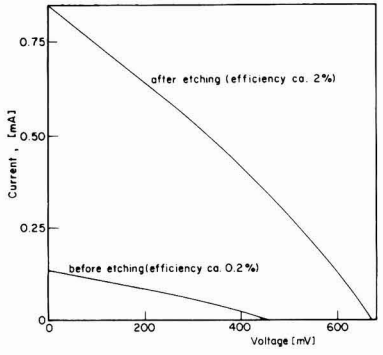

Fig. 3. Steady-state *I vs. V* curve for the polished and etched sample at which the transients of Fig. 2 were recorded.

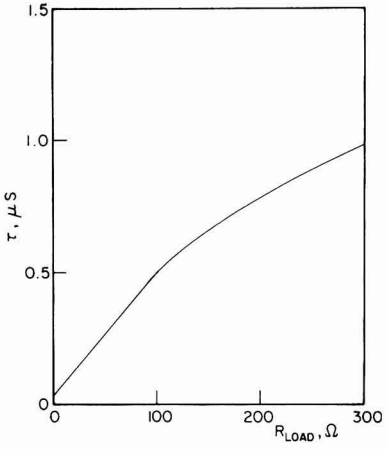

Fig. 5. τ *vs.* R_L recorded for an etched electrode under small photopotential perturbations. Surface area = 0.1 cm².

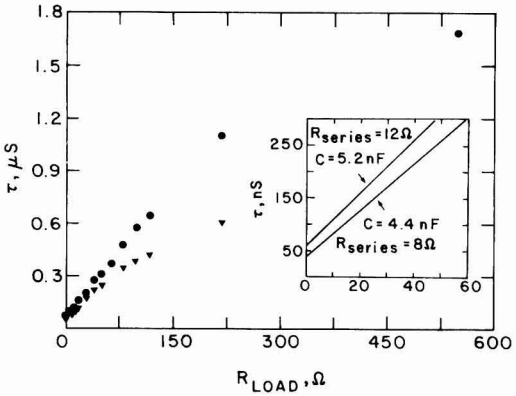

Fig. 6. τ *vs.* R_L plots taken before and after etching and recorded under small photopotential perturbations. Surface area = 0.1 cm² (same sample as in Fig. 4).

pulse width, revealed that the radiative band-to-band decay is completed in these CdSe samples (under small perturbation conditions) within 20 nsec. It thus seems from the above-mentioned arguments and results that in the time domain investigated ($t > 20$ nsec) photocurrent decay should be controlled by an R-C time constant.

The measured time dependence of τ on R_L (Fig. 5 and 6) verifies that τ is indeed controlled in our case by an R-C time constant which is determined by properties of the PEC and of the external circuit. The form of the measured variation of τ with R_L at small perturbations can be simulated by a very simple equivalent circuit, in which the semiconductor-electrolyte interfacial region is represented by a photocapacitor, C, with a shunt resistor, R_{in}, across it, while the rest of the cell and circuit is represented by a resistor R_{out}. R_{out} is given by

$$R_{out} = R_{series} + R_L$$

where R_{series} is a series combination of ohmic elements due to the PEC. To complete the equivalent circuit the photon flux is represented by a current source, according to the routine adopted in the analysis of solid-state solar cells (20), this leading to the circuit depicted in Fig. 7(a). The measured response of the real system to short light pulses can be simulated by the response of this simple R-C network to short current pulses. For a very short current pulse from the source (current delta function) the time variation of the current in the external circuit is calculated for circuit 7(a) [*e.g.*, by Laplace transformation (21)] as

$$i_{out} = \frac{\Delta Q}{R_{out}C} \exp(-t/\tau) \qquad [1]$$

where ΔQ is the charge injected by the source into the photocapacitor, and the decay time is given by $\tau = (R_{in}||R_{out})C$. For small values of R_L such that $R_{out} << R_{in}$, the decay time is given by $\tau = R_{out} \cdot C = (R_L + R_{series})C$. Under such conditions a plot of τ *vs.* R_L should be linear, with a slope of C and an intercept $R_{series} \cdot C$. On the other hand, at high values of R_L such that $R_{out} >> R_{in}$, the decay time is given by $\tau = R_{in}C$ and is thus expected to be independent of R_L. This is indeed the general form of the experimental τ *vs.* R_L plots depicted in Fig. 5 and 6. It thus seems that for small values of R_L photocarrier decay occurs via the external circuit, while for large values of R_L the decay takes place via an internal leakage route, in the same way as the capacitor in circuit 7(a) discharges primarily via R_{out} or via R_{in} depending on their relative values.

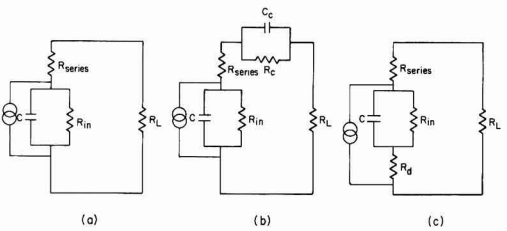

Fig. 7. Equivalent circuits used in the analysis of the photocurrent decay time (see text): C—photocapacitor; R_{series}—total series resistance of the PEC; R_L—load resistor; R_{in}—internal leakage resistor; R_c, C_c—the resistance and capacitance due to the counterelectrode-solution interface; R_d—resistance due to the damaged surface layer.

Although the very simple equivalent circuit of Fig. 7(a) seems to explain the general form of the experimental τ *vs.* R_L plots, its validity should be examined considering the complete photoelectrochemical cell it is expected to represent. Thus, when additional elements representing the counterelectrode are added, the more complex circuit of Fig. 7(b) is obtained. Analysis of this circuit shows that the solution for the current in the external cell, following a delta source current perturbation, has the form

$$I_{out} = A_1 \exp(-t/\tau_1) + A_2 \exp(-t/\tau_2) \qquad [2]$$

However, when $C_c >> C$, the following relationships apply: $\tau_1 \sim (R_{out}||R_{in})C$, $\tau_2 \sim R_cC_c$ and $A_2 << A_1$. This means that circuit 7(b) will generate transients with, practically, a single decay time: $\tau = (R_{out}||R_{in})C$, provided $C_c >> C$. This condition is fulfilled by the PEC employed, the counter being a metal electrode of large area. Any large capacitor in series with the small photocapacitor is expected, in fact, to act as a short during a fast transient measurement, and the simple circuit 7(a) is, thus, a high frequency form of 7(b) for $C_c >> C$. This was further verified experimentally by replacing the brass counterelectrode by a gold wire, (while employing a 50Ω resistor), resulting in no apparent effect on the measured transients, in accordance with the results reported in Ref. (16). Photocurrent transients with a single decay time may be, thus, expected for this cell when the decay is under pure R-C control, provided the potential perturbations are sufficiently small to ensure the constancy of C and R_{in}.

From the results of Fig. 6, it is seen that etching lowers the cell resistance, R_{series}, from 12 to 8Ω. Assuming that mechanical polishing produces a damaged surface layer (or a surface film) which can be removed by chemical etching, then such a layer may behave as an additional ohmic element through which photocarriers have to be transported. The effect of such an additional ohmic element on the form of the transient can be examined with the aid of the equivalent circuit in Fig. 7(c), where the damaged layer is represented by the additional resistor R_d. The solution for a delta perturbation in this circuit is

$$I_{out} = \frac{\Delta Q \cdot R_{out}}{(R_d + R_{out})^2 C} \exp(-t/\tau) \qquad [3]$$

where $\tau = C\,[R_{in}||(R_d + R_{out})]$. The resistor R_d thus explains the longer decay time and, to some extent, the lower amplitudes obtained in the presence of the surface film. Under short-circuit conditions, the amplitude is calculated to reduce by a factor of 2.5 due to the surface layer when $R_d = 4\Omega$ and $R_{out} = 8\Omega$. However, the description of the damaged layer in terms of the additional resistor, R_d, is not complete. From Fig. 3, it is clearly seen that this layer causes a substantial lowering of the open-circuit potential as well. This is not expected to occur due to the addition of R_d. It seems

that the damaged surface acts also as an active recombination region. If the recombinative process in this layer is very fast, it may not show up as a feature in the decay curve in the time window of our measurement ($t > 20$ nsec).[1] Its only apparent effect in terms of the equivalent circuit considered may be the lowering of the initial ΔQ on the photocapacitor, causing a reduction of the initial photopotential. The total amount of charge passing through the external load was indeed measured by us to increase 2-4 times after etching (Fig. 2). The role of the surface as a region of enhanced recombination has been described before by Nelson *et al.* (23) according to *ex situ* photoluminescence decay measurements. This may be the main kinetic significance of such a damaged layer under open-circuit conditions. However, the additional ohmic effect has to be considered when photocurrents are drawn from the cell.

The value of R_{series} evaluated from the photocurrent decay measurements after etching (8Ω in the case depicted in Fig. 6) is very close to the sum of bulk SC and electrolyte solution ohmic resistances calculated according to the specific resistivities, sizes, and geometries employed. The same value for the cell series was found also from the maximum photocurrent peak obtained for an etched electrode under saturation conditions (high pulse intensity): The maximum measured photocurrent peak was given by

$$(i_p)_{max} = \frac{\Delta\phi_{max}}{R_{series} + R_L}$$

where $\Delta\phi_{max} = 0.7V$ (complete band flattening) and $R_{series} = 8\Omega$. It is thus clear the value of R in the RC time constant found for photocurrent decay in this PEC is determined by the total series resistance of the cell. If R_{series} contains a contribution due to the finite rate of interfacial charge-transfer at the SC-electrolyte interface ("faradaic impedance") this contribution is apparently very small in this case. Further transient measurements with solutions containing less efficient hole acceptors should reveal if the faradaic impedance can be resolved when it is much larger than the ohmic elements due to the bulk SC and electrolyte.

Finally, the value of C evaluated from the τ *vs.* R_L plots is close to that found from a Schottky-Mott plot (80 nF cm^{-2}) for a similar CdSe electrode in an alkaline $S^=/S^\circ$ solution under the same applied potential (22). This simply means that the photocapacitor is located in the space-charge region of the semiconductor. Etching is expected to increase the value of C if its only effect were surface roughening. The slight lowering of C measured after etching (Fig. 6) probably means that some surface states contributing to the total C measured for a mechanically polished electrode are removed by etching, resulting in a lower capacity in spite of the increased surface area. It should be also noticed that the measured reduction in reflectance due to this mode of etching (24) is calculated to bring about not more than 20% enhancement of the photocurrent, *i.e.*, this cannot be considered a major contribution to the measured effects.

[1] Measurements conducted by us recently, using an Nd-YAG laser, showed that effects of the damaged surface layer on the effective lifetime of the photocarriers could be measured in the time window 10 psec-10 nsec.

Acknowledgment

One of us (S. G.) would like to thank Brookhaven National Laboratory for their assistance in the preparation of this manuscript for publication during his stay there as a Visiting Scientist (Summer 1980).

Manuscript received Aug. 6, 1980.

Any discussion of this paper will appear in a Discussion Section to be published in the December 1981 JOURNAL. All discussions for the December 1981 Discussion Section should be submitted by Aug. 1, 1981.

REFERENCES

1. "Semiconductor Liquid-Junction Solar Cells," A. Heller, Editor, The Electrochemical Society Softbound Proceedings Series, Princeton, N.J. (1977).
2. D. D. MacDonald, "Transient Techniques in Electrochemistry," Plenum Press, New York (1977).
3. S. M. Ryvkin, "Photoelectric Effects in Semiconductors," Consultants Bureau, New York (1969) and Ref. therein.
4. S. R. Dhariwal, L. S. Kothari, and S. C. Jain, *J. Phys. D: Appl. Phys.*, **9,** 631 (1976).
5. S. R. Dhariwal, L. S. Kothari, and S. C. Jain, *Solid State Electron.*, **20,** 297 (1977).
6. D. M. Bielle-Daspet and G. D. Gasset, *ibid.*, **21,** 1219 (1978).
7. H. Tade, *J. Appl. Phys.*, **37,** 4595 (1966).
8. J. L. Lindström, *Solid State Electron.*, **14,** 827 (1971).
9. J. E. Mahan, T. W. Ekstedt, R. I. Frank, and R. Kaplow, *IEEE Trans. Electron Devices*, **ed 26,** 733 (1979).
10. H. T. Weaver and R. D. Nasby, *Solid State Electron.*, **22,** 687 (1979).
11. V. A. Mayamlin and Y. V. Pleskov, "The Electrochemistry of Semiconductors," Plenum Press, New York (1967).
12. K. W. Frese and J. H. Kennedy, Paper 425 presented at The Electrochemical Society Meeting, Seattle, Washington, May 21-26, 1978.
13. G. A. Korsunovskii, *Russ. J. Phys. Chem.*, **53,** 123 (1979).
14. T. Sakata and T. Kawai, Paper 626 presented at The Electrochemical Society Meeting, Los Angeles, California, Oct. 14-19, 1979.
15. J. H. Richardson, S. B. Deutscher, J. E. Harrar, D. C. Johnson, S. P. Perone, and J. Zilmer, Paper 627 presented at The Electrochemical Society Meeting, Los Angeles, California, Oct. 14-19, 1979.
16. F. Kawai, H. Tributsch, and T. Sakata, *Chem. Phys. Lett.*, In press.
17. C. E. P. Krohn, Ph.D. Thesis, University of Texas at Austin (1978).
18. Z. Harzion, N. Croitoru, and S. Gottesfeld: (a) Bulletin of the Israel Physical Society, April 1980; (b) Extended Abstracts of the 3rd Intl. Conf. on Photochemical Conversion and Storage of Solar Energy, Boulder, Colorado, August 1980.
19. G. Hodes, J. Mannasen, and D. Cahen, Private communication.
20. A. Rothwarf and K. W. Böer, *Prog. Solid State Chem.*, **10,** 71 (1975).
21. See, for example, S. Goldman, "Laplace Transform Theory and Electrical Transients," Dover Publications, New York (1966).
22. D. Lando, Private communication.
23. R. J. Nelson, J. S. Williams, H. J. Leamy, B. Miller, H. C. Casey, Jr., B. A. Parkinson, and A. Heller, *Appl. Phys. Lett.*, **36,** 76 (1980).
24. R. Tenne, Private communication.

The Use of Rutherford Backscattering Spectroscopy for Characterization of Surface Films Produced by Aluminum/Water Reactions

R. C. McCune

Ford Motor Company, Engineering & Research Staff, Research, Dearborn, Michigan 48121

and C. J. Russo[1]

General Ionex Corporation, Newburyport, Massachusetts 01950

Surface films formed during the reaction between aluminum metal and aqueous electrolytes at elevated temperatures are of considerable interest in situations where such films may afford some measure of resistance to the onset of pitting attack in the presence of aggressive anions (*e.g.*, Cl^-). The reaction between aluminum or aluminum alloys and aqueous electrolytes may result in a variety of reaction products and surface film morphologies, and is reviewed in detail by Alwitt (1). For the specific case of aluminum alloy radiators in automotive cooling systems, the complexity of the electrolyte is accentuated by a variety of components including an antifreezant, various corrosion inhibitors, buffers, and antifoaming agents. Furthermore, the overall system may contain dissimilar metal components which can ultimately result in plating reactions on freshly exposed aluminum, in the absence of particular inhibitors for these reactions. Characterization of aluminum alloy surfaces used in an active cooling system involves not only an appraisal of aluminum/water reaction products on the surface, but also the degree of inhibitor uptake by the surface, the presence of any dissimilar metals, and the integrity of the surface film as a barrier to pitting attack.

The role of any films formed by surface reaction in the overall process of pitting attack is also of interest. While an initially dense oxide or oxyhydroxide (*e.g.*, pseudoboehmite) film may be advantageous in limiting the rate of aggressive ion ingress, its ultimate role may be deleterious if the film serves to isolate a developing pit from the bulk of the electrolyte (2, 3). In this latter case, the essentially unreactive film allows localized acidity conditions to develop within the pit so that metal dissolution proceeds without benefit of any diluent or buffering effects of the electrolyte external to the pit.

Electron and low energy (*i.e.*, <10 keV) ion beam spectroscopies are often limited in their ability to rapidly assess such features as apparent thickness and overall elemental composition for water-grown films on aluminum. This is due primarily to experimental sampling depths (usually $\sim$100Å or less) which can represent only a limited fraction of the thickest water-grown films [often approaching physical dimensions of $\sim$0.5 μm (1)]. Since elemental depth profiles in these techniques are often achieved by concurrent sputter etching, the results may often require extensive times for data collection, and result in limited depth resolution due to artifacts associated with the sputter process. In this work, the use of Rutherford Backscattering Spectroscopy (RBS) is described with particular application to reactions between a relatively clean aluminum surface and water containing a phosphate-based inhibitor. RBS has the distinct advantages in these applications of permitting the overall film characteristics to be assessed qualitatively, and in a relatively fast, (*ca.* 5 min spectrum acquisition time) though nondestructive manner.

The RBS technique has been employed by a number of investigators for analysis of surface oxides on aluminum and aluminum alloys (4-7). The experimental details are adequately described in the text by Chu, Mayer, and Nicolet (8). In general, a collimated source of monoenergetic high energy ions and associated scatter chamber and detector are used to acquire the energy distribution of ions scattered through a fixed angle from the target surface. For the simplest thin film, the mass of the surface atom is deduced from the kinetic energy of the backscattered ion, through application of simple binary scattering kinematics with the initial ion energy, its mass, and scattering angle as known quantities. Depth information may be obtained when energy losses in the target bulk are considered for the backscattered ions. For the case of $^4He^{2+}$ at primary energies of 2-3 MeV, the accessible depth is sufficient to permit penetration of the surface films, allowing extraction of compositional data for the free surface as well as the metal/oxide interface. Because of the relatively low atomic weights of aluminum and oxygen, the spectral peaks for heavier elements occur where there is minimal background contribution, and with somewhat larger sensitivities due to greater scattering cross sections (8).

In this work, the ion source consisted of a 3.0 MeV Tandetron accelerator manufactured by General Ionex Corporation. A scattering angle of approximately 160° was used, in conjunction with a barrier-type particle detector and counting electronics. The overall experimental resolution was estimated to be 25 keV.

Aluminum coupons of a commercial 1100 type material were prepared by mechanical and electrolytic polishing according to a procedure described elsewhere (9). Surface films were grown at 100°C by immersion of the coupons in either doubly distilled, deionized water or in similar water containing Na_2HPO_4 at 0.05M, which is a known inhibitor of the aluminum/water reaction (10). The surface treatments, as well as several experimental quantities are summarized in Table I.

[1] Present address: Varian Associates, Extrion Division, Gloucester, Massachusetts 01930.

Key words: backscattering, pseudobeohmite, aluminum, inhibitor.

Table I.

Specimen	Film growth time (min.) Water	Film growth time (min.) 0.05M Na_2HPO_4	ΔE_s Aluminum substrate energy shift (MeV)	O_{FWHM} (MeV)	Approximate film thickness (Å)*	Remarks
A	—	—	0.0	—	—	Electropolished surface only
B	15	0	0.079	0.081	1450	No iron peak observed
C	0	15	0.044	0.050	850	Distinct P and Fe
D	15	15	0.117	0.122	2150	Diffuse P and Fe

* Calculated using density of 3.0 g/cm² of AlOOH (boehmite) and tabulations outlined in Ref. (12) and (13).

The RBS spectra for the various surface treatments are shown in Fig. 1. The iron peak observed for the electropolished surface (spectrum A) is believed to be due to residual $FeAl_3$ particulates which remain on the surface following specimen preparation. Iron is the principal impurity in 1100 type alloys, present at levels typically less than 0.5% (wt). The role of the resultant $FeAl_3$ precipitates in corrosion of aluminum has been discussed elsewhere (11). In spectrum A scattering from the essentially clean aluminum substrate shows a spectral edge having the energy of the binary He-Al collision at roughly the half-height of the edge. The effect of growing a pseudoboehmite film in water (spectrum B) is evidenced by two new features of the spectrum: (*i*) the appearance of an oxygen peak due to growth of the oxyhydroxide film, and (*ii*) the displacement of the aluminum substrate scatter edge to a lower energy by the amount ΔE_s due to the associated loss of energy by the helium ions as the layer is traversed during the scatter process. As indicated in Table I, the aluminum substrate scatter edge is displaced by 0.079 MeV from the binary collision energy associated with the relatively clean surface in spectrum A. Because the surface pseudoboehmite film has a lower density of aluminum atoms per cm² than the aluminum metal substrate, the leading aluminum scatter edge occurs at an overall lower signal height. Thus, in principle, the film thickness is reflected in the breadth of the leading surface layer spectral edge (and corresponding ΔE_s for the substrate edge), while the height of this leading edge is a measure of the film density.

In spectrum C, the effect of the inhibitor is immediately apparent in that ΔE_s for the substrate, as well as the oxygen full width at half maximum (O_{FWHM}) are diminished from the values associated with the pure water grown film. The uptake of phosphorus in the surface layer is evidenced by the appearance of a distinct peak having the appropriate binary collision energy for He-P.

In spectrum D, the original 15 min pseudoboehmite film was exposed to an additional 15 min in the phosphate solution. The spectrum indicates continued film growth *i.e.*, increased O_{FWHM} and ΔE_s, but with noticeably less phosphate uptake than that which occurred on the relatively fresh aluminum surface. The passivation of the surface by the original pseudoboehmite film is apparently responsible for retarding the fixation of the aluminophosphate complex as occurred in spectrum C. The original film produced by 15 min water exposure continues to develop with only slight uptake of phosphate.

It can be seen that RBS offers a unique insight into the mechanisms of film formation and growth. The inhibitive effect of phosphate at the fresh metal surface, as reported by Vermilyea and Vedder (10) is clearly observable, as well as the resulting phosphate uptake by the surface. The ability of RBS to observe cumulative elemental compositions in depth, may prove to extend the utility of the technique to a range which is unattainable with many other surface spectroscopies.

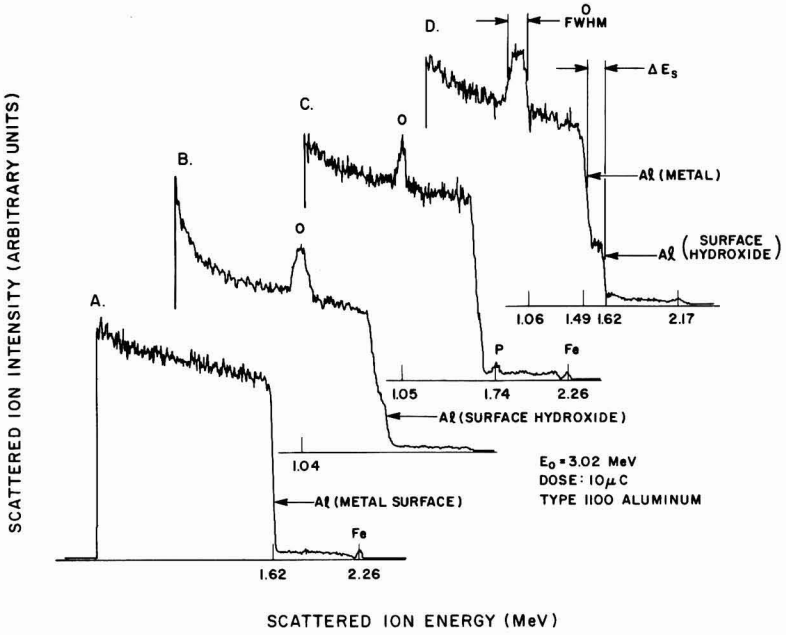

Fig. 1. Rutherford backscatter spectra for various surface treatments to type 1100 aluminum. A. Electropolished surface, B. 15 min pseudoboehmite film, C. 15 min film in phosphate inhibitor, D. combined 15 min pseudoboehmite, 15 min phosphate inhibitor.

Acknowledgments

The authors would like to thank P. J. Edwards for preparation of the specimens, and W. L. Winterbottom and R. R. Wiggle for review of the manuscript. The use of the General Ionex Facility and the cooperation of D. Mills and R. Suchanek for the work is appreciated.

Manuscript submitted July 22, 1980; revised manuscript received *ca.* Sept. 30, 1980.

Any discussion of this paper will appear in a Discussion Section to be published in the December 1981 JOURNAL. All discussions for the December 1981 Discussion Section should be submitted by Aug. 1, 1981.

Publication costs of this article were assisted by Ford Motor Company.

REFERENCES

1. R. S. Alwitt, "Oxides and Oxide Films," Vol. 4, J. W. Diggle and A. K. Vijh, Editors, p. 169, Marcel Dekker, Inc., New York (1976).
2. G. C. Wood, W. H. Sutton, J. A. Richardson, T. N. K. Riley, and A. G. Malkerbe, "Localized Corrosion," R. W. Staehle, B. F. Brown, J. Kruger, and A. Agrawal, Editors, p. 526. NACE, Houston (1974).
3. J. R. Galvele, "Passivity of Metals," R. P. Frankenthal and J. Kruger, Editors, p. 285, The Electrochemical Society, Princeton (1978).
4. M. Kamoshida, I. V. Mitchell, and J. W. Mayer, *J. Appl. Phys.*, **43**, 1717 (1972).
5. W. Bauer and R. G. Musket, *ibid.*, **44**, 2606 (1973).
6. F. Brown and W. D. Mackintosh, *This Journal*, **120**, 1096 (1973).
7. H. H. Strehblow, C. M. Melliar-Smith, and W. M. Augustyniak, *ibid.*, **125**, 915 (1978).
8. W. K. Chu, J. W. Mayer, and M. A. Nicolet, "Backscattering Spectrometry," Academic Press, New York (1978).
9. R. C. McCune, *J. Vac. Sci. Technol.*, **15**, 31 (1978).
10. D. A. Vermilyea and W. Vedder, *Trans. Faraday Soc.*, **66**, 2644 (1970).
11. J. Zahavi, A. Zavgvil, and M. Metzger, *This Journal*, **125**, 438 (1978).
12. J. F. Ziegler, "Helium Stopping Powers and Ranges in All Elemental Matter," Pergamon, New York (1977).
13. R. L. Shilts, Western Michigan University, Kalamazoo, MI (Private communication).

Erratum

In the paper "A Thermodynamic Theory of Dissolution Potential and Further Tests of the Theory" by R. P. Rastogi and S. A. Kahn, which appeared in the September 1980 issue of the JOURNAL, Vol. 127, No. 9, the following corrections should be noted: On page 1989, paragraph 3 should precede paragraph 2; on page 1990, in the third paragraph, it should read M = mass of phase; also on p. 1990, the right-hand side of Eq. [8] should read X_2 instead of J_c. On page 1991, the left-hand side of Eq. [34] should read $(\Delta\phi)$ instead of $(\phi\Delta)$; on page 1991, Eq. [44] should read as $\frac{a_2^{(sat'd)}}{a_2^{\beta}}$ instead of $\frac{a_1^{(sat'd)}}{a_2^{\beta}}$. The title of Table II on p. 1993 should be "Dissolution potential of KCl in KCl-HCl aqueous mixtures." Also in Table II, the fourth line in the first column should read 0.025M HCl + 0.075M KCl.

JOURNAL OF THE ELECTROCHEMICAL SOCIETY

SOLID-STATE SCIENCE AND TECHNOLOGY

MARCH 1981

Preparation and Properties of Zinc Oxide Films Grown by the Oxidation of Diethylzinc

James R. Shealy and B. Jayant Baliga*

General Electric Company, Corporate Research and Development Center, Schenectady, New York 12345

and R. Jett Field and Sorab K. Ghandhi*

Electrical and Systems Engineering Department, Rensselaer Polytechnic Institute, Troy, New York 12181

ABSTRACT

This paper describes the preparation and properties of zinc oxide films grown by the oxidation of diethylzinc. It is shown that growth above 250°C, with an oxygen to diethylzinc mole ratio in excess of 10, results in stable films of zinc oxide, free from carbon contamination or zinc-ethyl groups. Details are provided of these growth conditions and also of the resulting growth parameters in this paper. The physical properties of films grown by this technique are also described, with particular emphasis on their *IR* absorption characteristics, stoichiometry, refractive index, and crystallographic orientation, as a function of the growth conditions. Films are shown to have an oxygen deficiency which increases with growth temperature, as does their refractive index. Film orientation, along the c-axis, is also found to improve with increasing growth temperatures.

The properties of zinc oxide films have allowed the fabrication of devices such as heterojunction solar cells, surface acoustic wave devices, and optical waveguides. The highly aligned C-axis films which are obtained with the technique to be described display piezoelectric properties (1) and provide a medium for surface acoustic wave propagation (2). The bandgap of zinc oxide (3.3 eV) is sufficiently large to be transparent to most of the solar spectrum, and its conductivity may be controlled over a broad range. These facts together make zinc oxide useful in heterojunction solar cells application. For example, an n-ZnO/p-CdTe heterojunction solar cell has produced solar efficiencies of 4.6% and short-circuit current collection of 19 mA/cm^2 (3). The optical transmission spectrum for the zinc oxide films shows a strong absorption edge at wavelengths around 0.4 μm, with a transparent region in the range of 0.4-2.3 μm. This transparent window makes zinc oxide suitable for optical waveguide fabrication (4). In addition, the authors have used zinc oxide films as a source of zinc for open tube diffusions of zinc in gallium arsenide (5).

This paper describes the growth of zinc oxide utilizing a metal-organic chemical vapor phase deposition (CVD) process. These films are characterized using infrared transmission, resistivity measurements, x-ray diffraction, Auger analysis, and ellipsometry. The conditions for the deposition of stable, C-axis oriented, zinc oxide films grown by the oxidation of diethylzinc have been determined. It appears that zinc oxide films obtained with this process have desirable optical, electrical, and acoustical properties which are potentially suitable for the many applications mentioned above.

* Electrochemical Society Active Member.

Key words: zinc oxide, chemical vapor deposition, organometallic CVD.

Apparatus

The apparatus used for the zinc oxide depositions was a resistance heated, cold wall system which is schematically illustrated in Fig. 1. The substrate heater was approximately 1½ in. in diameter. The reaction chamber geometry was vertical with gas flow normal to the substrate surface. The chamber was maintained at essentially atmospheric pressure with reactants entering at the top and exhausted out of the bottom of the chamber. The chamber was a 12 in. long, 3 in. diam quartz tube. Gases provided to this system were argon[1] and oxygen.[1] The diethylzinc[2] was contained in a stainless steel bubbler maintained at 25°C, and was transported into the reaction chamber by passing argon through the bubbler. An additional argon line was used for dilution purposes. Oxygen was introduced through a separate port at the top of the reaction chamber.

Film Deposition

In this study, the zinc oxide films were deposited by the reaction of diethylzinc with oxygen. Diethylzinc is a pyrophoric liquid which is known to react with air even at room temperature. The deposition of zinc oxide films using diethylzinc vapors was, therefore, studied over a wide range of temperatures ranging from room temperature (25°C) up to 500°C. The oxidation of diethylzinc may be expected to proceed by the following reaction

$$(C_2H_5)_2Zn + 7\ O_2 \rightarrow ZnO + 4CO_2 + 5H_2O \qquad [1]$$

This equation indicates that it is necessary to perform the deposition under a high O_2/DEZ mole ratio to ensure complete oxidation of the diethylzinc.

[1] UHP grade, Union Carbide Corporation.

[2] 5*N* Electronic grade, Ventron Corporation, Danvers, Massachusetts.

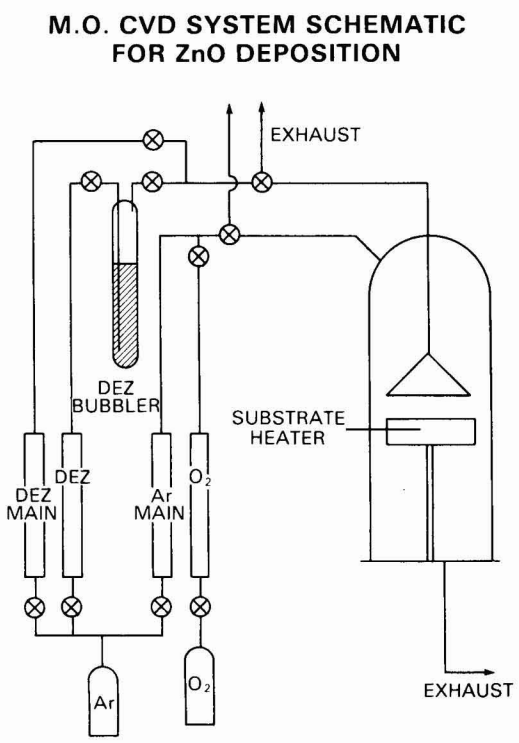

Fig. 1. Schematic diagram of zinc oxide deposition system

The deposition of the zinc oxide films was studied on (111) ± 0.5° oriented, 30 Ω-cm, phosphorus-doped, silicon substrates under the following conditions:

(*i*) For a fixed partial pressure of diethylzinc and a fixed deposition temperature, the effect of the partial pressure of oxygen was observed by changing the oxygen flow.

(*ii*) Keeping the partial pressure of oxygen and the deposition temperature fixed, the effect of the partial pressure of diethylzinc was observed by changing the argon flow through the diethylzinc bubbler. Full saturation conditions were assumed for the argon passing through the bubbler.

(*iii*) Keeping the partial pressures of diethylzinc and oxygen fixed, the effect of the deposition temperature was observed. Prior to film deposition, the substrates were cleaned by degreasing, immersion in Caros solution, and a dip in HF prior to loading into the reactor. After deposition, the film thickness was determined by ellipsometry.

Oxygen flow.—In the absence of oxygen, diethylzinc will decompose at elevated temperatures into zinc-ethyl groups or even into elemental zinc if the temperature is sufficiently high. In this study, it was found that the films deposited with little or no oxygen present showed rapid changes in appearance upon exposure to air after deposition. The effect the introduction of oxygen had upon the growth rate of the films was examined at a deposition temperature of 350°C while maintaining all other gas flows constant. To obtain this data, the argon flow through the diethylzinc bubbler was maintained at 23 cm³/min and a total argon flow of 6.9 liters/min was used. The growth rate was found to be independent of oxygen flow when the oxygen to diethylzinc mole ratio exceeded 10. Films grown at oxygen to diethylzinc mole ratios of less than 10 showed changes in appearance on exposure to air. This is in accordance with the high ratio of oxygen to diethylzinc indicated by Eq. [1] to ensure complete reaction. Consequently, care was taken in the experiments described below to maintain an oxygen to diethylzinc ratio of greater than 10 to ensure the deposition of stable zinc oxide films.

Diethylzinc flow.—The growth rate of the zinc oxide films could be varied over a broad range by controlling the argon flow through the DEZ bubbler while maintaining all other growth parameters constant. For a deposition temperature of 350°C, an oxygen flow of 12 cm³/min and a total argon flow of 6.9 liters/min, the growth rate was found to increase linearly with increasing argon flow through the DEZ bubbler as shown in Fig. 2. Similar results were obtained at other deposition temperatures. It should be noted that even at the highest DEZ concentrations used to obtain the growth rate data in Fig. 2, the oxygen to DEZ ratio was maintained at greater than 10 to ensure the formation of zinc oxide films.

Growth temperature.—The growth rate of the zinc oxide films was measured as a function of the deposition temperature over the range from room temperature (25°C) to 500°C, while maintaining all the gas flows constant. The gas flows chosen for these experiments were an argon flow through the DEZ bubbler of 23 cm³/min, an oxygen flow of 12 cm³/min, and a total argon flow of 6.9 liters/min. It was found that the films deposited at below 250°C changed their appearance on exposure to air. Consequently, the growth rate of films deposited at 250°-500°C is shown in Fig. 3. It can be seen that the deposition rate decreases when the growth temperature is increased. Reactant depletion at the substrate surface with increasing deposition temperature was found to be responsible for this decrease in the growth rate. This depletion in the reactant concentration at the substrate surface occurs due to a competing gas phase reaction between the diethylzinc and

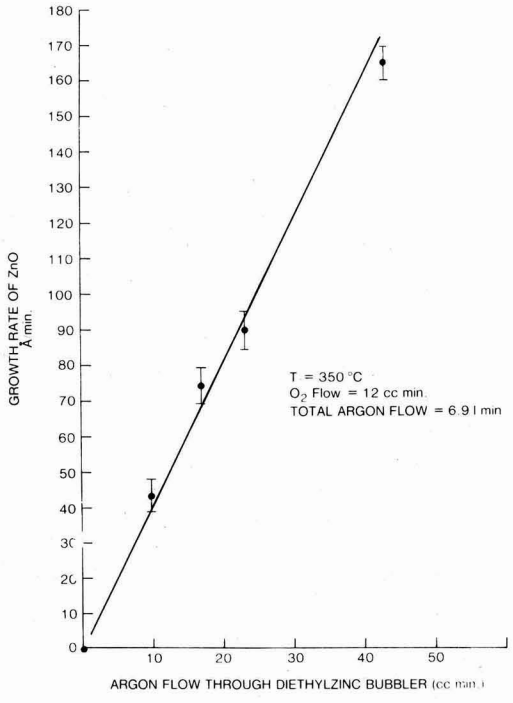

Fig. 2. Increase in the deposition rate of zinc oxide films with increase in argon flow through the diethylzinc bubbler.

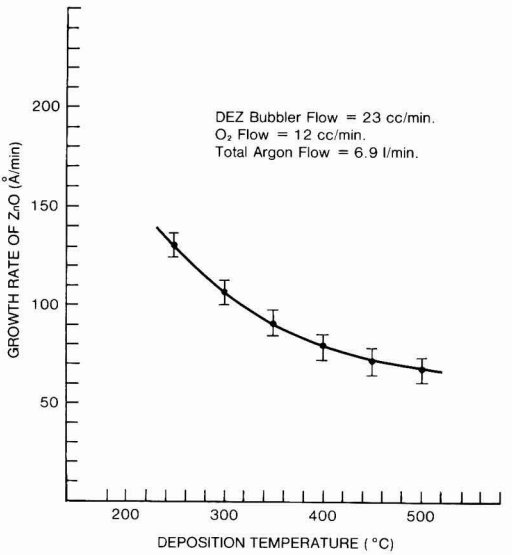

Fig. 3. Dependence of the growth rate of zinc oxide films upon the substrate temperature.

oxygen. Evidence supporting this was obtained by measuring the growth rate, at a fixed deposition temperature, while changing the spacing between the DEZ inlet to the reactor and the substrate surface. For a fixed partial pressure of DEZ in the reaction chamber, the growth rate showed a rapid increase with decreasing spacing between the DEZ inlet and the substrate surface. Although it may be concluded from these results that a small spacing between the DEZ inlet and the substrate surface is desirable for obtaining high growth rates, in practice the DEZ inlet position must be chosen so as to obtain the desired uniformity in the film thickness over the entire substrate area. As an example, for the above growth conditions, a spacing of 3 in. between the DEZ inlet and the substrate surface resulted in a variation in film thickness of less than ±10% over an area of 1.5 in. in diameter.

Film Properties

Chemical, physical, and electrical properties of the zinc oxide films deposited under various growth conditions are described below. This data can be used to evaluate the quality of these films for potential applications.

Infrared absorption.—Infrared absorption measurements over wavelengths ranging from 1 to 40 microns were taken on films deposited at temperatures ranging from room temperature (25°C) to 500°C. Films which were deposited at temperatures above 250°C showed the presence of an absorption band at a wavelength of 23 microns which was not observed in the case of films deposited at below 250°C. Typical absorption spectra for films deposited at 150° and 500°C are shown in Fig. 4 for comparison. Since this absorption band has been observed in bulk zinc oxide and is associated with the zinc-oxygen molecular bond, it can be concluded that zinc oxide films are deposited at substrate temperatures above 250°C, while films deposited below this temperature probably consist of unstable zinc ethyl groups.

Composition.—The stoichiometry of zinc oxide films deposited at temperatures ranging from 250° to 500°C was measured by Auger analysis using a polycrystalline zinc oxide sample as the standard. Films were found to contain an excess of zinc which increased with increasing deposition temperatures as shown in Fig. 5. A similar behavior has been observed in the case of the deposition of tin oxide films by the oxidation of tetramethyltin (6). The presence of excess zinc in the films, as detected by the Auger analysis, is important for understanding the variation in their refractive index and resistivity with growth temperature. It is also worth pointing out that the Auger analysis, taken on these films after ion milling approximately 50Å from the surface, showed that they were free of the carbon contamination that could arise from the use of the organometallic zinc source.

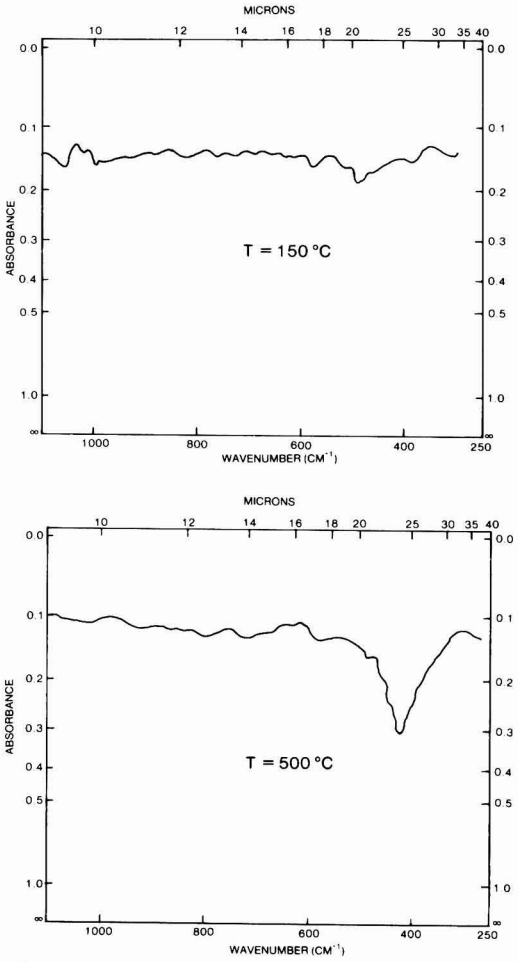

Fig. 4. Infrared absorption spectra of films deposited at substrate temperatures of 150° and 500°C.

Refractive index.—The index of refraction was measured for films at a wavelength of 5461Å by ellipsometry. The conditions used to deposit these films on the silicon substrates were identical to those used to obtain the data shown in Fig. 3. The variation in the refractive index with deposition temperature is shown in Fig. 6. It can be seen that the index of refraction increases when the deposition temperature is increased. This increase in the refractive index with deposition temperature correlates with the observed increase in the excess zinc concentration as was shown in Fig. 5. While a refractive index of 2.03 has been reported for bulk ZnO (8), values similar to those given

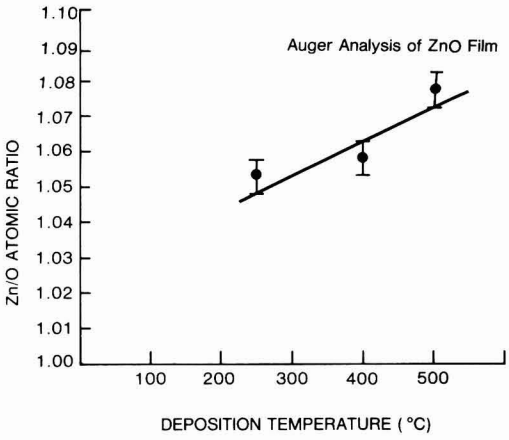

Fig. 5. Auger data of zinc oxide films revealing the increase of excess zinc in the films with increasing deposition temperatures.

in Fig. 3 have been observed for ZnO films deposited by other chemical vapor deposition techniques (9).

Crystal orientation.—X-ray diffraction measurements were made on films deposited on Corning Type 7059 glass at deposition temperatures ranging from 250° to 500°C. No diffraction peaks were observed for films grown at and below 300°C, indicating that these films were amorphous. However, films deposited at above 300°C showed x-ray diffraction peaks as illustrated in Fig. 7 for a film deposited at 400°C. This and other x-ray data taken on these films shows that the films have a high C-axis orientation which improves with increasing deposition temperature. This data as well as the results of deposition on other substrates has been discussed in greater detail elsewhere (7).

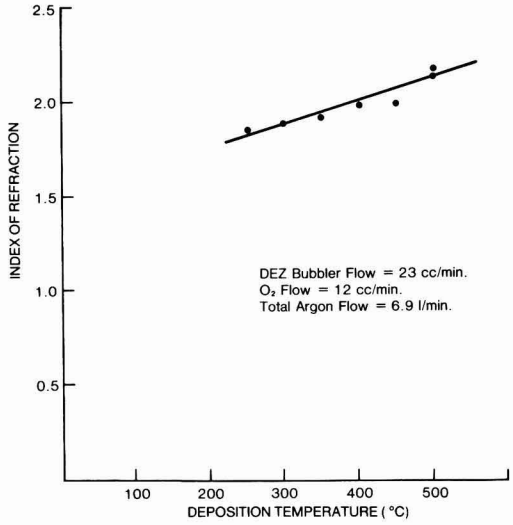

Fig. 6. Refractive index of zinc oxide films grown at deposition temperatures ranging from 250° to 500°C.

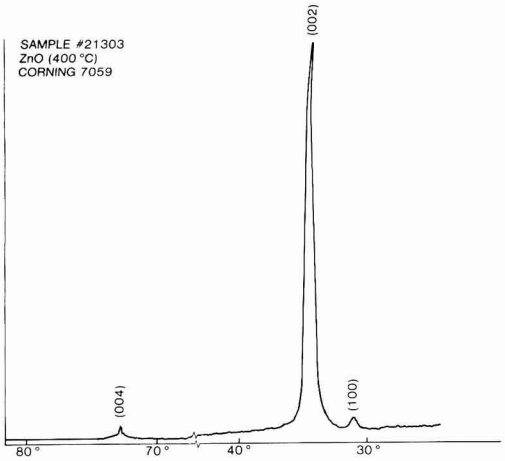

Fig. 7. X-ray diffraction data of a zinc oxide film grown at 400°C on Corning 7059 glass obtained using Copper K_α radiation.

Conclusions

A novel technique for the deposition of zinc oxide films at relatively low temperatures has been outlined. The physical properties of this material, which are of interest for a number of electronic applications, have also been described. It has been shown that films grown in this manner are highly oriented, and should find use in surface acoustic wave application. The use as a zinc source for open tube gallium arsenide diffusion has been outlined in an earlier paper. Further work needs to be done to explore other uses for zinc oxide thin films grown by this CVD technique.

Acknowledgment

The authors would like to thank R. Rafun for manuscript preparation. This work was partially supported (S.K.G. and R.J.F.) by Contract No. XI-9-8000-1 from the Solar Energy Research Institute, Golden, Colorado.

Manuscript submitted June 20, 1980; revised manuscript received Aug. 13, 1980.

Any discussion of this paper will appear in a Discussion Section to be published in the December 1981 JOURNAL. All discussions for the December 1981 Discussion Section should be submitted by Aug. 1, 1981.

Publication costs of this article were assisted by General Electric Company.

REFERENCES

1. A. R. Hutson, *Phys. Rev. Lett.*, **4**, 505 (1960).
2. T. Shiosaki, T. Yamamoto, A. Kawabata, R. S. Muller, and R. M. White, *IEDM Digest*, 151 (1979).
3. A. L. Fahrenbrach, J. Aranovich, F. Courregas, T. Chynoweth, and R. H. Bube, IEEE Photovoltaic Spec. Conf., 13th, Washington, D.C., p. 281 (1978).
4. T. Shiosaki, S. Ohnishi, and A. Kawabata, *J. Appl. Phys.*, **50**, 3113 (1979).
5. J. R. Shealy, B. J. Baliga, and S. K. Ghandhi, *IEEE Electron Device Lett.* **edl-1**, 119 (1980).
6. B. J. Baliga and S. K. Ghandhi, *This Journal*, **123**, 941 (1976).
7. S. K. Ghandhi, R. J. Field, and J. R. Shealy, *Appl. Phys. Lett.*, **37**, 449 (1980).
8. E. Mollwo, *Z. Agnew Phys.*, **6**, 257 (1954).
9. T. Shiosaki, S. Ohnishi, Y. Hirokawa, and A. Kawabata, *Appl. Phys. Lett.*, **33**, 406 (1978).

Comparison of the Properties of Molybdenum Silicide Films Deposited by D-C Magnetron and RF Diode Co-Deposition

Ronald S. Nowicki* and John F. Moulder

Perkin-Elmer, Physical Electronics Division, Mountain View, California 94043

ABSTRACT

We report a preliminary study in which the physical and electrical properties of d-c magnetron and co-deposited rf diode molybdenum silicide films of varying stoichiometry are compared. It is shown that the d-c magnetron films deposited from a composite target tend to be non-optimal in comparison to the rf diode co-deposited films of the same stoichiometry. Extensive degradation of the d-c magnetron films was frequently observed during heat-treatment at 1000°C in nitrogen or argon ambient. The rf diode films, however, appear to withstand heat-treatment without signs of degradation. There appear to be significant differences in film stress changes during heat-treatment, *i.e.*, the d-c magnetron films exhibit a severe change in stress level resulting in a highly tensile state which causes film cracking and loss of adhesion, whereas the rf diode co-deposited film stress changes to minimal values during heat-treatment. Additional data on crystal morphology, resistivity change during heat-treatment, and general film properties are also discussed.

Refractory metal silicides have been proposed as alternatives to polycrystalline silicon ("polysilicon") for gate electrode or interconnection metallizations in field effect transistor devices of VLSI dimensions (1-4). This trend has evolved as a consequence of the prohibitive values of resistance encountered in conventional polysilicon gate technology as device geometries are reduced.

One significant problem with these newer materials appears to be the relatively high levels of contaminants (*e.g.*, oxides, carbon, and alkalies) presently found in composite, hot-pressed sputtering sources (targets). These contaminants not only can alter device characteristics irreversibly, but also may result in the loss of film integrity during subsequent high temperature (1000°C) device processing steps.

Another potential problem with refractory silicide thin films may be the high levels of intrinsic film stress often found in these films. Additionally, many commercial sputter deposition systems do not provide a means of controlling this film stress through controlled d-c or rf substrate bias (5, 6). Films deposited with high levels of intrinsic stress can also fail in subsequent high temperature processing, where thermal expansion coefficient mismatch between film and substrate is exaggerated.

In this preliminary study, we describe a co-deposition technique in which rf sputtering is done from separate high purity targets of the refractory metal and silicon with and without substrate bias. Additionally, we compare the physical and electrical properties of molybdenum silicide films prepared by this technique with films deposited from a composite target by the d-c magnetron technique.

Experimental

D-C magnetron deposition of molybdenum silicide.—All d-c magnetron depositions were done in a Perkin-Elmer Model 4400 cryo-pumped sputtering system equipped with a hot-pressed source (target) of molybdenum disilicide of 99.9 purity (Metron). The target was solder-bonded to a standard water-cooled copper backing plate and magnet assembly. Depositions were done at *ca.* 7 W/cm^2 (averaged over entire target area of *ca.* 300 cm^2) and 5 mTorr (0.67 Pa) of argon pressure at system base pressure of *ca.* 5×10^{-7} Torr (7×10^{-5} Pa) and 10 rpm substrate table rotation. Deposition rates were typically *ca.* 35 nm/min. Films of *ca.* 250 nm nominal thickness, determined via profilometry of an etched step (HNO_3:HF-200:1), were deposited onto silicon wafers previously coated with *ca.* 100 nm of thermal silicon oxide, 100 nm of rf sputtered silicon nitride, and *ca.* 500 nm of LPCVD-deposited (640°C) polycrystalline silicon (polysilicon). Additional depositions with and without rf substrate bias were done onto 5 × 25 mm, 63 μm thick sapphire beams for evaluation of film stress and film integrity during subsequent heat-treatment.

Deposition of molybdenum silicide via the rf diode co-deposition technique.—These depositions were done in the same sputter system described above from separate targets of 99.99 purity molybdenum and silicon using the rf power-splitting feature of the system at 10 mTorr (1.33 Pa) argon pressure. For deposition of the silicon-rich ($MoSi_{2.8}$) films, typical target voltages and wattages were: Mo 850V, 300W; Si 2400V, 1500W. Substrate pallet rotation was 10 rpm in all cases. Under these conditions, *ca.* 0.1 nm of molybdenum and *ca.* 0.2 nm of silicon were deposited per one pallet revolution. The resultant deposition rate was *ca.* 2.7 nm/min. Deposition temperature was found to be *ca.* 120°C under these conditions (PTC Model 575 CM surface thermometer).

To study the influence of rf substrate bias on the film properties, additional depositions were done with varying degrees of bias. The effects of this parameter are elaborated upon later in the text (Results section).

Additional rf diode depositions were done from a composite target of 99.9 purity at 10 mTorr argon pressure and 5 W/cm^2 power density. The resultant deposition rate was *ca.* 4.7 nm/min.

Other experimental techniques.—Conventional four-point probe measurements were used for resistivity determinations.

All heat-treatments were carried out with a Lindberg "table top" (Model SB 54542) furnace and quartz diffusion tube using high-purity sources of nitrogen or argon at *ca.* 10 liters/min flow.

CV plotting was done with an MDC controller/plotter and Signatone probe with hot stage.

* Electrochemical Society Active Member.
Key words: films, gates, sputtering, analysis.

Auger and SIMS analyses were done with a Perkin Elmer Model 590 scanning Auger Microprobe.

The elemental sensitivity values reported by Davis *et al.* (7) were used to quantify the Auger electron spectra.

Helium ion backscatter analysis was done with the Cal Tech 3 MeV Van de Graaff accelerator using $4He^+$ ions in the technique reported by Chu *et al.* (8).

Scanning electron microscopy (SEM) was done with a Hitachi S-450-1 system.

Determination of film stress was done on thin sapphire beams using the method reported (9) earlier.

X-ray diffractometry was done with a GE XRD diffractometer using CuKα radiation at 35 kV.

Results

Determination of molybdenum-silicon stoichiometry. —Molybdenum/silicon ratios for both d-c magnetron and co-deposited rf diode films were determined initially in films deposited directly on silicon wafers. This was particularly essential for the co-deposited films, where no prior correlations existed between deposition parameters and stoichiometry. It was hoped that the d-c magnetron and rf diode films deposited from a single composite target of $Mo_{33}Si_{67}$ would serve as "standards" for the stoichiometric determinations. However, it can be seen (Fig. 1) that good stoichiometric correlation between the two deposition methods was not obtained, as shown by the Auger depth profiles of the resultant films. It is apparent that molybdenum/silicon atomic ratio appears to be *ca.* 32:68 for the d-c magnetron films, whereas the ratio appears to be *ca.* 39:61 for the rf diode films.

In an attempt to resolve the question of film stoichiometry and to obtain a "standard" film, a sample of an rf diode co-deposited film having an apparent Mo/Si ratio of 32:68 by Auger analysis was analyzed via helium ion backscattering spectrometry (HIBS). The resultant Mo/Si ratio was found to be 26:74. Since the HIBS analyses are assumed to have an accuracy of approximately $\pm 5\%$, it is apparent that the Auger results are providing ratios that are Mo rich. It is possible that either differential sputtering effects or matrix effects on the shape of the Auger lines are contributing to this error (10). If the error is assumed to be constant (which may not be the case) a correction factor can be obtained by comparing the Auger and HIBS data. In this case the HIBS Mo/Si ratio was 0.35; the Auger Mo/Si ratio was 0.47. Therefore, a correction factor of 0.74 should be used as an attempt to correct the Auger data.

Figure 2 presents Auger depth profiles which depict the stoichiometry of two rf diode films, co-deposited with differing target voltages on the molybdenum and silicon. From Fig. 2(B), it is apparent that silicon enrichment may be present near the film surface. Appli-

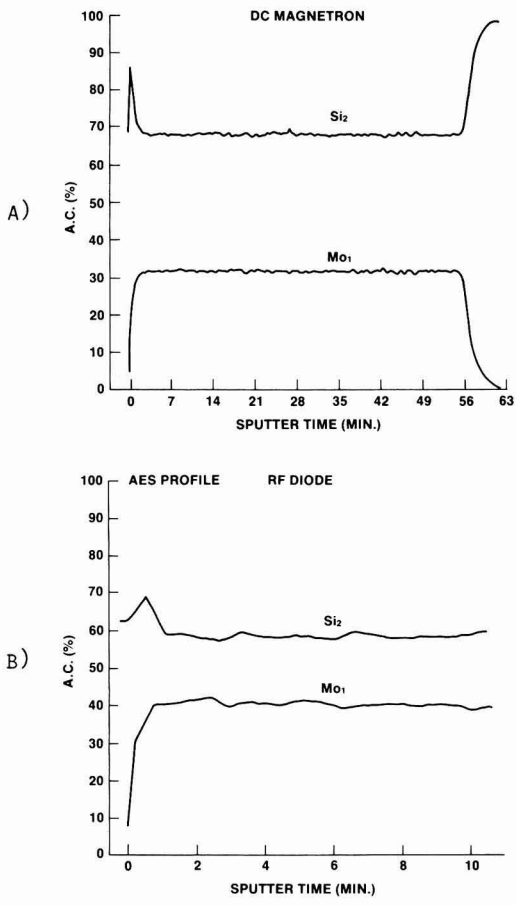

Fig. 1. Auger depth profiles of (A) d-c magnetron and (B) rf diode films sputtered from single composite targets of composition $Mo_{33}Si_{67}$.

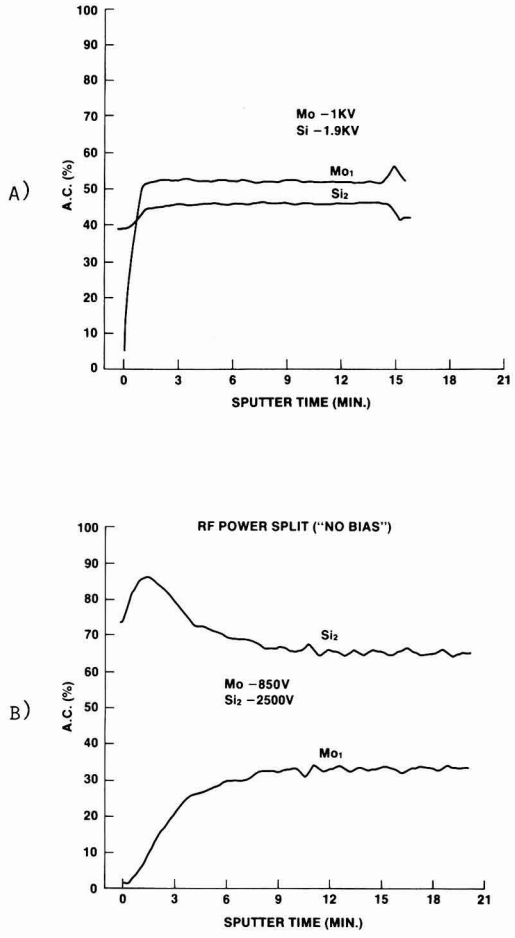

Fig. 2. Auger depth profiles of rf diode co-deposited molybdenum silicide films sputtered at different target voltages.

cation of the above correction factor to these spectra results in stoichiometric ratios of (a) $Mo_{46}Si_{54}$ and (b) $Mo_{26}Si_{74}$. For simplification, these films will be designated (a) "MoSi" and (b) "$MoSi_{2.8}$."

Comparison of morphology and integrity of as-deposited and heat-treated d-c magnetron and rf diode films.—The as-deposited films from all three types of depositions were metallic in appearance and exhibited no visible crystallinity or surface features at magnification up to 30 kX (SEM) on silicon oxide or nitride-coated silicon and sapphire. On polysilicon, all the as-deposited films tended to replicate the crystal morphology of the polysilicon. This observation is evident in Fig. 3(A), which shows the morphology of undoped polysilicon before (insert) and after deposition of the d-c magnetron molybdenum silicide without substrate bias. When this structure was subjected to 1000°C heat-treatment for 30 min in nitrogen or argon, severe cracking was observed in many instances, as shown in Fig. 3(B). Additionally, white fumes, presumably molybdenum oxide, were seen to evolve from the film during heat-treatment. The severity of this degradation precludes further processing. From Fig. 3, one may surmise that these cracks appear to be associated with a grain boundary or film stress phenomenon. The film stress-induced mode of degradation is supported by the observation that the films tended to peel away from the substrate with concavity (Fig. 4A), indicative of tensile stress in the film. (See section on Film stress below for further comment.) This degradation is more severe in films deposited under high values of substrate bias (−120V).

For rf diode co-deposited films having Mo/Si ratios <0.5 on polysilicon, silicon oxide, or nitride, no observable film degradation was observed during and after heat-treatment, as shown by Fig. 4(B) and Fig. 5. From Fig. 4(B), it should be noted that the largest visible crystallites were <100 nm in width. Auger depth profile analysis of the films deposited under rf bias indicated that Mo-Si stoichiometry remained unchanged as a result of the heat-treatment [Fig. 6(A)] when the Mo/Si ratio was <0.5. However, one change which became apparent during heat-treatment was the appearance of a thin (*ca.* 5 nm) layer of silicon nitride on the surface of the silicide film. Figure 6(B) shows the Auger spectrum of the heat-treated film. No molybdenum was detected on the surface. The nitrogen peak, however, is readily apparent in the spectrum. For co-deposited films of molybdenum-rich stoichiometry (Mo/Si>0.5), extensive surface degradation was observed during heat-treatment. It should be noted that no detectable changes in thickness were observed for MoSi or $MoSi_{2.8}$ films on silicon nitride or oxide as a result of heat-treatment.

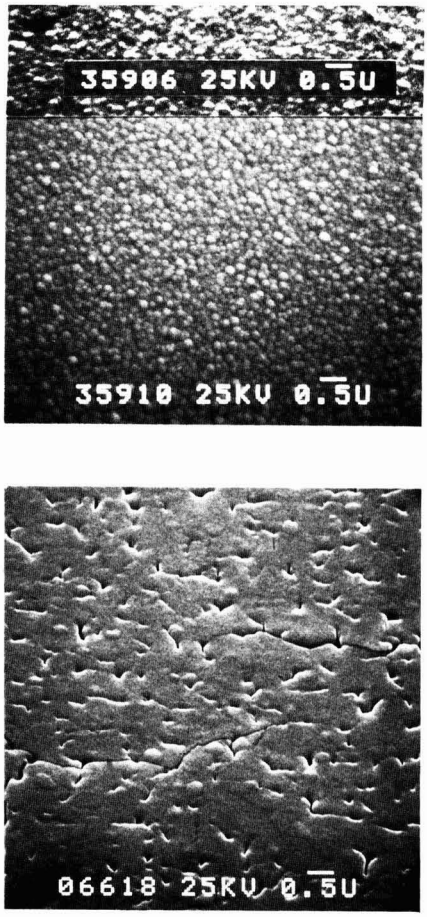

Fig. 3. SEM micrographies of d-c magnetron sputtered molybdenum silicide films on polysilicon, (A) as-deposited and (B) heat-treated in nitrogen at 1000°C for 30 min. Insert in (A) shows the uncoated polysilicon surface.

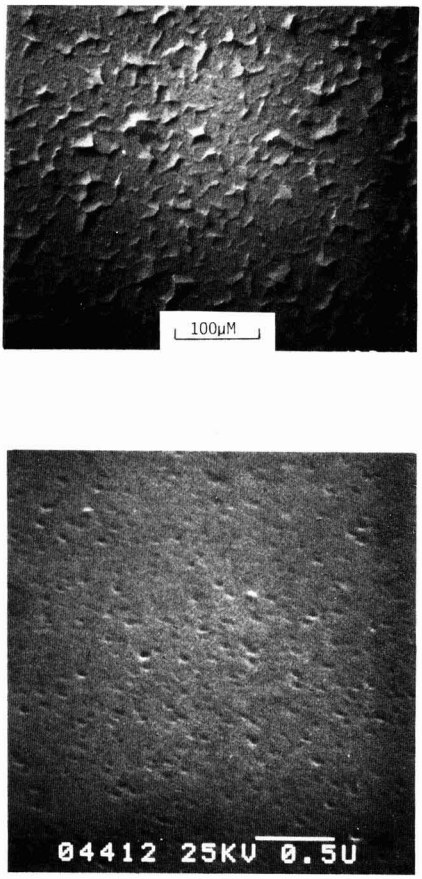

Fig. 4. Micrographs of (A) heat-treated d-c magnetron molybdenum silicide on polysilicon showing peeling morphology, and (B) heat-treated $MoSi_{2.8}$ on oxide.

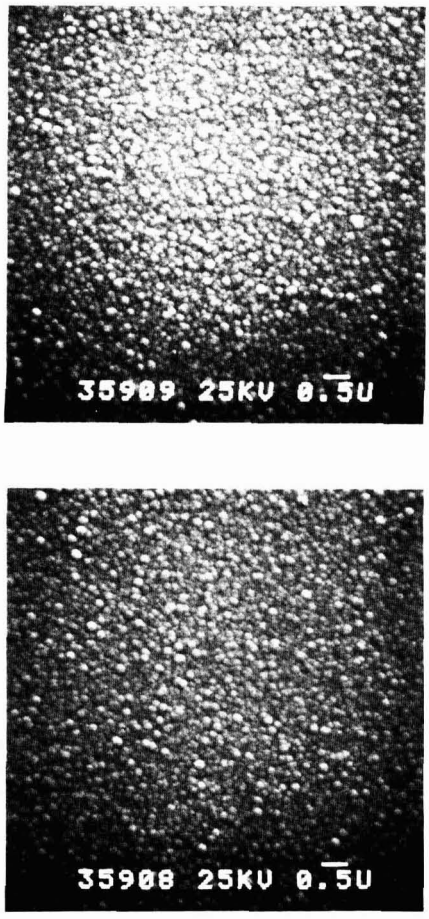

Fig. 5. SEM micrographs showing (A) as-deposited and (B) heat-treated $MoSi_{2.8}$ on polysilicon.

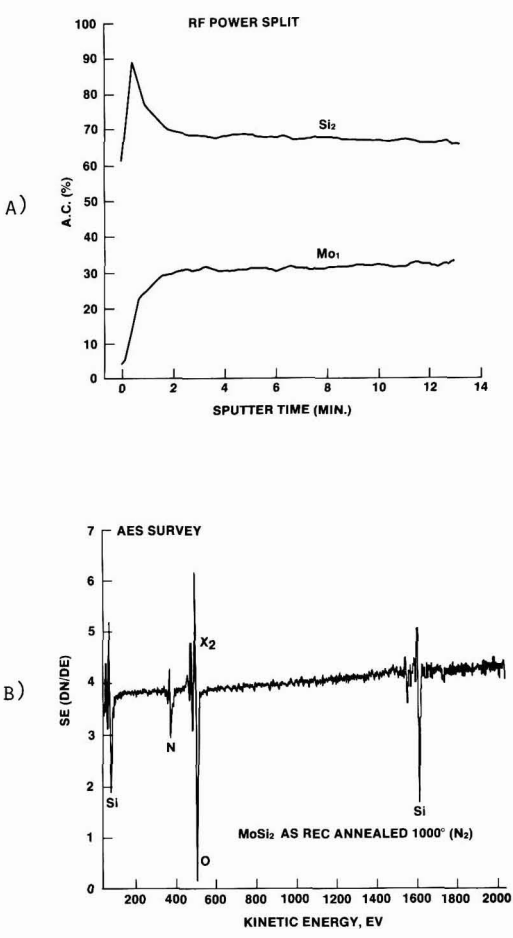

Fig. 6. Auger plots showing (A) depth profile of heat-treated rf diode co-deposited molybdenum silicide having as-deposited composition of $Mo_{32}Si_{68}$ (Auger), and (B) AES survey of film surface.

Comparison of the electrical properties of the d-c magnetron and co-deposited rf diode films.—The as-deposited d-c magnetron films had sheet resistance of *ca.* 20 Ω/sq on silicon oxide or nitride. After heat-treatment at 1000°C in nitrogen or argon, the sheet resistance lowered to 4-5 Ω/sq in cases when the film integrity was retained.

For the rf diode co-deposited films, the as-deposited sheet resistance values were dependent on molybdenum-silicon stoichiometry, as expected. Figure 7(A) shows the sheet resistance values plotted as a function of thickness for the composition $MoSi_{2.7}$. Figure 7(B) shows the resistivity plots as a function of Mo:Si ratio for as-deposited and heat-treated molybdenum silicide films of varying composition deposited under "no bias" (floating) conditions. With biased substrate depositions, (−25 to 50V), the heat-treated film resistivity appears to lower *ca.* 50% from the values shown. Thus, resistivity values of *ca.* 8×10^{-5} Ωcm can be obtained.

Capacitance-voltage plots of the d-c magnetron and rf diode co-deposited films were done before and after heat-treatment after using a metal mask to define 750 μm diam electrodes of the silicide on *ca.* 100 nm of thermal oxide on n-type silicon wafers. Figure 8 shows the resultant plots for the as-deposited d-c magnetron film and the rf diode film after heat-treatment. The plot for the as-deposited rf diode film is not shown due to its severe distortion, presumably due to oxide "damage" during deposition. From Fig. 8, it is apparent that alkali and hydrogen-induced flatband shifts (Qm) (11) are excessively high (*ca.* 3×10^{12} charges/cm²) for the d-c magnetron films, whereas the heat-treated rf diode films have Qm values of *ca.* 8×10^{10}/cm². The high Qm values of the d-c magnetron films were considerably reduced to levels comparable to the rf diode films after heat-treatment at 1000°C in cases where film degradation did not occur. This reduction in Qm with heat-treatment was reported by Learn (12).

X-ray diffractometry.—X-ray diffractometry was done on the as-deposited and heat-treated d-c magnetron and rf diode co-deposited films on silicon nitride coated wafers. The resultant spectra are shown in Fig. 9. Examination of these spectra show that both the as-deposited d-c magnetron and rf diode films [Fig. 9(a), their spectra were superimposable] exhibited minimal crystallinity. The silicon (211) cubic reflection in these spectra may be attributable to unreacted silicon in the as-deposited films; the intensity of this reflection is considerably diminished, or absent, after heat-treatment. Additionally, the heat-treated d-c magnetron film (b) shows strong tetragonal $MoSi_2$ reflections only. The rf diode co-deposited film designated "MoSi" (c) shows tetragonal and hexagonal $MoSi_2$ and cubic Mo_3Si reflections, whereas the film designated "$MoSi_{2.8}$" (d)

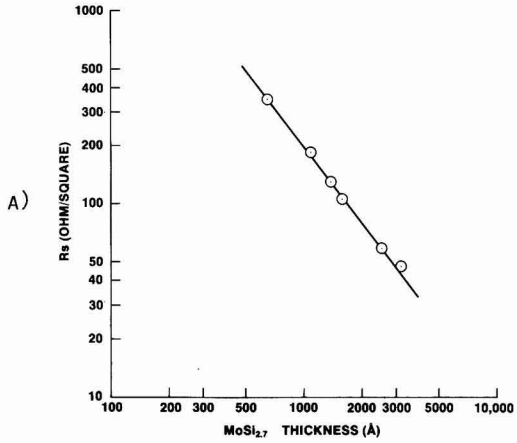

Fig. 7. Plots showing (A) sheet resistance vs. thickness for $MoSi_{2.7}$, and (B) as-deposited and heat-treated film resistivities for molybdenum silicide films of various stoichiometry.

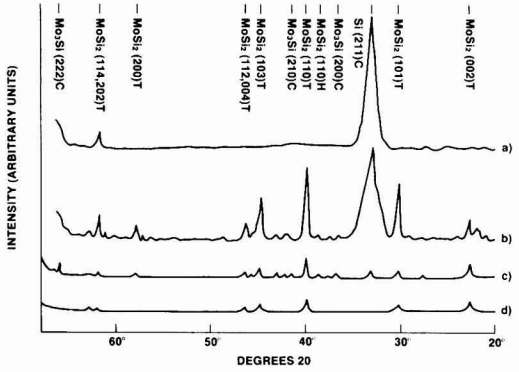

Fig. 9. X-ray spectra showing (a) as-deposited d-c magnetron and rf diode co-deposited $MoSi_{2.8}$ films, (b) d-c magnetron film after heat-treatment, (c) MoSi, and (d) $MoSi_{2.8}$ films after heat-treatment.

shows only weak tetragonal $MoSi_2$ reflections consistent with the SEM micrograph shown earlier (Fig. 4B), indicative of very small crystallite size.

Film stress.—In the as-deposited d-c magnetron films on sapphire, film stress was compressive and was calculated to be *ca.* 1×10^{10} dyne/cm^2. During 1000°C heat-treatment, however, the intrinsic film stress changed to high tensile stress values. This change could actually be observed during heat-up of the film; the substrate could be seen to curl rapidly from a convex to a concave condition, after which the film would tear away from the substrate producing fine particulates. In extreme cases, silicon wafers were seen to fracture during heat-treatment (13), especially when the deposition was done under high (−120V) substrate bias.

No such degrative changes in film stress were observed with the rf diode co-deposited films having Mo/Si ratios between 0.33 and 0.5. As-deposited, the film stress was minimally unmeasurable for films sputtered under "no bias" conditions or at −75V bias. Between −25 and −50V bias, film stress was *ca.* 5×10^{10} dyne/cm^2 (compressive). However, 1000°C heat-treatment of these films yielded a reduction of this stress to unmeasurable values. For films having Mo/Si ratios between 1.0 and 0.5, the film stress appeared to be in varying degrees of tension. Heat-treatment also appeared to reduce this stress to unmeasurable values. This stress behavior during heat-treatment differs from that reported (14) for co-sputtered titanium silicide.

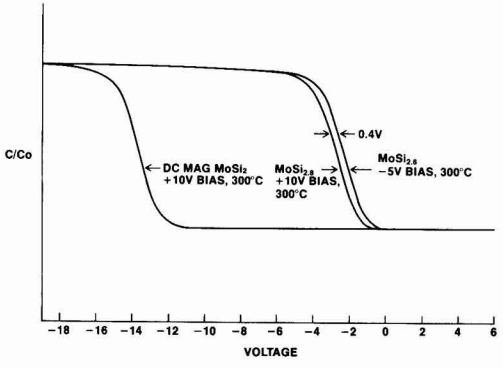

Fig. 8. Capacitance voltage plots of as-deposited d-c magnetron film and heat-treated rf diode co-deposited $MoSi_{2.8}$ film.

Analysis of trace elements.—Analysis for trace elements and hydrogen was done on the as-deposited d-c magnetron and rf diode co-deposited films using the SIMS capability of the Physical Electronics 590 system. Additionally, film samples were also electron beam heated *in situ* and the resultant evolved gases were measured by mass spectrometry. The resultant spectra showed hydrogen and fluorine to be present in all the films. Quantification of the spectra could not be carried out easily using this technique.

Step coverage.—A 250 nm thick co-deposited film of composition $MoSi_{2.8}$ was sputtered onto an oxide-stepped silicon wafer at −50V substrate bias. The film was heat-treated at 1000°C, then photolithographically masked and etched in a parallel plate prototype reactor using Freon-14 as the etch gas. Figure 10 shows the SEM micrograph (in cross section) of the etched film over a one micron oxide step which is slightly "undercut." From Fig. 10, it is apparent that acceptable step coverage was obtained in the as-deposited film.

Oxidation rate.—RF diode co-deposited films of composition $MoSi_{2.8}$ and $MoSi_2$ were oxidized in dry oxygen at *ca.* 6 liters/min flow at 1000°C. The resultant oxidation rate (at *ca.* 50 nm oxide thickness) for the $MoSi_{2.8}$ was only *ca.* 3 Å/min, whereas the rate for the $MoSi_2$ was *ca.* 400 Å/min (resultant oxide thickness *ca.* 300 nm). Additional studies are underway in an attempt to gain more information on the oxidation of these films (15).

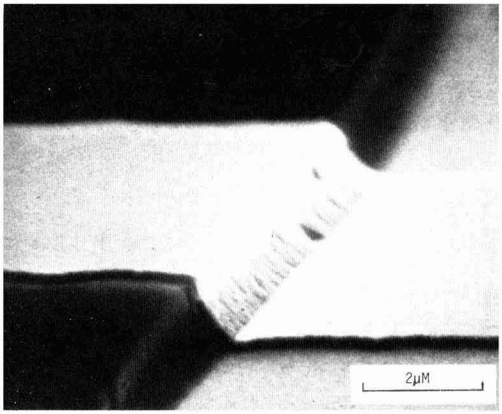

Fig. 10. SEM micrograph showing coverage of rf diode co-deposited film over oxide step.

Summary and Conclusions

This study has shown that molybdenum silicide films deposited by d-c magnetron sputtering from a composite target tend to be non-optimal during subsequent heat-treatment, *i.e.*, film degradation is often encountered for no easily apparent reason. The problem is more acute for films deposited under high values (−120V) of rf substrate bias.

RF diode films co-deposited from separate sources of molybdenum and silicon, however, do not exhibit this degradation when the Mo/Si ratio is $\leq$ 0.5, providing that the films have not been subjected to acidic cleaning procedures (DI water cleans only are recommended) and annealing ambient is ensured to be inert. The reason for the difference in behavior between the d-c magnetron and rf diode co-deposited films is unclear at the present time. A possible model for the degradation is that trace impurities, *e.g.*, hydrogen, in the d-c magnetron films may result in severe changes in film stress during subsequent heat-treatment. This severe change in film stress level is indeed observed during heat-treatment of the d-c magnetron films and is not observed with the rf diode co-deposited films. However, film analysis by Auger and SIMS shows little differences, if any, in trace element content between the two types of films. Thus, it may be possible that the instrumental sensitivity to trace elements is insufficient to allow for correlations with film properties. However, the Auger analyses done on the rf diode co-deposited films were shown to be essential for the establishment and monitoring of molybdenum-silicon stoichiometry in such a study.

In summary, it appears that the rf diode co-deposition technique is viable for the production of good quality molybdenum silicide films of low resistivity. Fully-operational gate arrays have been fabricated from these films, thus supporting the feasibility of the technique. Further details regarding these devices cannot be provided at this time due to proprietary considerations.

Manuscript submitted June 3, 1980; revised manuscript received Aug. 25, 1980. This was Paper 163 presented at the St. Louis, Missouri, Meeting of the Society, May 11-16, 1980.

Any discussion of this paper will appear in a Discussion Section to be published in the December 1981 JOURNAL. All discussions for the December 1981 Discussion Section should be submitted by Aug. 1, 1981.

Publication costs of this article were assisted by Perkin-Elmer.

REFERENCES

1. T. Mochizuki, K. Shibata, T. Inoue, K. Ohuchi, and M. Kashigawi, *Jpn. J. Appl. Phys.*, **17**, 37 (1978).
2. B. L. Crowder and S. Zirinsky, *IEEE J. Solid State Circuits*, **sc-14**, 291 (1979).
3. K. C. Saraswat, F. Mohammadi, and J. D. Meindl, Abstract 144, p. 388, The Electrochemical Society Extended Abstracts, Boston, Massachusetts, May 6-11, 1979.
4. S. Mantovani, G. Ottaviana, G. Magni, and F. Nava, Abstract 382, p. 967, The Electrochemical Society Extended Abstracts, Los Angeles, California, Oct. 14-19, 1979.
5. R. S. Nowicki, W. D. Buckley, W. D. MacKintosh, and I. V. Mitchell, *J. Vac. Sci. Technol.*, **11**, 675 (1974).
6. R. S. Nowicki, J. M. Harris, M.-A. Nicolet, and I. V. Mitchell, *Thin Solid Films*, **53**, 195 (1978).
7. L. E. Davis, N. C. MacDonald, P. W. Palmberg, G. E. Riach, and R. E. Weber, "Handbook of Auger Electron Spectroscopy," 2nd ed., Physical Electronics Industries, Inc., Eden Prairie, Minn. (1976).
8. W. K. Chu, J. W. Mayer, M.-A. Nicolet, T. M. Buck, G. Amsel, and F. Eisen, *Thin Solid Films*, **17**, 1 (1973).
9. R. S. Nowicki, *J. Vac. Sci. Technol.*, **14**, 127 (1977).
10. H. F. Winters and J. W. Coburn, *Appl. Phys. Lett.*, **28**, 176 (1976).
11. B. E. Deal, *This Journal*, **127**, 979 (1980).
12. A. J. Learn, *ibid.*, **122**, 1127 (1975).
13. F. Courreges, Private communication.
14. S. P. Murarka and D. B. Fraser, *J. Appl. Phys.*, **51**, 350 (1980).
15. K. C. Saraswat and R. S. Nowicki, Unpublished.

Fluorescent Screens for High-Resolution Real-Time X-Ray Topography

W. Hartmann

Max-Planck-Institut für Festkörperforschung, 7 Stuttgart 80, Germany

ABSTRACT

High-resolution real-time x-ray topography requires a fluorescent screen with high spatial resolution and good conversion efficiency of x-rays into visible light. We studied the spectral yield and the integral output with respect to screen thickness of common polycrystalline fluorescent materials. Gd_2O_2S:Tb has the best conversion efficiency and shows the highest spatial resolution with a grain size ≤ 1 μm. The optimal screen thickness for our applications was 5 μm. This choice results in a spatial resolution of about 10 μm.

Real-time x-ray topography is a recent tool to study nondestructively the dynamics of defects, like dislocations, and strain fields in crystals under externally applied forces, for example temperature, strain, or magnetic and electric fields. A typical application is reported by Hagen, Miltat, and the present author (1). There are in principle two methods for real-time x-ray topography, the single-stage or direct *vs.* the multiple-stage or indirect method (2). In the single-stage arrangement the x-ray pattern is directly converted into an electronic charge pattern which is read out by an electron beam of a television tube. The resolution of such method is limited to typically 30 μm (3). In the multiple-stage method the x-ray pattern is first converted into an optical picture by a fluorescent screen and then imaged onto the target of a TV camera by a lens system (4). The most important part in this arrangement is the fluorescent screen. It requires a high spatial resolution of a few micrometers and additionally a good conversion efficiency. Many studies have been made about resolution and yield of phosphors (5-12), but no information is available for this special x-ray topography purpose. This paper describes experiments about the spectral yield and the integrated intensity *vs.* screen thickness of various materials. We also investigated the spatial resolution.

Key words: fluorescent screen, real-time x-ray topography, spectral yield, spatial resolution.

Experimental

The experimental setup to study the spectral yield is shown in Fig. 1. A collimated x-ray beam enters an Si-crystal which is set in Bragg condition for the {220} reflection of MoK_α radiation. The diffracted beam is converted into an optical picture by a fluorescent screen. The resulting visible light is focused onto the entrance slit of a ¼ m-spectrometer which analyzes the emission spectra. The intensity is measured by a photomultiplier and amplified by an electrometer. The intensity *vs.* wavelength recording is made with an X-Y plotter. The fluorescent screens are prepared in the following way. A defined quantity of the material is weighed on a balance and then mixed with alcohol. The polycrystalline powder is deposited on a glass substrate by a centrifuge. The screen is characterized by density and thickness. The density is investigated

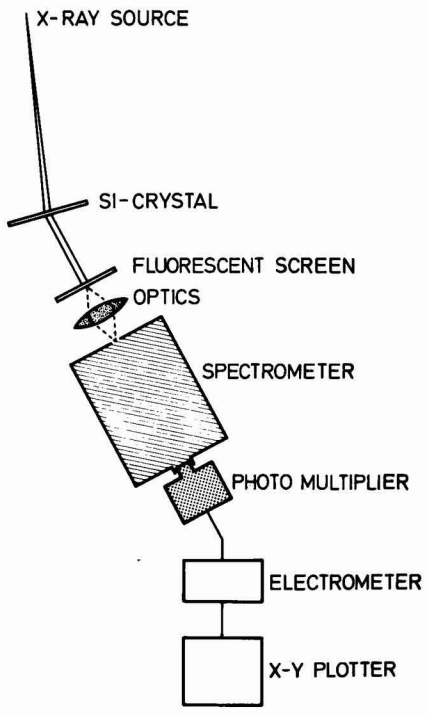

Fig. 1. Experimental setup to study the spectral yield of fluorescent screens for MoK_α radiation.

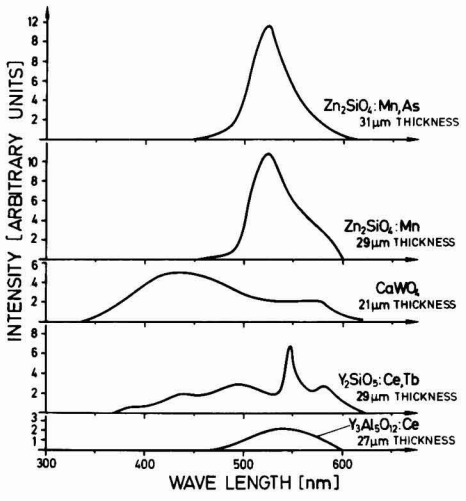

Fig. 2a. Emission spectra of Zn_2SiO_4:Mn, As, (31 μm thick) Zn_2SiO_4:Mn (29 μm thick), $CaWO_4$ (21 μm thick) Y_2SiO_5:Ce,Tb (29 μm thick), $Y_3Al_5O_{12}$:Ce (27 μm thick).

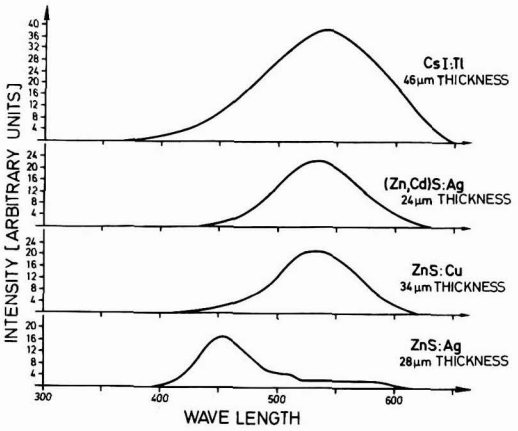

Fig. 2b. Emission spectra of CsI:Tl (46 μm thick), (Zn,Cd)S:Ag (24 μm thick), ZnS:Cu (34 μm thick), ZnS:Ag (28 μm thick).

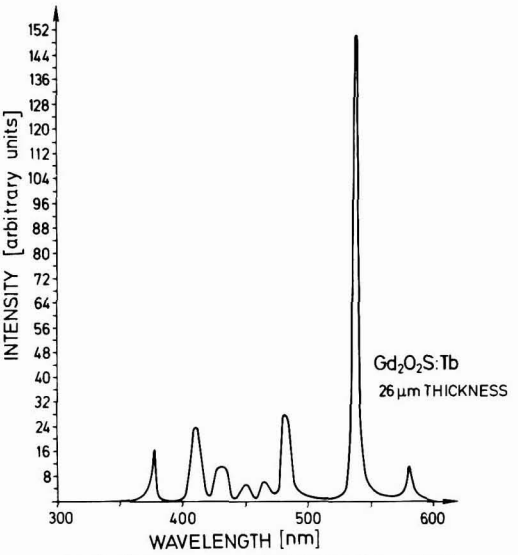

Fig. 2c. Emission spectra of Gd_2O_2S:Tb (26 μm thick)

by the weight of the screen minus the weight of the substrate divided by the screen area. The screen thickness is measured by an optical microscope.

Results and Discussion

Figures 2a-c show the spectral efficiency of the studied materials (Zn_2SiO_4:Mn,As; Zn_2SiO_4:Mn; $CaWO_4$; Y_2SiO_5:Ce,Tb; $Y_3Al_5O_{12}$:Ce; CsI:Tl, (Zn,Cd)S:Ag; ZnS:Cu; ZnS:Ag; and Gd_2O_2S:Tb) for one screen thickness.[1] Most of these materials emit light with a spectral intensity distribution over a broad wavelength region. Only Gd_2O_2S:Tb has eight sharp intensity peaks. This localized spectral recombination indicates that the ground and excited states of Tb, which are responsible for the emission spectra, have a small kinetic energy. That means the recombination centers are spatially localized in the material. This fact guarantees that the material is well suited for high spatial resolution.

[1] Some emission spectra differ slightly from the literature. The differences may be caused by contamination either from the producer of the fluorescent material and/or during screen preparation in our laboratory. However, these differences do not affect very much the results.

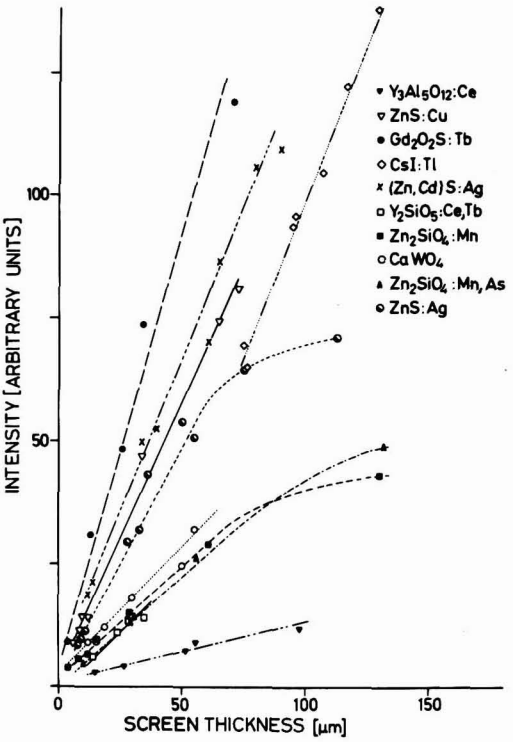

Fig. 3a. Integrated intensity *vs.* screen thickness of the studied materials. The intensity is calculated by digitizing the emission *spectra and integrating the area below the curves.*

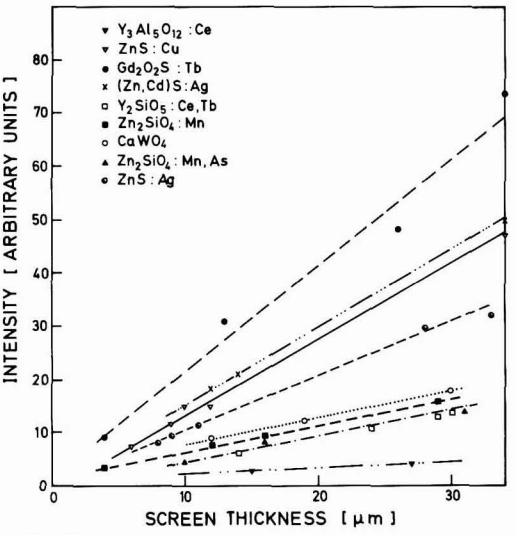

Fig. 3b. Blow-up of Fig. 3a in the thickness region up to about 30 μm. It shows more details at thinner screens which are important *for real-time x-ray topography.*

We have digitized the curves and integrated the area under each curve. Figure 3a shows the integrated intensity *vs.* the screen thickness. Gd_2O_2S:Tb has the best available efficiency. Figure 3b is a blow-up of Fig. 3a which shows more details of intensity differences in the thickness up to about 30 μm. One problem

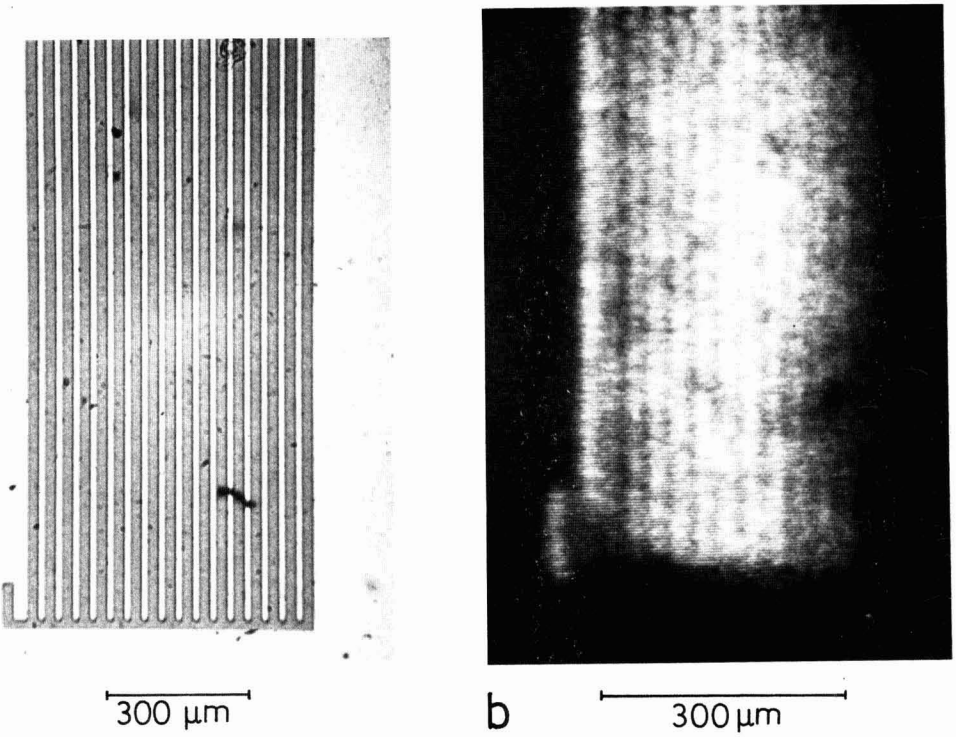

Fig. 4. (a) Optical micrograph of an excise stripe pattern on an Si-substrate with a periodicity of about 15 µm. (b) Corresponding video topograph directly photographed off the TV monitor.

of polycrystalline fluorescent screens still remains The density of Gd_2O_2S:Tb is 7.4 g/cm³, but the density of a screen with 5 µm thickness is only about 2-3 g/cm³. Thus, the achieved density is still well below the theoretical density and, therefore, we suffer a loss in the absorption of x-rays and in efficiency.

We need to achieve the highest possible spatial resolution in combination with sufficient yield. That means the grain size of the material used should be ≤1 µm, with as little decrease as possible of internal conversion due to such a small grain size. The other parameter which limits the resolution is the screen thickness. The highest possible resolution is roughly twice the screen thickness. We achieved an optimal screen thickness of 5 µm and, therefore, a spatial resolution of ~10 µm. Figure 4a shows an optical micrograph of an oxide stripe pattern on an Si substrate and Fig. 4b is the corresponding video topograph directly photographed off the TV monitor. The contrast of the test pattern has a stripe periodicity of about 15 µm and shows the limitation of our present screens. The most difficult problem in fabricating the screens lies in achieving uniformity in thickness over the entire screen area. The screen preparation is rather difficult to handle. However, because of these difficulties it would be very helpful to have a single crystalline phosphor with a high spatial resolution. A single crystal with special features would combine the high material density and a good thickness uniformity. It would be possible to achieve thinner (~2-3 µm) screens and, therefore, a better spatial resolution at the same conversion efficiency. Such experiments are currently under progress in our laboratory.

Acknowledgment

We gratefully acknowledge the support by the Bundesministerium für Forschung und Technologie. We thank K. Düker for assistance in screen preparation and especially R. Kniep and W. Schmettow, who are members of the chemistry department in our institute, for discussions and collaboration in material preparation.

Manuscript submitted June 25, 1980; revised manuscript received Sept. 22, 1980.

Any discussion of this paper will appear in a Discussion Section to be published in the December 1981 JOURNAL. All discussions for the December 1981 Discussion Section should be submitted by Aug. 1, 1981.

Publication costs of this article were assisted by the Max-Planck-Institut für Festkorperforschung.

REFERENCES

1. W. Hartmann, W. Hagen, and J. Miltat, *Appl. Phys. Lett.*, **36,** 483 (1980).
2. W. Hartmann, in "Topics in Applied Physics," Vol. 22, H. J. Queisser, Editor, pp. 191-219, Springer-Verlag, Berlin, Heidelberg, New York (1977).
3. J. Chikawa, *J. Cryst. Growth*, **24/25,** 61 (1974).
4. W. Hartmann, in the Proceedings of the NATO Advances Study Institute, "Characterization of Crystal Growth Defects by X-Ray Methods," Durham, 1979 (To be published).
5. H. W. Leverenz and F. Seitz, *J. Appl. Phys.*, **10,** 479 (1939).
6. T. Yoshioka and O. J. Sovers, in "Proc. Rare Earth Res. Conf. 7th," pp. 575-583 (1968).
7. A. P. Wilska, in "Proc. Sept. Congrès Int. Mikroscopic Electr.," pp. 347-348, Grenoble (1970).
8. R. A. Buchanan, *IEEE Trans. Nucl. Sci.*, **19,** 81 (1972).
9. R. K. Swank, *J. Appl. Phys.*, **44,** 4199 (1973).
10. A. F. Shlensky, R. A. Buchanan, T. G. Maple, and H. N. Bailey, *This Journal*, **122,** 1089 (1975).
11. J. A. De Poorter and A. Bril, *ibid.*, **122,** 1086 (1975).
12. A. L. N. Stevels and A. D. M. Schrama-de Pauw, *ibid.*, **123,** 886 (1976).

Degradation of Bonding Strength (Al Wire-Au Film) by Kirkendall Voids

Katsuya Okumura

Toshiba Corporation, Toshiba Semiconductor Division, Kawasaki, Japan

ABSTRACT

Degradation in bonding strength of the Al wire-plated Au film system has been studied. When this bonding system is stored at elevated temperatures, the bonding strength degrades following one of the three degradation modes: (*i*) A-mode in which the bonding strength decreases with increasing thermal annealing period until reaching a certain value, (*ii*) B-mode in which the strength starts separating into two values after a certain period of annealing, and (*iii*) C-mode in which the strength rapidly drops down to zero. The physical mechanisms for the three degradation modes have been well explained by Kirkendall void formation at the gold-rich intermetallic phase of the aluminum-gold interface, where the growth rate of the gold-rich intermetallic phase plays a very important role on deciding the degradation modes. When gold film includes a large amount of Pb or Tl, this rate decreases and C-mode or B-mode will take place. Doping of Ag into the gold film sometime results in less degradation in the bonding strength.

The reliability of gold-aluminum bonding strength has a strong influence on the reliability of IC and LSI. Although there have been many reports about bonding of gold wire to evaporated aluminum film on silicon chip, only a few reports about bonding of aluminum wire to gold film have been published (1-4). It has already been discussed that the bonding of aluminum wire to gold film has a higher reliability than of gold wire to aluminum film as long as the ratio of the width of the aluminum wire bonding area to the thickness of the gold film is greater than four (1).

However, the physical mechanism as to why the value four appears to be a threshold value for the degradation in bonding strength has not been made clear.

The purpose of the present study is to obtain a better understanding of the nature of the gold film-aluminum wire metallurgical system and to reveal the degradation mechanism of the bonding strength.

Experimental Results

Sample preparation.—Substrates for bonding were prepared by plating nickel and gold sequentially on rectangular Kovar plates of 50 × 7 × 0.25 mm. Typical layer thickness are 2 μm for nickel and 2-5 μm for gold. The plating solutions for nickel are a Watt bath and for gold a commercial cyanide solution.

Aluminum bonding wire of 2 mil in diameter, ultrasonic bonding grade including 1% silicon, is used, and 300 wires are bonded on each substrate. Here, bonding operations were made on the same ultrasonic wire bonder by the same technician in order to avoid poor reproducibility due to fluctuations coming from a different person and machine. Bonding strength was measured destructively on an automatic vertical pull tester, before and after annealing. Approximately 25 pull testings were carried out under each condition.

Thermal annealing was carried out in an air circulating oven controlled at 200° ± 5°C. After a certain period of annealing, 25 bonded wires were destructively pulled and the break strength was recorded for each test.

Pull strength as a function of annealing time.—The degradation modes of the pull strength at 200°C are phenomenologically classified into three kind of modes, as follows.

A-mode: The pull strength gradually decreases with annealing time and finally reaches a certain time-independent value as shown in Fig. 1. This value remained after 5000 hr at 200°C.

B-mode: The pull strength first decreases, and when annealing time exceeds a certain threshold, the degradation mode is divided distinctly into either A- or C-modes as shown in Fig. 2.

C-mode: The pull strength sharply drops down and becomes zero within a few hours as shown in Fig. 3.

Impurities in the plated gold film.—Impurities in the plated gold film are investigated by using ion mi-

Key words: electrode, failure and reliability, impurity.

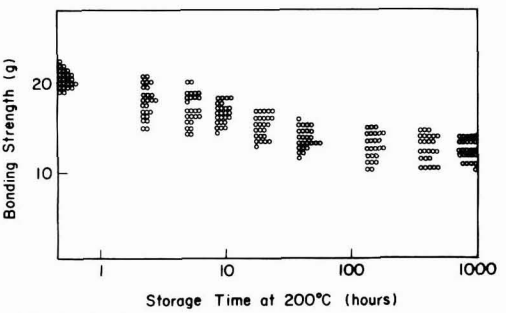

Fig. 1. The degradation appears to be A-mode. The bonding strength decreases with increasing heat-treatment until reaching a certain value.

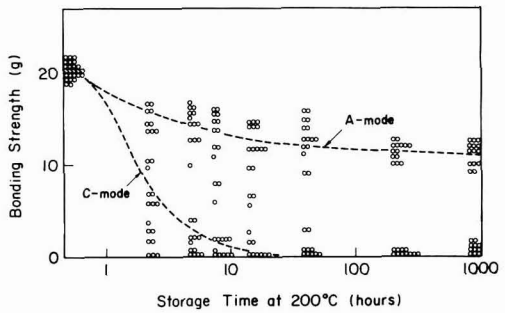

Fig. 2. The degradation appears to be B-mode. The bonding strength starts separating into two values after a certain period of the heat-treatment.

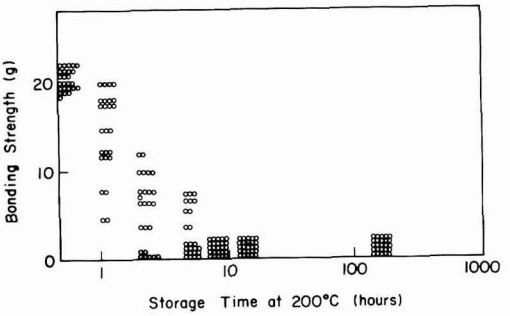

Fig. 3. The degradation appears to be C-mode. The bonding strength rapidly drops down and becomes zero within a few hours.

cromass analysis, IMA. The measuring conditions are as follows: Ar ions are used and accelerating voltage is 10 kV. Beam size is 760 μm in diameter, and the maximum measuring mass number is $M/e = 240$. The detected impurities are F, Na, K, Si, Al, Cl, Ca, Mg, Fe, Ni, Co, Ag, Tl, and Pb.

Results and Discussion

Correlations between impurities in Au film, thickness, and bonding strength.—Measured results of impurity concentration in gold, degradation mode, and gold film thickness are listed in Table I. Several characteristic features can be derived from Table I: (*i*) When a sample includes less Pb and Tl, the mode always becomes A-mode. (*ii*) When a sample has a large amount of Pb or Tl, the mode always becomes C-mode. (*iii*) When a sample has a few Ag even though it has a few Pb or Tl, the mode becomes A- or B-mode, but never C-mode. (*iv*) The thicker the gold film is, the more frequently B- and C-modes appear.

The effect of silver.—As pointed out above, even though there was a large amount of Pb or Tl in gold film, the influence of Pb or Tl was canceled by the presence of a small amount of silver. So, the following tests were carried out.

The substrate with a large amount of Tl and few Ag like in the sample No. 8 was prepared by depositing silver in a vacuum of $\sim 10^{-6}$ Torr. After being annealed, Al wire bondings were made on the preceding ultrasonic bonder. When about 400Å of Ag film is deposited, it is difficult to make bonds because of the hardness of the silver-evaporated gold surface. On the other hand, it is easy to make bonds when about 50Å of silver film is deposited and annealing is carried out at 250°C for 30 min. The degradation mode of this sample has completely changed from C-mode to A-mode. In addition to this sample, other samples were also deposited with silver (50Å) by the same procedure. The results of these tests are summarized in Table II.

Mechanism of pull strength degradation.—Let us consider a mechanism that explains what happens when aluminum and gold films are coexisting and are stored at elevated temperatures, and why the pull strength significantly degrades in some cases, but not in other cases.

Many studies, (1, 5-7) have been reported that in the aluminum-gold binary system the growth rate of the gold-rich intermetallic phase is approximately 10 times as large as the growth rate of the aluminum-rich intermetallic phase, and the formation of Kirkendall voids is observed at the interface of the gold-rich intermetallic phase and gold.

At this point, let us set up two working hypotheses as follows: (*i*) The Kirkendall voids formed at the interface have a constant radius, r_0, and the number of voids, n, is directly proportional to the square root of time. (*ii*) The Kirkendall voids are always at the interface. These voids pile up and condense to form an almost continuous line. This has a deleterious effect on the pull strength.

Kidson (8) has shown that if the mechanism of intermetallic phase formation is interdiffusion predominated by volume diffusion, growth rate of the intermetallic layer should follow a parabolic rate law as follows

$$d = k\sqrt{t} \qquad [1]$$

where d is the intermetallic thickness, t is the storage time, and k is the growth rate of the phase.

In fact, the intermetallic phase layer thickness has been observed (3, 7), showing the square root of time dependence even though the storage temperature was as low as 200°C.

As illustrated in Fig. 4, aluminum wire comes in contact with gold film with bonding width W. The length along the gold-rich intermetallic phase-gold interface is given by

$$l = \pi d + W \qquad [2]$$

By substituting Eq. [1] into Eq. [2]

$$l = \pi k\sqrt{t} + W \qquad [3]$$

Table I. Correlations between impurities in gold film, thicknesses, and degradation modes

	Sample number														
	1	2	3	4	5	6	7	8	9	10	11	12	13	14	15
Peak height in IMA (mm)															
Ag	2.1	180	20	75	6.2	150	6.1	8.4	6.2	4.1	4.2	1.1	1.2	17	5
Pb	0	0	1.9	1.2	1.4	1.0	1.2	0	1.1	0	0	2.2	30	26	0
Tl	8.4	84	2.3	3.8	3.0	4.2	1.5	8.1	1.1	30	10	0.1	0.1	0.1	40
Au thickness	4.0	3.6	4.8	2.5	3.2	2.0	4.0	2.0	3.8	2.2	2.2	2.5	2.7	1.5	3.8
Degradation mode	C	B	B	A	A	A	A	C	A	C	B	A	C	A	C

Table II. Changes in the degradation mode after silver doping

Sample number	Initial degradation mode	Mode after silver doping	Au thickness (μm)	Peak height in IMA (mm)			
				Tl	Pb	Ag	
						Initial	After doping
1	C	B	4.0	8.4	0	2.1	7
8	C	A	2.0	8.1	0	8.4	18
10	C	B	2.2	30	0	4.1	13
13	C	B	2.7	0.1	30	1.2	9
15	C	C	3.8	40	0	5.1	10
2	B	B	3.6	84	0	180	185
3	B	A	4.8	2.3	1.9	20	23
11	B	A	2.2	10	0	4.2	13

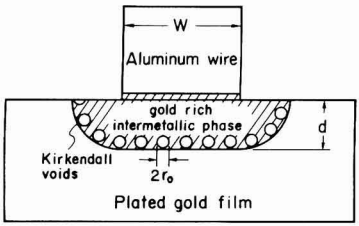

Fig. 4. Schematic representation of the degradation of bonding strength. Kirkendall voids are formed at the intermetallic phase-gold interface.

according to these working hypotheses, when the intermetallic phase grows up to the depth d, the number of Kirkendall voids, n, will be given by

$$n = \alpha\sqrt{t} \qquad [4]$$

where α is the rate constant.

Total length of the voids projected to the intermetallic phase-gold interface is given by

$$v = 2r_o n \qquad [5]$$

and thus

$$v = 2r_o\alpha\sqrt{t} \qquad [6]$$

where r_o is the radius of voids.

When Eq. [3] and [6] become equal, the Kirkendall voids form a continuous line and, consequently, the pull strength becomes catastrophically weak.

Equations [1], [3], and [6] are illustrated schematically in Fig. 5. When line 1 intersects line 2 at t_c, the voids form a continuous line at the intermetallic phase-gold interface and the pull strength degrades enormously. The depth of the intermetallic layer at t_c is defined as d_c.

The influence of gold film thickness.—Let us consider the influence of gold film thickness, D, the growth rate, k, and bonding width, W on the formation of Kirkendall voids. As shown in Fig. 6, the intermetallic phase-gold interface is divided into two parts; one is "P," the length of which grows as a function of πd and the other is "Q," the length of which stays constant at W.

When D is thicker than d_c, the voids will form a continuous line at both P and Q in the depth d_c and then the catastrophic weakness occurs, in other words, C-mode will appear.

Now, let us consider what can happen if D is thinner than d_c. When the intermetallic phase grows up and reaches the gold-nickel interface, the total projected length of the voids is represented as follows

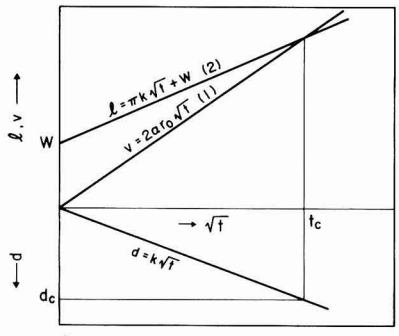

Fig. 5. Schematic representations for d, the intermetallic thickness; l, the length along the intermetallic phase-gold interface; and v, the total length of the voids projected to the interface as a function of t, the storage time.

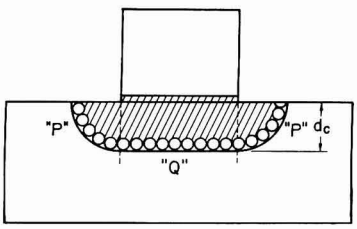

Fig. 6. Schematic representation. When gold film thickness is thicker than the critical depth, d_c, Kirkendall voids will form a continuous line along the intermetallic phase-gold interface.

$$v_o = 2r_o\alpha\sqrt{t_o} \qquad [7]$$

where t_o is the time when the intermetallic phase reaches the gold-nickel interface.

After t_o, there can be no increase in voids at Q, namely, the gold-nickel interface, on the other hand, the length of the interface along P, either $\overline{AB} + \overline{A'B'}$ or $\overline{CD} + \overline{C'D'}$ as shown in Fig. 7, is constant at πD but voids at P increase on and on until a continuous line is formed along $\overline{CD} + \overline{C'D'}$.

Let us find out the time t_1, when the continuous line is formed eventually by the voids at the interface along P. To obtain t_1, a graphical solution method is applied as shown in Fig. 8. The time when d grows up to D, namely, d_o, is t_o and at that time v and l are v_o and l_o, respectively. t_2 is imaginary time when v shall grow up to l_o, that is, v_2. The point X on $\overline{v_2t_2}$ divides v_2 into W ($= \overline{Xt_2}$) and $\pi k\sqrt{t_o} = \pi D$ ($= \overline{v_2X}$). The point Y is defined as the cross point of $\overline{v_ot_o}$ and $\overline{XO}$.

At time t_o, projected lengths of the voids on $\overline{AB} + \overline{A'B'}$ and $\overline{BB'}$, v_P, and v_Q, are given by dividing $\overline{v_ot_o}$ by the ratio $\pi D : W$. On the other hand, the point Y

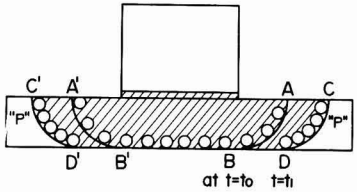

Fig. 7. Schematic representation. When gold film thickness is thinner than d_c, the intermetallic phase grows up and reaches the gold-nickel interface at the time t_o, and then there is still increase in voids at "P" until the voids form continuous line at the time t_1.

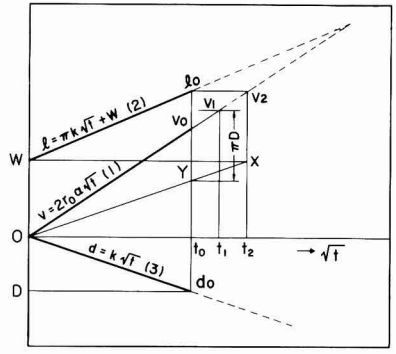

Fig. 8. Schematic representations of l, v, and d as a function of t when gold film thickness is thinner than d_c.

divides $\overline{v_o t_o}$ by the ratio $\pi D : W$, then v_p and v_Q are equal to $\overline{v_o Y}$ and $\overline{Y t_o}$, respectively.

After t_o, the length of the interface along P is constant at πD as shown in Fig. 7, but v_p still grows up from $\overline{v_o Y}$ to πD. t_1 is the time when v_p grows up to πD, that is, the voids along P form eventually a continuous line.

After t_1, both the voids and the gold-rich intermetallic phase stop growing up, because the continuous line of voids shuts off the gold supply to the intermetallic phase and the gold-rich intermetallic phase will change into an aluminum-rich intermetallic phase by being supplied with a sufficient amount of aluminum from the aluminum wire. If the bonding strength at Q is sufficiently strong, the pull strength does not degrade, which results in A-mode.

Whether the gold film is thinner or thicker than d_c, Kirkendall voids ultimately form a continuous line along the interface between the gold and the gold-rich intermetallic phase. This phase will change into an aluminum-rich intermetallic phase after a sufficiently long period of time.

The influence of bonding width.—As shown in Fig. 9, when the bonding width becomes narrower, the critical depth d_c becomes shallower. That means C-mode will appear more easily. When the gold film thickness is slightly thinner than d_c, W plays a dominant role on the degradation, namely, a narrower W will lead to C-mode and a wider W will lead to A-mode.

The influence of the intermetallic phase growth rate.—Figure 9 shows that the critical depth d_c decreases with decreasing k. The influence of k is more prominent than W, because k can affect both Eq. [1] and [2].

The value of k, W, and d_c.—The samples were polished in the cross sections, and then the thickness of the gold-rich intermetallic phase was measured by using an optical microscope and SEM. Figure 10 shows one of the SEM photographs of the A-mode samples. Here, a crack is observed around the periphery of the bond. Figure 11 shows one of the SEM cross-section photographs of the C-mode samples. As noticed, a crack is observed not only in P but also in Q.

Bonding width, W ranges from 26 to 60 μm and its mean value is 40 μm. The thicknesses of the phase of A-mode samples after annealing for 1 hr are in the range of 2.4-3.2 μm and its mean value is 2.8 μm. By this measurement, k for A-mode is found to be 2.8 $\mu m/\sqrt{hr}$.

On the other hand, Kashiwabara and Hattori have reported (1) that $W/d_c \geqq 4$ for the sample which is

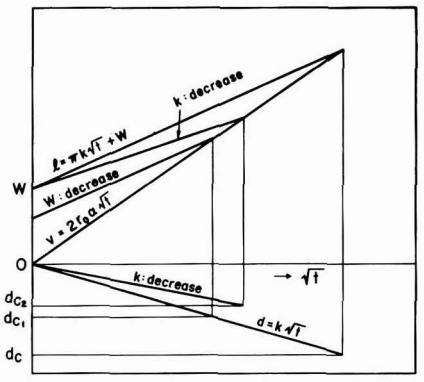

Fig. 9. Schematic representations of *l*, *v*, and *d* as a function of *t* taking bonding width *W* and intermetallic phase growth rate *k* as parameters.

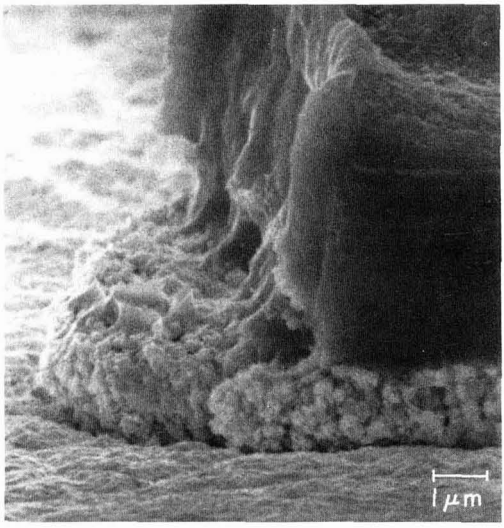

Fig. 10. An SEM photograph of Al-Au intermetallic compound formation (fluffy). A-mode sample stored at 200°C for 10 hr gives rise to the crack which is formed around the periphery of the bond.

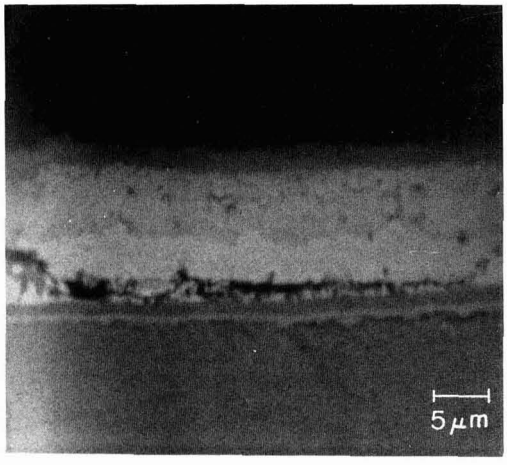

Fig. 11. An SEM cross-section photograph of Al-Au intermetallic phase. C-mode sample stored at 200°C for 10 hr demonstrates the continuous line of Kirkendall voids along the interface of intermetallic phase-gold, in "P" and "Q."

equivalent to A-mode. These are summarized as follows, $W = 40$ μm, $k = 2.8$ $\mu m/\sqrt{hr}$ and $W/d_c = 4$. Substituting these values into Eq. [1], [3], and [6]

$$10 = 2.8\sqrt{t_c} \quad [8]$$

$$l' = 2.8\pi\sqrt{t_c} + 40 \quad [9]$$

$$l' = 2r_o\alpha\sqrt{t_c} \quad [10]$$

at $t = t_c$, l' is equal to v', then

$$2.8\pi\sqrt{t_c} + 40 = 2r_o\alpha\sqrt{t_c} \quad [11]$$

From Eq. [8], $t_c = 12.7$ hr, then $2r_o\alpha = 20$ $\mu m/\sqrt{hr}$. The critical time t_c is in good agreement with the time when B-mode starts separating into A- and C-modes in Fig. 2.

Table III. Growth rate of the gold-rich intermetallic phase, k

Reference	k at 200°C ($\mu m/\sqrt{hr}$)	Purity of gold
Onishi (5)	1.1	Gold plate 99.99%
Kashiwabara (1)	2.6	Plated gold film
Philofsky (6)	3.9-4.4	99.999%
Campisano (7)	4.5-5.0	Evaporated gold film
This work	2.8	Plated gold film

Here, we compared the value of k with the previously published values which are summarized in Table III. As shown in Table III, Kashiwabara (1) obtained $k = 2.6\ \mu m/\sqrt{hr}$ for gold-plating film and Onishi (5) found $k = 1.1\ \mu m/\sqrt{hr}$ for gold plate where the purity of gold is 99.9%. Philofsky (6) and Campisano (7) found $k = 4\text{-}5\ \mu m/\sqrt{hr}$ for evaporated gold film, which had a purity of more than 99.99%. These indicate that the lower the purity of gold, the more the value of k decreases.

At $t = t_c$, l is equal to v and $d_c = k\sqrt{t_c}$, then

$$\frac{1}{d_c} = \frac{2r_0\alpha}{W}\left(\frac{1}{k} - \frac{\pi}{2r_0\alpha}\right) \qquad [12]$$

where

$$2r_0\alpha = 20$$

Figure 12 show the relationship between d_c and k for various values of W. When k decreases to be less than $1.4\ \mu m/\sqrt{hr}$ and the thickness of the gold film is more than 3.6 μm, C-mode will appear. Moreover, when k decreases to less than $0.8\ \mu m/\sqrt{hr}$, even though the thickness of gold film was 1.8 μm, C-mode should take place.

A large amount of Tl or Pb is found in the samples which provide B- or C-mode. Some of the samples have changed from C-mode to A- or B-mode by doping with a small amount of silver. This indicates that Tl or Pb may suppress the value of k drastically, but Ag has an ability to cancel this effect, although the mechanism for this is still uncertain.

Horsting (2) has experimentally shown that the presence of impurities in the gold caused the bondlift type of failure. However, he did not specify the kind of impurities responsible for the failure and the failure mechanism for the bondlift.

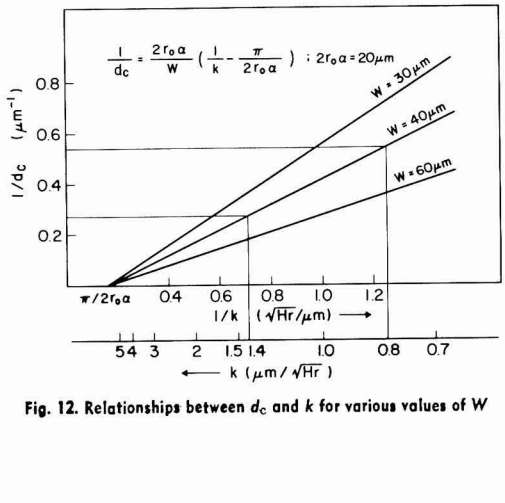

Fig. 12. Relationships between d_c and k for various values of W

On the contrary, in this study we have quantitatively made clear the mechanism of the degradation of bonding strength by introducing parameters such as k, n, W, and D. Our mechanism, described here, can also explain all of the facts which Horsting has found.

Conclusions

Degradation of bonding strength of the aluminum wire-gold film system has been investigated. The phenomena which take place at the aluminum-gold interface have been well explained by the Kirkendall void model.

1. When these bonding systems are heated at elevated temperatures, the degradation modes of the pull strength are classified into three modes: (*i*) A-mode in which the bonding strength decreases with increasing heat-treatment until reaching a certain value, (*ii*) B-mode in which the strength starts separating into two values after a certain period of heat-treatment, and (*iii*) C-mode in which the strength rapidly drops down to zero.
2. A large amount of Pb or Tl is found in the samples whose pull strength degrades rapidly and finally reaches zero.
3. Some of the samples including Pb or Tl are improved in the degradation mode by doping a small amount of silver into the gold film.
4. These phenomena can be well explained by the Kirkendall void model. According to this model, the growth rate of the gold-rich intermetallic phase plays a very important role on deciding the degradation modes. When this rate decreases, the pull strength frequently degrades very significantly.
5. The growth rate of the intermetallic phase, k, for A-mode, is found to be $2.8\ \mu m/\sqrt{hr}$ at 200°C.

Acknowledgments

Thanks are due to A. Ogawa and Y. Naruse for their technical assistance in this work. Y. Yamaguchi, who performed the IMA analysis is acknowledged. The author wishes also to thank K. Takahashi and Dr. Y. Nishi for their helpful discussions and for critical review of the manuscript.

Manuscript submitted March 10, 1980; revised manuscript received Sept. 1, 1980.

Any discussion of this paper will appear in a Discussion Section to be published in the December 1981 JOURNAL. All discussions for the December 1981 Discussion Section should be submitted by Aug. 1, 1981.

Publication costs of this article were assisted by the Toshiba Corporation.

REFERENCES

1. M. Kashiwabara and S. Hattori, *Rev. Elect. Commun. Lab.*, **17**, 1001 (1969).
2. C. W. Horsting, in 10th Annual Proceedings IEEE Reliability Physics Symposium, p. 155 (1972).
3. E. Philofsky, in 9th Annual Proceedings IEEE Reliability Physics Symposium, p. 11 (1971).
4. G. Riga, in 11th Annual Proceedings IEEE Reliability Physics Symposium, p. 26 (1973).
5. M. Onishi and K. Fukumoto, *J. Jpn. Inst. Metals*, **38**, 148 (1974).
6. E. Philofsky, *Solid State Electron.*, **13**, 1391 (1971).
7. S. U. Campisano, G. Foti, and E. Rimini, *Philos. Mag.*, 903 (1975).
8. G. U. Kidson, *J. Nucl. Mater.*, **3**, 21 (1961).

Densification of SIPOS

H. R. Maxwell, Jr.* and W. R. Knolle*

Bell Laboratories, Reading, Pennsylvania 19604

ABSTRACT

Semi-insulating polycrystalline silicon (SIPOS) can be used as part of a passivation scheme on semiconductor devices. During processing the film experiences temperatures several hundred degrees higher than the SIPOS deposition temperature of 640°C. We have investigated the effect of high temperature anneals on the physical properties of SIPOS films containing 25 atomic percent oxygen. Heat-treatments of 900°C or greater in inert ambients densify the film resulting in a film thickness decrease (densification) on the order of 10% and decrease the etch rate of the film by a factor of 6 in a $6H_2O_2$:1HF:10 NH_4F SIPOS etch solution. Also, the infrared transmission spectrum of the SIPOS film changes as a result of annealing. Similar infrared changes in SiO_2 films have been interpreted to be due to a relaxation of bond strain and a decrease in film porosity. Film stress has also been investigated before and after annealing and was found to change from tensile to compressive. This is consistent with the interpretation of the infrared data.

Semi-insulating polycrystalline silicon (SIPOS) films doped with oxygen (1) can be used as part of a passivation scheme on semiconductor devices. The film is deposited on the wafer by chemical vapor deposition (CVD) at a temperature of ~640°C. Typically, SIPOS is never used as the only passivation layer on a semiconductor device, but rather is followed by SiO_2 and Si_3N_4 layers deposited at 900°C or more. Therefore, it seemed natural to investigate more closely the behavior of SIPOS films after annealing in an inert ambient. In this paper we report the effects of high temperature anneals on the physical properties of SIPOS films containing 25 atomic percent (a/o) oxygen.

Experimental

SIPOS deposition.—An AMT low pressure (LPCVD) system was used to deposit the 25 a/o O SIPOS films by the reactive decomposition of silane (SiH_4) and nitrous oxide (N_2O) in N_2. For this work the deposition temperature was 637°C and the system pressure was 0.16 Torr. The reactant gas flow ratio, N_2O/SiH_4, was 0.22 with an N_2 carrier gas flow of 400 cm^3/min for a deposition rate of 35 Å/min. The SIPOS film thickness was nominally 5000Å.

Two-inch diameter n-type (111) Si wafers were used throughout except for the stress measurements that were made on 3 in. diam n-type (100) Si wafers. Silicon nitride covered Si substrates were used for determination of the oxygen content of the SIPOS films by a gravimetric technique previously reported (2). In order to obtain a representative oxygen content the nitrided and bare Si wafers were alternately placed on a quartz boat with 0.375 in. spacing between them, loaded into the LPCVD furnace, and SIPOS deposited.

Etch rate and film thickness determination.—The SIPOS etch solution consisted of a mixture, by volume, of 6 parts H_2O_2-30%, 1 part HF-48%, and 10 parts of a 40% NH_4F (6:1:10) solution (1). The etch solution was allowed to equilibrate to 30°C for 5 min prior to etching.

The as-deposited etch rate was determined by half-waxing a wafer, cutting it into strips, and etching the strips for various times in the 6:1:10 SIPOS etch. After etching, the wax was removed and the step height measured on a Taylor Hobson Talystep. The effects of annealing in N_2 on etch rate after various times and temperatures were determined in a similar manner.

* Electrochemical Society Active Member.

Key words: semiconductor passivation technology, infrared spectroscopy, thin films.

The thickness change (densification) after annealing was determined by half-waxing the SIPOS deposited Si wafers and etching them in the 6:1:10 solution until bubbling on the wafer surface stopped, indicating that the SIPOS-Si interface was reached (etch rate of Si in 6:1:10 is ~260 Å/min). The height of the step was then measured on the Talystep. These Talystep wafers were then remeasured for the determination of the SIPOS thickness after annealing and were used for the infrared measurements.

Infrared spectra measurements.—The infrared transmission spectrum of the SIPOS sample was taken before and after each anneal or densification process. A clean Si substrate was placed in the reference beam of the Perkin-Elmer Model 621 Grating Infrared Spectrophotometer. The Si in the reference beam nulls out the absorption signal from the Si substrate in the sample beam. The absorbance, A, of an infrared peak was measured by the baseline technique (3) and the area of the absorption was approximated by $A \cdot W$ where W is the full width at half of the maximum absorbance.

Stress measurements.—The stress of the SIPOS film was measured with an optically levered laser technique (4). The difference between the radius of curvature of the Si wafer measured before and after deposition can be related to the stress in the deposited SIPOS film (SIPOS must be etched off the back of the wafer before the measurement is made). The measurements were made on 3 in. diam, 0.020 in. thick (100) Si wafers. The precision of the measurement is about $\pm 1 \times 10^9$ dynes/cm^2.

Results

Etch rate.—The as-deposited SIPOS etch rate in the 6:1:10 SIPOS etch was determined and the data are plotted in Fig. 1 as the amount of SIPOS removed *vs.* etch time. The best fit for the data is shown and results in an average etch rate of ~1200 Å/min for the as-deposited 25 a/o O SIPOS film.

The effects of annealing temperature on etch rate are given in Fig. 2 where the SIPOS film etch rate in the 6:1:10 solution *vs.* annealing temperature is plotted. The anneals were done in N_2 for 1 hr. Initially, the etch rate decreases by a factor of 6 from the as-deposited value and then increases as the annealing temperature continues to increase. This increase in etch rate at the higher temperatures is attributed to the increase in the SiO_2 character of the film which will be discussed later. For reference, the etch rate of 1050°C steam-grown SiO_2 in 6:1:10 solution is shown.

The effect of annealing time on etch rate at the various temperatures is shown in Table I. The anneal

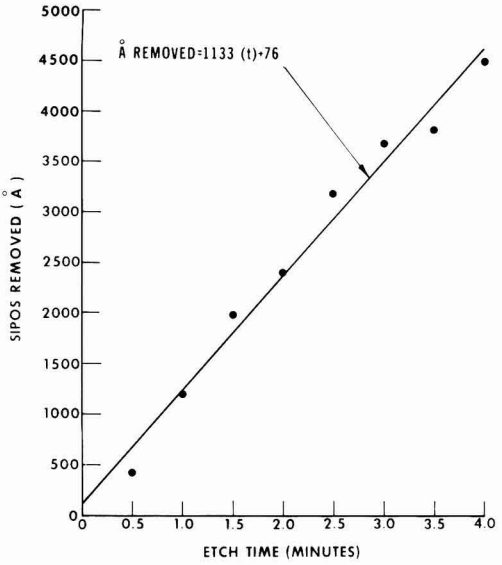

Fig. 1. Determination of the etch rate of 25 a/o O SIPOS in 6:1:10 SIPOS etch solution. The slope of the least squares line is the etch rate of the as-deposited SIPOS.

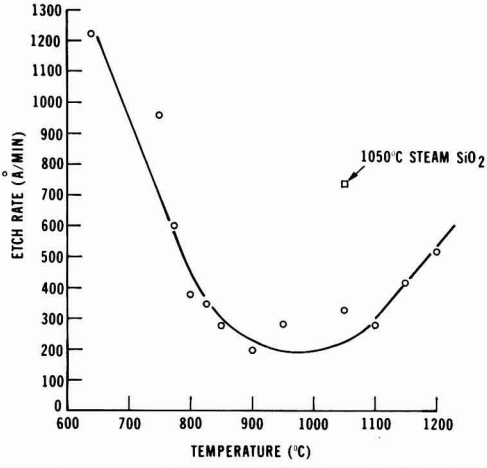

Fig. 2. Etch rate of 25 a/o O SIPOS in 6:1:10 SIPOS etch solution as a function of annealing temperature. Samples were annealed for 1 hr in N_2. The etch rate of a 1050°C steam-grown SiO_2 in 6:1:10 solution is represented by □.

times of 1/2, 1, and 2 hr were used for the three annealing temperatures of 800°, 900°, and 1100°C. The 800° and 900°C temperatures are representative of typical SiO_2 and Si_3N_4 deposition temperatures. As shown, the 800°C anneals are not as effective at lowering the etch rate as the 900° and 1100°C anneals. Also, the etch rate decreases with increasing annealing time for the 800° and 900°C anneals, but does not continue to decrease for the 1100°C anneal. From the change in etch rate it is apparent that the SIPOS films have changed character due to the anneals.

SIPOS densification.—The anneals also cause the films to shrink or densify as shown in Fig. 3 where the change in the SIPOS film thickness (densification) *vs.* time is plotted for a 900°C N_2 anneal. From this plot it is apparent that after 30 min the SIPOS film has densified as much as it will at this temperature.

Table I. SIPOS etch rate after annealing in nitrogen. (6:1:10) (Error in etch rate is ~35 Å/min)

Annealing temp (°C)	Annealing time (hr)	Etch rate (Å/min)
1100	2	240
	1	281
	0.5	250
900	2	150
	1	200
	0.5	225
800	2	350
	1	375
	0.5	500

In Fig. 4 the percent densification of the SIPOS films after a 1 hr N_2 anneal has been plotted *vs.* the reciprocal of T from ~800°-1150°C so that an activation energy associated with the densification might be ob-

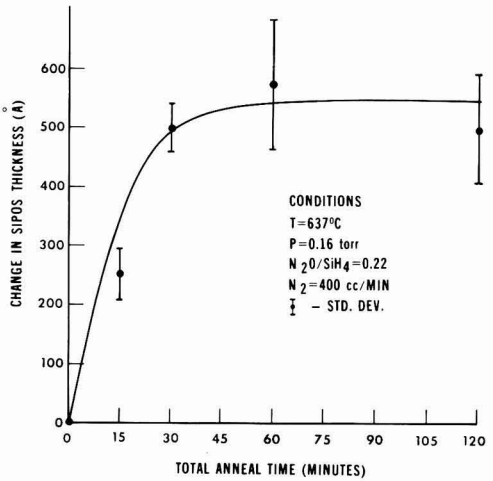

Fig. 3. Change in 25 a/o O SIPOS film thickness at 900°C in N_2 *vs.* annealing time. The change is a decrease in film thickness.

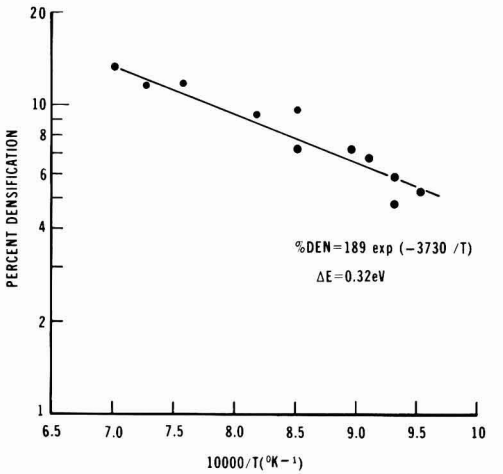

Fig. 4. Percent densification of 25 a/o O SIPOS *vs.* reciprocal temperature (K^{-1}). The SIPOS was annealed for 1 hr in N_2. Least squares analysis yields an activation energy of 0.32 eV.

tained. The least squares analysis of the Arrhenius-type plot results in an activation energy of 0.32 eV.

Infrared measurements.—Thus far, it has been shown that the SIPOS etch rate decreases from its unannealed value and the film densifies with annealing. It will now be interesting to show how the film physically restructures. To do this, one can examine the infrared spectrum as shown in Fig. 5. This spectrum is for an as-deposited 25 a/o O SIPOS film and shows a strong absorption peak at 1030 cm^{-1} and a weak peak at 865 cm^{-1}. No peak is noted at ~800 cm^{-1} which would be present in the infrared spectrum of SiO_2 (5).

The infrared spectra of SIPOS films after high temperature heat-treatments are shown in Fig. 6. This figure shows the effect of 1/2 hr N_2 anneals at 800°, 900°, and 1100°C on three different wafers. The major 1030 cm^{-1} absorption peak shifts to higher frequency with increasing annealing temperature. The strong absorption occurs at 1045 cm^{-1} for 800°C, 1080 cm^{-1} for 900°C, and 1095 cm^{-1} for the 1100°C anneal. Also the width of the major peak decreases from the initial value of 156 cm^{-1} to 125 cm^{-1} for 800°C, 121 cm^{-1} for 900°C, and 100 cm^{-1} for the 1100°C anneal. Moreover, the maximum absorbance increases in intensity as the temperature increases, yet the area of the strong absorption peak remains approximately the same for all temperatures and is an indication that the oxygen

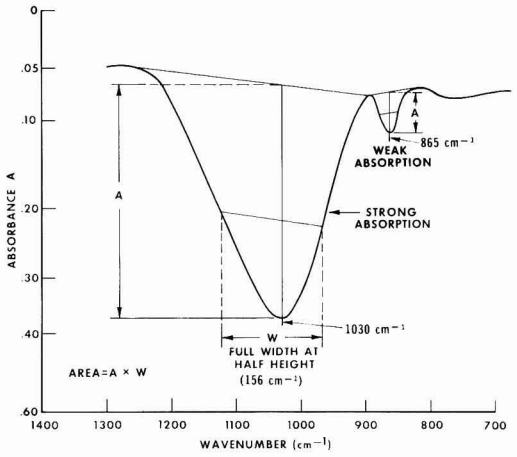

Fig. 5. Analysis of transmission infrared spectrum of 25 a/o O SIPOS film from 700 to 1400 cm^{-1}. The strong infrared absorption occurs at 1030 cm^{-1} while a weak absorption occurs at 865 cm^{-1}. area of the 1030 cm^{-1} absorption is approximated by $A \cdot W$.

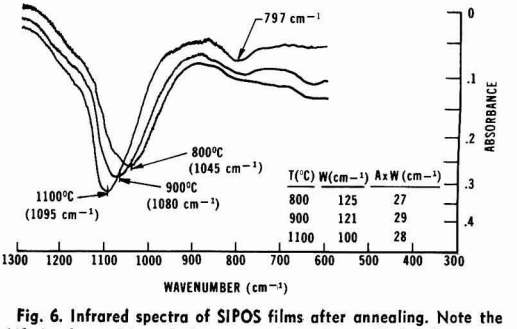

Fig. 6. Infrared spectra of SIPOS films after annealing. Note the shift in the position of the strong absorption to higher frequency with higher annealing temperature. The area of the strong absorption is constant, 28 ± 1 cm^{-1}, indicating no change in the oxygen content of the film.

Table II. SIPOS infrared peak and area ratios (2 hr nitrogen anneal)

Annealing temp (°C)	SiO_2 (797 cm^{-1}) / Si-O (1045-1095 cm^{-1}) Peak ratio	Area ratio
1100	0.071	0.041
900	0.071	0.035
800	0.044	0.019

content is not changing. (This is confirmed by electron microprobe analysis of the same films.) Furthermore, the 865 cm^{-1} peak is eliminated and at 900° and 1100°C a weak peak at 797 cm^{-1} appears. This peak is usually associated with SiO_2 (5).

Obviously the heat-treatments restructure the SIPOS film. A relative measure of this restructuring is given in Table II. The ratio of the intensity of the 797 cm^{-1} peak to the strong absorption peak at 1045-1095 cm^{-1} may be an indication of how much restructuring has been done. In Table II these ratios for peak height and area are given. The 2 hr 900° and 1100°C anneals are roughly comparable and apparently caused more restructuring than the 800°C anneal. The peak ratios indicate less SiO_2 component (797 cm^{-1}) is formed at 800°C as compared to 900° and 1100°C. Likewise, the area ratio would indicate the higher temperature anneals are more effective in forming the 797 cm^{-1} peak.

A measure of the activation energy associated with the restructuring is given in Fig. 7 where the shift of the strong infrared absorption *vs.* the reciprocal of the annealing temperature is plotted. The least squares analysis for this Arrhenius plot results in an activation energy of 0.27 eV.

Additional infrared data resulting in an Arrhenius plot are presented in Fig. 8. The change or narrowing of the full width at half of the maximum absorbance for the strong infrared absorption *vs.* the reciprocal of annealing temperature is plotted and yields an activation energy of 0.27 eV. These activation energies are in reasonable agreement with the activation energy determined for the percent densification, 0.32 eV, (Fig. 4) and are all approximately one-sixth of the energy associated with forming the SIPOS film.[1]

[1] The energy for formation of the SIPOS film was determined from an Arrhenius plot of deposition rate *vs.* reciprocal of deposition temperature (6).

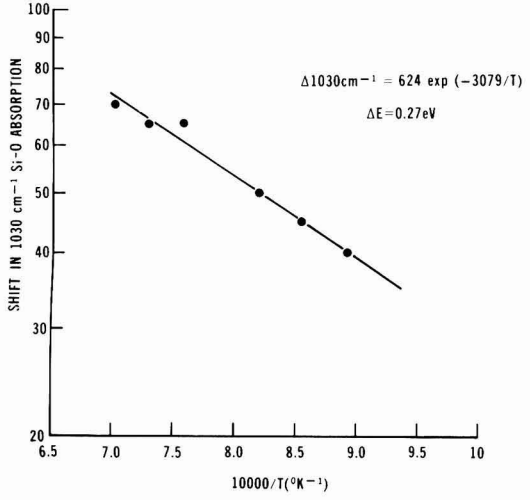

Fig. 7. Shift in the strong infrared absorption *vs.* reciprocal temperature (K^{-1}). The SIPOS films were annealed for 1 hr in N_2. The least squares analysis yields an activation energy of 0.27 eV.

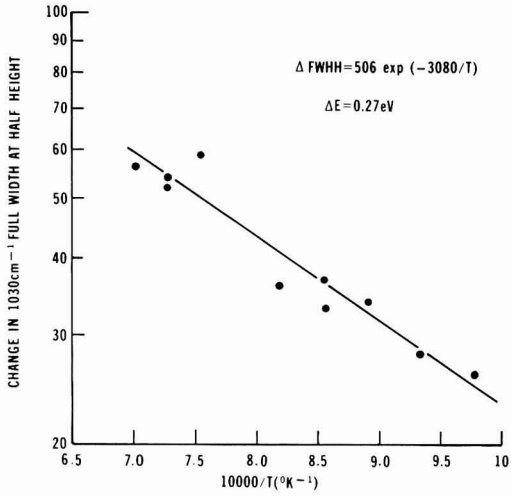

Fig. 8. Change in width of strong infrared absorption vs. reciprocal temperature (K^{-1}). The SIPOS films were annealed for 1 hr in N_2. The least squares analysis yields an activation energy of 0.27 eV.

The results discussed, thus far, are from control wafers that were heat-treated. However, the same effects are observed in device processing during subsequent film depositions such as Si_3N_4 passivation (see Fig. 9). This figure shows the infrared spectra for a SIPOS film before and after Si_3N_4 deposition. The Si_3N_4 was etched off the sample before the infrared spectrum was taken. For this work, the Si_3N_4 was deposited in a LPCVD reactor at a temperature of approximately 892°C by the reaction of SiH_2Cl_2 and NH_3. As shown, the major infrared peak for SIPOS has shifted from 1030 cm^{-1} to 1070 cm^{-1}, the 865 cm^{-1} peak has disappeared, and a new peak at 797 cm^{-1} has appeared. This infrared spectrum is similar to the infrared spectrum of a SIPOS film that has been annealed at 900°C (see Fig. 6).

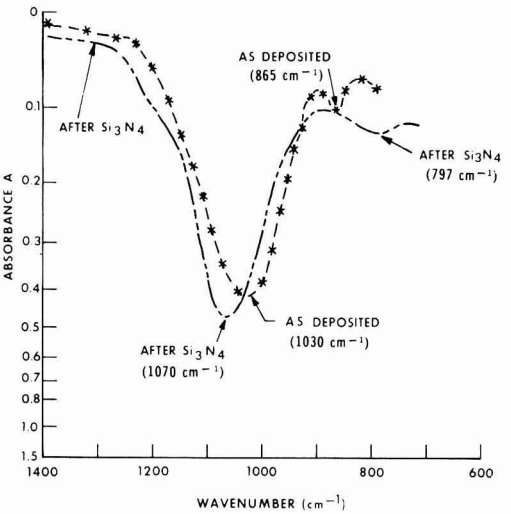

Fig. 9. Infrared spectra of SIPOS before and after deposition of Si_3N_4 at 892°C. —*— as-deposited SIPOS; — — — after Si_3N_4 deposition. Si_3N_4 was removed before infrared spectrum was recorded.

Stress measurements.—The restructuring caused by the high temperature anneals can be correlated with stress, as shown in Fig. 10, in which the measured stress is plotted for a 5000Å thick unannealed SIPOS film along with data after annealing at 900° and 1100°C for 1 hr in N_2. The stress for the as-deposited film is tensile and is $+1.2 \pm 0.9 \times 10^9$ dynes/cm². After the 1100°C anneal, the stress is compressive and is $-0.8 \pm 1.2 \times 10^9$ dynes/cm².

The total stress (σ_t) of a film is given by

$$\sigma_t = \sigma_{th} + \sigma_i$$

where σ_i is the intrinsic stress and σ_{th} the thermal expansion coefficient mismatch stress. The latter is given by (7)

$$\sigma_{th} = (\alpha_f - \alpha_{Si}) \frac{E_f}{1 - \nu_f} \cdot \Delta T$$

where α_f and α_{Si} are the thermal expansion coefficients of the deposited film and the Si substrate, E_f and ν_f are Young's modulus and Poisson's ratio for the film, and ΔT is the difference in temperature between the film deposition temperature and the temperature at which the stress is measured. For these films, ΔT is about 620°C. For a 25 a/o O SIPOS film α, $E/(1-\nu)$, and σ_i have been determined (8). These values are $\alpha = 2.18 \times 10^{-6}$/°C, $E/(1-\nu) = 1.31 \times 10^{12}$ dynes/cm², and $\sigma_i = +1.5 \times 10^9$ dynes/cm². Note that α lies between Si ($\alpha = 2.52 \times 10^{-6}$/°C) and SiO_2 ($\alpha = 0.55 \times 10^{-6}$/°C), as might be expected. Substituting the values for α and $E/(1-\nu)$ into the expression for σ_{th} yields $\sigma_{th} = -2.8 \times 10^8$ dynes/cm². If the high temperature annealing of SIPOS reduces the intrinsic stress, then SIPOS films should become more compressive according to the expression for σ_t and, in fact, this is what is observed, as shown in Fig. 10.

Discussion

The high temperature anneal of a 25 a/o O SIPOS film causes the film to shrink or densify about 10%. For deposited SiO_2, densification on the order of 3% to 5% has been reported (5) after annealing. The etch rate of the annealed SIPOS in the 6:1:10 SIPOS etch solution has also decreased from the as-deposited value. This observation is consistent with the elimination of voids (reduction of porosity) at anneal temperatures above the deposition temperature. Amorphous thin films commonly have a void network (9). Moreover, the infrared spectrum of the densified SIPOS has changed as well. The strong absorption peak narrows and shifts to higher frequency. Similar

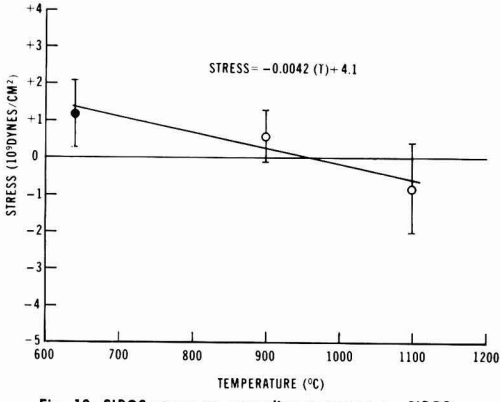

Fig. 10. SIPOS stress vs. annealing temperature. SIPOS was annealed for 1 hr in N_2. The units of stress are 10^9 dynes/cm². Tensile stress is positive and compressive stress is negative. The dark circle is the measured stress of the as-deposited SIPOS.

changes in the infrared spectrum of SiO_2 after annealing have been interpreted to be due to a relaxation of bond strain and a decrease in film porosity (5). In fact, if the temperature of the anneal is high enough, for example after an 1100°C anneal, the infrared spectrum of SIPOS resembles that of SiO_2. Even at 900°C, there is some SiO_2 character as evidenced by the presence of the weak 800 cm^{-1} peak in the infrared spectra.

Other changes occur in the SIPOS film with annealing. For example, from previous work (10), it is known that the as-deposited 25 a/o O SIPOS film is amorphous and that after a 1050°C anneal an average grain size of 40Å is observed. Given the above, it is possible that the formation of polycrystalline Si grains in the SIPOS during the anneal could exclude oxygen from the polycrystalline Si regions (there may still be some oxygen interstitially dispersed). Therefore, more of the remaining Si, not in the polycrystalline region, should be bonded to more than one oxygen atom. Evidence for this is suggested by the infrared spectrum of annealed SIPOS films that show no oxygen is lost during annealing. Thus, it is reasonable that after high temperature annealing the infrared spectrum of a SIPOS film should resemble SiO_2.

The stress measurements of SIPOS before and after an anneal are also consistent with more SiO_2 character of the annealed SIPOS film, in that the SIPOS film stress tends to change from tensile to compressive after annealing (SiO_2 is a film in compression on Si).

We interpret the etch rate data in the 6:1:10 SIPOS etch to indicate that at higher temperatures, more of the SIPOS has been converted to SiO_2 and polycrystalline Si since the etch rate actually starts to increase with the very high temperature anneal.[2] Thus the densification of the SIPOS film after anneal and the change in the infrared spectrum reported here support the models of annealed SIPOS presented by Hamasaki *et al.* (12) and McGinn and Goodman (13).

Conclusions

We conclude that with high temperature annealing the SIPOS films densify. For the 25 a/o O SIPOS films evaluated, this densification is a strong function of temperature. Some time dependence has also been noted for the lower temperature anneals (800°C). The densification is the result of a restructuring of the amorphous as-deposited SIPOS film as evidenced by the change in the infrared spectrum. This same densification takes place during high temperature deposition of Si_3N_4 or SiO_2 which are used as passivation layers on deposited SIPOS.

Evidence of grain growth at temperatures above the deposition temperature have been reported. Such grains exclude oxygen and result in the remaining Si atoms being bound to more than one oxygen atom (formations of SiO_2). The infrared changes and etch rate data are consistent with this interpretation. The change in the SIPOS stress due to the anneal is also consistent with more SiO_2 being formed. Finally, our results lend additional support to the models of annealed SIPOS presented by other workers.

[2] The etch rate variation of SIPOS with anneal temperature may also be interpreted in terms of the stress in the SIPOS films. In Fig. 2 the lowest etch rate is at ~980°C. In Fig. 10, this temperature corresponds to about zero stress in the SIPOS film. At any other temperature the film is stressed and so the etch rate is higher than that at 980°C (11).

Acknowledgment

We thank Dr. T. F. Retajczyk, Jr., at BTL-MH for the initial stress measurements.

Manuscript submitted March 19, 1980; revised manuscript received *ca.* Sept. 26, 1980. This was Paper 166 presented at the Boston, Massachusetts, Meeting of the Society, May 6-11, 1979.

Any discussion of this paper will appear in a Discussion Section to be published in the December 1981 JOURNAL. All discussions for the December 1981 Discussion Section should be submitted by Aug. 1, 1981.

Publication costs of this article were assisted by Bell Laboratories.

REFERENCES

1. H. Mochizuki, T. Aoki, H. Yamoto, M. Okayama, M. Abe, and T. Ando, *Suppl. Jpn. J. Appl. Phys.*, **15,** 41 (1976).
2. H. R. Maxwell, Jr. and W. R. Knolle, in "Semiconductor Characterization Techniques," P. H. Barnes and G. A. Rozgonyi, Editors, p. 180, The Electrochemical Society Softbound Proceedings Series, Princeton, N.J. (1978).
3. W. Bruegel, "An Introduction to Infrared Spectroscopy, p. 301, John Wiley & Sons, New York (1962).
4. A. K. Sinha, H. J. Levinstein, and T. E. Smith, *J. Appl. Phys.*, **49,** 2423 (1978).
5. W. A. Pliskin, *J. Vac. Sci. Technol.*, **14,** 1064 (1977).
6. H. R. Maxwell, Jr., Private communication.
7. A. K. Sinha, H. J. Levinstein, and T. E. Smith, *J. Appl. Phys.*, **49,** 2423 (1978).
8. T. F. Retajacyzk, Jr., Private communication.
9. A. G. Dirks and H. J. Leamy, *Thin Solid Films*, **47,** 219 (1977).
10. H. R. Maxwell, Jr., A. R. Hartman, and T. T. Sheng, RNP 27 presented at The Electrochemical Society Meeting, Boston, Massachusetts, May 6-11, 1979; see *This Journal*, **125,** 257C (1978).
11. S. Schwarz, H. R. Maxwell, Jr., and W. R. Knolle, To be published.
12. M. Hamasaki, T. Adachi, S. Wayakama, and M. Kikuchi, *J. Appl. Phys.*, **49,** 3987 (1978).
13. J. T. McGinn and A. M. Goodman, *Appl. Phys. Lett.*, **34,** 601 (1979).

Transmission Electron Observations of the Early Stage of Epitaxial Growth of Silicon on Sapphire

S. Hamar-Thibault

L.T.P.C.M./E.N.S.E.E.G.—Institut National Polytechnique de Grenoble, B.P.44 38401 Saint Martin d'Heres, France

and J. Trilhe

Laboratoire M.E.A., LETI/C.E.N. de Grenoble—85 X 38041 Grenoble Cedex, France

ABSTRACT

A discontinuous silicon layer was produced on $(01\bar{1}2)$ oriented sapphire. The early growth of silicon was examined by transmission electron microscopy. During a very short time of deposition, it is shown that islands of {100} orientation had nearly square or rectangular forms. We observed a very rapid decrease of {100} crystallite density together with a nearly constant {110} crystallite density. The lattice of epitaxial Si layers was measured to be distorted in the very early stage of the growth. The interfacial shear strain is calculated. The distortion of the silicon lattice decreases with growing time.

Devices fabricated from heteroepitaxial silicon films on sapphire sometimes presented backchannel leakage currents caused, at least in part, by the presence of defects and impurities in the silicon films. Several authors (1-4) using transmission electron microscopy have shown the presence of stacking faults and microtwins in silicon. Defect density in silicon is very high in the proximity of the sapphire interface, so it is very important to study the structure of the interface and the defects which are present.

In order to investigate the nature of the initially deposited silicon, we have studied, using transmission electron microscopy, the structure and the orientation of silicon islands at early stages of growth.

The presence of residual elastic stresses near the interface, which could affect electrical properties of integrated circuits, is proved by measuring lattice parameters by diffraction microscopy.

Experimental

The silicon was deposited from vapor phase at 980°C on $(01\bar{1}2)$ oriented CZ single crystal sapphire substrates by pyrolysis of diluted silane in H_2. The sapphire substrates were polished wafers from Union Carbide.

Deposition was stopped at various times; with a growth rate of 0.67 $\mu m \cdot mn^{-1}$, we obtained a series of samples with isolated islands of silicon. The samples examined were grown for 0.6, 1.2, 1.8, and 2.4 sec.

The samples were thinned by argon ion bombardment from the sapphire side only. Samples were observed by JEM 100 B electron microscope, operating at 100 keV.

Observations

We first present information contained in the diffraction patterns and electron microscopical images.

Diffraction pattern and electron micrographs.—The selected area diffraction pattern from a sample grown for 1.8 sec is shown in Fig. 1. The indexed pattern is given on the same figure with reference to the interpretation of Abrahams (1). It is seen in Fig. 1 that there are three orientations. The most important orientation of the silicon islands is {100}. For these {100} domains, the plane $(2\bar{1}\bar{1}0)$ is parallel to the (001) plane of the silicon.

There are also two other orientations of silicon islands, that is to say two kinds of {110} oriented domains. These three main orientations are always present with their twin configurations. Each two {110} oriented domains have their twin pairs. They twinned about the <111> axis, which lies parallel to the [011] and $[0\bar{1}1]$ directions of the (100) oriented domains. Only the two twin axes which are parallel to the substrate give well-developed twin crystals. All other spots may be due to multiple diffraction effects.

Bright and dark field electron micrographs of the sample grown for 2 sec are shown in Fig. 2. The micrograph 2a is the bright field image of a sample area. The micrograph 2b is a dark field image with an operative reciprocal lattice vector $\mathbf{g} = (004)$ of the same area. The {100} oriented silicon islands appear light. In the micrograph 2c corresponding to the <111> reflection parallel to the $[0\bar{1}1]$ direction of the {110} domains, the two {110} domains appear light.

It is seen that the silicon films consisted of differently oriented domains smaller than 100 nm in diameter. The crystallites are often composed of one or two {110} domains associated with {100} domains.

We also observed that {110} domains contain a very high density of twins and microtwins. Most of the twins are very thin, one or two atomic layers. The density of twins in {100} domains is much smaller. The results given above concerned developed films before complete coverage. The observations are slightly different at earlier stages under the present growth conditions.

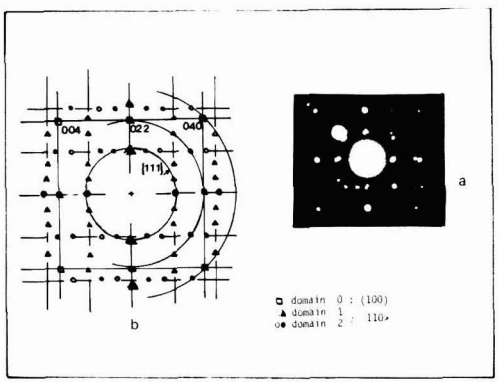

Fig. 1. Diffraction pattern of epitaxial silicon on sapphire. $(100)_{Si}/(01\bar{1}2)Al_{Al_2O_3}$. (a) Diffraction pattern, (b) indexed pattern of {100} and {110} domains.

Key words: dislocation, misfit, shear strain distortion.

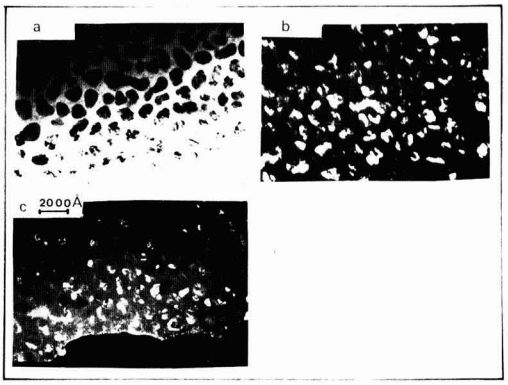

Fig. 2. Bright and dark fields electron micrographs: (a) bright field, (b) dark field {100} domain g = (022), (c) dark field {110} domains g = <111> || |0$\bar{2}$2|.

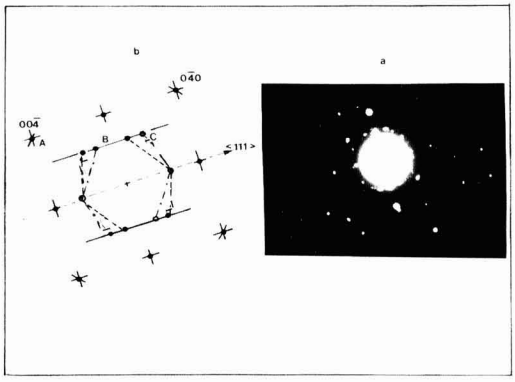

Fig. 4. Fine structure of a diffraction pattern

The size of the {100} domains is always larger than the corresponding {110} domain.

Figure 3 presents for different growing times the silicon islands deposed on sapphire. As seen in Fig. 3, the mean diameter of silicon crystallites increases with growing time, as the density of {100} domains decreases, as a result of island coalescence.

It is very interesting to note that for sample II (t = 1.2 sec, v = 0.67 μmn^{-1}), rectangular or square particles are present. They are much less numerous than the particles of other forms. The sides of the square particles are parallel to the [011] and [0$\bar{1}$1] directions. These particles are always smaller than other particles. The mean diameter seems to be smaller than 200 or 300Å. For longer growth time, the particles develop into larger conglomerates and the geometrical shape disappears.

Fine structure of electron diffraction patterns.—The fine structure in electron diffraction patterns for the sample with the smallest growth time shows: (*i*) elongation of spots (belonging to [100] and [110] domains) and (*ii*) distortion of the silicon lattice. Two distinct types of spot elongations are visible: circular elongation around the origin, and linear streaks. Figure 4 shows the diffraction pattern of [100] zone of {100} domains of silicon (sample II). Extreme variations in contrast made it difficult to obtain print that would preserve the details of the relrods. These are shown in the accompanying tracing. The most readily identifiable type is circular elongations of the spots, which are due to small misorientations of the {100} or {110} domains.

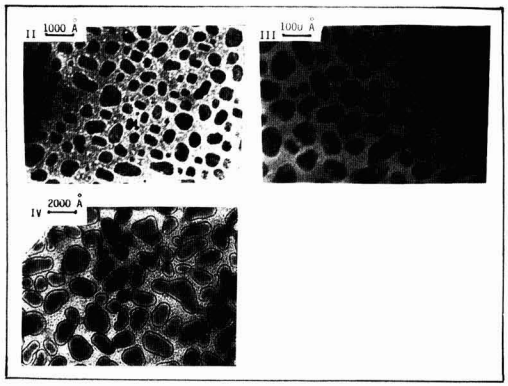

Fig. 3. Electron micrographs for different growing times. II = 1.2 sec; III = 1.8 sec; IV = 2.4 sec.

This elongation is due to small misorientations. The mean angular spread of the spots from the {100} domains is about 3° for the smallest growth time, and decreased to 1° for longer growth time. So experimentally, it is seen that silicon films on sapphire are like a mosaic of silicon islands, which becomes more perfect as the thickness of the films increases. This orientation spread of about 3° was interpreted by Abrahams (4) to nucleation of planes of the {100} silicon islands parallel to sapphire planes; if some of the (0$\bar{2}$2) planes of {100} silicon nucleate parallel to the ($\bar{2}$20$\bar{4}$) planes of sapphire, while some other of the (0$\bar{2}$2) planes nucleate parallel to (20$\bar{2}$4) planes of sapphire, the misorientation would be about 4°.

The second type of spot elongations in diffraction patterns appears as linear streaks in both {100} and {110} domains, arising from high density of stacking faults and microtwins (note B and C in Fig. 4). Diffraction patterns of the {110} domains (B) are present at very early stages of growing time; high density of microtwins shows linear streaks in the <111> direction. Only elongations along the <111> twin axis parallel to [011] and [0$\bar{1}$1] directions of {100} domains are well developed, as the twins. We obtain as the diffraction pattern, at very early stages of growth, a network with perpendicular streakings.

The {100} domains are also twinned about the <111> twin axes; at the exact [100] orientation, there are not spots due directly to the twins. But the spots noted C are extra spots due to double diffraction on those twins in {100} crystals. These spots disappear when the growing time increases. Linear streaks are also seen near (004), (022) spots and in the vicinity of the spots C, of the {100} domains. The streaks are parallel to the [010] and [001] directions; they can indicate a high density of stacking faults.

Angular distortion, misfit, and misfit dislocations.—At early stages of growth, before complete coverage, observations of diffraction patterns show that the silicon lattice is distorted. The distortion decreased for increasing growth time deposition. There is an angular distortion, and together a contraction of the reciprocal lattice vector. As the substrate is not cubic, a shear stress exists, which can be established from the nonorthogonality of (0$\bar{4}$0) and (00$\bar{4}$) reciprocal lattice vectors observed on the [100] silicon films patterns.

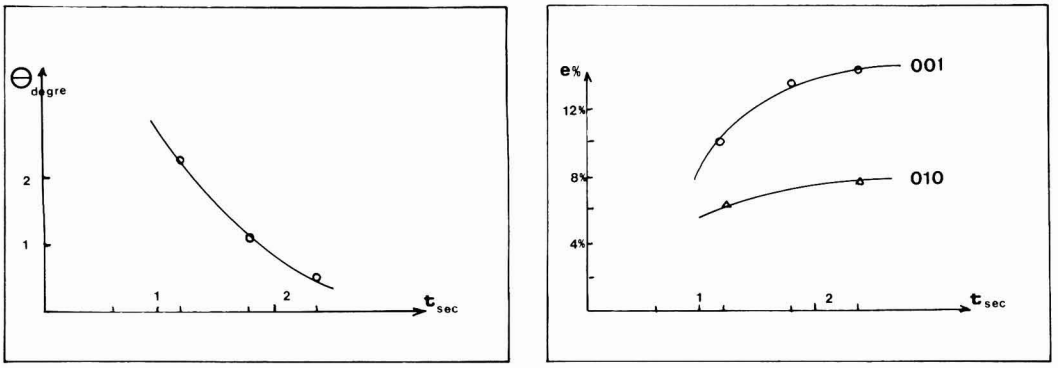

Fig. 5. Distortion of silicon lattice on sapphire at early stage of growth. (a) Deviation θ from theoretical angle between (004) and (040) reflections of epitaxial silicon, (b) misfit between distorted and nondistorted silicon lattice for the (004) and (040) reflection spots.

The angle between the $(0\bar{4}0)$ and $(00\bar{4})$ reciprocal lattice vectors was measured. This angle can be as large as 92°. The theoretical angle for the [100] orientation is 90°. 90° was substracted from the measured angle to give the shift named θ. The variation of θ for different growth time is shown in Fig. 5(a). θ decreases with increasing growth time. The maximum observed value of θ is as large as 2° for 1 sec of growth time. θ reached zero after 3 sec of growth time.

In diffraction patterns, a misfit between the silicon and sapphire lattices can be observed. From the separation of g_{SI} and g_{SA} where g_{SI} and g_{SA} are, respectively, the reflection (004) of the silicon and $(\bar{4}220)$ of the sapphire, we deduce that there is a progressive increase in the misfit between silicon and sapphire lattices with increasing deposit time. If the misfit is defined as

$$e = \frac{a_{SA} - a_{SI}}{a_{SA}}$$

where a_{SA} and a_{SI} are the interatomic spacings in the interfacial plane in sapphire and silicon, then in terms of g_{SI} and g_{SA}

$$e = \frac{|g_{SA}| - |g_{SI}|}{|g_{SA}|}$$

assuming $g_{SA}//g_{SI}$.

Figure 5(b) shows that the misfit e increases from about 8% to 14% compared with a natural misfit e^o of about 14%, for the (004) reciprocal lattice vector of silicon and the $(\bar{4}220)$ of sapphire. The misfits noted e_{004} and e_{040} are related to the (004) and (040) reflections spots for silicon.

The misfit is equal to the natural misfit after 2.4 sec of growth. For this sample, continuous networks of misfit dislocations are also seen in the silicon islands, as seen in Fig. 6. The fringes tend to lie parallel to the [011] and $[01\bar{1}]$ directions. The Burgers vector of the dislocations is consistent with $a/2$ [110] which is the $\bar{b}$ for dislocation in the diamond structure. Their spacing is equal to 38Å, which is in good agreement with the calculated value for pure edge type (37Å).

For this sample (2.4 sec of growing time) the linear density of misfit dislocations is $1/38\text{Å} = 2.6 \times 10^6$ dislocations·cm^{-1}. For the other samples with shorter growing time, we do not see any misfit dislocations. Misfit dislocations have also been observed by Abrahams (5).

It is very interesting to note the correlation between the lattice deformation of the silicon, which decreases with growing time, and the easy observation of misfit dislocations for longer growing time.

Results

Monoclinic distortion of the epitaxed layers.—If we assume the thickness of the epitaxial layer to be much smaller than the dimensions of the substrate, we may neglect the strains in the substrate. Substrates that were not very thick became curved due to the stresses in the epitaxial layer.

The observations indicate that the silicon lattice at early stages of epitaxy is distorted. From measurements of several d spacings, it is concluded that there are compressional and shear strains in the silicon islands. The simplest distorted lattice is a monoclinic lattice.

Figure 7 gives a schematic drawing of a monoclinic distortion of a silicon layer on sapphire. The lattice

Fig. 6. Misfit dislocations of silicon on sapphire (growth time 2.4 sec).

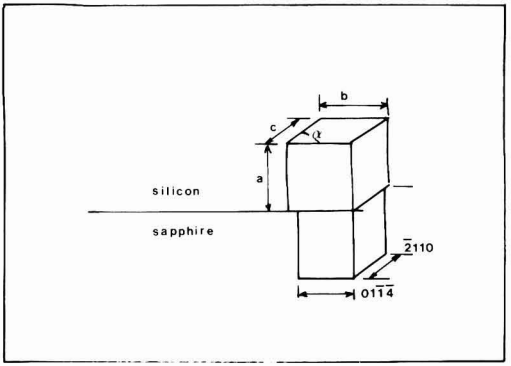

Fig. 7. Schematic representation of a monoclinic distorted silicon lattice on sapphire.

parameter of undistorted silicon is a_0. If ϵ_{100}, ϵ_{010}, ϵ_{001} are the strains along the three axes, the parameters of a distorted lattice become a b c

$$a = a_0(1 + \epsilon_{100})$$

$$b = a_0(1 + \epsilon_{010})$$

$$c = a_0(1 + \epsilon_{001})$$

where α is the monoclinic angle between the [010] and [001] axis, as shown in Fig. 7. α is 90° if the silicon layer is not distorted.

Relations between observable quantities and strain components.—From [100] diffraction pattern, we obtain information about strains in the wafer plane along the [001] and [010] axis, that is to say, c, b, and α. From the angular deviation between (010) and (001) reflections, spots on [100] diffraction pattern, we obtained α, which is related to θ.

Strains ϵ_{001} and ϵ_{010} are approximately related to misfits by

$$\epsilon_{001} = e_{004}^{o} - e_{004}$$

$$\epsilon_{010} = e_{040}^{o} - e_{040}$$

Strain ϵ_{100} related to the [100] axis perpendicular to the epitaxial plane must be calculated from the [110] pattern of the {100} silicon domains. The parameter a is more difficult to calculate, these parameters can only be obtained from relations between c, b, α, d_{400}, and d_{220}, where d_{400} and d_{220} measured on the {110} diffraction pattern are interplanar spacings of (400) and (220) planes of silicon.

Figure 8 shows variations of lattice parameters ϵ and α of a distorted silicon layer on sapphire with deposition time. As seen in the figure, the lattice parameter normal to the wafer surface increases, while the two lattice parameters parallel to the wafer surface decrease. This result suggests that the first layers of silicon on sapphire are deformed to accommodate the sapphire lattice.

Stresses in epitaxial layer.—The elastic stresses in a cubic crystal are correlated to the strains by a tensor, whose elements are the elastic stiffness coefficients. The elastic stiffness coefficients are given by Hornstra (6). In thin epitaxial layers, forces of the substrate act only in the interface plane, and as the substrate is not cubic, shear strains are present, which are to be added to compressional strains (8).

We calculate stresses along the different axes using the variation of the lattice parameters; the result is for 1.2 sec of growing time (sample II)

$$\sigma_{100} \simeq +1.2 \times 10^{10} \text{ dynes/cm}^2$$

$$\sigma_{010} \simeq +2.9 \times 10^{10} \text{ dynes/cm}^2$$

$$\sigma_{001} \simeq -5.9 \times 10^{10} \text{ dynes/cm}^2$$

The shear stress σ_S is calculated from the angular deviation θ by Abrahams (7)

$$\sigma_S = \text{tg } \theta \simeq 2.7 \times 10^{10} \text{ dynes/cm}^2 \text{ for sample II}$$

The decay of the compressional and shear strains is very quick. For the sample III ($t = 1.8$ sec) these strains are about a factor of 10 less than the strains of the sample II ($t = 1.2$ sec). Along the [001] direction, we calculate the values

$$\sigma_{II} = -5.9 \times 10^{10} \text{ dynes/cm}^2$$

$$\sigma_{III} = -0.7 \times 10^{10} \text{ dynes/cm}^2$$

We also observed a very important difference between strains in [001] and [010] directions, which gives rise to a shear strain in the wafer plane.

The precision of our results are best appreciated along the [001] axis, where the compressional strain is the most important. The compressional strain of sample IV ($t = 2.4$ sec) is impossible to estimate with our method; the precision of the diffraction patterns is too small. In opposition, the shear strain decreases slowly from $3 \cdot 10^{10}$ dynes/cm^2 for the sample II to 0.6×10^{10} dynes/cm^2 for sample IV, with increasing growth time.

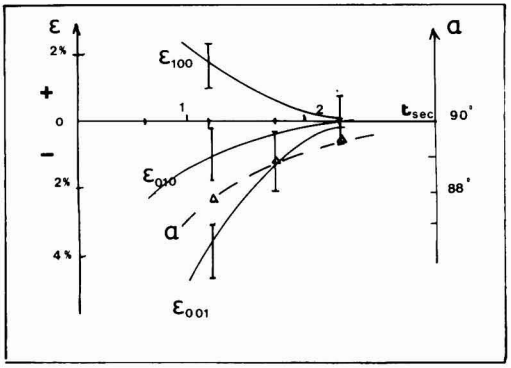

Fig. 8. Variation of lattice parameters of monoclinic silicon with deposit time.

Discussion

Two points are very important in our results, the geometrical form of the silicon islands and the stresses in the wafer plane before complete coverage. We compare first the morphology of the silicon islands with those of Abrahams (1); then some remarks are made concerning the magnitude of the calculated stresses and the asymmetric strains in the plane of the wafer.

The observations of the nucleation of silicon on sapphire are compared with the results of Abrahams. The growing conditions (temperature, growth rate) are approximately the same. They obtained near a rapid initial coverage rate, smooth forms of silicon islands. In opposition our silicon islands present geometric forms and the coverage of the substrate surface *vs.* time is represented by a sigmoid curve. Those islands present a partially coherent growth on the substrate. The morphology of the silicon islands differs only at a very early stage of growth. For longer growth time, our results are similar to those reported by Abrahams.

The important difference in the preparation of the substrate is hydrogen firing used by Abrahams. The surface of sapphire obtained by those authors seem to provide a high density of nucleation of silicon islands. As we do not use hydrogen firing, we obtain a lower density of silicon islands with a lower density of defects. Schmidt and Davey (13) have reported that after hydrogen firing, sapphire surfaces were ordered crystallographically but topologically poor.

Those silicon islands present, on the other hand, important compressional strains. Geometric or thermal considerations could explain the not equal compressional strains in the [001] and [010] directions, greater along the [001] axis. Stresses arise when the layers are cooled to room temperature. They are due to the difference between the thermal expansion coefficients of silicon and sapphire (8). The anisotropy of the thermal expansion coefficient of the sapphire (12) greater along c than perpendicularly gives rise to anisotropy of contraction of sapphire greater along the [010] than the [001] axis.

Crystallographical considerations could also induce stresses in the wafer plane. Nolder (11) compared the relative position of aluminum and oxygen atoms on a $(01\bar{1}2)$ plane in sapphire and the silicon atom on a (100) plane in the cubic lattice of the silicon.

It is seen that the aluminum sites form a face-centered array, which is similar to the arrangement of

silicon atoms in a (100) plane, with the [001] direction of silicon parallel to the $[2\bar{1}10]$ direction of the sapphire. The substitution of aluminum by silicon, leads to mismatches along the [001] and [010] directions of about 14 and 8% with reference to the $[2\bar{1}10]$ and $[01\bar{1}4]$ directions of sapphire. The observed strains are of the same order of magnitude and of the same direction as geometric strains.

In general, all the measurements of residual stresses in silicon films on sapphire lead to thermal stresses. Kamins and Meieran (9) calculated stresses of $7 \cdot 10^9$ dynes $\cdot$ cm^2, Dumin (10) found residual stresses to be about $5 \cdot 10^9$ dynes $\cdot$ cm^{-2}. Abrahams (7) gives shear stresses of $1.2 \cdot 10^{10}$ dynes $\cdot$ cm^{-2} near corners of silicon-sapphire interface. The magnitude of the calculated stresses ($5 \cdot 10^{10}$ dynes $\cdot$ cm^{-2} in the [001] direction) at an early stage of growth can exceed the thermal contribution by an order of magnitude. As the film grows, this contribution becomes very small rapidly. We think that there is a superposition of the two sorts of stresses. The crystallographical compressional strain, which is very important at early stage of growth, decreases very quickly with thickness. When the films are thicker, thermal compressional stresses remain the principal stresses.

Experimentally, we observed small islands at the first stage of the deposition of silicon on sapphire, which present the characteristics of partially coherent growth on the substrate surface. That is in opposition with the theory of Van Der Merve (14), which says that a totally coherent growth of a layer film (formed layer by layer) may be expected up until a certain thickness which is related with the misfit of the two lattices. This thickness is for the system Si/Al_2O_3 equal to 1Å, that is to say that the growth of silicon may be totally not coherent. In fact, the growth of islands of silicon instead of layers increases the possibility of coherent growing, by introducing a term of superficial energy of the island.

In conclusion, we observed at a very early stage of growth, a partial coherency of the silicon islands of sapphire. This partially coherent growth appears with compressional strains in wafer plane and at the same time, the coverage of the substrate surface by silicon islands is represented by a sigmoid curve.

Acknowledgment

Thanks are due to Mr. G. Cullen and Mr. M. S. Abrahams for very useful discussions.

Manuscript submitted Feb. 28, 1980; revised manuscript received *ca.* Sept. 29, 1980. This was Paper 329 presented at the Los Angeles, California, Meeting of the Society, Oct. 14-19, 1979.

Any discussion of this paper will appear in a Discussion Section to be published in the December 1981 JOURNAL. All discussions for the December 1981 Discussion Section should be submitted by Aug. 1, 1981.

Publication costs of this article were assisted by the Institut National Polytechnique de Grenoble.

REFERENCES

1. M. S. Abrahams, C. J. Buiocchi, R. T. Smith,, J. F. Corboy, Jr., J. Blanc, and G. W. Cullen, *J. Appl. Phys.*, **47**, 5139 (1976).
2. T. Hayashi and S. Kurosawa, *J. Cryst. Growth*, **45**, 426 (1978).
3. J. Trilhe, J. Borel, and J. P. Duchemin, *ibid.*, **45**, 439 (1978).
4. M. S. Abrahams and C. J. Buiocchi, *Appl. Phys. Lett.*, **27**, 324 (1975).
5. M. S. Abrahams, C. J. Buiocchi, J. F. Corboy, and G. W. Cullen, *ibid.*, **28**, 275 (1976).
6. J. Hornstra and W. J. Bartels, *J. Cryst. Growth*, **44**, 513 (1978).
7. M. S. Abrahams, J. Blanc, C. J. Buiocchi, and W. E. Hams, *J. Appl. Phys.*, **49**, 652 (1978).
8. D. M. Jefkins, *J. Phys. D. Appl. Phys.*, **3**, 770 (1970).
9. J. I. Kamins and E. S. Meieran, *J. Appl. Phys.*, **44**, 5064 (1973).
10. D. J. Dumin, *ibid.*, **36**, 2700 (1965).
11. R. Nolder and I. Cadoff, *Trans. Metal. Soc. AIME*, **233**, 549 (1965).
12. J. B. Wachtman, *J. Am. Ceram. Soc.*, **47**, 319 (1962).
13. W. A. Schmidt and J. E. Davey, *Nat. Bur. Stand. Spec. Publ.*, **348**, 259 (1972).
14. J. H. Van Der Merve, *J. Appl. Phys.*, **34**, 117 (1963).

Silicon Contamination of InP Synthesized under High Phosphorus Pressure

A. Yamamoto, S. Shinoyama, and C. Uemura

Nippon Telegraph and Telephone Public Corporation, Ibaraki Electrical Communication Laboratory, Tokai, Ibaraki 319-11, Japan

ABSTRACT

An experimental study has been made of processes causing Si contamination of polycrystalline InP synthesized under high phosphorus pressure (~30 atm) via the horizontal Bridgman technique. Silicon content of the grown ingots was determined by measurement of carrier concentrations and by spark source mass spectrometry. The Si content increased by about two orders of magnitude when the maximum temperature in the indium melt was varied from 1050° to 1180°C. The Si content scarcely depended on phosphorus pressure in the range of 5-30 atm. Presence of indium oxides in the indium melt was found to lower the incorporated Si content. As a result of these investigations, high purity InP ($N_d - N_a = 3.2 \times 10^{15}$ cm^{-3}, $\mu_{77K} = 37{,}000$ cm^2/V $\cdot$ sec) was reproducibly obtained by using a quartz boat at a growth rate of 3 mm/hr. The effective distribution coefficient for Si in InP was determined to be 0.53 by the analysis of intentionally Si-doped ingots.

Recent developments of InP-based devices such as InGaAsP-InP lasers or InP FET's require high quality InP crystals as substrates. Single crystals of InP are currently grown by the liquid encapsulated Czochralski (LEC) method. The LEC method uses polycrystalline InP as the starting material. Reduction of residual donor impurities in the starting material is essential

Key words: InP, Si contamination, effective distribution coefficient, synthesis of III-V compounds, horizontal Bridgman technique.

to grow semi-insulating crystals or p-type crystals with low carrier concentrations.

Silicon is known to be a major residual donor impurity in InP and to be introduced from the silica envelope during synthesis or crystal growth (1, 2). Use of pyrolytic boron nitride (PBN) boats in the synthesis of InP is effective in reducing carrier concentrations in the grown ingots (3). Furthermore, the synthesis at lower temperatures (~ 950°C) and under lower phosphorus pressure (~ 2 atm) is successful in obtaining high purity InP with carrier concentrations lower than 10^{15} cm^{-3} (4). Although the reaction of SiO_2 and phosphorus vapor, which provides a source for Si contamination, has been proposed by Bachmann *et al.* (1), details of Si contamination process during synthesis or crystal growth have not been systematically studied.

Segregation behavior of Si in InP, on the other hand, has been unclear since the effective distribution coefficient for Si in InP, k_e(Si), has been scattered in the wide range of 10^{-3} in LEC (5) to 30 in LPE (6). This uncertainty for k_e(Si) is thought to be mainly caused by Si contamination during synthesis or crystal growth (2). Therefore, segregation behavior of Si must be evaluated with intentionally Si-doped materials in which an Si contamination level can be neglected as compared with the Si doping level.

In this work, we studied experimentally the Si contamination process of undoped InP synthesized under high phosphorus pressure via the horizontal Bridgman technique. By carrier concentration measurements and spark source mass spectrographic analyses, we found some factors in the synthesis which governed Si content incorporated into grown ingots. As a result of that, it was proved that bulk polycrystalline InP with carrier concentrations as low as those synthesized using PBN boats could be obtained by using quartz boats. We also obtained a reliable value of k_e(Si) from the analyses of intentionally Si-doped ingots.

Experimental

Not intentionally doped polycrystalline InP was synthesized from the elements via the horizontal Bridgman technique. Approximately 200g of indium (6-9's purity, Mitsubishi Metals or Yamanaka Semiconductors) were charged in a quartz boat. The quartz boat was placed in a quartz ampul (ID: 35 mm, length: 600 mm) together with approximately 100g of red phosphorus (6-9's purity, Mitsubishi Metals) charged in a separate quartz boat. Prior to the sealing of the ampul, the indium was prebaked in vacuum (pressure: 1×10^{-6} Torr) at a temperature in the range of 450°-950°C for 3 hr. After being evacuated and then sealed, the ampul was set in a three-zone horizontal Bridgman furnace. The furnace was in a water-cooled chamber that could be pressurized up to 35 atm with N_2 gas. The furnace was heated to the conditions shown in Fig. 1. The phosphorus pressure in the ampul was controlled by the temperature in the zone A, T_A, and estimated from the pressure-temperature relationship data reported by Bachmann *et al.* (7). T_A was varied from 400° to 600°C, which corresponded to phosphorus pressure from 1.5 to 40 atm, respectively. To prevent breakage of the ampul due to such high phosphorus pressure, the N_2 gas pressure in the chamber was controlled to within ± 5 atm of the phosphorus pressure in the ampul. The indium was heated at the temperature in the zone B, T_B, and then traveled toward the zone A through the highest temperature zone C in which maximum temperature was T_{max}. T_B was fixed at 800°C through all experiments, and T_{max} was varied from 1050° to 1200°C. The ampul was moved at a constant speed of 3 mm/hr when the desired temperature in each zone was reached.

Silicon-doped InP was also synthesized to study the segregation behavior of Si in InP. For Si doping, small pieces (2-5 mg) of an Si wafer (phosphorus-doped, 50 Ω·cm) were added to the indium before the prebaking of the indium.

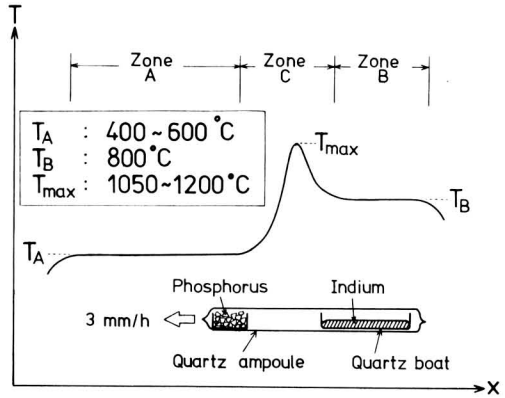

Fig. 1. Schematic of the horizontal Bridgman apparatus used for synthesis of InP.

The electrical properties of InP ingots synthesized were evaluated using Van der Pauw Hall measurements. The residual impurities in the ingots were determined using spark source mass spectrometry.

Results and Discussion

Silicon contamination of nominally undoped ingots.— We studied the dependence of carrier concentration or Si incorporated under various synthesis conditions such as maximum temperature in the zone C, T_{max}, phosphorus pressure in the ampul, P_P, and prebaking temperature of the charged indium, T_{pb}.

First, effects of T_{max} on carrier concentrations and Si contents in grown ingots will be described and discussed. Syntheses were performed under the following conditions: T_{pb} = 500°C, P_P = 7 atm, and T_{max} = 1050°-1180°C. The InP ingots grown under these conditions were fully stoichiometric excepting the last-to-freeze end at which excess indium remained. Figure 2 shows a typical grown ingot weighing 250g. Samples for electrical measurements were sliced perpendicular to the growth direction from each position of the ingots. Figure 3 shows carrier concentration profiles along the growth direction in the ingots grown at different T_{max}. It can be seen that, with increasing T_{max}, the carrier concentration increases drastically and its distribution becomes flat. To confirm that the increase in carrier concentration with increasing T_{max} is due to an increase in Si content in the ingots, spark source mass spectrographic analyses for the ingots were performed. The analytical results for typical two samples as indicated by numbered squares in Fig. 3 are pre-

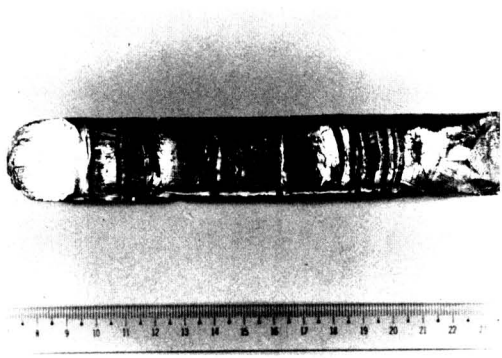

Fig. 2. A typical polycrystalline InP ingot grown, weighing 250g

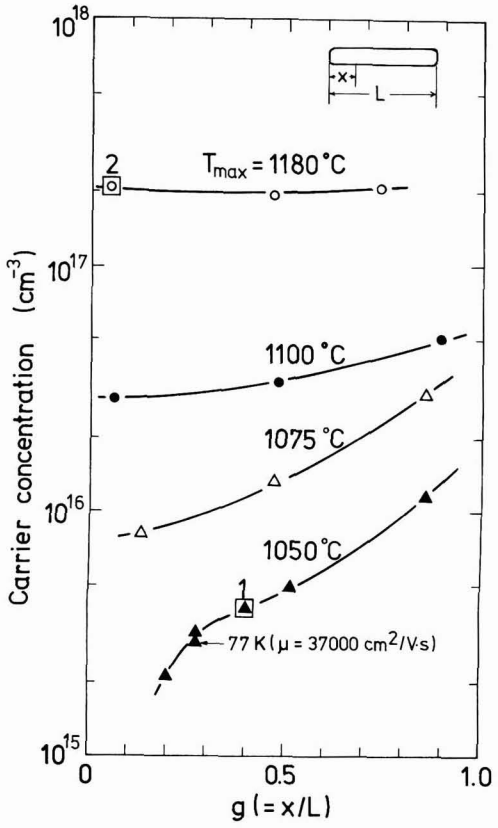

Fig. 3. Carrier concentration profiles along the growth direction for ingots grown at different maximum temperature in the indium melt (T_{max}).

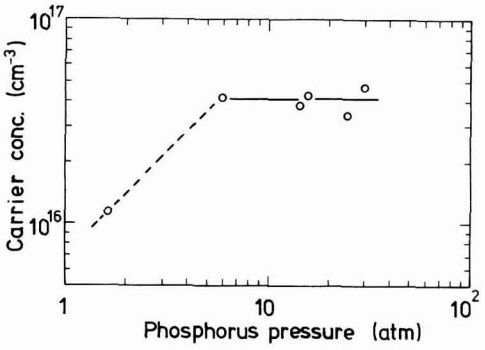

Fig. 4. Carrier concentrations at the first-to-freeze portion of grown ingots as a function of phosphorus pressure (P_P).

sented in Table I. A remarkable difference in Si concentrations between both samples are found, whereas no significant differences in concentrations of other impurities are found. Furthermore, no other donor impurities than Si are detected and the Si concentrations are in good agreement with the carrier concentrations. From these results, it is concluded that Si contents incorporated during synthesis dominate the carrier concentrations in the grown ingots and, also, that the increase in T_{max} drastically enhances the reaction for Si contamination. Although high concentrations of C, N, and O were detected, they are thought to be incorporated during the sample preparation processes for the analysis.

The results shown in Fig. 3 also show that carrier concentrations as low as those in PBN-grown InP (3) can be obtained at a comparable growth rate (3-4 mm/hr) even if quartz boats are used. Hall data for a typical ingot are $N_d - N_a = 3.2 \times 10^{15}$ cm^{-3} and $\mu_{77K} = 37{,}000$ cm^2/V·sec.

It is obvious that curves in Fig. 3 do not represent the segregation behavior of Si because the distribution of Si is governed by the Si contamination process. The increase in "apparent" effective distribution coefficient with increasing Si content incorporated is a phenomenon commonly observed in this study. The segregation behavior will be discussed in the next section.

Next, a phosphorus pressure dependence of the carrier concentration in the grown ingot will be described. The ingots were grown under the following conditions: $T_{pb} = 800$°C, $T_{max} = 1100$°C, and $P_P = 1.5$-30 atm. When the synthesis was carried out using 200g of charged indium, inclusions of excess indium were contained in the ingots grown at P_P lower than about 5 atm. To avoid the In inclusions, it was necessary to reduce either the growth rate or the amount of charged indium. In this experiment, the amount of charged indium was reduced to 20g and, consequently, ingots free from inclusions were obtained at P_P in the range of 1.5-30 atm. Carrier concentrations at the first-to-freeze portions of grown ingots are plotted in Fig. 4 as a function of P_P. The effect of P_P on the carrier concentration is not as large as that of T_{max}. The carrier concentration scarcely depended on P_P in the range of 5-30 atm. At lower P_P than about 5 atm, the carrier concentration seemed to depend on P_P. Similar P_P dependence of carrier concentration was found for InP crystals grown by the synthesis solute-diffusion method ($P_P = 0.6$-1.2 atm) (8). Therefore, it is reasonable to assume that Si contamination level increases with increasing P_P, and becomes saturated at higher P_P ($\gtrsim$5 atm).

We found that carrier concentrations in grown ingots were different depending on lot or supplier of the charged indium even if T_{max} and P_P were fixed to certain values, as shown in Fig. 5. Differences in the carrier concentration profiles in Fig. 5 were found to be closely related to differences in degree of oxidation of the charged indium. The lowest profile was obtained for the ingot synthesized using the most heavily oxidized indium. The degree of oxidation of the charged

Table I. Spark source mass spectrographic analyses of nominally undoped InP ingots

Sample (carrier conc.)	Impurity concentration (ppma)									
	Si	Sn	S	Te	Zn	Mg	Cu	C	N	O
No. 1 (4×10^{15} cm^{-3})	0.4 (1.6×10^{16} cm^{-3})	ND*	ND**	ND*	0.4	0.5	0.06	6	1	6
No. 2 (2×10^{17} cm^{-3})	15 (6×10^{17} cm^{-3})	ND*	ND**	ND*	0.2	0.6	0.04	5	4	8

ND*: <0.1 ppma, ND**: <0.05 ppma.

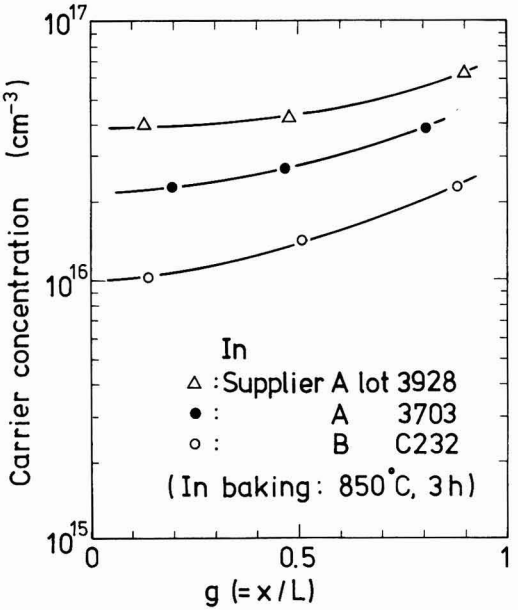

Fig. 5. Carrier concentration profiles for ingots grown by using charged indium of different lots or suppliers. Synthesis conditions are same for all samples.

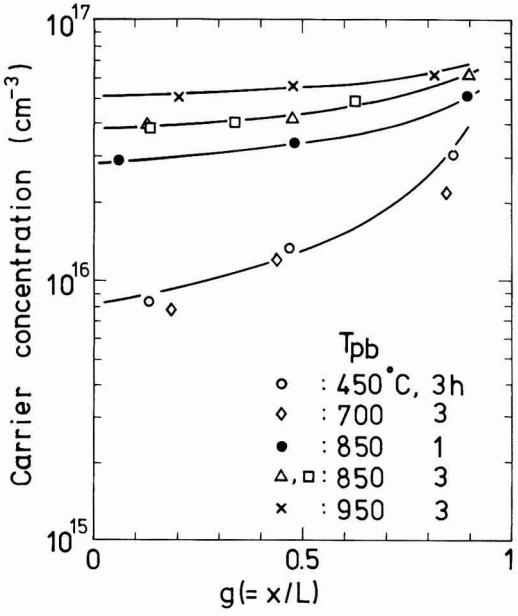

Fig. 6. Carrier concentration profiles for ingots grown by using charged indium prebaked at different temperature (T_{pb}).

indium was examined by an amount of a scum formed on a molten indium. This fact suggests that oxides of indium included in the charged indium have effects on the Si contamination process. Therefore, we tried to eliminate indium oxides contained in the charged indium, and examined effects of the elimination on the carrier concentration. The elimination was made by prebaking the charged indium in vacuum before synthesis. The prebaking temperature T_{pb} was varied from 450° to 950°C. All charged indium used here were from the same lot. The ingots were grown by using 200g of charged indium under the following conditions; P_P = 8 atm and T_{max} = 1100°C. Figure 6 shows carrier concentration profiles for the ingots grown by using the charged indium baked at different T_{pb}. With increasing T_{pb}, the carrier concentration increases and its distribution becomes flat. Especially, a remarkable difference is observed in carrier concentrations between T_{pb} = 700°C and 800°C. This difference can be explained by the difference in removal rates of indium oxides at both temperatures, because indium oxides such as In_2O_3, In_2O, or InO are sublimated or decomposed in vacuum at temperatures higher than about 800°C. From these results, it can be concluded that indium oxides in the charged indium suppress the reactions causing Si contamination. The effect of indium oxides on the reaction causing Si contamination can be understood qualitatively as follows. According to Bachmann *et al.* (1), an SiO vapor as a source for Si contamination is provided via the reaction

$$10\,SiO_2(s) + P_4(g) \rightleftharpoons 10\,SiO(g) + P_4O_{10}(g) \quad [1]$$

When indium oxides are present in the charged indium, they will be reduced by phosphorus vapor and a P_4O_{10} vapor will be produced prior to the reduction of SiO_2. An increase in P_4O_{10} partial pressure in the ampul by the reduction of the indium oxides can force reaction [1] to proceed to the left-hand side, *i.e.*, suppress the production of SiO vapor.

When the charged indium was prebaked in vacuum, most of the indium oxides were transported to a lower temperature region in the ampul. The presence of indium oxides at a lower temperature region during synthesis had no effect on carrier concentrations in grown ingots. This fact means that the reduction of indium oxides, as well as the reduction of silica, by phosphorus vapor requires a high temperature (~ 1000°C).

Effective distribution coefficient for Si in InP, k_e(Si). —As described in the previous section, distributions of Si concentration in nominally undoped ingots are remarkably different depending on the Si contamination level. Therefore, it is meaningless to evaluate k_e(Si) for those ingots. We prepared Si-doped ingots with carrier concentrations higher than 10^{18} cm^{-3} to examine k_e(Si). The ingots were grown under the following conditions: T_{pb} = 700°C, T_{max} = 1050°C, and P_P = 7 atm. For successful Si doping, it was necessary to dissolve completely the Si pieces into the indium melt before the synthesis. When the Si pieces floated on the surface of the indium melt during the synthesis, they were attacked by phosphorus vapor and transferred to a low temperature region in the ampul and, consequently, Si doping was unsuccessful.

Typical carrier concentration profiles for Si-doped ingots along the growth direction are shown in Fig. 7. Doping efficiencies of Si for these ingots were about 50%. It is reasonable to assume that the profiles represent the segregation behavior of Si because the Si contamination levels in these ingots are estimated, from the growth conditions, to be lower than 2×10^{16} cm^{-3}. The profiles obey the normal freezing relationship and their slopes give k_e(Si) = 0.53. Figure 7 also shows carrier concentration profiles in LEC single crystals grown by using the nominally undoped ingots described in the previous section. We found that the average carrier concentrations in the LEC crystals were in good agreement with those in the starting materials (9). The profiles for the LEC crystals also obey the normal freezing relationship and have a same slope as that for the Si-doped ingots. These facts indicate that the carrier concentrations in the LEC crystals are dominated by Si contents involved in the starting materials.

Summary

We studied experimentally Si contamination of polycrystalline InP ingots synthesized using quartz boats

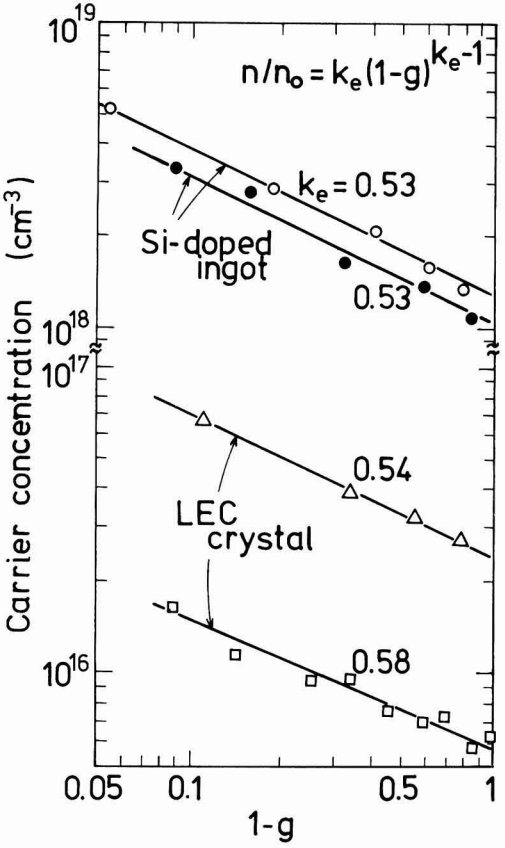

Fig. 7. Carrier concentration profiles for Si-doped ingots and for LEC crystals grown by using nominally undoped ingots. All curves obey the normal freezing relationship.

via the horizontal Bridgman technique. Silicon contamination levels were evaluated by measurements of carrier concentrations and by spark source mass spectrographic analyses. Good agreements between carrier concentrations and Si contents were obtained. Dependences of the Si contamination level on the synthesis conditions such as maximum temperature in the indium melt, phosphorus pressure in the ampul, and prebaking temperature of the charged indium were investigated. Among these conditions, maximum temperature in the indium melt was found to be the most dominant factor. Silicon contamination levels scarcely depended on phosphorus pressure in the range of 5-30 atm, while they decreased at lower phosphorus pressure than about 5 atm with decreasing phosphorus pressure. With increasing prebaking temperature of the charged indium, Si contamination levels were increased. This result is explained by taking into account the fact that indium oxides in the charged indium, which suppress the reaction for Si contamination, are eliminated through the prebaking process.

As a result of the investigations described above, it has been enabled to prepare high purity InP ($N_d - N_a = 3.2 \times 10^{15}$ cm^{-3}, $\mu_{77K} = 37{,}000$ cm^2/V · sec) at a growth rate of 3 mm/hr even if quartz boats are used.

To examine the segregation behavior of Si in InP, we also prepared intentionally Si-doped ingots in which Si contamination levels were neglected as compared with Si doping levels. Carrier concentration profiles for these ingots along the growth direction obeyed the normal freezing relationship and, consequently, gave the effective distribution coefficient for Si in InP, k_e(Si) = 0.53. Carrier concentration profiles for LEC single crystals grown by using nominally undoped ingots contaminated by Si also obeyed the normal freezing relationship and had a same slope as that for the Si-doped ingots. This result indicates that carrier concentrations in the LEC crystals are dominated by Si contents involved in the starting materials.

Acknowledgment

The authors would like to thank Dr. N. Niizeki, Dr. H. Takata, and Dr. K. Kudo for their encouragement and support through this work, and Mr. C. Honma, Musashino Electrical Communication Laboratory, for spark source mass spectrographic analysis.

Manuscript submitted May 21, 1980; revised manuscript received Oct. 17, 1980.

Any discussion of this paper will appear in a Discussion Section to be published in the December 1981 JOURNAL. All discussions for the December 1981 Discussion Section should be submitted by Aug. 1, 1981.

Publication costs of this article were assisted by Nippon Telegraph and Telephone Public Corporation.

REFERENCES

1. K. J. Bachmann, E. Buehler, J. L. Shay, and D. L. Malm, "Gallium Arsenide and Related Compounds 1974," (Inst. Phys. Conf. Ser. No. 24) p. 21 (1975).
2. K. J. Bachmann, L. Clark, Jr., E. Buehler, D. L. Malm, and J. L. Shay, *J. Electron. Mater.*, **4**, 741 (1975).
3. R. L. Henry and E. M. Swiggard, *ibid.*, **7**, 647 (1978).
4. G. A. Antipas, "Gallium Arsenide and Related Compounds 1976," (Inst. Phys. Conf. Ser. No. 33b) p. 55 (1977).
5. J. B. Mulline, A. Royle, B. W. Straughan, P. J. Tufton, and E. W. Williams, *J. Cryst. Growth*, **13/14**, 640 (1972).
6. G. G. Baumann, K. W. Benz, and M. H. Pilkun, *This Journal*, **123**, 1232 (1976).
7. K. J. Bachmann and E. Buehler, *ibid.*, **121**, 835 (1974).
8. A. Yamamoto and C. Uemura, *Jpn. J. Appl. Phys.*, **17**, 1869 (1978).
9. C. Uemura, S. Shinoyama, A. Yamamoto, and S. Tohno, Proceedings of ICCG-6, To be published.

Optical Properties of GaAs and Its Electrochemically Grown Anodic Oxide from 1.5 to 6.0 eV

D. E. Aspnes,* G. P. Schwartz,* G. J. Gualtieri, A. A. Studna, and B. Schwartz*

Bell Laboratories, Murray Hill, New Jersey 07974

ABSTRACT

Spectroscopic ellipsometry has been used to nondestructively study the optical and interface properties of the GaAs-electrochemically grown anodic oxide system over the energy range 1.5-6.0 eV. Values of the dielectric function of GaAs differ by up to 30% from previously published spectra due to improved sample preparation techniques. Values of the dielectric function of the oxide agree within several percent with previous measurements. Upper limits to the thickness of a layer modeled as amorphous arsenic (a-As) at the GaAs-oxide interface are 3 and 10Å for 60 and 75V oxides grown on <111>B and <100> surfaces, respectively, at 0.1 mA cm^{-2} constant current in a phosphoric acid/glycol based electrolyte. The major discrepancy between measurements and ideal three-phase model calculations arise from the interface region between oxide and ambient. This region shows a total distributed density deficit equivalent to 10Å lost material, probably due to leaching of As_2O_3. A complete description of the optical properties of the oxide requires a small absorptive component in the nominally transparent energy range below 4.5 eV. This absorptive component is equivalent to 0.2% and 0.9% by volume of a-As for the 60 and 75V oxides, respectively. The infrared refractive indexes for the two oxides, calculated from a Sellmeier dispersion relation with the absorptive component removed, are 1.777 and 1.717, respectively.

Intrinsic advantages of GaAs as a material for high-speed electronic devices have stimulated widespread research to develop a passivating oxide by thermal, plasma, and electrochemical anodization techniques. However, the composition, uniformity, and interface properties of native oxides on GaAs all depend rather strongly on the method by which the oxides are prepared. Thermally grown oxides consist almost entirely of Ga_2O_3 owing to the volatility of As and As_2O_3 at typical growth temperatures (1-4). Plasma-grown oxides are primarily mixtures of Ga_2O_3 and As_2O_3, but show accumulations of elemental As in both bulk and interface regions (3, 5-9). Although bulk uniformity and interface widths in electrochemically grown anodic oxides also depend on electrolyte and anodization conditions (10-12), recently reported Raman studies of thermal (13), plasma (14), and electrochemical (14) grown oxide films on GaAs indicate that the elemental arsenic content of the as-grown electrochemically formed oxides can be suppressed for low current density growth. A second feature associated with lowering the current density, and consistent with the Raman scattering results, appears to be a decrease in the width of the oxide-substrate interface region for electrochemically grown anodic oxides (12).

Preliminary reductions of complex reflectance ratio ($\tan\psi$, $\cos\Delta$) spectra that we measured for electrochemically grown anodic oxides supported the above conclusions, and indicated that nonuniformity and interface effects could be as much as an order of magnitude smaller than those observed in our previous work on films produced by rf-plasma (8, 9) and constant-voltage electrochemical (15) anodization methods. This suggested that more accurate values of the intrinsic dielectric response of anodic oxide films could be obtained. These data not only would be of interest in their own right, but also would serve as input data for determining more accurately from their dielectric response the composition, density, interface, and other microstructural parameters of other native oxides grown by different techniques. Moreover, since our previous investigations (15), methods using automatic spectroscopic ellipsometers have been developed (16, 17) for assessing the effectiveness of chemical stripping and cleaning procedures in real time, allowing dielectric function data that are more accurate than previously published spectra (18) to be obtained for the GaAs substrate material. Because these substrate data are used to determine interface and oxide parameters, more accurate analysis is made possible. Finally, we wished to establish new limits to the widths and possible compositions of the interface regions of the electrochemically grown oxides, taking advantage of the sensitivity of spectroscopic ellipsometry to these parameters (7-9, 19).

Since dielectric dispersion data are not available for both Ga_2O_3 and As_2O_3, we found it necessary to generalize the procedure that was previously developed for interface analysis with spectroscopic ellipsometry as it was applied to the thermally grown oxide on Si (20). This was done by using a Sellmeier representation to separate the slowly varying intrinsic dielectric response of the oxide from the more rapidly varying interface-related residual interference oscillations that appear in an approximate three-phase model solution. Thus both oxide and interface parameters could be obtained. This more general approach should also be useful for other oxide systems which can only be obtained in thin film form and for which bulk analytic dispersion expressions have not or cannot be determined.

Experimental

In this work, we analyze in detail two oxide films grown under 0.1 mA cm^{-2} constant current conditions in a phosphoric acid/glycol-based [AGW (21)] electrolyte. The substrates used were n-type GaAs single crystals with carrier concentrations 2×10^{16} cm^{-3} and $\sim 1 \times 10^{18}$ cm^{-3}. The surface orientation of the lightly doped sample was <111>B and that of the heavily doped sample was <100>. Surfaces were prepared by chemomechanical etch-polishing in bromine-methanol solutions. Surface quality was checked by measuring pseudo-(apparent) dielectric function spectra of chemically etched samples prior to anodization. Anodization was performed under white-light illumination to flood the space-charge region with carriers and eliminate any doping dependence of the anodization process. Final oxide thicknesses were ~1200 and

* Electrochemical Society Active Member.
Key words: ellipsometry, dielectrics, interface.

~1500Å corresponding to limiting potentials of 60 and 75V for the lightly and heavily doped samples, respectively.

Optical data were obtained from 1.5 to 6.0 eV with an automatic spectroscopic ellipsometer described in detail elsewhere (22). The angle of incidence was 67.08°. The data were corrected for the optical activity of the quartz Rochon polarizers (23). Anodized samples were rinsed with methanol prior to measurement. Substrate spectra were obtained after chemically stripping the anodic films in a 1:1 mixture of HCl/methanol. This procedure yielded the highest ϵ_2 value [cleanest, least disordered, and/or microscopically smoothest surface (17)] at the 4.75 eV E_2 peak for these substrates. The peak ϵ_2 values after anodizing and stripping were ~0.5 higher than the corresponding values before anodizing, indicating that the anodizing/stripping sequence was improving surface quality (24). To minimize oxidation and contaminant adsorption effects, all chemical processing steps were performed with the samples already aligned in the ellipsometer and enclosed in a dry N_2 atmosphere in a windowless cell. Tanψ, cosΔ, and pseudodielectric function spectra were obtained for the anodized and nominally bare stripped samples, respectively.

Optical Analysis

The basic procedure for determining interface properties from spectroscopic ellipsometric data was developed initially for application to the Si-SiO_2 system and is discussed in detail elsewhere (8, 20, 25). Briefly, in the previous work dielectric function data for crystalline Si, fused quartz, and various possible interface materials were used to calculate in an n-phase laminar model tanψ, cosΔ spectra from 1.5 to 5.8 eV in terms of three frequency-independent free parameters, d_{ox}, f_v, and d_{int}. These free parameters represented the thickness and void fraction (density deficit) of the oxide and the thickness of the interface region, respectively. The calculated spectra were then compared to the measured spectra, with the best-fit values of the free parameters and the residual mean square deviation being determined systematically and objectively by linear regression analysis (LRA) (26). The LRA analysis also provided correlation coefficients and 90% confidence limits to show whether the data were in fact determining the parameters in addition to showing how well the models were fitting the data.

For the Si-SiO_2 system, the method was based on the existence of an accurate analytic Sellmeier expression for the dielectric response of fused quartz (27), which was used with the density deficit parameter f_v to represent the dielectric response of the SiO_2 overlayers. Although Sellmeier expressions have been given for GaAs oxide films (28, 29), the known sensitivity of oxide properties to preparation method suggests that a better approach in the absence of accurate bulk data would be to determine the Sellmeier coefficients themselves in the data reduction process. This is the procedure that we develop here.

Why should a Sellmeier representation by necessary? In principle, the dielectric response of the oxide can be obtained directly by solving the three-phase (substrate, oxide, ambient) laminar model given the tanψ, cosΔ spectra and the dielectric functions of substrate and ambient. For example, the measured tanψ, cosΔ spectra of the 60V AGW oxide on the <111>B GaAs substrate shown in Fig. 1 and the approximate bulk dielectric response of this substrate shown in Fig. 2 can be used in the ideal three-phase model to calculate the approximate dielectric function of the oxide as shown in Fig. 3. Here, the thickness d_{ox} = 1203Å was chosen to make ϵ_2 "zero" in the transparency region below 4.5 eV. These results are calculated without regard to interface effects because the three-phase model supposes mathematically sharp boundaries.

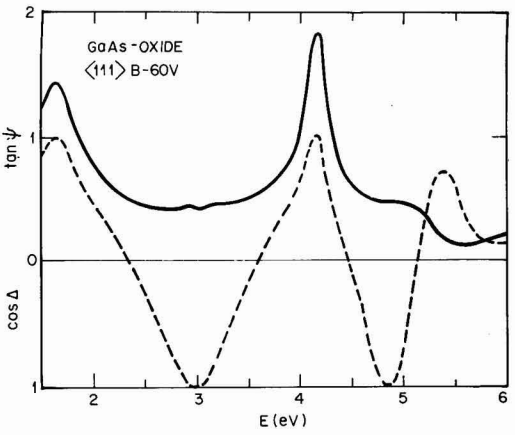

Fig. 1. tanψ, cosΔ spectra for a <111>B GaAs sample electrochemically anodized to 60V.

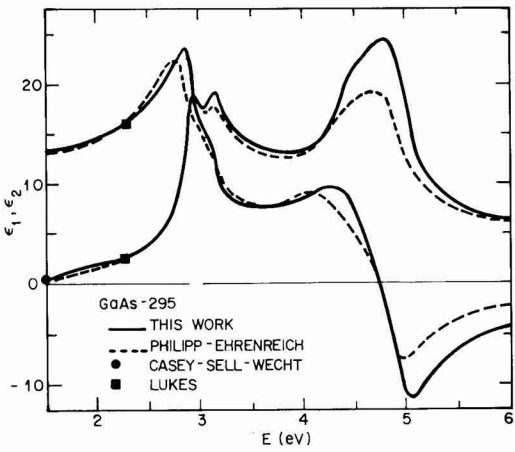

Fig. 2. Ellipsometrically determined dielectric response of the GaAs substrate for the sample of Fig. 1. Also shown for comparison are previous spectra [after Ref. (18)] and single-wavelength results [after Ref. (34) and (35)].

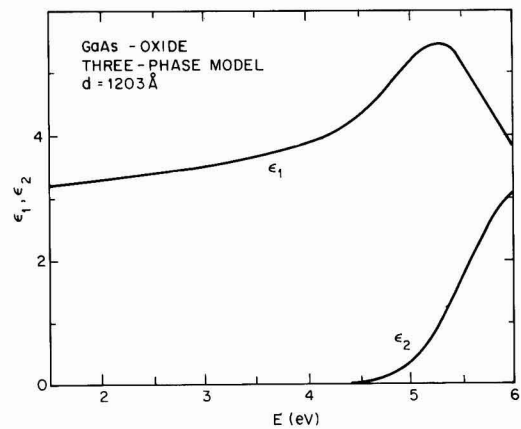

Fig. 3. Approximate dielectric response of a <111>B-60V anodic oxide calculated in the three-phase model from the data of Fig. 1 and 2.

In fact, ϵ_2 is not zero but rather exhibits small oscillations about a slowly varying background. This can be seen clearly in Fig. 4, which shows the ϵ_2 results of Fig. 3 on an expanded scale. The period of the oscillations follows the thickness (compare 60V <111>B and 75V <100> oxide calculations), which shows that they are not part of the intrinsic response of the oxide. Rather, they appear because the three-phase model, with its mathematically sharp boundaries, does not fully describe this system. As previously discussed (8), these oscillations arise from the growth and collapse of s- and p-polarized standing waves within the oxide as the wavelength is scanned. The standing waves modify the field strengths at the film boundaries and consequently the sensitivity to the interface regions. They therefore carry the information desired about the interface regions. Qualitatively, Fig. 4 appears to show that the interface regions of the 60V <111>B AGW oxide are narrower than those of the 75V <100> oxide, but not so narrow as those of the Si-SiO_2 system (20) whose data are also shown for comparison. In fact, we shall show that the major source of the oscillations for the GaAs-oxide system is the oxide-ambient interface region, and that the GaAs-AGW oxide interface region is actually narrower than that between Si and its thermally grown oxide.

To analyze these data for the properties of the interface regions, it is clear that these oscillations must be separated from the slowly varying intrinsic dielectric response of the oxide. Because the oscillations are very small for the 60V oxide, of the order of 1% of $|\epsilon|$, the three-phase-model solution is already a fairly good approximation to the intrinsic response. Accordingly, for simplicity we first use LRA to fit a Sellmeier function to the three-phase solution for ϵ_1 in the region of transparency below 4.5 eV and therefore average out the oscillations that contain the interface information. ϵ_2 in the same region is simply set equal to zero. These analytic expressions are now used as the initial approximation to the oxide response.

A complete description of the oxide film (excluding interface regions) can now be accomplished over the region of transparency with the Sellmeier expression and three frequency-independent free parameters representing, respectively, the oxide thickness, d_{ox}, a volume void fraction or distributed density deficit, f_v, and a volume fraction of optically absorbing material, f_a. The total dielectric response of the oxide film can then be calculated by effective-medium theory (30) using these parameters, the Sellmeier expression for the approximate "intrinsic" response of the oxide, $\epsilon = 1 + i0$ for the voids, and a suitable representation for the dielectric response of the optically absorbing component. Based on available data for this system, we choose the latter to be given by that of amorphous arsenic (a-As) (31), in which case $f_a = f_{a-As}$.

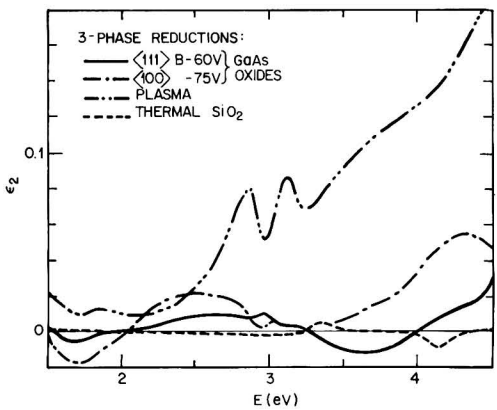

Fig. 4. Energy dependence of ϵ_2 on an expanded scale for selected oxide films in the region of transparency of oxides on GaAs.

The reason for treating an optically absorbing component as an extrinsic feature can be understood by examining the absorptive tails in ϵ_2 in Fig. 4. These differ in all three cases, which shows that optical absorption is clearly not part of the intrinsic response of the oxide. The justification for f_v is less obvious. It concerns the boundary condition that d_{ox} shall be chosen so ϵ_2 is "zero" in the transparency region. This condition obviously cannot be satisfied over the entire transparency range because of the small interface oscillations. Model calculations quickly show that these oscillations may average about zero, or above zero, or below zero depending on interface compositions and widths. The requirement that ϵ_2 oscillate about zero is a fact completely arbitrary, and to make it imposes unintended constraints on the solution.

Now because the optical thickness $n_{ox}d_{ox} = \sqrt{\epsilon_{ox}}d_{ox}$ is the fundamental parameter describing interference effects in a thin transparent film, it is clear that changing d_{ox} to properly position ϵ_2 with respect to zero will also affect ϵ_1 since the energy at which interference structures occur is also fixed by the properties of the film. Thus ϵ_1 must be decoupled from d_{ox}. This is the purpose of f_v, which acts essentially as a simple scaling parameter, but one which also describes the amount of polarizable material per unit volume in the film. By incorporating f_v into the model we have generalized the boundary condition to the simple requirement that the interface oscillations shall vanish in the correct laminar model solution for the oxide properties. We re-emphasize that the use of an intermediate Sellmeier representation with corrections as outlined above is legitimate because the GaAs-AGW oxide system is already well approximated by the three-phase model, and that the interface corrections are very small.

Results

Dielectric function of GaAs.—The dielectric function that we consider to be most representative of the bulk dielectric response of the 2×10^{16} cm^{-3}, <111> B-oriented n-type substrate used for the 60V anodization, and therefore that most appropriate for interface analysis, is shown in Fig. 2. This was obtained by *in situ* stripping of the AGW oxide with 1:1 HCl/methanol solution. The peak value observed for ϵ_2 was 23.89 at 4.75 eV. To obtain a better estimate of the intrinsic dielectric response of the substrate in the absence of etching-induced surface disorder, an additional 2Å of a-GaAs (32) was removed mathematically, bringing the ϵ_2 peak to 24.34. A direct experimental proof of the existence of such a disordered layer is not possible, but its presence can be inferred from similar measurements on Ge (33) and because the "bare substrate" dielectric function so obtained gave a somewhat lower residual in the interface analysis.

Whether the dielectric function obtained here accurately represents the intrinsic dielectric response of pure single crystal GaAs is a separate question and one more difficult to assess, but we believe that the ϵ spectra in Fig. 2 do so to within 5%. Bromine-methanol polished and anodized <111>B samples could be stripped with HCl/methanol, HCl/H_2O, or NH_4OH/H_2O solutions and consistently produced peak ϵ_2 values in the 23.0-23.9 range. By the "biggest-is-best" criterion (16, 17) the spectra corresponding to the largest peak value is the best approximation to the true response. Differences may represent surface roughness on a microscopic scale; the highest ϵ_2 values were generally observed by stripping once, with repeated treatments usually resulting in a gradual decline. This history-dependent sample behavior shows that in general the dielectric function spectrum actually used for analysis of very thin interfaces must be that measured on the

stripped sample itself, and not taken from a different sample or from the literature.

Also shown for comparison in Fig. 2 are the previous best spectra for GaAs, obtained from a Kramers-Kronig transform of reflectance data measured over the range 1-27 eV (18). The differences in energy positions of the structures are probably due to the fact that the ellipsometric data were obtained with a 17 meV energy spacing, approximately one-third that of the reflectance data. Consequently, the ellipsometric data were able to follow the intrinsic GaAs structure more faithfully. The substantial discrepancy in absolute values is almost certainly due to the presence of natural oxide or contamination layers on the reflectance samples, which could not be stripped *in situ* as were the ellipsometric samples.

Other single-wavelength values also shown in Fig. 2 are those of Casey *et al.* (34) who found $\alpha = 1.6 \times 10^4$ cm^{-1} at 1.5 eV compared to our value of 1.5×10^4 cm^{-1}, and Lukes (35), who obtained $\epsilon = (16.11 \pm 0.08) + (i2.41 \pm 0.40)$ at 5461Å (2.27 eV), compared to our value $16.13 + i2.80$. The agreement is satisfactory. We add that the ϵ_1 and ϵ_2 spectra obtained here were Kramers-Kronig consistent to better than 0.5%.

Approximate dielectric function of GaAs oxide.—The substrate dielectric function described above was used in the three-phase model to obtain the approximate dielectric response shown in Fig. 3. We now fit a four-term Sellmeier dispersion curve of standard form

$$\epsilon_1(E) = 1 + \sum_{i=1}^{4} \frac{E_{gi}E_{oi}}{E_{gi}^2 - E^2} \qquad [1]$$

to these data over the region of transparency. Two of the values E_{gi} are fixed by the known energies of the centroids of the lattice transitions at $E \cong 600$ $cm^{-1} = 0.075$ eV (28, 36) and the ultraviolet bonding-antibonding transitions at $E \cong 16$ eV (37).

The value of E_{01} that pertains to lattice absorption follows immediately from E_{g1} and the difference between the infrared dielectric constant [$\epsilon_\infty \sim 3.20$ (28)] and the 1 kHz dielectric constant ($\epsilon_0 \sim 8.2$) (38), that is, $E_{01} \cong 0.35$ eV. This presumes a contribution no greater than a few percent from water contained within the as-grown oxide, as seems reasonable from infrared absorption measurements on similar oxides (28), although the assumption is noncritical because this term has very little effect in the visible-near u.v. spectral range. Because the dispersion representation must describe near-edge absorption, Fig. 3 shows that 5.5 eV is a natural choice for E_{g2}. E_{g3} is essentially arbitrary, but a value of 7.5 eV will adequately describe midrange absorption.

The remaining three parameters are the amplitudes E_{02}, E_{03}, and E_{04}. We determine them by fitting Eq. [1] by LRA to the real part of ϵ_1 in Fig. 3 from 1.5 to 4.8 eV, obtaining 1.62 ± 0.27 eV, 5.5 ± 1.9 eV, and 18.8 ± 3.7 eV, respectively. The large uncertainties in E_{03} and E_{04} do not result from a poor fit, but rather originate because the third and fourth oscillators are highly correlated ($C_{34} = -0.994$). Since these values simply define a starting point for interface analysis, we shall defer a discussion about the fitted values until the section "Intrinsic oxide response."

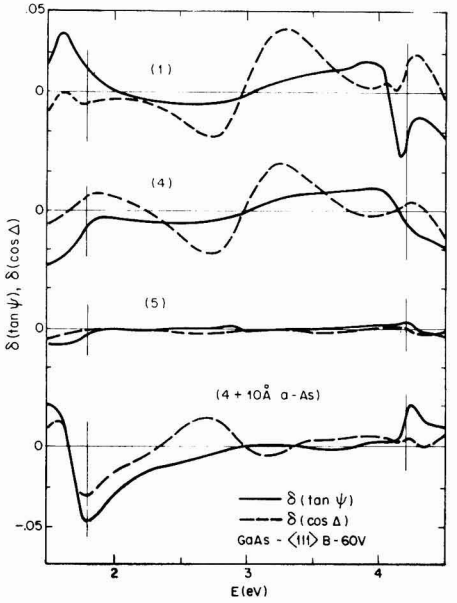

Fig. 5. Spectral dependences of discrepancies between experimental and theoretical spectra for various models for the ⟨111⟩ B-60V AGW oxide on GaAs: (top) 1-parameter model, using the Sellmeier oxide thickness as the single free parameter; (upper middle) 4-parameter model including an a-As interface, voids, and a-As in the oxide; (lower middle) as above, but including a density-deficient outer region; (lower) as above but with 10Å of a-As assumed at the GaAs-oxide interface.

Interface analysis.—Wavelength-dependent discrepancies between the tanψ, cosΔ data of Fig. 1 and the predictions of selected models are shown for the electrochemically grown 60V anodic oxide in Fig. 5. Model parameters for this oxide are listed in Table I.

The simplest model assumes that the Sellmeier expression derived in the preceding section is directly applicable and that there are no interfaces. Then the only free parameter is the oxide thickness, d_{ox}. This is determined by LRA to be 1197.5 ± 0.5Å with a residual 0.020 as summarized in Table I. The actual fitting was done over the range 1.8-4.2 eV to eliminate the effects of experimental artifacts at the low-intensity long-wavelength limit of the ellipsometer, and to eliminate intrinsic oxide absorption at higher energies which is not included in the Sellmeier model. The range is indicated by the vertical lines in Fig. 5. Neither tanψ nor cosΔ has its wavelength dependence predicted very accurately, but this is not surprising since interface effects are completely neglected. The result essentially establishes a point of reference from which to judge more elaborate models. It should be noted

Table I. Values of free parameters, 90% confidence limits, and residuals for models of an anodic oxide electrochemically grown to 60V on a ⟨111⟩B GaAs substrate with $N_0 \sim 2 \times 10^{16}$ cm^{-3}

Model	Inner interface		Oxide		Outer interface		Residual
	Composition	d (Å)	$10^3 f_{a\text{-}As}$	$10^3 f_v$	d (Å)	Composition	d (Å)	$10^3 \delta$
(1)	—	—	—	—	1197.5 ± 0.5	—	—	20.0
(2)	—	—	—	−2.9 ± 3.9	1195.3 ± 3.2	—	—	19.6
(3)	—	—	1.8 ± 0.6	20.5 ± 7.9	1212.16 ± 6.0	—	—	15.4
(4)	a-As	−0.9 ± 1.9	1.4 ± 0.8	19.3 ± 8.1	1211.9 ± 6.1	—	—	15.3
(5)	a-As	0.31 ± 0.29	2.1 ± 0.1	14.9 ± 1.1	1151.8 ± 1.9	15% void	67.6 ± 2.1	2.08
(6)	—	—	2.0 ± 0.1	14.6 ± 1.2	1151.8 ± 2.1	15% void	67.6 ± 2.3	2.11
(7)	a-As	0.22 ± 0.30	1.8 ± 0.1	15.5 ± 1.3	1178.1 ± 1.5	25% void	43.3 ± 1.6	2.37
(8)	a-As	0.18 ± 0.32	2.4 ± 0.4	15.1 ± 0.3	1121.2 ± 3.1	10% void	96.9 ± 3.3	2.46
(9)	a-As	10Å (fixed)	5.3 ± 1.0	13.8 ± 10.5	1136.4 ± 19.6	15% void	77.6 ± 21.9	20.3

that the maximum excursion in $\delta(\tan\psi)$ is only 2% of the peak value in Fig. 1, re-emphasizing our earlier point that the three-phase model is already a very good approximation by the usual standards applied to ellipsometric data.

As the model is made more general by allowing a density change and an absorptive fraction in the oxide, very little improvement occurs as shown in Table I. Virtually no change occurs upon introducing the void fraction f_v, but that is expected because the initial solution from which the Sellmeier coefficients were determined had already set a zero-order density scale. A 25% reduction in the residual occurs when an absorptive component is allowed through a volume void fraction, f_{a-As}, of amorphous arsenic.

We now investigate the effect of interfaces. Since elemental arsenic is known or anticipated to be at the substrate-oxide interface from previous studies, we suppose an interface layer of a-As and determine its thickness by LRA. The results are shown in Table I and at the bottom of Fig. 5. The results show quite definitely that no a-As appears at the interface of this electrochemically grown anodic oxide. In fact, even with three additional free parameters with respect to the original three-phase model we have only succeeded in reducing the residual by 25%, with nearly all of that coming through the assumption of an absorbing fraction in the bulk oxide. Thus the main source of discrepancy between measurement and model must be due to yet another effect.

The small value of interface thickness makes it clear that the calculation has already been optimized with respect to the GaAs-oxide interface, and simply substituting other possible interface materials such as a-GaAs or mixtures of a-As with the oxide will not reduce the discrepancy between theory and experiment. We are thus led to look elsewhere for the cause of the remaining discrepancy.

Noting that radioactive tracer (10), photoemission (39, 40), and ISS (12) studies have all shown As_2O_3 depletion at the oxide-electrolyte interface for anodizations in glycol-based electrolytes, we are led to suppose a density-deficient outer layer at the oxide surface. We therefore generalize the model to include an exterior interface region by allowing an additional density deficit in the outer region of the oxide and using the thickness of this region as a fifth free parameter in an LRA analysis. The results assuming a 15% density-deficient outer layer are shown in Fig. 5 and Table I. The assumption of a density-deficient outer layer results in a sevenfold decrease in the residual and thus accomplishes what the preceding three free parameters could not, *i.e.*, the virtual elimination of discrepancies between the experimental measurement and the $\tan\psi$, $\cos\Delta$ spectra. Furthermore, the discrepancies are essentially eliminated not only over the fitted region but also over the end regions as well. Thus the greatest single source of the discrepancy between the actual GaAs-oxide system and the ideal three-phase model does not occur at the GaAs-oxide interface, but rather at the oxide-ambient interface. The GaAs-oxide interface for electrochemically grown anodic oxides is in fact exceedingly sharp.

To emphasize that the sensitivity to the GaAs-oxide interface region is indeed real, we have calculated the result of minimizing the remaining four parameters in LRA supposing that 10Å of a-As exists at the GaAs-oxide interface. As shown in Fig. 5 and Table I, this artificially imposed condition results in a residual that is larger than that calculated in the initial three-phase model solution, and the good agreement between measured and calculated $\tan\psi$, $\cos\Delta$ spectra is eliminated. We may conclude that 10Å of a-As or its equivalent, as for example an interface 40Å wide consisting of 25 volume percent (v/o) a-As, would be easily detected. Clearly, the statistically negligible thickness of the interface, 0.3 ± 0.3Å, makes meaningless the question of its composition. The point can be emphasized by noting that the residual increases only by 0.00003 if the GaAs-oxide interface region is eliminated from the model entirely.

We have also investigated the effect of changing the void fraction of the outer interface. As can be seen from Table I, the data do not discriminate among density deficits in the 10-25 v/o range. However, all solutions converge on an effective density deficit of 10Å. Our measurements cannot distinguish whether this represents a nonstoichiometry resulting from surface leaching or microscopic roughness. As mentioned above, however, this result is entirely consistent with previous observations of As_2O_3 depletion in the outer film surface of these systems (10, 12, 39, 40). Because the actual depletion depth is sensitive to details of the electrolyte pH, current density, and maximum applied voltage, a further detailed comparison with previous results is not warranted.

The results of a similar analysis for the 75V anodic oxide electrochemically grown on the <100> surface are given in Table II. From Fig. 4, it can be anticipated that a larger absorbing fraction will be necessary to describe this oxide. As expected, the fraction is about four times larger and nearly equivalent to 1 v/o of a-As. The absorbing component of the bulk oxide now represents the single most significant factor in reducing the residual.

Once again, a full five-parameter LRA shows "no" GaAs-oxide interface region to within statistical uncertainty, although the solution is sufficiently indeterminate to allow a few Å to be present. However, the presence of an oxide-ambient interface region very similar to that detected on the 60V oxide is unambiguous. It is interesting to note that the density of the <100>-75V oxide is significantly less than that of the <111>B-60V oxide, indicating that oxide properties may be rather critically dependent on growth and substrate parameters.

Intrinsic oxide response.—The intermediate four-term Sellmeier oscillator representation of the oxides obtained in the three-phase model can now be replaced with expressions representing more accurately the intrinsic dielectric response of these oxides. We retain the characteristic oscillator energies, E_{gi}, and the amplitude, $E_{01} = 0.35$ eV, of the lowest oscillator and determine the remaining three amplitudes by an LRA fit to the dielectric function calculated in the effective-medium approximation from the intermediate representation and the void and a-As fractions calculated in the previous section. Values are given in Table III with and without the a-As contribution, although only

Table II. As Table I, but for an anodic oxide grown to 75V on a <100> GaAs substrate with $N_D \sim 10^{18}$ cm^{-3}

Model	Inner interface Composition	Inner interface d (A)	$10^3 f_{a-As}$	Oxide $10^3 f_v$	d (A)	Compositional	Outer interface d (A)	Residual $10^3 \delta$
(1)	—	—	—	—	1439.6 ± 0.8	—	—	36.8
(2)	—	—	—	−7.4 ± 5.7	1432.6 ± 5.5	—	—	34.5
(3)	—	—	8.2 ± 1.1	91 ± 14	1518.0 ± 12.7	—	—	17.1
(4)	a-As	4.3 ± 3.6	9.1 ± 1.3	91 ± 12	1515.9 ± 11.2	—	—	16.3
(5)	a-As	3.4 ± 3.3	9.3 ± 1.4	89 ± 11	1468.5 ± 12.4	15% void	50.6 ± 15.9	14.8
(6)	a-As	3.4 ± 3.3	8.8 ± 1.5	87 ± 15	1492 ± 19.5	25% void	26.7 ± 14.1	14.6
(7)	a-As	13.4 fixed	11.0 ± 1.4	82 ± 17	1445.6 ± 38	15% void	65 ± 34	18.2

Table III. Sellmeier oscillator energies for electrochemically grown anodic oxides on GaAs

	E_{g1}	60V with a-As	60V without a-As	75V with a-As	75V without a-As
E_{01}	0.075 eV	0.35 eV	0.35 eV	0.35 eV	0.35 eV
E_{02}	5.5	1.56	1.59	1.28	1.42
E_{03}	7.5	5.48	5.35	5.35	4.75
E_{04}	16.0	18.51	18.46	16.98	16.93
n_∞	—	1.781	1.777	1.734	1.717

the latter have meaning with respect to the intrinsic dielectric response of the oxide. Values of the infrared refractive index calculated from these results are also given.

Not surprisingly, a-As has its greatest effect on the lower-energy oscillators because its oscillator strength is greatest there. The reduction in amplitude of all oscillators, except that of the fixed term, E_{01}, is about 10% indicating a common dispersion characteristic (similar composition) for both, with basically a density difference responsible for the difference in dielectric response.

Discussion

The initial Sellmeier representation, together with the void and effective a-As volume fractions, define the wavelength-dependent dielectric response of these oxides over the region of transparency. The results for the 60 and 75V oxides of Tables I and II are shown in Fig. 6. The real and imaginary parts of the refractive index calculated from these spectra are shown in Fig. 7 along with selected results from the literature (28, 29, 36, 41-45) where with one exception (41) the effects of interfaces were neglected.

Figure 7 shows general agreement among refractive index values for as-grown oxides formed in glycol-based electrolytes. Specifically, our 60 and 75V spectra, those of Palik *et. al.* (28), and the single-wavelength datum of Umeno (36) are reasonably close. Data from Dinges (41) represent AGW oxides heat-treated in hydrogen for 1 hr at 300°C and have a slightly higher index. Choosing 5461Å = 2.27 eV as a common point, it is clear that the scatter is of the order of ± 0.03 units in n. This scatter may reflect differences in density as modeled here, but it could also represent small differences in the bulk film stoichiometry which arise from selective dissolution of one component in the electrolyte during growth. One should note that this latter feature is both current density and electrolyte

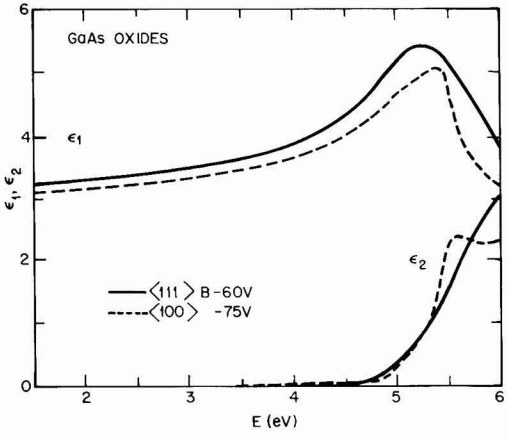

Fig. 6. Intrinsic dielectric functions for <111>B-60V and <100>-75V electrochemically grown anodic oxides deduced from the analysis of the section "Optical Analysis."

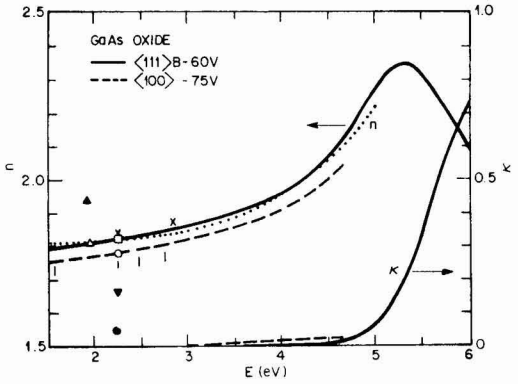

Fig. 7. As Fig. 6, but for refractive indexes. Selected data points and spectra are shown for comparison: AGW, as-grown: (. . . .) Palik *et al.*, Ref. (28); (△) Umeno *et al.* Ref. (36). AGW, heat-treated: (||||) Barnes and Schinke, Ref. (29); (▲) Umeno *et al.*, Ref. (36) (×) Dinges, Ref. (41). Aqueous anodization: (□) Dell'Oca *et al.*, Ref. (42). Oxygen plasma: (○) Weinreich, Ref. (43). Thermal: (▼) Löschke, *et al.*, Ref. (44); (●) Navratil, Ref. (45).

dependent, making it difficult to compare these oxides directly. Oxides produced in nonglycol-based electrolytes show similar scatter; our previous results (15) on samples heat-treated 2 hr at 200°C are essentially identical to our 60V AGW data (and are not shown for that reason), while the Barnes-Schinke data (29) are systematically lower. The single datum of Dell'Oca *et al.* (42) coincides with our 60V AGW result, while the oxygen plasma-grown value of Weinreich (43) coincides with our 75V AGW result.

Similar scatter also appears in the infrared refractive index evaluated from the Sellmeier dispersion expressions. The values of Palik *et al.* (28) and of Barnes and Schinke (29), 1.79 and 1.707, respectively, can be compared with our values including a-As in Table III, which are 1.78 and 1.73 for the <111>B-60V and <100>-75V oxides, respectively.

The measurement presented in Fig. 7 suggests that the index rises slightly by heat-treating in the 200°-300°C range, although it should be noted that Barnes and Schinke (29) reported a reduction in refractive index on five films heat-treated in N_2 at 250°C. We associate the general increase with heat-treating observed in most refractive index data with water removal and a slight densification. Ishii and Jepson (46) have studied the thermally induced desorption of products mass spectrometrically and observe that water is the primary species evolved below 300°C.

Heat-treatments above 300°C subject the film components to a variety of chemical reactions dependent on the nature of the ambient. In an inert atmosphere, the primary reactions involve the direct volatilization of As_2O_3 into the ambient and the reaction of As_2O_3 with the substrate according to the equation

$$As_2O_3 + 2GaAs \rightarrow Ga_2O_3 + 4As \qquad [2]$$

The latter reaction has been verified experimentally using Raman scattering (47, 48) and explained thermodynamically based on a determination of the Ga-As-O phase diagram (49). Heat-treatments in reducing atmospheres (principally H_2) will reduce both oxides to their respective elemental forms starting at the oxide-ambient interface at sufficiently high temperatures; the interfacial reaction between As_2O_3 and GaAs will occur simultaneously at the substrate interface. The resulting oxide composition will be difficult to specify and will be dependent on the temperature and length of the heat-treatment. Heating at elevated temperatures in an oxidizing ambient (O_2 or air, typically)

produces similar changes as described for an inert ambient, but in addition the oxide-ambient surface region may contain some fraction of $GaAsO_4$ (50). The diversity of the oxide compositions resulting from the various heating procedures probably accounts for the contradictory nature of reported index of refraction data for films treated above 350°C.

An analysis of the separate Ga_2O_3 and As_2O_3 contents in these films is presently not feasible by spectroscopic ellipsometry due to lack of comprehensive dielectric response data on the structural forms of Ga_2O_3 and As_2O_3 likely to be found in these amorphous films. More definitive information on composition has generally been obtained from photoemission (11, 39, 50), RBS (46), ion-induced x-ray emission (51), ion scattering (12), radioactive tracer (10), and Auger profiling (3) studies. There is some variance in the literature concerning the As_2O_3/Ga_2O_3 ratio of the bulk films, but it should be kept in mind that selective dissolution into the electrolyte during growth coupled with the growth rate (current density) would need to be evaluated for each data set separately before a valid comparison could be made. In addition, ion profiling techniques are subject to selective sputtering during analysis and compensation for ion and electron beam reduction must also be induced. The generally observed trend for AGW oxides grown at current densities of ~ 1 mA/cm^2 yields a bulk oxide of $\sim 1{:}1$ ratio between As_2O_3 and Ga_2O_3.

In our opinion, the question of elemental arsenic content in these films is better addressed by the nondestructive optical techniques such as spectroscopic ellipsometry and Raman scattering than by either photoemission or Auger profiling. One does not have to contend with electron and ion beam reduction artifacts of As_2O_3 nor with background interferences close to the substrate which greatly complicate the separation of elemental arsenic and substrate signals. Comparison of our data with profiling data would also require, among other things, careful attention to the question of sample annealing, since it is now known (47-49) that As can be generated at the oxide-substrate interface even if it were not present in as-grown samples. The interface width obtained in spectroscopic ellipsometry is also not subject to sputtering rate, selective sputtering, and ion knock-on effects. The liability of spectroscopic ellipsometry is clearly that it requires either *a priori* knowledge of the disposition of oxide interfaces or considerable physical intuition before a viable model can be constructed.

Our data additionally allow us to draw some inferences about overall film homogeneity. Initial three-phase model analysis of the 60V AGW oxide yielded $|\epsilon_2| < 0.01$ (0.2% in $|\epsilon|$) in the region of film transparency. This represents roughly a factor of 5 improvement over previously analyzed oxides (15) grown in a dilute aqueous solution of orthophosphoric acid at high current densities. Moreover, the AGW oxides showed no ambiguities in the three-phase solutions above the oxide absorption edge. Such ambiguities result from a convergence of substrate and ambient branches of the mathematical solution as absorption in the film gradually closes off optical contact to the substrate. If the film is inhomogeneous so that the three-phase model solutions do not strictly apply, the result is a loss of continuity in the calculated spectra. This effect was observed previously (15) in anodic films and tends to be pronounced in d-c and rf plasma oxidized films [see, *e.g.*, Fig. 5 and 6 in Ref. (8)]. The AGW oxides studied here display comparable bulk uniformity with thermally grown SiO_2 layers on Si. If the refractive indexes for Ga_2O_3 and As_2O_3 are taken to be of order 1.5 and 2.0, respectively, then these anodic films are homogeneous over the bulk (excluding boundary interfaces) to better than 2%.

The inner and outer interfaces deserve some final comment. The density-deficient oxide-air interface has been mentioned previously; it is modeled here as a distributed density deficit equivalent to 10Å of material lost uniformly from a 60Å surface region. Available experimental results (10, 12, 39, 40) strongly suggest that the actual physical situation corresponds to nonuniform As_2O_3 depletion from a comparable region. With respect to the width and elemental arsenic content of the oxide-GaAs interface, our present measurements are at variance with numerous published Auger and photoemission profile studies. Once again we wish to stress the importance of accounting for the current density and any subsequent heat-treating steps before directly comparing data. The present measurements are in fact capable of much higher detection sensitivity than those of Raman scattering (48), another nondestructive analysis technique that failed to observe elemental As in as-grown films. The present results show essentially no (0.3 ± 0.3Å) accumulated arsenic at the oxide-GaAs interface in the 60V oxide, although we feel that due to the possibility of systematic errors an absolute upper limit of 3Å is more reasonable. In addition to this elemental arsenic at the oxide-substrate interface, the bulk oxide would contain $\sim 0.2\%$ or another 2-3Å of absorbing material. The oxide-substrate interface width is essentially nil for AGW oxides produced under optimal (typically $I \leq 0.1$ mA/cm^2) current density conditions. It is somewhat surprising to note that the present measurements indicate that oxide-GaAs interfaces can in fact be obtained with widths comparable to or less than those found in thermally oxidized Si-SiO_2 systems (20). This suggests that the high density of interface states typically observed in oxide-GaAs *C-V* studies may have its origin in parameters unrelated to or at least not dominated by interfacial sharpness.

Manuscript received Aug. 12, 1980.

Any discussion of this paper will appear in a Discussion Section to be published in the December 1981 JOURNAL. All discussions for the December 1981 Discussion Section should be submitted by Aug. 1, 1981.

Publication costs of this article were assisted by Bell Laboratories.

REFERENCES

1. I. Shiota, N. Miyamoto, and J. Nishizawa, *This Journal*, **124,** 1405 (1977).
2. D. N. Butcher and B. J. Sealy, *J. Phys. D*, **11,** 1451 (1978).
3. K. Watanabe, M. Hashiba, Y. Hirohata, M. Nishino, and T. Yamashina, *Thin Solid Films*, **56,** 63 (1979).
4. I. Sakai, M. Hirose, and Y. Osaka, *This Journal*, **127,** 713 (1980).
5. L. A. Chesler and G. Y. Robinson, *Appl. Phys. Lett.*, **32,** 60 (1978).
6. C. C. Chang, R. P. H. Chang, and S. P. Muraka, *This Journal*, **125,** 481 (1978).
7. J. B. Theeten, D. E. Aspnes, and R. P. H. Chang, *J. Appl. Phys.*, **49,** 6097 (1978).
8. D. E. Aspnes, J. B. Theeten, and R. P. H. Chang, *J. Vac. Sci. Technol.*, **16,** 1374 (1979).
9. J. B. Theeten, R. P. H. Chang, D. E. Aspnes, and T. E. Adams, *This Journal*, **127,** 378 (1980).
10. J. C. Verplanke and R. P. Tijberg, *ibid.*, **124,** 802 (1977).
11. Y. Mizokawa, H. Iwasaki, R. Nishitani, and S. Nakamura, *J. Appl. Phys. Jpn.*, **17,** 327 (1978).
12. M. Croset, J. Diaz, D. Dieumegard and L. Mercandalli, *This Journal*, **126,** 1543 (1979).
13. R. L. Farrow, R. K. Chang, S. Mroczkowski, and F. H. Pollak *Appl. Phys. Lett.*, **31,** 768 (1977).
14. G. P. Schwartz, B. Schwartz, J. E. Griffiths, and T. Sugano, *This Journal*, **127,** 2269 (1980).
15. D. E. Aspnes, B. Schwartz, A. A. Studna, L. Derick, and L. A. Koszi, *J. Appl. Phys.*, **48,** 3510 (1977).
16. D. E. Aspnes, in *Surf. Sci.*, **101,** 84 (1980).
17. D. E. Aspnes, *J. Vac. Sci. Technol.*, **17,** 1057 (1980).
18. H. R. Philipp and H. Ehrenreich, *Phys. Rev.*, **129,** 1550 (1963).

19. J. B. Theeten and D. E. Aspnes, *Thin Solid Films*, **60**, 183 (1979).
20. D. E. Aspnes and J. B. Theeten, *Phys. Rev. Lett.*, **43**, 1046 (1979); *This Journal*, **127**, 1359 (1980).
21. H. Hasegawa, K. E. Forward, and H. L. Hartnagel, *Appl. Phys. Lett.*, **26**, 567 (1975); *This Journal*, **123**, 567 (1976); H. Hasegawa and H. L. Hartnagel, *ibid.*, **123**, 713 (1976).
22. D. E. Aspnes and A. A. Studna, *Appl. Opt.*, **14**, 220 (1975); *SPIE Proceedings*, **112**, 62 (1977); *Rev. Sci. Instrum.*, **49**, 291 (1978).
23. D. E. Aspnes, *J. Opt. Soc. Am.*, **64**, 812 (1974).
24. C. C. Chang, P. H. Citrin, and B. Schwartz, *J. Vac. Sci. Technol.*, **14**, 3602 (1978).
25. D. E. Aspnes, J. B. Theeten, and F. Hottier *Phys. Rev. B*, **20**, 3292 (1979).
26. E. S. Keeping, "Introduction to Statistical Interference," Chap. 12, Van Nostrand, Princeton, N.J. (1962).
27. I. H. Malitson, *J. Opt. Soc. Am.*, **55**, 1205 (1965).
28. E. D. Palik, N. Ginsburg, R. T. Holm, and J. W. Gibson, *J. Vac. Sci. Technol.*, **15**, 1488 (1978).
29. P. A. Barnes and D. P. Schinke, *Appl. Phys. Lett.*, **30**, 26 (1977).
30. D. A. G. Bruggeman, *Ann. Phys. (Leipzig)*, **24**, 636 (1935).
31. G. N. Greaves, E. A. Davis, and J. Bordes, *Philos. Mag.*, **34**, 265 (1976).
32. J. Stuke and G. Zimmerer, *Phys. Status Solidi B*, **49**, 513 (1972).
33. D. E. Aspnes and A. A. Studna, *Surf. Sci.*, **96**, 294 (1980).
34. H. Casey, Jr., D. D. Sell, and K. W. Wecht, *J. Appl. Phys.*, **46**, 250 (1975).
35. F. Lukes, *Optik*, **31**, 83 (1970).
36. M. Umeno, M. Yoshimoto, H. Shimizu, and Y. Amemiya, *Surf. Sci.*, **86**, 314 (1979).
37. R. N. Dexter, Private communication.
38. S. Varadarajan, I. Littlejohn, and J. R. Hauser, *Thin Solid Films*, **56**, 235 (1979).
39. P. A. Breeze, H. L. Hartnagel, and P. M. A. Sherwood, *This Journal*, **127**, 454 (1980).
40. G. P. Schwartz and G. J. Gualtieri, To be published.
41. H. W. Dinges, *Thin Solid Films*, **50**, L17 (1978).
42. C. J. Dell'Oca, G. Yan, and L. Young, *This Journal*, **124**, 1784 (1977).
43. O. A. Weinreich, *J. Appl. Phys.*, **37**, 2924 (1966).
44. K. Löschke, G. Kühn, H.-J. Bilz, and G. Leonhardt, *Thin Solid Films*, **19**, 81 (1973).
45. K. Navratil, *Czech. J. Phys. B*, **18**, 266 (1968).
46. T. Ishii and B. Jeppson, *This Journal*, **124**, 1784 (1977).
47. G. P. Schwartz, B. Schwartz, D. DiStefano, G. J. Gualtieri, and J. E. Griffiths, *Appl. Phys. Lett.*, **34**, 205 (1979).
48. G. P. Schwartz, J. E. Griffiths, and B. Schwartz, *J. Vac. Sci. Technol.*, **16**, 1383 (1979).
49. C. D. Thurmond, G. P. Schwartz, G. W. Kammlott, and B. Schwartz, *This Journal*, **127**, 1366 (1980).
50. G. P. Schwartz, G. J. Gualtieri, G. W. Kammlott, and B. Schwartz, *ibid.*, **126**, 1737 (1979).
51. L. C. Feldman, J. M. Poate, F. Ermanis, and B. Schwartz, *Thin Solid Films*, **19**, 81 (1973).

The Electromigration Directions of Liquid Au-Ag Alloy Droplets in Single Crystals of Si

T. R. Anthony

General Electric Research and Development Center, Schenectady, New York 12301

ABSTRACT

The electromigration directions and velocities of liquid Au-Ag alloy droplets in single crystals of Si were measured as a function of alloy composition at a temperature at which the electromigration velocities of Ag-Si and Au-Si liquid droplets are equal in magnitude, but opposite in direction. The electromigration null point composition of these ternary alloy droplets occurs at an alloy work function that roughly agrees with an electromigration-null-point work function previously determined with binary alloy droplets in Si.

Liquid metal droplets in a silicon single crystal through which a direct electric current is passing will migrate either towards the anode (+) or the cathode (−) (1-6). The motion of the liquid droplets is caused by a flux of dissolved silicon atoms across the inclusion, induced by the electric current passing through the liquid inclusion. To feed this flux of silicon atoms across the inclusion, silicon atoms dissolve into the inclusion at the forward face, while dissolved silicon atoms deposit on the rear face of the inclusion.

In the redeposited silicon trail left behind the electromigrating inclusion (Fig. 1), trace amounts of the metals comprising the droplet are left behind equal to the solid solubility limit of the metals in crystalline silicon. If one of the metals making up the inclusion is a donor or an acceptor element in silicon, then the redeposited silicon trail will be doped either n-type or p-type, respectively. By electromigration of an acceptor liquid metal droplet through n-type silicon or a donor liquid metal droplet through p-type silicon, p-n junctions can be formed in the silicon crystal. Because the electromigration velocities of liquid metal droplets are orders of magnitude greater than solid-state diffusion coefficients of the same metals, liquid droplet electromigration provides a means of forming p-n junctions all the way through silicon wafers in a manner of minutes instead of days.

Not all liquid metal droplets electromigrate in the same direction in silicon. As shown in Table I, a liquid

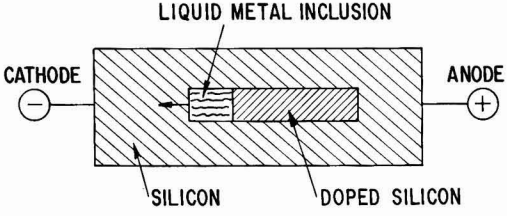

Fig. 1. A metal-rich liquid droplet electromigrating through a silicon single crystal toward the cathode. The redeposited silicon trail behind the electromigrating droplet contains the solid solubility limit in crystalline silicon of the metals comprising the inclusion.

Key words: electromigration, alloy, crystals.

Table I. The electromigration directions of nine liquid metal droplets in silicon and the work functions of these metals. The null-point work function for silicon is 4.55 eV. The work function of silicon is 4.85 eV. The electromigration directions are taken from Ref. (5) and the work functions from Ref. (8)

Element	Electromigration direction	Work function (eV)
Palladium	Anode (+)	5.12
Gold	Anode	5.10
Copper	Anode	4.65
Antimony	No electromigration	4.55
Tin	Cathode (−)	4.42
Aluminum	Cathode	4.28
Silver	Cathode	4.26
Gallium	Cathode	4.20
Indium	Cathode	4.12

droplet of a metal with a work function greater than 4.55 eV electromigrates toward the anode, while a liquid droplet of a metal with a work function less than 4.55 eV electromigrates toward the cathode (5, 6) in silicon.

To manufacture a particular semiconductor device, it may be desirable to have a liquid droplet that electromigrates toward the anode and that dopes the silicon p-type. From Table I, it is seen that all of the acceptor droplets (Al, Ga, and In) electromigrate toward the cathode. Hence, to obtain an inclusion that will both electromigrate toward the anode and dope the silicon p-type, an alloy inclusion must be formed of, say, Al and Pd in the right proportions.

In order to be able to obtain the correct inclusion composition in this and other cases, some information is required on the electromigration directions of inclusions composed of more than one metal. *A priori*, one would expect that the correlation of the work function of the metal comprising the droplet with the electromigration direction of the droplet found for the pure metals might carry over to droplets made up of more than one metal.

To test this hypothesis, the electromigration directions of droplets of Au-Ag alloys of varying compositions were measured. Au and Ag were selected for several reasons. First, both of these noble metals are chemically similar and have almost identical atomic radii. In addition, they form continuous solid and liquid solutions so that extraneous factors such as eutectic points, intermetallics, or liquid immiscibility do not complicate the study. Of particular importance to the investigation is the fact that inclusions of these two noble metals electromigrate in opposite directions: Au-Si droplets move toward the anode, while Ag-Si droplets move toward the cathode (5). Also, a temperature (880°C) can be selected where the absolute magnitudes of the oppositely directed velocities of Au and Ag droplets are equal (5) (Fig. 2). Finally, the work functions of Au-Ag alloys of varying compositions are available in the literature (7) so that a comparison of the electromigration direction of a particular alloy composition with its work function is possible.

Experimental

Sample preparation.—Rectangular samples 4 × 1 × 1 cm were cut from an n-type 10 Ω-cm Si ingot. The long dimension of the rectangular specimen was parallel to the <111> direction. The top and side faces were perpendicular, respectively, to the $<1\bar{1}0>$ and the $<11\bar{2}>$ directions. On the top $(1\bar{1}0)$ face of the sample, thirteen holes were ultrasonically drilled halfway through the crystal (Fig. 3). One hole was 2 mm in diameter and served as the thermocouple cavity, while the other twelve holes were 0.75 mm in diameter and were used to hold Au-Ag alloy droplets of varying composition.

Eleven Au-Ag alloys of various compositions from 0 to 100% Au at 10% composition intervals (*i.e.*, 0%, 10%, 20%, etc.) were cut and weighed from 99.99% Au and Ag wires and melted under vacuum in sealed quartz tubes. During melting the sealed quartz ampuls were mechanically jostled to ensure complete homogeneous mixing of the Au and Ag. Following melting, the alloys were quenched in water. The cast alloys

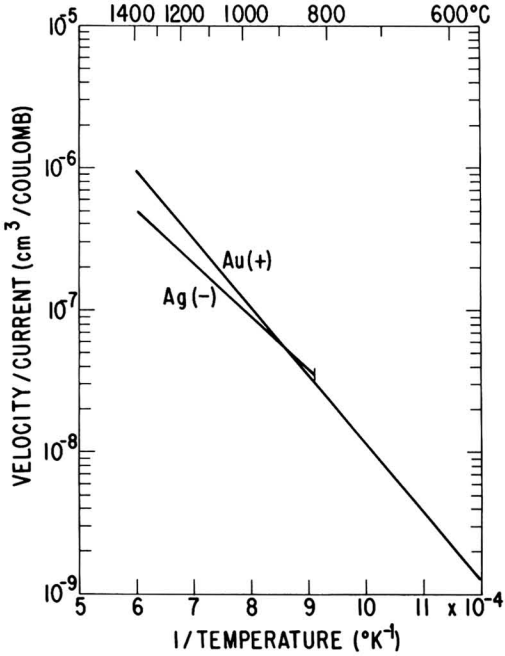

Fig. 2. The electromigration velocities of liquid droplets of Ag and Au in Si. In the temperature range of 880°-900°C, the electromigration velocities of Au and Ag-rich droplets are equal and opposite with Au migrating toward the anode (+) and Ag migrating toward the cathode (−).

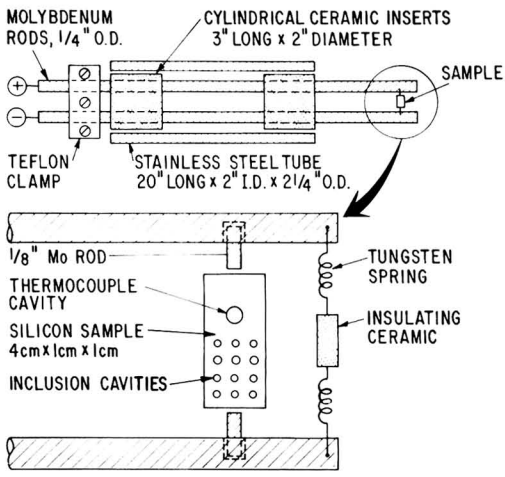

Fig. 3. The electrode jig used to pass current through the Si sample. The stainless steel tube is inserted part way into a diffusion furnace and current is passed through the Si sample in the furnace via the 1/4 in. molybdenum rods that extend outside of the furnace. The replaceable 1/8 in. molybdenom contact electrodes are pressed against the silicon sample throughout the electromigration experiment by the adjacent tungsten springs.

were hammered into thin sheets from which were cut small pieces that were inserted into the sample cavities in the silicon crystal (Fig. 3).

The silicon specimen with the eleven different alloy compositions in eleven separate sample cavities was placed in an annealing furnace with flowing H_2 at 1100°C for 3 hr to form the series of eleven Au-Ag liquid alloy droplets that would later be electromigrated. The silicon specimen was then cooled and removed from the annealing apparatus.

The electromigration apparatus.—The electromigration apparatus consisted of a diffusion furnace to attain the temperature of the electromigration run and an electrode jig, shown in Fig. 3, to apply current to the sample. One-eighth in. replaceable molybdenum electrodes were used as electrode contacts to the silicon sample. A tungsten spring provided contact pressure between the molybdenum electrodes and the Si sample during the high temperature electromigration experiments. A direct current of 15 A/cm² at a temperature of 884°C was used in the electromigration experiments. The temperature was selected so that the liquid inclusions of pure Ag and pure Au would have equal and opposite velocities (5). The current was produced by a Hewlett-Packard 6269B constant direct current power supply. A constant current supply was necessary, because the decrease in the resistivity of silicon with temperature would otherwise lead to an unstable situation. A voltage drop of 4.1V was required by the power supply to drive the 15 A/cm² current in the silicon specimen. Most of this voltage drop occurred at contact points in the circuit rather than in the specimen itself.

Measurement of Au-Ag electromigration directions.—Infrared transmission micrographs were taken of the pre-annealed silicon sample with a Research Devices (Elizabeth, New Jersey) infrared microscope. The silicon sample had been previously polished to a 1 μm finish and fiduciary lines had been scribed on the top surface of the sample with a diamond marker. These fiduciary lines were used as reference points to measure the movement of the alloy liquid droplets through the silicon.

The specimen was then placed in the electrode jig shown in Fig. 3 and inserted in a diffusion furnace. After temperature equilibration at 884°C, a constant direct current of 15 A/cm² was passed through the silicon sample for 24 hr. The temperature of the sample was continuously monitored during the experiment with a Chromel-Alumel thermocouple inserted in the thermocouple cavity (Fig. 3) of the specimen. A flow of a nonexplosive gas mixture of 95% N_2 + 5% H_2 was used to prevent oxidation of the electrode jig.

Following the electromigration anneal, the electrode jig was withdrawn from the furnace tube and allowed to cool. The Si sample was removed from the jig and infrared transmission micrographs were taken again of the Si sample to determine the movement of the eleven liquid Au-Ag alloy droplets through the silicon. Measurements of the inclusion displacements were made on the photomicrographs with respect to the diamond-scribed fiduciary lines on the surface of the sample. Care was taken to center each droplet in the middle of its respective photomicrograph to avoid parallax errors arising from the difference in depths between the droplets in the middle of the sample and the fiduciary lines on the surface of the sample.

Experimental Results

Figure 4 shows the electromigration velocities of eleven Au-Ag alloys *vs.* composition. The velocities are averages of several experiments. Ag-rich alloys electromigrated toward the cathode, while Au-rich alloys electromigrated toward the anode. The null-point crossover composition is approximately 79 atomic percent (a/o) Au-21 a/o Ag. Between 30-60 a/o Ag, the droplet velocity is independent of composition with experimental error.

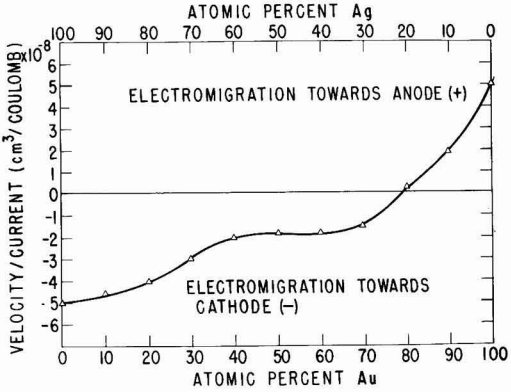

Fig. 4. The electromigration velocities and directions of a series of Au-Ag liquid droplets at 884°C *vs.* composition of the droplet. Droplets with more than 21 a/o Ag electromigrate toward the cathode, while droplets of Au-Ag alloys of less than 21 a/o Ag electromigrate toward the anode.

Discussion of the Electromigration Direction

In a previous paper, it was found that the electromigration directions of pure metals in silicon (5, 6) and germanium (11) show a strong correlation with the work functions (5) of the pure metals comprising the droplets. Table I shows that droplets of metals with work functions greater and less than 4.55 eV electromigrate, respectively, toward the anode and cathode in a silicon single crystal. In germanium crystals, liquid droplets of metals with work functions greater and less than 5.0 eV (the work function of Ge) electromigrate toward the anode and cathode, respectively, as shown in Table II.

A rationale for the relation between the work function of a metal and its electromigration direction as a liquid droplet in a host semiconductor crystal can be made qualitatively in terms of the electron-atom momentum exchange force that drives electromigration. [Electric field drift and Peltier-induced TGZM contribute less than a few percent of the observed electromigration velocities (2, 5, 6).] The work function of an element is a measure of the attraction between that element and an electron. That is, the larger is the work function, the greater will be the attraction. If two elements are mixed together, one would expect, as a first-order approximation, that some electron transfer would occur from the element with the small work function to the element with the large work function. Because the ion size of an element is a very sensitive function of

Table II. The work functions and electromigration directions of liquid metal droplets in germanium. The work function of germanium is 5.0 eV. The work functions are taken from Ref. (8) and the electromigration directions from Ref. (1)

Element	Electromigration direction	Work function (eV)
Platinum	Anode (+)	5.65
Nickel	Anode	5.15
Palladium	Anode	5.12
Gold	Anode	5.10
Tellurium	Cathode (−)	4.95
Copper	Cathode	4.65
Antimony	Cathode	4.55
Tin	Cathode	4.42
Aluminum	Cathode	4.28
Silver	Cathode	4.26
Lead	Cathode	4.25
Bismuth	Cathode	4.22
Gallium	Cathode	4.20
Magnesium	Cathode	3.66

its valence state, the electron scattering cross section for an element losing electrons (the low work function element) would be expected to decrease, while the scattering cross section for the element gaining electrons would increase. These respective changes in electron scattering cross sections would be in the direction such that when the liquid alloy is subjected to a direct electric current, the electron wind would tend to preferentially blow the element with the larger work function toward the anode in accord with the experimental observations listed in Tables I and II.

A simple dilute solution theory using the difference in the work function of the metal comprising the droplet and an empirical null-point work function, as the driving force for electromigration, can be formulated as follows.

At the rear interface of the electromigrating droplet, conservation of mass requires that the flux J of silicon atoms impinging on the rear interface equal the velocity V of the inclusion times the difference in silicon concentrations per unit volume between the solid and the liquid

$$J = V(C_s - C_L) \quad [1]$$

where C_s and C_L are, respectively, the concentrations of silicon per unit volume in crystalline silicon and in the liquid droplet.

The flux J of silicon atoms in the liquid metal is given by

$$J = \text{Force} \times \text{Mobility} \times \text{Solubility} \quad [2]$$

The force f on the dissolved silicon atoms can be represented by

$$f = \alpha I \Delta W \quad [3]$$

where I is the electric current density, ΔW is the difference between the work function of the metal comprising the droplet and the empirical null-point work function, and α is an unknown numerical factor. This is a result of an empirical relationship found earlier (5).

The mobility M of dissolved silicon atoms in the inclusion is given by the Einstein Relation

$$M = \frac{D}{RT} \quad [4]$$

where D is the diffusion coefficient of dissolved silicon atoms in the liquid metal droplet, R is the gas constant, and T is the absolute temperature. The combination of Eq. [1]-[4] gives

$$\frac{V}{I} = \left[\alpha\left(\frac{C_L}{C_s - C_L}\right)\frac{D}{RT}\right]\Delta W \quad [5]$$

Unfortunately, no data are available for silicon in Au-Ag alloys that would allow one to evaluate the bracketed expression. However, the null-point composition at which the electromigration velocity passes through zero can be predicted by the Au-Ag composition where the work function deviation ΔW of the alloy equals zero.

Figure 5 shows the work function of Au-Ag alloys plotted *vs.* composition. The null-point work function for silicon of 4.55 eV corresponds to a predicted electromigration null-point composition of 60% Au-40% Ag. Since at the temperature of the electromigration experiments, the electromigration velocities of pure Au and pure Ag droplets are equal and opposite, a simple use of the law of mixtures would indicate that the null-point composition would be 50 a/o Au-50 a/o Ag. In the experiments, a shift of the null point to a gold-rich composition is found instead. This shift to a gold-rich composition is predicted by the nonlinear work function of Au-Ag alloys that shows a much steeper change on the gold-rich side of the work-function-composition diagram than on the silver side. Thus, there is qualitative agreement between the experimental null point and the null point predicted by the work functions of the alloys as far as the shift to the gold-rich side of the diagram. However, quantitatively, the predicted null-point alloy composition of 60% Au-40% Ag does not agree with the experimentally observed null-point composition of 79% Au-21% Ag. This quantitative disagreement is not surprising, since the work function of a pure alloy crystal at room temperature, no doubt, does not equal the work function of the same alloy liquid containing dissolved silicon at 880°C. In view of this quantitative disagreement in the alloy case, the perfect correlation of electromigration directions with work functions found for the pure liquid metal droplets (5) is even more remarkable.

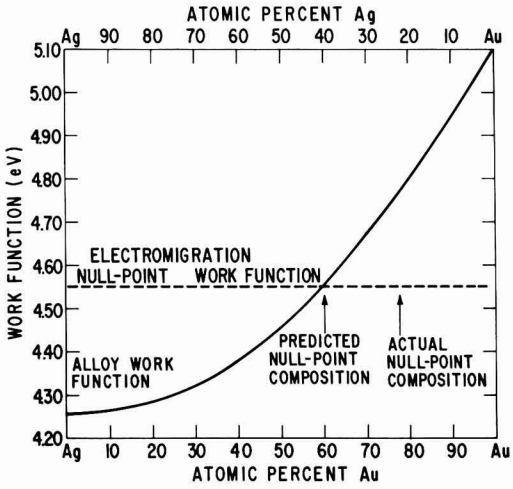

Fig. 5. The work function *vs.* composition of Au-Ag alloys taken from Ref. (7) and (8). The electromigration null-point work function for various metals is shown along with the predicted and experimental null-point alloy compositions.

Summary

The electromigration directions of a series of liquid Au-Ag droplets were measured as a function of composition in Si. The electromigration experiments were carried out at a temperature where the electromigration velocities of Au-Si and Ag-Si liquid droplets are equal in magnitude but opposite in direction. Although the law of mixtures would predict an electromigration null-point composition of 50% Au-50% Ag, the actual null-point composition was shifted to a gold-rich composition of 79% Au-21% Ag. This gold-rich shift is predicted qualitatively by a model relating the driving force of electromigration to the deviation of the nonlinear work function of Au-Ag alloys from an electromigration-null-point work function determined previously with simple liquid metal inclusions in Si.

Manuscript submitted May 12, 1980; revised manuscript received Sept. 8, 1980.

Any discussion of this paper will appear in a Discussion Section to be published in the December 1981 JOURNAL. All discussions for the December 1981 Discussion Section should be submitted by Aug. 1, 1981.

Publication costs of this article were assisted by General Electric Company.

REFERENCES

1. W. G. Pfann, K. E. Benson, and J. H. Wernick, *J. Electron*, **2**, 597 (1957).
2. D. T. J. Hurle, J. B. Mullin, and E. R. Pike, *Philos. Mag.*, **9**, 423 (1964).
3. J. K. Howard, *J. Appl. Phys.*, **46**, 1910 (1975).
4. J. K. Howard, *ibid.*, **44**, 1977 (1973).
5. T. R. Anthony, *ibid.*, **51**, 6348 (1980).
6. T. R. Anthony, *ibid.*, **51**, 6356 (1980).
7. S. C. Fain, Jr. and J. M. McDavid, *Phys. Rev. B*, **9**, 5099 (1974).
8. H. B. Michaelson, *IBM J. Res. Dev.*, **22**, 72 (1978).

An Improved Model for Analyzing Hole Mobility and Resistivity in p-Type Silicon Doped with Boron, Gallium, and Indium

L. C. Linares[1] and S. S. Li*

Department of Electrical Engineering, University of Florida, Gainesville, Florida 32611

ABSTRACT

Using the relaxation time approximation, and a three-band model (*i.e.*, nonparabolic light-hole band, parabolic heavy-hole, and split-off bands), theoretical calculations of hole mobility and resistivity were carried out for p-type silicon doped with boron, gallium, and indium for dopant densities from 10^{14} to 10^{18} cm^{-3} and temperatures between 100 and 400 K. The theoretical analysis did not consider the effects of compensation, but scattering contributions from acoustical and optical phonons, and ionized and neutral impurities were considered. In addition, interband scattering, the effect of hole-hole scattering, and the nonparabolic nature of the valence bands were also taken into account in the mobility formulations. To verify our theoretical calculations, resistivity measurements were performed on silicon samples (relatively free of compensating inpurities) doped with boron, gallium, and indium with dopant densities ranging from 4.25×10^{15} to 9.05×10^{17} cm^{-3}, for $100 \leq T \leq 400$ K. Agreement between the calculated and measured resistivity values and the published mobilities (4) was within 10% over the range of temperature and dopant density studied.

For purposes of device design it is necessary to know the correct relationship between resistivity and dopant density at different temperatures. Evaluation of the characteristics of semiconductor devices and the study of transport phenomena in semiconductors requires an accurate knowledge of variations in ohmic mobility and carrier density with changes in temperature and dopant density. Because of this, numerous studies of mobility, resistivity, and carrier density in p-type silicon have been carried out (1-15). However, due to the complexity of the valence band of silicon and the various scattering mechanisms involved, these studies, for the most part, have either been conducted in temperature and dopant density ranges designed to explore only a particular type of scattering mechanism, or have not advanced the theory necessary to describe the experimental results. For example, Costato and Reggiani (1) calculated the mobility of holes for pure p-type silicon in which lattice scattering dominates; Braggins (2) considered the nonparabolicity of the valence band and all the relevant scattering mechanisms with the exception of hole-hole (h-h) scattering, but he limited his investigation to dopant densities below 5×10^{16} cm^{-3} and low temperatures; Morin and Maita (3) considered wide ranges of temperature and dopant concentration, but did not provide a theoretical examination of the data. Recently, Li (4) developed a theoretical model capable of describing the mobility and resistivity of p-type silicon over a wide range of temperatures and dopant densities. This improved model was applied to the case of boron-doped silicon with great success (4). The improvement in Li's theoretical treatment of mobility and resistivity consists mainly of the inclusion of h-h scattering effects, and consideration of the nonparabolic nature of the valence band.

With some exceptions (13-15), most of the research in p-type silicon has been conducted with boron as the doping impurity, since boron is the shallowest acceptor in silicon and this material is widely available. A limited amount of data is available on silicon doped with deeper impurities such as gallium and indium. These dopants, especially indium, are of great interest to modern technology because of their application to photo-detector devices. Curves of resistivity and mobility as a function of dopant density (5-7) have been applied to characterizing boron-doped starting material and diffused boron layers in silicon, and have proven to be highly useful. Similar curves developed in this study may be expected to be equally useful for characterizing and integrating infrared detectors based on the deeper levels of indium and gallium with on-chip silicon electronics.

The purpose of this paper is to improve Li's (4) theoretical model by including consideration of interband transitions in the development of scattering relaxation time due to lattice phonons, and to apply this theory to the study of silicon doped with boron, gallium, and indium. The theoretical investigation is carried out over a temperature range from 100 to 400 K and a dopant density range from 10^{14} to 10^{18} cm^{-3}. Because of the complexities brought about by heavy doping effects and uncertainties in accounting for hole density and impurity density at high dopant densities, we have restricted the present analysis to densities below 10^{18} cm^{-3} in which the use of Boltzmann statistics is justified.

In the next section we describe the theoretical approach, presenting the formulation of effective mass in the nonparabolic valence band, and the relaxation time and mobility formulation. Resistivity and carrier density are also analyzed in this section. Next, the theoretical and experimental results are compared. The theory is further verified by comparison with other published data. The section "Summary and Conclusions" summarizes the main conclusions derived from this work.

Theoretical Approach

In this section we present the model used for the valence band of silicon, and the approach used to determine effective masses in the nonparabolic band. The mobility and resistivity in p-type silicon is obtained by considering contributions from lattice, ionized impurity, and neutral impurity scattering. The effects of h-h scattering and valence band nonpara-

* Electrochemical Society Active Member.
[1] Present address: U.S. Air Force Academy, Physics Department, Colorado Springs, Colorado 80840.
Key words: hole mobility, resistivity, dopant.

bolicity are also taken into account in the scattering relaxation time formulation. Interband transitions are considered only for lattice phonon scattering.

Valence band and hole effective masses.—The valence bands of silicon have an extremum at $\bar{k} = 0$ and are degenerate there. The constant energy surfaces for this case are warped spheres. Although warped, the bands are parabolic for small values of $\bar{\kappa}$. However, for larger values of $\bar{k}$, the bands become nonparabolic, and along the <100> and <111> directions the heavy- and light-hole bands are parallel over most of the Brillouin zone. The derivation of an expression for a valence band effective mass which incorporates the nonparabolic nature of the individual bands begins with a simplified model of the warped structure based on the work of Kane (16) and Barber (17). In this model, the heavy-hole band is characterized by holes with an energy independent but direction dependent effective mass, and the light-hole band is characterized by holes with an energy and direction dependent effective mass. The split-off band is separated at $\bar{\kappa} = 0$ by an energy $\Delta = 0.044$ eV (18), and is characterized by an effective mass which is temperature dependent. Thus the heavy-hole band is treated as parabolic for the range of temperature considered in this work, while the light-hole band is parabolic only for very low values of $\bar{k}$. At higher values of $\bar{\kappa}$, the light-hole band has an energy dependent curvature which takes on the same characteristics as the heavy-hole band for energies greater than 0.02 eV.

Using the above band model, expressions were derived for density-of-states and conductivity effective masses, based on the following definitions (19): the density-of-states effective mass, m_D*, enters in the normalization of the distribution function, and the conductivity effective mass, m_C*, is the mass of a mobile charge carrier under the influence of an external electric field. Since the crystal structure of silicon has cubic symmetry, ohmic mobility will be isotropic. The warping and nonparabolic character of the bands enters the isotropic mobility via the effective mass formulation. The values of m_C* and m_D* calculated in (19) were obtained assuming the Fermi-Dirac distribution function, and unequal relaxation times in the individual bands (20). These values are valid in the temperature range considered in this study, where the warping nature of the heavy-hole band is not strong and this band can be assumed parabolic. The values of m_C* and m_D* calculated in Ref. (19) for $100 \leq T \leq 400$ K are listed in Table I.

Mobility and scattering relaxation time formulation.—The calculation of the mobility of holes in the valence band of silicon is accomplished by evaluating the mobility separately in the heavy-hole band, the light-hole band, and the split-off band considering all appropriate scattering mechanisms. The overall mobility is then evaluated as a weighted average of the single-band mobilities over the individual hole densities in each band.

The conductivity mobility in each of the three valence bands is calculated from

Table I. Density-of-states and conductivity effective masses of holes in p-type silicon for $N_A = 10^{14}$cm^{-3} and $100 \leq T \leq 400$ K (19) (masses in units of electron rest mass)

T (K)	100	150	200	250	300	350	400
m_{D1}*	0.5503	0.5547	0.5592	0.5638	0.5685	0.5733	0.5782
m_{D2}*	0.2486	0.3092	0.3533	0.3865	0.4123	0.4337	0.4502
m_{D3}*	0.0680	0.0249	0.0443	0.0627	0.0793	0.0940	0.1071
m_D*	0.6567	0.6997	0.7340	0.7624	0.7865	0.8081	0.8265
m_{C1}*	0.4271	0.4323	0.4375	0.4429	0.4484	0.4541	0.4599
m_{C2}*	0.3285	0.4319	0.4839	0.5099	0.5222	0.5283	0.5286
m_{C3}*	0.2410	0.2443	0.2474	0.2511	0.2532	0.2598	0.2596
m_C*	0.3604	0.4143	0.4454	0.4633	0.4743	0.4820	0.4859

$$\mu_i = \frac{e<\tau_i>}{m_{Ci}^*} \quad [1]$$

where

$$<\tau_i> = \frac{\int \epsilon^{3/2}\,\tau_i(\partial f_o/\partial\epsilon)\,d\epsilon}{\int \epsilon^{3/2}\,(\partial f_o/\partial\epsilon)\,d\epsilon} \quad [1]$$

for the case of Fermi-Dirac statistics, $\epsilon = E/koT$ is the reduced energy, and m_{Ci}* and τ_i are the conductivity effective mass (19), and the total scattering relaxation time in band i, respectively.

At temperatures above absolute zero, in any semiconductor, the charge carriers may be scattered by a number of different mechanisms. Because each scattering mechanism has its own dependence on scattering energy, a simple closed form expression for total scattering relaxation time as a function of temperature cannot be obtained. The use of numerical techniques is necessary to solve for the relaxation time. In the case of p-type silicon, the peculiarities of a degenerate, warped, and nonparabolic valence band must be taken into account (2). The possibility of interband as well as intraband transitions must also be taken into account in the analysis. With the inclusion of interband scattering as given by Bir *et al.* (21), the total relaxation time in the heavy- (i = 1) and light- (i = 2) hole bands is given by

$$\tau_i = \frac{1}{\delta}\left(1 + \frac{m_{Di}^*}{m_{Dj}^*}\,\frac{\tau_{jj}}{\tau_{ij}}\right)\tau_{ii} \quad i \neq j;\quad i = 1, 2;\quad j = 1, 2 \quad [3]$$

where

$$\delta = 1 - \frac{\tau_{11}\tau_{22}}{\tau_{12}\tau_{21}} \quad [4]$$

and τ_{ii} is obtained by adding reciprocally the contributions from scattering by acoustical phonons, optical phonons, ionized impurities, and neutral impurities with i as the band index. The total relaxation time in the split-off band (i = 3) is obtained in the same manner. Only transitions between the light- and heavy-hole bands are considered; the relaxation time τ_{ji} takes into account a transition from band i to band j.

The procedure for including the nonparabolicity of the band structure into calculations of relaxation time, consists of modifying the relaxation time for a given scattering process by replacing the temperature independent effective mass of the parabolic band by the temperature dependent effective mass of the nonparabolic band. This procedure has been successfully applied to the study of acoustic phonon scattering in nonparabolic bands by Radcliffe (22). Optical phonon and ionized impurity scattering in nonparabolic bands have been considered by Barrie (23) in the same manner. Braggins (2) has used the same method to include nonparabolicity in his study of p-type silicon. In this work, the relaxation times appropriate to degenerate, parabolic valence bands have been used and modified according to the prescription of Radcliffe (22), Barrie (23), and Braggins (2). The anisotropy of the energy spectrum is not considered in this model, because from the transport theory for parabolic bands it is known that this anisotropy has no influence on the temperature dependence of mobility, but only on its absolute value (24). Each of the four scattering mechanisms will now be discussed.

Acoustical phonon scattering.—The relaxation time for scattering by acoustical phonons includes both the possibility of interband as well as intraband scattering. The treatment of the acoustical phonons has been based on the theory of Bir, Normantas, and Pikus (21) where the relaxation times can be expressed in terms of a single constant, τ_o which controls the overall magnitude of the scattering. Both transverse and longitudinal phonons participate in the scattering so that

$$\tau_{ac1}^{-1} = \frac{m_{D1}^{*3/2}}{\tau_o}\left\{ L_{11}^{(2)} + \gamma^3 L_{11}^{(1)} + \frac{C_l^2}{C_t^2}\eta^2 (T_{11}^{(2)} + \gamma^3 T_{11}^{(1)}) \right\} T^{3/2}\epsilon^{1/2} \quad [5]$$

and

$$\tau_{ac2}^{-1} = \frac{m_{D2}^{*3/2}}{\tau_o}\left\{ L_{22}^{(2)} + \gamma^3 L_{22}^{(1)} + \frac{C_l^2}{C_t^2}\eta^2 (T_{22}^{(2)} + \gamma^3 T_{22}^{(1)}) \right\} T^{3/2}\epsilon^{1/2} \quad [6]$$

for intraband scattering, while

$$\tau_{ij}^{-1}\gamma^{-5} = \tau_{ji}^{-1} = \frac{m_{Di}^{*3/2}}{\tau_o}\left\{ L_{ij}^{(2)} + \frac{C_l^2}{C_t^2}\eta^2 (T_{ij}^{(2)}) \right\} T^{3/2}\epsilon^{1/2} \quad [7]$$

for interband scattering. In the split-off band, the scattering relaxation time is given by

$$\tau_{ac3}^{-1} = \frac{m_{D3}^{*3/2}}{\tau_o}(\epsilon - \Delta/k_oT)^{1/2} T^{3/2} \quad [8]$$

In these equations

$$\frac{1}{\tau_o} = \frac{k_o^{3/2}a^2 m_o^{3/2}}{\sqrt{2}\pi\hbar^4 \rho_s C_l^2}, \quad \gamma^2 = \frac{m_{D2}^*}{m_{D1}^*}, \quad n = b/a$$

a and b are valence band acoustic deformation potential constants in the Picus and Bir (25) notation, ρ_s is the density, C_l and C_t are the longitudinal and transverse sound velocities in silicon, and L_{ij} and T_{ij} are the functions of η and γ defined in (21).

Optical phonon scattering.—Optical phonon scattering, while negligible at very low temperatures, cannot be ignored at high temperatures. Ehrenreich and Overhouser (26) have calculated the mobility of holes in silicon and its dependence on temperature. The calculated mobility follows a $T^{-2.3}$ dependence for reasonable choices of the parameters which describe the mixing of optical and acoustical phonon scattering. This agrees with experimental results (3, 7). The relaxation time for scattering by nonpolar optical phonons is given by (27)

$$\tau_{oi}^{-1} = \frac{m_{Di}^{3/2}}{\tau_o} W\theta T^{1/2}\{(n_o + 1)(\epsilon - \theta/T)^{1/2} + n_o(\epsilon + \theta/T)^{1/2}\}, \quad i = 1, 2, 3 \quad [9]$$

where θ is the Debye temperature, $n_o = (\exp(\theta/T) - 1)^{-1}$ is the phonon distribution function, and W is a constant which determines the relative coupling strength of the holes to the optical phonon mode compared to the acoustical phonon mode, $W = D_o^2h^2C_l^2/2k_o^2a^2\theta^2$, where D_o^2 is the optical deformation potential constant. The first term in the brackets of Eq. [9] corresponds to optical phonon emission and is relevant only when this is energetically possible ($\epsilon > \theta/T$). The second term in the brackets corresponds to optical phonon absorption.

Ionized impurity scattering.—The Coulombic interaction between ionized impurities and charge carriers drifting through the crystal under the action of an applied electric field causes scattering of the charge carriers. Scattering by ionized impurities was first considered by Conwell and Weisskopf (28). The basic assumption is that the Coulomb field is cut off at half the distance between charged impurities. This is equivalent to assuming that a charge carrier sees only one charged impurity at a time, the effect of the other charged impurities being sufficiently screened as to be negligible. This approach was improved by Brooks (29) and Herring (30) who associated the cutoff of the Coulomb potential with a screening distance, the free carriers being assumed to provide screening against the charge of the impurities. We have used the Brooks-Herring formula in our calculations.

Neutral impurity scattering.—Scattering by neutral impurities in semiconductors has been considered by Erginsoy (31) as a variation of the problem of the scattering of electrons by neutral hydrogen atoms. The result is a temperature independent relaxation time. Sclar (32, 33) has included the possibility of bound states in the evaluation of electron-hydrogen impurity scattering by using a three-dimensional square well to estimate the influence of a weakly bound state on the scattering. In this case the relaxation time is given by

$$\tau_{Ni}^{-1} = \frac{2^{3/2}\pi\hbar^2 N_N}{(k_oT)^{1/2}m_{Di}^{*3/2}}\left\{ \epsilon^{1/2} + \frac{E_1}{k_oT\epsilon^{1/2}} \right\}, \quad i = 1, 2, 3 \quad [10]$$

where

$$E_1 = 1.136 \times 10^{-19}\left(\frac{m_D^*}{m_o}\right)\left(\frac{\epsilon_o}{\epsilon_s}\right)^2$$

is the binding energy of neutral acceptors.

McGill and Baron (34) report a more accurate calculation of neutral impurity scattering which is not subject to any of the previous approximations to the scattering, and represents an accurate implementation of the neutral-hydrogen approximation. Using this calculation, Baron *et al.* (35) show that neutral impurity scattering is inversely proportional to the ionization energy of the impurity. McGill and Baron's calculations, while predicting significant deviations from the results of Erginsoy and Sclar at low temperatures, agree in general with the predictions of Eq. [10] at higher temperatures ($36 < T < 181$ K for In).

For silicon doped with shallow impurities, neutral impurity scattering is important at low temperatures where neutral impurities may outnumber ionized impurities. The more accurate calculations of McGill and Baron are appropriate in this case, especially for the deeper level impurities. In this study, however, because of the temperature range involved, we felt that Sclar's calculation could accurately represent neutral impurity scattering.

Effect of hole-hole scattering.—The expressions thus far presented for scattering relaxation time neglect the effect of hole-hole (h-h) scattering. Although h-h scattering does not affect the current density directly since it cannot alter the total momentum, it tends to randomize the way in which this total momentum is distributed among holes of different energies. When the scattering mechanism is such as to lead to a nonuniform distribution, h-h scattering gives rise to a net transfer of momentum from holes which dissipate momentum less efficiently to those which dissipate momentum more efficiently, resulting in an overall greater rate of momentum transfer, and lower mobility (36). Thus the size of the effect of h-h scattering on the scattering relaxation time is a function of the energy dependence of the relaxation time. The h-h factor, γ_{hh}, can be derived by means of a classical formulation introduced by Keyes (37). When hole-hole collisions are much more frequent than hole-acceptor collisions, the average relaxation time for a parabolic band in the Keyes (37) approximation approaches the limiting form

$$\langle\tau_{hh}\rangle = \frac{\int \epsilon^{3/2}(\partial f_o/\partial\epsilon)\,d\epsilon}{\int \epsilon^{3/2}\tau^{-1}(\partial f_o/\partial\epsilon)\,d\epsilon} \quad [11]$$

where f_o is the Fermi-Dirac distribution function. On the other hand, if h-h collisions are neglected, the average relaxation time is given by Eq. [2].

Thus the h-h reduction factor (*i.e.*, the ratio of $\langle\tau_{hh}\rangle$ to $\langle\tau\rangle$) can be expressed as

$$\gamma_{hh} = \left\{ \frac{\int \epsilon^{3/2}\tau(\partial f_o/\partial\epsilon)\,d\epsilon \; x \int \epsilon^{3/2}\tau^{-1}(\partial f_o/\partial\epsilon)\,d\epsilon}{[\int \epsilon^{3/2}(\partial f_o/\partial\epsilon)\,d\epsilon]^2} \right\}^{-1} = \frac{1}{\langle\tau\rangle\langle\tau^{-1}\rangle} \quad [12]$$

For optical phonon scattering, and $\gamma_{hh}°$, the h-h reduction factor is evaluated from Eq. [12].

For acoustical phonon scattering it is assumed that $\gamma_{hh}{}^a$ decreases linearly with increasing dopant density from a value of one to a value of $\gamma_{hh}{}^a = 9\pi/32 \triangleq 0.88$ (4) in a certain range of impurity concentration. The exact relationship ($\gamma_{hh}{}^a = 1.0004 - 4.013378 \times 10^{-19} N_A$, $10^{15} \leq N_A \leq 3 \times 10^{17}$) is determined empirically with a best fit of the experimental data.

Luong and Shaw (38) using a one-particle-like approximation from the Hartree-Fock theory, have shown that by inclusion of h-h scattering, the Brooks-Herring (29, 30) formula is reduced by a factor which can be expressed in closed form as

$$\gamma_{hh}{}^i = (N_A{}^-/p')\,[1 - \exp(p'/N_A{}^-)] \quad [13]$$

where $N_A{}^-$ is the ionized acceptor density and p' is the screening hole density.

In the case of neutral impurity scattering, h-h scattering has no significance because τ_N is independent of hole energy. Thus the overall scattering relaxation time in each hole band is calculated by adding the contributions from the different scattering mechanisms, each properly corrected for the effects of h-h scattering. The conductivity mobility in each individual band is calculated from Eq. [1] and the combined conductivity mobility in the valence band is then evaluated as a weighted average of the single-band mobilities over the population of holes in each band.

Resistivity and hole density.—The resistivity for p-type silicon is given by

$$\rho = \frac{1}{e\mu_C p} \quad [14]$$

where μ_C is the hole conductivity mobility and p is the hole density

$$p = \frac{4}{\sqrt{\pi}}\left[\frac{2\pi k_o T m_D{}^*}{h^2}\right]^{3/2} F_{1/2}(\eta) \quad [15]$$

for the general case of Fermi-Dirac statistics. Here, $m_D{}^*$, the density-of-states effective mass, contains information pertaining to the nonparabolic nature of the valence band (19). In the limit of low dopant densities, Eq. [15] reduces to $p = N_v \exp(-\eta)$ where $N_v = 2(2\pi m_D{}^* k_o T/h^2)^{3/2}$ is the effective density of valence band states. For the range of temperatures considered in this study, the hole density is determined by assuming that the density of carriers is determined by the impurities present in the silicon sample. The density of ionized acceptor impurities in p-type silicon is computed from the charge neutrality equation, which reduces to $p \simeq N_A{}^-$ for the case of uncompensated materials.

The density of ionized acceptors is (39)

$$N_A{}^- = \frac{N_A}{1 + g\exp\left(\frac{E_A - E_F}{k_o T}\right)} \quad [16]$$

where E_A is the acceptor ionization energy, and g is the ground state degeneracy. Excited states have a very minor influence on the carrier concentration due to the large separation between the ground state and the excited states (2, 39). Letting

$$g = 4 + 2\exp(-\Delta/k_o T) \quad [17]$$

enables us to include contributions from the lowest energy state associated with the split-orbit band. Equation [17] assumes that this state is bound to the split-orbit band with the same energy as the ground state is bound to the light- and heavy-hole bands. Calculations of Zwerdling, *et al.* (18) and Baldereschi and Lipari (40) show that this assumption leads to underestimation of the percentage of impurity ionization. On the other hand, tacit acceptance of $g = 6$ (41), overestimates ionization density and introduces a larger error than the assumption of Eq. [17]. The density of ionized acceptors is computed by iterating E_F in Eq. [15] and [16] until $|p - N_A{}^-| < 0.001$.

Experimental evidence shows that the acceptor ionization energy E_A is not a constant, but decreases with increasing dopant density (9). Penin *et al.* (42) have determined in a study of heavily doped silicon from 4 to 300 K that for shallow impurities such as boron and phosphorus the ionization energy decreases and finally disappears altogether for impurity densities greater than 3×10^{18} cm^{-3}. For impurities with deeper activation energies, it is also expected that at some impurity concentration, the impurity activation energy should become a function of the impurity concentration. However, in this case this should happen at higher impurity concentrations than for the shallower level impurities. This is due to the smaller geometrical dimensions of the wave functions applicable to the deeper levels, so that overlapping effects which promote the reduction in activation energy require higher impurity concentrations (13). For shallow impurities such as boron and phosphorus, empirical expressions (9, 42) relating the dependence of ionization energy to dopant density have been established. In the case of Ga, there are data (14) on activation energy *vs.* concentration, but not enough on which to base an accurate relationship. For this reason the value of $E_A = 0.065$ eV (43, 44) was used. For In, $E_A = 0.156$ eV (45) was used.

Theoretical and Experimental Results

Using the theoretical expressions derived in the previous section and the parameters listed in Table II, we have calculated the hole mobility as a function of hole density at 300 K for boron-doped silicon. The constant, τ_o, was found by fitting the mobility to experimental points in the lattice-scattering-limited range. Our value of τ_o is equivalent to an acoustic deformation potential constant of 8.099 eV. The optical phonon coupling constant, W, was then found by fitting the mobility to the high temperature experimental data. Our value of W is equivalent to an optical deformation potential constant of 6.024×10^8 eV/cm. Curve I in Fig. 1 represents this theoretical calculation, and curve 2 was reproduced from Wagner (7). Our calculated values are within 6% of the values reported by Wagner for $N_A \leq 3 \times 10^{17}$ cm^{-3}. For higher values of hole density our calculated values are substantially higher than those of Wagner. As previously explained by Li (4), this discrepancy is due to Wagner's assumption of complete ionization of boron impurities. This assumption is valid only at low dopant densities or at high temperatures where full ionization

Table II. Values of physical parameters used in the calculations of hole mobility in p-type silicon

Parameter	Value	Unit
Δ	44.0	meV
a	−6.4*	eV
b	−1.36*	eV
Cl/Ct	2.09*	
Θ	735	K
ρ_s	2.329×10^3	kg/m^3
ϵ_s	11.7	ϵ_o
τ_o	6.96×10^{-10}	sec K$^{2/3}$
W	2.44	

* J. C. Hensel and G. Feher, *Phys. Rev.*, 129, 1041 (1963).

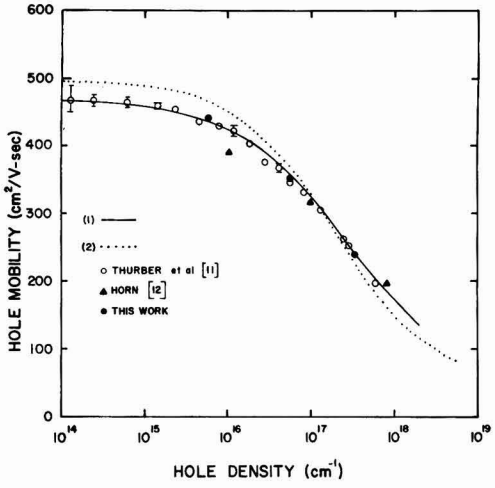

Fig. 1. Hole mobility vs. hole density for boron-doped silicon at 300 K. Curve 1 is the theoretical calculation and curve 2 is reproduced from Wagner (7). Shown also are the experimental results of this work, Horn (12), and Thurber *et al.* (11). All data points have been corrected for deionization effects.

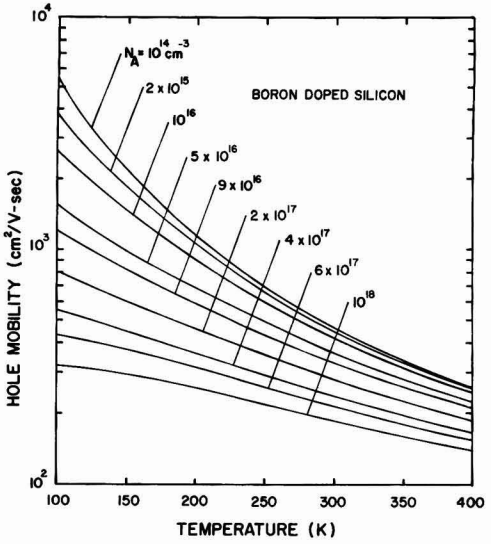

Fig. 2. The calculated hole mobility vs. temperature for boron-doped silicon with dopant density as a parameter.

of boron atoms prevails. The inclusion of interband scattering in the theoretical development results in a minor improvement in the quantitative agreement between theoretical and experimental results for boron-doped silicon. While Li's (4) model predicts a mobility of 475 cm²/V-sec for low-doped silicon at 300 K, the model presented in this paper predicts a mobility of 465 cm²/V-sec, and provides better agreement with the data of Thurber *et al.* (11). This value also agrees closely with direct measurements of drift mobility reported by Otaviani *et al.* (46). The theoretical calculation is in excellent agreement (within 3%) with experimental data reported by Thurber *et al.* (11). This gives support to the validity of ionization calculations based on Eq. [15] through [17]. Mobility values reported by Horn (12) are also in reasonable agreement with our theoretical results. The data points shown in Fig. 1 were corrected for deionization effects via Eq. [15] through [17].

The equations derived in the previous section were used to calculate the hole mobility for silicon doped with boron, gallium, and indium as a function of temperature with dopant density as a parameter, for $100 \leq T \leq 400$ K. The results are displayed in Fig. 2 through 4. A major use for Ga- and In-doped silicon is as infrared detectors. In this use it is essential that any residual boron be overcompensated. In the calculations of mobility in silicon doped with gallium and indium, we assumed that very lightly compensated boron impurities were also present. The Ga- and In-doped samples used in this study were specifically prepared with minimum compensation. Values of net background boron density (10^{13} and 5×10^{13} cm^{-3} in the gallium- and indium-doped samples, respectively) were deduced from a best fit of the experimental data. For this reason, especially in the case of indium-doped silicon, the actual role of the impurities at low temperatures and/or low dopant densities is masked by the action of the always present boron impurities. As the dopant density and temperature increase, the assumed background density of boron impurities becomes insignificant compared to the density of ionized dopant atoms, and Fig. 2 through 4 accurately depict the influence of the particular type of impurity on the mobility of holes in p-type silicon. The figures also show that for the case of the shallower ionization energies, mobility depends more strongly on temperature for the lightly doped case where lattice scattering is dominant, and becomes less temperature dependent as the dopant density increases.

In order to verify the adequacy of the theoretical model developed in this work, resistivity measurements were performed on silicon slices doped with boron, gallium, and indium for temperatures between 100 and 400 K. The data were obtained from NBS-4 test patterns fabricated on the silicon slices. Resistivity measurements were made on four-probe square array resistors and collector Hall effect resistors, while the net dopant density in the specimens was determined by the junction *C-V* method on a gated base-collector diode. These test structures are part of the test pattern NBS-4 (47), and are described in detail elsewhere

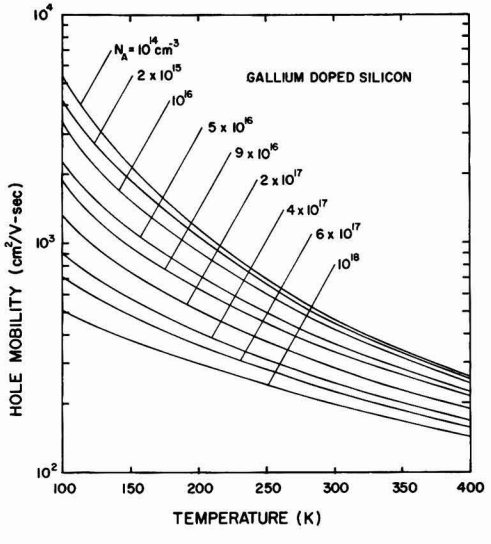

Fig. 3. The calculated hole mobility vs. temperature for gallium-doped silicon with dopant density as a parameter.

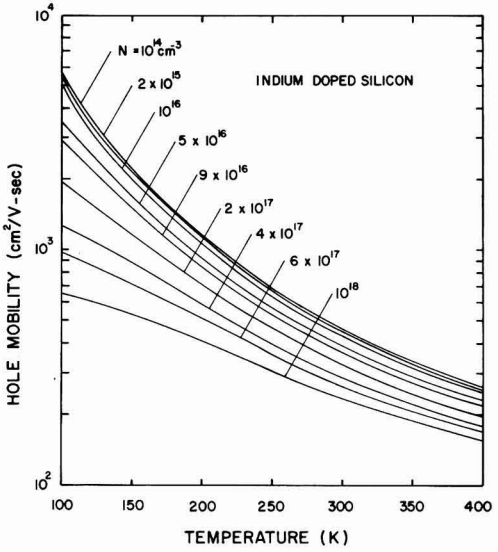

Fig. 4. The calculated hole mobility *vs.* temperature for indium-doped silicon with dopant density as a parameter.

(47, 48). Mean values of resistivity were determined by measuring 5-8 selected test cells with a standard deviation in resistivity values under 5%. Figure 5 shows the resistivity *vs.* dopant density relationship for boron-doped silicon at 300 K. The solid line presents theoretical calculations using Eq. [14], and the solid dots are our experimental data from boron-doped silicon. Resistivity values predicted by this model differ from those calculated by Li (4) by no more than 2% (at 300 K, for $N_A = 10^{14}$ cm^{-3}, our model predicts a resistivity of 134.1 Ω-cm, while Li's model predicts a value of 131.4 Ω-cm). Wagner's (7) resistivity curve and the theoretical line coincide over most of the total boron density range. Our theoretical calculations agree with Wagner's resistivity data within 6% over the entire range of boron densities considered at $T = 300$ K. Excellent agreement exists between our experimental data and the theoretical calculations at $T = 300$ K. Figure 5 also shows excellent agreement between our theoretical calculations and the data of Thurber *et al.* (11). Good agreement was obtained with the data of Thurber and Carpenter where total boron density was obtained by the nuclear track technique (49).

Figure 6 shows the resistivity of gallium- and indium-doped silicon as a function of total dopant density for $T = 300$ K. As expected, because of the deeper ionization energy of indium as compared to gallium, values of resistivity for gallium-doped silicon are lower than values of resistivity for indium-doped silicon at the same total dopant density. Figure 6 does not show this at low dopant densities because of the assumed values of background boron impurity densities. Excellent agreement was obtained between our experimental data and that obtained from Wolfstirn (14) for gallium-doped silicon, and our theoretical calculations at $T = 300$ K. Wolfstirn's data quotes values for activation energy ranging from 0.052 to 0.070 eV as the dopant density changes from 1.62×10^{18} to 1.26×10^{16} cm^{-3}. While Wolfstirn acknowledges that compensation plays a significant role in determining the degree of ionization of excess acceptors, she does not specify the degree of compensation of the samples used. Data obtained from the two indium-doped samples showed good agreement with the theoretical calculations, but the same was not true for the data of Schroder *et al.* (50), and Backenstoss (15). As seen in Fig. 6, for each value of measured resistivity, Schroder *et al.* (50) report two different values of measured indium density. The lower value of indium density was obtained by C-V and junction breakdown methods, while the higher value was obtained by Hall measurements and curve fitting. Because of uncertainties in the value of the Hall scattering factor, Schroder

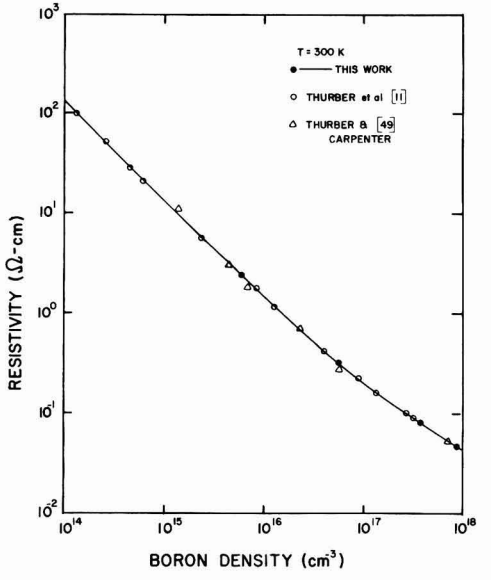

Fig. 5. Resistivity *vs.* dopant density for boron-doped silicon at 300 K. Shown are the theoretical calculations from Eq. [19] and the experimental results of this work, Thurber and Carpenter (49), and Thurber *et al.* (11).

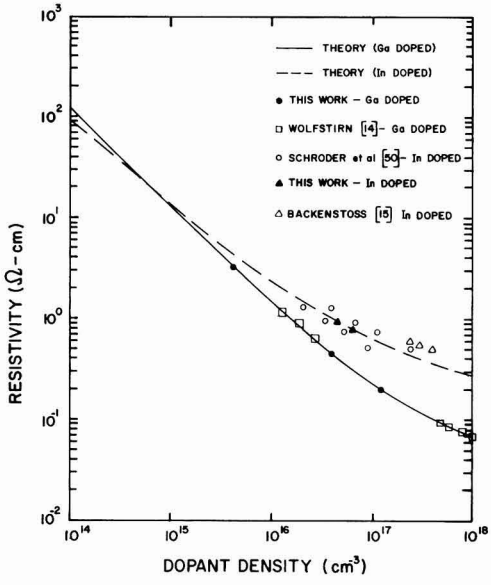

Fig. 6. Resistivity *vs.* dopant density for gallium- and indium-doped silicon at 300 K. Shown are theoretical calculations from Eq. [19] and the experimental results of this work, Wolfstirn (4), Schroder *et al.* (50), and Backenstoss (15).

et al. consider the lower value of density more reliable. Note that our theoretical calculation falls between the two values of dopant density reported by Schroder *et al.* (50). Values of resistivity of indium-doped silicon reported by Backenstoss (15) are about 25% higher than our calculated values. The work of Backenstoss (15), however, was done in the high doping region where dopant densities approach the limit of solid solubility. Backenstoss found that for dopant densities greater than 4×10^{17} cm^{-3} there was a considerable amount of indium precipitation. Thus it is possible that part of the discrepancy between our theoretical calculations and the data of Backenstoss is due to the low solid solubility limit of indium in silicon. Recent theoretical results of Sclar (13) for In-doped silicon also agree very closely with our theoretical calculations at 300 K. Neither Schroder *et al.* (50) nor Backenstoss (15) have indicated the degree of compensation of the samples used in their work.

To find out the adequacy of our theoretical model for temperatures other than 300 K, we compared the calculated and measured values of resistivity for silicon samples doped with boron, gallium, and indium for temperatures ranging from 100 to 400 K. Figure 7 shows the comparison between theoretical and measured resistivities for boron-doped silicon. Except for a couple of data points, agreement between the theoretical and measured values was within 8% over the entire range of temperatures. Figures 8 and 9 show the comparison between theoretical and measured resistivities for gallium- and indium-doped silicon, respectively. Agreement here was not as good as in the boron-doped case, but except for a couple of data points, agreement between theory and experiment was within 10%. For indium-doped samples, the largest discrepancies occurred at low temperatures. This is suggestive of some degree of compensation in the samples. Because the materials used were very carefully prepared to minimize compensation, an experimental estimate of percentage of compensation was not made for any of the silicon samples studied in this work.

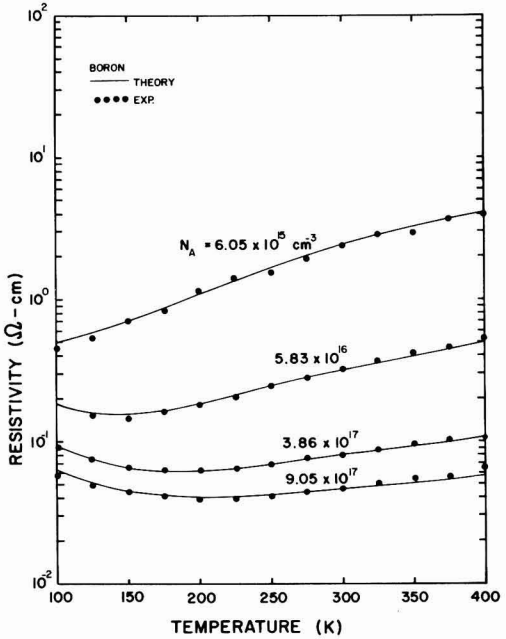

Fig. 7. Resistivity *vs.* temperature for the boron-doped silicon samples. Solid lines are the theoretical calculations and solid dots are the experimental data.

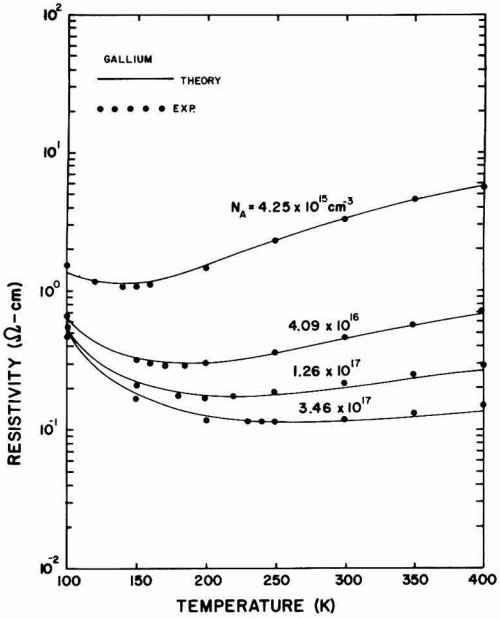

Fig. 8. Resistivity *vs.* temperature for the gallium-doped silicon samples. Solid lines are the theoretical calculations and solid dots are the experimental data.

Summary and Conclusions

Theoretical expressions have been derived to compute hole mobility and resistivity as functions of dopant density and temperature for silicon doped with boron, gallium, and indium. The valence band of silicon was represented by a three-band model which takes into account the nonparabolic nature of the bands. This attribute of the valence band is included in the

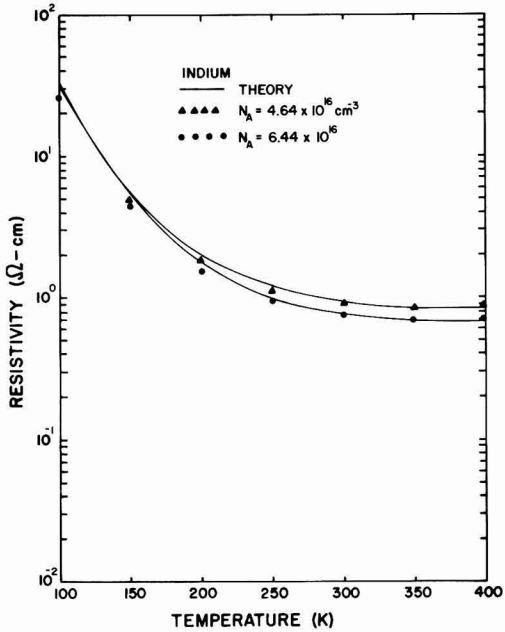

Fig. 9. Resistivity *vs.* temperature for the indium-doped silicon samples. Solid lines are the theoretical calculations.

effective mass calculations. Contributions from scattering by acoustical and optical phonons, ionized impurities, and neutral impurities were considered in the calculation of average relaxation time. In addition, our model also takes into account the effect of (h-h) scattering on both lattice and ionized impurity scattering relaxation times, and the effect of interband transitions on the acoustic phonon scattering relaxation time.

The resistivity analysis for the boron-, gallium-, and indium-doped silicon samples showed agreement between experimental and theoretical results within 10% over the entire range of temperature, $100 \leq T \leq 400$ K. Note that best agreement between theory and experiment was obtained for boron-doped samples, followed by gallium- and indium-doped samples. This may be due to the fact that we neglect the compensation effect and the possible dependence of ionization energy on dopant density in the theoretical calculations for gallium- and indium-doped samples. An experimental estimate of degree of compensation was not made for any of the silicon samples studied here. Data points representing a resistivity-dopant density pair are estimated to have a total error of around 6%.

A comparison between our calculated mobility values with those of Wagner's (7) data on boron-doped silicon at 300 K shows that agreement is within ±6% for $N_A \leq 3 \times 10^{17}$ cm^{-3}. Discrepancies at higher dopant densities can be eliminated if the effect of deionization of boron impurities were included in Wagner's calculations (7). Excellent agreement was found between our theoretical calculations of mobility in boron-doped silicon and the data of Thurber *et al.* (11) at 300 K. We have obtained excellent agreement between theoretical values of resistivity and our experimental data for boron-, gallium-, and indium-doped silicon at 300 K; our theoretical calculations also agreed with the resistivity data by Thurber *et al.* (11) for boron-doped silicon, and Wolfstirn (14) for gallium-doped silicon. From this study, we have found that the theoretical expressions derived in this work are adequate for mobility and resistivity calculations for p-type silicon valid for $10^{14} \leq N_A \leq 10^{18}$ cm^{-3} and $100 \leq T \leq 400$ K. The work presented here may be considered as a further refinement and extension over that published recently by Li (4) for p-type silicon.

Acknowledgment

The financial support received from the National Bureau of Standards and the National Science Foundation is gratefully acknowledged. Thanks are due to Dr. W. M. Bullis and W. R. Thurber of the National Bureau of Standards for their critical review of the manuscript, and their continued interest in this work.

The authors are also indebted to M. R. Riley for preparation and measurement of the boron-doped test structures, and to D. Yuen for resistivity measurements on the gallium- and indium-doped samples. Assistance by H. Mehta in carrying out the numerical computations is also gratefully acknowledged. This research was jointly supported by the National Bureau of Standards Contract 7-35741 and the National Science Foundation Grant ENG 76-81828.

Manuscript submitted July 30, 1979; revised manuscript received Sept. 15, 1980. This was Paper 551 presented at the Los Angeles, California, Meeting of the Society, Oct. 14-19, 1979.

Any discussion of this paper will appear in a Discussion Section to be published in the December 1981 JOURNAL. All discussions for the December 1981 Discussion Section should be submitted by Aug. 1, 1981.

Publication costs of this article were assisted by the University of Florida.

REFERENCES

1. M. Costato and L. Reggiani, *Il Nuovo Cimento*, **68**, 64 (1970).
2. T. T. Braggins, Thesis, Syracuse University (1975).
3. F. J. Morin and J. P. Maita, *Phys. Rev.*, **96**, 28 (1954).
4. S. S. Li, *Solid State Electron.*, **21**, 1109 (1978).
5. J. C. Irvin, *Bell Syst. Tech. J.*, **16**, 387 (1962).
6. S. M. Sze and J. C. Irvin, *Solid State Electron.*, **11**, 599 (1968).
7. S. Wagner, *This Journal*, **119**, 1570 (1972).
8. G. W. Ludwig and R. L. Watters, *Phys. Rev.*, **101**, 1699 (1956).
9. G. L. Pearson and J. Bardeen, *ibid.*, **75**, 865 (1949).
10. M. Prince, *ibid.*, **93**, 1204 (1954).
11. W. R. Thurber, R. L. Mathis, and Y. M. Liu, *Nat. Bur. Stand. Spec. Publ.*, **400-36** (1978).
12. F. H. Horn, *Phys. Rev.*, **97**, 1521 (1955).
13. N. Sclar, *IEEE Trans. Electron Devices*, **ed-24**, 709 (1977).
14. K. B. Wolfstirn, *J. Phys. Chem. Solids*, 16, 279 (1960).
15. G. Backenstoss, *Phys. Rev.*, **108**, 1416 (1957).
16. E. O. Kane, *J. Phys. Chem. Solids*, **1**, 82 (1956).
17. H. D. Barber, *Solid State Electron.*, **10**, 1039 (1967).
18. S. Zwerdling, K. J. Button, B. Lax, and L. M. Roth, *Phys. Rev. Lett.*, **4**, 173 (1960).
19. L. C. Linares and S. S. Li, *Phys. Status Solidi.*, To be published (1980).
20. M. Tiersten, *J. Phys. Chem. Solids*, **25**, 1151 (1964).
21. G. H. Bir, E. Normantas, and G. E. Pikus, *Soviet Phys. Solid State*, **4**, 867 (1962).
22. J. M. Radcliffe, *Proc. Phys. Soc. London Ser. A*, **68**, 675 (1955).
23. R. Barrie, *Proc. Phys. Soc. London Ser. B*, **69**, 553 (1956).
24. M. Ashe and J. vonBorzeszkowski, *Phys. Status Solidi*, **37**, 433 (1970).
25. G. E. Pikus and G. L. Bir, *Sov. Phys. Solid State*, **1**, 136, 1502 (1959).
26. H. Ehrenreich and A. W. Overhauser, *Phys. Rev.*, **104**, 649 (1956).
27. E. M. Conwell, *J. Phys. Chem. Solids*, **8**, 234 (1959).
28. E. M. Conwell and V. F. Weisskopf, *Phys. Rev.*, **77**, 388 (1950).
29. H. Brooks, in "Advances in Electronics and Electron Physics," Vol. 7, L. Marton, Editor, pp. 85-182, Academic Press, New York (1955).
30. C. Herring, *Bell Syst. Tech. J.*, **36**, 237 (1955).
31. C. Erginsoy, *Phys. Rev.*, **104**, 1559 (1956).
32. N. Sclar, *ibid.*, **104**, 1548 (1956).
33. N. Sclar, *ibid.*, **104**, 1559 (1956).
34. T. C. McGill and R. Baron, *Phys. Rev. B*, **11**, 5208 (1975).
35. R. Baron, M. H. Young, and T. C. McGill, in "Proc. of 13th Conf. on the Physics of Semiconductors," L. G. Fumi, Editor, p. 1158, Tipographia Marves, Rome (1977).
36. S. S. Li, *Nat. Bur. Stand. Spec. Publ.*, **400-33**, March (1977).
37. R. S. Keyes, *J. Phys. Chem. Solids*, **6**, 1 (1958).
38. M. Luong and A. W. Shaw, *Phys. Rev. B*, **4**, 2436 (1971).
39. J. S. Blakemore, "Semiconductor Statistics," Pergamon Press, New York (1962).
40. A. Baldereschi and N. O. Lipari, in "Proc. of 13th Int. Conf. on The Physics of Semiconductors," L. G. Fumi, Editor, p. 595, Tipographia Marves, Rome (1977).
41. H. J. Mason, Jr. and J. S. Blakemore, *J. Appl. Phys.*, **43**, 2810 (1972).
42. N. A. Penin, B. G. Zhurkin, and B. A. Volkov, *Sov. Phys.-Solid State*, **7**, 2580 (1966).
43. A. G. Milnes, "Deep Impurities In Semiconductors," John Wiley & Sons, New York (1973).
44. S. M. Sze, "Physics of Semiconductor Devices," John Wiley & Sons, New York (1969).
45. W. Scott, Paper presented at IRIS Specialty Group on IR Detectors, Colorado Springs, CO, March 21-23, 1977.
46. G. Ottaviana, L. Reggiani, C. Canali, F. Nava, and A. Alberigi-Quaranta, *Phys. Rev. B*, **12**, 3318 (1975).
47. W. R. Thurber and M. G. Buehler, *Nat. Bur. Stand. Spec. Publ.* **400-32**, April (1978).
48. M. Buehler and W. R. Thurber, *IEEE Trans. Electron Devices*, **ed-23**, 968 (1976).
49. W. R. Thurber and B. S. Carpenter, *This Journal*, **125**, 654 (1978).
50. D. K. Schroder, T. T. Braggins, and H. M. Hobgood, *J. Appl. Phys.*, **49**, 5256 (1978).

Measurement and Identification of Distortion, Alignment, and Mask Errors in IC Processing

K. H. Nicholas,* I. J. Stemp, and H. E. Brockman

Philips Research Laboratories, Redhill, Surrey, England

ABSTRACT

Measurement and identification of misregistration between patterns in integrated circuits is becoming increasingly important as finer geometry processes are being developed for VLSI. Various forms of the Stickman resistor pattern are described. These enable measurement of the alignment errors, mask errors, and distortions that occur when using any alignment apparatus. The properties of the different forms of Stickman resistors are compared and examples of applications to studying mask making errors, slice/mask distortions, projection distortions, and process induced slice distortions are described. It is shown that misregistrations of 0.1 micron or even less can be measured and identified. Direct measurements on simple apparatus are shown to be reproducible to ± 0.003 micron and accuracy is estimated at 5% of the misregistration with simple apparatus and 2% for a one micron misregistration if on chip measurement of sheet resistance is made.

Automatic measurement of the misregistration between patterns in integrated circuits and identification of the causes are necessary to the development of high packing density circuits. A resistor pattern for measuring misregistrations automatically has been described (1) that is more accurate and sensitive than other methods (2-5). In this paper three forms of the pattern (1), called the Stickman pattern from its shape, are described. They enable measurement of mask errors, alignment, and distortion in any alignment apparatus.

The basic pattern is first outlined and then the standard, small displacement, and protected edge forms are described and compared. Examples of measurements of mask faults and slice and image distortions are given to illustrate the flexibility and accuracy of the methods.

Throughout the paper misalignment is used to describe errors in aligning the new pattern with the slice as a whole and generally has only one value per slice. There can be several values with steppers. Misregistrations refer to errors at each measurement site including misalignment. Residual misregistrations are the values when apparent alignment errors have been removed. Distortions are the misregistrations when alignment and mask errors have been eliminated.

Stickman Types

Basic pattern.—The basic Stickman resistor pattern is shown in Fig. 1. It can be formed by a conducting layer on a mask or slice substrate or by doping in a silicon slice. The two resistors connected at one end are formed by two definition stages. One defines the outside edges shown with a solid line while the inside edges, shown by a dotted line, are defined at the other stage. Misregistration leads to differences in widths and hence to differences in resistances. It can be shown (1) that the misregistration, Δx, is given by

$$\Delta x = \tfrac{1}{2}\,\rho L(R_1^{-1} - R_2^{-1})$$

where ρ is the sheet resistance, L is the resistor length, and R_1 and R_2 are the resistances. The length of the resistor and sheet resistance are scaling factors. The sheet resistance can be measured on van de Pauw patterns adjacent to the Stickman patterns and the length is made large. The value for Δx is independent of resistor width and so is independent of systematic lithographic variations. Accuracy is better than 2% (0.02 micron for 1 micron misregistration) with typical measuring apparatus and linewidths.

Devices to measure misregistrations in X and Y directions are generally formed at each site. A pattern of resistors to do this is shown in Fig. 2. A constant current is passed from I to 0 and voltages across the resistors (1-2, 2-3, etc.) measured to evaluate their resistances.

The values can be analyzed in a computer to produce misregistrations and these are further analyzed in the computer in terms of position on the slices.

Standard.—The two patterns used to define resistors in the standard method are on two separate masks if conventional lithography is used. The patterns are indicated by different cross hatching in Fig. 3. Such patterns can be included on appropriate mask levels in production integrated circuit processes. The standard form is therefore ideal for monitoring total misregis-

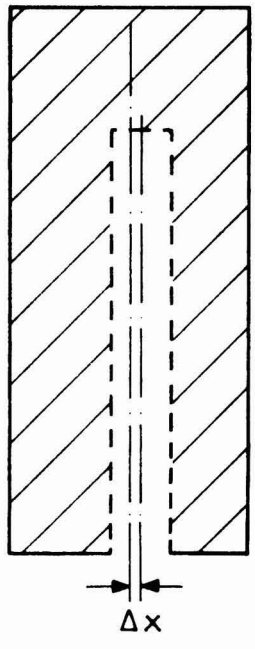

Fig. 1. Basic resistor pattern

* Electrochemical Society Active Member.

Key words: integrated circuits, resistivity, semiconductor.

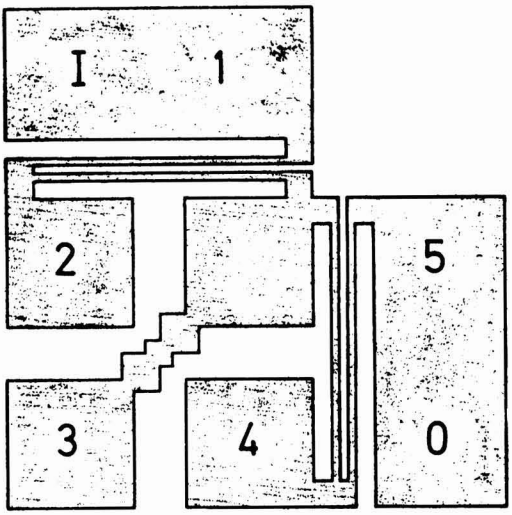

Fig. 2. Pattern with probe pads for misregistrations in both directions.

trations in integrated circuit process lines and can be used on any aligner.

Errors in alignment can generally be separated from other effects in the computer analysis program (6) but mask effects and distortions cannot necessarily be separated. In principle mask errors can be checked by using a "low distortion" process and finding errors that are reproduced on several slices. Some errors can be observed by this method or by studying the pattern of misregistrations but it is only generally possible if the errors are of the order of 0.1 μm or greater and a genuine "low distortion" process can be achieved. Subtracting the values of mask errors so obtained can allow distortion values to be derived but again the accuracy is limited.

The standard form can be used to assess mask makers directly. The two patterns are exposed successively on a bright chrome mask and the chrome layer defined. The thin film chrome resistors and the sheet resistance of the chrome can then be measured to give values for the misregistrations produced in the mask maker. This method can be extremely sensitive and accurate as will be shown in the Results section.

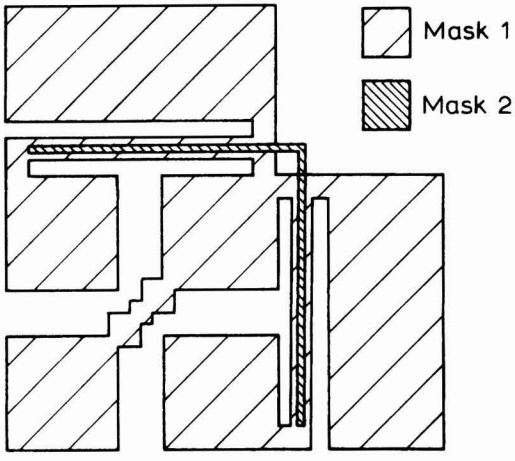

Fig. 3. Standard two mask level form

The mask stepping error can be greatly reduced by including both patterns on the same mask and displacing the second mask to superimpose it. Step and repeat errors of translation are virtually eliminated but any slight rotation of the chip leads to errors because the displacement has to be hundreds of microns to clear the pad areas. Also, it is not possible to misalign by hundreds of microns accurately in some aligners. The standard pattern is therefore unsuitable for accurate measurement of distortion.

Small displacement.—The small displacement pattern (7) was designed to eliminate mask stepping and some mask lithographic errors by using a single mask and reducing the displacement at the second alignment to a few microns. A single pattern has only to be misaligned by about ten microns. Chip rotation effects are negligible and the displacement only has to be accurate to about 2.5 μm. The pattern is shown in Fig. 4. If, for example a conducting layer is being etched, the layer is first defined to leave the shaded area. At the second definition stage the mask is misaligned by a small amount so that the small square at the top right falls in the larger one and the layer is redefined. The resulting pattern is shown in Fig. 4b, with the resistors indicated by heavy shading.

Distortion values are the misregistrations with the misalignment values removed by the computer (6) as mask errors are virtually eliminated. The misalignment values are not generally meaningful because of the special alignment situation associated with the displacement. The small displacement pattern cannot be used with most automatic aligners because of the need for a larger displacement to accommodate the larger autoalign mask.

Protected edge.—A new form for measuring distortion on an automatic aligner and for measuring alignment accurately has been developed. It is called the protected edge form because there are two edge protection masks as well as one critical mask. The critical mask is shown in Fig. 5a. It is designed to be like a perfectly aligned final pattern.

If a conducting layer is defined with negative resist the procedure is most straightforward because the layer has to remain where either the critical mask or

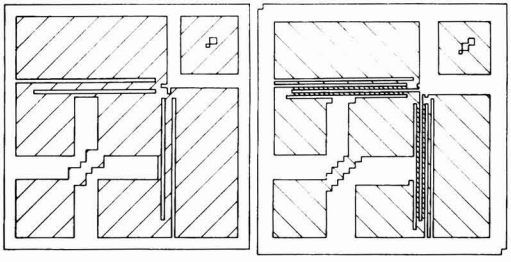

Fig. 4. Small displacement form

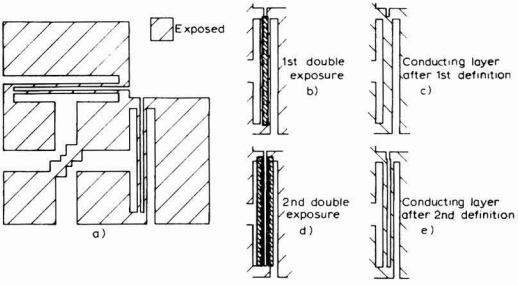

Fig. 5. Protected edge form

the edge protection mask is clear. The critical mask and the inner edge protection mask (dotted) are both exposed as shown for the X-direction in Fig. 5b. The layer is then etched leaving the layer shown in Fig. 5c with outside edges defined by the critical mask. At the second definition step the critical mask is again exposed but an outer edge protection mask is used for the second exposure as shown in Fig. 5d. This time the inside edges are defined by the critical mask and so after etching the final pattern shown in Fig. 5e is obtained.

The misregistration so measured is independent of step and repeat mask errors because resistor edges are defined by the same critical mask. The accuracy with which the resistors are matched on the critical mask will affect these results but this can be measured by a separate test in which only the critical mask is exposed and a measurement made. These measurements can then be removed from other results to give the true misregistration values. The matching on masks is often good enough to make the correction unnecessary.

The independence from step and repeat errors and smallness of other mask errors makes the protected edge form suitable for accurate measurement of distortion. It is ideal for measuring alignment as the same critical mask is used twice so that errors between alignment marks and patterns do not affect the results. The only disadvantages are the more complex processing and somewhat lower sensitivity. The lower sensitivity follows from the need for the protected edge masks to protect one edge of the resistors but not the other. This requires the resistors to be wider.

Comparison between different forms.—In this section the different forms of Stickman pattern are compared. The comparison is summarized in Table I. All forms can be used with any integrated circuit process though some modifications may be necessary.

Alignment apparatus can be assessed on both the standard and protected edge forms, but in the case of the standard form mask errors may be included particularly if alignment markers and measurement patterns are separately exposed. The small displacement pattern has special alignment requirements and so it is not generally suitable.

The standard form is ideal for overall misregistration measurements, particularly on work slices in production, and alignment errors can be separated even with the few process control sites normally present on such slices. The standard form is also the one to use for mask error studies. This can be done using a "low distortion" process, such as double exposure of a single resist layer to define resistors, and looking for common pattern of errors on different slices. The accuracy is then limited by residual distortions including temperature effects. The assessment of mask makers is best done using bright chrome mask layers to form thin film resistors after double exposure.

Distortions can be measured accurately by the small displacement and protected edge forms. The former cannot be used with most automatic aligners but has the advantage of simpler processing and higher accuracy.

Typical device length is 200 microns and an average resistor width of three microns is used to measure errors up to two microns. The minimum lithographic dimension on the mask is six microns as the resistor edges are defined in separate exposures. The only case of a complete resistor appearing on a mask is in the protected edge critical mask when the width is greater anyway. The greater width reduces sensitivity from 6.7% resistor difference per 0.1 μm to 3.3% difference in resistance per 0.1 μm. As misregistrations are decreased finer geometries can be used and sensitivity is further increased. The only limitation is that the resistivity is linear with width and so in general widths should be much greater than conductive layer thicknesses. It is generally possible to measure resistor values to better than 1% on a normal automatic probe and measurement apparatus if four terminal measurements are used. The accuracy is therefore better than 0.01 μm for a 1 μm misregistration. In the Results section it is shown that small misregistrations can be measured with a reproducibility of an order of magnitude smaller than this.

The different forms are suitable for different applications but at least one is suitable for any particular measurement.

Table I. Main properties of different Stickman forms

Device pattern	Standard (STD)	Small displacement (SD)	Protected edge (PE)
Measured directly			
Alignment	yes		yes
Overall misregistration	yes		
Mask errors	yes		
Distortions		yes	yes
Fabrication			
No. exposures	2	2	4
No. masks	2	1	3
On work slices	yes		
Typical geometries			
Length μm	200	200	200
Average width μm	3	3	6
Sensitivity			
% difference/0.1 μm	6.7	6.7	3.3
Lithography			
Photo-contact	yes	yes	yes
Photo-projection (P-E)	yes	yes	yes
Automatic stepper	yes		yes
Electron image proj.	yes	yes	yes
Direct slice writing	yes		
X-ray	yes		yes

Results

Applications are described that illustrate the usefulness of the technique in measuring and identifying causes of misregistration. The different forms can be used to study misalignments, mask errors, and distortions. The measurement of misalignment is straightforward, as described earlier, and the applications outlined here are to the measurement of mask errors and distortions.

Mask errors.—Mask errors have been identified by repetition of errors on different slices (6) and by the pattern of errors (1) using the standard form. Distortion variations were minimized but they do limit the accuracy.

A better method for studying errors on mask machines is to double define bright chrome layers in the mask making machine, again using the standard patterns, and measuring the thin film chrome resistors so formed. The technique has been applied to optical and electron beam mask makers.

Rotational misalignment has little meaning on mask makers or on direct slice writers working from marker arrays. It is useful in these cases to dispense with computer processing of data and have direct read-out of misregistrations. A circuit for direct reading onto a chart recorder is shown in Fig. 6. The resistors r_1 and r_2 are chosen to have the same value but much lower than the Stickman resistors R_L and R_R. By applying the same circuit and voltage V to X and Y direction devices and the outputs to an X-Y recorder, misregistration vectors can be drawn. The technique is also applicable on slices to Y-misregistrations in columns and X-misregistrations in rows where displacements due to rotation are virtually constant. The technique is not applicable if sheet resistance of the conducting layer is variable or if contact resistance is large and variable.

The two standard patterns had to be exposed consecutively on a widely used commercial mask maker as there was no facility for aligning reticles accurately with masks. Even so some misregistrations were ob-

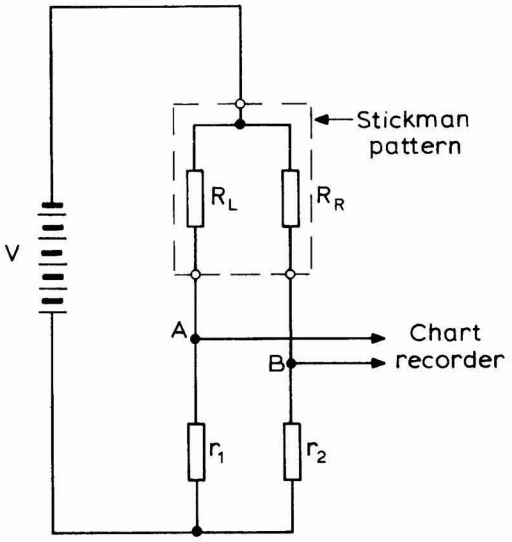

Fig. 6. Circuit for direct recording of misregistrations

served. The reticle contains an 8 × 8 array of devices. Misregistrations in the X-direction for two rows of devices (extending in the X-direction) are shown in Fig. 7(a) and (b). There is a repetitive pattern every 3.8 mm equal to the step and repeat distance. Errors within the pattern (up to 0.06 μm) are due to errors or distortion in the reticle or rotational errors in its placement. It was made on widely used commercial equipment. Misregistration values for each position in a chip are compared to the equivalent position in the first chip to evaluate step and repeat errors. The average values and standard deviations for the 16 positions are plotted against chip number in Fig. 8. Reproducibility over the chip is generally about ± 0.003 μm (a few atomic layers) showing how sensitive the technique is. The absolute accuracy is limited by sheet resistance variations and accuracy of the voltage measuring apparatus to about 5% of the misregistration. Step and repeat errors are less than 0.04 μm except for the relatively large change by about 0.15 μm around chip 7. This represents two $\lambda/8$ counts on the laser interferometer (λ = 633 nm). The reason for the counting error is being investigated.

It is possible to position patterns on masks with some more advanced mask makers enabling patterns to be written at well-separated times. This gives a more realistic measurement of alignment between different masks or different layers in direct slice writing. Results on an experimental electron beam pattern generator, with a six weeks gap between exposures and

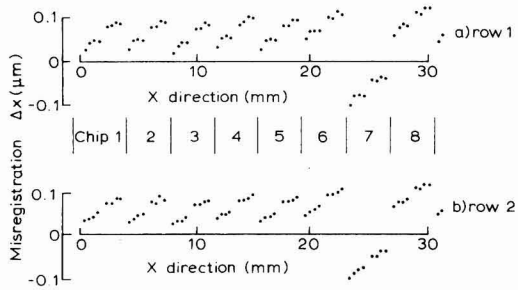

Fig. 7. Misregistrations in double written mask from optical mask maker.

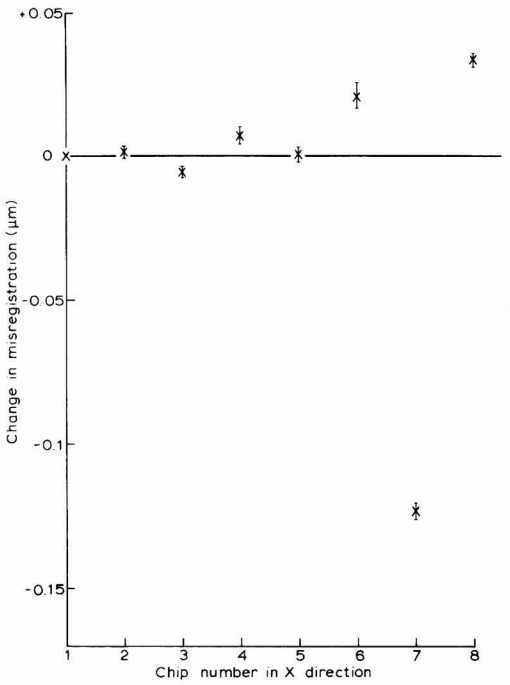

Fig. 8. Step and repeat errors in optical mask makers

incorrect adjustment the second time, are shown in Fig. 9. The outside rectangle represents the edge of the chip and the vectors give errors at 16 places in the chip. The scale for the vectors is given at the top. The sets of three vectors represent three different chips. There can be seen to be a general magnification error common to all chips which is due to a setting up error, but closer inspection shows an additional error in the X-direction. The corners of each chip are defined by markers. The markers in chip 3 (crosses) were read correctly but it appears that the bottom left-hand marker in chip 1 (diamonds) which determines the origin in the X-direction was differently read on the two occasions by about 0.08 μm. This led to differences in the X-direction from chip 3 on the left-hand side of the chip but improving agreement on moving to the right. The same marker was misread in chip 2 (plus signs) but this time it was the right-hand marker and so there is a magnification error causing increasing errors to the right of the chip. This illustrates how the causes even

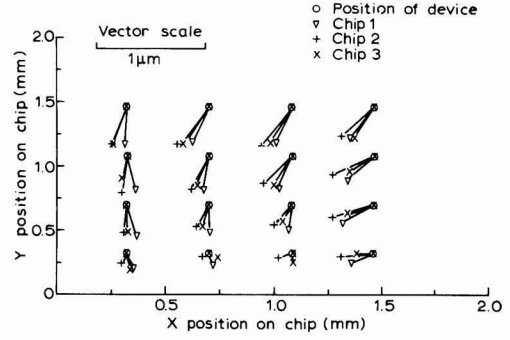

Fig. 9. Repetitive errors in different chips due to electron beam machine adjustment errors.

of small errors can be identified so that steps can be taken to reduce them. Errors were generally less than 0.1 μm when the machine was correctly adjusted (1).

Matching of pairs of resistor patterns is required for the critical mask in the protected edge form. If the critical mask alone is used to define resistors the matching can be investigated. Even with a mask made on an experimental pattern generator errors were only $+0.007$ μm and correction for such errors is normally unnecessary.

Distortions.—Misregistrations caused by lateral distortions can be measured with the small displacement or protected edge forms. The three common causes are (*i*) mask/slice distortion in the alignment equipment, (*ii*) pattern distortion on projection, and (*iii*) process-induced slice distortion. Distortions only contribute to misregistrations if they change between the two alignment stages.

An example of mask/slice distortion difference is shown in Fig. 10. Vectors representing misregistrations with alignment effects removed are shown in their position on the slice. The misregistrations are due to thermal expansion as the temperature (6) at the two alignment stages differed and the mask had a much higher temperature coefficient of expansion than the silicon slice. The effect can be reduced in some advanced alignment apparatus but such expansion is still important.

One way of compensating for the effect in some aligners is by intentional pattern distortion (8). Such distortion is shown in Fig. 11 where a contraction has been produced intentionally on an electron image projector. Analysis shows the contraction to be linear. On this machine any expansion can be compensated for automatically using signals from markers on the slice.

Distortion of slices by processing have also been observed. Most distortions are roughly linear but if stresses are very large nonlinear effects can occur. An example is shown in Fig. 12 where large stress was intentionally produced by a 0.14 micron thick layer of silicon nitride with a very thin oxide layer below. Such nonlinear distortions have only been found in the presence of a large density of defects.

Conclusions

Three forms of the Stickman resistor pattern (*i*) the standard (*ii*) the small displacement, and (*iii*) the protected edge forms have been described and compared.

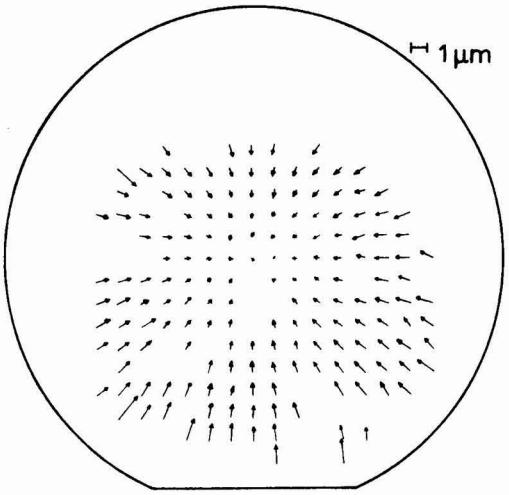

Fig. 11. Contraction of patterns in an electron image projector

It has been shown that alignment, mask errors, and distortions can be measured on any aligner using the appropriate form.

Identifications of errors in optical and electron beam mask makers have been described and observations of slice/mask distortion, projection distortion, and slice distortion outlined.

It has been shown that sensitivity and reproducibility are such that misregistration effects much less than 0.1 μm can be identified and measured to reproducibility of ± 0.003 μm using simple apparatus. Accuracy of measurement is limited to about 5% of the total misregistration if the simple apparatus is used but improved to 2% for 1 micron misregistration if sheet resistance is measured on each chip.

Acknowledgments

We would like to acknowledge the assistance of Mrs. C. Glaister in fabrication of devices and useful discussion with Dr. P. J. Daniel. We would also like to thank colleagues in Philips for providing masks and slices for measurement.

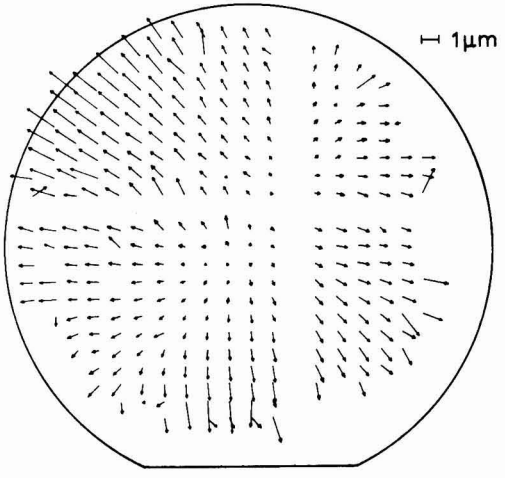

Fig. 10. Expansion due to temperature change

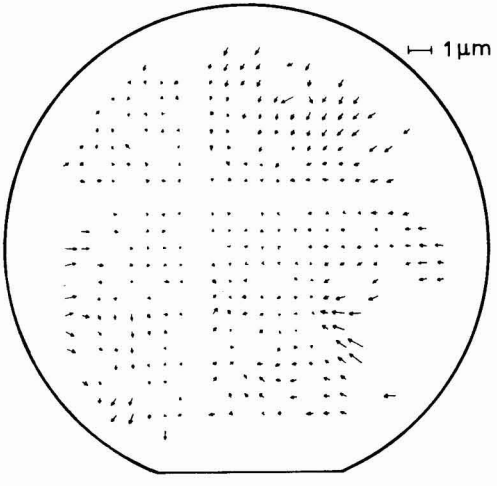

Fig. 12. Nonlinear distortions due to a silicon nitride layer

Manuscript submitted June 19, 1980; revised manuscript received *ca.* Sept. 16, 1980. This was Paper 184 presented at the Pittsburgh, Pennsylvania, Meeting of the Society, Oct. 15-20, 1978.

Any discussion of this paper will appear in a Discussion Section to be published in the December 1981 JOURNAL. All discussions for the December 1981 Discussion Section should be submitted by Aug. 1, 1981.

Publication costs of this article were assisted by Philips Research Laboratories.

LIST OF SYMBOLS

$\Delta x, \Delta y$	misregistration in X and Y direction (μm)
ρ	sheet resistance $\Omega/\square$
L	length of resistors (μm)
R_1 R_2	Stickman resistor values (Ω)
R_L, R_R	left and right resistor values (Ω)
r_1, r_2	measurement resistors (Ω)
V	applied voltage V (volts)

REFERENCES

1. I. J. Stemp, K. H. Nicholas, and H. E. Brockman, Proc. Conf. Microcircuit Engineering '78, Cambridge, England, April 1978.
2. D. S. Perloff, *IEEE J. Solid State Circuits*, **sc-13**, 436 (1978).
3. T. J. Russell, T.F. Leedy, and R. L. Mattis, *Tech. Dig. IEDM*, p. 7A (IEEE), Dec. 1977.
4. R. G. Gegenworth and R. P. Lamming, *S.P.I.E. V100 Semiconductor Microlithography II*, p. 66 (1977).
5. L. D. Yau, *Appl. Phys. Lett.*, **33**, 756 (1978).
6. I. J. Stemp, K. H. Nicholas, and H. E. Brockman, *IEEE Trans. Electron Devices*, **ed-26**, 729 (1979).
7. I. J. Stemp, K. H. Nicholas, and H. E. Brockman, Abstract 184, p. 491, The Electrochemical Society Extended Abstracts, Pittsburgh, Pennsylvania, Oct. 15-20, 1978.
8. R. Ward, To be published.

Surface Charges in a Zinc-Borosilicate Glass/Silicon System

Y. Misawa, H. Hachino, S. Hara, and T. Ogawa

Hitachi Limited, Hitachi Research Laboratory, Hitachi, Ibaraki, Japan

and H. Yagi

Hitachi Limited, Hitachi Works, Hitachi, Ibaraki, Japan

ABSTRACT

Surface charges in a zinc-borosilicate glass/silicon system were studied by measuring capacitance-voltage curves of metal-glass-silicon capacitors at various temperatures. The capacitance-voltage curves change remarkably with measurement frequency and temperature. The density of positive fixed charge decreases significantly with increasing glass firing temperature and also when nitrogen gas is added to the oxygen firing atmosphere. On the other hand, the density of the surface state is about (2-6) $\times$ 10^{12} $cm^{-2} \cdot eV^{-1}$ and insensitive to glass firing conditions. The surface charge is positive for n-type silicon and negative for p-type silicon when the Fermi level is near the intrinsic energy level. The surface charges are reversed, however, when the Fermi level is near the bandedge.

Surface passivation using glass powder is effective for achieving good reliability in high voltage silicon power devices since glass is electrically stable, easy to coat as a thick film, resistant to humidity, and has a low ion mobility. Therefore, many glass passivated silicon devices, such as thyristors, transistors, and diodes, have recently been developed.

Glasses as passivants for silicon devices are classified roughly into zinc-based glass and lead-based glass. Zinc-based glass is very stable at high temperature and high electric fields (1, 2), and therefore, is more suitable for achieving high reliability.

It is necessary to know better the surface charge configuration in a glass/silicon system in order to design glass passivated silicon devices accurately. However, not many investigations on this topic have been reported before. It is known that surface charge density changes with glass firing conditions, such as firing temperature and the content of the ambient (3). Many surface states exist at the glass/silicon interface (1, 2) and the flatband voltage is positive for n-type silicon and negative for p-type silicon (2).

However, the changes of surface charge configuration in a glass/silicon system with glass firing conditions have not been studied.

Key words: charge, films, glass.

In this paper, the variations of fixed charge density and surface state density with glass firing conditions and the conductivity-type of silicon substrates are discussed by measuring capacitance-voltage (C-V) curves at various temperatures.

Experimental

In this work, surface charge in a glass/silicon system was measured by metal-glass-silicon (MGS) capacitors at various temperatures. This method, as proposed by Gray and Brown (4), can separate the effects of the fixed charge in glass and surface states at glass/silicon interface, on the surface potential. Table I shows the properties of silicon substrates. The composition of the glass used is: ZnO, 65 weight percent (w/o); B_2O_3, 21 w/o; SiO_2, 8.5 w/o; PbO, 4 w/o; SnO, 1 w/o; and Sb_2O_3, 0.5 w/o. This glass has a

Table I. Properties of silicon substrates

Conduction type	N	P
Dopant	Phosphorus	Boron
Resistivity, $\Omega \cdot$ cm	9-15	8-12
Crystal orientation	(111)	(111)
Method of production	CZ	CZ
Surface	Mirror polish	Mirror polish

softening point of 645°C, crystallization point of 719°C, and thermal expansion coefficient of 4.0 10^{-6}/°C. MGS capacitors were prepared by following procedure. The glass powder was deposited on the silicon substrate by the electrophoretical method. The colloidal suspension used consisted of isopropyl alcohol as a suspension medium with a small amount of additive electrolyte and glass powder whose size was controlled by decantation. The glass film thickness was controlled to about 10 μm. The deposited glass powder was fired in an oxygen or a nitrogen-oxygen (4:1) mixture at various temperatures. The metal electrodes were formed on the glass film by evaporating aluminum. Capacitance of the MGS was measured in the evacuated chamber at various temperatures by a capacitance bridge. The measurement frequency was 1 MHz unless otherwise noted.

Results and Discussion

Effects of measurement frequency and temperature on the C-V curves.—Figure 1 shows the effect of measurement frequency on the C-V curves for samples made with the glass fired on n-type silicon at 710°C in a nitrogen-oxygen mixed atmosphere. The C-V curve shifts to the positive voltage direction with increasing frequency. It can be seen from this that many surface states with various time constants exist. Figure 2 illustrates the effect of measurement temperature on the C-V curves for the same sample. Here the C-V curve shifts significantly to the negative voltage direction with increasing measurement temperature.

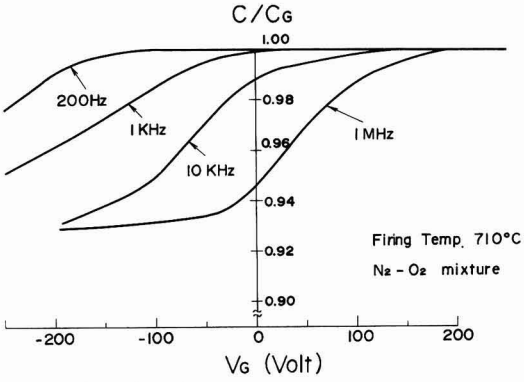

Fig. 1. The effect of measuring frequency on the capacitance-voltage curves of the sample made with the glass fired on n-type silicon at 710°C in a nitrogen-oxygen mixture.

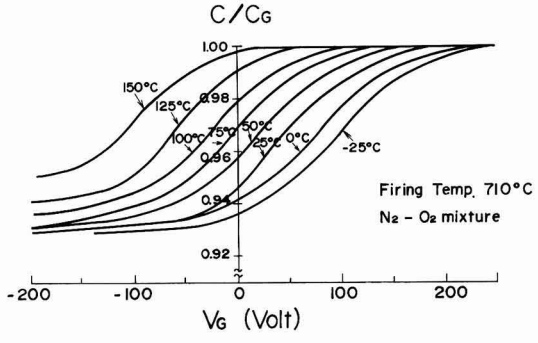

Fig. 2. The effect of measuring temperature on the capitance-voltage curves of the sample made with the glass fired on n-type silicon at 710°C in a nitrogen-oxygen mixture.

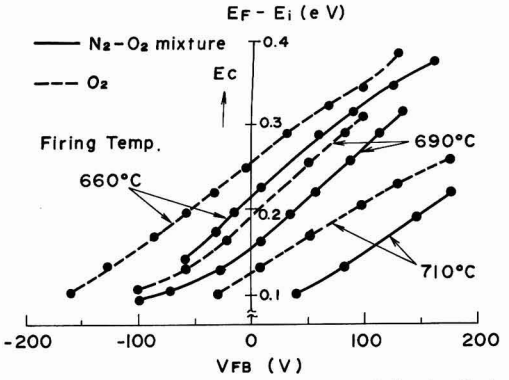

Fig. 3. Flatband voltage of the samples made with the glass fired on n-type silicon at various conditions *vs.* energy level.

This shows that the surface states are distributed over a wide range of energy levels.

Effect of glass firing condition on surface charge configuration.—Figure 3 shows flatband voltage (V_{FB}) of the samples made with the glass fired on n-type silicon at various temperatures in an oxygen or a nitrogen-oxygen mixed atmosphere *vs.* energy level $E_F - E_i$, where E_F is the Fermi level and E_i is the intrinsic level. The energy level decreases with increasing measurement temperature. The flatband voltage increases with increasing energy level and the curves shift in the positive voltage direction as the glass firing temperature increases. That is, the net surface charge density is more negative as the glass firing temperature increases. These curves are nearly linear and their slopes, nearly equal. That is, the surface state density is nearly equal over a wide range of energy levels. The surface state density for glass firing temperature of 660°C is shown in Fig. 4, as calculated

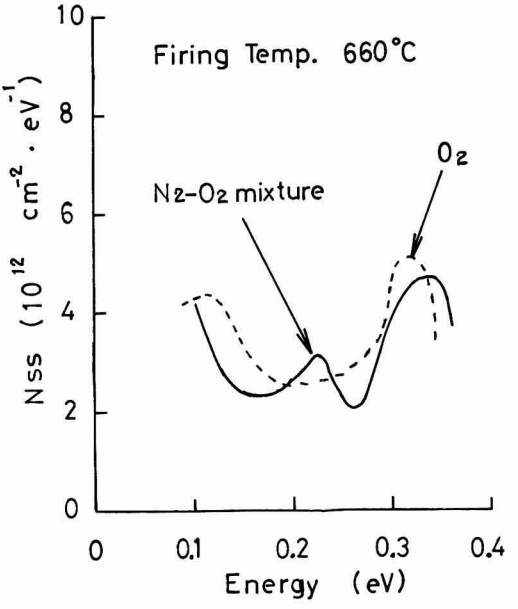

Fig. 4. Surface states density of the samples made with the glass fired on n-type silicon at 660°C in an oxygen or nitrogen-oxygen mixture *vs.* energy level.

from the experimental results given in Fig. 3. The surface state density is (2-6) $\times$ 10^{12} $cm^{-2} \cdot eV^{-1}$. Therefore, it is felt that the variation of the flatband voltage with the glass firing temperature is due to the fixed charge rather than surface states. So, the positive fixed charges decreases as the glass firing temperature increases. The flatband voltage for the firing atmosphere of a nitrogen-oxygen mixture is larger than that for an oxygen alone. The positive fixed charge decreases when nitrogen is added to the oxygen firing atmosphere.

Effect of the conductivity type of silicon substrate on surface charge configuration.—Figure 5 shows the flatband voltage of the samples made with the glass fired on n-type and p-type silicon *vs.* energy level. The flatband voltage of the glass fired on p-type silicon decreases as the Fermi level moves closer to the valence band. On the other hand, the flatband voltage of the glass fired on n-type silicon shifts to the positive voltage direction, as the energy level moves closer to the conduction band. That is, the flatband voltage of the glass fired on p-type silicon varies differently with measurement temperature as compared to that of the glass fired on n-type silicon. However, the change of flatband voltage with energy level for n-type and p-type silicon are qualitatively the same. The slopes of curve for n-type silicon is nearly equal to that for p-type silicon. Saying it differently, the surface states are distributed similarly in the energy level of the conduction band side and the valence band side as in Fig. 6 calculating from Fig. 5. Only the displacement of the curve along the flatband axis is different. Flatband voltage for p-type silicon at room temperature is negative and that for n-type silicon is positive. These results agree with the results of Goodwin (2). This difference is considered as the difference of the sign of fixed charge. That is, the fixed charge for n-type silicon is positive, that for p-type silicon is negative.

Conclusions

Surface charges in a zinc-borosilicate glass/silicon system were studied by measuring capacitance-voltage

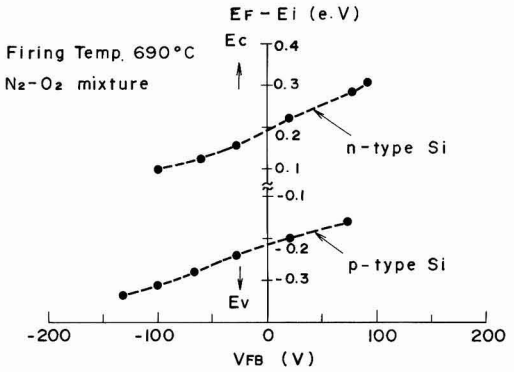

Fig. 5. Flatband voltage of the samples made with the glass fired on n-type or p-type silicon at 690°C in a nitrogen-oxygen mixture *vs.* energy level.

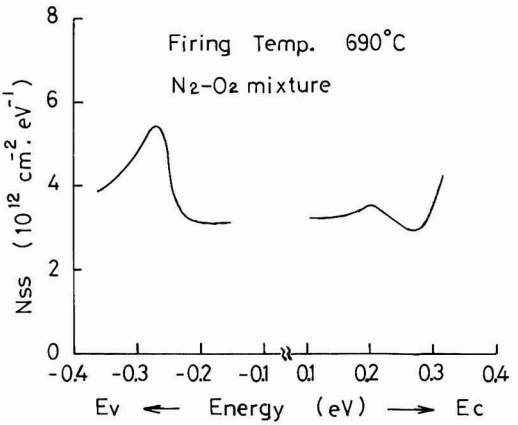

Fig. 6. Surface states density of the samples made with the glass fired on n-type or p-type silicon at 690°C in a nitrogen-oxygen mixture *vs.* energy level.

curves of metal-glass-silicon capacitors at various temperatures. Capacitance-voltage curves changed remarkably with measuring frequency and temperature due to the existence of many surface states. Net surface charge density varies with glass firing conditions as follows. The positive fixed charge density decreased remarkably with increasing glass firing temperature and also when nitrogen gas was added to the oxygen firing atmosphere. On the other hand, surface state density was about (2-6) $\times$ 10^{12} $cm^2 \cdot eV^{-1}$ and hardly changed with glass firing conditions. Moreover, the surface charge was positive for n-type silicon and negative for p-type when the Fermi level is near the intrinsic energy level. On the other hand, the surface charge was reversed when the Fermi level is near the bandedge.

Acknowledgments

The authors wish to thank Messrs. S. Kawai, K. Wajima, and K. Morita and Dr. Okamura for their helpful suggestions and encouragements during this study.

Manuscript submitted Dec. 17, 1979; revised manuscript received Sept. 8, 1980.

Any discussion of this paper will appear in a Discussion Section to be published in the December 1981 JOURNAL. All discussions for the December 1981 Discussion Section should be submitted by Aug. 1, 1981.

Publication costs of this article were assisted by Hitachi, Limited.

REFERENCES

1. K. Miwa, K. Ikeda, and K. Aoki, *NEC Res. Dev.*, **42**, 1 (1976).
2. C. A. Goodwin, Paper 353 presented at The Electrochemical Society Meeting, Las Vegas, Nevada, Oct. 17-22, 1976.
3. K. Miwa, Y. Moriguchi, M. Kanno, T. Kawamura, and T. Shibuya, *Denki Kagaku*, **40**, 478 (1972).
4. P. V. Gray and D. M. Brown, *Appl. Phys. Lett.*, **8**, 321 (1965).

Tapered Windows in SiO_2, Si_3N_4, and Polysilicon Layers by Ion Implantation

J. Götzlich and H. Ryssel

Fraunhofer-Institut für Festkörpertechnologie, 8000 München 60, Germany

ABSTRACT

In integrated circuit production, tapered windows are important for good step coverage of subsequent deposited layers. We show that by implantation of Ar and As ions into SiO_2, Si_3N_4, and polysilicon layers the slope angle of window walls can be reduced. The slope angle is determined by the ratio of the etch rates of the undamaged region to the damaged top region of the layer. Depending on ion species, ion dose, ion energy, and etching conditions we could achieve minimum angles of about 10° in these layers.

In semiconductor technology, the definition of structures in layers of SiO_2, Si_3N_4, or polycrystalline silicon is usually made by photolithography, which is followed by chemical or plasma etching of the film. If the etched structure is coated by another film, the step coverage of this second film at the windows is determined by the wall contour of the window. The step coverage is especially important with metal layers, since at a steep edge the metal is thinner and can cause severe problems with reliability (1). Many investigations have been performed to optimize step coverage by a proper design of the evaporation equipment. New evaporation techniques using magnetron sputtering have brought a significant improvement. The most reliable method is, however, the tapering of the slope of window walls.

Since all layers to be tapered are amorphous or polycrystalline, they are etched isotropically using wet chemical etches or standard plasma etching. If the adherence of the etching mask is good, the slope of the window wall will reach asymptotically 90° in case of overetching (2). Shallow slopes in homogeneous films can be produced by lifting-off the photoresist during the etching process. The slope angle is then determined by the ratio of lateral lift-off rate to the etching rate of the film. However, this technique is hard to control and therefore the results are not well reproducible.

A more reliable and very often used method is the reflow of phosphorus-silicon-glass (PSG). PSG is deposited at low temperatures from silane, oxygen, and phosphine in a nitrogen atmosphere and reflowed at about 900°C, resulting in very smooth window edges (9). Another reliable method for tapering windows is the application of a two-level structure, in which the top part of the layer etches faster than the lower part. The sine of the slope angle of the lower part of the layer is given by the ratio of the etching rates of the two components of the film. Even if the layer is overetched, this angle will have a constant value (3). This sandwich structure can be achieved in two different ways: First, by changing the chemical compounds during the deposition of the layer (*e.g.*, CVD layers) (4), and second, by bombardment of the layer with energetic ions which damage the surface and thus enhance the etching rate.

Moline *et al.* (5) reported on the tapering of SiO_2 using Ar ions. North *et al.* (3) also used Ar ions to taper PSG glass and Bell and Hoepfner (6) used Ar ions from an ion-etching machine for tapering SiO_2 layers.

In this paper we report on the tapering of window walls in SiO_2-, Si_3N_4-, and polysilicon layers by ion implantation using argon, arsenic, and boron ions with subsequent chemical or plasma etching.

Key words: ion implantation, tapered windows, damage enhanced etching.

Experimental Techniques

For all experiments, phosphorus-doped <111>-oriented silicon with a resistivity of 1-10 Ωcm was used. For the experiments with SiO_2, the silicon wafers were oxidized at 1000°C for 1 hr in a wet oxygen atmosphere, forming an SiO_2 layer of about 0.4 μm. The silicon nitride layers were deposited in an SiH_4-NH_3-N_2 atmosphere at 800°C. The film thickness was 0.4 μm. The deposition of the polysilicon layers was done in an SiH_4-N_2 atmosphere at 700°C. The 0.9 μm thick polysilicon was deposited on a thin SiO_2 layer, which acted as an etch stop.

The wafers were then implanted with Ar-, As-, and B-ions at energies between 50 and 200 keV and doses of 10^{12}-10^{16} cm^{-2}. To obtain the different implantation doses, a variable beam stopper was used, which made it possible to implant up to six various doses on one wafer. Thus, all samples to be compared were processed in the same way during the photolithographic and etch processes.

Before applying the photoresist to define the etch windows in SiO_2 and polysilicon, the wafers were baked in a nitrogen atmosphere at 300°C for 30 min. Nevertheless, it was necessary to apply an adhesion promoter solution to obtain reliable results. The nitride layers were CVD coated with a 200 nm thick oxide layer in an SiH_4-O_2-N_2 atmosphere at 450°C. The SiO_2 was etched in buffered hydrofluoric acid. The Si_3N_4 was etched at 160°C in conc H_3PO_4, using the SiO_2 layer as a mask. The etching solution for the polysilicon consisted of 100 HNO_3:3HF:4H_2O. Besides these procedures, polysilicon layers were etched in a CF_4 plasma in order to compare plasma etching with wet chemical etching.

The etching times were 2-4 min for the SiO_2, 60-80 min for the Si_3N_4, and 0.5-1 min for the polysilicon layers. The relative amount of overetching after etching through the layer was about 10%. After etching, the samples were cleaned using organic solvents and then cleaved. The cross section of the window wall was determined using a scanning electron microscope (SEM). The uncertainty in the determination of the slope angle of the window walls was ± 2°. The reproducibility was also ± 2°.

Results and Discussion

In Fig. 1, SEM photographs are shown for typical etched structures in Si_3N_4 layers implanted with argon ions. For all doses shown, a reduction in the slope angle can be seen. The top layer of 1000Å shows a steeper slope. This can be attributed to the thickness of the damaged layer, which shows a nearly constant enhanced etching rate. Using lower implantation energies, this effect can be reduced.

The implantation of Si_3N_4 layers with As ions (80 keV) reduced the taper angle to 11° for a dose of

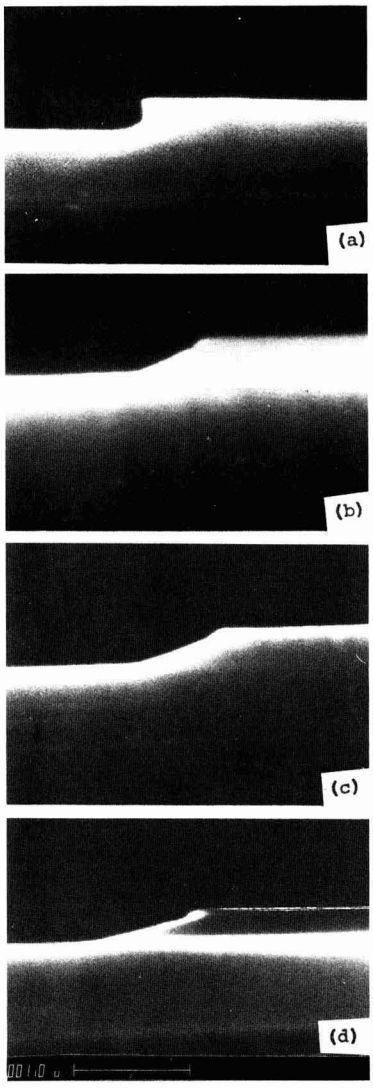

Fig. 1. Scanning electron micrographs of wall profiles in Si_3N_4 layers after Ar implantation with 50 keV and various doses: (a) no implantation; (b) $1 \cdot 10^{15}$ cm^{-2}; (c) $5 \cdot 10^{15}$ cm^{-2}; (d) $1 \cdot 10^{16}$ cm^{-2}.

10^{16} cm^{-2} (Fig. 2). There seems to be a saturation effect for the higher ion doses. This saturation does not occur until doses greater than 10^{15} cm^{-2}. The same dependence is observed for the implantation of 50 keV Ar ions; the slope angle decreases continuously to 14° for the 10^{16} cm^{-2} dose. In both cases (Ar and As ions), there was a step in the profile for doses greater than 5×10^{14} cm^{-2} (see Fig. 1). This step was not taken into consideration for the results in Fig. 2. The height of this step (about 0.1 μm) should indicate the depth to which the enhanced etching occurs.

In Fig. 3, the slope angles of window walls in SiO_2 after implantation with Ar and As ions, respectively, with different ion doses are shown. Implanting Ar ions with 50 keV or As ions with 80 keV, the slope angle can be reduced to 11° or 12°, whereas by implantation of Ar ions with 200 keV the minimum angle is about 24°. In all cases there is a saturation effect which depends on ion dose, species, and energy. This saturation

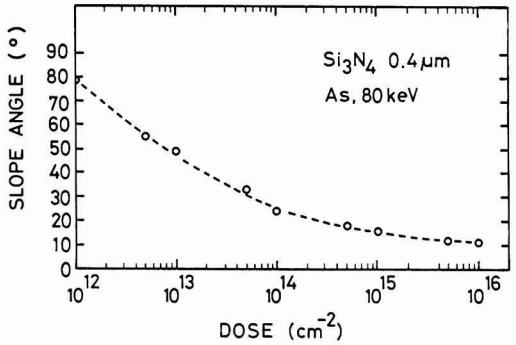

Fig. 2. Slope angles of window walls in Si_3N_4 vs. ion dose after implantation with 80 keV As.

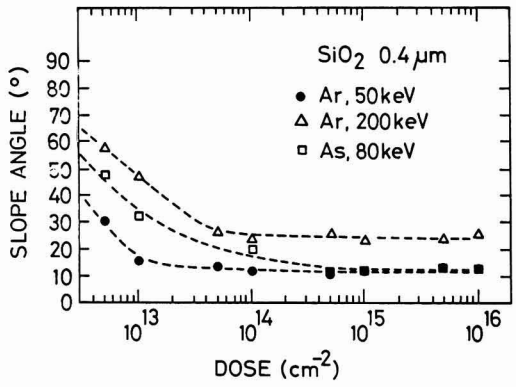

Fig. 3. Slope angles of window walls in SiO_2 vs. ion dose after implantation with 50 keV and 200 keV Ar and 80 keV As.

effect should be correlated with the saturation of defects produced by ion implantation. The As-implanted samples showed a step in the window profile for doses greater than 5×10^{13} cm^{-2}. The height was the same as for the Si_3N_4 layers (see above). In the case of Ar implantation, no step could be observed.

The results of the experiments with polysilicon layers are shown in Fig. 4 and 5. These measurements showed no effect of the ion implantation on the etching rate for doses up to 10^{13} cm^{-2}, *e.g.*, a steep slope of 80°-90° was observed. For ion doses greater than

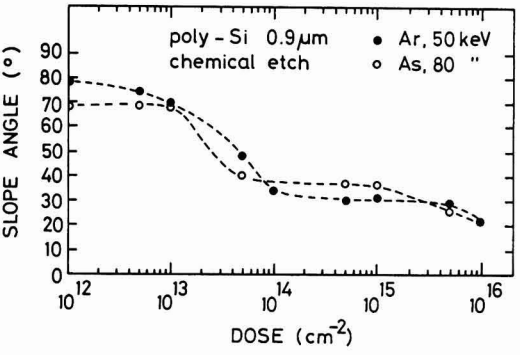

Fig. 4. Slope angles of window walls in polysilicon vs. ion dose after implantation with 50 keV Ar and 80 keV As and chemical etching.

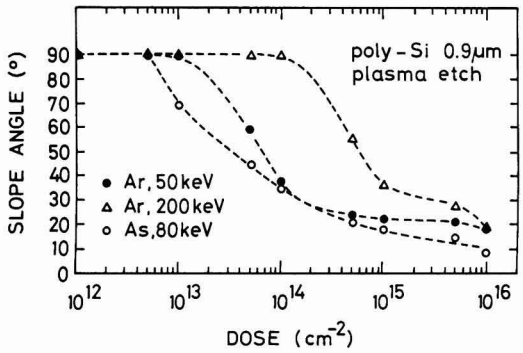

Fig. 5. Slope angles of window walls in polysilicon *vs.* ion dose after implantation with 50 keV and 200 keV Ar, 80 keV As and plasma etching.

10^{13} cm^{-2} there was a reduction of the slope angle in the case of the 50 keV Ar and the 80 keV As implantation for the chemically etched samples as well as for the plasma-etched layers. The minimum slope angle achieved with plasma-etched samples was 9° (1×10^{16} As/cm^2, 80 keV), whereas with the chemically etched samples the angle could only be decreased to 23° (1×10^{16} cm^{-2}, 80 keV As and 50 keV Ar). There is also a different behavior in respect to the formation of a step in the wall profile between the two sets of samples. The chemically etched samples showed no step, whereas for the plasma-etched samples, there was a step with a height of 0.1 μm (Ar, 50 keV) or 0.2 μm (As, 80 keV) for doses greater than 5×10^{14} cm^{-2}. The implantation of Ar with 200 keV in polysilicon layers only had an influence on the slope angle for ion doses greater than 1×10^{14} cm^{-2}. The slope angle of these 200 keV samples could only be measured in the case of plasma etching because of the steep overhanging step in the case of chemical etching. The height of this step was about 0.25 μm. This step can be explained by a lower etch rate at the surface, since the damage is produced predominantly in a deeper region. The plasma-etched samples showed only a step for the 10^{16} cm^{-2} implantation; the height was as above.

The implantation of B ions with 60 keV in SiO_2 and polysilicon layers gave no reliable results. At the higher ion doses (10^{15}-10^{16} cm^{-2}) a taper angle of about 40° could be observed but the reproducibility was only ± 10°. Most of the samples also showed a high step of about 0.3 μm in the wall profile, due to the large range of the ions.

All layers (SiO_2, Si_3N_4, poly-Si) showed the formation of a step profile for some implantation conditions such as high ion energy or high ion doses. The height of this steeper step on top of the layers was generally greater than the range of the implanted ions, and especially greater than the range of the damage created during the ion bombardment. Usually, the height of this step is about 0.05 to 0.1 μm more than the projected range of the ions. A possible explanation is that there exists a transition region with the above thickness, in which the steep slope at the surface is passed into the reduced slope (which is determined by the ratio of the etching rates of the damaged to the undamaged region). This observation should be taken into account if one adjusts the ion energy for tapering window walls. Moreover, one should take into consideration that any annealing of the implantation damage could change the slope angle of the wall profile. Such an annealing can occur not only during technological processes at low temperatures, but also already during the implantation process due to substrate heating (7, 8).

Conclusion

We have shown that in SiO_2, Si_3N_4, and polysilicon layers, the slope angle of window walls can be tapered by ion implantation. The slope angle depends on ion species, ion dose, and ion energy. The minimum angles achieved here were about 10°, *e.g.*, the etch rate of the damaged surface region showed a maximum enhancement of about 6 by ion implantation. The observed step in the profile can be reduced by reducing the ion energy. The reduction of the energy at lower ion doses gives the same slope angle as with the higher energy.

Acknowledgment

The authors wish to thank Mr. H. Kranz and Miss E. Traumüller for the implantations, Mrs. M. Ramin for the photolithography, and Miss D. Boehm for the SEM investigations.

Manuscript submitted July 15, 1980; revised manuscript received Sept. 12, 1980.

Any discussion of this paper will appear in a Discussion Section to be published in the December 1981 JOURNAL. All discussions for the December 1981 Discussion Section should be submitted by Aug. 1, 1981.

Publication costs of this article were assisted by the Institut für Festkörpertechnologie.

REFERENCES

1. J. L. Vossen, G. L. Schnable, and W. Kern, *J. Vac. Sci. Technol.*, **11,** 60 (1974).
2. R. G. Brandes and R. H. Dudley, *This Journal,* **120,** 140 (1973).
3. J. C. North, T. E. McGahan, D. W. Rice, and C. Adams, *IEEE Trans. Electron Devices,* **ed-25,** 809 (1978).
4. B. A. Boxall, *Solid-State Electron.*, **21,** 1173 (1978).
5. R. A. Moline, R. R. Buckley, S. E. Haszko, and A. U. MacRae, *IEEE Trans. Electron Devices,* **ed-20,** 840 (1973).
6. G. Bell and J. Hoepfner, in "Etching for Pattern Definition," H. G. Hughes and M. J. Rand, Editors, p. 47, The Electrochemical Society Softbound Proceedings Series, Princeton, N.J. (1976).
7. P. D. Parry, *J. Vac. Sci. Technol.*, **15,** 111 (1978).
8. P. D. Parry and S. P. Bristol, *ibid.*, **15,** 664 (1978).
9. W. Kern and R. S. Rosler, *ibid.*, **14,** 1082 (1977).

Neutron Activation Study of a Gettering Treatment for Czochralski Silicon Substrates

L. E. Katz and P. F. Schmidt*

Bell Laboratories, Incorporated, Allentown, Pennsylvania 18103

and C. W. Pearce*

Western Electric Company, Allentown, Pennsylvania 18103

ABSTRACT

A pre-process gettering treatment is described for Czochralski silicon substrates which removes essentially any transition group metal contaminants present in the wafer and continues to getter contaminants during subsequent device processing. Laser induced damage (LID) on the back surface of the wafer, a modified high temperature HCl treatment, and formation of oxygen precipitates in the bulk of the wafer only, are used as a three-step gettering process. Neutron activation analysis (NAA) was used to monitor the gettering behavior of each individual contaminant species and shows that the combined treatment is indeed nearly 100% effective in removing impurities, both from starting substrates and from processed wafers. Removal of impurities from the starting substrates is important in order to prevent the formation of oxidation induced stacking faults (OSF), which are nucleated by impurities and then become decorated with impurities making them much harder to getter (1). Holdtime performance of 4K and 16K dynamic RAM's fabricated on substrates treated in this manner served to evaluate the effectiveness of the treatment. Significant improvement can be achieved for bulk substrates. However, the performance of epitaxial silicon on low resistivity substrates cannot be matched since the low resistivity substrate in the EPI case additionally suppresses the minority carrier diffusion current from the bulk of the wafer. The individual steps of the treatment are: (*i*) produce laser induced damage on the back surface of the wafers by means of powerful, partially overlapping laser pulses; (*ii*) ramp from 950° to 1250°C in 0.5% O_2, 0.5% HCl, balance argon; (*iii*) oxidize at 1250°C for 8 hr in dry O_2 + 0.5% HCl, then ramp down to 950°C. Keeping the oxygen concentration to 0.5% during step (*ii*) is important to prevent formation of a thick oxide film during this step. The long oxidation at 1250°C both depletes interstitial oxygen at the Si surface, thus preventing formation of OSF, and causes formation of oxygen precipitates in the bulk if the initial O_i concentration is high enough. Oxygen precipitates in the bulk are a valuable means of gettering.

The detrimental effect of transition group metal impurities on device performance is well documented, both through the formation of microdefects in the silicon lattice during high temperature treatments and through their action as regeneration-recombination centers. The microdefects are in fact decorated by impurity precipitates. Impurities located at the surface are implicated in the formation of oxidation-induced stacking faults. Careful cleaning, prior to oxidation is a necessary but often insufficient condition for avoiding the OSF. The device sensitivity to transition group metal contamination depends on the required performance of the device and on the process technology used.

Metal impurities can be "gettered" from the bulk of the silicon by a variety of means, such as volatilization as chlorides during heat-treatment in Cl-containing ambients, diffusion into regions of enhanced metal solubility (N+ or P+ regions), or precipitation at deliberately introduced crystal defects. A number of techniques have been used for the controlled introduction of such crystal defects, such as ion implantation damage, stress-inducing surface films, surface abrasion, and oxygen precipitates, to which now is being added lattice damage from laser pulses of sufficient power to cause local melting of the silicon. The wavelength employed determines the distance over which the energy is absorbed by the silicon, and hence the depth of damage introduced. All of the lattice-damage-type gettering procedures require that the damaged region be located remote from the device areas; usually the back side of the wafer is used for this purpose (except in certain ion implantation applications) (2). The metal impurities are then made to diffuse into the deliberately damaged regions during a high temperature treatment, where they are held quite tenaciously and are not then involved in space charge leakage currents, provided the lattice damage survives the subsequent heat-treatments.

Gettering by oxygen precipitates poses certain problems of its own. Oxygen is a regular unintentional dopant in Czochralski grown silicon, though the level of oxygen concentration depends on several factors, such as rotational speed during crystal growth (3), ingot diameter, distance from the seed end, etc. If the oxygen concentration is high enough for precipitation of oxygen to occur during heat-treatments, then precipitates can form in the device areas, giving rise to microdefects and deterioration of device performance. On the other hand, oxygen precipitates are a valuable means of gettering. Their presence is thus desirable, but only in the bulk of the silicon, not in the device areas near the front surface of the wafer. The means of achieving this oxygen distribution was previously (4) described; it requires a prolonged heat-treatment in oxygen at 1250°C.

Gettering treatments are usually applied fairly well into the processing sequence, often as one of the last high temperature treatments. At this stage, however, the original crystal perfection of the surface-near layers of the wafer may already have been degraded, and impurities are precipitated at lattice defects where they are difficult to getter. In a way, the gettering treatment is being applied too late. Table I shows how

* Electrochemical Society Active Member.
Key words: gettering, HCl, laser damage, silicon defects.

inefficient N+ diffusion gettering from the back surface can sometimes be at this stage. In this example, a 4K dynamic RAM wafer pulled from the processing sequence, the gold contamination was reduced significantly, but the copper contamination remained high; the inverse occurs just as frequently, sometimes even both Au and Cu remain high.

Gettering studies in the past have mostly utilized device performance after the gettering step as the main diagnostic criterion. However, no detailed information about the concentrations of the different contaminant species present in the device regions of silicon wafers before and after the gettering step can be obtained in this way. In view of the exceedingly small amounts of contaminants already sufficient to degrade device performance, only neutron activation analysis has the necessary sensitivity to produce such information. NAA has therefore been applied throughout this study and has given firm quantitative results. Device performance after gettering confirmed the predictions based on NAA and expected from general principles. Systematic NAA is also a valuable and versatile method of process control.

Table II illustrates the correlation between level of contamination and generation lifetime or device holdtime. Concentrations of more than a few times 10^{12} atoms of Cu or Au per 3 in. silicon wafers are definitely to be avoided. While Cu and Au are among the most deleterious contaminants, other transition group metals also give rise to deep lying recombination-generation levels in silicon and can be equally detrimental. The concentration at which a given impurity species begins to cause trouble is a complex function of its capture cross sections for electrons and holes, its solubility and diffusivity, etc. However, one may expect that these concentrations will be higher than for Cu or Au.

The ideal gettering treatment for transition group metals in silicon should accomplish the following objectives:

1. It should remove detrimental impurities from the surface-near layers of the silicon wafer prior to the first high temperature oxidation step while maintaining the perfection of the silicon lattice near the surface where devices will be located.

2. It should continue to exert a gettering action throughout the device fabrication process, *i.e.*, the gettering mechanism must be able to survive prolonged high temperature treatments.

3. In particular, it must prevent impurities introduced into the silicon during later steps of device fabrication from becoming lodged at crystal defects near the sensitive front surface, in other words, it must prevent formation of oxidation-induced stacking faults throughout the device fabrication process.

These objectives can be achieved by a 3-step gettering process which consists of the following steps:

1. Applying laser induced damage (LID) to the back surface of the silicon wafers. The resulting damage is so severe that it survives essentially any annealing steps without losing its gettering ability, as demonstrated in separate experiments (5).

2. A high temperature HCl treatment in the presence of only a trace of oxygen. Some oxygen is necessary to prevent attack on the silicon, but higher concentrations of oxygen would cause growth of a thick (≥1000Å) oxide film; this impedes the outdiffusion of many transition group elements which therefore cannot react with and be transported away by the chlorine. Gold and the platinum group metals cannot be gettered by the HCl treatment because of the thermodynamic instability of their chlorides at high temperatures. For the gettering of these elements, a solid-state sink (LID layer, oxygen precipitates, or N+ diffused layers) is thus indispensable.

3. Depletion of interstitial oxygen (O_i) in the surface-near layers of the silicon wafers to a depth of about 120 microns by means of a high temperature anneal in oxygen (4). Formation of a thick oxide film eventually starves the Si/SiO_2 interface of oxygen from the gas phase (parabolic rate law), so that apparently the interstitial oxygen near the silicon/SiO_2 interface is consumed by this reaction. This depletion of oxygen in the surface-near layers has been proved both by charged particle activation analysis ($^{16}O(^3He, xp)F^{18}$; work performed for Bell Labs at the Texas A&M University, Center for Trace Characterization), and by microscopic examination in conjunction with cleavage and Secco-etch studies.

We have chosen 450 min at 1250°C in dry O_2 + 0.5% HCl for this step. In silicon wafers with an initial (O_i) content of more than about 30 ppm,[1] this treatment also results in the simultaneous precipitation of oxygen-silicon complexes in the bulk, but not in the surface-near layers of the wafers. These precipitates then become sinks for impurities introduced via the front surface during device processing. On silicon wafers with less than about 30 ppm (O_i) such precipitates cannot form and here the LID layer on the back surface continues to exert its gettering action. This is an important point because the interstitial oxygen concentration on some ingots can be less than 30 ppm and can also be nonuniform, so that even an average oxygen content above 30 ppm does not really guarantee formation of oxygen precipitates forming a continuous sheet in the bulk of any given wafer. This is particularly true of the butt end of an ingot. The thick oxide film grown during the 1250°C anneal can also be used as the initial oxide for device fabrication.

Table I. Gettering of impurities by N+ diffusion on back surface of processed bulk silicon wafers. (A 4K dynamic RAM wafer pulled from processing sequence.)

	Cu (atoms cm^{-2})	Au (atoms cm^{-2})
After phosphorus diffusion	3.8E12	6.2E12
After removal of N+ region and P-glass by etching	2.6E12	1.8E11

Table II. Correlation between copper and gold contamination and generation lifetime or device holdtime

Impurity concentration per 3 in. diam wafer			
MOS wafers			
Mos generation lifetime	100 μsec		2.0 μsec
Copper	—		5.0E14
Gold	2.5E11		3.1E12
4K dynamic RAM's on bulk silicon			
Holdtime at room temperature	100 sec	3 sec	0.8 sec
Copper	1.0E12	6.8E13	2.5E14
Gold	1.7E12	8.2E12	7.3E13

Experimental

Materials preparation.—All of the silicon wafers were cut from Czochralski boron-doped (100) oriented ingots of 3 in. diam and a fairly high oxygen content (~35 ppm). The resistivity ranged from 5.5-9.3 Ω-cm, and nominal thickness of the finished substrates was 20 mils. They were chem-etched on both sides and polished on one. Their back surfaces were subjected to laser damage as detailed in Table III. Prior to use they were again cleaned in hot ammonium hydroxide-hydrogen peroxide solution.

In many experiments previously oxidized and then neutron activated wafers were used for investigation of the three separate gettering mechanisms (HCl, LID, layer, oxygen precipitates). The activity of these samples had decayed to essentially zero over periods of

[1] The infrared oxygen concentration determination is based on ASTM F-121-79 "Interstitial atomic oxygen content of silicon by infrared absorption."

Table III. Details of laser treatment used

Laser type	ND:YAG, 8W-Cw, TEMoo
Dislocaton density produced	3oo/mm (counted along a cleavage face)
Propagation distance after a 1100°C, 1 hr oxidation	50 microns
Laser repetition rate	20 kHz
Machined spot diameter	45 microns
Spot overlap	30%

many months of storage, but their impurity contents were accurately known from the previous NAA results. These wafers, of course, contain initially very severe lattice damage from the previous neutron activation step. Some but not all of this damage can be annealed out. [During our neutron irradiation, fast neutrons with energies above 1 MeV were present as well, at a concentration of about 10% of the thermal neutrons. While fast neutrons do not contribute to the activity of isotopes formed by (n,gamma) reactions, they cause most of the lattice damage; this severe damage, in conjunction with appreciable contamination, makes complete annealing of lattice defects very difficult.] These wafers are therefore especially difficult to getter, and results obtained on them represent "worst possible cases."

High temperature treatments.—Table IV summarizes the separate steps of the cleaning-gettering-oxidizing treatment. Step 2 details the HCl cleaning and gettering during ramp-up from 950° to 1250°C, step 3 the 1250°C anneal in dry O_2 + 0.5% HCl. Neither the oxygen nor the HCl concentration is very critical; in fact, it is quite difficult to maintain a flow rate of exactly 0.5%. However, the oxygen concentration, on the one hand, should be kept to the level necessary to prevent pitting of the silicon surface, but, on the other, should be low enough that not more thon 100-200Å of oxide will grow during step 2. The HCl concentration, on the one hand, should be kept high enough to remove contaminants from the silicon as chlorides and to prevent indiffusion of additional impurities during the 8 hr 1250°C anneal in dry O_2, but, on the other hand, must be low enough to avoid any trouble due to phase segregation at the Si/SiO_2 interface (6). Throughout this work we have not observed troubles neither due to phase segregation, nor due to penetration of dislocations from the LID layer to the front surface, however, these are potential difficulties one has to watch for.

Neutron activation and analysis.—Many of the transition group metals, especially those of the stainless steel family, produce only very long-lived radioisotopes under neutron bombardment. In order to have sufficient sensitivity for these elements at the concentration levels at which they can be detrimental in silicon, long irradiation and long spectrum acquisition times are required (the saturation factor of the activity reached during neutron irradiation is given by $S = 1 - e^{-\ln 2 \cdot T_{irr}/T_{1/2}}$, where T_{irr} is the time in the reactor, and $T_{1/2}$ the half-life of any given isotope, both measured in the same time units. It is obvious that S will remain very small if $T_{irr}/T_{1/2}$ is a small quantity). Samples were therefore routinely irradiated for 120 hr at core face of the Union Carbide Research Reactor at Tuxedo, New York 10987; the flux at this position is approximately 7E12 thermal neutrons cm^{-2} sec^{-1} (averaged over the diameter of a 3 in. wafer), with an epithermal component of about 3%. Further details are given in the preceding paper by Schmidt and Pearce. (7).

Table IV. Details of gettering procedure

1. Subject back surface to laser-induced damage (LID).
2. Ramp up from 950° to 1250°C over a period of about 20 min in a mixture of 0.5-1% O_2, 0.5-1% HCl, balance argon.
3. At 1250°C, substitute dry O_2 for the argon, but keep HCl flowing; keep at 1250°C for about 8 hr. Ramp down to 950°C in the same ambient.

After cleaning, wafers were measured for 18 hr in close proximity to the end cap of a 46 cm^3, closed-one-end coaxial lithium-drifted detector, connected via a spectroscopy amplifier and ADC to a computerized 4096 channel analyzer. The measuring system and the concentration evaluation have been described in Ref. (8). It should perhaps be pointed out that the volume of data generated by this study as well as by continual production control was so large that it could not have been handled readily by conventional neutron activation analysis in which a standard for each element to be determined is co-irradiated with the unknown samples. The Absolute Counting method of analysis does not require such standards and is consequently much faster. It is also described in Ref. (8).

Distribution of impurities between the silicon wafer and the LID layer were determined by measuring the same wafer before and after etch-off of the LID layer in 5 parts nitric, 3 parts hydrofluoric, 3 parts acetic acid mixture. The acid etch was always followed by a double clean in hot $HCl-H_2O_2$ solution to remove chemisorbed impurities from the silicon surface; without this precaution, especially gold determination can give completely misleading results.

Device fabrication.—4K and 16K dynamic memory devices were fabricated on substrates of the description given under "Materials preparation." Half of the wafers received the laser treatment only, the other half received LID plus the "full treatment"[2] (see Table IV) prior to being fed into the normal device fabrication process. Split lots of the normal production served as controls. In the case of 4K dynamic RAM's, comparison was made between the performance of devices on untreated bulk substrates and on bulk substrates having undergone the procedures of Table IV described before. In the case of 16K dynamic RAM's, a comparison was also made between the performance of devices on gettered bulk substrates and on epitaxial silicon on highly doped but nongettered substrates.

Results

Table V shows impurity concentrations on two starting substrates of good crystal quality before and after removal by etching of the LID layer. Only a few impurities show up, and their concentration with the exception of gold, is very low. This is a consequence either of the purity of the starting material or of the gettering by the HCl treatment. Removal of the LID layer then eliminates the remaining impurities.[3]

The situation changes drastically if previously oxidized and then neutron activated substrates are used for the experiment as shown in Table VI. As shown in a companion paper (7), oxidation in steam or in dry oxygen without HCl leads to a strong contamination of the silicon. These impurities are tightly held at crystal defects produced by the oxidation and by the neutron irradiation and mostly refuse to be gettered into the LID layer. Note, in particular, the very high

[2] By "full treatment" we mean LID + 0.5% HCl-0.5% O_2 ramp-up in argon + 8 hr heat-treatment at 1250°C in dry oxygen.

[3] The high temperature treatments were performed in a furnace located in a laboratory otherwise engaged in gold metallurgy on silicon. As a consequence, contamination with small amounts of gold was very difficult to avoid.

Table V. Effectiveness of "full LID treatment" on starting substrates of good lattice perfection. Wafers activated after LID treatment.

	Cu	Cr	Fe	Co	Ni	Au
Before removal of LID layer	*	*	*	1.8E11	6.9E13	6.2E11
After removal of LID layer	*	*	*	—	—	3.6E11
Before removal of LID layer	*	*	*	*	8.4E13	1.3E11
After removal of LID layer	*	*	*	*	—	1.3E10

* These impurities already gettered by the HCl step of the "full treatment."

Table VI. Relative inefficiency of LID gettering if the HCl treatment is omitted on silicon wafers with strong lattice damage from previous neutron activation

	Cu	Cr	Fe	Co	Ni	Au	Ta
Before removing LID layer	3.9E14	7.3E14	6.9E15	2.7E13	5.6E14	1.1E12	2.7E12
After removing LID layer	1.0E14	6.1E12	—	8.9E12	2.7E14	3.1E10	1.0E12
Before removing LID layer	2.8E14	3.6E13	1.2E15	1.1E13	2.3E14	9.0E11	1.1E12
After removing LID layer	2.5E14	—	3.0E14	6.6E12	1.2E14	9.0E11	8.0E11

remaining copper concentration, a consequence of the omission of the HCl gettering step in this experiment.

Table VII shows that the combination of gettering by HCl and LID layer is capable of extracting the impurities even from a severely damaged silicon lattice. Only the gold concentration remained unchanged. As pointed out in footnote 3, we cannot be sure in the case of gold that we are not looking at an accidental recontamination after the high temperature treatment. Combining the information of Table VI and VII leads to an interesting conclusion. If depleting impurities at the silicon/ambient interface were the only function of the HCl at high temperature, *i.e.*, providing a concentration gradient, then one would expect that the concentration gradient provided by the LID layer should also suffice to attract impurities into the LID layer (case of Table V); this, however, essentially does not happen in the absence of HCl.

In the presence of HCl, however, impurities do diffuse into the LID layer and remain there, at least in part, in spite of the presence of the HCl. It appears that the impurities in the silicon are mobilized in the presence of HCl in a high temperature ambient.

It is generally considered that chlorine (the active species resulting from the interaction of HCl with oxygen) does not penetrate into the silicon. Neutron activation studies on silicon wafers oxidized in dry oxygen + 1% HCl at 1150°C have indeed shown that essentially all of the chlorine present on the sample is contained in the oxide film near the SiO_2/Si interface, and disappears from the sample upon etching in HF.[4] This result, however, was obtained on wafers cooled down to room temperature after the oxidation in dry O_2 + 1% HCl and does not give information about the presence of chlorine in the silicon at the high temperature.

All observed facts would find a logical explanation if chlorine is indeed to some extent soluble in silicon at high temperature, but is expelled from the crystal during cool-down due to a strong retrograde solubility as a function of temperature.

The effect of oxide films on suppressing the outdiffusion of certain impurities during the 950°-1250°C ramp-up in 0.5% HCl (no LID gettering) is shown in Table VIII. Only copper is always gettered under these circumstances. The getterability of Fe and of Cr depends on their location: if contained in the oxide film itself (probably even in the outer layers of the oxide film) they are quantitatively removed. But if contained in the silicon substrate, they are not. This effect is discussed in a companion paper (7). Co and Ni are very difficult to getter from a damaged Si lattice in the presence of an oxide film. Data on gold have been omitted in this table since gold cannot be gettered by high temperature HCl treatment due to the thermodynamic instability of its chloride. The conventional "dry oxygen + 1% HCl" treatment at 1000°-1100°C is thus not really a gettering treatment. It keeps additional impurities from getting into the silicon, but the concentration of impurities already in the silicon, with the exception only of copper, will not be strongly decreased by this treatment.

Oxygen precipitates forming in the bulk of the silicon wafer will eventually compete with the LID layer for the available impurities. Thus removing a LID layer from the wafer which has seen the 1250°C anneal in oxygen +0.5% HCl will result in a wafer which appears to be slightly more contaminated than a wafer which was merely subjected to the ramp-up-and-down in 0.5% each of O_2 and HCl, balance argon, with the LID layer in place. However, the impurities remaining on the wafer are tied down in oxygen precipitates and are not located near the surface of the wafer.

A comparison between device performance on gettered *vs.* nongettered bulk substrates, and also between gettered bulk substrates *vs.* epi on low resistivity p-type substrates, is given in Table IX in terms of the ratio of the percentage of devices failing the 4.4 msec Holdtime test. The gettered bulk substrates outperform the nongettered bulk substrates significantly, but the devices made on epitaxial silicon also outperform the devices on gettered bulk substrates by a similar margin.

[4] P. F. Schmidt, unpublished work.

Table VII. Effectiveness of "full LID treatment" including HCl step on previously neutron activated wafers containing strong lattice damage

	Cu	Cr	Fe	Co	Ni	Au
Before removing LID layer	2.0E13	5.3E12	*	8.0E11	2.0E14	1.0E12
After removing LID layer	—	—	—	—	—	1.0E12

* Iron completely removed, concentration of other impurities decreased by the ramp-up 950°-1250°C in 0.5% HCl-0.5% O_2.

Table VIII. High temperature HCl gettering of impurities from oxidized silicon wafers containing strong lattice damage from previous neutron activation step. 20 min in 0.5% HCl at 950°-1250°C.

		Cu	Cr	Fe	Co	Ni
Other thickness						
10,800A	Before HCl treatment	5.7E14	2.2E14	9.7E14	8.1E12	6.7E14
	After HCl treatment	—	2.0E13	+	8.1E12	6.0E14
8500A	Before HCl treatment	6.5E14	8.8E13	3.9E14	5.0E12	4.6E14
	After HCl treatment	—	1.0E13	—	5.0E12	4.1E14
		Cu	Cr	Fe	Co	Ni
Oxide thickness						
1000A	Before HCl treatment	2.4E16	1.6E13	3.9E14	+	9.1E13
	After HCl treatment	—	1.3E13	—	—	5.0E12
Initially bare	Before HCl treatment	1.4E13	1.4E14	9.6E14	2.8E12	1.1E14
200A grown during HCl treatment	After HCl treatment	—	—	—	1.8E12	5.7E13

Table IX. Improvement of hold time by pre-gettering of substrates

Dynamic RAM's on bulk Czochralksi silicon	Ratio % of device failing 4.4 millisecond test (at 90°C)
4K Dynamic RAM, lot 819	Non-gettered / Gettered = 3.28
4K Dynamic RAM, lot 7228	Non-gettered / Gettered = 1.91
16K Dynamic RAM, lot 1044	Non-gettered / Gettered = 1.57
16K Dynamic RAM's, lot 1044 and devices made on epi on low resistivity substrates	Gettered bulk substrates / Epi on low resistivity p-type = 2.52

This is a consequence of the suppression of the minority carrier diffusion current from the bulk of the wafer by the low resistivity epi substrates. This component of the leakage current is especially significant at elevated temperatures (9). Suppression of the diffusion component of the leakage current on bulk silicon can also be achieved by buried isolation diffusions.

Conclusions

The treatment described removes essentially any transition group metals from the front surface-near layers of the silicon, thus preventing formation of OSF, and resulting in improved holdtime performance of devices prepared on bulk Czochralski substrates gettered in this manner. However, the performance of devices fabricated on epitaxial silicon on low resistivity substrates cannot be matched since the low resistivity substrates suppress the minority carrier diffusion current from the bulk of the wafer.

To our knowledge this is the first deliberate gettering approach in which the gettering action continues throughout the device fabrication process and is not eliminated by high temperature treatments.

High temperature HCl gettering in the presence of only a very thin oxide film has been shown to be a much more effective means of removing transition group metals than is the conventional "dry oxygen + 1% HCl" treatment.

Manuscript submitted April 14, 1980; revised manuscript received July 31, 1980.

Any discussion of this paper will appear in a Discussion Section to be published in the December 1981 JOURNAL. All discussions for the December 1981 Discussion Section should be submitted by Aug. 1, 1981.

Publication costs of this article were assisted by Bell Laboratories.

REFERENCES

1. G. A. Rozgoni, S. Mahajan, and D. Brasen, *Appl. Phys. Lett.*, **29**, 531 (1976).
2. G. A. Rozgonyi, R. P. Deysher, and C. W. Pearce, *This Journal*, **123**, 1910 (1976).
3. L. E. Katz and D. W. Hill, *ibid.*, **125**, 1151 (1978).
4. C. W. Pearce and G. A. Rozgonyi, in "Semiconductor Silicon, 1977," H. Huff and E. Sirtl, Editors, pp. 606 ff, The Electrochemical Society Softbound Proceedings Series, Princeton, N.J. (1977).
5. V. J. Zaleckas and C. W. Pearce, Unpublished work.
6. J. Monkowski, R. E. Tressler. and J. Stach, *This Journal*, **125**, 1867 (1978); D. H. Hess and R. C. McDonald, *Thin Solid Films*, **42**, 127 (1977).
7. P. F. Schmidt and C. W. Pearce, *This Journal*, **128**, 630 (1981).
8. P. F. Schmidt and D. J. McMillan, *Anal. Chem.*, **48**, 1962 (1977); P. F. Schmidt, J. E. Riley, and D. J. McMillan, *ibid.*, **51**, 189 (1979).
9. R. Sun and J. T. Clemens, Abstract 499, p. 1266, The Electrochemical Society Extended Abstracts, Los Angeles, California, Oct. 14-19, 1979. See also U.S. Pat. 4,216,489 (August 1980).

AES Investigation of the Chemical Structure of Plasma-Deposited Silicon Nitride

H. H. Madden

Sandia Laboratories, Albuquerque, New Mexico 87185

ABSTRACT

Auger electron spectroscopy (AES) measurements have been made on a 500Å thick, plasma-deposited silicon nitride film. The refractive index of the film was 2.06, and it was deposited at 300°C. The silicon-$L_{2,3}VV$ uncorrected derivative signal had a sharp, high energy feature whose energy location and shape were suggestive of those from elemental silicon. Based on the supposition that the Si-$L_{2,3}VV$ signal from the plasma nitride is a superposition of signals, the background-corrected, loss-deconvoluted integral signal could be resolved into three signals: one which represented elementally bound silicon (and which was modeled by the signal from the silicon substrate); a second which was representative of silicon-hydrogen bonding; and a third which was found to have the shape of a signal from pyrolytically deposited silicon nitride. Because hydrogen is not directly detectable by AES measurement, and its effects on the shape of the Si-$L_{2,3}VV$ signal are small and more subtle than those of either oxygen or nitrogen, the effects of hydrogen on the Si-$L_{2,3}VV$ signal decomposition could only be assessed by making use of auxiliary data from a separate study of the silicon-hydrogen system. The uncorrected peak-to-peak, first derivative signals from oxygen and silicon in the plasma nitride indicated an oxygen content of less than 0.5 atomic percent (a/o). This was consistent with the lack of any indication of oxygen influence on the shape of the plasma-nitride Si-$L_{2,3}VV$ signal. These results for plasma-nitride are compared with the results of a similar study of silicon-oxynitride samples.

Silicon nitride is a dielectric material that has been found useful for a number of applications in the semiconductor-device industry. It is mostly used in the form of amorphous films, and although a number of other film growth techniques have been studied, chemical vapor deposition (CVD) and reactive plasma deposition are the most common thin film fabrication processes used. Films deposited by these methods may have electrical and structural properties which are strongly influenced by the presence of excess silicon or of contaminants in the films. The most important contaminants are thought to be oxygen, which results for oxidants present during the deposition reactions, and hydrogen derived from the hydrogen-bearing gases, silane and ammonia, used in both the CVD and plasma processes. The effects of nonstoichiometry and of oxygen and hydrogen impurities in silicon-nitride films are subjects of continuing interest. The persisting uncertainties in these subjects are consistent with the complex nature of silicon-nitrogen chemistry (1).

Of the many physical properties used in defining the characteristics of silicon nitride films, the index of refraction is the most widely used in practice. It has been found that excess silicon in a film causes an increase in the refractive index above the value of ~2 which is thought to be indicative of stoichiometric Si_3N_4. An oxygen contamination causes a decrease in the refractive index toward a value of 1.44 characteristic of SiO_2. The effect of hydrogen on the refractive index has not been clearly delineated.

Direct Si, N, and O signals appear in the AES spectrum and they have been employed for compositional analysis (2). There have been some disagreements in the interpretations of the lineshape of the silicon signals, however. Some authors (3, 4) have described the shape of the uncorrected derivative silicon $L_{2,3}VV$-AES signal from stoichiometric Si_3N_4 as being composed of a strong negative peak on its high energy side, with a broader shoulder at its low energy end. The energy location of the high energy peak is close to that of the corresponding signal from elemental silicon. This has led other workers (2, 5) to interpret this peak as being due to elemental or "free" silicon and thus the shape of the Si-$L_{2,3}VV$ signal as being due to the superposition of a low energy signal from silicon in silicon nitride and a high energy signal due to free silicon.

Key words: silicon nitride. hydrogen, chemical bonding.

In contrast to these interpretations, recent results from our laboratories (6) have indicated that the $L_{2,3}VV$ lineshapes from oxygen-contaminated CVD silicon-nitride films may also have the high energy peak/low energy shoulder structure but that the high energy peak is due to the presence of oxygen in the films. These results are in agreement with the AES and x-ray photoelectron spectroscopy (XPS) results of Wittberg, Hoenigman, Moddeman, Cothern, and Gulett (7), also on oxygen-contaminated CVD nitride films, which showed that the "free" silicon in such CVD films was less than 3 a/o. In our study the CVD nitride film with the least oxygen contamination exhibited only a single peak in the location (~84 eV) of the shoulder of the two-feature signals. This single peak line was judged to be the "true" AES lineshape for silicon bonded to nitrogen.

The apparent contradiction in interpretation of the high energy peak in the more complex AES lineshape, together with an expectation that the signal from a silicon-rich nitride film should be the simple superposition of a nitride-related signal and a signal from "free" silicon, prompted the measurements reported below. The plasma-nitride films used in this new investigation had an Si/N ratio closer to 1.05 than to the stoichiometric value of 0.75; and although oxygen was detectable, its level was very low. After corrections for instrumental and electron-energy-loss distortions, the integral $[N(E)]$ silicon-$L_{2,3}VV$ signal from our plasma-nitride samples could indeed be resolved into a "free"-silicon signal suprimposed on a silicon-nitride-like (6) signal, but with a third component representing silicon-hydrogen bonding in the film.

Other measurements (8) on nitride films deposited under nearly identical conditions to those in this AES

study indicate that the films contain some 20-25 a/o hydrogen. A large portion of this hydrogen is bonded to the excess silicon and the question naturally arises as to the role that hydrogen plays in determining the shape of the $L_{2,3}VV$ silicon line. Although direct AES signals from hydrogen do not exist, the effects of hydrogen could be reflected in silicon lineshape changes. This possibility has been ignored in the interpretations cited above (2-6). While separate studies (9) on the chemisorption of hydrogen onto a clean silicon surface have shown that the changes in the silicon AES lineshape due to hydrogen-silicon bonding are less dramatic than the changes that accompany nitrogen- or oxygen-bonding to a silicon surface, the changes are discernable and the results of our plasma-nitride silicon lineshape decomposition are consistent with the idea that the high energy component is due to some hydrogen-bonded silicon and not solely to excess "free" silicon.

Experimental

The plasma-nitride films were deposited to a thickness of ~500Å in an AMT Plasma I reactor. This is a production scale system incorporating a rotating horizontal platen, capacitive-coupling to drive the glow discharge in a radially flowing gas mixture, and a stationary resistance-heater block positioned below the rotating platen to control its temperature. The temperature of the 3 Ω-cm, n-type (111) Si wafers onto which the films were deposited was 300°C; and the gas-discharge mixture consisted of an N_2 carrier gas fed at a rate of 670 std cm^3/min with ammonia and silane fed at a flow ratio of 2.67:1 (NH_3-360 cm^3/min; SiH_4-135 cm^3/min). The refractive index of our film was 2.06. Other predeposition processing and deposition conditions were identical to those described in the report by Stein, Wells, and Hampy (8), where the results of a series of optical, structural, and electrical measurements made on these films are discussed. The major difference between the films used for our AES investigations and those studied by Stein *et al.* was the thickness. Their films were some 8-10 times thicker. Anderson (10) has discussed the effects on radiation hardness in the use of these plasma-nitride films for passivation of CMOS integrated circuits.

The AES data are taken with a single-pass cylindrical-mirror analyzer (CMA) using a 5 keV, 5 μA primary electron beam from an electron gun coaxial with the CMA. The modulation voltage was 2V p-p and the data was recorded using signal-averaging techniques in the first-derivative mode. Before processing to arrive at a loss-corrected integral $[N(E)]$ signal the data were first corrected for the linear dependence of the CMA response on energy. The "true" Auger signal must be extracted from the raw data by corrections for electron-energy-loss features. These include simple subtraction of a secondary-electron-background function (11) and a subsequent iterative deconvolution procedure (12) to remove a low energy tail from the background-corrected $N(E)$ signal. This tail results from Auger electrons which have suffered energy losses before leaving the solid. The deconvolution technique makes use of a near-elastic spectrum of backscattered electrons as an approximation to the total system (spectrometer resolution and Auger-electron loss features) response function. It was the loss-corrected $N(E)$ signal that was analyzed in terms of a superposition of signals from silicon atoms in different chemical environments.

During the transfer of the samples from the deposition system to the AES unit, the nitride films developed an oxide layer (13). This layer was removed by sputtering with 1 keV argon ions prior to analysis. A representative sputter profile recorded during our investigations of oxynitride films (6) is shown in Fig. 1 with the $L_{2,3}VV$-silicon AES signals taken at various sputter depths given in the insert to this figure. The silicon lineshape taken before sputtering, A, is "SiO_2-

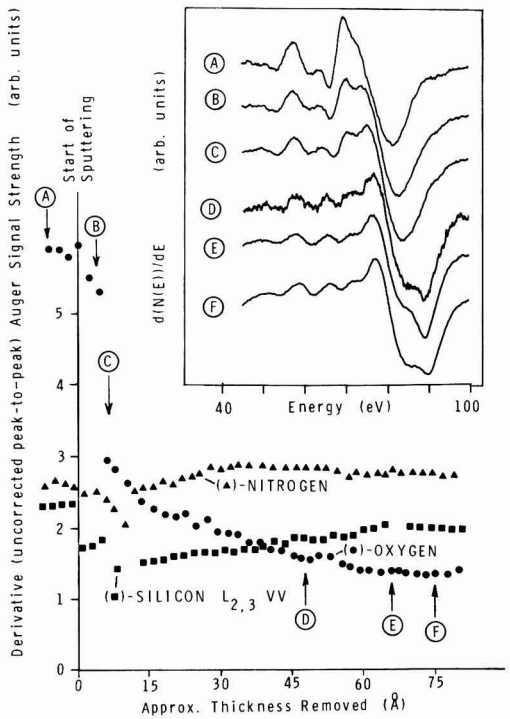

Fig. 1. AES sputter profile for a silicon-oxynitride film with ~10 a/o bulk oxygen [this film denoted as "74 ppm" in Ref. (6)]. Insert gives silicon-$L_{2,3}VV$ spectra taken at various points indicated on the sputter profile. The differences in signal-to-noise for curves D through F in the insert are the result of differing numbers of scans used in data averaging. For general survey work one set of scans (*e.g.*, curve D) was taken while, for data that were to be used in deconvolution (curve E or F) a larger number of scans was taken so that the buildup of noise expected in the deconvolution process [Ref. (12)] could be mitigated.

like," but without the electron-beam-reduction peak (6, 14) at ~ 90 eV. Signals B and C are typical of a superposition of an SiO_2 and an oxynitride line. Only when a "plateau" was reached, *e.g.*, curves D-F in Fig. 1, did the silicon lineshape become "nitride-like." Similar changes in the Si-$L_{2,3}VV$ lineshape with sputter depth were observed for the plasma-nitride film. All of the AES data presented below were taken in the sputter-plateau region, *i.e.*, after the surface oxide layer had been removed.

The AES data were taken with the ion-bombardment beam off and only after the argon pressure in the experimental chamber had fallen below 7×10^{-7} Pa (the base pressure was $\sim 3 \times 10^{-8}$ Pa). In earlier work (14) it was found that AES data taken during ion bombardment were subtly distorted. These distortions were found to be related to the presence of argon gas at ion-bombardment pressures ($\sim 5 \times 10^{-3}$ Pa) in the experimental system during AES measurements. The samples in the present work were not annealed and hence contained embedded argon. Studies (15) of argon-ion bombarded, single crystal silicon samples, however, indicated that the presence of embedded argon and the associated damage does not have a very significant effect on the silicon AES lineshape. Carbon was a persistent contamination but for the data discussed below the carbon level was always low enough that it did not have an effect on the silicon lineshape (15).

Results and Discussion

Si-N, Si-Si, and Si-H contributions to the Auger lineshape.—Figure 2 shows both the uncorrected derivative $L_{2,3}VV$ signal (left-hand column) and the corresponding, loss-corrected $N(E)$ signal (right-hand column) from a plasma-nitride sample. For comparison, signals from elemental silicon, from our lowest-oxygen-content CVD nitride sample (6), our 74 ppm CVD oxynitride sample (6), and from an SiO_2 sample (16) are also plotted in this figure. The elemental silicon signals were obtained from the silicon substrate after sputtering through the plasma-nitride film. The energy location and shape of the high energy feature in the derivative spectra from our plasma-nitride and oxynitride samples are indeed suggestive of elemental Si. The SiO_2 data shown in Fig. 2 were recorded (16) in the presence of an oxygen atmosphere in order to minimize the electron beam reduction effects which give rise to a sharp peak commonly seen in the derivative spectrum from silicon dioxide at ~ 90 eV, which is also interpreted as due to elemental Si. Of the other $N(E)$ signals of Fig. 2 (right-hand column) the plasma-nitride signal most closely resembles the CVD nitride and oxynitride signals on their low energy sides in shape and energy location.

In order to test the supposition that the high energy feature in the uncorrected, derivative spectrum from the plasma nitride is due to elemental or "free" silicon, an elemental-silicon signal in the loss-corrected $N(E)$ form (Fig. 2) was subtracted from the $N(E)$ plasma-nitride signal (Fig. 2) to get a difference signal whose shape could be checked against the CVD-nitride signal (Fig. 2). The elemental-silicon signal was scaled in the resolution such that it had the maximum amplitude without resulting in a difference signal exhibiting negative $N(E)$ portions. This is a condition that one would expect for a simple superposition of signals. For the results presented here the curves involved in the resolution were not shifted in energy relative to one another. Allowing relative energy shifts would have introduced an additional (undesirable) adjustable parameter into the curve resolution. Some shifts might indeed be appropriate due to core-level shifts or to differences in work functions for the surfaces involved. Such differences, although not measured, were assumed to be negligible however, and the only adjustable parameter in the curve resolution was the scaling factor, as was also true for the our oxynitride studies published earlier (6).

The difference signal from our plasma-nitride curve resolution, using the elemental silicon signal as one of only two components, is shown as the solid curve in Fig. 3a. It is seen to closely resemble (6, 14) a signal from an oxynitride sample with appreciable oxygen content. This might be interpreted to suggest that there is a third, oxygen-related component in the difference signal for plasma nitride, but the low oxygen concentration in the film determined by AES peak-height analysis runs counter to this suggestion. What was needed to obtain a more nitride-like difference curve was a different component signal which was more-or-less elemental-Si-like in shape but which occurred ~ 1 eV lower in energy than the elemental-Si signal used in Fig. 3a. Such a signal was found (9) in the $L_{2,3}VV$ signal from a hydrogen-covered silicon surface. A component curve that reflects Si-H bonding might indeed have been expected because infrared measurements indicated appreciable Si-H bonding in these plasma-nitride films (8).

Although a direct AES signal from hydrogen does not exist, hydrogen may be detected indirectly by its effects on an AES line of its host material. Such an effect of hydrogen on the Si-$L_{2,3}VV$ line is shown in Fig. 4, the results of a study of the chemisorption of hydrogen onto a clean (100) silicon surface (9). The amount of hydrogen on the hydrogen-covered surface for the signal shown in Fig. 4 was enough to have two

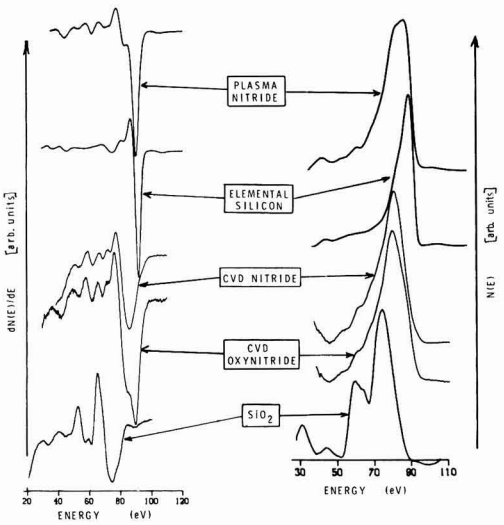

Fig. 2. Silicon-$L_{2,3}VV$ signals from plasma-nitride; elemental-silicon; CVD-nitride [Ref. (6)]; CVD-oxynitride [74 ppm, Ref. (6)]; and SiO_2 [Ref. (16)] samples. The left-hand side of this figure gives uncorrected, first-derivative signals while corresponding background-corrected, loss-deconvoluted integral signals are shown as the right-hand side. Zero levels for the integral signals are given by the right-hand side of each $N(E)$ curve.

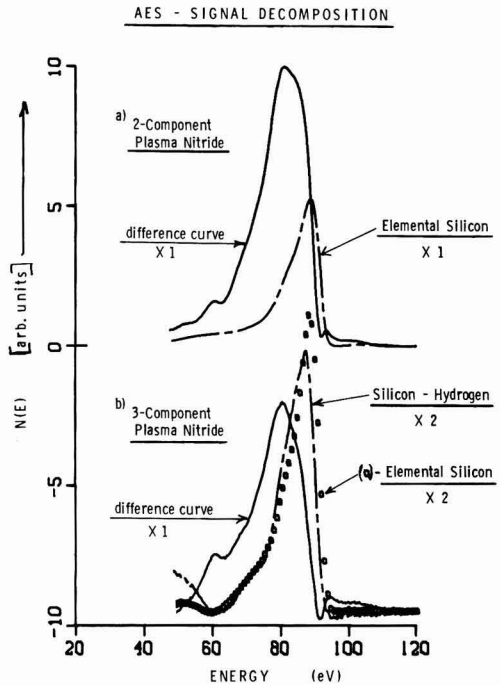

Fig. 3. $L_{2,3}VV$-silicon component signals for a plasma-nitride sample. a) 2-component decomposition using only an elemental-Si signal as the high energy component; b) 3-component decomposition using both the elemental-Si and the Si-H signals from Fig. 4 as the high energy components. The solid curves are the difference curves in both cases.

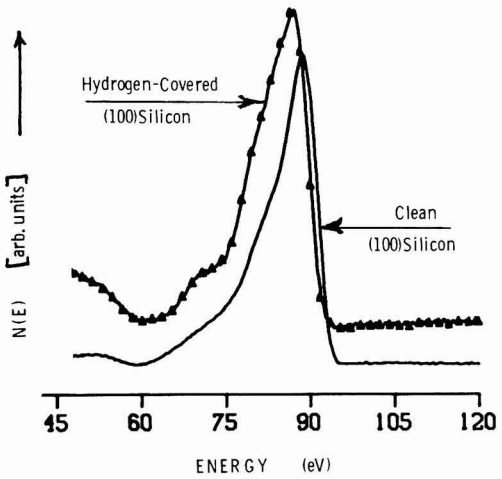

Fig. 4. Loss-corrected $N(E)$, $L_{2,3}VV$ signals from a clean, and a hydrogen-covered (100) silicon surface. Zero levels for the signals are given by the right-hand side of each curve. Triangles mark the curve for the hydrogen-covered surface.

hydrogen atoms bonded to each surface silicon atom (17). Thus each surface silicon atom is bonded to two hydrogen atoms and to two substrate silicon atoms. The hydrogen chemisorption caused the reconstructed (2 × 1) surface characteristic of the clean (100) surface to form a (1 × 1) structure characteristic of the dihydride layer on this substrate (17). The $L_{2,3}VV$ signal from the hydrogen-covered surface (Fig. 4) is a superposition of a hydrogen-influenced signal from the surface region and an elemental-Si signal from the substrate. This signal by itself was thus thought to be a better approximation to the high energy component curve in the plasma-nitride-film case than is the elemental-Si signal.

Subtracting this hydrogen-covered-surface signal from the plasma-nitride signal did produce a difference curve that was a better fit to the CVD nitride signal in the region near the peak but the lower part of the high-energy side of the difference curve was still too broad. The best-shaped difference curve was obtained by using both the hydrogen-covered-surface signal and the elemental-Si signal from Fig. 4. This difference curve is shown as the solid curve in Fig. 3b and once again in Fig. 5a. For comparison the CVD-nitride signal is also plotted in Fig. 5a. The good agreement in shape between these two curves indicates that the $L_{2,3}VV$ signal from our plasma-nitride sample can indeed be regarded as the superposition of three components: the silicon-nitride signal, the elemental-Si signal, and a signal due to Si-H bonding in the film.

Comparison of spectra from plasma-nitride and CVD-oxynitride.—These results for the plasma-nitride film are in sharp contrast to our earlier results (6) for CVD-oxynitride films. There the uncorrected derivative Si-$L_{2,3}VV$ signal also had a high energy feature that had earlier been interpreted as being due to free silicon but which our curve-resolution results found to be more indicative of silicon-oxygen bonding than to free silicon. The difference curve for the CVD oxynitride had a double-peak structure that resembled the SiO_2 signal more closely than it did the elemental-Si signal. Despite the similarities in shape of the oxynitride-difference and SiO_2 curves, there are significant differences that should be discussed. The prominent peak of the difference signal occurs some 13 eV higher than the corresponding peak in the SiO_2 signal. The peak separation in the difference signal is also somewhat less than in the SiO_2 curve. This is seen in Fig. 5b where the SiO_2 curve has been shifted up in energy so that the prominent peaks of the two curves are aligned.

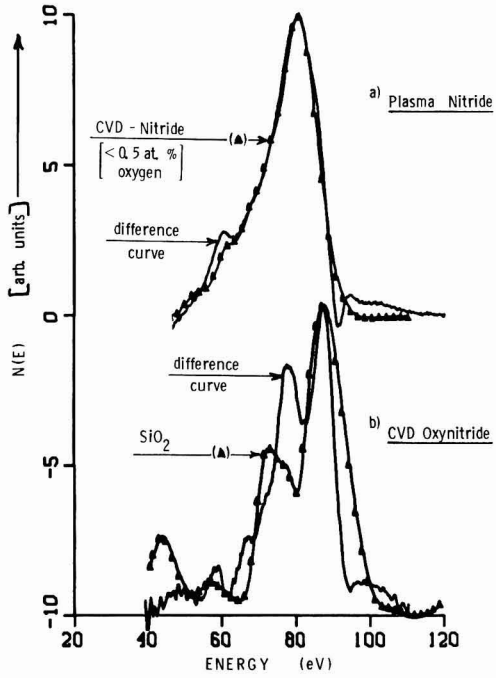

Fig. 5. Comparisons of a) curve-resolved difference curve from 3-component plasma-nitride decomposition results of Fig. 3b with our CVD-nitride signal [Ref. (6) and Fig. 2] and b) curve-resolved difference curve from our CVD-oxynitride results [Fig. 2 of Ref. (6)] with an SiO_2 signal [Ref. (16)]. The SiO_2 signal has been shifted higher in energy by 13 eV, but the CVD-nitride signal is in its original energy location. Both the CVD-nitride and SiO_2 signals are marked with triangles.

The differences in shape between the two curves in Fig. 5b suggest that the difference curve is not simply an SiO_2-like curve shifted up in energy relatable, perhaps, to formation of a suboxide in the films. The prominent peak of the SiO_2 curve occurs fairly close to (~ 3 eV below) the secondary peak of the difference curve. Thus the high energy peak of the difference curve could alternatively be interpreted as a spectrum feature peculiar to the incorporation of oxygen in the amorphous silicon nitride matrix. It should be remembered that AES is a local probe of a material's electronic configuration. The prominent peak in the oxynitride difference curve could signal a local configurational change in the nitride. If the oxygen enters the nitride substitutionally, as suggested in our earlier report (6), the divalent oxygen will leave one unsaturated bond which could lead to so-called dangling-bond states at the local sites of the replaced trivalent nitrogen.

Alternatively, the incorporation of oxygen into the nitride could be accompanied by a local restructuring of the nitride matrix and the formation of new and different Si-Si and Si-H bonds. Such local "disordering of the nitride skeleton by oxygen" has already been suggested by the results (18) of a study of short-range order in silicon-oxynitride films using the method of radial distribution functions determined from electron diffraction measurements. AES is a probe of the local electronic structure of a material and should hence be sensitive to such local disorder. In any case the AES

data indicate that, below an oxygen level of ~ 50 a/o, the incorporation of oxygen into the nitride does not lead to a simple mixture of SiO_2 and silicon nitride but to a more unique substance. On the other hand, the fact that signals indicating Si-Si and Si-H bonding can be reasonably shown to be components of the Si-$L_{2,3}$VV lineshape for plasma nitride suggests that excess silicon and silicon bonded to hydrogen may exist as independent entities in a two (or three) phase amorphous mixture with silicon nitride in plasma-nitride films.

Comments and Conclusions

The high energy peak in the uncorrected, derivative Si-$L_{2,3}$VV signal from a plasma-nitride film is due to Si-Si bonds in the film. In our sample this peak is also identifiable with some Si-H bonding. The overall $L_{2,3}$VV lineshape for our plasma-nitride sample is thus consistent with the presence of excess silicon, of silicon bonded to hydrogen, and of silicon bonded to nitrogen in the film. The AES signal decomposition indicates that the Si-Si and Si-H bonding in the plasma nitride can be detected as separate signals from the Si-N signal. This suggests that plasma-nitride films prepared with excess silicon may be simple mixtures of silicon (with incorporated hydrogen) and silicon nitride.

These decomposition results are in contrast to our earlier results (6) for CVD silicon-oxynitride films where the Si-$L_{2,3}$VV signal, which in its uncorrected derivative form also has a high energy peak that has been interpreted as being due to free silicon, was found to be composed only of a component indicating silicon-nitrogen bonding and a second component indicating silicon-oxygen bonding. No clear-cut elemental (or "free") silicon component was found. This contrast indicates that the assignment of compositional information based primarily on the energy locations of AES lines in uncorrected, derivative spectra can be misleading and that more careful attention should be given to the shape of the AES lines in interpreting AES results.

The analysis of our $N(E)$ data might perhaps be considered speculative. It is based on the supposition that the background-corrected, loss-deconvoluted AES signal is a simple superposition of component signals. This is certainly not unreasonable; and the decomposition (or curve-resolving) that was done was performed with the restriction that no adjustments of relative energy positions of the as-measured component signals was allowable. This meant that whereas the high energy portion of the plasma-nitride signal could actually have been modeled by two elemental-Si signals shifted relative to one another, the physical and chemical significance of such a pair of elemental-Si signals must be considered unclear, at the least. The Si-H signal used in the curve-resolving presented above, while not differing greatly in shape from the elemental-Si signal, does give the energy shift needed with a chemically identifiable reason for the shift. In this regard, it should be noted that the 13-eV shift made to the SiO_2 signal in Fig. 5b was not involved in the curve-resolving procedure (6), but was made merely to make the shape comparison with the silicon-oxynitride difference curve easier.

These results illustrate the utility of AES as a probe of the chemical, as opposed to merely elemental, composition of solid surfaces. Energy (chemical) shifts of Auger lines can be larger than corresponding shifts of XPS lines; and, with care, these shifts can provide useful information about the chemistry of materials. Auger lineshape changes have been shown to aid in such interpretations.

Acknowledgments

The preparation of the plasma nitride films by J. J. Clement and the assistance of W. O. Wallace in making the Auger measurements are gratefully acknowledged. Very useful information concerning other measurements on these films was supplied by H. J. Stein prior to publication. This work was supported by the U.S. Department of Energy under Contract DE-AC04-76-DP00789.

Manuscript submitted Jan. 24, 1980; revised manuscript received Aug. 6, 1980.

Any discussion of this paper will appear in a Discussion Section to be published in the December 1981 JOURNAL. All discussions for the December 1981 Discussion Section should be submitted by Aug. 1, 1981.

Publication costs of this article were assisted by Sandia Laboratories.

REFERENCES

1. U. Wannagat, in "Advances in Inorganic Chemistry and Radiochemistry," H. J. Emeleus and A. G. Sharpe, Editors, pp. 225-277, Academic Press, New York (1964).
2. S. Thomas and R. J. Mattox, *This Journal*, **124**, 1942 (1977).
3. W. A. Lanford and M. J. Rand, *J. Appl. Phys.*, **49**, 2473 (1978).
4. P. H. Holloway, *Surf. Sci.*, **54**, 506 (1976).
5. Y. E. Strausser and J. S. Johannessen, NBS Special Publ. 400-23, ARPA/NBS Workshop IV, "Surface Analysis for Silicon Devices," A. G. Lieberman, Editor, p. 119 (March 1976); J. S. Johannessen, W. E. Spicer, and Y. E. Strausser, *Phys. Scr.*, **19**, 355 (1979).
6. H. H. Madden and P. H. Holloway, *J. Vac. Sci. Technol.*, **16**, 618 (1979).
7. T. N. Wittberg, J. R. Hoenigman, W. E. Moddeman, C. R. Cothern, and M. R. Gulett, *ibid.*, **15**, 348 (1978).
8. H. J. Stein, V. A. Wells, and R. E. Hampy, *This Journal*, **126**, 1750 (1979).
9. H. H. Madden, 39th Annual Conference on Physical Electronics, Univ. of Maryland, June 20, 1979; and to be published.
10. R. E. Anderson, *IEEE Trans. Nucl. Sci.*, **ns-26**, 5180 (1979).
11. E. N. Sickafus, *Rev. Sci. Instrum.*, **42**, 933 (1971).
12. H. H. Madden and J. E. Houston, *J. Appl. Phys.*, **47**, 3071 (1976); *Adv. X-Ray Anal.*, **19**, 657 (1976).
13. S. I. Raider, R. Flitsch, J. A. Aboaf, and W. A. Pliskin, *This Journal*, **123**, 560 (1976).
14. H. H. Madden, G. Moore, and P. H. Holloway, "An Auger-Electron Line-Shape Study of CVD Silicon Nitride Films," Report No. SAND77-0584, Sandia Labs., Albuquerque, NM (1977), Unpublished work.
15. J. E. Houston, G. Moore, and M. G. Lagally, *Solid State Commun.*, **21**, 879 (1977).
16. J. E. Houston and M. G. Lagally, *J. Vac. Sci. Technol.*, **13**, 361 (1976); and unpublished results.
17. T. Sakurai and H. D. Hagstrum, *Phys. Rev. B*, **14**, 1593 (1976).
18. F. L. Edelman, B. N. Zaitsen, V. Z. Latula, and A. A. Khoromenko, *Phys. Status Solidi A*, **51**, 49 (1979).

A Neutron Activation Analysis Study of the Sources of Transition Group Metal Contamination in the Silicon Device Manufacturing Process

P. F. Schmidt*

Bell Laboratories, Allentown, Pennsylvania 18103

and C. W. Pearce*

Western Electric Company, Allentown, Pennsylvania 18103

ABSTRACT

A survey is given of the sources, species, and quantities of transition group metals residing on starting silicon substrates and introduced during the device manufacturing process. The survey begins with the polysilicon feed for silicon ingot fabrication and extends through all customary device fabrication steps, such as wafering, polishing, oxidations, epitaxy, ion implantation, etc. High temperature furnace operations in the absence of HCl, such as steam oxidations, are presently the major source of contamination if all other steps of the fabrication process are under full control. However, contaminated polishing slurries, contaminated handling tools or carriers, impure SiC boats or susceptors, or choice of unsuitable materials for beam catcher plates, etc. in ion implantation, can also lead to trouble. Several options are available to avoid the contamination introduced during high temperature treatments, and these are reviewed.

Minority carrier lifetime is an important parameter in silicon (integrated) device technology. However, the amounts of contaminants which suffice to degrade lifetime are so small that they cannot be detected and quantified by conventional chemical analysis. Only neutron activation analysis (NAA) has this capability among techniques applicable to measuring the total impurity concentration.[1] A systematic application of NAA to the silicon device manufacturing process does not seem to have been carried out before.

We report here on NAA starting with the polysilicon used for crystal growth and extending through the fabrication process. Some of the results are what one would expect to find, others came as surprises.

Some Background Information

Gamma-ray spectrometry of reactor neutron activated samples has a very high sensitivity for most elements of the periodic system beyond neon. Notable exceptions are the light elements B, P, and S, and the heavy elements Tl, Pb, and Bi, which do not become gamma-ray emitters but only beta emitters.[2] Since the electrons emitted in beta decay have a continuous spectrum, beta spectroscopy is not an attractive tool to identify individual elements among a multitude of beta emitters. However, determination of the half-life and maximum beta energy can sometimes be used to measure some beta emitters, especially phosphorus. We shall limit ourselves here to gamma-ray emitters.

Among the gamma-ray emitters, there exist also a few elements (V, Al, Cl, and F being the most important) whose half-lives are so short that their determination must be carried out immediately after end of reactor irradiation, and these elements are therefore not seen at all if analysis is carried out a day or so after end of irradiation. Manganese, too, has a relatively short half-life (2.58 hr) and will be detectable a day after end of irradiation only if the total number of manganese atoms in the sample approaches about 1E15.

Si-31, the only radioisotope formed during reactor irradiation of silicon, has a short half-life of 2.62 hr. This fact is of great help in the instrumental analysis of silicon samples: about 27 hr after even a long irradiation, the emission intensity from the silicon matrix has decayed to the extent that the samples can be analyzed nondestructively, without any need for chemical separations. The high purity of semiconductor silicon also guarantees that there are no self-shielding effects for any of the impurities contained in the silicon, and the thermal cross sections and infinite dilution resonance integrals given in the literature for the various isotopes can be used without correction factors for concentration determinations. This fact makes absolute counting of silicon samples especially attractive. In this method, one does not need standards for each element to be determined, one must merely measure accurately the thermal and epithermal flux in the reactor at the time and location of irradiation. A method of measuring the thermal and epithermal flux in a very convenient manner has been described before (1). Since silicon is a light element, there is also very little self-absorption of the emitted gamma rays, and again one does not have to worry about correction factors when applying instrumental analysis.

Two of the common dopants in silicon, boron, and phosphorus do not become gamma-ray emitters after irradiation. Phosphorus, however, becomes a 14-day half-life emitter of high energy betas, which in turn give rise to copious generation of Bremsstrahlung x-rays, raising instrumental deadtime and background at lower energies to unacceptable levels. Thus highly phosphorus-doped silicon samples are not very suitable for nondestructive analysis. Boron, on the other hand, is an ideal dopant for NAA purposes. The fission reaction of B-10 with thermal neutrons, resulting in the emission of Li-7 or of alpha particles, generates no radioactivity, and the beta activity resulting from the B-11 (n,gamma) B-12 reaction has a half-life of much

* Electrochemical Society Active Member.

Key words: carrier lifetime, diffusion, silicon dioxide, IC processing, contaminants.

[1] Ion microprobes have similar sensitivities as NAA in terms of total number of atoms needed for detection, but in the microprobe case these atoms are confined to the very small volume being sputtered, *i.e.*, representing relatively high concentrations. NAA is a global technique, does not give information about impurity distributions in very small volumes, and is most useful for determination of impurities present in extreme dilution, The two techniques are thus complementary.

[2] Except boron.

less than 1 sec. Thus boron-doped silicon is ideally suited for investigating at which process steps contaminants are being introduced. Most of the work described in this paper was performed with 3" ϕ boron-doped Czochralski silicon.

There are certain practical constraints on the maximum or minimum number of samples one usually activates together during a reactor irradiation. Since the irradiations are fairly expensive, one clearly wants to co-irradiate as many samples as possible. On the other hand, one should be able to measure all samples before the short-lived species on the last samples to be measured have decayed to too low levels of activity. One thus needs a high throughput capability of the measuring equipment and computer evaluation of the gamma-ray spectra becomes a practical necessity.

There are many computer programs described in the literature which take spectrum evaluation to the point where identification of the isotopes present as well as determination of the intensities of the various photopeaks has been accomplished. Converting these intensities to concentrations, however, is usually done by comparison to the intensities of standards for each element co-irradiated with the unknown samples. A hybrid technique in which standards for each element are irradiated in a very well-known flux, and comparison to the spectra obtained in another reactor or a different flux is made possible through the co-irradiation of so-called comparators, has also been described (2). These techniques, however, involve a considerable amount of computation and [in the hybrid technique (2)] some degree of control over the irradiation facility.

The method of absolute counting (1), by contrast, requires the co-irradiation of only two flux monitors and the use of a minicomputer and is applicable to irradiations in any reactor. It is therefore much faster and only slightly less accurate than the relative method. Altogether, in survey work of this type precision is more important than accuracy, and the precision of absolute counting is excellent. The large volume of data generated in this study could not readily have been handled by a relative method.

Experimental

Whenever feasible, boron-doped silicon wafers were used, mostly in the resistivity range 4-9 Ω-cm, and of (100) or (111) orientations. Samples were cleaned in hot H_2O_2-NH_4OH and H_2O_2-HCl solutions prior to insertion into the process steps to be tested, prior to measurement after neutron irradiation, and, of course, also prior to neutron irradiation if the purpose of the test was to determine the impurities worked into the silicon surface rather than deposited on the surface (slicing, lapping, and polishing of wafers).

Samples were irradiated for 120 hr with rotation at core face of the Union Carbide reactor[3] at Tuxedo, New York, and were measured nondestructively the next day. All samples were measured first for 2000 sec only for determination of short-lived species and were then measured again for 18.2 hr for determination of the long-lived species. Coarse profiling of impurity distributions was done by removal of oxide films in HF followed by cleaning in HCl-H_2O_2, by etching in 5:3:3 nitric:hydrofluoric:acetic acid mix (sometimes with one surface masked against attack) followed by cleaning in H_2O_2-HCl, and also by removing the peripheral portions of the wafer by scribing and breaking in order to learn about the lateral distribution of the impurities. Autoradiography served the same purpose on wafers with only one predominant emitter.[4]

[3] Typical flux of 1.5 $\times$ 10^{13} thermal neutrons cm^{-2} sec^{-1}, with 3-5% epithermal neutron.

[4] One should bear in mind that the sensitivity of the photographic plate is much higher for betas than for gammas and that presence of pure beta emitters could completely falsify an autoradiograph. Presence or absence of beta emitters can usually be inferred from the low energy x-ray background (below 100 keV) generated by a given sample.

Both the measuring equipment and the method of absolute counting used, as well as the method of flux determination by means of Fe-Ru flux monitors, has been discussed before (1).

In irradiating high purity materials it is necessary to use high purity materials as irradiation containers. Impurities contained in the irradiation container can be transferred and implanted into the unknown sample by knock-on events of fast neutrons and cannot always be removed by nondestructive cleaning. One also needs a container material which does not become very radioactive even after long irradiations, so that samples can be handled readily after irradiation, and the containers reused after some cool-down periods to let induced activities decay. These considerations limit the practical choice of irradiation containers to silicon, quartz, graphite, or vanadium, all of the highest purity. The half-lives of V-51 and of Si-31 are 3.76 min and 2.62 hr, respectively, thus containers made from quartz, silicon, or vanadium can be handled after conveniently short waiting periods. On the other hand, the neutron capture cross section of C-13 is so low (0.9 millibarns, at an abundance of 1.11%) and the half-life of C-14 so long (5730 years) that the activity generated in the matrix is very low even after long irradiations[5] and in any case stems only from a very low energy beta emitter. We have chosen 7 nines pure graphite for irradiation containers, both because of its ready availability and its ease of machinability.

While the graphite matrix is extremely pure, surfaces of graphite workpieces can be significantly contaminated from contact with metal or carbide tools during fabrication. We have especially noted significant molybdenum contamination on some batches. Fortunately, these surface contaminants can be removed by the manufacturer by means of a high temperature cleaning treatment at little extra cost. Their elimination is necessary because of the knock-on and implant events during irradiation already mentioned. Especially molybdenum seems to diffuse quite deeply into silicon during reactor irradiation. Contamination of graphite containers inevitably will also occur from contact with the (contaminated) silicon wafers placed into the containers. It is, however, possible to repurify the graphite (at a somewhat lower temperature than the original heat-treatment) after the activities of these surface contaminants have decayed. Long-lived impurities located deeper in the graphite will have little tendency to be released since they were not removed by the original heat-treatment at the higher temperature.

Our graphite containers consisted of 1.5 in. high cylindrical boxes with screw-on lids, and 1 mm thick graphite spacers to be inserted between the 10 silicon wafers (full load) for avoidance of cross contamination between wafers.

Results

Starting materials and fabrication of starting substrates.—Crystal growth.—The polysilicon used for crystal growth is extremely pure, with only weak traces of impurities detectable.[6] The crystals grown from this polysilicon also proved to be exceedingly pure, with only traces of Cr, Co, Ta, W, Sb, and Na being present. The polysilicon residue in the quartz crucible, however, turned out to be severely contaminated as shown in Table I. The residue constitutes

[5] The activity generated as a function of irradiation time is given by the saturation factor $S = 1 - \lambda/t_{irr}$, with $\lambda = \ln 2/T_{1/2}$; $T_{1/2}$ is the half-life of the radioactive species formed.

[6] By weak traces we mean photopeaks which are still clearly discernible as to their position in energy, but too weak for meaningful quantitative evaluation because of the statistical uncertainty involved. Detection limits for the more important transition group metals, using our detectors, irradiation, and counting conditions, as stated above, and decay times of about 2 weeks, would be approximately (for 3" ϕ silicon wafers): Fe, 1E14 atoms; Ni, 5E13; Zr, 7E13; Cr, 1.5E12; Mo, 1E11; Co, 5E10; Au, 1E9. Detection limits depend, of course, on the background, i.e. are higher in the presence of longer lived species having photopeaks at higher energies.

Table I.

Silicon residue in crucible I		Silicon residue in crucible II	
Cu	2.6×10^{-1} ppm (= (5.7E15 cm^{-3})*	Cu	1.5×10^{-1} ppm
Au	5.3×10^{-6} ppm	Au	5.0×10^{-5} ppm
Cr	$4.2 \times 10^{+0}$ ppm	Cr	7.2×10^{-1} ppm
Mn	2.9×10^{-1} ppm	Mn	4.5×10^{-2} ppm
Fe	$2.3 \times 10^{+1}$ ppm	Fe	$4.2 \times 10^{+0}$ ppm
Co	6.8×10^{-2} ppm	Co	1.7×10^{-2} ppm
Ni	$4.1 \times 10^{+0}$ ppm	Ni	$1.1 \times 10^{+0}$ ppm
Mo	2.0×10^{-1} ppm	Mo	7.1×10^{-2} ppm
Ag	4.7×10^{-2} ppm	Ag	n.d.
Hf	Positive	Hf	7.2×10^{-3} ppm
Ta	3.6×10^{-5} ppm (= 2.8E11 cm^{-3})*	Ta	4.4×10^{-5} ppm
W	8.2×10^{-3} ppm	W	2.2×10^{-3} ppm
As	1.9×10^{-3} ppm	As	2.9×10^{-3} ppm
Sb	2.5×10^{-3} ppm	Sb	1.8×10^{-3} ppm

* Conversion from ppm to atoms/cm^3 involves the atomic weight of the impurity species. For readers more familiar with the atoms/cm^3 notation, the concentrations have been expressed in this manner for a typical light (Cu) and a typical heavy (Ta) metal.

about 10% of the original charge, its level of contamination subsequent to crystal growth thus cannot be due simply to the reduced volume. Since the hot silicon melt dissolves a substantial amount of the crucible during a run, it was initially thought that impurities in the crucible were responsible for the buildup of contamination in the melt, and the quartz from several suppliers was analyzed (see Table II). While the amount of impurities in the quartz is not negligible, it is not sufficient to explain the massive contamination of the melt; the contamination had to originate somewhere else in the crystal grower. Next we suspected the quality of the graphite susceptor, but it, too, proved to be quite clean (Table III). However, when the upper edge of the susceptor was examined, it was found to be severely contaminated with molybdenum and with the various components of stainless steel (Table IV). The source of contamination turned out to be seed shafts made from molybdenum or stainless steel and attached to the graphite chuck carrying the silicon seed crystal. These were positioned close enough to the hot portions of the crystal grower to reach obviously excessive temperatures. Since not only the silicon melt became contaminated, but the edge of the surrounding graphite susceptor as well, a major portion of the contamination must have occurred through the vapor phase.

Table II. Impurities detected in various crucible quartz. Concentrations given in ppm.

	Quartz from crucible I	Quartz from crucible II	Quartz from supplier* 1	2	3	4
Cr	2.0E−1	3.7E−1	n.d.	1.3E−1	n.d.	n.d.
Mn	n.d.	n.d.	1.7E−1	7.5E−1	7.2E−3	9.0E−3
Fe	5.9E−0	n.d.	1.3E−0	1.6E−0	n.d.	3.3E−1
Co	1.0E−2	n.d.	7.6E−3	3.8E−3	n.d.	6.2E−4
Ni	9.0E−1	n.d.	Not meas.	Not meas.	Not meas.	Not meas.
Cu	2.3E−1	1.6E−1	n.d.	3.4E−1	9.3E−2	1.4E−1
Zn	1.1E+1	n.d.	1.5E−2	5.5E−2	n.d.	n.d.
Zr	1.1E+1	8.6E−0	Not meas.	Not meas.	Not meas.	Not meas.
Mo	5.1E−0	4.1E−0	7.0E−1	n.d.	n.d.	n.d.
Hf	2.7E−1	5.8E−1	1.6E−1	2.1E−1	n.d.	n.d.
Ta	3.9E−3	2.4E−0	2.1E−3	9.0E−3	2.8E−3	n.d.
W	4.8E−2	7.1E−2	2.5E−1	2.8E−1	n.d.	6.0E−4
Ag	4.9E−2	n.d.	n.d.	n.d.	n.d.	n.d.
Au	n.d.	1.4E−5	n.d.	n.d.	n.d.	n.d.
Pt	n.d.	n.d.	7.5E−0	9.7E−1	n.d.	n.d.
Ir	n.d.	n.d.	2.0E−4	2.0E−4	n.d.	n.d.
Na	3.7E−0	1.2E−0	7.0E−1	2.2E−0	2.0E−1	1.3E−0
K	n.d.	n.d.	6.6E−1	3.3E−0	n.d.	n.d.
As	5.1E−3	1.4E−3	n.d.	n.d.	2.0E−2	3.4E−3
Sb	2.6−3	2.3E−3	3.5E−2	2.7E−2	4.2E−2	7.0E−3
Sn	9.8E−0	n.d.	Not meas.	Not meas.	Not meas.	Not meas.
U	n.d.	n.d.	2.6E−1	1.3E−1	n.d.	n.d.
Ce	1.1E−0	n.d.	3.1E−2	4.6E−2	n.d.	n.d.

* Note: The data for these 4 quartz samples by J. E. Riley, M. T. Kelley and G. Gleason, Talk presented at the American Nuclear Society Conference, Mayaguez, 1978.

Table III. Graphite from center of susceptor. All concentrations in ppm.

V	5.6E−1
Cr	1.5E−1
Mn	1.0E−1
Fe	n.d.
Co	n.d.
Ni	4.0E−1
Mo	1.1E−01
Zr	3.2E+0
Hf	1.9E−2
Au	3.7E−4
Ca	1.0E+2
Sr	1.2E+0
Sc	2.3E−1
Sn	2.3E+0
Sb	7.4E−3
Se	+
La	2.1E+0
Ce	2.8E+0

Rare earths in the 10^{-2}-10^{0} range

Table IV. Graphite from edge of susceptor. All concentrations in ppm.

V	5.0E−1
Cr	1.6E+0
Mn	4.6E−1
Fe	3.7E+2
Co	6.6E−1
Ni	3.1E+1
Mo	6.3E+1
Zr	3.6E+0
Hf	n.d.
Au	2.4E−4
Ca	9.1E+1
Sr	1.2E+0
Sc	1.2E−1
Sn	1.8E+0
Sb	5.9E−3
Se	4.1E+0
La	1.5E+0
Ce	1.6E+0

Rare earths in the 10^{-2}-10^{0} range

The high purity of the silicon crystals pulled from the contaminated melt is thus due to the large segregation coefficient for transition group metals. A rough calculation based on the observed concentrations of the various impurities in the crucible residue showed that the impurity traces in the silicon ingot just correspond to the segregation factors. Since the quality of the ingot material is adequate, the observed contamination of the melt is not serious as long as the polycrystalline residue in the crucible is indeed discarded and is not added to further silicon charge. Somewhat surprising is the purity of the silicon ingot in spite of its contact with the vapors of the contaminants.

Slicing, mechanical and chemical lapping, and polishing.—Slicing and mechanical lapping are very dirty operations, carried out on industrial equipment not designed for maintaining cleanliness. Wafers at this stage are therefore badly contaminated with a variety of impurities, not always removable by simple cleaning. The level and species introduced during slicing and mechanical lapping depend on the kind of slicing saw, the lapping compound, and the composition and corrosion resistance of other metal parts involved in the process. Fortunately, almost all of this contamination is again removed in the chem-etching step, thus there is little purpose in listing specific contaminants observed in the slicing or mechanical lapping process. Some comments, however, are in order concerning the edge beveling and the chem-etching steps.

Until recently, edge beveling wheels had their diamonds embedded in a solder consisting of a mixture of Cu, Ni, Mn, and Sn. This type of wheel deposited large amounts of impurities at the wafer periphery, which, strangely enough, could not be efficiently removed by chem-etching, even when the duration of the chem-etching step was extended by a factor of 4. The only reasonable explanation for this kind of behavior appears to be the assumption that the high density of vacancies generated at the silicon surface during beveling, in conjunction with local high tempera-

Table V.

Impurities in a silica based polishing slurry as determined by neutron activation

Impurity species	V	Mn	Cr	Fe	Co	Ni	Cu	Zn	Zr	In	Hf	Ta
Conc in ppm	7.5	3.3	0.45	96.8	5.7E−2	2.52	2.6	3.8	145	0.45	3.3	8.8E−3

Impurities in ppm in polishing compounds from different manufacturers. Determination by means of atomic absorption spectrometry.

	V	Cr	Fe	Cu
Supplier 1	<0.5	0.30	47	0.20
Supplier 2	<0.5	0.45	43	1.0
Supplier 3	<0.5	0.35	40	0.28
Supplier 4	<0.5	0.28	124	0.20
Supplier 5	<0.5	0.50	84	3.8
Supplier 6	<0.5	3.20	228	1.9

tures, caused impurity diffusion into the silicon and that these impurities retreated before the advancing solution/silicon interface during chem-etching in the manner described by Wagner for copper in aluminum during electrolytic polishing (3).

More recently, beveling wheels have become available in which the diamonds are embedded in nickel only, with an increased ratio of diamonds/nickel binder. These wheels seem to deposit next to no contamination, not even nickel, at least when new.

In view of the heavy contamination of sliced or mechanically lapped wafers with transition group metals, it is necessary to change the etching solution frequently enough to prevent impurity buildup in the solution. Otherwise the electrochemical potential of the impurities can rise to the point where the solution ceases to be an effective cleaning agent. This phenomenon is quite analogous to the deposition of heavy metals on silicon from contaminated nitric acid-hydrofluoric acid solutions reported by Politycki and Rädlein (4).

Polishing slurries usually appear to be clean enough not to deposit large amounts of impurities on the polished silicon surfaces (Table V), but again it is necessary to limit the length of time the same solution may be reused by recycling. Table VI shows the disastrous results of using a polishing slurry for too long.[7]

The analysis of an alumina-based lapping compound is given in Table VII. These are only examples and may not be typical of other lapping compounds or slurries. An interesting aspect of contamination during polishing is the difference in susceptibility to contamination of differently doped and differently oriented silicon surfaces. (100) and (111) oriented silicon wafers, boron (p-type) and phosphorus (n-type) doped in the 10^{14} cm^{-3} range, were polished using an alkaline, SiO_2-based slurry deliberately contaminated with very dilute copper sulfate. The (100) oriented surface of the p-type wafers became plated with a continuous copper film, the (111) oriented large surface of the n-type wafers remained visually free of any copper, but showed some copper deposition on the edge; the amount of copper on the other two combinations, (111) oriented p-type and (100) oriented n-type silicon, was intermediate. This behavior is in accord with the known electrochemical behavior of silicon crystals, but should be kept in mind: (100)-oriented p-type silicon is most prone to contamination during polishing.

Device fabrication.—Wafer handling.—Prior to entering the device fabrication process, polished substrates are cleaned in different ways, all of which seem to do an adequate job of removing impurities adhering to the surfaces. The wafers are then subjected to a variety of processing steps, which require handling of the wafers for inspection, insertion in furnaces,

[7] Impurities on silicon wafers are usually concentrated in surface near layers, but their exact distribution is not known. We prefer to give impurities detected on silicon wafers in terms of atoms/wafer. Conversion of atoms/wafer to ppm requires knowledge of the wafer thickness at a given diameter. A 20 mil thick, 3 in. diam silicon wafer contains about 1.15E23 atoms silicon, and weighs about 5.39g.

Table VI. Impurities on a wafer polished with an alkaline SiO_2 based polishing slurry which became contaminated during excessive use of the same solution

	Concentrations in atoms/3" ϕ wafer
Cr	5.9E15
Fe	8.5E15
Co	4.0E15
Ni	3.4E15
Cu	1.4E15
Zn	+
Mo	3.6E15
Ta	1.6E12
W	1.4E14

Table VII.

Impurities in a fresh alumina lapping compound. Concentration in ppm.

Cr	7.2
Fe	1100
Zn	34.2
Cu	Not meas.
Ni	28.7
Mo	4.1
Hf	2.1
W	3.9
Au	0.023
Na	4600

Other elements detected: As, Ga, Sc, La, Ce, Nd, Eu, Tb, Yb

Impurities in alkaline solution (density 1.18 g/ml) of colloidal silica.* Concentration in ppm of liquid.

Cr	0.14
Fe	31.0
Zn	0.43
Cu	0.085
Ni	0.084
Mo	0.025
Mn	0.125
V	0.250

* Atomic Absorption Data courtesy of T. Y. Kometani, Bell Labs, Murray Hill, N.J.

application of photoresist, etc. Until fairly recently, metal tweezers were in widespread use for this purpose. Table VIII shows that this is not the best way of handling wafers, especially bare silicon wafers which are hard enough to abrade the tweezer material; an oxidized wafer is much "softer" in this respect. More recently, plastic tweezers have been substituted, and the "roll-over" technique from one (plastic) container

Table VIII. Contamination of bare silicon wafers handled with metal tweezers

	Control (atoms/3" ϕ wafer)	Wafer lifted 20 times with metal tweezer (atoms/ 3" ϕ wafer)	Tweezer composition concentration (%)
Fe	–	4.2E13	73.15
Cr	5.0E11	1.3E13	14.30
Ni	1.4E13	5.6E13	10.90
Cu	–	–	0.059
Au	1.1E11	1.5E11	Contaminated

to another has eliminated much of the handling of individual wafers, resulting in a considerable reduction in the degree of contamination with stainless steel components. There persist two rather insidious modes of contamination: use of the same containers or of the same tweezers for handling metallized and virgin wafers. Containers or tools used for handling metallized wafers should not be used at earlier fabrication steps.

Once oxidized, the silicon surface becomes much less vulnerable to contact contamination, including contact with liquids. Etching with HF, however, generates a highly active silicon surface on which noble metals, if present, will readily plate out by contact potential. If a contamination problem seems to exist on the line, an HF etching step exposing bare Si should always be followed by a cleaning in hot H_2O_2-HCl, which both cleans and oxidizes the silicon surface.

Deposition of epitaxial silicon.—In the MOS technology epitaxial silicon is usually deposited on low resistivity substrates, which has a high solubility for transition group metals. This is a fortunate feature in that the substrate effectively blocks the transfer of impurities, emanating from impure graphite or SiC susceptors, into the epitaxial layer by solid-state diffusion. Because of the lower metal solubilities at lower temperatures, there is, of course, a practical limit to the degree of blockage even a low resistivity substrate can exert (5), and cleanliness of the susceptors, especially absence of particulate impurities, is still very important. Diffusion of impurities from the susceptors through the vapor phase into the growing epitaxial layer is essentially prevented by the presence of chlorine or chlorine-containing species during the epitaxial deposition process. In addition, the low oxygen content and the purity of the higher resistivity epitaxial silicon offers few sites for precipitation of contaminants.

The effect of particulate (*i.e.*, highly concentrated) contamination in the susceptor was demonstrated by Pearce and McMahon (6). Dragging a stainless steel tweezer over the surface of an SiC susceptor resulted in the appearance of the same pattern in the epitaxial layer of a wafer placed over the contaminated area for epitaxy. The pattern in the epilayer consisted of stacking faults and saucer pits (after Secco etching). Contamination of graphite susceptors with nickel and copper-containing particulate matter was revealed also by laser-induced emission spectroscopy (7) and by autoradiography of wafers neutron-activated after epitaxial deposition: the radioactive spots were confined to the back surface of the wafer. These particulate sources of contamination probably stem from the machining process and could perhaps be removed by the manufacturer by a cleaning treatment subsequent to the shaping operation.

Oxidation.—High temperature oxidations, in the absence of HCl, especially steam oxidations for production of the "initial oxide" are probably the process step normally introducing the largest quantities of detrimental impurities. Yet this need not be so.

Table IX shows the typical contamination resulting from a high temperature steam oxidation as well as from an oxidation in dry oxygen (no HCl) at about the same temperature and for the same length of time. There is not much difference between the level of contamination, thus it is not necessary to speculate on transportation of volatile impurity species by the steam: the impurities must be diffusing out of the quartz tube. Table X gives the analysis of a piece of an unused quartz tube. While the level of contamination is not insignificant, it is obvious that the total amount of impurities present could not possibly act as the reservoir for the observed contamination of the silicon wafers over an extended period of time. In steady state, impurities must be diffusing from the outside through the walls of the quartz tube.

Quartz tubes are conventionally operated inside mullite or SiC liners; both of these materials are, however, very impure and can serve as a virtually inexhaustible reservoir of impurities. Table XI gives impurity concentrations in mullite and in SiC from furnace liners.

Diffusion of transition group metals through quartz furnace tubes possesses an extremely steep temperature dependence. In one set of experiments the existing temperature gradient in a furnace was utilized, with silicon wafers positioned at locations of accurately measured temperatures. The concentrations of Fe, Co, Ni, and Cr were all found to increase by a factor of 200 over a temperature range of only 30°C (1140°-1170°C), whereas copper and tantalum increased only by a factor of 3. The ambient, dry oxygen or steam, did not appear to be a factor. We believe, however, that these results do not reflect a true activation energy for diffusion, but rather a different degree of devitrification of the quartz tube kept at the different temperatures for a long period of time, and thus providing more or

Table IX. Typical level of contamination observed after oxidation in steam or in dry O_2 without HCl. Concentrations in atoms/3" θ wafer.

	Cu	Cr	Fe	Co	Ni
Steam at 1170°C for 1 hr	1.3E15	4.8E14	2.1E15	1.2E14	5.4E14
Dry O_2 at 1150°C for 1 hr	1.5E15	1.3E15	6.6E16	2.7E14	3.8E15

Table X. Impurities in an unused quartz furnace tube. Concentrations in ppm.

Cr	3.3E−2
Mn	Not meas.
Fe	3.4
Co	8.6E−3
Ni	2.4E−1
Zn	2.4E−1
Cu	0.28
Mo	0.26
Zr	5.3
Hf	0.17
Ta	5.6E−3
Se	0.57
Te	0.08
Th	0.15
U	0.55
Na	1.8
Cd	0.72

Other elements detected: Ca, Ba, La, Sc, rare earth (in part fission products from the reactions on U and Th).

Table XI.

Impurities in a SiC furnace liner. Concentrations in ppm.**

Fe	19,300
Co	51.1
Ni	195
Zr	9,300
Hf	3.5
Mn	10.3
Cr	75.1
Ir	0.23
W	0.42
Na	19,900
K	1,860

La, Sc, Sm, Eu—all in the 0.X ppm range

Impurities in a mullite furnace liner. Concentrations in ppm.**

Fe	8,180	Ga	75.0
Co	5.7	Na	980
Ni	9.4	K	7,570
Cr	62.9	Ca	2,200
W	8.2	Cs	12.7*
Ta	3.6	Ba	152*
Th	2.2	Sc	15.6
U	0.12	Zr	210*
Hf	6.2	Yb	35.6
Sb	0.77	La	6.26
Au	0.12		

* There may be some contribution from the fission of U-235.
** Cu could not be determined nondestructively on this sample but was present.

easier diffusion paths. Fe, Co, Ni, and Cr thus appear to diffuse preferentially along (incipient) grain boundaries, the lower "activation energy" of copper may be indicative of a bulk diffusion process.

Table XII shows impurity concentrations on silicon wafers oxidized at the same temperature, but for different periods of time in steam. It can be seen that there exists probably a sublinear time dependence. Combining these two results suggests that from the contamination point of view it would be advantageous to carry out steam oxidations at the lowest feasible temperature.

Table XIII gives the impurities on a wafer oxidized in dry oxygen + 1% HCl at 1000°C for 1 hr. The presence of the HCl prevents contamination of the silicon; unfortunately, no such protection occurs during steam oxidation in HCl, not to mention the exceedingly corrosive nature of the steam-HCl mixture.

A particularly insidious, but easily avoidable, source of contamination during high temperature furnace treatments are impure SiC boats or paddles (or impure graphite coated with a thin layer of SiC). Table XIV shows the enormous contamination that can result from the use of such boats. This particular oxidation was carried out in dry O_2 + 1% HCl, otherwise the contamination would have been even worse. Autoradiography also showed that the contamination was heaviest where the wafer had been in contact with the boat. Contamination can also result from the use of impure diffusion sources. Table XV shows the impurity content of a BN diffusion disk. This BN disk, as well as others, were found to be very nonuniform, and segments from one and the same disk gave strongly different results. The isotopes Cu and Mn could not be determined on this sample, the 511 keV peak of the positron annihilation radiation due to Cu-64 being interfered by pair-production from other high energy gamma emitters, and the Mn-56 emission having decayed due to the short half-life of Mn-56 (2.58 hr). From the absence of the weak 1345.6 keV gamma line of Cu-64 it can be inferred that the Cu concentration must have been less than about 10^{14} atoms cm^{-3}.

By analyzing the impurities not in the BN disk but on silicon wafers diffused from BN disks it has been shown that Cu and Mn are in fact impurities transferred from the BN disks to the silicon during diffusion treatment. Which impurities are significantly volatile will depend on the activity coefficient of the impurity in the BN matrix, a topic on which essentially nothing is known. In calculating the impurity concentrations in boron or BN from the gamma-ray spectra of neutron-activated samples one must take into consideration the reduction in thermal neutron flux inside the sample, due to the extremely large cross section of B-10 for thermal neutrons (8).

Ways to avoid contamination during steam oxidation.— 1. A guaranteed way to eliminate contamination would be the use of a double-walled quartz tube with an HCl-containing gas being passed between the inner and outer walls of the tubes (and discharged into a separate outlet from the steam). This would increase the outer diameter of the tube, but would eliminate the need for a furnace liner.

2. High purity alumina liners are available, an analysis of this material is shown in Table XVI. The high purity alumina is orders of magnitude cleaner than the customary mullite liners (and therefore also more expensive). There should be very little transition group metal diffusion into quartz tubes heated inside high purity alumina liners, as long as the alumina liner does not become saturated with impurities diffusing from the heating elements of the furnace, etc. We do not have at this time experimental data to clarify this question.

3. Another attractive approach is the use of low temperature-high pressure steam oxidation. Table XVII shows results obtained on wafers oxidized in a system built at Bell Labs, Allentown (9). In this particular system the steam comes in direct contact with a highly corrosion resistant cobalt alloy, a condition avoided in commercially available systems. The contamination with cobalt, nevertheless, is moderate. The wafers after oxidation are rather clean, except for an unaccounted for contamination with some copper. Es-

Table XII. Impurity buildup as a function of oxidation time in steam at 950°C. Concentrations in atoms/3″ θ wafer.

	Cu	Fe	Co	Ni	Cr	W
60 min	2.8E14	3.2E15	1.7E13	5.9E14	7.5E14	4.1E11
122 min	5.1E14	3.9E15	2.0E13	1.5E15	1.0E15	3.1E12

Table XIII. Typical level of contamination observed on a very clean substrate after oxidation for 1 hr at 1000°C in dry oxygen + 1% HCl. Atoms/3″ θ wafer

Cu	–
Cr	–
Fe	–
Co	3.8E11
Ni	+
Ta	1.5E11

Table XIV. Impurities on originally clean substrate oxidized in dry O_2 + 1% HCl for 1 hr at 1000°C in SiC boat. Atoms/3″ θ wafer.

Cu	2.8E16
Co	6.6E12
Ni	3.5E14
Ta	8.4E11

Table XV. Impurities on a BN diffusion disk. Concentrations in ppm.

Fe	97.0E−0
Co	1.0E−2
Ni	1.3E−3
Mo	5.0E−4
Zr	4.6E−1
Pt	1.1E−1
Hf	3.0E−0
Ta	3.0E−1
Au	3.0E−4
W	6.4E−1
U	7.0E−1
Th	8.1E−1

Many rare earths, in part from the fission reaction of U-235

Table XVI. Impurities on a piece of high purity alumina furnace liner. Concentrations in ppm.

Cu	Not measured because of interference
Cr	7.1
Fe	512
Co	0.37
Ni	9.4
Zr	1,000
Mo	0.30
Hf	1.72
W	1.61
Na	350
K	143
Ca	217

Other elements detected: Ba, Ce, La, Ga, Sc, Nd, Eu, Tb, Yb

Table XVII. Contamination during low temperature (750°C)-high pressure (20 atm) oxidation for 70 min in steam. Steam in direct contact with pressure vessel alloy. Atoms/3″ θ wafer.

	Before oxidation	After oxidation
Cu	5.8E13	1.9E14
Cr	6.1E13	6.1E13
Co	–	2.3E12
Ni	Very weak	2.1E13
Fe	Very weak	Very weak
W	–	1.3E11
Na	1.5E14	1.1E14
As	8.7E11	7.3E11
Sb	9.9E10	7.6E10

sentially all contamination should be avoidable, at 750°C!, in a system which prevents the steam from coming in contact with any metal parts.

Ion implantation.—Our experiments were carried out on two different types of implanters. One is a high voltage, low current commercial machine in which only one wafer at a time is being implanted. The other is a low voltage, high current machine designed and built internally. In this latter machine up to 30 wafers may be implanted simultaneously, a large target holder moving in front of the stationary beam. The commercial high voltage-low current machine has excellent focusing and mass resolution, and no contamination with transition group metals attributable to the implantation step was detectable. In the low voltage, high current machine, on the other hand, the ion beam is permitted to strike the walls of the waveguide, the beam stop, and the beam catcher plate. Impurities can and are being sputtered off these metal parts, and attention must therefore be paid to the material from which they are made. Table XVIII shows an example of the contamination resulting from the use of a stainless steel beam catcher plate. The contamination was not confined to the back surface of the wafer, about 1/3 was found on the front surface. Impurities from the material of the hot cathodes were also shown to find their way to the silicon wafers, but this does not appear to constitute a major problem.

Plasma etchers.—Plasma etching is beginning to replace wet chemical etching steps due to the better resolution and avoidance of undercutting. The plasma, however, constitutes a very effective means of redistributing impurities deposited outside the target area in previous runs. Thus, for instance, plasma etchers which have been used to pattern gold metallurgy should not be used for other work without very thorough cleaning if the sample to be etched will undergo still some high temperature treatments after the plasma etch. Exposed copper parts also have been shown to be a source of contamination, as is the copper contained in aluminum-copper alloys used as the base plate in some etchers; in the latter case, however, the aluminum plate becomes oxide covered if the working gas in the etcher contains oxygen, and the contamination decreases with time.

Packaging.—At this stage, wafers are no longer exposed to high temperatures, thus contaminants other than those that give rise to electrolytic conduction, such as NaCl, are no longer of importance. A special case, however, is the packaging of static memories in alumina ceramics. Information in static memories is not periodically refreshed, but must be maintained indefinitely. Alumina ceramics, however, often contain small amounts of uranium and thorium and other members of the uranium decay chain, all of them alpha emitters. Due to the large energy of alpha particles, and the very small charge stored on an individual capacitor in such memory arrays, direct hits by alpha particles can result in loss of information. This fact requires that static memories be shielded against direct alpha hits, a relatively easy task in view of the very short range of alpha particles in matter. Most of the alpha emission, incidentally, does not stem from the very long-lived U-238, but from shorter lived members of the decay chain. However, the (n,gamma) reaction on U-238 is the most convenient method for determining the uranium content, and hence establishing the presence or absence of the problem (Table XIX).

Table XVIII. Impurities on a silicon wafer boron implanted at a dose of 6.7E16/wafer at a beam current of 0.5 mA with a low voltage-high current implanter built internally. Tungsten hot filament, stainless steel beam catcher plate. Atoms/3" θ wafer.

Cu	Fe	Co	Ni	Cr	W	Mo
1.9E14	5.4E15	1.6E13	6.0E14	1.6E15	7.4E11	1.7E13

Table XIX. Impurities from the ceramic of an integrated circuit package. Concentration in ppm or in %.

Na	0.48%
Ca	5.1%
Cr	0.51%
Zr	0.35%
Hf	130 ppm
W	21 ppm
Ta	7 ppm
U	0.79 ppm
La	0.34 ppm
Sc	0.42 ppm
Sm	0.25 ppm
Yb	1.70 ppm

Summary

A survey has been given of the sources of contamination in silicon device processing. The polysilicon used for growing ingots is very pure, but very strong contamination of the silicon melt can occur from the exposure of metal parts (Inconel and/or molybdenum in our case) in the crystal growers to high temperatures. Transfer of the contamination appears to occur preponderantly through the vapor phase. The large segregation coefficients of the transition group metals protect the silicon ingot against significant contamination provided the polysilicon residue in the crucible is not recycled.

Lapping and polishing can be sources of very undesirable contamination of the starting substrate surface if the lapping and polishing compounds are dirty to start with or are being reused for too long. Edge beveling wheels of a new design were found to introduce very little if any contamination as compared to older types of wheels. High temperature oxidations in the absence of HCl were shown to be preponderant sources of contamination. The impurity diffusion through the walls of the quartz tubes and into the silicon approximately follows an exponential behavior with temperature. Presence of HCl suppresses this contamination. Possible alternatives for preventing contamination during high temperature furnace treatments are described. The special role of HCl (or other chlorine-containing compounds) in removing contaminants as chlorides during high temperature gettering is examined in a companion paper.

Acknowledgment

The authors are indebted to T. Y. Kometani, Bell Labs, Murray Hill, New Jersey, for atomic absorption spectrometric determinations of impurities in polishing compounds.

Manuscript submitted April 14, 1980; revised manuscript received July 31, 1980.

Any discussion of this paper will appear in a Discussion Section to be published in the December 1981 JOURNAL. All discussions for the December 1981 Discussion Section should be submitted by Aug. 1, 1981.

Publication costs of this article were assisted by Bell Laboratories.

REFERENCES

1. P. F. Schmidt and D. J. McMillan, *Anal. Chem.*, **48,** 1962 (1976); P. F. Schmidt, J. E. Riley, Jr., and D. J. McMillan, *ibid.*, **51,** 189 (1979).
2. R. Van der Linden, F. De Corte, and J. Hoste, *Anal. Chim. Acta*, **71,** 267 (1974); L. Moens, F. De Corte, J. Haste, and A. Simonits, *J. Radioanal. Chem.*, **45,** 221 (1978).
3. H. W. Pickering and C. Wagner, *This Journal*, **114,** 698 (1967); see also H. H. Strehblow, C. M. Melliar-Smith, and W. M. Augustyniak, *ibid.*, **125,** 915 (1978).
4. A. Politycki and G. Rädlein, *Z. Naturforsch., Teil A*, **19,** 1216 (1964).

5. R. N. Hall, *J. Phys. Chem. Solids*, **3**, 63 (1957); R. N. Hall and J. H. Racette, *J. Appl. Phys.*, **35**, 378 (1964).
6. C. W. Pearce and R. G. McMahon, *J. Vac. Sci. Technol.*, **14**, 40 (Jan/Feb. 1977).
7. T. H. Briggs, Personal communication.
8. Y. U. Yakovlev and N. N. Dogadkin, *Uspekhi Anal. Khim.*, 124 (1974).
9. L. E. Katz and B. F. Howells, *This Journal*, **126**, 1822 (1979).

Metal Silicon Reactions Induced by CW Scanned Laser and Electron Beams

T. Shibata,[1] T. W. Sigmon,* J. L. Regolini,[2] and J. F. Gibbons*

Stanford Electronics Laboratories, Stanford, California 94305

ABSTRACT

Scanned CW-laser and electron beams have been utilized to react thin metal films of Pd, Pt, Mo, W, and Nb deposited by electron beam evaporation onto single crystal silicon substrates to form silicides. Formation of large area uniform layers of Pd_2Si or PdSi is controlled by selection of the power level of the scanning laser or electron beam. Single phase $MoSi_2$, WSi_2, and $NbSi_2$ are also found after CW-beam reaction. For the Pt/Si system mixed phase silicides are found after CW-laser reaction with a superconducting ($T_c \cong 4$ K) metastable compound, Pt_2Si_3, observed as the dominant phase. In contrast, single-phase PtSi is found after electron-beam reaction. Comparison is also made with electron beam evaporated films and argon sputter-deposited films.

The reaction of thin metal films with both single and polycrystalline silicon to form silicide compounds is an area which has received wide attention in the past few years. Future integrated circuit technology will require increased device packing density along with decreased dimensions resulting in a need for low resistance interconnects. Desirable properties of these interconnects will include high temperature process compatability and controlled metal-silicon-interface reactions for both Schottky and ohmic contact reliability (1-3). The bulk of the research to date has been carried out in thermal equilibrium furnace reactions and an excellent review is given in Ref. (4). There both the film deposition and furnace annealing processes are discussed in detail along with useful measurement techniques for determining reacted film composition and quality.

Certain limitations have been found in the furnace thermal equilibrium processing, however. As a result of these limitations, within the last year, the use of energetic beams to react metal silicon films has been investigated by a number of research groups. Both laser (5-7) and electron beam (8) reaction and ion beam mixing (9) have been used in this work. Each of these techniques has led to several unique results, differing in many cases from that found for standard furnace processing.

The main features offered by the laser or electron beam processing of these films include shorter reaction times, localized heat-treatment, and rapid heating and cooling rates. Similar to the case of energetic beam annealing of semiconductors, a natural division of the physical mechanisms and results can be made for pulsed *vs.* scanned CW energetic beam-induced reactions. In this paper we will discuss results we have obtained using scanned CW-laser and electron beams to react various metal/silicon systems. In contrast to the results found for the pulsed case, uniform, essentially single-phase silicide films are obtained with the scanned CW beams. However, under certain conditions, metastable mixed-phase systems are also obtained. Both MeV Rutherford backscattering and glancing angle x-ray diffraction analysis have been utilized for characterizing the structure of the layers. Four-probe resistivity measurements have been utilized to obtain bulk resistivity using the film thickness data obtained from the backscattering.

Experimental

In Table I we list the various metal/silicon systems reacted in this work. Also listed are the pertinent properties characterizing each system, such as thickness and whether or not a silicon overcoating is used. All metal films were deposited by electron beam evaporation onto p-type <100> silicon substrates in a high vacuum oil-free system, unless otherwise noted. Thin amorphous silicon layers were deposited on the metal layers to be reacted by the laser to provide an antireflection coating for the metal surface. Without the silicon overcoating, a high laser power is required to compensate for the power reflected from the metal surface. However, the smaller reflectance of the silicide compound results in an increased power absorption in the film during the reaction, leading to difficulty of control of the reaction. This problem can be avoided by the use of this thin silicon overcoating. Naturally, since the reflectance does not change for the electron beam this overcoating layer is not required for the scanned electron beam experiments.

The laser used in this work was a CW argon laser operating in the multiline mode. The laser output was focused by a 135 mm lens onto the sample and scanned by the apparatus described in Ref. (10). Typical pa-

Table I. Summary of samples used in the experiments

Beam process	Si-overcoating	Metal layer		Substrate
Scanned-laser beam	Si (200Å)	Pd	(1300Å)	p-type <100> Si
		Pt	(1000Å)	
		Mo	(530Å)	
		W	(440Å)	
		Nb	(1100Å)	
Scanned-electron beam	None	Pd	(1400Å)	
		Pt	(1100Å)	
		Nb	(1250Å)	

* Electrochemical Society Active Member.
[1] On leave from Integrated Circuits Laboratory, Toshiba R and D Center, Toshiba Corporation, Kawasaki, Japan.
[2] Present address: CNEA Bariloche, Argentina.
Key words: silicides, laser anneal, e-beam anneal, contacts.

rameters used in these experiments were, approximately 50 μm spot size and 12 cm/sec beam scan speed. The substrate was held at fixed temperatures during the laser irradiation. The substrate temperatures used for the various reactions are listed in Table II. Electron beam irradiation was performed in a Hamilton Standard electron beam welder, Model EBW7.5 at a working vacuum of 10^{-4} Torr. The samples were mounted on a copper heat sink with Dow Corning 340 heat sink compound and maintained near room temperature during the reaction. Typical electron beam parameters used for the reactions were, substrate temperature approximately 50°C, electron beam energy 31 keV, current 0.1-0.3 mA, beam spot size (as measured by the reacted path) approximately 100 μm, scan rate of 13 cm/sec, and a step size of less than 100 μm. All reacted layers were studied by MeV ^{4}He ion backscattering, glancing angle x-ray diffraction analysis in a Read camera, Nomarsky optical microscopy, and four-probe resistivity measurements.

Results and Discussion

Pd/Si.—In Fig. 1 we show an optical micrograph of a sample consisting of Si (200Å)/Pd (1300Å)/Si <100> laser beam scanned as a function of laser power levels. It can be seen from Fig. 1 that the reaction of the Pd/Si is initiated at about 4W of laser power. The laser-induced reaction is easily detected by the unaided eye through a surface color change. For this particular sample the reaction began at a power level of 4W where the surface color changed from blue (unreacted film) to yellow (reacted film, low power phase). This low power phase was found to be stable to a threshold power of about 7.0W, above which a different high power phase appears in the center of the beam scan line. At this power level, the surface color changes to a gray color characteristic of the high power phase. In order to obtain uniformly annealed areas, overlapped scans were performed in such a way that each adjacent scan line overlapped by at least 40%.

For the remainder of this paper we will normalize the output power level of the laser (P) to the power at which the surface of a virgin silicon wafer just begins to melt (P_o). This normalized power ($p \equiv P/P_o$) is experimentally reproduceable, thereby minimizing the dependence on the laser system and/or other conditions. For our experimental configuration. typical values of P_o are 9.0 and 5.0W for 50° and 350°C substrate temperatures, respectively. This normalized laser power is also related to the important parameter of the CW-beam process, *i.e.*, the ratio of beam power to the spot radius (P/w). This relation is given by P/w (W/μm) = $0.337p$ or $0.191p$ for T_{sub} = 50° or 350°C, respectively, using the formulation of Ref. (11). Here the beam radius, w, is defined by the $1/e$ point of the beam intensity assuming a Gaussian distribution. Since

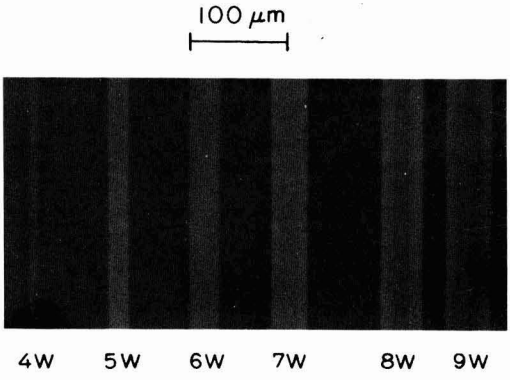

Fig. 1. Optical micrograph of a sample consisting of Si (200Å)/Pd (1300Å)/Si <100> after single laser scans at various laser power levels. The low power phase is formed between 4 and 7W and the high power phase at and above 8W.

the actual power absorbed by the sample is reduced by the reflection, the essential power parameter is $(1 - R)\ P/w$, where R denotes the reflectance of the sample. This parameter is listed in Table II and has been calculated by using experimentally determined values for R. Since reflectance is not important for the electron beam experiments the actual P/w values are listed in Table II. For the electron beam data the beam diameter used was determined by measuring the width of the reacted material for a single scan. This technique gives a slightly different value for w as compared to the laser case, where w is determined from the melting power (P_o).

Backscattering spectra for the Pd/Si samples which were laser annealed at p = 0.71 (low power phase) or p = 1.1 (high power phase) are shown in Fig. 2(a). The spectrum for the unreacted sample is shown by the solid line. Since this is a sample prepared for laser annealing, the peak in the solid line near 1.2 MeV on the energy scale is the signal from the 200Å of silicon antireflection overcoating previously discussed. The peak at higher energy is the signal from the Pd, and the step in the backscattered yield at about 1.1 MeV represents the signal from the underlying silicon substrate. It is clearly seen in Fig. 2(a) that the entire metal layer has been reacted with the substrate and surface silicon after laser irradiation. From the areas underlying the backscattering spectra for the different atomic species, one can determine the average composition of the reacted materials. This was determined to be Pd_2Si for the low power phase and PdSi for the

Table II. Summary of beam process parameters and resultant reactions

	Metal film	Reacted phase	Reacted thickness* (Å)	p (normalized laser power)	Power parameter** (W/μm)	T_{sub} (°C)	Resistivity ($\mu\Omega \cdot$ cm)
Laser beam reacted	Pd	Pd_2Si	1930	0.71	0.154	50 (±0.5)	37
	Pd	PdSi	2600	0.9 ~ 1.4	0.2 ~ 0.3	50 (±0.5)	31
	Pt	Pt_2Si†	—	0.69		50 (±0.5)	—
	Pt	$PtSi_2$†	—	0.86	0.185	50 (±0.5)	—
	Mo	$MoSi_2$	1450	0.88	0.093	350 (±1.0)	190
	W	WSi_2	1200	0.85 (10 scans)	0.087	350 (±1.0)	110
	Nb	$NbSi_2$	1350	0.9 (21 scans)	0.089	350 (±1.0)	—
Electron beam reacted	Pd	Pd_2Si	2280		0.112	~50	39
	Pd	PdSi	2730		0.136	~50	20
	Pt	PtSi	1670		0.093	~50	28
	Nb	$NbSi_2$	1200‡		0.173	~50	—

* Calculated from backscattering spectra using the near-surface approximation for the energy loss.
** Calculated values of absorbed power/beam radius: $(1 - R)P/w$.
† A mixed phase compound including metastable Pt_2Si_3.
‡ Thickness of a partially reacted film.

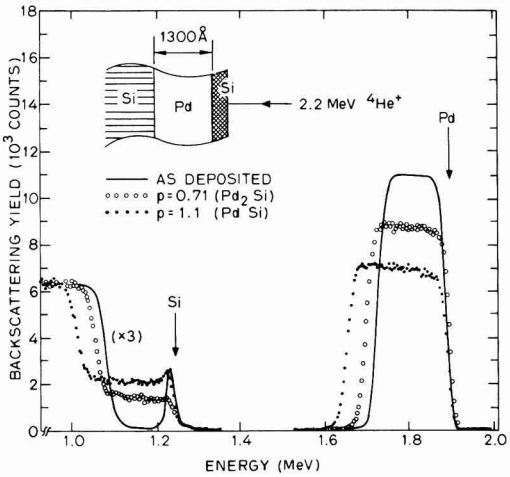

Fig. 2. (a). Backscattering spectra for Si/Pd/Si laser annealed samples for various normalized laser power levels. The solid line (——) represents data taken on unreacted samples, the circles (○ ○ ○) on samples reacted at low powers, and the closed circles (● ● ●) samples reacted at high power levels.

high power phase. It should be noted that the spectrum of the high power phase (PdSi) did not change significantly with laser powers ranging from $p = 0.9$ to 1.4. This result is quite different from those obtained using a pulsed laser beam, where the average composition of the silicide layers are observed to change continuously with increasing laser power (5, 12). In Fig. 2(b) we show the x-ray diffraction pattern obtained from the sample reacted at high power ($p = 1.1$) using a Read x-ray camera. The lines from the PdSi phase are indicated by the solid circles and the most intense lines from the Pd_2Si phase by the open circles. It can be seen from this diffraction pattern that the compound is essentially single-phase PdSi containing a trace amount of Pd_2Si, thereby verifying the backscattering results. Similar results were obtained for the sample reacted at low power where the compound was found to be mainly Pd_2Si, with a trace amount of PdSi observed. Identical results were also found for the electron beam reacted Pd/Si samples. These results are also in contrast with those obtained using a pulsed laser beam, where the reacted layer was found to consist of PdSi, Pd_2Si, Pd_4Si, Pd_5Si, and Si precipitations (12, 13).

It should be noted that the formation of uniform PdSi layers is difficult by conventional furnace techniques unless ion beam mixing (14) is used, usually leading to a PdSi island microstructure containing Si between or inside the islands (15). In Table II various properties of the PdSi and Pd_2Si films formed by both the laser and electron beams are presented.

The surface morphology of the Pd_2Si layers can be best described as a rather patchy surface appearance similar to that obtained in the furnace reacted case (15). The effective temperature calculated for the laser-scanning conditions used to form the Pd_2Si is about 778°C for $p = 0.71$, with an effective annealing time of $T_{eff} = 12.1$ msec. This results in a calculated Pd_2Si thickness of about 1530Å assuming that the furnace annealing data (16) holds for the laser process. [The formulas in Ref. (11) have been used for the calculation.] These calculations are in good agreement with the experimentally observed result (1930Å) determined by backscattering (Table I). These results indicate that the formation of Pd_2Si by the CW laser occurs by a process quite similar to that of the furnace reaction. Using recently obtained furnace annealing data for the activation energy of the Pd_2Si formation (17), we have concluded that the formation of this phase proceeds via a solid-state interdiffusion mechanism (18).

The PdSi films exhibit a laminar-like surface morphology indicative of a spontaneous nucleation process. A Nomarsky interference micrograph of the surface is shown in Fig. 3. Although the mechanism responsible for the PdSi formation is not completely understood, we have evidence indicating that a nucleation-induced process is responsible (7).

Pt/Si.—Scanned laser reaction of the Si (200Å)/Pt (1000Å)/Si <100> samples resulted in surface color changes similar to those found for the Pd/Si samples. The reaction was found to begin at $p = 0.5$ with the transition from a low power to a high power phase occurring at a value $p = 0.74$. The backscattering and x-ray diffraction results were found to be quite different from those obtained for the Pd/Si films. In Fig. 4(a) we show backscattering data for the laser-reacted Pt/Si films, and in Fig. 5 similar data is shown for the electron-beam reacted layers.

The average composition calculated from the backscattering spectrum in Fig. 4 for the low power laser-reacted sample is close to Pt_2Si; however, it was found from x-ray analysis that the layer consisted mainly of Pt_3Si and PtSi with trace amounts of $Pt_{12}Si_5$ and Pt_2Si.

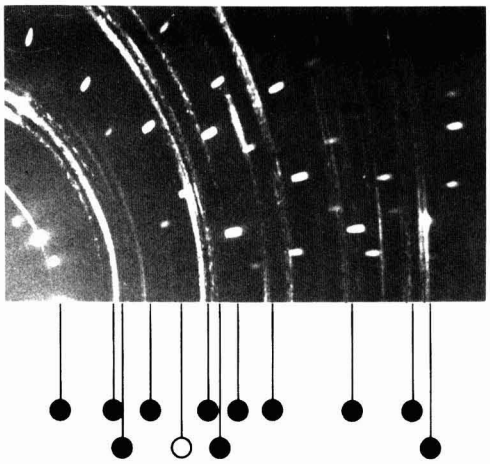

Fig. 2. (b) Glancing angle x-ray diffraction pattern from a Read camera on the sample reacted at high power as shown in Fig. 2(a). The line indicated by ○ is the most intense diffraction line from Pd_2Si.

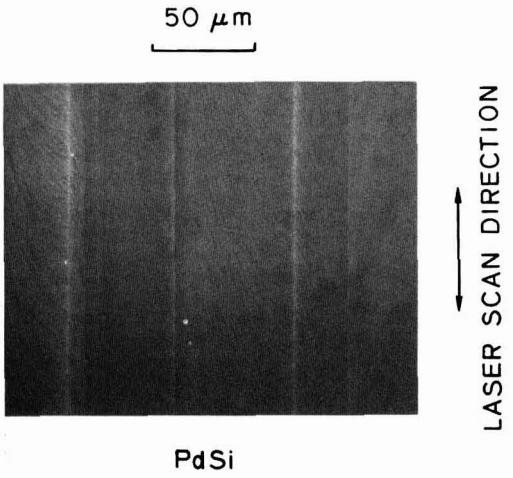

Fig. 3. Nomarsky interference micrograph of a PdSi layer formed by scanned laser reaction.

The average composition determined from Fig. 4 for the high power phase was approximately $PtSi_2$. This compound does not exist in the equilibrium phase diagram (19). The x-ray diffraction pattern obtained from the high power phase ($PtSi_2$) is shown in Fig. 4(b). The intense lines appearing in this diffraction pattern cannot be fit by any equilibrium Pt/Si compounds. However, they are found to fit very well the diffraction pattern of metastable Pt_2Si_3 (20). Small amounts of Pt_2Si_3 were also found in the samples reacted at low power. To further verify the existence of this phase for these samples we performed superconductivity measurements. The observed transition temperature (T_c) was found to be approximately 4 K corresponding well to that observed in Ref. (20).

In Fig. 5 backscattering data obtained for the Pt/Si films reacted by scanned electron beams are shown. Using the near-surface approximation for the energy loss and cross section, this data indicates the entire film has been reacted to form PtSi. That this is a uniform reaction is indicated by the uniformity of the platinum and silicon signals corresponding to the PtSi layer.

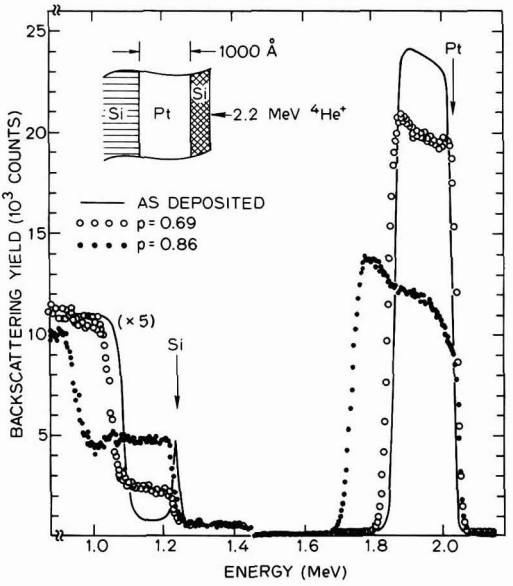

Fig. 4. (a) Backscattering spectra for as-deposited (——) Si/Pt/Si structures and laser annealed [(○○○) $p = 0.69$ and (●●●) $p = 0.89$] Si/Pt/Si structures.

This is in contrast to that observed in Fig. 4(a), for the Pt/Si layers reacted by the laser. Glancing angle x-ray diffraction analysis of the electron-beam reacted layers confirm the results of the backscattering that we do indeed have single-phase PtSi. Further parameters measured for these films are listed in Table II.

The observed difference between the laser and electron beam ability to form PtSi can be caused by two phenomena. The basic physical differences between the laser and electron beam experiments are sample structure and beam energy deposition profile. Although we cannot rule out the possibility of interfacial effects (such as bond breaking) created by penetration of the electron beam into the Pt/Si interface, we speculate

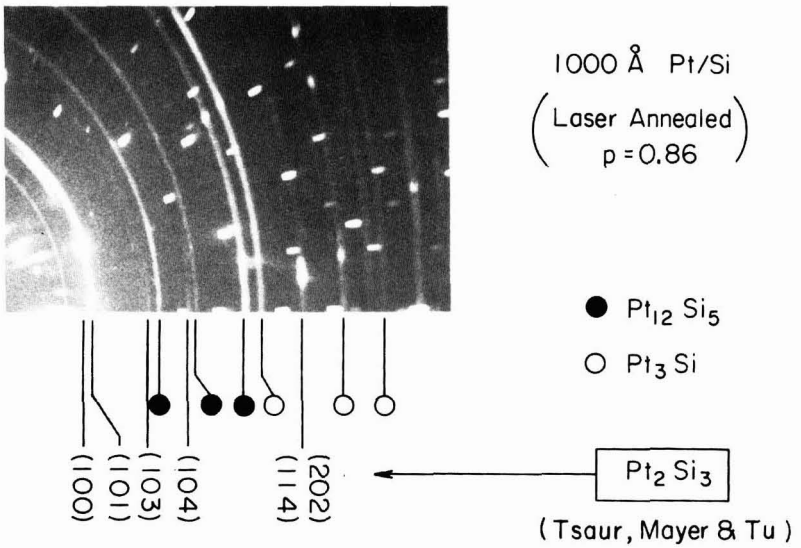

Fig. 4. (b) Glancing angle x-ray diffraction pattern for the Pt/Si structure laser annealed at $p = 0.86$ as shown in Fig. 4(a). Formation of superconducting Pt_2Si_3 phase is evident.

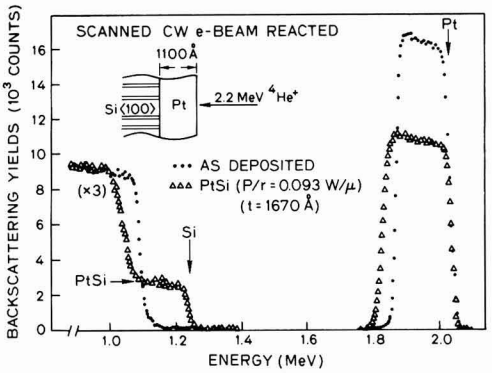

Fig. 5. Backscattering spectrum shown for Pt/Si film reacted by a scanning electron beam. The closed circles (● ● ●) represent the spectrum from the as-deposited film while the triangles (△△△) are for the e-beam reacted.

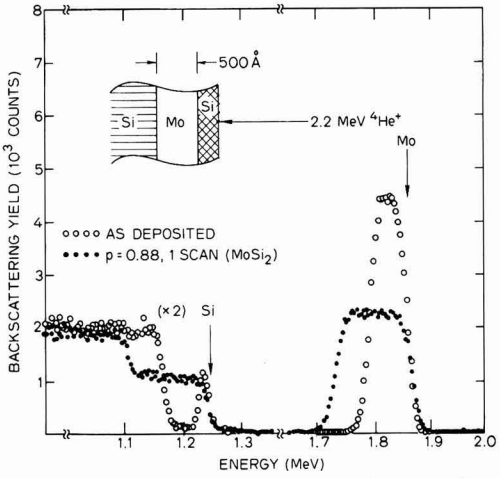

Fig. 6. (a) Backscattering spectra for Si (200Å)/Mo (530Å)/Si ⟨100⟩ structures before (○ ○ ○) and after (● ● ●) laser reaction. A layer of $MoSi_2$ of about 1450Å thickness was obtained after 1 laser scan at $p = 0.88$.

that the observed difference is due to the presence of the thin overcoating of silicon on the laser-reacted samples.

Refractory metals (Mo, W, Nb)/silicon.—We have successfully used the scanned CW laser and/or electron beam to react thin films of Mo, W, and Nb with Si. For films to be reacted by the laser a thin overcoating of silicon was again used to control reflectivity. In Fig. 6(a) we show backscattering spectra for both before and after CW laser irradiation of Si(200Å)/Mo (530Å)/Si ⟨100⟩ samples. It can be seen from this data that the deposited film of Mo was completely reacted with the Si after laser irradiation at a normalized power of $p = 0.88$. The average composition of resulting layer can be calculated from the spectrum and was found to be $MoSi_2$. The x-ray diffraction pattern, shown in Fig. 6(b), also verifies that the reacted layer is single-phase $MoSi_2$ free from unreacted Mo or Si precipitates.

For both the W/Si and Nb/Si samples multiple laser scans were required to fully react the metal with the underlying silicon. For example, for the Si (200Å)/W (440Å/Si ⟨100⟩ and Si (200Å)/Nb (1100Å)/Si ⟨100⟩, laser irradiation at a normalized power of $p = 0.85$ and 0.90, respectively, resulted in only a limited amount of reaction observed at the interface between the metal and silicon. The results of backscattering analysis for both the W/Si and Nb/Si samples are shown in Fig. 7(a) and 8, respectively. In Fig. 7(a) it can be seen that the 440Å tungsten layer was completely reacted forming a WSi_2 layer of about 1200Å in thickness. It should also be noted that ten passes with the laser were required to complete this reaction. The backscattering data show that the film is quite uniform with a well-defined interface at the silicide/silicon crystal interface. In Fig. 7(b) the x-ray diffraction pattern obtained for this sample is shown. The maor lines of WSi_2 are seen without presence of W and/or Si precipitate lines.

In Fig. 8 the backscattering spectra for the Nb/Si samples are shown. Here we see the advancement of the interface between the silicon and niobium occurring for constant laser power as a function of the number of laser scans. It can be seen that the thickness of the silicide film ($NbSi_2$) increases with the number of scans. The average composition of this reacted layer is found to be $NbSi_2$, determined from the backscattering spectra and verified by x-ray diffraction analysis. Using the near-surface S factor, $[S_0]_{Nb}^{NbSi_2} = 83.7$ eV/Å, the film thickness *vs.* the number of scans are plotted in Fig. 9. One can clearly see that a parabolic growth behavior exists for the $NbSi_2$ film since the number of scans is proportional to an effective annealing time. This result is in agreement with the general behavior of the refractory metals which form disilicides

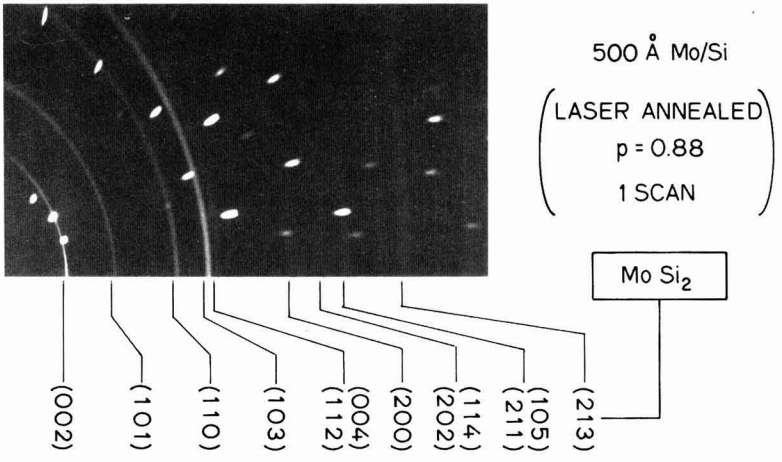

Fig. 6. (b) X-ray diffraction pattern obtained from the Mo/Si sample laser annealed at $p = 0.88$.

by furnace annealing (4). The facts suggest that the laser-induced reaction for $NbSi_2$ formation occurs essentially by a solid-phase diffusion mechanism.

In Fig. 10 we show backscattering data taken on unreacted Nb/Si and e-beam reacted $NbSi_2$ for two different values of P/w (0.155, 0.173 W/μ). The growth front of the $NbSi_2$ layer into the Nb/Si couple can be seen directly from this data. Verification of the $NbSi_2$ phase has been done again using x-ray diffraction. The calculated thicknesses of the two layers are 780 and 1200Å for the 0.155 and 0.173 W/μ power levels, respectively.

Sputtered films (Pd, W)/Si.—The thin film samples used in the experiments discussed so far were all prepared by e-beam evaporation of the metal and silicon layers in an oil-free free vacuum system. Similar experiments have been performed on samples prepared by argon sputtering of the layers. However, significant differences have been found in the resulting reacted films from those prepared by evaporation.

The Si(200Å)/Pd (1000Å)/Si <100> samples prepared by argon sputtering were laser irradiated at power levels of $p = 0.5$-1.4. For the lower power

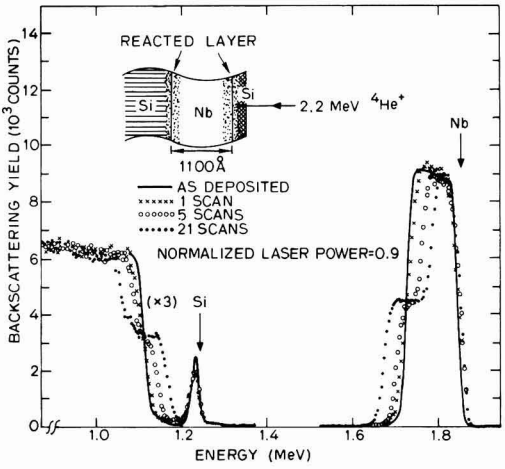

Fig. 8. Backscattering spectra for Si (200Å)/Nb (1100Å)/Si <100> samples with multiple laser scans. The thickness of the silicide ($NbSi_2$) increases with the number of scans.

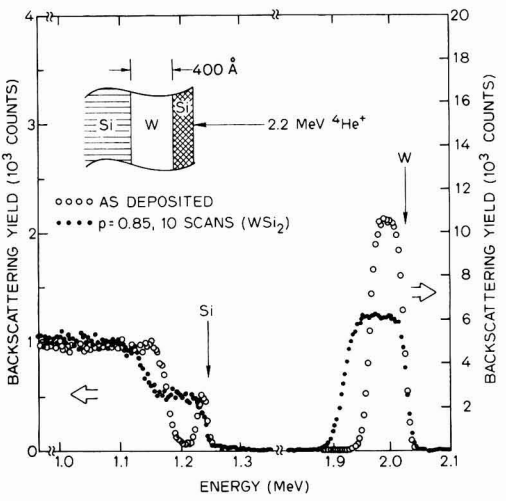

Fig. 7. (a) Backscattering spectra for Si (200Å)/W (440Å)/Si <100> structures. About 400Å of W (○○○) is completely reacted to form a WSi_2 film (●●●) of about 1200Å thickness after 10 laser scans at $p = 0.85$.

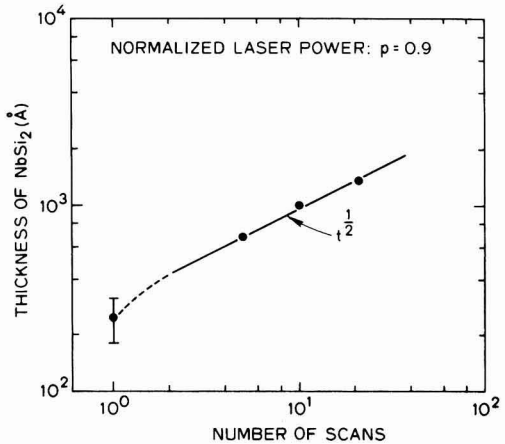

Fig. 9. Thickness of $NbSi_2$ as a function of the number of laser scans. The data show the parabolic growth for $NbSi_2$ formation since the number of scans is proportional to the annealing time.

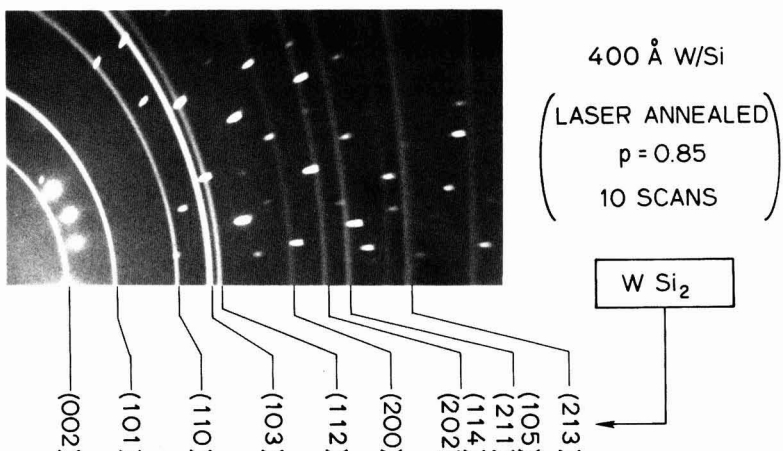

Fig. 7. (b) X-ray diffraction pattern obtained from the Si/W/Si structure laser annealed at $p = 0.85$ for 10 scans.

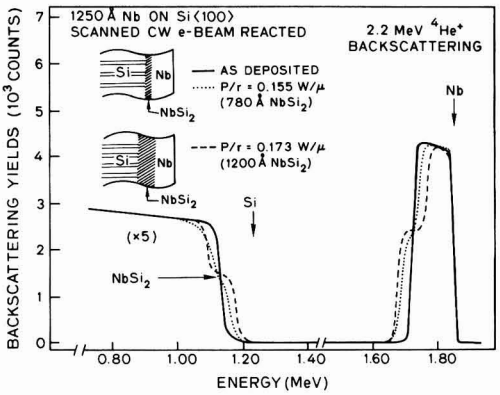

Fig. 10. Backscattering spectra for Nb (1250Å)/Si <100> samples electron beam scanned at various power levels. The thickness of the silicide is seen to increase with increasing power.

levels (0.5-1.0), the surface color changes observed optically were similar to those observed for the e-beam evaporated films, *i.e.*, the surface color changed from blue (unreacted film) to yellow (low power reaction). However, at the higher power levels ($p \gtrsim 1.0$), a damaged surface was observed optically in contrast to the high power phase appearing for the e-beam, evaporated samples.

In Fig. 11(a) we show an optical micrograph of a sputtered Pd/Si sample laser irradiated at a power level of $p = 1.2$. A severely damaged surface can be seen to result. This micrograph should be compared to that shown in Fig. 3 for the e-beam evaporated Pd/Si sample laser irradiated under similar conditions. The backscattering spectrum of a sputtered sample which was laser irradiated at a power of $p = 0.98$, slightly below the power causing surface damage, is shown by the solid line in Fig. 11(b). The spectrum for an unreacted sample is also shown by the solid circles in this figure for comparison. Only a limited amount of reaction is observed from this data at the Pd/Si interfaces (to be compared with Fig. 1). Also a small peak can be seen at an energy of 1.48 MeV in the spectrum of the as-deposited sample, corresponding to argon in the near-surface region. Although it is not observed in the backscattering spectrum, considerable amounts of Ar can exist in the Pd films. The argon atoms and/or other possible impurities (such as carbon, oxygen, etc.) can be incorporated during the sputtering process. These impurities can have a crucial effect on the silicide-forming reactions (21). Similar results were obtained for the W/Si samples prepared by argon sputtering.

Conclusions

Silicide-forming reactions induced by scanned CW laser and electron beams have been described. The characteristic features of the scanned CW-beam process found differentiating it from those using pulsed beam systems are: scanned CW beams can be used to form large area, uniform, essentially single-phase silicides; different phases within a particular system (such as Pd_2Si or PdSi) can be formed by adjusting the beam power level; and the reactions proceed basically by a solid-phase mechanism.

We have also succeeded in forming both the PdSi silicide and metastable Pt_2Si_3 silicide phases. These phases are difficult or impossible to form by conventional furnace annealing techniques. Both laser and electron beams have exhibited similar reaction effects for most of the metal/Si systems examined here, an exception occurring for the Pt/Si system. We speculate that the effects from the thin overcoating of silicon on

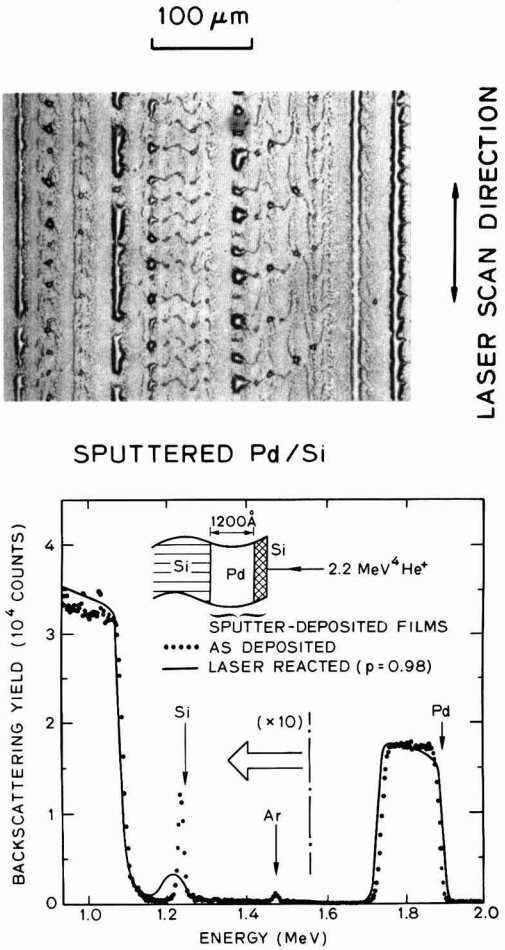

Fig. 11. (a) Optical micrograph of a sputtered Si/Pd/Si sample laser irradiated at a power level of $p = 1.2$. (b) Backscattering spectra of as-deposited (● ● ●) and laser reacted (——) Si/Pd/Si sputter deposited films. A small peak corresponding to Ar in the surface Si layer is seen.

the laser-reacted samples could be responsible for this difference. At this writing further experiments are underway to verify this hypothesis. Finally, it is pointed out that for the case of sputter-deposited metal films impurities incorporated into the films during sputter deposition have a deleterious effect on silicide formation.

Acknowledgments

We would like to thank Dr. S. S. Lau, Cal Tech for providing the e-beam evaporations and D. Keith, CMR Stanford for providing the sputter-deposited films. We also would like to acknowledge Dr. R. Reynolds for continued encouragement and support of this work through DARPA contracts MDA903-78-C-0290 and MDA903-78-C-0128 and one of us (T. Shibata) would like to acknowledge partial support of Toshiba Corporation during the course of this work.

Manuscript received May 27, 1980.

Any discussion of this paper will appear in a Discussion Section to be published in the December 1981 JOURNAL. All discussions for the December 1981 Discussion Section should be submitted by Aug. 1, 1981.

Publication costs of this article were assisted by Stanford University.

REFERENCES

1. B. L. Crowder and S. Zirinsky, *IEEE Trans. Electron Devices*, **ed-26,** 369 (1979).
2. P. L. Shah, *ibid.*, **ed-26,** 631 (1979).
3. H. N. Yu, A. Reisman, C. M. Osburn, and D. L. Critchlow, *ibid.*, **ed-26,** 318 (1979).
4. "Thin Films Interdiffusion and Reactions," J. M. Poate, K. N. Tu, and J. W. Mayer, Editors, Wiley-Interscience, New York (1978).
5. J. M. Poate, H. J. Leamy, T. T. Sheng, and G. K. Celler, *Appl. Phys. Lett.*, **33,** 918 (1978).
6. Z. L. Liau, B. Y. Tsaur, and J. W. Mayer, *ibid.*, **34,** 221 (1979).
7. T. Shibata, J. F. Gibbons, and T. W. Sigmon, *ibid.*, **36,** 569 (1980).
8. T. W. Sigmon, J. L. Regolini, J. F. Gibbons, S. S. Lau, and J. W. Mayer, Abstract 388, p. 981, The Electrochemical Society Extended Abstracts, Los Angeles, California, Oct. 14-19, 1979.
9. B. Y. Tsaur, Z. L. Liau, and J. W. Mayer, *Appl. Phys. Lett.*, **34,** 168 (1979).
10. A. Gat and J. F. Gibbons, *ibid.*, **32,** 142 (1978).
11. R. B. Gold and J. F. Gibbons, *J. Appl. Phys.*, **51,** 1256 (1980).
12. M. von Allmen and M. Wittmer, *Appl. Phys. Lett.*, **34,** 68 (1979).
13. M. Wittmer and M. von Allmen, *J. Appl. Phys.*, **50,** 4786 (1979).
14. B. Y. Tsaur, S. S. Lau, and J. W. Mayer, *Appl. Phys. Lett.*, **35,** 225 (1979).
15. G. A. Hutchins and A. Shepela, *Thin Solid Films*, **18,** 343 (1979).
16. R. W. Bower, D. Sigurd, and R. E. Scott, *Solid State Electron.*, **16,** 1461 (1973).
17. N. Cheung, S. S. Lau, M.-A. Nicolet, and J. W. Mayer, in "Thin Film Interfaces and Interactions," J. E. E. Baglin and J. M. Ponte, Editors, p. 494, The Electrochemical Society Softbound Proceedings Series, Princeton, N.J. (1980).
18. T. Shibata, T. W. Sigmon, and J. F. Gibbons, Proceedings of Laser and Electron Beam Processing of Materials Symposium of Materials Research Society, Boston (1979), To be published.
19. M. Hansen, "Constitution of Binary Alloys," McGraw-Hill Book Co., New York (1958).
20. B. Y. Tsaur, J. W. Mayer, and K. N. Tu, in "Thin Film Interfaces and Interactions," J. E. E. Baglin and J. M. Ponte, Editors, p. 264, The Electrochemical Society Softbound Proceedings Series, Princeton, N.J. (1980).
21. Ref. (4), p. 103.

Evaluation of Dislocation Generation at Si_3N_4 Film Edges on Silicon Substrates by Selective Oxidation

Y. Tamaki, S. Isomae, S. Mizuo, and H. Higuchi*

Hitachi Limited, Central Research Laboratory, Kokubunji, Tokyo 185, Japan

ABSTRACT

The density of dislocations generated at Si_3N_4 film edges on silicon substrate by selective oxidation is measured and the relation between the selective oxidation conditions and dislocation generation at the film edges is investigated. Dislocations are observed using Secco etching. The results show that the density of dislocations does not continuously increase with oxidation temperature, but decreases markedly at temperatures above 1000°C. A further experiment with recessed oxide structure reveals that the generation of dislocations depends strongly on the cross-sectional structure of the sample These results are interpreted in terms of viscous flow of SiO_2 film. Another experiment suggests that high pressure oxidation is not effective for suppressing dislocation generation, although it is useful for reducing oxidation time. Finally, collector-emitter shorts of transistors in bipolar integrated circuits are examined quantitatively using a simple statistical method in relation to the dislocations generated at Si_3N_4 film edges.

In silicon device technology, chemical vapor deposited (CVD) Si_3N_4 films on silicon substrates have been widely used as selective oxidation masks or passivating films. These Si_3N_4 films on silicon substrates have a large intrinsic stress of about 10^9 N/m^2 that often leads to the generation of dislocations in silicon substrates during thermal treatment (1-3). Since these dislocations are detrimental to the characteristics of transistors, insertion of SiO_2 film between Si_3N_4 film and silicon substrate has been used in order to avoid generation of dislocations. However, in selective oxidation the SiO_2 film causes the formation of a long bird's beak at the perimeter of the silicon islands (4, 5). This bird's beak constitutes an insuperable barrier to reducing the dimensions of oxide-isolated devices. Therefore, selective oxidation conditions that can prevent the generation of dislocations on silicon substrate without inserting an SiO_2 film have been sought. Although several papers dealing with the generation of dislocations in selective oxidation have been reported (5-8), no reports which quantitatively examine the oxidation condition have been published.

In this paper, first the relation between the heat-treatment conditions (Si_3N_4 film thickness, temperature, time, atmosphere, etc.) and dislocation generation at the film edges is described quantitatively using the dislocation density per unit length of Si_3N_4 film edge. From this experiment the difference in the temperature dependence of dislocation generation between N_2 annealing and selective oxidation becomes clear. Then the cause of this phenomenon is discussed, taking the behavior of SiO_2 films grown during oxidation into account. The effects of Si etching and high pressure oxidation on dislocation generation are also examined. The influence of sample structure on dislocation gen-

* Electrochemical Society Active Member.

Key words: defect density, mechanical property, viscosity of SiO_2, bipolar transistor.

eration and the suitability of high pressure oxidation are also discussed. Next, in order to examine the effect of dislocations on collector-emitter shorts of transistors, defect density obtained from transistor yield was compared to the dislocation density after selective oxidation.

Experimental Procedures

Sample preparation.—The samples were (001) oriented p-type, 0.2-0.3 Ω-cm, dislocation-free, 350 μm thick Czochralski-grown silicon wafers with 10 × 10 μm square masks consisting of only an Si_3N_4 film. The Si_3N_4 film was deposited by reacting SiH_4 and NH_3 in N_2 at 950°C. The deposition rate was 25 nm/min and the NH_3/SiH_4 flow rate ratio was 150. The films were 100-200 nm thick. The pattern of the film was formed by conventional H_3PO_4 etching technique using phosphorus-doped SiO_2 film as a mask.

The force acting on the Si_3N_4 film edge is proportional to the film thickness, with a constant of proportionality of about 9.2×10^{-1} N/m per nanometer of film thickness (9). For some samples the exposed silicon substrate was anisotropically etched 0.9 μm using KOH solution containing isopropyl alcohol in order to make a recessed oxide structure.

Thermal treatment and oxidation.—In order to investigate dislocation generation at the film edges, the samples were divided into three groups. The samples in the first group were annealed at 950°-1150°C for 2 hr in N_2 atmosphere. The samples in the second group were oxidized at 900°-1150°C for 2 or 16 hr in wet O_2 atmosphere. Some of the samples were silicon-etched before oxidation for comparison. The samples in the third group were silicon-etched and oxidized to grow 1.8 μm thick SiO_2 at 900°-1125°C in wet O_2 under atmospheric pressure (1 atm) or high pressure (7 atm) to form recessed oxide structures. The conditions for the third sample group correspond to those for isolation oxidation of bipolar integrated circuits. Cross sections of the samples were observed by scanning electron microscope (SEM) to evaluate the bird's beak and bird's head.

Dislocation observation.—In order to detect dislocations generated at the film edges, surface films were removed from the samples using diluted hydrofluoric acid after heat-treatment. Photographs of dislocations revealed by Secco etching (10) are shown in Fig. 1. In this figure, dislocation pits appear near the film edges. Since the force acting on the Si_3N_4 film edge is very large, it is expected that the density of dislocations depends on the perimeter length of the film edges. If the occurrence of dislocations can be represented by a Poisson distribution, the yield of patterns (the probability that a pattern has no dislocations) is given by

$$Y = e^{-\lambda l}$$

where λ is the dislocation density per unit length of the film edge and l is the perimeter length of the pattern. Consequently the dislocation density can be obtained by measuring the yield of 10 × 10 μm square patterns.

Transistor fabrication.—In order to apply the above results to the fabrication of integrated circuits and investigate the relations between dislocations generated by selective oxidation and collector-emitter shorts of bipolar transistors, npn array-transistors were fabricated by a conventional planar process. A 150 nm thick Si_3N_4 film was deposited directly on the silicon substrate and selective oxidation was performed at 1100°C in wet O_2 under high pressure (7 atm) to reduce oxidation time. The time required to grow 1.8 μm thick SiO_2 film was only 50 min. The base and emitter were formed by boron ion-implantation and arsenic diffusion in an ampul tube, respectively.

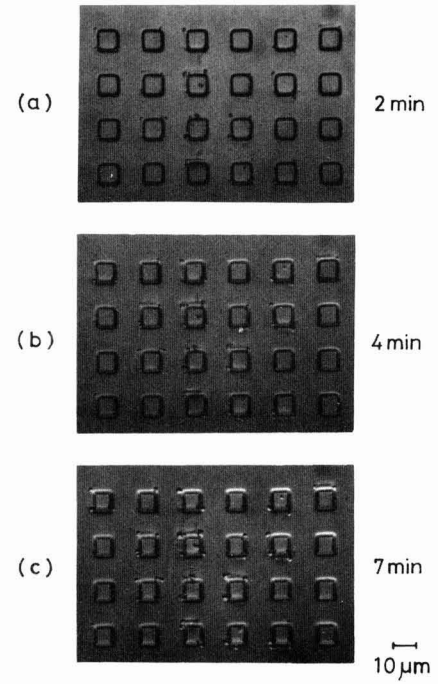

Fig. 1. Photographs of dislocation pits revealed by Secco etching for various etching time. Dislocation pits become more clear as the etching time increases. The square patterns were the regions covered by 150 nm thick Si_3N_4 film during oxidation.

Results and Discussion

Dislocation generation in N_2 annealing.—The samples in the first group were annealed for 2 hr in N_2 at 950°-1150°C. Dislocation densities of these samples are shown in Fig. 2, where "x," "Δ," and "o" represent the results for 200, 150, and 100 nm thick Si_3N_4 films, respectively. It is easily seen that the dislocation density increases with annealing temperature. This is because the critical stress for dislocation generation in Si becomes smaller as temperature increases. Since the force acting on the Si_3N_4 film edges is proportional to the film thickness, dislocation density increases with Si_3N_4 film thickness. Figure 3 shows the annealing time dependence of the dislocation densities at 1000°C. This figure indicates that the dislocation density becomes larger with annealing time.

From these results it is clear that the dislocation generation depends on the force acting on the Si_3N_4 film edges, annealing temperature, and annealing time. The data of a creep experiment (11) indicate that the time required to generate dislocations becomes shorter with increasing temperature.

Dislocation generation in oxidation.—The samples in the second group were oxidized for 2 or 16 hr in wet O_2 at 900°-1150°C. Dislocation densities of the samples oxidized for 2 and 16 hr are shown in Fig. 4 and 5, respectively. A distinguishing feature of both figures is that the dislocation density decreases with increasing temperature above 1000°C. It should be noted that the present results are entirely different from the results obtained in N_2, which are shown in Fig. 2. This suggests that SiO_2 film grown during oxidation plays an important role in dislocation generation.

Two factors that reduce the stress effect during oxidation are considered. One is reduction in Si_3N_4 film thickness. During oxidation the surface of Si_3N_4 film is gradually converted to SiO_2 film (12). The reduc-

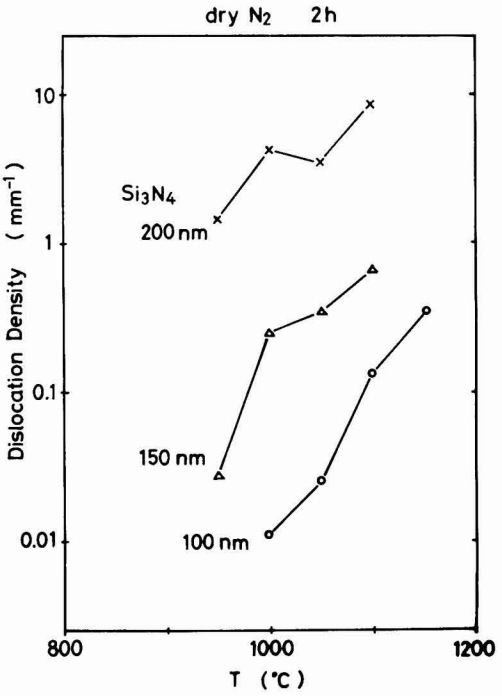

Fig. 2. Temperature dependence of dislocation densities of the samples annealed for 2 hr in N_2. The marks "×", "△", and "○" show that the thickness of Si_3N_4 films were 200, 150, and 100 nm, respectively.

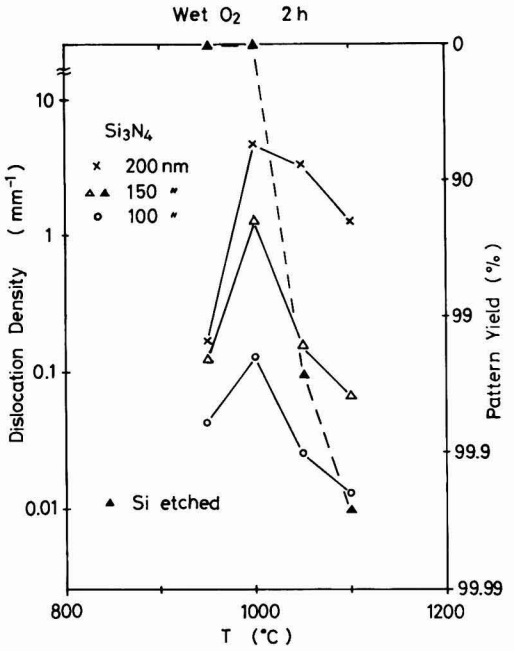

Fig. 4. Temperature dependence of dislocation densities of the samples oxidized for 2 hr in wet O_2. Pattern yield means the probability that a 10 × 10 μm square pattern has no dislocations. Dashed line shows the results for samples with 0.9 μm Si etching before oxidation.

tion in Si_3N_4 film thickness by oxidation are shown in Table I. The other is relaxation due to the viscous flow of SiO_2 film grown under the Si_3N_4 film edges. The dislocation density of the sample with 150 nm Si_3N_4 film oxidized in wet O_2 at 1100°C is smaller than that of the sample with 100 nm Si_3N_4 film annealed in N_2 at 1100°C, as seen from Fig. 2 and 4. This suggests that the effect of the latter factor is much larger than that of the former. It is known that the viscosity of SiO_2 decreases rapidly with increasing temperature and that viscous flow of SiO_2 occurs at temperatures around 950°C (13-15). Consequently, it is expected that the dislocation density tends to decrease with temperature, as shown in Fig. 5. Since relaxation of the stress

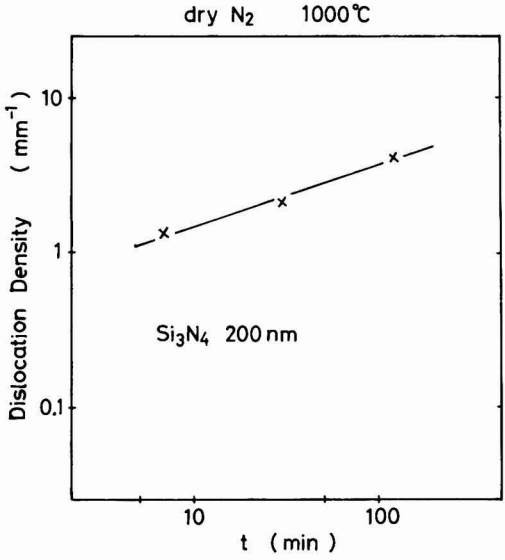

Fig. 3. Annealing time dependence of dislocation densities at 1000°C.

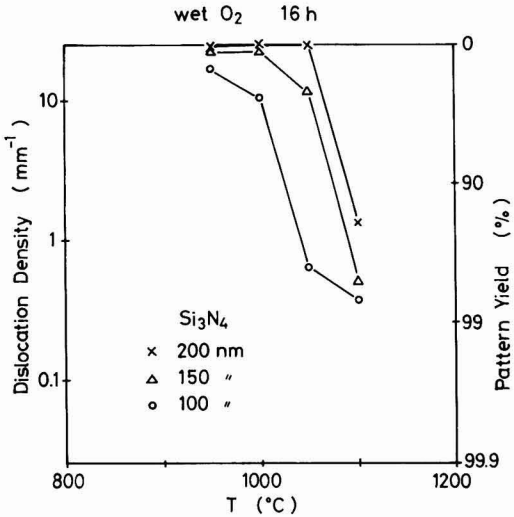

Fig. 5. Temperature dependence of dislocation densities of the samples oxidized for 16 hr in wet O_2.

Table I. Reduction in Si_3N_4 film thickness by oxidation (in wet O_2 at 1 atm)

		Oxidation time	
		2 hr	16 hr
Oxidation Temperature	1000°C	6 nm	30 nm
	1100°C	22 nm	98 nm

is caused by the SiO_2 film grown under the Si_3N_4 film, the degree of the relaxation depends on the stress fields in the silicon substrate under the Si_3N_4 film edges and the extent of lateral oxidation (in this case this is nearly half of the SiO_2 film thickness). Therefore, when the SiO_2 film is thin, relaxation will not occur. Although the stress fields near the film edges are different from the theory of elasticity (9, 16), the extent of lateral oxidation that the generation of dislocations can be suppressed is estimated to be 0.4-0.5 μm from the thickness of the SiO_2 film (0.8 μm) grown at 1050°C in wet O_2 for 2 hr. Because the temperature that the dislocation density in Fig. 4 becomes smaller than that in Fig. 2 is about 1050°C. As the results of oxidation for 2 hr at temperatures under 950°C are similar to those of N_2 annealing, stress relaxation due to oxide does not occur in these conditions. Thicknesses of SiO_2 films were about 0.4 μm at 950°C and 0.3 μm at 900°C. For these reasons, the maximum of dislocation density is found at about 1000°C in Fig. 4 (solid line).

In order to examine the effect of Si etching on dislocation generation, Si substrate is etched and oxidized for 2 hr. As the stress due to the expansion of SiO_2 grown by oxidation concentrates, the effect of viscous flow of SiO_2 film becomes dominant. Therefore, the dislocation densities of these samples are large at temperatures below 1000°C and decrease rapidly with temperature at temperatures above 1000°C, as shown in Fig. 4 (dashed line).

From these results it is concluded that the dislocation generation at Si_3N_4 film edges by selective oxidation depends on the strength of Si crystal, the thickness of Si_3N_4 film, the viscosity of SiO_2, and the topological structure of the Si substrate. Although the latter two factors are not so important in N_2 annealing, they play an important role in selective oxidation.

Dislocation generation in recessed oxide structure.— The samples in the third group were silicon-etched and oxidized to grow 1.8 μm thick SiO_2 at 900°-1125°C in wet O_2 under atmospheric pressure or high pressure. This coplanar structure is used for high speed bipolar integrated circuits. As the oxidation time is inversely proportional to the pressure, high pressure oxidation is useful to reduce the oxidation time drastically (17). Dislocation densities and oxidation times of the samples with this structure are shown in Fig. 6 and Table II, respectively. It is seen that the dislocation density decreases rapidly with temperature. The results are ascribed to the effect of viscous flow of SiO_2 film. The effect may be understood by observing the cross section of the sample. Photographs of the samples observed by SEM are shown in Fig. 7. The shape of SiO_2 film grown by selective oxidation changes with oxidation temperature. Inspecting the shape near the edge of SiO_2, Si is lifted up and a number of etch patterns

Table II. Oxidation times of the samples in Fig. 6

		Oxidation pressure	
		1 atm	7 atm
Oxidation Temperature	900°C	32 hr	200 min
	1000°C	16 hr	100 min
	1050°C	10 hr	68 min
	1100°C	7 hr	50 min

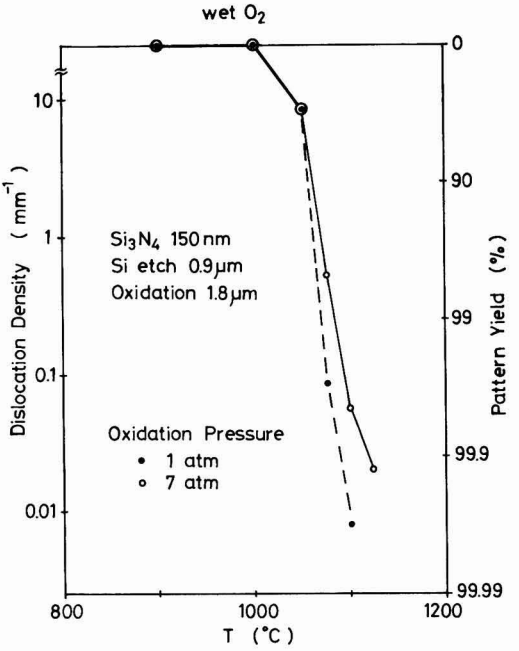

Fig. 6. Temperature dependence of dislocation densities of the samples with recessed oxide structure. After Si substrate was etched 0.9 μm, 1.8 μm thick SiO_2 was grown under atmospheric pressure (solid line) or high pressure (dashed line).

produced by large strain in Si are seen at temperatures of 1000° and 1050°C. The amounts of the lift-up were 0.15, 0.09, and 0 μm at 1000°, 1050°, and 1100°C, respectively. The higher the oxidation temperature is, the smaller the deformation of Si becomes. The lift-up and etch patterns correspond to the generation of dislocations in Si substrate. This temperature dependence of dislocation generation coincides with that in Fig. 6. Since the viscosity of SiO_2 becomes very small at 1100°C, the stress produced by the growth of SiO_2 is almost relaxed by the viscous flow of SiO_2. The stress acting on Si substrate is reduced to a great extent, and thus dislocation generation is prevented. Although the generation of dislocations can be suppressed by oxidizing at 1100°C, the bird's beak lengthens to about 0.3 μm. The bird's beak is defined as the distance between the Si_3N_4 mask edge and the top of the beak. From Fig. 7 the beaks were 0.60, 0.61, and 0.92 μm at 1000°, 1050°, and 1100°C, respectively. It is expected that the bird's beak reduces the stress acting on the silicon substrate. In order to evaluate the increment in bird's beak, the oxidation mechanism of Si, and the mechanical strength of Si, SiO_2 and Si_3N_4 at high temperatures must be considered. Further investigation will be necessary.

Next, the effect of pressure during oxidation is discussed. It is seen that the dislocation density at 7 atm is larger than that at 1 atm. As the growth rate of SiO_2 is proportional to the oxidation pressure, the time required to grow SiO_2 of a given thickness becomes shorter with increasing pressure. If the generation of dislocations depended only on oxidation time, the dislocation density at 7 atm might be smaller than that at 1 atm. Therefore it is concluded that the generation of dislocations depends not only on oxidation time but on oxidation rate. This behavior is considered to be related to the relaxation time τ of viscous flow of SiO_2 Here, τ is defined by $\tau = \eta/E$, where η and E are, respectively, the viscosity and the shear modulus of the

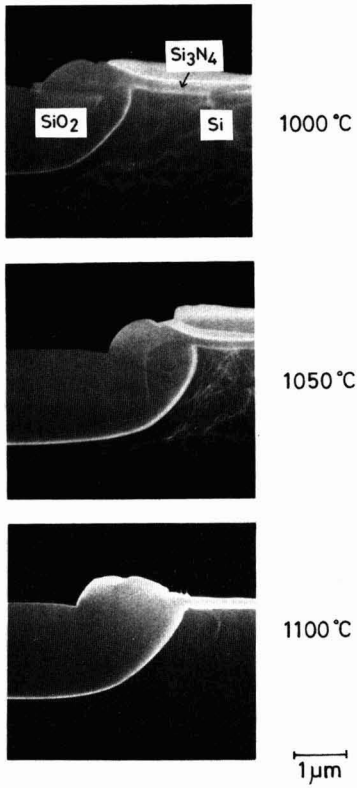

Fig. 7. Cross sections of recessed oxide structure for various oxidation temperatures. The samples were lightly etched by HF-HNO_3 before SEM observation.

SiO_2 film. Using the values of η and E for vitreous silica (18, 19), τ is estimated to be around 1 min at 1100°C. This is different from EerNisse's estimated time, which is only a few seconds (14). Although it is not certain which time is correct, it is clear that the effect of viscosity appears at the beginning of the oxidation. As the initial oxidation rate is very large, the effect is reduced in high pressure oxidation.

Transistor characteristics.—It is known that process-induced dislocations cause collector-emitter shorts of bipolar transistors (20). However, the relation between the collector-emitter shorts and the dislocation density after selective oxidation has seldom been investigated. In this study, in order to treat the shorts quantitatively, collector-emitter breakdown voltages (BV_{CEO}) of fabricated transistors were measured and the transistors with $BV_{CEO} > 5V$ at $I_{CE} = 10\ \mu A$ were defined as good. If the occurrence of defects can be represented by a Poisson distribution, the yield of good transistors is given by (21)

$$Y = e^{-(\lambda_A A + \lambda_L L)}$$

where λ_A is the defect density per unit emitter area, λ_L is the defect density per unit length of the emitter perimeter, and A and L are the emitter area and perimeter length per transistor, respectively. From the yield of transistors with emitter size of $3 \times 5\ \mu m^2$ and $70 \times 110\ \mu m^2$, $\lambda_A = 0.24\ mm^{-2}$ and $\lambda_L = 0.048\ mm^{-1}$ were obtained. Comparison of λ_L with λ at 1100°C in Fig. 6 shows that they are in good agreement. Since the size of the emitter is about 1/3 that of the pattern with selective oxidation, it is expected that about 1/3 of the transistors with dislocations generated by selective oxidation fail by collector-emitter shorts. In order to examine the close relation between the dislocations and the collector-emitter shorts, further investigation of multiplication and movement of dislocations are needed.

Conclusions

From the results obtained in this study, several conclusions can be made.

1. The density of dislocations generated at Si_3N_4 film edges by selective oxidation decreases with increasing oxidation temperature. This phenomenon is explained by the effect of the viscous flow of SiO_2 film.
2. When Si is etched and oxidized to form a recessed oxide structure, the effect of the viscosity of SiO_2, *i.e.*, oxidation temperature dependence of dislocation generation, becomes significant. This effect is confirmed by observation of cross sections of samples. Furthermore, the Si substrate is deformed by selective oxidation with Si_3N_4 mask at temperatures below 1050°C.
3. The dislocation generation at Si_3N_4 film edges by selective oxidation depends on Si_3N_4 film thickness, oxidation temperature, oxidation time, and oxidation rate.
4. The dislocations generated by selective oxidation cause collector-emitter shorts of bipolar transistors. The probability of the occurrence of collector-emitter shorts caused by dislocations depends on the heat-treatment conditions and the pattern geometry. This is considered to be related to the multiplication and movement of dislocations.

Acknowledgments

The authors wish to thank Drs. K. Sugawara, M. Maki, and M. Ogirima for useful discussions.

Manuscript submitted May 28, 1980; revised manuscript received Aug. 15, 1980.

Any discussion of this paper will appear in a Discussion Section to be published in the December 1981 JOURNAL. All discussions for the December 1981 Discussion Section should be submitted by Aug. 1, 1981.

Publication costs of this article were assisted by Hitachi Limited.

REFERENCES

1. W. A. Westdorp and G. H. Schwuttke, in "Thin Film Dielectrics," F. Vratny, Editor, p. 546, The Electrochemical Society Softbound Proceedings Series, Princeton, N.J. (1969).
2. M. Tamura and H. Sunami, *Jpn. J. Appl. Phys.*, **11**, 1097 (1972).
3. E. A. Irene, *J. Electron. Mater.*, **5**, 287 (1976).
4. J. A. Appels and M. M. Paffen, *Phil. Res. Rep.*, **26**, 157 (1971).
5. E. Bassous, H. N. Yu, and V. Maniscalco, *This Journal*, **123**, 1729 (1976).
6. B. O. Kolbesen and H. Strunk, "Proc. 5th Int. Conf. on High Voltage Electron Microscopy," p. 637, Kyoto (1977).
7. A. Bohg and A. K. Gaind, *Appl. Phys. Lett.*, **33**, 895 (1978).
8. K. Shinada, S. Shinozaki, K. Kurosawa, and K. Taniguchi, "Int. Electron Devices Meet. Dig. Tech. Papers," p. 344, IEEE (1979).
9. S. Isomae, Y. Tamaki, A. Yajima, M. Nanba, and M. Maki, *This Journal*, **126**, 1014 (1979).
10. F. S. d'Arogona, *ibid.*, **119**, 948 (1972).
11. S. Isomae, M. Nanba, Y. Tamaki, and M. Maki, *Appl. Phys. Lett.*, **30**, 564 (1977).
12. I. Franz and W. Langheinrich, *Solid State Electron.*, **14**, 499 (1971).
13. J. R. Patel and N. Kato, *J. Appl. Phys.*, **44**, 965 (1973).
14. E. P. EerNisse, *Appl. Phys. Lett.*, **30**, 290 (1977).
15. E. P. EerNisse, *ibid.*, **35**, 8 (1979).
16. S. M. Hu, *ibid.*, **32**, 5 (1978).
17. J. R. Ligenza, *This Journal*, **109**, 73 (1962).
18. R. Brückner, *J. Non-Cryst. Solids*, **5**, 123 (1970).
19. R. Brückner, *ibid.*, **5**, 177 (1971).
20. F. Barson, *IEEE J. Solid-State Circuits*, **sc-11**, 505 (1976).
21. S. M. Hu, S. P. Klepner, R. O. Schwenker, and D. K. Seto, *J. Appl. Phys.*, **47**, 4098 (1976).

Interdiffusion of Titanium and Gold: A Comparison of Thin Films Deposited in Technical Vacuum and Ultrahigh Vacuum

G. W. B. Ashwell and R. Heckingbottom

British Telecom Research Laboratories, Martlesham Heath, Ipswich IP5 7RE, England

ABSTRACT

Thin films of 0.5 μm Ti and 0.5 μm Au have been deposited on Si and SiO_2 substrates in technical vacuum (HV, $\leq 10^{-6}$ Torr) and ultrahigh vacuum (UHV, 10^{-9} Torr). After deposition and subsequent annealing in N_2 containing $\leq 1\%$ O_2 at 300°-350°C, the films were analyzed, principally using Auger sputter ion profiling, but also using electrical resistivity, x-ray, Rutherford backscattering, and SEM/microprobe measurements. While the UHV films were clean to the techniques used, several percent of C and O were present in the HV deposited Ti films. On SiO_2 substrates the reaction proceeded via formation of Au_4Ti and oxidation of Ti to TiO_2 as it came in contact with the air interface. The rate of alloy formation was almost an order of magnitude faster in the UHV deposited films and the oxidation rate was also enhanced. The importance of these usually unmonitored impurities in determining the reactivity of films deposited in technical vacuum is stressed.

Gold is widely accepted as the preferred metallic conductor for interconnection patterns on semiconductors, particularly where high current densities are encountered. Its advantages include high electrical conductivity, corrosion resistance, and full compatibility with gold wire thermocompression bonding. Its two main drawbacks, poor metallurgical bonding to the semiconductor and catastrophic reduction of carrier lifetime in the semiconductor, can both be solved by the use of an intermediate layer of titanium between the gold and the semiconductor. While more complex three-layer metallizations incorporating a third layer of Pd or Pt to reduce the Au-Ti interaction are widely used, extremely reliable transistors can be fabricated using Au-Ti metallization only (1).

The interaction of Au-Ti thin film couples under thermal stressing and varying humidity has been studied previously (2-4), reflecting its importance both individually and as part of the three-layer metallization schemes. All these studies used films prepared in technical vacuum comparable with that used in device fabrication. As part of a wider program aimed at optimization of the Ti-Au system we have also studied films prepared in ultrahigh vacuum. This paper describes the significant differences between films formed in the two different ways. Resistivity/anneal time plots have been used to identify distinct stages in the interaction and compositional analysis, principally by Auger electron spectroscopy with sputter ion profiling, was carried out at these points. The importance of low levels of impurities such as oxygen and carbon in determining the stability of the layers used in device fabrication is clearly illustrated.

Experimental

Sample preparation.—The main series of Au-Ti layers were deposited on a thermally grown SiO_2 layer (3500Å thick) on Si(111) slices to allow simple resistivity determinations. Other series of Au-Ti layers, deposited directly on Si(111) substrates, were also subjected to compositional analysis to check for any effects due to the introduction of the SiO_2 layer. A standard deposition sequence involved (*i*) deposition of 0.5 μm Ti with a substrate temperature of 75°C, (*ii*) increase of the substrate temperature to 250°C followed by deposition of a further 250Å of Ti, and (*iii*) deposition of 0.5 μm Au with the substrate at 250°C. Matched deposition sequences were carried out in technical vacuum (HV) and in ultrahigh vacuum (UHV). In both cases beam pressures were $\simeq 5 \cdot 10^{-6}$ Torr with background pressures of $\simeq 10^{-6}$ and $\simeq 10^{-9}$ Torr, respectively. There was a detectable drop in the former background pressure during Ti evaporations. Additional samples with only 0.1 μm Au layers were prepared for Rutherford backscattering analysis (RBS).

Key words: reaction rate, impurities, Auger profiling.

Analysis techniques.—Auger analysis was performed with a conventional CMA analyzer at 3 keV primary beam energy. The sputter ion profiling used argon ions at 500 eV from a broad focused gun. RBS spectra were generated using 1.5 MeV He^+ ions and were provided by Dr. P. L. F. Hemment of the University of Surrey, England. A separate examination for nitrogen was carried out using x-ray photoelectron spectroscopy (XPS) because of a partial overlap between N and Ti peaks in the Auger spectrum. The XPS analysis was provided by Dr. R. M. Waghorne at Fulmer Research Institute, England. The x-ray data was produced using a cylindrical texture camera (5). In this technique the sample is rotated normal to its surface which is at a glancing angle to the incident x-ray beam. The resulting pattern of arcs of diffracted x-ray reveals the extent of any orienation effects in the thin surface layers in addition to the lattice spacings. Scanning electron microscopy (SEM) with energy dispersive microprobe facilities was also used to check for any spatial heterogeneity in the samples.

Results

Electrical resistivity.—Standard 0.5 μm Ti-0.5 μm Au layers on SiO_2 were annealed in N_2 containing $\leq 1\%$ O_2 for varying times at 350°C The changes in sheet resistance with anneal time are shown in Fig. 1 for layers formed in HV and UHV systems. Several distinct stages in the plots are present for both samples, with the time taken to reach a given stage being almost an order of magnitude shorter for the UHV plot. The actual values of resistance at each stage are also significantly lower for the UHV samples for reasons considered in the discussion. These differences show through in Fig. 1, even though R_T/R_0 is plotted, as R_0 values were similar in the two cases: 3-4 10^{-6} Ω cm for HV films and 3.5-4.0 10^{-6} Ω cm for UHV films, cf. 2.06-2.44 10^{-6} Ω cm for bulk Au. For convenience in the following descriptions we may distinguish the following regions in the plots. First a slow initial in-

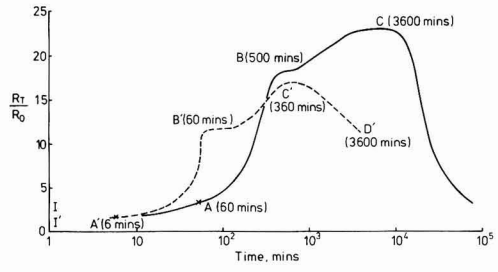

Fig. 1. Resistivity *vs.* anneal time plots for Au-Ti films deposited on SiO_2 in technical vacuum — and ultrahigh vacuum - - -, and annealed in air at 350°C. Points A, A' etc. are described in the text.

crease with time (stage A), second a rapid climb to a plateau (stage B), third a further steady climb to a peak (stage C), and finally a fall off (stage D). The UHV plot stages will be further distinguished by a prime *e.g.*, A'.

Auger sputter ion profiles.—Auger profiles were recorded at each of the key stages identified in the resistivity plots. First, however, the as-deposited films were examined. In Fig. 2a a standard film on SiO_2, deposited in technical vacuum is shown. Several important features are immediately apparent. The gold film is clean by Auger criteria, with a small amount of carbon contamination on the surface. The titanium film, on the other hand, has up to $\simeq$10% of oxygen and carbon impurity, levels which increase as the deposition continues, *i.e.*, they are quite different from an initial surface contamination broadened by the sputtering process. In contrast, the SiO_2 surface was free from carbon contamination. By comparison, both the metal films deposited in UHV (Fig. 2b) were free from impurities. In both cases there was a detectable amount of apparent interdiffusion at the Au/Ti interface with a significant Au tail extending into the Ti. In neither case had the Ti penetrated to the Au surface.

The initial stage of interaction on annealing is shown in Fig. 3. The profile was taken after annealing a UHV deposited film for 6 min (stage A'). The major change is that Ti has penetrated to the Au surface and has accumulated with oxygen. Though there has been measurable broadening of the Au/Ti interface, the Ti level within the gold film has remained undetectable. An example of slightly increased reaction (still in stage A) is shown in Fig. 4. In the HV deposited film annealed for 60 min, some Ti is detectable throughout the Au film, but there is a marked concentration gradient approximately half-way through the Au film. An increased amount of Ti and O have accumulated on the Au surface.

Stage B is illustrated in Fig. 5 where the profile was obtained from a sample deposited in technical vacuum and annealed for 500 min. The new feature is the alloying of all the Au layer. The titanium oxide buildup on the surface has increased toward 2000Å and the Au tail has extended to the SiO_2 substrate. Traces of Fe and Ni are detectable on the outer surface in this sample. Oxygen is present throughout the film with Ti. All the same major features were present at stage B' for the UHV deposited sample (not shown). As this stage was

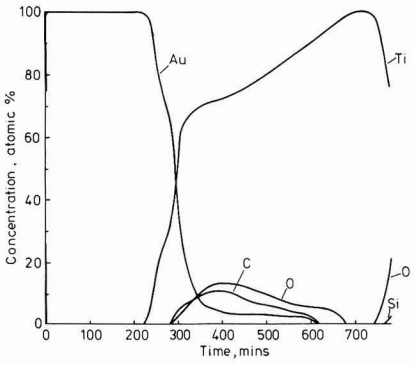

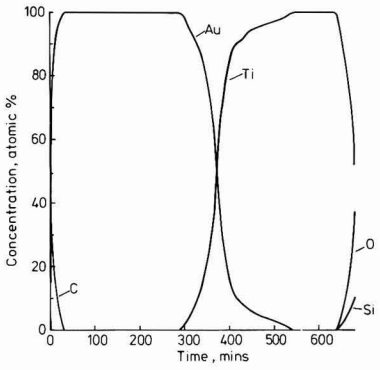

Fig. 2. Compositional depth profiles of as-deposited films determined by Auger electron spectroscopy with sputter ion profiling, (a, top) deposited in technical vacuum and (b, bottom) deposited in ultrahigh vacuum.

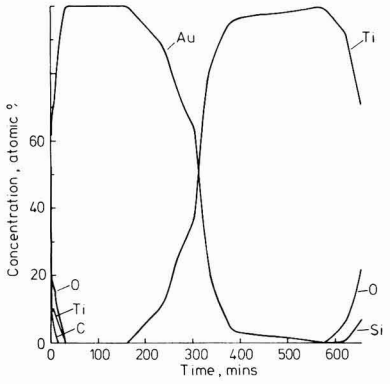

Fig. 3. Composition/depth profile of an Au-Ti film deposited in UHV on an SiO_2 substrate and annealed for 6 min at 350°C.

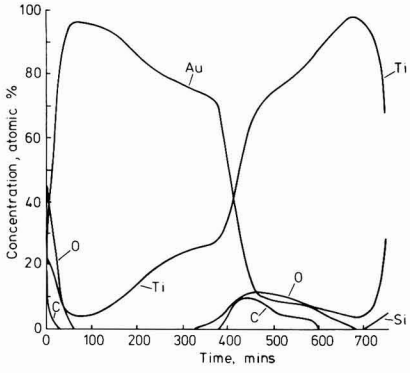

Fig. 4. Composition/depth profile of an Au-Ti film deposited in HV on an SiO_2 substrate and annealed for 60 min at 350°C.

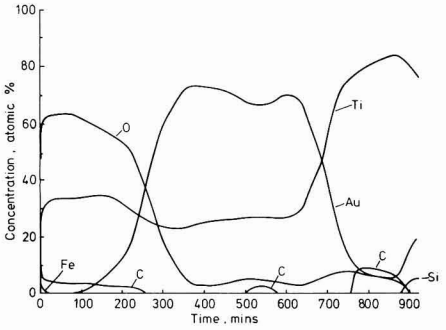

Fig. 5. Composition/depth profile of an Au-Ti film deposited in HV on an SiO_2 substrate and annealed for 500 min at 350°C.

reached after only a 60 min anneal the oxide buildup on the surface amounted to only a few hundred angstroms. A more substantial level of Fe impurity persisted throughout the film in this sample.

The final distinctive stage in the reaction is shown in Fig. 6. This profile corresponds to stage C′ on a UHV deposited sample annealed for 360 min. Here the key feature is that the oxidation of the Ti is so extensive that all elemental Ti has reacted either with O or Au. As in the earlier samples, several percent of C are present in the oxide film. Again Fe persists as an impurity throughout the films on this sample. A comparison of the fourth stage, D′, with C′ shown in Fig. 6 revealed no major differences. There was, however, a measurable enhancement of the Au level *vs.* Ti both near the peak of the Au signal and at the interface with the SiO_2. Stage C was only reached after annealing for 4000 min and, although the outlines of the profiles were similar to those shown in Fig. 6, there had clearly been much more intermixing in C between the Au/Ti alloy and the titanium oxide layers.

The similar series of samples prepared on Si substrates proved unsuitable for Auger profiling after annealing at 350°C. Although after a 6 min anneal of the UHV deposited sample the reaction had started in a similar manner to that shown in Fig. 3 a separate heterogeneous interaction (described later) rapidly began to dominate.

Further series of samples with 0.1 μm Au on 0.5 μm Ti on both Si and SiO_2 substrates were prepared and annealed at 300°C. These samples were more suitable for RBS analysis. Anneal times of 960 and 1380 min were used and no differences due to the two kinds of substrates were observed in the Auger profiles under these conditions. Both anneal periods were sufficient for the whole of these thinner layers of Au to have reacted with the Ti. The longer anneal periods differed only in that a thicker layer of titanium oxide formed above the Au/Ti layer. The extent of oxidation was also greater on the UHV prepared samples. That is a thicker oxide layer had formed after 960 min on the UHV sample than had formed after 1380 min on an HV sample. On the other hand, the surface oxygen did not penetrate beyond the Au/Ti layer in the UHV deposited sample, whereas in the HV deposited sample oxygen from the surface merged with that already in the Ti as shown in Fig. 5.

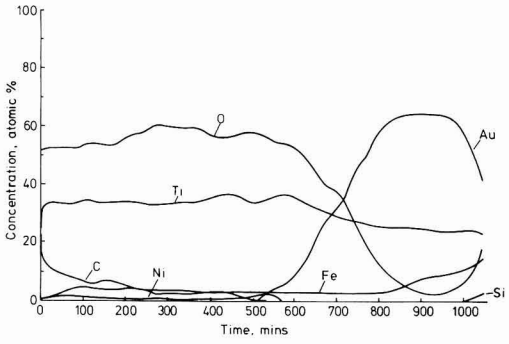

Fig. 6. Composition/depth profile of an Au-Ti film deposited in UHV on an SiO_2 substrate and annealed for 360 min at 350°C.

X-ray, RBS, XPS, and SEM/electron microprobe.— The x-ray diffraction data were dominated by the contributions from the layers containing gold. In addition to Au itself, the only phase detected was Au_4Ti, as identified in earlier work (3). This phase was present in all the films where Auger indicated significant interaction between Au and Ti. Both identifiable layers showed marked texturing.

As can be seen from Fig. 7 the RBS analysis supported the overall results from Auger and x-ray measurements. The slight interdiffusion during deposition was confirmed, particularly by the high energy edge of the Ti signal. Following the anneal, the appearance of Ti on the surface and throughout the gold layer is clearly evident. It is also clear, however, (particularly from the rounding of the gold peak in the annealed sample spectrum) that there is some continuous variation of composition with depth. The composition of the Au/Ti is not quite as straightforward as might be inferred from the x-ray data. While the identification of the main phase as Au_4Ti is supported, the Au/Ti ratio corresponding to the Au peak in the annealed sample RBS spectrum is $\simeq$4.7.

No nitrogen could be detected in the films, using XPS combined with argon ion sputtering.

SEM/electron microprobe analysis on the majority of the samples confirmed that the layers remained intact, so that the averaging implict in the broad area technique described above retained validity. Two conditions occurred where this situation broke down, however. First, after very long anneal times at 350°C for layers on SiO_2 substrates (stage C) where the Auger profiles for different elements showed much overlapping, this was shown to be due to a physical mixing of different matrices. SEM/microprobe analysis following a light etch in 40% HF solution showed that the Au_4Ti remaining had been honeycombed with titanium oxide.

A second, more serious exception, invalidated the profiling approach for layers on Si substrates annealed at 350°C. After about 10 min anneal a reaction involving film break-up began to spread from local

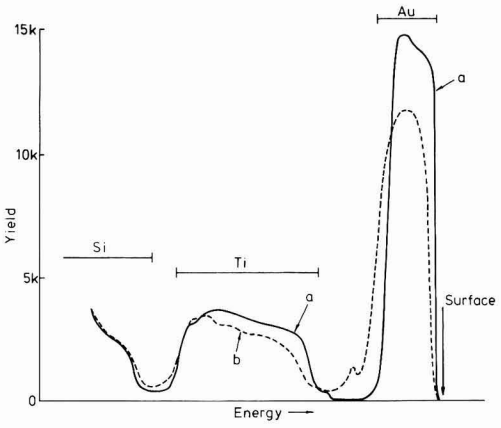

Fig. 7. Rutherford backscattering spectra of 0.1 μm Au/0.5 μm Ti films deposited in HV on SiO_2 substrates, (a) as deposited — and (b) after annealing for 23 hr at 300°C - - -.

areas often at the sample edge. By 30 min the reaction had occurred over the entire surface. High magnification pictures of the reaction at different stages are shown in Fig. 8. The Ti_5Si_3 crystallites were identified by electron microprobe analysis and x-ray diffraction following removal of the surrounding Au in I_2 solution. This etching also revealed that the formation of pinholes in the Ti film preceded the crystallite formation (Fig. 8c). Subsequent removal of the crystallites in 40% HF solution revealed small amounts of Au between them and the Si substrate, which had been protected from the earlier iodine etch.

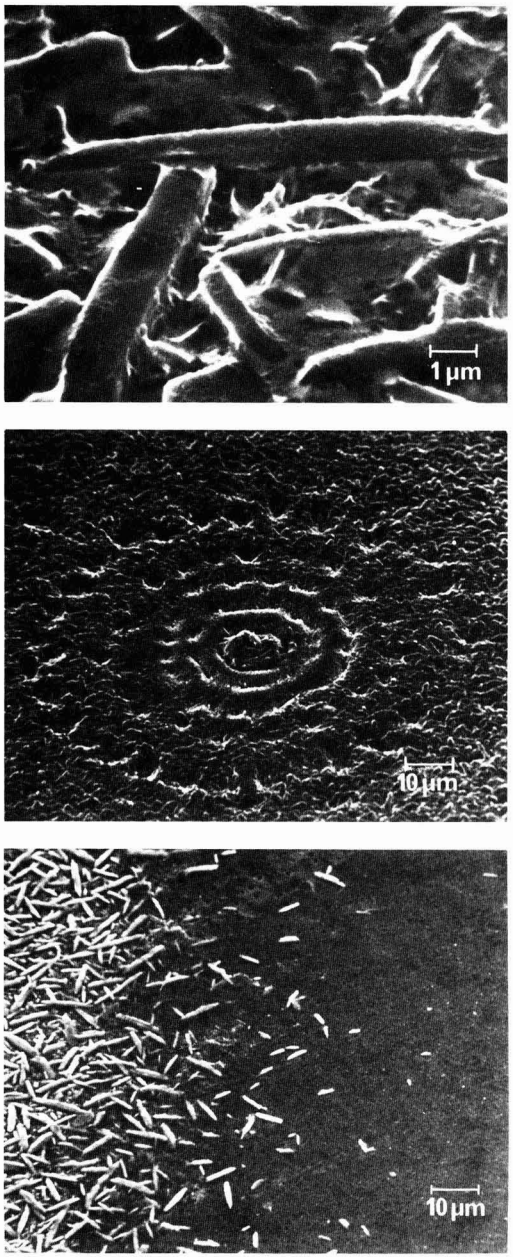

Fig. 8. Scanning electron micrographs of stages in the Au-Ti-Si interaction at 350°C: (a, top) the reaction product of elongated Ti_5Si_3 crystallites in an Au matrix, (b, center) the center of a reacted zone, and (c, bottom) the edge of a reaction zone (after removing the gold).

Discussion

The detailed Auger profiles in Fig. 2-6 allow considerable progress to be made in understanding the basic resistivity data of Fig. 1 and the underlying interaction between Au and Ti. The basic difference between the HV and UHV deposited layers is the significant concentration of C and O in the Ti layers of the former. These impurities are the most likely cause of the slower interdiffusion rates (by almost an order of magnitude) in the HV samples. The higher resistivity at stage B compared with B′ is also likely to be dominated by these impurities, though in the comparison of C with C′ the honeycombing of the intermetallic layer by oxide will also be important. It should be stressed that these contaminant levels are to be expected for all evaporations of active metals in vacuum systems with background pressures of $\simeq 10^{-6}$ Torr. Most films studied previously (2-4) and in general use will be of the contaminated kind. The "pumping" of the background gases during the evaporation is exactly the same phenomenon that makes titanium sublimation pumps an effective aid to obtaining UHV. As a first approximation the contaminant content will reflect the ratio of the bombardment rate of the background gas molecules on the sample ($\simeq 10^{15}$ cm^{-2} sec^{-1} at 10^{-6} Torr) and the evaporant flux (which may be calculated from the amount of film deposited in a given time).

The main interaction sequence appears to be similar in the UHV and HV deposited films. It simply occurs faster in the former. Thus from Fig. 3 it seems most likely that the Ti has reached the surface by grain boundary diffusion through the gold. This mechanism is thus identified as the fastest process, as first recognized by Tisone and Drobek (2). However, as pointed out by Hall and Morabito (6) in their studies of the Au/Pd system, diffusion within the grains is also required to explain any substantial compositional change in the Au layer. Simple application of the formula $x = (Dt)^{1/4}$ to the position of the diffusion front in Fig. 4 allows an estimate of this bulk diffusion constant D. Taking x as 3000Å for $t = 3600$ sec gives $D \simeq 2.5\ 10^{-13}$ cm^2 sec^{-1}. As noted previously for Pd-Au (6), values of this kind are five or six orders of magnitude higher than would be expected by extrapolation of data obtained for bulk diffusion couples at higher temperatures (2). In general this result would be expected in samples cooled from high temperatures; at some point the activation energy obtained in high temperature measurements (which includes both formation and mobility of defects) would cease to apply and a lower value (which represents only the mobility term) would replace it. What is interesting is that it seems to be the norm that films formed directly at lower temperatures also have extremely high values of defects in them. Any growth methods that reduced these nonequilibrium concentrations of defects could lead to much improved metallization systems.

Figure 4 also shows that these enhanced diffusion rates within the grains are becoming comparable to the grain boundary diffusion rate. Thus the original Ti/Au interface is a more effective source of Ti than the grain boundaries, at least when the latter are also acting as a source for the oxidation. Otherwise one would not see a concentration gradient in Ti but a steady rise with time of a flat Ti level through the Au layer as discussed by Poate *et al.* (3) in their analysis of RBS profiles of the Pd-Au system.

Although the experiments were primarily designed to study the intermetallic layers, it is also possible to learn something from them about the accompanying oxidation of titanium which reaches the surface. First, it is clear that the UHV deposited layers also oxidized much faster than the HV deposited layers. Thus in Fig. 6 there is approximately three times as much oxide as

in Fig. 5 even though the anneal time in the former is shorter. A similar conclusion is provided by the data from the 300°C anneals. Second, all the oxidation rates are much greater than expected from extrapolation of literature values obtained at high temperatures. Close comparison is difficult because of the variety of rate laws reported for low temperature oxidation of titanium (7). However, the size of the effect can be gauged from the following estimate. At 600°C a parabolic oxidation law is followed (8) with $kp = 0.16 \exp(-45{,}000/RT)$ g^2 cm^{-4} sec^{-1}. Extrapolation to 350°C gives $kp \simeq 2.8 \times 10^{-17}$ g^2 cm^{-4} sec^{-1}, whereas from Fig. 5 with 3000Å of oxide formed in $3 \cdot 10^4$ sec $kp = 5.3 \times 10^{-13}$ g^2 cm^{-4} sec^{-1} which is some four orders of magnitude higher. Even without assuming the parabolic rate law at 350°C there is the simple comparison that a slightly thicker oxide layer has grown at 350°C than in the earlier experiments with titanium (8) at 600°C. More recent work on titanium (9, 10) also shows no evidence of the faster oxidation rates reported here. However Poate *et al.* (3) did find a comparable amount of oxidation, suggesting that the faster rate is characteristic of the gold-rich Au/Ti alloys. In both these studies of the Au/Ti alloys the presence of excess nitrogen in the gas phase had no detectable effect.

The above discussion of diffusion has not depended on accurate quantitative elemental concentrations from the Auger profiles. However, it is clear from Fig. 2-6 that the Auger data is providing a good quantitative guide at many points. The values shown were obtained using Chang's basic formula (11) together with our own elemental and compound standards. The thicker layers of oxide are very close to TiO_2. The apparent excess of Ti is due to the presence of TiC also, as it is clear from the shape of the C_{272} peak that the carbon is present as carbide not in a graphitic form. In the Au/Ti alloy, on the other hand, the composition indicated by the Auger profile is too rich in Ti; in Fig. 5 the Au/Ti ratio is only $\simeq$2.7 not 4. Errors in alloy composition are to be expected when elemental standards are used (12). For instance the Ti signal in the alloy should be enhanced due to the greater backscattering coefficient from the Au in the alloy. Also, as reported earlier for Ti and TiO samples (13), the Ti Auger spectrum undergoes strong changes in the relative intensities of the two peaks at 387 and 418 eV with matrix. Although this makes detailed quantitative work difficult it can be turned to advantage and used as a guide to the chemical state of the titanium. In Fig. 9 this region of the Ti spectrum is illustrated for the four distinct matrices occurring in the present work. The Ti_5Si_3 spectrum was recorded after an iodine etch removal of the Au, similar to that described in the SEM results section, but on a completely reacted sample. These peak intensity differences may often be amplified for ease of detection during profiling by choice of appropriate modulation voltage (14).

Following the chemical analysis, the main features of the resistivity plots shown in Fig. 1 can be interpreted as follows. The initial slow rise in resistivity is due to "removal" of free Au by alloying with Ti, as the Au layer is expected to carry $\simeq$95% of the current initially (15). By stage B no free Au remains and

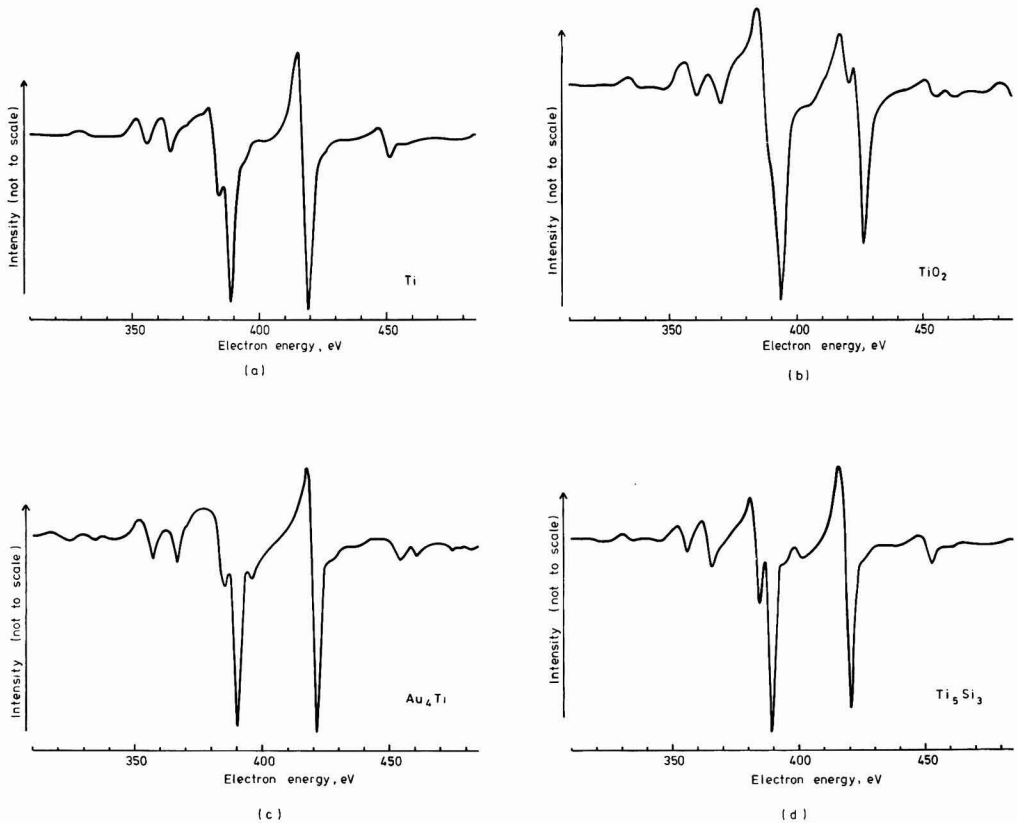

Fig. 9. Auger spectra from titanium in the 350-450 eV energy range taken with an energy resolution of 0.6% and showing the effect of different chemical matrices on the relative peak intensities: (a) metallic Ti, (b) TiO_2, (c) Au_4Ti, and (d) Ti_5Si_3.

the current is carried by both Au_4Ti and Ti layers. At stage C all the Ti has been oxidized and only the Au_4Ti layer remains conducting. A comparison between stages C and B suggests the conductivity of the Au_4Ti is comparable with that of Ti, perhaps $\simeq$30% higher. Finally, as oxidation proceeds further, some free Au is regenerated and the resistance falls again quite markedly.

Sylwestrowicz *et al.* (4) have rightly stressed that some of the mechanisms of interaction studied at high temperature may not be relevant to metallizations used on devices operated nearer room temperature. On SiO_2 substrates we have three mechanisms at least, grain boundary diffusion, bulk diffusion of Ti-Au, and oxidation of Ti, all influencing the reaction. In principle these reactions could all show quite different dependences on temperature. In practice, however, they are all likely to be quite similar. The temperature dependence of the defect mobility term in the bulk diffusion coefficient has been found to be 0.80-0.85 eV for several metals in Au (16, 17). Similarly the equivalent defect mobility term in TiO_2 has been estimated at $\simeq$ 1.0 eV (7). There appears to be no direct measurement of the activation energy for grain boundary diffusion of Ti in Au but an estimate of 0.87-0.9 eV has been calculated for Pd in Au (3, 6) and initial penetration of Ti through Au occurs at similar temperatures to Pd in Au (3). Thus in the system studied here the high temperature results reported should provide a worthwhile guide to the expected behavior of metallizations used in long-lived devices.

The results from high temperature anneals (350°C) of Au-Ti on Si substrates clearly illustrate Sylwestrowicz's point, and it is likely that they were quite unrepresentative of room temperature behavior. The detailed mechanism is not established, but it appears that a Ti-Au-Si eutectic which is molten at 350°C must form. Starting at discrete flaws in the film, the reaction then spreads rapidly. A similar phenomenon was reported by Sinha in the $Si/SiO_2/W/Au$ system (18). Both the appearance of the reaction zone in Fig. 8b and the complete envelopment of the Ti_5Si_3 crystallites in the Au matrix strongly support the idea of melting during reaction. Figure 8c suggests that the spread of the molten zone, like many other reactions, proceeds first at grain boundaries. Independent of the precise details of the reaction mechanism, it is evident that the reaction product Ti_5Si_3 is more stable than the possible Au-containing alloys, a point that it might be possible to exploit in future metallization schemes.

Conclusions

Auger sputter ion profiling has shown that deposition of Ti films in technical vacuum results in the incorporation of C and O impurities at the 1-10% level. Comparison with films deposited in UHV, and so free from the above impurities, shows that the C and O play a crucial role in determining the interdiffusion rates and hence effective lifetimes of Ti-Au thin film couples. The results suggest that monitoring and control (even controlled introduction) of such impurities, normally ignored in device production, might lead to significant improvements in current metallization schemes.

Acknowledgments

The authors would like to thank C. H. Ling, P. Walmsley, and S. J. Wright for film preparation, C. H. Ling for resistivity measurements, P. J. Carter for x-ray measurements, and A. P. Skeats for SEM/microprobe determinations. Acknowledgment is also made to the Director of the British Telecom Research Laboratories for permission to publish this paper.

Manuscript submitted June 18, 1980; revised manuscript received Sept. 18, 1980.

Any discussion of this paper will appear in a Discussion Section to be published in the December 1981 JOURNAL. All discussions for the December 1981 Discussion Section should be submitted by Aug. 1, 1981.

Publication costs of this article were assisted by British Telecom Research Laboratories.

REFERENCES

1. D. Baker, P.O. Res. D. Report No. 641 (1977).
2. T. C. Tisone and J. Drobek, *J. Vac. Sci. Technol.*, **9**, 271 (1971).
3. J. M. Poate, P. A. Turner, W. J. De Bonte, and J. Yahalom, *J. Appl. Phys.*, **46**, 4275 (1975).
4. W. D. Sylwestrowicz, H. A. Elkholy, and G. W. Kammlott, *J. Mater. Sci.*, **14**, 873 (1979).
5. C. A. Wallace and R. C. Ward, *J. Appl. Crystallogr.*, **8**, 255 (1975).
6. P. M. Hall, J. M. Morabito, and J. M. Poate, *Thin Solid Films*, **33**, 107 (1976).
7. O. Kubaschewski and B. E. Hopkins, "Oxidation of Metals and Alloys," p. 214, Butterworths, London (1962).
8. A. E. Jenkins, *J. Inst. Met.*, **84**, 1 (1955).
9. W. D. Sylwestrowicz, *This Journal*, **122**, 1504 (1975).
10. T. Smith, *Surf. Sci.*, **38**, 292 (1973).
11. C. C. Chang, *ibid.*, **48**, 9 (1975).
12. P. M. Hall and J. M. Morabito, *ibid.*, **83**, 391 (1979).
13. J. T. Grant, T. W. Haas, and J. E. Houston, *J. Vac. Sci. Technol.*, **11**, 227 (1974).
14. J. T. Grant, T. W. Haas, and J. E. Houston, *Surf. Sci.*, **42**, 1 (1974).
15. "Handbook of Chemistry and Physics," R. C. Weast, Editor, p. f145, Chemical Rubber Co., Cleveland, Ohio (1973).
16. W. Jost, "Diffusion in Solids, Liquids and Gases," p. 234, Academic Press Inc., New York (1952).
17. P. G. Shewmon, "Diffusion in Solids," p. 74, McGraw-Hill, New York (1963).
18. A. K. Sinha, *Thin Solid Films*, **20**, 115 (1974).

Liquid Phase Epitaxial Growth of $(Hg_{1-x}Cd_x)Te$ from Tellurium-Rich Solutions Using a Closed Tube Tipping Technique

J. A. Mroczkowski* and H. R. Vydyanath*

Honeywell Electro-Optics Center, Lexington, Massachusetts 02173

ABSTRACT

The liquidus temperatures for $(Hg_{1-x}Cd_x)_{1-y}Te_y$ have been determined for $x = 0.067$, $x = 0.10$, and $0.7 \leq y < 1.0$ compositions by differential thermal analyses. $(Hg_{1-x}Cd_x)Te$ films with compositions of $x = 0.35$, 0.31, and 0.24 have been grown by liquid phase epitaxy on CdTe (111)A oriented substrates. The Cd segregation coefficient has been determined to be $k = 3.5 \pm 0.1$. Films grown at around 550°C from 3 mm thick melts at slow cooling rates showed thicknesses close to those expected for equilibrium growth. The residual impurity in the LPE films was usually n-type and was less than 10^{15} cm^{-3} in the better films. Photovoltaic diodes fabricated in the films have shown performance comparable to those fabricated in bulk grown crystals.

The II-VI compounds of CdTe and HgTe form a continuous series of solid solutions with cubic zincblende structure. $(Hg_{1-x}Cd_x)Te$ consists of a mixture of the wide gap semiconductor CdTe ($E_g = 1.6$ eV) with the semimetallic compound HgTe which can be considered as a semiconductor having a negative energy gap. The gap in the alloys varies nearly linearly with x between the two end-point values. Alloys of $Hg_{1-x}Cd_xTe$ with x-values in the range 0.2-0.4 corresponding to bandgap energies in the range 0.1-0.5 eV are of particular interest for the detection of infrared radiation in the 2-20 micron range.

Initial LPE $(Hg_{1-x}Cd_x)Te$ film growth was pursued from pseudobinary melts due to the absence of phase diagram information in the Hg-rich and Te-rich corners. Since the pseudobinary film growth involved temperatures around 700°C and Hg pressures on the order of 10 atm a closed tube tipping technique was adopted. The work reported here concerns the subsequent determination of liquidus temperatures and LPE $(Hg_{1-x}Cd_x)Te$ film growth development from Te-rich solutions.

LPE $(Hg_{1-x}Cd_x)Te$ film growth from Te-rich solutions has only recently been reported in "open" systems (1-3), but no liquidus data covering a range of x, y values has been documented. Our initial use of a closed tube system for film growth at temperatures around 550°C, where the Hg pressure is about 1/3 atm, has permitted the study of film growth under near equilibrium conditions without concern over melt composition changes from Hg loss due to evaporation.

With phase diagram information limited to binary and pseudobinary compositions initial work was concentrated on determining the liquidus temperatures for Te-rich $(Hg_{1-x}Cd_x)_{1-y}Te_y$ solutions suitable for $x = 0.20$ to $x = 0.40$ film growth. Subsequently, stoichiometric $(Hg_{1-x}Cd_x)Te$ films were grown from slightly undersaturated 3 mm thick LPE melts. Measured film thicknesses and composition gradings obtained from slow growth conditions were then compared with calculated values based on measured liquidus temperatures and the Cd segregation coefficient.

Liquidus Temperatures

Thermal analyses were conducted by the slow cooling of homogenized $(Hg_{1-x}Cd_x)_{1-y}Te_y$ liquid samples. Charges with weights close to 15g were placed in 12 mm ID, 1 mm thick wall quartz ampuls with a thin 2 cm re-entrant thermocouple well. The free space inside the ampuls was about 5 cm^3. The change in composition due to evaporation was calculated to result in an error in the liquidus temperature interpolation of much less than 1°C. A similar ampul containing silicon was used as a reference. After sealing, the ampuls were placed very close together in two symmetrical cavities drilled in a nickel cylinder fitted with a nickel lid. A Chromel-Alumel thermocouple was inserted in each ampul, and the two were connected for simultaneous recording of the sample temperature and the temperature difference between the sample and reference as a function of time. To obtain high sensitivity sample and differential temperature readings, the sample signal was largely balanced out with a potentiometer, and the differential signal was amplified ten times. The two signals were then fed into an XYY′ recorder.

Temperature data for each composition were taken after at least 6 hr of solution homogenization at temperatures at least 15°C above the anticipated liquidus temperatures. Cooling rates were typically 2°C/min, an order of magnitude larger than used in the subsequent LPE film growths. Supercooling was observed in all the thermal analysis runs, and from later liquidus temperature interpolations supercooling at the cooling rates used was found to range mostly between 5° and 15°C.

The actual liquidus temperatures were estimated by extrapolation from a plot of the degree of supercooling *vs.* temperature at which supercooling stopped. The amplitude of the differential temperature overshoot was used as a measure of the degree of supercooling.

Heating runs for the eutectic temperatures gave a range of values lying between 410° and 420°C. Since the eutectic compositions cannot be specifically defined under nonequilibrium cooling conditions the eutectic temperatures are not displayed.

The thermal analysis data taken for $x = 0.067$ and $x = 0.10$ compositions together with $x = 0$ data for Hg_1Te^4 are summarized in Table I and displayed in Fig. 1. The data for the liquidus slopes at varying compositions x, y defined as $m_x = \partial T/\partial x)_y$ °C/mole and $m_y = \partial T/\partial y)_x$ °C/mole were obtained from the best slope fitting of the data shown in Fig. 1.

LPE Film Growth Procedures and Results

LPE film growth using the tipping technique was accomplished in a POCO DFP 3-2 grade graphite boat shown in Fig. 2. The outer radius of the base of the graphite boat was designed to fit the inside radius of an evacuated sealed quartz ampul. The component

* Electrochemical Society Active Member.

Key words: LPE, II-VI ternary semiconductor, phase diagram, equilibrium growth theory.

Table I. Liquidus temperature and slope data for low x-value Te-rich $(Hg_{1-x}Cd_x)_{1-y}Te_y$ solutions

	Liquidus temperatures (°C)		Liquidus surface	
			$\left(\frac{\partial T}{\partial y}\right)_x$ °C/mole	$\left(\frac{\partial T}{\partial x}\right)_y$ °C/mole
y	$x =$ 0.067	$x =$ 0.10	$0.067 \lesssim x \lesssim 0.10$	$0 < x \lesssim 0.10$
0.70	585 ± 4	597 ± 8	−672	500
0.725	—	590 ± 3	−707	530
0.75	551 ± 4	568 ± 3	−770	600
0.775	—	545 ± 3	−862	630
0.80	506 ± 3	530 ± 3	−960	645
0.825	—	499 ± 5	−1170	650
0.85	445 ± 10	—	—	—
0.90	430 ± 10	—	—	—

preparation and the film growth processes are described in the following.

The LPE melt was usually obtained from a section of a rapidly quenched $(Hg_{1-x}Cd_x)_{1-y}Te_y$ ingot. Six nines purity quadruply zone refined Cominco Cd and Te were used for the compounding. *In situ* preparation of the melt from HgTe, CdTe, and Te in the graphite boat just before growth was also used. In both of the preparation methods the elements were homogenized in closed ampuls in the LPE tipping furnace used in a rocking mode. In the case of the *in situ* preparation method, the rocking angles were chosen such as to prevent the melt contacting the CdTe substrates before the actual growth process was initiated.

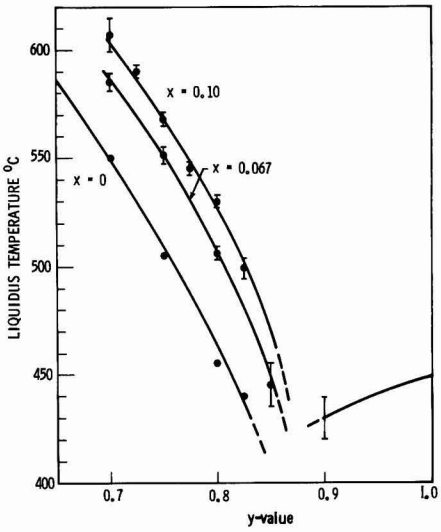

Fig. 1. Liquidus temperature data on $x = 0.067$ and $x = 0.10$ $(Hg_{1-x}Cd_x)_{1-y}Te_y$ solutions. $x = 0$ data is from Ref. (4).

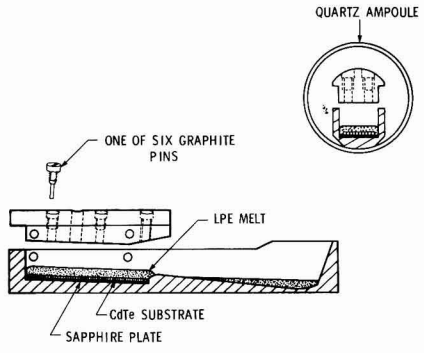

Fig. 2. Exploded view of LPE graphite boat shown in the growth position with the Te-rich solution tipped over the substrate.

The dimensions of the CdTe substrates used were typically 10 × 37 mm; the substrates, purchased from II-VI Incorporated, were also prepared from 6 nines pure Cd and Te obtained from Cominco. Almost all the substrates used were (111)A oriented. The initial polishing of the substrates to mirror flatness involved a method using diamond milling with a single diamond edge along a select direction (5). Subsequent surface preparation involved light chemical-mechanical and chemical etching in a bromine methanol solution with the final chemical etch being performed immediately before the loading of the growth ampul.

To ensure a minimum of process contamination, the $(Hg_{1-x}Cd_x)_{1-y}Te_y$ compounding and the pre-LPE growth component assembly procedures were all performed in a VAC argon glove box which included a Mettler Electronic balance. Quartz ampuls used for compounding or film growth were baked out at 800°C under ion pump vacuum. LPE graphite boats were rf baked before each film growth run for 3 hr at 1600°C under a diffusion pump vacuum of 2×10^{-7} mm pressure. Component transfer between the glove box and vacuum stations either under vacuum or with the glove box atmosphere was performed with the use of closed bellows valves which isolated the inside of the ampuls from the ambient.

For each LPE film growth run, 10 ± ½g of $(Hg_{1-x}Cd_x)_{1-y}Te_y$ were used. The CdTe substrate and $(Hg_{1-x}Cd_x)_{1-y}Te_y$ were placed at opposite ends of the graphite boat. To prevent substrate to graphite sticking a 0.010 in. thick sapphire plate was placed in between.

After loading the graphite boat and components into a quartz ampul and subsequent evacuation and sealing, the quartz ampul with the contents was placed in the growth furnace near the center of a 12 in. sodium heat pipe. The steady-state temperature profile was ± ¼°C over the 6 in. length of the ampul. The thermal history of each growth run was recorded using the analog output of an Omega 2176A thermometer with simultaneous digital display reading to 0.2°C. The temperature and the times involved in a typical growth run are shown in Fig. 3. The recording thermocouple was checked against the melting point of Te; the melting point of Te was recorded at 452.6°C.

In most growth runs slight undersaturation was used. The CdTe substrate was then allowed to equilibrate with the solution at constant temperature for about 15 min before a slow linear cool was initiated for typically a 5°-7°C temperature drop. Figure 4 illustrates the small changes in liquidus composition after the 15 min equilibration time, and at the end of near equilibrium film growth. At the end of the cooling cycle, the solution was decanted off the film and the ampul was removed from the furnace.

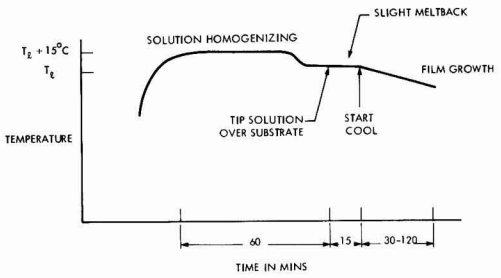

Fig. 3. Typical thermal history of an LPE film growth run; the liquidus temperature is denoted by T_L.

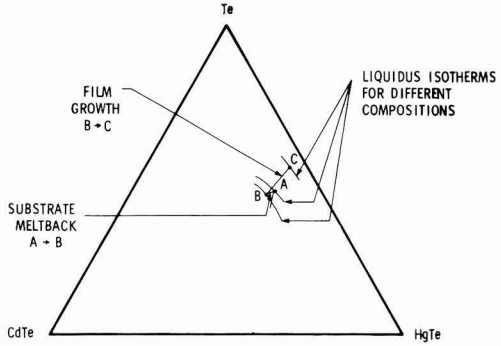

Fig. 4. Schematic of changes in the LPE solution composition (A→B→C) following the growth conditions shown in Fig. 3.

Some problems that develop in the LPE film surface morphology during growth can be traced to local changes in the melt depletion region composition. Several triggering situations are possible, including initial surface uneveness and/or substrate contamination affecting the initial nucleation and melt trace impurities. Any of these situations can result in an increasingly irregular interface, as melt diffusion in the affected areas takes on a nonuniform three-dimensional aspect. Depressed growth areas can then become increasingly covered by slightly lower liquidus temperature compositions resulting in further slow down of the growth rate in those areas and the problem can escalate, particularly under severely diffusion-limited growth conditions. Since, in the initial portion of this work, fast film growth rates appeared to be detrimental to film surface morphology, most of the film growth concentrated on slow growth rates controlled by slow cooling rates.

Film thickness *vs.* temperature drop data for films grown from solution compositions initially compounded as $(Hg_{0.90}Cd_{0.10})_{0.225}Te_{0.775}$ and $(Hg_{0.933}Cd_{0.067})_{0.25}Te_{0.75}$ are shown in Fig. 5. All of the solutions used for growing these films were undersaturated by 0 to 3°C at the time of the initial contact with the substrate. Under these conditions, after 15 min of equilibration, the new very slightly different solution compositions were considered to be very close to their liquidus temperatures.

The film thickness measurements were made optically from cleaved $(1\bar{1}0)$ planes perpendicular to the (111)A film surface. The film thickness was readily identified from a distinctly different visible reflectivity of $(Hg_{1-x}Cd_x)Te$ compared to that of the CdTe substrate. The film growth thickness was taken as the total thickness less 4 microns of interdiffusion into the substrate side of the interface.

Measured film growth thicknesses *vs.* temperature drop data given in Fig. 5 show that for cooling rates on the order of 0.05°C/min the film thicknesses were close to those expected for equilibrium film growth from 3 mm thick solutions.

X-ray microprobe analyses were performed across $(1\bar{1}0)$ cleaved surfaces of the films perpendicular to the (111)A surface. HgTe and CdTe were used as standards and the composition of films was determined using a KEVEX Magic 5 program with a ZAF correction. Composition profiles shown in Fig. 6 were made on lightly etched film surfaces and also on as-grown surfaces.

The microprobe measurements on the as-grown films and films which were lightly etched indicated that the Cd concentration increases near the as-grown surface. Evidence of an increase in the Cd concentration near the film surface was also provided by visible color differences of the film surfaces before and after etching which were the same as those seen in cleaved film sections between the CdTe substrate and the $(Hg_{1-x}Cd_x)Te$ film. Auger and ellipsometer analyses on the as-grown and etched surface areas confirmed that the composition increased by abut $\Delta x = 0.5$ within about a tenth of a micron of the surface.

The increase in surface x-value occurs after the LPE solution is decanted off, and the closed ampul cools to ambient temperatures in about 5 min. The probable explanation for this is that during cooldown the ratios of the activities of Hg and Cd over the melt and film change in a manner that favor the formation of a CdTe-rich surface layer on the film.

Infrared transmission scans were used to determine the composition of films with x-values around $x = 0.35$. For a linearly graded film composition the fraction of energy transmitted relative to the peak transmission can be expressed as (6)

$$I_{tr} = I_{pk} \exp - (2K/3\beta m)(E - E_s)^{3/2} \quad [1]$$

where E_s denotes the surface bandgap energy, E the

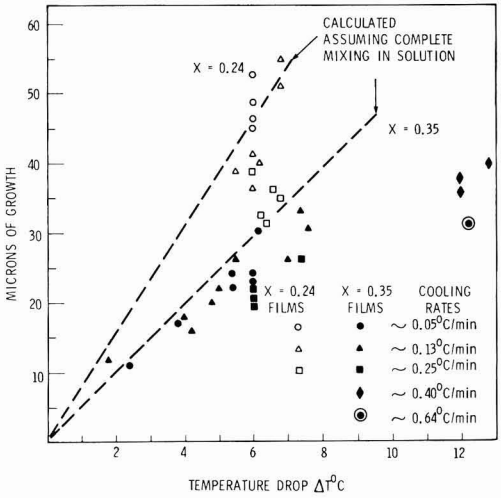

Fig. 5. Film growth thicknesses *vs.* temperature drop for $(Hg_{0.90}Cd_{0.10})_{0.225}Te_{0.775}$ and $(Hg_{0.933}Cd_{0.067})_{0.25}Te_{0.75}$ solutions.

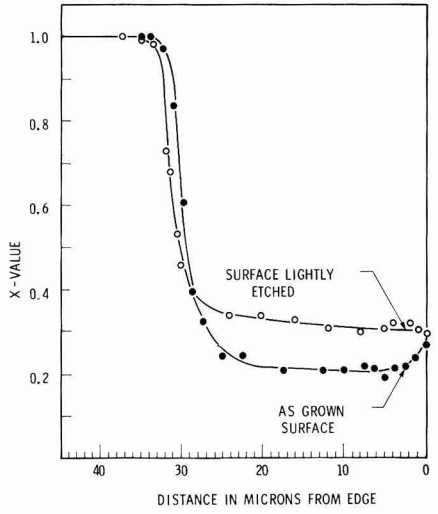

Fig. 6. X-ray microprobe data on films grown from $(Hg_{0.90}Cd_{0.10})_{0.225}Te_{0.775}$ and $(Hg_{0.933}Cd_{0.067})_{0.25}Te_{0.75}$ solutions.

photon energy satisfies $E_s + \beta md \geq E \geq E_s$, m is the composition grading/unit distance, β is the incremental change in energy gap/Cd mole, d is the depth from the film surface in which absorption can take place, and the parameter K is related to the bandgap energy E_g through the standard expression $\alpha = K(E - E_g)^{1/2}$ where α is the absorption coefficient at the photon energy E. Transmission curve fitting to Eq. [1] and the use of calibrated data for the absorption coefficient at $\alpha(E) = 500$ cm^{-1} *vs.* x-value (7) enabled an accurate assessment of the film surface composition to be made.

Films grown from $(Hg_{0.90}Cd_{0.10})_{0.225}Te_{0.775}$ solutions around 550°C with thicknesses around 25 microns beyond the interdiffused region showed surface x-values close to $x = 0.345$. Films which were grown from $(Hg_{0.91}Cd_{0.09})_{0.232}Te_{0.768}$ solutions at the same temperatures showed surface compositions of around $x = 0.31$ close to those expected for a 10% reduction in solution x-value. A few films which were grown from $(Hg_{0.90}Cd_{0.10})_{0.175}Te_{0.825}$ solutions at around 500°C indicated essentially no discernible change in the segregation coefficient with increase in y-value.

The segregation coefficient of Cd, k, obtained from the more extensively investigated $x = 0.10$ and $x = 0.09$ LPE solutions at growth temperatures around 550°C was taken to be $k = 3.5 \pm 0.1$. The more accurate composition determinations of films grown from $x = 0.067$ solutions at around 550°C were made using infrared spectral response measurements at 77 K; the composition of these films was $x = 0.235$, which agreed with the value kx expected from the definition of k.

Most of the film growths were carried out on (111)A CdTe substrate surfaces rather than on the (111)B and (100) surfaces. Evaluation of over 100 films grown from Te-rich solutions has shown that the best films were grown using only about 1°C of undersaturation resulting in a slight meltback of the substrate surface which could not be detected in optical examination of the film cross sections.

For 3°C of undersaturation, substrate meltback was uneven and film morphologies were very uneven, particularly when relatively fast cooling rates were used. In addition, the LPE solution was trapped in the more heavily depressed film regions after the melt decanting operation. When growth conditions used solutions estimated to be supersaturated by 2°C the quality of the film surface was generally poorer and homogeneously precipitated $(Hg_{1-x}Cd_x)Te$ crystals deposited on the film surface. It appeared that without some undersaturation, initial nucleation on the substrate may have been inhibited by traces of oxides on the substrate in the closed tube growth. The cross section of a typical LPE film is shown in Fig. 7.

A feature observed to some degree on most film surfaces was the presence of isolated, very flat plateau areas surrounded by depressed areas as seen in the micrograph of Fig. 8. The completely flat areas were exact (111)A planes with dimensions up to 1 mm across. The changes in film thickness between these areas were fairly gradual and generally within 3 microns for film thicknesses typically averaging 30 microns. However, in a few cases, thicknesses varied by more than a factor of two over distances on the order of 1 mm. These features appeared most prominently in films grown at slow cooling rates, when initial undersaturation was relatively high and when (111)A substrates oriented to within 5 min were used. Figure 8 shows the plateau areas adjacent to the more depressed areas. These morphological features are believed to be caused by convection currents in the melt since the lower, more depleted melt regions are less dense. Estimates of the solution stability using a Reynolds number criterion such as reported by Crossley and Small (8) support the possibility of solution convection during LPE film growth from Te-rich solutions, particularly when slow cooling rates are used.

Electrical characteristics.—Electrical characterization of the LPE films was used to determine the residual impurity concentration, the carrier mobilities, and the carrier concentrations. Since the CdTe substrates used for the growth of the LPE films were almost insulating it was assumed that the LPE films were electrically isolated from the CdTe substrates and therefore the electrical measurements were made on the films without etching away the substrate. Hall effect and resistivity measurements were made using the Van der Pauw method (9).

The residual impurity as measured from the Hall effect measurement at 77 K (subsequent to an Hg-rich anneal at a temperature of 250°C or less) was usually of the donor type (possibly indium) and varied between 3×10^{14} to 1×10^{15} cm^{-3} in the better films.

The electron mobility at 77 K in the better films exceeded 10^5 cm/V sec for $x = 0.2$ and 2×10^4 cm/V sec for $x = 0.3$ compositions. These values compare well with those reported for the bulk grown crystals (10) and, hence, indicate the crystallinity of the films to be sound.

Diode characteristics.—Some n^+-p diodes were fabricated in the LPE films. Figure 9 shows the characteristics of these diodes at 130 K in terms of R_oA (product of the zero bias resistance and p-n junction area) *vs.* the material cutoff wavelength $\lambda_{1/2}$. Data for some of the better diodes fabricated in bulk grown material are included in Fig. 9 for comparison purposes. Details of

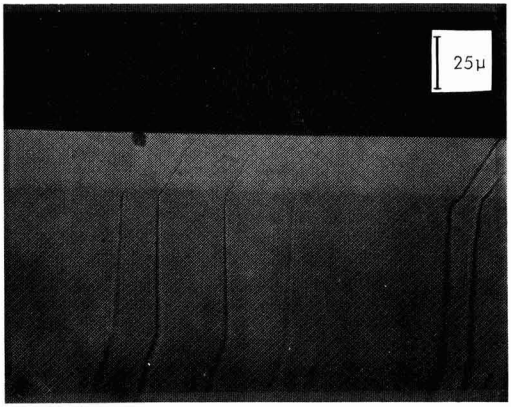

Fig. 7. Section of an $(Hg_{0.65}Cd_{0.35})Te$ film at 400×

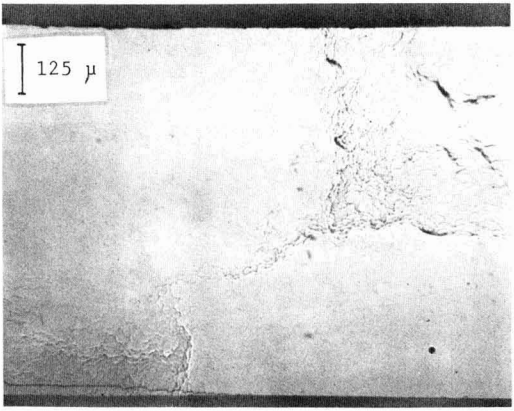

Fig. 8. Micrograph of film showing slightly elevated flat plateau areas surrounded by terraced areas.

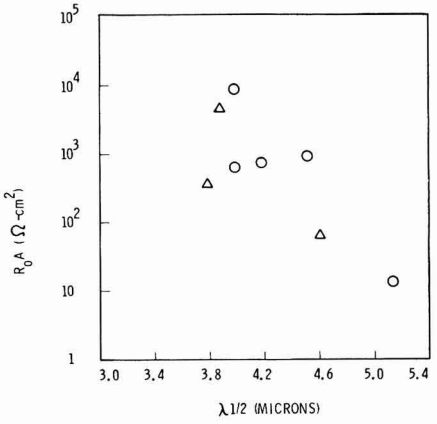

Fig. 9. R_0A data measured at 130 K vs. $\lambda_{1/2}$. Circles represent diodes fabricated in bulk grown material while triangles refer to diodes fabricated in the LPE material.

the LPE diode characteristics will be presented elsewhere.

Discussion

Calculations of the film thicknesses and composition gradings due to Cd and Hg depletion in the solution, based on equilibrium growth conditions, have been made. These calculations provided an additional method for estimating solution liquidus temperatures based on the depth of meltback from excessively undersaturated solutions. Solution undersaturation was then optimized to provide the best film surface morphology.

A slight change in the LPE solution composition occurs during the heat up of the growth system and subsequent homogenization of the solution. This composition change is due to the interaction of the CdTe substrate with the vapor species in the growth ampul before the melt contacts the substrate. In order to assess the extent of this interaction, a CdTe substrate that was exposed only to the vapor interaction was microprobed as shown in Fig. 10. If one assumes that all the Cd loss from the CdTe substrate in exchange for Hg is uniformly dissolved in the $(Hg_{1-x}Cd_x)_{1-y}Te_y$

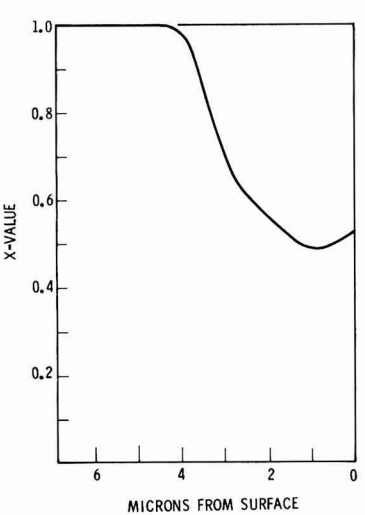

Fig. 10. X-ray microprobe analysis of a CdTe substrate exposed to the vapor (Hg, Cd, and Te_2 species) of a $(Hg_{1-x}Cd_x)_{1-y}Te_y$ growth solution during heat up and homogenization of an LPE growth run.

solution, the increase in x-value of the solution can be estimated to be about $\Delta x = 0.003$ resulting in an increase of the liquidus temperature of 2°C. These changes were expected to be reproducible in film growth runs using comparable homogenization times and temperatures.

Consider N mole fractions of $(Hg_{1-x}Cd_x)_{1-y}Te_y$ very slowly precipitating ΔN moles of stoichiometric solid $(Hg_{1-kx}Cd_{kx})_{0.5}Te_{0.5}$ following a temperature drop ΔT°C below the liquidus temperature. Cd precipitation satisfies the follwing equation

$$\Delta[Nx(1-y)] = \Delta Nx(1-y) + \Delta xN(1-y) - Nx\Delta y = 0.5kx\Delta N \quad [2]$$

Similarly, Te precipitation gives

$$\Delta[Ny] = N\Delta y + y\Delta N = 0.5\Delta N \quad [3]$$

An additional constraint on the final solution composition is given by

$$\Delta T = \frac{\partial T}{\partial x}\Big)_y \Delta x + \frac{\partial T}{\partial y}\Big)_x \Delta y \quad [4]$$

where $\partial T/\partial x)y = m_x$ and $\partial T/\partial y)x = m_y$ are the liquidus slopes for $(Hg_{1-x}Cd_x)_{1-y}Te_y$. From Eq. [2] to [4]

$$\Delta x = \left[\frac{x(k-1)}{m_x x(k-1) - m_y(2y-1)(1-y)}\right]\Delta T \quad [5]$$

$$\Delta y = \left[\frac{-(2y-1)(1-y)}{m_x x(k-1) - m_y(2y-1)(1-y)}\right]\Delta T \quad [6]$$

$$\frac{\Delta N}{N} = 2\left[\frac{(1-y)}{m_x x(k-1) - m_y(2y-1)(1-y)}\right]\Delta T \quad [7]$$

The change in the Cd concentration C in the solution for a given change in x and y is given by

$$\Delta C = (1-y)\Delta x - x\Delta y$$

Using Eq. [5] and [6], the liquidus slope for equilibrium growth defined in terms of the Cd concentration is given by

$$m = \frac{\partial T}{\partial C} = \frac{m_x x(k-1) - m_y(2y-1)(1-y)}{(1-y)(k+2y-2)x} \quad [8]$$

For film thickness determination the densities of the LPE melt and precipitated solid $(Hg_{1-x}Cd_x)Te$ are taken as $\rho_m(x,y)$ and $\rho_f(kx,0.5)$, respectively. The LPE film thickness l_f for equilibrium growth can then be obtained with the use of Eq. [7] and [8], while noting that the ΔN for the film is opposite in sign to that for the solution. Denoting the molecular weights of the film and melt by M_f and M_m we obtain

$$l_f = -\frac{\rho_m(x,y)M_f}{\rho_f(kx,0.5)M_m}\left[\frac{2l_m\Delta T}{mx(k+2y-2)}\right]$$

Estimates of $\rho_m(x,y)$ were obtained from the sum of the proportionately weighted stoichiometric solid and pure Te densities $\rho(x,0.5)$ and ρ_{Te}, respectively, *i.e.*

$$\rho_m(x,y) = 2(1-y)\rho(x,0.5) + (2y-1)\rho_{Te}$$

The density of solid $(Hg_{1-x}Cd_x)Te$ at room temperature (11) was taken as

$$\rho(x,0.5) = 2.226(3.628 - x)$$

and the density of pure Te at 550°C (12) was taken as 5.75 g/cm^3.

Table II lists some of the growth parameters used to obtain films with compositions of $x = 0.35$ and $x = 0.24$, and also the calculated equilibrium values of film growth thickness/°C of temperature drop and the composition grading/micron of growth from 3 mm thick solutions.

Under equilibrium growth conditions the change in the solution x-value due to the depletion of Cd and Hg

Table II. Summary of film growth parameters and calculated substrate meltback depths and film composition changes due to initial solution undersaturation, and film thickness and composition gradings in subsequent film growth

		Film compositions	
		$Hg_{0.65}Cd_{0.35}Te$	$Hg_{0.765}Cd_{0.235}Te$
Parameters			
Melt thickness	l_m mm	3	3
Melt composition	$(Hg_{1-x}Cd_x)_{1-y}Te_y$	$(Hg_{0.90}Cd_{0.10})_{0.225}Te_{0.775}$	$(Hg_{0.933}Cd_{0.067})_{0.25}Te_{0.75}$
Liquidus slopes	m_x °C/mole	630	600
	m_y °C/mole	−862	−770
	m °C/Cd mole	3850	3915
Densities: melt	$\rho_m(x,y)$ g/cm³	6.7	6.8
film	$\rho_f(kx,0.5)$ g/cm³	7.3	7.5
Segregation coefficient	k (Cd ratio)	3.5	3.5
Film growth			
Thickness	l_f microns/°C	4.9	7.35
Film grading	$\frac{d(kx)}{dl_f}$ Cd moles/micron	−0.0007	−0.0004
Meltback $Hg_{0.5}Cd_{0.5}Te$ surface			
Effective segregation coefficient	k' Cd ratio	5.0	7.46
Liquidus slope	m' °C/mole	3504	3053
Film x-value increase	$k\Delta x$ Cd moles/°C	0.0039	0.0043
Meltback depth	l_d microns/°C	−3.6	−4.0
Meltback CdTe surface			
Effective segregation coefficient	k' Cd ratio	10.0	14.9
Liquidus slope	m' °C/mole	3135	2716
Film x-value increase	$k\Delta x$ Cd mole/°C	0.0047	0.0050
Meltback depth	l_d microns/°C	−1.9	−2.2

during growth results in proportional changes in the precipitated solid composition x-values. From Eq. [5] and [8], $\Delta x/x$ in solution can be expressed as

$$\frac{\Delta x}{x} = \frac{(k-1)\Delta T}{(k+2y-2)(1-y)mx}$$

The change in the x-value of the film is then

$$k\Delta x = \frac{k(k-1)\Delta T}{(k+2y-2)(1-y)m} \qquad [9]$$

Using Eq. [9], the change in x-value as a function of film thickness can be obtained

$$\frac{d(kx)}{dl_f} = -\frac{\rho_f(kx,0.5)M_m}{\rho_m(x,y)M_f}\left[\frac{(k-1)kx}{2(1-y)l_m}\right] \qquad [10]$$

To estimate substrate meltback depths and the increase in the film composition profile resulting from a Cd and Hg increase in the solution the same formalism as used for growth can be used for meltback, provided that k and m are appropriately redefined by their effective values in meltback, that is k' and m'. On the basis of the microprobe data shown in Fig. 10 two values of k' have been considered for the meltback process. First, for the case of light meltback of no more than about 2 microns of the substrate surface with x-value around $x = 0.5$, k' was taken as $0.5/x$ where x is the solution x-value. Second, for the case of significant meltback involving essentially pure CdTe k' was taken as $1/x$. The increase in the whole film x-value profile for $\Delta T'$°C of undersaturation could then be obtained from

$$k\left[\frac{(k'-1)\Delta T'}{(k'+2y-2)(1-y)m'}\right] \qquad [11]$$

With most undersaturated solution contact temperatures controlled to within ±½°C of each other the measured film x-value variations between films of comparable thickness, grown from the same solution compositions, were observed to be within $\Delta x = \pm 0.002$. These results are consistent with the composition variations expected on the basis of Eq. [11] and listed in Table II.

Average meltback depths l_d into $Hg_{0.5}Cd_{0.5}Te$ and separately into CdTe substrate surface compositions were determined from

$$l_d = -\frac{\rho_m(x,y)M_s}{\rho_s(k'x,0.5)M_m}\left[\frac{2l_m\Delta T'}{m'x(k'+2y-2)}\right]$$

where M_s and ρ_s denote the molecular weight and density of the surface with composition $k'x$. The calculated values of l_d in Table II show that the meltback depth per °C of undersaturation is significantly less on CdTe than on $Hg_{0.5}Cd_{0.5}Te$. In films grown from supersaturated solutions the Cd/Hg interdiffusion depth on the CdTe substrate was typically 4 microns. Based on this information, the meltback depth data in Table II and observation on over a hundred films showing that excessive undersaturation led to uneven meltback reaching into the CdTe, we have associated an undersaturation of about 2°C as the temperature at which meltback could just be seen. Using meltback observations as a reference point for estimating solution undersaturation, it was estimated that the optimum degree of solution undersaturation for the best film morphology appeared to be about 1 ± ½°C.

Two liquidus temperatures estimated from thermal analyses and meltback considerations are given in Table III. The liquidus temperature data obtained from thermal analysis appear to be about 3°C higher than those interpreted from LPE film growth. This temperature difference is believed to be largely due to the interaction between the substrate and solution via the vapor phase before solution tipping over the substrate. Allowing also for the solution depletion during growth, the Cd segregation coefficient for solutions with $y \geq 0.75$ and low x-values is estimated to be $k = 3.5 \pm 0.1$.

Summary

Thermal analyses have been made of Te-rich $(Hg_{1-x}Cd_x)_{1-y}Te_y$ solutions with compositions suitable for growing $(Hg_{1-x}Cd_x)Te$ films with compositions

Table III. Liquidus temperatures obtained by DTA and from LPE films

Solution composition		Film surface kx	Liquidus temperatures determined from	
x	y		DTA	LPE
0.10	0.775	0.35	545 ± 3°C	549 ± 1°C
0.067	0.75	0.24	551 ± 4°C	554 ± 1°C

$x = 0.2$-0.4. The liquidus temperatures obtained in this way are consistent with estimates inferred from substrate meltback prior to the film growth process.

LPE $(Hg_{1-x}Cd_x)Te$ films grown at slow cooling rates under almost nondiffusion limited conditions showed thicknesses and composition gradings close to those calculated for equilibrium growth. In the absence of Hg loss in the closed system used, an accurate assessment of the Cd segregation coefficient was possible for low x-value $(Hg_{1-x}Cd_x)_{1-y}Te_y$ solutions with $y \geq 0.75$; the value obtained was $k = 3.5 \pm 0.1$.

Using slight undersaturation, smooth films up to 40 microns thick were grown. Electrical characterization of the LPE films showed electron mobility and residual impurity concentration characteristics comparable to bulk grown material. In addition, the performance of photodiodes made in the LPE films was similar to those made in the bulk grown material.

Acknowledgments

The authors wish to express their thanks to Mr. P. Guzelf for growing films and P. Crickard for electrical evaluation. This work was supported, in part, by the Air Force Materials Laboratory, Air Force Systems Command, United States Air Force, Wright Patterson AFB, Ohio 45433, under Contract No. F33615-78-C-5156.

Manuscript submitted April 28, 1980; revised manuscript received Sept. 12, 1980.

Any discussion of this paper will appear in a Discussion Section to be published in the December 1981 JOURNAL. All discussions for the December 1981 Discussion Section should be submitted by Aug. 1, 1981.

Publication costs of this article were assisted by Honeywell Electro-Optics Center.

REFERENCES

1. T. C. Harman, in Abstracts of the 1979 Electronic Materials Conference, June 28, 1979.
2. J. L. Schmit and J. E. Bowers, *Appl. Phys. Lett.*, **35**, (6) (1979).
3. C. C. Wang, S. H. Shin, M. Chu, M. Lanir, and A. H. B. Vanderwyck, *This Journal*, **127**, 175 (1980).
4. R. Brebrick and A. Strauss, Private communication.
5. J. A. Mroczkowski, To be published.
6. J. Mroczkowski, P. Lovecchio, D. Polla, and H. R. Vydyanath, "$(Hg_{1-x}Cd_x)Te$ Technology Development for MSP Support," Interim annual report to Air Force Materials Laboratory under Contract No. F33615-73-C-5156 (1979).
7. M. W. Scott, *J. Appl. Phys.*, **40**, 4077 (1969).
8. M. B. Crossley and I. Small, *J. Cryst. Growth*, **27**, 35 (1974).
9. L. J. Van der Pauw, *Philips Tech. Rev.*, **20**, 220 (1959).
10. W. Scott, *J. Appl. Phys.*, **43**, 1055 (1972).
11. J. Blair and R. Newman, in "Metallurgy of Elemental and Compound Semiconductors," Vol. **12**, p. 393, Wiley-Interscience, New York (1961).
12. CRC Handbook, 55 ed., p. B-237 (1974-1975).

Stress-Induced Dark Line Defect Formation in GaAlAs:Si LED's

A. K. Chin,* W. C. King, T. J. Leonard, R. J. Roedel, C. L. Zipfel, V. G. Keramidas,* and F. Ermanis

Bell Laboratories, Murray Hill, New Jersey 07974

ABSTRACT

Homojunction, graded bandgap GaAlAs:Si LED's have been demonstrated to be highly reliable. During accelerated aging (30 mA forward bias, 250°C), these LED's generally degrade slowly without the formation of dark lines or dark spots. It has recently been found, however, that some LED's show a rapid reduction of light output even when aged without current bias at 200°C. <110> oriented dark lines appeared in the electroluminescence image of heavily degraded devices. To determine the source of the DLD's, the material quality of degraded LED's and unaged LED's from the same wafer was assessed using etch pitting and transmission cathodoluminescence. Examination of the devices revealed the presence of small pyramids, composed mainly of silicon, on the p-surface of some of the LED's; no unusual features were found on the remaining LED's. A dislocation network surrounding each pyramid was found to be initially present. Due to bonding and thermal stresses applied to the pyramids, these networks enlarged with aging along the {111} planes and appeared as <110> DLD's in the electroluminescence image upon reaching the p-n junction. In degraded LED's from pyramid-free regions of the wafer with pyramids, <110> DLD's initiate at dicing damage and regions of the p-surface subject to high bonding stress, *i.e.* edges and corners. The growth of these DLD's is identical to those initiating at pyramids. A similar study of LED's from a wafer that is totally free of pyramids shows that DLD's are not formed in devices that degrade slowly.

Graded-bandgap, homojunction GaAlAs:Si LED's are presently used as high efficiency light sources for opto-isolators (1, 2). Bias tests of these devices, accelerated by applying a thermal stress, demonstrated high reliability; with 30 mA forward current bias, a mean-time-to-failure (MTTF) of $\sim 10^5$ hr at 250°C (1) and $\sim 10^8$ hr at 25°C (3) was determined. The electroluminescence of degraded diodes appears to differ from unaged devices only in relative brightness. Both degraded and undegraded LED's exhibit uniform light emission; no dark lines or spots are observed. Recently, however, aging studies (4) have shown that some LED's degrade rapidly when aged at 200°C even without current bias; degradation to 10% of initial efficiency occurred within 400 hr. Examination of the

* Electrochemical Society Active Member.

Key words: cathodoluminescence, electron microscopy, reliability.

electroluminescence image of many of the most heavily degraded devices showed the presence of <110> oriented dark line defects (DLD's). The drop in LED efficiency is thus attributed to nonradiative recombination at the DLD's. Since dark line formation has not been previously observed in graded bandgap GaAlAs:Si LED's, this paper reports on their origin and growth behavior.

Formation of dark spots and dark lines oriented in the <100> and <110> directions is a degradation mode for LED's fabricated from many semiconductors, *e.g.*, GaP (5), GaAs/GaAlAs (6-13), and GaAsP (14, 15). <110> DLD's grow by glide motion of dislocations on the {111} slip planes (6, 7, 9, 10) whereas the growth of <100> DLD's is consistent with climb of dislocations (11-13). Studies have shown that formation of <100> DLD's require minority carrier injection whereas <110> DLD formation can be induced with either minority carrier injection or stress (7). Since the GaAlAs:Si LED's under discussion developed <110> DLD's without current bias, a source of stress was searched for.

Studies of stress-induced DLD's in GaAs/GaAlAs double heterostructure crystals provide a useful background for the present study. These studies showed that a threshold stress is required to form <110> DLD's (6, 7, 9, 10). This threshold level decreases for increasing minority carrier injection (6, 7, 10). For no injection, the threshold stress is $\sim 8 \times 10^9$ dynes/cm^2 (7). This value rapidly decreases to $\sim 2 \times 10^9$ dynes/cm^2 under the low excitation level of 3 W/cm^2 from a 6471Å Kr-ion laser beam, equivalent to a current density of $J \sim 1$ A/cm^2 (7). A lower stress level of $\sim 6 \times 10^8$ dynes/cm^2 is found for $J = 58$ A/cm^2 (10). These stress values are comparable with values from typical sources of stress. Stresses from dielectric coatings can be as high as 10^{10} dynes/cm^2 (15), stresses due to dicing damage are 2-7 $\times 10^7$ dynes/cm^2 (14), and the thermal stress on a mounted LED, assuming a 100°C temperature difference between header and LED, can be $\sim 10^9$ dynes/cm^2 (8).

In a reliability study by King (4), LED's from the same wafer as those that showed poor reliability were examined visually. Pyramidal protrusions of various sizes were found on the p-surface of some of the LED's (4). These pyramids occasionally occur in this device material and their exact cause is presently under investigation. LED's from the same wafer were separated into groups with and without pyramids. Bonded LED's with pyramids were found to degrade at a faster rate than those without pyramids, but both groups degraded faster than previous devices (1, 3, 4). A mean-time-to-failure (MTTF) of $\sim 10^5$ hr (250°C, 30 mA forward current) has been found for the latter whereas the LED's with pyramids show a MTTF of $\sim 4 \times 10^2$ hr even under reduced stress conditions (200°C, 0 mA forward current). Dark regions and lines in the electroluminescence image were observed only in the devices degraded to less than ~10% of their initial efficiency.

In the present study, the material quality of unaged and aged devices from a wafer exhibiting pyramids on the p-surface was determined by KOH etch pitting (17) and transmission cathodoluminescence (TCL) (18). A dislocation network was found to surround each pyramid initially. During aging, <110> DLD's develop from these networks. In the pyramid-free LED's, <110> DLD's initiate at processing damage and at high stress points (*e.g.*, edges and corners) on the p-surface. To determine whether bonding stress or internal stress is responsible for the growth of the DLD's, a defect study was made of similar unbonded LED's aged at 200°C without current bias. Finally, a high dislocation density ($\sim 10^5$ cm^{-2}) and stacking faults were found in the degraded devices. This result suggests that the susceptibility of the pyramid-free LED's to stress-induced DLD's may be simply due to a high dislocation density or to the presence of stacking faults. Low and high defect density GaAlAs:Si LED's fabricated from a wafer without pyramids on the p-surface were then tested. High reliability was found for the LED's irrespective of the defect density. The degradation of these LED's did not involve the formation of DLD's. These experiments and results are summarized in Table I. The remainder of this paper comprise the details of this study.

Experimental

Device characteristics.—The GaAlAs:Si LED's were grown by a single-step liquid phase epitaxy (LPE) technique as described by Dawson (1). A schematic of the LED structure is presented in Fig. 1. An epitaxial layer of ~200 μm thickness is grown on a <100> oriented GaAs substrate. The aluminum content of this

Table I.

Experiment	Analysis technique	Results
1. Material evaluation	Nomarski interference microscopy	Pyramids on p-surface
	Secondary electron imaging in SEM	Dicing damage
		Etch used to remove dicing damage removes more of the n-layer
	TCL	10^5 dislocation/cm^2
	KOH etch pitting	Stacking faults
		Dislocation network surrounding pyramids
	X-ray microanalysis on SEM	Pyramids consist mainly of silicon
2. Reliability of bonded LED's with pyramids	Aging at 200°C, 0 mA	MTTF $\lesssim$ 400 hr
	Electroluminescence imaging	DLD's observed for $\eta/\eta_0 \lesssim 0.1$
	TCL of p-surface	DLD's initiate from dislocation networks surrounding pyramids
	TCL of LED side	DLD's propagate on {111} planes and terminate at p-n junction
3. Reliability of unbonded LED's with pyramids	Aging at 200°C, 0 mA	Aging time = 10^3 hr
	Electroluminescence imaging	No DLD's
	TCL	No change in dislocation networks surrounding pyramids
4. Reliability of pyramid-free bonded LED's from wafer with pyramids	Aging at 200°C, 0 mA	MTTF $\lesssim 10^3$ hr
	Electroluminescence imaging	DLD's observed for $\eta/\eta_0 < 0.1$
	TCL of p-surface	DLD's initiate from dicing damage and high stress points on p-surface
	TCL of LED side	DLD's propagate on (111) planes and terminate at p-n junction
5. Reliability of bonded LED's from pyramid-free wafer	Aging at 250°C, 30 mA, 5-15 dislocations/LED	MTTF ~ 10^5 hr
	Aging at 250°C, 30 mA, 20-40 dislocations/LED and stacking faults	MTTF ~ 10^5 hr
	TCL of p-surface	LED's do not degrade by DLD formation
		Dislocations and stacking faults not sources of DLD's

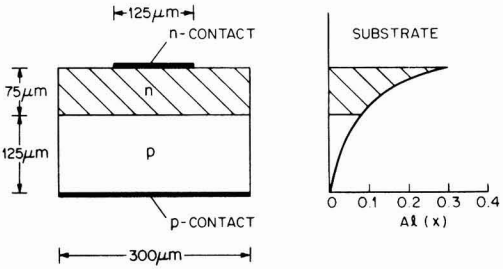

Fig. 1. Schematic of GaAlAs:Si LED

layer varies from an initial value of $x \sim 0.30$ to a final value of $x \sim 0.0$. The p-n junction is formed by Si amphoteric doping; the aluminum concentration is $x \sim 0.08$ at this junction which is located ~75 μm from the substrate-epilayer interface. After epi-growth, the GaAs substrate is chemically removed from the LPE layer, contacts are evaporated, and the wafer is diced into 300 × 300 μm square diodes. The p-surface receives a full surface metallization of 1% BeAu alloy whereas the n-contact consists of a 125 μm diam dot of SnAu. To minimize dicing damage, the saw cuts are aligned along the <100> directions (45° from the <110> cleavage directions) and then etched to remove the sawing damage. The etch consists of 30% H_2O_2 whose *p*H is adjusted to 8.4 by the addition of NH_4OH (1). The devices are bonded with epoxy with the p-surface toward the header so that the higher aluminum content, *i.e.*, higher bandgap, n-layer forms a window for the light emitted at the p-n junction. The typical operating condition is 10 mA forward current, corresponding to a current density of $J \sim 10$ A/cm².

Material evaluation technique.—As noted above the material quality of degraded and undegraded devices was assessed using KOH etch pitting (17) and transmission cathodoluminescence (TCL) (18). Dislocations appear as dark spots in the TCL image due to nonradiative recombination. An exact one-to-one correspondence between dislocation pits produced by the KOH etch and dark spots in TCL images of the {100} surface of GaAlAs:Si has been previously established (18). For most of the study the TCL technique was used since etch pitting of small devices is difficult.

Both etching and TCL require removal of the LED from the header used for aging and testing. Other techniques for detecting material defects, *e.g.*, cathodoluminescence (CL) and electron beam induced current (EBIC), that do not require demounting of the LED, were tried unsuccessfully. Although mechanical damage appears as a dark region in TCL, CL, and EBIC images, grown-in dislocations and DLD's are apparent only in the TCL images (19, 20).

For TCL measurements, the devices were carefully demounted from the TO-18 headers by softening the bonding epoxy with heat ($T \sim 300$°C) applied to the header. The residual epoxy was removed using an oxygen plasma. The contact metallization was chemically stripped with a solution of 450g KI, 150g I_2, and 400 ml H_2O. Since the contact is alloyed into the semiconductor and since the metallization etch mildly attacks GaAlAs, the etched surfaces are rougher than the as-grown surface. This surface is, however, sufficient for TCL imaging.

Material quality and degradation.—Figure 2 shows an electroluminescence image of a typical, rapidly degraded LED. The dark circle in the center is the n-contact. Several <110> oriented DLD's are observed. These dark lines are located at the p-n junction where the light is emitted. To determine the source of the DLD's, the degraded LED's were first visually inspected on the headers using the SEM and Nomarski interference microscopy. Some damage was found, but it was not considered unusual or excessive. After demounting the LED's, small pyramids of various sizes were found on the p-surface of some of the LED's. Figure 3a is a secondary electron (SE) image of an unaged LED with several pyramids. X-ray microanalysis on an SEM showed that these pyramids are composed mainly of silicon (21).

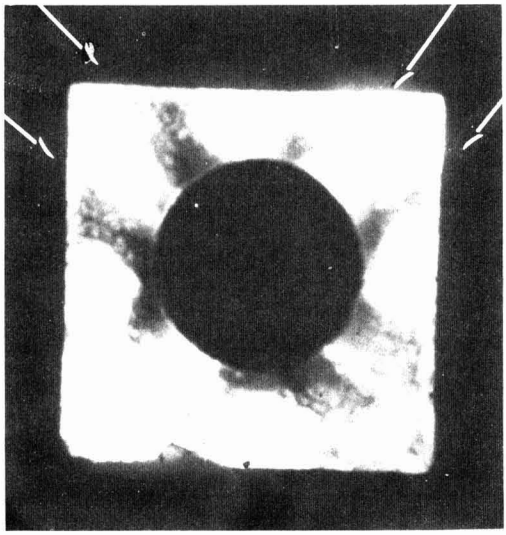

Fig. 2. Electroluminescence image of the n-surface of a degraded LED. The black dot in the center is the n-contact. The arrows indicate the <110> DLD's.

Figure 3b is the TCL image of the region shown in Fig. 3a. The pyramids appear dark due to the low luminescence efficiency of these regions. In addition to dark regions, dark lines extending from the pyramids along the <110> directions are observed. These dark regions and lines are part of a dislocation network and have no corresponding features in the SE image of Fig. 3a. These dislocation networks are probably a result of lattice mismatch between the GaAlAs epilayer and the Si pyramid. Using the KOH defect etchant (17), these dislocation networks are also revealed. The surface of a wafer, examined with Nomarski interference microscopy before and after etching, is shown in Fig. 4a and 4b. A comparison of the two figures shows that the pyramids have been etched away by the KOH. The dislocation network surrounding the pyramids appears as a rectangular region containing a high density of etch pits. The <110> dark lines appear as a series of pits after KOH etching.

Figures 5a and 5b are, respectively, the SE and TCL images of the p-surface of typical degraded, bonded LED's. Although Fig. 3 and 5 correspond to two different LED's, comparison of these figures shows clearly that with aging the dislocation networks originating at the pyramids enlarge along the <110> directions and form <110> DLD's. A similar study of unbonded LED's was performed to determine whether bonding stress or internal strain was responsible for the growth of the DLD's. The TCL images of the aged, unbonded LED's were similar to Fig. 3b. No noticeable growth of the dislocation networks was found. It is thus concluded that bonding stresses applied to the pyramids is one source of DLD's. These stresses include those that result from the differences in the thermal expansion coefficient of the LED, header, and bonding material.

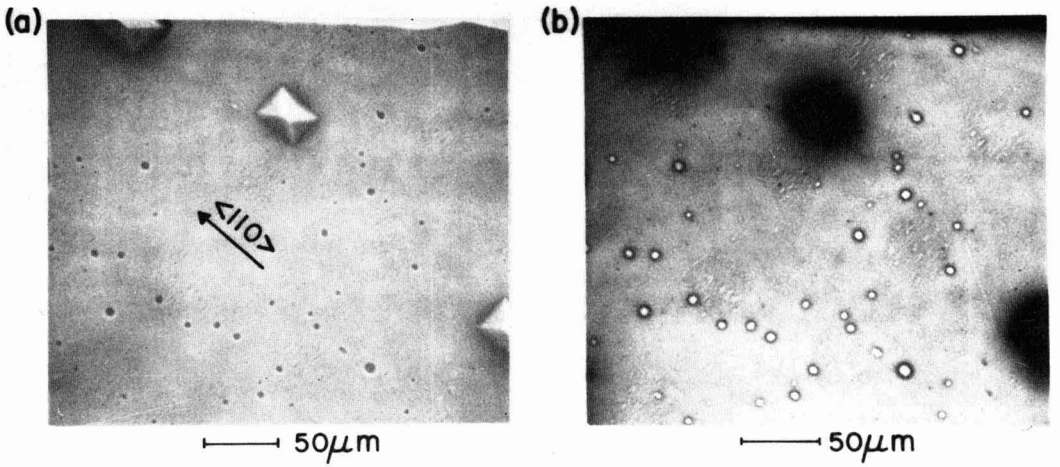

Fig. 3. a. Secondary electron image of the p-surface of an unaged LED with pyramids. The sides of the pyramids are parallel to the <110> directions. b. TCL image of the region in Fig. 3a. The dark area surrounding each pyramid is a dislocation network. The short dark lines are dislocations extending along the <110> directions.

Bonded devices without pyramids selected from the same wafer as the LED's in Fig. 3 and 5 were also found to degrade although at a slower rate (4). After 10^3 hr at 200°C without current bias, the efficiency is generally reduced to $\lesssim$ 0.1 of its initial efficiency. As in diodes with pyramids, <110> DLD's were observed in the electroluminescence image only after the efficiency had fallen below $\lesssim$ 0.1 of its initial efficiency. TCL examination shows <110> DLD's initiating at dicing damage and high stress points, *e.g.*, edges and corners, on the p-surface. Typical DLD's are shown in Fig. 6. Dicing damage is visible in the SE image of Fig. 6a; DLD's extending from the dicing damage are visible in the TCL image of Fig. 6b. These DLD's are found in the TCL image of all aged LED's examined, even those that do not show DLD's in the electroluminescence image. Although similar damage was found

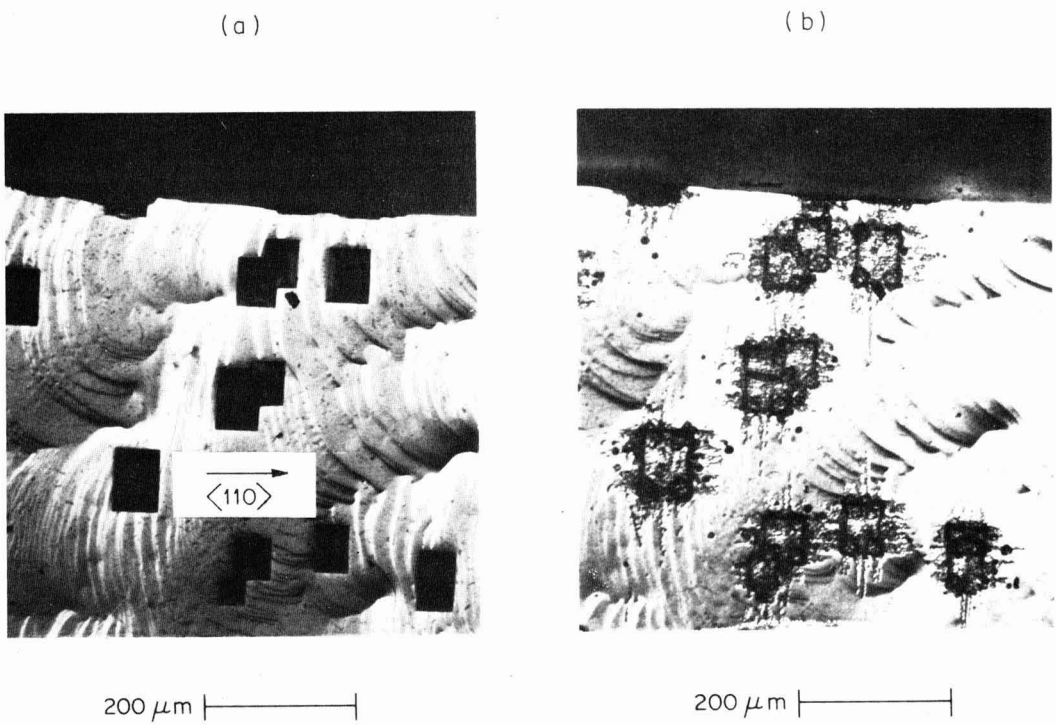

Fig. 4. a. Region of p-surface containing pyramids. b. Region of p-surface after etching in KOH. The pyramids have been removed by the etch and a high density of etch pits is observed beneath the pyramid (rectangular regions of pits). Linear arrays of pits extend along the <110> directions.

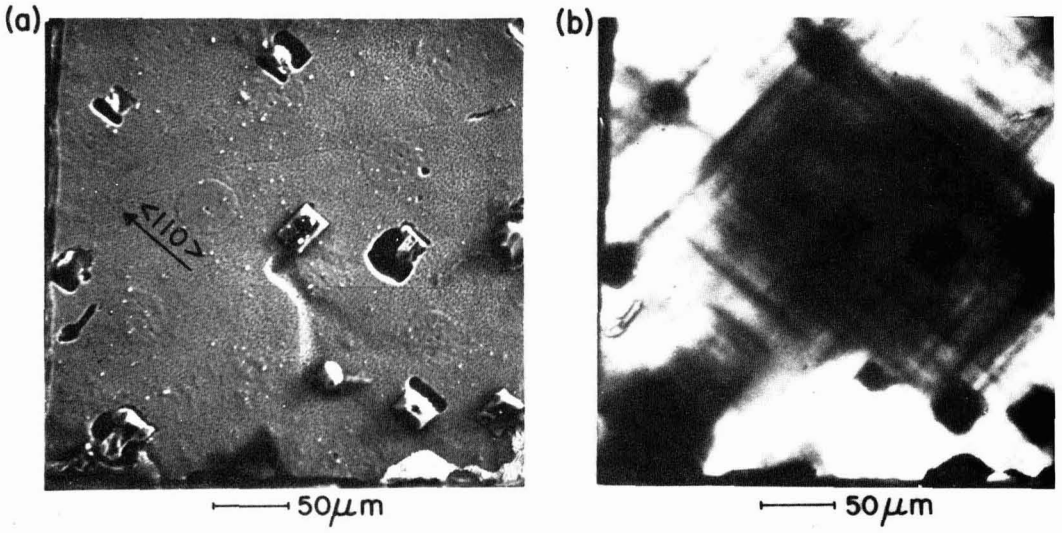

Fig. 5. a. SE image of the p-surface of a degraded LED with pyramids. b. TCL image of region in Fig. 5a. <110> DLD's initiate at the pyramids.

in unaged devices, only dark regions and not dark lines were associated with them. It will be shown below that the susceptibility to DLD formation is peculiar to the device wafers with silicon pyramids.

DLD growth behavior.—The study in the above section concentrated on the p-surface due to the presence of pyramids there. To determine whether the DLD's originate only on the p-surface, the top n-surface and (100) sides of the LED's need to be examined. In unaged devices, the usual dislocations, stacking faults, and processing damage were found on these surfaces. In degraded devices, TCL images of the n-surface were similar to those of unaged LED's, but <110> DLD's were found on the sides. By examining the sides of partially and highly degraded LED's, the DLD's were found to initiate at the p-surface and propagate

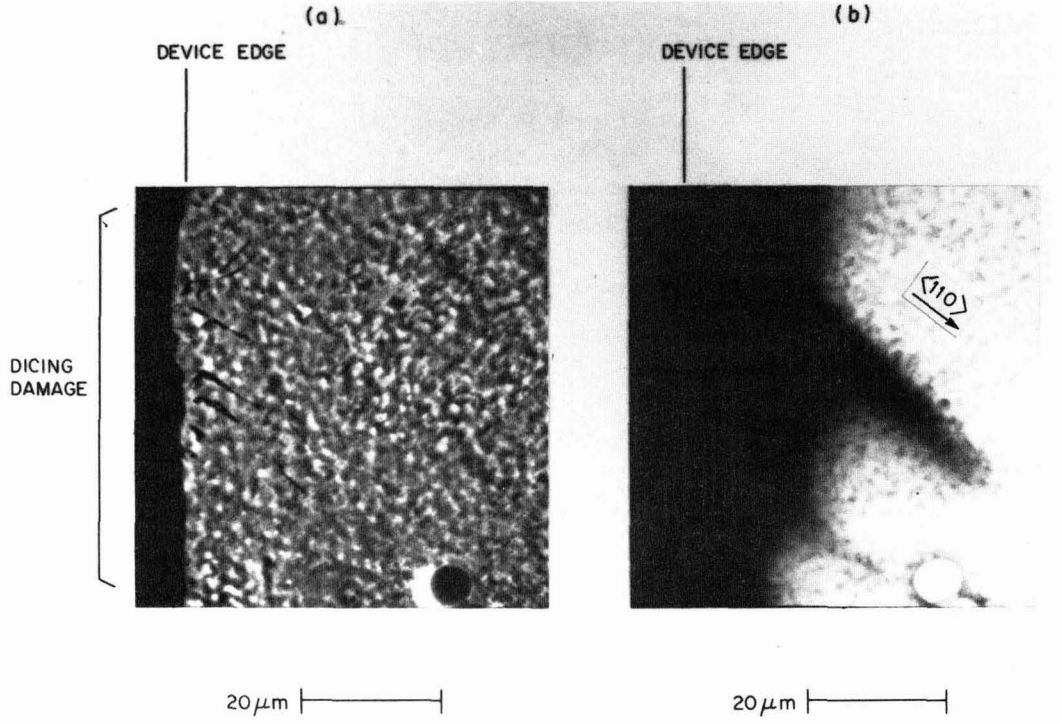

Fig. 6. a. SE image of the p-surface of an LED showing dicing damage along an edge. b. TCL image of the region in Fig. 6a. <110> DLD's initiate at the damage.

toward the p-n junction; the DLD's did not extend beyond the p-n junction into the n-region even in the most heavily degraded LED's ($\eta/\eta_0 < 0.01$).

SE and TCL images of the (100) side of a partially degraded LED are shown in Fig. 7. The SE image shows that the etch used to remove dicing damage removes more of the n-layer. The p-n junction appears as a dark line in the TCL image since the built-in electric field separates the electron-hole pairs generated by the electron beam and prevents recombination (22). The n-layer is brighter than the p-layer due to higher intrinsic luminescence efficiency rather than a result of degradation. DLD's were not observed in the electroluminescence image although the luminescence efficiency was 0.62 of its initial efficiency. However, DLD's were found by TCL imaging of the p-surface and the sides. The DLD's initiate at dicing damage on the p-surface and extend up the side as shown in Fig. 7b. The DLD's intersect the {100} p-surface at an angle of 45°, suggesting that the DLD's lie on the {111} slip planes.

Figures 8a and 8b are the SE and the TCL image of the {100} sides of heavily degraded LED. After aging, this {100} side was ground with 3 μm alumina grit and etched in Br/methanol to observe the p-n junction clearly. The efficiency was $\lesssim 0.01$ of the initial value; DLD's were observed in the electroluminescence image. As shown in Fig. 8b, the DLD's propagate up to the p-n junction, but do not penetrate into the n-layer. Similar examination of LED's with various degrees of degradation shows that the DLD's always initiate at the p-surface and propagate toward the p-n junction.

The DLD's stop their growth upon reaching the p-n junction probably due to lower stress in the n-layer. Since the etch used to remove the saw damage removes more of the n-layer than the p-layer, the n-layer may have a lower surface damage induced stress. A high internal electric field at the p-n junction is unlikely to hinder the propagation of the DLD's. Similar stress-induced <110> DLD's in GaAs/GaAlAs wafers have been shown to propagate through the p-n junction (23). Further study, *e.g.*, an examination of degraded LED's using transmission electron microscopy or a reliability study of LED's that have been etched more uniformly, is required to determine the exact cause of this effect. Such studies are beyond the scope of this work.

Degradation of high and low defect density LED's.— During evaluation of device wafers with pyramids, a high dislocation density (up to $\sim 10^5$ cm^{-2}, $\sim$100 dislocations/LED) and stacking faults were found. Additionally, the dislocation networks beneath the pyramids were resolved as individual dislocations or parts of dislocation loops even after 50-100 μm of material have been chemically etched from the p-layer. The susceptibility of the pyramid-free LED's to DLD formation was thus possibly a result of a high defect density. To investigate the influence of such defects, a separate set of LED's from a wafer completely free of

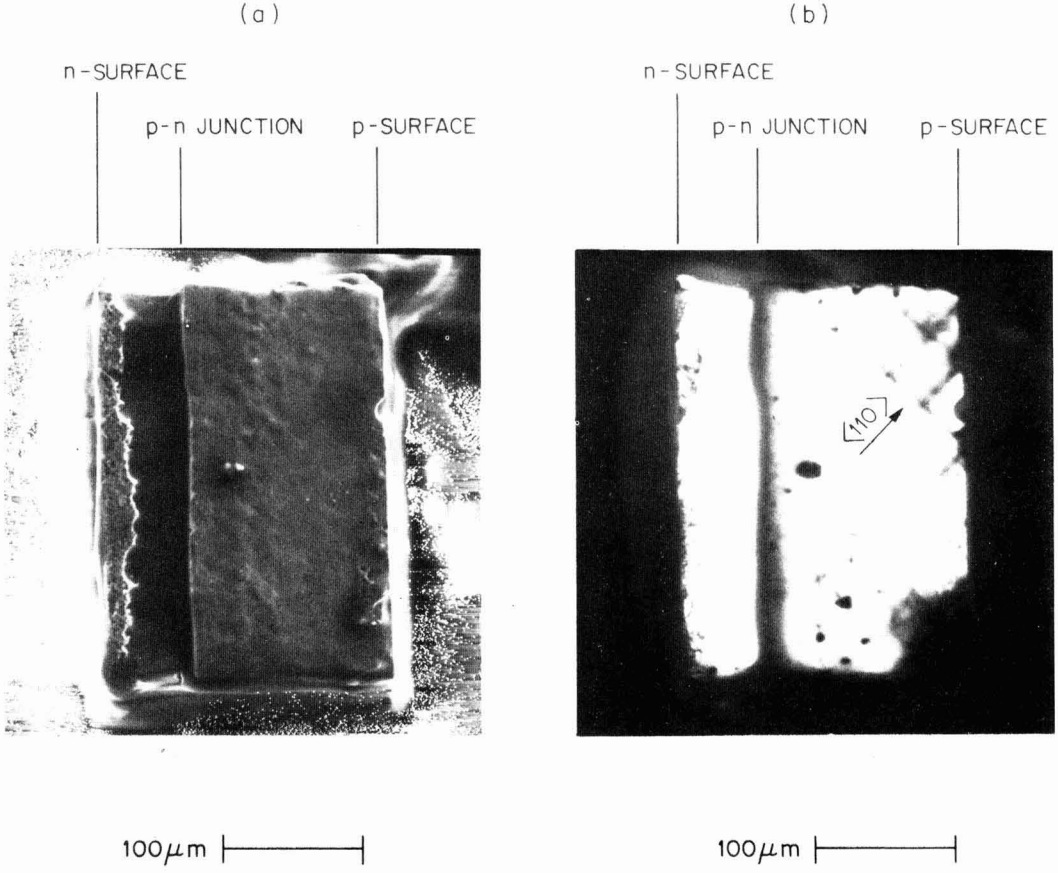

Fig. 7. a. SE image of {100} side of a partially degraded ($\eta/\eta_0 = 0.62$) LED. b. TCL image of the region in Fig. 7a. <110> DLD's initiate at the p-surface and propagate along the (111) planes toward the p-n junction.

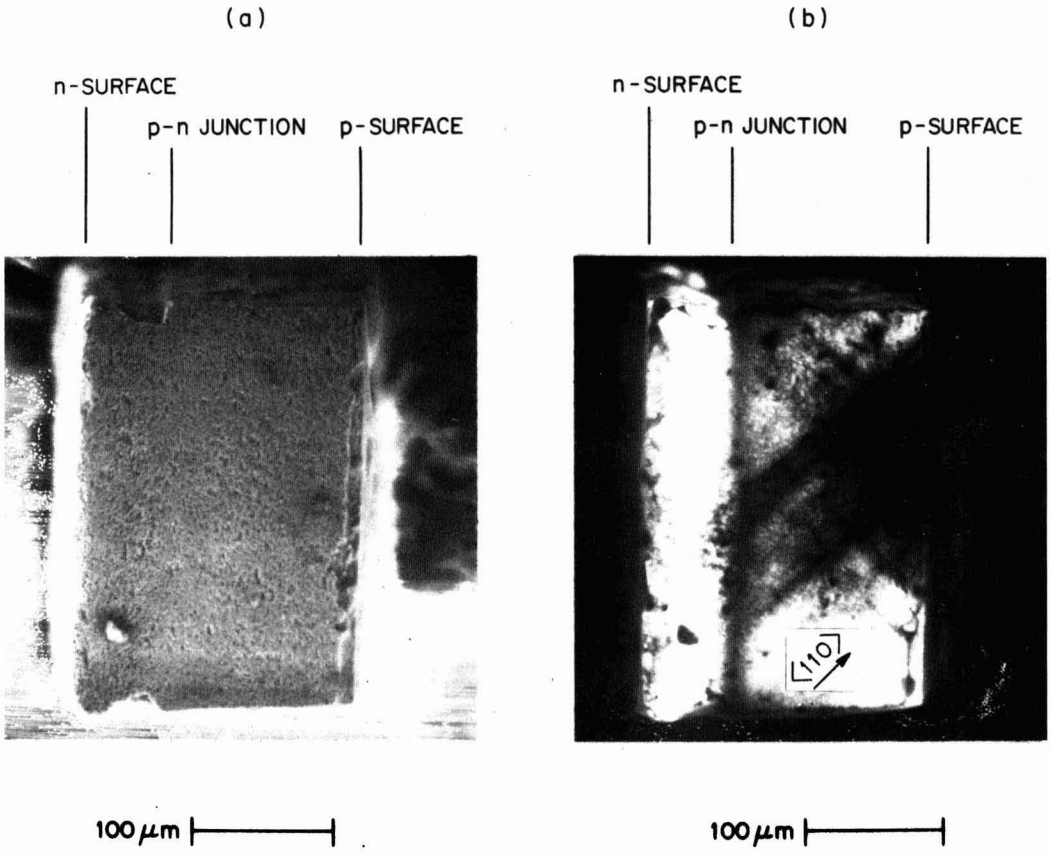

Fig. 8. a. SE image of the {100} side of a heavily degraded ($\eta/\eta_0 = 0.01$) LED. The surface has been ground and etched. b. TCL image of the region in Fig. 8a. <110> DLD's initiate at the p-surface, propagate along the {111} planes toward the p-n junction, and terminate at the p-n junction.

pyramids was separated into a group containing a high defect density (stacking faults and 20-40 dislocations/LED) and a group containing a low defect density (5-15 dislocations/LED). The two groups were then tested in the usual fashion (250°C, 30 mA forward bias).

The defect density of each diode was determined in the following manner. The surface of the device wafer was Br/methanol polished to provide a smooth surface; ~25 μm of material was removed. Saw cuts, 25 μm deep, were made into the wafer to define the locations of the LED's. The p-surface of each LED was imaged using TCL to determine the defect content. After processing, the wafer was diced along the original saw marks. The LED's were demounted from the cutting block and individually etched to preserve their identity.

The results of the reliability study on these LED's are plotted in Fig. 9. The average efficiency of each group is plotted *vs.* the square root of time in hours; each group contains 10 LED's. Essentially, the results show that the defect density of the devices from a wafer free of pyramids has little or no effect on the reliability. From the data in Fig. 9, an MTTF of $\gtrsim 10^5$ hr at 250°C with 30 mA forward current is estimated for both high and low defect density LED's. These values of MTTF are similar to those found by Dawson (1). No catastrophic degradation was observed in any of the devices, and no DLD's were observed in the electroluminescence image after the ~4000 hr of operation.

Ten of the LED's were demounted and examined using TCL. In general, some additional dark spots developed during aging, but short ($\lesssim 25$ μm), dark lines were found only in one of the devices. These dark lines were present at the edge of the LED on the p-surface as shown in Fig. 10. Figures 10a and 10b are the SE and TCL images, respectively. Two <110> DLD's and

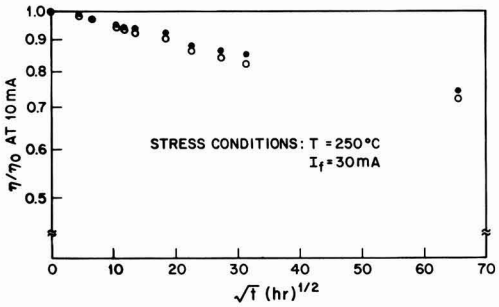

Fig. 9. Normalized efficiency *vs.* $\sqrt{t}$ for two sets of LED's. LED's in set 1 (dots) contain stacking faults and 20-40 dislocations. LED's in set 2 (open circles) contain 5-15 dislocations.

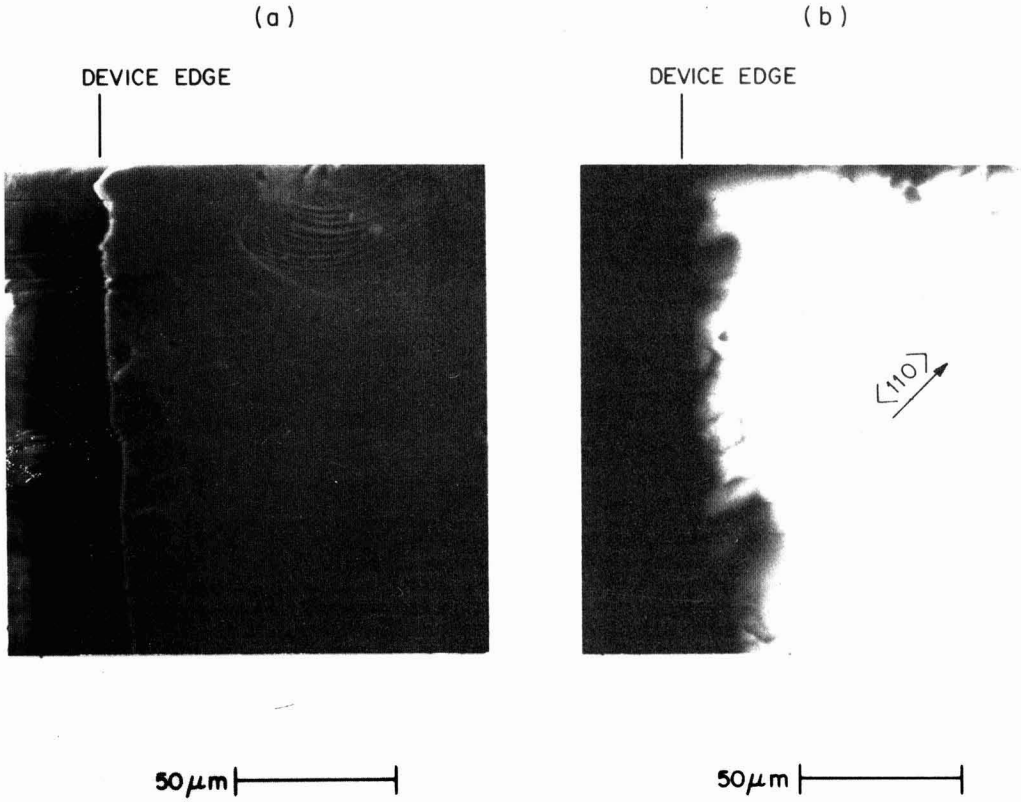

Fig. 10. a. SE image of the p-surface of an LED aged for 4000 hr at 250°C and I_f = 30 mA. b. TCL image of region in Fig. 10a. Two <110> DLD's and one <100> DLD are apparent at the device edge.

one <100> DLD are observed in Fig. 10b. The presence of this <100> DLD is unusual and suggests that these DLD's are not stress induced (11-13).

Summary and Conclusions

The present results show that GaAlAs:Si LED's fabricated from wafers with Si pyramids on the p-surface are prone to stress-induced <110> DLD formation. The origin of the silicon pyramids is not presently known and requires further study. Two sources of DLD's were found. First, a dislocation network was shown to initially surround the pyramids. These networks with the addition of bonding and thermal stresses extended on {111} planes toward the p-n junction. When they reached the p-n junction they were observed in the electroluminescence image. No DLD's were found in the n-layer. The etch used to remove dicing damage removes more of the n-layer and thus reduces the associated stress.

An internal stress of 2-7 $\times$ 10^7 dynes/cm^2 due to dicing damage was found by Hirahara *et al.* (16) in GaP LED's; this stress was sufficient to enhance the degradation rate of such devices. A similar stress is probably present in the GaAlAs:Si LED's. At room temperature, it is known that a threshold stress level of 8 $\times$ 10^9 dynes/cm^2 produces <110> DLD's in GaAlAs/GaAs double heterostructure crystals (7). This threshold level is probably greatly reduced for the GaAlAs:Si LED's at 200°C and the presence or absence of internal stress may cause the total strain to either exceed or be below the threshold required for stress-induced DLD's. Additionally, DLD's on devices selected from pyramid-free regions of the wafer with pyramids were found to initiate at mechanical damage or high stress points of the p-surface. The DLD growth proceeded as in devices with pyramids, but at a slower rate. Since LED's from pyramid-free wafers do not degrade by DLD formation, the presence of pyramids indicates a material problem. A high density of precipitates, unresolved either by KOH etching or TCL, may be present in wafers with pyramids.

The susceptibility of the LED's from wafers with pyramids to stress-induced DLD's was shown not to be a result of a high dislocation density or the presence of stacking faults. The tests used to determine the influence of such defects showed that the reliability of normal GaAlAs:Si LED's seems to be relatively independent of the diode defect density. Examination of normal LED's operated at 250°C, and 30 mA forward bias for 4000 hr shows that the degradation mechanism is not DLD formation.

Acknowledgments

We wish to thank H. Temkin for aging the LED's and for helpful discussions, E. Lassiter for mounting and demounting the LED's, D. D. Roccasecca for some device processing, K. B. Bauer for electroluminescence imaging, S. Jabbar for supplying some of the LED's, and O. G. Lorimor and R. H. Saul for helpful discussions.

Manuscript submitted Aug. 22, 1980; revised manuscript received Oct. 21, 1980. This was Paper 515 presented at the Hollywood, Florida, Meeting of the Society, Oct. 5-10, 1980.

Any discussion of this paper will appear in a Discussion Section to be published in the December 1981 JOURNAL. All discussions for the December 1981 Discussion Section should be submitted by Aug. 1, 1981.

Publication costs of this article were assisted by Bell Laboratories.

REFERENCES

1. L. R. Dawson, *J. Appl. Phys.*, **48,** 2485 (1977).
2. J. S. Jayson and S. Knight, *Appl. Solid State Sci.*, **6,** 119 (1976).
3. C. L. Zipfel, Unpublished.
4. W. C. King, Unpublished.
5. M. Iwamoto and A. Kasami, *Appl. Phys. Lett.*, **28,** 591 (1976).
6. S. Kishino, N. Chinone, H. Nakashima, and R. Ito, *ibid.*, **29,** 488 (1976).
7. H. Nakashima, S. Kishino, N. Chinone, and R. Ito, *J. Appl. Phys.*, **48,** 2771 (1977).
8. G. Zaeschmar and R. S. Speer, *ibid.*, **50,** 5686 (1979).
9. K. Ishida, T. Kamejima, and J. Matsui, *Appl. Phys. Lett.*, **31,** 397 (1977).
10. T. Kamejima, K. Ishida, and J. Matsui, *Jpn. J. Appl. Phys.*, **16,** 233 (1977).
11. P. W. Hutchinson and P. S. Dobson, *Philos. Mag.*, **32,** 745 (1975).
12. P. Petroff and R. L. Hartman, *Appl. Phys. Lett.*, **23,** 469 (1973).
13. P. Petroff and R. L. Hartman, *J. Appl. Phys.*, **45,** 3899 (1974).
14. N. Shimano, *Jpn. J. Appl. Phys.*, **17,** 1323 (1978).
15. N. Shimano, Y. Kawai, and M. Sakuta, *J. Appl. Phys.*, **51,** 1227 (1980).
16. K. Hirahara, Y. Iizuka, T. Beppu, and A. Kasami, 3rd IEEE Specialist Conference on the Technology of Electroluminescent Diodes, Session B1 (1978).
17. J. G. Grabmaier and C. B. Watson, *Phys. Status Solidi.*, **32,** K13 (1969).
18. A. K. Chin, H. Temkin, and R. J. Roedel, *Appl. Phys. Lett.*, **34,** 476 (1979).
19. R. J. Roedel, A. R. Von Neida, R. Caruso, and L. R. Dawson, *This Journal*, **126,** 637 (1979).
20. A. K. Chin, V. G. Keramidas, W. D. Johnston, Jr., S. Mahajan, and D. D. Roccasecca, *J. Appl. Phys.*, **51,** 978 (1980).
21. F. Ermanis, Unpublished.
22. D. B. Wittry and D. F. Kyser, *J. Appl. Phys.*, **36,** 1387 (1965).
23. K. Ikeda, T. Tanaka, M. Ishii, and A. Ito, *GaAs Relat. Comps.*, **24,** 174 (1974).

The Properties of Iron in Silicon

K. Graff and H. Pieper

AEG-Telefunken, Serienprodukte AG, Semiconductor Division, D-7100 Heilbronn, West Germany

ABSTRACT

The properties of iron in n-type and p-type silicon were studied by means of DLTS, carrier lifetime measurements, and infrared absorption spectroscopy. Only one donor level was observed, situated at $E_v + 0.43$ eV and correlated to iron on an interstitial site. In p-Si:B iron-boron pairs were formed at room temperature. Their activation energy was determined to be $E_v + 0.10$ eV. The reaction proceeded in two phases. In the second phase a thermal equilibrium between iron and iron-boron pairs was found which could be shifted by annealing and illuminating the specimen, respectively. In aluminum-doped silicon crystals two levels were observed after iron diffusion correlated to iron-aluminum pairs. Their activation energies were determined to be $E_v + 0.21$ and 0.13 eV. It is assumed that iron-boron pairs form also two levels, a donor and an acceptor. The acceptor must be situated in the upper half of the silicon bandgap. Reaction mechanisms are discussed.

Iron is one of the main heavy metal impurities in silicon devices. Because of its considerable high solubility and fast diffusion at high temperature iron is easily introduced into silicon crystals during heat-treatments. Hence it has been detected even after presumably clean annealing and quenching processes (1-3).

First investigations on the behavior of iron in silicon were carried out in the fifties and early sixties applying radiotracer techniques, resistivity measurements, and ESR spectroscopy (4-7). The fundamental knowledge about the properties of iron in silicon are based on these results: after quenching iron-doped specimens from high temperature iron forms a deep donor level at $E_v + 0.4$ eV which is paramagnetic in neutral state and detectable by ESR as iron on an interstitial site. This interstitial iron reacts with shallow acceptors such as B, Al, Ga, and In even at room temperature forming pairs which are oriented in <111>-direction with the exception of FeIn showing <100>-symmetry. These pairs dissociate during annealing at moderate temperatures and finally iron precipitates at somewhat higher temperature (100°-200°C).

Recently an increasing number of papers concerning the properties of iron in silicon was published showing a growing interest in this subject. This may be due to further increasing requirements to device performance accompanied by the development of improved measurement techniques including Deep-Level-Tansient-Spectroscopy (DLTS) (8), Mössbauer-spectroscopy, and neutron activation analysis of higher sensitivity (9). On the other hand, investigations on thermally induced donors resulted in a correlation of these defects to electrically active iron impurities (2, 10-12). Most of the publications show, however, a wide spread in results as shown in Fig. 1. Various experimentally determined activation energies of iron in silicon are scaled in the bandgap of silicon (2, 5, 7, 11, 13-23). The histogram deduced from these values at the right side of the figure shows a peak at $E_v + 0.42$ eV and a second broader one at $E_c - 0.60$ eV. The spread of values can be caused by (*i*) additional undesired impurities introduced especially during extended treatments of the specimens at high temperatures, (*ii*) iron reactions with dopant atoms or other impurities, and (*iii*) precision of differing method for the determination of the activation energy (resistivity, photoconductivity, Hall-measurements, and DLTS).

In order to avoid systematic errors, more sophisticated experiments were carried out in the present study, regarding specifications of the silicon crystals and utmost cleanliness of specimen preparation and heat-treatment. The undesired introduction of additional impurities was checked and the concentrations

Key words: iron-boron pairs, iron-aluminum pairs, room temperature impurity reactions, haze.

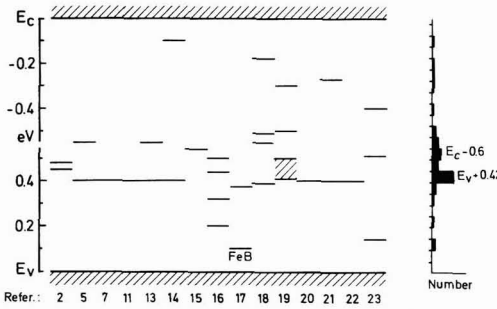

Fig. 1. Activation energies of iron in silicon as published in the literature and histogram deduced from these results.

of defect levels were monitored. The reaction mechanism of iron in p-type silicon was studied by observing variations of the levels as a function of time elapsed after quenching the specimen. This paper shall contribute to clarify the properties of iron in silicon taking into account results obtained by the following measurement techniques: four-point probe, DLTS, carrier lifetime measurements, infrared absorption, and Sirtl-etch technique.

Experimental Procedure

Specimen preparation.—Iron doping experiments were performed on p-type and n-type silicon wafers with resistivities in the range 1-100 Ωcm. The crystals were grown dislocation-free by Czochralski and floating-zone techniques, respectively. Most of the crystals were free of swirl-defects.

Iron contamination was performed either by evaporation of iron onto the polished clean surface of the wafer or by scraping with a piece of iron wire on the rougher back side. Before scraping the iron wire was etched. This procedure, so far, seems to be the cleanest method to obtain intentional impurity contamination.

Diffusion of iron was carried out in an oven with silica tube and specimen holder. The silicon wafer was mounted on top of two oxidized silicon specimens preventing a direct contact of the wafer to the silica substrate holder. The atmosphere in the furnace tube consisted of oxygen or nitrogen. Some diffusions were performed in argon and hydrogen, respectively. High cooling rates were achieved by quenching the specimen in Diffilen, ethylene glycol, or liquid nitrogen. In order to achieve low cooling rates the power of the furnace was switched off.

After diffusion 50-100 μm were removed from both surfaces by etching the specimen in a mixture of nitric acid, hydrofluoric acid, and acetic acid. For applying DLTS, Schottky contacts 1 mm in diameter were evaporated using Pd for n-type and Ti or Mg for p-type silicon. Silicon specimens $2.5 \times 5 \times 25$ mm^3 in size were used for the determination of the carrier lifetime. Ohmic contacts were prepared onto the two small opposite sites of these specimens by rubbing gallium onto the silicon surfaces.

Measurement techniques.—Several measurement techniques were applied in order to gain more information about the properties of iron in silicon. Usual Sirtl-etch technique revealed the distribution of iron after diffusing wafers containing iron scratches on the surface. Four-point probe measurements exhibited the degree of free-carrier compensation after diffusion of iron in p-type silicon. Measurements of the recombination lifetime of minority carriers were carried out by applying an improved photoconductive decay (PCD) technique as reported previously (24).

The reactions of iron with shallow acceptors boron and aluminum were studied by means of infrared absorption spectroscopy which enabled us to determine the concentration of boron and aluminum at low measurement temperatures. For this purpose a Perkin-Elmer 621 double-beam grating infrared spectrometer was used. Specimens 2×2 cm^2 in size were cut from the wafers and cooled to about 25 K with the aid of a CTI Cryogenics refrigerator, which was mounted in the measurement beam. The boron concentration [B] was calculated from the absorption coefficient α of the main absorption band at 320 cm^{-1} applying the following calibration factor (25)

$$[B] = 3.5 \times 10^{13}\, \alpha\ \text{cm}^{-3}$$

No absolute values were determined for the concentration of aluminum.

For deep-level analysis the improved double-correlation equipment (DDLTS) of Lefèvre and Schulz (26) was applied. Spectra were recorded during the cooling cycle of the refrigerator mentioned above. The specimen temperature was determined by means of a calibrated silicon diode. The Schottky diodes were usually supplied with a reverse bias of 5V. The first pulse of 5V resulted in a final reverse bias of zero volts. The second pulse was adjusted to 1V. Pulse durations of 70 μsec were used. An emission time of 1.42 msec was achieved by adjusting the correlator-windows at 1 and 2 msec, respectively. Most of the spectra were recorded between 310 and 50 K.

In order to determine the activation energy of an unknown defect level the temporal signal decay was studied for several fixed temperatures in the region of maximum DDLTS-signal. The decay curves were stored in 100 storage channels of a Waveform Eductor and the corresponding lifetime was determined with the aid of a digital voltmeter and a calculator. The activation energy finally resulted from the best fit of an Arrhenius plot.

Experimental Results

Intentionally iron-doped silicon.—Intentionally iron-doped n- and p-type silicon specimens exhibited no deep-level impurities in DLTS if slow cooling rates were applied after iron diffusion. Quenching n-type silicon specimens after iron diffusion resulted in two levels of minor concentrations in the upper half of the bandgap which, however, were not correlated to iron. They appear after any etching procedure showing a steeply decreasing concentration towards the bulk of the wafer.

Quenching p-type silicon specimens after diffusion of iron resulted in one strongly marked deep-level impurity with an activation energy of $E_v + 0.43$ eV. This level was also observed in n-type silicon when light pulses were applied for discharging the defects. The same level was found in iron-doped p-type silicon specimens which were slowly cooled from 900°C for the first time, shortly annealed at 900°C for a second time, and finally quenched to room temperature. The concentration of this level depended on the diffusion temperature applied and to a minor extent on the atmosphere during annealing. A reducing atmosphere yielded somewhat higher final impurity content in the silicon crystal than an inert gas atmosphere or oxygen. The impurity concentration as a function of annealing temperature was found to be in good agreement with the solubility of interstitial iron as published by Weber and Riotte (ESR results) (1). After iron diffusion in p-type silicon the resistivity of the specimens increased more or less depending on its initial value and the respective iron concentration. At the same time the minority carrier lifetime was considerably reduced.

Room temperature reactions in boron-doped silicon.—In iron-doped p-type silicon crystals containing higher boron concentrations a second shallower impurity level was observed. Its activation energy was

determined to be $E_v + 0.10$ eV. This level was also obtained in high resistivity crystals after a certain period of time elapsed after quenching the specimen. The appearance of this shallower level was accompanied by the disappearance of the deeper level, the sum of both concentrations remaining constant. The time required for this transmutation of impurity levels was found to depend on the initial boron concentration of the starting material, being short for high concentrations and longer for low boron content. After an appropriate time the deep level disappeared completely in all specimens studied so far. Investigations were performed, however, in specimens where the boron concentration always exceeded the iron content in order to enable quantitative measurements by means of DLTS.

During this level transmutation no changes were observed neither in resistivity nor in carrier lifetime, both of which were compatible with the respective change in impurity concentration. Soon after quenching the iron-doped specimens the concentration of the boron acceptor was strongly reduced, as determined by means of infrared absorption spectroscopy. A further storage of this specimen at room temperature for several days resulted only in an additional minor reduction in boron concentration although the level transmutation in similar material took place within this period of time.

Reaction in aluminum-doped silicon.—Experiments performed on a p-type silicon crystal doped with boron and aluminum resulted in the formation of two further levels after a certain period of time elapsed after quenching the iron-doped specimen. The activation energies of these levels were determined to be $E_v + 0.13$ and $E_v + 0.21$ eV, respectively. Besides the disappearance of the boron acceptor, infrared absorption spectra showed a considerable reduction in the absorption bands correlated to the aluminum acceptor. These results are shown in Fig. 2. The concentration of the aluminum acceptor still decreased with the storage time of the specimen at room temperature. The two additional DLTS signals $E_v + 0.13$ and $E_v + 0.21$ eV correlated to aluminum increased in the same way with the elapsed time as the boron-correlated signal ($E_v + 0.10$ eV), whereas the deep level ($E_v + 0.43$ eV) decreased simultaneously as shown in Fig. 3.

Reactions during illumination of boron-doped silicon.—When the level transmutation in boron-doped p-type silicon was terminated, resulting in only one impurity level at $E_v + 0.10$ eV, the reaction could be

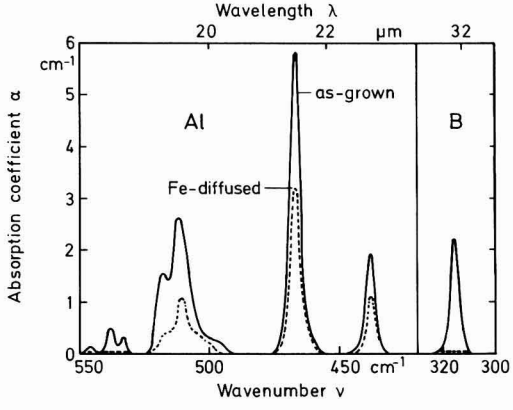

Fig. 2. Reduction of aluminum and boron infrared absorption bands due to complexing with iron observed at 25 K in a p-type silicon wafer doped with boron and aluminum before (solid curve) and after (dashed curve) iron diffusion.

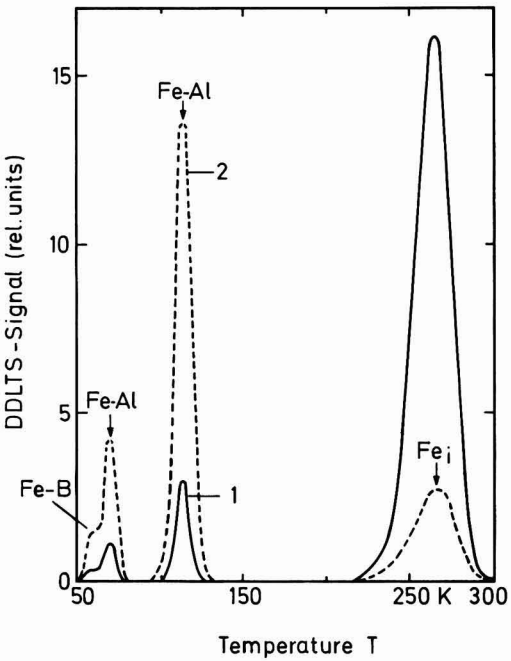

Fig. 3. Deep-level spectra after iron diffusion in a p-type silicon crystal doped with boron and aluminum at two different elapsed times (1: solid curve = initial, 2: dashed curve = final) after quenching of the specimen.

reversed in a rather short time by illuminating the specimen with intense white light. This was carried out by focusing the light of a 50W halogen lamp on the surface of the silicon specimen. The illuminated area amounted to about 0.5 cm in diameter. During illumination the specimen was kept at room temperature by mounting it on a heat sink which was cooled by the aid of compresed air. After illuminating the specimen for 1 hr Schottky contacts were evaporated again and deep levels were monitored. As in the initial state soon after quenching the specimen the impurity was concentrated in the 0.43 eV level. This is shown in Fig. 4. Similar results were obtained repeatedly in crystals of various specifications. Infrared absorption spectra showed an increase in boron concentration with the duration of the illumination. For the application of infrared absorption the illuminated area was considerably extended and the intensity of the light correspondingly reduced. After illumination was terminated the level transmutation from the deeper to the shallower one preceeded as observed soon after quenching the specimen.

Annealing properties of boron-doped silicon.—During transmutation of the 0.43 eV level into the 0.10 eV level a storage of the iron-doped specimen at elevated temperature (100°C) was obviously of no influence. This is shown in Fig. 5 phase 1, where the ratio of the concentration of 0.10 eV level to the total concentration is plotted as function of storage time at 100°C. When, however, the transmutation was terminated (after about 10 days room temperature storage, phase 2) the ratio of the concentration of the shallow level to the total iron content proved to be dependent on the temperature resulting in a thermal equilibrium. This is shown in Fig. 5 and 6 as function of annealing duration at 100° and 130°C and temperature, respectively. At higher temperatures this equilibrium shifted to increasing deep level and vanishing shallow level.

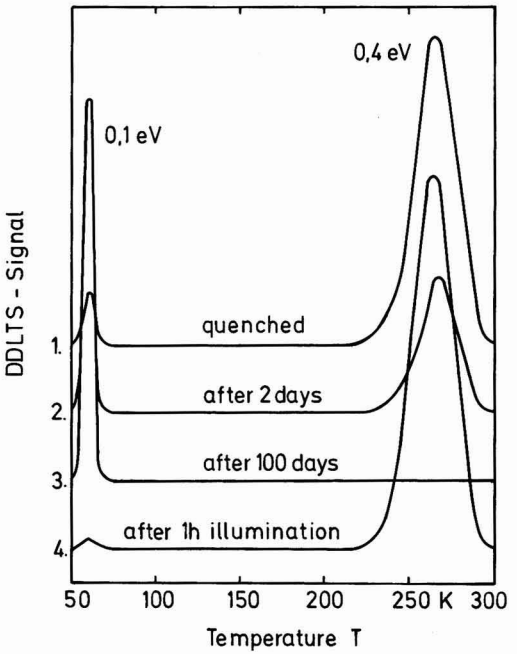

Fig. 4. Deep-level spectra after iron diffusion in boron-doped p-type silicon at three different elapsed times after quenching of the specimen and finally after illumination of the specimen.

Beyond about 150°C the total concentration of both levels decreased after extended annealing durations. This latter reaction was accelerated at higher temperatures. At the same time the boron (and aluminum) acceptor increased finally up to the initial value of the starting material as deduced from infrared absorption spectra and shown in Fig. 7. Simultaneously the resistivity of the specimen was restored. The electrical activity of the iron impurity could not be restored before a second treatment at high temperatures and quenching was performed.

Diffusion properties of iron.—Even during quenching iron-doped silicon wafers from high temperatures iron tends to diffuse to the surfaces of the specimen. This resulted in lower iron contents for shallow penc tration depths. In order to obtain bulk values the surfaces were removed after heat-treatment. Moderately fast cooling rates after iron diffusion (within 5 min from 1050°C to room temperature) already resulted in the formation of precipitates which were detected by x-ray topography. Whereas the Lang-topography exhibited the area of distorted silicon lattice the section topography showed an accumulation of precipitates within the middle of the wafer. Towards both surfaces the density of precipitates was strongly reduced. The distribution of iron after diffusion was also detected by usual Sirtl-etching of the wafer showing an accumulation of shallow etch pits in the same area as marked by the Lang-topography. The distribution of these etch pits is frequently called "haze." One example is shown in Fig. 8. The symbol "Fe" was scratched on the back side of a Czochralski-grown p-type silicon wafer with the aid of a piece of iron wire. The wafer was then annealed at 1150°C for 10 min, moderately cooled to room temperature within 5 min, and treated by Sirtl-etch. For taking the photograph the wafer was illuminated by means of a spot light. Whereas the Sirtl-etch technique works for Czochralski-grown and floating-zone silicon, x-ray topography resolved precipitates and strain only in the case of Czochralski-grown silicon. This is probably caused by the larger size of precipitates in pulled crystals due to initially formed oxygen agglomerates.

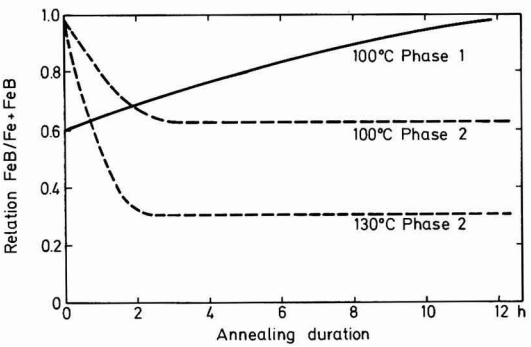

Fig. 5. Ratio of the concentration of the 0.10 eV level and the total iron content as function of storage time at elevated temperatures (100° and 130°C). Phase 1 (solid curve): soon after quenching the specimen, phase 2 (dashed curve): after completing complex formation about 10 days later.

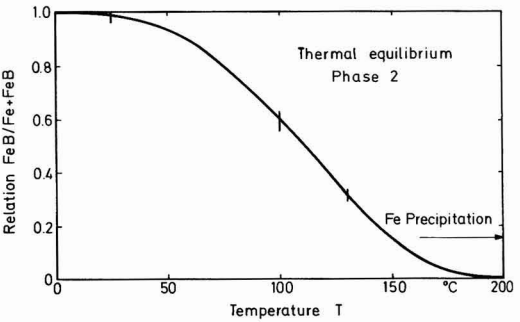

Fig. 6. Ratio of the concentration of the 0.10 eV level and the total iron content as function of storage temperature in phase 2.

Iron content in as-grown silicon crystals.—After having investigated intentionally iron-doped silicon crystals the undesired iron content of some commercially available crystals of various specifications was determined. Measurements were carried out in as-received state and after a short heat-treatment at 1000°C and quenching. Utmost clean conditions were observed for handling and heat-treating the specimens. The iron content of as-received silicon crystals

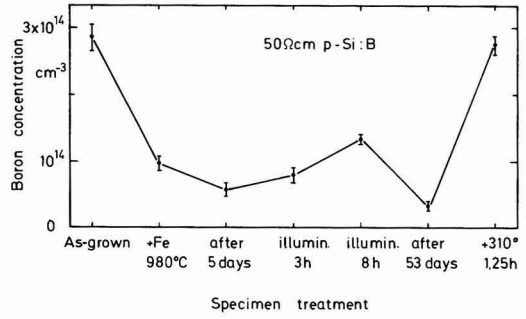

Fig. 7. Boron concentration calculated from infrared absorption of a boron-doped p-type silicon wafer before and after iron diffusion, illumination, and annealing of the specimen.

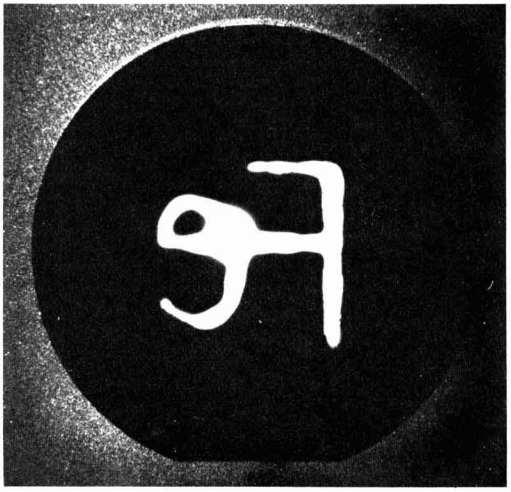

Fig. 8. Czochralski-grown silicon wafer with "Fe" scratched on the back side with the aid of a piece of iron wire, annealed at 1150°C for 10 min and treated in Sirtl-etch.

investigated so far did not exceed the detection limit (about 10^{-4} of the carrier concentration). After quenching these specimens, rather low iron concentrations were observed not exceeding 5×10^{11} cm^{-3} in floating-zone and 5×10^{12} cm^{-3} in Czochralski-grown crystals. These results are in contrast to previous publications (1, 12).

Discussion

From the experimental results the following properties of iron in silicon were deduced: only one impurity level is formed by electrically active iron in n- and p-type silicon situated at $E_v + 0.43 \pm 0.04$ eV. This level is obviously correlated to iron on an interstitial site as detectable by means of ESR spectroscopy. This level has the properties of a donor. The best fit to our experimental results for the solubility of iron in silicon as function of the temperature [Fe] is represented by the Arrhenius equation published by Weber and Riotte (1)

$$[\mathrm{Fe}] = 5 \times 10^{22} \exp(7.3 - 2.87\ \mathrm{eV/kT})\ \mathrm{cm}^{-3}$$

Because of the high diffusion coefficient of iron in silicon even at rather low temperatures, iron tends to precipitate during a cooling cycle if the specimen is not quenched rapidly. The precipitates can be dissolved once more by a second heat-treatment of the specimen up to a concentration corresponding to the respective solubility.

So far no infrared absorption bands correlated to iron in silicon were observed. As a deep level impurity iron reduced the carrier lifetime in n- and p-type silicon. The capture cross section for holes in n-type silicon $\sigma_p^{\circ} = 3 \times 10^{-16}$ cm^2 (27) seemed to be in reasonable agreement with most of our experimental lifetime results. The electron capture cross section in p-type silicon $\sigma_n^{+} = 15 \times 10^{-16}$ cm^2 (27), however, is still doubtful, since the iron donor is not stable in p-type silicon but reacts with all common shallow acceptors even at room temperature.

The iron-boron pairs formed in p-type silicon after quenching the specimen were detected by means of DLTS and a level at $E_v + 0.10$ eV was found. This value is identical with recent results of Feichtinger (17). So far no infrared absorption bands could be correlated to this complex. If the boron concentration exceeded the iron content in the crystal all interstitial iron reacted with boron in an appropriate time which depended on the boron concentration. In the first stage after quenching the specimen this reaction took place quantitatively, independent of the storage temperature within the range 20°-150°C. In a second phase, after termination of the level transmutation, a thermal equilibrium between interstitial iron and iron-boron pairs was observed, following the mechanism

$$\mathrm{FeB} \rightleftharpoons \mathrm{Fe_i}^{+} + \mathrm{B_s}^{-} \quad \text{(phase 2)}$$

This equilibrium could be shifted to the right side by increasing the temperature and by illuminating the specimen, respectively. At higher temperatures exceeding about 150°C most of the complexes were dissociated. Since the thermal mobility of iron is rather high, the iron then precipitated irreversibly after an appropriate time.

In order to explain the reaction mechanism in phase 1 two facts were illuminating: the thermal equilibrium was not observed soon after quenching the specimen and at the same time the concentration of the boron acceptor was strongly reduced although almost no pairs were detected. To explain these observations it was assumed, that the boron acceptor reacted with an intrinsic defect during quenching the specimen. Then the following reaction may take place

$$\mathrm{Fe_i} + \mathrm{B_sI} \rightarrow \mathrm{FeB} + \mathrm{I} \quad \text{(phase 1)}$$

I symbolizes an intrinsic defect being a vacancy or self-interstitial, which is formed at high temperatures in the silicon lattice and which is highly mobile even at room temperature. In the present case a self-interstitial seems more likely to react in the same way as iron on an interstitial site. After the formation of the iron-boron pairs the isolated intrinsic defect can react with a second boron atom or finally diffuse to the surface of the specimen. This reaction proceeds only in one direction because one participant disappears. When all the intrinsic defects have disappeared then the phase 2 reaction takes place.

During the reaction of iron with boron no strongly marked change in carrier lifetime was observed as would be expected during the change of a deep-level impurity into a shallow one. This could be explained by assuming the existence of a second level for the pair which must be situated in the upper half of the silicon bandgap and which must be a deep level. Usually a level in the upper half of the bandgap cannot be observed by DLTS in p-type material by applying Schottky contacts. On the other hand the iron-boron pair is not formed in n-type silicon, so the second level of this pair is not detectable by this method. In some specimens which were highly compensated because of high iron concentrations, however, an additional level was observed after the formation of the complexes was completed. The activation energy of this level was determined to $E_v + 0.6$ eV, so it must be situated in the upper half of the bandgap. This result agrees well with the value $E_c - 0.55$ eV published repeatedly in the literature as an additional impurity level of iron in silicon (Fig. 1). Furthermore in aluminum-doped silicon two levels were detected which were correlated to iron-aluminum pairs.

If an ionic binding in the iron-boron pairs predominates, the charge carriers may be bound to one atom. Only the following three charge states are possible: ($\mathrm{Fe^{\circ}B^{-}}$), ($\mathrm{Fe^{+}B^{-}}$), and ($\mathrm{Fe^{+}B^{\circ}}$). ($\mathrm{Fe^{\circ}B^{\circ}}$) is not existent, since $\mathrm{Fe^{\circ}}$ and $\mathrm{B^{\circ}}$ are always situated on opposite sites of any Fermi level as shown in Fig. 9. The sum of the charge states of iron and boron determines the charge of the complex. From the figure it is deduced that the $E_v + 0.10$ eV level then forms a donor (change from positive to neutral charge) whereas the $E_c - 0.55$ eV level forms an acceptor (change from neutral to negative charge). This assumption would explain all experimental findings and can be extended in the same way to explain the two levels of the iron-

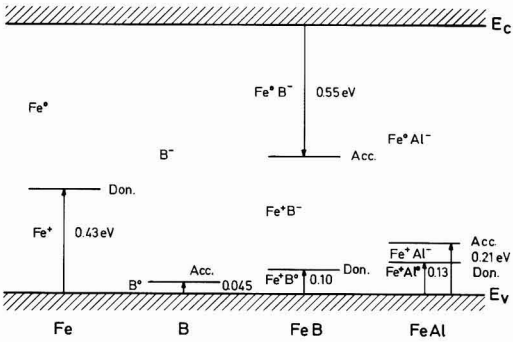

Fig. 9. Activation energies of iron, boron, iron-boron, and iron-aluminum pairs in silicon.

aluminum pairs. In this pair the ionic character of the binding may be reduced so the two levels approach one another. The formation and detection of the iron-boron acceptor level and its correlation to the iron-boron pair should be proved, however, by another measurement technique.

Conclusion

The knowledge of the impurity level of iron in silicon and those of the most frequent iron-acceptor pairs is quite useful for the examination of the impurity content in silicon crystals especially after technological processes for device production. Usually iron is precipitated at least partly. Therefore a certain preparation technique is needed to transform it into a detectable electrically active impurity. The experimental finding, that iron-boron pairs dissociate during illumination of the specimen facilitates the detection of the total iron content of a specimen. The iron analysis is then limited to usual measurement temperatures (270 K). The DLTS-signal of the FeB, however, is not observed at temperatures exceeding 60 K applying an emission time constant of 1.42 msec.

The present investigations were limited to impurity reactions of iron with boron, aluminum, and phosphorus. In order to complete the knowledge about possible reaction mechanisms further impurities should be added intentionally and the resulting deep-level spectra studied.

Acknowledgment

The authors want to thank J. Hilgarth for performing x-ray topographies. They are grateful to Dr. Goldbach for his interest and for stimulating discussions. This work was supported by the Bundesministerium für Forschung und Technologie of the FRG.

Manuscript submitted June 19, 1980; revised manuscript received *ca.* Aug. 29, 1980.

Any discussion of this paper will appear in a Discussion Section to be published in the December 1981 JOURNAL. All discussions for the December 1981 Discussion Section should be submitted by Aug. 1, 1981.

Publication costs of this article were assisted by AEG-Telefunken.

REFERENCES

1. E. Weber and H. G. Riotte, *J. Appl. Phys.*, **51,** 1484 (1980).
2. J. D. Gerson, L. J. Cheng, and J. W. Corbett, *ibid.*, **48,** 4821 (1977).
3. H. Feichtinger, A. Gschwandtner, and J. Waltl, *Phys. Status Solidi A*, **53,** K71 (1979).
4. J. D. Struthers, *J. Appl. Phys.*, **27,** 1560 (1956).
5. C. B. Collins and R. O. Carlson, *Phys. Rev.*, **108,** 1409 (1957).
6. H. H. Woodbury and G. W. Ludwig, *ibid.*, **117,** 102 (1960).
7. W. H. Sheperd and J. A. Turner, *J. Phys. Chem. Solids*, **23,** 1967 (1962).
8. D. V. Lang, *J. Appl. Phys.*, **45,** 3023 (1974).
9. U. Herpers, H. G. Riotte, and E. Weber, To be published.
10. Y. H. Lee, R. L. Kleinhenz, and J. W. Corbett, *Inst. Phys. Conf. Series*, **46,** 521 (1979).
11. H. J. Rijks, J. Bloem, and L. J. Giling, *J. Appl. Phys.*, **50,** 1370 (1979).
12. E. Weber and H. G. Riotte, *Appl. Phys. Lett.*, **33,** 433 (1978).
13. N. T. Bendik, V. S. Garnyk, and L. S. Milloskii, *Sov. Phys. Solid State*, **12,** 1340 (1970).
14. B. J. Boltaks, M. K. Baknadyrkanov, and G. S. Kulikov, *ibid.*, **13,** 2240 (1972).
15. L. K. Ermakov, *Sov. Phys. Sem.*, **12,** 732 (1978).
16. A. O. Evwaraye and P. L. Andersson, in "Semiconductor Characterization Techniques," P. A. Barnes and G. A. Rozgonyi, Editors, p. 61, The Electrochemical Society Softbound Proceedings Series, Princeton, N.J. (1978).
17. H. Feichtinger, *Inst. Phys. Conf. Series*, **46,** 528 (1979); The Institute of Physics, Bristol, London (1979).
18. M. Okuyama, N. Matsunaga, J. W. Chen, and A. G. Milnes, *J. Electron. Mater.*, **8,** 501 (1979).
19. M. A. Abdugafurova, L. M. Kapitanova, L. S. Kostina, A. A. Lebedev, and S. L. Makhkamov, *Sov. Phys. Sem.*, **9,** 450 (1975).
20. M. A. Abdugafurova, A. A. Lebedev, A. T. Mamadalimov, and Sh. Makhkamov, *ibid.*, **8,** 1409 (1975).
21. J. W. Chen and A. G. Milnes, in "Proc. Nat. Workshop on Low-Cost Polycryst. Silicon Solar Cells," T. L. Chu and S. S. Chu, Editors, Dallas (1976).
22. K. D. Glinchuk and N. M. Litovchenko, *Sov. Phys. Solid State*, **6,** 2963 (1965).
23. W. Fahrner and A. Goetzberger, *Appl. Phys. Lett.*, **21,** 329 (1972).
24. K. Graff and H. Fischer, "Carrier Lifetime in Silicon and Its Impact on Solar Cell Characteristics, Topics in Appl. Phys.," Vol. 31, B. O. Seraphin, Editor, p. 173, Springer Verlag, Berlin (1979).
25. B. O. Kolbesen, *Appl. Phys. Lett.*, **27,** 353 (1975).
26. H. Lefèvre and M. Schulz, *IEEE Trans. Electron. Devices*, **ed-24,** 973 (1977).
27. E. Schibli and A. G. Milnes, *Mater. Sci. Eng.*, **2,** 229 (1967/68).

Effects of Multiple Slice Epitaxy and Front End Processing on Generation Threshold Current in Bubble Memory Devices

R. L. Guldi, R. E. Fontana, Jr., and D. C. Bullock

Texas Instruments, Incorporated, Dallas, Texas 75265

ABSTRACT

The factors affecting generate threshold current, Ig, (the minimum current required to reliably nucleate a bubble under a hairpin generator) are reviewed. Ig data are presented for bubble memory devices fabricated using YSL-CaGe garnet (1) epitaxial films with nominal bubble sizes of 5.3 and 3.8 microns. Where multiple slice epitaxy employing large vertical stacks (up to 16 singly spaced slices/stack) is used, it is found that Ig measured on an aluminum generator without overlying Permalloy elements or passivation is shown to depend on position in the epitaxy stack, decreasing by as much as 4 mA (1%) per slice position with increasing depth of slices in the melt. In contrast, slices ion milled to remove a 0.4 micron thick surface layer show no dependence of Ig on stack position. Removal of the surface layer has the additional effect of significantly decreasing the variation of Ig across a slice by up to 67%. These observations are interpreted in terms of the existence of a low anisotropy surface layer approximately 0.2-0.5 microns thick grown as slices are slowly withdrawn from the epi melt without rotation. The properties of this layer are discussed. In particular, the layer is shown to have a lower anisotropy than the bulk film, and it is estimated that the growth rate appropriate to the surface layer is approximately 20% of the value for normal film growth (0.4-1.0 microns/min). Finally the dependence of Ig on subsequent front end processing is presented, and it is shown that the Ig value measured on an aluminum generator without overlying oxide and Permalloy is reduced by approximately 30% after subsequent oxide and Permalloy processing steps.

Generate threshold current (Ig), or the minimum current required to reliably nucleate a bubble under a hairpin generator, is a parameter that must be understood and controlled in order to produce reliable, interchangeable, and easily used bubble memory devices. Some of the factors contributing to Ig variations in devices have been discussed previously by Wolfe and Johnson (2) who have related Ig variation to stress effects in the epitaxial garnet layer due to the silicon oxide and the aluminum metallization and to changes in the stress because of the presence of the overlying layers, and through annealing effects arising during oxide and Permalloy deposition.

This paper describes another major source of Ig variation that can be found in slices grown using multiple slice epitaxy employing large vertical stacks of slices, namely a contribution from an anomalous surface layer on the top of the epitaxial garnet film.

Experimental

Figure 1 shows an artist's concept of the particular type of multiple slice holder used in this study. This holder has capacity for 16 singly spaced, 2 in. diam slices. The circular ring that ties the legs of the holder together for extra strength in the center of the holder separates the top eight slices from the bottom eight and increases the distance between the eighth and ninth slices in the stack, producing an effect on the stack dependence of Ig that will be discussed later.

The generator geometry for this investigation is shown in Fig. 2. The generator element is a conventional hairpin generator, made of evaporated aluminum containing approximately 2 weight percent (w/o) copper, separated from the epitaxial film by a plasma-deposited silicon oxide layer, and patterned by ion milling at an angle of 45 degrees. Silicon oxide and aluminum thicknesses are 4000 and 5000Å, respectively, for five micron bubble circuits and 4000 and 4000Å for three micron bubble circuits. The dimensions given in Fig. 2 apply to a three micron bubble circuit which is a scaled-down version of a five micron circuit as far as considerations dealing with the generator are concerned. All data reported were taken on neon-implanted slices (2.5 E14 at 100 keV for 5 micron films and 2.0 E14 at 100 keV for 3 micron films).

Generate threshold data as reported in this paper are taken on the structure shown in Fig. 2 without overlying oxide and Permalloy layers in order to avoid effects due to stress or problems with the alignment of aluminum and Permalloy elements. Ig measurements are made by contacting the generator lead structure with fine-tipped probes, pulsing the generator with a 500 nsec current pulse with a rep rate of 500 Hz to minimize heating, and increasing the pulse amplitude until the first bubble is observed optically. It is estimated that the Ig values obtained are reproducible

Key words: magnetic garnet epitaxy, liquid phase epitaxy, generate threshold current, multiple slice epitaxy, bubble memory devices.

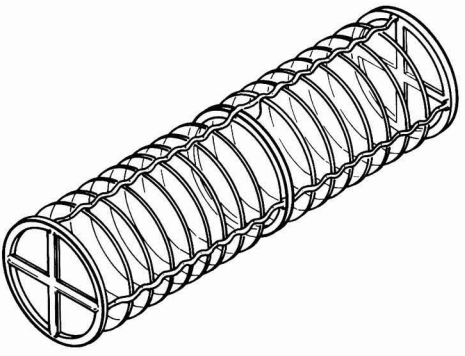

Fig. 1. Slice holder for LPE of 16 singly spaced wafers

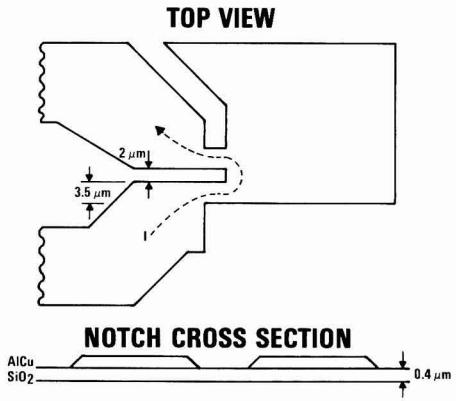

Fig. 2. Generator design for 3 micron bubble circuits

to about ±5 mA. All data presented were taken at room temperature. For consistency the threshold is measured with the bias field 10 Oe below free bubble collapse. It will be noticed that the Ig values discussed throughout the paper are approximately 30% higher than those found in actual packaged devices. This discrepancy arises because Ig decreases with annealing during the high temperature processing used in depositing subsequent oxide and Permalloy layers, as will be described later.

Results

The dependence of Ig on position in the epitaxy holder for a typical epitaxial run is shown in Fig. 3 for three micron bubble films. The X-axis is drawn using a linear distance scale as measured from the top slice holder ring, with numbers labeling the position of each slice in the stack, starting with the No. 1 slice at the top of the stack. The larger than average separation between the eighth and ninth slices results from the presence of the middle support ring on the slice holder (see Fig. 1). The top eight slices in the stack show practically no dependence of Ig upon stack position, but slices in the lower eight positions show a decrease in Ig with stack position of up to 7 mA/slice position.

This type of dependence of Ig on stack position is typical of both 5 and 3 micron bubble films. Run-to-run variations in the degree of stack dependence in the range of approximately 2-7 mA/stack position exist and these are correlated with a variation in epitaxial film anisotropy throughout the stack which is associated with small vertical temperature gradients in the epi-melt. Runs for which the measured film anisotropy is higher for slices from the top of the stack than for slices from the bottom show an increased Ig stack variation compared to runs for which the measured film anisotropy gradient is reversed, but in all cases Ig decreases with increasing stack position. Another common trend is for the Ig value for slices in position 1 and 9 to be slightly less than the average for adjacent slices in the stack, and it is interesting that these films are grown with the device side faced down whereas all other films are grown with the device side faced up. However, the universal trend is that slices from the bottom of the stack exhibit reduced Ig. It should be noted that there is a minimal dependence of Ig on spacer oxide thickness, aluminum thickness, and generator linewidth provided these parameters are controlled within ± 5%.

As an explanation for the dependence of Ig upon stack position, it was proposed that a low anisotropy surface layer grown on the epitaxial film during withdrawal from the melt is responsible for controlling Ig. In order to investigate this hypothesis, 5 micron films from alternating stack positions were ion-milled to remove a 5000Å thick surface layer before ion implanting and beginning generator processing. The results of this experiment are shown in Fig. 4. The unmilled slices exhibit a strong dependence of Ig on stack position, but the milled slices do not. Hence the existence of a surface epi layer which controls Ig was verified.

To investigate this effect further, four slices, one each from positions 2, 6, 10, and 16 of a sixteen slice 5 micron bubble stack, were quartered and each quarter was ion-milled to remove either 0, 2000, 4000, or 6000Å of material before generator processing (see Fig. 5), and generators were fabricated on these quartered slices. The measured Ig values were independent of milled thickness for slices 2 and 6, which are from the top of the stack, but increased dramatically with increasing thickness milled for slice 16, which was grown at the bottom of the stack.

Slices No. 10 and 11 were processed as whole slices. Slice No. 10, which was not milled, showed an Ig value approximately 20 mA less than the slice grown in the adjacent stack position No. 11, which had 6000Å of material removed by milling before generator processing.

Again the quarters of all four slices which received no milling show the same type of dependence of Ig on stack position presented in Fig. 3 and 4, while practically no stack dependence is found on the quarters of the slices which had a sufficiently large thickness removed, namely 6000Å. Hence, one could estimate the maximum thickness of the surface layer for the 16th slice in the stack as approximately 6000Å.

In a related experiment, the variation of Ig over a single slice was investigated. Figure 6 shows the distribution of Ig measured for slices number 2 and num-

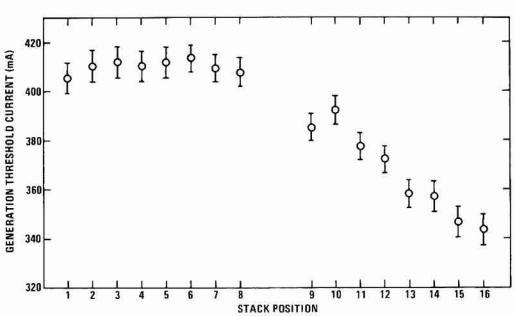

Fig. 3. Average generation threshold current, Ig, on aluminum generators without overlying oxide and Permalloy elements vs. position in the epitaxy slice holder for 3 micron bubble films. Stack position No. 1 is located toward the top of melt.

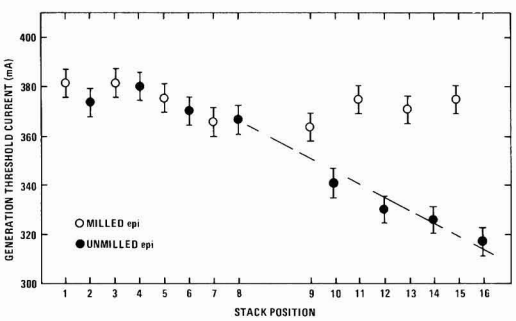

Fig. 4. Average generation threshold current, Ig, on aluminum generators without overlying oxide and Permalloy elements vs. position in the epitaxy slice holder for 5 micron bubble films. Alternate slices were ion milled to remove a 5000Å thick surface layer before beginning generator processing.

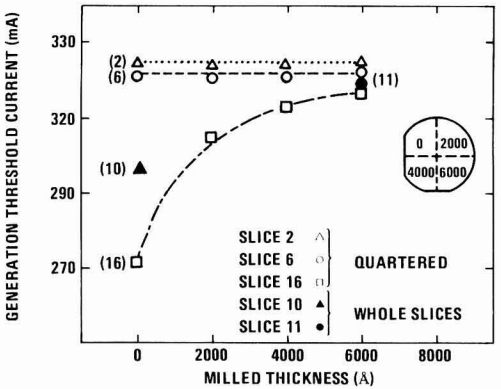

Fig. 5. Average generation threshold current, Ig, on aluminum generators *vs.* thickness of material removed by ion milling before beginning generator processing as a function of stack position. Slices No. 2, 6, and 16 were quartered, and each quarter had a different amount of material removed before processing. Slices No. 10 and 11 were processed as whole slices.

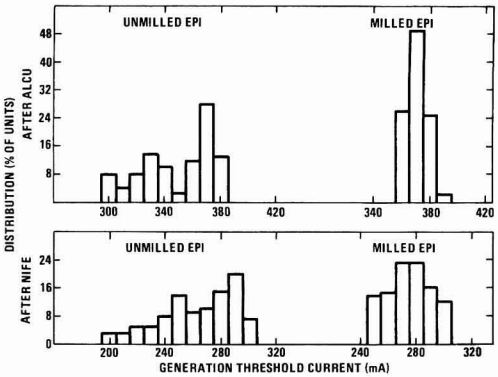

Fig. 7. Ig distribution for all chip positions in a lot of 16 slices from the same 3 micron epitaxial run. Alternating slices were either unmilled or ion milled to remove a 5000Å layer before generator fabrication. Distributions are shown for measurements after AlCu patterning without overlying oxide and Permalloy elements and for measurements after NiFe patterning.

ber 15 in a sixteen slice stack of three micron bubble films. A tighter distribution of Ig about the mean value is found for the slice from the top of the stack (σ = 3.8 mA for slice No. 2 *vs.* σ = 6.7 mA for slice No. 15). Consistent with previous data, slice No. 15 also shows a lower value of Ig.

The Ig distribution for all chip positions in all 16 slices from the same three micron epitaxial run was also investigated. Alternating slices were either unmilled or milled to remove a 5000Å layer before generator fabrication. The Ig distributions measured after aluminum patterning and also after Permalloy patterning are shown in Fig. 7. For this lot after aluminum patterning, a fairly narrow distribution was observed for milled slices, while a broader distribution was observed for unmilled slices. After the NiFe was patterned, both distributions broadened somewhat with the unmilled distribution still broader than the milled. In this example, the Ig broadening arising from epi-related effects is approximately 3 times more significant than broadening related to aluminum or Permalloy processing.

In order to confirm the existence of a surface layer of composition different from the bulk, SIMS or ion probe profiles of composition *vs.* depth were obtained for epitaxial films. Figure 8 shows one such profile for a three micron bubble film. For simplicity the Y, Ca, and Fe profiles which were relatively constant are not shown. Similar results have been obtained for both three and five micron films. In general there exists on all films a surface region with a composition significantly different from the bulk of the film, although the exact nature of the profiles in the surface region varies considerably from epi run to epi run. For the slice at the bottom of the stack, the thickness of the surface region is approximately 5000Å. Usually the surface region is lower in components that contribute to anisotropy such as samarium and lutetium, or it is lower in germanium content than the bulk, a condition that would tend to increase $4\pi M_s$ and decrease anisotropy.

The existence of an anomalous surface layer on epitaxial films is consistent with the basic understanding of the epitaxial growth process. During the growth of the primary film, extensive melt mixing occurs because of the stirring action of the rotating slices. Indeed mixing is required in order to maintain the proper concentrations of the various components sufficiently near the surface of the growing film to incorporate the correct amount of each component into the film as required to achieve desired film properties (3-5). It has also been shown that the rotation conditions used during immersion of slices into an epi melt can significantly affect film coercivity and lattice parameter because of compositional variations near the film-substrate interface (6). After primary film growth terminates, the stack of slices is slowly withdrawn from

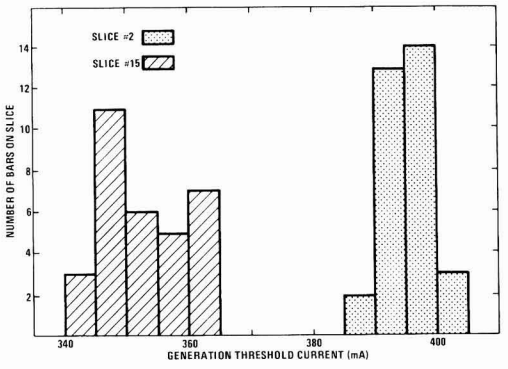

Fig. 6. Distribution Ig for slices No. 2 and 15 in a 16 slice stack of 3 micron films.

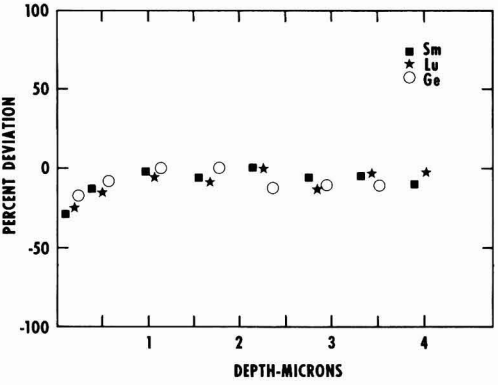

Fig. 8. Composition profiles of garnet wafer determined by ion probe (SIMS). The Y, Ca, and Fe contents were relatively constant.

the melt without rotation in order to minimize the occurrence of flux droplets which cause defects on the slice. The lack of rotation during withdrawal from the melt significantly reduces melt mixing so that growth then occurs under drastically different conditions such as with a reduced growth rate, a wider diffusion boundary at the film-melt interface, and changed values of the segregation coefficients of the constituents. Reduced surface anisotropy at reduced growth rate is consistent with reduced segregation coefficients of high anisotropy components such as samarium and lutetium and with a reduced effective segregation coefficient for germanium, all of which have segregation coefficients less than unity. The reduced samarium and lutetium concentrations directly decrease the anisotropy of the surface layer, while the reduced incorporation of germanium leads to a tendency toward higher $4\pi M_s$ and lower l, conditions which are also associated with reduced anisotropy.

One can estimate the reduction in growth rate that occurs during withdrawal of slices from an epitaxial melt without rotation in the following manner. The milling experiments suggest that the surface layer thickness, t, for a bottom slice in a 16 slice stack is approximately 0.5 microns. For the withdrawal rate of slices from the melt used in this work, 7.5 cm/min, and for conditions in which the bottom slice is grown at a depth of 18 cm below the melt surface, the withdrawal time, T, for the bottom slice is calculated to be 2.4 min. The average growth rate, R' appropriate for growth of the surface layer is then calculated as t/T or 0.21 microns/min. Since R, the growth rate which applies during the growth of the primary portion of the epitaxial film while slice rotation and melt mixing are present, is of the order of 1 micron/min, one can calculate a value for the growth rate reduction factor during withdrawal as $R'/R = 0.21$. Hence during withdrawal, the growth rate drops to approximately 1/5 its normal value.

In order to relate measurements of Ig on aluminum generators without overlying Permalloy elements to measurements on finished devices, we have measured Ig after specific stages of front end processing. Figure 9 shows the reduction that occurred in the average Ig for a slice as it progressed through normal processing and was measured after plasma resist stripping at 75°C, plasma oxide deposition at 350°C, NiFe sputtering at 375°C followed by ion milling and plasma resist stripping. All temperatures cited are nominal. When Ig was measured on slices after generator patterning and then remeasured after annealing the slices through the NiFe time-temperature schedule, a 14% decrease in Ig was found, compared with a 30% decrease when oxide and NiFe layers were actually deposited and patterned. These results are similar to data presented by Wolfe and Johnson (2) who attributed the Ig reduction to a localized decrease in film anisotropy caused by stresses from overlying oxide and metallization layers and to annealing effects which modify the stresses of the conductor metallization on the garnet film.

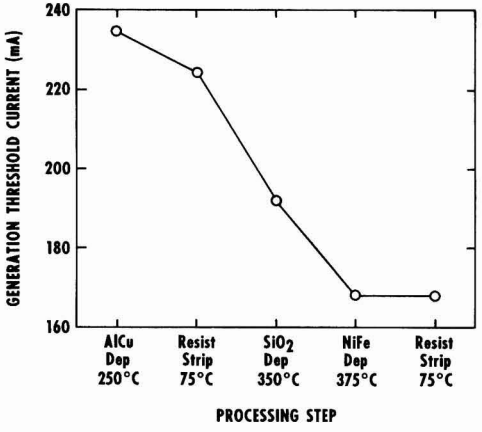

Fig. 9. Generation threshold current after various front end processing steps.

Conclusions

An anomalous surface layer with composition and anisotropy different from the bulk exists on slices grown in large vertical stacks in LPE melts and withdrawn slowly from the melt. Although the composition and anisotropy of this layer depend upon melt temperature and on melt temperature gradient, the primary dependence of surface layer thickness is on stack position, with a maximum surface layer thickness approximately 0.5 micron being found for a slice in the lowest position of a sixteen slice stack. For the withdrawal speeds used, the growth rate during withdrawal from the melt (without mixing) is estimated as 0.2 micron/min for melts in which the nominal film growth rate is 1.0 micron/min.

The variation in generation threshold current due to the anomalous surface layer presents a problem that may become increasingly more severe as film thickness is reduced to produce smaller bubble films required for advanced devices. Although Ig is the only device parameter presently identified as being sensitive to the presence of the surface layer, it is reasonable to expect other device parameters to be influenced by this layer. The control of Ig and other such parameters may involve techniques to reduce the surface layer thickness such as increasing the withdrawal rate or reducing stack height, or it may involve techniques to remove the layer such as milling or etching. Alternatively, new device designs which are less sensitive to epi surface film layers would be attractive.

Acknowledgment

The authors wish to thank Dr. C. Castro and Dr. S. Parker for illuminating discussions leading to the identification of the anomalous surface layer.

Manuscript submitted June 9, 1980; revised manuscript received Sept. 10, 1980.

Any discussion of this paper will appear in a Discussion Section to be published in the December 1981 JOURNAL. All discussions for the December 1981 Discussion Section should be submitted by Aug. 1, 1981.

Publication costs of this article were assisted by Texas Instruments, Incorporated.

REFERENCES

1. S. L. Blank, J. W. Nielsen, and W. A. Biolsi, *This Journal*, **123**, 856 (1976).
2. R. Wolfe and W. A. Johnson, *IEEE Trans. Mag.*, **mag-13**, 1595 (1977).
3. S. L. Blank, B. S. Hewitt, L. K. Shick, and J. W. Nielson, *A.I.P. Proc.*, **10**, 256 (1972).
4. J. E. Davies, G. Galli, and J. C. Suits, *J. Appl. Phys.*, **49**, 1859 (1978).
5. S. J. Lewis, *IBM J. Res. Dev.*, **22**, 422 (1978).
6. S. G. Parker, *Solid State Commun.*, **31**, 403 (1979).

Chemical Reaction of Sulfur Dioxide at High Humidity and Temperature: Implications for Accelerated Testing

Daniel L. Flamm, D. D. Bacon, E. Kinsbron, and Alan T. English

Bell Laboratories, Murray Hill, New Jersey 07974

ABSTRACT

The interaction of SO_2 with humid air was studied in a Teflon chamber (SEAT facility) as a function of flow rate (50-180 std. liters/min), humidity (7-87%), temperature (23°-85°C), and SO_2 concentration (2-9 ppm). Both SO_2 and the reaction products were monitored using wet chemical and pulsed fluorescence techniques. Sulfur dioxide is oxidized to SO_3/H_2SO_4 in dark reactions at elevated temperature and humidity. The experimental data were represented by the rate equation

$$\frac{dp_{SO_2}}{dt} = -k(T)p_{SO_2}p_w$$

where p_{SO_2} is the partial pressure of SO_2 in the chamber, p_w the partial pressure of water vapor, and $k(T)$ the rate constant. The reaction has a low activation energy ($\lesssim$ 5 kcal/mole) and appears to occur in the gas phase rather than on the chamber walls. The significance of secondary corrosive products in the design and use of accelerated tests is covered in detail. When field failure of a device occurs via the attack of SO_2 and water vapor alone, the quantity of product acid in accelerated test chambers should be carefully limited. It is shown how this requirement can be quantitatively specified in the form of an operating diagram derived from the rate expression. Other simulation regimes and the significance of catalytic oxidation processes are also discussed.

Introduction

Accelerated test environments.—Assurance of long-term reliability is an important consideration for most mechanical and electronic equipment in the telecommunications industry. The development of a sound basis for prediction and specification of reliability is thus a vital research and engineering objective. Typically, components are expected to function continuously and without interruption for a number of years. To provide timely information, reliability tests must be short; therefore, they must somehow be "accelerated" with respect to normal conditions of use in order to produce failures within a reasonable period of time.

Usually, elevated temperature and/or high humidity have been used to realize this acceleration: tests at 85°C and 85% relative humidity (RH) have been extensively employed for Bell System studies. Accelerated reliability tests have been used to make qualitative comparisons which are useful for device selection or for identification of the predominant modes of failure (1, 3b, 4). In a few cases there has been a post hoc attempt to determine scaling factors which relate failure times under field conditions to those observed in the laboratory test (2). More often, the extrapolation from laboratory to use conditions is based on some assumptions concerning the mechanism of failure and the dependence of the kinetics of that process on accelerated test parameters.

The concern with chemical pollutants in our environment has extended to reliability studies (3). A number of workers (3b, 4, 6) have introduced various pollutants into the test environment in an attempt to mimic the effects of atmospheric contaminants on chemical or "corrosion" sensitive failure. A crucial problem in this work is the unavailability of scientific or empirical guidelines which can be used to specify a suitable polluted atmosphere for use in accelerated tests, or a method to calculate or even to estimate the resulting acceleration factors.

Key words: atmosphere, oxidation, kinetics, corrosion.

Recently, Schwartz and Bacon (5) proposed theoretical guidelines for "Simulated Environment Accelerated Tests" (SEAT). It was assumed that the effect of atmospheric contaminants on failure could be attributed to the solution of these compounds in a thin adsorbed layer of water and by the sequential reaction of dissolved species with devices. With the exception of those involving NO and NO_2, the rate of chemical degradation processes leading to failure were assumed to be of the form

$$r_p = A_p \prod_i C_{is}^{n_i} C_{H_2O,s} e^{-\Delta E/kT} \qquad [1]$$

where A_p is a numerical coefficient, $C_{H_2O,s}$ is the surface concentration of adsorbed water, C_{is} are the average concentrations of contaminants on the surface, n_i is the reaction order (exponent) of the i^{th} component, ΔE is the activation energy, and kT, the Boltzmann constant and temperature. It was further assumed that the surface concentrations, C_{is}, could be obtained by Henry's law equilibria and that $C_{H_2O,s}$ would be nearly a function of relative humidity alone. In general it was presumed that the various atmospheric contaminants underwent no synergistic reactions (outside of the failure interaction, Eq. [1]) as long as the temperature in the accelerated environment was restricted to 85°C.[1]

According to the procedure stipulated by Schwartz and Bacon, accelerated failure would be accomplished by a manipulation of the variables in the rate expression, Eq. [1]. In particular, it was proposed that the rate could be increased by an increase in temperature, thereby relating failure rate in the field to failure rate under accelerated conditions by an Arrhenius law

$$\frac{r_p^{accel}}{r_p^{field}} = e^{\frac{-\Delta E}{k}\left(\frac{1}{T_{accel}} - \frac{1}{T_{field}}\right)} \qquad [2]$$

where ΔE is the activation energy for the failure re-

[1] Several exceptions to this scheme were explicitly given.

action. Relative humidity (RH) was to be held constant—it was argued that the surface concentration of water, $C_{H_2O,s}$, would be nearly unchanged under these conditions. Finally, the concentration of each species in aqueous solution was to be maintained near the upper end of the range of values encountered in field use (3a). It was stated that this would occur if the gas phase partial pressure of each component was adjusted at each temperature in proportion to the corresponding value of its Henry's law constant in a pure solution

$$\frac{p_i^{\text{accel}}}{p_i^{\text{field}}} = \frac{H(T_{\text{accel}})}{H(T_{\text{field}})} \quad [3]$$

There was no experimental confirmation of these propositions.

Schwartz and Bacon (5) constructed a heated Teflon chamber (SEAT facility) in order to apply these principles to actual failure tests in the presence of SO_2, NO_2, and ozone. In initial experiments, employing humid air and SO_2 analysis of the chamber ambient was attempted using a pulsed fluorescence analyzer to monitor the concentration of SO_2; there was an apparent discrepancy between the quantity of SO_2 entering the chamber and that detected in the humid air emerging downstream. This effect was again confirmed in subsequent reliability studies involving the electroplated leads of light emitting diodes (LED's) (6). Furthermore, when SO_2, NO_2, and O_3 were introduced in various combinations, there was a large interaction between contaminants as the loss of each was dependent on the concentrations of the other components.

These results are highly significant since other workers have carried out accelerated tests under the assumption that gases introduced into a test chamber maintain their chemical integrity (7). Kemmerer and Hartwig (7a), for example, assumed that 0.5 ppm SO_2 introduced into a stream of air at 85°C and 80% RH provides an atmosphere containing 0.5 ppm SO_2 for the exposure of metallizations in a test chamber; however the SEAT studies (5, 6) demonstrate that large SO_2 losses occur and, as will be shown, SO_3 and sulfuric acid are the main corrosive agents under those test conditions.

Restrictions on the simple model.—Clearly there are a number of additional assumptions implicit in the simple model, Eq. [1]. As noted by the authors (5), it is assumed that the relative humidity is a proper scaling factor. Consecutive chemical processes of all kinds are neglected. For instance, if pollutant A forms a product B and B is the corrosive agent, then the corrosion process

$$A \rightarrow B \quad [4a]$$

$$B + (\text{Device}) \rightarrow C \quad [4b]$$

cannot, in general, be characterized by a single reaction and activation energy. Thus the attack of metallizations by sulfuric acid, alluded to above, falls outside of the scope of this model. Of course far more complex multiple reaction schemes are conceivable and the actual failure process (as opposed to precursor formation, as illustrated above) may involve several consecutive reactions and even alternate pathways.

The elementary model also neglects mass transfer limitations. A pollutant must be transferred to the interface solution and, ultimately, to the liquid-device interface. In addition, the actual corrosive agent may be formed through intermediate reactions at the gas-liquid or solid-liquid phase boundaries. A simple universal rate of the form given in Eq. [1] can only apply when consumption or transport of reactant in one of these processes is always slow (and therefore dominant) compared with the others. If these requirements are not met, then the rate law and detailed chemistry of failure will be a function of the specific concentrations, temperature, humidity, and gas flow parameters in the test.

Previous studies of SO_2 oxidation.—The oxidation of SO_2 in the atmosphere is an important process in the chemical evolution of air pollutants and as such has received a great deal of attention (8). While there seems to be many parallels with the present study, including synergistic effects on the reaction from NO_2 and water vapor (9), the atmospheric process is photochemical and therefore differs fundamentally from the dark reaction occurring in the present study. In the polluted atmosphere, hydroxyl radicals are formed from photochemical reactions involving other species (*e.g.*, NO, hydrocarbons) and the oxidation process can be quite complex (10). In the laboratory, the formation of SO_3 and subsequent nucleation of sulfate has been studied through photochemical oxidation involving excited states of SO_2 and the ground state of oxygen. In any case the homogeneous photo-oxidation of SO_2 in the atmosphere is very slow ($\sim$ 2%/hr in sunlight at solar zenith) (11). In the presence of water, laboratory photolysis rates (12) are greatly increased (about 200 times), presumably due in part to hydration of SO_2 molecules which promotes H_2SO_4 formation. Negligible oxidation occurs at ambient temperature in the absence of irradiation (12).

The homogeneous dark oxidation of SO_2 has, by comparison, been little studied. Tokunaga *et al.* (13) found that in dry mixtures of SO_2 and high purity synthetic air, no oxidation could be observed, even at 100°C and after irradiation by 10 Mrad of 1-2 MeV electrons. In the presence of water, irradiation produces substantial oxidation. However these workers did not report the rate, if any, of oxidation of the wet mixtures without irradiation. Urone *et al.* (14) found no homogeneous reaction in an SO_2/air mixture ($\sim$ 10-20 ppm) at 25°C and 50% RH. Evidently there are no other published data for the homogeneous oxidation of SO_2 in air at elevated temperature.

A number of workers have investigated the oxidation of SO_2 by molecular oxygen in aqueous solution (15). At 25°C, the oxidation proceeds via the mechanism[2] (15a)

$$SO_{2(g)} \rightleftarrows SO_{2(\text{aqueous})} \quad [5a]$$

$$H_2O \rightleftarrows H^+ + OH^- \quad [5b]$$

$$SO_{2(\text{aqueous})} + H_2O \rightleftarrows HSO_3^- + H^+ \quad [5c]$$

$$SO_{2(\text{aqueous})} + OH^- \rightleftarrows HSO_3^- \quad [5d]$$

$$HSO_3^- \rightleftarrows SO_3^- + H^+ \quad [5e]$$

$$SO_3^= + \tfrac{1}{2} O_2 \rightarrow SO_4^= \quad [5f]$$

where the oxidation of $SO_3^=$ to $SO_4^=$ occurs by a first-order reaction as indicated and no oxidation of HSO_3^- occurs directly. To a good approximation, the rate of oxidation is given by (15a)

$$\frac{d[SO_4^=]}{dt} = 1.58 \times 10^{11} [H]^{-2.16} p_{SO_2} \frac{\text{moles } SO_4^=}{\text{liter-s-atm.}} \quad [6]$$

where p_{SO_2} is the partial pressure of SO_2 in equilibrium with water; the overall reaction appears to be rate controlled by the oxidation of sulfite (Eq. [5f]), even in a static chamber, and the rate was verified for pH between 2 and 6 and temperatures of 3° and 25°C. The reaction rate was zero order with respect to O_2 over a wide range of concentrations.

Finally, it is well known that certain metal oxides catalyze the air oxidation of SO_2 to SO_3 (14) and a number of transition metal ions catalyze the oxidation of sulfite to sulfate in solution (17). The action of some catalysts is clearly very temperature sensitive since, for instance, vanadium and chromium oxides produce very slow oxidation at room temperature (14, 18), whereas vanadium pentoxide is a catalyst for sulfuric acid

[2] It should be noted that some workers studying the oxidation of other sulfur species in aqueous solution were apparently unaware of this previous work and utilized erroneous assumptions for the oxidation of sulfite (16).

production at ~400°C (18). Metallic catalysts also can enhance the photochemical oxidation of SO_2 (14).

In this connection it should also be noted that higher alcohols and phenols inhibit the aqueous oxidation of sulfite (18, 19). The wet chemical analysis, described below, utilized isopropanol as an inhibitor in order to separately collect sulfate.

Scope of the investigation.—SO_2 is one of the most pervasive pollutants and it is known to accelerate failure and corrosion in a variety of situations. Compared to the complex chemistry which occurs in many gas mixtures, or even with other elementary pollutants such as NO_2, SO_2 represents a simple contaminant system. Nevertheless, as mentioned above, several investigators have been unable to obtain a mass balance on humid, SO_2-contaminated air streams entering an empty Teflon chamber; one objective of the present study was to characterize any chemical processes which occur and could account for the loss of SO_2. A second objective was to identify those conditions for which the loss of SO_2 and the formation of secondary corrosive agents would be negligible—only under these circumstances would there be some hope of establishing an analytical relationship between SO_2-induced failure processes in the field and those observed in an accelerated laboratory test environment.

Low concentrations (1-5 ppm) of SO_2 were added to the humid air and the effluent composition was measured as a function of temperature (23°-85°C), humidity (7-87% RH), and flow rate (50-185 std. liters per minute [slpm]) in an empty Teflon (SEAT) chamber. Wet chemical and instrumental analyses were in good agreement and revealed that substantial amounts of SO_2 in the feed gas were converted to SO_3 and sulfuric acid. The kinetics of this reaction were determined and it was found that the loss of SO_2 in an accelerated environment can be minimized by the judicious selection of residence time, temperature, and humidity.

Apparatus and Technique

SEAT flow system.—The SEAT test facility, which has been described previously (5), was modified and used to conduct the present investigation. Its construction and current mode of operation will be discussed briefly.

A schematic of the entire apparatus is shown in Fig. 1. Dry nitrogen and oxygen were metered in a 1:4 ratio through a Tylan mass flowmeter gas blending unit. This stream passed through a packed column containing activated charcoal and molecular sieves to insure the absence of reactive trace impurities. This "synthetic air" then flowed over a humidification tray in the oven that housed the Teflon SEAT chamber and into a mixing plenum leading to the chamber proper (Fig. 2). A precalibrated SO_2 mixture (5% SO_2 in N_2) was metered through a separate mass flowmeter and injected into the mixing plenum (Fig. 2) of the 16 × 17 × 15 in. chamber.

The chamber temperature was measured using a sheathed thermocouple inserted via the exhaust port, and humidity was measured with a Humitemp Model PCRC-55HPT humidity/temperature sensor, a wet/dry bulb system built into the oven, and water collected by condensation of the chamber effluent (water collection

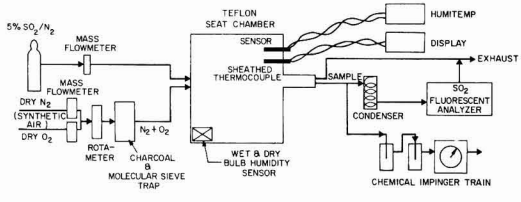

Fig. 1. Schematic of apparatus

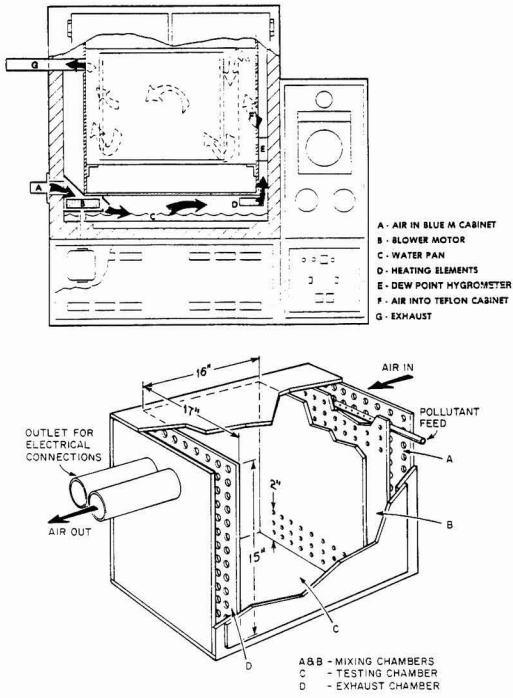

Fig. 2. SEAT Chamber. (a, top) humidity oven and airflow, (b, bottom) chamber detail.

occurred as part of the chemical analysis—see below). SO_2 concentrations in the effluent were determined by pulsed fluorescence while an independent chemical technique was used to analyze SO_2 and the combined quantity of SO_3 and H_2SO_4.

The SO_2 flowmeter was periodically calibrated against a Brooks mercury-sealed piston displacement calibrator and the N_2 and O_2 flow rates were calibrated against a wet test meter. The wick of the wet/dry bulb sensor deteriorated with use and this measurement was not consistently made through all the experiments. In order to insure against chemical degradation of the Humitemp sensor, the remote element was regularly replaced with a new, calibrated unit. The precision of water collection was best at high temperatures and moderate to high humidity; under favorable conditions the humidity determined in this way was in good agreement with the humitemp measurements (±3°C dewpoint).

Sampling and analyses.—SO_2 concentrations reported in previous investigations with the SEAT facility (5, 6a) were determined using the sampling system in Fig. 1 and a Thermoelectron Model 43 pulsed Fluorescence SO_2 Analyzer. While this method of analysis was continued throughout the present investigation, *a priori* its accuracy was uncertain due to possible losses in the sampling process and the failure of previous investigators to obtain an SO_2 mass balance (5, 6a). However, parallel wet chemical determinations made during the present study were in good agreement with the analyzer and thus verified its accuracy (Fig. 3).

The fluorescent analyzer is essentially a transfer standard and must be carefully calibrated to make absolute measurements. Periodically, the analyzer was zeroed and spanned against a dry, standard 1 ppm (nominal) SO_2/N_2 mixture and a dynamic SO_2 permeation tube system. Independently, the 5% SO_2/N_2 supply tank was standardized using the wet chemical procedure (see below) and diluted with "synthetic air" to

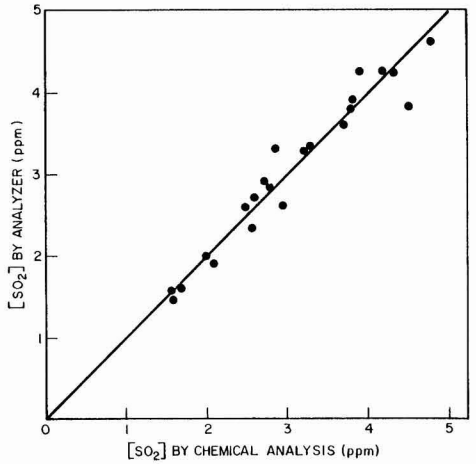

Fig. 3. SO_2 analyzed chemically vs. SO_2 measured by pulsed fluorescence (46°-85°C, 7-90% RH).

verify the analyzer calibration. These procedures were also used to standardize new tanks of SO_2/N_2 mixture.

The atmosphere emerging from the Teflon SEAT chamber is generally hot and humid. Since the analyzer will not function under such conditions, a glass water-cooled condenser was used to cool and dehumidify the gas (Fig. 1). Evidently, negligible SO_2 is absorbed during this process because (*i*) the condensate is acidic due to dissolved sulfuric acid and SO_2 is relatively insoluble in neutral and acid solution and (*ii*) the contact time is short.

A possible cause for the earlier mass balance discrepancies was the oxidation of SO_2 in the chamber. In order to quantify the significance of this process and to account for all products in the effluent, we added a wet chemical sampling train (Fig. 4) and titrimetrically analyzed SO_2 and its oxidation products. The method used was a modification of the hydrogen peroxide "stack sampling" technique (20, 17, 19b). Approximately 100 liters of the chamber effluent was sampled at 0.25-0.5 liter/min into two Smith-Greenberg impingers (Fig. 4). A small auxiliary vacuum pump was used to draw the sample and total gas volume was measured with an in-line wet test meter. Typical collection times were ~2-4 hr. Both impingers were immersed in an ice bath to condense water vapor and the short sample line sloped downward in order to drain any condensate into the first impinger.

Impinger 1 was charged with 150 ml of a fresh solution containing 80% isopropanol in distilled water. The second impinger contained 150 ml of 3% hydrogen peroxide solution. SO_3, H_2SO_4 aerosol, and water vapor in the sampled stream are collected in the first impinger, while SO_2 is captured in impinger 2. After the sample has been collected, dry air is passed through the train for several minutes to sweep any traces of SO_2 in the first impinger out and into the second impinger. SO_2 is relatively insoluble in the aqueous, acidic isopropanol solution in impinger 1 and the isopropanol inhibits the slow oxidation of SO_2 to sulfate in solution (17, 19). The hydrogen peroxide in impinger 2, on the other hand, rapidly absorbs SO_2 and oxidizes it to sulfate (17). The quantity of water vapor collected in impinger 1 was measured by the volume or weight change and provided an independent measure of relative humidity. Negligible water accumulated in impinger 2 under these conditions.

The efficacy of this collection process was verified in several distinct ways. Blank runs using SO_2 alone confirmed that negligible SO_2 was collected in the first impinger. A third impinger with peroxide absorbent was temporarily inserted into the train after impinger 2; this also failed to collect SO_2 and thus proved that impinger 2 had a high absorption efficiency. The combination of SO_2 and SO_3/H_2SO_4 determined by this analysis consistently agreed with the total quantity of SO_2 fed to the chamber. Finally, as already mentioned, these SO_2 analyses were in good agreement with pulsed fluorescence.

The absorbent solutions were analyzed as follows. 80 ml of isopropanol was added to 20 ml aliquots of the impinger samples. These were then titrated with 0.005m $BaClO_4$ using 6 drops of 0.013% methylene blue solution and 6 drops of 0.2% thorin as an indicator (17). At the endpoint of the reaction

$$Ba^{++} + SO_4^{=} \rightarrow BaSO_4\downarrow \qquad [7]$$

the greenish color changes to pink.

Results and Discussion

Reaction and rate.—The chemical analysis revealed that SO_2 is converted to SO_3 and H_2SO_4 in the SEAT chamber. Under steady-state operation, the total sulfur determined by chemical analysis of the product gas was ordinarily within 5% of that based on the feed gas flow rates and there was no accumulation of water or acid in the chamber; therefore any H_2SO_4 so formed must emerge as an aerosol or fine mist. Reaction data for 100 slpm air feed rate and various temperatures are shown in Fig. 5. At high temperature and humidity more than 70% of the SO_2 was converted to products. No significant reaction was observed at 23°C. Experiments performed at constant temperature, humidity, and air flow rate, but with varying concentrations of SO_2 in the feed (2-9 ppm), revealed that the extent of reaction is independent of SO_2 concentration. Thus at least in this 0-10 ppm SO_2 range, the curves in Fig. 5 apply for any concentration of pure SO_2 introduced into the SEAT chamber.

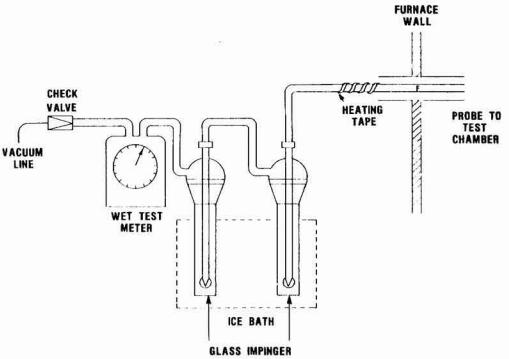

Fig. 4. Impinger train for sample collection

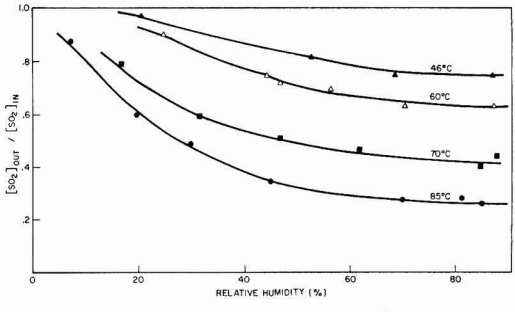

Fig. 5. Unreacted fraction of SO_2 vs. relative humidity at 100 slpm and various temperatures. SO_2 concentrations were 5-7 ppm.

If the kinetics of this reaction process were of the form given by Eq. [1], where relative humidity determines $C_{H_2O,surf}$, then the logarithm of SO_2 conversion plotted against RH would be a straight line at each temperature; however the data do not support this hypothesis. In fact the data are consistent with the first-order rate equation

$$\frac{dp_{SO_2}}{dt} = -k(T)p_{SO_2}p_w \qquad [8]$$

This may be seen as follows. Equation [8] is integrated to give

$$\ln\frac{p_{SO_2,out}}{p_{SO_2,in}} = -k(T)p_w\tau \qquad [9]$$

where τ is the mean residence time. If the chamber gas is well mixed

$$\tau = \tau_0 \equiv V/F \qquad [10]$$

where V is the volume of the chamber, approximately 66.86 liters, and F is the total combined volumetric flow rate of air and water vapor entering the chamber (the volume of SO_2 is neglected). On the other hand, even if mixing were incomplete, τ and τ_0 would only differ by a constant factor as long as the degree of mixing were insensitive to changes in the flow rate. Equation [9] may then be rewritten in the form

$$\log_{10}\frac{p_{SO_2,out}}{p_{SO_2,in}} = -k'(T)p_w\tau_0 \qquad [11]$$

where

$$k'(T) = k(T)\frac{\tau}{\tau_0}\log_{10}e \qquad [12]$$

If the data obey this relation, a plot of log ($p_{SO_2,out}/p_{SO_2,in}$) against p_w will form a distinct straight line at each temperature. Figures 6 and 7 show the experimental data plotted in this fashion. If the 85°, 50 slpm data (upper line) in Fig. 7 are temporarily disregarded, it may be concluded that the results are indeed in satisfactory agreement with Eq. [11].

As noted, the 85°C, 50 slpm data form a distinct group. While superficially, this appears to be contrary

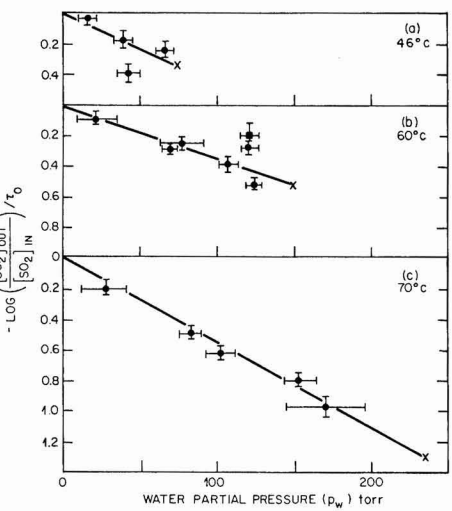

Fig. 6. $-\log\frac{[SO_2]_{out}}{[SO_2]_{in}}/\tau_0$ vs. p_w at (a) 46°C, (b) 60°C, and (c) 70°C. The dry air flow rate was 100 slpm except (■) 50 slpm. Inlet SO_2 concentrations ranged from 5 to 13 ppm. The lines terminate at saturation (100% RH denoted by x's).

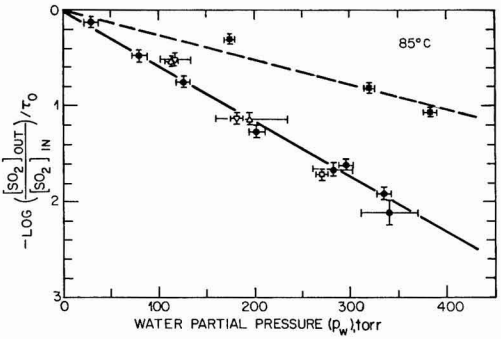

Fig. 7. $-\log\frac{[SO_2]_{out}}{[SO_2]_{in}}/\tau_0$ vs. p_w at 85°C. (■) 50 slpm, (●) 100 slpm, (▽) 120 slpm, (□) 150 slpm, (△) 180 slpm dry air flow rates. SO_2 concentrations ranged from 5 to 11 ppm. The lines terminate at 100% RH [p_w (85°C) = 433.6 Torr].

to Eq. [11], it is possible to rationalize these data within the above framework. Feed gas entering the bottom of the chamber wall (Fig. 2) creates a complex flow pattern due to entrainment of the surrounding fluid, the effect of nearby surfaces, and, possibly, flow separation. Temperature gradients may also influence the flow. Since the Peclet number (based on the lengths subtended by the feed jet array) is large (~350) and the Reynolds number is moderate ($N_{Re} \approx 500$), the mixing within the chamber is primarily brought about by flow circulation rather than diffusion or turbulence. By analogy to other hydrodynamic phenomena, it is reasonable to assume that this circulation pattern will exhibit drastic changes at particular values of the Reynolds number. Thus without direct experimental evidence, it might be assumed that there is less circulation at the lowest flow (50 slpm, 85°C); this will lower τ. A decrease in τ results in a smaller $k'(T)$, (Eq. [12]) which is in accordance with the data.

The available precision and range of the present data foreclose the possibility of detecting a similar mixing effect at the lower temperatures (60°and 46°C). At low p_w and temperature, little SO_2 reacted and the variability in conversion was comparable to its magnitude. A large p_w cannot be used under these conditions since p_w is limited by the vapor pressure at saturation and this decreases rapidly with temperature (Fig. 6 and 7).

The slopes of the (high flow) 85°C and 60°C lines (Fig. 7 and 8) correspond to rate constants [$k'(T)$] of 0.0058 and 0.0035 $Torr^{-1}$ min^{-1}, respectively. The derived activation energy is ~5 ± 2 kcal/mole, but this is a very crude estimate because of the scatter and the possibility that part of it can be attributed to systematic changes in τ/τ_0.

Mechanism of reaction.—There is insufficient information to infer detailed mechanisms for the oxidation of SO_2 in the SEAT chamber. However, some rather general observations suggest that the reaction does not take place on the chamber walls. A combination of homogeneous reaction, and reaction at the surface of sulfuric acid aerosol nuclei is consistent with recent photochemical oxidation studies and the present data.

Since water vapor is required for the reaction to proceed at a measurable rate, the direct oxidation of SO_2 to SO_3 on the Teflon walls may be excluded. Furthermore, in the presence of water, sulfuric acid should be the principal oxidation product. Sulfuric acid has a negligible vapor pressure and thus any acid produced on wall sites would accumulate in the chamber and absorb additional water vapor from the humid

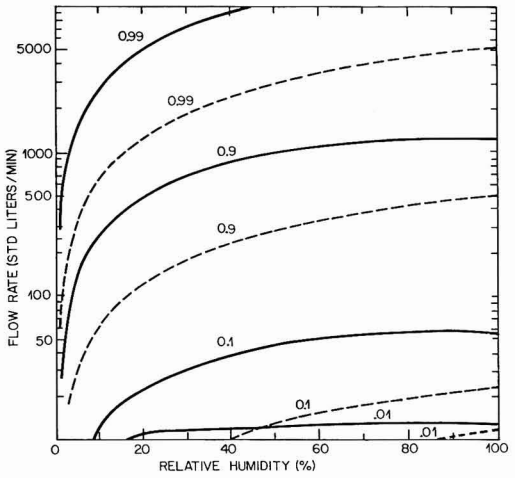

Fig. 8. Theoretical air flow/relative humidity operating curves for a constant fraction of unreacted SO_2 in the SEAT chamber (based on Eq. [13]). Fraction noted on curves. Solid lines (——) at 85°C; dashed lines (- - - -) at 60°C.

gas. Since (*i*) liquid did not normally accumlate in the chamber and (*ii*) essentially all sulfur was accounted for in the emerging product gas, this type of process can be excluded.

It has been proposed (21) that SO_2 may cluster with water molecules in the gas phase at high humidity. Such hydration would facilitate its oxidation and nucleation to form an H_2SO_4 aerosol. The surface of aerosol droplets could, in turn, provide sites for subsequent heterogeneous oxidation within the gas phase. Substantial homogeneous reaction within the liquid phase of aerosol droplets is unlikely, since the total volume of liquid would be small and the rate of this oxidation process (Eq. [5]-[6]) is retarded by low *p*H.

Significances of reliability tests.—These experiments show that secondary products can be highly significant in contaminative humid atmospheres at elevated temperature. Since the temperature, humidity, residence time, and flow profile will greatly influence the chemical environment, the chamber composition should be monitored and these variables manipulated to attain the desired test composition.

Ideally, a test should not be sensitive to small fluctuations in the operating parameters. Thus the temperature, flow rate, and humidity should be chosen so that only a small extent of reaction is possible or, alternatively, so that gaseous reactions proceed to near-completion. These requirements may be expressed as a series of "operating curves" as shown in Fig. 8. In Fig. 8, SEAT isothermal $[SO_2]_{out}/[SO_2]_{in}$ isopleths are shown on the RH-air flow plane. The curves are computed from Eq. [11] using $k'(T)$ values determined from Fig. 6 and 7 (see above). Thus more than 90% of SO_2 in the inlet gas will be unreacted for values of flow and RH which lie above and to the left of the $[SO_2]_{out}/[SO_2]_{in} = 0.9$ isopleths. Likewise, for example, the extent of reaction will be more than 90% for flow and RH values which lie below and to the right of the $[SO_2]_{out}/[SO_2]_{in} = 0.1$ isopleths. In fact, the curves in Fig. 8 may overstate conversion somewhat since they do not include possible effects of flow rate on τ (see Reaction and Rate, above).

Another consideration is the relation of chamber data to field conditions. If field failure of a device occurs via the attack of SO_2 and water vapor alone, exposure to SO_3 and H_2SO_4 may lead to unrepresentative failure modes. In this case the test should be conducted in the low conversion regime of Fig. 8. In other instances, field failure may be induced by sulfuric acid from the dark or photo-oxidation of SO_2 on oxide or metallic surfaces. In that event, a test environment containing SO_2 and its oxidation products may be quite appropriate.

This point has been overlooked in previous studies. Feinstein and Sbar (7b), for example, report that both nickel sulfite and nickel sulfate were formed on the metallizations in their accelerated tests using 0.5 ppm SO_2 at 85°C and 85% RH. While those workers and others (7) attribute the sulfate corrosion to SO_2 attack, this premise should be carefully scrutinized in light of the present findings.

Even when SO_3 and H_2SO_4 are normal ingredients in SO_2 induced field failure processes, more sophisticated analyses will be required to carry out scalable accelerated tests. Consider a case in which SO_2 is catalytically oxidized on the surface of a component under test. The product acid may be responsible for failure in both field and accelerated test environments; however surface reactions will be rate limiting in the field, whereas the supply of SO_3/H_2SO_4 in a chamber can be governed by volume production.

Conclusions

Sulfur dioxide is oxidized during accelerated life test at elevated temperature and humidity. The products are sulfuric acid, and possibly, SO_3. The reaction is first order in SO_2 and water concentrations and appears to occur in the gas phase, either homogeneously or on aerosol nuclei, rather than on the walls of a Teflon test chamber. A rate equation has been formulated to represent the experimental data, but at present its numerical values should only be applied to the SEAT test facility.

In order to conduct meaningful tests which mimic the effects of atmospheric contaminants, it is necessary to consider the oxidation and interaction of pollutants since secondary corrosive agents are formed under accelerated conditions. The acceleration guidelines proposed by Schwartz and Bacon (5) require stringent assumptions which do not appear to be met in practice.

The formation of product acid from SO_2 can be controlled by a judicious selection of operating parameters. The manifolds of constant product formation are two dimensional; it is therefore possible to select various combinations of temperature and humidity which accelerate failure, and simultaneously to control product formation by adjusting the gas flow rate.

Manuscript received July 21, 1980.

Any discussion of this paper will appear in a Discussion Section to be published in the December 1981 JOURNAL. All discussions for the December 1981 Discussion Section should be submitted by Aug. 1, 1981.

Publication costs of this article were assisted by Bell Laboratories.

REFERENCES

1. F. G. Peters and N. Schwartz, TM 77-1528-31; G. T. Kohman. H. W. Hermance. and G. H. Poanes, *Bell Syst. Tech. J.*, **34,** 1115 (1955).
2. J. C. Harrison, *Microelectron. Reliab.*, **16,** 233 (1977).
3. (a) T. E. Graedel and N. Schwartz, *Materials Performance*, **16,** 17 (1977); (b) K. L. Schiff and N. Harmsen, *Z. Elecktrotech (ETZ-B)*, **28,** 896 (1976).
4. N. Harmsen, *ibid.*, **28,** 902 (1976).
5. N. Schwartz and D. D. Bacon, *This Journal*, **125,** 1487 (1978).
6. (a) N. N. Schwartz, G. L. Link, D. D. Bacon, and D. R. Falcone, Unpublished results (1977); (b) E. Kinsbron, D. D. Bacon, and A. T. English, Unpublished results (1978).
7. (a) C. T. Kemmerer and C. T. Hartwig, Unpublished results (1979); (b) L. G. Feinstein and N. L. Sbar, *IEEE Trans. Comp. Hybrids Manuf. Tech.*, **chmt-2,** 159 (1979); (c) L. G. Feinstein

and N. L. Sbar, Unpublished results (1975).
8. R. B. Husar, J. P. Lodge, Jr., and D. J. Moore, Editors, "Sulfur in the Atmosphere," Proceedings of the International Symposium on Sulfur in the Atmosphere, Dobrovnik, Yugoslavia, September, 1977 (Pergamon Press, 1978).
9. K. Iwamoto, N. Presser, and J. Ross, *J. Chem. Phys.*, **68,** 663 (1978).
10. T. E. Graedel, *Rev. Geophys. Space Phys.*, **15,** 421 (1977); T. E. Graedel, "Atmospheric Photochemistry," in *Hand. Env. Chem.*, O. Hutzinger, Editor, In press, Springer (Berlin) 1980; J. T. Herron, R. E. Huie, J. A. Hodgeson, Editors, "Chemical Kinetic Data Needs for Modeling the Lower Troposphere," NBS Special Publ. 57, U.S. Dept. Commerce, Wash. D.C. (1979); R. D. Cadle and E. R. Allen, *Science,* **167,** 243 (1970).
11. H. W. Sidebottom, C. C. Badcock, G. E. Jackson, J. G. Calvert, G. W. Reinhardt, and E. K. Damon, *Env. Sci. Tech.*, **6,** 72 (1972).
12. J. P. Smith and P. Urone, *ibid.*, **8,** 742 (1974).
13. O. Tokunaga, K. Nishimura, and M. Washino, *Int. J. Appl. Rad. Iso.*, **29,** 87 (1978).
14. P. Urone, H. Lutsep, C. M. Noyes, and J. F. Parcher, *Env. Sci. Tech.*, **2,** 611 (1968).
15. (a) S. Beilke, D. Lamb, and J. Müller, *Atmos. Environ.*, **9,** 1083 (1975); (b) W. D. Scott and P. V. Hobbs, *J. Atmos. Sci.*, **24,** 54 (1967); (c) J. M. Miller and R. G. de Pena, *J. Geophys. Res.*, **77,** 5905 (1972); (d) H. A. C. McKay, *Atmos Environ.*, **5,** 7 (1971).
16. D. J. O'Brien and F. B. Birkner, *Env. Sci. Tech.*, **11,** 1114 (1977).
17. J. N. Driscoll and A. W. Berger, "Improved Chemical Methods For Sampling and Analysis of Gaseous Pollutants from the Combustion of Fossil Fuels, Vol. I Sulfur Oxides," National Tech. Inform. Service PB 209 267/APTD 1106 (1971).
18. D. Bienstock, L. W. Brunn, E. M. Murphy, and H. E. Benson, "Sulfur Dioxide—Its Chemistry and Removal From Industrial Waste Gases," U.S. Bureau of Mines, Circular 7836 (1958).
19. (a) H. N. Alvea and H. L. J. Bäckström, *J. Am. Chem. Soc.*, **51,** 90 (1929); (b) D. Flint, *JSCI,* **67,** 2 (1948).
20. Texas Department of Health, Air Pollution Central Services "Compliance Sampling Manual," II41-II-50, Austin, Texas (1972).
21. (a) D. C. Marvin and H. Reiss, *J. Chem. Phys.*, **69,** 1897 (1978); (b) P. Mirabel and J. L. Clavelin, *ibid.*, **68,** 5025 (1978); (c) R. H. Heist and H. Reiss, *ibid.*, **61,** 573 (1974).

Preparation of Tin Oxide Films from Ultrafine Particles

Hisahito Ogawa, Atsushi Abe, Masahiro Nishikawa, and Shigeru Hayakawa

Matsushita Electric Industrial Company, Limited, 1006 Kadoma, Osaka, 571 Japan

ABSTRACT

A highly reproducible procedure for preparing films from ultrafine particles of metal oxides has been developed. The ultrafine particles of several tens of angstroms in size are grown by the evaporation of the metal in low oxgen gas pressure, and subsequently, the film is constructed from the ultrafine particles aligned in a specific direction on the substrate. The particles' size and film structure were studied under various deposition conditions, *i.e.*, oxygen gas pressure, rf activation power, evaporation temperature, and others. The ultrafine particle films prepared with this procedure may serve as a highly sensitive gas sensor.

Increasing attention is being paid to studies on tin oxide materials, especially on the method of preparation of sintered materials and thin films of tin dioxide and evaluation of their electrical properties for gas sensors. It is important to pay special attention to the surface quality of the tin oxide materials, because the change in conductance of gas sensors takes place at the boundary between the gaseous and solid states.

The specific surface area of crystals, *i.e.*, the surface area of the crystals per unit weight (cm^2/g), increases as the particle size decreases. Hence, if one studies the physical properties associated with the crystal surface, such as gas adsorption and light dispersion, the properties are strongly dependent on the particle size (1-3), and may be enhanced with ultrafine particles. In order to supply samples for studying the physical properties of ultrafine particles, we have studied the preparation of ultrafine particles in the size range of several tens of angstroms and films of these particles deposited on a glass substrate.

The preparation methods for fine particles which are usually considered are the following: (*i*) mechanically grinding large particles to a smaller desired size, and (*ii*) nucleation and growth of particles by chemical reaction of the constituent elements under controlled conditions. The latter method, combined with a gas-evaporation technique, which can easily produce low surface distortion, high purity, and small size particles, is preferable to the grinding one. Many studies on the growth and morphology of metallic particles (4-8) have been carried out by the gas-evaporation technique. A few reports have been made on metal oxides (9, 10). None of these studies, however, supplies enough information on the formation of films made with ultrafine particles of metal oxides which is the subject of this report.

We found a new procedure for growing the appropriate ultrafine particles of certain metal oxides in oxygen atmosphere, and subsequently, a method for producing films consisting of the ultrafine particles aligned in a specific direction on the substrate. The details of the preparation and the optimized conditions will be described below.

Key words: ultrafine particle films, tin oxide, gas-evaporation technique, oxygen gas plasma, gas sensor.

Deposition of Metal Oxides

The vacuum deposition chamber used in this study is illustrated in Fig. 1. The specific features arranged in the chamber were (*a*) a quartz cylinder guiding the ultrafine particles from an evaporator boat to a substrate, and (*b*) an rf coil electrode consisting of several turns of stainless steel tubing. The rf coil was operated with a 13.56 MHz oscillator through a matching box.

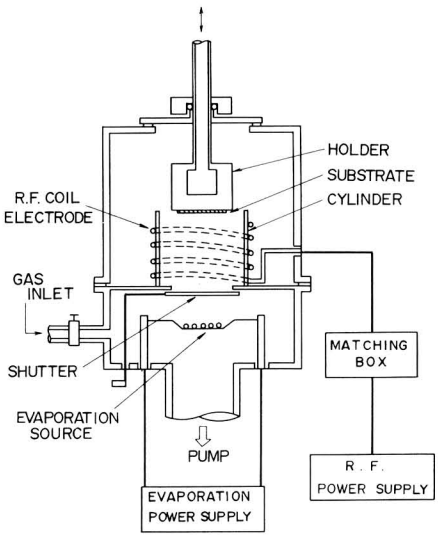

Fig. 1. The apparatus arrangement in this experiment

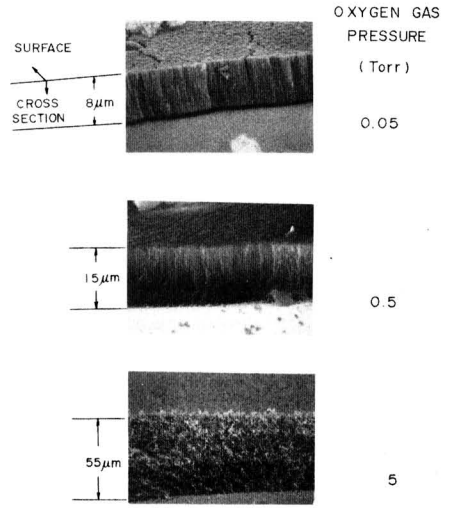

Fig. 2. Scanning electron micrographs showing the stucture of tin oxide ultrafine particle films deposited at three different oxygen gas pressures.

The glow discharge of the oxygen in the vacuum chamber was produced in the region adjacent the rf coil by applying the high oscillating field between the coil and chamber.

The samples were prepared using the following procedures. A glass substrate was supported by a sample holder. A high purity metal (greater than 99.99%) such as Sn, Mn, Zn, or Cu was placed in the evaporator boat. The chamber was pumped down to approximately 2×10^{-6} Torr and then oxygen gas was introduced into the chamber. A glow discharge in the oxygen gas (white color) was produced by applying the rf power. Then power was supplied to the boat to evaporate the metal. The growth of the ultrafine metal oxide particles in the glow discharge of oxygen gas was easily detected with the observation of the discharge color turning to purple (in the case of tin oxide) from white.

When the boat temperature was stabilized, a shutter was opened to deposit the ultrafine metal oxide particles on the substrate. The deposition was continued for several minutes, depending on the desired thickness of the final ultrafine particle film.

The metal oxides deposited on the substrate were significantly dependent, both physically and chemically, upon the oxygen gas pressure in the vacuum chamber. Most of our studies were with Sn as the metallic reactant and are thus the principal subject of this report. Evaporation of Sn metal yields a film consisting of a mixture of SnO_2 and SnO for oxygen gas pressures between 0.1 and 10 Torr. It can be seen that no peaks from tin metal ultrafine particles exist in the x-ray diffraction spectrum, indicating extensive chemical reaction between evaporating tin atoms and oxygen molecules in the chamber. The percentage (Γ) of SnO_2 content in the final products was estimated from the ratio of the intensities of the given x-ray diffraction lines of SnO_2 (at $2\theta = 26.6°$) and SnO (at $2\theta = 29.9°$), with the aid of a calibration curve made from a physical mixture of SnO_2 and SnO powders. As described later, the value of Γ was a sensitive function of the oxygen gas pressure, evaporation temperature, and activation power in the plasma.

The appearance of the metal oxide ultrafine particle films deposited on the substrate is also affected by the oxygen gas pressure. Figure 2 shows photomicrographs, taken by a scanning electron microscope, of tin oxide ultrafine particle films deposited at oxygen gas pressures of 0.05, 0.5, and 5.0 Torr, respectively. It may be seen that the structure and thickness of the ultrafine particle films are markedly dependent upon the oxygen gas pressure and vary from oriented columnar to spongy structures. When the oxygen gas pressure is less than 0.05 Torr, the ultrafine particle film has a smooth, flat surface with an inferior columnar structure perpendicular to the surface of the substrate. For oxygen gas pressures greater than 0.2 Torr, derangement occurs in the columnar structure and the thickness of the ultrafine particle film is increased. The growth of the ultrafine particle film is accelerated with the oxygen gas pressure at 5 Torr, resulting in a spongy appearing film with a rough surface.

Determination of Particle Size

An ultrafine particle film, even a single column in the film, consists of an agglomeration of many ultrafine particles, of the order of tens of angstroms in size. The particle sizes and crystallization of the ultrafine particles were determined first from observation with an electron microscope.

Figure 3 shows an electron micrograph and an electron diffraction pattern of ultrafine tin oxide particles.

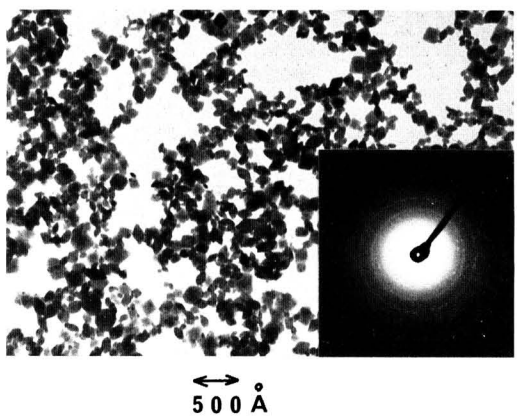

Fig. 3. Transmission electron micrograph and electron diffraction pattern of ultrafine tin oxide particles.

One may see the spotty diffraction rings, indicating that the ultrafine particles are crystallized well. This is consistent with the observation of flat crystal faces in the micrograph. Microcrystallites consisting of octahedra and truncated octahedra are clearly evident (9). The distribution of sizes of the ultrafine particles is log-normal. The sizes of 185 particles on the micrograph were measured by a ruler, and the result is shown in Fig. 4 in a size distribution histogram. The calculated curve of the log-normal distribution is also shown with a solid line. The median particle size (4) D is calculated from the data to be 152Å.

The determination of particle size distribution by the electron microscope may be accurate and precise, but is very tedious. It is found that the mean particle size D of the ultrafine particles can also be estimated from the broadening of the lines in the x-ray diffraction spectrum, by applying Hall's equation (11)

$$\frac{\beta\cos\theta}{\lambda} = \frac{1}{D} + 2\epsilon\frac{\sin\theta}{\lambda} \qquad [1]$$

where λ is the wavelength of x-ray used (in this case, $\lambda = 1.5404$Å), β is the width of the line at the half-maximum intensity, and ϵ is the degree of crystal distortion. The estimated values of D and ϵ (for the same sample observed in the electron microscope) were $D = 160$Å and $\epsilon = 3 \times 10^{-3}$, respectively. This means particle size D is in good agreement with the value of the median particle size D measured using the electron microscope. Thus, we can determine the size of the ultrafine particles by means of the x-ray diffraction lines, instead of the tedious method by the electron microscope. We used the x-ray diffraction method for further size measurements of ultrafine particles in deposited films.

Particle Size Dependence on the Oxygen Gas Pressure

Figure 5 shows the curves of the D values for ultrafine tin oxide particles determined from the x-ray diffraction spectrum as a function of oxygen gas pressure under the evaporation conditions of the evaporation temperature $T = 1100$°C, the rf power $RF = 0$ watt (*i.e.*, no plasma), and the distance between the evaporation source and substrate $L = 7$ cm. Similar results were also obtained with different T and L. The results shown in Fig. 5 indicate that the growth rate dependence of ultrafine particle films of SnO_2 on oxygen gas pressure (P) can be expressed by

$$D = kP^{1/2} \qquad [2]$$

where k is a constant determined by T and L.

The growth mechanism of ultrafine metal oxide particles on the substrate is not yet well understood, even though a mutual collision-coalescence of particles and a complicated chemical reaction of the oxidation between metal atoms and oxygen molecules have obviously occurred during the deposition. Therefore, we cannot propose a model to explain the sublinear dependence of the particle size on the oxygen gas pressure.

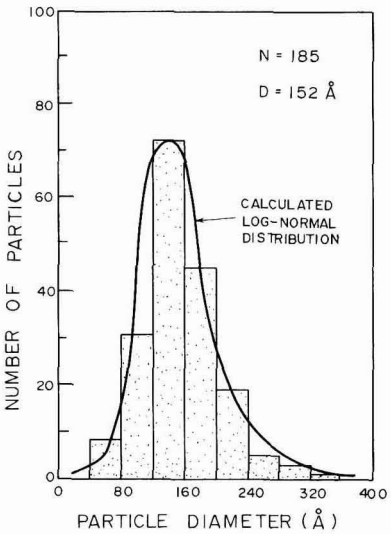

Fig. 4. A histogram of the particle size of tin oxide (shaded). The solid curve represents a log-normal distribution calculated for $\bar{x} = 152$, $\bar{\sigma} = 1.4$.

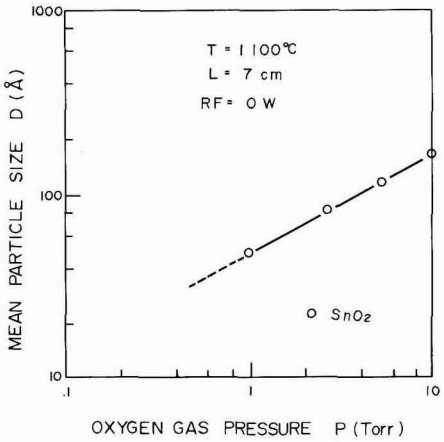

Fig. 5. The mean particle size D of SnO_2 particles as a function of oxygen gas pressure.

Evaporation Conditions for Tin Oxide Films

As already mentioned, the composition of the film of the ultrafine tin oxide particles (*i.e.*, SnO_2 and SnO), as revealed by the x-ray diffraction analysis, is markedly dependent on the evaporation conditions. Figure 6 shows the values of D and Γ as a function of the distance L between the evaporation source and substrate, for two evaporation temperatures of 1100° and 1350°C. For evaporation temperatures below 1100°C, the values of D and Γ are essentially independent of both T and L, ($D_{SnO_2} = 40$Å and $\Gamma = 16\%$). For $T >$ 1100°C, the values of D and Γ are increased with increasing T and L, showing an increase in the content of large SnO_2 particles in the film with T and L. The measured temperature of the oxygen atmosphere for different values of L are also plotted in Fig. 6. These temperature profiles show that in the case of $T =$ 1350°C, the oxygen gas at $L < 7$ cm is heated enough for the conversion of SnO to SnO_2 (the conversion easily occurs above 170°C, as described later). Thus, the increase in the values of both D and Γ is caused by the reaction in the oxygen gas. If $SnO \rightarrow SnO_2$ is the sequence of the reaction of the evaporating metal particles with the active oxygen gas, this reaction would be favored by the particles travelling longer distances, *i.e.*, large D and Γ would result for large L. The heated oxygen gas may be active at the evaporation temperature of 1350°C. When an rf field is applied, the oxygen plasma gas should be very active for oxidation even at a lower temperature. This has been examined for $T = 1100$°C.

The rf power (RF) was varied from 0 to 500W. Figure 7 shows the dependence of D and Γ on the rf power. The mean particle size D_{SnO_2} of SnO_2 particles in the film increased from 40 to 52Å as the rf power was increased to 150W, and the percentage of SnO_2 progressively increased from 16 to 66%. The values of

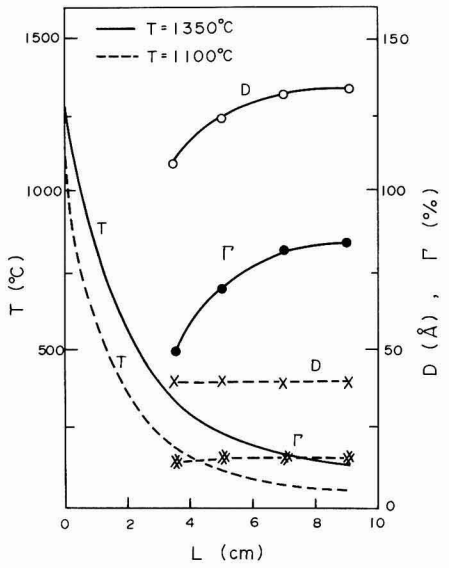

Fig. 6. The mean particle size *D* of tin oxide particles and the percentage Γ of SnO_2 content in films as a function of the distance *L* between the substrate and source. The tin oxide particles were prepared at temperatures *T* = 1350°C and 1100°C.

D and Γ increased linearly with rf power up to 100W and, for rf power greater than 150W, the values of *D* and Γ were almost constant ($D \sim 50$Å and $\Gamma \sim 70\%$). The temperature of the oxygen gas slightly increased during the operation of the rf discharge, less than 150°C even with an rf power of 500W, therefore, the growth of SnO_2 ultrafine particles could not be attributed solely to the temperature rise of the oxygen gas. Thus, the oxidation of SnO ultrafine particle is promoted in the active oxygen gas plasma even though the oxidation is not completed; the value of Γ is saturated at 67%. To obtain a pure SnO_2 film with $D = 52$Å, another treatment was necessary.

In order to understand the conversion of SnO to SnO_2, we have studied the thermogravimetry (TG) and differential temperature analysis (DTA) of the film in air. Two samples prepared under the following conditions were tested.

Sample No. 1 $P = 1$ Torr, $T = 1100$°C, $RF = 150$W, $\Gamma = 66\%$

Sample No. 2 $P = 1$ Torr, $T = 1100$°C, $RF = 0$W, $\Gamma = 16\%$

Figure 8 shows the TG and DTA curves obtained with the temperature rising at a rate 10°C/min. The results show the complete oxidation of SnO to SnO_2 at 300°C. This is confirmed by the x-ray diffraction analysis. The SnO is stable below 150°C. As the temperature is raised, the DTA curve shows an exothermic band, between 170° and 300°C with the peak at 220°C, showing that the oxidation of SnO to SnO_2 occurs in this temperature region. The TG curve shows an increase in weight, in the same temperature range, also indicating the oxidation of SnO to SnO_2. On the basis of these observations, we could say that the conversion of SnO to SnO_2 by means of the heat-treatment is dependent on the initial value of Γ. To confirm the oxidation of SnO to SnO_2, the ultrafine particle films prepared were annealed at various temperatures up to 250°C. Each sample was held for 30 min in air at the given temperature. The results obtained are shown in Fig. 9.

For the ultrafine particle film prepared under no plasma ($RF = 0$W) (Sample No. 2), the values of *D* and Γ increased progressively with annealing temperature, to a maximum of $D = 70$Å and $\Gamma = 84\%$ which did not fit our requirements. Because, in detecting combustible gases, the tin oxide film comprising 100% SnO_2 ultrafine particles (*i.e.*, $\Gamma = 100\%$) has high sensitivity as compared with the film comprising mixed SnO-SnO_2 ultrafine particles. It is also found that there is an optimum particle size for the gas sensing film.

On the other hand, the samples deposited under $RF = 150$W (Sample No. 1) convert completely to pure SnO_2 with only a small increase in size (from 52 to 56Å at 250°C). Observation of the annealed ultrafine particle film with the scanning electron microscope re-

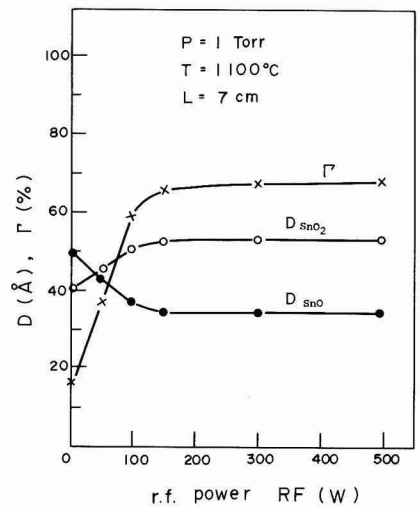

Fig. 7. The mean particle sizes D_{SnO_2} and D_{SnO} and the percentage Γ of SnO_2 content in films as a function of rf power (*RF*).

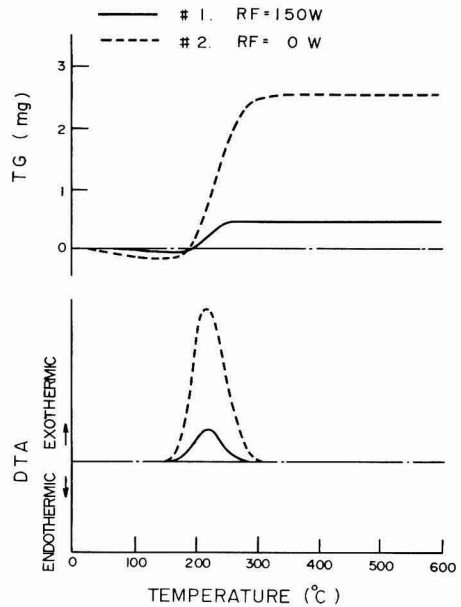

Fig. 8. Thermogravimetry and differential temperature analysis curves of tin oxide particles prepared with two different rf powers, *RF* = 150W and 0 W.

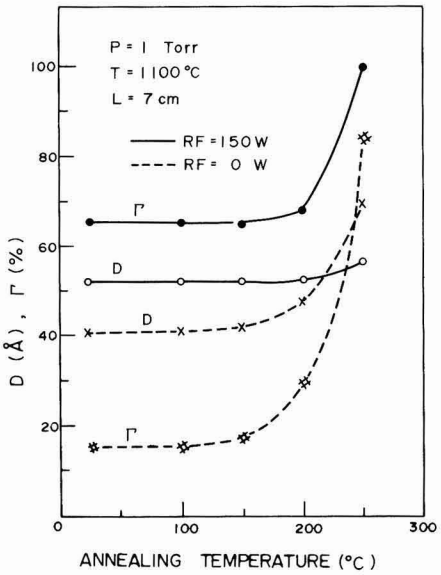

Fig. 9. The mean particle size *D* of SnO_2 particles and the percentage Γ of SnO_2 content in films of Fig. 7 as a function of annealing temperature.

vealed the columnar structure. Thus, the film structure is not altered by the annealing. Because the *D*-values of SnO_2 and SnO ultrafine particles grown at 1100°C in $RF = 150$W are less sensitive to deposition conditions, good reproducibility was obtained for the film.

Summary and Conclusions

We have developed a procedure for preparing a columnar structure film of SnO_2. A film comprising 100% SnO_2 particles about 50Å in size was realized with a high reproducibility by the following procedure. An initial deposit of mixed SnO-SnO_2 ultrafine particles was prepared in an oxygen gas plasma with an rf power input of 150W, subsequent heating of this deposit at 250°C in air for 30 min fully converted the film to SnO_2 without significant particle growth. This film may serve as a highly sensitive gas sensor.

Acknowledgments

The authors would like to express our hearty thanks to Dr. T. Nemoto, Dr. S. Sekido, and Dr. M. Mikoda for their deep interest throughout the progress of the work, and Professor R. Kiriyama and Dr. L. Ozawa for many useful discussions, and Messrs. T. Murakami and M. Fujii for the electron micrograph analysis. This work was supported by MITI subsidy for important technological research and development.

Manuscript submitted July 28, 1980; revised manuscript received Oct. 20, 1980.

Any discussion of this paper will appear in a Discussion Section to be published in the December 1981 JOURNAL. All discussions for the December 1981 Discussion Section should be submitted by Aug. 1, 1981.

Publication costs of this article were assisted by Matsushita Electric Industrial Company, Limited.

REFERENCES

1. D. B. Tanner, A. J. Sievers, and R. A. Buhrman, *Phys. Rev. B*, **11**, 1330 (1975).
2. J. R. Anderson, R. F. Macdonald, and Y. Shimojama, *J. Catal.*, **28**, 147 (1970).
3. J. C. Slater and K. H. Johnson, *Phys. Today*, Oct., 34 (1974).
4. C. G. Graugvist and R. A. Buhrman, *J. Appl. Phys.*, **47**, 2200 (1976).
5. K. Kimoto, Y. Kamaya, M. Nonoyama, and R. Uyeda, *Jpn. J. Appl. Phys.*, **2**, 702 (1963).
6. Y. Saito, S. Yatsuya, K. Mihama, and R. Uyeda, *ibid.*, **17**, 291 (1978).
7. G. H. Comsa F. Hensel, and F. Ringelmann, *Le Vide*, **30**, 113 (1975).
8. M. Rappaz and F. Feas, *J. Appl. Phys.*, **46**, 3273 (1975).
9. C. Kaito, K. Fujita, H. Shibahara, and M. Shiojiri, *Jpn. J. Appl. Phys.*, **16**, 697 (1977).
10. M. Kato, *ibid.*, **15**, 757 (1976).
11. W. H. Hall, *Proc. Phys. Soc., A*, **62**, 741 (1949).

On the Kinetics of the Thermal Oxidation of Silicon

III. Coupling with Other Key Phenomena

William A. Tiller

Department of Materials Science and Engineering, Stanford University, Stanford, California 94305

ABSTRACT

A new model of transformation is proposed which leads to a much reduced excess free energy storage. Silicon is transformed to α-cristobalite plus interstitial Si ions. Subsequent oxidation of these interstitials produces rapid distortion of the lattice and speedy transformation of the structure to vitreous silica. The model allows a satisfactory qualitative explanation of both the orientation and temperature dependence of oxidation-enhanced diffusion (OED), oxidation-induced stacking faults (OISF), interface states (N_{it}), fixed oxide charge (Q_f), oxidation velocity (V), oxide density interface stoichiometry (SiO_x), and silicon interstitial partition coefficient (k_I).

In Part I (1) of this series a general overview was given of the partitioning of the total driving force for the oxidation process into the key parallel subprocesses. Attention was focused on the free volume supply condition needed to sustain such a transformation and on the specific mechanism available for free volume generation. In Part II (2), the transport subprocess was predicted to be electric field and orientation dependent and to involve charged as well as neutral species. The excess free energy subprocess due to the

Key words: semiconductor processing, thermodynamics, point defects, silicon dioxide, interstitials.

large molecular volume difference between Si and SiO_2 was shown to dominate the Si/SiO_2 oxidation and to lead to a possible interface structure wherein a cross-grid of extra half-planes terminated at the Si side of the Si/SiO_2 interface. Propagation of the interface to the Si phase required continuous removal of these extra atoms via one of several mechanisms.

Associated with the oxidation process in Si, there are a number of other phenomena that beckon for understanding. There is the oxidation-enhanced diffusion (OED) phenomenon (3-6), the oxidation-induced stacking fault (OISF) formation phenomenon (5, 7), plus the interface charge (N_{it}) and fixed oxide charge (Q_f) phenomena which all need to be understood in relationship to the oxidation process. One would also wish to understand their orientation and temperature dependences.

The primary purpose of this paper is to present a new way of looking at the oxidation process that allows one to qualitatively explain all of the foregoing phenomena with their associated orientation and temperature dependences as well as the orientation and temperature dependence of the oxidation velocity, V, the interface oxide density, and the interface stoichiometry SiO_x. Some quantitative assessment of these phenomena is given as well.

Analysis

Structural model of phase change.—Let us first consider what crystalline phase of SiO_2 would be the best match to continuously transform Si in the <100> direction. We shall assume that the system selects that phase which lowers the excess free energy contribution, ΔG_E (1, 2), the most, and then we shall look at the consequences of this choice and this approach.

The SiO_2 molecular volume increases from β-quartz (38.8Å^3) to α-cristobalite (43.6Å^3), β-cristobalite (45.3Å^3), and then to tridymite (52.0Å^3) compared to the atomic volume of Si (20.0Å^3) and vitreous silica (44.5Å^3). Transformation of the Si phase to these SiO_2 phases requires massive reconstruction except for the cristobalites and the vitreous phase. Direct intrusion of O atoms between each Si-Si bond in the Si lattice creates the β-cristobalite lattice under a compressive strain of 31%. Similar direct formation of vitreous SiO_2 from the Si lattice results in an amorphous film under a 30% compressive strain. However, the direct formation of α-cristobalite seems to offer a potentially much lower value of ΔG_E.

Consider the (100) face of the Si unit cell and the (100) face of the tetragonal α-cristobalite unit cell whose projections are shown in Fig. 1. In the Si unit cell we have 8 atoms. By completely removing the 4-Si atoms at the ¼ and ¾ positions and slightly displacing the other 4-Si atoms followed by oxidation of these 4 remaining Si atoms, we obtain the α-cristobalite unit cell. This produces a biaxial tension in the film parallel to the interface of $\sim$ 9% and no strain in the perpendicular direction because the unit cell can expand freely in this direction. This would yield a strain energy < 9% of that generated by forming the β-cristobalite directly. However, we still have the 4 removed Si atoms per unit cell to place back into the system in interstitial positions and this will move the system toward compressive strain and will increase the excess free energy. Placing these interstitials into the Si and the SiO_2 at the interface will stretch the respective unit cells to varying degrees depending on the degree of partitioning of these 4 extra Si atoms between the two phases. Thus, if the majority of these extra Si atoms enter the SiO_2, we can expect relaxation to occur at the interface such that some extra half-planes on the Si side will terminate at the interface (see Fig. 2). The number of these planes per unit area of interface will depend on the partitioning ratio of the Si interstitials between the two phases. Since the dangling bonds at the interface ends of these half-planes constitute interface electronic states, this is probably the source of N_{it} (8). We thus see that the magnitude of N_{it} depends critically on the interstitial partitioning ratio at the interface. In addition, we note in Fig. 1 that, at 45° to the α-cristobalite unit cell, the structure is pseudo diamond-cubic with a lattice spacing slightly smaller than that of β-cristobalite. Thus, the proposed transformation leads to a relatively well-matched diamond-cubic phase that is then stressed in compression by the interstitials placed therein. This leads to an increased density of the interfacial silicate and to an interface silicate stoichiometry of SiO_x where $x \approx 1$. If the β-cristobalite phase or the vitreous phase had formed directly from the Si, it would not have been possible to obtain this interface stoichiometry or excess interfacial density.

The key point of this concept is that the SiO_2 forms a suitable structure with extra atoms being placed in interstitial positions rather than forms a structure without interstitials. We shall see later that the former choice is the energetically favorable one. The second point concerning this concept relates to the actual structure that the interface SiO_2 takes. There is only a slight preference for α-cristobalite over β-cristobalite since both produce extra half-planes of Si at the interface that must end up in interstitial positions. There is less reason to choose vitreous SiO_2 because this requires some additional disordering mechanism and there is no rationale for choosing which Si atoms are destined to become interstitial species. We shall see later that a mechanism exists for the rapid transition of the crystalline SiO_2 phase to the vitreous SiO_2 phase within a few molecular distances of the interface. The crystalline SiO_2 phase thus exists only as a buffer layer between the Si and the vitreous SiO_2, but it plays a crucial role in the overall transformation process.

Point defect thermodynamics.—Neglecting any electric field or strain field effects, Appendix A gives the

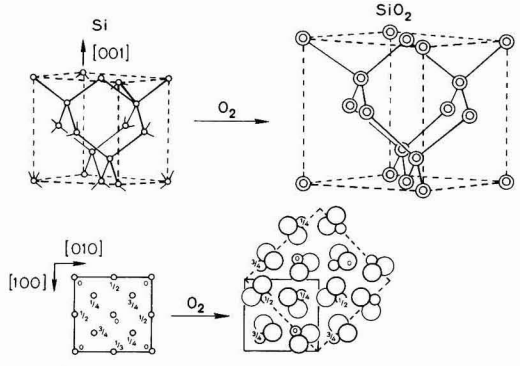

Fig. 1. Projection of the Si and the α-cristobalite unit cells onto their (100) planes. The dashed square represents the pseudo-diamond cubic unit cell of α-cristobalite.

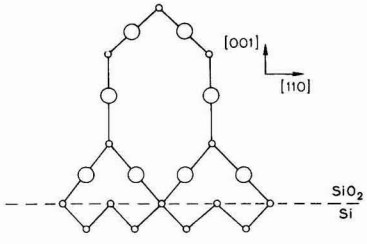

Fig. 2. Projection of Si/SiO_2 interface cross section illustrating the extra half-planes of Si that terminate at the interface with α-cristobalite.

chemical potential of defect species i, i = vacancy (V) or interstitial (I), in each phase j = Si or SiO_2 to be (9)

$$\mu_{ij} = kT \ln \left[\frac{n_{ij}(n_{sij} - n_{ij}^*)}{n_{ij}^*(n_{sij} - n_{ij})} \right] \quad \begin{matrix} i = V, I \\ j = Si, SiO_2 \end{matrix} \qquad [1]$$

Here, n_i is the average number of i-defects per unit cell, n_{si} is the number of possible i-defect sites per unit cell, and n_i^* is the average equilibrium number of i-defects given by

$$\frac{n_i^*}{n_{si} - n_i^*} = e^{\Delta S_i^V/k} e^{-\Delta H_i/kT} \qquad [2]$$

where ΔS_i^V is the vibrational entropy contribution and ΔH_i is the enthalpy of formation of the i-defect. In general, we expect $n_i^* << n_s$ for each phase. For Si, $n_{sV} = 8$, $n_{sI} = 5$ (10), $\Delta H_V = 2.4$ eV while $\Delta H_I \sim 8$ eV (11). For α-cristobalite, $n_{SV} = 4$ for Si, O, or SiO_2 vacancies, while $n_{sI} \sim 15$ (one I-defect adjacent to each O site in a ring), and no information is available on the ΔH values; however, it is well known that many different kinds of interstitial ions enter the interstitial spaces in natural β-cristobalite so it is expected that ΔH_I will be small for this defect in SiO_2 (10). Certainly, it is expected that $\Delta H_I^{SiO_2} << \Delta H_I^{Si}$ (11, 12). For the vacancy species as well as the interstitial species in SiO_2, one must consider Si, O, O_2, SiO, SiO_2, SiO_3, SiO_4, and $(O\text{-}Si\text{-}O)_n$ chains as candidates. For each of these defect species, the free energy change for the phase, ΔG_{ij}, has the form given by Fig. 3 where the minimum gives the location of the equilibrium i-defect content, $n_i^*(\mu_i^* = 0)$. For our interest here, we will generally be interested in i-defect contents far removed from n_i^* where ΔG_{ij} is no longer negative, but may have a large positive value.

Since so little is known about point defects in SiO_2, let us consider the consequences of adding large numbers of I-defects to the Si phase. Since the I-defects are so much more energetic than the V-defects, the free energy of the system will be lowered by recombination events between I- and V-defects. If there were no vacancy sources in the system, the V-concentration would be greatly reduced until its chemical potential, μ_V, had been sufficiently reduced that

$$\frac{\partial G}{\partial n_I} + \frac{\partial G}{\partial n_V} = 0 \qquad [3a]$$

or

$$\frac{n_V n_I}{n_V^* n_I^*} \left[\frac{(n_s - n_I^*)}{(n_s - n_I)} \right] \approx 1 \qquad [3b]$$

Thus, since μ_I will be large and positive, μ_V will be large and negative. At this point, the recombination process no longer lowers the free energy of the system and it will stop. This leaves us with $n_I >> n_I^*$ and $n_V << n_V^*$. In general, we can expect two or three types of vacancy sources in the system. The first is the small voids in the Si created by vacancy supersaturation due to initial cooling of the crystal from the melting temperature. This should give a total potential vacancy supply of $\sim 10^{15}/cm^3$ (*i.e.*, all those formed at the melting point). The second is dislocation lines which can climb in a direction so as to generate vacancies (total potential supply $< 10^{14}/cm^3$, *i.e.*, $\sim 10^3$ lines/$cm^3 \times \sim 4 \times 10^7$ sites/line $\times \lesssim 2500$ climb steps/site). The third is the Si/SiO_2 interface where vacancies in the SiO_2 lattice may transfer to the Si phase. Depending on the kinetics of supply of vacancies from these sources, the vacancy concentration of bulk Si may or may not be reduced to levels such that Eq. [3] is satisfied.

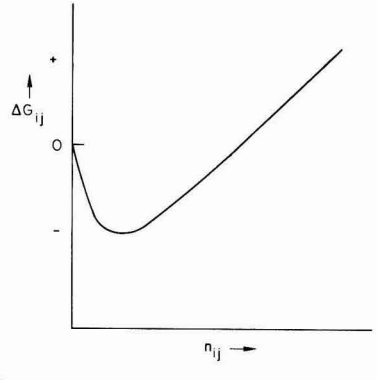

Fig. 3. Excess free energy of formation, ΔG_{ij}, of i-type defects in phase j as a function of number of defects per unit cell, n_{ij}.

The probability of interstitial annihilation, P_A, is given by the product of P_{VN} = probability that a vacancy is in a neighboring site and P_J = probability of a net jump into the vacant site. Thus, since there are 6 possible lattice sites in the ring surrounding each interstitial site, we have

$$P_A = 6X_V \frac{\nu}{6} e^{-Q_A^*/kT}(1 - e^{-(\mu_I - \mu_V)/kT}) = P_A' n_V \qquad [4]$$

where X_V is the fraction of vacancies, $P_A' = P_A/8$, ν is the vibrational frequency, and Q_A^* is the activation barrier between the ring center and a lattice site on the ring. The differential equation governing the interstitial content is

$$D_I \nabla^2 n_I - P_A' n_V n_I = \frac{\partial n_I}{\partial t} \qquad [5]$$

While that governing the vacancy content is

$$D_V \nabla^2 n_V - P_A' n_I n_V + \dot{Q}_V^S = \frac{\partial n_V}{\partial t} \qquad [6a]$$

where $\dot{Q}_V^S$ is the volume source supply rate per unit cell of Si. The strength of this vacancy source is given by (13)

$$\dot{Q}_V^S = \frac{A_V^S}{\Omega^{2/3}} \frac{\nu}{6} e^{-Q_S^*/kT} [f_V^S - X_V e^{(\mu_V - \delta E)/kT}] \qquad [6b]$$

where Ω is the atomic volume of Si, A_V^S is the active area of the vacancy source, f_V^S is the fraction of surface sites from which a vacancy can be introduced into the Si with activation energy Q_S^*, and δE is the energy change of the source due to the loss of one vacancy, *i.e.*

$$\delta E = \left(\frac{dE_V^S}{dr} \right) \Delta r = \frac{2\Omega\gamma}{r} \qquad [6c]$$

for a spherical source of radius r and surface energy γ. In Eq. [6b], μ_V is negative.

Interstitial partition coefficient.—The equilibrium partition coefficient, k_I^*, between the concentration of interstitial species in SiO_2 at the interface to the concentration in Si at the interface will be determined by the quality of the electrochemical potential, η_I, of this defect species, Si_I, in each phase at the interface

$$\eta_I^{Si} = \eta_I^{SiO_2} \quad \text{at} \quad Si/SiO_2 \qquad [7]$$

Neglecting any electric field or strain field effects, Eq. [1] is inserted in Eq. [7] with $\eta_I = \mu_I$. It should be noted in Eq. [1] that the value of n_{Ij}^* is dependent on the actual conditions applying at the interface; *i.e.*, on thermal expansion stresses, disregistry stresses due to interfacial orientation constraints when one alters the Si orientation, and on the presence of electric or macroscopic stress fields. Thus, in general, $\eta_I \neq \mu_I$. These refinements will be considered as second-order effects for this paper; however, it should be recognized that

there will undoubtedly be some circumstances when they may become first-order effects.

We are actually interested in the nonequilibrium partition coefficient, k_I, for the I-defect at the interface. The initial I-defects can be thought of as being created in the α-cristobalite lattice by the breaking of Si-Si bonds (thermally activated process) so that the corner Si atoms are free to become SiO_2 while the 4 inner Si atoms become I-defects. The entrance of the I-defects into the Si side of the interface then involves an activation step because the enthalpy of formation of the I-defect in Si is expected to be much higher than in SiO_2 (11, 12). This is conceptually illustrated in Fig. 4. Actually, instead of the two-step process proposed above, the process of I-defect partitioning is a single-step process which is outlined mathematically in Appendix B. However, because the two-step process is more tractable mathematically at this stage in our understanding, we shall utilize it.

For the two-step process, a chemical potential difference, $\Delta\mu_I(V, \theta)$, develops between the I-defects on the SiO_2 side of the interface compared to the I-defects on the Si side of the interface in order to supply I-defects to the Si at a rate determined by the oxidation rate, V. This can be thought of in analogy with water trickling through a leaky dam; the higher the water level, the greater the leak rate. As indicated in Appendix B, this leak rate is expected to be a function of orientation, θ, because the activation barrier existing right at the interface in Fig. 4 is expected to be a function of orientation. It is also expected to be a function of interface velocity, V, since the flux, J_{I1}, of I-defects into the Si depends on V. Using classical reaction rate theory for the two-step process (see Appendix B), we expect to find

$$J_{I1} \approx Ae^{-Q(\theta)/kT}e^{+\Delta\mu/kT} \qquad [8a]$$

where A is a constant with a slight orientation dependence for a given number of I-defects in the SiO_2 and

$$Q(\theta) = \Delta H_I^{Si} + Q^*(\theta) - \Delta H_I^{SiO_2} \qquad [8b]$$

(see Fig. 4). Thus, instead of Eq. [7], for the zero interface field case we must use

$$\Delta\mu(V, \theta) + \mu_I^{Si} = \mu_I^{SiO_2} \qquad [9]$$

to determine the nonequilibrium interface partition coefficient, $k_I(V, \theta)$.

Utilizing Eq. [9], [7], and [1], k_I is given by

$$k_I(V, \theta) = \frac{n_{I2}(O)}{n_{I1}(O)} = \frac{\beta}{\left[1 + \frac{n_{I1}(O)}{n_{s2}}\left(\beta - \frac{n_{s2}}{n_{s1}}\right)\right]} \qquad [10a]$$

where the subscripts 1 ≡ Si and 2 ≡ SiO_2 and where

$$\beta = \left[\frac{1 - n_{I1}^*/n_{s1}}{1 - n_{I2}^*/n_{s2}}\right]\frac{n_{I2}^*}{n_{I1}^*}\exp\left[\Delta\mu(V,\theta)/kT\right] \qquad [10b]$$

In our case, $n_{I1}^*/n_{s1} << 1$ and probably $n_{I2}^*/n_{s2} << 1$ as well so that the first term on the right of Eq. [10b] is ~1. From Eq. [8a], we also note that $\beta \propto J_{I1}$. Although we do not have any information on $\Delta\mu(V,\theta)$ or on n_{I2}^*/n_{I1}^*, we can evaluate k_I in terms of β. In Fig. 5, plots of k_I and $n_{I2}(O)$ are given as a function of $n_{I1}(O)/n_{s2}$ for a range of β-values. We note that k_I decreases from its saturation value of ~β at very small values of $n_{I1}(O)$ to an inverse dependence on $n_{I1}(O)$ at large values of $n_{I1}(O)$. We note from the previous discussion that $n_{I2}(O) = k_I n_{I1}(O)$ increases toward its ultimate value of 4 per unit cell of Si transformed as $n_{I1}(O)$ increases and at a rate less than linear.

If we make the approximation that $n_{I2}(O) \approx 4$ in the derivation leading to Eq. [10a], then we are led to the result that

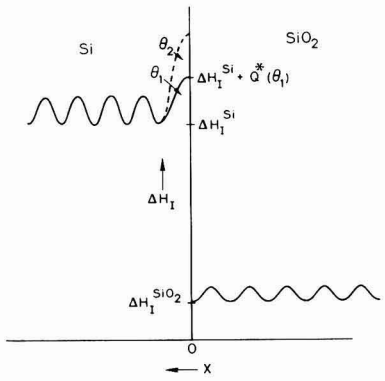

Fig. 4. Schematic illustration of the enthalpy of formation, ΔH_I, for I-defects as a function of distance from the interface. Also included is the interface barrier for two different Si wafer orientations θ_1 and θ_2.

$$k_I \approx \beta\left(1 - \frac{4}{n_{s2}}\right) + \frac{4}{n_{s1}} \qquad [11]$$

since $k_I \approx 4/n_{I1}(O)$. Thus, in this limit, from Eq. [8a] and [10a], we see that $k_I \propto J_{I1}$. For this same approximation, we shall find the excess free energy stored in I-defects, ΔG_E, to be given by (see Appendix A)

$$\Delta G_E = mkT\left\{4\ln\left[\frac{4(n_{s2} - n_{I2}^*)}{n_{s2}n_{I2}^*}\right] + (n_{s2} - 4)\ln\left(\frac{n_{s2} - 4}{n_{s2}}\right)\right\} \qquad [12a]$$

$$\approx mkT\{4\ln(4/n_{I2}^*) + 11\ln(11/15)\} \qquad [12b]$$

assuming that $n_{s2} = 15$ for α-cristobalite. For $n_{I2}^* = 10^{-2}$ and 10^{-4}, this amounts to values of $\Delta G_E \approx 6.5$ and 12.4 kcal/mole, respectively, at ~1100°C. Thus by the type of structural transition involving interstitials proposed here rather than a direct transition with no interstitials, the value of ΔG_E is reduced from ~150 kcal/mole to ~20 kcal/mole for this step in the process.

Interstitial conservation condition.—There are 4 Si atoms per unit cell of Si transformed that become

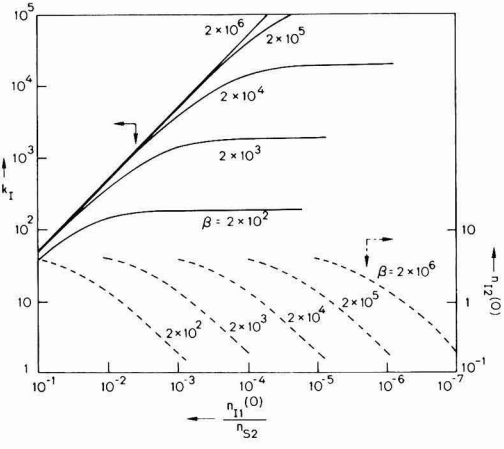

Fig. 5. Plot of k_I and $n_{I2}(O) = k_I n_{I1}(O)$ as a function of $n_{I1}(O)/n_{s2}$ for several values of the parameter β.

I-species. Thus, the interface conservation condition is given, on an Si unit cell basis, as

$$\frac{4V}{\lambda_o^3} = J_{I1} - J_{I2} \qquad [13a]$$

where λ_o is the unit cell size of the Si. Neglecting any interface field effects, this becomes

$$\frac{4V}{\lambda_o^3} = -\frac{D_{I1}\nabla n_{I1}}{\lambda_o^3} - \frac{Vn_{I1}}{\lambda_o^3} + \frac{D_{I2}\nabla n_{I2}}{\lambda_o^3} + \frac{Vn_{I2}}{\lambda_o^3} \qquad [13b]$$

Here, D_{Ij} is the interstitial diffusion coefficient in the j-phase. From Eq. [13b]

$$[4 - (k_I - 1)n_{I1}(O)]V \approx \frac{D_{I1}[n_{I1}(O) - n_{I1}(x_1^*)]}{x_1^*} + \frac{D_{I2}[n_{I2}(O) - n_{I2}(x_2^*)]}{x_2^*} \qquad [13c]$$

where x_j^* is the characteristic diffusion length in the j-phase. In Eq. [13b]and [13c], drift of the interstitial species in either an electric or a stress field at the interface has been neglected. In phase 2, subsequent oxidation of the I-defects tends to fill the interstitial spaces with SiO complexes. This increases the formation energy and decreases the diffusion coefficient of the I-defect with increasing distance from the interface. Thus, an interface field effect must really be introduced to model J_{I2}. Diffusion in this phase extends only a short distance ($x_2^* \sim$ 15Å-25Å) before it is almost completely stopped and D_{I2} has dropped to very small values. This leakage into the region $|x| > |x_2^*|$ is the limiting value of $J_{I2} - (Vn_{I2}/\lambda_o^3)$. The value of $x_1^* \approx \sqrt{\pi D_{I1} t}$ should be used for semi-infinite Si and $x_1^* \approx l$ for an Si slab of thickness $2l$ at times $t \gtrsim l^2/\pi D_{I1}$.

From the earlier discussion, it is clear that $n_{I1}(O)$ and k_I are functions of time, especially since J_{I1} and V are functions of time in the oxidation process. In the limit where almost all of the I-defects remain in the SiO_2, $k_I \propto J_{I1}$ from Eq. [11] and $n_{I1}(O) = b/J_{I1}$ where b is an orientation-dependent constant. With this approximation, the flow of interstitials into the Si can be uncoupled from the flow into the SiO_2 and we can treat each phase in turn. For the SiO_2 phase, we choose $J_{I1} << -J_{I2}$ in Eq. [13a] and let $n_{I2}(O) \approx 4$. For the Si phase, we choose $n_{I2}(O) \approx 4$ and let k_I have the value given by Eq. [11]. Following this procedure, we can consider time-dependent events in each phase.

Consequences for the Si-phase.—The I-defects partitioned into the Si slab of thickness $2l$ will diffuse into the bulk Si and some will recombine with vacancies to deplete the population. At short times, Eq. [5] will govern the diffusion of the I-defects subject to the conditions (*i*) $n_I = 0$ at $t = 0$ for all x, (*ii*) $\partial n_I/\partial x = 0$ at $x = 0$ for all t, and (*iii*) $J = J_{I1}$ from Eq. [8a] at $x = \pm l$ for all t. Initially, let us assume that $P_A' = 0$ (no interstitial sinks) and look for a solution in the time domain $t \gtrsim 10^3$ sec. In this time domain, diffusion in a slab $l \sim 10^{-1}$ cm with $D_I \sim 10^{-5}$ cm²/sec is almost complete. If we assume that diffusion is complete, then we have the average slab I-defect concentration, $\bar{n}_{I1}$

$$\bar{n}_{I1} \approx n_{I1}(O) = \frac{1}{l}\int_o^t J_{I1}dt' \qquad [14]$$

which leads to

$$\frac{dn_{I1}(O)}{dt} = \frac{J_{I1}}{l} \qquad [15]$$

Combining Eq. [1] and [9] with [8a], we find that

$$J_{I1} = Ae^{-Q(\theta)/kT}\left[\frac{(n_{I2}/n_{I1})(n_{s2}/n_{s1})n_{s1}}{(n_{I2}^*/n_{I1}^*)(n_{s2} - n_{I2})}\right] \qquad [16a]$$

which yields

$$n_{I1}(O) \approx \frac{4}{J_{I1}}Ae^{-Q(\theta)/kT}\left[\frac{n_{s2}(n_{I1}^*/n_{I2}^*)}{(n_{s2} - 4)}\right] \qquad [16b]$$

Inserting Eq. [16a] into Eq. [15] leads to

$$n_{I1}^2(O) \approx \frac{8Ae^{-Q(\theta)/kT}}{l}\left[\frac{n_{s2}(n_{I1}^*/n_{I2}^*)}{(n_{s2} - 4)}\right]t \qquad [17]$$

Thus, in the time domain $t \gtrsim t_o \sim 0$, $n_{I1}(O)$ increases as $t^{1/2}$ provided we neglect recombination events with vacancies or other sinks. Incorporating the effects of such events will decrease the time exponent in this relationship.

To incorporate the effect of vacancy recombination events, let us assume that $P_A'n_V$ in Eq. [5] is independent of x and is a slowly varying function of t. Then, following Carslaw and Jaeger (14), we find our new I-defect content in the Si, $n_{I1}^\dagger$, to be given by

$$n_{I1}^\dagger = n_{I1}e^{-P_A'n_V(t-t_o)} + P_A'n_V\int_o^{t-t_o} n_{I1}(t')e^{-P_A'n_Vt'}dt' \qquad [18]$$

where $n_{I1}(t)$ is given from Eq. [17].

Because n_V has been so strongly decreased in the Si close to the oxidizing interface, vacancies flow in from the bulk Si to reduce n_V close to the interface. This diffusion of V-defects along substitutional sites produces a type of "vacancy wind" which moves substitutional solutes deeper into the Si. The movement of I-defects deeper into the Si also produces an "interstitial wind" of strength proportional to J_{I1}. The analogue for this wind effect comes from electromigration experiments where the momentum exchange between electrodes and lattice ions often causes movement in the opposite direction from that expected based on ionic charge. In terms of the thermodynamics of multicomponent systems, the flux, J_a, of species a is given in terms of the mobilities, M_{ia}, and the electrochemical potential gradients, $\nabla\eta_i$, of the various species i by (15)

$$\bar{J}_a = -\sum_{i=1}^{n} M_{ia}\nabla\eta_i \qquad [19]$$

Thus, depending on the sign of M_{ia} and the $\nabla\eta_i$ ($i \neq a$), the diffusion of a may be greatly enhanced. Here, for i = I, $\nabla\eta_I \propto J_{I1}$. This enhanced drift of the substitutional species has been labeled oxidation enhanced diffusion (OED). We see that it arises from the interstitial flux generated at the Si/SiO_2 interface as a natural consequence of the oxidation model described here.

From Eq. [18] we expect $n_{I1}^\dagger$ to build up in the Si slab in a manner proportional to t^p where $p < \frac{1}{2}$. At some time, t_1, the supersaturation of I-defects will be sufficient that stacking faults will nucleate and begin to grow and Eq. [5] must then be replaced by

$$D_I\nabla^2 n_I - P_A'n_Vn_I - \dot{Q}_{SF} = \frac{\partial n_I}{\partial t} \qquad [20a]$$

where

$$\dot{Q}_{SF} = \frac{2\pi bN_{SF}}{\Omega_I}\bar{r}\frac{d\bar{r}}{dt} \qquad [20b]$$

with N_{SF} and $\bar{r}$ as the number and average radius, respectively, of the stacking faults as a functions of time, b is the thickness of the fault, and Ω_I is the atomic volume of the condensed I-defect in Si. This interstitial sink should deplete the supply in the bulk Si. However, it is noted that significantly changing N_{SF} has a negligible effect on $d\bar{r}/dt$ (16), which suggests that the interface source strength is so strong. I-defect diffusion in Si is so fast, and the barrier to attachment at the stacking fault edge so large that $n_{I1}(O)$ remains relatively unaltered by the increased sink strength. Eventually, of course, the total line length of stacking fault increases to the point that the drain of interstitials

exceeds the supply and $d\bar{r}/dt$ must shrink to zero. The retrograde portion of the stacking fault growth curve can then come about either by continued vacancy supply from bulk sources plus from the Si/SiO_2 interface or by a change in diffusive flux of I-defects into the bulk SiO_2 from the interface so that N_{I2} decreases. If the latter occurs, N_{I1} begins to decrease and I-defects begin to flow from the Si to the SiO_2 so that the stacking faults then become the I-defect sources.

Consequences to the SiO_2.—Let us now look in the opposite direction, *i.e.*, to the interstitials flowing into the SiO_2. It is most probable that these will be partially charged, but they will not be nearly as mobile as those in the Si. In fact, they may be fairly immobile because of the incoming oxygen species. These interstitials, almost 4 per unit cell, will swell the unit cell in the direction lateral to the interface making the interface SiO_x more dense than the bulk SiO_2 (17, 18). As oxygen diffuses through the SiO_2 and reaches the interface region, it will oxidize these interstitial Si ions partially blocking the outward diffusion paths of other Si ions. This immobilized group reacts further to form O-Si-O polymer chains. These chains may be thought to interconnect the interstitial spaces in the diamond cubic structure until flow produces enough volume that the more stable SiO_4 tetrahedra may form. It is well known that SiO_4 tetrahedra link together by sharing two of the four corners to form a continuous chain of composition $(SiO_3)_n$ (12) constituting the pyroxene group of chain silicates. In the amphibole group, the SiO_4 tetrahedra are linked to form chains having double the pyroxene chain width and having a composition $(Si_4O_{11})_n$. The mica group of silicates form sheet structures with hexagonal nets which lead to a composition of Si_4O_{10} (12).

Several features are important to note about the proposed interstitial chains. First, they may be considered to have a range of enthalpies of formation and some particular distribution of chain lengths will minimize the free energy of SiO_2 (short chain lengths probably). Second, the strain energy will increase with the degree of advancement of the oxidation process and very quickly exceed a few kcal/mole so that the α-cristobalite lattice will quickly distort to the vitreous-type structure. Third, the incompletely oxidized Si (chain ends) are expected to contain unsatisfied bonds which will be positively charged. Since the positive ions occupy less space, the reduced strain energy favors the ionization. This is proposed as the origin of Q_f. Fourth, since these chains place the unit cell under swelling stresses, there will be a slow yielding of the SiO_x as free volume flows into the interface region from the bulk SiO_2 via viscoelastic processes (19). As the system yields, complete oxidation of these interstitial I-defects become possible and they may make the transition to stable SiO_4 tetrahedra which completely transforms the SiO_x to vitreous SiO_2. Thus, an interface layer of enhanced density and thickness, ΔZ, exists wherein the stoichiometry is of the form SiO_x with $1 \lesssim x < 2$. This layer becomes a steady-state condition moving with the interface wherein new bare Si or SiO interstitials enter at one side and completely oxidized interstitial chains or interstitial tetrahedra exit at the other side. The point here is not to make a case for chains *vs.* partial tetrahedra, but to allow both possibilities at this qualitative stage. Important thermodynamic calculations need to be made concerning these various interstitial defect species and such subsequent calculations will allow discrimination between these two possibilities. A residual interstitial density, such as to produce a swelling stress equal to the SiO_2 flow stress at the oxidation temperature, is predicted in accordance with the findings of Taft (20). For high pressure oxidation, this residual density effect will be higher because of the decreased SiO_2 viscosity at the higher pressure.

An important point to be underlined here is that the oxidation of Si occurs via two streams. In the first stream, 4 Si atoms per unit cell of Si oxidize directly to SiO_2 and form the lattice of α-cristobalite. In the second stream, almost 4 I-defects per unit cell of transformed Si oxidize in steps as SiO_x with an increased activation energy and decreased free energy release being associated with oxidation as x increases from 1 to 2. The larger x is for this stream, the slower the oxidation process because of the associated strain energy. From qualitative theoretical reasoning, one expects x to increase from ~ 1 to ~ 2 in about 4 unit cell distances. This internal swelling and flow process cannot help but produce a highly densified and integral oxide.

Temperature dependence.—As the temperature is increased, the yield stress of the α-cristobalite is reduced and the system flows more easily. Thus, the stored strain energy due to the I-defects in SiO_2 will be reduced, which will reduce $\Delta\mu$ for the same value of N_{I2}. This will cause a decrease in $J_{I1}(O)$ and an increased fraction of the I-defects are partitioned to the SiO_2. Since there are fewer I-defects flowing into the Si as T increases, the driving force for both the OED and the OISF phenomena must decrease beyond a certain temperature as T increases. From the work of Eernisse (19), we see that the critical temperature range for strong changes in the vitreous SiO_2 flow properties is $\sim 950°$-$1000°C$. Thus, changes in OED and OISF should begin to be seen at $T \gtrsim 1000°C$.

With respect to expected Q_f and n_{it} changes with T, since $J_{I1}(O)$ decreases and k_I increases as T increases, one might expect that the total positive charge at chain ends would increase and that Q_f should increase also. However, n_{I2} increases only very slightly as T increases but, because the system flows more easily at the higher temperatures, the oxidation should be more complete, the number of oxy-silicon chain ends should decrease, and Q_f should decrease in accord with the results of Deal (8). At the higher T, the reaction between the Si atoms at the ends of the extra half-planes and oxygen will be more rapid and, thus, more complete so that N_{it} should also decrease as T increases. Of course, the reactivity of minor constituents like H or C should also be altered, which will, in turn, alter the observable N_{it} (21).

Orientation dependence.—We assume the same epitaxial match, $(100)Si//(100)SiO_2$, but now we focus attention on the (111) plane of Si as the interfacial plane and notice that it is lined up with the (120) plane of the pseudo-diamond cubic cell of α-cristobalite (see Fig. 1). As Herman *et al.* (22) have noted, the interface model of (100)Si parallel to (100)β-cristobalite, with this latter rotated by 45°, is the simplest interface model constructable between these two phases. In our case, the $(100)Si//(100)\alpha$-cristobalite with parallel <100> directions gives almost exactly the result of Herman *et al.* (22). If we look into the α-cristobalite pseudo cube along the <120> or into the β-cristobalite along this direction, we note easy access to the <110> tunnels through the diamond cubic structure.

Thus, for this direction, the second term of Eq. [13c] may be larger than for Si orientations where the interface normal is not lined up with the tunnel direction. If this is so, then $n_{I1}(O)$ will be reduced and so will the OED and the OISF. We are not yet in a position to evaluate the magnitude of this effect. The dominant orientation effect, however, is expected to arise as a consequence of its influence on the magnitude of β. As V increases at fixed $n_{I2}(O)$, J_{I1} is fixed; however, for fixed oxide thickness, $\bar{n}_{I1}$ is reduced because it takes less time to form this layer and thus t, in Eq. [14], is smaller. For constant diffusive transport rate in the oxide, $n_{I2}(O)$ should increase as V increases (less transported away per unit film thickness). Thus, $\bar{n}_{I1}$ should decrease as V increases, but a little less than

linearly with V. Since V increases as p_{O_2} increases, a similar change in $n_{II}(O)$ should develop for increasing p_{O_2}. In changing the Si wafer orientation from (100) to (111), the change in $n_{II}(O)$ arises from the fact that $V_{(111)} > V_{(100)}$. Thus, this effect is expected to lower $n_{II}(O)$ for the (111)Si wafers compared to the (100)Si wafers for fixed oxide thickness, in accord with observations.

Because of the increase of k_I for the (111)Si compared to the (100), Q_f will increase, OED will decrease, and OISF will decrease. Since larger k_I means more I-defects in the SiO_2, this means greater lateral swelling stresses as the interstitial Si becomes oxidized. The increased lateral swelling stresses are expected to cause the SiO_2 at the interface to relax to a larger average spacing and leave more Si half-planes per unit interface area on the Si side terminating at the interface. Thus, we also expect N_{it} to increase for the (111) over that for the (100).

Oxidation velocity.—Because the number of I-defects in Si is greater for the (100) orientation than for the (111) orientation, the reverse situation holds for the SiO_2 phase. The greater Q_f for the (111) orientation means an enhanced electric field in the oxide for this orientation. Since the Q_f is associated with positive charge, the interface region will be more positive for the (111) orientation than for the (100). This means that the diffusion rate of $O^=$ ions through the oxide will be enhanced for the (111) oxidation compared to the (100) so the oxidation velocity for (111) oxidation will be greater than for the (100) oxidation. As shown in Part II (2), the field effects enter both the linear and parabolic rate coefficients so both the short-time and the long-time oxidation rates should be affected by this mechanism. Of course, as the temperature is increased, the enhanced flow process allows almost all of the I-defects to enter the SiO_2 phase and differences in the field-driven diffusion for the two orientations disappear. Thus, the oxidation velocities for the (111) and the (100) become almost equal at high temperatures.

Discussion

The most important concept of this paper is the formation of a transitory crystalline SiO_2 layer containing interstitial species. The utilization of this concept allows one to see how a host of ancillary phenomena can occur and be associated with the oxidation process. Consideration of a direct transition to vitreous SiO_2 without interstitial species leaves one with no ready pathway to simply account for these other phenomena. Certainly there is no apparent way to see their interconnectedness. Since the free energy difference between any one SiO_2 phase and another is only $\sim$ 2 kcal/mole, which is $\sim$ 1%-2% of the total free energy available for the reaction, the choice of specific interface SiO_2 structure is of second order to the overall process. In this paper, the slight favorite has been α-cristobalite.

The paper has, for reasons of simplicity, considered that the Si atoms at the ends of the extra half-planes remain unoxidized until after they jump into SiO_2 interstitial positions. In actual fact, many of these atoms will have formed a single Si-O bond and some may have formed O-Si-O bonds. Thus, not only will we have Si interstitials being generated from this interface source but SiO interstitials and some O-Si-O interstitials as well. Of course, this will increase the interface density and the value of x somewhat in the overall interface stoichiometry, SiO_x. We would expect that, in the interface reaction control regime at low temperatures or high O_2 pressures, the oxygen supersaturation at the interface would be greatest, so more of the terminating Si atoms would be partially oxidized, more SiO interstitials would enter the SiO_2, and x would be larger for SiO_x at the interface. At the other extreme, for thick oxides where diffusion control is dominant, the interface oxygen supersaturation will be small and most of the terminating Si atoms will be bare and will enter the SiO_2 interstitial positions as bare Si. Of course, during cooling to room temperature, the excess oxygen in the SiO_2 will move to the interface and partially oxidize these terminating Si species.

For the bare Si atoms in terminal positions at the interface, one might picture them with dangling bonds; however, it is more likely that bond reconstruction will occur and only a few dangling bonds will exist. The density of these dangling bonds is likely to be much lower at room temperature than at oxidation temperatures and to depend on both the quenching rate from high temperature and the quenching environment. This should be governed by the natural bond reconstruction rate which is expected to be a function of the orientation of the extra half-planes terminating at the interface; *i.e.*, it should be a function of interface orientation. We should always expect some bare dangling bonds, even in the equilibrium reconstructed state, for entropic reasons. Given the difference in bond energy, ΔE^*, between the dangling and reconstructed states, the fraction of dangling bond sites, x_{db}, in the equilibrium reconstructed state is simply

$$x_{db} \sim e^{-\Delta E^*/kT} \qquad [21a]$$

When some of these terminal atoms are partially oxidized, we must mix the three unique species (dangling bonds, reconstructed bonds, and oxygenated bonds) among these available terminating atoms. For a fixed fraction x_o of oxygenated terminal Si species, Eq. [21a] becomes

$$x_{db} = (1 - x_o)\, e^{-\Delta E^*/kT} \qquad [21b]$$

As x_o approaches unity, it can no longer be held fixed in the calculation and we return to a result like Eq. [21a], but with ΔE^* replaced by $\Delta E^* + \Delta E_B$ where ΔE_B is the decrease in bond energy in going from a bare reconstructed bond to a singly oxidized bond.

The conceptual features of this overall model are expected to be fairly representative of the experimental reality for the thermal oxidation of Si. However, much fine tuning of the model is still needed to produce the desired quantitative match with experiment. Many significant theoretical hurdles still stand in the way of this goal.

Conclusions

A qualitative model has been proposed based on the initial transformation of silicon to α-cristobalite plus almost 4 interstitial Si ions per unit cell of Si transformed, with the remainder interstitial Si ions rejected into the bulk silicon phase. Subsequent oxidation of the interstitial Si ions in the SiO_2 matrix produces rapid distortion and transformation of the structure to the vitreous form. The following are the qualitative predictions of the model:

1. OED, OISF, N_{it}, and Q_f can be accounted for.
2. The orientation dependence gives, in accordance with experiment

$$k_{I(100)} < k_{I(111)}$$

$$OED_{(100)} > OED_{(111)}$$

$$OISF_{(100)} > OISF_{(111)}$$

$$Q_{f(100)} < Q_{f(111)}$$

$$N_{it(100)} < N_{it(111)}$$

$$V_{(111)} > V_{(100)}$$

3. The temperature dependence gives k_I increasing as T increases above $\sim$950°C so that all the orientation dependences tend to decrease.
4. At the lower growth temperatures, a layer of increased density SiO_2 will exist at the Si interface which will yield an increased index of refraction for the layer in accordance with experiment (17). The chemical stoichiometry of the layer will range from almost SiO

(slightly Si deficient) at the interface with Si to almost SiO_2 (slightly O deficient) at the transition with bulk density vitreous SiO_2 which occurs within ~3-5 unit cell distances of the interface.

In addition, a quantitative expression for k_I has been derived and the I-defect content in the Si is predicted to increase for short times as t^p, where $p < 0.5$.

Acknowledgments

This work was partially supported by the Defense Advanced Research Projects Agency under Contracts No. DAAB07-77-C-2684 and MDA 903-79-C-0484. The author wishes to thank Dr. A. Lin for many informative discussions.

Manuscript submitted Feb. 22, 1980; revised manuscript received June 26, 1980.

Any discussion of this paper will appear in a Discussion Section to be published in the December 1981 JOURNAL. All discussions for the December 1981 Discussion Section should be submitted by Aug. 1, 1981.

Publication costs of this article were assisted by Stanford University.

APPENDIX A

Neutral Interstitial Partition Coefficient at the Si/SiO_2 Interface

Let the neutral interstitial enthalpy of formation in Si and in SiO_2 be given by ΔH_{I1} and ΔH_{I2}, respectively. In each phase, the entropy of the I-species, S_p, permuted amongst the mn_s available interstitial sites for m unit cells, is given by

$$S_p = k \ln [(mn_s)!/(mn_I)!(mn_s - mn_I)!] \quad [A\text{-}1]$$

Here, $n_s = 5$ for diamond cubic with one atom or ion per site. However, in SiO_2 it may be possible to have more than one I-species per interstitial site because the sites are so large. Thus, $n_s^{SiO_2}$ is not fully specifiable at this time.

The equilibrium number of interstitials per unit cell, n_I^*, in each phase is given by

$$\frac{n_{Ij}^*}{n_{sj} - n_{Ij}^*} = e^{\Delta s_j^v/k}\, e^{-\Delta H_{Ij}/kT} \quad j = 1, 2 \quad [A\text{-}2]$$

where ΔS^v is the vibrational entropy contribution of the I-defects. Both n_{I1}^* and n_{I2}^* are expected to be small relative to n_{s1} and n_{s2} and $n_{I1}^* << n_{I2}^*$ is also expected. In our area of interest, large values of n_I are being generated at the Si/SiO_2 interface and the excess free energy of each phase for $n_{Ij} >> n_{Ij}^*$ is given by (9)

$$\Delta G_{ex\,j} = mkT \left\{ n_{Ij} \ln \left[\frac{n_{Ij}(n_{sj} - n_{Ij}^*)}{n_{Ij}^* n_{sj}} \right] + (n_{sj} - n_{Ij}) \ln \left[\frac{n_{sj} - n_{Ij}}{n_{sj}} \right] \right\} \quad j = 1, 2 \quad [A\text{-}3]$$

for the m unit cells ($m = N/8$ for a mole of Si or α-cristobalite where N = Avogadro's number). The chemical potentials of the interstitials at these excess concentrations are, in turn, given by

$$\mu_{Ij} = \frac{\partial G_{ex\,j}}{\partial n_j} = kT \ln \left[\frac{n_{Ij}(n_{sj} - n_{Ij}^*)}{n_{Ij}^*(n_{sj} - n_{Ij})} \right] \quad j = 1, 2 \quad [A\text{-}4]$$

APPENDIX B

Interstitial Partitioning of Si

One-step process.—Consider unit area of interface where the environment for Si I-defects is like that in Fig. 4. The concentration of the I-defects in SiO_2 is such that a chemical potential difference, $\Delta\mu_o$, exists between SiO_2 and Si for this species. The number of Si atoms jumping out of the interface layer per unit time into interstitial sites in Si ≡ 1 and SiO_2 ≡ 2 is given by

$$R_{out} = \frac{N_s(\theta)}{2} \frac{\nu}{6} (e^{-Q_2^*/kT} + e^{-Q_1^*/kT}) \quad [B\text{-}1]$$

where $N_s(\theta)$ is the average number of atoms per unit area of the interface and ν is the vibrational frequency. The number jumping back into the interface layer per unit time from these phases is

$$R_{in} = N_{I2} \frac{\nu'}{6} e^{-[Q_1^* - (\Delta H_{I2} + \Delta\mu)]/kT} + N_{I1} \frac{\nu''}{6} e^{-[Q_1^* - \Delta H_{I1}]/kT} \quad [B\text{-}2]$$

The net result arising as a result of interface motion is

$$R_{out} - R_{in} = \frac{4V(\theta)}{\lambda_o^3} \quad [B\text{-}3]$$

where λ_o is the Si unit cell size and V is the interface velocity. Placing Eq. [B-1] and [B-2] into [B-3] leads to

$$\frac{4V(\theta)}{\lambda_o^3} = \left[\frac{N_s(\theta)\nu}{12} - \frac{N_{I2}\nu'}{6} e^{(\Delta H_{I2} + \Delta\mu)/kT} \right] e^{-Q_2^*/kT} + \left[\frac{N_s(\theta)\nu}{12} - \frac{N_{I1}\nu''}{6} e^{\Delta H_{I1}/kT} \right] e^{-Q_1^*/kT} \quad [B\text{-}4]$$

At $V = 0$, $\Delta\mu = 0$ and $N_{I2} = k_I^* N_{I1}$, so a relationship between some of the parameters is possible; however, it is essentially too complex to be readily useful.

Two-step process.—Let all of the I-defects first be liberated into the SiO_2 (with an activation energy that requires Si-Si bond breaking). Then, some of the I-defects are partitioned into the Si interstitial spaces. For this second step, we have

$$R_L = N_{I2} \frac{\nu}{6} e^{(Q^* - \Delta\mu)/kT} \quad [B\text{-}5]$$

and

$$R_R = N_{II} \frac{\nu}{6} e^{-Q^*/kT} \quad [B\text{-}6]$$

where R_L means from the SiO_2 to the Si, while R_R is from the Si to the SiO_2. Therefore, the number of I-defects entering the Si per unit time, J_1, is given by

$$J_1 = R_L - R_R = N_{I2} \frac{\nu}{6} e^{-Q^*/kT} \left(e^{\Delta\mu/kT} - \frac{1}{k_I} \right) \quad [B\text{-}7a]$$

$$\approx \frac{N_{I2}\nu}{6} e^{-Q^*/kT}\, e^{\Delta\mu/kT} \quad [B\text{-}7b]$$

since k_I^{-1} is very small and $\Delta\mu/kT >> 1$ generally. It should also be noted that J_1 is somewhat proportional to V since the interface conservation condition is

$$\frac{4V}{\lambda_o^3} = J_1 - J_2 \quad [B\text{-}8]$$

and the minus sign is used because J_2 is in the opposite direction to J_1.

REFERENCES

1. W. A. Tiller, *This Journal*, **127**, 619 (1980).
2. W. A. Tiller, *ibid.*, **127**, 625 (1980).
3. P. S. Dobson, *Philos. Mag.*, **24**, 567 (1971).
4. P. S. Dobson, *ibid.*, **26**, 1301 (1972).
5. S. M. Hu, *J. Appl. Phys.*, **45**, 1567 (1974).
6. D. A. Antoniadis, A. M. Lin, and R. W. Dutton, *Appl. Phys. Lett.*, **33**, 1030 (1978).
7. S. P. Murarka, *Phys. Rev. B*, **16**, 2849 (1977).
8. B. E. Deal, *This Journal*, **121**, 198C (1974).
9. R. A. Swalin, "Thermodynamics of Solids," p. 218, John Wiley & Sons, Inc., New York (1962).
10. R. G. Rhodes, "Imperfections and Active Centers in Semiconductors," p. 12, MacMillan, Pergamon Press, New York (1964).
11. J. S. Van Vechten, *Phys. Rev. 5*, **17**, 3197 (1978).
12. W. A. Deer, R. A. Howie, and J. Zussman, "An Introduction to the Rock-Forming Minerals," John Wiley & Sons, Inc., New York (1966).
13. K. A. Jackson, *Philos. Mag.*, **5**, 43 (1960).
14. H. S. Carslaw and T. C. Jaeger, "Conductor of Heat

in Solids," p. 63, Clarendon Press, Oxford (1959).
15. P. G. Shewmon, "Diffusion in Solids," p. 122, McGraw-Hill Book Co., New York (1963).
16. A. Lin, Private communication.
17. E. Taft and L. Cordes, *This Journal*, **126**, 131 (1979).
18. H. Z. Massoud and J. A. Plummer, Private communication.
19. E. P. Eernisse, *Appl. Phys. Lett.*, **30**, 290 (1977).
20. E. A. Taft, *This Journal*, **125**, 968 (1978).
21. C. M. Svensson, in "The Physics of SiO_2 and Its Interfaces," S. T. Pantelides, Editor, p. 328, Pergamon Press, New York (1979).
22. F. Herman, I. P. Batra, and R. V. Kasowski, in "The Physics of SiO_2 and Its Interfaces," S. T. Pantelides, Editor, p. 333, Pergamon Press, New York (1979).

Technical Notes

Formation of Recombination Centers in Epitaxial GaAs due to Rapid Changes of the Growth Velocity

L. Jastrzebski

RCA Laboratories, Princeton, New Jersey 08540

and J. Lagowski and H. C. Gatos*

Department of Materials Science and Engineering, Massachusetts Institute of Technology, Cambridge, Massachusetts 02139

It was established that recombination centers in epitaxial GaAs are formed upon abrupt acceleration of the growth. The corresponding effect of abrupt deceleration of the growth is only minor. In the case of backmelting, recombination centers are also introduced, however, not due to backmelting itself, but rather due to the subsequent acceleration of the growth. The abrupt changes in growth velocity were achieved by corresponding changes in the current density during electroepitaxial growth.

It has been recently demonstrated experimentally and theoretically that liquid phase electroepitaxy provides a unique means for achieving essentially independent control of the interface temperature and the growth velocity (1, 2). In the present study we have utilized this feature of electroepitaxy in the growth of GaAs with intentionally imposed controlled changes of the growth velocity in order to study the role of growth dynamics in the formation of recombination centers.

In electroepitaxy growth is initiated and sustained by passing an electric current through the solution-substrate interface. An electric field, $E = \rho J$, (ρ is the resistivity and J is the current density) in the solution (GaAs in the present case) causes electromigration of solute species (As in the present case) to the interface providing an effective means for the mass transport required for epitaxial growth (1). In addition, electric current flow leads to a change, ΔT_p, of the interface temperature due to the Peltier effect; $\Delta T_p \sim \pi J d$ where π is the Peltier coefficient with a sign depending on the conductivity type of the substrate (n or p) and d is the thickness of the substrate. It is apparent that by using thin substrates, current-induced change of the interface temperature can be minimized (down to a fraction of 1°C) and thus growth can be controlled by electromigration. The velocity (1, 2), $v_E = C_0 \mu E J/(C_s - C_0)$, (where C_0 and C_s are the equilibrium solute concentration in the solution and in the solid, respectively, and μ is the mobility of solute species) can be programmed by programming the current density as a function of time. The electromigration flux adjusts instantaneously to changes in electric current density and thus the time-lag between rapid changes of J and of the growth velocity, v_E, is negligible. For thick substrates, ΔT_p becomes of significance (of the order of a few degrees C). However, the thermal relaxation time of the interface temperature is typically of the order of 0.1 sec, which is much longer than the relaxation time of the growth velocity associated with solute electromigration changes.

In the present study controlled growth velocity changes were introduced during electroepitaxial growth of Sn-doped ($n \simeq 6 \times 10^{16} cm^{-3}$) GaAs from Ga-rich solution at 950°C with an apparatus described elsewhere (3). The minority carrier lifetime microprofiling in the grown layers was performed utilizing SEM-electron beam-induced current (EBIC).

A current collecting Schottky barrier was formed by evaporating gold on the surface of the epitaxial layer cleaved parallel to growth direction. As shown in Fig. 1, the collection efficiency of the electron beam-induced current was measured while scanning the beam across the regions subjected to changes of growth velocity. The position of these regions (and thus the corresponding values of growth velocity) was determined with differential etching (AB etchant).

EBIC measurements were carried out under plasma generation conditions so that the observed changes of collection efficiency reflect primarily the changes of minority carrier lifetime and thus the concentration of recombination centers (a decrease in collection efficiency corresponds to an increase in the concentration of recombination centers). The experimental results showing the effect of growth velocity changes on the formation of recombination centers are shown in Fig. 2 and 3.

It is evident from Fig. 2a that an abrupt increase of growth velocity[1] from 2 to 4 μm/min produces a pronounced minimum in collection efficiency in the corre-

* Electrochemical Society Active Member.
Key words: growth, electroepitaxy, current.

[1] The change of the current level was brought about in 1 msec; it is believed that the corresponding change of growth velocity took place in approximately the same period of time.

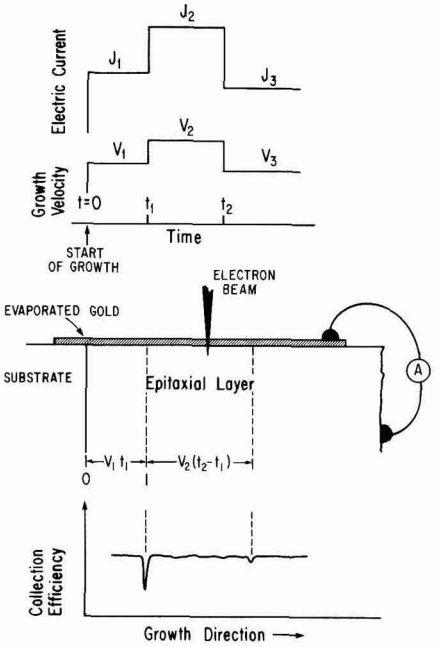

Fig. 1. Schematic representation of current-controlled changes of the growth velocity (upper portion) and corresponding configuration employed in SEM-electron beam-induced current (EBIC) measurements.

sponding transition region. Higher growth velocity changes (from 2 to 14 μm/min; or from 8 to 20 μm/min) reduce the collection efficiency by as much as 30%. It should be pointed out that the recovery of the

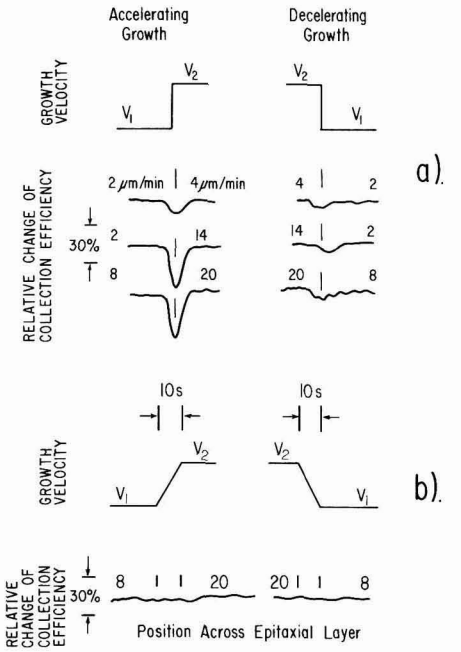

Fig. 2. EBIC microprofiles reflecting formation of recombination centers upon abrupt changes of growth velocity (a) and upon similar changes spread over a period of 10 sec (b).

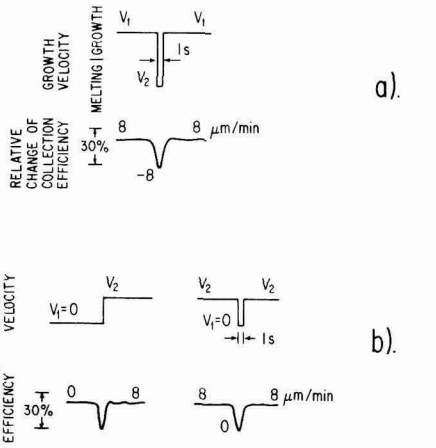

Fig. 3. EBIC microprofiles corresponding to backmelting (a) and to abrupt changes of growth velocity without backmelting (b). (See text.)

collection efficiency (concentration of recombination centers) following the step-like change in growth velocity indicates that the acceleration of the growth (dV/dt) rather than the absolute value of growth velocity (V) is responsible for the formation of recombination centers. This conclusion is confirmed by the results of Fig. 2b, whereby the growth velocity was changed from 8 to 20 μm/min, however, not instantaneously but during a period of 10 sec. In this case no noticeable amount of recombination centers was introduced.

The results shown on the right-hand side of Fig. 2(a, b) indicate that the effect of deceleration of the growth on recombination centers is about one order of magnitude smaller than that of acceleration of the growth.

Experiments, as discussed above, were also carried out with substrates of different thickness, and thus under different current-induced changes of the interface temperature. No significant differences were observed from the results of Fig. 2 obtained with thin substrates. Apparently, changes in interface temperature are of secondary importance compared to changes in growth velocity.

Typical results regarding the effect of backmelting on the formation of recombination centers are shown in Fig. 3. In the upper portion of Fig. 3 backmelting is introduced with 1 sec electric current pulse of polarity opposite than required for growth. It is seen that a minimum in collection efficiency is introduced by this pulse.

In order to verify whether the observed increase in concentration of recombination centers is caused by phenomena taking place during backmelting of the grown crystal or by the subsequent increase of the growth velocity to the original value of 8 μm/min, the following experiments were carried out. Growth was arrested for an extended period and then it was abruptly increased to 8 μm/min. In addition, the growth was interrupted for 1 sec and then restored abruptly to its original value of 8 μm/min. As seen in the lower part of Fig. 3, the results are the same as those obtained for backmelting (upper part of Fig. 3). Thus, it is concluded that the recombination centers introduced into the epitaxial layer during backmelting are formed primarily by the acceleration of the growth following backmelting.

In summary, we have demonstrated the importance of growth dynamics, and in particular, the importance of the acceleration of growth in the formation of re-

combination centers during liquid phase epitaxy. It is likely that these recombination centers originate from point defects generated at the growth interface in response to abrupt increases in growth velocity (abrupt deviations from steady-state growth conditions). It is apparent that surface nucleation effects commonly considered of no significance in the LPE process with slowly varying growth velocity can in fact be of primary importance in the case of abrupt increases in growth velocity. The limited framework of existing theoretical treatments of point defect formation on growth interfaces (4-7) does not provide an adequate basis for further, even qualitative explanation of the present findings.

Acknowledgments

The authors are grateful to the National Aeronautics and Space Administration and to the National Science Foundation for financial support.

Manuscript received Sept. 12, 1980.

Any discussion of this paper will appear in a Discussion Section to be published in the December 1981 JOURNAL. All discussions for the December 1981 Discussion Section should be submitted by Aug. 1, 1981.

Publication costs of this article were assisted by the Massachusetts Institute of Technology.

REFERENCES

1. L. Jastrzebski, J. Lagowski, H. C. Gatos, and A. F. Witt, *J. Appl. Phys.*, **49**, 5909 (1978).
2. T. Bryskiewicz, J. Lagowski, and H. C. Gatos, *ibid.*, **51**, 988 (1980).
3. L. Jastrzebski, Y. Imamura, and H. C. Gatos, *This Journal*, **125**, 1140 (1978).
4. W. W. Webb, *J. Appl. Phys.*, **33**, 1961 (1962).
5. J. A. Van Vechten, *Appl. Phys. Lett.*, **26**, 593 (1975).
6. A. J. R. de Koch, P. J. Roksnner, and P. G. T. Boonen, *J. Cryst. Growth*, **22**, 311 (1974).
7. J. Chikawa and S. Shirai, *Jpn. J. Appl. Phys.*, **18**, Supplement 18-1, 153 (1979).

The Archival Stability of Tellurium Films for Optical Information Storage

David Y. Lou

Philips Laboratories, Briarcliff Manor, New York 10510

Optical storage of information by means of laser micromachining of thin metal films is currently the subject of a great deal of interest (1-3). One of the major potential applications of this technology is the high density, low cost archival storage of information. Thus, the archival properties of the recording medium are examined. We report in this paper data obtained for tellurium films deposited on polymethyl methacrylate (PMMA) substrates, where the recording medium is fabricated into a protective air sandwich structure (2, 3).

Experimental Procedure

Several options exist in the choice of parameters to monitor the degradation of optical disks. One possibility is to monitor the degradation in the recording characteristics of the disk, such as the sensitivity to laser machining and the recovered bit error rate. This would yield information about the shelf life of the optical disk (4). Another important parameter concerns the degradation in the characteristics of a recorded disk, which gives us the archival life of stored information. Obviously, a complete map of errors over the entire disk gives the most information. Such data are, however, also most expensive to come by. Measurements of the fundamental optical properties of the film material, such as reflection, transmission, or subjective appearance, undoubtedly give information directly related to film degradation, and are much easier to perform (5). However, the translation of these properties into degradation characteristics of digital information is problematic, especially when the degradation is nonuniform over the disk surface. The most representative description of the degradation of recorded digital information is the bit error rate, averaged over a meaningful portion of the recordable disk surface area. This is the parameter we have chosen to measure.

Figure 1 shows the electronic instrumentation that was used to measure the bit error rate. The clock for the pattern generator section of the HP 3780A was derived from a Syntest frequency synthesizer for a data rate of 1.85 Mbits/sec. Two bit patterns were used for testing, a 16 bit word, 1010 1010 1010 1010 (1010//4) and a pseudorandom bit sequence 2^{15}-1 bits long (PRBS-15). The Miller modulated version of these bit sequences were used to drive the acousto-optic modulator in the recorder.

The experiments were carried out on air sandwiches (2) assembled from two tellurium-coated disks. The recorder used in this series of experiments was of fairly standard design. Laser radiation of 633 nm was obtained from an He-Ne laser and modulated by an

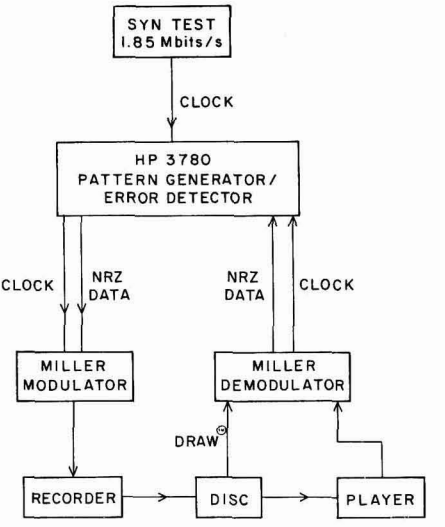

Fig. 1. Electronic system

Key words: aging, humidity, metals.

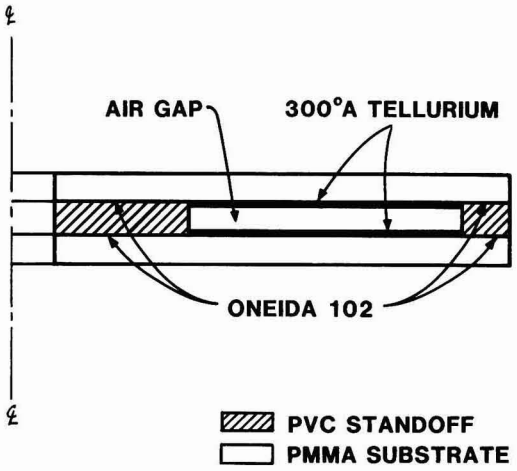

Fig. 2. The air sandwich™ structure

acousto-optic modulator. The sandwiches were mounted on an air-bearing spindle driven by a pancake motor. The focusing lens was a 0.45 N.A. Zeiss objective designed for the Philips Videodisc player. The calculated spot size of the recording beam is 0.7 μm FWHM. Active focusing was obtained by sensing the error signal with an infrared side beam system, and driving the objective with a standard Videodisc type voice coil. The entire focusing optics assembly was mounted on a rectangular Dover air-bearing sled and driven by a linear motor. The readout signal was obtained by splitting off a portion of the laser beam before modulation and aligning it to trail the main recording beam by a few microns on the recorded track.

Typically, each disk has four recorded bands of information, each approximately 2 mm wide, 120 sec long. Recordings of the 1010//4 pattern were made at the inner (75 mm), middle, and outer (95 mm) radii of the disk, together with a PRB5-15 pattern somewhere in between. For each recorded band, the recording parameters were adjusted to minimize the bit error rate of the readout signal.

After recording, the disks were stress aged in a temperature humidity oven at 45°C 95% relative humidity. Periodically, the disks were taken out, and the bit error rates were measured. Playback was on a modified version of the standard Philips Videodisk player. The Miller output from the player preamplifier was

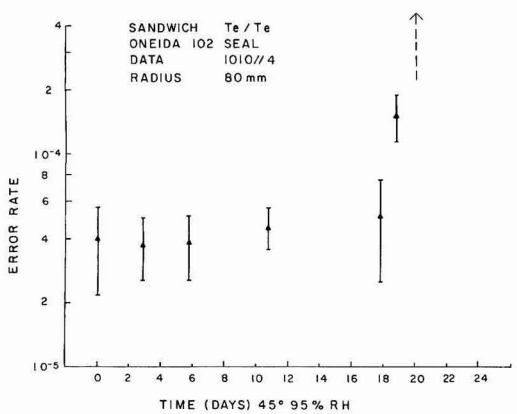

Fig. 3. Error rate degradation for double-sided tellurium air sandwich™, inner radius.

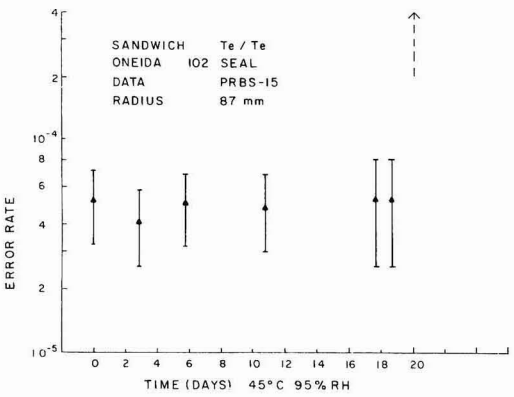

Fig. 4. Error rate degradation for double-sided tellurium air sandwich™, middle radius.

demodulated. The bit error rate of the recorded data was measured in the error detector section of the HP 3780A over data segments 10^6 bits in length. With a gating time of 1 sec on the HP 3780A, each recorded band contains approximately 100 readings. The average and standard deviation of these bit error rate readings are taken as the descriptor for the condition of the disk.

Results

Figures 3-5 show the data obtained for a double-sided sandwich, which has 300Å Te coated on both recordable surfaces. Standard Glasflex PMMA disks were cleaned by an acetone/alcohol rinse, immersion in an ultrasonic detergent bath, and deionized water rinse. The sandwich was bonded together with a polyvinyl chloride standoff using Oneida 102 cyanoacrylate as a seal (Fig. 2). Figure 3 gives the behavior for a 1010//4 pattern recorded at a radius of 80 mm. The recorded data show an initial error rate in the mid 10^{-5} range and are stable at 45°C 95% relative humidity for up to 18 days, after which it rapidly deteriorates. Figure 4 shows the behavior of PRB5-15 data at 87 mm, and Fig. 5 shows the behavior of 1010//4 data at 95 mm, on the same disk. The degradation in the fundamental signal characteristics, as measured by the carrier to noise ratio and carrier to second harmonic ratio, is given in Fig. 6. Figure 7 gives the data for a 1010//4 pattern on a double-sided sandwich which has extensive recordings made on the opposite recordable

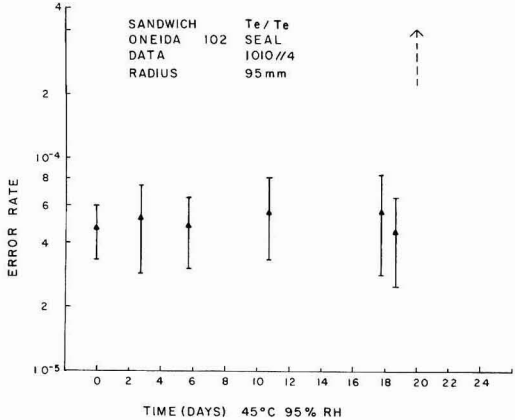

Fig. 5. Error rate degradation for double-sided tellurium air sandwich™, outer radius.

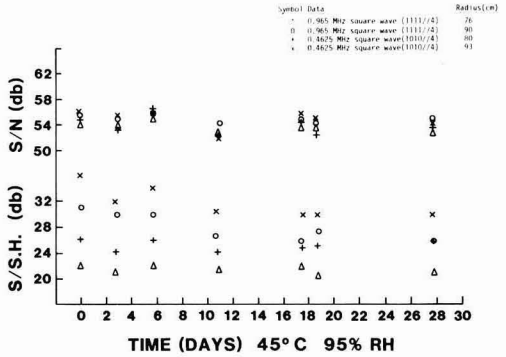

Fig. 6. Signal-to-noise and signal-to-second-harmonic degradation for double-sided tellurium air sandwich™.

surface. The results are typical of the behavior of tellurium air sandwiches.

Conclusions

Recorded data on these tellurium sandwich disks will remain stable in a 45°C and 95% relative humidity environment for at least 15 days. Stability is independent of recording radius, recorded data patterns, and whether recordings have been made on the opposite side. At present, extrapolation of these data to room ambient is uncertain. If one were to adopt the model proposed by Milch and Tasaico (4), developed

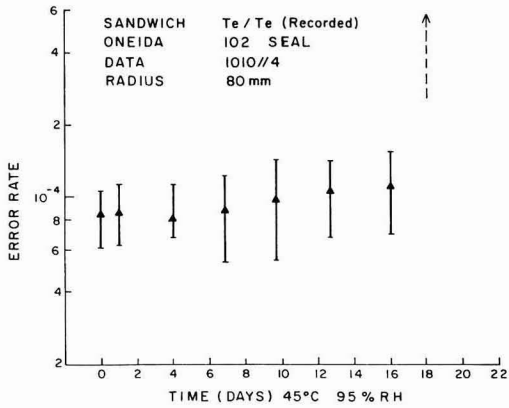

Fig. 7. Error rate degradation for double-sided tellurium air sandwich™ with recordings on opposite side.

for the extrapolation of shelf-life data, these results imply an archival life of at least 10 years for tellurium sandwiches at room ambient (25°C, 50% relative humidity). Failure of the air sandwich consists of a dramatic increase (several orders of magnitude) in the error rate, developing over a comparatively short time (a day or so). The direct cause of failure is apparently the development of localized defects on the disk. The catastrophic failure was not observed in the macroscopic signal characteristics, the film properties, or the integrity of the air sandwich structure. Lifetime data based on macroscopic optical measurements of transmission and reflection may well give overly optimistic results. Analogue information storage based on these macroscopic signal characteristics will probably have substantially longer lifetimes than 14 days at high humidity.

Several possible pathways exist for improving the archival life of the tellurium sandwich. The degradation is primarily associated with humidity. Hermetic sealing of the sandwich (6), or storage at elevated temperatures (4), have been used successfully. Substantially improved stability has also been observed by introducing appropriate impurities in the tellurium film. These results will be reported in a subsequent paper.

Acknowledgments

We would like to thank A. Chan and J. Nadan for the electronics instrumentation used in these experiments, and F. Zernike for the recorder. Sandwiches were fabricated by A. Weeks and M. Jaso, and S. Tan carried out the data analysis. We would also like to acknowledge G. Blom and G. Kenney for reviewing the manuscript.

Manuscript submitted June 24, 1980; revised manuscript received Sept. 15, 1980.

Any discussion of this paper will appear in a Discussion Section to be published in the December 1981 JOURNAL. All discussions for the December 1981 Discussion Section should be submitted by Aug. 1, 1981.

Publication costs of this article were assisted by Philips Laboratories.

REFERENCES

1. R. Bartolini, H. Weakleim, and B. Williams, *Opt. Eng.*, **15**, 99 (1976).
2. G. Kenney, D. Lou, R. McFarlane, A. Chan, J. Nadan, T. Kohler, J. Wagner, and F. Zernike, *IEEE Spectrum*, **16**, No. 2, 33 (1979).
3. K. Bulthuis, M. G. Carasso, J. P. J. Heemskerk, P. J. Kivits, W. J. Kleuters, and P. Zalm, *ibid.*, **16**, No. 8, 26 (1979).
4. A. Milch and P. Tasaico *This Journal*, **127**, 884 (1980).
5. S. Yonezawa, T. Maeda, T. Sugiyama, and H. Takahashi, *Tech. Dig.*, CLEOS (1980).
6. M. deHaan, *ibid.*, CLEOS (1980).

Tarnishing of Silver by Sulfur Vapor: Film Characteristics and Humidity Effects

B. T. Reagor* and J. D. Sinclair*

Bell Laboratories, Holmdel, New Jersey 07733

In laboratory and field studies over the past several years, we have noted that in some environments the average tarnishing rate of silver seemed to be less dependent on relative humidity (RH) than the dramatic dependence that has commonly been observed in the laboratory with hydrogen sulfide (1-15). We have also noted that the tarnish film thickness was often nonuniform. These effects were especially evident

* Electrochemical Society Active Member.
Key words: sulfidation, dendrite, SEM, growth.

in laboratory studies in which sulfur vapor was the tarnishing agent and in field studies at Artesia, New Mexico.

While sulfur vapor is a significant atmospheric tarnishing agent in only a few field environments (16), mercaptans and organic sulfides and disulfides can be more widely found as a result of natural processes and anthropogenic activity. Crossland *et al.* (11) have reported that mercaptans do not tarnish silver, but work in this laboratory indicates that atmospheres generated from organic sulfides and disulfides rapidly tarnish silver, especially in the presence of light (17). Very recently carbonyl sulfide, a major atmospheric sulfur-containing constituent was found to tarnish silver at elevated RH (18). The effect of RH on tarnishing by any of these carbon containing agents is unknown.

In a paper on precious metal alloys, Abbott (19) briefly reported on the tarnishing of silver by sulfur at 30°C in a flowing atmosphere. His data were summarized in a single linear plot that represented all N_2-O_2-SO_2-sulfur-H_2O environments studied. Chiarenzelli (5) claimed tarnishing would not occur in the absence of moisture. We report here the results of a study on sulfide film uniformity and humidity effects, using sulfur vapor as the tarnishing agent for silver coupons exposed in a closed environment at room temperature and 50°C.

Experimental

Tarnish film morphology was studied with an AMR-1000 Scanning Electron Microscope (SEM) in the secondary electron mode using an accelerating voltage of 30 kV. Average sulfide film thickness was measured by cathodic reduction (20). Nonuniformity in film thickness was estimated from sulfur ($K\alpha$) to silver ($L\alpha$) x-ray intensity ratios using a calibration plot based on cathodic reduction measurements. The x-ray intensities were measured with a Princeton Gamma-Tech x-ray detector and Tracor Northern 880 multichannel analyzer in conjunction with the SEM.

Square silver coupons (½ in. on a side) were cut from 0.005 in. thick Sargent-Welch silver foil. The coupons were cleaned and etched by two sets of successive immersions in concentrated nitric acid and then ammonia, the first set involving 10 min immersions and the second set 5 min immersions. Each immersion was followed by multiple rinses in pure water. The coupons were air dried for several hours prior to initiation of the experiments. This procedure produced a uniform and reproducible white matte surface on the coupons.

Sulfide films were grown on coupons suspended individually by glass hooks in bell jars that were approximately 8 cm high with a diameter of 6.5 cm. Sulfur vapors were evolved from a large excess of aged flowers of sulfur spread across a crystallization dish that was placed at the bottom of the bell jar. The vapor pressure of sulfur at room temperature is approximately 0.2 mPa (21), while that at 50°C is approximately 10 mPa (21). The molecular composition of sulfur vapor in equilibrium with the solid is approximately 96% S_8 and 4% S_6 at 50°C (22). A saturated salt solution, pure water, or Drierite, each contained in a 10 ml beaker, was placed at the bottom of the bell jar in the center of the crystallization dish for RH control. The salts used were lithium chloride, calcium nitrate, and ammonium sulfate. A survey of literature data on the vapor pressures of saturated salt solutions (23-32) indicated that the RH over the calcium nitrate solution used at room temperature was approximately 51%, while the RH's over the lithium chloride, ammonium sulfate, and calcium nitrate solutions used at 50°C were 11, 79, and 35-45%, respectively.

Coupon exposures at room temperature (23° ± 2°C) were accomplished on laboratory benches under ordinary fluorescent lighting. Studies at elevated temperatures were carried out in a GCA/Precision Scientific oven that was modified to include a Leeds and Northrup temperature controller. The temperature of the oven was 50° ± 2°C.

Results and Discussion

The sulfide tarnish film thickness on freshly cleaned and etched silver coupons that were exposed for up to 50 and 18 days at room temperature and at 50°C, respectively, is shown in Fig. 1 and 2 as a function of exposure time. The error bars indicate 95% confidence limits. The data confirm that in a closed environment relative humidity does not have an appreciable effect on the average rate of silver sulfide formation in the presence of sulfur vapor either at room temperature or at 50°C. The independence of the rate on relative humidity is further evidence that the probable function of moisture in tarnishing by hydrogen sulfide is to provide a medium for the oxidation of hydrogen sulfide to free sulfur (2, 10).

The average rate of silver sulfide film formation (at all humidities) was 0.5 Å/hr at room temperature and 13.3 Å/hr at 50°C. Similar to previous work, the observed linearity of the sulfiding rate at the conditions of this study indicates that the process is controlled by the arrival of sulfur at the silver surface (12, 19, 33, 34). An approximation for the rate of arrival of S_8 vapor to the coupon surface was calculated with the equation

$$S/t = DqCe/l$$

from the cylindrical model of Jost (35), where S is the quantity of S_8 arriving in time t, D is the diffusivity of S_8 in air, l is the distance from the sulfur source to the center of the coupon (5 cm), q is the cross-sectional

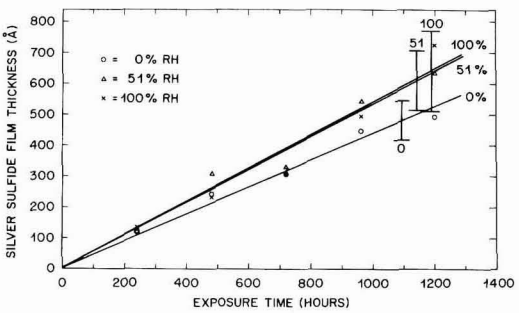

Fig. 1. Sulfide tarnish film formation on silver by sulfur vapor at room temperature.

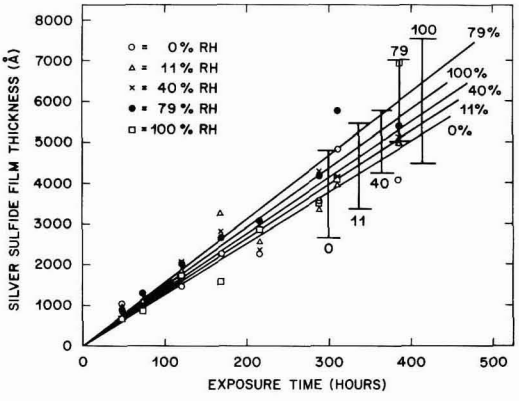

Fig. 2. Sulfide tarnish film formation on silver by sulfur vapor at 50°C.

area of the bell jar, and C_e is the equilibrium concentration of S_8 obtained from the vapor pressure above the solid. The model assumes an S_8 concentration of zero at the silver surface, *i.e.*, all S_8 striking the coupon surface is consumed by silver. The diffusivity of S_8 at room temperature was estimated from the diffusivity of air and the relationship

$$\frac{D_{sulfur}}{D_{air}} = \sqrt{\frac{MW_{air}}{MW_{sulfur}}}$$

to be 0.036 cm²/sec. With this model the calculated rate of silver sulfide formation at room temperature was 0.7 Å/hr in reasonable agreement with the experimental rate. Unfortunately the diffusivity of silver in silver sulfide is not well known below 90°C, which prohibits calculating a silver diffusion limited tarnishing rate. Parabolic kinetics have been observed at considerably higher tarnishing agent concentrations (> 1 ppm hydrogen sulfide) (6). For initial film formation rates in excess of approximately 10 Å/hr at room temperature, the diffusivity of silver in silver sulfide appears to be rate controlling.

The morphology of the tarnish films formed at 50°C under the conditions of this study was not appreciably affected by the relative humidity, as the micrographs in Fig. 3 and 4 indicate. The high magnification micrographs in Fig. 3 of approximately 5000Å sulfide films exhibit the crystallinity in the surface film that was observed on the tarnished coupons. The apparent greater crystallinity seen in micrograph d relative to that in micrographs b and c is a result of random variations across the coupon surfaces.

In all cases examined, the tarnish film thickness at the coupon edges was greater than the thickness at the center. The micrographs in Fig. 4 show the extensive dendritic growths observed at the coupon edges and a rapid drop in dendrite density immediately interior to the edges. The tarnish film thickness variations on these coupons, as determined by the SEM/x-ray method, are summarized in Table I. The tarnish film thickness at the coupon centers is from 1240 to 2940Å less than the average thickness at the corners. The trend toward increasing thickness away from the center can be attributed to the statistical distribution of the sulfur diffusion paths as affected by convection currents from the sulfur source to the coupon surface. Most of the film thickness measurements for the four corners are within 200Å of the average of the corners and can be considered essentially identical. However, the corners of the coupons exposed at 0 and 100% RH that exhibited thicknesses of 6500 and 5180Å, respectively, are significantly different from the average.

Table I. Silver sulfide tarnish film thicknesses by S/Ag x-ray intensity ratio (18 day exposure at 50°C)

Percent RH of test atmosphere	Thickness (A)		
	Four corners of coupon	Average of the corners	Coupon center
0	5770, 5770, 6500, 5710	5940	3000
51	5120, 5250, 5180, 5370	5230	3990
100	5180, 5960, 5820, 5770	5680	4020

These nonuniformities indicate that the wide scatter in tarnish rate data found for films analyzed by cathodic reduction in this study and in others could be at least partially caused by random fluctuations in the surface condition prior to tarnishing that may be experimentally caused but that would be most difficult if not impossible to avoid. They could also relate, in part, to convective effects on the sulfur arrival rates. Mechanistic interpretations utilizing film thickness data based on cathodic reduction or other averaging techniques may not always be as straightforward as is often thought. In some cases, for example the mixed oxide, sulfide films that usually form on copper, regional fluctuations in the rates of competing reactions may occur across the surface of test coupons. For silver, the variations in sulfide thickness could result in or be caused by localized mechanistic differences or nonuniform surface energetics but do not appear to influence the average rate of the sulfur limited reaction.

Some of the previous studies of sulfidation of silver have documented the growth of dendrites, whiskers, or platelets. Drott (3), using 2% hydrogen sulfide in water saturated air at room temperature, noted that the appearance of whiskers occurred simultaneously with a sudden increase of the reaction rate. The whisker growth was uniformly distributed and oc-

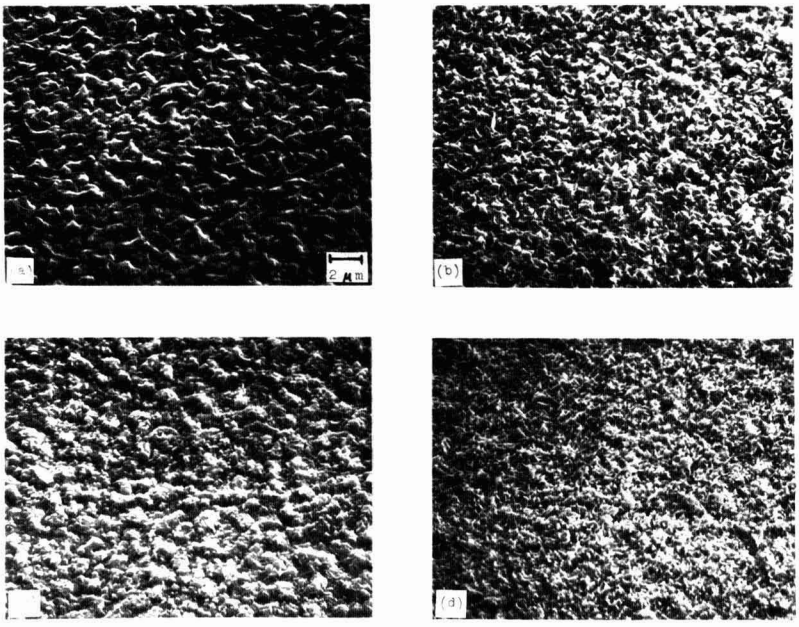

Fig. 3. Morphology of the interior surfaces of silver coupons: (a) untarnished coupon; (b-d) coupons tarnished to a sulfide film thickness of approximately 5000Å at 0, 51, and 100% RH, respectively.

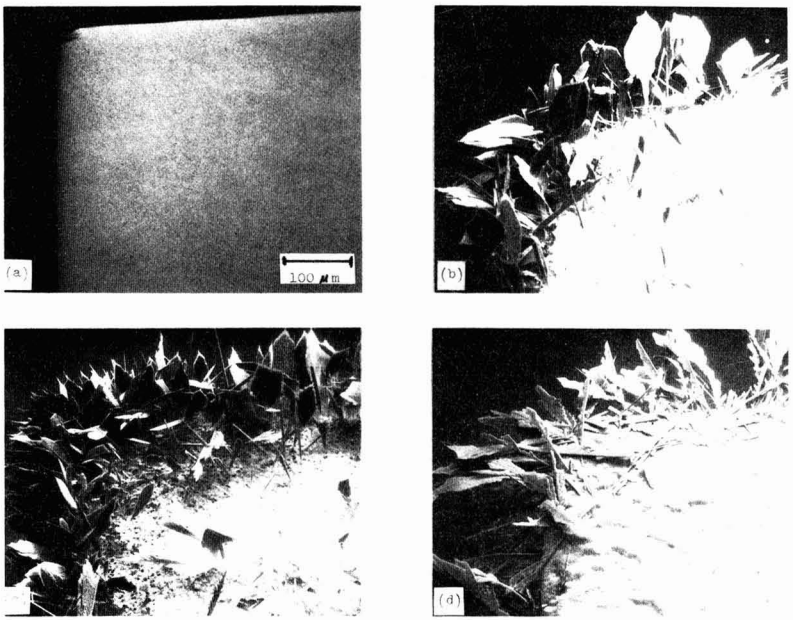

Fig. 4. Dendritic growths at the corners of silver coupons: (a) untarnished coupon; (b-d) coupons tarnished to a sulfide film thickness of approximately 5000Å at 0, 51, and 100% RH, respectively.

curred after the formation of discrete mounds whose distribution was unrelated to the grain structure of the metal. It was suggested that whiskers sprouted when critical mound conditions existed that were brought about by mechanical tension due to rapid growth. Backland *et al.* (4) and Bennett *et al.* (9) reported similar findings.

At the very high tarnishing agent concentrations of Drott the increase in tarnishing rate coincident with whisker growth can be attributed to the sudden availability of silver in a silver-limited environment. In the sulfur limited environment of this study an increased growth rate coincident with whisker growth would not occur. The preferential growth of dendrites at the edges indicates that the rate of arrival of sulfur there was sufficiently large to create a mechanically stressed surface. The surplus silver available at the outer ends of the easy diffusion paths apparently allows whisker growth to start. After initiation, the sulfur arrival process and the surface diffusion paths available on the dendrites would probably be expected to produce preferential growth on the whiskers. The average growth rate would remain linear.

Manuscript submitted June 12, 1980; revised manuscript received *ca.* Sept. 24, 1980.

Any discussion of this paper will appear in a Discussion Section to be published in the December 1981 JOURNAL. All discussions for the December 1981 Discussion Section should be submitted by Aug. 1, 1981.

Publication costs of this article were assisted by Bell Laboratories.

REFERENCES

1. W. H. J. Vernon, *Trans. Faraday Soc.*, **31,** 1668 (1935).
2. S. Lilienfeld and C. E. White, *J. Am. Chem. Soc.*, **52,** 885 (1930).
3. J. Drott, *Arkiv För Kemi,* **15,** 181 (1960).
4. P. Backlund, B. Fjellström, S. Hammerbäck, and B. Maijgren, *ibid.*, **26,** 267 (1966).
5. R. V. Chiarenzelli, *IEEE Trans. Parts, Mater., Packag.*, **pmp-3,** 89 (1967).
6. D. Pope, H. R. Gibbens, and R. L. Moss, *Corros. Sci.*, **8,** 883 (1968).
7. W. H. Abbott, "Proceedings of the Holm Seminar on Electrical Contact Phenomena," p. 53, Chicago, Ill. (1968).
8. W. E. Campbell and U. B. Thomas, *ibid.*, p. 233 (1968).
9. H. E. Bennett, R. L. Peck, D. K. Burge, and J. M. Bennett, *J. Appl. Phys.*, **40,** 3351 (1969).
10. J. A. Lorenzen, "Proceedings of the Institute of Environmental Sciences," p. 110, Mt. Prospect, Ill. (1971).
11. W. A. Crossland, E. Knight, and C. R. Wright, "Proceedings of the Holm Seminar on Electrical Contact Phenomena," p. 265, Chicago, Ill. (1973).
12. W. H. Abbott, *IEEE Trans. Parts, Hybrids, Packag.*, **php-10,** 24 (1974).
13. H. Schmidt-Brücken and W. Betz, *Mettalloberflaeche Angew Elektrochem.*, **28,** 373 (1974).
14. K. L. Schiff and H. Becker, *Electr. Contacts,* **24,** 295 (1978).
15. D. Simon, J. Bardolle, and M. Bujor, "Proceedings of the Holm Seminar on Electrical Contact Phenomena," p. 55, Chicago, Ill. (1979).
16. B. T. Reagor, Publication in preparation, unpublished work.
17. J. D. Sinclair, Publication in preparation.
18. T. E. Graedel, G. W. Kammlott, and J. P. Franey, Publication in preparation.
19. W. H. Abbott, *IEEE Trans. Parts, Mater., Packag.*, **pmp-5,** 156 (1969).
20. W. E. Campbell and U. B. Thomas, *Trans. Electrochem. Soc.*, **76,** 303 (1939).
21. A. N. Nesmeyanor, "Vapor Pressure of the Chemical Elements," translated from 1961 Russian ed., pp. 314-320, Elsevier, New York (1963).
22. "The Sulphur Data Book," W. N. Tuller, Editor, pp. 26-28, McGraw-Hill Book Co., New York (1954).
23. F. E. M. O'Brien, *J. Sci. Instr.*, **25,** 73 (1948).
24. C. P. Hedlin and F. N. Trofimenkoff, "Humidity and Moisture," Vol. 3, A. Wexler and W. A. Wildhack, Editors, 1963 International Symposium on Humidity and Moisture, Washington, D.C.
25. A. Wexler and S. Hasegawa, *J. Res. Nat. Bur. Stand.*, **53(1),** 19 (1954).
26. R. H. Stokes and R. A. Robinson, *Ind. Eng. Chem.*, **41,** 2013 (1949); R. A. Robinson and R. H. Stokes, "Electrolytic Solutions," 2nd ed., Butterworths, London (1959).
27. W. A. Wink and G. R. Sears, *TAPPI,* **33,** 96 (1950); *Chem. Abstr.*, **44,** 10416 (1950).
28. F. H. Huttig and F. Reyscher, *Z. Anorg. Chem.*, **137,** 155 (1924).
29. G. Edgar and W. O. Swan, *J. Am. Chem. Soc.*, **44,** 570 (1922).
30. J. R. Adams and A. R. Merz, *Ind. Eng. Chem.*, **21,** 305 (1929).

31. J. Obermiller and M. Goertz, Z. *Phys. Chem.*, **109,** 145 (1924).
32. A. Lannung, *ibid.*, **A170,** 134 (1934).
33. H. Rickert, *Werkst. Korros.*, **19,** 869 (1968).
34. H. Rickert and K. H. Tostmann, *ibid.*, **21,** 965 (1970).
35. W. Jost, "Diffusion in Solids, Liquids, Gases," p. 9, Academic Press Inc., New York (1970).

Niobium Triselenide in a Lithium Dioxolane Cell

M. Stanley Whittingham*,[1] and Gerald H. Newman*

Exxon Research and Engineering Company, Linden, New Jersey 07036

For many applications there is a need for a secondary battery with a high volumetric energy density. Although the lithium titanium disulfide cell has very good rechargeability and gravimetric energy density, it has a rather low volumetric energy density compared with some primary cathodes such as MnO_2 and FeS_2. The oxide has a higher potential and the sulfide reacts with about two lithium:

$$Li + MnO_2 \rightarrow LiMnO_2 \qquad 2.8 \text{ volts}$$

$$Li + TiS_2 \rightarrow LiTiS_2 \qquad \sim 2.1 \text{ volts}$$

$$2Li + FeS_2 \rightarrow Li_2FeS_2 \qquad \sim 1.5 \text{ volts}$$

In contrast to the disulfide, titanium trisulfide will react with three lithium to give the compound Li_3TiS_3. However, this compound shows very poor reversibility, less than one lithium being discharged on the 2nd cycle, because of structural changes (1). Niobium triselenide is much more reversible (2), but even here the best reported cycling showed a 60% loss in capacity in going from the first to the third cycle (3). The capacity then fell in the range 26-30% of the first cycle capacity for the next sixty cycles.

The reversibility of the Li/TiS_2 cell was maximized when dioxolane was used as the electrolyte solvent (4). We therefore conducted experiments on the trichalcogenides using dioxolane as the solvent. The cells were constructed as described earlier (5), using as electrolyte a 2.5 molar solution of lithium perchlorate in dioxolane. They were then cycled (6) continuously at 2 ma/cm^2 between voltage limits of 2.65 and 1.45 volts. On the first discharge 2.33 lithium were incorporated into the niobium triselenide lattice, 78% of the theoretical value. This decayed slowly on cycling as shown in Fig. 1. This figure also compares the data in the dioxolane solvent with that obtained (3) in a $LiClO_4$/propylene carbonate cell to which 3 wt.% of an ether additive, tetraglyme, has been added. The latter in turn was much improved over a pure propylene carbonate solvent (3). Just as for titanium disulfide, dioxolane gives the best cycling performance for niobium triselenide. The reason for this is not clear but is related to a number of factors, probably including its lithium plating capability which minimizes formation of lithium "sludge", its greater resistance than propylene carbonate to react at the cathodic lithium potentials and better wetting of the cathode and separators.

The experiments were extended to two other trichalcogenides, NbS_3 and TiS_3, to see whether their cycling could also be improved. The NbS_3 was discharged at 2 ma/cm^2 for the first two cycles and then at 1 ma/cm^2 thereafter; charging throughout was at 1 ma/cm^2. The TiS_3 cathode was discharged at 2 ma/cm^2 but due to the very low capacities the charge rate was only 0.5 ma/cm^2; this was further reduced to 0.25 ma/cm^2 after the 27th discharge. The cycling behavior of these two cathodes are compared with despite the less demanding cycling regime. Thus on the 20th cycle, the capacities are 66%, 30% and 2.6% for $NbSe_3$, NbS_3 and TiS_3 respectively. This behavior is probably a result of an inherent irreversibility of at least part of the lithium in the two sulfides, rather than a function of the electrolyte, as described elsewhere (1,5,7-9). When TiS_2 cells are cycled under similar conditions the loss of capacity over 60 cycles is about 20%. This was reduced to about 0.1%/cycle by applying pressure to the cells (10), and it is anticipated that the capacity of $NbSe_3$ cells would be similarly improved as Jacobson (11) has shown in very slow cycling tests that $NbSe_3$ is inherently totally reversible. In addition, a low capacity, 4 mAHr, $NbSe_3$ cell has recently been cycled to over 80% of 3 Li/Nb sixty times (12).

*Electrochemical Society Active Members

1. Present Exxon Address: P. O. Box 101, Florham Park, N. J. 07932

REFERENCES

1. M. S. Whittingham, J. Electrochem. Soc. 123, 315 (1976).
2. J. Broadhead and F. A. Trumbore, Abstract 178 p. 445, The Electrochemical Society Extended Abstracts, Chicago, Illinois, May 13-18, 1973 and U.S. Pat. 3,864,167.
3. J. Broadhead, T. M. Putvinski & F. A. Trumbore, U.S. Patent 3,928,067.
4. L. H. Gaines & G. H. Newman, Can. Pat. 1,066,766.
5. M. S. Whittingham, Progress in Solid State Chem., 12, 41 (1978).
6. M. S. Whittingham & G. H. Newman, U.S. Patent 4,086,403.
7. R. R. Chianelli & M. B. Dines, Inorg. Chem., 14, 2417 (1975).
8. D. W. Murphy & F. A. Trumbore, J. Electrochem. Soc., 123, 960 (1976).
9. G. L. Holleck, F. S. Shuker & S. B. Brummer, Proc. 10th IECEC Mtg., Delaware, 10, 444 (1975).
10. M. S. Whittingham & J. A. Panella, Mat. Res. Bull., 16, 1 (1981).
11. A. J. Jacobson, to be published.
12. J. Broadhead, 5th Australian Electrochemistry Conference, to be published.

Manuscript submitted Sept. 29, 1980; revised manuscript received Dec. 17, 1980.

Publication costs of this article were assisted by Exxon Research and Engineering Company.

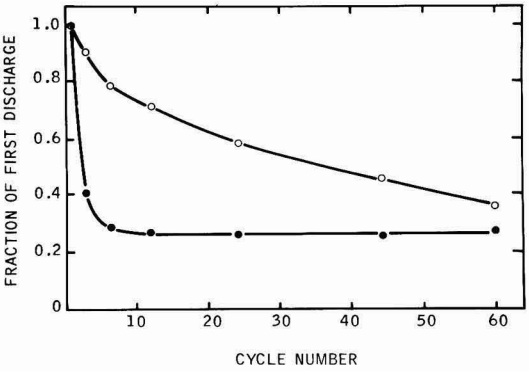

FIG 1 Discharge capacity of $NbSe_3$ in lithium cells containing as electrolyte solvent (o) dioxolane and (●) propylene carbonate/3% tetraglyme

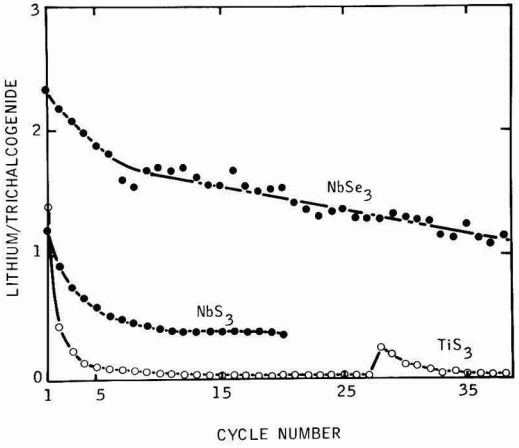

FIG 2 Discharge capacity of $NbSe_3$, NbS_3 and TiS_3 in lithium cells using a lithium perchlorate/dioxolane electrolyte and no conductive diluent in the cathode

Low Pressure Deposition of Silicon Nitride by $SiCl_4$ and NH_3 Reaction

I. Szendro and E. Marton

TUNGSRAM, H-1340, Budapest, Hungary

Low pressure deposition processes utilizing SiH_4-NH_3 and SiH_2Cl_2-NH_3 have been reported. The former reaction is extremely sensitive to wafer spacings and system configurations /1.,2./. The SiH_2Cl_2-NH_3 /1.,3./ reaction yields excellent film uniformities and reproducibilities. However, to achieve this, care should be taken of the control of temperature and pressure, and at 900°C it requires a rather high capacity vacuum system /1./.

In our study we have applied the $SiCl_4$-NH_3 reaction /which is well known at atmospheric, cold wall conditions/ to a low pressure hot wall system as this nitride forming process was expected to be less sensitive to process variations.

Experiments. -- The LPCVD system consisted of a normal resistance heated furnace and a quartz tube /80/74 mm/ without any special tube inserts. The 2 inch diameter wafers were held in four basket type quartz carrier with wafer plane perpendicular to the tube axis. One wafer carrier consisted 25 slots with 3,2 mm spacings. The vacuum exhaust system was based on a LN_2 trap followed by a mechanical vacuum pump of 585 l/min capacity. The pressure could be independently controlled by introducing N_2 gas directly into to vacuum inlet line of the pump. Pressure was measured at the front of the tube by a Baratron 221 type capacitance manometer, temperatures reported here were measured in the subatmospheric reaction zone.

Gases were controlled by taper tube flowmeters /Matheson Gas Prod./, the $SiCl_4$/Merck, zur Synthese/ was held in a stainless steel reservoir, and its vapour was introduced into the reactor zone by N_2 carrier gas. In some experiments undiluted, pure $SiCl_4$ vapour was introduced into the reactor with the help of a mass flow controller, connected between the outlet of the reservoir and the inlet of the reactor quartz tube. In those cases, the N_2 gas inlet of the $SiCl_4$ reservoir was closed and only the $SiCl_4$ vapour / ~260 mbar at 20°C/ feeded the MFC inlet. This set up is useful if one needs a high $SiCl_4$ partial pressure in the reactor, because no N_2 carrier is needed. The E.G. ammonia and diclorosilane /for comparative nitride depositions/ was supplied by Matheson Gas Prod., the N_2 was obtained from liquid nitrogen source and after purification its oxygen and water concentration was less than 2 ppm. All thickness and refractive index measurements were made with a laser ellipsometer.

Results.-- The deposition rate was studied as a function of temperature and the results are plotted in Fig. 1. The Arrhenius curves show that the $SiCl_4$-NH_3-N_2 process is about half as sensitive to temperature change / ~0,9 %/°C/ as the SiH_2Cl_2-NH_3 process /~1,7 %/°C/. On Fig.2. the $SiCl_4$ and SiH_2Cl_2 partial pressure effect on the nitride growth rate is shown and the advantages of $SiCl_4$ over SiH_2Cl_2 are significant as to deposition rate change versus pressure change. Deposition rate versus wafer spacing was determined for several system pressures and there was no difference between the two nitride forming process.

Film uniformity within a wafer and

Key words: LPCVD, silicon nitride

within wafer to wafer in a 100 wafers load was studied as a function of pressure and temperature slope. In order to get a better uniformity within a wafer than ± 2,5 % and a better than ± 4 % within wafer to wafer the pressure must be below 1,1 mbar, wafer spacings 3,2 mm, and as high as 1,5°C/cm temperature slope should be achieved in the reactor zone declining towards the gas inlet.

The physical and chemical properties of the silicon nitride layers produced by the $SiCl_4$-NH_3 LPCVD process was found to be similar to those deposited by the $SiCl_4$-NH_3 reaction at atmospheric conditions /4./ or by the SiH_2Cl_2 - NH_3 LPCVD process /1./. The refractive index is 1,98 ±0,01, the etch rate in 40 % HF at 25°C is 11 nm/min, the i.r. absorption maximum is at 830 cm^{-1}.

It is known that at atmospheric deposition conditions trace amounts of oxygen and water can cause off stoichiometric silicon nitride layers /5./. We have carried out some experiments to see how the gas phase O_2 and H_2O contamination affects the LPCVD silicon nitride film properties. The preliminary results are suprising and futher experiments have to be made. It is found that up to 50 ppm O_2 concentration in the SiH_2Cl_2-NH_3 process and 50 ppm H_2O in the $SiCl_4$-NH_3 process has no effect on such nitride properties as refractive index, etch rate, i.r. absorption. The possible explanation is that in the hot wall reactors the O_2 and H_2O can not reach the wafers surface because they react in the hot gas phase much faster with SiH_2Cl_2 and $SiCl_4$ than NH_3 does, and the oxide forming reaction is finished already in the colder inlet side of the reactor.

Acknowledgment. -- Authors are grateful to Gy. Mótal for his encouragement during this work and to F. Nagel for his help in building the LPCVD equipment.

Manuscript submitted March 26, 1980; revised manuscript received Dec. 9, 1980.

REFERENCES

1. R.S. Rosler, Solid State Technology, vol. 20, pp. 63-70. Apr. 1977
2. E.Tanikawa, O. Takayama and K.Maeda, Proc. 4th Int. Conf. on C.V.D., 1973. pp 261-274
3. W-A. Brown, T.I. Kamins, Solid State Technology, pp 51-57. July 1979.
4. M.J. Grieco, F.L. Worthing and B. Schwartz, J. Electrochem. Soc. vol. 115, no.5. pp 525-531 May 1968.
5. V.A. Wells and M.V. Hanson, Proc. 7th. Int. Conf. on C.V.D., 1979 pp 190-197.

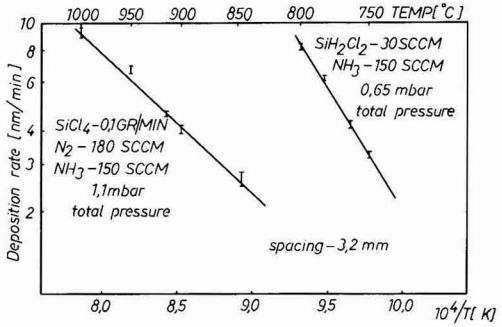

Fig.1. Silicon nitride deposition rate versus 1/T.

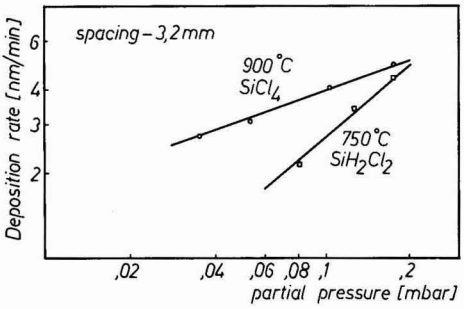

Fig.2. Silicon nitride deposition rate versus $SiCl_4$ and SiH_2Cl_2 partial pressure

Al/FeS_2 Secondary Cells Using Organic Electrolytes

Setsuko Takahashi and Nobuyuki Koura*

Department of Industrial Chemistry, Faculty of Science and Technology, Tokyo University of Science, 2641 Yamazaki, Noda Chiba 278, Japan

Aluminum is a common and inexpensive metal with a high theoretical capacity and a negative potential, but for use as the negative electrode of cells, it has some drawbacks, oxide film formation, self corrosion, and dendritic deposit. Therefore, there are few practical cells with an Al electrode (1).

It is considered that if the above drawbacks can be overcome, aluminum is highly promising as the active material for the negative electrode of advanced secondary cells. We have investigated Al/$AlCl_3$-NaCl-MCl_x/FeS_2 cells for load-leveling applications and in electric vehicles (2), and there are many other investigations (1) showing that a smooth, dense aluminum deposit forms in organic electrolytes. For this reason, Al/$AlCl_3$-organic solvent/FeS_2 cells have been developed. It was expected that these cells will offer a long service life and high terminal voltage at around room temperature.

The Al electrodes were spiraled rods (ϕ5 mm, 99.99% purity) with areas five to seven times the areas of the FeS_2 electrodes. Details of the FeS_2 electrode are given elsewhere (2). The FeS_2 electrode (7 mm thick, ϕ25 mm) was degassed and immersed in the organic bath in vacuo to wet both the FeS_2 powder and the current collector completely with the electrolyte.

$AlCl_3$ and lauryl pyridinium chloride (LPC) were dried at 80°C for 10 h in vacuo. In tetrahydrofuran (THF) system, $LiAlH_4$ was added to the THF, the solution was refluxed at 70°C for 6 h, and the $AlCl_3$ was put in a THF-benzene or a THF solution to which was added the THF-$LiAlH_4$ solution. Electrolyte preparation was done under a dry N_2 atmosphere. The cell comprises an upper Al electrode and a lower FeS_2 electrode (distance: 5 ∿ 10 mm). Cell performance was observed during about 30 repetitions (1 ∿ 2 months) of the discharge (cutoff: 0.5 V) - charge (cutoff: 2.1 ∿ 3.0 V) cycle under the N_2 atmosphere. The ohmic drop (IR drop) was checked once every 30 minutes with a relay. Potential-current curves were given potentiostatically.

After several cycles the cell performance was steady, therefore, the data (IR-free) of each 10th cycle are presented. Although charge curves are not shown, the coulombic efficiencies were from 80 to 100%. Discharge curves for the LPC systems are shown in Fig. 1. In the case of a 63.0 mol% $AlCl_3$ - 37.0 mol% LPC bath, in which the current density at the FeS_2 electrode was 3 mA/cm^2 and bath temperature was 125 °C, although the discharge capacity was only 0.03 Ah and the IR drop was large (0.5 V), the open circuit voltage (OCV) was 1.50 V. When toluene was added to the bath to lower its temperature, discharge capacity fell to 0.02 Ah at 100°C. For an FeS_2 electrode with a 38% graphite additive, however, discharge capacity for the above bath rose to 0.07 Ah at 60°C and 0.1 Ah at 100°C. The additive had no pronounced effect either on OCV or IR drop. Since THF baths are very favorable to Al deposition, and can be operated at relatively low temperatures, it was decided to test this system (Fig. 2). The discharge capacity rose no higher than 0.32 Ah (ca. 20% of the theoretical capacity). However at room temperature and 5 mA/cm^2, the discharge curve showed a high voltage plateau of about 2.3 V and a low voltage plateau of about 1.0 V. Moreover, in the case of a vitreous carbon current collector, the high voltage plateau capacity increased significantly. These facts indicate that THF systems are very promising.

Potential-current curves for Al

*Electrochemical Society Active Member

Key words: aluminum, FeS_2, secondary cell, organic electrolyte

anode in LPC and THF systems showed the limiting current of 0.7 mA/cm^2 for the LPC systems and 7 mA/cm^2 for the THF systems. In THF systems the reactions are considered to be as follows:

$AlCl_3+LiAlH_4 \rightleftharpoons 2AlH_2Cl+LiCl$,

$AlH_2Cl+LiCl \rightleftharpoons LiAlH_2Cl_2 \rightleftharpoons Li^+ + AlH_2Cl_2^-$.

It is also known that the lower the concentration of $LiAlH_4$, the smaller is the conductivity of the electrolyte (3). In the case of the bath B in Fig. 2, the conductivity was 5.47×10^{-3} Ω^{-1}/cm. We suggest that ionic species ($AlH_2Cl_2^-$, etc.) may be present in insufficient quantities in the electrolyte, and that this is the reason why this cell has a big IR drop and a small discharge capacity. Thus the immediate need is to improve the electrolyte. The fact that the addition of graphite greatly raised the discharge capacity but had little effect on IR drop further corroborate the above reasoning. In a molten-salt cell (Li-Al/LiCl-KCl/FeS_2), it is known that the problem of FeS_2 electrode conductivity is not so severe, due to the existence of certain phases (4), while in the organic solvent cells studied, such phases were not detected by X-ray analysis. Therefore, it is considered that a conductive material should be added to the FeS_2 electrode of organic cells in order to raise the discharge capacity. Since the graphite did not affect the OCV, it would seem that there can have been no effect from a 'carbon-metal complex' (5).

If the cell reactions are:

$(2/3)Al+FeS_2 \rightleftharpoons FeS+(1/3)Al_2S_3$,

$(2/3)Al+FeS \rightleftharpoons Fe+(1/3)Al_2S_3$,

two plateaus should appear in the discharge curve as seen in Fig. 2. FeS and Al_2S_3 were detected by X-ray analysis of a discharged FeS_2 electrode. But the e.m.f. values calculated from free energy values for the above reactions do not correspond to those observed. It should be considered that some complex compounds may be formed in the FeS_2 electrode by the interaction of Al_2S_3 with iron-sulfur compounds such as in the Li-Al/FeS_2 cell (4).

It is suggested that through improvement of the electrolyte and investigation of suitable additives for the FeS_2 electrode, the promise of this cell can be realized in the development of an advanced, high-capacity secondary cell.

REFERENCES

1. N.Koura and S.Takahashi, Alutopia, 10, 49 (1980) and references cited.
2. N.Koura, This Journal, 127, 1529 (1980).
3. M.Yoshio and N.Ishibashi, J. Appl. Electrochem., 3, 321 (1973).
4. F.C.Mrazek and J.E.Battles, This Journal, 124, 1556 (1973).
5. E.S.Buzzelli, U. S. Patent, 3650834 (1972).

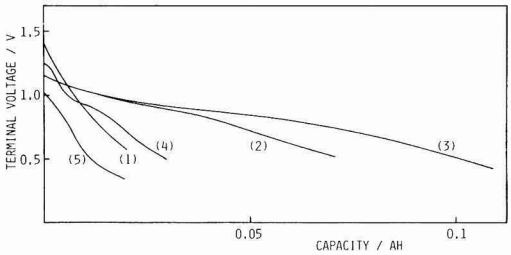

Fig. 1 Discharge curves for (A) 63mol% $AlCl_3$+37mol% LPC bath or (B) (A)+sat. toluene bath. (1) bath B, 50°C, FeS_2 4 g+C 3g; (2) bath B, 60°C, FeS_2 4g+C 3g; (3) bath B, 100°C, FeS_2 4g+C 3g; (4) bath A, 125°C, FeS_2 8g; (5) bath B, 100°C, FeS_2 8g. C.D.: 3 mA/cm^2.

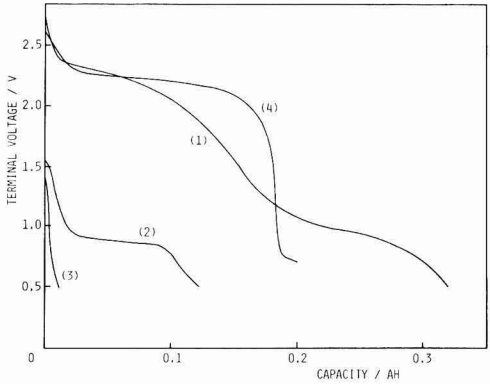

Fig. 2 Discharge curves for (A) 1.5M $AlCl_3$+0.3M $LiAlH_4$+80vol% THF+20vol% benzene bath and (B) 0.5M $AlCl_3$+0.5M $LiAlH_4$+THF bath. (1) bath B, room temperature, 5 mA/cm^2, FeS_2 4g+C 3g; (2) bath A, 50°C, 3 mA/cm^2, FeS_2 4g+C 3g; (3) bath A, 50°C, 3 mA/cm^2, FeS_2 8g; (4) bath B, room temperature, 5 mA/cm^2, FeS_2 4g, vitreous carbon c. c.

Manuscript received Sept. 11, 1980.

Publication costs of this article were assisted by Tokyo University of Science.

Surface Treatment Induced Sub-Band Gap Photoresponse of GaP Photoelectrodes

M. A. Butler* and D. S. Ginley*

Sandia National Laboratories, Albuquerque, New Mexico 87185

The efficiency and behavior of most photoelectrodes depend strongly on the nature of the surface and near surface region of the semiconductor. Thus it is to be expected that the electrodes are sensitive to surface treatment.[1] The predominant mechanism is thought to be the introduction or removal of localized states near the surfaces which can act as recombination centers or can modify the kinetics of the redox reaction. Such localized states, which may be in the band gap of the semiconductor, can provide a mechanism for a photoresponse at energies below the band gap.[2] In this paper we demonstrate that such a sub-band gap photoresponse can be generated in GaP photoelectrodes either by mechanically damaging the surface or by cathodic aging of the electrode.

The p-GaP samples were single crystal wafers cut perpendicular to the [111] axis and Zn doped to a density of $5x10^{17}cm^{-3}$. The contacts were made by sputtering In:Zn alloy and then annealing in vacuum. A conventional 3-electrode electrochemical cell was used with a PAR 173 potentiostat and a saturated calomel reference electrode. The illumination was by a quartz iodine lamp with a Schoeffel grating monochromator. Unless specified otherwise all experiments were run in 0.1M $HClO_4$ electrolyte. Typical sub-band gap spectra for various surface treatments are shown in Figure 1.

Figure 1a shows that etching of the photoelectrodes ~4 μm with a specific GaP etchant[3] removes any sub-band photoresponse that may have existed.

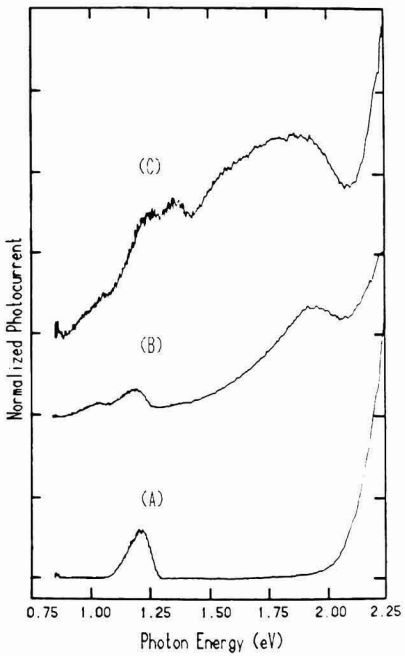

Figure 1. The sub-band-gap photoresponse of p-GaP with various surface treatments. The spectra are normalized to light intensity and the zero level is offset for (b) and (c) by an amount indicated by the left side of the spectra. All measurements were made at -2.0 V(SCE) in 0.1M $HClO_4$ using a filter to cut off the optical response above ~2.5 eV. (a) Polished surface etched 4 μ. (b) Surface mechanically polished using 1/4 μ diamond paste. (c) Cathodic aging under constant current conditions 5 mA for 1 hr. The peak at 1.2 eV is due to the second order reflection of the grating.

*Electrochemical Society Active Member.

Polishing the surface either wet or dry using various materials including diamond paste, aluminum oxide and SiC produces a sub-band gap response such as shown in Figure 1b. Similar behavior but with somewhat broader spectral features is produced by cathodic aging of the sample as shown in Figure 1c.

A sub-band gap response has also been observed in an n-GaP photoanode which was doped with sulfur to a density of 2×10^{18} cm^{-3}. The general features were the same as observed in p-GaP although a complete set of experiments on this sample have not been performed.

Etching for fixed time periods to profile the surface treatment effects shows that both polishing and cathodic aging produce damage extending ~1500Å into the surface. These results are confirmed by the potential behavior of the photocurrent shown in Figure 2. For a small optical absorption coefficient α it has been shown[4] that the photocurrent is:

$$J = \phi\alpha\left(\frac{2\varepsilon q}{N_D}\right)^{1/2}\left(V - V_{fb}\right)^{1/2} \quad [1]$$

where ϕ is the photon flux, ε the dielectric constant, q the electronic charge, N_D the dopant density and V the applied potential. Since the width of the depletion layer is given by:

$$W = \left(\frac{2\varepsilon}{qN_D}\right)^{1/2}\left(V - V_{fb}\right)^{1/2} \quad [2]$$

the linear relationship between J^2 and V shown in Figure 2 means that $J \propto W$. The observed photoresponse is a bulk effect arising throughout the depletion layer region. The maximum applied potential, - 4V(SCE), corresponds to a depletion layer thickness of ~0.09 μm. Thus, the linear region in Figure 2 indicates that the surface treatment effects are uniform between ~0.06 μm and ~0.09 μm. The deviation from linearity between 0 and -1V has been shown to arise from recombination in the near-surface region[5].

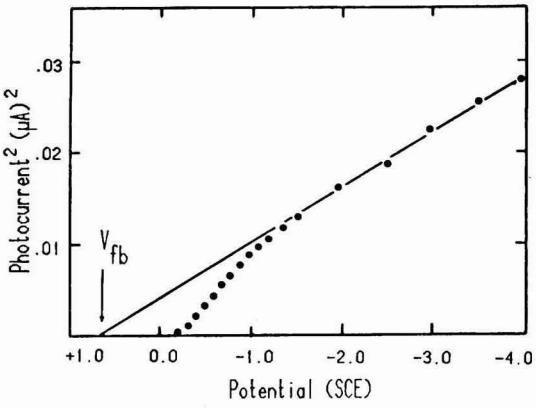

Figure 2. Potential behavior of the photoresponse at 1.75 eV of a polished sample taken in 0.1M $HClO_4$. Note the difference between photocurrent onset and flatband potential (V_{fb}) as determined by capacitance measurements.

In addition to etching, which removes the damaged near surface region, the sub-band gap photoresponse can be removed by anodic aging or by heat treating the sample. Treatment at 800°C for 1 hr. in vacuum totally removes the effect. Since at this temperature the partial pressure of P is higher than the partial pressure of Ga,[6] the heat treatment should change the stoichiometry of the near surface region by lowering the P/Ga ratio. Thus the sub-band gap response may arise from Ga vacancy related defects.

This idea is consistent with the production of a sub-band gap response by cathodic aging and its removal by anodic aging. These two bias conditions represent reductive and oxidative surface conditions which tend to remove Ga and P respectively from the sruface.[5] The exact nature of the defects responsible for the states in the gap is not known.

While the sub-band gap photoresponse induced by mechanical damage or cathodic aging can be removed by similar means, there are differences in such treated electrodes other than the obvious spectral differences

which can be observed. Simultaneously with the sub-band gap photoresponse measurements the capacitance of the interface and the photoresponse above the band gap were measured. Both of these measurements provide further information concerning the nature of the induced electronic states.

For a freshly etched surface in a 0.1M $HClO_4$ electrolyte a Mott-Schottky plot gives a straight line with an intercept of ~ + 0.7 V(SCE) and a slope indicative of a donor density of ~ $7 \times 10^{17} cm^{-3}$. The flat band potential is in good agreement with previously reported values(5) and the donor density is in agreement with the known bulk value of $5 \times 10^{17} cm^{-3}$. Anodic or cathodic aging of the sample does not significantly change either slope or intercept of the Mott-Schottky plot even though the cathodic aging induces a sub-band gap photoresponse. The photoresponse in 0.1M $HClO_4$ at 500nm (2.48eV) of a freshly etched surface has an onset at ~ 0.0V(SCE) again consistent with previously reported results. The discrepancy between the photocurrent onset and the flatband potential arises from recombination at bulk states in the band gap.(5) This behavior is also observed for anodically and cathodically aged samples.

For the mechanically damaged (polished) samples considerable changes are observed. The capacitance is drastically reduced although the intercept remains the same. The slope of the linear part of the Mott-Schottky plot suggests a reduction of the doping density by an order of magnitude with some variation from sample to sample. This interpretation is supported by the photoresponse at 500nm (2.48eV) which shows that the photocurrent increases by approximately a factor of three as would be expected for a lower doping levels and consequently increased depletion layer widths.

Thus it seems that the two processes which produce a sub-band gap photoresponse induce states of considerably different character. Cathodic aging produces states which do not change the overall doping level while polishing results in states which seem to compensate the p-type GaP samples. Both of these processes produce sub-band gap responses which are similar in spectral dependence.

REFERENCES

1. R. H. Wilson, L. A. Harris and M. E. Gerstner, J. Electrochem. Soc. 127, 884 (1979).

2. M. A. Butler, M. Abramovich, F. Decker and J. F. Juliao, J. Electrochem. Soc. (in press).

3. Manufactured by the TRANSENE Company Rt. 1, Rowley, Mass. 01969.

4. M. A. Butler, J. Appl. Phys. 48, 1914 (1977).

5. M. A. Butler and D. S. Ginley, J Electrochem. Soc. 127, 1273, (1980).

6. M. Ilegums, M. B. Panish and J. R. Arthur, J. Chem Thermodynamics 6, 157 (1974).

ACKNOWLEDGMENT

This work was supported by the Materials Sciences Division, Office of Basic Energy Sciences, U.S. Department of Energy, under Contract DE-AC04-76-DP00789.

Manuscript received July 22, 1980.

Publication costs of this article were assisted by Sandia National Laboratories.

Transference Number Measurements for the Polymer Electrolyte Poly(ethylene oxide) NaSCN

R. Dupon, D. H. Whitmore,* and D. F. Shriver

Departments of Chemistry and Materials Sciences, and Materials Research Center, Northwestern University, Evanston, Illinois 60201

Current interest in the development of high energy density batteries has focused considerable attention on solid electrolytes. The leading solid electrolytes in developmental batteries are hard ceramic materials, which usually are employed at elevated temperatures with liquid electrodes. A more compliant solid electrolyte, such as a polymer electrolyte, should enable contact to be maintained at the electrode-electrolyte interfaces in an all solid state battery and lower operating temperatures might be facilitated. Potential application of ion-containing polymers as battery electrolytes, and electrical measurements on salt complexes with poly(ethylene oxide) and with poly(propylene oxide) have been presented by Armand (1,2), and structural studies of poly(ethylene oxide) salt complexes have been reported from our laboratory (3). The original synthesis and characterization of these materials was reported by Wright (4,5) and extended by James (6).

A fundamental parameter in the characterization of any solid electrolyte is the fraction of the total current which is carried by the mobile ion, i.e. the transference number. Prior to the present work, a rigorous determination of the transference number for poly(ethylene oxide) based electrolytes was not available. The present study is based on the measurement of emf between ion reversible amalgam electrodes which are separated by the solid electrolyte in a concentration cell (7,8).

Experimental Procedure. -- Poly(ethylene oxide) with an average molecular weight 600,000 was obtained from Aldrich. The polymer was purified by ion-exchange of an aqueous solution and the solvent was subsequently removed under high vacuum. Reagent grade NaSCN (B & A) was recrystallized from methanol and dried under high vacuum. Reagent grade methanol (MCB) was dried by distillation from iodine-activated magnesium under a nitrogen atmosphere.

A PEO·NaSCN complex, 4.5:1 mole ratio of polymer repeat unit to salt, was prepared from stoichiometric quantities of the polymer and salt in anhydrous methanol. Following complete dissolution of the two solids, the methanol was removed under vacuum. All manipulations were carried out using standard inert atmosphere techniques (9). The identity of the PEO·NaSCN complex was confirmed by infrared spectroscopy and differential scanning calorimetry, and in previous research the material prepared by this same procedure has been characterized by optical microscopy and x-ray diffraction, which demonstrate the absence of free NaSCN.

Amalgams were prepared with triple distilled mercury and reagent grade sodium (MCB). Molten sodium was filtered through fritted glass to remove sodium oxide. The concentration of the stock amalgam, solution No. 1, Table I, was determined gravimetrically and checked by the gasometric method based on the amount of hydrogen evolved from the reaction of the sodium amalgam with hydrochloric acid. Concentrations of the remaining solutions were determined gravimetrically by successive dilution of the stock amalgam.

The sample and amalgams were placed in a cell which permitted exclusion of the atmosphere, Fig. 1. A pressed pellet of the PEO·NaSCN complex, 4.5:1, was fitted into an o-ring which was then clamped between the side arms. All loading of the polymer complex was carried out in a nitrogen filled dry box. One side arm was filled with the stock amalgam solution while the other was successively filled with the dilutions of the stock. Introduction of amalgam solutions was done with a gas-tight syringe under a flush of dry nitrogen.

Key words: Solid electrolyte, polymer electrolyte, transference number, poly(ethylene oxide).

*Electrochemical Society Active Member.

The potentials of the cell were measured using a Keithley 177 multimeter together with an electrometer containing an RCA CA3140 E MOS/FET operational amplifier designed to increase the input impedance of the measuring device to 10^{12} ohms. All measurements were made at room temperature, 23.5 ± 0.2 °C, which was monitored using an iron-constantan thermocouple and millivolt meter. The cell and connecting leads were placed in an aluminum box designed to shield the system from extraneous radiation. Reversing the cell polarity produced insignificant changes in the magnitude of the observed potentials. The emf was read after the potential had maintained a stable (± 0.3 mV) value over a period of one hour. Typical stabilizaton times were of the order of one to two hours. The measured results are given in Table I. As a check on these measurements, emf values were determined on a different batch of the polymer electrolyte using different amalgam preparations. Agreement between the data sets was good.

A value of the cell impedance was obtained by loading standard resistors in parallel with the cell and observing the change in emf. The observed room temperature cell impedance of 3.9×10^6 Ω was well within the capability of the measuring device and yielded a D.C. conductivity of 6.3×10^{-8} $(\Omega\ cm)^{-1}$, which is in general agreement with the A.C. value shown by Armand (2).

The emf of the concentration cell $Hg\text{-}Na(x_1) \mid PEO{\cdot}NaSCN \mid Hg\text{-}Na(x_2)$ is expressed by (8):

$$E_{obs} = (1 - t_e)E_{id} = (1 - t_e)\frac{RT}{nF} \ln \frac{a_1}{a_2} =$$

$$(1 - t_e)\frac{RT}{nF} \ln \frac{\gamma_1 x_1}{\gamma_2 x_2}$$

The activity coefficients for dilute amalgams (present case) may be calculated from the relationship (10):

$$\text{Log } \gamma = Qx$$

where

$$Q = 18.720 - 8.00 \times 10^{-3}\ T$$

From this, E_{id} may be calculated:

$$E_{id} = \frac{RT}{F} 2.303 \log \frac{x_1}{x_2} + \frac{RT}{F} 2.303\ Q(x_1 - x_2)$$

A plot of E_{obs} vs. E_{id} for each x_2 (x_1 being fixed as the stock amalgam, solution No. 1) yields a straight line (Fig. 2) of slope $(1\text{-}t_e)$.

Results and Discussion. -- For a purely ionic conductor the value of $(1 - t_e)$ should be unity. Least squares treatment of E_{obs} vs. E_{id} produced slope 1.005 ± 0.005, Fig. 2. This result establishes that the electronic contribution to the total electrical conductivity of PEO·NaSCN is negligible and that the ionic component is responsible for the conduction. Since sodium-reversible electrodes were employed and since the conductivity is close to the published A.C. data, the sodium ion is implicated as the major charge carrier in the PEO·NaSCN complex.

Table I. Ideal and observed emf's of concentration cell at room temperature.

Solution No.	x_{Na}	E_{id} (mV)	E_{obs} (mV)
1	0.04103	-	-
2	0.03426	11.13	10.98
3	0.02944	19.64	19.47
4	0.02406	29.99	29.11
5	0.01928	40.25	40.89
6	0.01440	52.36	52.10
7	0.009477	67.84	68.34

E_{obs} = the measured emf
t_e = electronic transference number
E_{id} = ideal emf, value of E_{obs} when $t_e = 0$
R = universal gas constant
T = absolute temperature
n = number of electrons transferred
F = Faraday constant
a_1, a_2 = activities of sodium in the amalgams
γ_1, γ_2 = activity coefficients of sodium in the amalgams
x_1, x_2 = mole fractions of sodium in the amalgams

Acknowledgment. -- We wish to thank Mr. J. R. Anderson for discussions and help with the instrumentation. This research was supported in part by the Office of Naval Research.

REFERENCES

1. M. Armand, J. M. Chabagno, and M. J. Duclot, Abstract 6.5, Extended Abstracts, Second International Conference on Solid Electrolytes, St. Andrews, Scotland, Sept. 20-22, 1978.

2. M. Armand, J. M. Chabagno, and M. J. Duclot, in "Fast Ion Transport in Solids," P. Vashishta, J. N. Mundy, and G. K. Shenoy, Editors, p. 131, North-Holland, Amsterdam (1979).

3. B. L. Papke, M. A. Ratner, and D. F. Shriver, J. Phys. Chem. Solids, in press.

4. D. E. Fenton, J. M. Parker, and P. V. Wright, Polymer, 14, 589 (1973).

5. P. V. Wright, Br. Polym. J., 7, 319 (1975).

6. D. B. James, R. S. Stein, and W. J. Macknight, Bull. Am. Phys. Soc., 24, 479 (1979).

7. L. Hsueh and D. N. Bennion, This Journal, 118, 1128 (1971).

8. R. Galli, F. A. Tropeano, P. Bazzarin, and U. Mirarchi, in "Fast Ion Transport in Solids," W. van Gool, Editor, p. 573, North-Holland, Amsterdam (1973).

9. D. F. Shriver, "The Manipulation of Air-Sensitive Compounds," McGraw-Hill, New York (1969).

10. T. Mussini, A. Maina, and A. Pagella, J. Chem. Thermodyn. 3, 281 (1971).

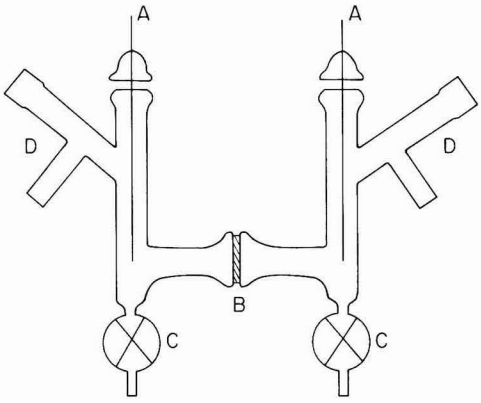

Fig. 1. Cell for transference number measurements. A, nickel electrode; B, polymer electrolyte; C, stopcock; D, Teflon in glass valves for N_2 inlet.

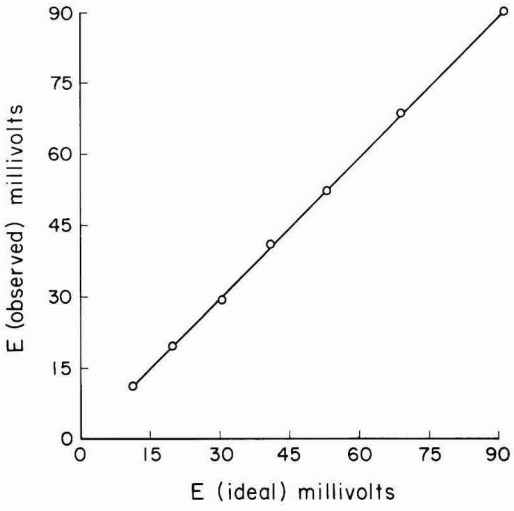

Fig. 2. Observed vs. ideal emf values for a Na/Hg concentration cell with NaSCN·PEO polymer electrolyte.

Manuscript received Nov. 17, 1980.

Publication costs of this article were assisted by Northwestern University.

THE ELECTROCHEMICAL SOCIETY
SHORT COURSE
PLASMA CHEMISTRY FOR IC FABRICATION
MINNEAPOLIS, MINNESOTA

Sunday, May 10, 1981, Leamington Hotel

Limited attendance—Advance registration required

The Electrochemical Society will sponsor a short course in conjunction with the 159th Meeting of the Society in Minneapolis, Minnesota, at the Leamington Hotel on Sunday, May 10, 1981. The course will consist of four lectures, two from 9:00 AM to 12:00 noon, and two from 1:30 to 4:30 PM. Copies of the slides, along with an outline and bibliography will be distributed to each registrant at the time of the course. The registration fee is $100 for members and $150 for nonmembers. The fee covers the course, luncheon, and text material; it is not applicable to any other activities of the Society's 159th Meeting. The attached registration form and a check for the correct registration fee must be received not later than **April 15, 1981,** at The Electrochemical Society, Inc., 10 South Main St., Pennington, N.J. 08534.

FUNDAMENTALS AND APPLICATIONS OF PLASMA CHEMISTRY FOR IC FABRICATION

Alexis T. Bell and Dennis W. Hess

Department of Chemical Engineering, University of California, Berkeley, California

This course will emphasize the physics and chemistry of rf glow discharges as they pertain to the fabrication of integrated circuits. The course is intended to serve as an introduction to plasma processing for those involved in the production of semiconductor devices. Course attendees should have the background normally contained in a standard undergraduate program with a major in physics, chemistry, or electrical engineering.

The first half of the course will cover basic principles of plasma physics and chemistry and will discuss some of the techniques available for plasma diagnostics. The fundamental physical characteristics of low pressure, nonequilibrium plasmas will be defined and their relationship to the kinetics of forming chemically active species will be demonstrated. The relationship of the free atoms, radicals, and ions produced in a plasma to the progress of overall chemical reactions (e.g., film deposition, etching, etc.) will be shown and a brief introduction to the modeling of plasma-chemical processes will be presented. The physical and chemical characterization of plasmas by means of electrical probes, mass spectrometry, and optical spectroscopy will be surveyed for the purpose of identifying the type of information obtainable from each technique.

The second half of the course will be devoted to a discussion of the applications of high frequency discharges to thin film etching and deposition processes used in integrated circuit fabrication. Examples will be chosen from the areas of photoresist stripping; semiconductor, insulator, and metal film etching; and silicon-based materials deposition. Recent results will be presented and discussed in terms of plasma physics and chemistry. Chemical and physical models which generate insight into the "tailoring" of etch rates and profiles, and deposited film properties will be indicated. Degradation of device properties due to plasma exposure will be considered.

SHORT COURSE REGISTRATION FORM

PLASMA CHEMISTRY FOR IC FABRICATION

Payment enclosed:

☐ ECS Member—$100.00 ☐ Nonmember—$150.00

Name_____

Address_____

City, State, Zip_____

Business Affiliation_____

Please return this form by April 15, 1981, with your payment to:
The Electrochemical Society, Inc., 10 South Main St., Pennington, N.J. 08534

JOURNAL OF THE ELECTROCHEMICAL SOCIETY

REVIEWS AND NEWS

MARCH 1981

Minneapolis—"City of Lakes"

The Leamington Hotel

Lake of the Isles, one of 22 lakes and lagoons in Minneapolis, with a view of the city in the background.

Minneapolis, Minnesota, site of the 159th Meeting of The Electrochemical Society, is well known as the "twin" city to its neighbor St. Paul, and as the educational, cultural, and entertainment center of the area. But Minneapolis is also called the "City of Lakes," and for good reason. It contains 11 major bodies of water, and can be most accurately described as a city of lakes, lagoons, waterfalls, rivers, creeks, and acres of rich rolling parks. During your stay in Minneapolis, you will see the many facets of this multidimensional town.

The home-base during your stay in Minneapolis will be the Leamington or Curtis Hotel, conveniently located in the Downtown area. From here you will find easy access to the "heart" of the city, with immediate proximity to all the unique opportunities that Minneapolis has to offer.

The Nicollet Mall in downtown Minneapolis, a gently curving pedestrian walkway flanked by trees, flowers, and fountains, is the heart of the city's exciting shopping scene. Lined by five major department stores and scores of specialty shops and boutiques, the Mall is where the visitor can shop in a unique and interesting atmosphere.

A visit to the Nicollet Mall will give you the perfect opportunity to utilize the extraordinary Minneapolis Skyway System. Fourteen glass-enclosed, climate-controlled overhead bridges provide weather-proof access between some 40 buildings in 32 blocks of the Downtown area.

Among the many interesting attractions on the agenda for the nontechnical registrants is The American Swedish Institute, headquartered in the former Swan J. Turnblad mansion. Turnblad was the publisher of the "biggest and best" (in his words) Swedish language newspaper in America. Today, the mansion serves as an extraordinary setting for the American Swedish Institute. It is a splendid example of a turn of the century interpretation of stately Romanesque chateau architecture. Coming close to our childhood visions of a medieval castle, it contains 33 rooms, three turrets, five chimneys, and 14 flues. Within its elegantly appointed rooms are displayed social and cultural artifacts spanning over 150 years of the Swedish experience in America.

Beautiful Loring Park and Lake, just a short stroll from downtown Minneapolis.

Other points of interest the visitor to Minneapolis will not want to miss are the Betty Crocker Kitchens; Foshay Tower, a Minneapolis landmark designed after the Washington Monument; and the Minnesota Zoological Garden. Just a short bus ride from Downtown, this conservatory of living things provides a blend of interior and exterior nature-imitating habitats amidst rolling hills and lakes for over 250 species of animals, and 2000 varieties of plants.

The magnitude of culture and arts also adds a special vitality to Minneapolis, which boasts a long list of fine museums and theaters. Among these are the world-renowned Guthrie Theater, offering the finest in repertory theater; the Minneapolis Institute of Arts and the Walker Art Center; and the Minnesota Orchestra, which ranks among the best in the nation.

Make it a point while in Minneapolis to enjoy the city's trademark and greatest blessing—its glistening lakes and wooded parks—the focal point of a recreation system unsurpassed in the nation. To make your trip complete, view the majestic 53 foot Minnehaha Falls, located in the wooded 155 acre Minnehaha State Park. Immortalized by the poet Longfellow, near these grand falls you will find bronze statues of the central figures of Longfellow's poem, Hiawatha and Minnehaha.

Enjoy your stay in Minneapolis. With a multitude of informative, exciting, and unusual things to see and do, you will have no trouble understanding why this metropolitan city has come to be admired and enjoyed by visitors from all over the world.

The Electrochemical Society, Minneapolis, Minnesota, Meeting
The Leamington-Curtis Hotels, May 10-15, 1981

		Monday May 11	Tuesday May 12	Wednesday May 13	Thursday May 14	Friday May 15
Iowa Room Lobby	**A.M.** **P.M.**	**Electronics/D&I—** 4th International Symposium on Silicon Materials Science and Technology	**Electronics/D&I—** 4th International Symposium on Silicon Materials Science and Technology	**Electronics/D&I—** 4th International Symposium on Silicon Materials Science and Technology	**Electronics/D&I—** 4th International Symposium on Silicon Materials Science and Technology	**Electronics/D&I—** 4th International Symposium on Silicon Materials Science and Technology
	Evening			**Electronics/D&I—** 4th International Symposium on Silicon Materials Science and Technology Informal Discussion		
Illinois Room Lobby	**A.M.** **P.M.**	**D&I/E&M—** Adhesion Aspects of Polymeric Coatings	**D&I/E&M—** Adhesion Aspects of Polymeric Coatings	**D&I/E&M—** Adhesion Aspects of Polymeric Coatings	**D&I/E&M—** Adhesion Aspects of Polymeric Coatings	
Michigan Room Lobby	**A.M.** **P.M.**	**Electronics/D&I—** Joint General Session	**Electronics/D&I—** Joint General Session	**Electronics/D&I—** Joint General Session	**Electronics/D&I—** Joint General Session	**Electronics/D&I—** Joint General Session
Twin Cities Lower Lobby	**A.M.** **P.M.**				**Electronics/D&I—** Recent News Papers	
New York Room Lower Lobby	**A.M.** **P.M.**	**E&M—** Thermochemistry of Intermetallic Compounds	**E&M—** Thermochemistry of Intermetallic Compounds	**Corrosion/Physical Electrochemistry—** Nonaqueous Electrolytes	**Corrosion/Physical Electrochemistry—** Nonaqueous Electrolytes	
Chicago Room Lower Lobby	**A.M.** **P.M.**	**Organic and Biological Electrochemistry—** Electrochemistry in the Study of Novel Organic Compounds	**Energy Technology—** General Session	**Organic and Biological Electrochemistry—** Mechanisms and Mechanistic Techniques in Organic Electrode Reactions	**Organic and Biological Electrochemistry—** Mechanisms and Mechanistic Techniques in Organic Electrode Reactions	**Organic and Biological Electrochemistry—** General Session

Milwaukee Room Lower Lobby	**A.M.** **P.M.**	**Organic and Biological Electrochemistry/Energy Technology—** Electrochemistry of Biomass Derived Compounds	**Organic and Biological Electrochemistry/Energy Technology—** Electrochemistry of Biomass Derived Compounds		**D&I—** Electrolytic Capacitor Technology	
Lincoln Room Second Floor	**A.M.** **P.M.**	**Battery/Energy Technology/Industrial Electrolytic—** Porous Electrodes	**E&M/Corrosion/Physical Electrochemistry/New Technology Subcommittee—** Vibrational Spectroscopy in Electrochemistry (Laser, Raman, and Infrared)	**E&M/Corrosion/Physical Electrochemistry/New Technology Subcommittee—** Vibrational Spectroscopy in Electrochemistry (Laser, Raman, and Infrared)	**E&M/Energy Technology—** Thermionic and Thermoelectric Generation Conversion	
Jefferson Room Second Floor	**A.M.** **P.M.**	**Education Committee—** Selected Movies	**Education Committee—** Selected Movies	**Education Committee** Selected Movies	**Physical Electrochemistry—** General Session	
Roosevelt Room Second Floor	**A.M.** **P.M.**	**Physical Electrochemistry/ Energy Technology—** Electrocatalysis	**Physical Electrochemistry/ Energy Technology—** Electrocatalysis	**Physical Electrochemistry/ Energy Technology—** Electrocatalysis	**Physical Electrochemistry—** Solid Electrolyte Interfaces	
Cardinal Room The Curtis, Lobby	**A.M.** **P.M.**	**Corrosion/D&I—** Anodic Oxidation	**Corrosion/D&I—** Anodic Oxidation	**Corrosion/D&I—** Anodic Oxidation	**Corrosion/D&I—** Anodic Oxidation	
East Room The Curtis, Lobby	**A.M.** **P.M.**	**Industrial Electrolytic—** Chlorine	**Industrial Electrolytic—** Chlorine	**Industrial Electrolytic—** Chlorine		
Solarium Room The Curtis, Lobby	**A.M.** **P.M.**	**Electronics—** Luminescence Display Technology and Special Purpose Cathode Ray Tubes	**Electronics—** Luminescence Display Technology and Special Purpose Cathode Ray Tubes **Electronics—** Luminescence Luminescence of II-VI Compounds	**Electronics—** Luminescence Luminescence of II-VI Compounds	**Electronics—** Luminescence General Session	
ABC Room The Curtis, Lower Lobby	**A.M.** **P.M.**	**Corrosion—** General Session				

Program

Minneapolis, Minnesota, Meeting

THE ELECTROCHEMICAL SOCIETY, INC.

May 10-15, 1981

Sunday through Friday

GENERAL INFORMATION

The 1981 Spring Meeting will be held at the Leamington and Curtis Hotels, 10th and 3rd Avenue South, Minneapolis, Minnesota. In the event you need to be contacted during the meeting, the telephone number is 612-370-1100.

In order to accommodate anticipated attendance, rooms have been reserved at these two hotels at comparable rates. Be sure to make your reservations early and, to obtain convention rates, use the hotel reservation card provided. All reservations should be made through the headquarters hotel, the Leamington. Room assignments will be made according to the receipt date of the reservation card and, insofar as is possible, at the rate requested. **ALL RESERVATIONS MUST BE RECEIVED AT THE LEAMINGTON HOTEL NO LATER THAN APRIL 17, 1981.**

TRAVEL INFORMATION

Check with your travel agent for super-saver or any other special air fares.

REGISTRATION

The registration area will be located in the Dakota Room, Lobby Level, in the Leamington Hotel.

Advance Registration

We suggest that all those planning to attend the 1981 Spring Meeting take advantage of ADVANCE REGISTRATION. If you need an advance registration form, please write to: Minneapolis Meeting, The Electrochemical Society, Inc., 10 South Main Street, Pennington, New Jersey 08534. The deadline for advance registration is April 24, 1981. Attendees who have used advance registration may pick up their packets during registration hours at a special desk.

Registration at the Meeting

The registration hours are as follows:

Sunday, May 10	4:00 P.M. to	9:00 P.M.
Monday, May 11	7:30 A.M. to	3:30 P.M.
Tuesday, May 12	8:00 A.M. to	4:00 P.M.
Wednesday, May 13	8:00 A.M. to	4:00 P.M.
Thursday, May 14	8:00 A.M. to	4:00 P.M.
Friday, May 15	8:00 A.M. to	10:00 A.M.

REGISTRATION FEES

All attendees are required to pay a registration fee according to the following schedule:

Technical Session Registration	
Members	$55.00
Nonmembers	80.00*
Emeritus and Honorary Members	Complimentary
Members (not currently employed)	2.00
Student Members	Complimentary
Student Nonmembers	2.00
Last Day Registration	
Members	15.00
Nonmembers	25.00
Nontechnical Registration	10.00

***If a nonmember submits an Application for Admission within four months of the meeting and is subsequently elected to membership in the Society, the difference between the nonmember and member registration fee will be applied to the first year's dues.**

MEETING INFORMATION

The technical sessions will be held in both hotels; for details, refer to the technical session program. All social functions, committee meetings, and luncheons will be held in the Leamington Hotel.

Society Headquarters Office	Washington A Room
Nontechnical Registrants Headquarters	Bali Room
Information/Message Center	Main Lobby

GENERAL FUNCTIONS

Sunday Evening Get-Together

An informal Sunday Evening Get-Together will be held in the Iowa Room, Lobby Level, from 8:00 to 10:00 P.M. All those registered for The Electrochemical Society Meeting are invited to attend.

Monday—Plenary Session

At 9:00 A.M., the Plenary Session will be held in the Iowa Room, Lobby Level. Gordon Moore, Intel Corporation, will deliver The Electrochemical Society Lecture, "A Perspective on VLSI."

Monday Evening Mixer

An informal social gathering will be held in the Minnesota Room, Lobby Level, from 6:00 to 7:30 P.M. Beer, soft drinks, and snacks will be served on a complimentary basis. In addition, there will be a cash bar for those who prefer mixed drinks. All meeting registrants are invited to attend.

Tuesday

Awards and Recognition Session

An Awards and Recognition Session will begin at 4:30 P.M. in the Iowa Room, Lobby Level.

Honorary Membership in the Society will be conferred upon Michael J. Pryor. In addition, other recognitions and awards will be presented including the Electronics Division Award.

In recognition of his outstanding contributions to the field of solid state science and technology, Gerald L. Pearson, Stanford Electronics Laboratories, has been named the recipient of the Solid State Science and Technology Award Medal and Prize. He will deliver the Solid State Science and Technology Award Address entitled, "Solid State Science and Technology in Retrospect."

Solid State Science and Technology Award Reception

Immediately following the award address (approximately 6:00 P.M.), everyone is cordially invited to attend a reception in the Illinois Room, Lobby Level, honoring Gerald L. Pearson, the recipient of the Solid State Science and Technology Award Medal and Prize.

COMMITTEE MEETINGS

Sunday, May 10, 1981

3:30 P.M.— Vittorio de Nora-Diamond Shamrock Award Selection Committee, Hoover B Room, Second Floor
3:30 P.M.— Electronics Division Subcommittee on VLSI, Hoover A Room, Second Floor
4:00 P.M.— Electronics Division Audit and Budget Committee and Ad Hoc Committee on Finances, Wilson Room, Second Floor
5:30 P.M.— Electronics Division Planning Committee, Adams Room, Second Floor
5:30 P.M.— Energy Technology Group Executive Committee, Taft Room, Second Floor
7:00 P.M.— Council of Local Sections, Jefferson Room, Second Floor
8:00 P.M.— Electronics Division Executive Committee, Lincoln Room, Second Floor

Monday, May 11, 1981

7:15 A.M.—Electrothermics and Metallurgy Division Executive Committee, Hoover B Room, Second Floor
10:00 A.M.—Education Committee, Washington B Room, Second Floor
10:00 A.M.—Olin Palladium Medal Award Subcommittee, Hoover B Room, Second Floor
12:15 P.M.— Dielectrics and Insulation Division Executive Committee and Planning Committee, Hoover A Room, Second Floor

1:30 P.M.— Society Meeting Committee, Washington B Room, Second Floor
2:00 P.M.— New Technology Subcommittee, Hoover B Room, Second Floor
3:30 P.M.— Electronics Division Planning Committee on Informal Discussions, Hoover A Room, Second Floor
4:30 P.M.— Honors and Awards Committee, Washington B Room, Second Floor
4:30 P.M.— Electronics Division Award Selection Committee, Room 224, Second Floor
4:30 P.M.— Representatives to the Individual Membership Committee, Wilson Room, Second Floor

Tuesday, May 12, 1981

7:30 A.M.—Symposium Subcommittee, Hoover B Room, Second Floor
9:30 A.M.—Technical Affairs Committee, Washington B Room, Second Floor
11:00 A.M.—Editorial Committee, Adams Room, Second Floor
1:30 P.M.— Publication Committee, Washington B Room, Second Floor
7:00 P.M.— Solid State Division Chairmen, Hoover B Room, Second Floor

Wednesday, May 13, 1981

7:30 A.M.—Dielectrics and Insulation Division Long Range Planning Committee, Hoover A Room, Second Floor
7:30 A.M.—Finance Committee, Washington B Room, Second Floor
7:30 A.M.—Council of Past Presidents, Room 224, Second Floor
8:00 A.M.—Industrial Electrolytic Division Executive Committee, Hoover B Room, Second Floor
10:00 A.M.—Ways and Means Committee, Washington B Room, Second Floor
12:15 P.M.— Contributing Membership Committee, Room 224, Second Floor
1:30 P.M.— Financial Policy Advisory Committee, Hoover B Room, Second Floor

Thursday, May 14, 1981

9:00 A.M.—Board of Directors, Wilson Room, Second Floor

LUNCHEONS AND BUSINESS MEETINGS

Monday, May 11, 1981

12:15 P.M.— Electronics Division, Twin Cities Room, Lower Lobby
12:15 P.M.— Electrothermics and Metallurgy Division, Adams Room, Second Floor
12:15 P.M.— Physical Electrochemistry Division, Minnesota Room, Lobby Level

Tuesday, May 12, 1981

11:40 A.M.—Dielectrics and Insulation Division Business Meeting (Election of Officers), No Luncheon, Michigan Room, Lobby
12:15 P.M.— Annual Society Luncheon and Business Meeting, Twin Cities Room, Lower Lobby

Wednesday, May 13, 1981

12:15 P.M.— Energy Technology Group, Twin Cities Room, Lower Lobby
12:15 P.M.— Industrial Electrolytic Division, Minnesota Room, Lobby Level
12:15 P.M.— Organic and Biological Electrochemistry Division, Milwaukee Room, Lower Lobby

Thursday, May 14, 1981

12:15 P.M.— Luminescence-Electronics Division, Minnesota Room, Lobby Level

TECHNICAL SESSION CHAIRMEN ORIENTATION

All Session Chairmen and Vice-Chairmen are required to attend a breakfast meeting at 8:00 A.M. on the day of their participation in the Adams Room, Second Floor.

EDUCATION COMMITTEE

The Education Committee has arranged for movies to be shown on Monday, Tuesday, and Wednesday in the Jefferson Room, Second Floor. The schedule may be found in the technical session program. A brief description of each film may be found at the end of the technical session program.

NONTECHNICAL REGISTRANTS PROGRAM

The headquarters for the nontechnical registrants will be in the Bali Room, Lobby Level. This will be the starting point for daily activities. The nontechnical registrants are cordially invited to visit here each morning to meet old friends and make new ones.

Sunday, May 10—On Sunday evening, the nontechnical registrants are invited to attend the Sunday Evening Get-Together which will be held in the Iowa Room, Lobby Level.

Monday, May 11—Coffee and rolls will be available in the Bali Room from 9:00 to 10:00 A.M.

At 10:00 A.M., buses will depart for a tour of the highlights of Twin Cities and St. Anthony Main. See the "Skyway Cities" from the 57-story IDS center in downtown Minneapolis and then drive past the Tyrone Guthrie Theater, through the mansion and cathedral areas, and around the city lakes and lagoons. After a stop at Minnehaha Falls, the tour follows the Mississippi River in St. Paul to famous Summit Avenue where the cathedral, the capitol, and the University of Minnesota are visited. Next, off to St. Anthony Main, the "birthplace of Minneapolis," now an exciting panorama of the old milling district, cobblestone streets, waterfront restaurants, and the charming stone arch bridges. You can stop to enjoy lunch at the restaurant of your choice, at your own expense, in one of the six interesting, ethnic restaurants. Return to the hotel will be approximately 2:30 P.M. The cost of tickets will be $7, excluding luncheon, per person.

On Monday evening, the nontechnical registrants are invited to attend the Monday Evening Mixer which will be held in the Minnesota Room, Lobby Level.

Tuesday, May 12—Coffee and rolls will be available in the Bali Room, Lobby Level, from 9:00 to 10:00 A.M.

At 10:00 A.M., buses will depart for a day at the Minneapolis Institute of Arts, one of the most exciting art complexes in the country. The Children's Theater, the Minneapolis School of Art and Design, and the Institute of Arts are all here in spectacularly designed buildings. Furnished period rooms, priceless oriental pieces, African art and sculpture, Paul Revere silver tea service, and the most valuable collection of archaic jade in the Western World are in the permanent collection. After the tour, there will be time to browse in the gift shop with its variety of gifts from all over the world. Enjoy a gourmet lunch, at one's own expense, in the Link Restaurant. Return to the hotel will be approximately 2:00 P.M. The cost of tickets will be $8, excluding luncheon, per person.

On Tuesday evening at 6:00 P.M., the nontechnical registrants are invited to attend the Solid State Science and Technology Award Reception in the Illinois Room, Lobby Level.

Wednesday, May 13—Coffee and rolls will be available in the Bali Room, Lobby Level, from 9:00 to 10:00 A.M.

At 10:00 A.M., buses will depart for a tour of the Swedish Castle, Butler Square, and Betty Crocker Kitchens. The tour starts with a visit to the American Swedish Institute which is one of the showplaces of Minneapolis and was built by a Swedish immigrant for his residence (His stone castle is more breathtaking than a Disneyland fantasy!). It is massive and has carved ceilings, exquisite porcelain fireplaces, and a superb Scandinavian import shop. Next, on to Butler Square, a nationally renowned, restored warehouse. It now houses boutiques, galleries, and collections of all kinds, in multilevel clusters around the nine-floor high central atrium. It is an environmental as well as a shopping experience! Enjoy lunch at the restaurant of one's choice, at one's own expense. After lunch, tour the General Mills' Corporate "estates." This tour begins with a multimedia presentation and a guided tour of the seven test kitchens where Betty Crocker and her associates develop and test their famous recipes. Refreshments will be served, everyone will receive a "goodie bag" and can shop in the boutique full of special cookbooks and gifts. Return to the hotel will be approximately 4:00 P.M. The cost of tickets will be $9, excluding luncheon, per person.

Thursday, May 14—Coffee and rolls will be available in the Bali Room, Lobby Level, from 9:00 to 10:30 A.M.

This day is free for relaxing, shopping, or visiting with friends.

COST OF VARIOUS FUNCTIONS

(Other than Registration)

Sunday Evening Get-Together	Complimentary
Monday Evening Mixer	Complimentary
Annual Society, Divisional and Group Luncheons (each)	$ 6.00
Nontechnical Registrants Activities	
Monday Highlights of Twin Cities and St. Anthony Main (excluding lunch)	7.00
Tuesday Tour of the Minneapolis Institute of Arts (excluding lunch)	8.00
Wednesday Tour of Swedish Castle, Butler Square, and Betty Crocker Kitchens (excluding lunch)	9.00

DISCUSSION

No recording will be made of oral discussion. Those contributing to the discussion of a paper and desiring their remarks to be published should send the discussion to the Publication Editor of the **Journal of The Electrochemical Society,** 10 South Main Street, Pennington, New Jersey 08534. The discussion will then be referred to the author for reply. Publication of the discussion and the comments of the author(s) depends on publication of the paper in the **Journal.**

Written discussion of a published paper should be submitted within two months following publication of an article.

EMPLOYMENT POSTERS

There will be a special bulletin board in the Registration Area for employment posters. Companies desiring to recruit employees are requested to place their announcement on this special board. These announcements should be no larger than 8-1/2" × 11".

NOTE

Photographing of lantern slides, charts, etc., will be permitted unless specifically prohibited by the speaker. **PHOTO FLASH AND PHOTO FLOODS ARE PROHIBITED. Tape recordings, except on behalf of the Society, are prohibited.**

TECHNICAL SESSIONS

Monday, May 11, 1981

9:00 A.M.—Society Plenary Session, Iowa Room, Lobby Level. Gordon Moore will deliver The Electrochemical Society Lecture, "A Perspective on VLSI."

12:15 P.M.—Electronics Division Luncheon and Business Meeting, Twin Cities Room, Lower Lobby
12:15 P.M.—Electrothermics and Metallurgy Division Luncheon and Business Meeting, Adams Room, Second Floor
12:15 P.M.—Physical Electrochemistry Division Luncheon and Business Meeting, Minnesota Room, Lobby Level

EDUCATION COMMITTEE MOVIES

J. Horkans, Chairman

(JEFFERSON ROOM, Second Floor)

A.M.

10:00—Energy: A Conversation with Linus Pauling, George Wald, and Philip Morrison
10:30—Natural Gas Fuel Cell

P.M.

2:00—An Interview with the Transistor's Inventors
2:30—Crystal Growth Morphologies
3:00—Turbulence

BATTERY/ENERGY TECHNOLOGY/ INDUSTRIAL ELECTROLYTIC

Porous Electrodes

T. Katan, Chairman; D. N. Bennion, Vice-Chairman

(LINCOLN ROOM, Second Floor)

A.M. **Abs.**

10:00—"Distribution of Potential in Lead-Acid Battery Electrodes" by W. G. Sunu and B. W. Burrows **1**
10:20—"Ratios of AgO/Ag_2O in Porous Silver Oxide Electrodes" by T. Katan and P. J. Carlen **2**
10:40—"Observations within a Porous, Segmented Wire Silver Oxide Electrode" by T. Katan and H. F. Bauman **3**
11:00—"Current Distribution in Porous Zinc Electrode. II. The Effect of Electrolyte Conductance" by M.-B. Liu, B. R. Faulds, G. M. Cook, and N. P. Yao **4**
11:20—"Effect of A-C Charging Methods on Zinc Electrode Morphology" by R. Sethi, D-T. Chin, and J. McBreen **5**
11:40—"Mathematical Model of the Controlled-Micro-Geometry (CMG) Nickel Hydroxide Electrode" by J. W. Oldfield and T. S. Turner **6**

H. Wroblowa, Chairman; S. Srinivasan, Vice-Chairman

P.M.

2:00—"Porous Nickel-Coated Steel Anodes for Moderate Temperature Alkaline Electrolysis: Corrosion Resistance" by D. E. Hall **7**
2:20—"Thickness of Films in Porous Electrodes" by G. Wilemski and J. Mitteldorf **8**
2:40—"Composite Model of Electrode-Matrix Structures and Their Performance in the Molten Carbonate Fuel Cell" by H. C. Maru, D. Patel, and L. Paetsch **9**
3:00—"Comparison of Results to Theory of Potentiostatic Charging of the Double Layer of Porous Electrodes" by N. A. Fleischer **10**
3:20—Ten-minute intermission
3:40—"Electrosorption of Organics on Flow-Through Porous Electrodes" by R. C. Alkire and R. S. Eisinger **11**
4:00—"Microporous Flow-Through Electrodes" by S. M. Mohnot and E. L. Cussler **12**
4:20—"Electrochemical Reactor with Flow Through Electrodes for Wastewater Cleanup" by J. L. Weininger and B. M. Kim **13**
4:40—"Thermomechanical Behavior of Simulated Electrodes for Li-Al/FeS Battery Cells" by G. Bandyopadhyay and J. E. Battles **14**

CORROSION

General Session

R. P. Frankenthal, Chairman; R. B. Diegle, Vice-Chairman

(ABC ROOM, The Curtis, Lobby)

A.M. **Abs.**

10:00—"Microcalorimetry as a Tool for Assessing Corrosion and Parasitic Reactions" by M. A. Norenberg, M. A. Pehl, G. M. Phillips, and D. F. Untereker **15**
10:20—"Mössbauer Spectroscopic Study of the Chemical State of Cobalt in an Electrodeposited Zinc-Cobalt Alloy" by H. Leidheiser, Jr., A. Vertes, and M. L. Varsanyi **16**
10:40—"A Finite Element Method of Calculating Current Distribution in Galvanic Corrosion" by J. W. Fu **17**
11:00—"Investigations of Corrosion Layers on Mild Steel with a Direct Imaging Mass Spectrometer" by A. Pebler **18**
11:20—"Flow Effects During Repassivation of Iron and Cobalt" by R. C. Alkire and K. R. Weisbrod **19**
11:40—"Study on Flow-Through Packed Iron Anode" by Y.-X. Zhang and Z.-B. Hu **20**

P.M.

R. B. Diegle, Chairman; R. P. Frankenthal, Vice-Chairman

2:00—"Passivation Mechanism of Iron in Concentrated Caustic Solution at Room Temperature" by A. K. Agrawal and R. B. Diegle **21**
2:25—"Anodic Dissolution of Aluminum in Alkaline Solutions" by K. C. Tsai and J. L. Morris **22**
2:50—"Adsorbed Polymers Effect on Salt Water Corrosion" by M. R. Van De Mark and J. W. Truesdell **23**
3:15—"Anodic Corrosion and Passivation Behavior of Metals in Molten LiCl-KCl Containing Oxide Ions" by X. K. Feng and C. A. Melendres **24**
3:40—Ten-minute intermission
3:50—"Tarnishing of Silver by Organic Sulfur Vapors: Rates and Film Characteristics" by J. D. Sinclair **25**
4:15—"Oxidation Behavior of 20/25/Nb Stainless Steel Containing Dispersed Phases" by O. T. Goncel **26**
4:40—"Oxidation Behavior of Fe-Cr Alloys after Coating by Inorganic Salts" by O. T. Goncel **27**

CORROSION/DIELECTRICS AND INSULATION

Anodic Oxidation

J. P. S. Pringle, Chairman; J. S. Llewelyn Leach, Vice-Chairman

(CARDINAL ROOM, The Curtis, Lobby)

A.M. **Abs.**

10:00—Introductory remarks by B. MacDougall
10:05—"Ionic Pickup during Anodic Oxidation" by J. S. Llewelyn Leach, C. Panagopoulos, and B. R. Pearson **28**

Monday continued

10:35—"Distribution of Anions in Oxide Films Anodically Formed on Aluminum in a Neutral Phosphate Solution" by H. Takahashi, H. Konno, K. Fujimoto, and M. Nagayama **29**

11:05—"Anodic Film Formation on Aluminum in Neutral Solutions" by G. E. Thompson, K. Shimizu, and G. C. Wood **30**

11:35—"A-C Anodizing Processes of Aluminum Alloys" by J. Zahavi, H. Kerbel, O. Korotkina, and M. Metzger **31**

J. S. Llewelyn Leach, Chairman; J. P. S. Pringle, Vice-Chairman

P.M.

2:00—"The Difference Between Barrier and Porous Anodic Oxides on Aluminum" by J. P. S. Pringle **32**

2:25—"Study of Patterns of Breakdown Processes in Anodic Oxide Films Formed on Aluminum in Sulfuric Acid" by J. Zahavi and M. Metzger **33**

2:50—"The Phenomenology of the Electrical Breakdown during Anodizing of Aluminum in Borate Solutions" by K. Shimizu, G. E. Thompson, and G. C. Wood **34**

3:15—"Voids in Anodic Aluminum Oxide Films" by R. S. Alwitt, C. K. Dyer, and B. Noble **35**

3:40—Ten-minute intermission

3:50—"Wear Properties of Thin to Thick Anodic Oxide Films on Aluminum" by H. Leidheiser, Jr., S.-M. Chou, W. Bilder, and M. C. Hughes **36**

4:15—"Initial Oxide Growth Rate on Newly Generated Surfaces of Aluminum and Zirconium" by T. R. Beck **37**

4:40—"Dissolution Behavior of the Barrier Layer of Porous Anodic Films on Aluminum" by S. Ono and T. Sato **38**

DIELECTRICS AND INSULATION/ELECTROTHERMICS AND METALLURGY

Adhesion Aspects of Polymeric Coatings

K. L. Mittal, Chairman; W. Brockmann, Vice-Chairman

(ILLINOIS ROOM, Lobby)

A.M. **Abs.**

10:00—"Adhesion Aspects of Polymeric Coatings: An Overview" by K. L. Mittal **98**

10:40—"Acid Base Interactions Between Oxide Surfaces and Polar Organic Compounds" by J. C. Bolger **99**

11:20—"Adhesion of Polymers to Metals: The Role of Surface Topography" by D. E. Packham **100**

K. L. Mittal, Chairman; H. Schreiber, Vice-Chairman

P.M.

2:00—"Detection of Contamination and Chemical Variance on Surfaces Prepared for Polymeric Coatings" by G. R. Sparrow **101**

2:30—"Surface Chemistry and Electrochemical Properties of Sulfuric-Chromic Acid (FPL) Etched Aluminum" by A. V. Pocius **102**

2:50—"Investigation of the Effect of Plasma Pretreatment on the Adhesion of Parylene to Various Substrates" by T. J. Riley, T. C. Mahuson, and K. Seibert **103**

3:10—"Adhesion Properties of Styrene/Acrylic Polymers: Influence of Process Conditions" by H. P. Schreiber **104**

3:30—"Variables Affecting the Adhesion of Bisphenol A Diglycidyl Ether/Aliphatic Amine Epoxy Resin to Metal and Ceramic Substrates" by A. Coury, A. Jevne, and P. Cahalan **105**

3:50—"Adhesion of Polyimide to Aluminum for Printed Circuit Armatures" by K. N. Karol **106**

4:10—"Importance of Preliminary Treatment of Surfaces by Blasting from the Standpoint of Adhesive and Tribological Properties of Polymer Coatings" by D. Kniewald, K. Takác, E. Grutka, and M. Sefara **107**

ELECTRONICS—LUMINESCENCE

Display Technology and Special Purpose Cathode-Ray Tubes

A. Hardy, Chairman; M. Tecotzky, Vice-Chairman

(SOLARIUM ROOM, The Curtis, Lobby)

A.M. **Abs.**

10:00—Introductory remarks by F. M. Ryan

10:05—"Phosphors for Special Cathode Ray Tubes" by P. Seats **144**

11:00—"Panel Displays Based on Electron-Beam Technology" by B. Kazan **145**

11:35—"Advances and Applications of Storage Cathode Ray Tubes" by I. F. Chang **146**

G. Knutsen, Chairman; P. N. Yocom, Vice-Chairman

P.M.

2:00—"Color Write-Thru Direct View Storage Tubes" by R. O. Petersen **147**

2:25—"A New Cathodoluminophor with Long Persistence" by J. J. Wei, Z. H. Wang, S. Y. Zhao, Y. Wu, S. H. Lu, and S. H. Xu **148**

2:50—"Temperature Dependence of Luminescence and Photostimulation in Single Crystals of Zn_2SiO_4:Mn with and Without As Addition" by I. F. Chang, E. A. Giess, and E. E. Mendez **149**

3:15—Ten-minute intermission

3:25—"Correlation of Phosphor Emission Decay Kinetics with Flicker Perception" by J. R. McColl **150**

3:50—"The Cathodoluminescence of $Zn_2Si_{1-2x}(Al, P)_xO_4$:Mn, As Phosphors" by T. E. Peters and J. R. McColl **151**

4:15—"Low Current Density Aging" by R. L. Donofrio **152**

4:40—"The Novel Characterization of Lanthanum Oxybromide Phosphors Used in the Projection Cathode-Ray Tubes" by J. Liu **153**

ELECTRONICS/DIELECTRICS AND INSULATION

Fourth International Symposium on Silicon Materials Science and Technology

VLSI Overview

H. R. Huff, Chairman; R. Kriegler/Y. Takeishi, Vice-Chairmen

(IOWA ROOM, Lobby)

A.M. **Abs.**

10:00—Introductory remarks by H. R. Huff

10:05—"Basic Technology for VLSI" by Y. Tarui and Y. Takeishi **184**

10:45—"VLSI Trends" by E. Bloch **185**

11:25—"Fundamental Aspects of Czochralski Silicon Crystal Growth for VLSI" by K. E. Benson, W. Lin, and E. P. Martin **186**

Silicon Crystals

B. O. Kolbesen, Chairman; T. Abe, Vice-Chairman

P.M.

2:00—"Impurities in Silicon Single Crystals—A Current View" by T. Abe, K. Kikuchi, S. Shirai, and S. Muraoka **187**

2:30—"Photoluminescence Analysis of Silicon Crystals" by M. Tajima, T. Masui, T. Abe, and T. Iizuka **188**

2:50—"CZ Silicon Crystals Grown under a Transverse Magnetic Field" by T. Suzuki, K. Hoshi, N. Isawa, and Y. Okubo **189**

3:10—"Control of Oxygen Concentration in CZ Silicon Growth" by K. Hoshikawa, H. Hirata, H. Nakanishi, and K. Ikuta **190**

3:30—Ten-minute intermission

T. Abe, Chairman; B. O. Kolbesen, Vice-Chairman

3:40—"Mechanisms of Oxygen Incorporation in Czochralski-Grown Silicon" by A. Murgai **191**

4:00—"Oxygen-Free Silicon Single Crystal Grown from Silicon Nitride Crucible" by M. Watanabe, T. Usami, H. Muraoka, S. Matsuo, Y. Imanishi, and H. Nagashima **192**

4:20—"Electronic Characteristics of Float Zone Grown Silicon" by L. Jastrzebski and P. Zanzucchi **193**

4:40—"Current Aspects of Silicon Material Processing for Solar Cell Application" by E. Sirtl **194**

5:10—"Photovoltaic Performance Related to Properties of Various Forms of Silicon" by H. I. Yoo and P. A. Iles **195**

Joint General Session

Measurements

A. Reisman, Chairman; G. Cullen, Vice-Chairman

(MICHIGAN ROOM, Lobby)

A.M. **Abs.**

10:00—"Silicon Film Characterization by Correlation of Surface Analysis and Electrical Data" by G. D. O'Clock, Jr., S. L. Kruchten, T. E. Brady, C. L. Gruber, and L. D. Feisel **262**

Monday continued

10:20—"A Novel Contactless Method for Measuring Collector/Isolation P-N Junction Capacitance in LSI Wafers" by R. L. Verkuil **263**

10:40—"Pulse Scanning C-V Technique for the Analysis of Carrier Generation in Si" by S. Kawazu, T. Matsukawa, and H. Nakata **264**

11:00—Ten-minute intermission

11:10—"Microscale Characterization of Heteroepitaxial Silicon-on-Sapphire by Scanning Photovoltage Measurements" by L. Jastrzebski, G. W. Cullen, and J. Lagowski **265**

11:30—"Investigation of Threshold Voltage Variations of Ion-Implanted Depletion and Enhancement-Mode MOSFET Devices" by S. W. Netherton and G. M. Oleszek **266**

11:50—"Analysis of the "Write" and the "Erase" Operations in a Floating-Gate MNOS Memory Device" by R. Abderrassoul and M. Shabana **267**

Measurements and General Topics

D. Shaw, Chairman; K. Pickar, Vice-Chairman

P.M.

2:00—"Charge Storage Model for SNOS Memory Devices" by J. A. Topich **268**

2:20—"ICECREM, a New Program for Process Modeling" by H. Ryssel, K. Hoffmann, K. Haberger, G. Prinke, and R. Dümcke **269**

2:40—"Capacitance Modeling and Measurements of Fine-Patterned Interconnects" by T. Shibata, N. Shigyo, K. Kurosawa, R. Nakayama, R. Dang, and H. Iizuka **270**

3:00—"Process Design Optimization for Submicron MOS Devices" by T. Shibata, M. Konaka, S. Mimura, R. Dang, and H. Iizuka **271**

3:20—"Process Check Technology in P-MOS IC Fabrication" by C. Kim, T. Komatsu, and K. Shohno **272**

3:40—Ten-minute intermission

3:50—"CW Lasar Trimming Phenomenon of Heavily Doped Polycrystalline Silicon" by S. Matsumoto, J. F. Gibbons, and T. J. Magee **273**

4:10—"DSC Mask. An Implant Identification and Contact Coding Method" by M. R. Tennyson and J. E. Martin **274**

4:30—"Semiconductor Device Technology in Chemical Abstracts" by C. W. Moulton **275**

4:50—"Low Resistivity Spray Pyrolyzed Films" by J. Recktenwald, C. W. Bates, Jr., A. Raza, J. B. Mooney, L. McIntosh, R. H. Lamereaux, and K. Nelson **276**

ELECTROTHERMICS AND METALLURGY

Thermochemistry of Intermetallic Compounds

P. J. Meschter, Chairman; R. Schiffman, Vice-Chairman

(NEW YORK ROOM, Lower Lobby)

A.M. **Abs.**

10:00—Introductory remarks by P. J. Meschter

10:05—"Abnormal Properties of the Transition Metals and Their Alloys" by L. Brewer **333**

10:45—"High Temperature Thermodynamic Properties of Intermetallic Compounds in the Platinum-Tantalum System" by S. K. Lau and W. L. Worrell **334**

11:10—"A High-Temperature Thermodynamic Investigation of the Platinum-Rich Region of the Al-Pt System" by J. Major and W. L. Worrell **335**

11:35—"Activity Measurements in the Ti-Cu, Ti-Ni, and Mg-Cu Systems by Metal-Hydrogen Equilibration" by M. Arita, R. Kinaka, K. Shimizu, and M. Someno **336**

W. L. Worrell, Chairman; S. K. Lau, Vice-Chairman

P.M.

2:00—"Low Temperature (1-20 K) Heat Capacity Measurements on Metallic Systems" by K. A. Gschneidner, Jr. **337**

2:40—"Thermodynamics of the Incongruent Subliming Aluminum-Niobium System" by R. A. Schiffman and I. Shilo **338**

3:05—"Coulometric Titrations to Study Solid Ca-Au Alloys" by H.-P. Pfeiffer, R. J. Heus, and J. J. Egan **339**

3:30—Fifteen-minute intermission

3:45—"Calorimetric Determination of the Phase Stability of Ni_4Mo" by C. R. Brooks and P. J. Meschter **340**

4:10—"XIr_3 Intermetallic Compound Catalysts" by M. B. Brodsky and P. W. Ensign **341**

4:35—"A Thermodynamic Analysis of Fission Product Reaction Behavior in Reactor Fuel Elements" by R. Kohli **342**

INDUSTRIAL ELECTROLYTIC

Chlorine

Hydrodynamics

D. C. Johnson, Chairman; W. B. Darlington, Vice-Chairman

(EAST ROOM, The Curtis, Lobby)

A.M. **Abs.**

10:00—Introductory remarks

10:10—"A Close View of Gas Evolution" by P. J. Sides and C. W. Tobias **392**

10:45—"Chlorine Evolution. The Role of Transient Thermodynamics in Clarification of Steady-State Polarization Curves" by I. V. Kadija **393**

11:15—"Influence of Bubble Dynamics on Chlorine Saturation Levels at the Anode Surface" by I. V. Kadija **394**

Electrodes

E. Rudd, Chairman; J. Bennett, Vice-Chairman

P.M.

2:00—"Chlorine Anodes: The Metal Anode Revolution" by J. M. Kolb **395**

2:20—"Chlorine Evolution Kinetics on Electrochemically Modified Anodic Oxide Films at Ir and Ru Electrodes" by B. E. Conway and J. Mozota **396**

2:40—"Chlorine Ion Adsorption Effects on Surface Oxidation of Noble Metal Anodes and Kinetics of Cl_2 Evolution" by B. E. Conway, D. M. Novak, and J. Mozota **397**

3:00—"Surface Structure of Ruthenium Dioxide Based Electrodes and Kinetics of Chlorine Evolution" by A. Carugati, G. Lodi, and S. Trasatti **398**

3:20—Twenty-minute intermission

3:40—"The Photoelectrochemical Production of Sodium Hydroxide and Chlorine" by V. Guruswamy, G. Hildreth, and J. O'M. Bockris **399**

4:00—"Photoproduction of Cl_2, Br_2, and I_2 on an n-Semiconducting Powder" by B. Reichman and C. E. Byvik **400**

4:20—"Catalytically Active Coatings for Hydrogen Evolution in Brine Electrolyses" by M. D. Spasojevic, N. V. Krstajic, K. I. Popov, and R. T. Atanasoski **401**

ORGANIC AND BIOLOGICAL ELECTROCHEMISTRY

Electrochemistry in the Study of Novel Organic Compounds

W. Geiger, Chairman; A. J. Fry, Vice-Chairman

(CHICAGO ROOM, Lower Lobby)

A.M. **Abs.**

10:00—"Reoxidative Cleavage and Reductive Formation of Cyclopropane Derivatives" by P. G. Gassman **419**

10:45—"The Electrochemistry of Novel Pi-Systems" by A. J. Fry **420**

11:30—"Dual Reactivity in the Reduction of β-Mercapto-α-ketoacids" by M. Fleury, J. Tohier, and P. Zuman **421**

A. J. Fry, Chairman; R. Rieke, Vice-Chairman

P.M.

2:00—"Long Lived Radical Cations with Small Pi Systems" by S. F. Nelsen, C. R. Kessel, W. C. Hollinsed, R. Akaba, and D. J. Steffek **422**

2:45—"Electrochemical Studies on Novel Arenetricarbonylchromium Complexes and Potential New Electron Acceptors" by R. D. Rieke, S. N. Milligan, I. Tucker, B. Willeford, and L. I. Rieke **423**

3:30—"Influence of Metal Oxidation State on the Structure of Pi-Complexed Polyolefins" by W. E. Geiger, Jr. and J. Moraczewski **424**

ORGANIC AND BIOLOGICAL ELECTROCHEMISTRY/ENERGY TECHNOLOGY

Electrochemistry of Biomass Derived Compounds

N. Weinberg, Chairman; H. Chum, Vice-Chairman

(MILWAUKEE ROOM, Lower Lobby)

P.M.

2:00—Introductory remarks

Monday continued

2:05—"Electrochemistry of Biomass and Derived Materials" by H. L. Chum and M. M. Baizer **449**

2:35—"Depolarizing Water Electrolysis Via Biomass Derived Materials" by M. R. St. John, A. J. Furgala, and A. F. Sammells **450**

2:55—"Hydrogen and Single Cell Protein from Biomass by Electrolysis" by M. P. Steinberg, D. L. Day, and R. R. Kravets **451**

3:15—Fifteen-minute intermission

3:30—"Polarography in the Study of Physicochemical Properties of Lignin" by P. Zuman, S. Ainso, B. Pethica, and R. Smith **452**

Paper 453 withdrawn

3:50—"Electroreduction of Lignin from 'Explosively Depressurized' Wood" by D. W. Sopher, H. A. Schroeder, and H. L. Chum **454**

PHYSICAL ELECTROCHEMISTRY/ENERGY TECHNOLOGY

Electrocatalysis

F. G. Will, Chairman; P. N. Ross, Vice-Chairman

(ROOSEVELT ROOM, Second Floor)

A.M. **Abs.**

10:00—"Electrocatalysis: Fundamental Aspects and Recent Developments" by E. Yeager and D. Scherson **496**

10:45—"Cluster Model Study of Chemisorption on Heavy Transition Metal Surfaces" by C. Y. Yang **497**

11:10—"Oxygen Reduction on Transition Metal Cluster Catalysts in Alkaline Electrolyte" by P. N. Ross, Jr. **498**

11:35—"Electrocatalysis on Ion-Implanted Electrode Surfaces" by W. E. O'Grady and G. K. Wolf **499**

P. N. Ross, Chairman; F. G. Will, Vice-Chairman

P.M.

2:00—"Comparison of Electrochemical Proton Transfer from the Unhydrated H_3O^+ Ion and from $H_9O_4^+$ in Excess Water" by B. E. Conway and D. Tessier **500**

2:25—"Chemical and Electrochemical Surface Reactivity. Role of Competition Between Solvent and Reaction Intermediate Adsorption" by S. Trasatti **501**

2:50—"Changes of the Electrochemical Characteristics of Rhodium Electrodes Induced by Potentiodynamic Perturbation" by C. Pallotta, N. R. de Tacconi, and A. J. Arvia **502**

3:10—Ten-minute intermission

3:20—"Study of O_2 Involving Reactions at Potentials of the Hydrogen Region in Acid Solution on Smooth and Platinized Platinum Covered by $Co_{ad.}$" by M. W. Breiter **503**

3:45—"The Growth and the Stabilization of the O-Containing Species on Pt in Molten $KHSO_4$" by M. E. Folquer, N. R. de Tacconi, and A. J. Arvia **504**

4:05—"Electrode Kinetics of Hydrogen Oxidation and Oxygen Reduction on Carbon-Supported Pt Fuel Cell Electrodes in H_3PO_4" by J. McBreen, H. Olender, and S. Srinivasan **505**

4:25—"Electronic Structure of Iron Phthalocyanine and Its Analogs—A Theoretical Study" by N. Sabelli, L. K. Lee, and C. A. Melendres **506**

4:45—"Electrocatalytic Study of a Series of Metals and Alloys under Physiological Conditions" by B. J. Piersma and W. Greatbatch **507**

5:05—"An Electrocatalyst for Hydrogen Electrodes" by D. E. Brown, S. M. Hall, M. N. Mahmood, M. C. M. Man, A. K. Turner, D. Wood, and S. Anderson **507A**

Tuesday, May 12, 1981

12:15 P.M.—Annual Society Luncheon and Business Meeting, Twin Cities Room, Lower Lobby

4:30 P.M.—Awards and Recognition Session, Iowa Room, Lobby Level. Gerald L. Pearson will deliver the Solid State Science and Technology Award Address, "Solid State Science and Technology in Retrospect."

EDUCATION COMMITTEE MOVIES

J. Horkans, Chairman

(JEFFERSON ROOM, Second Floor)

A.M.

10:00—Energy: A Conversation with Linus Pauling, George Wald, and Philip Morrison

10:30—Natural Gas Fuel Cell

P.M.

2:00—An Interview with the Transistor's Inventors

2:30—Crystal Growth Morphologies

3:00—Turbulence

CORROSION/DIELECTRICS AND INSULATION

Anodic Oxidation

H. Leidheiser, Jr., Chairman; D. D. Macdonald, Vice-Chairman

(CARDINAL ROOM, The Curtis, Lobby)

A.M. **Abs.**

9:00—"A Theory of Electron Transfer Reactions at Oxide Electrodes Involving Adsorbate States" by W. Schmickler **39**

9:25—"A Comparative Analysis of the Kinetics of Growth of Thin Anodic Films at Pt and Ni Electrodes" by A. Damjanovic, J. F. Wolf, and L. S-R. Yeh **40**

9:50—"Kinetics of Transitional Growth in Sub-Monolayer to Multilayer Oxide Film Formation at Au" by H. Angerstein-Kozlowska, B. Barnett, and B. E. Conway **41**

10:15—"Kinetics of Distinguishable Stages in Oxide Film Reduction at Au" by B. Barnett, H. Angerstein-Kozlowska, and B. E. Conway **42**

10:40—Ten-minute intermission

10:50—"Kinetics and Mechanisms of O_2 Evolution at Pt Electrodes Covered by Thin Anodic Oxide Films" by A. Damjanovic **43**

11:15—"Oxygen Evolution and Passivation Behavior of Cu_xTi_{1-x} Alloys" by G. G. Scherer, K. Müller, and S. Stucki **44**

11:40—"Optical Studies of the Anodic Passivation of Tin" by S. D. Kapusta **45**

D. D. Macdonald, Chairman; H. Leidheiser, Jr., Vice-Chairman

P.M.

2:00—"Mechanism of Growth of Thick Anodic Oxide Films on Nickel" by B. MacDougall **46**

2:25—"Structure of Hydrous Electrochromic Oxide Films as Deduced from Potential-pH Response" by L. D. Burke, M. E. G. Lyons, E. J. M. O'Sullivan, and D. P. Whelan **47**

2:50—Ten-minute intermission

3:00—"Electrochemical Properties of Iridium Oxide Films in a Buffered Electrolyte" by M. L. Gopikanth, J. Crossen, and E. Luksha **48**

3:25—"Kinetics of the Anodic Oxidation of Precipitated Nickel Hydroxide" by R. E. Carbonio, V. A. Macagno, M. C. Giordano, J. R. Vilche, and A. J. Arvia **49**

DIELECTRICS AND INSULATION/ ELECTROTHERMICS AND METALLURGY

Adhesion Aspects of Polymeric Coatings

K. L. Mittal, Chairman; H. Yasuda, Vice-Chairman

(ILLINOIS ROOM, Lobby)

A.M. **Abs.**

9:00—"An Overview of the Adhesion Properties of Inks and Coatings" by G. V. Calder **108**

9:30—"Adhesion of Plasma-Polymerized Coatings" by H. Yasuda **109**

10:00—"Epoxy Adhesion to Copper" by J. M. Park and J. P. Bell **110**

10:20—"Wet Adhesion of Latex Paints" by S. M. Kambanis **111**

Tuesday continued

10:40—"Infrared Spectroscopic Investigation of Polymer Coating-Metal Substrate Interaction" by W. Suetaka 112
11:00—"The Relationship Between Adhesion and Polyelectrolyte Solution Conformation as Studied by Fourier Transform IR Spectroscopy" by D. J. Belton and S. I. Stupp 113
11:20—"Dynamics of an Adsorbed Polymer Molecule Subjected to Flow" by G. G. Fuller 114
11:40—"PTFE Film Adhesion to Electronically Conducting Materials" by K. A. Klinedinst 115

K. L. Mittal, Chairman; L. Rothman, Vice-Chairman

P.M.

2:00—"Adhesion, Wettability, and Surface Chemistry: SiO_2 and Resist Materials" by C. A. Deckert and D. A. Peters 116
2:30—"Recognition and Discussion of Basic Adhesion Mechanisms in Photopolymeric Systems" by L. Fullwood 117
2:55—"Organosilanes as Process Compatible Adhesion Promoters for Resist Materials" by J. N. Helbert and H. G. Hughes 118
3:20—"Liquid Negative Working Photoresist for Through Hole Printed Circuitry" by S. Simoliunas 119
3:40—"Dry Film Photoresist Adhesion on Electroless Copper Surfaces" by W. L. Hamilton 120

ELECTRONICS—LUMINESCENCE

Display Technology and Special Purpose Cathode-Ray Tubes

P. Toch, Chairman; M. Royce, Vice-Chairman

(SOLARIUM ROOM, The Curtis, Lobby)

A.M. **Abs.**

9:00—"Inorganic Electrochromics" by G. Beni 154
9:35—"Electro-Wetting Displays" by S. Hackwood and G. Beni 155
10:00—"Analysis of Color-Changing Penetration-Type Cathodoluminescent Phosphor Screens" by W. Lehmann 156
10:25—"Preparation, Optimization, and Cathodoluminescent Properties of a Line Emission Penetration Phosphor" by T. E. Clark, C. T. Burilla, and G. Knutsen 157
10:50—"A New Design of Voltage Penetration Phosphor" by W. L. Li, Z. X. Zhang, and S. H. Xu 158

Luminescence of II-VI Compounds

D. J. Robbins, Chairman; F. M. Ryan, Vice-Chairman

(SOLARIUM ROOM, The Curtis, Lobby)

P.M. **Abs.**

2:00—Introductory remarks by D. J. Robbins and F. M. Ryan
2:05—"Recent Advances in Electrical and Optical Properties of II-VI Compound Semiconductors" by P. J. Dean 159
3:00—"Properties of Low Resistivity N-Type ZnSe Prepared by Organometallic CVD" by W. Stutius 160
3:20—"Luminescence and EPR of Chloride-Doped ZnTe" by N. Magnea, K. Saminadayar, D. Galland, J. L. Pautrat, and R. Triboulet 161
3:40—"Photoluminescence Study of Shallow Acceptors in Refined Cadmium Telluride" by E. Molva, J. P. Chamonal, and J. L. Pautrat 162

ELECTRONICS/DIELECTRICS AND INSULATION

Fourth International Symposium on Silicon Materials Science and Technology

Oxygen in Silicon

T. Abe, Chairman; B. O. Kolbesen, Vice-Chairman

(IOWA ROOM, Lobby)

A.M. **Abs.**

8:00—"Recent Problems on Oxygen in Silicon" by J. R. Patel 196
8:20—"Dislocation Behavior and Mechanical Strengths of Float-Zone Silicon Crystals and Czochralski Silicon Crystals" by K. Sumino 197
8:40—"Plastic Deformation and Preannealing Effects in CZ and FZ Silicon Crystals" by Y. Kondo 198
9:00—"Activation of the Oxygen Donor in Si on a Microscale" by P. Rava, H. C. Gatos, and J. Lagowski 199
9:20—"Oxygen Precipitation in Czochralski Silicon" by R. A. Craven 200
9:40—"Oxygen and Carbon in Heat-Treated Silicon Crystals" by C-C. Hsu, B-K. Sun, S-N. Jiang, W-N. Wang, and C-Y. Sung 201
10:00—Ten-minute intermission

B. O. Kolbesen, Chairman; T. Abe, Vice-Chairman

10:10—"Nucleation and Growth of Oxide Precipitates in Silicon" by H. F. Schaake, R. F. Pinizzotto, and S. C. Baber 202
10:30—"Oxygen Precipitation in Czochralski Silicon—Mechanism and Application" by N. Inoue, K. Wada, and J. Osaka 203
10:50—"Denuded Zone and Microdefect Formation in Czochralski-Grown Silicon Wafers by Thermal Annealing" by K. Kugimiya, S. Akiyama, and S. Nakamura 204
11:10—"The Influence of Precipitate Size and Capillarity Effects on the Surface Denuded Zone in Thermally Processed Cz-Wafers" by R. W. Series, K. G. Barraclough, and W. Bardsley 205
11:30—"Oxygen Precipitation in Silicon Between 600° and 800°C" by K. Tempelhoff, R. Gleichmann, and B. Hahn 205A
11:50—"Minority Carrier Lifetime and Reverse Current Inhomogeneities in PN Diode Arrays Resulting from Microdefects in Czochralski Grown Silicon Crystals" by C. J. Varker, J. D. Whitfield, K. V. Rao, and L. J. Demer 206

Metallic Impurities in Silicon

P.M.

1:45—"The Behavior of Transition and Noble Metals in Silicon Crystals" by K. Graff and H. Pieper 207
2:05—"The Role of Metallic Impurities in the Formation of Haze Defects" by W. T. Stacy, D. F. Allison, and T-C. Wu 208
2:25—"Thermal Conditions for the Formation of Fog in Silicon Wafers" by D. E. Hill 209
2:45—Five-minute intermission

Deposited Silicon Films

T. I. Kamins, Chairman; D. J. DiMaria, Vice-Chairman

2:50—"The Nucleation and Growth of Silicon via Chemical Vapor Deposition" by W. A. P. Claassen and J. Bloem 210
3:15—"Growth Reaction Mechanisms of Vapor Phase Si Epitaxy" by T. Aoyama, Y. Inoue, and T. Suzuki 211
3:35—"Electrical Properties of Grain Boundaries in Silicon Bicrystals" by L. J. Cheng and C. M. Shyu 212
3:55—"The Mobility and Lifetime of Injected Holes and Electrons in a-Si-H Thin Films" by C. Y. Chang, Y. K. Fang, W. L. Lin, and W. C. Hsu 213

Joint General Session

Si/SiO_2

N. Goldsmith, Chairman; M. Kestigian, Vice-Chairman

(MICHIGAN ROOM, Lobby)

A.M. **Abs.**

9:00—"Barrier Heights at the Polycrystalline Silicon-SiO_2 Interface" by T. W. Hickmott and R. D. Isaac 277
9:20—"Polysilicon Oxide Interface Microtexture and Dielectric Breakdown" by T. T. Sheng and R. B. Marcus 278
9:40—"Temperature Dependent Boron Segregation at the SiO_2/Si Interface" by R. K. Jain 279
10:00—Twenty-minute intermission
10:20—"Annealing of Gate Insulators at Elevated Pressure" by A. Reisman, J. M. Aitken, A. K. Ray, M. Berkenblit, C. J. Merz, and R. P. Havreluk 280
10:40—"Structural Changes in SiO_2 Films during Thermal Growth" by A. G. Revesz 281
11:00—"Thermal Oxidation of Heavily Doped Polycrystalline Silicon Thin Films" by H. Singh and K. C. Saraswat 282
11:20—"Si Oxidation in O_2/N_2 in the Presence of HCl" by M. K. Lee, S. D. Liu, and C. L. Lee 283

Tuesday continued

Dielectrics and Insulation Division Business Meeting

11:40—Dielectrics and Insulation Division Business Meeting

Metallization and Silicides

G. C. Schwartz, Chairman; R. Pinizzotto, Vice-Chairman

P.M.

2:00—"Ohmic Contacts to Silicon by Electroless Nickel-Boron Alloy" by R. S. Korde, V. K. Gupta, and M. S. Tyagi **284**

2:20—"Thin Tungsten Films by Low Pressure CVD" by N. E. Miller and R. B. Herring **285**

2:40—"Electromigration Resistance of Narrow Metal Lines" by S. H. Lee and P. Brusius **286**

3:00—"Transmission Electron Microscopy of Silicon-Silicide Interfaces" by H. Föll **287**

3:20—"Effects of Ion Implantation on the Thermal Growth of Pt and NiPt Silicides" by T. W. Orent, J. A. Sartell, S. Lee, and T. L. Brewer **288**

3:40—"Rare Earth Silicide Formation Through Contact Reaction with Silicon" by R. D. Thompson, B. Y. Tsaur, and K. N. Tu **289**

ELECTROTHERMICS AND METALLURGY

Thermochemistry of Intermetallic Compounds

L. Brewer, Chairman; K. A. Gschneidner, Jr., Vice-Chairman

(NEW YORK ROOM, Lower Lobby)

A.M. **Abs.**

9:00—"Thermodynamics and Defect Structure of Intermetallic Phases" by Y. A. Chang **343**

9:40—"Thermodynamic Equations for the Liquids of $(A_{1-u}B_u)_{2-y}C_y(s),y$ Near Unity, and Associated Solution Models" by R. F. Brebrick, T. Tung, C-H. Su, and P-k. Liao **344**

10:05—"Quantitative Fit to the Phase Diagram and Thermodynamic Data for the Hg-Cd-Te System" by T. Tung, C-H. Su, P-k. Liao, and R. F. Brebrick **345**

10:30—Fifteen-minute intermission

10:45—"Solid-State Electrochemical Study of Indium-Antimony Liquid Alloys" by T. J. Anderson and L. F. Donaghey **346**

11:10—"Analysis of the In-Sb System Using an Associated Solution Model for the Liquid" by C-H. Su, P-k. Liao, T. Tung, and R. F. Brebrick **347**

11:35—"Analysis of the Ga-Sb System and the Ga-In-Sb Ternary Used an Associated Solution Model for the Liquid" by P-k. Liao, C-H. Su, T. Tung, and R. F. Brebrick **348**

Y. A. Chang, Chairman; R. F. Brebrick, Vice-Chairman

P.M.

2:00—"Metastable Intermetallic Compounds in Some Binary and Ternary Systems" by M. Ellner and B. Predel **349**

2:25—"Relationship Between Structural and Thermodynamic Properties of Some Phases of the Cu-Family" by M. Ellner **350**

2:50—"Solid Solubility Trends in Divalent Alloys" by J. R. Chelikowsky **351**

3:15—"A Mechanism for Growth and the Hydrogen Reduction of Black Molybdenum Thin Films" by K. Seshan, P. D. Hillman, E. E. Chain, K. A. Gesheva, and B. O. Seraphin **352**

3:40—"Magnetoresistive Properties of $Cd_{3-x}Zn_xAs_2$ Compound Semiconductors" by Y. K. Su, Y. L. Tsai, B. D. Liu, C. C. Wei, and C. Y. Chang **353**

ELECTROTHERMICS AND METALLURGY/CORROSION/PHYSICAL ELECTROCHEMISTRY/NEW TECHNOLOGY SUBCOMMITTEE

Vibrational Spectroscopy in Electrochemistry (Laser, Raman, and Infrared)

W. A. Adams, Chairman; R. H. Heidersbach, Vice-Chairman

(LINCOLN ROOM, Second Floor)

A.M. **Abs.**

9:00—"Raman Studies of the Vibrational Properties of Adsorbed Species and Films at Electrochemical Interfaces" by E. Yeager, R. Kötz, and G. Nazri **354**

9:50—"Raman Spectroscopy as an In Situ Probe of Corrosion at Elevated Temperatures" by R. E. Benner, A. S. Nagelberg, and J. C. Hamilton **355**

10:10—Twenty-minute intermission

10:30—"Characterization of the High Temperature Corrosion of Stainless Steels by Raman Scattering" by A. S. Nagelberg, R. E. Benner, and J. C. Hamilton **356**

10:50—"Surface Enhanced Raman Scattering (SERS) as a Probe of Solar Mirror Degradation" by R. E. Benner, J. Vitko, Jr., J. C. Hamilton, and J. E. Shelby **357**

11:10—"Adatom-Molecule Complex in Surface Enhanced Raman Scattering" by J. R. Lombardi and R. L. Birke **358**

11:30—"The Structure of Water on Emersed Electrodes. ATR and Raman Spectra" by J. G. Gordon, B. Pettinger, and M. R. Philpott **359**

R. A. Osteryoung, Chairman; L. Faulkner, Vice-Chairman

P.M.

2:00—"Applications of Raman Spectroscopy in Molten Salt Electrochemistry" by G. Mamantov, K. Tanemoto, G. M. Begun, R. Marassi, and R. Huglen **360**

2:20—"Raman Spectroscopic Studies of Lithium Sulfur Dioxide and Lithium Thionyl-Chloride Batteries" by K. C. Lee, W. A. Adams, C. L. Gardner, D. T. Fouchard, and G. J. Donaldson **361**

2:40—"In Situ Monitoring of Electrode Surface Phases by Laser Raman Spectroscopy during Anodization and Sulfation of Tetra Basic Lead Sulfate in Sulfuric Acid" by R. Varma, G. Cook, N. P. Yao, and W. Molinorolo **362**

3:10—"Optical Properties of Complexes at the Metal/Electrolyte Interface Measured by Surface Plasmon Excitation (SP)" by A. Tadjeddine and D. M. Kolb **363**

3:35—"Interpretation of Surface-Enhanced Raman Scattering as a Resonance Raman Effect: Spectrum of 1,2-bis-(4-pyridyl)-ethylene" by J. J. McMahon, K. L. Guyer, G. T. Babcock, and M. J. Weaver **364**

ENERGY TECHNOLOGY

General Session

J. McBreen, Chairman; S. Wagner, Vice-Chairman

(CHICAGO ROOM, Lower Lobby)

A.M. **Abs.**

9:00—"Shallow Electron States and Linear Boundaries in EFG Ribbon Silicon" by J. I. Hanoka, R. O. Bell, and B. Bathey **381**

9:25—"The Structure of Silicon Grain Boundaries Formed by Growing Silicon on Intersecting Sapphire Planes" by K. A. Jones **382**

9:50—"Solid-State Electrochemical Modification of Photoanodes" by C. Y. Yang, F. T. Lious, S. Levine, and S. Srinivasan **383**

10:15—Ten-minute intermission

10:25—"Studies on Photoanodic Dissolution of n-CdS Electrodes" by J. R. Wilson and S.-M. Park **384**

10:50—"Effects of the Electrolyte Concentration on Flat-band Potentials of n-TiO_2 Electrodes" by J. R. Wilson and S.-M. Park **385**

11:15—"Efficient and Stable Photoelectrochemical Cells Constructed with WSe_2 and $MoSe_2$ Photoanodes" by G. Kline, K. Kam, D. Canfield, and B. A. Parkinson **386**

11:35—"Improvement of Energy Conversion Efficiency by Specific Chemical Treatments of $MoSe_2$ and WSe_2 Photoanodes" by D. Canfield and B. Parkinson **387**

S. Wagner, Chairman; J. McBreen, Vice-Chairman

P.M.

2:00—"Bipolar Zn-Br_2 Batteries for Electric and Hybrid Vehicles" by P. A. Malachesky, H. Einstein, R. Bellows, P. G. Grimes, E. Kantner, and K. Newby **388**

2:25—"Design of Electrolysis under Cost-Optimal Thermal Conditions" by T. Z. Fahidy **389**

2:50—"Effects of Several Trace Contaminants on Molten Carbonate Fuel Cells" by S.-M. Park, and T. J. O'Brien **390**

3:15—"Second Law Performance of Solid Electrolyte Fuel Cells" by R. A. Gaggioli, T. J. Murphy, and G. A. Lopez **391**

INDUSTRIAL ELECTROLYTIC

Chlorine

Electrodes

D. Caldwell, Chairman; R. Bellows, Vice-Chairman

Tuesday continued

(EAST ROOM, The Curtis, Lobby)

Abs.

9:00—"Metal Anodes and Hydrogen Cathodes: Their Activity Towards ClO_3^- Formation, O_2 Evolution, and ClO_3^- Reduction" by B. V. Tilak and D. Pouli 402
9:20—"Chlorine Anodes and Their Effects on Diaphragm Cell Performance" by M. P. Grotheer 403
9:40—"Modified Cathode for Chlor-Alkali Electrolysis" by K. Kawasaki and I. Matsuda 404
10:00—Twenty-minute intermission

Reactors

D. Bennion, Chairman; J. M. Ford, Vice-Chairman

10:20—"Characteristics of Two-Phase Flow in Electrochemical Chlorate Reactors" by E. M. Spore 405
10:40—"Optimization of Electrolytic Cells Having Large Numbers of Design Variables" by R. C. Alkire, G. D. Cera, and M. A. Stadtherr 406
11:00—"Hybrid Cell—A New Process for Improving the Energy Efficiency and Reducing the Cost of Chlor-Alkali Production" by B. Broniewski, B. Warszawski, A. T. Emery, and H. P. Silverman 407

J. Bennett, Chairman; E. Rudd, Vice-Chairman

P.M.

2:00—"Power Dissipation in Shunt-Current Parasitic Process in Series-Connected Electrochemical Cells with Common Electrolyte" by P. Grimes, R. Bellows, and M. Zahn 408
2:20—"Parasitic Current Elimination in Series-Connected Electrochemical Cell Systems with Shared Electrolyte. III. Channel Interconnects" by P. Grimes, R. Bellows, and M. Zahn 409
2:40—"Mechanisms of Shunt Current Production in Series-Connected Electrochemical Cells with Common Electrolyte" by P. Grimes and R. Bellows 410
3:00—Twenty-minute intermission
3:20—"Effects of the Brine Impurities on the Cell Performance of the Diaphragm-Type Chlor-Alkali Cell" by F. Hine, M. Yasuda, and K. Fujita 411

ORGANIC AND BIOLOGICAL ELECTROCHEMISTRY/ENERGY TECHNOLOGY

Electrochemistry of Biomass Derived Compounds

J. G. Osteryoung, Chairman; P. Zuman, Vice-Chairman

(MILWAUKEE ROOM, Lower Lobby)

A.M. Abs.

9:00—"Nonpetroleum Feedstock in Electro-organic Synthesis" by D. Cipris 455
9:30—"Polarographic Studies of Some Reactions of Fural" by E. Woodman, M. A. Wells, and P. Zuman 456
9:50—"Steric Factors Influencing the Rate of Anodic Oxidation of Aldehydes in Alkaline Media" by R. M. Van Effen, B. S. Hui, and D. H. Evans 457
10:10—Fifteen-minute intermission
10:25—"Hydration, Enolization, and Acid-Base Properties in Polarographic Reduction of 1,2-Diketones" by J. Segretario, N. Sleszynski, and P. Zuman 458
10:45—"Review of the Electrochemistry of Levulinic Acid-Acid Degradation Product of Cellulosic Materials" by H. L. Chum and M. Ratcliff 459
11:05—"Electrochemical Conversion of Natural Chiral Compounds into Chiral Synthetic Blocks" by S. Torii, T. Inokuchi, and R. Oi 460
11:25—General discussion

J. Wagenknecht, Chairman; D. Evans, Vice-Chairman

P.M.

2:00—"Conversion of Biomass-Derived Organic Acids to Liquid Fuels by Electrochemical Oxidation in Aqueous Solutions" by J. E. Sanderson, G. W. Barnard, and P. F. Levy 461
2:20—"Semiconductor Powder Catalysts for Photo-Kolbe Electrolysis of Volatile Fatty Acids" by J. S. Cantrell 462
2:40—"The Photo-Kolbe Reaction: A Promise Wrapped in a Puzzle" by R. E. Schwerzel, H. J. Byker, D. G. Vutetakis, and V. E. Wood 463
3:00—Fifteen-minute intermission
3:15—"The Photoelectrochemical Behavior of Levulinic Acid on Platinized Anatase Powders" by H. L. Chum, M. Ratcliff, K. Moran, J. Turner, and A. Nozik 464
3:35—"Light Catalyzed Electro-oxidation of Alcohols and Hydrocarbons" by J. M. Bobbitt, J. P. Willis, and L. L. Kulkarni 465

PHYSICAL ELECTROCHEMISTRY/ENERGY TECHNOLOGY

Electrocatalysis

W. O'Grady, Chairman; M. W. Breiter, Vice-Chairman

(ROOSEVELT ROOM, Second Floor)

A.M. Abs.

9:00—"Electrocatalysis at Oxide-Covered Metal-Electrodes" by S. Gottesfeld and S. Srinivasan 508
9:25—"The Oxygen Evolution Reaction on Ruthenium and RuO_2/TiO_2-Coated Electrodes" by R. Woods 509
9:50—"Questions on the Kinetics of O_2 Evolution on Oxide Covered Metals" by B. D. Cahan and C. T. Chen 510
10:15—Ten-minute intermission
10:25—"Anodic Evolution of Oxygen on Sputtered Iridium Oxide Films" by S. Hackwood, L. M. Schiavone, and G. Beni 511
10:45—"Oxygen Gas Evolution at Rhodium Oxide Anodes" by L. D. Burke and E. J. M. O'Sullivan 512
11:05—"Thin Catalytic Films on Silicon" by L. A. Harris and J. A. Hugo 513
11:25—"Study of a Decomposing Hydride Phase by Measurement of Open-Circuit Potential Decay" by H. Angerstein-Kozlowska and B. E. Conway 514

M. W. Breiter, Chairman; W. O'Grady, Vice-Chairman

P.M.

2:00—"Mass Spectroscopic Cyclic Voltammetry for Mechanistic Studies in Organic Electrocatalysis" by O. Wolter, C. Giordano, J. Heitbaum, and W. Vielstich 515
2:25—"Oxidation of Formic Acid and Methanol on Single Crystal Platinum Electrodes" by R. R. Adzic, A. V. Tripkovic, W. O'Grady, and S. Srinivasan 516
2:45—"Electrocatalysis of the Carbon Monoxide Methanation Reaction on Stabilized Zirconia" by T. M. Gür and R. A. Huggins 517
3:05—"Crystallographic Anisotropies in Chemical and Electrochemical Etching of Pt" by R. Caracciolo and L. D. Schmidt 518
3:20—"The Potentiodynamic Electrooxidation of CO on Pt and Rh Both 'Free' and 'Oxidized' in Acid Solution" by S. A. Bilmes, N. R. De Tacconi, and A. J. Arvia 519
3:40—"Electro-Organic Oxidations on Lead Ruthenate" by H. H. Horowitz, H. S. Horowitz, and J. M. Longo 520

Wednesday, May 13, 1981

12:15 P.M.—Energy Technology Group Luncheon and Business Meeting, Twin Cities Room, Lower Lobby
12:15 P.M.—Industrial Electrolytic Division Luncheon and Business Meeting, Minnesota Room, Lobby Level
12:15 P.M.—Organic and Biological Electrochemistry Division Luncheon and Business Meeting, Milwaukee Room, Lower Lobby

EDUCATION COMMITTEE MOVIES

J. Horkans, Chairman

(JEFFERSON ROOM, Second Floor)

A.M.

10:00—Energy: A Conversation with Linus Pauling, George Wald, and Philip Morrison
10:30—Natural Gas Fuel Cell

P.M.

2:00—An Interview with the Transistor's Inventors
2:30—Crystal Growth Morphologies
3:00—Turbulence

Wednesday continued

CORROSION/DIELECTRICS AND INSULATION

Anodic Oxidation

L. Young, Chairman; J. L. Ord, Vice-Chairman

(CARDINAL ROOM, The Curtis, Lobby)

A.M. Abs.

9:00—"Electrostriction in Anodic Oxides" by J. L. Ord 50
9:25—"Optical and Dielectric Properties of Anodic Ta_2O_5" by D. J. Smith and L. Young 51
9:50—"Optical Properties and Poole Frenkel Conduction in Anodic Films of Sputtered Tantalum and Tantalum Nitride" by C. J. Miner, R. W. Streater, B. K. MacLaurin, and W. Westwood 52
10:15—Fifteen-minute intermission
10:30—"Investigation of High Field Induced Oxygen Movements in Thin Solid Electrolyte Films of Calcia Stabilized Zirconia (CSZ)" by J. Perriere, J. Siejka, and M. Croset 53
11:00—"Anodization of Superimposed Metallic Layers: Effects of Different Movement Probabilities and Ionic Conductivities" by J. Perriere and J. Siejka 54
11:30—"Mechanism of the Anodic Oxidation of Zirconium" by C. Ortega and J. Siejka 55

J. L. Ord, Chairman; L. Young, Vice-Chairman

P.M.

2:00—"Kinetics of High Field Ionic Conduction in Anodic Tantalum Pentoxide Films" by D. J. Smith and L. Young 56
2:25—"Kinetic Parameters for Growth of Barrier-Type Anodic Oxide on Valve Metals from Galvanostatic Anodization" by I. A. Ammar, S. Darwish, and M. W. Khalil 57
2:50—"Electroluminescence during the Anodic Growth of Tantalum Pentoxide" by V. Kadary and N. Klein 58
3:15—"A-C Ionic Conductivity of Thin Tantalum Pentoxide Films" by A. H. M. Shousha 59
3:40—Ten-minute intermission
3:50—"The Activation Energy for Ion Transport during Anode Film Growth on Nb and Ti" by I. A. Ammar, S. Darwish, and M. W. Khalil 60
4:15—"Titanium Electrodes: Electronic Properties of Thin Passive Films" by U. Stimming and J. W. Schultze 61
4:40—"Investigation of Fixed Electric Charges Induced in Oxides during Anodization Processes" by J. Siejka, A. Morawski, J. Lagowski, and H. C. Gatos 62

CORROSION/PHYSICAL ELECTROCHEMISTRY

Nonaqueous Electrolytes

R. D. Rauh, Chairman; E. J. Cairns, Vice-Chairman

(NEW YORK ROOM, Lower Lobby)

A.M. Abs.

9:00—Introductory remarks by R. D. Rauh
9:10—"Selected Aspects of the Characterization of Organic Electrolytes" by J. F. Coetzee 75
9:50—"Chemical and Electrochemical Studies in a Room Temperature Ionic Liquid" by R. A. Osteryoung, R. J. Gale, J. Robinson, H. Linga, and G. Cheek 76
10:30—Fifteen-minute intermission
10:45—"Novel Aspects on Electrolyte Systems" by V. Gutmann and G. Resch 77
11:25—"Properties and Structure of Nonaqueous Electrolytes" by H. V. Venkatasetty 78

V. R. Koch, Chairman; H. V. Venkatasetty, Vice-Chairman

P.M.

2:00—"Solvent Effects on the Kinetics of Simple Electrode Reactions: A Test of Theoretical Models of Solvent Reorganization" by S. Sahami and M. J. Weaver 79
2:25—"Ion Association in High Concentration Nonaqueous Solutions" by G. E. Blomgren 80
2:50—"Conductivities in Thionyl Chloride: II" by M. Salomon 81
3:15—Fifteen-minute intermission
3:30—"Conductivity Studies of Thionyl Chloride in the Presence of Halogen Compound" by R. W. Bennett, M. L. Gopikanth, and E. Luksha 82
3:55—"Electrocatalytic Reduction of Thionyl Chloride by Organometallic Complexes" by N. Doddapaneni 83

DIELECTRICS AND INSULATION/ ELECTROTHERMICS AND METALLURGY

Adhesion Aspects of Polymeric Coatings

K. L. Mittal, Chairman; H. Leidheiser, Jr., Vice-Chairman

(ILLINOIS ROOM, Lobby)

A.M. Abs.

9:00—"Durability of Metal Polymer Bonds" by W. Brockmann 121
9:25—"Adhesion of Coatings and Its Loss Due to Corrosion" by R. A. Dickie 122
10:00—"Cathodically Induced Deadhesion of Polymer Coating/Metal Substrate Interfaces" by H. Leidheiser, Jr., L. Igetoft, W. Wang, and K. Weber 123
10:25—"The Effects of Environment on Paint Adhesion to Steel" by R. T. Ruggeri and T. R. Beck 124
10:45—"Correlation of Surface Chemistry and Mechanical Properties of Aluminum Substrates Bonded to Polymer Coatings. I. Surface Chemistry" by T. S. Sun, B. M. Ditchek, J. S. Ahearn, and J. D. Venables 125
11:10—"Correlation of Surface Chemistry and Mechanical Properties of Aluminum Substrates Bonded to Polymer Coatings. II. Mechanical Properties" by J. S. Ahearn, T. S. Sun, B. M. Ditchek, and J. D. Venables 126
11:30—"A Case Study of Water Sensitivity of Polymeric Coating-Substrate Interface for Two Aluminum Surface Preparations" by K. K. Knock and M. C. Locke 127
11:50—"Effect of Age of Pigmented Polymeric Films on Adhesion to Metal Substrate" by M. N. Sathyanarayana, P. S. Sampathkumaran, and M. A. Sivasamban 128

K. L. Mittal, Chairman; P. A. Engel, Vice-Chairman

P.M.

2:00—"Adhesion Measurement of Polymeric Coatings" by K. L. Mittal 129
2:40—"Resin Coating Adhesion Tests" by G. G. Gray 130
3:10—"Indentation Debonding Test for Adhered Thin Polymer Layers" by P. A. Engel and G. C. Pedroza 131
3:30—"Thermographic Detection of Polymer/Metal Adhesion Failures" by B. E. Dom and H. E. Evans 132
3:50—"Ultrasonic Inspection Potential for Polymeric Coatings" by J. L. Rose and J. B. Nestleroth 133
4:20—"Pull-Off Test, An Internationally Standardized Method for Adhesion Testing—Assessment of the Relevance of Test Results" by J. Sickfeld 134
4:40—"Bond Strength of Baked Electropaints and the Electrical Resistance per Coulomb of Electrodeposits—A Comparative Study" by S. Guruswamy 135

ELECTRONICS—LUMINESCENCE

Luminescence of II-VI Compounds

D. H. Smith, Chairman; L. Ozawa, Vice-Chairman

(SOLARIUM ROOM, The Curtis, Lobby)

A.M. Abs.

9:00—"Nitrogen as a Shallow Acceptor in ZnSe" by B. J. Fitzpatrick and P. M. Harnack 163
9:25—"Impurity-to-Conduction Band Electron Transfer Transitions in ZnSe:Co" by D. J. Robbins, P. J. Dean, and C. West 164
9:55—"Cathodoluminescence Measurements in the Range of 500-6000V" by R. R. Wengert 165
10:20—Ten-minute intermission
10:30—"$Zn_{1-x}Cd_xS$:Ag,Al Phosphors for Vacuum Fluorescent Displays" by H. Kukimoto, K. Morimoto, H. Toki, and E. Imaizumi 166
10:55—"Preparation and Luminescent Properties of ZnS Phosphors with Large Plate Microcrystals" by T. Matsuoka, F. Fukushima, Y. Fukuda, and T. Nitta 167
11:20—"Multiple Emission from Tellurium-Doped Cadmium Sulfide Photoelectrodes and Implications Regarding Excited-State Communication" by A. B. Ellis, B. R. Karas, H. H. Streckert, and R. Schreiner 168

Wednesday continued

B. J. Fitzpatrick, Chairman; M. S. Waite, Vice-Chairman

P.M.

2:00—"Light Emission and Current in A-C Thin-Film Electroluminescent Devices" by H. Venghaus and D. Theis 169

2:20—"Energy Spectra of the Bulk and Interface States within ZnS:Mn A-C Thin Film EL" by K. W. Yang, S. J. T. Owen, and D. H. Smith 170

2:40—"The Preparation and Characterization of Tb and TbF_3 Doped ZnS Thin Film Electroluminescent Devices" by R. T. Tuenge, R. E. Coovert, and W. A. Barrow 171

3:00—"Electrochemical Process in DCEL ZnS (Mn,Cu) Devices" by D. Pecile, C. Brunel, J. Thomas, and A. Godin 172

3:20—"Effect of Particle Distribution and Second Dopant on the Characteristics of ZnS: Mn DCEL Panels" by X. Luo and L. Zhou 173

3:40—"Low Field Recombination at Self-Activated Centers in II-VI D.C.E.L. Cells" by M. S. Waite 174

4:00—"Kinetics of Radiative Recombination in ZnSe-ZnTe Electroluminescence Diodes" by F. Firszt and E. J. Łożykowski 175

4:20—Ten-minute intermission

Informal Discussion

4:30—Informal discussion on Luminescence of II-VI Compounds

ELECTRONICS/DIELECTRICS AND INSULATION

Fourth International Symposium on Silicon Materials Science and Technology

Silicon Oxides and Their Interfaces

D. J. DiMaria, Chairman; C. M. Osburn, Vice-Chairman

(IOWA ROOM, Lobby)

A.M. **Abs.**

8:00—"Very Thin Gate Insulators" by S. K. Lai 214

8:25—"Ionizing Radiation Effects in SiO_2 and RF Plasma Annealing" by T. P. Ma 215

8:50—"The Role of the Si/SiO_2 Interface in Silicon Oxidation Kinetics" by J. D. Plummer 216

9:15—"The Structural and Chemical Properties of the $Si-SiO_2$ Interface" by C. R. Helms 217

9:40—"Experimental Evidence for the Interpretation of MOS Interface States" by M. Schulz 218

10:05—Fifteen-minute intermission

Laser/Electron Beam Processing

R. G. Wilson, Chairman; G. Foti, Vice-Chairman

10:20—"Laser Annealing–A Novel Regime of Crystal Growth" by J. M. Poate 219

10:45—"Fast Anneal Processing for Improved Device Performance" by J. F. Gibbons 220

11:10—"Enhanced Solubility of Implanted Carbon in Silicon after Q-Switched Laser Annealing" by A. G. Cullis, R. Series, H. C. Webber, and N. G. Chew 221

11:30—"Pulsed Laser Annealing of BF_2^+-Implanted Amorphized Silicon" by A. Bhattacharyya, L. A. Reinisch, and B. G. Streetman 222

11:50—"Pulsed Electron Beam Annealing of Ion-Implanted Semiconductors" by A. V. Dvurechensky, B. P. Kashnikov, and L. S. Smirnov 223

Electronics Division Award Address

P.M.

2:00—"Semiconductor Materials Engineering via Defect Diagnostics" by G. A. Rozgonyi 224

Refractory Metal Silicides

T. I. Kamins, Chairman; C. M. Osburn, Vice-Chairman

3:00—"Silicides: Which, Why, and How?" by S. P. Murarka 225

3:30—"A Comparison of $TiSi_2$ Films Formed by Alloy Sputtering and Coevaporation" by R. F. Pinizzotto, K. L. Wang, and S. Matteson 226

3:50—"One Micron Single Polycide (WSi_2 on Poly-Si) MOSFET Technology" by M. Y. Tsai, H. H. Chao, L. M. Ephrath, B. L. Crowder, A. Cramer, R. S. Bennett, C. J. Lucchese, and M. R. Wordeman 227

4:10—"Low Temperature CVD Growth of Tungsten Disilicide" by W. I. Lehrer and J. M. Pierce 228

4:30—Ten-minute intermission

4:40—"Phosphorus-Doped Molybdenum Silicide Films for LSI Applications" by S. Inoue, N. Toyokura, T. Nakamura, and H. Ishikawa 229

5:00—"Molybdenum Silicide: Is It Suitable for Interconnections in VLSI?" by P. Cappelletti, F. Mori, G. Pignatel, G. Ferla, F. Nava, and G. Ottaviani 230

Silicon Crystal Technology: Informal Session

H. R. Huff, Chairman; K. E. Benson, Vice-Chairman

7:30—Film "Dislocation Phenomena in Silicon Crystals at High Temperature"—K. Sumina

8:00—Informal discussion

Joint General Session

Dry Processing Technologies

L. Rothman, Chairman; F. Schwettmann, Vice-Chairman

(MICHIGAN ROOM, Lobby)

A.M. **Abs.**

9:00—"Electron Beam Resist Materials for Microfabrication" by O. Kogure, K. Sukegawa, S. Imamura, K. Miyoshi, and S. Sugawara 290

9:20—"All Dry Lithographic Processes and Mechanistic Studies with Poly(methacrylonitrile) and Related Polymers" by H. Hiraoka 291

9:40—"A Fully Dried Mask Making Process" by T. Yamazaki, Y. Suzuki, K. Tanaka, and H. Nakata 292

10:00—"Simultaneous Temperature and Etch Rate Measurements during Plasma Stripping of Photoresist" by R. A. Bond, S. Dzioba, and H. M. Naguib 293

10:20—Twenty-minute intermission

10:40—"Temperature and Reactant Gas Effects on Plasma-Deposited Silicon Nitride Characteristics" by R. Chow, D. Rosler, W. A. Lanford, and K.-M. Wang 294

11:00—"Conductivity Change in Polycrystalline Silicon Films by Plasma Deposition of Si-N Layer" by T. Yamaji, S. Hagiwara, and S. Ushio 295

11:20—"Silicon Nitride Passivation for Short-Channel Molybdenum Gate Devices" by T. P. Chow, M. Ghezzo, A. J. Steckl, and D. M. Brown 296

11:40—"Comparison of PSG Films Deposited by Three Different CVD Methods" by Y. Shioya, M. Maeda, and M. Takagi 297

12:00—"The Effect of Glow Discharge Characteristics on the Properties of Plasma-CVD Silicon Nitride Films" by A. Hiraiwa, K. Mukai, S. Takahashi, and S. Harada 298

Dry Processing/Contact Metallization

M. Jones, Chairman; B. Streetman, Vice-Chairman

P.M.

2:00—"Reactive Ion Milling of Aluminum and Alloys" by J. Kiddon, J. Sellers, T. Coutumas, and T. Brewer 299

2:20—"VLSI Reactive Ion Beam Etching" by F. Z. Custode, W. Fewer, M. Splinter, and D. F. Downey 300

2:40—"Polycide Etching in a Flexible Diode Reactor" by R. S. Bennett, L. M. Ephrath, M. Y. Tsai, and C. J. Lucchese 301

3:00—"An Mo-Nitride/Mo Gate MOS Structure" by H. Okabayashi, K. Higuchi, and T. Nozaki 302

3:20—Ten-minute intermission

3:30—"The Diffusion Kinetics of Si in Plasma-Deposited SiO_2" by L. A. Nesbit 303

3:50—"Silicon Epitaxial Growth on Porous Silicon by Plasma CVD with Silane" by T. Itoh, H. Takai, and M. Horiuchi 304

4:10—"Plasma-Activated Deposition and Some Properties of PSG Films" by A. Takamatsu, M. Shibata, H. Sakai, and T. Yoshimi 305

4:30—"Al/Ti as Contact Metallurgy for VLSI Applications. I. Electrical Properties" by C. Y. Ting and B. L. Crowder 306

4:50—"Al/Ti as Contact Metallurgy for VLSI Applications. II. Annealing of Radiation Damage in MOSFET's" by J. M. Aitken and B. L. Crowder 307

Wednesday continued

ELECTROTHERMICS AND METALLURGY/CORROSION/PHYSICAL ELECTROCHEMISTRY/NEW TECHNOLOGY SUBCOMMITTEE

Vibrational Spectroscopy in Electrochemistry (Laser, Raman, and Infrared)

R. VanDuyne, Chairman; R. Varma, Vice-Chairman

(LINCOLN ROOM, Second Floor)

A.M. **Abs.**

9:00—"Surface Enhanced Raman Spectroscopy: A Discussion of Mechanisms and a Guide to Applications" by T. E. Furtak 365

9:40—"Surface Enhanced Raman Scattering from Benzotriazole on Cu" by J. Kester and T. Furtak 366

10:00—Twenty-minute intermission

10:20—"Reactive Interfacial Chemistry and SERS" by R. P. Cooney, M. W. Howard, and M. Mahoney 367

11:00—"Surface Enhanced Raman Spectra of Azide Ion and Other Molecules on Silver and Copper Electrode" by M. R. Philpott, R. E. Kunz, and J. G. Gordon 368

T. Furtak, Chairman; W. A. Adams, Vice-Chairman

P.M.

2:00—"Raman Spectroscopic Study of the Radical Ions Stabilization at a Silver Electrode" by A. Regis and J. Croset 369

2:20—"Surface Enhanced Raman Scattering of Cyanide Chemisorption Layers on Silver: Potential and Time Dependence" by W. Plieth, B. Roy, and H. Bruckner 370

2:40—"In Situ Vibrational IR Spectroscopy of Adsorbed Species on Metal Electrodes in Aqueous Systems" by A. Bewick, K. Kunimatsu, and J. W. Russell 371

3:00—Ten-minute intermission

Recent News Papers

3:20—Recent News Papers

INDUSTRIAL ELECTROLYTIC

Chlorine

Separators

K. E. Woodard, Chairman; M. P. Grotheer, Vice-Chairman

(EAST ROOM, The Curtis, Lobby)

A.M. **Abs.**

9:00—"A Comparison of Properties of Films of Perfluorinated Carboxylate and Sulfonate Ion Exchange Polymers" by Z. Twardowski, L. Clarke, and H. L. Yeager 412

9:20—"Diffusional Properties of a Perfluorinated Carboxylate Film in Chlor-Alkali Solution Environments" by H. L. Yeager and B. O'Dell 413

9:40—"Measurement of Ionic and Water Transport Numbers in a Membrane Chlor-Alkali Cell" by H. L. Yeager and Z. Twardowski 414

10:05—Fifteen-minute intermission

10:20—"Estimation of Minimum Thickness for a Chlor-Alkali Diaphragm" by K. Viswanathan 415

11:00—"Electrochemical Hypochlorination of Allyl Chloride in Dilute HCl" by C. Comninellis and E. Plattner 416

11:20—"Membrane for Chlor-Alkali Electrolysis" by M. Seko 417

11:40—"Energy Saving in Brine Electrolysis with Oronzio deNora SPE Cell" by A. Nidola 418

ORGANIC AND BIOLOGICAL ELECTROCHEMISTRY

Mechanisms and Mechanistic Techniques in Organic Electrode Reactions

H. B. Mark, Jr., Chairman; J. F. Evans, Vice-Chairman

(CHICAGO ROOM, Lower Lobby)

A.M. **Abs.**

9:00—Introductory remarks

9:05—"Derivative Cyclic Voltabsorptometry: A New Spectroelectrochemical Technique for the Study of Organic Electrode Reactions" by E. E. Bancroft and H. N. Blount 425

9:35—"Thin Layer Spectroelectrochemical Kinetic Study of Viologen Cation Radicals Reacting at Hydrogen-Evolving Gold and Nickel Electrodes" by E. F. Bowden and F. M. Hawkridge 426

10:05—Twenty-minute intermission

10:25—"Diffractive Spectroelectrochemistry—Enhanced Optical Probes for Monitoring Electrogenerated Species" by P. Rossi, R. Robinson, and R. L. McCreery 427

10:55—"Development of a Spectrofluoroelectrochemical Cell for Studying Biological Systems" by M. J. Simone, W. R. Heineman, and G. P. Kreishman 428

11:25—"Comparison of Stopped-Flow Kinetic Spectrophotometry and Open-Circuit Relaxation Spectroelectrochemistry in the Study of the Kinetics and Mechanism of Reactions of Electrogenerated Species" by J. F. Evans 428A

B. S. Pons, Chairman; H. N. Blount, Vice-Chairman

P.M.

2:00—Introductory remarks

2:05—"Electrocatalysis of Chemical Reactions—The Effect of Electrogenerated Bases on Several 9-Substituted Fluorenes and Bifluorenyls" by C. Nuntnarumit, F. M. Triebe, and M. D. Hawley 429

2:35—"The Electroreduction of PhCOR and PhRC=CHCN" by E. M. Abbot, A. J. Bellamy, J. B. Kerr, and I. S. MacKirdy 430

3:05—Fifteen-minute intermission

3:20—"Mechanisms of Acid and Base Catalyzed Dehydration of Geminal Diols" by J. Rusling, J. Segretario, and P. Zuman 431

3:50—"Electrochemical Generation of Arenetricarbonylchromium Anions. A Study of Their Reactions with Electrophiles" R. D. Rieke, W. P. Henry, G. D. Venburg, S. N. Milligan, and J. Arney 432

4:20—"Electrochemical Reduction of Carbonium Ions in $AlCl_3$-Containing Melts" by G. Luer and D. Bartak 433

PHYSICAL ELECTROCHEMISTRY/ ENERGY TECHNOLOGY

Electrocatalysis

S. Bruckenstein, Chairman; E. Yeager, Vice-Chairman

(ROOSEVELT ROOM, Second Floor)

A.M. **Abs.**

9:00—"The Structure of Metal Adsorbates Formed at Underpotentials" by D. M. Kolb 521

9:30—"Some Recent Developments in Electrocatalysis on Surfaces Modified by Foreign Metal Adatoms" by R. R. Adzic 522

10:00—"The Effect of pH on the Electrocatalytic Properties of Adsorbed Metal Ions" by P. Bindra 523

10:25—Ten-minute intermission

10:35—"Electrocatalytic Effects of Underpotential Metal Deposits on the Cathodic Reduction of Oxygen on Single Crystal Surfaces" by K. Juttner and W. J. Lorenz 524

11:05—"Catalytic Effect of Copper Ion on the Anodic Oxidation of Cyanide Ion" by A. Katagiri, S. Yoshimura, Y. Deguchi, and S. Yoshizawa 525

11:30—"The Influence of Underpotential Deposition on the Electrooxidation of Methanol in Acid Solutions" by E. P. M. Leiva and M. C. Giordano 526

E. Yeager, Chairman; S. Bruckenstein, Vice-Chairman

P.M.

2:00—"Factors Governing the Choice of Semiconducting Oxides for the Evolution of Oxygen in Alkaline Media" by A. C. C. Tseung and P. Rasiyah 527

2:20—"Oxygen Electrocatalysis on Some Oxide Pyrochlores" by H. S. Horowitz, H. H. Horowitz, and J. M. Longo 528

2:40—"Mechanism of Oxygen Evolution on Li-Doped Co_3O_4" by P. Rasiyah and A. C. C. Tseung 529

3:00—"Mechanism of Oxygen Evolution on $NiCo_2O_4$. II. Kinetic Studies" by P. Rasiyah and A. C. C. Tseung 530

3:20—Ten-minute intermission

3:30—"Inner-Sphere Reactivity at Solid Metal Surfaces: The Reduction of Co(III) Ammine Complexes at Platinum and Gold Electrodes" by S. W. Barr and M. J. Weaver 531

Wednesday continued

3:50—"Inner-Sphere Reactivity at Solid Metal Surfaces: Rate-Structure Correlations for Transition-Metal Complexes at Silver Electrodes" by K. L. Guyer, J. T. Hupp, and M. J. Weaver **532**

4:10—"Electrocatalytic Properties of Transition Metal Macrocyclics for Anodic Reactions" by J. Zagal, C. Fierro, E. Munoz, and R. Rozas **533**

4:30—"Influence of Anion Adsorption on O_2 Reduction Kinetics. Interest of Mo and Fe Naphthalocyanine Impregnations on Carbon Black Supports" by G. Magner, M. Savy, and G. Scarbeck **534**

Thursday, May 14, 1981

12:15 P.M.—Luminescence-Electronics Division Luncheon, Minnesota Room, Lobby Level

CORROSION/DIELECTRICS AND INSULATION

Anodic Oxidation

B. MacDougall, Chairman; C. R. Clayton, Vice-Chairman

(CARDINAL ROOM, The Curtis, Lobby)

A.M. **Abs.**

9:00—"RHEED and X.P.S. Studies of the Passive Films Formed on 304 Stainless Steels" by C. R. Clayton, K. G. K. Doss, Y-F. Wang, and J. Warren **63**

9:25—"Influence of B and P on Corrosion and Passivation Properties of Ni Films" by V. Brusic, J. Aboaf, R. D. MacInnes, and E. Alessandrini **64**

9:50—"Comparative Approach of the Corrosion and Passivation of Nickel and Iron in Aqueous Solutions" by J. R. Vilche and A. J. Arvia **65**

10:15—Fifteen-minute intermission

10:30—"Corrosion and Oxidation of Silver and Silver/10% Palladium Electrodes under Physiological Conditions" by B. J. Piersma and W. Greatbatch **66**

10:55—"The Anodic Oxidation of Steel in Sodium Metasilicate Solutions" by L. L. Gruss and E. Silvestre **67**

11:20—"An Assessment of the Processes Leading to Pit Nucleation on Iron" by M. Janik-Czachor **68**

C. R. Clayton, Chairman; B. MacDougall, Vice-Chairman

P.M.

2:00—"A Critical Consideration of the Flade Potential" by K. Juttner and W. J. Lorenz **69**

2:30—"Anodic Oxidation of UO_2" by S. Sunder, D. W. Shoesmith, M. G. Bailey, and N. S. McIntyre **70**

2:55—"The Chemiconductor Model of the Passive Film on Iron" by B. D. Cahen and C. T. Chen **71**

3:25—Ten-minute intermission

3:35—"A Point Defect Model for the Growth and Breakdown of Anodic Oxide Films" by C-Y. Chao, L.-F. Lin, and D. D. Macdonald **72**

4:05—"The Anodic Oxidation of Ni-Cr Alloys in Molten Sodium Sulfate" by J. Truhan and T. Jeys **73**

4:30—"Mechanism of Growth of Ferric Oxide Films by Anodic Oxidation of Fe^{2+} in Nearly Neutral Solutions" by S. Ardizzone and L. Formaro **74**

CORROSION/PHYSICAL ELECTROCHEMISTRY

Nonaqueous Electrolytes

G. Blomgren, Chairman; B. Scrosati, Vice-Chairman

(NEW YORK ROOM, Lower Lobby)

A.M. **Abs.**

9:00—"Selective Electrowinning Using a Liquid Membrane" by M. Gökalp and E. L. Cussler **84**

9:25—"Electrical Conductivity in Solutions of Bromine and Pyridine Derivatives" by P. M. Skarstad and T. G. Hayes **85**

9:50—"Photoelectrochemical Cells Using the Liquid Ammoniate of Sodium Iodide at Room Temperature" by J.-L. Sculfort, D. Guyomard, and M. Herlem **86**

10:15—Fifteen-minute intermission

10:30—"Determination of Water in Propylene Carbonate Electrolytes by Cyclic Voltammetry" by R. T. Atanasoski, H. H. Law, and C. W. Tobias **87**

10:55—"Effect of Electrolyte Variables on the Polarization of the Lithium Electrode in Sulfuryl Chloride Solutions" by F. Alessandrini, B. Scrosati, F. Bonino, and M. Lazzari **88**

11:20—"Cycling Efficiency Behavior of Lithium in Nonaqueous Electrolytes at Ambient Temperature" by M. Garreau and J. Thevenin **89**

DIELECTRICS AND INSULATION

Electrolytic Capacitor Technology

R. S. Alwitt, Chairman, W. J. Bernard, Vice-Chairman

(MILWAUKEE ROOM, Lower Lobby)

A.M. **Abs.**

9:00—"Electrical Breakdown of Insulating Films by Impact Ionization" by N. Klein **90**

9:40—"The Scintillation Behavior of Anodic Ta_2O_5 and Its Relation to Electrolytic Capacitors" by J. M. Martinez-Duart, I. Montero, M. Fernandez, and J. M. Albella **91**

10:00—"A-C Etching Technology for Aluminum Electrolytic Capacitor in Japan" by S. Watase and T. Kudo **92**

10:25—Ten-minute intermission

10:35—"D.C. Etching for Low Voltage Foils. Regulation of Pit Initiation at the Etching Bath Incoming" by M. Badia, G. Laslaz, and J. Dubruelh **93**

10:55—"Factor Determining the Etch Gain of Hard Aluminum Foil in Electrolytic Capacitors" by H. H. Nee **94**

11:15—"Effect of Trace Elements on Etching of Aluminum Electrolytic Capacitor Foil" by K. Arai, T. Suzuki, and T. Atsumi **95**

11:35—"The Anodization of Etched Aluminum Foil" by H. J. de Wit, C. Crevecoeur, and J. Bruinink **96**

11:55—"A Method for Estimating Size Distribution of Etch Tunnels in DC-Etched Al Foil" by R. S. Alwitt **97**

DIELECTRICS AND INSULATION/ ELECTROTHERMICS AND METALLURGY

Adhesion Aspects of Polymeric Coatings

K. L. Mittal, Chairman; L. Rothman, Vice-Chairman

(ILLINOIS ROOM, Lobby)

A.M. **Abs.**

9:00—"Silane Adhesion Promoters for Polymeric Coatings" by E. P. Plueddemann **136**

9:35—"Structure and Effects of Organosilane or Organotitanate Adhesion Promoters on Al_2O_3/Polyethylene Joints" by N. H. Sung, A. Kaul, S. Ni, C. S. P. Sung, and I. J. Chin **137**

10:05—"The Use of Coupling Agents to Improve the Adhesion of Polymer Matrices for Electronic Applications" by D. J. Vaughan and R. C. Peek, Jr. **138**

10:25—"Adhesion Promotion and Polymer Composite Performance with Titanate Coupling Agents" by S. J. Monte and G. Sugerman **139**

10:45—"Improved Metal-Polymer Wet Strength Adhesion" by L. Graham and J. A. Emerson **140**

11:05—"Adhesion of Aromatic Polyimide to Silicon Wafer" by Y. K. Lee and J. D. Craig **141**

11:25—"Effect of Residual Chemical Contaminants on Polyimide/Surface Interface Adhesion" by M. Chaker and R. J. Clark **142**

11:45—"The Study of Some β-Diketones as Complexing Agents for the Adhesion Promotion Between Carbon Steel and Polymeric Coating" by T. T. Kam and P. K. Hon **143**

ELECTRONICS—LUMINESCENCE

General Session

C. F. Chenot, Chairman, M. V. Hoffman, Vice-Chairman

(SOLARIUM ROOM, The Curtis, Lobby)

A.M. **Abs.**

9:00—"Synthesis and Characterization of Cerium- **176**

Thursday continued

Activated Fluoroapatite Phosphors" by R. G. Pappalardo, T. Peters, A. Kasenga, and C. F. Chenot

9:25—"On Scattering Coefficients of Lamp Phosphore" by K. Narita 177

9:50—"Kubelka-Munk Theory of the Performance of Pigmented Phosphor Screens" by J. R. McColl 178

10:15—Five-minute intermission

10:20—"Dye-Laser Spectroscopy of Y_2O_3:Eu Lamp Phosphors" by R. B. Hunt, Jr. and R. G. Pappalardo 179

10:45—"The Emission Color of Y_2O_2S:Tb^{3+} Phosphor with Dy^{3+} Coactivator" by K. Inoue, M. Watanabe, T. Takahara, T. Wakatsuki, and T. Nishimura 180

11:10—"The Relationship Between Emission Intensity from Tb^{3+} $^5D_3$ $^5D_4$ Level in LaOBr and Temperature, Concentration" by C-S. Shi, W-P. Zhang, and C-X. Guo 181

11:35—"Mechanism of Energy Transfer from a Trace of Tb^{3+} to RE^{3+} (Eu^{3+}, Sm^{3+}, Dy^{3+}) in Y_2O_2S Phosphor" by C-X. Guo, W-P. Zhang, and C-S. Shi 182

M. J. Brines, Chairman; G. R. Gillooly, Vice-Chairman

P.M.

2:30—"Host Sensitization Mechanism of Eu^{3+} Luminescence in $(Y,In)_2O_3$:Eu^{3+}" by H. Yamamoto 183

2:55—Five-minute intermission

Recent News Papers

3:00—Recent News Papers

ELECTRONICS/DIELECTRICS AND INSULATION

Fourth International Symposium on Silicon Materials Science and Technology

Advanced IC Process Technology

A. F. Tasch, Jr., Chairman; C. M. Osburn, Vice-Chairman

(IOWA ROOM, Lobby)

A.M. **Abs.**

9:00—"Dry Etching for VLSI—A Review" by L. M. Ephrath 231

9:30—"Effects and Chemistry of the Addition of Oxygen-Containing Compounds to Halocarbon Plasmas" by F. H. M. Sanders and J. Dieleman 232

9:50—"Anisotropic Etching of Polysilicon and Metal Silicides in Fluorine Containing Plasma" by W. Beinvogl and B. Hasler 233

10:10—"Plasma Oxide FET Devices" by A. K. Ray and A. Reisman 234

10:30—Ten-minute intermission

C. M. Osburn, Chairman; A. F. Tasch, Jr., Vice-Chairman

10:40—"A Microlithography Scenario" by J. H. Bruning 235

11:10—"Multilevel Interconnections for VLSI" by P. B. Ghate and C. R. Fuller 236

11:40—"Submicron Ohmic Contacts on n-Type Polysilicon for Integrated Circuits" by J. Y. Chen, G. Eckhardt, and L. D. Hess 237

Defects/Device Performance

G. J. Declerck, Chairman; L. E. Katz, Vice-Chairman

P.M.

1:30—"Considerations Regarding Gettering in Integrated Circuits" by C. W. Pearce, T. E. Seidel, and L. E. Katz 238

2:00—"Heavy Metal Gettering by Segregation Annealing" by G. F. Cerofolini and G. Ferla 239

2:20—"Impact of a Chlorine Oxidation on the Properties of Silicon Bulk Defects" by C. Claeys, G. Declerck, R. Van Overstraeten, H. Bender, J. Van Landuyt, and S. Amelinckx 240

2:40—"Annealing Effect of Mechanical Damage on Minute Defect, Heavy Metal and Oxygen Atom in Silicon Crystal" by Y. Takano, H. Kozuka, M. Ogirima, and M. Maki 241

3:00—"Process Modelling with High Oxygen Content CZ Silicon" by D. Huber, P. Stallhofer, and M. Blätte 242

3:20—"The Predominant Intrinsic Point Defects in Silicon: Vacancies or Interstitials" by U. Goesele, H. Foell, W. Frank, and H. Strunk 243

3:40—Twenty-minute intermission

L. E. Katz, Chairman; G. J. Declerck, Vice-Chairman

4:00—"Defects Produced in Silicon by High Energy Electron and γ-Irradiation and Their Effects upon Recombination Lifetime" by S. D. Brotherton and P. Bradley 244

4:20—"The Use of Photoinjection to Determine Minority Carrier Lifetime and Doping Level Profiles of Low-Doped MOS Structures" by U. Efron and J. Grinberg 245

4:40—"Bird's Beak Configuration of Isolation Oxide in Bipolar Technology" by R. Lemme and H. Oppolzer 246

5:00—"Crystal Defects Induced by Local Oxidation of Silicon" by G. Franz, B. O. Kolbesen, and H. Strunk 247

5:20—"Wet HCl Oxidation of BBr_3 Open Tube Duffused Bases" by D. C. Ahlgren 248

5:40—"A Study of Dislocations Induced in Emitter Phosphorus during Silicon Planar Transistor Production: Generation, Elimination, and Effect on Characteristics" by N. D. Stojadinovic and R. S. Popovic 249

Joint General Session

Defects in Si

H. F. Schaake, Chairman; S. Mahajan, Vice-Chairman

(MICHIGAN ROOM, Lobby)

A.M. **Abs.**

9:00—"Improvement of the Crystalline Quality of SOS Films by Beam Processing" by R. E. Reedy and T. W. Sigmon 308

9:20—"Regional Low-Level Leakage Distribution and Pipe Characteristics in LSI Silicon Wafers" by M.-S. Fung 309

9:40—"Microdefects during Phosphorus Diffusion" by S. Blackstone, W. Henry, L. Jastrzebski, and W. Fisher 310

10:00—"A Preferential Etch Study of Swirls and Stacking Faults in CZ Silicon" by K. V. Rao, L. J. Demer, and C. J. Varker 311

10:20—Twenty-minute intermission

10:40—"Discriminating Electronically Active and Inactive Defects by Anodic Etching" by H. Föll 312

11:00—"Oxygen Striation Observed by Scanning IR Absorption Method in CZ-Grown Silicon Crystals" by A. Ohsawa, K. Honda, S. Shibatomi, and S. Ohkawa 313

11:20—"Exit Chipping in ID Diamond Sawing of Silicon Crystals" by L. D. Dyer 314

11:40—"The 'Feathering' of Striations in LPE and CZ Crystals: An Explanation Using Lateral Microscopic Growth Concepts" by E. Bauser and G. A. Rozgonyi 315

Diffusion, Implants, Gettering, III-V

J. Mauer, Chairman; A. Voshchenkov, Vice-Chairman

P.M.

2:00—"High Dose Field Implantation for Channel Stopping" by T. C. Gwo and W. C. Ko 316

2:20—"Partial Vacuum Boron Diffusion III (Boron Silicide Phase Growth and Oxidation)" by D. Flowers and S. Thompson 317

2:40—"Arsenic and Boron Diffusion in Polycrystalline Silicon" by C. H. Lee and A. C. Yen 318

3:00—"Oxidation-Enhanced Diffusion of Boron in Steam" by M. R. Oliver, S. Matteson, and R. E. Yankley 319

3:20—Twenty-minute intermission

3:40—"Effect of Poly-Si Gettering Scheme on the Quality of Si Epitaxial Film" by M. C. Chen, J. Y. Lee, and H. J. Wu 320

4:00—"Si Epitaxial Quality Improvement by Post-Epi Poly-Si Gettering" by M. C. Chen and V. J. Silvestri 321

4:20—"In Situ Monitoring of GaAs LPE Growth Rate" by A. Okamoto, S. Isozumi, J. Lagowski, and H. C. Gatos 322

4:40—"Characterization of Implanted GaAs and InP Using Raman Scattering" by L. L. Abels, S. Sundaram, and J. Comas 323

Recent News Papers

G. C. Schwartz, Chairman; P. J. Tsang, Vice-Chairman

(TWIN CITIES ROOM, Lower Lobby)

A.M.

9:00—Recent News Papers

W. A. Pliskin, Chairman; G. C. Schwartz, Vice-Chairman

P.M.

2:00—Recent News Papers

Thursday continued

ELECTROTHERMICS AND METALLURGY/ ENERGY TECHNOLOGY

Thermionic and Thermoelectric Generation Conversion

D. Tuomi, Chairman; T. Jayadev, Vice-Chairman

(LINCOLN ROOM, Second Floor)

A.M. **Abs.**

9:00—Introductory remarks by D. Tuomi
9:10—"Thermionic Energy Conversion: Its Potential and Problems" by G. O. Fitzpatrick **372**
9:50—"Thermally Regenerative Electrochemical Systems—An Update" by H. L. Chum **373**
10:30—Ten-minute intermission
10:40—"A New Photothermogalvanic System" by H. L. Chum, R. Pitts, and R. F. Fahlsing **374**
11:00—"High Efficiency Thermoelectric Conversion with Solid Electrolytes. The Sodium Heat Engine" by T. Cole, N. Weber, and T. K. Hunt **375**

T. Cole, Chairman; T. Jayadev, Vice-Chairman

P.M.

2:00—"Lattice Thermal Conductivity of Semiconductors: A Chemical Bond Approach" by D. P. Spitzer **376**
2:40—"Thermoelectricity. V. Seebeck Quality Optimization" by D. Tuomi **377**
3:00—Ten-minute intermission
3:10—"Rare Earth Chalcogenides as Thermoelectric Materials" by T. Takeshita, B. J. Beaudry, and K. A. Gschneidner, Jr. **378**
3:30—"The Thermoelectric Properties of the Boron-Carbon System" by A. Lockwood, C. Wood, G. Reynolds, and N. Elsner **379**
3:50—"Considerations Involved in the Development of a Viable Design for a Copper-Silver Selenide Thermoelectric Element" by P. B. Hogerton, W. C. Mitchell, and J. D. Hinderman **380**

ORGANIC AND BIOLOGICAL ELECTROCHEMISTRY

Mechanisms and Mechanistic Techniques in Organic Electrode Reactions

G. P. Kreishman, Chairman; R. L. McCreery, Vice-Chairman

(CHICAGO ROOM, Lower Lobby)

A.M. **Abs.**

9:00—Introductory remarks
9:05—"Applications of Fast Fourier Transform Faradaic Admittance Measurements (FFT-FAM) to Organic Electrode Reaction Heterogeneous Charge Transfer Rates" by J. H. Begemann, M. Grzeszczuk, and D. E. Smith **434**
9:35—"Reverse Pulse Polarographic Study of 1-methyl-4-cyanopyridinium Ion" by A. Webber, E. Kirowa-Eisner, and J. Osteryoung **435**
10:05—Fifteen-minute intermission
10:20—"Identification of Electrolysis Mechanism Using Cyclic Voltammetry and Computerized Pattern Recognition" by S. P. Perone and S. D. Schachterle **436**
10:50—"Conformational Effects on the Electrochemical Oxidation and Reduction of Sterically Hindered Ethylenes" by R. W. Busch and D. H. Evans **437**
11:20—"Catalytic and Electrocatalytic Behavior of Ruthenium Dioxide" by L. D. Burke and J. F. Healy **438**

M. D. Hawley, Chairman; F. M. Hawkridge, Vice-Chairman

P.M.

2:00—Introductory remarks
2:05—"Electrochemical Determination of Cation Radical Stabilities of Methylbenzo[a]pyrenes" by D. A. Tryk and S.-M. Park **439**
2:35—"Electrochemically Activated Binding of Benzo[a]pyrene and Other Polycyclic Aromatic Hydrocarbons to DNA" by D. A. Tryk and S.-M. Park **440**
3:05—Fifteen-minute intermission
3:20—"Mechanisms of Mediated NADH Electrooxidations" by L. L. Miller and A. Kitani **441**
3:50—"Electrochemical Regeneration of NAD" by G. L. Cahen, Jr., D. J. Kirwan, J. W. Parcells, and G. E. Stoner **442**
4:20—"Electrochemistry of Uric Acid and Related Biological Purines" by R. N. Goyal, A. Brajter-Toth, and G. Dryhurst **443**

PHYSICAL ELECTROCHEMISTRY

Solid Electrolyte Interfaces

M. W. Breiter, Chairman; B. Dunn, Vice-Chairman

(ROOSEVELT ROOM, Second Floor)

A.M. **Abs.**

9:00—"Characterization of Solid Electrolyte-Inert Electrode Interfaces" by D. O. Raleigh **466**
9:20—"Interface Polarization of Sodium Beta Alumina in Aqueous and Nonaqueous Solutions of Sodium Salts" by F. G. Will and K. Kalapis **467**
9:40—"Time Dependence of the Asymmetric Behavior of Polycrystalline Beta" Alumina" by M. W. Breiter and B. Dunn **468**
10:00—"The Sodium/Beta Alumina Interface" by D. S. Demott, M. L. Wright, and M. D. Hames **469**
10:20—Twenty-minute intermission
10:40—"Study of the AgF-LaF_3 Reversible Interface by Auger Spectroscopy and Impedance Technique" by T. A. Fjeldly and J. S. Johannessen **470**
11:00—"Theoretical Analysis of Liquid-Junction Photovoltaic Cells" by M. E. Orazem and J. Newman **471**
11:20—"Properties of Solid Electrolyte Film Grown on Fresh Surface Lithium Electrode" by M. Yaniv, K. M. Abraham, and G. L. Holleck **472**

B. Dunn, Chairman; M. W. Breiter, Vice-Chairman

P.M.

2:00—"Studies of Internal Interfaces in Solid Electrolytes by Impedance Spectroscopy" by C. K. Chiang, A. L. Dragoo, and A. D. Franklin **473**
2:20—"Oxygen Diffusion in Liquid Metal Studied by Impedance Spectroscopy" by E. J. L. Schouler, C. Couture, and M. Kleitz **474**
2:40—"Electrochemical and Surface Spectroscopic Studies of Metal/Solid Electrolyte Interfaces" by C. Y. Yang, H. S. Isaacs, and W. E. O'Grady **475**
3:00—"The H_2/H_2O Reaction at Noble Metal Electrodes on Zirconia Electrolytes" by E. J. L. Schouler and H. S. Isaacs **476**
3:20—Twenty-minute intermission
3:40—"Electrical Conductivity of Tetragonal Zirconia Below the Transformation Temperature" by T. K. Gupta and R. B. Grekila **477**
4:00—Round table discussion

PHYSICAL ELECTROCHEMISTRY

General Session

E. J. Cairns, Chairman; J. P. Hoare, Vice-Chairman

(JEFFERSON ROOM, Second Floor)

A.M. **Abs.**

9:00—"The Effect of Electrolyte Anion Adsorption on Current Efficiencies for the Evolution of Ozone" by P. C. Foller and C. W. Tobias **478**
9:15—"A Simple Technique for the Estimation of the Bulk Resistivity of Powdered Materials" by J. R. Whyte, Jr., and K. Seshan **479**
9:30—"Experimental and Theoretical Study of Porous Electrodes Having Perpendicular Direction of Current and Electrolyte" by A. Storck and M. A. Enriquez-Granados **480**
9:45—"General Equations for the Chemical Potential and Its Isobatic, Isochoric, Isentropic and Isothermal Changes, Variation of Gas Constant and Its Thermodynamic Implications" by R. Heyrovska **481**
10:00—"An Estimate of the Heat of Adsorption of the Hydroperoxyl Radical on Platinum" by J. P. Hoare **482**
10:15—Ten-minute intermission
10:25—"Electrochemical Reduction of Cobalt Carbon Bonded Organometallic Compounds of Cobaloxime Type. Electrocatalytical Applications" by J. Devynck, C. Bied-Charreton, M. D. Le Hoang, A. Gaudemer, and B. Tremillon **483**
10:40—"Error Analysis of the Potential and Voltage Step Relaxation Techniques for the Measurement of the Kinetics of Electrode Reactions" by Z. Nagy **484**
10:55—"Theory of Transition Time: Anodic Passivation" by K. C. Tsai and S. Venkatesh **485**

Thursday continued

11:05—"Double-Layer Measurements at Silver and Lead Electrodes" by K. L. Guyer, J. T. Hupp, D. Larkin, H. Y. Liu, and M. J. Weaver **486**

11:20—"Van't Hoff's Factor for Nonideality of Gases and Aqueous Solutions, Hydration Numbers from Osmotic Coefficients, Langmuir's Formula Extended for Space Coverage" by R. Heyrovska **487**

J. P. Hoare, Chairman; E. J. Cairns, Vice-Chairman

P.M.

2:00—"Photocurrent Spectroscopy of Some Semiconducting Layered Compounds (WSe_2, $MoSe_2$, WS_2, and InSe)" by K.-K. Kam and B. A. Parkinson **488**

2:20—"Electrochemical Disinfection of Recirculating Fluids" by P. Natishan, G. E. Stoner, and G. L. Cahen, Jr. **489**

2:40—"Electrochemical Studies of Chromium in Molten LiF-NaF-KF (FLINAK)" by T. Yoko and R. A. Bailey **490**

3:00—"Investigation of Anion Adsorption on Platinum in Trifluoromethanesulfonic Acid and Related Alkanesulfonic Acids" by G. W. Walker and R. T. Foley **491**

3:20—Ten-minute intermission

3:30—"Current-Potential Characteristics of the Bromine/Bromide Electrode Reaction" by S. E. Lorimer and R. E. White **492**

3:50—"Electrocatalysis in Electroless Copper Deposition" by J. Duffy, L. Pearson, and M. Paunovic **493**

4:10—"The Effect of Cathodic Polarization on the Creep Rate of Gold" by C. H. van der Wekken **494**

4:30—"Electrocatalysis of the Oxygen Reduction Reaction—Electrolyte and Anion Effects" by S. Srinivasan, H. Olender, E. A. Klaus, and M. H. Miles **495**

Friday, May 15, 1981

ELECTRONICS/DIELECTRICS AND INSULATION

Fourth International Symposium on Silicon Materials Science and Technology

Process/Device Monitors

M. G. Buehler, Chairman; D. S. Perloff, Vice-Chairman

(IOWA ROOM, Lobby)

A.M. **Abs.**

8:00—"Test Vehicles for the Measurement and Analysis of VLSI Lithographic and Etching Parameters" by T. F. Hasan, D. S. Perloff, and C. L. Mallory **250**

8:20—"A Modular Concept for a Bipolar Oxide-Isolated Test Vehicle" by R. Klein, R. O'Connor, W. Wright, and S. Hutchings **251**

8:40—"Test Patterns for a Bipolar Process Using High-Reduction Projection Printers" by S. Wetterling **252**

9:00—"Characterizing and Analyzing Critical Integrated Circuit Process Parameters" by L. W. Linholm, R. L. Mattis, R. C. Frisch, and C. P. Reeve **253**

9:20—"A Test Pattern for the Evaluation of Bipolar Integrated Circuit Processes" by C. M. Drum and P. T. Panousis **254**

9:40—Twenty-minute intermission

Process/Device Modeling

D. A. Antoniadis, Chairman; M. Gosney, Vice-Chairman

10:00—"A Review of Submicron Device Modelling" by P. K. Chatterjee **255**

10:30—"Oxidation Induced Point Defects in Silicon—A Review" by D. A. Antoniadis **256**

11:00—"Modeling Anomalous Phenomena in Arsenic Diffusion in Silicon" by R. B. Fair **257**

M. Gosney, Chairman; D. A. Antoniadis, Vice-Chairman

P.M.

1:00—"Modelling of Double-Diffusion Processing" by N. Mallam, C. L. Jones, and A. F. W. Willoughby **258**

1:20—"Measurement of Local Diffusion Coefficients in Planar Device Structures" by C. Hill **259**

1:40—"Grain Growth Mechanisms in Polysilicon" by L. Mei, M. Rivier, Y. Kwart, and R. W. Dutton **260**

2:00—"SUBMODAN—A Composite Process/Device Simulation System for Short-Channel MOS FET's" by S. Onga, M. Konaka, K. Taniguchi, H. Iwai, and L. M. Dang **261**

Joint General Session

Silicon Crystal Growth

R. E. Enstrom, Chairman; Y. S. Chiang, Vice-Chairman

(MICHIGAN ROOM, Lobby)

A.M. **Abs.**

9:00—"Electrodeposited Silicon and Its Characterization" by G. M. Rao, D. Elwell, and R. S. Feigelson **324**

9:20—"Technique to Cast Silicon for Solar Cells" by A. Sanjurjo **325**

9:40—"Modeling of Ambient-Meniscus Melt Interactions Associated with Carbon and Oxygen Transport in EFG of Silicon Ribbon" by J. P. Kalejs and L.-Y. Chin **326**

10:00—Twenty-minute intermission

10:20—"Computer-Controlled Czochralski Puller with Recharging Possibility for Large Diameter Silicon Crystals" by B. Altekrüger, H. Birck, and D. Drechsel **327**

10:40—"Improvements to the Czochralski-Silicon Pulling Process" by K. G. Barraclough, R. W. Series, and W. Bardsley **328**

11:00—"A New Compact Production Float Zoner for Large Diameter Silicon Crystals" by B. Altekrüger and D. Drechsel **329**

11:20—"Suppression of Thermal Convection by Transverse Magnetic Field" by K. M. Kim **330**

11:40—"Silicon Wafers Critical Shear Stress Enhancement by Annealing near 800°C" by C. Plougonven, B. Leroy, and E. Trevisan **331**

12:00—"Influence of CW Laser Scan Speed in Solid Phase Crystallization of Amorphous Silicon on Si_3N_4/Glass Substrate" by G. Auvert, D. Bensahel, V. T. N'Guyen, P. Henoc, J. Morin, and P. Coissard **332**

ORGANIC AND BIOLOGICAL ELECTROCHEMISTRY

General Session

L. Miller, Chairman, F. Plattner, Vice-Chairman

(CHICAGO ROOM, Lower Lobby)

A.M. **Abs.**

9:00—"Electrochemical Production of Manganic Sulfate in Concentrated H_2SO_4" by C. Comninellis and E. Plattner **444**

9:20—"Preparative Gas Phase Electrochemical Production of Hydrogen and Fluoride Atom Reactions with Aromatic Compounds" by L. L. Miller and P. W. Schmalzl **445**

9:40—"Preparative Gas Phase Electrochemical Production of Acrylonitrile from Ethylene" by N. Henis, Y.-H. So, and L. L. Miller **446**

10:00—"Preparative Gas Phase Electrochemical Production of Cyanoaromatics" by Y.-H. So and L. L. Miller **447**

EDUCATION COMMITTEE

Description of Movies

Energy: A Conversation—Three very eminent scientists in a film discussion of the most basic, but elusive, concept . . . energy. They are Dr. Linus Pauling of Stanford, chemist and two-time Nobel Prize winner; Dr. George Wald of Harvard, Nobel Prize winner in biology; and Dr. Philip Morrision of MIT, a physicist deeply involved in science education. Dr. Morrision acts as both participant and moderator in this intense and absorbing exchange.

Natural Gas Fuel Cell—This film traces the development of the natural gas fuel cell from the discovery of its basic concepts through to its application as a self-contained power plant for home and industrial use. It shows natural gas converted into electricity through chemistry, without heat, without burning, without turning any mechanical device at all.

An Interview with the Transistor's Inventors—This film features John Bardeen, Walter Brattain, and William Shockley recalling how the transistor was invented at Bell Laboratories in 1947.

Crystal Growth Morphologies—This film illustrates crystal growth in materials that have various entropies of fusion. Some of the effects of impurities or second components are shown.

Turbulence—This film illustrates many of the important aspects of turbulence: effect of Reynolds number on inception, increased pressure drop in pipe-flow, efficient mixing, turbulent transport of momentum and scalar properties, Reynolds stress, influence of Reynolds number on fully developed turbulent flows, turbulent energy cascade, isotropy and similarity of small-scale motions in diverse turbulent fields, effects of buoyancy, the non-Gaussian intermittent character of the small-scale structure at high Reynolds number.

Abstracts*

BATTERY/ENERGY TECHNOLOGY/INDUSTRIAL ELECTROLYTIC

Porous Electrodes

Abstract No. 1

Distribution of Potential in Lead-Acid Battery Electrodes

W. G. Sunu* and **B. W. Burrows,** Gould Laboratories, Rolling Meadows, IL 60008

The potential distribution in thin electrodes of the automotive battery type was determined experimentally and predicted from a model. Potentials at various locations on the plates were measured in cells at various discharge rates, temperatures and for different plate geometries. A model, based on the application of Kirchoff's first law to each intersection of grid members, was solved numerically to predict potential distribution. The measured and calculated potential distributions were in good agreement. The implications of the results are discussed with emphasis on the effect of grid configuration on high rate behavior.

Abstract No. 2

Ratios of AgO/Ag_2O in Porous Silver Oxide Electrodes

T. Katan and **P. J. Carlen,*** Lockheed Palo Alto Research Laboratory, Palo Alto, CA 94304

Preselected ranges of galvanostatic charge/discharge treatments are imposed on planar silver electrodes in 10M KOH, saturated Ag_2O. In this manner, trends toward certain idealized ratios of the charges required for formation and discharge of AgO and Ag_2O could be distinguished. These ratios and deviations from these ratios provide clues to the electrochemical steps and gradations in oxide ratios that develop in porous electrodes, influencing open-circuit potential and performance.

Abstract No. 3

Observations within a Porous, Segmented Wire Silver Oxide Electrode

T. Katan and **H. F. Bauman,*** Lockheed Palo Alto Research Laboratory, Palo Alto, CA 94304

Porous silver electrodes are prepared from 0.6 cm lengths of 25μ diameter wire and subjected to galvanostatic charge and discharge. In this way, subsequent SEM and optical microscopy can be used to observe morphological changes with reference to a known surface position, enabling accurate determinations of oxide thickness for a known porosity and surface area. Agreement is found with electrodes prepared from silver particles and also with planar silver electrodes.

Abstract No. 4

Current Distribution in Porous Zinc Electrode. II. The Effect of Electrolyte Conductance

M.-B. Liu,* **B. R. Faulds, G. M. Cook,** and **N. P. Yao,** Chemical Engineering Division, Argonne National Laboratory, Argonne, IL 60439

The specific conductivity of 7.32*N* KOH with different zincate concentrations (0-1.5M) in an Ni/Zn cell has been measured. The result indicates that the specific conductivity of the electrolyte decreases linearly with increasing zincate concentration. This linearity would be predicted using a mixture rule. The current distribution in porous zinc electrode in electrolyte was interpreted in terms of our conductivity data. The nonuniformity of current distribution in the electrode was attributed to the low conductivity in the electrolyte in the pores of the electrode.

Abstract No. 5

Effect of A-C Charging Methods on Zinc Electrode Morphology

R. Sethi and **D-T. Chin,*** Dept. of Chemical Engineering, Clarkson College of Technology, Potsdam, NY 13676 and **J. McBreen,** Dept. of Energy and Environment, Brookhaven National Laboratory, Upton, NY 11973

The behavior and morphology of zinc electrodes charged with either superimposed square-wave alternating voltage or current was investigated. Studies were made on deposition on rotating zinc disks and on deposition of zinc in pasted zinc electrodes in small nickel-zinc cells. At the normal low overvoltages encountered in battery operation, superimposition of an alternating voltage greatly improved the morphology of the deposit. Even with zinc-on-zinc deposition, stable deposits with good compact morphology were obtained. In the case of pasted plates, superimposition of alternating current encouraged zinc growth close to the current collector grid. These preliminary results indicate that modified charging methods may be a promising approach to the zinc-on-zinc deposition problem in all zinc batteries.

Abstract No. 6

Mathematical Model of the Controlled-Micro-Geometry (CMG) Nickel Hydroxide Electrode

J. W. Oldfield* and **T. S. Turner,** INCO, European Research and Development Centre, Birmingham, England B16 0AJ

The CMG electrode is a novel porous electrode; it consists of layers of thin perforated nickel foil, each coated with nickel hydroxide and then stacked in register and pressed together. A mathematical model has been developed which clearly demonstrates the effect of electrode geometry and active mass parameters on the discharge characteristics of this electrode and shows how the electrode can be optimized to meet the needs of any given application.

Abstract No. 7

Porous Nickel-Coated Steel Anodes for Moderate Temperature Alkaline Electrolysis: Corrosion Resistance

D. E. Hall, Inco Research & Development Center, Inc., Sterling Forest, Suffern, NY 10901

A previous paper described anodes for alkaline water electrolysis made by coating steel substrates with porous nickel. Coatings were applied for polysilicate paints containing the particles in suspension, and sintered to produce cohesion and firm bonding to the substrates. Anodes prepared in this manner produced low oxygen evolution overpotentials in 30 w/o KOH at 80°C, conditions typical of commercial electrolyzer operation. The present paper reports a study of the corrosion resistance of such anodes. It is shown that the anodes are stabilized by formation of a protective Ni-Fe alloy layer at the steel surface, resulting from the interdiffusion of nickel and iron during sintering.

Abstract No. 8

Thickness of Films in Porous Electrodes

G. Wilemski and **J. Mitteldorf,** Physical Sciences Inc., Woburn, MA 01801

We adapt the Derjaguin-Landau-Verwey-Overbeek (DLVO) theory of colloid stability to calculate the thickness of liquid electrolyte films on walls of unflooded pores in gas diffusion electrodes. We show that these films are considerably thinner than those observed on plates or wires dipping into free electrolyte. The effects of pore size and geometry and of electrolyte concentration on film thickness are also considered.

Abstract No. 9

Composite Model of Electrode-Matrix Structures and Their Performance in the Molten Carbonate Fuel Cell

H. C. Maru, * **D. Patel,** and **L. Paetsch,** Energy Research Corp., Danbury, CT 06810

The application of a capillary model describing the electrolyte distribution in a "fixed" electrolyte system such as the molten carbonate fuel cell is discussed. The model uses complete pore size distributions of all porous components competing for electrolyte. Experimental verification of the model, and the effect of electrolyte content on electrode performance and cell resistance are also described. The electrolyte distribution model has been combined with existing kinetic models of gas diffusion electrodes to estimate electrode performance as a function of electrode and matrix pore structure, thickness, and electrolyte inventory.

*** An asterisk by a name indicates which author will present the paper.**

The information has been employed in molten carbonate fuel cell design.

Abstract No. 10

Comparison of Results to Theory of Potentiostatic Charging of the Double Layer of Porous Electrodes

N. A. Fleischer (Present address: Ray-O-Vac, Madison, WI 53703), Dept. of Membrane Research, Weizmann Institute of Science, Rehovot, Israel

Experiments were performed to optimize porous electrode design. A theoretical model of potentiostatic charging of the double layer in porous electrodes was tested for the first time. The model agreed extremely well with experimental results for static and fluidized beds of carbon blacks. A new equation was derived from this model for cyclic voltammetry in the double layer region of potentials. It allows the entire capacity to be calculated at conveniently fast scan rates even though the charging process is not complete by the end of a scan. Finally, the potentiostatic and linear sweep charging modes are compared experimentally and theoretically.

Abstract No. 11

Electrosorption of Organics on Flow-Through Porous Electrodes

R. C. Alkire* and **R. S. Eisinger,** Dept. of Chemical Engineering, University of Illinois, Urbana, Ill. 61801

Electrosorption, the phenomenon in which the adsorption of a species from solution is potential-dependent, can be used as a separation process. An example of such an application is adsorption of organic species from aqueous solution in a flow-through porous electrode. Experiments were carried out on electrosorption of β-naphthol onto packed beds of glassy carbon microspheres. An engineering model of the process has been developed which considers mass transfer, ohmic resistance, and charging of the electrical double layer for a porous electrode and has been applied to the experimental system which exhibited a modified Langmuir adsorption isotherm. Predictions of the model are compared with experimental measurements of adsorbate effluent concentration, current, and potential distribution.

Abstract No. 12

Microporous Flow-Through Electrodes

S. M. Mohnot* and **E. L. Cussler,** Dept. of Chemical Engineering and Materials Science, University of Minnesota, Minneapolis, MN 55455

Thin microporous flow-through electrodes are made from uniform micron-sized nickel and platinum powders. Slow sweep rate current-polarization curves obtained for the ferrocyanide/ferricyanide system show an enhancement of the radial mass transfer coefficient of many orders of magnitude. This demonstrates how the rate-controlling step can be changed from radial mass transfer to electron transfer reaction.

Abstract No. 13

Electrochemical Reactor with Flow Through Electrodes for Wastewater Cleanup

J. L. Weininger and **B. M. Kim,** General Electric Co., Corporate Research and Development, Schenectady, NY 12301

Electrolytic deposition of copper and nickel from dilute solutions is described. An electrochemical reactor has been constructed which has flow-through electrodes with large surface area. For the removal of metallic waste from industrial effluent, the reactor was tested in a flow system in which 99% copper was removed from a plating solution in 1 hr at 89% current efficiency. Reactor design factors are discussed with regard to critical mass transfer and electrochemical parameters, and a brief economic evaluation is also given.

Abstract No. 14

Thermomechanical Behavior of Simulated Electrodes for Li-Al/FeS Battery Cells

G. Bandyopadhyay* and **J. E. Battles,** Argonne National Laboratory, Argonne, IL 60439

Particle rearrangement, densification, and deformation of cold-pressed compacts of simulated negative and positive electrode compositions representing various charge conditions were examined in the presence of molten LiCl-KCl eutectic and external load. The results indicate that the sintering characteristics, deformation behavior, and microstructural development of both electrodes are strongly dependent on the electrode composition (*i.e.*, the state of charge), the amount of electrolyte, and the stresses present. These observations are significant in relation to understanding the in-cell microstructural development and swelling of the electrodes.

CORROSION

General Session

Abstract No. 15

Microcalorimetry as a Tool for Assessing Corrosion and Parasitic Reactions

M. A. Norenberg, M. A. Pehl,* G. M. Phillips, and **D. F. Untereker,** Energy Technology/Medtronic, Brooklyn Center, MN 55430

Microcalorimetry has been demonstrated to be an effective tool for estimating the rate of chemical reactions such as self-discharge in battery systems (1-4). We have extended this technique to assessing the rates of other types of reactions, such as corrosion, which are often difficult to observe except over extended periods of time. We used this technique to estimate the rate of corrosion of a variety of materials including stainless steel, Ni, Ta, and other metals by a mixture of iodine and poly(2-vinylpyridine). The technique is sensitive enough to detect corrosion rates on the order of 0.001 cm/yr on samples with a surface area of 1-2 cm^2. Several other examples using this technique will also be discussed.

1. E. J. Prosen and J. C. Colbert, "Microcalorimetry Study of Cardiac Pacemakers and Batteries," NBS1R 77-1310.
2. W. Greatbatch, R. McLean, W. Holmes, and C. Holmes, "IEEE Transport Biomedical Engineering," Vol. BME-26, No. 5, 1979.
3. L. D. Hansen and R. M. Hart, *J. Electrochem. Soc.*, **125,** 842 (1978).
4. D. F. Untereker, *ibid.*, **125,** 1907 (1978).

Abstract No. 16

Mössbauer Spectroscopic Study of the Chemical State of Cobalt in an Electrodeposited Zinc-Cobalt Alloy

H. Leidheiser, Jr.* and **A. Vértes,** Center for Surface and Coatings Research, Lehigh University, Bethlehem, PA 18015, and **M. L. Varsanyi,** Lorand Eötvös University, Budapest, Hungary

An electrogalvanized steel containing small amounts of cobalt and chromium is of interest because of its claimed corrosion resistance under service conditions. Electrodeposited zinc-cobalt alloys containing 0.01-2% cobalt represent supersaturated solutions of cobalt in zinc. Cobalt probably functions as a corrosion inhibitor because of its influence on the properties of the surface oxide film which it enters during active corrosion.

Abstract No. 17

A Finite Element Method of Calculating Current Distributions in Galvanic Corrosion

J. W. Fu, Westinghouse Research and Development Center, Pittsburgh, PA 15235

Recent advances in numerical analysis of galvanic corrosion processes have demonstrated that accurate current and potential distributions of galvanic couples can be obtained using a finite element numerical analysis. In this method, the corrosive environment is modeled as an assembly of elements called an element mesh and the metal surfaces are modeled as the surface of those elements at the boundary of the element mesh. The method and the current distribution analysis of a galvanic couple under thin condensed film are given in this paper.

Abstract No. 18

Investigations of Corrosion Layers on Mild Steel with a Direct Imaging Mass Spectrometer

A. Pebler, Westinghouse Research & Development Center, Pittsburgh, PA 15235

The growth of magnetite (Fe_3O_4) on mild (carbon) steel surfaces immersed in high temperature water is of considerable practical importance to the electrical power industry because of the extensive use of mild steel in commercial boiler applications. A direct imaging mass analyzer has been used for the identification and distribution of corrodants and corrosion products in the crevice corrosion of mild steel in aqueous acid chloride environments. The identification and distribution of borate deposits has led to a plausible explanation for the inhibiting effect of boric acid on acid chloride corrosion of mild steel.

Abstract No. 19

Flow Effects during Repassivation of Iron and Cobalt

R. C. Alkire* and **K. R. Weisbrod,** Materials Research Laboratory and Dept. of Chemical Engineering, University of Illinois, Urbana, IL 61801

The mechanism by which iron and cobalt reform protective passive layers in the presence of fluid flow was studied in neutral and acidic aqueous solutions at ambient temperature. Experiments consisted of observing electrical transients following galvanostatic or potentiostatic step-changes from an initial state where there was no protective film. A flow channel permitted studies up to Re = 60,000. A mathematical model was developed based on the hypothesis that a metal salt film is a necessary precursor to passivation. The model agreed with experimental data under conditions when repassivation occurred slowly.

Abstract No. 20

Study on Flow-Through Packed Iron Anode

Y.-X. Zhang and **Z.-B. Hu,** Dept. of Chemistry, Beijing Shi Fan University, Beijing 100009, China

The behavior of flow-through packed iron anode has been studied. Anodic dissolution of iron particles in the packed electrode together with oxidation by hexavalent chromium electrolyte were investigated. The distributions of overpotential have been determined and the amount of iron dissolved and chromium (VI) reduced at various regions within the electrodes were also measured. A one-dimensional model for flow-through electrode operating far from the equilibrium has been assumed. The manner of distributions of currents, potentials as well as concentrations throughout the packed bed electrodes can be described mathematically by means of semi-empirical equations. Satisfactory agreements between calculations and experimental data all over the reactor performance have been obtained with an average error of a few percent. As the reactor is of high efficiency in the treatment of hexavalent chromium pollution, this study can be utilized in the treatment of industrial waste water for plants of moderate scales.

Abstract No. 21

Passivation Mechanism of Iron in Concentrated Caustic Solution at Room Temperature

A. K. Agrawal* and **R. B. Diegle,** Battelle, Columbus Laboratories, Columbus, OH 43201

Passivation kinetics of iron in 12M NaOH solution at ~25°C have been studied over a wide potential range by using a scratch technique. The current transients following the scratching of potentiostated specimens were monitored on a digital transient recorder. The current decay, after the initial peak, followed a semilogarithmic relationship with time, *i.e.*, $I = I_0 \exp(-t/\tau)$. The slope $(-1/\tau)$ of the transients in the potential range −1.15 to −0.3V SCE was ~0.43. The results indicate that a dissolution-precipitation model for passivation is applicable to this system, and iron dissolution is the rate-determining step.

Abstract No. 22

Anodic Dissolution of Aluminum in Alkaline Solutions

K. C. Tsai and **J. L. Morris,*** The Continental Group, Inc., Energy Systems Laboratory, Cupertino, CA 95014

Anodic dissolution of Al and its alloys in strongly alkaline solutions was studied via RDE technique. A typical polarization curve comprising active and passive polarization regions resembles corrosion characteristics of many metals in aqueous electrolytes. It was further observed that (*i*) the addition of minor constituents to Al substantially increases critical current density, i_{crit}, (*ii*) the *i-E* characteristics of an Al alloy anode are fairly insensitive to increasing $Al(OH)_4^-$ concentrations, and (*iii*) the magnitude of i_{crit} and the *i-E* characteristics were almost invariant toward rotating speed suggesting that the anodic dissolution of Al in alkaline solution is limited by either kinetics of $Al(OH)_3$ formation or the rate of $Al(OH)_4^-$ complex formation. An attempt to ascertain the mechanism of anodic dissolution of Al in alkaline solutions is presented.

Abstract No. 23

Adsorbed Polymers Effect on Salt Water Corrosion

M. R. Van De Mark* and **J. W. Truesdell,** Dept. of Chemistry, University of Miami, Coral Gables, FL 33124

The effect of adsorbed polymers from dilute solution in tetrahydrofuran on the corrosion rate of low carbon (0.08%) cold rolled steel in an ocean environment was investigated. The study included condensation polymers of thiodiglycolic or 3,3′-thiodipropionic acid chlorides with 1,2-ethanedithiol, 1,3-propanedithiol, or dimercaptothiadiazole (DMTD). The corrosion rates are compared to uncoated and noncoordinating adsorbed polymers such as polyvinyl chloride.

Abstract No. 24

Anodic Corrosion and Passivation Behavior of Metals in Molten LiCl-KCl Containing Oxide Ions

X. K. Feng,* Tianjin Institute of Power Sources, Tianjin, China and **C. A. Melendres,** Argonne National Laboratory, Argonne, IL 60439

The anodic polarization of some selected metals (*e.g.*, Fe, Co, Ni, etc.) had been studied in molten LiCl-KCl eutectic containing lithium oxide at 375° and 450°C. Current-potential curves obtained show characteristic corrosion-passivation behavior similar to that found in aqueous systems. Anodic corrosion rates are compared with the metals in pure LiCl-KCl electrolyte. Reversibility in the reduction of the oxide films formed was examined by cyclic voltammetry. Other electrochemical kinetic measurements on typical systems were undertaken and results are presented.

Abstract No. 25

Tarnishing of Silver by Organic Sulfur Vapors: Rates and Film Characteristics

J. D. Sinclair, Bell Laboratories, Holmdel, NJ 07733

The rate of formation of sulfide films on silver coupons by atmospheres generated with organic sulfur vapors, especially dimethyldisulfide, has been measured at room temperature. The rate increases with sulfur chain length and is light dependent, decreasing in the order intense u.v. > fluorescent > dark. A mechanism involving formation of free sulfur is proposed. Sulfide morphology tends to be more like field grown films than the highly structured films generated by sulfur flowers vapor.

Abstract No. 26

Oxidation Behavior of 20/25/Nb Stainless Steel Containing Dispersed Phases

O. T. Goncel, Cukurova University, Adana, Turkey

20/25/Nb Stainless steel has been internally nitrided in an atmosphere containing 0.1 and 0.95 atm. nitrogen. The alloys which were prenitrided in a higher nitrogen potential later denitrided to remove retained nitrogen. Internal oxidation pretreatment were carried out in a "Rhines pack." Isothermal and cyclic oxidation tests were carried out at 1000° and 1100°C. The results obtained are discussed in detail.

Abstract No. 27

Oxidation Behavior of Fe-Cr Alloys after Coating by Inorganic Salts

O. T. Goncel, Cukurova University, Adana, Turkey

The high temperature oxidation behavior of Fe-Cr base alloys after coating with zirconium nitrate and cerium nitrate has been studied under thermal cycling and isothermal conditions at 1100°C. The coating has been carried out under various conditions. However the best oxidation results are obtained when the hot sample has been immersed into the molten salt and taken out while it is hot. It should be noted that the sample has to be dried out in the furnace to let the gases out. If this is not done, blistering of the oxide layer occurs. The oxidation resistance of the coated alloys is quite superior to that of the uncoated alloys, but not as outstanding as observed in the alumina-coated alloys.

CORROSION/DIELECTRICS AND INSULATION

Anodic Oxidation

Abstract No. 28

Ionic Pickup during Anodic Oxidation

J. S. Llewelyn Leach, C. Panagopoulos, and **B. R. Pearson,** Dept. of Metallurgy and Materials Science, University of Nottingham, University Park, Nottingham NG7 2RD, England

Ions other than oxygen and metal are incorporated into anodic oxides from surface contamination of the substrate metal and from the electrolyte. The amount of incorporation from the electrolyte is a function of the current density for growth and the pH of the electrolyte at the electrode surface. Incorporated ions cause changes in the field for growth, the oxide crystallinity, and the oxide stresses. The theory of surface pH change is outlined and experimental results for the influence of pH and current density on the pickup of ions from the electrolyte are given. Some examples of effects of incorporated ions on the oxidation process and on the properties of the oxide are also presented.

Abstract No. 29

Distribution of Anions in Oxide Films Anodically Formed on Aluminum in a Neutral Phosphate Solution

H. Takahashi, H. Konno, K. Fujimoto, and **M. Nagayama,*** Analytical Chemistry Laboratory, Faculty of Engineering, Hokkaido University, Sapporo 060, Japan

Oxide films were formed on Al by anodizing in a neutral phosphate solution, and the concentration profiles of PO_4^{3-} and OH^- ions were examined as functions of anodizing time and C.D., using a chemical sectioning technique combined with XPS, capacitance measurement, and solution analysis. It was found that both ions are included in the outer part, OH^- ions are missing in the middle part, and the inner part consists of pure Al_2O_3.

Abstract No. 30

Anodic Film Formation on Aluminum in Neutral Solutions

G. E. Thompson,* K. Shimizu, and **G. C. Wood,** University of Manchester Institute of Science and Technology, Manchester, England M16 1QD

Direct transmission electron microscopy of stripped films and ultramicrotomed sections has been employed in order to gain further insight into the general and local anodizing behavior of aluminum and selected alloys in borate and phosphate solutions. Crystallization experiments and STEM/EDAX analysis allow rapid assessment of apparent transport numbers. Observations of films formed on the alloys, possessing different flaw-types and population densities, show clearly the results of local processes occurring at flaws and their relationship with the general film composition.

Abstract No. 31

A-C Anodizing Processes of Aluminum Alloys

J. Zahavi,* IBM Corp., Poughkeepsie, NY 12602, **H. Kerbel** and **O. Korotkina,** Technion Israel Institute of Technology, Haifa, Israel, and **M. Metzger,** University of Illinois, Urbana, IL 61801

Studies have been made of a-c anodizing processes of aluminum alloys in order to examine, characterize, and gain better understanding of the main factors associated with and affecting film growth and properties. Films were formed at constant a-c voltages in sulfuric acid, oxalic acid, and a mixture of these electrolytes. Kinetic film growth was studied by recording current-time curves under various anodizing conditions. Film topography, structure, and composition were characterized through direct transmission, replica and scanning microscopy, and electron probe microanalyzer. Film thickness increased with increases in anodizing time, electrolyte concentration and temperature, and anodizing voltage. Micrographs of film surface and cross section showed the porous structure together with dispersed intermetallic compounds. Further results and possible explanation are discussed.

Abstract No. 32

The Difference Between Barrier and Porous Anodic Oxides on Aluminum

J. P. S. Pringle, Atomic Energy of Canada Limited Research Company, Chalk River, Ont., Canada K0J 1J0

Barrier oxides have been used as electrolytic capacitors since about 1900, and porous oxides as corrosion-resistant coatings since about 1923. No adequate explanation for the difference between the two types of anodic oxides has, however, ever been presented. It is shown here that the difference arises naturally from four properties of anodic aluminum oxide: its anodizing kinetics, its amorphous structure, the migration of the aluminum and oxygen atoms, and the Pilling Bedworth ratio.

Abstract No. 33

Study of Patterns of Breakdown Processes in Anodic Oxide Films Formed on Aluminum in Sulfuric Acid

J. Zahavi (Permanent address: Israel Institute of Metals, Technion, Haifa, Israel) and **M. Metzger,*** Dept. of Metallurgy and Mining Engineering, University of Illinois at Urbana-Champaign, Urbana, IL 61801

Previous electron microscopic studies of transient pitting by the authors were extended to examine nucleation and spreading of breakdown-pitting-repair processes in the early stages of anodizing and their relation to substrate orientation. Streaks of very small events parallel to the substrate slip planes were followed by larger events nucleated on the streaks and often exhibiting preferred growth in cube directions. Models for the propagation of breakdown and the resulting distribution of events are presented. Substrate grain boundaries were associated with preferential transient pit growth, not breakdown. The processes occurring appeared to be similar in the presence of small amounts of chloride.

Abstract No. 34

The Phenomenology of the Electrical Breakdown during Anodizing of Aluminum in Borate Solutions

K. Shimizu,* G. E. Thompson, and **G. C. Wood,** University of Manchester Institute of Science and Technology, Manchester, England M16 1QD

High resolution scanning and transmission electron microscopy of the anodic film and stripped films and ultramicrotomed sections have been employed to gain further insight into the mechanisms of the electrical breakdown during anodizing of aluminum in borate solution. Attention has been focused on the following fundamental parameters: (*i*) the sites at which breakdown initiate, (*ii*) the development of breakdown, and (*iii*) the structure of the films after breakdown. The observations indicate the breakdown is possibly of thermal nature and triggered by local heating effects caused by highly localized conduction at flaws.

Abstract No. 35

Voids in Anodic Aluminum Oxide Films

R. S. Alwitt* and **C. K. Dyer** (Present address: Bell Laboratories, Murray Hill, NJ 07974), United Chemi-Con, Inc., Northbrook, IL 60062, and **B. Noble,** Dept. of Metallurgy and Materials Science, University of Nottingham, Nottingham NG7 2RD, England

Al_2O_3 films were examined by transmission electron microscopy using defocus contrast. Voids were observed in both amorphous and crystalline anodic Al_2O_3 films. Discrete voids are 2-4 nm in diameter and are present at densities in the range of $10^{11} \sim 10^{12}cm^{-2}$. Strings of connected voids were seen in crystalline oxide, and these may be the cross section of cracks that are thought responsible for the electrical instability of these films. There were no voids in several anodic Ta_2O_5 films that were examined.

Abstract No. 36

Wear Properties of Thin to Thick Anodic Oxide Films on Aluminum

H. Leidheiser, Jr.,* S.-M. Chou, W. Bilder, and **M. C. Hughes,** Center for Surface and Coatings Research, Lehigh University, Bethlehem, PA 18015

A previously developed method has been applied to the study of the wear of anodized aluminum and of polymer-coated anodized aluminum. The rate of wear was determined on anodized aluminum prepared under different conditions. Interference fringe techniques and optical absorption were utilized as methods for determining the thickness of the anodic coating and the polymer coating as a function of wear. The results have significance to the wear of lithographic plates.

Abstract No. 37

Initial Oxide Growth Rate on Newly Generated Surfaces of Aluminum and Zirconium

T. R. Beck, Electrochemical Technology Corp., Seattle, WA 98107

New surfaces of aluminum and of zirconium were generated in solution by a fast fracture method previously used by the author for titanium. Transient anodic current was measured under potentiostatic conditions in sulfate and chloride solutions. Current decayed rapidly with time due to oxide film growth. The linear region of the $\log i$ *vs.* $\log \tau$ plots from 0.1 to 100 s are in good agreement with predictions of transient current from an integrated form of the high field conduction equation and published data for aluminum and zirconium obtained by other methods.

Abstract No. 38

Dissolution Behavior of the Barrier Layer of Porous Anodic Films on Aluminum

S. Ono* and **T. Sato,** Dept. of Industrial Metallurgy, Shibaura Institute of Technology, 3-9-14 Shibaura, Minato-ku, Tokyo, Japan

The structural change of the barrier layer with chemical dissolution has been studied using the "pore-filling" technique and electron microscopy. Micropores in the barrier layer of porous films formed in phosphoric acid solution are clearly confirmed after the 2/3rd thinning of the layer. The nature of the defects is affected significantly by the forming voltage.

Abstract No. 39

A Theory of Electron Transfer Reactions at Oxide Electrodes Involving Adsorbate States

W. Schmickler, Institut für Physikalische Chemie II, Universitäts-Düsseldorf, 4000 Düsseldorf, Germany

A general theory is presented for electron transfer reactions via an intermediate state, in which all three states are strongly coupled to the solvent. The theory is applied to redox reactions at oxide electrodes; it is shown that adsorbates on the oxide surface can catalyze the reaction by providing intermediate states with a suitable energy. An explicit expression for the corresponding current is derived. Recent experimental findings are discussed in terms of this theory.

Abstract No. 40

A Comparative Analysis of the Kinetics of Growth of Thin Anodic Films at Pt and Ni Electrodes

A. Damjanovic,* J. F. Wolf, and **L.S-R. Yeh,** Allied Chemical Corp., Corporate Research & Development, Morristown, NJ 07960

Kinetics of growth of thin anodic oxide films at Pt in acid and alkaline and at Ni in alkaline solutions of different *p*H's and temperatures are analyzed and compared. The kinetics at both electrodes follows the high field-assisted formation of oxide films. Comparison of the activation energies and the exchange current densities lead to the conclusion that the rate-determining steps, both at Ni and at Pt electrode, must be located at the oxide film/solution interface and therefore the field at that interface controls the rate of growth. This interpretation, however, poses a difficulty as it requires a particular charge distribution at the complex metal-solution interfaces. Potentials at which anodic films begin to grow and their *p*H dependences are discussed.

Abstract No. 41

Kinetics of Transitional Growth in Sub-Monolayer to Multilayer Oxide Film Formation at Au

H. Angerstein-Kozlowska,* B. Barnett, and **B. E. Conway,** Chemistry Dept., University of Ottawa, Ottawa, Ont., Canada K1N 9B4

The transition from sub-monolayer, through monolayer to multilayer anodic oxide film growth at Au was studied as a function of time ($10^{-4} \leq t < 100$ sec) and potential, V, with particular reference to the states of surface oxide that can be distinguished in the course of development of the monolayer to various coverages, θ. Integrated θ *vs.* $\log t$ data reveal that oxide growth takes place in several distinguishable stages. Electrochemically controlled growth can be distinguished at low V and t and is represented by linear $\log (1-\theta)$ *vs.* t. Slower growth in two stages is observed at larger V and t, and proceeds with linear θ *vs.* $\log t$ kinetics exhibiting clearly distinguishable slopes for the two stages. For each of the stages, the transfer coefficients for the kinetics are evaluated together with the g parameters characterizing lateral interactions in the distinguishable states of the oxide film as it grows. The growth process appears to be continuous in nature from sub-monolayer, through monolayer to multilayer oxide film formation. Models are considered for the quasi-chemical step that is required to account for the growth and aging effects observed, and the observed hysteresis between oxide formation and reduction.

Abstract No. 42

Kinetics of Distinguishable Stages in Oxide Film Reduction at Au

B. Barnett,* H. Angerstein-Kozlowska, and **B. E. Conway,** Chemistry Dept., University of Ottawa, Ottawa, Ont., Canada K1N 9B4

The kinetics of reduction of the several distinguishable states of surface oxide that are developed in controlled monolayer oxide formation at Au, are evaluated using several techniques. Partial reduction of an anodically characterized oxide film is made in a cathodic sweep to some controlled but variable potential, V_r. The kinetics of continuing reduction at V_r are measured as a function of time and V_r, *i.e.*, for various initial coverages, θ_i. The results of these experiments reveal that the reduction proceeds, surprisingly, by an irreversible, electrochemically controlled process for which $\log \theta_i$ is linearly dependent on reduction time, t. Transfer coefficients for the distinguishable surface processes are evaluated from peak potential *vs.* $\log$ [sweep rate, s] information derived from linear potential-sweep experiments. The reduction processes are too irreversible for the reversibility parameter, s_n, to be evaluated. Mechanistic examination of the results indicates that a quasi-chemical step, such as reverse place-exchange of O/Au, does not control the reduction kinetics nor does reduction involve hole growth following nucleation of holes. The oxide reduction behavior is related to the growth processes treated in our previous paper at this Symposium.

Abstract No. 43

Kinetics and Mechanisms of O_2 Evolution at Pt Electrodes Covered by Thin Anodic Oxide Films

A. Damjanovic, Allied Chemical Corp., Corporate Research & Development, Morristown, NJ 07960

Kinetics of O_2 evolution at Pt electrodes is examined in H_2SO_4 and $HClO_4$ solutions with *p*H's ranging from 0.1 to 3.2 with and without a supporting electrolyte. Fractional reac-

tion order with respect to H_3O^+ is now confirmed. It cannot be accounted for in terms of any simple electrode kinetics criteria. This pH dependence, as well as a strong isotope effect observed in D_2O solutions, are discussed and related to possible mechanisms of O_2 evolution at electrodes covered by thin, insulating anodic oxide films of varying thicknesses which make the structure of the metal/insulator/solution interface complex.

Abstract No. 44

Oxygen Evolution and Passivation Behavior of Cu_xTi_{1-x} Alloys

G. G. Scherer,* K. Müller, and **S. Stucki,** BBC Research Center, CH-5405 Baden, Switzerland

Oxygen evolution and passivation behavior of Cu_xTi_{1-x} electrodes have been investigated. Three different types of alloys in the range x = 0.1-0.8 have been prepared: arc melted alloys, amorphous alloys, and alloys made by electrolytical copper deposition onto porous titanium sheets and subsequent heat-treatment. A strong enhancement of the oxygen evolution with rising copper concentration is observed. Low copper concentration alloys ($x \leq 0.2$) tend to passivate. No passivation occurs with alloys $x \geq 0.4$ due to the corrosion of the alloy.

Abstract No. 45

Optical Studies of the Anodic Passivation of Tin

S. D. Kapusta, Dept. of Chemistry, Rice University, Houston, TX 77001

Relative reflectivity changes due to the formation and removal of the passivating film on tin in 0.2M borate buffer were measured at different angles of polarization of the reflected light. The optical constants of the substrate and the film and the thickness of the latter were obtained over a wide range of potentials and wavelengths. The results are compared with those obtained from electrochemical and photoelectrochemical measurements, and good correlation found.

Abstract No. 46

Mechanism of Growth of Thick Anodic Oxide Films on Nickel

B. MacDougall, National Research Council of Canada, Div. of Chemistry, Ottawa, Ont., Canada K1A 0R9

The anodic oxidation of nickel in pH 7.65 borate buffer solution has been studied by a combination of electrochemical and surface-analytical techniques. A compact film of NiO is formed in the passive potential range while a thick finely porous film of NiOOH is generated in the oxygen evolution region. The kinetics of porous film growth have been determined and it appears that the stability of the underlying passive film is the main factor controlling the growth rate of the porous film. A detailed mechanism is suggested to explain porous film formation.

Abstract No. 47

Structure of Hydrous Electrochromic Oxide Films as Deduced from Potential-pH Response

L. D. Burke, M. E. G. Lyons, E. J. M. O'Sullivan, and **D. P. Whelan,** Dept. of Chemistry, University College, Cork, Ireland

Electrochemically produced hydrous oxides on transition metals such as gold and iridium show unusual pH responses which may be interpreted by assuming (*i*) an open polymeric structure for the oxide and (*ii*) complex formation between metal ions in the film and hydroxide species from solution. Structures for these hydrous films, deduced on the basis of pH effects, provide an interesting contrast with those of compact films produced either by potentiostatic techniques or thermal decomposition of chlorides.

Abstract No. 48

Electrochemical Properties of Iridium Oxide Films in a Buffered Electrolyte

M. L. Gopikanth, J. Crossen, and **E. Luksha,** Cardiac Pacemakers, Inc., St. Paul, MN 55164

Iridium oxide electrode has drawn attention in varied application areas from electrochromic devices to a stable electrode. The behavior of these electrodes prepared under different conditions do have different electrochemical properties. This paper deals with the behavior of the iridium oxide electrodes prepared by two methods, viz., electrochemical and air-oxidation, toward electrochemical kinetics. An attempt has been made to explain the electrochemical behavior, like linear, Tafel and potentiodynamic polarizations for the above electrodes.

Abstract No. 49

Kinetics of the Anodic Oxidation of Precipitated Nickel Hydroxide

R. E. Carbonio, V. A. Macagno, and **M. C. Giordano,** Departamento de Fisicoquímica, Facultad de Ciencias Quimicas, Universidad Nacional de Córdoba, Córdoba, Argentina and **J. R. Vilche** and **A. J. Arvia,** Instituto de Investigaciones Fisicoquímicas Teóricas y Aplicadas (INIFTA) Casilla de Correo 16, Sucursal 4, La Plata, Argentina

The electrochemical behavior of colloidal nickel hydroxide formed on various conducting materials (Pt, Au, and vitreous-C) is studied in aqueous alkaline solutions. Under a systematic choice of the potential perturbation conditions a change of the rate-controlling step in the reaction $Ni(OH)_2 = NiOOH + H^+ + e$ can be evaluated. This change in the kinetic overall reaction depends on the film thickness and the electrolyte concentration. The stability and electrochemical properties of the film are also discussed.

Abstract No. 50

Electrostriction in Anodic Oxides

J. L. Ord, Dept. of Physics, University of Waterloo, Waterloo, Ontario, Canada N2L 3G1

The 0.1% to 1.0% increase in film thickness observed when the anodizing field is applied to most valve-metal oxides has several important implications for the theory of electrostriction, the dielectric properties of the oxides, and the anodic oxidation process. The ellipsometric and dielectric constant measurements on which the observations are based are looked at in detail, as in the type of theory required to account for the unexpected sign and magnitude of the field-induced strain.

Abstract No. 51

Optical and Dielectric Properties of Anodic Ta_2O_5

D. J. Smith and **L. Young,** Dept. of Electrical Engineering, University of British Columbia, Vancouver, B.C., Canada V6T 1W5

Single crystal tantalum was anodized at constant current, and the oxide film thickness was measured by *in situ* ellipsometry. The ellipsometer data show the effect of surface roughness on the apparent refractive index of the substrate. The film thicknesses are compared with the values obtained by a spectrophotometric method and calculated from equations fitted to published steady-state data. The small signal a-c capacitance of the oxide film, measured *in situ* at 1 kHz, was also investigated.

Abstract No. 52

Optical Properties and Poole Frenkel Conduction in Anodic Films of Sputtered Tantalum and Tantalum Nitride

C. J. Miner,* R. W. Streater, B. K. MacLaurin, and **W. Westwood,** Bell-Northern Research, Ottawa, Ont., Canada K1Y 4H7

Conduction in anodic tantalum oxide and oxynitride is strongly dependent on the nitrogen doping level. The insulator thickness and optical dielectric constant ϵ, obtained by reflectance spectrophotometry and ellipsometry are used to explain this phenomenon in terms of the Poole Frenkel conduction equation $J = \kappa \exp \beta V^{1/2}$. Variations with increasing nitrogen doping in ϵ from 3.61 to 2.99 and in the calculated oxide growth field, F, from 5.34 to 6.81 $\times 10^6$ V/cm account for the range of β observed.

Abstract No. 53

Investigation of High Field Induced Oxygen Movements in Thin Solid Electrolyte Films of Calcia Stabilized Zirconia (CSZ)

J. Perriere and **J. Siejka,*** Groupe de Physique des Solides de l'E.N.S., 75221 Paris Cedex 05, France and **M. Croset,** L.C.R. Thomson-C.S.F., Domaine de Corbeville, 91401 Orsay, France

As we have shown previously it is possible to anodize metals and GaAs in aqueous electrolytes or oxygen plasma through thin (<300 nm) deposited films of CSZ. Analysis of oxide growth kinetics in aqueous electrolytes on GaAs/CSZ and Metal/CSZ samples evidences an initial potential drop V in the CSZ layer which is independent of the nature of the substrate being oxidized. V depends linearly on the CSZ thickness d and increases with the current density J. The electric field $E(E = V/d)$ is much lower than that deduced from Verwey-Mott relationship: $J = D/a\ C(x) \sinh qa\ E/kT$. Moreover the relation $J = f(E)$ is similar to that found during anodization of pure zirconium. Oxygen 18 tracing experiments show that oxygen movements take place through easy paths although the concentration of oxygen vacancy in the CSZ films is of the order of 8 a/o. These results strongly suggest that the ionic oxygen current is not carried out by oxygen vacancies.

Abstract No. 54

Anodization of Superimposed Metallic Layers: Effects of Different Movement Probabilities and Ionic Conductivities

J. Perriere* and **J. Siejka,** Groupe de Physique des Solides de l'Ecole Normale Supérieure, 75221 Paris Cedex 05 France

We have found previously that the anodization of superimposed metallic films leads either to the conservation of the order of metal and oxygen atoms or to a partial inversion of the order for the two species. Two distinct phenomena are responsible for the inversion of order: differences in ionic conductivities and differences in movement probabilities. We have evidenced separately their effects. When both phenomena contribute, two possible approaches exist in order to describe the results: (*i*) a liquid type model in which ions move like in an electrolyte with equal probabilities to take part in transport events, but moving different distances; and (*ii*) a locally perturbed solid model in which the different cations have different probabilities to take part in transport events which depend on the oxide and on the cationic concentration. Consequences on transport numbers, nature of the transport events, and lateral uniformity of the oxides are examined and discussed.

Abstract No. 55

Mechanism of the Anodic Oxidation of Zirconium

C. Ortega* and **J. Siejka,** Groupe de Physique des Solides de l'Ecole Normale Supérieure, 75221 Paris Cedex 05, France

We have found that during anodic oxide growth on zirconium in aqueous solutions, the oxygen migrates through easy paths. The density of easy paths near the oxide surface is higher at $pH = 6$ than at $pH = 13$, increases with the formation current at $pH = 6$, but is independent of the formation current at $pH = 13$. The lateral distribution of the easy paths changes continuously during the growth. All these results are well explained if one assumes that the OH^- ions are injected into interstitial sites from oxide surface groups, inducing in the oxide extended defects which favor further oxygen injection and movement. An easy path is hence an extended defect which connects the two interfaces.

Abstract No. 56

Kinetics of High Field Ionic Conduction in Anodic Tantalum Pentoxide Films

D. J. Smith and **L. Young,** Dept. of Electrical Engineering, University of British Columbia, Vancouver, B.C., Canada V6T 1W5

The ionic conduction process was investigated under steady-state, stepped-current, and open-circuit discharge conditions using computerized data acquisition. The results were compared with previous data and tested for consistency with models.

Abstract No. 57

Kinetic Parameters for Growth of Barrier-Type Anodic Oxide on Valve Metals from Galvanostatic Anodization

I. A. Ammar,* **S. Darwish,** and **M. W. Khalil,** Dept. of Chemistry, Faculty of Science, Cairo University, Giza, Egypt

Galvanostatic charging curves have been used to calculate kinetic parameters such as oxide formation rate, reciprocal capacity, electric field, constants of exponential law, effective activation distance, etc. for a number of metals with varying valve-metal behavior including Ta, Nb, Zr, Ti, Al, W, Bi, Sb, Te. With all recent developments in the field, the simple theory of galvanostatic anodization is still the best medium for interpretation and prediction of the behavior during industrial anodization.

Abstract No. 58

Electroluminescence during the Anodic Growth of Tantalum Pentoxide

V. Kadary (Present address: Israel Aircraft Industries, Yahud, Israel) and **N. Klein,** Dept. of Electrical Engineering, Technion, Israel Institute of Technology, Haifa, Israel

Light emission during the anodic growth of tantalum pentoxide was found to grow quasi-exponentially with electric field and oxide thickness. Data on the spectrum were obtained with six narrow band-pass filters. Largest light output was found for 4.8 eV photons. This light component was strongly absorbed in the oxide, since its bandgap is 4.6 eV. The light emission was interpreted as an electroluminescent (EL) effect due to electron avalanching and to recombination of hot electrons with trapped holes for most of the light components. The not absorbed light components could in part be due also to first-order kinetics EL processes. Relations derived for the EL output fitted experimental results well giving $\alpha = 1.12 \times 10^5$/cm for the coefficient of impact ionization at a field of 6.26 MV/cm. Earlier breakdown investigations resulted in $\alpha = 1.4 \times 10^5 \pm 10$ %/cm. The difference in α values can be due to approximations made in deriving relations for the two phenomena. Since both breakdown and EL theories were developed with the same avalanche model, independent evidence was obtained on impact ionization in tantalum pentoxide from two phenomena.

Abstract No. 59

A-C Ionic Conductivity of Thin Tantalum Pentoxide Films

A. H. M. Shousha, Dept. of Physics, United Arab Emirates University, Al Ain, United Arab Emirates

Growth kinetics and ionic conductivity of thin Ta_2O_5 films are investigated using a small a-c signal superimposed on the d-c polarizing voltage. Both resistive and capacitive current components are monitored during the film growth. The results indicate that the a-c ionic conductivity is proportional to the formation current density and decreases from its highest value at d-c measurements to its lowest value at transient measurements as the signal frequency increases. On switching off the d-c voltage, the film conductivity decreases nonlinearly with time, reaching a value independent of the formation current density. The results presented are discussed in terms of a model with distributed parameters.

Abstract No. 60

The Activation Energy for Ion Transport during Anode Film Growth on Nb and Ti

I. A. Ammar, S. Darwish,* and **M. W. Khalil,** Dept. of Chemistry, Faculty of Science, Cairo University, Giza, Egypt

The effect of temperature on galvanostatic anodic charging curves has been used to calculate the activation energy

and to estimate the effect of temperature on the width of energy barrier for ion transport in thin (Ti) and thick (Nb) films. Based on the simple exponential law, it is demonstrated here that the activation energy can be directly calculated from the effect of temperature on either of: the constant (A), the field, or the current density.

Abstract No. 61

Titanium Electrodes: Electronic Properties of Thin Passive Films

U. Stimming* and **J. W. Schultze,** Institut für Physikalische Chemie II der Universität Düsseldorf, D-4000 Düsseldorf, Germany

Anodic passive films of TiO_2 (d = 2-12 nm) were investigated concerning the charge distribution within the film, the kinetics of electron transfer reactions, the influence of doping on the electronic conductivity, and photoelectrochemical properties. With various data (donor concentration, flatband potential, dielectric constant, bandgap, absorption coefficient, etc.) obtained from these measurements, a bandstructure model of the passive film is derived which explains the electrochemical properties investigated with these electrodes.

Abstract No. 62

Investigation of Fixed Electric Charges Induced in Oxides during Anodization Processes

J. Siejka,* Groupe de Physique des Solides de l'E.N.S., 75221 Paris Cedex 05, France, **A. Morawski,** Institute of Physics, Polish Academy of Science, Warsaw, Poland, and **J. Lagowski** and **H. C. Gatos,** Dept. of Materials Science and Engineering, Massachusetts Institute of Technology, Cambridge, MA 02139

The density and polarity of fixed charges in GaAs and Al native oxides were measured using the Kelvin probe (contact potential difference). Negative surface charges as high as 10^{12} q./cm^2 were found on all anodic oxides independently of their thickness. At room temperature this charge can be screened out by adsorption of polar molecules which can be desorbed by thermal annealing at $T < \sim 70°C$. The annealing at higher temperatures ($T > \sim 70°C$) reduces the surface charges by more than one order of magnitude. The partial dissolution of oxides (~500Å thick surface layer) in basic or acid solutions has affected neither polarity nor density of this charge. This charge seems to be due to the homogeneous distribution of oriented dipoles in whole oxide. The possible implication of this finding on the mechanism of anodization is discussed.

Abstract No. 63

RHEED and X.P.S. Studies of the Passive Films Formed on 304 Stainless Steels

C. R. Clayton,* **K. G. K. Doss, Y-F. Wang,** and **J. Warren,** Dept. of Materials Science and Engineering, State University of New York at Stony Brook, Stony Brook, NY 11794

Preliminary studies have been carried out to investigate the structure and composition of the passive films formed on 304 stainless steel. Samples have been investigated after passivation for 1 hr at constant potential in deaerated 1N H_2SO_4 and after the same treatment followed by injection of NaCl solution into the acid to produce a solution of 2% NaCl. The nature of the structural and compositional changes observed in the passive film as a function of passivation potential and Cl^- ion content is discussed.

Abstract No. 64

Influence of B and P on Corrosion and Passivation Properties of Ni Films

V. Brusic, J. Aboaf, R. D. MacInnes, and **E. Alessandrini,** IBM T. J. Watson Research Center, Yorktown Heights, NY 10598

Influence of B and P on corrosion and anodic oxide film formation on Ni thin films in acid environment has been evaluated. The study relies on electrochemical techniques combined with *in situ* applied ellipsometry and *ex situ* utilized Auger/ESCA and reflection electron diffraction analyses. The results are discussed in terms of film composition, structure, and presence or absence of the crystalline state.

Abstract No. 65

Comparative Approach of the Corrosion and Passivation of Nickel and Iron in Aqueous Solutions

J. R. Vilche* and **A. J. Arvía,** Instituto de Investigaciones Fisicoquímicas Teóricas y Aplicadas (INIFTA), Casilla de Correo 16, Sucursal 4, La Plata, Argentina

The E/I response of both Ni and Fe electrodes in acid and neutral aqueous solutions under complex programmed potentiodynamic perturbations exhibit some common features which can be related to the formation of various hydroxide and oxohydroxide species within the potential range of water stability. The products of the anodic corrosion and passivation reactions formed in the different potential regions involve the formation of a mixture of species which present different chemical reactivities. The complex kinetics can be accounted for in terms of a reactions pattern including aging type processes of the species participating in the overall reactions.

Abstract No. 66

Corrosion and Oxidation of Silver and Silver/10% Palladium Electrodes under Physiological Conditions

B. J. Piersma* and **W. Greatbatch,** Dept. of Chemistry, Houghton College, Houghton, NY 14744

Silver and silver/10% palladium wires have been studied in 0.15M NaCl at 37°C using steady-state potentiostatic and cyclic voltammetric techniques. The steady-state behaviors of silver and silver-palladium alloy are similar, particularly in the anodic region, however, the cyclic voltammograms show distinct differences. The behavior of silver in NaCl solution is distinctly different from results observed in alkaline solutions. We have compared our results with those for a noble metal (Pt) and a valve metal (Ti).

Abstract No. 67

The Anodic Oxidation of Steel in Sodium Metasilicate Solutions

L. L. Gruss* and **E. Silvestre,** ARRADCOM, FC&SCWSL, Dover, NJ 07821

The anodic behavior of high carbon steel was investigated in 0.1N solutions of reagent grade sodium metasilicate with and without a surfactant (aerosol O/T) as a function of pH. Solution pH (reduction) was adjusted with CO_2 (dry ice). A current density of 2.4 A/cm^2 was employed in all reactions. The reaction cell was thermostated at 18.5° ± 0.5°C. An initial efficient anodization, as evidenced by the large slope in the chronopotentiogram was observed with solutions containing Aerosol O/T in the pH range of 9.0 to 11.5. The anodic products are hard and bear some resemblance to the slags which form on furnace refractories. The deposited coatings were identified as iron metal dispersed in silicate glass. The effect pH, anion, and surfactant have on the anodic process utilizing a variety of organic and inorganic acids for pH reductions are compared and discussed.

Abstract No. 68

An Assessment of the Processes Leading to Pit Nucleation on Iron

M. Janik-Czachor (Permanent address: Institute of Physical Chemistry, Polish Academy of Sciences, Warsaw, Poland), Dept. of Chemistry, Northwestern University, Evanston, IL 60201

The recent findings relating to the stages prior to and during pit initiation on iron in aggressive environments such as halides are reviewed. Electrochemical conditions for pit nucleation are discussed. Evidence is presented on the controversial issues regarding possible aggressive anion entry into the film and relating to passive film thinning and salt accumulation. Effect of surface defects is emphasized.

Abstract No. 69

A Critical Consideration of the Flade Potential

K. Jüttner and **W. J. Lorenz,*** Institut für Physikalische Chemie und Elektrochemie, Lehrstuhl III, Universität Karlsruhe, 7500 Karlsruhe 1, Germany

The importance of the Flade potential on the active-passive transition of metals is critically reconsidered. Measurements of the active-passive transition of iron show that this transition is represented by a continuous current density-potential curve having a negative Tafel slope in the so-called passive layer formation range. In this potential range, the nonporous passive film consisting of Fe_3O_4 and γ-Fe_2O_3 is formed by topochemical reactions including bi- and tri-valent iron oxide coverages. The Flade potential corresponds to the boundary between the passive layer formation range and the passive range.

Abstract No. 70

Anodic Oxidation of UO_2

S. Sunder, D. W. Shoesmith,* M. G. Bailey, and **N. S. McIntyre,** Atomic Energy of Canada Ltd., Whiteshell Nuclear Research Establishment, Pinawa, Manitoba, Canada R0E 1L0

The electrochemical oxidation of UO_2 in neutral sodium sulfate solutions has been studied by potentiostatic and cyclic voltammetric techniques. The surface oxide films formed have been identified by x-ray photoelectron spectroscopy. The surface oxidation progresses through a sequence of film formation reactions ($UO_2 \rightarrow UO_{2+x} \rightarrow U_3O_7 \rightarrow U_2O_5 \rightarrow U_3O_8$), dissolution as U^{VI} species occurring simultaneously. At high anodic potentials ($\geq$ + 0.4V *vs.* SCE) a film of UO_3 is formed by precipitation from a supersaturated U^{VI} solution. The relative importance of the film formation reactions varies with potential, time of oxidation, and pH.

Abstract No. 71

The Chemiconductor Model of the Passive Film on Iron

B. D. Cahan and **C. T. Chen,** Dept. of Chemistry, Case Laboratories for Electrochemical Studies, Case Western Reserve University, Cleveland, OH 44106

On the basis of the results from a wide range of experimental techniques such as ellipsometric spectroscopy, wide-frequency range impedance and electroreflectance studies, and pulse discharge techniques, a new model has been developed for the passive film on iron. This model is applicable from the Flade (or dissolution) potential to oxygen evolution. We show that the experimental results are incompatible with the semiconductor and the sandwich models. A chemiconductor is a material whose local stoichiometry can be varied semireversibly by the electrochemical environment, thereby changing its electronic properties from an insulator to a pseudo-semiconductor or an ionic and/or electronic conductor without significantly changing the basic form of the material.

Abstract No. 72

A Point Defect Model for the Growth and Breakdown of Anodic Oxide Films

C-Y. Chao, L.-F. Lin, and **D. D. Macdonald,*** Fontana Corrosion Center, Dept. of Metallurgical Engineering, The Ohio State University, Columbus, OH 43210

A point defect model for the growth of oxide films on metal surfaces is described. The essential mechanism of growth involves the movement of oxide vacancies from the metal/film interface to the film/solution interface, or equivalently due to movement of oxide ions in the reverse direction. The movement of cation vacancies (or cations) does not result in film growth but only in dissolution. However, the movement of cation vacancies from the film/solution interface to metal/film interface provides a rationale for the chemical breakdown of passive films.

Abstract No. 73

The Anodic Oxidation of Ni-Cr Alloys in Molten Sodium Sulfate

J. Truhan* and **T. Jeys,** Lawrence Livermore National Laboratory, Livermore, CA 94550

We studied anodic polarization of Ni-Cr binaries in molten Na_2SO_4 at 900°C. The corrosion potential shifted in the noble direction as the chromium content was increased but never attained an equilibrium value as a function of time in the environment. While pure nickel exhibits active-passive behavior, chromium additions cause both apparent spontaneous passivation at the corrosion potential and the passive current to decrease. Scale products are thin, coherent, and apparently all chromium oxide.

Abstract No. 74

Mechanism of Growth of Ferric Oxide Films by Anodic Oxidation of Fe^{2+} in Nearly Neutral Solutions

S. Ardizzone and **L. Formaro,*** Laboratory of Electrochemistry, The University, Milan, Italy

The electrochemical oxidation of Fe^{2+} ions on inert metal electrodes in neutral solutions occurs with the quantitative precipitation of a ferric (oxo)hydroxide film on the electrode surface. The reaction has been studied in the limiting current region as a function of solution parameters ($C_{Fe^{2+}}$, pH). The oxide layer behaves as a diffusion path of increasing thickness for Fe^{2+} transport from solution to the metal-oxide interface where the oxidation reaction occurs. The limiting current dependence on pH is determined by the oxide surface dissociation which increases with pH.

CORROSION/PHYSICAL ELECTROCHEMISTRY

Nonaqueous Electrolytes

Abstract No. 75

Selected Aspects of the Characterization of Organic Electrolytes

J. F. Coetzee, Dept. of Chemistry, University of Pittsburgh, Pittsburgh, PA 15260

The characterization of nonaqueous electrolytes is a broad and complex field which requires a variety of experimental and theoretical approaches. This paper deals with a few such approaches and also with typical experimental problems that must be overcome if meaningful data are to be obtained. One such problem which is discussed is the purification of the solvent and the determination of residual impurities. The rest of the paper deals with selected aspects of ion solvation and its influence on the thermodynamics and kinetics of ion reactivities, as well as on the transport properties of electrolytes.

Abstract No. 76

Chemical and Electrochemical Studies in a Room Temperature Ionic Liquid

R. A. Osteryoung,* R. J. Gale, J. Robinson, H. Linga, and **G. Cheek,** Dept. of Chemistry, State University of New York at Buffalo, Buffalo, NY 14214

A mixture of aluminum chloride and N-butylpyridinium chloride (BuPyCl) is an ionic liquid, technically a molten salt, with a liquidus temperature at about 30°C. The mole ratio of $AlCl_3$ to BuPyCl may be varied from about 0.6:1 to 2:1 with marked changes in the acid-base properties of the solvent. The dominant acid base equilibrium may be written as

$$2\,AlCl_4^- = Al_2Cl_7^- + Cl^-$$

A general overview of chemical and electrochemical studies in this nonaqueous solvent is presented, with emphasis on the electrochemistry of solutes showing marked acid-base dependent behavior. This system is perhaps the first of a large group of new ionic liquids whose acid-base properties are variable, which are nonaqueous, and excellent solvents for both electrochemical and spectroscopic studies.

Abstract No. 77

Novel Aspects on Electrolyte Systems

V. Gutmann* and **G. Resch,** Technical University, Institute of Inorganic Chemistry, Vienna A-1060, Austria

After a brief review of the existing theories on electrolyte solutions, both usefulness and limitations of the extended donor-acceptor approach are demonstrated with reference to so-called nonaqueous systems. With the aim to obtain a more profound understanding, a nonstatistical approach is presented. The differences of the constituent parts are ordered according to their significance for the whole system

under consideration and the concept of a "hierarchic order" is proposed. Its application is illustrated also for electrode-electrolyte interface phenomena.

Abstract No. 78

Properties and Structure of Nonaqueous Electrolytes

H. V. Venkatasetty, Honeywell Corporate Material Sciences Center, Bloomington, MN 55420

This paper will review briefly various techniques used in purification and characterization of nonaqueous electrolyte solutions. Data on transport properties and structure of various electrolytes, particularly at high concentration, in single and mixed solvent systems are presented and discussed in terms of ion-ion, ion-solvent, and solvent-solvent interactions.

Abstract No. 79

Solvent Effects on the Kinetics of Simple Electrode Reactions: A Test of Theoretical Models of Solvent Reorganization

S. Sahami* and **M. J. Weaver,** Dept. of Chemistry, Michigan State University, East Lansing, MI 48824

The one-electron reduction kinetics of $Co(en)_3^{3+}$ (en = enthylenediamine), $Co(NH_3)_6^{3+}$, and $Co(NH_3)_5F^{2+}$ have been studied in aqueous solution and in six nonaqueous solvents at mercury electrodes. The use of such substitutionally inert reactants allows tests to be made of conventional theoretical models that describe the outer-shell solvent contribution to the reorganization barrier. Substantial solvent effects upon the experimental rate parameters were observed that are not predicted by the dielectric continuum model. Possible reasons for these discrepancies are discussed in the light of corresponding measurements of solvent dependences of the redox thermodynamics.

Abstract No. 80

Ion Association in High Concentration Nonaqueous Solutions

G. E. Blomgren, Union Carbide Corp., Battery Products Div., Cleveland, OH 44101

Recent interpretations of the structure of solutions of high concentrations of salt in low to moderate dielectric constant solvents are critically reviewed. The role of ion pairs and higher association complexes as the salt concentration increases to the limit of the fused salt is discussed in terms of ion-ion and ion-solvent interactions. The relative importance of chemical and electrostatic interactions in determining the formation of association complexes is also discussed.

Abstract No. 81

Conductivities in Thionyl Chloride: II

M. Salomon, U. S. Army Electronics Technology and Devices Laboratory, Power Sources Div., Fort Monmouth, NJ 07703

New studies on the conductometric behavior of various electrolytes in thionyl chloride are reported. The electrolytes include NaCl, KCl, the tetraalkyl chlorides of methyl-, ethyl-, n-propyl-, n-butyl-, and a number of salts containing tetraphenyl arsonium and tetraphenyl borate ions. The limiting molar conductivities at infinite dilution for individual ions, λ^∞, are evaluated using the assumption that $\lambda^\infty(Ph_4As^+) = \lambda^\infty(Ph_4B^-)$. The results are discussed in terms of specific ion-solvent interactions. The solubilities of various salts were determined from the electrolytic conductivities of saturated solutions, and the results are discussed in terms of the medium effect.

Abstract No. 82

Conductivity Studies of Thionyl Chloride in the Presence of Halogen Compounds

R. W. Bennett,* **M. L. Gopikanth,** and **E. Luksha,** Cardiac Pacemakers, Inc. St. Paul, MN 55164

Lithium-thionyl chloride cells are very high energy density systems and there have been many studies on improving performance. The conductivity of the system would play an important role in cell performance. Thus a study was undertaken to determine the effect on conductivity of thionyl chloride solutions with the addition of the halogen compounds chlorine, bromine, iodine-monochloride, iodine-trichloride, lithium aluminum chloride, and lithium chloride.

Abstract No. 83

Electrocatalytic Reduction of Thionyl Chloride by Organometallic Complexes

N. Doddapaneni, Honeywell Inc., Power Sources Center, Horsham, PA 19044

The electrochemical reduction of thionyl chloride, $SOCl_2$ in an $Li/SOCl_2$ system takes place at the cathode surface and strongly depends on the electrode material. Moderate to high discharge rates are achieved only by the use of carbon blacks. We have found that organometallic complexes of transition metals increase the electrochemical reduction rate of $SOCl_2$. Impregnation of transition metal complexes of macrocyclic compounds such as Phthalocyanines, porphyrines onto carbon substrates has increased the $Li/SOCl_2$ cell voltage drastically. As much as 300 mV increase is observed in both acid and neutral electrolyte. Performance data showing the electrocatalytic effect are presented.

Abstract No. 84

Selective Electrowinning Using a Liquid Membrane

M. Gökalp* and **E. L. Cussler,** Dept. of Chemical Engineering and Materials Science, University of Minnesota, Minneapolis, MN 55455

A potential gradient applied across an organic liquid membrane is used to selectively separate metal ions in aqueous solution. This work describes one such selective electrowinning process in detail. The specific system used separates Ag^+ or Cu^{++} from Fe^{++} and Ni^{++}.

Abstract No. 85

Electrical Conductivity in Solutions of Bromine and Pyridine Derivatives

P. M. Skarstad and **T. G. Hayes,*** Energy Technology/Medtronic, Brooklyn Center, MN 55430

Although bromine is a nonpolar liquid at 25° C with a low conductivity, bromine is known to dissolve certain salts, notably CsBr and various quaternary ammonium bromides, to give solutions with conductivities greater than $10^{-2}\Omega^{-1}cm^{-1}$. Similarly high levels of conductivity can be achieved by dissolving in bromine small amounts of any of a large number of organic compounds such as amines. It is thought in this case that the amine forms a charge-transfer complex with the bromine, and that conductivity arises in the solution through ionic dissociation of the complex. We have investigated the conductivity of bromine solutions of pyridine and various substituted pyridines. Maximum conductivities greater than $10^{-2}\Omega^{-1}cm^{-1}$ were observed in most cases. Plots of equivalent conductivity *vs.* (concentration)$^{\frac{1}{2}}$ show features typical of electrolyte solutions in nonpolar or weakly polar solvents. The results are contrasted with data from quaternary ammonium bromide solutions.

Abstract No. 86

Photoelectrochemical Cells Using the Liquid Ammoniate of Sodium Iodide at Room Temperature

J.-L. Sculfort,* **D. Guyomard,** and **M. Herlem,** Laboratoire d'Electrochimie Interfaciale du CNRS, 92190 Meudon, France

Endurance tests under illumination showed that most of S.C. electrodes (n-type photoanodes such as: GaP, $Ga_rIn_{1-r}P$, CdS, Si, and CdTe, and p-type photocathodes such as: GaP, Cu_2O, Si, ZnTe, and CdTe) seem to be stable in ammonia and in liquid ammoniate of sodium iodide NaI $3.3NH_3$. In this last solvent, like in other nonaqueous solvents, efficiency and lifetime of the photoelectrochemical cells are very sensitive to the presence of water. Since it is difficult to obtain anhydrous solvents, to prevent the S.C. material against the photocorrosion due to the remaining water, the surface of the S.C. electrodes can be coated with SiO, silicium monoxide. In these conditions, the S.C. electrodes can be used even in aqueous solutions.

Abstract No. 87

Determination of Water in Propylene Carbonate Electrolytes by Cyclic Voltammetry

R. T. Atanasoski (Present address: Institute of Electrochemistry, Belgrade, Yugoslavia), **H. H. Law*** (Present address: Bell Laboratories, Murray Hill, NJ 07974), and **C. W. Tobias,** Materials and Molecular Research Div., Lawrence Berkeley Laboratory, and Dept. of Chemical Engineering, University of California, Berkeley, CA 94720

The influence of water on the electrochemical behavior of propylene carbonate electrolytes was investigated. Cyclic voltammograms and chronopotentiograms were obtained to detect the processes occurring on platinum and stainless steel electrode surfaces. The amount of water present was quantitatively determined in KPF_6 and $KAlCl_4$ solutions by comparing the magnitude of current peaks of the cyclic voltammograms obtained before and after the addition of known amounts of water to the electrolyte. Less than 1 ppm of water was present in the electrolyte prepared.

Abstract No. 88

Effect of Electrolyte Variables on the Polarization of the Lithium Electrode in Sulfuryl Chloride Solutions

F. Alessandrini and **B. Scrosati,** Istituto di Chimica Fisica, University of Rome, Rome, Italy and **F. Bonino** and **M. Lazzari,*** Centro Studio Processi Elettrodici del C.N.R., Istituto di Electrochimica, Polytechnic of Milan, P. le L. daVinci 32,20133 Milan, Italy

The behavior of lithium electrode in sulfuryl chloride solutions is strongly influenced by electrolyte variables, such as composition and additives. In this work results obtained by varying the nature and the concentration of the electrolyte are reported and discussed in terms of lithium electrode polarization and voltage delay effect after storage.

Abstract No. 89

Cycling Efficiency Behavior of Lithium in Nonaqueous Electrolytes at Ambient Temperature

M. Garreau* and **J. Thevenin,** Groupe de Recherche du CNRS, Physique des Liquides et Electrochimie, Associé à l'Université Pierre et Marie Curie, 75230 Paris Cedex 05, France

A study of the coulombic efficiency limitations of the lithium charge-discharge processes on either pure lithium or on aluminum substrates is presented. The evolutions with time of the potential, overpotential, and open-circuit potential of the electrode during the cyclings are investigated in an attempt to obtain a basic understanding of the role of several parameters—nature of solvent and substrate, cycling conditions, initial formation methods—on the premature battery failures. Applications to the determination of optimal cycling conditions in dioxolane and propylene carbonate based electrolytes are discussed.

DIELECTRICS AND INSULATION

Electrolytic Capacitor Technology

Abstract No. 90

Electrical Breakdown of Insulating Films by Impact Ionization

N. Klein, Dept. of Electrical Engineering, Technion, Israel, Institute of Technology, Haifa, Israel

Impact ionization by both holes and electrons can produce electrical breakdown in semiconductors. In contrast impact ionization by one type of carrier can result in electrical breakdown in insulators. The breakdown develops through a regenerative process by mutual enhancement of current injection and impact ionization. The mechanism of this breakdown process is described qualitatively. Results of theory are compared with experimental observations gained during the anodization of tantalum and aluminum. Good agreement of theory and experiment is illustrated.

Abstract No. 91

The Scintillation Behavior of Anodic Ta_2O_5 and Its Relation to Electrolytic Capacitors

J. M. Martínez-Duart,* I. Montero, M. Fernández, and **J. M. Albella.** Dept. de Física Aplicada, and Instituto de Física del Estado Sólido, CSIC. Universidad Autónoma. Cantoblanco. Madrid-34, Spain

Recent experimental results on scintillation in anodic Ta_2O_5 are discussed according to modern theories based in the injection of electrons across the electrolyte/oxide interface. It is proposed that two competitive processes, attack and recrystallization of the oxide, occur during the scintillation phenomenon. The influence of the anodizing conditions in the scintillation process and in the resulting oxide's dielectric properties is studied for tantalum foil samples and anodes employed in tantalum electrolytic capacitors. Finally, the scintillation in the $Ta/Ta_2O_5/MnO_2$/electrolyte structures is considered.

Abstract No. 92

A-C Etching Technology for Aluminum Electrolytic Capacitor in Japan

S. Watase, Nippon Chemical Condensor Co., Ltd., Higashi-ome, Ome city, Tokyo, Japan and **T. Kudo,** Hitachi Denkaihaku Kenkyujo Co., Ltd., Arakawa, Takahagi City, Ibaragi-ken, Japan

Etching technology is one of the important production processes to obtain miniature but high-capacitance electrolytic capacitors. The etching method is classified as d-c or a-c etching according to the power source. In the a-c etching system, a-c is directly supplied between two electrodes that sandwich the aluminum foil in an electrolyte. This gives higher production speed by two to five times than that of d-c etching. Another advantage is that mechanically strong etched foil can be obtained with sufficient capacitance. In view of foil materials, etching solution, etching process, capacitance, structure of etched foil, mechanical strength, waste solution treatment, electricity efficiency, current a-c etching technology are reviewed comparing with d-c etching system.

Abstract No. 93

D. C. Etching for Low Voltage Foils. Regulation of Pit Initiation at the Etching Bath Incoming

M. Badia, G. Laslaz,* and **J. Dubruelh,*** Pechiney Research Center, B. P. 24 38340 Voreppe, France, and Satma, 38570 Goncelin, France

For low voltage etching processes a pretreatment of the foil is usual: oil removing and surface cleaning or brushing treatment in order to cause cracks in oxide film. These pretreatments develop numerous favored locations for pit initiation on foil surface avoiding large and localized etch pits. Our study shows clearly that a new important factor of pit initiation is the current density profile when the foil is entering the etching bath. Regulating this profile allows us to avoid the above pretreatments.

Abstract No. 94

Factor Determining the Etch Gain of Hard Aluminum Foil in Electrolytic Capacitors

H. H. Nee, Sprague Electric Co., North Adams, MA 01247

The anode foils used for aluminum electrolytic capacitors are usually heavily cold worked and of 99.96-99.99% purity. Strong correlation was found between capacitance (at 60V anodic formation) and x-ray line broadening for various commercial and heat-treated foils. The correlation can be expressed as $Cap = \alpha B_h^2$ with Cap, the capacitance at 60V; B_h, the half-width of the (220) diffraction peak; and α, a constant. The multiple correlation coefficient for our data is 0.995. It has been demonstrated in the literature that a relationship between x-ray diffraction half-width and dislocation density exists, namely, $B_h^2 = C\,N$, with N being the dislocation density and C a constant. The tentative conclusion is that the capacitance of Al foils for a given d-c etch process is a linear function of dislocation density.

Abstract No. 95

Effect of Trace Elements on Etching of Aluminum Electrolytic Capacitor Foil

K. Arai, T. Suzuki, and **T. Atsumi,** Showa Aluminum Corp., 6-224, Kaisancho, Sakai, Osaka, Japan

An investigation was made of the effects of trace impurities, particularly bismuth and boron, on etching morphology and capacitance of aluminum electrolytic capacitor foil. It was found that as little as 2 wt-ppm bismuth in foil strongly accelerated surface etching, inhibited tunneling, and consequently lowered capacitance. Three ppm boron also enhanced surface etching but lowered capacitance less than bismuth. The reason for these results is discussed.

Abstract No. 96

The Anodization of Etched Aluminum Foil

H. J. de Wit,* C. Crevecoeur, and **J. Bruinink,** Philips Research Laboratories, Eindhoven, The Netherlands

The capacitance C_s of etched low voltage capacitor foil has been measured as a function of anodization voltage U_f and frequency f. The etched structure was also examined by electron microscopy. The results cannot be understood with the model that narrow tunnels are closed during anodization. The decrease of $C_s \cdot U_f$ with U_f is ascribed instead to the process that the oxide layers of tunnels lying closely together grow against each other. Results of anodization-dissolution of oxide-anodization experiments support this view.

Abstract No. 97

A Method for Estimating Size Distribution of Etch Tunnels in DC-Etched Al Foil

R. S. Alwitt, United Chemi-Con, Inc., Northbrook, IL 60062

A mathematical expression is derived from which the tunnel size distribution can be estimated using experimental C-V data for anodized specimens. The relationship depends upon the properties of cylindrical capacitors and the closure of a tunnel at an oxide film thickness determined by the anodizing voltage and initial tunnel radius. Some examples are presented of distributions in H-temper foil etched for low voltage applications.

DIELECTRICS AND INSULATION/ELECTROTHERMICS AND METALLURGY

Adhesion Aspects of Polymeric Coatings

Abstract No. 98

Adhesion Aspects of Polymeric Coatings: An Overview

K. L. Mittal, IBM Corp., Hopewell Junction, NY 12533

Polymeric coatings are used for a number of purposes and irrespective of their intended function, their adhesion to the substrate is of paramount importance. Among the topics to be covered in this overview are: factors which influence adhesion (substrate cleaning, deposition mode, material properties of substrate and coating, etc.); ascertainment of the precise locus of failure; understanding of interfacial interactions; adhesion improvement techniques; and durability of the bond. Some areas of research which need intensified efforts are highlighted.

Abstract No. 99

Acid Base Interactions Between Oxide Surfaces and Polar Organic Compounds

J. C. Bolger, Amicon Corp., Lexington, MA 02173

A model for the hydrated oxide layer present on all metals, glasses and other "oxide" surfaces, published in 1967, described how these surfaces could interact with polar organic compounds by a combination of dispersion forces plus acid-base forces. The free energy change for the acid-base interactions can be calculated from equations involving only the isoelectric point of the surface and the pK_a of the polar group. The present paper uses these equations to interpret adhesion, flotation, surfactant adsorption, and water displacement data (1).

1. J. C. Bolger and A. S. Michaels, in "Interface Conversion," P. Weiss, Editor, Chap. 1, Elsevier, New York and Amsterdam (1969).

Abstract No. 100

Adhesion of Polymers to Metals: The Role of Surface Topography

D. E. Packham, School of Materials Science, University of Bath, Bath, BA2 7AY, England

In the formation of an adhesive joint or coating the substrate surface topography can influence the extent of actual contact with the adhesive. Depending on the details of topography, surface energies, and whether the extent of contact is thermodynamically or kinetically determined, either complete contact or various degrees of void formation may occur. The effect of topography on measured strength is complex. There are many reports of poorer adhesion to rough surfaces, many of which may be attributed to the stress concentrating effects of interfacial voids. Some reports of improved adhesion to rough surfaces result from cognate effects such as surface cleaning rather than to the production of roughness per se. In other cases the improvement is explicable in terms of the effect of the roughness on the stress field at the interface during debonding.

Abstract No. 101

Detection of Contamination and Chemical Variance on Surfaces Prepared for Polymeric Coatings

G. R. Sparrow, Advanced R&D, Inc., St. Paul, MN 55101

The role of surface contamination and chemical surface treatments on polymer coating application is discussed. Emphasis is on use of modern surface analytical techniques to analyze the outer few angstroms of polymers and substrates.

Abstract No. 102

Surface Chemistry and Electrochemical Properties of Sulfuric-Chromic Acid (FPL) Etched Aluminum

A. V. Pocius, 3M Co., Adhesives, Coatings and Sealers Div., St. Paul, MN 55144

The aerospace industry has used the sulfuric-chromic acid (FPL) etch for many years as a surface preparation for aluminum. Workers in the past have found that the efficacy of the FPL etch as a surface preparation is increased if an appropriate concentration of Cu^{++} is present in the etch bath. We have investigated the electrode kinetics of FPL etched 2024T-3 aluminum in aqueous chloride solution as a function of $[Cu^{++}]$ in the etch bath and found no correlation with increased performance. Surface chemistry as a function of $[Cu^{++}]$ was also determined by Auger spectroscopy. The only correlation noted was an increase in the Al and O concentration as a function of $[Cu^{++}]$ in the etch bath. In addition, the number of microscopic pits increases as a function of $[Cu^{++}]$ in the etch bath. The conclusion we draw is that the increased performance of FPL etch as a surface preparation as a function of $[Cu^{++}]$ is not due to increased corrosion resistance or to a modification of surface chemistry. Rather, it must be due to a surface morphology change.

Abstract No. 103

Investigation of the Effect of Plasma Pretreatment on the Adhesion of Parylene to Various Substrates

T. J. Riley,* T. C. Mahuson, and **K. Seibert,** NASA-Lewis Research Center, Cleveland, OH 44135

An experimental effort has been undertaken to examine the effect of plasma pretreatment of various substrate materials coated with a polymer in the parylene family. This paper describes the procedure and discusses initial data which indicate using plasmas of argon and oxygen to promote adhesion of parylene coatings upon many difficult-to-bond substrates. Substrates investigated were gold, nickel, kovar, Teflon (FEP), kapton, silicon, tantalum, titanium, and tungsten. Without plasma treatment, 180° peel tests yield a few g/cm (oz/in.) strengths. With d-c plasma treatment in the deposition chamber, followed by coating, peel strengths are increased by one to two orders of magnitude.

Abstract No. 104

Adhesion Properties of Styrene/Acrylic Polymers: Influence of Process Conditions

H. P. Schreiber, Dept. of Chemical Engineering, Ecole Polytechnique de Montréal, Montreal, Qué., Canada H3C 3A7

The bond strength of Al joints using styrene-acrylic copolymers as adhesives, varies appreciably within a narrow range of formation temperatures. The magnitude of the effect depends on the amount of acrylic component present, and originates in the melt flow properties of these polymers. These are dominated by entanglement couplings at higher temperatures and by thermolabile H-bonds at lower process temperatures. Films produced under the latter conditions tend to be strained, cohesively weaker, and deteriorate more rapidly than controls.

Abstract No. 105

Variables Affecting the Adhesion of Bisphenol A Diglycidyl Ether/Aliphatic Amine Epoxy Resin to Metal and Ceramic Substrates

A. Coury,* A. Jevne, and **P. Cahalan,** Energy Technology, A Div. of Medtronic, Brooklyn Center, MN 55430

Bisphenol A diglycidyl ether/aliphatic polyamine-based epoxy resins find use as general-purpose adhesives. Their adhesive strength and durability are very dependent on application conditions. As coatings for medical electronic device substrates and packaging, maximum adhesion is sought. In an adhesion study, high cure temperatures, thin film application, properly-applied silane coupling agents and scrupulous atmospheric control during cure promoted high initial adhesion and bond durability of the epoxy to metal and ceramic substrates.

Abstract No. 106

Adhesion of Polyimide to Aluminum for Printed Circuit Armatures

K. N. Karol, IBM General Products Div., Tucson, AZ 85744

The need of creating a high temperature low inertia motor armature dictated the conception, design and development of a combination of glass cloth, polyimide, and aluminum of high adhesive strength into a thin laminate suitable for a printed circuit process. To achieve the results, it was necessary to start with the basic raw materials and develop the various processes to achieve the necessary adhesive strength of the laminate. The material development, configuration, and process that resulted together with some of the facts that established the high strength requirement peculiar to this particular need are discussed.

Abstract No. 107

Importance of Preliminary Treatment of Surfaces by Blasting from the Standpoint of Adhesive and Tribological Properties of Polymer Coatings

D. Kniewald, K. Takáč, E. Grutka, and **M. Šefara,** Technical University Košice, 040 01 Košice, Sverdlovova 74, Czechoslovakia

The paper contains the results of several years' research in the field of mechanical preliminary treatment of surfaces of the parent metal material by blasting from the point of view of formation of protective and functional coatings. It presents an analysis of the effect of the quality of the preliminary treated surfaces by blasting on adhesion of coatings to the surface of the parent material. In addition, it will bring forward a study into tribological properties and processes of polymer coatings under the conditions of sliding friction.

Abstract No. 108

An Overview of the Adhesion Properties of Inks and Coatings

G. V. Calder, S. C. Johnson & Son, Inc., Racine, WI 53403

This paper contrasts the approaches and methods used by scientists studying the physical phenomenon of adhesion and the approaches and methods used by scientists studying the desirable technological property of an ink or coating, also referred to as adhesion. Unfortunately, the physical phenomenon and the desirable technological property often have little to do with one another. The complex problems facing the applications scientist trying to obtain and understand adhesion within the ulterior constraints placed on him are illustrated.

Abstract No. 109

Adhesion of Plasma-Polymerized Coatings

H. Yasuda, Graduate Center for Materials Research, University of Missouri-Rolla, Rolla, MO 65401

Because of unique mechanisms of polymer formation, plasma polymerization can be utilized to create relatively water insensitive adhesion between plasma-polymerized coatings and various substrates. A review of recent work on adhesion of plasma-polymerized coatings investigated by using various tests, such as a boiling test in a saline solution, adhesive strength measurement after boiling in a saline solution, a test using repeated small strain flexion, and cyclic voltammetry, is presented.

Abstract No. 110

Epoxy Adhesion to Copper

J. M. Park* and **J. P. Bell,** Institute of Materials Science, University of Connecticut, Storrs, CT 06268

To improve the water resistance of copper-epoxy adhesive bonds, chemical bonding between the resin and the copper surface is being studied. Several coupling agents, capable of bonding with both copper and the epoxy adhesive, have been prepared and evaluated by a torsional joint testing method. A long term aging test in boiling water showed that 5-amino-benzo-triazole can be an effective coupling agent for improvement of the water-resistance of copper-epoxy adhesion. Several additional experiments have been performed to understand the mechanism of failure.

Abstract No. 111

Wet Adhesion of Latex Paints

S. M. Kambanis, Reichhold Ltd., Weston, Ont., Canada M9M 1B1

Wet adhesion is defined as the property of emulsion polymers enabling latex paints to maintain adhesion to precoated surfaces under severe exposure to water and film dislodging forces such as scrubbing and peeling. The tests used by the industry to measure this property were reviewed and a modified version of the Canadian Government Test 1-GP-138 was adopted for this study. Using this test, the effect of polymer and paint parameters were investigated, and it was found that wet adhesion is improved by introducing certain polar groups by increasing the molecular weight, decreasing the particle size of the emulsion polymer and by proper selection of surfactants, thickeners, and coalescing agents.

Abstract No. 112

Infrared Spectroscopic Investigation of Polymer Coating-Metal Substrate Interaction

W. Suëtaka, Laboratory of Interface Science of Metals, Faculty of Engineering, Tohoku University, Aramaki Aoba, Sendai 980, Japan

Infrared spectroscopy can provide information about the interaction of polymer coating with metal substrate. The obtained information can be divided in two categories: (*i*) The interaction of polymer-substrate bonding can be obtained from the spectrum of polymer molecule in the first monolayer on the substrate. (*ii*) The polymer-metal interaction can be deduced from molecular orientation in the thin coating film, and the orientation, in its turn, corresponds to mechanical strength of the polymer film.

Abstract No. 113

The Relationship Between Adhesion and Polyelectrolyte Solution Conformation as Studied by Fourier Transform IR Spectroscopy

D. J. Belton,* Signetics Corp., Sunnyvale, CA 94086 and **S. I. Stupp,** Dept. of Ceramic Engineering, University of Illinois at Urbana Champagne, Urbana, IL 61801

The absorption behavior of polyelectrolyte macromolecules at an ionic interface, in part, defines the ability of that polymer to function as an adhesive. The effects of altering macromolecular solution conformation, via added electrolyte and salts, upon the structure of the absorbed layer can be monitored by Fourier transform infrared spectroscopy coupled with the technique of attenuated total reflectance. The results are expressed in terms of the amount of polymer absorbed, and the apparent fraction of bound segments on absorbed molecules.

Abstract No. 114

Dynamics of an Adsorbed Polymer Molecule Subjected to Flow

G. G. Fuller, Dept. of Chemical Engineering, Stanford University, Stanford, CA 94305

The imposition of a velocity gradient at the polymer/solid interface can have important consequences regarding the durability and conformation of a polymer coating residing on that surface. This paper examines the response of an adsorbed polymer molecule to a surface velocity gradient modelled as a simple dumbbell attached to a surface. It is shown that exact, time-dependent expressions can be obtained with this model for the moments of the probability distribution function describing the conformation and for the power dissipation. The model is further generalized to include the finite volume of the polymer as well as the hydrodynamic interaction between the polymer and the solid surface.

Abstract No. 115

PTFE Film Adhesion to Electronically Conducting Materials

K. A. Klinedinst, GTE Laboratories, Inc., Waltham, MA 02154

Composites of PTFE with electronically conducting materials are generally made by heating (above the melting point of the PTFE) mixtures or contacting layers of the two substances. The resulting interactions between the polymer and the contacting material have been elucidated. In addition to the apparent rheological characteristics and thermal degradation of the polymer, the effects of varying electrochemical potential upon the stability of the adhesive bond between the PTFE and the electronically conducting material have been examined.

Abstract No. 116

Adhesion, Wettability, and Surface Chemistry: SiO_2 and Resist Materials

C. A. Deckert,* Shipley Company, Newton, MA 02146 and **D. A. Peters,** RCA Laboratories, Princeton, NJ 08540

Several problem areas related to photo- or electron-beam-resist/SiO_2 interfaces are examined. These areas include adhesion measurement, effect of chemical and thermal treatment on SiO_2 surface chemistry, resist surface chemistry, correlation of surface chemistry with adhesion, and wettability of SiO_2 surfaces by resist materials. Surface energy measurements have been used as a means of elucidating SiO_2 and resist film surface chemistry. The polar component of surface energy, γ^p, of both resist and substrate is found to be of prime importance in determining adhesion and wettability of resist/SiO_2 composites. Best adhesion during wet etching is achieved if γ^p of both resist film and substrate is small. However, in the case of a resist with fairly large γ^p, it is necessary to make γ^p of the substrate sufficiently large to permit good wetting. Large effects of processing procedures on SiO_2 wettability and adhesion are observed, and these effects are correlated with measured changes in surface energies.

Abstract No. 117

Recognition and Discussion of Basic Adhesion Mechanisms in Photopolymeric Systems

L. Fullwood, Thiokol/Dynachem Corp., Tustin, CA 92680

Standard manufacturing procedures for printed wiring boards require the application of dry film photopolymeric resists onto a copper substrate. This is accomplished by using heated lamination techniques. This paper examines the chemical and mechanical surface condition required to provide good adhesion. Scanning electron micrographs and surface profilometry are used to define various topographic configurations. Finally, there is a discussion of the use of adhesion promoting chemicals to improve bonding.

Abstract No. 118

Organosilanes as Process Compatible Adhesion Promoters for Resist Materials

J. N. Helbert* and **H. G. Hughes,** Motorola, Phoenix, AZ 85008

Resist adhesion is strongly dependent upon the condition of the wafer substrate surface. For example, wafers stored for long periods of time in humid conditions exhibit poorer resist adhesion than those recently processed. Organosilanes have been commonly used to treat these hydrated substrates to achieve better resist adhesion. While many organosilanes are available, only a limited number have been successfully employed. A brief review of the chemistry of organosilane coupling agents and several practical applications for positive and negative resists are presented.

Abstract No. 119

Liquid Negative Working Photoresist for Through Hole Printed Circuitry

S. Simoliunas, Kimplate Inc., Detroit, MI 48201

The industrial realization of liquid photocrosslinkable negative working resist for etch mask in PTH printed circuit manufacturing yields copper circuitry, which can be solder masked and then hot air solder leveled or tin immersed. The application of liquid photoresist is not only simple, but also the transformation from a liquid state to an amorphous solid on the work itself creates excellent adhesion between the photoresist and the copper substrate. Thus, the exposed photoresist can be developed not only in cold solvents, but also in hot degreasers.

Abstract No. 120

Dry Film Photoresist Adhesion on Electroless Copper Surfaces

W. L. Hamilton, E. I. du Pont de Nemours & Co., Inc., Riston Products Center, Newark, DE 19713

Printed wiring board manufacturers electroless-plate drilled panels to deposit copper in through holes. Until recently, shops flash-electroplated copper over this electroless before laminating resist to ensure reliable plating in the holes. But improved electroless baths have encouraged many shops to eliminate flash plating and laminate resist directly to the electroless surface. To be successful, however, such shops must know and control the factors affecting resist adhesion to electroless during electroplating. This report discusses these factors, and describes conditions maximizing resist adhesion. Topics covered include effects of: resist type, post-electroless scrubbing, post-electroless rinsing/neutralization/drying, resist exposure level (step held), electroless copper thickness, deburring method used before electroless, copper plating bath type ($CuSO_4$ or Cu-Pyro), electroless line maintenance, and electroless bath type. The process conditions recommended should allow printed wiring shops to achieve excellent resist adhesion during plating when laminated to electroless copper equal to that on scrubbed electroplated copper.

Abstract No. 121

Durability of Metal Polymer Bonds

W. Brockmann, Dept. Structures and Composites, Fraunhofer Institut für angewandte Materialforschung, 2820 Bremen 77, Germany

The most important factor for the long term properties of metal polymer composites is the stability of adhesion against humidity. Failure mechanisms like hydrolysis of chemical bonds between polymers and metal oxides, hydration of the oxides itself, and depolymerization of the polymers near the boundary layer by aggressive reaction products of water with impurities of the metal surface layers are discussed. This hypotheses is compared with the

results of surface analyses of so-called adhesional failures to set a better grasp of the problem and hints with reference to systematical methods of optimization of the compounds.

Abstract No. 122

Adhesion of Coatings and Its Loss Due to Corrosion

R. A. Dickie, Ford Motor Co., Dearborn, MI 48121

Modern surface analytical techniques have contributed greatly to the understanding of the interaction between organic coatings and the substrates to which they are applied. This paper reviews results on the effect of moisture and corrosion products on the coating/substrate interface. Mechanical, and corrosion induced de-adhesion are compared for model coatings. Corrosion induced de-adhesion is often associated with chemical degradation of the organic polymer; the locus of de-adhesion is closer to the substrate than in the case of mechanical de-adhesion.

Abstract No. 123

Cathodically Induced De-adhesion of Polymer Coating/Metal Substrate Interfaces

H. Leidheiser, Jr.,* L. Igetoft, W. Wang, and **K. Weber,** Center for Surface and Coatings Research, Lehigh University, Bethlehem, PA 18015

A summary is given of research at Lehigh on the de-adhesion of polybutadiene and epoxy-polyamide coatings from various metallic substrates during cathodic treatment in different electrolytes. New data on the effect of coating thickness, ionic transport, and substrate pretreatment are presented.

Abstract No. 124

The Effects of Environment on Paint Adhesion to Steel

R. T. Ruggeri* and **T. R. Beck,** Electrochemical Technology Corp., Seattle, WA 98107

The adhesion of five different paints to a steel substrate has been quantitatively measured using a mechanical cutting device. The paints were unpigmented and contained no corrosion inhibitors. One-coat systems without primers were investigated. Tests were conducted to evaluate the effects of water, sodium chloride solution, anodic or cathodic currents, caustic solution, and various solvent cleaning methods on paint adhesion. Results indicate that water has the most disruptive influence on adhesion, but at short times the effects are reversible when water is removed.

Abstract No. 125

Correlation of Surface Chemistry and Mechanical Properties of Aluminum Substrates Bonded to Polymer Coatings. I. Surface Chemistry

T. S. Sun, B. M. Ditchek, J. S. Ahearn, and **J. D. Venables,** Martin Marietta Laboratories, Baltimore, MD 21227

By utilizing the chemical and quantitative information from an x-ray photoelectron spectroscopic analysis, we have been able to explain the evolution of the surface composition of Al adherends allowed to degrade in a humid environment and to determine the effects of some inhibitors on the degradation process. In this paper we will show that (*i*) degradation proceeds step-wise—first, Al OOH forms on the surface, then Al $(OH)_3$ growth follows and (*ii*) the presence of some P-containing compounds can effectively retard the initiation of the hydration process.

Abstract No. 126

Correlation of Surface Chemistry and Mechanical Properties of Aluminum Substrates Bonded to Polymer Coatings. II. Mechanical Properties

J. S. Ahearn, T. S. Sun, B. M. Ditchek, and **J. D. Venables,** Martin Marietta Laboratories, Baltimore, MD 21227

The importance that the chemical composition of the oxide film formed on Al adherend surfaces has on durability has recently been determined by wedge tests of the adherend-adhesive bond in a moist environment. Analysis of the durability tests has suggested that the conversion of the oxide on the Al adherend to a hydroxide is responsible for bond degradation. In the present work, we describe the treatment of Al adherends with amino phosphonic acids that adsorb on Al-oxide surfaces and thereby delay the conversion of Al-oxide to Al-hydroxide. Accelerated tests conducted in a moist environment demonstrate that the presence of adsorbed phosphonate molecules significantly improves the durability of bonds to 2024 Al adherends. Results using STEM in the high resolution SEM mode, Auger/ESCA, ellipsometry, and mechanical tests are presented and correlated with a view toward understanding in detail the mechanism of degradation of the adhesive/adherend interface.

Abstract No. 127

A Case Study of Water Sensitivity of Polymeric Coating-Substrate Interface for Two Aluminum Surface Preparations

K. K. Knock and **M. C. Locke,** The Boeing Co., Seattle, WA 98124

The relationship between the microstructure of aluminum oxide and the water resistance of the adhesive-oxide bond has been investigated. Phosphoric acid anodize (PAA) oxide on clad 2024 after formation under two process conditions was studied. Mechanical strength data are presented along with electron photomicrographs illustrating microstructural differences. A load transfer mechanism is presented which is consistent with both the general superior durability of PAA bondments and the wet failure tendency of poorly prepared adherends.

Abstract No. 128

Effect of Age of Pigmented Polymeric Films on Adhesion to Metal Substrate

M. N. Sathyanarayana, P. S. Sampathkumaran, and **M. A. Sivasamban,*** Surface Coatings Div., Regional Research Laboratory, Hyderabad-500 009, India

The aging of pigmented polymeric films is likely to affect their properties of cohesion and adhesion. In the present work the effect of aging under ambient conditions of coatings formulated at two pigmentation levels using alkyd resin and titanium dioxide (anatase), zinc oxide or their combinations on their practical adhesion to mild steel substrate has been investigated. Adhesion was determined by sandwich pull-off method and cohesive strength determined on free films. The results are discussed.

Abstract No. 129

Adhesion Measurement of Polymeric Coatings

K. L. Mittal, IBM Corp., Hopewell Junction, NY 12533

There exists in the literature a plethora of the so-called adhesion measurement techniques ranging from very primitive to very sophisticated. The potentialities and limitations of some of these techniques are discussed. The phrase "adhesion measurement" is fraught with confusion so the concept of "practical adhesion" (experimentally measured value) is emphasized. Various examples are given to illustrate the relationship between the practical adhesion and the adhesion determined by interfacial interactions (fundamental adhesion).

Abstract No. 130

Resin Coating Adhesion Tests

G. G. Gray, Eastman Kodak Co., Paper Service Div., Rochester, NY 14650

Two photographic papers, one made using polyethylenimine (PEI) in the tub size, and one using an in-line corona discharge treatment (CDT), were extruded with polyethylene (PE) at a series of melt temperatures to compare adhesion of the resin layer. Adhesion was studied using a variety of testing procedures supplemented with scanning electron micrographs (SEM) of the PE-paper interfaces. It was found that excellent adhesion can be obtained with either PEI or CDT methods provided adequate melt temperature and backing roll pressure are maintained. Using conventional and unique testing procedures that are described in detail, it was found that strength of paper substrates, and the rate, mode, and direction of applied force can influence adhesion ratings. In some instances

judgments made only on the amount of fiber removed in peel testing can be misleading. Advantages and limiting factors of the test methods employed are described.

Abstract No. 131

Indentation Debonding Test for Adhered Thin Polymer Layers

P. A. Engel* and **G. C. Pedroza,** IBM System Products Div., Endicott, NY 13760

The indentation-debonding test has been introduced for the verification of mechanical bond resistance between epoxy coatings and underlying metal substrates. If bond strength is inferior, then pressing a sharp indenter against the surface provokes delamination, observed through a microscope. The strength of the bond, when delamination occurs, can be related to the force of indentation and the debonding radius. For the quantitative relations an engineering analysis is presented.

Abstract No. 132

Thermographic Detection of Polymer/Metal Adhesion Failures

B. E. Dom and **H. E. Evans,*** IBM Corp., Boulder, CO 80302

Loss of adhesion at a polymer/metal interface leads to an increase in interface thermal impedance. Such areas may be detected by inducing a thermal gradient across the interface and subsequently monitoring the polymer surface temperature profile utilizing a computer-interfaced infrared thermal imaging unit. This technique has been applied to various materials systems (*e.g.*, silicone rubber/aluminum, Hypalon/bronze and urethane steel) and diverse geometrical configurations (*e.g.*, flat plates and cylindrical rollers).

Abstract No. 133

Ultrasonic Inspection Potential for Polymeric Coatings

J. L. Rose and **J. B. Nestleroth,** Mechanical Engineering and Mechanics Dept., Drexel University, Philadelphia, PA 19104

The nondestructive measurement of adhesion quality in a coating process is critical to ensure the good quality control and coating performance. A computer based ultrasonic test bed system has been successfully used to solve similar problems related to the prediction of adhesive bond strength. The basic concepts of ultrasonics, data acquisition, signal analysis, feature extraction, and pattern recognition as they pertain to the measurement of the adhesion quality of polymeric coatings are discussed. New approaches in ultrasonics that utilize special transducers and pattern recognition methodologies are also reviewed.

Abstract No. 134

Pull-Off Test, An Internationally Standardized Method for Adhesion Testing—Assessment of the Relevance of Test Results

J. Sickfeld, Bundesanstalt für Materialprüfung, D-1000 Berlin 45, Germany

The first part of the report reviews results concerning the influences of test-parameters cited below on "adhesion"-values obtained with the pull-off method which have influenced the wording of ISO4624: Test assemblies, diameter and geometrical dimensions of test cylinders, testing area isolation, coating and substrate thickness. Testing equipment is introduced which fulfills the requirements of the standard. In the second part it is demonstrated also by SEM pictures that one should not rely too much on absolute values of adhesion. For interpretation of adhesion phenomena it is more important to describe the nature of failure and changes in the nature of failure as a consequence of resistance tests.

Abstract No. 135

Bond Strength of Baked Electropaints and the Electrical Resistance per Coulomb of Electrodeposits—A Comparative Study

S. Guruswamy, Central Electrochemical Research Institute, Karaikudi 623 006, South India

The bond strength (psi) of a baked electrodeposit is related to the electrical resistance per coulomb (p, Ω/C) of electrodeposits, evaluated from current-time data. The value of m in the equation

$$\text{Bond strength (psi)} = \left\{\frac{1}{1 - (p \times 10^{-3})}\right\}^{m}$$

depends on the resin-metal-system chosen for studies. Since p is more easily evaluated than the bond strength values, it is possible to estimate the latter for comparative studies when p values are known for a particular system.

Abstract No. 136

Silane Adhesion Promoters for Polymeric Coatings

E. P. Plueddemann, Dow Corning Corp., Corporate Research, Midland, MI 48640

In order for trace amounts of silane additives to function effectively in coatings, there must be some mechanism for concentrating the silane at the interface where it provides a boundary layer (interphase region) with optimum chemical and mechanical properties for adhesion. These conditions are discussed with applications in PVC plastisols, urethanes, and epoxy coatings. Some anomalous results in performance of pigmented coatings are described and explained.

Abstract No. 137

Structure and Effects of Organo Silane or Organo Titanate Adhesion Promoters on Al_2O_3/Polyethylene Joints

N. H. Sung, A. Kaul, and **S. Ni,** Dept. of Chemical Engineering, Tufts University, Medford, MA 02155, and **C. S. P. Sung*** and **I. J. Chin,** Dept. of Materials Science and Engineering, Massachusetts Institute of Technology, Cambridge, MA 02139

The structure of organo silane or organo titanate when adsorbed on single crystalline aluminum oxide has been studied by combining Fourier-Transform IR spectroscopy and Electron Spectroscopy for Chemical Analysis. Adsorbed organo silanes have undergone hydrolysis and polymerization to form somewhat cross-linked polysiloxane, but oligomers or unreacted silanols are still present in adsorbed silane, the exact composition of which seems to depend on concentration, pH, and drying conditions. In contrast, adsorbed titanates show more subtle changes, only after prolonged heating. Correlation of the structure of the adsorbed layer with the peel strength of Al_2O_3/polyethylene joint was attempted. Organo silanes are much more effective than organo titanates. Extensive drying of adsorbed silane which drives the cross-linking reaction significantly reduces the peel strength. Based on these results, interdiffusion between polyethylene and silane was tentatively suggested as a responsible mechanism for improved adhesion.

Abstract No. 138

The Use of Coupling Agents to Improve the Adhesion of Polymer Matrices for Electronic Applications

D. J. Vaughan and **R. C. Peek, Jr.,*** Clark-Schwebel Fiber Glass Corp., Anderson, SC 29622

The data obtained on the effects of varying the interface on electrical properties have proven helpful in understanding interfacial bonding applications. It is possible that adhesion measured by a composite's mechanical performance involves factors that have not been thought essential for adhesion of polymers on a molecular scale. The improved performance, specifically electrical properties, imparted to a number of composites by the use of coupling agents suggests that these materials may play an important role in better understanding the theory of adhesion.

Abstract No. 139

Adhesion Promotion and Polymer Composite Performance with Titanate Coupling Agents

S. J. Monte* and **G. Sugerman,** Kenrich Petrochemicals, Inc., Bayonne, NJ 07002

Titanate coupling agents act as molecular bridges at the interface of an inorganic filler and an organic polymer matrix. Their reaction with the free protons at the inorganic interface results in the formation of organic monomolecular layers on the inorganic surface providing, among other significant effects: viscosity reduction; hydrophobicity; adhesion promotion; corrosion protection; controlled catalysis; increased electrical conductivity; increased elongation and impact. Chemical mechanisms, illustrative effects, data and patent literature references explain as well as substantiate the claims.

Abstract No. 140

Improved Metal-Polymer Wet Strength Adhesion

L. Graham* and **J. A. Emerson,** Western Electric Co., Engineering Research Center, Princeton, NJ 08540

Improved wet strength adhesion of epoxy coated steel substrates is accomplished by wetting tin hydrosol and organic coupling agent treatment of the clean steel. The adhesion is measured by a 90¼ peel test. The adverse effect of water on adhesion for a series of metal treatments were examined. For the steel/epoxy substrate, it was found that: (*i*) clean only samples showed approximately 80-100% reduction in adhesion, (*ii*) iron or zinc phosphate samples varied from 60-90% reduction, and (*iii*) organic modified wetting tin hydrosol showed 0-50%.

Abstract No. 141

Adhesion of Aromatic Polyimide to Silicon Wafer

Y. K. Lee and **J. D. Craig,** E. I. du Pont de Nemours & Co., Philadelphia, PA 19146

The adhesion of polyimide on a silicon wafer is poor if no adhesion promoter is used. Organic silane compounds are often used as the adhesion promoter. In this paper we propose the mechanism of silane to promote adhesion and experimental evidence to support the hypothesis. The intercoat adhesion of polyimide is important when the PI is used as a dielectric for multilevel metallization. Attempts are made to study this property for different polyimide coatings.

Abstract No. 142

Effect of Residual Chemical Contaminants on Polyimide/Surface Interface Adhesion

M. Chaker and **R. J. Clark,*** IBM Corp., Essex Junction, VT 05452

The presence of a chemical contaminant on a substrate (ceramic, silicon, or metallic surface) will effect the adhesion of a polyimide film to that surface. Quantitative measurements for the level of contamination were performed, using chemical extraction techniques of the suspect samples, which in turn were followed by the separation of the solution in a high pressure liquid chromatograph. Subsequently, contact angle measurements of the polymeric solutions on different substrates were used as an indicator and monitor for the cleanliness of those surfaces. The addition of a silane coupling agent to the polymeric solution before application reduces the effect of the contaminant and the sensitivity to the process environment.

Abstract No. 143

The Study of Some β-Diketones as Complexing Agents for the Adhesion Promotion Between Carbon Steel and Polymeric Coating

T. T. Kam* (Present address: Abteilung Korrosion, Technische Universitat Clausthal, D-3392 Clausthal-Z., Germany), and **P. K. Hon,** Dept. of Chemistry, The Chinese University of Hong Kong, Shatin, N.T., Hong Kong

The polymeric coating of carbon steel with methyl/n-butyl methacrylate copolymer resin for corrosion protection can be strengthened by some Fe(III) β-diketonate complexes firstly developed on the metallic (iron) surface by reaction with the corresponding β-diketone complexing agent. Increase in corrosion protection has been demonstrated and related to the kind of complexes developed. Reinforcement of adhesion in the polymeric coating probably resulted from chemical interactions between the polymeric components and the functional groups of the complex.

ELECTRONICS—LUMINESCENCE

Display Technology and Special Purpose Cathode-Ray Tubes

Abstract No. 144

Phosphors for Special Cathode Ray Tubes

P. Seats, Thomas Electronics, Inc., Wayne, NJ 07470

Some 50 or more phosphors are in use either singly or in combination for special cathode ray tube screens. The origins of some of the more important phosphors are reviewed. Many of these were developed with stimulation from the commercially important fields of television tubes, fluorescent lamps, and x-ray intensifier screens. Despite the wide range of available characteristics encompassed in many phosphor types, however, important gaps exist, some of which are identified and discussed.

Abstract No. 145

Panel Displays Based on Electron-Beam Technology

B. Kazan, Xerox Research Center, Palo Alto, CA 94304

During the past decade it had been hoped that progress in the newer display technologies would lead to large-screen panels for TV applications. However because of increasing doubts that any of these technologies will result in devices capable of achieving the performance levels necessary to compete with cathode-ray tubes, the applicability of electron-beam technology itself is being investigated for panel displays. Towards this end, work is presently under way on several promising new vacuum structures.

Abstract No. 146

Advances and Applications of Storage Cathode Ray Tubes

I. F. Chang, IBM T. J. Watson Research Center, Yorktown Heights, NY 10598

Storage CRT's have wide applications as oscilloscopes, signal converters, and imaging and display devices. Different storage CRT technologies are in use for these applications. Facing strong competition, some significant technological advances have been made in storage CRT's for information display applications where CRT's with special phosphor screens such as long persistence phosphors, secondary electron emitting phosphors (bistable phosphor screen), cathodochromic phosphors (dark trace faceplate), and electroluminescent phosphors (memory EL faceplate) were utilized. These storage CRT's are reviewed.

Abstract No. 147

Color Write-Thru Direct View Storage Tubes

R. O. Petersen, Tektronix, Inc., Beaverton, OR 97077

Color in computer graphics aids the user in discernment of data. Color write-thru in direct view storage tubes (DVST's) is discussed. Write-thru in a DVST is the refresh luminance that occurs when the writing beam is sweeping at sufficient vector speed and low Ib as not to store. Use of special coatings on P-1 and P-22R phosphors provides green storage and orange write-thru. These two phosphors are discussed along with DVST performance.

Abstract No. 148

A New Cathodoluminophor with Long Persistence

J. J. Wei, Z. H. Wang, S. Y. Zhao, Y. Wu, S. H. Lu, and **S. H. Xu,*** Changchun Institute of Physics, Changchun 130021, Jilin, China

A new phosphor, $SrAl_2O_4$, activated with Dy^{3+} is synthesized which shows a decay time of more than 200 msec to decrease to an intensity of 1/10 of its initial value after the removal of cathode ray excitation. The luminescence spectrum is characteristic of Dy^{3+}, appearing yellow-white in color. The cathodoluminescence brightness is comparable to commercial MgF_2:Mn, or about 60% that of Zn_2SiO_4:Mn,As(P39). The luminescence decay is nonexponential. Thermoluminescence after CR excitation shows the existence of deep traps which are responsible for the slow decay.

Abstract No. 149

Temperature Dependence of Luminescence and Photostimulation in Single Crystals of Zn_2SiO_4:Mn with and Without As Addition

I. F. Chang,* E. A. Giess, and **E. E. Mendez,** IBM T. J. Watson Research Center, Yorktown Heights, NY 10598

Photoluminescence (PL) and excitation spectra, photostimulated luminescence (PSL) (1) and decay characteristics of clear rhombohedral zinc silicate crystals grown from a melt, fluxed with the Pb analog of hardy-stonite, and doped with Mn, and with and without As, were investigated over the temperature range of 77-300 K. The crystal with Mn alone exhibits intrinsic Mn^{2+} PL decay, and t^{-1} type PSL decay with deviation at longer times. Its PSL intensity is strongly dependent on temperature, exhibiting a peak around 150-175 K, in contrast with the Mn-As doped crystal. The latter does show larger temperature dependence in PL and PSL decay characteristics.

1. I. F. Chang and G. A. Sai-Halasz, *J. Electrochem. Soc.*, **127,** 2458 (1980).

Abstract No. 150

Correlation of Phosphor Emission Decay Kinetics with Flicker Perception

J. R. McColl, GTE Laboratories, Inc., Waltham, MA 02254

Many computer terminal display cathode ray tubes are operated at low frame rates (~30 frames/sec) to minimize component costs and information transfer rates. As a result, long persistent phosphors are required to prevent perception of flicker. Measurement of the flicker sensitivity of four observers to emission from phosphor blends shows that the standard JEDEC test for persistence is inadequate for testing flicker performance. The "ripple ratio" suggested by DeLange, on the other hand, correlates admirably with observed flicker sensitivity. Results on red and green-emitting long persistence phosphor blends are presented to illustrate these points.

Abstract No. 151

The Cathodoluminescence of $Zn_2Si_{1-2x}(Al,P)_xO_4$:Mn,As Phosphors

T. E. Peters* and **J. R. McColl,** GTE Laboratories, Inc., Waltham, MA 02254

The increasing use of low-refresh-rate CRT's in computer displays has stimulated the search for phosphors of higher efficiency and longer persistence than those currently available. Recently Chang and Shafer reported an efficiency enhancement in Zn_2SiO_4:Mn(P-1) arising from the substitution of $AlPO_4$ for part of the SiO_2 in the phosphor. In an extension of this work, we have synthesized Zn_2SiO_4:Mn,As(P-39) phosphors with analogous $AlPO_4$ substitutions and describe some of the cathodoluminescence emission and decay properties of these materials.

Abstract No. 152

Low Current Density Aging

R. L. Donofrio, GTE Products Corp., Seneca Falls, NY 13148

Historically, aging data have been analyzed with respect to Pfahnl's aging equation and its associated burn constant. Our studies show that for the low charge accumulation region (*i.e.*, below 1 C/cm^2), a new relationship is recommended which is a better fit to experimental data. It is shown that Pfahnl's burn parameter can be expressed as a function of accumulated charge. Data are presented using P4 and P31 phosphors in data display tubes which show the new functional relationship.

Abstract No. 153

The Novel Characterization of Lanthanum Oxybromide Phosphors Used in the Projection Cathode-Ray Tubes

J. Liu, Research Dept., General Institute of Nonferrous Metal Metallurgical Industry Ministry, Beijing, China

The temperature effects of various hosts on Tb^{3+} luminescence have been investigated such hosts as Y_2O_2S, Gd_2O_2S, and LaOBr. Excellent properties were found in the LaOBr host for projection tube use. The present paper describes the luminescent properties, especially the emission intensity and the color stability, under electron excitation of the following phosphors, LaOBr:Tb, Y_2O_2S:Tb, and $(YGd)_2O_2S$:Tb. Measurements show that the LaOBr:Tb projection tube provides an emission intensity 1.2-1.5 times greater than $(YGd)_2O_2S$:Tb at 30 kV and 150 mA operating conditions and the performance of the former is almost independent of temperature. Also, the LaOBr:Tb projection tube has considerably greater color stability over a wide range of operating currents and temperatures. The stability of color is in the following order: LaOBr:Tb, Y_2O_2S:Tb, $(YGd)_2O_2S$:Tb.

Abstract No. 154

Inorganic Electrochromics

G. Beni, Bell Laboratories, Holmdel, NJ 07733

We review the most recent research in inorganic electrochromic materials and its relevance for display devices. The materials most likely to emerge as technologically viable are WO_3 and iridium oxide films. For both materials, lifetimes in excess of 10^7 cycles have been demonstrated. Response times are < 500 msec for WO_3 and < 50 msec for iridium oxide films. Low temperature operability of the latter has been demonstrated, with response times < 1 sec at temperatures > −20°C. Development of displays based on solid electrolytes is more advanced for WO_3, partly because the mechanism of electrochromism is much more clearly understood in this material. For iridium oxide films further evidence has been provided for a low activation energy anion mechanism. Solid-state display cells based on fluoride electrolytes have been fabricated. Finally, it has been shown that, in principle, electrochromic display cells can be intrinsically matrix-addressed.

Abstract No. 155

Electro-Wetting Displays

S. Hackwood* and **G. Beni,** Bell Laboratories, Holmdel, NJ 07733

We report the general operating parameters of displays based on the dynamics of a liquid moving within a solid matrix of characteristic length ≈1 to 10μ~. The dynamic is due to electro-wetting, which in a 3-phase system (solid, liquid electrolyte, and a second fluid), we define as the change in solid-electrolyte contact angle due to an applied potential difference between the solid and the electrolyte. Electro-wetting is akin to, but distinct from electrocapillarity (1). We show how electro-wetting can be the basis of a display device which (*i*) can be switched between a transparent and a white (diffusely reflecting) state; (*ii*) has fast response time (~1 msec); and (*iii*) has a low operating voltage and power consumption. We also report experiments on electro-wetting of gold, demonstrating the concept of these displays.

1. G. Beni and S. Hackwood, *Appl. Phys. Lett.*, In press.

Abstract No. 156

Analysis of Color-Changing Penetration-Type Cathodoluminescent Phosphor Screens

W. Lehmann, Westinghouse R&D Center, Pittsburgh, PA 15235

Electron penetration through solid barrier layers into polycrystalline cathodoluminescent phosphors can be described by a relatively simple mathematical equation which, in turn, permits the computation of color changes available from phosphor blends containing such coated particles. An extension of the analysis covers also multilayer cathodoluminescent films. The calculations permit predetermination of the efficiencies and color characteristics of such screens and design of screens to meet given specifications.

Abstract No. 157

Preparation, Optimization, and Cathodoluminescent Properties of a Line Emission Penetration Phosphor

T. E. Clark* and **C. T. Burilla,** Sperry Research Center, Sudbury, MA 01776 and **G. Knutsen,** Sperry Flight Systems, Phoenix, AZ 85036

A line emission penetration phosphor, suitable for use in high brightness CRT's, has been developed. The penetration phosphor powder particles consist of a coating of small red emitting YVO_4:Eu particles on the surface of larger core particles containing a nonluminescent surface layer of $La_2O_2SO_4$:Tb and a green emitting center of La_2O_2S:Tb. Optimization of this system with respect to brightness and color range has resulted in a material comparable to other high brightness penetration phosphors except for the exploitable advantage of being a narrow band emitter. The preparation, optimization, and cathodoluminescent properties of this system are discussed.

Abstract No. 158

A New Design of Voltage Penetration Phosphor

W. L. Li, Z. X. Zhang, and **S. H. Xu,** Changchun Institute of Physics, Changchun 130021, Jilin, China

A new design of a voltage penetration phosphor of the onion skin type is proposed and demonstrated by a material with its main composition $SrAl_2O_4$, of which the core is activated by Eu^{2+}, emitting in the blue-green region while the exterior is activated by Eu^{3+}, emitting red light under cathode ray excitation. It is prepared by first synthesizing $Sr_{0.80}Ca_{0.10}Ba_{0.05}(Al_{0.97}Ga_{0.03})_2O_4$:$Eu^{2+}_{0.05}$ in a reducing atmosphere and subsequently firing in air to oxidize Eu^{2+} ions in the outer part of the crystals to Eu^{3+}. The color change under different excitation voltages shows the feasibility of this technique.

Luminescence of II-VI Compounds

Abstract No. 159

Recent Advances in Electrical and Optical Properties of II-VI Compound Semiconductors

P. J. Dean, Royal Signals and Radar Establishment, Great Malvern, Worcestershire, WR14 3PS England

The II-VI semiconductors ZnSe, ZnS, and their alloys provide efficient luminescence throughout the visible spectrum and are very suitable for thin film CRT screens and various high-field EL devices made from powders, thin films, or single crystals. Recent renewal of interest in these materials springs from the need for active, thin panel displays, application of improved material preparation techniques and new insights into the control of their electrical and optical properties, long regarded as intractible.

Abstract No. 160

Properties of Low Resistivity N-Type ZnSe Prepared by Organometallic CVD

W. Stutius, Xerox Corporation, Palo Alto Research Centers, Palo Alto, CA 94304

Low resistivity n-type ZnSe has been grown epitaxially on (100) GaAs substrates by a low-pressure low-temperature organometallic CVD process. Aluminum is used as a dopant. The as-grown layers show a strong near-bandgap photoluminescence (PL) peak. The much weaker PL intensity at longer wavelength indicates that the concentration of deep centers is lower than in doped ZnSe prepared by other methods. The relationship between the electrical and the PL properties is discussed.

Abstract No. 161

Luminescence and EPR of Chloride-Doped ZnTe

N. Magnea, K. Saminadayar, D. Galland, J. L. Pautrat,* and **R. Triboulet,** CEN-G/DRF-Physique du Solide, 85 X, 38041 Grenoble, Cedex, France

The shallow hydrogenic donor related to chlorine has been identified from two electron transitions revealed by resonant and photoexcitation spectra. From the shift between 1S and 2P state we obtain $E_D^{Cl} = 20.1$ meV to be compared to $E_D = 18.3$ meV for the "native" donor commonly observed in ZnTe. On the same crystal, a photosensitive and isotropic EPR signal is detected with a well-resolved structure. The characteristics of this signal are $g = 1.964 \pm 0.001$, $A_{Cl^{35}} = 47\ 10^{-4}$ cm. Moreover the hyperfine interaction with Cl^{37} is also observed. All these results indicate that chlorine introduces simultaneously a shallow donor and a deep level in ZnTe, this latter level can be a substitutional Cl^- ion on a Te site.

Abstract No. 162

Photoluminescence Study of Shallow Acceptors in Refined Cadmium Telluride

E. Molva, J. P. Chamonal, and **J. L. Pautrat,*** CEN-G/DRF-Physique du Solide, 85 X, 38041 Grenoble, Cedex, France

We report on the first observation of "two hole" transitions in low temperature photoluminescence spectra of high purity p-type cadmium telluride. The undoped samples reveal two acceptors with binding energies of 108 and 149 meV. Li and Na incorporated by low temperature diffusion introduce hydrogenic acceptor levels at 58 and 59 meV. The accurate binding energies which are obtained are quite different from published data.

Abstract No. 163

Nitrogen as a Shallow Acceptor in ZnSe

B. J. Fitzpatrick* and **P. M. Harnack,** Philips Laboratories, Briarcliff Manor, NY 10549

Nitrogen should be a good acceptor in ZnSe, but no evidence of acceptor action due to nitrogen has been seen in as-grown material. Using epitaxial techniques, evidence of incorporation in a variety of ways has been obtained from photoluminescence and electrical measurements. In LPE material grown at normal temperatures (950°-800°), an exciton with a binding energy of 10.8 meV (typical for a shallow acceptor) has been observed. At higher temperatures, a band at ~2.73 eV is seen, which we believe is the donor-acceptor pair band of the nitrogen acceptor. This band has been seen in material grown from both the liquid and the vapor phase, using several doping sources (NH_3, Zn_3N_2, NH_4Br). We believe that these data indicate that nitrogen is a shallow acceptor with an ionization energy of ~85 meV.

Abstract No. 164

Impurity-to-Conduction Band Electron Transfer Transitions in ZnSe:Co

D. J. Robbins,* P. J. Dean, and **C. West,** Royal Signals & Radar Establishment, Malvern, Worcestershire, WR14 3PS, England

Three weakly-phonon-coupled absorption bands have recently been reported (1) for ZnSe:Co^{2+}, together with several associated luminescence transitions. This paper will report Zeeman and uniaxial stress data for the lowest energy absorption band, strongly supporting an assignment as impurity → CB electron transfer, *i.e.*, $Co^{2+}(d^7) \rightarrow [Co^{3+}(d^6)]e_b$ where e_b is a bound electron with an s-like wavefunction having significant CB parentage. This represents the first positive evidence for such an excited state of a transition metal impurity in any semiconductor. The observation of luminescence from this state with excitation by above-gap radiation suggests that the dominant energy relaxation channel through the Co^{2+} center involves sequential carrier capture.

1. D. J. Robbins, P. J. Dean, S. G. Bishop, and P. Porteous, *Solid State Commun.*, **36,** 61 (1980).

Abstract No. 165

Cathodoluminescence Measurements in the Range of 500-6000V

R. R. Wengert, Siemens AG, Grundlagenentwicklung Bereich Bauelemente, Postfach 801709, D-8000 München 80, Germany

An apparatus is described to perform CL measurements of phosphor brightness and efficiency in the range between 500 and 6000V. The electron beam current at the sample is calibrated by a special method which allows the use of not aluminized samples also. It is shown how the luminous efficiency of ZnS-phosphors and of some reference samples decreases with increasing brightness by current density enhancement at constant voltage. MgO, BeO, and Zn_2SiO_4 proved to be excellent coating materials, but the best efficiency was obtained with uncoated material.

Abstract No. 166

$Zn_{1-x}Cd_xS$:Ag,Al Phosphors for Vacuum Fluorescent Displays

H. Kukimoto,* Tokyo Institute of Technology, Midori-ku, Yokohama 227, Japan, and **K. Morimoto, H. Toki,** and **E. Imaizumi,** Futaba Corp., Mobara, Chiba 297, Japan

Low voltage cathodoluminescence can be achieved with low resistivity phosphors of $Zn_{1-x}Cd_xS$:Ag,Al. We have investigated optimum concentrations of the activator (Ag) and coactivator (Al) impurities especially in yellow ($x = 0.5$) and red ($x = 0.75$) emitting phosphors. The results obtained are good enough for the practical application of these phosphors for vacuum fluorescent displays.

Abstract No. 167

Preparation and Luminescent Properties of ZnS Phosphors with Large Plate Microcrystals

T. Matsuoka,* F. Fukushima, Y. Fukuda, and **T. Nitta,** Matsushita Electric Ind., Co. Ltd., Materials Research Laboratory, 1006 Kadoma, Osaka, Japan

An attempt to taking out more emission produced in phosphor crystals in the screen of a cathode-ray picture tube has been made by means of improvement in the shape of the phosphor microcrystals, *i.e.*, large plate crystals. The optical geometry of the screen of these large plate crystals is certainly improved as compared with the screen constructed from conventional phosphor crystals. The preparation of ZnS large plate crystals by sulfurizing of basic zinc sulfate is presented.

Abstract No. 168

Multiple Emission from Tellurium-Doped Cadmium Sulfide Photoelectrodes and Implications Regarding Excited-State Communication

A. B. Ellis,* B. R. Karas, H. H. Streckert, and **R. Schreiner,** Dept. of Chemistry, University of Wisconsin-Madison, Madison, WI 53706

Samples of single-crystal, n-type, 100 ppm Te-doped CdS (CdS:Te) exhibit two emission bands (λ_{max} ~510, 600 nm) when excited at several ultraband gap wavelengths as the photoanode in photoelectrochemical cells (PEC's) employing aqueous sulfide electrolyte. Examination of decay times and the influence of PEC variables (temperature, electrode potential, electrolyte) on the two emission bands can be used to infer the existence of excited-state communication. These results and communication schemes compatible therewith are presented.

Abstract No. 169

Light Emission and Current in A-C Thin Film Electroluminescent Devices

H. Venghaus and **D. Theis,*** Siemens AG, FL OHL, D 8000 München 83, Germany

The brightness of ZnS:Mn (1%) a-c thin film electroluminescent structures was measured as a function of conduction current i_c on samples with 0.6 μm thickness of the ZnS layer. We found a correlation between $\Delta i_c/\Delta V$ well above threshold and the brightness saturation level; the steeper $\Delta i_c/\Delta V$, the higher the maximum brightness (V = driving voltage). We show that i_c is limited by clamping of the electric field over the ZnS layer, and suggest that lower brightness is due to inactive regions in our samples, which do not contribute to conduction and consequently to light output.

Abstract No. 170

Energy Spectra of the Bulk and Interface States within ZnS:Mn A-C Thin Film EL

K. W. Yang* and **S. J. T. Owen,** Dept. of Electrical and Computer Engineering, Oregon State University, Corvallis, OR 97330 and **D. H. Smith,** Tektronix, Inc., Display Research Group, Beaverton, OR 97077

The energy spectra of both bulk and interface states within ZnS:Mn a-c thin film EL devices have been studied by optical probing and TSC measurements. The effects of these states on the electrical characteristics are described. Systematic measurements have been developed to detail the energy distribution of both types of states and to identify the physical basis for their generation.

Abstract No. 171

The Preparation and Characterization of Tb and TbF_3 Doped ZnS Thin Film Electroluminescent Devices

R. T. Tuenge,* R. E. Coovert, and **W. A. Barrow,** Tektronix, Inc., Beaverton, OR 97077

Green-colored a-c thin film electroluminescent devices have been prepared by coevaporating ZnS with either metallic terbium or TbF_3 powder. A saturation brightness of 200 fL at 5 kHz drive frequency with efficiency as high as 0.3 L/W has been obtained for ZnS:TbF_3 films sandwiched between highly insulating layers. The concentration dependence of the brightness, efficiency, and decay time of the TbF_3 luminescent center has been determined. Postdeposition thermal annealing effects on device performance have been examined. The role of fluorine in improving the efficiency of this rare earth doped EL device is discussed.

Abstract No. 172

Electrochemical Process in DCEL ZnS (Mn,Cu) Devices

D. Pecile, C. Brunel, J. Thomas, and **A. Godin,** Centre National d'Etudes des Télécommunications, 92220 Bagneux, France

DCEL ZnS (Mn,Cu) devices have gained a renewed interest during the last few years. Powder technique and coevaporation technique are used. In both cases the elaboration of the device requires an electrochemical process called forming. According to a current assumption, copper migrates from the anode and a highly resistive copper-depleted layer is formed. Small signal harmonic analysis gives useful information on that resistive layer. For a typical electroluminescent device the layer thickness is in the micron range.

Abstract No. 173

Effect of Particle Distribution and Second Dopant on the Characteristics of ZnS:Mn DCEL Panels

X. Luo* and **L. Zhou,** Changchun Institute of Physics, Chinese Academy of Science, Changchun, 130021 China

The effect of particle size distribution of ZnS raw materials on DCEL characteristics was investigated. An explanation based on DCEL mechanism, *i.e.*, the high field region being concentrated in a layer of one particle closed to the anode, is presented. Improvement of brightness, efficiency, and lifetime of copper-coated ZnS:Mn phosphors by second dopant were also examined. Photoluminescent spectra, DCEL spectra, and PL excitation spectra of ZnS:Mn,Cu powders and time variation of brightness and of current of DCEL panels are described. The brightness, efficiency, and lifetime of copper-coated ZnS:Mn,Cu DCEL panels are given.

Abstract No. 174

Low Field Recombination at Self-Activated Centers in II-VI D.C.E.L. Cells

M. S. Waite, School of Materials Science and Physics, Thames Polytechnic, London, SE18 6PF, England

Direct current electroluminescent powder cells, with ZnS:Cl and ZnSe:Cl phosphors, show two emission pulses (other than avalanche emission) when excited by rectangular d-c pulse. One appears on the leading edge of the pulse and the other follows the pulse, delayed by 5 → 10 microseconds. The emission corresponds to the SAL at 2.67 eV for ZnS:Cl at 2.0 eV for ZnSe:Cl and appears to involve both thermal and field release of carriers from traps. The effect of temperature is described and the possible relevance to pulse addressed displays discussed.

Abstract No. 175

Kinetics of Radiative Recombination in ZnSe-ZnTe Electroluminescence Diodes

F. Firszt and **H. J. Łożykowski,** Institut of Physics Nicholas Copernicus University, 87-100 Toruń Grudziadzka 5, Poland 21065

The electroluminescence properties of ZnSe-ZnTe heterostructure grown by liquid phase epitaxy have been investigated by means of T.R.S. The El. spectra was determined in the temperature range 20-300 K. The spectra at low temperature showed four emission bands with maxima at: a = 460 nm, b = 535 nm, c = 628 nm, and d = 635 nm. From the application of T.R.S. to the decay of the four broad band emission peaks it is clear that the a and d emission results from D-A recombination and that the b and c emission results from F-B recombination. The anti-Stokes El. emission are explained by tunneling and Auger mechanisms.

General Session

Abstract No. 176

Synthesis and Characterization of Cerium-Activated Fluoroapatite Phosphors

R. G. Pappalardo* and **T. Peters,** GTE Laboratories, Precision Materials Technology Laboratory, Waltham, MA 02254, and **A. Kasenga** and **C. F. Chenot,** GTE Precision Materials, Towanda, PA 18848

In a search for efficient co-activated phosphors for lamp applications, we have examined the performance characteristics of Ce-activated fluoroapatite phosphors, following on some early work by Henderson and Ranby. A series of calcium and strontium fluoroapatites were prepared, using initially excess fluoride over the standard apatite formulation, and later also charge compensation of Ce^{3+} in order to optimize the emission efficiency both in the u.v. region (singly activated materials) and in the yellow spectral region (co-activated materials). The resulting co-activated phosphors are comparable in plaque brightness to the standard halophosphate phosphors. The Ce-activated fluoroapatite phosphors, though, degrade in efficiency after lamp fabrication noticeably more than the standard halophosphate phosphors. The mechanisms of this phosphor degradation are currently under study.

Abstract No. 177

On Scattering Coefficients of Lamp Phosphors

K. Narita, Toshiba Corp., Consumer Products Engineering Laboratory, 1, Komukai Toshibacho, Saiwaiku, Kawasaki 210, Japan

Although knowledge on phosphor scattering coefficient (s) is essential for theoretical study of fluorescent lamp output, available data are not abundant. Thus measurements of s were undertaken in the wavelength region of 350-700 nm. Samples were sedimented on nonreflecting black plates and the reflectance (R_0) was measured. Values of s were then calculated by a Kubelka-Munk equation which describes the relation between $R_{inf.}$, R_0, coating weight, and s. Data on some representative lamp phosphors are presented. They show little dependence on wavelength in the region mentioned above. Dependence of s on particle size is also discussed.

Abstract No. 178

Kubelka-Munk Theory of the Performance of Pigmented Phosphor Screens

J. R. McColl, GTE Laboratories, Inc., Waltham, MA 02254

Kubelka-Munk theory is extensively and successfully used in the paint and dye industries for calculating reflectance spectra; its use for pigmented phosphors is straightforward. In this work, the theory is intended to treat pigmented phosphor emission spectra and intensity. Calculated results on color shift, reflectance, and brightness loss *vs.* pigment concentration are presented. The calculations are in reasonable accord with experimental results on contrast improvement and optimum pigment level. The calculations bear out the experimental observation that green pigmentation is not advantageous.

Abstract No. 179

Dye-Laser Spectroscopy of Y_2O_3:Eu Lamp Phosphors

R. B. Hunt, Jr.* and **R. G. Pappalardo,** GTE Laboratories, Precision Materials Technology Laboratory, Waltham, MA 02254

Dye-laser excitation was used in detailed studies of the spectral properties of commercial Y_2O_3:Eu phosphors for lighting applications. Computer-controlled measurements of excitation spectra, emission spectra, and emission decay kinetics were performed over the temperature range from 300 K to ~4 K. At the Eu concentrations present in these materials, efficient energy transfer was found to occur between C_{3i} and C_2 sites even at temperatures as low as 55 K. The decay of the dominant emission line at 611-612 nm was generally exponential at ~4 K, but became longer and nonexponential with the increase in temperature up to 300 K.

Abstract No. 180

The Emission Color of $Y_2O_2S:Tb^{3+}$ Phosphor with Dy^{3+} Coactivator

K. Inoue, M. Watanabe, T. Takahara, T. Wakatsuki, and **T. Nishimura,** Toshiba Corp., Electron Tube and Device Div., 72, Horikawacho, Saiwai-ku, Kawasaki-city, Kanagawa, 210, Japan

Luminescence properties of $Y_2O_2S:Tb^{3+}$ phosphor with Dy^{3+} coactivator ($Y_2O_2S:Tb^{3+},Dy^{3+}$) are investigated to obtain effective green emitting phosphor for color picture tubes. The emission color of $Y_2O_2S:Tb^{3+},Dy^{3+}$ phosphor is a desirable yellowish green as compared with that of $Y_2O_2S:Tb^{3+}$ phosphor without the decrease of cathodoluminescence efficiency. This effect is due to the energy transfer between Tb^{3+} and Dy^{3+}. The practical applications of $Y_2O_2S:Tb^{3+},Dy^{3+}$ phosphor are also discussed.

Abstract No. 181

The Relationship between Emission Intensity from Tb^{3+} $^5D_3$,$^5D_4$ Level in LaOBr and Temperature, Concentration

C-S. Shi, W-P. Zhang, and **C-X. Guo,** Dept. of Physics, The University of Science and Technology of China, Hofai, Anhwei, China

The temperature dependence of Tb^{3+} $^5D_{3,4} \rightarrow {}^7F_J$ (J = 0, 1 . . . 6) emission in $La_{1-x}Tb_xOBr$ under u.v. excitation in 300-580 K has been studied. Thermal stability of Tb^{3+} luminescence in LaOBr is much better than in Y_2O_2S and Gd_2O_2S. Concentration dependence of Tb^{3+} $^5D_{3,4} \rightarrow {}^7F_J$ emission in LaOBr under u.v. and cathode ray excitation has been studied also. It is shown that the possible way concentration quenching of $^5D_3 \rightarrow {}^7F_J$ emission is not $^5D_3 \rightarrow {}^5D_4$ cross relaxation, but it is resonance transfer of $^5D_3$ of Tb^{3+} and excitation energy transfer to quenching centers or other shunt.

Abstract No. 182

Mechanism of Energy Transfer from a Trace of Tb^{3+} to RE^{3+} (Eu^{3+}, Sm^{3+}, Dy^{3+}) in Y_2O_2S Phosphor

C-X. Guo, W-P. Zhang, and **C-S. Shi,** Dept. of Physics, The University of Science and Technology of China, Hofei, Anhwei, China

The enhancement effect of cathodoluminescence and ultraviolet excitation luminescence efficiencies of Eu^{3+}, Sm^{3+}, and Dy^{3+} in Y_2O_2S by codoping with a trace of Tb^{3+} have been investigated. The factors responsible for the enhancement are: (*i*) decreasing of bulk charge in the phosphors by addition Tb^{3+}, (*ii*) existing energy transfer from Tb^{3+} to RE^{3+}. The experiments indicate that the sort of energy transfer is not due to a resonance energy transfer, a reabsorption of emission light, and a hole transfer, but it is due to energy transfer of free exciton, into which is changed exciton bound by isoelectronic trap of Tb^{3+} because of thermal disturbance.

Abstract No. 183

Host Sensitization Mechanism of Eu^{3+}-Luminescence in $(Y,In)_2O_3:Eu^{3+}$

H. Yamamoto, Hitachi Ltd., Central Research Laboratory, Kokubunji, Tokyo, Japan

Host sensitization mechanism in the solid solution $(Y_{1-x}In_x)_2O_3:Eu^{3+}$ is discussed on the assumption that Eu^{3+} works as a recombination center. The charge transfer band of Eu^{3+} is found below the absorption edge for small x, but is buried in the fundamental absorption when $x \gtrsim 0.05$. This

result indicates that poor host sensitization in In-rich compositions is due to boiling-off of an electron trapped by Eu^{3+}.

ELECTRONICS/DIELECTRICS AND INSULATION

Fourth International Symposium on Silicon Materials Science and Technology

Abstract No. 184

Basic Technology for VLSI

Y. Tarui,* Electrotechnical Laboratory, 1-1-4 Umezono, Sakura-mura, Niihari-gun, Ibaragi 305, Japan and **Y. Takeishi,** Toshiba Corp., Semiconductor Device Engineering Laboratory, Komukai, Saiwai-ku, Kawasaki 210, Japan

Original scope and main achievement of basic study of VLSI technology in the VLSI Cooperative Laboratories in the past four years are reviewed. Successful results cover a variety of technologies concerning 1 μm or less geometry, such as electron-beam and optical lithography, defects and distortion of silicon wafers, dry processing, various diagnostic techniques, and devices of new structures.

Abstract No. 185

VLSI Trends

E. Bloch, IBM Corp., DSD East Fishkill Facility, Hopewell Junction, NY 12533

VLSI is not just an extension of silicon monolithic circuit development as it was practiced over the last 15 years, but requires a different viewpoint and different approaches to its design, manufacture, and support functions as well as to its application. This paper summarizes the status of design, manufacture, and application of VLSI in the United States today, and discusses the VHSIC program and presents an outlook of its impact on future directions. Emphasis is placed on new requirements that are important to continue the advance of VLSI, particularly packaging, tooling, and design automation.

Abstract No. 186

Fundamental Aspects of Czochralski Silicon Crystal Growth for VLSI

K. E. Benson,* W. Lin, and **E. P. Martin,** Bell Laboratories, Allentown, PA 18103

The major progress achieved during the last four years as related to the science and engineering of large diameter Czochralski silicon crystal growth is reviewed. Our present understanding of some of the important aspects of crystal growth such as growth morphology, dopant distribution, oxygen and carbon incorporation, growth-induced defects, and trace metal impurities is presented. Thermal considerations relating to hot zone characteristics, melt convection, and crystal stress are discussed.

Abstract No. 187

Impurities in Silicon Single Crystals—A Current View

T. Abe, K. Kikuchi, S. Shirai, and **S. Muraoka,** Shin-Etsu Handotai Co., Annaka-Shi, Gunma-ken, 379-01 Japan

Various requirements for wafer quality become severe. Resistivity distributions within a wafer and slice-to-slice variations of resistivity should be in a narrow range. In addition, oxygen-concentration and distribution control of CZ wafers becomes of importance. Low oxygen concentrations are desired for suppression of oxygen precipitates and obtaining higher resistivity. Whereas, for purposes of intrinsic gettering and of restraining of slippage due to heat cycle, higher concentrations are required. Therefore, oxygen concentration is chosen to meet the device processes. For impurities incorporated accidentally such as carbon and some heavy metals, their concentration should be as low as possible. In this paper, recent progress of impurity control is reviewed and important roles of doped nitrogen and gold are pointed out.

Abstract No. 188

Photoluminescence Analysis of Silicon Crystals

M. Tajima,* Electrotechnical Laboratory, Umezono, Sakura-mura, Ibaraki 305, Japan, **T. Masui,** and **T. Abe,** Shin-Etsu Handotai Co. Ltd., Annaka, Gunma 379-01, Japan, and **T. Iizuka,** Electrotechnical Laboratory, Umezono, Sakura-mura, Ibaraki 305, Japan

The photoluminescence (PL) method for the quantitative impurity analysis has been calibrated by using the samples whose impurity concentrations are controlled by the neutron-transmutation doping and vacuum multipass float-zone techniques. The simultaneous determination of B and P in commercial Si crystals has been successfully performed with the use of the revised calibration curves. The various types of oxygen donors which are generally produced in CZ crystals by annealing at temperatures ranging from 400° to 800°C have been investigated by the PL method together with the resistivity and infrared absorption measurements. The effects of heat-treatment history and carbon on the generation and annihilation of the oxygen donors are discussed.

Abstract No. 189

CZ Silicon Crystals Grown under a Transverse Magnetic Field

T. Suzuki, K. Hoshi, N. Isawa, and **Y. Okubo,** SONY Corp., Semiconductor Div., Asahi-cho, Atsugi City, Kanagawa, Japan 243

We have applied a transverse magnetic field during the CZ silicon crystal growth stage, and found that the convection and temperature fluctuation in the molten silicon were remarkably suppressed by the magnetic field of more than 1500G. The growth striations caused by the thermal convection can be reduced by the magnetic field. This method permits the control of oxygen concentration ($\sim 1 \times 10^{17}$ atoms/cm^3), the lower defect generation, and the growth of high resistivity (up to about 300 Ω-cm) crystals.

Abstract No. 190

Control of Oxygen Concentration in CZ Silicon Growth

K. Hoshikawa,* H. Hirata, H. Nakanishi, and **K. Ikuta,** Musashino Electrical Communication Laboratory, Nippon Telegraph and Telephone Public Corp., 3-9-11 Midori-cho Musashino-shi, Tokyo 180, Japan

A control technique for oxygen concentration has been investigated by analyzing an oxygen incorporation mechanism into CZ silicon crystal. Three to five inch diameter ingots with 2 to 8 $\times$ 10^{17} atoms/cm^3 oxygen concentration [calculated by multiplying the infrared absorption coefficient (cm^{-1}) at 9 μm by 2.45 $\times$ 10^{17} atoms/cm^3] have controllably been obtained, at the same time realizing uniform oxygen concentration along the pulling direction and parallel to the growth interface. They have been grown by controlling the crystal and the crucible rotation in conjunction with the circular fluid flow caused by the rotating magnetic field in the three phase a-c heating system.

Abstract No. 191

Mechanisms of Oxygen Incorporation in Czochralski-Grown Silicon

A. Murgai, IBM Corp., General Technology Div., East Fishkill Facility, Hopewell Junction, NY 12533

Oxygen incorporation was studied in Czochralski growth of (100) silicon crystals (diameters: 85-130 mm) pulled from large melts (7-20 kg). Axial variation in oxygen concentration in the crystals was modeled quantitatively through the prevailing rates of silica crucible dissolution, oxygen evaporation at the melt surface, and an equivalent distribution coefficient for oxygen (dependent among other parameters on the crystal growth rate). The radial variation in oxygen concentration was investigated empirically and shown to be controlled primarily by the melt thermohydrodynamics prevailing in the presence of crystal and crucible rotation.

Abstract No. 192

Oxygen-Free Silicon Single Crystal Grown from Silicon Nitride Crucible

M. Watanabe,* **T. Usami,** and **H. Muraoka,** Toshiba R&D Center, Kawasaki-shi, Kanagawa-ken 210 Japan, and **S. Matsuo, Y. Imanishi,** and **H. Nagashima,** Toshiba Ceramics, R&D Center, Hatano-shi, Kanagawa-ken 257 Japan

Crucible materials other than fused quartz have long been tried in vain to grow silicon single crystals. New pure and dense α-Si_3N_4 crucible was made by chemical vapor deposition method. Silicon single crystals without any oxide film on their surface could be grown from the new crucibles, even though nitrogen was dissolved into the melt by slow erosion of crucibles. Not only nitrogen but also oxygen was detected in the single crystals by infrared absorption measurement.

Abstract No. 193

Electronic Characteristics of Float Zone Grown Silicon

L. Jastrzebski* and **P. Zanzucchi,** RCA Laboratories, David Sarnoff Research Center, Princeton, NJ 08540

Due to a characteristically low grown-in defect density and high lifetime relative to Czochralski (CZ) grown silicon, or chemical vapor deposited (CVD) epitaxial films, the use of float zone (FZ) grown silicon for CCD imagers or power devices is of special importance. The need to control and optimize the electrical properties of such devices has generated a great deal of interest in understanding grown-in point and aggregated defects. This work deals with characterization of defects in commercially available, float zone silicon, with an emphasis on the effect which heat-treatment will have on electrical parameters.

Abstract No. 194

Current Aspects of Silicon Material Processing for Solar Cell Application

E. Sirtl, Heliotronic GmbH, Postfach 11 29, D-8263 Burghausen, Germany

In the framework of worldwide long-range efforts to provide real low-cost silicon we would like to characterize silicon quality by the term "terrestrial solar grade" (TSG). This includes economical aspects (set-up, throughput) as well as particular impurity situations. The various types of solar devices and their modification in future years make the present definition of TSG silicon a rather difficult one. Solidification of a silicon melt can be performed in two ways, basically: (*i*) Production of maximum size ingots per time unit, mono- or poly-crystalline, requiring parallel development of unconventional slicing processes, and (*ii*) Growth of sheet- or ribbon-like material to be applied directly in solar cell technology. Accomplishments, trends, and needs in this technology package are discussed.

Abstract No. 195

Photovoltaic Performance Related to Properties of Various Forms of Silicon

H. I. Yoo* and **P. A. Iles,** Applied Solar Energy Corp., City of Industry, CA 91746

The photovoltaic performance of a wide variety of silicon sheet forms is analyzed. The sheets were formed by ingot growth, by casting, or as ribbons. The photovoltaic *I-V* data were supported by other physical measurements. The overall PV performance was correlated with silicon sheet properties such as impurity content, crystalline defects, or physical properties. The analysis led to application of improved processing, to determine present upper limits to the cell performance obtainable from the various sheet forms.

Abstract No. 196

Recent Problems on Oxygen in Silicon

J. R. Patel, Bell Laboratories, Murray Hill, NJ 07974

Since the last review of oxygen in silicon in "Semiconductor Silicon 1977," there has been an explosion of interest in this subject. In particular the behavior of oxygen in silicon subjected to simple and complex thermal treatments has been extensively probed. Recent advances in our experimental and theoretical understanding of the nucleation and precipitation of oxygen in silicon are outlined. Certain areas in which gaps in our knowledge still exist on the fundamental behavior of oxygen in silicon are discussed.

Abstract No. 197

Dislocation Behavior and Mechanical Strengths of Float-Zone Silicon Crystals and Czochralski Silicon Crystals

K. Sumino, The Research Institute for Iron, Steel and Other Metals, Tohoku University, 2-1-1 Katahira, Sendai 980, Japan

Various dislocation processes and the mechanical behavior in both float-zone-grown and Czochralski-grown silicon crystals are investigated by means of *in situ* observations utilizing x-ray topography and high-voltage electron microscopy as well as tensile tests. Oxygen atoms in silicon crystals are shown to affect the behavior of dislocations through their locking action upon segregating on the latter and to be responsible for the large difference in the thermomechanical responses of the two types of silicon crystals.

Abstract No. 198

Plastic Deformation and Preannealing Effects in CZ and FZ Silicon Crystals

Y. Kondo, Nippon Electric Co., Ltd., Basic Technology Research Laboratories, Takatsu-ku Kawasaki 213, Japan

To investigate the oxygen role in plastic deformation of silicon crystals, oxygen-rich (CZ) and -poor (FZ) crystals bent with a static load were yielded by heating from room temperature up to 1100°C with a constant ramp rate (5°C/min). Deformation temperatures measured when plastic deflection reached at 50, 100, 500, and 1000 μm, were correlated with stress (S) as $S \propto \exp(U/kt)$, where $U = 0.68$ eV/1.10 eV in CZ/FZ crystals without preannealing. Preannealing effects (800°C, 1050°C) are also discussed with results of defect observation after chemical etching and oxygen precipitation measured by the infrared (IR) absorption method.

Abstract No. 199

Activation of the Oxygen Donor in Si on a Microscale

P. Rava,* **H. C. Gatos,** and **J. Lagowski,** Dept. of Materials Science & Engineering, Massachusetts Institute of Technology, Cambridge, MA 02139

Concentration profiles of interstitial oxygen were obtained by scanning *IR* absorption in Si crystals and, upon thermal activation at 450°C, oxygen donor profiles were determined with spreading resistance measurements on the identical locations of the oxygen profiles. In contrast to accepted premise, it was found that the oxygen donor concentration is not consistently related to the oxygen concentration, and that in fact the oxygen donor distribution does not necessarily coincide with the oxygen distribution. Vacancy distribution and vacancy gettering defects are believed to be intimately related to oxygen donor activation. It was also found that the type of dopant present influences the donor activation rate.

Abstract No. 200

Oxygen Precipitation in Czochralski Silicon

R. A. Craven, Monsanto Co., St. Louis, MO 63166

Experimental data are presented which indicate that oxygen can precipitate both homogeneously and heterogeneously. Samples with high densities of heterogeneous nucleation centers have been used to determine the solubility of oxygen. $O_s/cm^3 = 10^{(20.77-4210/T(K))}$ (ASTM). The critical radius for an oxygen precipitate at 1100°C for $1.5 \times 10^{18}/cm^3$ is extrapolated to be 10Å. Ambient gas, time, and temperature affect the size of denuded zones on material with controlled interstitial oxygen content. N_2 + 3%HCl + 3%O_2 ambient during denuding anneal results in small (<5 μm) or nonexistent denuded zones. O_2 and N_2 ambients can have ≥ 10 μm denuded zones under identical conditions. The influence of carbon on oxygen precipitation is also discussed.

Abstract No. 201

Oxygen and Carbon in Heat-Treated Silicon Crystals

C-C. Hsu, B-K. Sun, S-N. Jiang, W-N. Wang, and **C-Y. Sung,** Institute of Semiconductors, Academia Sinica, Peking, China

Czochralski crystals commonly used for LSI manufacture have been heat-treated over a wide temperature-time range to explore the basic annealing behavior of oxygen and carbon in silicon. The nature and an electronic structure model of the thermal donor has been put forward and discussed. The mechanism of carbon suppression effect on the formation of the thermal donor has been also studied. The precipitates of oxygen, carbon and their interaction after heat-treatment at 700°C and 1050°C have also been studied using x-ray topography, IR absorption, TEM, AES, and ESCA. The precipitate formation depends strongly upon the conditions of the crystal growth.

Abstract No. 202

Nucleation and Growth of Oxide Precipitates in Silicon

H. F. Schaake,* R. F. Pinizzotto, and **S. C. Baber,** Texas Instruments Inc., Dallas, TX 75265

The nucleation of oxygen precipitation in silicon at very low temperatures ($T < 525$°C) manifests itself as the well-known oxygen donor. Recent *IR* data support a model in which the donors are a result of precipitates with a coherent interface between the precipitate and the matrix, *i.e.*, that they arise from Guinier-Preston zones in silicon. Concurrent with this, and extending to higher temperatures, precipitates with a semicoherent interface are energetically feasible.

Abstract No. 203

Oxygen Precipitation in Czochralski Silicon—Mechanism and Application

N. Inoue, K. Wada,* and **J. Osaka,** Musashino Electrical Communication Laboratory, Nippon Telegraph and Telephone Public Corp., Musashino-shi, Tokyo, Japan

Oxide precipitate nucleation, growth, and shrinkage in CZ silicon have been investigated. Both annealing temperature and oxygen content dependencies of the nucleation rate are well explained by the classical nucleation theory suggesting homogeneous nucleation taking place below 950°C. Carbon content dependence is ambiguous in the presently available content range ($\leq 10^{16}$ atoms/cm^3). Preexisting precipitates in as-grown crystals are nucleated in growth cooling through homogeneous and heterogeneous mechanisms. The precipitates larger than 100Å proceed with oxygen diffusion-limited growth, whereas with the smaller precipitate growth is retarded. Precipitate shrinkage and denuded zone formation mechanisms in highly precipitated wafers are discussed. The above results have successfully been utilized in establishing the intrinsic gettering conditions.

Abstract No. 204

Denuded Zone and Microdefect Formation in Czochralski-Grown Silicon Wafers by Thermal Annealing

K. Kugimiya,* S. Akiyama, and **S. Nakamura,** Central Research Laboratory, Matsushita Electric Ind. Co., Ltd., 3-15 Yagumonakamachi, Moriguchi, Osaka 570, Japan

Thermally induced microdefects in Czochralski-grown silicon wafers were examined by transmission electron microscopy, optical microscopy and infrared absorption measurements. The formation of denuded zones was dependent on the content of interstitial oxygen and the out-diffusion of oxygen subsequently followed by the heat-treatments for nucleation and growth. No microdefect was found in denuded zones. Homogeneous nucleation was assumed to take place at the low temperature annealing of silicon supersaturated by oxygen while inhomogeneous nucleation at the high temperature annealing.

Abstract No. 205

The Influence of Precipitate Size and Capillarity Effects on the Surface Denuded Zone in Thermally Processed Cz-Wafers

R. W. Series, K. G. Barraclough,* and **W. Bardsley,** RSRE Malvern, Great Malvern, Worcestershire, England

The effect of heat-treatments on the formation of a near-surface zone denuded of microdefects has been studied in Czochralski-silicon wafers. Controlled denuded zones and bulk intrinsic gettering centers can be produced by a two-stage process involving first a high temperatuture (*e.g.*, 1150°C) then a low temperature (*e.g.*, 750°C) heat-treatment, whereas the reverse process produces a nonuniform denuded zone. The results illustrate the importance of oxide precipitate size on denuded zone formation in the silicon wafer.

Abstract No. 205A

Oxygen Precipitation in Silicon Between 600° and 800°C

K. Tempelhoff,* R. Gleichmann, and **B. Hahn,** Akademie der Wissenschaften der DDR, Zentralinstitut für Elektronenphysik, 1080 Berlin, Germany

Electron microscopic and infrared absorption investigations were undertaken to identify the nature of oxygen precipitation-induced defects in Cz-silicon at annealing temperatures below 800°C. Precipitation kinetics and kinds of formed defects in this temperature region are different from those at higher temperatures. The primary defect in the 600°-800°C region is the "rod-like" which is stable below 700°C. Above 700°C a simultaneous transformation into elongated (<110>) narrow dislocation loops (b = a/2 <110>) occurs. The influence of a low temperature preannealing of Cz silicon wafers has been studied.

Abstract No. 206

Minority Carrier Lifetime and Reverse Current Inhomogeneities in PN Diode Arrays Resulting from Microdefects in Czochralski Grown Silicon Crystals

C. J. Varker* and **J. D. Whitfield,** Motorola Inc., Semiconductor Research and Development Laboratories, Phoenix, AZ 85008, **K. V. Rao,** Texas Instruments Inc., Houston TX 77001, and **L. J. Demer,** Dept. of Metallurgical Engineering, University of Arizona, Tucson, AZ 85721

Computerized test methods are used to investigate the spatial distribution of minority carrier lifetime (τ) and reverse current (I_R) on gated N^+P diode arrays fabricated on "dislocation free" Czochralski crystals. Computer graphic displays are used to reveal spatial inhomogeneities in τ and I_R measurements which are dependent on the axial and radial distribution of microdefects in the crystal and the subsequent thermal history during wafer processing. Experimental results are presented which provide graphic evidence for electrical inhomogeneities resulting from impurity precipitation involving oxygen, defect nucleation, and growth, for a two-step thermal anneal and oxidation process.

Abstract No. 207

The Behavior of Transition and Noble Metals in Silicon Crystals

K. Graff* and **H. Pieper,** AEF-TELEFUNKEN, Semiconductor Div., D-7100 Heilbronn, Germany

3 d transition metals from Ti to Ni and the noble metals Cu, Ag, Au were diffused intentionally into n- and p-type silicon crystals. The deep level impurities were investigated by means of DLTS. Measured activation energies of the levels in the silicon bandgap were reported as well as cross sections of the majority carriers. Results were compared to values published in the literature and related to the position of the respective element in the periodic table.

Abstract No. 208

The Role of Metallic Impurities in the Formation of Haze Defects

W. T. Stacy, Philips Research Laboratories Sunnyvale, c/o Signetics Corp., Sunnyvale, CA 94086, **D. F. Allison,** Signetics Corp., Sunnyvale, CA 94086, and **T-C. Wu,** Philips Research Laboratories Sunnyvale, c/o Signetics Corp, Sunnyvale, CA 94086

Using a TEM equipped with an x-ray spectrometer, we have found haze microdefects to be decorated by either Cu- or Ni-containing precipitates. Contact with stainless steel

(Ni, Cr, Fe) induced Ni-decorated defects; Fe and Cr were found only in the region of contact. Cu-decorated defects were found at lower densities in wafers which had not been intentionally contaminated.

Abstract No. 209

Thermal Conditions for the Formation of Fog in Silicon Wafers

D. E. Hill, Monsanto Co., Electronics Div., St. Louis, MO 63166

The formation of "S" pits, or fog, on silicon wafers after oxidation and preferential etching is shown to be relatively independent of the details of the oxidation process. Fog is also shown to be a precursor for the formation of surface stacking faults occurring after subsequent oxidations. Sequential oxidation experiments indicate that fog forms during the cooldown after oxidation at temperatures below 500°C.

Abstract No. 210

The Nucleation and Growth of Silicon via Chemical Vapor Deposition

W. A. P. Claassen* and **J. Bloem,** Philips Research Laboratories, Eindhoven, The Netherlands

An experimental study of nucleation of silicon on SiO_2 and Si_3N_4 substrates shows the influence of hydrogen adsorption notably on SiO_2 substrates at temperatures below 900°C. Additional experiments on the growth of silicon from silane show that the growth rate at high temperatures is only influenced by the total pressure. At low growth temperatures the growth rate becomes independent of the total pressure but instead the partial pressure of hydrogen is an important parameter.

Abstract No. 211

Growth Reaction Mechanisms of Vapor Phase Si Epitaxy

T. Aoyama, Y. Inoue, and **T. Suzuki,** Hitachi Research Laboratory, Hitachi, Ltd, 4026 Kuji-cho, Hitachi-shi, Ibaraki-ken 319-12 Japan

Gas phase reaction mechanisms in Si epitaxial growth with horizontal rf heated reactor have been investigated by means of *in situ* measurements of reaction gas concentration profiles using mass spectrometry and *IR* absorption spectroscopy. Five species, $SiCl_4$, $SiHCl_3$, SiH_2Cl_2, $SiCl_2$, and HCl are observed in the reaction gas. Not only $SiCl_4$ (source gas) but the other Si chlorides contribute to the surface growth reaction; the primary reaction species which contribute to the growth rate shift from $SiCl_4$ to the other Si chlorides with decreasing gas velocity and with increasing temperature and position along the susceptor.

Abstract No. 212

Electrical Properties of Grain Boundaries in Silicon Bicrystals

L. J. Cheng and **C. M. Shyu,*** Jet Propulsion Laboratory, California Institute of Technology, Pasadena, CA 91103

Experimental results of a study on electrical properties of grain boundaries in boron-doped silicon bicrystals grown by Czochralski technique are reported. The techniques used include temperature dependence measurement of zero-bias conductance and deep level transient spectroscopy. The double-depletion-layer model of the electronic structure of grain boundaries in semiconductors is employed for data analysis. The result not only reveals important information concerning properties of the boundaries in silicon, but also shows the suitability of the combined technique used for grain boundary characterization. (The research described in this paper was carried out at Jet Propulsion Laboratory, California Institute of Technology, and was sponsored by the Low-Cost Solar Array Project of the U.S. Department of Energy through an interagency agreement with NASA.)

Abstract No. 213

The Mobility and Lifetime of Injected Holes and Electrons in a-Si-H Thin Films

C. Y. Chang, Y. K. Fang, W. L. Lin, and **W. C. Hsu,** Research Institute of Electronics & Electrical Engineering National Cheng Kung University, Tainan, Taiwan, China

The mobility and lifetime of electrons and holes in a-Si-H films are measured as a function of temperature. Hall effect measurement and transit time experiment methods are used for mobility measurement, while the transient *c-t* method is adopted as lifetime test. The a-Si-H films were prepared by rf glow discharge in silane under various conditions, *i.e.*, various substrate materials, substrate temperature, various dopant gases, and rf power. The experimental results indicate that the mobility and lifetime are varied with these process factors. A model base on Mott's assumption is used to interprete these effects.

Abstract No. 214

Very Thin Gate Insulators

S. K. Lai, IBM T. J. Watson Research Center, Yorktown Heights, NY 10598

Very thin gate insulators (50-200Å) are very important in electrically alterable read only memories (EAROM's) and future VLSI circuits. The major problem in silicon dioxide is yield and reliability. The reliability problem may be controlled by the use of trapping. Such oxides also show increased resistance to radiation damage and with reduction of bulk effects, interface effects beome important. Thermally grown silicon oxynitride films may be used as a substitute for oxide films. (This research was supported in part by the Defense Advanced Research Projects Agency, and was monitored by the Deputy for Electronic Technology (RADC) under contract No. F19628-78-C-0225.)

Abstract No. 215

Ionizing Radiation Effects in SiO_2 and RF Plasma Annealing

T. P. Ma, Dept. of Engineering and Applied Science, Yale University, New Haven, CT 06520

In the first part of this paper process-induced radiation effects in SiO_2 are reviewed. The physical phenomena pertinent to such effects are presented in terms of MOS device properties. Several possible mechanisms are discussed. In the second part, the rf plasma annealing technique is presented. Experimental results are given to demonstrate the effectiveness of this technique in removing radiation damage. The annealing mechanism is discussed based on a recombination-enhanced defect reactions model.

Abstract No. 216

The Role of the Si/SiO_2 Interface in Silicon Oxidation Kinetics

J. D. Plummer, Integrated Circuits Laboratory, Stanford University, Stanford, CA 94305

For many years the basic linear parabolic growth law of Deal and Grove has been used to describe silicon oxidation kinetics. For thinner oxides and lower temperature oxidations, the overall rate limiting step is the reaction at the Si/SiO_2 interface. This is modeled in the Deal/Grove growth law as an effective rate constant k_s. Substantial work in recent years has been aimed at understanding the physical mechanisms "hidden" in k_s. Considerable indirect evidence exists that generation of silicon interstititals and consumption of silicon vacancies at the Si/SiO_2 interface during oxidation occurs. Such evidence includes the correlation of oxidation rate dx/dt with: substrate doping level, enhanced diffusion coefficients of substitutional impurities in the substrate, growth and retrogrowth of oxidation induced stacking faults and oxide charge densities. This paper reviews the evidence for the role of point defects in the oxidation process including recent results obtained at Stanford, and attempts to provide an overall perspective of the oxidation process and its relationship to other phenomena.

Abstract No. 217

The Structural and Chemical Properties of the $Si-SiO_2$ Interface

C. R. Helms, Stanford Electronics Laboratories, Dept. of Electrical Engineering, Stanford University, Stanford, CA 94305

This paper reviews recent studies of the $Si-SiO_2$ interface by transmission electron microscopy, Rutherford backscattering, ellipsometry, x-ray photoelectron spec-

troscopy, and Auger electron spectroscopy. Results of these studies are viewed within the framework of a nanoscopic model of the interface with amorphous SiO_2 matched to crystalline silicon. Properties of this interface are compared to more idealized models of the interface such as cristobalite to silicon.

Abstract No. 218

Experimental Evidence for the Interpretation of MOS Interface States

M. Schulz, Institute for Applied Physics, University of Erlangen, D-8520 Erlangen, Germany

Interface state distributions have been analyzed in state-of-the-art clean MOS capacitors by CC-DLTS, conductance technique, and infrared optical excitation. The comparison of the results obtained by different techniques and the properties of interface states observed are discussed in the light of models for interpretation. The observations are in favor for tunneling into a discrete level in SiO_2 at an energy position which is dependent on the distance from the interface.

Abstract No. 219

Laser Annealing—A Novel Regime of Crystal Growth

J. M. Poate, Bell Laboratories, Murray Hill, NJ 07974

The ability to rapidly heat the surface layers of solids using pulsed irradiation has created a new area of Si crystal growth. Liquid phase regrowth takes place typically at velocities of 1-5 m/sec. We review the phenomena associated with this exceptionally rapid regrowth. In particular we consider the trapping of dopants at the liquid-solid interface.

Abstract No. 220

Fast Anneal Processing for Improved Device Performance

J. F. Gibbons, Stanford Electronics Laboratories, Stanford University, Stanford, CA 94305

This paper reviews the potential of both pulsed and cw beam processing for VLSI applications. Use of these processes for annealing source/drain implants in small MOSFET structures is discussed first, followed by a description of beam-processed silicides for gate and interconnect layers. The paper concludes with a discussion of MOSFET devices made directly on beam recrystallized polysilicon and their potential advantages for VLSI.

Abstract No. 221

Enhanced Solubility of Implanted Carbon in Silicon after Q-Switched Laser Annealing

A. G. Cullis, R. Series,* H. C. Webber, and **N. G. Chew,** Royal Signals and Radar Establishment, Great Malvern, Worcestershire, England WR14 3PS

Q-switched ruby laser annealing of high dose carbon implants in silicon has been investigated. In addition to the formation of SiC as monitored by electron microscopy, *IR* absorption measurements showed that high concentrations of substitutional carbon had been introduced into the regrown lattice, exceeding the equilibrium solubility limit by about 2 1/2 orders of magnitude. The mode of formation and the thermal stability of this metastable solution are described.

Abstract No. 222

Pulsed Laser Annealing of BF_2^+-Implanted Amorphized Silicon

A. Bhattacharyya,* L. A. Reinisch, and **B. G. Streetman,** Coordinated Science Laboratory, University of Illinois, Urbana, IL 61801

We present here for the first time a detailed theoretical and experimental investigation of the dynamics of surface melting and regrowth and electrical activation of BF_2^+-implanted amorphous silicon annealed with a Q-switched Nd:glass laser ($\lambda = 1.06\ \mu m$). The technique of finite difference equations is used to solve the one-dimensional heat conduction equations for the solid and liquid phases taking into account the temperature dependence of all the parameters involved, especially the substrate parameters to give us a realistic model. The melting model is supported by time-resolved reflectivity measurements using a He-He and an Ar laser. We use SEM to investigate the channelling pattern to study the quality and orientation of crystalline regrowth. To investigate the electrical activation after laser annealing we determine the sheet resistivity as a function of the laser fluence.

Abstract No. 223

Pulsed Electron Beam Annealing of Ion-Implanted Semiconductors

A. V. Dvurechensky, B. P. Kashnikov, and **L. S. Smirnov,** Institute of Semiconductor Physics, Novsibirsk, USSR

High-intensity electron beams have been used to anneal ion-implantation damage in Si and GaAs. The electron energy was both the higher and lower the threshold value of defect production. The high energy (1 MeV) electron irradiation was shown to reduce the temperature of the defect annealing more than by 100°C. The comparison of annealing at high (1 MeV) and low (10 keV) energy of electrons allows to develop the important role of the Frenkel pairs at reordering of the implanted layer.

Abstract No. 224

Semiconductor Materials Engineering via Defect Diagnostics

G. A. Rozgonyi (Present address: Visiting Scientist, CNET, 38240 Meylin-Grenoble, France) Bell Laboratories, Murray Hill, NJ 07974

We describe how optical, x-ray, and electron microscopy, coupled with preferential chemical etching and the basic crystallography of dislocations, as presented by the Thompson tetrahedron, can be used as tools for understanding what is structurally imperfect in the fabrication of electronic devices. The author has used the information obtained with this approach to obtain engineering solutions to basic problems encountered turning crystal growth and high temperature processing of semiconductors, *e.g.*, in gettering, laser annealing, lattice matched heterojunction lasers and in visualizing microscopic crystal growth processes.

Abstract No. 225

Silicides: Which, Why, and How?

S. P. Murarka, Bell Laboratories, Murray Hill, NJ 07974

The low resistivity of the silicides, which can be formed directly on silicon, polysilicon, or SiO_2, makes these silicides highly attractive for lowering of the resistance at the gate and interconnect level and of the contact resistance in the windows. In this paper the usefulness of the various silicides in the silicon integrated circuits is reviewed with special reference to the disilicides of refractory metals molybdenum, tantalum, titanium, and tungsten.

Abstract No. 226

A Comparison of $TiSi_2$ Films Formed by Alloy Sputtering and Coevaporation

R. F. Pinizzotto* and **K. L. Wang,** VLSI Device Technology Branch and **S. Matteson,** Materials Characterization Branch, Texas Instruments Inc., Dallas, TX 75265

Refractory metal silicides are currently being considered as replacements for polysilicon as the gate electrode in MOSFET's. These materials have low resistivities, are compatible with current IC processing technology, and can be passivated using thermally grown oxides. This paper presents our evaluation of one candidate silicide, $TiSi_2$, formed either by sputtering of a $TiSi_2$ target or by the coevaporation of Ti and Si. Emphasis is placed on the effects of the sample preparation procedure on the physical properties of the films. Low angle x-ray diffraction, Auger electron spectroscopy, Rutherford backscattering spectroscopy and transmission electron microscopy were used for sample characterization. Film resistivity was monitored as a function of both anneal time and temperature. Determination of the electrical properties of MOS capacitors and FET's is in progress. It is proposed that differences in the

oxygen concentration in the films due to processing are responsible for the difference in the annealing characteristics.

Abstract No. 227

One Micron Single Polycide (WSi_2 on Poly-Si) MOSFET Technology

M. Y. Tsai,* H. H. Chao, L. M. Ephrath, B. L. Crowder, A. Cramer, R. S. Bennett, C. J. Lucchese, and **M.R. Wordeman,** IBM T. J. Watson Research Center, Yorktown Heights, NY 10598

An n-channel single level polycide (WSi_2 on poly-Si), 22.5 nm gate oxide technology, using electron-beam direct writing for lithography with minimum feature size of 1 μm, has been developed to fabricate NMOS circuits. Low resistance (2.7 $\Omega/\square$) polycide interconnections and small dimension (1 μm) devices are the unique features of this process. A six-mask polycide process has been implemented for single-polycide dynamic RAM applications. This polycide process is to be presented. Devices with normal characteristics and functional dynamic RAM arrays are achieved by this technology.

Abstract No. 228

Low Temperature CVD Growth of Tungsten Disilicide

W. I. Lehrer and **J. M. Pierce,*** Fairchild Camera and Instrument Corp., Research and Development Laboratory, Palo Alto, CA 94304

A process is described for preparing bilayer films of Si and WSi_2 at 600°C by sequential deposition of Si and W using SiH_4/N_2 and WCl_6/H_2 at atmospheric pressure. The resulting films were analyzed before and after annealing with Rutherford backscattering, x-ray diffraction, TEM, and resistivity monitoring. During W deposition, a crystalline WSi_2 layer grows on the Si layer with grain size the order of 10 nm. After anneal, the grain size is 30-50 nm and the electrical resistivity is as low as 65 $\mu\Omega$-cm.

Abstract No. 229

Phosphorus-Doped Molybdenum Silicide Films for LSI Applications

S. Inoue, N. Toyokura, T. Nakamura, and **H. Ishikawa,** Fujitsu Laboratories Ltd., 1015 Kamikodanaka, Nakahara-ku, Kawasaki, 211, Japan

Phosphorus-doped molybdenum silicide has been developed as a gate and interconnecting material for LSI's. The doped silicide was able to diffuse phosphorus into silicon substrate, to provide good ohmic contact to silicon, and to produce highly reliable MOS gates. The doped silicide was deposited by co-sputtering Mo and Si in Ar containing PH_3. Phosphorus was doped uniformly in the as-deposited films. In wet O_2 oxidation at low temperature, the oxidation rate of doped silicide was enhanced as in that of doped polysilicon, the oxidized surface of the doped silicide (Mo/Si = 0.5) is rough and that of the Si-rich doped silicide (Mo/Si = 0.35) is smooth. The excess silicon in Si-rich silicide on Si was precipitated at the silicide/Si interface, and the film was recrystallized as a double layer of $MoSi_2$ and Si after high temperature annealing.

Abstract No. 230

Molybdenum Silicide: Is It Suitable for Interconnections in VLSI?

P. Cappelletti, F. Mori, G. Pignatel, and **G. Ferla,*** SGS-ATES, Agrate Brianza, Milano, Italy, **F. Nava** and **G. Ottaviani,** Istituto di Fisica, 41100 Modena, Italy

Molybdenum silicide has been used as a metallization scheme for providing interconnections at low resistance in silicon devices. A systematic investigation has been performed on molybdenum-silicon interaction. Molybdenum film deposited on silicon produces only $MoSi_2$ after annealing. Oxygen and carbon eventually contained in the original metal film are segregated at the silicide boundaries. $MoSi_2$ sputter deposited originally amorphous is crystallized after annealing. Annealing in SiO_2 promotes the growth of SiO_2 and the formation of metal rich phases. The impurities play a relevant role. Data on the stress associated with volume change during recrystallization are presented. Various systems to reduce stress are discussed.

Abstract No. 231

Dry Etching for VLSI—A Review

L. M. Ephrath, IBM T. J. Watson Research Center, Yorktown Heights, NY 10598

Dry etching in rf generated plasmas is currently used in semiconductor manufacturing and development labs to pattern a number of films including silicon, silicon compounds, resist, and aluminum. A variety of reactors are used which differ markedly in geometry; for example in the area ratio of electrode to ground and in the position of substrates. In this review, four tools are contrasted: a barrel-type plasma etcher, a radial flow reactor, a reactive ion etching system, and a flexible diode reactor. Etching characteristics of each are described and related to the physical features of the reactor.

Abstract No. 232

Effects and Chemistry of the Addition of Oxygen-Containing Compounds to Halocarbon Plasmas

F. H. M. Sanders* and **J. Dieleman,** Philips Research Laboratories, 5600 MD Eindhoven, The Netherlands

In plasma etching the etch rates of polysilicon and photoresist as well as the etch homogeneity are influenced by adding an oxygen containing compound to, *e.g.*, a CF_4 plasma. While the selectivity of polysilicon to photoresist decreases with increasing oxidant content, the homogeneity increases. The effects of O_2, CO_2, or NO on the selectivity and the homogeneity are compared for the etching of polysilicon in a barrel etcher. The differences in etch rates of polysilicon and photoresist, and in the positions of the maximum etch rate are discussed in light of mass spectrometrical studies on these systems.

Abstract No. 233

Anisotropic Etching of Polysilicon and Metal Silicides in Fluorine Containing Plasma

W. Beinvogl* and **B. Hasler,** Siemens AG, FL HLT 41, Otto-Hahn-Ring 6, D-8000 München 83, Germany

Results on reactive sputter etching of polysilicon and silicides in a parallel plate reactor are reported. The dependence of the etching behavior on various process parameters has been investigated. Results obtained with CF_4 and SF_6 are compared. In an SF_6-plasma poly-Si is etched without undercut under the photoresist mask whereby both selectivity to SiO_2 and homogeneity are acceptable. Anisotropic etching of polycide double layers has been achieved whereby the etching behavior of the silicide was found to depend on metal concentration and layer preparation.

Abstract No. 234

Plasma Oxide FET Devices

A. K. Ray* and **A. Reisman,** IBM T. J. Watson Research Center, Yorktown Heights, NY 10598

Polysilicon gate FET devices were fabricated with optical lithography using plasma oxidation alone or in combination with thermal oxidation and the characteristics of these devices were compared to those fabricated using conventional high temperature oxidation. Plasma oxide devices had higher threshold voltages and higher sheet resistivity of the n^+ junctions compared to thermal oxide devices. Other device characteristics were found comparable. Plasma oxide devices have some distinct advantages over thermal oxide devices in terms of lower processing temperatures, junction depth containment, and dopant depletion.

Abstract No. 235

A Microlithography Scenario

J. H. Bruning, Bell Laboratories, Murray Hill, NJ 07974

This paper presents one view of an anticipated chain of events in the continuing evolution of lithographic technology for semiconductor fabrication. A perspective of the roles, limitations, lifetimes, and overlapping uses of optical, electron, ion, and x-ray lithographies are discussed as seen for the decade of the 1980's.

Abstract No. 236

Multilevel Interconnections for VLSI

P. B. Ghate* and **C. R. Fuller,** Texas Instruments Inc., Semiconductor Research and Development Laboratories, Dallas, TX 75265

Multilevel interconnections promise improved circuit performance and also a better utilization of chip area for active components. In this paper, multilevel interconnection requirements of both bipolar and MOS VLSI circuits are reviewed. The use of overlap vias *vs.* nested vias for maximum packing density and the metal coverage problems on oxide steps are examined. Also, a discussion of the film microstructure, electromigration-induced failures, and the VLSI interconnection reliability is presented.

Abstract No. 237

Submicron Ohmic Contacts on n-Type Polysilicon for Integrated Circuits

J. Y. Chen, G. Eckhardt, and **L. D. Hess,** Hughes Research Laboratories, Malibu, CA 90265

Properties of Al and W:Ti ohmic contacts on polysilicon were studied as a function of annealing procedures and contact geometry down to submicron dimensions. The test structures employed were horizontal-type polysilicon resistors with self-aligned contacts. Laser-annealed contacts were found to possess superior properties when compared to furnace-annealed contacts. Surface as well as interface morphology were markedly improved due to the elimination of interdiffusion, and contact resistance was significantly reduced.

Abstract No. 238

Considerations Regarding Gettering in Integrated Circuits

C. W. Pearce, Western Electric, Allentown, PA 18103; **T. E. Seidel** and **L. E. Katz,** Bell Laboratories, Allentown, PA 18103

A collection of processing techniques, collectively referred to as gettering methods, have been routinely used to compensate for the inadequacies of device fabrication processes. Gettering as a sub-branch of processing technology has grown in fundamental understanding and multiplicity of methods. This paper reviews the advances of the past several years. In particular, the effectiveness of gettering techniques for the fabrication of VLSI devices is discussed. For example, in such sophisticated processes a single gettering treatment is often inadequate to control all the defects and process contamination developed during the process, and multiple gettering steps are often required.

Abstract No. 239

Heavy Metal Gettering by Segregation Annealing

G. F. Cerofolini and **G. Ferla,** SGS-ATES, 20041 Agrate, Milano, Italy

Gettering by segregation annealing is a technique to remove metal impurities directly compatible with any MOS technology. It consists of a heat-treatment at moderate temperature (700°-900°C) for some hours, that allows metal impurities to segregate in p^+ and n^+ regions (scribe lines, contacts, or back side). This technique succeeds in reducing the concentration of generation-recombination centers below their levels of detectability.

Abstract No. 240

Impact of a Chlorine Oxidation on the Properties of Silicon Bulk Defects

C. Claeys,* G. Declerck, and **R. Van Overstraeten,** K. U. Leuven, ESAT Lab., 3030 Heverlee, Belgium, **H. Bender, J. Van Landuyt,** and **S. Amelinckx,** Universiteit Antwerpen, RUCA, 2020 Antwerpen, Belgium

The first part of the paper reviews the results on defect behavior during a chlorine oxidation reported in the literature since the last semiconductor silicon symposium. Important phenomena like, *e.g.*, the interstitial oxygen gettering, the inhibition effect, and the use of a Cl implantation for defect annihilation are analyzed. By using both preferential etching techniques and high voltage electron microscopy, the bulk behavior of the defects is studied. Some important new results on the in-depth distribution of the defects are discussed. In a last part of the paper, some practical considerations on the device applications of the use of a chlorine oxidation for defect annihilation are given.

Abstract No. 241

Annealing Effect of Mechanical Damage on Minute Defect, Heavy Metal and Oxygen Atom in Silicon Crystal

Y. Takano,* H. Kozuka, M. Ogirima, and **M. Maki,** Hitachi Ltd., Central Research Laboratory, Kokubunji, Tokyo, Japan 185

This paper is divided into three parts. The first part deals with the characterization of induced mechanical damage and the second part shows the gettering effects of the mechanical damage on minute defects and heavy metals. In the last part, it is shown that interstitial oxygen atoms in CZ crystals are enhanced to precipitate by mechanical damage during annealing. The mechanism of these effects is discussed in detail.

Abstract No. 242

Process Modelling with High Oxygen Content CZ Silicon

D. Huber, P. Stallhofer, and **M. Blätte,** Wacker-Chemitronic GmbH, D-8263 Burghausen/Obb., Germany

High oxygen content silicon offers the potential of a built-in internal or intrinsic getter. This getter has to be activated in different ways. One way is a special preannealing process which has some drawbacks for the following device processing. The getter can be activated by the device processes. But then special precautions have to be taken depending on the applied device technology.

Abstract No. 243

The Predominant Intrinsic Point Defects in Silicon: Vacancies or Interstitials

U. Goesele, and **H. Foell,** IBM T. J. Watson Research Center, Yorktown Heights, NY 10598, **W. Frank** and **H. Strunk,** Max-Planck-Institut fur Metallforschung, Stuttgart, Germany

At present, three essentially different point defect models have been proposed for silicon claiming that either predominantly vacancies or predominantly self-interstitials or both types of point defects in similar numbers are present in silicon under thermal equilibrium conditions. We review recent experimental and theoretical results on anomalous diffusion effects and on the diffusion of gold in silicon which clearly demonstrate that, contrary to common belief, the predominant intrinsic point defects in silicon are self-interstitials and not vacancies.

Abstract No. 244

Defects Produced in Silicon by High Energy Electron and γ-Irradiation and Their Effects upon Recombination Lifetime

S. D. Brotherton* and **P. Bradley,** Philips Research Laboratories, Redhill, Surrey, RH1 5HA, England

The defects produced by 1 and 12 MeV electrons and Co^{60} γ-rays have been studied in n-type silicon as a function of device processing. The introduction rates of the A-center and the E-center were found to be influenced by the process history of the slice as was the annealing characteristic of the divacancy. By examining the recombination lifetime in devices with different divacancy:A-center ratios it is shown that neither trap alone is responsible for lifetime control.

Abstract No. 245

The Use of Photoinjection to Determine Minority Carrier Lifetime and Doping Level Profiles of Low-Doped MOS Structures

U. Efron* and **J. Grinberg,** Hughes Research Laboratories, Malibu, CA 90265

The proposed method, aimed at independently determining doping level and minority carrier lifetime profiles of

semiconductors, is based on substituting the thermally generated charge with an externally photoinjected charge. The MOS device is first pulsed into deep depletion. A delayed photopulse is then applied to the sample causing partial collapse of the depletion region. The changes in fill-time and capacitance *vs.* the photocharge collected are then measured. This data is then used to determine minority carrier lifetime and doping level profiles.

Abstract No. 246

Bird's Beak Configuration of Isolation Oxide in Bipolar Technology

R. Lemme, Siemens AG, Integrated Circuit Div., Munich, Germany, and **H. Oppolzer,** Siemens AG, Research Laboratories, Munich, Germany

Selective oxidation provides isolation for bipolar IC components. The edges of the recessed oxide areas show a bird's head profile. Transmission electron microscopy of cross-sectional specimens was used to image this configuration with high accuracy. The variation of the shape of the bird's beaks with respect to the process parameters for the mask (thicknesses of pad oxide and nitride) and to oxidation parameters (temperature, pressure) are discussed in terms of oxidation kinetics and stress from the Si_3N_4 film.

Abstract No. 247

Crystal Defects Induced by Local Oxidation of Silicon

G. Franz, B. O. Kolbesen, and **H. Strunk,** Siemens AG, Grundlagenentwicklung Bauelemente, D-8000 München 80, Germany and Max-Planck-Institut für Metallforschung, D-7000 Stuttgart 80, Germany

Oxide-nitride-edge dislocations (OND) and stacking faults (ONSF) can be formed during local oxidation of silicon wafers for bipolar circuits with oxide isolation. These defects can cause malfunction of the devices by, *e.g.*, diffusion pipes. They can be eliminated: (*i*) by decreasing the stresses induced at oxide-nitride-edges both by optimizing the masking oxide-nitride-sandwich and the oxidation conditions taking advantage of the viscoelastic behavior of oxides and (*ii*) by reducing dislocation sources and nuclei for ONSF, in particular the impurity level.

Abstract No. 248

Wet HCl Oxidation of BBr_3 Open Tube Diffused Bases

D. C. Ahlgren, IBM General Technology Div., East Fishkill Facility, Hopewell Junction, NY 12533

Steam oxidation using a 1:1 mixture of concentrated hydrochloric acid and deionized water has proven to be a good method for reducing contamination and increasing oxide thickness uniformity. Here, we explore the use of "wet HCl" in the oxidation of a BBr_3 open tube diffused base on VLSI transistors. We show increased uniformity of post base oxidation sheet resistance, final device p' sheet rho, and transistor β. The three effects are due to increased oxide thickness uniformity achieved with a "wet HCl" base oxidation process.

Abstract No. 249

A Study of Dislocations Induced in Emitter Phosphorus Diffusion during Silicon Planar Transistor Production: Generation, Elimination and Effect on Characteristics

N. D. Stojadinović and **R. S. Popović,** Faculty of Electronic Engineering, University of Nis, Beogradska 14, 18000 Nis, Yugoslavia

It is shown that under certain conditions of emitter phosphorus diffusion, diffusion-induced dislocations and emitter edge dislocations can become the same dislocations, originally created inside diffused emitter areas, and then, during emitter oxidation, displaced towards the edges of these areas. It is shown that among dislocations induced in emitter phosphorus diffusion, emitter edge dislocations represent the main source of low frequency noise. We suggest a new method in which the gettering action of the emitter phosphorus diffusion itself is sufficient to ensure satisfactory characteristics.

Abstract No. 250

Test Vehicles for Measurement and Analysis of VLSI Lithographic and Etching Parameters

T. F. Hasan,* D. S. Perloff, and **C. L. Mallory,** Signetics Corp., Advanced Technology Center, Sunnyvale, CA 94086

The increasing complexity of VLSI processes and equipment makes techniques for automated measurement, collection, and analysis of data crucial for the control of critical process parameters. In this paper we discuss the use of such techniques for the characterization of a number of lithographic and etching parameters. These include registration accuracy, lens distortion effects, dimensional control, and etching uniformity associated with 10:1 wafer stepper lithography. Each of the techniques to be described involves automated data collection and analysis using commercially available equipment and rapid feedback of information by means of easily interpreted graphics displays.

Abstract No. 251

A Modular Concept for a Bipolar Oxide-Isolated Test Vehicle

R. Klein, R. O'Connor, W. Wright,* and **S. Hutchings,** Digital Equipment Corp., Hudson, MA 01749

A modular test chip for an oxide-isolated bipolar ECL process is presented. The advantages and constraints of the modular concept are outlined. The structures on the test chip are designed to provide an evaluation for many areas of integrated circuit engineering. Examples of different areas are shown: resistor modeling; design rule testing and development; and defect density measurements. These areas and the strategies for evaluating them are discussed.

Abstract No. 252

Test Patterns for a Bipolar Process Using High-Reduction Projection Printers

S. Wetterling, Tektronix, Inc., Beaverton, OR 97077

High-reduction optical projection printers expose only a limited area at a time, repeating this exposure many times over each wafer. The key problem in designing wafer test patterns for processes using this equipment is to minimize the consumption of the limited print field. A cellular approach is presented which adapts to a wide range of die sizes while providing comprehensive information about process parameters and device characteristics. Several novel test structures are discussed.

Abstract No. 253

A Technique for Identifying, Characterizing, and Analyzing Critical Integrated Circuit Process Parameters

L. W. Linholm,* R. L. Mattis, and **R. C. Frisch,** Electron Devices Div., and **C. P. Reeve,** Statistical Engineering Div., National Bureau of Standards, Washington, D.C. 20234

In order to control a developmental integrated circuit process, micro-electronic test structures can be used to measure the degree of process control. Test results from these structures must be obtained and interpreted in a timely fashion in order to be used for correcting or improving the process. This paper describes techniques for determining and displaying critical process parameters in forms convenient for characterizing the intrawafer variation of these parameters.

Abstract No. 254

A Test Pattern for the Evaluation of Bipolar Integrated Circuit Processes

C. M. Drum* and **P. T. Panousis,** Bell Laboratories, Allentown, PA 18103

A test die has been designed and used extensively for the d-c electrical characterization of several bipolar IC processes. The die includes a variety of IC structures including resistors, diodes, and transistors as well as structures for the measurement of sheet and contact resistances, linewidths, and alignment displacements. Representative results are presented in the form of computer-generated distributions, scatter plots, and vector alignment displacement plots.

Abstract No. 255

A Review of Submicron Device Modelling

P. K. Chatterjee, Texas Instruments Inc., Dallas, TX 75265

Physical understanding of submicron device phenomena is the key to the efficient use of these structures in circuits and the invention of new device structures. The major emphasis in submicron device models has been the influence of geometry and high field transport on active devices. At submicron geometries, modelling of parasitic devices like interconnection and isolation are important in determining circuit operation and performance. A review of the status of active and passive device models is presented.

Abstract No. 256

Oxidation Induced Point Defects in Silicon—A Review

D. A. Antoniadis, Massachusetts Institute of Technology, Cambridge, MA 02139

This paper reviews effects of process induced point defects in silicon from the standpoint of oxidation enhanced diffusion (OED) and oxidation stacking faults (OSF). It briefly reviews the current understanding of intrinsic diffusion mechanisms in silicon and outlines the competing theories. General models are presented that can explain OED and OSF behavior in a great range of temperatures and times and at various substrate orientations.

Abstract No. 257

Modeling Anomalous Phenomena in Arsenic Diffusion in Silicon

R. B. Fair, Bell Laboratories, Reading, PA 19604

A unified model of arsenic diffusion in silicon is presented which can be used to explain a number of anomalous phenomena such as (*i*) incomplete electrical activation, (*ii*) low temperature enhanced diffusion, (*iii*) the emitter push observed for the As/Ga combination, (*iv*) two-dimensional effects at window edges, (*v*) the difference between chemical-source As diffusion and ion-implated As diffusion, and (*vi*) As pile up at a growing Si/SiO_2 interface.

Abstract No. 258

Modelling of Double-Diffusion Processing

N. Mallam, C. L. Jones, and **A. F. W. Willoughby,*** Dept. of Mechanical Engineering, The University, Southampton, Hants, England SO9 5NH

Results of a computer simulation of sequential arsenic/boron and arsenic/gallium diffusion processes are presented, together with a preview of current progress in understanding interactions in double-diffusion processing. Interactions included in the model incorporate the Fermi-level effect, the electric-field effect, and excess point defect generation. Diffusion equations were solved numerically using finite difference techniques, and simulated profiles produced are shown to model experimental profiles very closely, in the specific cases examined.

Abstract No. 259

Measurement of Local Diffusion Coefficients in Planar Device Structures

C. Hill, Plessey Research (Caswell) Limited, Allen Clark Research Centre, Caswell, Towcester, Northants., England

A marker technique is described which permits accurate measurements of local diffusion coefficients of dopants in silicon under processing conditions. The use of marker slices incorporating a buried dopant layer, an inert marker zero and a built-in calibration scale enables accuracy of 300Å in diffusion profile movement in volumes down to 10^{-8} ccs. A systematic study of oxidation-enhanced diffusion coefficients has been made with the technique and the origin of apparent anisotropy identified.

Abstract No. 260

Grain Growth Mechanisms in Polysilicon

L. Mei, M. Rivier, Y. Kwart, and **R. W. Dutton,** Integrated Circuits Laboratory, Stanford University, Stanford, CA 94305

The electrical characteristics of polycrystalline silicon layers are intimately related to their grain structure. This paper discusses a comprehensive study of grain structure of poly under a variety of doping and process conditions. A theoretical model of grain growth has been developed and implemented in the SUPREM process simulator and comparisons of simulated results of grain size with those measured by transmission electron micrographs for As, P, and B-doped poly are presented and discussed. The results show that n-type dopants increase the grain growth rate whereas p-type dopant has a negligible effect.

Abstract No. 261

SUBMODAN—A Composite Process/Device Simulation System for Short-Channel MOS FET's

S. Onga,* **M. Konaka, K. Taniguchi, H. Iwai,** and **L. M. Dang,** Toshiba Research and Development Center and Toshiba Semiconductor Engineering Device Laboratory, Kawasaki-city 210 Japan

A composite process/device simulation system, SUBMODAN, which directly analyzes various characteristics of a short-channel MOS FET starting from the very process parameters, is developed. The system is composed essentially of two separate simulators, one for process simulation by improved SUPREM II and the other for original two-dimensional device simulation, interlinked with each other across a memory file. Several examples based on SUBMODAN are presented: (*i*) optimum ion-implantation condition to minimize punch-through currents in short-channel MOS FET, and (*ii*) threshold voltage sensitivity *vs.* process parameters etc., and also results simulated are discussed, comparing with experimental results.

Joint General Session

Abstract No. 262

Silicon Film Characterization by Correlation of Surface Analysis and Electrical Data

G. D. O'Clock, Jr.,* **S. L. Kruchten,** and **T. E. Brady,** Perkin Elmer, Physical Elect. Div., Eden Prairie, MN 55344 and **C. L. Gruber** and **L. D. Feisel,** Dept. of Electrical Engineering, South Dakota School of Mines and Technology, Rapid City, SD 57701

Auger, x-ray photoelectron spectroscopy, and electrical performance data can be combined to provide information on band structure, surface contamination, and interface quality for thin semiconductor films. Thin polycrystalline Si film structures, applicable to solar cells, were analyzed with these techniques. The data reveal a p$^+$p degenerate to nondegenerate doping profile with near-surface inversion and semi-insulating surface layer for Si-on-Al films grown at substrate temperatures of 577°C.

Abstract No. 263

A Novel Contactless Method for Measuring Collector/Isolation P-N Junction Capacitance in LSI Wafers

R. L. Verkuil, IBM Corp., East Fishkill Facility, Hopewell Junction, NY 12533

We have found that a combination of VHF inductive coupling (for photoconductivity sensing) and electrostatic coupling (for photovoltaic sensing) can provide a contactless indication of collector/isolation p-n junction capacitance. The photoconductivity and photovoltaic signals are used to yield an effective change in junction capacitance, per change in junction voltage, which increases monotonically with increasing junction capacitance. Good agreement is shown between conventional contacting capacitance measurements and the contactless method.

Abstract No. 264

Pulse Scanning C-V Technique for the Analysis of Carrier Generation in Si

S. Kawazu, T. Matsukawa, and **H. Nakata,** Mitsubishi Electric Corp., LSI Research and Development Laboratory, 4-1 Mizuhara, Itami, Hyogo, Japan 664

A very simple and sensitive new technique is presented which can be applied to determine the carrier generation lifetime in the depletion layers of MOS diodes. This method is based on the measurements of the transient capacitance before and after the carrier generation in the depletion layer. Carrier generation at the edge of the field oxide was measured by this method to improve the refresh time of MOS dynamic RAM's.

Abstract No. 265

Microscale Characterization of Heteroepitaxial Silicon-on-Sapphire by Scanning Photovoltage Measurements

L. Jastrzebski* and **G. W. Cullen,** RCA Laboratories, David Sarnoff Research Center, Princeton, NJ 08540, and **J. Lagowski,** Massachusetts Institute of Technology, Cambridge, MA 02139

The measurements of photovoltage spectroscopy provide a powerful means for nondestructive, contactless characterization of silicon-on-sapphire films in terms of defect levels, minority carrier trapping centers, and band structure. In present work the photovoltage measurements have been extended to characterize on a microscale (30 μm resolution) level of inhomogeneities in as grown SOS epilayers and inhomogeneities introduced by processing. Studies of SOS material homogeneities are considered to be of primary importance for device applications because some characteristics of SOS circuits, *e.g.*, stand-by leakage current can be limited by defective regions of unknown origin present in SOS layers.

Abstract No. 266

Investigation of Threshold Voltage Variations of Ion-Implanted Depletion and Enhancement-Mode MOSFET Devices

S. W. Netherton,* NCR Microelectronics, Colorado Springs, CO 80907 and **G. M. Oleszek,** University of Colorado, College of Engineering and Applied Science, Colorado Springs, CO 80907

In VLSI technology depletion-mode device V_T variation is much larger than enhancement-mode device V_T variation over many tested devices. This work will investigate the sensitivities of various process parameters in V_T control. Using Suprem II process simulation and fabricated devices it was determined that V_T variations are to first order ion-implant dose dependent for enhancement-mode and depletion-mode devices. Enhancement-mode V_T directly correlated with oxide thickness variation in conjunction with increasing ion-implant dose levels.

Abstract No. 267

Analysis of the "Write" and the "Erase" Operations in a Floating-Gate MNOS Memory Device

R. Abderrassoul* (Current address: SMU, Dallas, TX 75275) and **M. Shabana,** Dept. of Electrical Engineering, University of Alexandria, Alexandria, Egypt

The "Write" operation affected through charging the floating gate by avalanche-injected electrons from the underlying silicon substrate is analyzed. The avalanche-injection ratio and the charge accumulated on the floating gate are calculated. The "Erase" operation affected by current transport through the nitride layer is investigated. The current-transport mechanisms are analyzed. A geometry-dependent field factor is introduced to account for the presence of the floating gate between the oxide- and nitride layers. The constants of the nitride current component are estimated. Our theoretical model shows excellent agreement with the experimental reported results for both operations.

Abstract No. 268

Charge Storage Model for SNOS Memory Devices

J. A. Topich, NCR Corp., Microelectronics-Components Div., Miamisburg, OH 45342

Theories for charge trapping in MNOS devices deal only with charges near the oxide-nitride interface. Experimental evidence for N-channel SNOS devices show that for positive gate voltages, the dominant stored charge resides nearer to the silicon gate than to the substrate. This charge trapping is due to the difference in the nitride current and the charge injected by the gate. For negative gate voltages charge storage follows the traditional theories. This new model is based on results which show that (*i*) writing speed is essentially independent of memory oxide thickness, (*ii*) charge decay in the written state is not affected by the oxide thickness, (*iii*) quantity of stored charge does not decrease with increased oxide thickness, and (*iv*) the maximum written threshold does not vary with nitride thickness.

Abstract No. 269

ICECREM, A New Program for Process Modeling

H. Ryssel,* K. Hoffmann, K. Haberger, G. Prinke, and **R. Dümcke,** Fraunhofer-Institut für Festkörpertechnologie, 8000 München 60, Germany

A versatile program for process modeling of up to four dopant distributions is described. Steps which can be simulated are: ion implantation, concentration-dependent diffusion (including simultaneous oxidation), etching, and oxide or nitride deposition. The flexibility of the input language and extensive diagnostic features make the program easy to handle. To evaluate measured data of profiling experiments, the program contains an optimization section which extracts optimum parameters for further improvement of process modeling. An extended version of ICECREM is able to simulate two-dimensional process steps.

Abstract No. 270

Capacitance Modeling and Measurements of Fine-Patterned Interconnects

T. Shibata,* N. Shigyo, K. Kurosawa, R. Nakayama, R. Dang, and **H. Iizuka,** Toshiba Research and Development Center, IC Laboratory, 72 Horikawacho, Saiwaiku, Kawasaki, Kanagawa 210, Japan

The capacitance coupling of neighboring interconnect lines constitutes one of the limits to the performance of VLSI circuits. A two-dimensional capacitance simulation was performed and the results agreed quite well with measurements. Electron beam direct writing and reactive ion etching was used to delineate fine patterns of aluminum and polysilicon lines. Discussions are made of the constraints imposed on the design of VLSI circuits based on these results.

Abstract No. 271

Process Design Optimization for Submicron MOS Devices

T. Shibata,* M. Konaka, S. Mimura, R. Dang, and **H. Iizuka,** Toshiba Research and Development Center, IC Laboratory, 72 Horikawacho, Saiwaiku, Kawasaki, Kanagawa 210, Japan

An MOS fabrication process has been optimally designed for transistors with typical channel length of around 0.7 microns. Process parameters have been adjusted to yield desirable device characteristics based on the two-dimensional device simulation. Test devices covering a wide range of physical dimensions have been fabricated and the results are compared with simulation. Discussions are made of several new proposals conceived for the fabrication process of submicron devices.

Abstract No. 272

Process Check Technology in P-MOS IC Fabrication

C. Kim, T. Komatsu, and **K. Shohno,** Sophia University, Faculty of Science and Technology, Kioicho 7-1, Chiyoda-ku, Tokyo 102, Japan

Examples of process checks for the successful fabrication of p-MOS IC are presented. Silicon wafers were confirmed by checking the oxidation rate constants and the density of OSF. The photolithographic process was checked by comparing the test photomask pattern with those of the photoresists and also the films delineated. The cleanness in the quartz tubes was confirmed by checking the amount of contamination originated in donor or acceptor impurities. The yield of p-MOS transistors was estimated by checking those of both MOS and planar diodes.

Abstract No. 273

CW Laser Trimming Phenomenon of Heavily Doped Polycrystalline Silicon

S. Matsumoto,* J. F. Gibbons, and **T. J. Magee,** Stanford Electronics Laboratories, Stanford, CA 94305

A cw laser has been used to trim the resistance of heavily doped polycrystalline silicon. Resistance decrease by laser scans above a certain threshold power and resistance recovery by a first laser scan followed by a second scan are observed, which are similar to phenomena of electrical trimming of resistors. A cw laser is possible to trim the resistance even for the doping concentration less than 1.0×10^{20} cm^{-3}. Resistance decrease is attributed to the slight increase of grain size and the impurity activation, which occur separately.

Abstract No. 274

DSC Mask. An Implant Identification and Contact Coding Method

M. R. Tennyson* and **J. E. Martin,** Rockwell International, Electronic Devices Div., Anaheim, CA 92803

During MOS device fabrication, visible evidence of which ion implantation mask was used—or whether one was used at all—is lacking. A method which eliminates this problem while at the same time saving one step in the fabrication process is described in this paper. The method employs a depletion (D) mask which includes not only all the depletion devices, but also the buried contacts (SC), and so becomes a single DSC (depletion-silicon contact) mask. After this mask is employed for depletion implant, the photoresist is not removed. Another layer of photoresist is applied, and the SC mask is then exposed and developed, opening up buried contacts through both the DSC and SC photoresist layers. Then, at the SC oxide etch, permanent impressions are left in the gate oxide for both the DSC and SC mask revision, part number coding (if used) and alignments. Described in the paper are two particular illustrations of the circuit design innovations made possible by the DSC method: (*i*) implantation coded devices, and (*ii*) simplified strap option circuits.

Abstract No. 275

Semiconductor Device Technology in Chemical Abstracts

C. W. Moulton, Chemical Abstracts Service, Columbus, OH 43210

The extent of the coverage by *Chemical Abstracts* (*CA*) of the primary technical literature concerned with materials and chemical processing as they pertain to semiconductor technology is described. Examples of the content of relevant abstracts and their placement throughout the many *CA* sections are reviewed, and the various indexes to the abstracts described. Means of retrieval of information from the data base via printed, magnetic-tape and on-line services are discussed.

Abstract No. 276

Low Resistivity Spray Pyrolyzed Films

J. Recktenwald,* SRI International Menlo Park, CA 94025, **C. W. Bates, Jr.** and **A. Raza,** Stanford University, Stanford, CA 94305, **J. B. Mooney, L. McIntosh,** and **R. H. Lamereaux,** SRI International, Menlo Park, CA 94025, and **K. Nelson,** Stanford University, Stanford, CA 94305

A study of the preparation of low-resistivity CdS films by chemical spray pyrolysis and subsequent heat-treatment is presented for the range of cation/anion ratios of 1:10 to 1:0.7. The most stable, low resistivity films are obtained at a cadmium excess of 1:0.8 to 1:0.9 and at high substrate temperature. A short heat-treatment produces vacancies and a consequent three-orders-of-magnitude reduction of resistivity.

Abstract No. 277

Barrier Heights at the Polycrystalline Silicon-SiO_2 Interface

T. W. Hickmott* and **R. D. Isaac,** IBM T. J. Watson Research Center, Yorktown Heights, NY 10598

The variation of the position of the Fermi level with doping for degenerately doped silicon is uncertain, both experimentally and theoretically. Capacitance-voltage measurements of the dependence of flatband voltage of polycrystalline-silicon (polysilicon) gate MOS capacitors on oxide thickness are used to measure the position of the Fermi level in degenerately doped polysilicon as a function of the doping of the polysilicon.

Abstract No. 278

Polysilicon Oxide Interface Microtexture and Dielectric Breakdown

T. T. Sheng and **R. B. Marcus,*** Bell Laboratories, Murray Hill, NJ 07974

Transmission electron microscope studies were made of cross sections of oxidized P-doped, As-doped, and undoped polysilicon films and single crystal silicon substrates. The formation of protuberances and silicon inclusions in the polysilicon oxide is noted and mechanisms for inclusion formation are described. High fields at tips of protuberances are the probable cause of lower breakdown field strength of polysilicon oxides and the imaging of these sites as specimen current signals in the SEM.

Abstract No. 279

Temperature Dependent Boron Segregation at the SiO_2/Si Interface

R. K. Jain, Solid State Devices Div., Central Electronics Engineering Research Institute, Pilani (Rajasthan) India 333031

Silicon dioxide layers are widely used in microelectronics as dielectrics, diffusion masks, passivation layers, etc., but still the physics of impurity diffusion and segregation is not well understood. The present paper reports the temperature-dependent results of the boron segregation coefficient at the SiO_2/Si interface based on oxide masking experiments. These results are smaller than previous results obtained by redistribution experiments by one order of magnitude. This study suggests for the first time that oxide masking and redistribution mechanisms are quite different.

Abstract No. 280

Annealing of Gate Insulators at Elevated Pressure

A. Reisman,* J. M. Aitken, A. K. Ray, M. Berkenblit, C. J. Merz, and **R. P. Havreluk,** IBM T. J. Watson Research Center, Yorktown Heights, NY 10598

Post metal annealing studies have been conducted at forming gas pressures up to 50 atm at normal annealing temperatures, on metal-oxide-silicon and metal-polysilicon-oxide-silicon capacitors, as well as on polysilicon gate insulator field effect transistors. These studies were conducted on nonirradiated and irradiated samples to examine the elevated pressure annealing behavior of the above mentioned ambient atmosphere on removal of process-induced radiation damage. Interface trap density, D_{it}, levels following both high pressure and 1 atm forming gas or hydrogen annealing at 400°C were in the $1 \times 10^{10}/cm^2$ eV range, as might have been anticipated. Fixed charge levels, Q_f, on radiation damaged devices were, however, dramatically affected with high pressure annealing, showing only $10 - <20$, or so mV of equivalent residual positive charge in 35 nm insulators as compared to 100-200 mV in the 1 atm annealed devices.

Abstract No. 281

Structural Changes in SiO_2 Films during Thermal Growth

A. G. Revesz, COMSAT Laboratories, Clarksburg, MD 20734

During the thermal growth of SiO_2 films on Si in dry O_2 the rate of the oxidation reaction decreases and the rate of O_2 transport increases with increasing thickness, X, indicating that the structures of the Si/SiO_2 interface and the SiO_2 film change. These effects are particularly pronounced when the oxidation is interrupted by a heat-treatment at X_1, oxide thickness. Then the growth of the new oxide film can be associated with a transient regime provided that the

rate-limiting step is not the O_2 flux. In this case, the initial oxide growth at $X \approx X_n$ is similar to that characteristic of the growth at $X \approx 0$. The initial oxide growth is an extreme manifestation of the nonsteady-state under which the SiO_2 films grow. Their structure and transport properties are related to the growth conditions and can be significantly different from those of fused SiO_2.

Abstract No. 282

Thermal Oxidation of Heavily Doped Polycrystalline Silicon Thin Films

H. Singh and **K. C. Saraswat,** Integrated Circuits Laboratory, Stanford University, Stanford, CA 94305

This study addresses the wet and dry oxidation of LPCVD polysilicon films doped to solid-solubility limit with phosphorus. 0.5 and 1.0 μm thick poly-Si films were deposited on thermally oxidized silicon wafers by low pressure CVD at 620°C and were doped to solid solubility at 1000°C for 30 min with a $POCl_3$ source. Dry oxidations were carried out at temperatures of 1100°, 1000°, 900°, and 800°C for durations of 30 min to 88 hr. Wet oxidations were done at 850°, 800°, and 750°C for durations of 10 min to 4 hr. For the 800°C dry O_2 oxidation, additional samples were used where a 96 hr anneal in N_2 at 800°C, was done prior to the oxidation to segregate phosphorus at the grain boundaries. Oxide and polysilicon thicknesses were measured using an Alphastep profilometer. Sheet resistance measurements were made on the residual polysilicon films after stripping the grown oxides. From these experiments it is seen that concentration-enhanced oxidation of poly-Si is similar in nature to that of single crystal silicon. However, there are fundamental differences because of enhanced dopant diffusion at grain boundaries, dopant segregation at the grain boundaries, and at both the polysilicon-oxide interfaces, and due to the impervious boundary of SiO_2 underneath the polysilicon film.

Abstract No. 283

Si Oxidation in O_2/N_2 in the Presence of HCl

M. K. Lee, Electronic Research and Service Organization, Industrial Technology Research Institute, Hsin Chu, Taiwan, China, **S. D. Liu,** and **C. L. Lee,*** Semiconductor Research Center, National Chiao Tung University, Hsin Chu, Taiwan, China

SiO_2 of 200-900Å grown in O_2/N_2 (1:1) in the presence of various concentrations of HCl have studied for temperatures of 1000°, 1050°, and 1100°C. The linear growth rate, R, can be expressed by an empirical equation

$$R = (1.46 \pm 0.14) \times 10^9 P_{HCl}^{0.40 \pm 0.01} \exp[-(2.15 \pm 0.01)/kT] \text{Å/min}$$

N_2 presence tends to raise the oxidation potential. HCl presence has drastic effect on improving the pin-hole yield, and the pin-hole yield can exceed 90%.

Abstract No. 284

Ohmic Contacts to Silicon by Electroless Nickel-Boron Alloy

R. S. Korde,* **V. K. Gupta,** and **M. S. Tyagi,** Product and Process Development, Transit Semiconductors C.P., 110 Montes Claros 39400 MG Brasil

Owing to its excellent properties, nickel deposited by electroless plating using dimethylamine borane (DMAB) reducing agent bath has been recently suggested as a substitute for gold in military applications. This work investigates influence of type and resistivity of silicon and sintering temperature on contact resistance of this deposit to silicon. The contact resistance has been found to be minimum on n-type wafers in the sintering temperature range 400°-500°C and its value is comparable to that reported for other electroless nickel deposits to silicon.

Abstract No. 285

Thin Tungsten Films by Low Pressure CVD

N. E. Miller* and **R. B. Herring,** Applied Materials, Inc., Santa Clara, CA 95051

A process has been developed for the CVD preparation of thin films of tungsten in a low pressure, hot-walled reactor. The process exhibits surface control of the reaction kinetics leading to excellent uniformity of the deposit over a large load of semiconductor wafers. The thin (1200-1500Å) tungsten films have a sheet resistivity in the range 1.0-1.5 Ω/square. A unique feature is that the tungsten is deposited selectively leading to many types of self-aligned gate or interconnect structures.

Abstract No. 286

Electromigration Resistance of Narrow Metal Lines

S. H. Lee and **P. Brusius,** Honeywell, Solid State Electronics Center (SSEC), Plymouth, MN 55441

Electromigration tests were performed on lines with varying width for three metal systems which have potential usage in VLSI technology: aluminum, Al-Cr-Al sandwich, and Al-4% Cu. Accelerated test results at 200°C ambient and a current density of 3×10^6 A/cm^2 indicate that conventional linear scaling of mean time to failure (MTF) does not hold for geometries approaching the grain size of the metal. The MTF actually increases as the width of metal lines approaches the grain sizes. The results support the conclusions reported on other systems.

Abstract No. 287

Transmission Electron Microscopy of Silicon-Silicide Interfaces

H. Föll, (Present address: Siemens AG, ZFE-FL OPT 32, 8000 Munchen 83, Germany) IBM T.J. Watson Research Center, Yorktown Heights, NY 10598

Ni-, Pd- and Pt-silicides formed on Si substrates have been investigated by TEM, predominantly in the cross-sectional mode. It is found that the native oxide on the Si substrate can crucially influence the silicide formation and properties. Remainders of this oxide are visible in the silicide layers and can serve as diffusion markers. For Ni-silicides unusual epitaxial growth on substrates has been observed.

Abstract No. 288

Effects of Ion Implantation on the Thermal Growth of Pt and NiPt Silicides

T. W. Orent* and **J. A. Sartell,** Corporate Materials Science Center, Honeywell, Bloomington, MN 55420 and **S. Lee** and **T. L. Brewer,** Solid State Development Center, Honeywell, Bloomington, MN 55420

Ion implantation of Pt/Si and Ni/Pt/Si samples caused intermixing of the Pt and Si. The Si LVV Auger peak shape indicated silicide formation; however, the Pt to Si ratio varied with depth. Subsequent annealing caused additional Pt and Si interdiffusion, but the implanted specimens had to be annealed much longer than the unimplanted ones in order to produce equivalent silicide layers. TEM and x-ray diffraction data on the ion-induced changes in microstructure which inhibit the thermal growth of Pt_2Si and PtSi are presented.

Abstract No. 289

Rare Earth Silicide Formation Through Contact Reaction with Silicon

R. D. Thompson,* **B. Y. Tsaur,** and **K. N. Tu,** IBM T. J. Watson Research Center, Yorktown Heights, NY 10598

It has been found that thin films of rare earth metals (Ce, Gd, Dy, Ho, Er) and Y and La react with a silicon substrate to form disilicides at 300°-400°C (1 hr) as an apparent first and last phase. They have been found to be stable up to 900°C though oxidation is always a severe problem. Their measured Schottky barrier heights to n-Si are the lowest yet reported (<0.40 eV). Some alloying with near-noble and refractory metals have been tried and allow the barrier height to be tailored to desired values.

Abstract No. 290

Electron Beam Resist Materials for Microfabrication

O. Kogure, K. Sukegawa, S. Imamura, K. Miyoshi, and **S. Sugawara,** Nippon Telegraph and Telephone Public Corp., Ibaraki Electrical Communication Laboratory, Tokai, Ibaraki, Japan 319-11

Chloromethylated polystyrene and chloromethylated poly-α-methylstyrene have been developed as suitable negative resist materials for E-beam lithography and dry etching technique. The fundamental structure of these resists is the polystyrene which contains benzene rings with view of increasing dry etching durability. As a result of swelling measurement, a suitable developer for high resolution was obtained. Using this developer, the patterns whose linewidth was 3 μm and space was 1 μm were resolved. The obtained width of the narrowest line pattern was 0.1 μm.

Abstract No. 291

All Dry Lithographic Processes and Mechanistic Studies with Poly(methacrylonitrile) and Related Polymers

H. Hiraoka, IBM Research Laboratory, San Jose, CA 95193

Poly(methacrylonitrile) and related polymers have been found to be uniquely suited for all dry lithographic processes. The polymer patterns are generated by thermal treatment followed by oxygen plasma removal. Poly (methacrylonitrile) and copolymer(acrylonitrile-methacrylic acid) yield patterns with positive tone, while poly(α-chloroacrylonitrile) provides negative tone patterns. Oxygen plasma etch rate differs for the exposed and the unexposed parts. The polymer patterns, after heat-treatment, become highly CF_4 plasma etch resistant, providing well-defined Si patterns. Thus, with 2 μm thick films of poly(methacrylonitrile) exposed to a dose of 5×10^{-6} C/cm², 1.5-1.8 μm deep Si patterns are obtained with high resolution by all dry processes; the electron beam resist patterns of 1.5 μm width, depth, and spacing are obtained at 5×10^{-6} C/cm² with the wall angle of 65°. Mechanistic studies including EPR, ESCA, and mass spectroscopic measurements were carried out to provide a mechanism.

Abstract No. 292

A Fully Dried Mask Making Process

T. Yamazaki,* Y. Suzuki, K. Tanaka, and **H. Nakata,** Mitsubishi Electric Corp., LSI Research and Development Laboratory, 4-1, Mizuhara, Itami City, Japan

A fully dried LSI mask-making process has been established by means of the gas plasma. Both photoresist and electron beam resist were exposed by electron beam and developed in a wet air gas plasma. Nevertheless the obtained resist thickness was too thin to resist in a dry etching environment, chromium mask patterns have been successfully etched by the reverse gas plasma etching technique (1) with minimum 2 μm pattern width.

1. T. Yamazaki, Y. Suzuki, J. Uno, and H. Nakata, *J. Electrochem. Soc.*, **126,** 1794 (1979); T. Yamazaki, Y. Watakabe, Y. Suzuki, and H. Nakata, *ibid.*, **127,** 1859 (1980).

Abstract No. 293

Simultaneous Temperature and Etch Rate Measurements during Plasma Stripping of Photoresist

R. A. Bond,* S. Dzioba, and **H. M. Naguib,** Bell-Northern Research, Ottawa, Ont., Canada K1Y 4H7

Conventional approaches used to examine the temperature dependence of photoresist strip rate involve the measurement of initial and final film thickness, strip time, and average temperature representative of the run. This paper reports on a new interferometric method which simultaneously monitors the instantaneous glass substrate temperature and the instantaneous photoresist film thickness. Using this technique, strip rates of AZ 1350J photoresist were determined as a function of substrate temperature during its rise from ambient to the plasma-induced maximum. The resulting Arrhenius plots were nonlinear, indicating a complex dependence of the reaction mechanism on the stripped thickness. This effect is masked in the conventional approach where time-averaged rates are used.

Abstract No. 294

Temperature and Reactant Gas Effects on Plasma-Deposited Silicon Nitride Characteristics

R. Chow, D. Rosler, W. A. Lanford, and **K.-M. Wang,** National Semiconductor, Santa Clara, CA 95051

The properties of plasma-deposited silicon nitride are a strong function of the hardware design and the processing parameters. Previous publication has compared nine commercially available reactors with the emphasis on hardware design. This experimental work is performed in ASM's LPCVD-type reactor with temperature ranges from 150° to 380°C. In addition to the variation of the amount of reactant gas, the effects of replacing ammonia with nitrogen are investigated. The films are characterized with various techniques including nuclear resonance profiling, Rutherford backscattering, laser stress measurement, and IR spectroscopy.

Abstract No. 295

Conductivity Change in Polycrystalline Silicon Films by Plasma Deposition of Si-N Layer

T. Yamaji,* S. Hagiwara, and **S. Ushio,** OKI Electric Industry Co., Ltd., Hachioji, Tokyo 193, Japan

Low doped polycrystalline silicon film, used in MOS LSI as high resistance layer, decreases its electrical conductivity in the order of two or three by plasma deposition of silicon nitride layer on it and annealing. The mechanism of these phenomena has been investigated by electrical and optical measurements and by ESR. The conclusion is that the spins which act as electron traps in grain boundaries of polycrystalline silicon reduce its density after the deposition and annealing.

Abstract No. 296

Silicon Nitride Passivation for Short-Channel Molybdenum Gate Devices

T. P. Chow* and **M. Ghezzo,** General Electric Co., Corporate R&D, Schenectady, NY 12301, **A. J. Steckl,** Rensselaer Polytechnic Institute, Integrated Circuits Laboratory, Troy, NY 12181, and **D. M. Brown,** General Electric Co., Corporate R&D, Schenectady, NY 12301

A VLSI-oriented process which employs silicon nitride for surface passivation of molybdenum gate in MOS structures has been investigated. Plasma etching was used to selectively etch the nitride layer to make contact vias. The process was implemented to fabricate short channel linear and self-enclosed MOSFET's. Device parameters, such as threshold voltage and transconductance, have been characterized. For instance, a linear MOSFET with a nominal length of 1.25 μm and width of 10 μm has a threshold voltage of ~1V and a transconductance of ~260 μmho.

Abstract No. 297

Comparison of PSG Films Deposited by Three Different CVD Methods

Y. Shioya,* M. Maeda, and **M. Takagi,** Fujitsu Ltd., IC Process Engineering Div., 1015 Kamikodanaka Nakahara-ku, Kawasaki, Japan 211

PSG films were deposited using three different methods—plasma-enhanced CVD, low pressure CVD, and atmospheric CVD. The properties of these films were compared. The stress of films deposited by the plasma enhanced and low pressure CVD varies from compressive to tensile as the P concentration increases, while the stress of films deposited by the atmospheric CVD is tensile from the beginning, and its value decreases as the P concentration increases. Films deposited by the plasma enhanced and low pressure CVD are less brittle than those deposited by atmospheric CVD. The IR absorption coefficient (at the P=O bond) for films deposited by the low pressure CVD is about half that for films deposited by the other two CVD.

Abstract No. 298

The Effect of Glow Discharge Characteristics on the Properties of Plasma-CVD Silicon Nitride Films

A. Hiraiwa, K. Mukai, S. Takahashi, and **S. Harada,** Hitachi Ltd., Central Research Laboratory, Kokubunji, Tokyo, Japan

Plasma-CVD silicon nitride films have recently attracted notice of silicon semiconductor engineers, because of their high mechanical strength, good step coverage and low deposition temperature. The film properties are investigated in relation to plasma parameters such as plasma density, elec-

tron temperature, and plasma potential in a parallel plate reactor. The potential difference between plasma and substrate is found to have large effect on the mechanical strength of the films.

Abstract No. 299

Reactive Ion Milling of Aluminum and Alloys

J. Kiddon, J. Sellers, T. Coutumas, and **T. Brewer,** Honeywell, SSEC, Plymouth, MN 55441

The technique of ion milling is applied to the etching of aluminum alloys for VLSI circuit fabrication. Good results in terms of etch parameters, *e.g.*, etch rate, feature definition, redeposition effects, and etch selectivity are demonstrated for reactive ion beams comprised of Cl_2 or chlorine compounds. The effect of substrate heating on these etch parameters is also reported.

Abstract No. 300

VLSI Reactive Ion Beam Etching

F. Z. Custode,* W. Fewer, and **M. Splinter,** Rockwell International, Microelectronics Research & Development Center, Anaheim, CA 92803 and **D. F. Downey,** Varian Associates, Inc./Extrion Div., Blackburn Industrial Park, Gloucester, MA 01930

Modern (sub) micron VLSI device fabrication requires a reliable anisotropic etching technology capable of uniform selective etching of the basic material components; oxide, nitride, silicon (both single and polycrystalline), and aluminum (alloys). Reactive Ion Beam Etching (RIBE) meets these requirements. The results and the predominant mechanisms involved for the etching of these materials with CCL_4, CF_4, and C_2F_6 are discussed. In addition, the dependence of pattern replication on the lithographical techniques employed are reviewed.

Abstract No. 301

Polycide Etching in a Flexible Diode Reactor

R. S. Bennett,* L. M. Ephrath, M. Y. Tsai, and **C. J. Lucchese,** IBM T. J. Watson Research Center, Yorktown Heights, NY 10598

A two-step process for etching polycide structures has been developed for a 1μ single polycide MOSFET technology. The requirements of the etching process are to etch the WSi_2/n^+ polysilicon stack selectively to a thin gate oxide. Etching is carried out in a flexible diode RIE system in a CF_4-O_2 plasma. In the first step, RIE is used to remove the top CVD oxide, the WSi_2 film and about half of the n^+ polysilicon. Plasma etching selectively, but isotropically, removes the remaining polysilicon. Studies were carried out to determine the effect of doping and annealing processes on the plasma etch rate of the film.

Abstract No. 302

An Mo-Nitride/Mo Gate MOS Structure

H. Okabayashi,* K. Higuchi, and **T. Nozaki,** Nippon Electric Co., Ltd., Basic Technology Research Laboratories, Takatsu-ku, Kawasaki 213, Japan

A new metal gate MOS structure is presented. The new gate structure uses a sequentially sputtered bilayer of Mo-nitride and Mo, and was found to have the following superiorities over the conventional Mo gate structure.

1. No anomalous masking ability degradation for self-aligned implantation doping of source and drain regions.
2. Improved uniformity in FET characteristics.
3. Higher stability in long term bias-temperature stressing test.

There are no significant drawbacks in the new gate technology compared with the Mo gate. Therefore, the new gate will be promising for low resistivity interconnects and gates for VLSI's.

Abstract No. 303

The Diffusion Kinetics of Si in Plasma-Deposited SiO_2

L. A. Nesbit, IBM General Technology Div., Essex Junction, VT 05452

The diffusion kinetics of Si in plasma-deposited Si-rich SiO_2 are determined by means of Si precipitate growth in the Si-rich SiO_2 films. Thin films of various compositions are annealed at temperatures ranging from 700° to 1100°C. The Si precipitate size is determined from dark-field transmission electron microscopy.

Abstract No. 304

Silicon Epitaxial Growth on Porous Silicon by Plasma CVD with Silane

T. Itoh,* H. Takai, and **M. Horiuchi,** School of Science and Engineering, Waseda University, Shinjuku-ku, Tokyo 160, Japan

Porous silicon layers formed by anodization of Si single crystal in HF solution keep single crystal structure. Silicon single crystal films are grown on porous silicon layers by means of plasma CVD with the conditions of 800°C of substrate temperature and 0.01 Torr of SiH_4 pressure. Crystalline qualities of the grown films are evaluated by Rutherford backscattering measurements with 400 keV H^+, and it is confirmed that the grown films have good crystalline qualities. Silicon single crystal film on insulator can be obtained by oxidization of the porous silicon layer after silicon epitaxial growth, because porous silicon layers can be oxidized easily.

Abstract No. 305

Plasma-Activated Deposition and Some Properties of PSG Films

A. Takamatsu,* M. Shibata, H. Sakai, and **T. Yoshimi,** Musashi Works of Hitachi Ltd., Kodaira-shi, Tokyo 187, Japan

A plasma deposition method of PSG films was improved in order to obtain good properties for silicon devices. In this technique, a good step coverage and a high breakdown voltage in plasma PSG films in comparison with those of the conventional CVD-PSG films deposited under atmospheric pressure were achieved. The plasma PSG films are capable of applications for the multilayer insulation films and the chip passivation films in a silicon IC technology.

Abstract No. 306

Al/Ti as Contact Metallurgy for VLSI Applications. I. Electrical Properties

C. Y. Ting and **B. L. Crowder,*** IBM T. J. Watson Research Center, Yorktown Heights, NY 10598

The metallization systems Al/Ti and Si/Al/Ti were studied as a contact metallurgy applied to n^+ silicon with contact size around 1 μm^2 and junction depth as shallow as 0.1 μm. Electrical test results show that contact resistivity is lower than that provided by PtSi contact metallurgy, ranging from low 10^{-6} to middle 10^{-7} Ω-cm^2 depending upon surface concentration. Junction leakage is extremely low and has no significant degradation after 5 hr annealing at 400°C or 30 min annealing at 450°C. Contact resistance of 15-20Ω per contact has been achieved on 1 μm^2 size contacts.

Abstract No. 307

Al/Ti as Contact Metallurgy for VLSI Applications. II. Annealing of Radiation Damage in MOSFET's

J. M. Aitken* and **B. L. Crowder,** IBM T. J. Watson Research Center, Yorktown Heights, NY 10598

Al/Ti metallurgy has been used as a contact metal in MOSFET's fabricated with electron beam lithography. The thermal stability of this metallurgy on shallow (0.25 μm) n^+ junctions makes it ideally suited to withstand the extended low temperature anneals required to remove lithography-related damage from the oxides of MOSFET's. The removal of radiation-related charge from polysilicon gate MOSFET's fabricated with electron beam lithography is discussed. In addition, the presence of Ti metal on the filled oxide overlying the polysilicon gate is found to impede the annealing of damage from the oxide. The practical implications and resolution of this problem are discussed.

Abstract No. 308

Improvement of the Crystalline Quality of SOS Films by Beam Processing

R. E. Reedy,* Naval Ocean Systems Center, San Diego, CA 92152 and **T. W. Sigmon,** Stanford Electronics Laboratory, Stanford, CA 94305

In this work we report a detailed investigation of recrystallization and aluminum contamination of channeled Si implanted SOS films. The subsurface damage profile was positioned at the SOS interface. The use of both thermal and scanned CW argon laser annealing is discussed. Results from 2.2 MeV ^4He channeling analysis will be reported showing improved crystalline quality as a function of the implant and anneal parameters. Al redistribution as a function of these parameters has been characterized by SIMS and is reported. Device characteristics (channel mobility, leakage current, and 1/f noise) are reported and correlated to recrystallization parameters.

Abstract No. 309

Regional Low-Level Leakage Distribution and Pipe Characteristics in LSI Silicon Wafers

M.-S. Fung, IBM Corporation, General Technology Div., Essex Junction, VT 05452

This paper reports on the observation of a relationship between transistor pipes and the regional variation of p-n junction characteristics. Probability of a pipe occurrence is discussed in terms of p-n junction low-level leakage, soft characteristics, and premature breakdown. Furthermore, the observation of pattern behaviors in the regional low-level leakage distribution associated with the junction breakdown character is reported, which leads to better insight into the mechanisms of pipe formation.

Abstract No. 310

Microdefects during Phosphorus Diffusion

S. Blackstone, RCA Laboratories, Princeton, NJ 08540, **W. Henry,** RCA, Lancaster, PA 17604, and **L. Jastrzebski** and **W. Fisher,** RCA Laboratories, Princeton, NJ 08540

During a heavy $POCL_3$ deposition using only SiO_2 as a mask, a large number of unintentionally diffused regions (N^+ defects) have been found. These defects are in the order of a few tenths to a few square microns and vary in density from 30 to 60 cm^{-2}. The defects are not related to the pinholes initially present in the masking oxide. This study examines the microdefects as a function of diffusion source. The sources studied were doped oxides, PBr_3, P_2O_5 solid source wafers, and ion implantation. It was found that only PBr_3 and ion implantation are capable of forming N^+ regions without causing N^+ microdefects.

Abstract No. 311

A Preferential Etch Study of Swirls and Stacking Faults in CZ Silicon

K. V. Rao* and **L. J. Demer,** Dept. of Metallurgical Engineering, University of Arizona, Tucson, AZ 85721 and **C. J. Varker,** Motorola Semiconductor Group, Semiconductor Research & Development Laboratories, Phoenix, AZ 85008

"Swirl" patterns in CZ silicon, as revealed by preferential etching with a modified Sirtl etch, are most pronounced in seed-end. A two-step procedure (650°C anneal, followed by ≥800°C treatment) "intensifies" swirl patterns. For comparable oxide thicknesses, the swirl pattern is most severe at 900°C, whereas progressive dissolution of defects is observed for thermal oxidation at 1050° and 1200°C. These results are discussed in relationship to precipitation/dissolution processes involving oxygen inhomogeneities in silicon.

Abstract No. 312

Discriminating Electronically Active and Inactive Defects by Anodic Etching

H. Föll, (Present address: Siemens AG, ZFE-FL OPT 32, 8000 Munchen 83, Germany), IBM T.J. Watson Research Center, Yorktown Heights, NY 10598

An etching method for p-type Si has been developed which allows only electronically active defects or all the defects present in a sample to etch. The method is electrochemical in nature; the different etching behaviors are achieved by using different voltages. The method gives the same qualitative information as otherwise obtained by EBIC and chemical etching. Examples are given and compared to the conventional methods.

Abstract No. 313

Oxygen Striation Observed by Scanning IR Absorption Method in CZ-Grown Silicon Crystals

A. Ohsawa, K. Honda, S. Shibatomi, and **S. Ohkawa,** Fujitsu Laboratories Ltd., Nakahara-Ku, Kawasaki 211, Japan

A new scanning infrared (IR) absorption method has been developed by using IR semiconductor laser diode with the wavelength of 9.02 ± 0.02 μm. By applying the method to longitudinal CZ-grown silicon slices, the microdistribution of oxygen was determined with the spatial resolution of 100 and 200 μm. The correlation between oxygen striation with long period of (1-2 mm) and etch pits striation due to heat-treatment could be revealed. In addition to this striation, the superimposed fine structure with the period of 300-400 μm was observed in etch pits striations. However, the corresponding structure was not observed in oxygen striation. The paper discusses the mechanism of microdefects generation and oxygen striation formation from these and other results.

Abstract No. 314

Exit Chipping in ID Diamond Sawing of Silicon Crystals

L. D. Dyer, Texas Instruments, Inc., Sherman, TX 75090

A fracture analysis is presented of the exit chipping problem in ID diamond sawing of silicon, which is known to be more prevalent in the (100) orientation. Chips that are located where the ID diamond saw last cuts through a crystal are called exit chips in silicon wafer technology. These chips are shown to occur as a result of forces on the slice directed away from the crystal which cause the opening of normal saw microcracks.

Abstract No. 315

The "Feathering" of Striations in LPE and CZ Crystals: An Explanation Using Lateral Microscopic Growth Concepts

E. Bauser* and **G. A. Rozgonyi** (Permanent address: Bell Laboratories, Murray Hill, NJ 07974), Max-Planck-Institut für Festkörperforschung, 7000 Stuttgart 80, Germany

The "feathering", *i.e.*, splitting, recombining, merging, etc., of impurity striations has previously been shown (1) to be related to convective flows associated with both crucible and crystal rotation. We present a kinetic, atomistic model for feathering based on the microscopic configuration of the growth interface, whereby two types of striations are produced during lateral microscopic growth (LμG) of terraced layers (2). Type I striations are parallel to the instantaneous growth interface, while type II striations are the traces of terrace risers or misorientation-induced growth steps. Feathering occurs when type II striations interfere with type I striations or with type II striations.

1. A. Murgai and W. A. Westdorp, in "Semiconductor Silicon 1977," H. R. Huff and E. Sirtl, Editors, p. 83, The Electrochemical Society Softbound Proceedings Series, Princeton, N.J. (1977).

2. E. Bauser and G. A. Rozgonyi, *Appl. Phys. Letters*, Dec. 1980.

Abstract No. 316

High Dose Field Implantation for Channel Stopping

T. C. Gwo* and **W. C. Ko,** Fairchild Camera and Instrument Corp., Mountain View, CA 94042

High dose field implantation by boron ions and subsequent thermal oxidation are known to be causes of oxidation-induced stacking faults and/or dislocations. These bulk defects will degrade the isolation junction be-

tween active devices. This paper discusses the reduction or elimination of these defects by implanting through a layer of thin screen oxide followed by a short annealing cycle in inert gas before thermal oxidation. The mechanism of this defect elimination is presented.

Abstract No. 317

Partial Vacuum Boron Diffusion III (Boron Silicide Phase Growth and Oxidation)

D. Flowers* and **S. Thompson,** Motorola, Phoenix, AZ 85008

Boron silicide formation has been reported in partial vacuum predeposition. It can function as an "infinite" source for boron diffusion. Later it must be oxidized for further wafer processing. This paper presents data detailing boron silicide growth and oxidation at various temperatures. The latter provides information relating to boron redistribution after boron silicide phase clears and the effect on sheet resistance uniformity.

Abstract No. 318

Arsenic and Boron Diffusion in Polycrystalline Silicon

C. H. Lee and **A. C. Yen,** IBM Data Systems Div., East Fishkill Facility, Hopewell Junction, NY 12533

Polycrystalline silicon has been investigated for integrated circuit application for a number of years. The diffusion rates of the popular impurities for semiconductor doping have not yet been directly measured though they are needed for process design modeling for device fabrication. In this work, arsenic and boron diffusion characteristics in the low pressure polycrystalline film are investigated by using the redistribution profiles of ion implantation and the secondary ion mass spectrometry analysis. The diffusion rates and the activation energy in the temperature range from 700° to 1000°C are determined.

Abstract No. 319

Oxidation-Enhanced Diffusion of Boron in Steam

M. R. Oliver* (Present address: Intel Corp., Aloha, OR 97005), **S. Matteson,** and **R. E. Yankley,** Texas Instruments Inc., Dallas, TX 75223

Oxidation enhanced diffusion (OED) of boron has been examined over a range of conditions and some key features have been identified. OED was evaluated for boron-implanted {100} material for steam oxidations in the temperature range of 950°-750°C where it strongly dominates the intrinsic diffusion component. Variations of OED with temperature, pressure, starting material, and local oxidation conditions can be interpreted in a manner similar to that applied to the growth and shrinkage of oxidation-induced stacking faults, where silicon interstitials play a critical role.

Abstract No. 320

Effect of Poly-Si Gettering Scheme on the Quality of Si Epitaxial Film

M. C. Chen,* **J. Y. Lee,** Dept. of Electronics Engineering and the Institute of Electronics, National Chiao Tung University, Hsinchu, Taiwan, China and **H. J. Wu,** Electronic Research and Service Organization, Industrial Technology Research Institute, Hsinchu, Taiwan, China

Poly-Si films in the thickness range of 0.8-5.0 μm were deposited on the back side of Si substrate wafer by the CVD method (silane process) at temperatures ranging from 650° to 800°C prior to the silicon epitaxial deposition. By this pre-epi, in process poly-Si gettering, various epitaxial defects including the stacking faults, hillocks, and S-pits have been significantly reduced, presumably through the removal of the defects nucleation sites by the strain action of grain boundary. Wright etch and anodic etch techniques were used to investigate the defect's features. In addition, the MOS retention time method was also employed to investigate the epitaxial quality. Significant improvement of the retention time yield has been observed.

Abstract No. 321

Si Epitaxial Quality Improvement by Post-Epi Poly-Si Gettering

M. C. Chen,* Dept. of Electronics Engineering, National Chiao Tung University, Hsinchu, Taiwan, China, and **V. J. Silvestri,** IBM T.J. Watson Research Center, Yorktown Heights, NY 10598

Substantial improvement on the quality of silicon epitaxial film by post-epi poly-Si back side gettering has been observed. This manifested by the reduction of defect counts revealed by the Wright etch and anodic etch, and the improvement of carrier lifetime characterized by the increasing MOS retention time. Correlation between the defect etching pit and the retention time of the MOS devices was investigated.

Abstract No. 322

In Situ Monitoring of GaAs LPE Growth Rate

A. Okamoto, S. Isozumi, J. Lagowski, and **H. C. Gatos,** Massachusetts Institute of Technology, Cambridge, MA 02139

In situ determination of the LPE growth process was achieved for the first time employing an electroepitaxial system in which growth is initiated and sustained by electric current through a solid-solution interface. In this system, the resistance increase of the growing layer was accurately and continuously measured and simultaneously converted to layer thickness. This technique provides a powerful means for studying *in situ* growth behavior on a microscale. Results on the transient behavior of the growth rate caused by current modulation and the corresponding characteristics of the LPE layers are discussed.

Abstract No. 323

Characterization of Implanted GaAs and InP Using Raman Scattering

L. L. Abels,* and **S. Sundaram,** Dept. of Physics, University of Illinois, Chicago, IL 60680 and **J. Comas,** Naval Research Laboratory, Washington, DC 20375

The characterization of the III-V semiconductors GaAs and InP implanted with Se and Si has been investigated using Raman laser-induced scattering. The technique is shown to be very sensitive to lattice order and the effects of induced implantation damage and annealing have been studied as a function of implant fluence. The use of Raman scattering for optically characterizing implanted InP and GaAs and the results pertaining to damage production, partial self-annealing during implantation, and lattice regrowth are presented. (Work supported by the Naval Research Laboratory Electronics Materials Program.)

Abstract No. 324

Electrodeposited Silicon and Its Characterization

G. M. Rao,* D. Elwell, and **R. S. Feigelson,** Center for Materials Research, Stanford University, Stanford, CA 94305

Electrowinning of silicon from a solution of inexpensive fluorosilicate has the potential to reduce substantially the production cost of polycrystalline silicon for terrestrial solar cell application. We have recently reported that solar grade silicon could be electrogrown onto graphite and silver from the K_2SiF_6-KF-LiF melt system. Four-probe resistivity, spreading resistance, and Hall mobility measurements were made on these samples. Preliminary data indicated that the room temperature resistivity of electrodeposited silicon on graphite and silver were 1-3 and 0.01-0.05Ω cm, respectively. The unintentionally doped silicon films have a carrier mobility up to 125 $cm^2/V \cdot sec$ with free carrier concentration of the order of 10^{18} cm^{-3}. Depending on the impurities present in the electrodeposits, some silicon samples showed n-type character while the other samples showed p-type. The electrical characteristics of electrowon silicon are discussed, together with fluorescence and Auger analysis data.

Abstract No. 325

Technique to Cast Silicon for Solar Cells

A. Sanjurjo, SRI International, Menlo Park, CA 94025

A technique has been developed to form silicon sheet in a graphite die without the undesirable formation of SiC. Silicon is melted in the presence of a molten salt that wets the silicon, preventing it from reacting with the graphite walls. The silicon coalesces into a pool that is flattened to a disk by a graphite piston. Silicon is solidified in this condition to form flat sheets. High purity NaF has to be used as coating salt. Some Na is chemically pumped into the silicon sheet during melting, but it may be readily extracted by vacuum evaporation. With improved mechanical and thermal control and the use of high purity NaF, it may be possible to produce silicon sheet with geometry and structures suitable for solar cell fabrication.

Abstract No. 326

Modeling of Ambient-Meniscus Melt Interactions Associated with Carbon and Oxygen Transport in EFG of Silicon Ribbon

J. P. Kalejs* Mobil Tyco Solar Energy Corp., Waltham, MA 02254, and **L.-Y. Chin,** Dept. of Chemical Engineering, Clarkson College of Technology, Potsdam, NY 13676

Recent experimental work has shown that significant changes in properties of EFG silicon ribbon are associated with variations in the concentration of CO and CO_2 in the meniscus melt environment (1). Transport processes related to ambient-meniscus melt interactions have been studied by numerical solution of transport equations. Results show that interstitial oxygen observed in ribbon grown from graphite crucibles and with oxygen-containing gases in the meniscus environment is introduced by transport in the meniscus melt.

1. J. P. Kalejs *et al.*, Paper 329 presented at The Electrochemical Society Meeting, St. Louis, Missouri, May 11-16, 1980.

Abstract No. 327

Computer-Controlled Czochralski Puller with Recharging Possibility for Large Diameter Silicon Crystals

B. Altekrüger, H. Birck, and **D. Drechsel,** Leybold-Heraeus, D 6450 Hanau, Germany, and Leybold-Heraeus, Vacuum Systems Inc., Enfield, CT 06082

Improved productivity and crystal quality independent of operator's skill is expected from a newly developed computer-controlled CZ production machine for silicon crystals up to diameter of 6 in. More than 60 parameters of all process steps (automatic pump down, melting, dipping, neck, shoulder, cylindrical part, end cone) are controlled by a micro computer. A new cable drive system instead of a conventional pulling shaft results in a short overall puller height of 5.3m only in spite of its 2.2m pulling length. Recharging and multiple use of crucible is possible. Productivity numbers demonstrating the good capabilities of the machine are given.

Abstract No. 328

Improvements to the Czochralski-Silicon Pulling Process

K. G. Barraclough,* R. W. Series, and **W. Bardsley,** RSRE Malvern, Great Malvern, Worcestershire, England

Conventionally grown, 3 in. diam dislocation-free Czochralski silicon single crystals have been compared with those grown by a modified Czochralski process. The substitutional Al-dopant- and the interstitial oxygen distribution are compared using four point probe resistivity-, spreading resistance-, and IR absorption measurements. Improvements in uniformity, in particular the oxygen distribution, have been achieved. The significance of the results is discussed in relation to intrinsic gettering of impurities in Cz-silicon wafers during thermal processing (1).

1. R. W. Series, K. G. Barraclough, and W. Bardsley, Abstract 205, The Electrochemical Society Meeting, Minneapolis, Minnesota, May 10-15, 1981.

Abstract No. 329

A New Compact Production Float Zoner for Large Diameter Silicon Crystals

B. Altekrüger and **D. Drechsel,** Leybold-Heraeus, D 6450 Hanau, Germany and Leybold-Heraeus, Vacuum Systems Inc., Enfield, CT 06082

The compact design of a newly developed production float zoner for 3 and 4 in. silicon crystals with drive assemblies inside of the chamber instead of conventional pulling shafts avoids stability problems and enables a pulling length of 1450 mm at a total machine height of 5m only. The process can be performed under high vacuum and under inert gas up to 2 bar. Lateral set off of rf coil and crystal is possible. A special clamping device supports the growing crystal. The machine can be operated and maintained very easily. Its good production capabilities have been established by many pulling tests. Productivity numbers are given.

Abstract No. 330

Suppression of Thermal Convection by Transverse Magnetic Field

K. M. Kim, IBM East Fishkill, Hopewell Junction, NY 12533

Effect of a transverse magnetic field (B) on the suppression of thermal convection was investigated in a vertical column of InSb melt under a destabilizing temperature gradient (β). The melt height and β were 2.5 cm and 16°C/cm, respectively. At B=0, a turbulent thermal convection occurred as measured by a thermocouple inserted in the melt. At B=920-1420G, random temperature fluctuations of the turbulent thermal convection assumed some periodic variations. At B=1450G, a sinusoidal oscillation of 0.17 Hz (10 cpm) and 3°C amplitude appeared. With a further increase in B up to 1660G, the amplitude of the oscillation decreased, while the frequency stayed the same. At $B \cong 1690$G, no temperature fluctuations were measured, and the thermal convection was completely suppressed. Striation-free crystal growth was then achieved at $B \geq 1690$G, when the thermal convection was suppressed.

Abstract No. 331

Silicon Wafers Critical Shear Stress Enhancement by Annealing near 800°C

C. Plougonven, B. Leroy, and **E. Trevisan,** IBM France, 91102 Corbeil-Essonnes, France

The critical shear stress of Czochralski grown silicon wafers strongly depends on the amount of oxygen precipitated and on the precipitate's distribution and size. The critical shear stress of silicon wafers has been derived from experimental observations of the lowest temperature at which an imposed radial temperature gradient results in generation of ship. The plot of c thus calculated *vs.* amount of oxygen precipitated is given for precipitation heat-treatments in the 900°-1000°C range and for an 800°C anneal. The 800°C precipitation heat-treatment results in a 2x critical stress enhancement. This results from a different precipitate size distribution, at 800°C a large number of small precipitates are formed by homogeneous nucleation.

Abstract No. 332

Influence of CW Laser Scan Speed in Solid Phase Crystallization of Amorphous Silicon on Si_3N_4/Glass Substrate

G. Auvert, D. Bensahel, V. T. N'Guyen, P. Henoc, J. Morin, and **P. Coissard,** Centre National d'Etudes des Telecommunications, Meylan, France

In this paper, we report results of a morphology study (by optical microscope and TEM) of the CW laser crystallization of amorphous silicon film deposited on Si_3N_4/glass substrate as a function of the laser scan speed. Our results, obtained with the substrate temperature Ts = 300K, show for the first time that structural features of crystallized film (in particular the existence of periodic features) depend strongly on two well-defined ranges of the laser scan speed.

ELECTROTHERMICS AND METALLURGY

Thermochemistry of Intermetallic Compounds

Abstract No. 333

Abnormal Properties of the Transition Metals and Their Alloys

L. Brewer, Dept. of Chemistry, and MMRD Division of the Lawrence Berkeley Laboratory, University of California, Berkeley, CA 94720

The transition metals differ markedly in behavior from the normal metals. The distinction by N. Engel between outer shell and inner shell valence electrons, *e.g.*, 5s,p *vs.* 4d for Zr, makes it possible to make straightforward predictions. The predictions, contrary to common belief, that pressure stabilizes the bcc phase of 4th group metals over the close-packed structure and that hcp Ru or Os destabilize the hcp phases relative to the bcc phases, have been confirmed with 95-100% reliability. The present paper covers extension to predictions that transition metals will have entropies of fusion and high temperature heat capacities larger by a factor of two than normal metals.

Abstract No. 334

High Temperature Thermodynamic Properties of Intermetallic Compounds in the Platinum-Tantalum System

S. K. Lau,* Westinghouse R&D Center, Pittsburgh, PA 15235 and **W. L. Worrell,** Dept. of Materials Science and Engineering, University of Pennsylvania, Philadelphia, PA 19104

High temperature thermodynamic properties of solid platinum-tantalum alloys containing 2-29 a/o tantalum have been determined. An electrochemical cell technique using a thoria-based electrolyte has been employed over the temperature range of 1100-1300K. Tantalum activities exhibit large negative deviations from Raoult's law, while the platinum activities are almost ideal. The Gibbs energies of formation of the intermetallic compounds $TaPt_3$ and $TaPt_2$ indicate that these compounds are among the most stable intermetallics.

Abstract No. 335

A High-Temperature Thermodynamic Investigation of the Platinum-Rich Region of the Al-Pt System

J. Major, Research Inst. for Tech. Physics, Budapest, Hungary, and **W. L. Worrell,*** Dept. of Materials Science and Engineering K1, University of Pennsylvania, Philadelphia, PA 19104

The thermodynamic properties of platinum-aluminum alloys have been determined using the following electrochemical cell

$$NbO_2, Nb_2O_{1.8}/ThO_2(Y_2O_3)/Pt, Al_2O_3$$

where *Pt* represents Al-Pt alloys containing between 4 and 28 a/o aluminum. The thoria-yttria solid-oxide electrolyte exhibits negligible electronic conductivity over the experimental temperature and oxygen partial pressure range. To obtain stable and reproducible emf data, it was essential to pre-anneal the alloy-Al_2O_3 electrodes for as long as 60 days at temperatures between 950° and 1275°C. The thermodynamic results indicate that the aluminum activity is extremely negative in the platinum-rich alloys and that the standard Gibbs energy of formation (ΔG_f^0) for $AlPt_3$ is ~ 64 kcal/mole at 1000°C.

Abstract No. 336

Activity Measurements in the Ti-Cu, Ti-Ni, and Mg-Cu Systems by Metal-Hydrogen Equilibration

M. Arita,* and **K. Shimizu,** Dept. of Metallurgical Engineering, Tokyo Institute of Technology, Meguro-ku, Tokyo 152, Japan, **R. Kinaka,** Kawasaki Steel Corp., Chiba, Japan, and **M. Someno,** Nagaoka University of Science and Technology, Nagaoka, Japan

A technique has been developed to determine thermodynamic activities in a binary alloy by measuring the pressure of hydrogen gas equilibrated with the alloy and the hydride of one component. With the use of this technique, activities in the Ti-Cu, Ti-Ni, and Mg-Cu systems between 600 and 900 K have been determined. From the activities, the standard free energies, enthalpies, and entropies of formation for intermetallic compounds in these systems have been determined.

Abstract No. 337

Low Temperature (1-20 K) Heat Capacity Measurements on Metallic Systems

K. A. Gschneidner, Jr., Ames Laboratory-DOE and Dept. of Material Science and Engineering, Iowa State University, Ames, IA 50011

The low temperature heat capacities of nonmagnetic metallic solids yield information about both the electronic structure and lattice dynamics. These are, respectively, the electronic specific heat constant which is proportional to the density of electron states at the Fermi surface and the Debye temperature which is a measure of the lattice rigidity. Both of these properties, although not necessarily simultaneously, can influence the existence or formation of metallic phases. Specific examples of each are given.

Abstract No. 338

Thermodynamics of the Incongruent Subliming Aluminum-Niobium System

R. A. Schiffman* and **I. Shilo,** Ames Laboratory, Iowa State University, Ames, IA 50011

Vapor pressures of aluminum have been measured continuously across the total Nb-Al composition range by simultaneous weight-loss and mass-spectrometric Knudsen effusion techniques. Data over the series of single-and two-phase alloys were combined with data from target collection Knudsen effusion experiments at fixed compositions in the two-phase regions to evaluate thermodynamic parameters for the intermediate phases; $NbAl_3$, Nb_2Al, Nb_3Al. The three complementary methods were utilized to offset limitations of each individual method. Weight-loss data allowed calculation of location and width of phase regions in the Nb-Al temperature-composition diagram.

Abstract No. 339

Coulometric Titrations to Study Solid Ca-Au Alloys

H.-P. Pfeiffer, R. J. Heus, and **J. J. Egan,*** Brookhaven National Laboratory, Dept. of Energy and Environment, Upton, NY 11973

Several intermetallic compounds in the Ca-Au system were studied with the help of the cell

$$Ca\text{-}Sn(l)|CaF_2(s)|Ca\text{-}Au(s)$$

using a CaF_2 solid electrolyte and a liquid Ca-Sn reference electrode with a known activity of Ca. A gold foil (0.025 mm) served as the right-hand electrode and the Ca content was controlled by coulometric titration. Concentrations between 0 and 35 mole percent Ca were studied. The following intermetallic compounds were found: $CaAu_5$, Ca_2Au_9, Ca_2Au_7, $CaAu_2$, and their ranges of stoichiometry were determined. Two phase and single phase activities of calcium were measured and equations of Wagner and Schottky were applied to help determine the type and degree of disorder. (This work was supported by the Division of Chemical Sciences, U.S. Department of Energy, Washington, D.C. under Contract No. DE-AC02-76CH00016.)

Abstract No. 340

Calorimetric Determination of the Phase Stability of Ni_4Mo

C. R. Brooks and **P. J. Meschter,** Dept. of Chemical, Metallurgical, and Polymer Engineering, University of Tennessee, Knoxville, TN 37916

The heat capacities of ordered Ni_4Mo and the (stable or metastable) fcc Ni-Mo solid solution at 20 a/o Mo have been determined by adiabatic calorimetry. From these measurements and the heat of transformation at 1141 K, the free energy difference between the disordered and ordered phases is determined as a function of temperature. Anomalies in the heat capacity curve of the metastable disordered phase at intermediate temperatures give information on the nature of the ordering process.

Abstract No. 341

XIr_3 Intermetallic Compound Catalysts

M. B. Brodsky* and **P. W. Ensign,** Materials Science Div., Argonne National Laboratory, Argonne, IL 60439

The rates of ethane hydrogenolysis to methane and dehydrogenation to ethylene have been measured using $TiIr_3$, $CrIr_3$, $NbIr_3$, and Ir ("$IrIr_3$"), all of which occur in the ordered, fcc $AuCu_3$ structure. Catalytic activities varied over four orders of magnitude, with $CrIr_3$ being the most active catalyst. Variations in product specificity and self-poisoning are also observed. Possible surface reconstruc-

tions and magnetic properties are discussed relative to the catalytic results, also.

Abstract No. 342

A Thermodynamic Analysis of Fission Product Reaction Behavior in Reactor Fuel Elements

R. Kohli, Institut für Metallurgie, Österreichisches Forschungszentrum Seibersdorf GmbH, A-1082 Wien, Austria

A comprehensive thermodynamic model is presented to predict fission product reaction behavior in reactor fuel elements. Using recent experimental high temperature thermodynamic data and the in-reactor oxygen potential and temperature range of LWR fuel elements, the most plausible reactions of the various fission products with each other, the uranium dioxide UO_{2+x} fuel, and the Zircaloy cladding are considered in detail. The highly stable alkali-metal zirconates are predicted to form in preference to either the molybdates or the uranates. The implications of these predictions on fuel chemistry and on fuel-cladding interactions are discussed.

Abstract No. 343

Thermodynamics and Defect Structure of Intermetallic Phases

Y. A. Chang, Dept. of Metallurgical and Mineral Engineering, University of Wisconsin-Madison, Madison, WI 53706

Intermediate phases formed from two or more component elements rarely exist as line compounds, *i.e.*, at a single stoichiometric composition. This is particularly true for intermetallic phases. Since a perfectly ordered structure may be achieved only at absolute zero, any intermediate phase even with a narrow range of homogeneity must possess thermally activated structural defects at any finite temperature. The existence of many intermetallic phases with large deviations from the stoichiometric composition must be accompanied by the generation of large amounts of defects. In this presentation, we describe a statistical thermodynamic model for a class of intermetallic phases with the CsCl structure and triple defects, *i.e.*, vacancies and antistructure atoms in the lattice. The validity of the model is demonstrated using thermodynamic data available for a large number of systems. Furthermore, independent structural evidences also support the validity of the model.

Abstract No. 344

Thermodynamic Equations for the Liquidus of $(A_{1-u}B_u)_{2-y}C_y(s)$, y Near Unity, and Associated Solution Models

R. F. Brebrick,* T. Tung, C-H. Su, and **P-k. Liao,** Materials Science and Metallurgy, Marquette University, Milwaukee, WI 53233

Ternary and quatenary solids with desirable properties have revitalized interest in phase diagrams. Two important theoretical aspects concern the correct thermodynamic liquidus equations and models for the liquid phase. We present thermodynamic equations for the liquidus of an almost pseudobinary solid in a number of equivalent exact and useful approximate forms. We also discuss some general properties of the associated solution model. Analyses using this model have generally started with incorrect liquidus equations.

Abstract No. 345

Quantitative Fit to the Phase Diagram and Thermodynamic Data for the Hg-Cd-Te System

T. Tung,* C-H. Su, P.-k. Liao, and **R. F. Brebrick,** Materials Science and Metallurgy, Marquette University, Milwaukee, WI 53233

Phase diagram and thermodynamic data are simultaneously fit using an associated solution model for the liquid. HgTe and CdTe are taken as molecular species whose interactions are described by quadratic and cubic terms in their mole fractions. The data include liquidus points, partial pressures, and the ΔH_f and ΔS_f of the solid in the Hg-Te and Cd-Te binaries; partial pressures and phase lines in the pseudobinary; and the ternary liquidus surface.

Abstract No. 346

Solid-State Electrochemical Study of Indium-Antimony Liquid Alloys

T. J. Anderson,* Dept. of Chemical Engineering, University of Florida, Gainesville, FL 32611 and **L. F. Donaghey,** Chevron Research Co., Richmond, CA 94802

The chemical potential of In in liquid solution with Sb was measured as a function of composition and temperature with a solid-state galvanic cell. The results exhibit moderate deviations from ideal behavior and are shown to be consistent with the available thermochemical data and the reported phase diagram. Solution models are examined and a consistent thermochemical property data set is presented.

Abstract No. 347

Analysis of the In-Sb System Using an Associated Solution Model for the Liquid

C-H. Su,* P-k. Liao, T. Tung, and **R. F. Brebrick,** Materials Science and Metallurgy, Marquette University, Milwaukee, WI 53233

This analysis differs from earlier ones in taking the interactions among liquid phase species to depend upon the mole fractions of the species and in using a more correct liquidus equation. The relative (to the pure liquid elements) heat capacity of the 50% liquid is not zero so that the commonly used Vieland equation is incorrect. The fit includes liquidus points, chemical potential and heats-of-mixing in the melt, and heat capacity.

Abstract No. 348

Analysis of the Ga-Sb System and the Ga-In-Sb Ternary Used an Associated Solution Model for the Liquid

P-k. Liao,* C-H. Su, T. Tung, and **R. F. Brebrick,** Materials Science and Metallurgy, Marquette University, Milwaukee, WI 53233

An analysis of the Ga-Sb system similar to that for the In-Sb system is performed, and the results of both extended to the ternary. The approach is more correct and/or all-inclusive than published accounts in that the relative heat capacity of the 50% Ga-Sb liquid is not erroneously set to zero for an associated liquid model and the thermodynamic constraints imposed by the congruent melting of GaSb and InSb are included.

Abstract No. 349

Metastable Intermetallic Compounds in Some Binary and Ternary Systems

M. Ellner and **B. Predel,** Max-Planck-Institut für Metallforschung, Institut für Werkstoffwissenschaften, D-7000 Stuttgart 1, Germany

During supercooled solidification, the new metastable intermetallic compound $MgGa_2$(m) with the $CaIn_2$ type structure was found. Below 415 K, this metastable phase undergoes a transformation to the stable phase $MgGa_2$ ($MgGa_2$ type). Some metastable defect variants of the $CaIn_2$-type structure were observed with the stoichiometry $MgGa_3$. Using the splat cooling technique in the systems Au-Si and Pd-Pb-As, metastable intermetallic compounds were studied. The crystallographic relationship between these metastable compounds and stable intermetallic compounds is discussed.

Abstract No. 350

Relationship Between Structural and Thermodynamic Properties of Some Phases of the Cu-Family

M. Ellner, Max-Planck-Institut für Metallforschung, Institut für Werkstoffwissenschaften, D-7000 Stuttgart 1, Germany

The dependence of the mean atomic volume and the valence electron density on the chemical composition in the binary systems containing nickel, palladium, and platinum as the solid solvent and the metals of the IB . . . VB group as the solute was determined and analyzed. For the phases of the Cu- and Cu_3Au-type structure, some relationship be-

tween the partial atomic volume, partial valence electron density, and the partial molar enthalpy of formation were found.

Abstract No. 351

Solid Solubility Trends in Divalent Alloys

J. R. Chelikowsky, Exxon Research and Engineering Co., Corporate Research Laboratories, Theoretical Science Unit, Linden, NJ 07036

Using a macroscopic model for predicting solubility trends, a variety of solutes in seven prototypical simple divalent metal hosts are examined. Our model should prove more successful than the classical approaches of Hume-Rothery or Darken and Gurry. The method is an extension of a cellular scheme developed by Miedema and involves two chemical coordinates. Moreover, we will show that Miedema's coordinates describe recent experiments that involve site energy preferences of implants in Be. This dramatic result suggests that Miedema's coordinates may describe metastable systems and, as a consequence, are more widely applicable than might be expected.

Abstract No. 352

A Mechanism for Growth and the Hydrogen Reduction of Black Molybdenum Thin Films

K. Seshan, Dept. of Metallurgy, University of Arizona, Tuscon, AZ 85721, **P. D. Hillman, E. E. Chain, K. A. Gesheva,** and **B. O. Seraphin,** Optical Sciences Center, University of Arizona, Tucson, AZ 85721

Thin films of black molybdenum, deposited by CVD from MoO_2Cl_2, or from $Mo(CO)_6$ followed by annealing, are a composite of Mo in MoO_2. These films show spectrally selective properties desirable in high temperature photothermal solar energy conversion. The mechanism of film growth and microstructural changes, presented here, is based on analysis of thermodynamic and diffusion data, as well as results of structural and compositional studies of the films. This model correctly interprets experimentally observed results.

Abstract No. 353

Magnetoresistive Properties of $Cd_{3-x}Zn_xAs_2$ Compound Semiconductors

Y.K. Su, Y. L. Tsai, B. D. Liu, C. C. Wei, and **C. Y. Chang,** Research Institute of Electronics and Electrical Engineering, Tainan, Taiwan, China

$Cd_{3-x}Zn_xAs_2$ compound semiconductors are fabricated by using vertical Bridgman method. The mobility and carrier concentration are measured by means of van der Pauw method. These materials having a high magnetoresistivity ratio $\Delta\rho/\rho$ can be used as Hall elements. The thermoelectric power and thermoconductivity are also measured. These devices have a good potential as the thermoelectric elements whose figure of merit z are in the order of 10^{-3} ($°K^{-1}$).

ELECTROTHERMICS AND METALLURGY/CORROSION/PHYSICAL ELECTROCHEMISTRY/NEW TECHNOLOGY SUBCOMMITTEE

Vibrational Spectroscopy in Electrochemistry (Laser, Raman, & Infrared)

Abstract No. 354

Raman Studies of the Vibrational Properties of Adsorbed Species and Films at Electrochemical Interfaces

E. Yeager,* R. Kötz, and **G. Nazri,** Case Laboratories for Electrochemical Studies and the Dept. of Chemistry, Case Western Reserve University, Cleveland, OH 44106

The application of Raman spectroscopy in *in situ* studies of adsorbed species and thin films at metal- and semiconductor-electrolyte interfaces are surveyed with emphasis on the types of information which can be obtained. Specific topics to be considered include (*i*) the effects of interactions with the surface and the potential gradient at the interface on the Raman spectra of adsorbed species, (*ii*) the use of probe molecules to examine the properties of electrode surfaces, and (*iii*) studies of oxide layers and anodic films on electrode surfaces. (This research was supported by ONR.)

Abstract No. 355

Raman Spectroscopy as an *In Situ* Probe of Corrosion at Elevated Temperatures

R. E. Benner,* A. S. Nagelberg, and **J. C. Hamilton,** Sandia Laboratories, Livermore, CA 94550

Spontaneous Raman scattering techniques are being developed to characterize the corrosion products of structural metals at elevated temperatures in realistic combustion environments. Data obtained from a number of stainless steels and thermal barrier coatings provide identification of the corrosion products, simultaneously with determinations of surface temperatures. Exploiting the *in situ* and nonperturbing capabilities of the Raman technique requires rejecting blackbody radiation and strong elastic scattering from the as-grown corrosion scales, as well as optimizing detection efficiency. The use of a cavity-dumped laser in conjunction with gated electronics, a triple spectrometer/spectrograph, and multichannel detection in overcoming these difficulties are discussed. (This research was supported by the U.S. Department of Energy.)

Abstract No. 356

Characterization of the High Temperature Corrosion of Stainless Steels by Raman Scattering

A. S. Nagelberg,* R. E. Benner, and **J. C. Hamilton,** Sandia Laboratories, Livermore, CA 94550

Raman spectroscopy has been employed as an *in situ* technique to study the formation of corrosion scales at elevated temperatures. Spectra from 304 and 310 stainless steels obtained at 100°C increments between 350° and 950°C indicate a change from a predominantly Fe_2O_3 scale at lower temperatures to a Cr_2O_3 and spinel-based scale at higher temperatures. These oxidation results have been compared with Raman data for the corrosion scales formed with a molten $NaNO_3$ salt overcoating the alloy samples. Raman measurements have been supplemented by post-exposure analysis by Auger spectroscopy and electron microprobe techniques. (This work was supported by the U.S. Department of Energy.)

Abstract No. 357

Surface Enhanced Raman Scattering (SERS) as a Probe of Solar Mirror Degradation

R. E. Benner,* J. Vitko, Jr., J. C. Hamilton, and **J. E. Shelby,** Sandia Laboratories, Livermore, CA 94550

The observation of SERS from heliostats having a glass-700Å Ag- 300Å Cu-paint configuration has provided direct evidence that agglomerated silver is a major degradation product in field-exposed mirrors. Spectra from corrosion spots obtained through the glass superstrate exhibit the air absorbate bands recently attributed to graphitic carbon, as well as a band at ~240 cm^{-1}. SERS intensities have been correlated with the chemical composition and RMS roughness of the corroded region(s). (This research was supported by the U.S. Department of Energy.)

Abstract No. 358

Adatom-Molecule Complex in Surface Enhanced Raman Scattering

J. R. Lombardi* and **R. L. Birke,** Dept of Chemistry, The City College of the City University of New York, New York, NY 10031

The surface enhanced Raman spectrum of molecules adsorbed on Ag electrodes, Ag sols, and Hg electrodes show lines in the 150-300 cm^{-1} region which are not in the solution spectrum of the molecules. These lines are not due to a metal Cl^- vibration since in some cases the lines have been seen on Ag sols in the absence of Cl^- ions. These lines are attributed to the stretching vibration of a metal adatom molecule surface complex.

Abstract No. 359

The Structure of Water on Emersed Electrodes. ATR and Raman Spectra

J. G. Gordon,* B. Pettinger, and **M. R. Philpott,** IBM Research Laboratory, San Jose, CA 95193

Hansen and his co-workers have presented evidence that an electrode can be removed from solution with the interfacial region intact. We report here attenuated total reflection measurements that show when an electrode is pulled from a solution it removes with it a water layer about 40Å thick, thick enough to contain a nearly unmodified double layer. Both the potential and concentration dependence of the water thickness have been studied. We have also obtained the Raman spectrum of water on these emersed electrodes and compare it with the spectrum of water on immersed electrodes.

Abstract No. 360

Applications of Raman Spectroscopy in Molten Salt Electrochemistry

G. Mamantov,* **K. Tanemoto, G. M. Begun, R. Marassi,** and **R. Huglen,** Dept. of Chemistry, University of Tennessee, Knoxville, TN 37916, and Chemistry Div., Oak Ridge National Laboratory, Oak Ridge, TN 37830

In this paper the applications of Raman spectroscopy to studies of molten salt solutions are discussed. Examples are presented of the utility of Raman spectra for characterization of species in molten salt solvents, as well as of reactants and products in melt solutions used for electrochemical studies. Resonance Raman spectroelectrochemical studies of the oxidation of iodine in chloroaluminate melts are discussed.

Abstract No. 361

Raman Spectroscopic Studies of Lithium Sulfur Dioxide and Lithium Thionyl-Chloride Batteries

K. C. Lee, W. A. Adams, C. L. Gardner, D. T. Fouchard, and **G. J. Donaldson,** Defence Research Establishment Ottawa, Dept. of National Defence, Ottawa, Ont., Canada K1A 0Z4

The construction and operation of safe high rate Li/SO_2 and $Li/SOCl_2$ batteries depends on a thorough knowledge of the chemical reactions that can occur under all conditions of storage and use. The electrolyte of commercial cells has been observed by Raman spectroscopy prior to, during, and following discharge. Comparison of these spectra with reference spectra of appropriate electrolytes has provided information on cell reactions.

Abstract No. 362

In Situ Monitoring of Electrode Surface Phases by Laser Raman Spectroscopy during Anodization and Sulfation of Tetra Basic Lead Sulfate in Sulfuric Acid

R. Varma,* **G. Cook, N. P. Yao,** and **W. Molinorolo,** Argonne National Laboratory, Chemical Engineering Div., Argonne, IL 60439

Lead positive plates "formed" with tetrabasicleadsulfate (TBLS) have been suggested to improve cycle life. However, the electrode processes occurring during formation are not well understood. *In situ* monitoring by laser Raman spectroscopy of surface layers on TBLS-pasted electrodes in 0.1*N* H_2SO_4 has shown: (*i*) partial chemical sulfation into $PbO \cdot PbSO_4$ and $PbSO_4$ during open-circuit stand and $3PbO \cdot PbSO_4 \cdot H_2O$, during anodizations. Furthermore, a difference in electrochemical activity of the various sulfate species was observed.

Abstract No. 363

Optical Properties of Complexes at the Metal/Electrolyte Interface Measured by Surface Plasmon Excitation (SP)

A. Tadjeddine,* Laboratoire d'Electrochimie Interfaciale du CNRS, 92190 Meudon-Bellevue, France and **D. M. Kolb,** Fritz-Haber Institut der M.G.P., 1000 Berlin 33, Germany

SP excitation at Ag(Au) single crystal electrodes is used to investigate the optical properties of complexes electrochemically generated at the interface. The aim is to gain access to the electronic transitions of those complexes that are active in SERS and to contribute to the understanding of this phenomenon. Results for pyridine on Ag (Au) in halide solution are shown and discussed. Preliminary results on silver/silver deposition in pyridine-free solution are presented.

Abstract No. 364

Interpretation of Surface-Enhanced Raman Scattering as a Resonance Raman Effect: Spectrum of 1,2-bis-(4-pyridyl)-ethylene

J. J. McMahon,* **K. L. Guyer, G. T. Babcock,** and **M. J. Weaver,** Dept. of Chemistry, Michigan State University, East Lansing MI 48824

The surface-enhanced Raman scattering (SERS) spectrum of 1,2-bis-(4-pyridyl)-ethylene has been observed at a polycrystalline silver electrode. The SERS exhibits a dramatic dependence upon the electrode potential which is interpreted in terms of complex formation involving the ligand n and π^* states. A resonance Raman effect arising from surface complex electronic excitations is invoked as the enhancement mechanism. The appearance of *IR* modes indicates that the surface complex is of low symmetry. Increased enhancement in the red can be understood in terms of a high density of electronic states. The spectra indicate monolayer enhancement.

Abstract No. 365

Surface Enhanced Raman Spectroscopy: A Discussion of Mechanisms and a Guide to Applications

T. E. Furtak, Dept. of Physics, Rensselaer Polytechnic Institute, Troy, NY 12181

An explanation of the various proposed mechanisms for the anomalously large Raman scattering intensity which can be observed from molecules adsorbed on metal surfaces will be presented. An effort is made to provide guidance which will be useful for electrochemists interested in the application of this phenomenon for analytical purposes.

Abstract No. 366

Surface Enhanced Raman Scattering from Benzotriazole on Cu

J. Kester* and **T. Furtak,** Ames Laboratory-USDOE and Dept. of Physics, Iowa State University, Ames, IA 50011

The surface complexes formed by benzotriazole (BTA) on Cu have been investigated using surface enhanced Raman scattering (SERS). The applied voltage dependence of the observed intensities and frequencies are related to changes in the molecular configuration of the adsorbed layers closest to the Cu. In addition, we report the photocatalyzed electrochemical formation of a surface complex which demonstrates a much larger SERS signal. A connection exists between these surface complexes and corrosion inhibition by BTA layers on Cu.

Abstract No. 367

Reactive Interfacial Chemistry and SERS

R. P. Cooney,* **M. W. Howard,** and **M. Mahoney,** Dept. of Chemistry, University of Newcastle, N.S.W. Australia 2308

The surface-enhanced Raman scattering (SERS) from pyridine (and related organic molecules) and from cyanide on silver electrode surfaces is associated with the presence of secondary adsorbents on the silver surfaces. In the case of the organic adsorbates, the secondary adsorbent is disordered carbon generated either from trace quantities of carbon dioxide or from graphitization of the adsorbate. In the case of cyanide, the surface phase associated with SERS is *p*H sensitive and reducible and hence has been identified as a stabilized oxide film.

Abstract No. 368

Surface Enhanced Raman Spectra of Azide Ion and Other Molecules on Silver and Copper Electrode

M. R. Philpott, R. E. Kunz, and **J. G. Gordon,*** IBM Research Laboratory, San Jose, CA 95193

Studies of the surface enhanced Raman (SER) effect for some ions and neutral molecules adsorbed on silver electrodes from aqueous electrolyte solutions are described. For azide ion, only the oxidation portion of the usual oxidation-reduction activation cycle is required. In addition, the infrared modes are enhanced more than the Raman modes and a Fermi resonance between ν_1 and $2\nu_2$ is observed near 1242 cm^{-1}.

Abstract No. 369

Raman Spectroscopic Study of the Radical Ions Stabilization at a Silver Electrode

A. Regis* and **J. Corset,** Laboratoire de Spectrochimie Infrarouge et Raman, CNRS, 94320 Thiais, France

The electrochemical formation of the methylviologen radical MV^{+} in an aqueous media is compared through Raman spectroscopy at a silver and at a platinum electrode. After an oxido-reduction cycle Ag^{+}/Ag_n in an aqueous chloride media, an intense Raman spectrum of methyl biologen MV^{++} adsorbed at the electrode is observed. Such a spectrum is not observed with a platinum electrode. This phenomenon is discussed in relation with the radical MV^{+} stabilization at the silver electrode. The resonance Raman spectrum of this species is observed as soon as the oxido-reduction potential of MV^{++}/MV^{+} is approached.

Abstract No. 370

Surface Enhanced Raman Scattering of Cyanide Chemisorption Layers on Silver: Potential and Time Dependence

W. Plieth,* **B. Roy,** and **H. Bruckner,** Freie Universität Berlin, Institut für Physikalische Chemie, D-1000 Berlin 33, Germany

The Raman signal of chemisorbed CN^{-} ions on Ag at *ca.* 2110 cm^{-1} was investigated. Its dependence on the electrode potential was tested by a periodic impulse program applied to the electrode. The time dependence after anodic activation was registered for various cathodic potentials. In a second type of experiment silver was deposited on gold surfaces and again the time dependence of the Raman signal was followed. The experiments give hints that formation of small clusters is necessary for the enhancement effects.

Abstract No. 371

In Situ, Vibrational *IR* Spectroscopy of Adsorbed Species on Metal Electrodes in Aqueous Systems

A. Bewick,* **K. Kunimatsu,** and **J. W. Russell,** Dept. of Chemistry, The University, Southampton SO9 5NH, England

Vibrational *IR* spectra from species in the electrode/aqueous electrolyte interphase obtained by *in situ* modulated specular reflectance spectroscopy are presented. The structure of water in the inner region of the double layer and, in particular, the role of small clusters of molecules, is discussed together with data on adsorbed intermediates in electrocatalytic reactions such as hydrogen evolution and methanol oxidation at platinum electrodes.

ELECTROTHERMICS AND METALLURGY/ENERGY TECHNOLOGY

Thermionic and Thermoelectric Generation Conversion

Abstract No. 372

Thermionic Energy Conversion: Its Potential and Problems

G. O. Fitzpatrick, Rasor Associates, Inc. Sunnyvale, CA 94086

Thermionic energy converter is an electronic device for converting heat directly to electricity without the use of moving parts or high pressure. This paper reviews the field and points out the potential and problems in this field. The resources of the electrochemical research community may well be suited to assist in solving these problems.

Abstract No. 373

Thermally Regenerative Electrochemical Systems—An Update

H. L. Chum, Solar Energy Research Institute, Biomass Thermal Conversion and Exploratory Branch, Golden, CO 80401

Thermally regenerative electrochemical systems (TRES) are closed systems that convert heat into electricity in an electrochemical heat engine that is Carnot cycle limited in efficiency. Past and present work is reviewed and classified. Two broad classes of TRES are identified according to the type of energy input required to regenerate the electrochemical cell reactants: thermal input alone or the coupling of thermal and electrolytic energy inputs. These two broad categories are further divided into seven types of TRES. The subdivision is made according to significant differences in either the electrochemical cell or in the regeneration.

Abstract No. 374

A New Photothermogalvanic System

H. L. Chum,* **R. Pitts** and **R. F. Fahlsing,** Solar Energy Research Institute, Golden, CO 80401

Aqueous thermogalvanic cells, the solution analogs of solid-state thermoelectric devices, are investigated for power generation using low-grade heat. Measurements on the copper|copper formate|copper system yield thermoelectric powers. $(\Delta E/\Delta T)_{1-o}$, of 1.25-1.9 mV/degree, which are higher than those exhibited by other copper systems. In these solutions three copper formate complexes are present. Practical cells were built and tested. The power output is largely limited by cell resistance. The coupling of this thermogalvanic system with an electrochemical photovoltaic effect is described. XPS and SIMS techniques were employed in the investigation of the electrode surfaces.

Abstract No. 375

High Efficiency Thermoelectric Conversion with Solid Electrolytes. The Sodium Heat Engine.

T. Cole, Jet Propulsion Laboratory, Pasadena, CA 91109, and **N. Weber** and **T. K. Hunt,** Ford Motor Co., Dearborn, MI 48120

We report our recent work on the Sodium Heat Engine (SHE) a thermally regenerative concentration cell based on the unique properties of beta"-alumina. Liquid sodium is expanded isothermally through a beta"-alumina membrane into a low pressure vapor space at a temperature of 600°-1000°C. The sodium vapor is liquified on a condenser surface maintained at 100°-300°C and returned to the high temperature region by a pump. Power densities of 1.1 W/cm^2 and efficiencies of 15% have been achieved.

Abstract No. 376

Lattice Thermal Conductivity of Semiconductors: A Chemical Bond Approach

D. P. Spitzer, American Cyanamid Co., Stamford, CT 06904

Lattice thermal conductivity data at room temperature is compiled for more than 200 semiconductors. The data for over 70 semiconductors were obtained at our laboratory. Lattice thermal conductivity is correlated rather reliably with crystal structure. In general, increasing coordination of the ions is associated with decreasing thermal conductivity. Low thermal conductivity may also be caused by lattice vacancies. Using these correlations, an unknown thermal conductivity can generally be estimated to within a factor of two.

Abstract No. 377

Thermoelectricity. V. Seebeck Quality Optimization

D. Tuomi, Borg-Warner Corp., R. C. Ingersoll Research Center, Des Plaines, IL 60018

The Seebeck Quality Factor of a semiconductor alloy is defined through characteristic values of $Q_S = \mu_n(m^*/m_o)^{3/2}$ defined by the Seebeck coefficient-electrical conductivity data point pairs for varied samples. The composition and process variable dependence of Q_s describes the response surface for selecting conditions to maximize Q_s. Above 70 K, the range of Q_s for varied alloys parallels that of X_L, the lattice thermal conductivity.

Abstract No. 378

Rare Earth Chalcogenides as Thermoelectric Materials

T. Takeshita,* **B. J. Beaudry,** and **K. A. Gschneidner, Jr.,** Ames Laboratory-DOE, Iowa State University, Ames, IA 50011

Seebeck coefficients and electrical resistances of some rare earth sesquichalcogenides were measured from room temperature up to ~700°C. A comparison is made between the sesquichalcogenides of sulfur and selenium. Our results are also compared with data reported in the literature. The Seebeck coefficient and resistivity depend upon the rare earth to chalcogenide ratio, impurities, and thermal treatment.

Abstract No. 379

The Thermoelectric Properties of the Boron-Carbon System

A. Lockwood* and **C. Wood,** Jet Propulsion Laboratory, Pasadena, CA 91103 and **G. Reynolds** and **N. Elsner,** General Atomic Co., San Diego, CA 92138

The resistivity, Seebeck coefficient, and thermal conductivity have been investigated in hot-pressed powders of B_xC compositions, as a function of X (x = 24 to 2.4) and as a function of temperature in the range 300 to 1700 K. The electronic and thermal transport mechanisms in these materials are discussed and their potential is estimated for high temperature thermal to electric conversion.

Abstract No. 380

Considerations Involved in the Development of a Viable Design for a Copper-Silver Selenide Thermoelectric Element

P. B. Hogerton, W. C. Mitchell, and **J. D. Hinderman,** 3M Co., 3M Center, St. Paul, MN 55144

The TPM-217 p-type thermoelectric element is under development for use in space power systems. Extensive research has evolved a design structure promising to provide reproducible, long-lived performance. The critical unusual problems and their resolution by design modification are briefly discussed.

ENERGY TECHNOLOGY

General Session

Abstract No. 381

Shallow Electron States and Linear Boundaries in EFG Ribbon Silicon

J. I. Hanoka,* R. O. Bell, and **B. Bathey,** Mobil Tyco Solar Energy Corp., Waltham, MA 02254

Low temperature EBIC has been used to study the effects of oxygen concentration and ribbon growth conditions on the nature of shallow electron states found in EFG silicon ribbon. The defect structure of EFG ribbon is characterized by linear boundaries parallel to the growth direction. It has been found that shallow electron states near the conduction bandedge are associated with these boundaries and that they are spatially anchored there and not mobile at temperatures up to 900°C. Occupation of these states has been found to be sensitive to oxygen concentration and diffusion temperature. Their relation to the deeper lying recombination levels is discussed.

Abstract No. 382

The Structure of Silicon Grain Boundaries Formed by Growing Silicon on Intersecting Sapphire Planes

K. A. Jones, Dept. of Electrical Engineering, Colorado State University, Ft. Collins, CO 80523

The orientation relationship for silicon on sapphire is derived, and it is used to calculate the misorientation between the silicon growing on intersecting sapphire planes. The misorientation is measured using x-ray methods and is compared with the theoretical calculations. Possible theoretical structures are given for the grain boundary lying parallel to the line of intersection of the sapphire planes and formed when silicon growing on the two sapphire planes grows together. These structures are correlated with the traces of the grain boundary plane determined by etching.

Abstract No. 383

Solid-State Electrochemical Modification of Photoanodes

C. Y. Yang,* Dept. of Energy and Environment, Brookhaven National Laboratory, Upton, NY 11973, **F. T. Lious** and **S. Levine,** Dept. of Materials Science, SUNY, Stony Brook, NY 11790, and **S. Srinivasan,** Dept. of Electrochemical Engineering, Los Alamos Scientific Laboratories, Los Alamos, NM 87544

Fluorine-based solid electrolyte (*e.g.*, CaF_2) cells have been used to incorporate fluorine into semiconductors which are promising anodes for photoelectrochemical devices. The purpose of this study is to modify the flatband potentials of these photoanodes. Since the fluorine activity at the solid electrolyte/semiconductor interface can be controlled by applying a potential across the cell, the addition to or removal of fluorine from a semiconductor can be performed electrochemically. Experimental procedures, flatband potential characteristics, and grain boundary segregation effects are reported. (This work was performed under the auspices of the U.S. Department of Energy.)

Abstract No. 384

Studies on Photoanodic Dissolution of n-CdS Electrodes

J. R. Wilson and **S.-M. Park,** Dept. of Chemistry, The University of New Mexico, Albuquerque, NM 87131

The stability of a CdS electrode toward photoanodic dissolution was studied in an aqueous photoelectrochemical cell using a rotating ring disk electrode and Fe^{2+}-EDTA complex as a redox couple. The following experimental conditions were studied for their effect on the amount of the photoanodic dissolution current: (*i*) wavelength of incident light; (*ii*) incident light intensity; (*iii*) applied potential at the n-CdS disk electrode; (*iv*) pH of the solution; (*v*) concentration of the redox couple; and (*vi*) the concentration of supporting electrolyte. The most important parameters in controlling the extent of corrosion were (*ii*), (*iv*), (*v*), and (*vi*).

Abstract No. 385

Effects of the Electrolyte Concentration on Flatband Potentials of n-TiO_2 Electrodes

J. R. Wilson and **S.-M. Park,** Dept. of Chemistry, The University of New Mexico, Albuquerque, NM 87131

The flatband potentials (E_{fb}) of an n-TiO_2 electrode were measured by a photoresponse method as a function of the supporting electrolyte concentration. Thirteen compounds were studied for their concentration effect on the flatband potential in an aqueous system. Only two compounds, ethylenediaminetetraacetic acid (EDTA) and 8-hydroxyquinoline (8-HQ) were found to shift E_{fb} in a positive direction when their concentration was increased. This effect was attributed to the complexation of surface donor ions by EDTA or 8-HQ.

Abstract No. 386

Efficient and Stable Photoelectrochemical Cells Constructed with WSe_2 and $MoSe_2$ Photoanodes

G. Kline, K. Kam, D. Canfield,* and **B. A. Parkinson,** Ames Laboratory, Iowa State University, Ames, IA 50010

Single crystals of n-WSe_2 and n-$MoSe_2$ were grown and employed as the photoanode in a regenerative photoelectrochemical cell with an iodide/triiodide electrolyte. Solar to electrical power conversion efficiencies of 10.2 and 9.4% were achieved on selected crystals of WSe_2 and $MoSe_2$, respectively. Products of a photocorrosion reaction from an $MoSe_2$ electrode could not be detected in the electrolyte after one month of continuous operation.

Abstract No. 387

Improvement of Energy Conversion Efficiency by Specific Chemical Treatments of $MoSe_2$ and WSe_2 Photoanodes

D. Canfield and **B. Parkinson,*** Ames Laboratory, Iowa State University, Ames, IA 50011

Several novel chemical treatments are reported which reduce the deleterious effect of edge site surface states on the photoconversion efficiency of layered semiconductor transition metal dichalcogenide photoanodes. The first treatment involves direct binding of ligands such as phosphines to the unsaturated metal atoms. Another approach was the "semi-intercalation" of pyridine containing molecules exclusively where the lattice terminates. Power conversion efficiencies of poor crystals can be significantly improved with these treatments.

Abstract No. 388

Bipolar Zn-Br_2 Batteries for Electric and Hybrid Vehicles

P. A. Malachesky,* H. Einstein, R. Bellows, P. G. Grimes, E. Kantner, and **K. Newby,** Exxon Research and Engineering Co., Linden, NJ 07036

Bipolar flowing electrolyte Zn-Br_2 batteries, based on inexpensive conductive carbon-plastic electrode technology, are attractive for future use in electric and hybrid vehicles. Due to the ability to partially separate the power-producing capability of the system (the cell stack) from the energy storage capability of the system (the electrolyte reservoir), the Zn-Br_2 system is, in principle, well suited for the pure electric and ICE/electric hybrid missions. Battery system design considerations for both applications are discussed, along with initial test results on Zn-Br_2 battery performance during simulated driving profiles.

Abstract No. 389

Design of Electrolysis under Cost-Optimal Thermal Conditions

T. Z. Fahidy, Dept. of Chemical Engineering, University of Waterloo, Waterloo, Ont., Canada N2L 3G1

A rapid approximate method to design electrolytic processes, where production rates and thermal losses are optimized with respect to amortized investment costs and the price of energy is described. Based on appropriate heat balances and heat transport equations, steady-state electrolyte temperature, cost-optimal thickness of thermal insulation on the electrolytic tank and optimal electrical energy requirements may be computed by a fast-converging successive iteration scheme. The method is numerically illustrated for a practical case of metal deposition.

Abstract No. 390

Effects of Several Trace Contaminants on Molten Carbonate Fuel Cells

S.-M. Park,* Dept. of Chemistry, The University of New Mexico, Albuquerque, NM 87131 and **T. J. O'Brien,** Morgantown Energy Technology Ctr., U.S. Dept. of Energy, Morgantown, WV 26805

The electrochemical reactivity of various trace contaminants in coal gas, *i.e.*, Hg/HgS, PbS, CdS, Sn/$SnCl_2$/$SnCl_4$, and TiO_2, in coal gas at the nickel anode and the nickel oxide cathode in a molten carbonate fuel cell have been examined thermodynamically. Calculations indicate that only $SnCl_4$ would undergo reduction at the cathode to $SnCl_2$. Possible chemical interactions between contaminants and electrodes or electrolytes have been examined. Reactions of Sn^{2+}, HgS, H_2S, and HCl with the nickel anode have negative free energies. Mercury would interact physically with the anode by forming an alloy. Reactions of Sn, $SnCl_2$, H_2S, and HCl with the nickel oxide cathode also have negative free energies. Reactions of Sn^{2+}, HCl, H_2S, and SO_2 with carbonates have large negative free energies. Born's model of ion transfer was used to calculate the free energy change for the transfer of ions from aqueous solutions to the molten carbonate solution.

Abstract No. 391

Second Law Performance of Solid Electrolyte Fuel Cells

R. A. Gaggioli,* Dept. of Mechanical Engineering, Marquette University, Milwaukee, WI 53233, **T. J. Murphy,** Dept. of Mechanical Engineering, University of California, Berkeley, CA 94720, and **G. A. Lopez,** Dept. of Mechanical Engineering, Marquette University, Milwaukee, WI 53233

A computer program has been developed to simulate solid electrolye fuel cells and has been validated by comparison with experimental data. The principal results are 2nd Law efficiencies P^*, cell power divided by fuel energy, and η^*, cell power divided by fuel minus exhaust energy, as functions of fuel rate, air-fuel ratio, cell current, temperature, and several geometric factors. Second Law cost accounting is used to get the unit costs (¢/kW-hr, $/$10^6$ Btu, etc.) for the outputs from multiproduct energy complexes which incorporate cells as one component as well as within a complex to get unit costs of power and flow streams between units thereby greatly facilitating the optimal design of the plant.

INDUSTRIAL ELECTROLYTIC

Chlorine

Abstract No. 392

A Close View of Gas Evolution

P. J. Sides* and **C. W. Tobias,** Materials and Molecular Research Div., Lawrence Berkeley Laboratory and Dept. of Chemical Engineering, University of California, Berkeley, CA 94720

The rapid events of electrolytic gas evolution were magnified and slowed with a high speed motion picture camera. A 0.2 μm thick film of tin oxide doped with antimony served as a transparent electrode which allowed oxygen evolution to be photographed from the back side where the growing and departing bubbles could not interfere with the view of the electrode surface. The movies show that coalescence of bubbles is important in their growth; coalescing bubbles cause significant fluid motion close to the electrode; bubbles can detach and return; bubbles evolve in a sequence of growth by diffusion and by different modes of coalescence.

Abstract No. 393

Chlorine Evolution. The Role of Transient Thermodynamics in Clarification of Steady-State Polarization Curves

I. V. Kadija, Olin Chemical, Charleston, TN 37310

An investigation of steady-state chlorine evolution by means of rotating double ring system indicated a considerable super-saturation of molecular chlorine in anode adjacent liquid. Polarization curves are interpreted by means of variable thermodynamic conditions at the interface.

Abstract No. 394

Influence of Bubble Dynamics on Chlorine Saturation Levels at the Anode Surface

I. V. Kadija, Olin Chemical, Charleston, TN 37310

We have previously investigated the chlorine saturation levels in the electrolyte adjacent to the anode surface under mass transport conditions defined by rotating double ring. We have extended our investigation to more practical situations with regular stationary electrodes. Here the mass transport is being controlled by bubble dynamics. Theoretical and experimental polarization curves have been developed and interpreted from the point of mass transport limitations.

Abstract No. 395

Chlorine Anodes: The Metal Anode Revolution

J. M. Kolb, Diamond Shamrock Corp., Dallas, TX 75201

Coated metal anodes have rapidly replaced graphite in the commercial production of chlorine. The availability of titanium in the 1950's led to the development of two major types of thermally deposited coatings—platinum iridium and mixed oxides of precious and nonprecious metals. These developments are reviewed, and an outline given of the physical and electrochemical properties of each. The impact metal anodes have had on the chlorine-caustic industry since their adoption in the early sixties is discussed.

Abstract No. 396

Chlorine Evolution Kinetics on Electrochemically Modified Anodic Oxide Films at Ir and Ru Electrodes

B. E. Conway* and **J. Mozota,** Dept. of Chemistry, University of Ottawa, Ottawa, Ont., Canada

At Ir and Ru, a monolayer surface oxide can be initially formed and well characterized in cyclic-voltammetry experiments. Further and prolonged cycling of potentials between certain required limits produces progressively thickened hydrated oxide films exhibiting solid-state reversible redox currents proportional to film thickness, d. d can be related to the redox charge Q, passed in anodic/cathodic potential sweeps and the increase of Q over the initial monolayer charge, Q_1, is referred to as the charge enhancement factor, CEF. Cl_2 evolution currents, i, were measured as a function of CEF over a wide range. For Ir, i is proportional to CEF up to CEF's of $ca.$ 150 x. This is shown to be due to microscopic real area change. At Ru, i is not increased with CEF, due to a different state of the thick oxide layer that is electrochemically formed at Ru. Because of a substantial change of conductivity of the Ir oxide film between 1.4 V and 0.3V E_H, (due to a change of oxidation state), interesting large differences of apparent electrocatalytic activity of the oxide layer surface for H_2 and for Cl_2 evolution are observed.

Abstract No. 397

Chlorine Ion Adsorption Effects on Surface Oxidation of Noble Metal Anodes and Kinetics of Cl_2 Evolution

B. E. Conway, D. M. Novak, and **J. Mozota,** Dept. of Chemistry, University of Ottawa, Ottawa, Ont., Canada

Experiments over a wide concentration range (10^{-7} to 10^{0} M) on the effects of Cl^- ion on the monolayer surface oxidation process of Pt and Ir anodes are described. Cl^- ion adsorption is competitive with electrodeposition of OH/O species and the competitive adsorption isotherm is quantitatively evaluated. A long linear-logarithmic behavior in $[Cl^-]$ is observed over most of the concentration range. Cl^- selectively blocks the initially formed monolayer OH film on Pt whereas, comparatively, Br^- adsorption is less selective. This is attributed to a difference in the electrosorption valency (effective charge) of adsorbed Cl^- and Br^- ions. Differences and similarities in Cl^- adsorption effects at Ir and Pt are noted in relation to the behavior of Cl^- at thick oxide films formed at Ir and Ru electrodes. The Cl^- dependent state of the monolayer oxide films on Pt and Ir is a major factor determining anodic Cl_2 evolution kinetics of these surfaces.

Abstract No. 398

Surface Structure of Ruthenium Dioxide Based Electrodes and Kinetics of Chlorine Evolution

A. Carugati, G. Lodi, and **S. Trasatti,*** Laboratory of Electrochemistry, The University, 20133 Milan, Italy

The kinetics of chlorine evolution on ruthenium dioxide based films supported on titanium and quartz is investigated as a function of the intimate structure of the catalyst surface. The latter is modified by changing the temperature of pyrolysis of $RuCl_3$ and is characterized by measuring the amount of charge exchanged with the solution when the potential is varied within a range where no electrode reaction takes place. The results allow to distinguish between macro- and microroughness of the surface. Chlorine evolution appears to be sensitive to the former but not to the latter.

Abstract No. 399

The Photoelectrochemical Production of Sodium Hydroxide and Chlorine

V. Guruswamy, G. Hildreth, and **J. O'M. Bockris,** Dept. of Chemistry, Texas A&M University, College Station, TX 77843

An examination of the evolution of chlorine from a salt solution was made by photoirradiation of certain photo anodes using an Xe lamp. These electrodes were prepared by heating T_2O_3 or TO_2, with transition metals, (T = Cr, Ru, Pt) with rare earth oxides, (La_2O_3). The current-potential curves were examined and found to be quasi-exponential. The onset potential is −1.3V with respect to the reversible anode potential; on the cathode side the electrode potential is +0.4V. The photoelectrochemical spectrum shows a maximum quantum efficiency for La CrO_3 on Ti, and it increases with increase of anode potential.

Abstract No. 400

Photoproduction of Cl_2, Br_2, and I_2 on an n-Semiconducting Powder

B. Reichman* (Present address: Energy Conversion Devices, Troy, MI 48084) and **C. E. Byvik,** NASA Langley Research Center, Hampton, VA 23665

The halogen molecules, Cl_2, Br_2, and I_2 have been successfully photoproduced in oxygen-saturated aqueous solutions containing the respective halide ion and platinized semiconducting n-TiO_2 powder. While the latter is produced photocatalytically, the first two are clear examples of products of photosynthetic reactions. The photooxidation of the halogens was carried out at several pH values and for various conditions, and conclusions concerning the efficiency of the overall process are discussed.

Abstract No. 401

Catalytically Active Coatings for Hydrogen Evolution in Brine Electrolyses

M. D. Spasojević, N. V. Krstajić, K. I. Popov, and **R. T. Atanasoski,*** Institute of Electrochemistry ICTM, and Faculty of Technology and Metallurgy, University of Beograd, Beograd, Yugoslavia

The reaction of hydrogen evolution has been successfully catalyzed on both titanium and stainless steel substrates. On titanium, a coating has been developed consisting of a protective layer of thermally decomposed lanthanum and titanium salts on top of which molybdenum and cobalt has been electrodeposited. On stainless steel only a layer of cobalt and molybdenum has been applied. Good polarization characteristics of these coatings have been preserved for more than a year so far. No signs of corrosion of the coatings nor of the substrate has been noticed.

Abstract No. 402

Metal Anodes and Hydrogen Cathodes: Their Activity Towards ClO_3^- Formation, O_2 Evolution, and ClO_3^- Reduction

B.V. Tilak and **D. Pouli,*** Hooker Chemicals, Research Center, Grand Island, NY 14072

Two parasitic processes occurring in chlor-alkali and chlorate cells include: (*i*) co-generation of O_2 and (*ii*) chlorate formation and reduction. Factors influencing the kinetics of these reactions on some noble-metal based anodes and nonsteel based cathodes are discussed and exemplified in an effort to develop additional criteria involved in the selection of electrode materials.

Abstract No. 403

Chlorine Anodes and Their Effects on Diaphragm Cell Performance

M. P. Grotheer, Hooker Chemicals & Plastics Corp., Niagara Falls, NY 14302

It is well known that the conversion of diaphragm cells from graphite to metal anodes produced an energy savings of up to 15%. Other effects of this conversion, such as higher anolyte pH's, higher concentrations of active chlorine in anolyte, higher concentrations of chlorate in cell liquor and higher oxygen concentrations in the hydrogen produced, have been discussed very little if at all. This paper discusses these effects in terms of commercial operating data and attempt to provide some insight into the chemistry behind the observation.

Abstract No. 404

Modified Cathode for Chlor-Alkali Electrolysis

K. Kawasaki* and **I. Matsuda,** Showa Denko K.K., 13-9, Shiba Daimon 1-chome, Minato-ku, Tokyo, Japan

The present report relates to the porous iron-alloy coated cathode for salt electrolysis, featuring low hydrogen overvoltage, prepared by electroplating the conventional cathode. The electroplating process features the use of a

special iron alloy bath. The plating procedure is identical to that of the conventional plating process. The cathode prepared by this process imparts a hydrogen overvoltage that is about 0.3V lower than the conventional mild steel cathode having smooth surface.

Abstract No. 405

Characteristics of Two-Phase Flow in Electrochemical Chlorate Reactors

E. M. Spore, Hooker Chemical, Niagara Falls, NY 14302

Gas evolution in chlorate cells, particularly H_2 and water, have a dramatic effect on cell voltage and efficiency. Pilot plant scale experiments utilizing the pumping characteristics of H_2 gas lift and the vapor pressure of H_2O with temperature have yielded a 500 mV voltage reduction and up to 6% increase in cell current efficiency. Computer programs accurately predict interelectrode cell liquor velocities and voltage with various pumping tower designs and electrode geometry.

Abstract No. 406

Optimization of Electrolytic Cells Having Large Numbers of Design Variables

R. C. Alkire,* G. D. Cera, and **M. A. Stadtherr,** Dept. of Chemical Engineering, University of Illinois, Urbana, IL 61801

A reduced gradient optimization technique was applied to a simple nonlinear model of a single electrolytic cell. A model of a percolating diaphragm chlor-alkali cell was used for the investigation reported here, although any other cell for which model equations are available could be optimized by the technique described. An objective function (profit) was maximized over thirty-nine variables and thirty-six constraints. Information relating to the sensitivity of the optimum with respect to perturbations in the variables and constraints was also elicited from the study.

Abstract No. 407

Hybrid Cell—A New Process for Improving the Energy Efficiency and Reducing the Cost of Chlor-Alkali Production

B. Broniewski, B. Warszawski, A. T. Emery, and **H. P. Silverman,** Occidental Research Corp., Irvine, CA 92713

A new device for improving the energy efficiency and reducing the cost of chlor-alkali production is described. The device combines two energy efficient processes: a fuel cell (for converting the chemical energy content of hydrogen into electrical energy) and an electrodialysis cell (for concentration and purification of sodium hydroxide). This combined operation recovers almost 20% of the electrical energy used in chlor-alkali production and minimizes caustic evaporation. The hybrid cell is separate from the chlor-alkali cell and operates in a chlorine-free environment. It uses low cost all plastic cell components and inexpensive hydrocarbon membranes. The hybrid cell can be used to retrofit existing plants as well as for new "grass-roots" plants.

Abstract No. 408

Power Dissipation in Shunt-Current Parasitic Process in Series-Connected Electrochemical Cells with Common Electrolyte

P. Grimes* and **R. Bellows,** Exxon Research and Engineering Co., Linden, NJ 07036 and **M. Zahn,** Dept. of Electrical Eng. and Computer Sci., Massachusetts Institute of Technology, Cambridge, MA 02139

Expressions are described for the estimation of power dissipation in cells, channels, and manifolds in systems with series-connected cells with common electrolyte, at open circuit, power input, and power production modes. Comparisons are made to power requirements for shunt-current protection processes.

Abstract No. 409

Parasitic Current Elimination in Series-Connected Electrochemical Cell Systems with Shared Electrolyte. III. Channel Interconnects

P. Grimes* and **R. Bellows,** Exxon Research and Engineering Co., Linden, NJ 07036 and **M. Zahn,** Dept. of Electrical Eng. and Computer Sci., Massachusetts Institute of Technology, Cambridge, MA 02139

Parasitic current effects can be reduced in series-connected electrochemical cell systems with shared electrolyte by passing an appropriate current through interconnections between channels which connect the cells to the manifolds. The current requirements will be compared to the manifold protection current (Part I, II) (1).

1. Abstracts 120 and 121 presented at The Electrochemical Society Meeting, Hollywood, Florida, Oct. 5-10, 1980.

Abstract No. 410

Mechanisms of Shunt Current Production in Series-Connected Electrochemical Cells with Common Electrolyte

P. Grimes* and **R. Bellows,** Exxon Research and Engineering Co., Advanced Energy Systems Laboratory, Linden, NJ 07036

Four electrochemical processes can contribute to the production of shunt currents in series-connected electrochemical cells with common shared electrolyte. These processes are described and their relative potential for product contamination, yield reduction, reactant consumption, and electrode corrosion is discussed.

Abstract No. 411

Effects of the Brine Impurities on the Cell Performance of the Diaphragm-Type Chlor-Alkali Cell

F. Hine,* M. Yasuda, and **K. Fujita,** Nagoya Institute of Technology, Gokiso-cho, Showa-ku, Nagoya 466 Japan

A laboratory cell equipped with the deposited asbestos diaphragm was operated with impure brine to investigate the effects of the hardness on the cell performance. The concentration distribution of NaOH in the diaphragm is established by three factors: diffusion, migration, and the hydraulic flow. It was pointed out that the migration flux was larger than the diffusion flux under the operating conditions of the diaphragm cell.

Abstract No. 412

A Comparison of Properties of Films of Perfluorinated Carboxylate and Sulfonate Ion Exchange Polymers

Z. Twardowski,* L. Clarke, and **H. L. Yeager,** Dept. of Chemistry, The University of Calgary, Calgary, Alta., Canada T2N 1N4

Several properties of a film of a perfluorinated carboxylate ion exchange polymer and perfluorosulfonate film (Nafion® 120), are compared here. Film self-diffusion coefficients for Na^+, Cs^+, and water have been determined in dilute solution environments from 0° to 40°C. In addition, water sorption in alkali metal ion forms and ion exchange selectivities for Na^+ and Cs^- exchange with hydrogen ion have been measured. Both film types exhibit excellent cationic diffusion capability; differences in various film properties are discussed in terms of possible mechanisms for film diffusion.

Abstract No. 413

Diffusional Properties of a Perfluorinated Carboxylate Film in Chlor-Alkali Solution Environments

H. L. Yeager* and **B. O'Dell,** Dept. of Chemistry, The University of Calgary, Calgary, Alta., Canada T2N 1N4

The diffusional behavior of a film of a perfluorocarboxylate polymer has been investigated at elevated temperatures in the concentrated brine and caustic solution environments which are found in chlor-alkali cells. Film self-diffusion coefficients of Na^+ were measured as a function of caustic concentration and as a function of brine *p*H. Ionic dialysis and osmosis were studied in systems where the film separated brine and caustic solutions. Results are discussed in terms of the potential advantages of using membranes based on films of this type in the production of chlorine-caustic.

Abstract No. 414

Measurement of Ionic and Water Transport Numbers in a Membrane Chlor-Alkali Cell

H. L. Yeager* and **Z. Twardowski,** Dept. of Chemistry, University of Calgary, Calgary, Alta., Canada T2N 1N4

A new membrane test cell has been built to measure the Na^+ and water transport numbers in a brine-caustic electrolysis system. The experiment uses sodium-22 radiotracer and weighing methods to yield results with improved accuracy. The cell has been applied to the study of a perfluorosulfonate (Nafion® 120), a film of a perfluorocarboxylate ion exchange polymer. The carboxylate material shows dramatic increases in the Na^+ transport number. Results are discussed in terms of water sorption and related properties of these polymers.

Abstract No. 415

Estimation of Minimum Thickness for a Chlor-Alkali Diaphragm

K. Viswanathan, Hooker Chemical, Niagara Falls, NY 14302

A mathematical model proposed by Stender is used to predict the performance of a chlor-alkali cell diaphragm. For a given caustic current efficiency, catholyte percolation flow, current density, and porosity of the diaphragm, the minimum thickness that a diaphragm must have can be calculated. Knowing the average specific conductivity of the liquid medium within the diaphragm, the voltage drop across the separator may then be calculated. Typical calculations are performed for a Hooker H-4 cell and compared with the actual performance.

Abstract No. 416

Electrochemical Hypochlorination of Allyl Chloride in Dilute HCl

C. Comninellis* and **E. Plattner,** Institut de Génie chimique, Ecole Polytechnique Fédérale de Lausanne, Ecublens, 1015 Lausanne, Switzerland

In the synthesis of organochlorine compounds hydrogen chloride is obtained as a by-product which can be used in the electrochemical hypochlorination of olefins. In this work we have studied the electrochemical hypochlorination of allyl chloride in dilute HCl solution in a cell without a diaphragm to produce dichloropropanols (2.3 + 1.3). The yield and selectivity of the process were found to be influenced by the reaction conditions, anode material, hydrochloric acid concentration, and current density. The following optimum conditions for the hypochlorination of allyl chloride were found: current yield 80-90%, selectivity 85-92%, when using 0.8-1.5*N* HCl, current density of 50-100 mA/cm^2 and temperature 25°-30°C. An economical study of the process has been effected.

Abstract No. 417

Membrane for Chlor-Alkali Electrolysis

M. Seko, Asahi Chemical Industry Co., Ltd., Chiyodaku, Tokyo, Japan

The membrane should contain perfluoro carboxylic acid as functional group to prevent the backmigration of hydroxide ion. However the membrane which has only carboxylic acid is not appropriate for the industrial operation because of its high electric resistance due to low moisture content. Asahi came to the conclusion that the best membrane should consist of sulfonic acid on the anode side and carboxylic acid on the cathode side, with an optimal layer thickness of 0.1-0.5 mil.

Abstract No. 418

Energy Saving in Brine Electrolysis with Oronzio deNora SPE Cell

A. Nidola, Oronzio deNora Impiante Elettrochimici S.p.A., 20134 Milano, Italy

Commercial cation exchange membrane activated *in situ* on the anodic side with an anode catalyst which very selectively promotes the chlorine evolution reaction over the undesirable oxygen evolution reaction and further is activated on the opposite side with a cathode catalyst activated to promote the hydrogen evolution reaction, shows important energy savings over conventional chlor-alkali membrane cell technology.

ORGANIC AND BIOLOGICAL ELECTROCHEMISTRY

Electrochemistry in the Study of Novel Organic Compounds

Abstract No. 419

Reoxidative Cleavage and Reductive Formation of Cyclopropane Derivatives

P. G. Gassman, Dept. of Chemistry, University of Minnesota, Minneapolis, MN 55455

Recently, both the oxidative cleavage of cyclopropane derivatives and the reductive synthesis of fused ring cyclopropane derivatives have attracted considerable interest in our laboratories. Special emphasis has been devoted to the electrochemical oxidation of a variety of highly strained polycyclic molecules with special emphasis on the bicyclo[1.1.0]butane nucleus. Both the ease of oxidation and products of oxidation have been investigated. In terms of the synthesis, the reductive cyclization of appropriate electrophilic species to radical anions generated electrochemically from α,β-unsaturated ketones has been explored. Fused ring cyclopropane derivatives and other bicyclic systems have been prepared using this methodology.

Abstract No. 420

The Electrochemistry of Novel Pi-Systems

A. J. Fry, Dept. of Chemistry, Wesleyan University, Middletown, CT 06457

The broad features of the electrochemical cathodic behavior of aromatic hydrocarbons are known in some detail. The present study examines some less-studied aspects of the electrochemistry of aromatic systems, including extreme forms of ion-pairing and the electrochemistry of stable free radicals.

Abstract No. 421

Dual Reactivity in the Reduction of β-Mercapto-α-ketoacids

M. Fleury, Laboratoire de Chimie Analytique, Faculté des Sciences Pharmoceutiques et Biologiques, University Paris V, 75270 Paris, Cedex 06, France, **J. Tohier,** Laboratoire de Chimie de l'E.N.S.E.T., 94230 Cachan, France, and **P. Zuman,*** Clarkson College, Potsdam, NY 13676

In the majority of cases compounds of the type Y-CH(Z) COR (where Y=OR, SR, SR^+_2, NR_2, NR^+_3, and PR^+_3) are reduced with a cleavage of the C—Y bond. For R'S—CH(Z) COCOOH reduction of CO predominates, in R'S—CH(Z)COCOO$^-$ both CO and C—S are reduced in competitive reactions, in $^-$S—CH(Z) CO COO$^-$ cleavage of C—S predominates. In the same sequence hydration of the CO group decreases. For the isopropyl derivative (Z = $CH(CH_3)_2$) and thioether (R'=CH_3) hydration is suppressed.

Abstract No. 422

Long Lived Radical Cations with Small Pi Systems

S. F. Nelsen,* C. R. Kessel, W. C. Hollinsed, R. Akaba, and **D. J. Steffek,** Dept. of Chemistry, University of Wisconsin, Madison, WI 53706

Radical cations which have an odd electron formally localized on one or two pi centers are usually too short-lived to allow their CV to be reversible, so $E°$ cannot be determined. Choosing alkyl groups which hold the α-hydrogens perpendicular to the pi orbital axis of the radical cation allows isolation of hydrazine radical cations, and $E°$ measurement for trialkylamines, dialkylchloramines, and monoolefins. Thermodynamic effects of the choice of alkyl groups are discussed.

Abstract No. 423

Electrochemical Studies on Novel Arenetricarbonylchromium Complexes and Potential New Electron Acceptors

R. D. Rieke,* S. N. Milligan, I. Tucker, B. Willeford, and **L. I. Rieke,** Dept. of Chemistry, University of Nebraska, Lincoln, NE 68588

Electrochemical oxidation of complexes of the type dimethylbis (phenyltricarbonylchromium)M where M = C, Se, Ge, Sn, and Pb result in a stable dication. The electrochemical results indicate two noninteracting phenyltricarbonylchromium groups. Proper substitution on the phenyl rings provides for additional stabilization of the dications. Reduction of the binaphthylbistricarbonylchromium complex yields a stable dianion. Redox properties of several new organic electron acceptors are discussed.

Abstract No. 424

Influence of Metal Oxidation State on the Structure of Pi-Complexed Polyolefins

W. E. Geiger, Jr.* and **J. Moraczewski,** Dept. of Chemistry, University of Vermont, Burlington, VT 05405

The manner in which a cyclic polyolefin, such as cyclooctatetraene (COT) or cyclooctadiene (COD) bonds to transition metals in metal pi-complexes can be changed by reduction of the metal pi complex to its radical anion. We have studied the reduction of (COT)CoCp(Cp= $\eta^5-C_5H_5$), (COT)Co($\eta^5-C_5Me_5$), and (COD)CoCp in nonaqueous solvents by a number of voltammetric and spectroscopic techniques. The electrochemically-induced hydrocarbon isomerizations we observe are discussed in terms of the bonding in the radical anions.

Mechanisms and Mechanistic Techniques in Organic Electrode Reactions

Abstract No. 425

Derivative Cyclic Voltabsorptometry: A New Spectroelectrochemical Technique for the Study of Organic Electrode Reactions

E. E. Bancroft and **H. N. Blount,*** Brown Chemical Laboratory, The University of Delaware, Newark, DE 19711

A new spectroelectrochemical technique for the study of mechanisms of organic electrode reactions has been developed. This method couples cyclic linear sweep potential perturbation of an optically transparent electrode with optical monitoring of the product of the electrode reaction. The observed absorbance is differentiated with respect to the linearly varying potential to yield a waveform which is analogous to cyclic voltammetry. Unique advantages of this technique are demonstrated for E, EC, ECE, and half-regeneration mechanisms.

Abstract No. 426

Thin Layer Spectroelectrochemical Kinetic Study of Viologen Cation Radicals Reacting at Hydrogen-Evolving Gold and Nickel Electrodes

E. F. Bowden and **F. M. Hawkridge,*** Dept. of Chemistry, Virginia Commonwealth University, Richmond, VA 23284

The kinetics of viologen cation radicals reacting at hydrogen-evolving gold and nickel electrodes in pH 6 to 8 electrolytes have been investigated. Visible absorption spectroscopy was used to follow the course of the reaction in an optically transparent thin layer electrochemical cell under quasi-steady-state conditions. The spectroelectrochemical data were analyzed using classical kinetics and yielded zero-order behavior. For methyl viologen cation radical at gold, a formal zero-order rate constant evaluated at zero hydrogen overpotential was found to be 1×10^{-13} moles/sec-cm^2. At nickel the comparable rate constant was *ca.* two orders of magnitude larger than at gold. Increasing pH from 6 to 8 at gold electrodes shifted both the hydrogen evolution and the methyl viologen cation radical reaction 60-70 mV/pH unit in a negative direction. The diquat cation radical behaved in a similar manner. The proposed mechanism involves a fast, non-rate-limiting, chemical reaction between the viologen cation radical and adsorbed hydrogen atom(s).

Abstract No. 427

Diffractive Spectroelectrochemistry—Enhanced Optical Probes for Monitoring Electrogenerated Species

P. Rossi, R. Robinson, and **R. L. McCreery,*** Dept. of Chemistry, Ohio State University, Columbus, OH 43210

Commonly used techniques for obtaining UV-VIS spectral information about solution components involved in electrode reactions suffer from lower sensitivity, and are usually limited to strong chromophores with moderate lifetimes. By using light diffracted by an electrode for absorbance measurements, the region very close to the electrode surface is monitored, yielding improved sensitivity and time resolution. Increases of factors of 3000 in absorbance over conventional techniques have been observed, and the useful time scale of the approach has been extended down to 10 μsec.

Abstract No. 428

Development of a Spectrofluoroelectrochemical Cell for Studying Biological Systems

M. J. Simone, W. R. Heineman, and **G. P. Kreishman,*** Dept. of Chemistry, University of Cincinnati, Cincinnati, OH 45221

An optically transparent thin layer electrode with a gold minigrid as the working electrode of standard design can be used for detecting changes in fluorescent properties of a molecule as a function of its oxidation state. Fluorescence spectrum in the 300-450 nm range can easily be obtained. At longer wavelengths, due to excessive light scattering by the minigrid detection of fluorescence is difficult. Reduction potentials have been determined for cobalamin and cytochrome *c* at 1 to 10 μM concentrations.

Abstract No. 428A

Comparison of Stopped-Flow Kinetic Spectrophotometry and Open-Circuit Relaxation Spectroelectrochemistry in the Study of the Kinetics and Mechanism of Reactions of Electrogenerated Species

J. F. Evans, Dept. of Chemistry, University of Minnesota, Minneapolis, MN 55455

The techniques of stopped flow kinetic spectrophotometry (SFKS) and open-circuit relaxation spectroelectrochemistry (OCRSE) as they apply to the study of reaction rates and mechanisms of absorbing electrogenerated species are compared and contrasted. Whereas SFKS can be utilized at much lower concentrations of reacting absorber than OCRSE, these techniques in combination are shown to be complimentary in examining systems over a much wider concentration range than availed by only one approach. Thus, the concentration range over which a proposed mechanism can be tested is considerably increased. Moreover, numerical analytical approaches are presented that allow for conversion of OCRSE absorbance-time transients to conventional kinetic plots for higher order reactions (*e.g.*, second order in absorber), thereby simplifying the analysis of the kinetic data and the elucidation of mechanism.

Abstract No. 429

Electrocatalysis of Chemical Reactions—The Effect of Electrogenerated Bases on Several 9-Substituted Fluorenes and Bifluorenyls

C. Nuntnarumit, F. M. Triebe, and **M.D. Hawley,*** Dept. of Chemistry, Kansas State University, Manhattan, KS 66506

Three types of chain reactions which are induced by electrogenerated bases have been studied for a series of 9-substituted fluorenes and bifluorenyls. In the first series hydroxide ion electrogenerated by the cleavage of the carbon-oxygen bond in 9-hydroxybifluorenyl and 9,9-dihydroxybifluorenyl anion radicals effects a chain reaction in which carbon-carbon bond cleavage in unreacted starting material gives monomeric, fluorenyl products. In the second type, electrogenerated methoxide ion causes the elimination of methanol from 9-methoxybifluorenyl to give bifluorenylidene. In the last type, azobenzene anion radical

electrogenerated in the presence of 9-fluorenylamine and 9-fluorenol causes a chain reaction that results in the formation of hydrazobenzene and the oxidation of 9-fluorenylamine and 9-fluorenol to fluorenone imine and fluorenone, respectively.

Abstract No. 430

The Electroreduction of PhCOR and PhRC=CHCN

E. M. Abbot and **A. J. Bellamy,** Dept. of Chemistry, University of Edinburgh, Edinburgh EH9 3JJ, Scotland, **J. B. Kerr,*** Hooker Chemical Co., Electrochemicals R&D, Niagara Falls, NY 14302, and **I. S. MacKirdy,** Dept. of Chemistry, University of Edinburgh, Edinburgh EH9 3JJ, Scotland

The electroreduction of PhCOR and PhRC=CHCN (R=Ph, Me, H) in dry acetonitrile has been studied. Significant amounts of adducts arising by reaction of the substrate with the cyanomethyl anion were obtained. The conditions for promoting and suppressing such reactions were evaluated and the reaction mechanisms were investigated. The effect of residual water upon the stereochemistry of dimeric products was also studied.

Abstract No. 431

Mechanisms of Acid and Base Catalyzed Dehydration of Geminal Diols

J. Rusling, J. Segretario, and **P. Zuman,*** Clarkson College, Potsdam, NY 13676

Polarographic studies indicate when an acid-base equilibrium preceding the dehydration proper is the rate-determining step of the dehydration and when the loss of water or hydroxide ions governs the rate of dehydration. In the case of the rate-determining formation of a geminal diol anion followed by rapid loss of OH^- the conjugate base is effectively reduced. Examples of reductions of pyridinecarboxaldehydes, 1,2-diketones, and some α-ketoacids are given.

Abstract No. 432

Electrochemical Generation of Arenetricarbonylchromium Anions. A Study of Their Reactions with Electrophiles

R. D. Rieke,* W. P. Henry, G. D. Venburg, S. N. Milligan, and **J. Arney,** Dept. of Chemistry, University of Nebraska, Lincoln, NE 68588

Electrochemical reduction of arenetricarbonylchromium complexes generally is a two electron process. The resulting dianions show varying degrees of reactivity towards water. This reactivity is highly dependent on the arene. Heterocyclic complexes as well as monothiocarbonyldicarbonylchromium complexes have been prepared to probe the origin and degree of reactivity towards water. The reaction products as well as their redox properties are discussed.

Abstract No. 433

Electrochemical Reduction of Carbonium Ions in $AlCl_3$-Containing Melts

G. Luer and **D. Bartak,*** Dept. of Chemistry, University of North Dakota, Grand Forks, ND 58202

The electrochemical reduction of free carbonium ions to their respective radicals was studied in a room temperature aluminum chloride-n-butylpyridinium chloride melt. The carbonium ions were generated from alkyl chlorides via reaction [1]

$$RCl + Al_2Cl_7^- \underset{k_b}{\overset{k_f}{\rightleftarrows}} R^+ + 2AlCl_4^- \quad [1]$$

$$R^+ + e^- \rightarrow R\cdot \quad [2]$$

$$2R \rightarrow RR \quad [3]$$

where R = Ph_3C—, Ph_2CH—, $PhCH_2$—, $(CH_3)_3C$—. U.V. and visible spectrophotometric techniques were used to determine the concentration of R^+ as a function of melt acidity (pCl); the equilibrium constant for reaction [1] was determined. Cyclic voltammetry, chronoamperometry, and controlled potential coulometry were used to establish reactions [2] and [3]. Rotating disk voltammetry of the carbonium ion established that k_f was relatively slow.

Abstract No. 434

Applications of Fast Fourier Transform Faradaic Admittance Measurements (FFT-FAM) to Organic Electrode Reaction Heterogeneous Charge Transfer Rates

J. H. Begemann, M. Grzeszczuk, and **D. E. Smith,*** Dept. of Chemistry, Northwestern University, Evanston, IL 60201

Instrumentation used in our laboratory for FFT-FAM measurements is described, including empirical performance specifications based on several years of application to electrochemical systems of widely varying properties. Recent applications of this instrumentation to investigations of heterogeneous charge transfer rates of homologous series of organic molecules in aprotic organic solvents are surveyed. Our latest studies have focused on nitroaliphatics, nitroaromatics, and substituted biphenyls. We describe and rationalize effects of solvent, electrolyte, and electrode material.

Abstract No. 435

Reverse Pulse Polarographic Study of 1-methyl-4-cyanopyridinium Ion

A. Webber, E. Kirowa-Eisner, and **J. Osteryoung,*** Dept. of Chemistry, State University of New York at Buffalo, Buffalo, NY 14214

The cathodic reduction of 1-methyl-4-cyanopyridinium ion in acetonitrile solutions exhibits two one-electron reductions, the second irreversible, which are coupled to homogeneous reactions such as the attack of carbanion on the cation substrate. The reaction mechanism is elucidated by using normal and reverse pulse polarography.

Abstract No. 436

Identification of Electrolysis Mechanism Using Cyclic Voltammetry and Computerized Pattern Recognition

S. P. Perone and **S. D. Schachterle,** Dept. of Chemistry, Purdue University, West Lafayette, IN 47907

This work reports the development of a pattern recognition method for identifying the mechanism of an electrode process using the shape information contained in a single cyclic voltammetry experiment. Experimental voltammograms are classified using a training set composed of nearly 900 theoretical curves, which allow a broad coverage of types of electrode processes (nine) and values of electrochemical parameters (k_s, n, etc). The method was applied to 12 different electrode processes under a variety of conditions. The mechanism was correctly identified with 93% accuracy under conditions where a single process prevailed.

Abstract No. 437

Conformational Effects on the Electrochemical Oxidation and Reduction of Sterically Hindered Ethylenes

R. W. Busch and **D. H. Evans,*** Dept. of Chemistry, University of Wisconsin, Madison, WI 53706

The thermochromic substance, bianthrone, formally may be regarded as a sterically hindered ethylene. Earlier studies have shown that great differences exist between the electrochemical behavior of the low temperature, quasiplanar, A form and the high temperature, twisted, B form of bianthrone. Similar behavior has been noted for the reduction of various substituted bianthrones. Related conformational effects were discovered involving oxidation of 2,2′-dimethoxybianthrone, dixanthylene, and dithioxanthylene.

Abstract No. 438

Catalytic and Electrocatalytic Behavior of Ruthenium Dioxide

L. D. Burke* and **J. F. Healy,** Chemistry Dept., University College, Cork, Ireland

The commercial development of dimensionally stable anodes has resulted in increasing interest in the redox behavior of RuO_2 and related compounds. The involvement of higher oxidation states of the metal in electro-organic oxidation reactions at this type of substrate is demonstrated. The use of this type of material as a catalyst for oxidations carried out in a nonelectrochemical manner is also described.

Abstract No. 439

Electrochemical Determination of Cation Radical Stabilities of Methylbenzo[a]pyrenes

D. A. Tryk and **S.-M. Park,** Dept. of Chemistry, The University of New Mexico, Albuquerque, NM 87131

All twelve monomethylbenzo[a]pyrenes were studied using cyclic voltammetry, current-reversal chronopotentiometry, single- and double-potential step chronoamperometry, and double-potential step chronocoulometry in dry and wet acetonitrile in order to determine the stability of the cation radicals. EC and ECE rate constants were obtained for certain aspects of the overall EC . . . EC process (6 electrons). Rate constants and half-wave potentials were compared with molecular orbital calculations and carcinogenicities.

Abstract No. 440

Electrochemically Activated Binding of Benzo[a]pyrene and Other Polycyclic Aromatic Hydrocarbons to DNA

D. A. Tryk and **S.-M. Park,** Dept. of Chemistry, The University of New Mexico, Albuquerque, NM 87131

Benzo[a]pyrene (B[a]P) has been subjected to anodic oxidation in single- and double-phase solutions in contact with DNA. The DNA was recovered, washed, and, using fluorescence spectroscopy, levels of chemical binding were estimated to be about 3000 and 600 μmol B[a]P per mol nucleotide in single- and double-phase experiments respectively and about 1600 μmol 6-methyl[a]P per mol nucleotide in a single-phase experiment. Five other hydrocarbons were tested in double-phase experiments.

Abstract No. 441

Mechanisms of Mediated NADH Electrooxidations

L. L. Miller* and **A. Kitani,** Dept. of Chemistry, University of Minnesota, Minneapolis, MN 55455

NADH oxidations have been mediated by a variety of oxidants. Rate constants for the homogeneous reaction between oxidized mediator and NADH have been measured. It has been demonstrated that orthoquinone by diimines are especially effective. The mechanistic approach and results are discussed.

Abstract No. 442

Electrochemical Regeneration of NAD

G. L. Cahen, Jr.,* Dept. of Materials Science, University of Virginia, Charlottesville, VA 22901, **D. J. Kirwan,** Dept. of Chem. Engineering, University of Virginia, Charlottesville, VA 22901, and **J. W. Parcells** and **G. E. Stoner,** Dept. of Materials Science, University of Virginia, Charlottesville, VA 22901

The use of the cofactor nicotinamide adenine dinucleotide (NAD) requiring enzymes in chemical processes is dependent on regeneration and multiple reuse of the cofactor. The behavior of several composite electrodes in the regeneration of NAD are compared to bulk graphite and platinum. The reaction is no longer apparently first order and there are no apparent end product nor substrate concentration dependencies. In addition, the specificity of the regeneration has improved significantly.

Abstract No. 443

Electrochemistry of Uric Acid and Related Biological Purines

R. N. Goyal, A. Brajter-Toth, and **G. Dryhurst,*** Dept. of Chemistry, University of Oklahoma, Norman, OK 73019

The electrochemical oxidation of uric acid, a naturally occurring purine, has been examined between *p*H 1.5 and 10 using cyclic voltammetry, thin layer spectroelectrochemistry, and extensive analysis of reaction intermediates and products. Intermediates have been characterized electrochemically, spectrally, and kinetically and at least one has been trapped and analyzed by gas chromatography-mass spectrometry. Initial oxidation leads to formation of a very reactive diimine which rapidly hydrates to an imine-alcohol. The latter intermediate then undergoes a rapid ring contraction to form a bicyclic carboxylic acid which can be trapped and analyzed. The bicyclic carboxylic acid is also unstable in aqueous solution and further decomposes to the ultimate products which are largely controlled by *p*H.

General Session

Abstract No. 444

Electrochemical Production of Manganic Sulfate in Concentrated H_2SO_4

C. Comninellis and **E. Plattner,** Institut de Génie chimique, Ecole Polytechnique Fédérale de Lausanne, Ecublens, 1015 Lausanne, Switzerland

The electrochemical oxidation of manganous sulfate to manganic sulfate can be effected with high current efficiency (80-90%) in moderate H_2SO_4 concentration but with low current efficiency in concentrated H_2SO_4 (15-16M). In this work we have found that the presence of catalytic amount of Ag_2SO_4 increases considerably the current efficiency of manganous sulfate oxidation in concentrated H_2SO_4. The process has been applied for the oxidation of some organic compounds.

Abstract No. 445

Preparative Gas Phase Electrochemical Production of Hydrogen and Fluorine Atom Reactions with Aromatic Compounds

L. L. Miller* and **P. W. Schmalzl,** Dept. of Chemistry, University of Minnesota, Minneapolis, MN 55455

The reaction, in an inductively coupled radio frequency plasma discharge, of aromatic compounds with hydrogen produces hydrogenation and fragmentation of the substituted benzenes. Fluorination and trifluoromethylation result from the reaction of perfluoroalkanes (CF_4, C_2F_6) with aryl compounds. The nature of the products and their dependence upon flow rates, applied power, and reactor pressure are discussed.

Abstract No. 446

Preparative Gas Phase Electrochemical Production of Acrylonitrile from Ethylene

N. Henis, Y.-H. So, and **L. L. Miller,*** Dept. of Chemistry, University of Minnesota, Minneapolis, MN 55455

The production of nitriles from cyanogen and various alkenes in an inductively coupled radio frequency plasma discharge has been investigated. Formation of acrylonitrile from ethylene occurs in particularly high yield. The effects of flow rate and power on the yields are discussed. Heavier alkenes, such as *cis*-2-butene produce nitrile products in lower yields.

Abstract No. 447

Preparative Gas Phase Electrochemical Production of Cyanoaromatics

Y.-H. So* and **L. L. Miller,** Dept. of Chemistry, University of Minnesota, Minneapolis, MN 55455

Aromatic compounds are directly cyanated by passing cyanogen and the respective compounds through a radiofrequence generated and inductively coupled glow discharge zone. Benzene and a wide variety of substituted benzenes (C_6H_5X, X = CH_3, *t*-butyl, CF_3, OH, F, Cl, Br, CHO) are cyanated providing a good use of ortho, meta, para, and ipso substituted products. A mechanism involving cyano radicals is supported by a Hammett plot ρ value of -0.4.

ORGANIC AND BIOLOGICAL ELECTROCHEMISTRY/ENERGY TECHNOLOGY

Electrochemistry of Biomass Derived Compounds

Abstract No. 449

Electrochemistry of Biomass and Derived Materials

H. L. Chum, Solar Energy Research Institute, Biomass Thermal Conversion and Exploratory Research Branch, Golden, CO 80401 and **M. M. Baizer,*** School of Engineering and Applied Science, University of California, Los Angeles, CA 90024

After defining the scope of what is included in the term "biomass and derived materials," this paper discusses the pretreatments for converting the natural material to possible electrochemical feedstocks, the categories of substances so produced, and the electrochemical reactions and technologies for transforming these intermediates into organic chemicals useful as fuels and/or valuable building blocks or products. Current and planned work is cited.

Abstract No. 450

Depolarizing Water Electrolysis Via Biomass Derived Materials

M. R. St. John,* **A. J. Furgala,** and **A. F. Sammells,** Institute of Gas Technology, Chicago, IL 60616

Electrolytic hydrogen generation by conventional methods is uneconomical for large scale production because of the high electrical-energy cost resulting from a rather high operating potential. This high potential is a consequence of a relatively high reversible potential and high overpotential for the direct water electrolysis reaction. One approach to the reduction of the electrolysis cell potential is to substitute a more desirable reaction for the oxygen evolution reaction, or in other words, to depolarize the anode. The desirability of any reaction rests on its ability to reduce the reversible potential of the cell and/or the anode overpotential. The work presented discusses the oxidation of the biomass derived material, glucose, as a possible depolarizing reaction for the anode in water electrolysis. Cyclic voltammetry results on the oxidation of glucose in H_2SO_4 electrolyte under varying conditions of temperature, glucose concentration, acid concentration, and anode material are presented along with the cyclic voltammograms of possible oxidation products. The controlled potential electrolysis results of glucose oxidation in H_2SO_4 electrolyte and at a platinized platinum anode are discussed.

Abstract No. 451

Hydrogen and Single Cell Protein from Biomass by Electrolysis

M. P. Steinberg,* **D. L. Day,** and **R. R. Kravets,** Dept. of Agricultural Engineering, University of Illinois, Urbana, IL 61801

This process couples electrolysis of water to oxygen and hydrogen with an aerobic fermentation which converts biomass to single cell protein and other constituents between the electrodes. Cell design, especially anode material, is extremely important. Electrode arrangement is one cathode sandwiched between two anodes. A diaphragm is not necessary, greatly reducing cell electrical resistance. Cell voltage was only 2.8V. The cell was operated with liquid swine manure and cheese whey. Electricity to hydrogen conversion efficiency is high.

Abstract No. 452

Polarography in the Study of Physicochemical Properties of Lignin

P. Zuman,* **S. Ainso, B. Pethica,** and **R. Smith,** Dept. of Chemistry, Clarkson College, Potsdam, NY 13676 and **L. Jurasek,** Pulp and Paper Research Institute, Montreal, Que., Canada

Polarographic and spectrophotometric methods were used in the study of some reaction rates and equilibria involving lignin. Examples are studies of the reaction of lignin with hydroxide ions and of acid-base equilibria involved, as well as of adsorption of nitrosamines, inorganic cations, and bile acids by lignin. In the latter case the dehydration of bile acids in sulfuric acid was investigated. At low concentration levels differential pulse polarography was found useful.

Abstract No. 453

Abstract Withdrawn.

Abstract No. 454

Electroreduction of Lignin from "Explosively Depressurized" Wood

D. W. Sopher* and **H. A. Schroeder,** Dept. of Wood Science, Colorado State University, Fort Collins, CO 80523 and **H. L. Chum,** Biomass Thermal Conversion Branch, Solar Energy Research Institute, Golden, CO 80401

The "steam explosion" treatment of lignocellulosic materials, principally hardwoods, effectively separates the three main biomass components: cellulose, hemicelluloses, and lignins. The lignin obtained by this technique has a low degree of polymerization, is less cross-linked, and is more soluble in solvents than lignins obtained by most other pretreatments. This paper reviews the polarography of lignins resulting from several pretreatments in several solvents, and compares these results with those obtained from the "steam exploded" aspen lignin.

Abstract No. 455

Nonpetroleum Feedstock in Electro-organic Synthesis

D. Cipris, Allied Chemical Corp., Corporate Research and Technology, Morristown, NJ 07960

The utilization of small, gaseous molecules has received an increased attention in both organic and electro-organic synthetic chemistry in recent times. The attraction of "small molecules," such as carbon monoxide, carbon dioxide, hydrogen, and ammonia, as the building blocks for commercial chemicals lie in their nonpetroleum origin and their abundance. We have been engaged in the studies of several systems involving the electrochemistry of carbon monoxide in recent years. This work has been reviewed, along with the studies of both carbon monoxide and carbon dioxide conducted by other workers. A number of interesting reactions had been observed for the first time, leading to the products including squaric acid, organic carbonates, methanol, ethylene glycol, and urea (based on CO) as well as formic, oxalic, malic, and glycollic acids (based on CO_2). New promising routes to important chemicals have thus emerged; these are discussed in some detail.

Abstract No. 456

Polarographic Studies of Some Reactions of Fural

E. Woodman,* **M. A. Wells,** and **P. Zuman,*** Clarkson College, Potsdam, NY 13676

At low concentrations, used in polarographic and spectrophotometric studies of reactions of fural in alkaline media, it has been shown that Cannizzaro reaction of this aldehyde competes with a reaction first order in fural, probably involving a ring opening. This reaction is photocatalyzed. In 5-nitrofural the first hydroxide ion adds to the aldehyde group, the second attacks the ring in a nucleophilic substitution, with NO_2^- as a leaving group.

Abstract No. 457

Steric Factors Influencing the Rate of Anodic Oxidation of Aldehydes in Alkaline Media

R. M. Van Effen, B. S. Hui, and **D. H. Evans,*** Dept. of Chemistry, University of Wisconsin, Madison, WI 53706

Aldehydes are prominent examples of biomass-derived compounds. In earlier research, anodic reactions of aldehydes were observed at silver and gold electrodes at potentials as negative as $-8V$ *vs.* SCE. It was demonstrated that the gem-diolate, **1**, was the electroactive species, that

C-H bond breaking occurs in the rate-determining step and that adsorption of reactant and/or an intermediate was a mandatory component of the reaction scheme. A number of ortho-substituted and 2,6-disubstituted benzaldehydes have been studied to probe the effect of steric bulk in the vicinity of the carbonyl function on the rate of the oxidation.

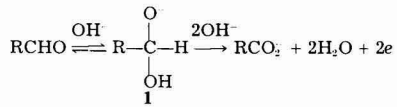

1

Abstract No. 458

Hydration, Enolization, and Acid-Base Properties in Polarographic Reduction of 1,2-Diketones

J. Segretario,* N. Sleszynski, and **P. Zuman,** Clarkson College, Potsdam, NY 13676

1,2-Diketones react with arginine groups of enzymes. To study this interaction species present in aqueous solutions of 1,2-diketones at various *p*H values must be identified. Combination of polarography, u.v. spectrophotometry, and NMR spectroscopy enables studies of hydration, enolization, and acid-base reactions involved. Acid and base catalysis of these reactions was studied.

Abstract No. 459

Review of the Electrochemistry of Levulinic Acid-Acid Degradation Product of Cellulosic Materials

H. L. Chum* and **M. Ratcliff,** Solar Energy Research Institute, Biomass Thermal Conversion and Exploratory Research Branch, Golden, CO 80401

Lignocellulosic materials are the most abundant polymers on earth. These materials and their chemical components can constitute the basis of a substantial chemicals industry in perpetuity. Levulinic acid (4-oxopentanoic acid) is the major product of glucose acid degradation. It is obtained in nearly quantitative yields, with a straightforward recovery of the mineral acid catalyst. This paper discusses the electrochemical behavior of this compound and describe possible electrochemical routes to useful chemicals and/or fuels.

Abstract No. 460

Electrochemical Conversion of Natural Chiral Compounds into Chiral Synthetic Blocks

S. Torii,* T. Inokuchi, and **R. Oi,** Dept. of Industrial Chemistry, School of Engineering, Okayama University, Tushima-Naka-3, Okayama, Japan 700

In order to provide chiral synthetic blocks for fine organic synthesis, electrochemical fragmentation of easily available natural products such as monoterpenes and saccharides are examined. Anodic cleavage of the carbon-carbon bond of 4-hydroxy-p-menth-8-en-3-one derived from (3R)-pulegone by epoxidation followed with acid-catalyzed rearrangement provided methyl (3R)-3,7-dimethyl-6-oxo-7-octenoate. The preparation of such kinds of chiral synthetic blocks by electrolysis procedure as well as their synthetic applications is discussed.

Abstract No. 461

Conversion of Biomass-Derived Organic Acids to Liquid Fuels by Electrochemical Oxidation in Aqueous Solutions

J. E. Sanderson,* G. W. Barnard, and **P. F. Levy,** Dynatech R/D Co., Cambridge, MA 02139

Organic acids such as acetic, propionic, butyric, valeric, and caproic acids are readily produced in dilute aqueous solution by the anaerobic fermentation of biomass. These acids, when concentrated by extraction to 0.5-1.0 molar aqueous solutions, are readily converted electrochemically to linear alkanes, olefins, and alcohols, all of which have use as feedstock or blending components for liquid fuels. These electrochemical oxidations, commonly called Kolbe Electrolysis and the Hofer-Moest reaction, have been the subject of considerable mechanistic speculation over the years. Gas chromatographic analysis of the products of electrochemical oxidation under a variety of conditions has shed additional light on the mechanisms of these reactions.

Abstract No. 462

Semiconductor Powder Catalysts for Photo-Kolbe Electrolysis of Volatile Fatty Acids

J. S. Cantrell, Chemistry Dept., Miami University, Oxford, OH 45056

Semiconductors (n-type) are prepared from screened (80-100 mesh) powders of such materials as TiO_2, MoO_3, WO_3, and ZnWO, by heating to 600°C in a quartz tube with hydrogen gas flowing over the material until the crystals turn navy blue (~2 hr). Platinum metal is photochemically deposited (partial coverage) using H_2PtCl_6 and formic acid (*p*H ~ 3.5 Na_2CO_3) to produce photodiodes. The photodiodes catalyze VFA (acetic, propionic, butyric, valeric and caproic) to form CO_2 and hydrocarbons. X-ray diffraction studies of the photodiode materials have been made to help elucidate the mechanisms of these reactions. (Support of the Miami University Faculty Research Committee is gratefully acknowledged.)

Abstract No. 463

The Photo-Kolbe Reaction: A Promise Wrapped in a Puzzle

R. E. Schwerzel,* H. J. Byker, D. G. Vutetakis, and **V. E. Wood,** Battelle Columbus Laboratories, Columbus, OH 43201

The photo-Kolbe reaction, the anodic oxidation of carboxylic acids to produce CO_2 and hydrocarbon products, has been shown by us and by other workers to occur to the exclusion of oxygen production at illuminated n-type oxide photoanodes in aqueous solutions of acetic acid or other carboxylic acids. Because these acids are abundantly available from the enzymatic hydrolysis of biomass materials, we have previously suggested that a "tandem" strategy be employed, with a photoelectrolysis device deriving its aqueous input from a biomass conversion system. The photo-Kolbe reaction is perplexing, however, in that it seems to be controlled by interfacial kinetics rather than energetics; it therefore sometimes fails to proceed under condition where it is allowed thermodynamically. Our observations on this reaction, and the "ground rules" which govern it, are discussed in this paper.

Abstract No. 464

The Photoelectrochemical Behavior of Levulinic Acid on Platinized Anatase Powders

H. L. Chum, M. Ratcliff,* K. Moran, J. Turner, and **A. Nozik,** Solar Energy Research Institute, Biomass Thermal Conversion and Exploratory Branch and Photoconversion Branch, Golden, CO 80401

Levulinic acid (4-oxopentanoic acid) is the major product of the acid degradation of cellulosic materials. Under the experimental conditions described by Kraeutler and Bard [*J. Am. Chem. Soc.*, **100,** 5985 (1978)], suspensions of levulinic acid (*p*H 3-7) and platinized n-TiO_2 powders decarboxylate ~3 times faster than in the absence of the powders. Direct photochemical reactions of the acid are minimal under the experimental conditions. Acetaldehyde, acetone, and isopropanol were identified as organic reaction products. Yields and possible reaction mechanisms are discussed.

Abstract No. 465

Light Catalyzed Electro-oxidation of Alcohols and Hydrocarbons

J. M. Bobbitt,* J. P. Willis, and **C. L. Kulkarni,** Dept. of Chemistry, University of Connecticut, Storrs, CT 06268

Photoexcited quinones are strong oxidizing agents and can be used for the oxidation of numerous compounds such as alcohols and aromatic hydrocarbons. In the process, the quinones are reduced to hydroquinones. When an electrochemical system is added, the hydroquinone can be oxidized back to quinone with hydrogen production at the cathode. Thus, the quinone serves as a light catching catalyst. Such a system is of interest both as a means of oxidizing biomass compounds with the production of hydrogen and as a means for using solar energy.

PHYSICAL ELECTROCHEMISTRY

Solid Electrolyte Interfaces

Abstract No. 466

Characterization of Solid Electrolyte-Inert Electrode Interfaces

D. O. Raleigh, Rockwell International Science Center, Thousand Oaks, CA 91360

The solid-state electrochemical arrangement termed a polarization cell can be used to characterize solid electrolyte-inert electrode interfaces in considerable (sometimes exquisite) detail. Capacitance-voltage measurements can indicate the mechanism by which the interface stores charge and how well-formed an interface it is. Galvanostatics differentiates between nucleated and underpotential deposition and sometimes provides submonolayer activity-coverage data. Chronocoulometry can characterize diffusion of discharged ions into the electrode material.

Abstract No. 467

Interface Polarization of Sodium Beta Alumina in Aqueous and Nonaqueous Solutions of Sodium Salts

F. G. Will,* General Electric Corporate Research and Development, Schenectady, NY 12301, and **K. Kalapis,** Institute for Physical Chemistry, University of Bonn, 53 Bonn, Germany

The transfer of sodium ions through the interface between sodium beta alumina and solutions of sodium iodine in water and propylene carbonate has been studied. In aqueous solution, the interface polarization was found to be small, linearly dependent upon current, and symmetrical for ion transfer from the solid into the liquid and vice versa. For propylene carbonate solution, the polarization was found to be significantly larger, nonlinear with current, and highly unsymmetrical. Sodium ion transfer from the solid into the organic electrolyte yields currents which increase exponentially with polarization, indicating activation control. However, sodium ion transfer from the organic into the solid electrolyte yields currents which increase parabolically with polarization as it would be expected for space charge-limited currents in polarizable solids.

Abstract No. 468

Time Dependence of the Asymmetric Behavior of Polycrystalline Beta″ Alumina

M. W. Breiter and **B. Dunn,*** General Electric Corporate Research and Development, Schenectady, NY 12345

The time dependence of the asymmetric resistive behavior of polycrystalline tubes of beta″ alumina was studied by several electrochemical techniques. It was found different for ceramic tubes of various compositions fabricated at GE and elsewhere. The results are interpreted as an interfacial phenomenon.

Abstract No. 469

The Sodium/Beta Alumina Interface

D. S. Demott, M. L. Wright, and **M. D. Hames,** British Railways Research and Development Div., Railway Technical Centre, Wilmorton, Derby England.

Interfacial polarization at the sodium/beta alumina interface has been shown to be responsible for a goup of related phenomena often observed in sodium sulfur cells. These are: resistance rise, asymmetry of resistance, nonohmic resistance, and transient high resistance. The causes of these phenomena have been investigated and methods of controlling them have been developed. Results are presented which illustrate the efficacy of these methods.

Abstract No. 470

Study of the AgF-LaF_3 Reversible Interface by Auger Spectroscopy and Impedance Technique

T. A. Fjeldly* and **J. S. Johannessen,** Electronics Research Laboratory, The Norwegian Institute of Technology, The University of Trondheim, Trondheim, Norway N-7034

Lanthanum fluoride (LaF_3) has great practical importance as a membrane in fluoride-specific ion-selective electrodes. In an effort to produce all-solid-state ion-selective electrodes with integral amplifier electronics, silver fluoride (AgF) has been found to provide a satisfactory solid contact with the LaF_3-membrane. Structural and electrical properties of this junction have been studied by means of Auger depth profiling and electrical impedance measurements. Structurally, the interface, prepared by melting AgF onto the LaF_3 substrate, is found to be a fused, gradual one in terms of chemical composition. From the impedance measurements an equivalent circuit for the structure is derived, revealing the nonblocked behavior of the interface.

Abstract No. 471

Theoretical Analysis of Liquid-Junction Photovoltaic Cells

M. E. Orazem* and **J. Newman,** Chemical Engineering Dept. and Materials and Molecular Research Div., University of California, Berkeley, CA 94720

A one-dimensional theoretical model is presented for the liquid-junction photovoltaic cell. The model incorporates dilute-solution transport relationships for the semiconductor and for the electrolyte. Adsorption, desorption, and charge transfer reactions couple the semiconductor to the solution at the semiconductor-electrolyte interface. This coupling includes the effect of the space-charge region, diffuse region, and surface concentrations. The effect of kinetic and transport parameters on cell performance is investigated. Current-voltage curves are presented for illuminated electrodes, as well as for the semiconductor in the dark. The results are compared with experimental observations.

Abstract No. 472

Properties of Solid Electrolyte Film Grown on Fresh Surface Lithium Electrode

M. Yaniv,* K. M. Abraham, and **G. L. Holleck,** EIC Laboratories, Inc., Newton, MA 02158

The kinetics and properties of surface films are studied on Li electrode freshly cut *in situ* in thionyl-chloride electrolyte solutions. Correction is made between film properties and discharge curves at various film growth stages taking into account film porosity and electrode pretreatment. The validity of the solid electrolyte interface model is tested and a modified duplex model is suggested and checked with respect to the experimental results.

Abstract No. 473

Studies of Internal Interfaces in Solid Electrolytes by Impedance Spectroscopy

C. K. Chiang, A. L. Dragoo, and **A. D. Franklin,*** National Bureau of Standards, Washington, DC 20234

The frequency dependence of the impedance of the system electrode/solid electrolyte/electrode contains information about charge transport processes not only at the solid electrolyte/electrode interfaces and within the single crystal grains of the solid electrolyte itself, but also at internal interfaces within the solid electrolyte. Data from Mg- and Y-doped ceramics and bi-crystals, Y-doped CeO_2 ceramics, and Sr-doped $LaCrO_3$ and Ca-doped $YCrO_3$ illustrate how grain boundaries may be studied.

Abstract No. 474

Oxygen Diffusion in Liquid Metal Studied by Impedance Spectroscopy

E. J. L. Schouler,* C. Couture (Permanent address: Université de Sherbrooke, Quebec, Canada), and **M. Kleitz,** Laboratoire d'Energétique Electrochimique, ENSEEG, 38401 Saint Martin d'Hères, France

The oxygen-liquid silver/stabilized zirconia electrode was investigated by impedance spectroscopy in various oxygen environments ($5 \cdot 10^{-6} < P_{O_2} < 1$atm). The diagrams show a pure Warburg impedance over an extended frequency range (10^2-10^{-2}Hz). The analysis of the results indicates that the corresponding limiting step of the electrode reaction is a slow diffusion of atomic oxygen in the liquid metal. This type of measurement provides an accurate and convenient determination of the diffusion coefficient of oxygen in liquid metals.

Abstract No. 475

Electrochemical and Surface Spectroscopic Studies of Metal/Solid Electrolyte Interfaces

C. Y. Yang,* H. S. Isaacs, and **W. E. O'Grady,** Dept. of Energy and Environment, Brookhaven National Laboratory, Upton, NY 11973

A high temperature solid electrolyte (yttria-stabilized zirconia) cell has been incorporated into an ultrahigh vacuum surface analysis chamber. Electrochemical techniques (cyclic voltammetry, potential-step transients, etc.) and surface spectroscopic techniques (XPS, UPS, Auger, etc.) are used to study the interfaces between the electrolyte and metal electrodes such as nickel, iron and iron-based alloys. The emphasis of this investigation is on the transport of oxygen across the interfaces and the interaction between oxygen and the metals at elevated temperature. The results provide an understanding of the electrochemical redox processes at the electrolyte/metal interfaces and the initial stages of metal oxidation.

Abstract No. 476

The H_2/H_2O Reaction at Noble Metal Electrodes on Zirconia Electrolytes

E. J. L. Schouler* (Permanent address: ENSEEG, Grenoble, France) and **H. S. Isaacs,** Dept. of Energy and Environment, Brookhaven National Laboratory, Upton, NY 11973

The polarization behavior of single point contacts of platinum and gold have been studied as electrodes on zirconia electrolytes at 1000°C in mixtures of steam, hydrogen, and argon. The anodic and cathodic curves showed inflections characteristic of limiting currents associated with the oxidation and reduction reactions. The reactions, their dependence on the partial pressure of steam and hydrogen, and electrode materials have been analyzed. (This work was performed under the auspices of the U.S. Department of Energy.)

Abstract No. 477

Electrical Conductivity of Tetragonal Zirconia Below the Transformation Temperature

T. K. Gupta and **R. B. Grekila,** Westinghouse R&D Center, Pittsburgh, PA 15235

The electrical conductivity of tetragonal zirconia has been reported in the literature only above the transformation temperature because the tetragonal phase is not stable at room temperature. In this note, electrical conductivity has been studied on the recently developed stabilized tetragonal zirconia in the temperature range of 200°-900°C, which is below the transformation temperature. The conductivity has two temperature dependent regions, one above 300°C with an activation energy of about 0.9 eV, and the other below 300°C with an activation energy of about 0.5 eV.

General Session

Abstract No. 478

The Effect of Electrolyte Anion Adsorption on Current Efficiencies for the Evolution of Ozone

P. C. Foller* and **C. W. Tobias,** Dept. of Chemistry and Chemical Engineering, University of California, Berkeley, CA 94720

Ozone may be obtained in relatively high yield by the electrolysis of acidic aqueous solutions using beta-PbO_2 anodes. It has been found that the anionic coverage of the beta-PbO_2 electrode surface has a strong influence on the ozone current efficiencies obtained. Phosphorus 32 radiotracer measurements have demonstrated that where anion coverage of the anode surface is high, ozone current efficiencies are low. Anionic adsorption on PbO_2 at ozone evolution potentials is so persistent that the polarization history of the anode influences its subsequent ozone yields. Indications are that at these potentials, electrolyte anions may dermisorb into the PbO_2 surface. Such conclusions lead to adjusting the "adsorptivity" for anions of PbO_2 through reduction of surface Pb to O stoichiometry in a successful effort to enhance ozone current efficiency. It is speculated that anionic coverage acts to weaken the free energy of adsorption of oxygen, and it is through such an influence that the formation of ozone is affected.

Abstract No. 479

A Simple Technique for the Estimation of the Bulk Resistivity of Powdered Materials

J. R. Whyte, Jr., Phelps-Dodge Corp., Div. of Environmental Engineering and Research, Tucson, AZ 85701 and **K. Seshan,** Dept. of Metallurgical Engineering, The University of Tucson, Tucson, AZ 85721

A simple technique for room-temperature measurement of the electrical resistivity of particulate or powdered materials is reported here. The device used is a simplified four-point probe which gives resistivity as a function of compacting pressure. Measurements on powders of known composition showed the device to be capable of reasonable accuracy. Plots of powder resistivity against compacting pressure are given. The significance of the shape of these plots is discussed.

Abstract No. 480

Experimental and Theoretical Study of Porous Electrodes Having Perpendicular Direction of Current and Electrolyte

A. Storck* and **M. A. Enriquez-Granados,** Laboratoire des Sciences du Génie Chimique, CNRS-ENSIC, 54042 Nancy Cedex, France

A mathematical model is presented to describe the behavior of three-dimensional electrodes operating under limiting current conditions. Principal results are the effect of electrolyte resistivity, hydrodynamic and cell geometrical parameters on the distribution of the electrolyte potential and overpotential inside the structure. The study establishes the most pertinent parameters of the electrode, and application to the design of a reactor having perpendicular directions of current and electrolyte flow is given. The analytical solution is experimentally tested for packed bed electrodes of nickel particles using the reduction of ferricyanide ions. A very good agreement is observed for a large range of operating conditions.

Abstract No. 481

General Equations for the Chemical Potential and Its Isobaric, Isochoric, Isentropic and Isothermal Changes, Variation of Gas Constant and Its Thermodynamic Implications

R. Heyrovska, Na Šťáhlavce 6, 160 00 Praha 6, Czechoslovakia.

The chemical potential can be represented by the general equation, $\mu = P(V\text{-}b) = \pi(V_i^g - V_h^g) = i^*R_oT$ for gases and aqueous solutions. At STP, for $i^* = 1.0$, $\mu = 2271$ J·mole^{-1} and $E = \mu/F = 0.0235$V. On writing $i^*R_o = R$, a variable, and differentiating, $d\mu_P = -dF$, $d\mu_V = dE$, $d\mu_R = RdT$ and $d\mu_T = TdR$ at constant P, V, R, and T, respectively. Thus, R is a measure of the isothermal entropy of the given system in the given circumstances; and $C_P - C_V = R + T(dR/dT)$. For gases, at and above the van der Waals' temperature (*e.g.*, N_2, ≥ 400°C), $R = R_o$ for all P. For an ideal gas, $b = 0$ and $dR = 0$ at all P and T.

Abstract No. 482

An Estimate of the Heat of Adsorption of the Hydroperoxyl Radical on Platinum

J. P. Hoare, General Motors Research Laboratories, Electrochemistry Dept., Warren, MI 48090

In the two-electron reduction of O_2 in acid solution, an adsorbed hydroperoxyl radical, HO_2, must be discharged. The standard potential of the homogeneous discharge reaction is 1.5V which is ~0.7V higher than the potential (0.8V) at which O_2 is reduced at a Pt cathode. It is possible that the heat of adsorption lowers this high potential to the reaction potential of 0.8V. Assuming that the standard potential of the heterogeneous reaction occurs at 0.8V, subtraction of the heterogeneous from the homogeneous equations gives -16.49 kcal/mole for ΔG_{ads} of HO_2 radicals. From statistical thermodynamic calculations, the ΔS_{ads} is -28.23 eu for an immobile layer with $\theta = 0.01$. Then a value of -24.9 kcal/

mole is found for ΔH_{ads} for HO_2 radicals which is an acceptable value. A discussion of this result is given.

Abstract No. 483

Electrochemical Reduction of Cobalt Carbon Bonded Organometallic Compounds of Cobaloxime Type. Electrocatalytical Applications

J. Devynck,* C. Bied-Charreton, M. D. Le Hoang, A. Gaudemer, and **B. Tremillon,** Laboratory of Analytical and Applied Electrochemistry (associaté CNRS), Ecole Nationale Superieure de Chimie, Univesité Pierre et Marie Curie, 75231 Paris Cedex 05, France

The complexes of cobalt and dimethylglyoxime are organometallic compounds which form a metal-carbon bond with various organic substrates. Conditions of formation and breaking of the cobalt-carbon bond are analyzed by means of voltammetric and coulometric methods and with the ring-disk electrode. The solvent is dimethylsulfoxide. The stability of the Co-C bond is evaluated as a function of the organic substrate and new intermediate species are proposed to explain the general process of reduction and reoxidation. Applications to the electrocatalytic reduction of alkyl halides and double bonded carbonyl compounds are proposed.

Abstract No. 484

Error Analysis of the Potential and Voltage Step Relaxation Techniques for the Measurement of the Kinetics of Electrode Reactions

Z. Nagy, Argonne National Laboratory, Chemical Engineering Div., Argonne, IL 60439

An error analysis of the potential and voltage step techniques is reported, including the comparison of several graphical and numerical data evaluation methods. The errors are examined as a function of certain time constants of the electrode reaction system. To compare several data evaluation methods, "synthetic data" were generated using a computer program in which all error sources of the measurement are incorporated. This program uses a current density-time equation which fully takes into account the rise time of the potentiostat and all the effects of uncompensated resistance.

Abstract No. 485

Theory of Transition Time: Anodic Passivation

K. C. Tsai and **S. Venkatesh,*** The Continental Group, Inc., Energy Systems Laboratory, Cupertino, CA 95014

The current density-transition time relationship of the generalized form $(i - i_c) = kt_p^{-n}$ with $i_c \geq 0$ and $n = 1/2$ or 1 has been repeatedly observed for many metal-electrolyte systems. When $n = 1/2$, t_p is generally small (*i.e.*, 10^{-3} sec) and the equation can be successfully interpreted using the diffusion model. For example, at $i_c = 0$ this equation is reduced to the classical Sand equation $i = kt_p^{-1/2}$, and at $i_c > 0$, an analytical solution has been recently obtained by Littauer and Tsai. However, when $n = 1$, t_p is generally large (*i.e.*, $\geq 10^{-1}$ sec) and there is not a satisfactory model yet to account for the observed empirical equation, $(i - i_c) = kt_p^{-1}$. In this regard, a model based on mass transport limited process coupled with surface coverage phenomena is presented in this paper.

Abstract No. 486

Double-Layer Measurements at Silver and Lead Electrodes

K. L. Guyer, J. T. Hupp, D. Larkin,* H. Y. Liu, and **M. J. Weaver,** Dept. of Chemistry, Michigan State University, East Lansing, MI 48824

When interpreting electrochemical kinetic data it is desirable that the structure of the solution-electrode interface be known under the prevailing experimental conditions. Despite the importance of solid metals in electrocatalysis, relatively little such information is available. Some of our recent results for the double-layer capacitance at polycrystalline silver- and lead-aqueous interfaces using a-c bridge and automated potential-step methods are discussed. Particular reference is made to previous work reported with these systems and the problems inherently associated with obtaining such measurements.

Abstract No. 487

Van't Hoff's Factor for Nonideality of Gases and Aqueous Solutions, Hydration Numbers from Osmotic Coefficients, Langmuir's Formula Extended for Space Coverage

R. Heyrovská, Na Štáhlavce 6, 16000 Praha 6, Czechoslovakia

Experimental data show that $(PV/R_nT) = i = i^x + (bP/R_nT)$ for gases and $(\pi V_A^n/R_nT) = i = \nu\phi = \nu\phi^x + \nu m\phi V_h^n D_A$ for aq. nonelectrolyte and electrolyte solutions [b = van der Waals' const, V_A^n and V_h^n = volumes of total and bound (hydration) solvent A per mole of solute B, m = molality]. i^x and ϕ^x are factors characterizing intermolecular interactions and are ≤ 1.0. The spatial occupation of molecules follows the equations $b/(V - b) = B_1P$(gases) and $V_h^n/(V_A^n - V_h^n) = B_1m\phi$ (aq. solutions) over a wide range of T, P and m, where B_1 is the Langmuir's coefficient. $i = i^x = 1.0$ and $B_1 = 0$ for an ideal gas.

Abstract No. 488

Photocurrent Spectroscopy of Some Semiconducting Layered Compounds (WSe_2, $MoSe_2$, WS_2, and InSe)

K.-K. Kam* and **B. A. Parkinson,** Dept. of Physics, Iowa State University, Ames, IA 50010

Photocurrent spectra of some semiconducting layered compounds (WSe_2, $MoSe_2$, WS_2, and InSe) in electrolyte solutions have been measured for photon energy in the 1-3.5 eV range. The anisotropy of these materials was studied by using polarized light on crystal surfaces ($\perp$c or $\|$c) and varying the angle of incidence. The effects of the redox couple and the electrode potential on the photocurrent spectra were also investigated. The results are interpreted using the band structure of the materials.

Abstract No. 489

Electrochemical Disinfection of Recirculating Fluids

P. Natishan,* G. E. Stoner, and **G. L. Cahen, Jr.,** Applied Electrochemistry Laboratory, Dept. of Materials Science, University of Virginia, Charlottesville, VA 22901

As an alternate to present disinfection practices, a method for the on site generation of an oxidant in recirculating, low salt content fluids is being considered. A graphite composite is used as the electrode material and the reactor is powered by an alternating current. In order to optimize the system, the oxidant production and faradaic efficiencies are being compared as a function of flow rate, a-c frequency, type of electrolyte, electrolyte concentration, and applied current.

Abstract No. 490

Electrochemical Studies of Chromium in Molten LiF-NaF-KF(FLINAK)

T. Yoko* and **R. A. Bailey,** Dept. of Chemistry, Rensselaer Polytechnic Institute, Troy, NY 12181

Electrochemical reduction and oxidation of chromium in the molten LiF-NaF-KF eutectic have been studied by means of cyclic voltammetry and chronopotentiometry in the range of about 550°-1000°C. Reduction is a two step process, with the first step ($Cr^{3+} \rightarrow Cr^{2+}$) not mass-transfer limited at high temperatures. At lower temperatures, the first reduction shifts to more negative potentials, eventually almost merging with the second. The oxidation processes show analogous changes with temperature. Interpretation of the processes and their relationship to molten salt electrodeposition is considered.

Abstract No. 491

Investigation of Anion Adsorption on Platinum in Trifluoromethanesulfonic Acid and Related Alkanesulfonic Acids

G. W. Walker* (Present address: Bureau of Mines, Avondale, MD 20782), Mobility Equipment Research and Development Command, Ft. Belvoir, VA 22060 and **R. T. Foley,** Dept. of Chemistry, The American University, Washington, DC 20016

The search for new fuel cell electrolytes has focused on a number of alkanesulfonic acids, one of which is

trifluoromethanesulfonic acid (TFMSA). Increase in the oxygen open-circuit potential (≈150 mV) as well as increases in the hydrogen and propane oxidation rates have been observed in TFMSA, as compared to H_3PO_4. The improved performance in TFMSA has been attributed, at least in part, to the fact that the sulfonate anion ($CF_3SO_3^-$), in contrast to the phosphate anion, is nonsurface active, but thus far the exact nature of the surface activity of TFMSA anion has not been determined. This investigation has shown that the surface character of $CF_3SO_3^-$ is analogous to that of ClO_4^- or F^-, anions which have previously been shown to be nonadsorbing. The surface characteristics of other alkanesulfonic acids have also been examined in order to determine if the presence of fluorine is required in the hydrocarbon structure to retard surface activity.

Abstract No. 492

Current-Potential Characteristics of the Bromine/Bromide Electrode Reaction

S. E. Lorimer* and **R. E. White,** Dept. of Chemical Engineering, Texas A&M University, College Station, TX 77843

A new model for the bromine/bromide electrode reaction is presented. The model is developed for a rotating disk electrode and includes the effects of ion migration and the homogeneous complexation reaction forming the tribromide ion (Br_3^-). Simulated current-potential curves are compared to data to demonstrate the manner in which the model may be used in kinetic model discrimination and kinetic parameter determination. Due to the rapid kinetics of the electrode reaction, correction for mass transfer effects is essential; the model is used to evaluate critically several correction techniques. The ability of the model to account for the effects of complexing for a broad range of solution compositions and complexing reaction kinetic parameters is compared to prior limited analytical solutions.

Abstract No. 493

Electrocatalysis in Electroless Copper Deposition

J. Duffy, L. Pearson, and **M. Paunovic,*** PCK Technology Div., Kollmorgen Corp., Melville, NY 11747

A promoter added to the electroless copper solution can selectively accelerate the cathodic or the anodic partial reaction, or it can simultaneously accelerate both partial reactions, in an equal or different extent. The accelerating effects of promoters vary with the type of complexing agent for copper ion, ionic strength, and pH of the solution. Catalytic effects of pyridine, guanidine, derivatives of purine, benzotriazole, and pyrimidine are discussed in terms of the depolarization resulting from the presence of these promoters (accelerators) in the electroless copper solution.

Abstract No. 494

The Effect of Cathodic Polarization on the Creep Rate of Gold

C. J. van der Wekken, Laboratory of Metallurgy, Delft University of Technology, 2628 AL Delft, The Netherlands

After loading gold wires at 0 mN *vs.* SCE, extra creep resulting from cathodic polarization was measured at electrode potentials ranging from −200 to −1800 mV. The effects depend on the pH and on the oxygen content of the test solution. It is concluded that in alkaline environments the effects are associated with dislocation pinning at the metal surface by hydroxyl ions. In oxygenated acid solutions a similar role is played by other oxygen containing species.

Abstract No. 495

Electrocatalysis of the Oxygen Reduction Reaction—Electrolyte and Anion Effects

S. Srinivasan,* Los Alamos National Laboratory, Los Alamos, NM 87545, **H. Olender,** Brookhaven National Laboratory, Upton, NY 11973, and **E. A. Klaus** and **M. H. Miles,** Middle Tennessee State University, Murfreesboro, TN 37172

The choice of electrocatalysts for the oxygen electrode reaction is limited, particularly in acid media, because of competing reactions (*e.g.*, metal dissolution, oxide formation). An alternative approach to lower overpotentials is by change or modification of electrolytes. This paper reports results of experiments to determine effects of some electrolytes (H_2SO_4, $HClO_4$, H_3PO_4, CF_3SO_3H, $KHCO_3/K_2CO_3$, KOH) and of anion adsorption (Cl^- I^-, PO_4^{3-}) on the oxygen overpotential at Pt. (A few studies were also conducted on Ag.) Potentiostatic and/or slow potential sweep techniques were used. There is a progressive improvement of oxygen reduction kinetics at Pt with increase of pH (*i.e.*, i_o in H_2SO_4 < in $KHCO_3/K_2CO_3$ < in KOH). Of all acids tested, the exchange current density on Pt is highest in trifluoromethanesulfonic acid. The influence of anion adsorption on oxygen reduction kinetics decreases with increase of pH, probably due to a shift of the oxygen reversible potential in the more cathodic direction.

PHYSICAL ELECTROCHEMISTRY/ENERGY TECHNOLOGY

Electrocatalysis

Abstract No. 496

Electrocatalysis: Fundamental Aspects and Recent Developments

E. Yeager* and **D. Scherson,** Case Laboratories for Electrochemical Studies and the Dept. of Chemistry, Case Western Reserve University, Cleveland, OH 44106

Electrocatalysis involves the strong interaction of electrochemical reactants, intermediates and/or products with the electrode surface. These interactions can drastically reduce the energy barriers for electron and atom transfer processes, but the nature of the interactions and the relation to surface electronic properties and morphology are only beginning to be understood. The present status of understanding of various electrocatalytic reactions is summarized with special emphasis on hydrogen and oxygen electrocatalyst and the relation of electrocatalysis to solid-gas interface catalysis.

Abstract No. 497

Cluster Model Study of Chemisorption on Heavy Transition Metal Surfaces

C. Y. Yang, Surface Analytic Research, Inc, Mountainview, CA 94043

A relativistic description of a heavy metal d-band under different crystal fields is illustrated with Dirac-Slater calculations on small platinum clusters modeling various surfaces. This description agrees well with existing UPS data and serves as an improvement to previous interpretations of such data. These clusters are also used to study the chemisorption of oxygen and carbon monoxide. The electronic structure calculations with the model clusters revealed the site dependence of the adsorbate-metal bond. The ionization energies of CO and O are compared with UPS and XPS data.

Abstract No. 498

Oxygen Reduction on Transition Metal Cluster Catalysts in Alkaline Electrolyte

P. N. Ross, Jr., Lawrence Berkeley Laboratory, Materials and Molecular Research Div., Berkeley, CA 94720

Procedures were developed for synthesizing 2-3 nm clusters of all the Group VIII transition metals on carbon substrates. These clusters are metallic in the reduced state but most oxidize on air exposure or upon immersion in aqueous electrolyte to form oxide clusters of comparable size. Oxygen reduction in alkaline solution proceeds at a reasonable rate on all these catalysts with surprisingly small variations between metals. All catalysts showed very nearly the same apparent Tafel slope, 55 ± 5 mV per decade. The ranking in specific activity was in the order: Pt > Ru > Ir ≈ Rh ≈ Pd ≈ Ni ≈ Co (> factor of 10, ≈ factor of 2). The turnover numbers for Ni and Co clusters appear to be the same as for the most catalytically active Ni and Co macrocyclics. For Pt clusters, the kinetics and mechanism appear to be totally different than for smooth Pt. The specific activity of Pt clusters in alkaline solution is more than 100 times that in acid solution at the same potential and temperature. (This work was supported by the Division of Electrochemical Systems Research, Office of Conservation and Solar Energy, U.S. Department of Energy under Contract No. W-7405-Eng-48.)

Abstract No. 499

Electrocatalysis on Ion-Implanted Electrode Surfaces

W. E. O'Grady,* Brookhaven National Laboratory, Upton, NY 11973 and **G. K. Wolf,** University of Heidelberg, 69 Heidelberg, Germany

The use of ion implantation techniques for the development of new catalysts has received very little attention. We have developed several new electrocatalysts using ion implantation techniques. In this paper we report on the oxidation of formic acid, methanol and oxygen reduction and evolution on Pt implanted in RuO_2. (This work was performed under auspices of U.S. Department of Energy.)

Abstract No. 500

Comparison of Electrochemical Proton Transfer from the Unhydrated H_3O^+ Ion and from $H_9O_4^+$ in Excess Water

B. F. Conway* and **D. Tessier,** Dept. of Chemistry, University of Ottawa, Ottawa Ont., Canada

Use of the pure strong acid monohydrate, $CF_3SO_3H \cdot H_2O$, (which exists as the hydronium salt $CF_3SO_3^- H_3O^+$) and its solution in water, offers the possibility of comparing the rates of H_2 evolution from the unhydrated H_3O^+ ion (from liquid $CF_3SO_3^- H_3O^+$ at $T > 307$ K) and the fully hydrated proton as $H_9O_4^+$ (Ackermann-Eigen structure) in aqueous CF_3SO_3H (*ca.* 1M). Experiments of this kind have been carried out in which the exchange current densities, i_0, the H/D kinetic isotope effects and the apparent activation energies have been measured for H_2 evolution from H_3O^+ and $H_9O_4^+$, aq. at Ni and Pt. i_0 values are 100 times smaller for H_2 evolution from the H_3O^+ ion than from $H_9O_4^+$, aq, and, if concentration differences are allowed for, the rate constant would be *ca.* 900 times smaller. From measurements of the reversibility parameter, s_0, for the H peaks in upd of H at Pt, the corresponding differences of proton discharge/ionization rates from H_3O^+ and $H_9O_4^+$ are also evaluated.

The results provide a basis for critical examination of the role of direct and solvational reorganization in the activation process in theories of proton transfer/chemisorption and of proximate anion effects in proton discharge.

Abstract No. 501

Chemical and Electrochemical Surface Reactivity. Role of Competition Between Solvent and Reaction Intermediate Adsorption

S. Trasatti, Laboratory of Electrochemistry, The University, 20133 Milan, Italy

The surface reactivity of metals and oxides towards hydrogen, oxygen, oxygenated species, and chlorine is analyzed. Data of reactivity of the solid surfaces at the interface with the gas phase are compared with the behavior at the solid/aqueous solution interface. The comparison may reveal the role played by the competitive adsorption of solvent molecules in changing or even reversing the reactivity "scale" of the solid surfaces at the latter interface.

Abstract No. 502

Changes of the Electrochemical Characteristics of Rhodium Electrodes Induced by Potentiodynamic Perturbation

C. Pallotta, N. R. de Tacconi, and A. J. Arvía,* Instituto de Investigaciones Fisicoquimicas Teóricas y Aplicadas (INIFTA) Casilla de Correo 16, Sucursal 4, La Plata, Argentina

Two types of Rh electrodes which exhibit different electrochemical characteristics in the potential range covering from the hydrogen evolution to the oxygen evolution region are shown. Processes such as oxygen and hydrogen electrosorption and electrodesorption are different for each type of electrode. The electrocatalytic behavior of these electrodes is investigated in the O_2 evolution region. The results are interpreted taking into account the type of layer which is formed on the metal surface. The properties of these layers depend on the metal treatment, solution composites, and aging conditions.

Abstract No. 503

Study of O_2 Involving Reactions at Potentials of the Hydrogen Region in Acid Solution on Smooth and Platinized Platinum Covered by CO_{ad}

M. W. Breiter, General Electric Corporate Research and Development, Schenectady, NY 12345

The coverage of CO_{ad} on platinized platinum decreased only slightly during the reduction of O_2 at 0.1, 0.2, and 0.3V while it disappeared to a large extent within the initial 500 sec on smooth platinum in 0.5M H_2SO_4 at room temperature. The difference in behavior is attributable to the reaction of H_2O_2, formed during the O_2 reduction, with CO_{ad}. The net rate of O_2 reduction was not affected to a noticeable degree on platinized platinum at potentials of the hydrogen region by CO_{ad}.

Abstract No. 504

The Growth and the Stabilization of the O-Containing Species of Pt in Molten $KHSO_4$

M. E. Folquer, N. R. de Tacconi, and **A. J. Arvía,*** Instituto de Investigaciones Fisicoquímicas Teóricas y Aplicadas (INIFTA) Casilla de Correo 16, Sucursal 4, La Plata, Argentina.

The dynamic aging of O-containing species electroformed in the potential range of the O-monolayer produces energetically different Pt (O) species which are revealed through the corresponding electroreduction. The interphase was potentiodynamically perturbed so that only a fraction of the O-monolayer was periodically removed and reformed during a preset time (t). When the fraction removed is 70%, the cathodic current peak splits into two peaks. When the fraction removed is 30%, the cathodic sweep shows only one peak increasing monotonically with t. In both cases, the shifts of the peaks indicate a gradual stabilization of the electroformed species. The dynamic aging promotes the reconstruction of the metal lattice and the penetration of oxygen into the metal. These effects are favored at 245°C.

Abstract No. 505

Electrode Kinetics of Hydrogen Oxidation and Oxygen Reduction on Carbon-Supported Pt Fuel Cell Electrodes in H_3PO_4

J. McBreen,* **H. Olender,** and **S. Srinivasan,** Dept. of Energy and Environment, Brookhaven National Laboratory, Upton, NY 11973

Even though the phosphoric acid fuel cell is in an advanced stage of development, the electrode kinetics, particularly of the oxygen electrode, are not well understood. Considerable discrepancies exist between kinetic data obtained on smooth bulk platinum and platinum supported on carbon. This investigation used a specially designed cell to determine electrode kinetic parameters and *in situ* platinum surface area. When careful attention was paid to electrode purification, the kinetic data on carbon supported platinum was very similar to that obtained on smooth platinum. In the potential region of fuel cell operation, the Tafel slope for oxygen reduction was ~120 mV and the activation energy was between 8 to 12 kcal/mole. (This work was performed under the auspices of the U.S. Department of Energy.)

Abstract No. 506

Electronic Structure of Iron Phthalocyanine and Its Analogs—A Theoretical Study

N. Sabelli and **L. K. Lee,** Dept. of Chemistry, University of Illinois—Chicago Circle, Chicago, IL 60601, and **C. A. Melendres,*** Argonne National Laboratory, Chemical Engineering Div., Argonne, IL 60439

Molecular electronic structures of the dianions and iron complex of phthalocyanine and other macrocyclic compounds (*e.g.*, tetrabenzaporphine, tetrazaporphine, and porphyrin) which are of interest in oxygen electrocatalysis have been calculated using INDO molecular orbital methods. Differences are found between the phthalocyanine and porphyrin models that are correlated with their properties. The interaction of the compounds with oxygen was studied. The electronic configuration of the iron and the nature of the Fe-O_2 bond in phthalocyanine and porphyrin-

like complexes are discussed. Spectral information has also been derived.

Abstract No. 507

Electrocatalytic Study of a Series of Metals and Alloys under Physiological Conditions

B. J. Piersma* and **W. Greatbatch,** Dept. of Chemistry, Houghton College, Houghton, NY 14744

A series of 25 metals and alloys, including alloys of Ti and of Ta with Pt, Ir, and Ru have been studied in 0.15*N* NaCl at 37°C using galvanostatic pulses, analogous to those used by the heart pacemaker, and also using cyclic voltammetry. We have attempted to correlate polarization data and kinetic data with electronic properties of the electrode materials, particularly work functions.

Abstract No. 507A

An Electrocatalyst for Hydrogen Electrodes

D. E. Brown,* S. M. Hall, M. N. Mahmood, M. C. M. Man, A. K. Turner, D. Wood, and **S. Anderson,** BP Research Centre, Sunbury on Thames, Middlesex, TW16 7LN, England.

An electrocatalyst for hydrogen electrodes has been developed and performance data reported (1). The active component of this catalyst is a nickel-molybdenum alloy with a face centered cubic structure. The identification of the alloy structure in x-ray diffraction and thermogravimetric analysis studies is described together with data relating composition to electrochemical activity. Results from hydrogen reduction and oxidation studies are discussed in terms of the hydrogen transfer mechanisms on this new catalyst system.

1. D. E. Brown *et al.*, "Hydrogen Energy Progress (Proceedings 3rd World Hydrogen Energy Conference)," Vol. 1, p. 152, Tokyo (1980).

Abstract No. 508

Electrocatalysis at Oxide-Covered Metal-Electrodes

S. Gottesfeld, Dept. of Chemistry, University of Tel-Aviv, Tel-Aviv, Israel, and **S. Srinivasan,** Brookhaven National Laboratory, Upton, NY 11973

Rates of simple redox reactions and of more complex electrochemical processes (mainly OER) were measured at oxide-covered Ir, Rh, and Ru electrodes, as well as at some oxide-covered Ru-Ir alloys. The results point to the significance of catalytic mechanisms involving redox processes in the oxide film and particularly on its surface. Such internal redox reactions may serve as mediators in faradaic processes occurring at metal oxides of several stable oxidation states. The dependence of catalytic activity on film structure may also be related to structural effects on the activity of such internal redox mediators.

Abstract No. 509

The Oxygen Evolution Reaction on Ruthenium and RuO_2/TiO_2-Coated Electrodes

R. Woods, CSIRO, Div. of Mineral Chemistry, Port Melbourne, Victoria 3207, Australia

An oxide layer develops on ruthenium electrodes at potentials in the oxygen evolution region. The growth of the oxide results in an enhancement of the activity for oxygen evolution, the activity of thin layers increasing linearly with the quantity of oxide present. The kinetics of oxygen evolution on ruthenium and RuO_2/TiO_2-coated electrodes is interpreted by a mechanism involving the formation of a higher ruthenium oxide which decomposes releasing oxygen.

Abstract No. 510

Questions on the Kinetics of O_2 Evolution on Oxide Covered Metals

B. D. Cahan and **C. T. Chen,** Dept. of Chemistry, Case Laboratories for Electrochemical Studies, Case Western Reserve University, Cleveland, OH 44106

Traditional interpretation of the kinetics of oxygen evolution reaction has been based on measurements of the Tafel slope. New preliminary evidence which has been obtained from wide-frequency range impedance measurements indicates that this parameter may actually be controlled by a variable resistance in the oxide film itself. This implies that the true kinetics for O_2 evolution may be much faster than heretofore expected and that apparent catalytic improvements may be due to modification of the properties of the oxide itself.

Abstract No. 511

Anodic Evolution of Oxygen on Sputtered Iridium Oxide Films

S. Hackwood,* L. M. Schiavone, and **G. Beni,** Bell Laboratories, Holmdel, NJ 07733

We report on the electrocatalytic properties of sputtered iridium oxide films (SIROF's) in acidic electrolytes. Long-term stability (240 hr) is demonstrated. Typical steady-state currents are 75 mA/cm² at 1.85V(*vs.* RHE), which is 50% higher than previously reported (1). In addition, we introduce a new method of determining Tafel slopes based on the short-time decay of the oxygen evolution reaction (OER) current, corrected for the capacitative component. Tafel plots are presented for samples of different thickness and degree of hydration. The high current density and absence of corrosion demonstrate the superior catalytic properties of SIROF's *vs.* iridium over the entire voltage range investigated. Catalytic rejuvenation by voltage pulsing is also discussed.

1. G. Beni, L. M. Schiavone, J. L. Shay, W. C. Dautremont-Smith, and B. S. Schneider, *Nature,* **282,** 15 (1979).

Abstract No. 512

Oxygen Gas Evolution at Rhodium Oxide Anodes

L. D. Burke and **E. J. M. O'Sullivan,*** Dept. of Chemistry, University College, Cork, Ireland

Hydrous rhodium oxide films are readily produced on cycling the potential of a rhodium metal electrode in base. Such films are unusually reactive with regard to oxygen gas evolution as compared with the uncycled metal and the involvement of an intrinsic electrocatalytic effect is suggested by the lowering of the Tafel slope. The mechanism of oxygen gas evolution on these, and thermally prepared films of the same metal, is discussed.

Abstract No. 513

Thin Catalytic Films on Silicon

L. A. Harris* and **J. A. Hugo,** General Electric Corporate Research and Development, Schenectady, NY 12301

Smooth continuous films of platinum, as little as 20A thick, may be deposited on silicon that is sufficiently ion etched beforehand. The n-Si contact with Pt is ohmic, but on p-Si there is a small electronic barrier. The films display the electrochemical characteristics of platinum metal and are very stable under strongly oxidizing conditions.

Abstract No. 514

Study of a Decomposing Hydride Phase by Measurement of Open-Circuit Potential Decay

H. Angerstein-Kozlowska* and **B. E. Conway,** Dept. of Chemistry, University of Ottawa, Ottawa, Ont., Canada

The kinetics of decomposition of a surface or thin layer metal hydride, MH, coupled with the continuous Faradaic evolution of H_2, were evaluated by means of open-circuit potential decay, $V(t)$ measurements. A corrosion-type mechanism is treated, with a time-dependent self-discharge current, i_t, limited by the kinetics of H_2 evolution and the total charge passed determined by the quantity of MH initially present. The corrosion-type current i_t is given by $i_t = (C_\phi + C_{dl})dV/dt$ where C_ϕ is the pseudocapacitance arising from potential-dependence of coverage or lattice occupancy by the species H and C_{dl} is the double-layer capacitance. By analogy with adsorption pseudocapacitance, $C_\phi = Q_{MH}(F/RT)(X_{MH})(1-X_{MX})$ where X_{MH} is the lattice site fraction of H in the hydride phase. The slopes of V_t *vs.* log t at appreciable t for several limiting mechanisms of self-discharge are calculated and compared with the experimental behavior for hydride decomposition at some Ni and Ni-alloy cathodes. The behavior observed is found to be similar to that treated by Conway and Bourgault for self-discharge of nickel oxide battery cathodes.

Abstract No. 515

Mass Spectroscopic Cyclic Voltammetry for Mechanistic Studies in Organic Electrocatalysis

O. Wolter, C. Giordano, J. Heitbaum,* and **W. Vielstich,** Institute of Physical Chemistry, University of Bonn, D-5300 Bonn, Germany

The rate of the formation of the volatile products of an organic electrode reaction is on line detected by mass spectroscopy using a hydrophobic porous electrode as inlet system. The method allows the simultaneous measurement of the rates of oxidation and product formation as function of the potential applying scan rates up to 400 mV sec^{-1}. Thus, the instantaneous current efficiency can be calculated giving additional information on the mechanism. Examples for the electrooxidation of different organic fuels are presented.

Abstract No. 516

Oxidation of Formic Acid and Methanol on Single Crystal Platinum Electrodes

R. R. Adžić,* and **A. V. Tripković,** Institute of Electrochemistry, ICTM, Belgrade, Yugoslavia **W. O'Grady** and **S. Srinivasan,** Brookhaven National Laboratory, Upton, N.Y. 11973

The oxidation of these organic molecules involves a strong adsorption prior to the charge transfer process and the intermediates formed in these reactions are even more strongly adsorbed. It has been found that these processes are highly dependent on the surface orientation of the single crystal electrodes. The highest activity has been found with (111) orientation, and the lowest with (100). The highest activity of (111) orientation has been explained with the low hydrogen adsorption on this plane, and the low adsorption of strong bond intermediates which require three or two sites for their adsorption. This more than compensates for the low reactivity of the (111) plane toward formic acid and methanol themselves.

Abstract No. 517

Electrocatalysis of the Carbon Monoxide Methanation Reaction on Stabilized Zirconia

T. M. Gür,* The Continental Group, Inc., Energy Systems Laboratory, Cupertino, CA 95014, and **R. A. Huggins,** Stanford University, Stanford, CA 94305

The feasibility of electrochemically synthesizing hydrocarbons via a Fischer-Tropsch type reaction has been demonstrated on yttria stabilized zirconia featuring paste Pt, Au, and Ag electrodes. The electrocatalytic activity for the hydrogenation of CO has been controlled by a suitable potential drop imposed across the electrodes. This scheme drives the gas/catalyst interface to a very reactive state. The synthesis reaction has been carried out in a differential flow reactor at 1 atm between 400° and 900°C with an H_2/CO ratio from 1 to 3. Despite the severe polarization effects observed on these electrodes, the specific reaction rate for CO methanation is enhanced nearly tenfold on Pt and Au electrodes by the use of this electrochemical scheme.

Abstract No. 518

Crystallographic Anisotropies in Chemical and Electrochemical Etching of Pt

R. Caracciolo and **L. D. Schmidt,** Dept. of Chemical Engineering and Materials Science, University of Minnesota, Minneapolis, MN 55455

Single crystal microspheres of Pt are used to examine the crystallographic variations in the rates of etching and morphologies produced by chemical and electrochemical etching. In aqua regia the only stable plane is {110}, and attack begins on {210} regions and spreads until the {110}, {100} and finally {111} regions facet. An a-c electrochemical treatment in HCl/KCl produces only planes near {100}. Attack is more uniform with the {111} plane being faceted rapidly and extensively. These results are interpreted in terms of relative rates of attack of Cl atoms generated in the solution and at the surface.

Abstract No. 519

The Potentiodynamic Electrooxidation of CO on Pt and Rh Both "Free" and "Oxidized" in Acid Solution

S. A. Bilmes, N. R. de Tacconi, and **A. J. Arvía,** Instituto de Investigaciones Fisicoquímicas Teóricas y Aplicadas (INIFTA) Casilla de Correo 16, Sucursal 4, La Plata, Argentina.

Potentiodynamic current peaks associated with the electrooxidation of CO species on Pt and Rh both "free" and "oxidized" in 1*N* $HClO_4$ at 25°C are obtained through a systematic stepwise increase and decrease of the cathodic switching potential within the potential range where the O-electrosorption and O-electrodesorption take place. The comparative response of both systems is interpreted through different adsorption sites available for CO and the potential dependent energy distributions at the electrocatalyst which is related to the surface concentrations of the "free" metal, Me(OH) and Me-O-species.

Abstract No. 520

Electro-Organic Oxidations on Lead Ruthenate

H. H. Horowitz,* H. S. Horowitz, and **J. M. Longo,** Exxon Research & Engineering Co., Linden, NJ 07932

High surface area lead ruthenate, Pb $(Ru_{1-x}Pb_x)$ $O_{3-\epsilon}$, an exceptional catalyst for oxygen evolution and reduction, having variable oxygen stoichiometry, has been found to be active for the oxidation of organics in aqueous alkali. Besides oxidizing primary alcohols to acids, it was able to catalyze cleanly the cleavage of olefins and ketones. Propylene gave acetate and $CO_3^=$. Undecylenate gave sebacate. Butanone-2 and butanediol went to two moles of acetate. Sec-butanol went to the ketone at *pH* 9 but was cleaved at *pH* 14. Cyclohexanone and – ol went to adipic acid, etc.

Abstract No. 521

The Structure of Metal Adsorbates Formed at Underpotentials

D. M. Kolb, Fritz-Haber-Institut der MPG, D-1000 Berlin 33, Germany

In situ structural investigations of metal adsorbates are sparse as we suffer from the limitations given by the presence of the bulk electrolyte. Yet some information on structural details can be gained by a careful analysis of adsorption isotherms and by optical techniques such as normal incidence reflectance spectroscopy and surface plasmon excitation. More information can be obtained by using the structure sensitive electron diffraction methods on emersed electrodes. Analogous experiments may also be conducted in vacuum yielding complementary information on the structure of adsorbates.

Abstract No. 522

Some Recent Developments in Electrocatalysis on Surfaces Modified by Foreign Metal Adatoms

R. R. Adžić, Institute of Electrochemistry ICTM and Center for Multidisciplinary Studies, University of Belgrade, 11000 Belgrade, Yugoslavia

A review of the catalytic efforts of foreign metal adatoms on various electrochemical reactions will be given and their origins discussed. New results with the oxidation of organics in various electrolytes as a function of *p*H, temperature, and adatom coverages are presented, as well as detailed disk-ring measurements of oxygen reduction on gold, silver, and platinum electrodes. The examples of the effects of adatoms on carbon dioxide reduction and metal deposition are also reported. Different mechanisms of the catalytic action of foreign metal adatoms are discussed.

Abstract No. 523

The Effect of *p*H on the Electrocatalytic Properties of Adsorbed Metal Ions

P. Bindra, IBM, T. J. Watson Research Center, Yorktown Heights, NY 10598

The catalytic activity for O_2 reduction of gold in alkaline solution is substantially enhanced by the underpotential adsorption (UPD) of metal adatoms such as Cu and Pb. In acid media, however, the UPD of Cu on platinum lowers the catalytic activity of platinum for O_2 reduction. The aim of

this study is to elucidate the mechanism of action of these metal adatoms. The systems studied include O_2-Pb(II)-M and O_2-Cu(II)-M where M = Hg, Pt, or Au.

Abstract No. 524

Electrocatalytic Effects of Underpotential Metal Deposits on the Cathodic Reduction of Oxygen on Single Crystal Surfaces

K. Jüttner and **W. J. Lorenz,*** Institut für Physikalische Chemie und Elektrochemie, Lehrstuhl III, Universität Karlsruhe, 7500 Karlsruhe 1, Germany

The oxygen reduction process is strongly influenced by underpotential metal deposits. The electrocatalytic effects of well-ordered submonolayers and monolayers of Pb, Tl, and Bi on single crystal surfaces of Ag (hkl) and Au (hkl) have been studied in acid solutions using the rotating disk technique. The results can be correlated to the degree of coverage, the structural arrangement of the adsorbate and the specific interactions between adsorbed reaction intermediates and the modified substrate. Pseudocatalytical effects can be caused by competitive anion adsorption phenomena.

Abstract No. 525

Catalytic Effect of Copper Iron on the Anodic Oxidation of Cyanide Ion

A. Katagiri* (Present address: Dept. of Chemistry, University of Tennessee, Knoxville, TN 37916), **S. Yoshimura, Y. Deguchi,** and **S. Yoshizawa,** Kyoto University, Kyoto 606, Japan

The anodic oxidation of CN^- ion was found to be catalyzed by a small amount of copper ion. Cyanate, oxamide, oxalic acid, and/or ammonia were formed in exhaustive controlled-potential electrolysis, depending upon the pH of the solution. An unstable intermediate, $Cu(CN)_i^{2-}$, was detected by ESR spectroscopy, and kinetics of its decomposition was studied. The electrochemical reaction was also studied by RDE technique, chronopotentiometry, and steady-state current-potential measurement. A possible mechanism of the reaction is proposed.

Abstract No. 526

The Influence of Underpotential Deposition on the Electrooxidation of Methanol in Acid Solutions

E. P. M. Leiva and **M. C. Giordano,*** Departamento de Fisicoquímica, Facultad de Ciencias Químicas, Universidad Nacional de Córdoba, Cordoba, Argentina.

The influence of metal underpotential deposition (Cu, Sn, Bi, Ag, As, and Pb) on platinum electrocatalysts on the electrooxidation of methanol in 0.5M H_2SO_4 is investigated, through the application of potentiodynamic perturbation techniques, covering the potential range from 0.05 to 1.5V (NHE). The different potentiodynamic responses are comparatively presented to attempt a correlation of the results. Most of the underpotential deposited metals inhibit the electrooxidation process, except Sn. The latter under low surface coverage conditions produces an increase of the anodic current in the 0.45-0.75V range.

Abstract No. 527

Factors Governing the Choice of Semiconducting Oxides for the Evolution of Oxygen in Alkaline Media

A. C. C. Tseung* and **P. Rasiyah,** Dept. of Chemistry, The City University, Northampton Square, London ECIV OHB, England

Published data and experimental results on metals and semiconducting oxides have shown that there is a linear correlation between the minimum voltage required for oxygen evolution and the potential of lower oxide/higher oxide couple. Furthermore, there is a positive correlation between pseudo-exchange current density-Tafel slope and the lower oxide/higher oxide couple. The effect of electrical resistivity on the performance is also determined. These studies were conducted on RuO_2, PtO_2, IrO_2, $Li_xCo_{1-x}O_1$, $Li_xNi_{1-x}O$, PbO, PbO_2, Pb_3O_4, Fe_2O_3, Fe_3O_4.

Abstract No. 528

Oxygen Electrocatalysis on Some Oxide Pyrochlores

H. S. Horowitz,* H. H. Horowitz, and **J. M. Longo,** Exxon Research and Engineering Co., Linden, NJ 07036

A new class of bidirectional electrocatalysts with low overvoltage characteristics has been discovered. These catalysts, which have the pyrochlore structure, may be described by the formula $A_2[B_{2-x}A_x]O_{7-y}$ where: A = Pb or Bi, B = Ru or Ir, $O \leq x \leq 1$ and $O \leq y \leq 0.5$. In alkaline electrolyte between RT and 110°C, they give significantly lower polarizations than any other catalyst for oxygen evolution and are among the best for oxygen reduction. Life testing has demonstrated reasonable activity maintenance for long periods (500-1800 hr) of operation.

Abstract No. 529

Mechanism of Oxygen Evolution on Li-Doped Co_3O_4

P. Rasiyah and **A. C. C. Tseung,** Dept. of Chemistry, The City University, Northampton Square, London ECIV OHB, England

10 a/o Li-doped Co_3O_4 electrode gave an oxygen evolution performance of 1.538V (*vs.* DHE) at 75°C in 5*N* KOH, significantly better than other oxides tested. Coulometric studies show the formation of Co^{3+} and Co^{4+} species before oxygen evolution. A Tafel slope of ~60 mV per decade was obtained by steady state and transient studies. Kinetic consideration based on Tafel and reaction order parameters suggests that a proton abstraction step such as $MOH + OH^- \rightarrow MO^- + H_2O$, after the first electron transfer step is rate determining.

Abstract No. 530

Mechanism of Oxygen Evolution on $NiCo_2O_4$. II. Kinetic Studies

P. Rasiyah* and **A. C. C. Tseung,** Dept. of Chemistry, The City University, Northampton Square, London, EClV OHB, England

Oxygen evolution on $NiCo_2O_4$ at 25°C gave Tafel slopes of ~40 mV ($E < 1.56$V, [KOH] = 1.2*N*-5*N*) and ~120 mV ($E > 1.56$V, [KOH] = 0.1*N*-5*N*). The kinetic indicators

$$\left(\frac{\partial \log i}{\partial \log C_{OH^-}}\right)_{E,T}, \left(\frac{\partial \log i}{\partial \log C_{OH^-}}\right)_{\eta,T} \text{ and} \left(\frac{\partial \log i}{\partial \log C_{OH^-}}\right)_{i,T}$$

were found to be 1.12, 0.49, and 0.06 for the slope of 120 mV. This is in agreement with the kinetics where the second electron transfer involving an OH^- ion is rate determining at complete coverage. It is suggested that the slope of 40 mV is due to the same kinetics at low coverage.

Abstract No. 531

Inner-Sphere Reactivity at Solid Metal Surfaces: The Reduction of Co(III) Ammine Complexes at Platinum and Gold Electrodes

S. W. Barr* and **M. J. Weaver,** Dept. of Chemistry, Michigan State University, East Lansing, MI 48824

A number of Co(III) ammine complexes containing a variety of inorganic ligands have been shown to be strongly adsorbed at platinum- and gold-aqueous interfaces using several methods, including their effects upon the kinetics of simple, outer-sphere electrode reactions. Some of the complexes also reduce via extremely facile inner-sphere pathways. The likely influences of the surfaces upon the free energy barrier to electron transfer are discussed in the light of these data.

Abstract No. 532

Inner-Sphere Reactivity at Solid Metal Surfaces: Rate-Structure Correlations for Transition-Metal Complexes at Silver Electrodes

K. L. Guyer,* J. T. Hupp, and **M. J. Weaver,** Dept. of Chemistry, Michigan State University, East Lansing, MI 48824

The silver-aqueous interface provides a particularly interesting surface with which to explore electrocatalytic phenomena since a wide potential region is available where the surface is positively charged and capable of strongly binding a variety of reactants. Kinetic data for the ligand-

bridged reduction of some Cr(III) and Co(III) complexes at clean silver in comparison with those obtained at surfaces coated with u.p.d. thallium or lead layers indicates that the observed inner-sphere catalyses can be extremely sensitive to the electrode composition. Likely reasons for this behavior are discussed in terms of "intrinsic" and "thermodynamic" contributions to the electron transfer barrier.

Abstract No. 533

Electrocatalytic Properties of Transition Metal Macrocyclics for Anodic Reactions

J. Zagal,* C. Fierro, E. Muñoz, and **R. Rozas,** Departamento de Química, Facultad de Ciencia, Universidad Técnica del Estado, Casilla 5659, Santiago 2, Chile.

Tetrasulfonated metal phthalocyanines (M-TSPc) and metal phthalocyanines (M-Pc), where M= Co and Fe, have been found to possess catalytic activity for the anodic oxidation of hydrazine when adsorbed on pyrolytic graphite electrodes. The iron derivatives show higher activity than their cobalt parents. Co-TSPc also shows catalytic activity for the anodic oxidation of cysteine. The Tafel parameters and chemical orders for the reactions have been determined. The mechanisms and the kinetics of the processes are discussed.

Abstract No. 534

Influence of Anion Adsorption on O_2 Reduction Kinetics. Interest of Mo and Fe Naphthalocyanine Impregnations on Carbon Black Supports

G. Magner, M. Savy, and **G. Scarbeck,** Laboratoire d'Electrochimie Interfaciale du CNRS, 92190-Meudon-Bellevue, France

The interest of Mo naphthalocyanine catalyst for O_2 reduction and evolution in alkaline media has been stressed recently. In the present work using the RDE technique, strong differences have been shown between Fe and Mo samples. In the case of KOH supporting electrolytes only NO_3^- is not inhibiting the limiting current with Fe samples. With Mo, in contrast only a slight inhibition is apparent in the case of high Cl^- and ClO^- concentrations. The net result lies in the existence of a range of potentials where the O_2 reduction kinetics is important compared to the ClO^- anion reduction.

INDEX TO AUTHORS

Abstract No.

Abbot, E. M. 430
Abderrassoul, R. 267
Abe, T. 187, 188
Abels, L. L. 323
Aboaf, J. 64
Abraham, K. M. 472
Adams, W. A. 361
Adzic, R. R. 516, 522
Agrawal, A. K. 21
Ahearn, J. S. 125, 126
Ahlgren, D. C. 248
Ainso, S. 452
Aitken, J. M. 280, 307
Akaba, R. 422
Akiyama, S. 204
Albella, J. M. 91
Alessandrini, E. 64
Alessandrini, F. 88
Allison, D. F. 208
Alkire, R. C. 11, 19, 406
Altekruger, B. 327, 329
Alwitt, R. S. 35, 97
Amelinckx, S. 240
Ammar, I. A. 57, 60
Anderson, T. J. 346
Anderson, S. 507A
Angerstein-Kozlowska, H. 41, 42, 514
Antoniadis, D. A. 256
Aoyama, T. 211
Arai, K. 95
Ardizzone, S. 74
Arita, M. 336
Arney, J. 432
Arvia, A. J. 49, 65, 502, 504, 519
Atanasoski, R. T. 87, 401
Atsumi, T. 95
Auvert, G. 332

Babcock, G. T. 364
Baber, S. C. 202
Badia, M. 93
Bailey, M. G. 70
Bailey, R. A. 490
Baizer, M. M. 449
Bancroft, E. E. 425
Bandyopadhyay, G. 14
Bardsley, W. 205, 328
Barnard, G. W. 461
Barnett, B. 41, 42
Barr, S. W. 531
Barraclough, K. G. 205, 328
Barrow, W. A. 171
Bartak, D. 433
Bates, C. W., Jr. 276
Bathey, B. 381
Battles, J. E. 14
Bauman, H. F. 3
Bauser, E. 315
Beaudry, B. J. 378
Beck, T. R. 37, 124
Begemann, J. H. 434
Begun, G. M. 360
Beinvogl, W. 233
Bell, J. P. 110
Bell, R. O. 381
Bellamy, A. J. 430
Bellows, R. 388, 408, 409, 410
Belton, D. J. 113
Bender, H. 240
Beni, G. 154, 155, 511
Benner, R. E. 355, 356, 357
Bennett, R. S. 227, 301
Bennett, R. W. 82

Abstract No.

Bensahel, D. 332
Benson, K. E. 186
Berkenblit, M. 280
Bewick, A. 371
Bhattacharyya, A. 222
Bied-Charreton, C. 483
Bilder, W. 36
Bilmes, S. A. 519
Bindra, P. 523
Birck, H. 327
Birke, R. L. 358
Blackstone, S. 310
Blatte, M. 242
Bloch, E. 185
Bloem, J. 210
Blomgren, G. E. 80
Blount, H. N. 425
Bobbitt, J. M. 465
Bockris, J. O'M. 399
Bolger, J. C. 99
Bond, R. A. 293
Bonino, F. 88
Bowden, E. F. 426
Bradley, P. 244
Brady, T. E. 262
Brajter-Toth, A. 443
Brebrick, R. F. 344, 345, 347, 348
Breiter, M. W. 468, 503
Brewer, L. 333
Brewer, T. 299
Brewer, T. L. 288
Brockmann, W. 121
Brodsky, M. B. 341
Broniewski, B. 407
Brooks, C. R. 340
Brotherton, S. D. 244
Brown, D. E. 507A
Brown, D. M. 296
Bruckner, H. 370
Bruinink, J. 96
Brunel, C. 172
Bruning, J. H. 235
Brusic, V. 64
Brusius, P. 286
Burilla, C. T. 157
Burke, L. D. 47, 438, 512
Burrows, B. W. 1
Busch, R. W. 437
Byker, H. J. 463
Byvik, C. E. 400

Cahalan, P. 105
Cahan, B. D. 71, 510
Cahen, G. L., Jr. 442, 489
Calder, G. V. 108
Canfield, D. 386, 387
Cantrell, J. S. 462
Cappelletti, P. 230
Caracciolo, R. 518
Carbonio, R. E. 49
Carlen, P. J. 2
Carugati, A. 398
Cera, G. D. 406
Cerofolini, G. F. 239
Chain, E. E. 352
Chaker, M. 142
Chamonal, J. P. 162
Chang, C. Y. 213, 353
Chang, I. F. 146, 149
Chang, Y. A. 343
Chao, C-Y. 72
Chao, H. H. 227
Chatterjee, P. K. 255

Abstract No.

Cheek, G. 76
Chelikowsky, J. R. 351
Chen, C. T. 71, 510
Chen, J. Y. 237
Chen, M. C. 320, 321
Cheng, L. J. 212
Chenot, C. F. 176
Chew, N. G. 221
Chiang, C. K. 473
Chin, D-T. 5
Chin, I. J. 137
Chin, L.-Y. 326
Chou, S.-M. 36
Chow, R. 294
Chow, T. P. 296
Chum, H. L. 373, 374, 449, 454, 459, 464
Cipris, D. 455
Claassen, W. A. P. 210
Claeys, C. 240
Clark, R. J. 142
Clark, T. E. 157
Clarke, L. 412
Clayton, C. R. 63
Coetzee, J. E. 75
Coissard, P. 332
Cole, T. 375
Comas, J. 323
Comninellis, C. 416, 444
Conway, B. E. 41, 42, 396, 397, 500, 514
Cook, G. 362
Cook, G. M. 4
Cooney, R. P. 367
Coovert, R. E. 171
Corset, J. 369
Couture, C. 474
Coury, A. 105
Coutumas, T. 299
Craig, J. D. 141
Cramer, A. 227
Craven, R. A. 200
Crevecoeur, C. 96
Croset, M. 53
Crossen, J. 48
Crowder, B. L. 227, 306, 307
Cullen, G. W. 265
Cullis, A. G. 221
Cussler, E. L. 12, 84
Custode, F. Z. 300

Damjanovic, A. 40, 43
Dang, L. M. 261
Dang, R. 270, 271
Darwish, S. 57, 60
Day, D. L. 451
Dean, P. J. 159, 164
Declerck, G. 240
Deckert, C. A. 116
Deguchi, Y. 525
Demer, L. J. 206, 311
Demott, D. S. 469
de Tacconi, N. R. 502, 504, 519
Devynck, J. 483
de Wit, H. J. 96
Dickie, R. A. 122
Diegle, R. B. 21
Dieleman, J. 232
Ditchek, B. M. 125, 126
Doddapaneni, N. 83
Dom, B. E. 132
Donaghey, L. F. 346
Donaldson, G. J. 361
Donofrio, R. L. 152
Doss, K. G. K. 63
Downey, D. F. 300

Abstract No.

Dragoo, A. L. 473
Drechsel, D. 327, 329
Drum, C. M. 254
Dryhurst, G. 443
Dubruelh, J. 93
Duffy, J. 493
Dumcke, R. 269
Dunn, B. 468
Dutton, R. W. 260
Dvurechensky, A. V. 223
Dyer, C. K. 35
Dyer, L. D. 314
Dzioba, S. 293

Eckhardt, G. 237
Efron, U. 245
Egan, J. J. 339
Einstein, H. 388
Ellis, A. B. 168
Eisinger, R. S. 11
Ellner, M. 349, 350
Elsner, N. 379
Elwell, D. 324
Emerson, J. A. 140
Emery, A. T. 407
Engel, P. A. 131
Enriquez-Granados, M. A. 480
Ensign, P. W. 341
Eisinger, R. S. 11
Ephrath, L. M. 227, 231, 301
Evans, D. H. 437, 457
Evans, H. E. 132
Evans, J. F. 428A

Fahidy, T. Z. 389
Fahlsing, R. F. 374
Fair, R. B. 257
Fang, Y. K. 213
Faulds, B. R. 4
Feigelson, R. S. 324
Feisel, L. D. 262
Feng, X. K. 24
Ferla, G. 230, 239
Fernandez, M. 91
Fewer, W. 300
Fierro, C. 533
Firszt, F. 175
Fisher, W. 310
Fitzpatrick, B. J. 163
Fitzpatrick, G. O. 372
Fjeldly, T. A. 470
Fleischer, N. A. 10
Fleury, M. 421
Flowers, D. 317
Foell, H. 243
Foley, R. T. 491
Foll, H. 287, 312
Foller, P. C. 478
Folquer, M. E. 504
Formaro, L. 74
Fouchard, D. T. 361
Frank, W. 243
Franklin, A. D. 473
Franz, G. 247
Frisch, R. C. 253
Fry, A. J. 420
Fu, J. W. 17
Fujimoto, K. 29
Fujita, K. 411
Fukuda, Y. 167
Fukushima, F. 167
Fuller, C. R. 236
Fuller, G. G. 114
Fullwood, L. 117
Fung, M.-S. 309
Furgala, A. J. 450
Furtak, T. E. 365, 366

Abstract No.

Gaggioli, R. A. 391
Gale, R. J. 76
Galland, D. 161
Gardner, C. L. 361
Garreau, M. 89
Gassman, P. G. 419
Gatos, H. C. 62, 199, 322
Gaudemer, A. 483
Geiger, W. E., Jr. 424
Gesheva, K. A. 352
Ghate, P. B. 236
Ghezzo, M. 296
Gibbons, J. F. 220, 273
Giess, E. A. 149
Giordano, C. 515
Giordano, M. C. 49, 526
Gleichmann, R. 205A
Godin, A. 172
Goesele, U. 243
Gokalp, M. 84
Goncel, O. T. 26, 27
Gopikanth, M. L. 48, 83
Gordon, J. G. 359, 368
Gottesfeld, S. 508
Goyal, R. N. 443
Graff, K. 207
Graham, L. 140
Gray, G. G. 130
Greatbatch, W. 66, 507
Grekila, R. B. 477
Grimes, P. G. 388, 408, 409, 410
Grinberg, J. 245
Grotheer, M. P. 403
Gruber, C. L. 262
Gruss, L. L. 67
Grutka, E. 107
Grzeszczuk, M. 434
Gschneidner, K. A., Jr. 337, 378
Guo, C-X. 181, 182
Gupta, T. K. 477
Gupta, V. K. 284
Gur, T. M. 517
Guruswamy, S. 135
Guruswamy, V. 399
Gutmann, V. 77
Guyer, K. L. 364, 486, 532
Guyomard, D. 86
Gwo, T. C. 316

Haberger, K. 269
Hackwood, S. 155, 511
Hagiwara, S. 295
Hahn, B. 205A
Hall, D. E. 7
Hall, S. M. 507A
Hames, M. D. 469
Hamilton, J. C. 355, 356, 357
Hamilton, W. L. 120
Hanoka, J. I. 381
Harada, S. 298
Harnack, P. M. 163
Harris, L. A. 513
Hasan, T. F. 250
Hasler, B. 233
Havreluk, R. P. 280
Hawkridge, F. M. 426
Hawley, M. D. 429
Hayes, T. G. 85
Healy, J. F. 438
Heineman, W. R. 428
Heitbaum, J. 515
Helbert, J. N. 118
Helms, C. R. 217
Henis, N. 446
Henoc, P. 332
Henry, W. 310
Henry, W. P. 432
Herlem, M. 86

Abstract No.

Herring, R. B. 285
Hess, L. D. 237
Heus, R. J. 339
Heyrovska, R. 481, 487
Hickmott, T. W. 277
Higuchi, K. 302
Hildreth, G. 399
Hill, C. 259
Hill, D. E. 209
Hillman, P. D. 352
Hinderman, J. D. 380
Hine, F. 411
Hiraiwa, A. 298
Hiraoka, H. 291
Hirata, H. 190
Hoare, J. P. 482
Hoffmann, K. 269
Hogerton, P. B. 380
Holleck, G. L. 472
Hollinsed, W. C. 422
Hon, P. K. 143
Honda, K. 313
Horiuchi, M. 304
Horowitz, H. H. 520, 528
Horowitz, H. S. 520, 528
Hoshi, K. 189
Hoshikawa, K. 190
Howard, M. W. 367
Hsu, C-C. 201
Hsu, W. C. 213
Hu, Z.-B. 20
Huber, D. 242
Huggins, R. A. 517
Hughes, H. G. 118
Hughes, M. C. 36
Huglen, R. 360
Hugo, J. A. 513
Hui, B. S. 457
Hunt, R. B., Jr. 179
Hunt, T. K. 375
Hupp, J. T. 486, 532
Hutchings, S. 251

Igetoft, L. 123
Iizuka, H. 270, 271
Iizuka, T. 188
Ikuta, K. 190
Iles, P. A. 195
Imaizumi, E. 166
Imamura, S. 290
Imanishi, Y. 192
Inokuchi, T. 460
Inoue, K. 180
Inoue, N. 203
Inoue, S. 229
Inoue, Y. 211
Isaac, R. D. 277
Isaacs, H. S. 475, 476
Isawa, N. 189
Ishikawa, H. 229
Isozumi, S. 322
Itoh, T. 304
Iwai, H. 261

Jain, R. K. 279
Janik-Czachor, M. 68
Jastrzebski, L. 193, 265, 310
Jevne, A. 105
Jeys, T. 73
Jiang, S.-N. 201
Johannessen, J. S. 470
Jones, C. L. 258
Jones, K. A. 382
Jurasek, L. 452
Juttner, K. 69, 524

Kadary, V. 58
Kadija, I. V. 393, 394

Abstract No.

Kalapis, K. 467
Kalejs, J. P. 326
Kam, K. 386
Kam, K.-K. 488
Kam, T. T. 143
Kambanis, S. M. 111
Kantner, E. 388
Kapusta, S. D. 45
Karas, B. R. 168
Karol, K. N. 106
Kasenga, A. 176
Kashnikov, B. P. 223
Katagiri, A. 525
Katan, T. 2,3
Katz, L. E. 238
Kaul, A. 137
Kawasaki, K. 404
Kawazu, S. 264
Kazan, B. 145
Kerbel, H. 31
Kerr, J. B. 430
Kessel, C. R. 422
Kester, J. 366
Khalil, M. W. 57, 60
Kiddon, J. 299
Kikuchi, K. 187
Kim, B. M. 13
Kim, C. 272
Kim, K. M. 330
Kinaka, R. 336
Kirowa-Eisner, E. 435
Kirwan, D. J. 442
Kitani, A. 441
Klaus, E. A. 495
Klein, N. 58, 90
Klein, R. 251
Kleitz, M. 474
Kline, G. 386
Klinedinst, K. A. 115
Kniewald, D. 107
Knock, K. K. 127
Knutsen, G. 157
Ko, W. C. 316
Koch, V. R. 453
Kogure, O. 290
Kohli, R. 342
Kolb, D. M. 363, 521
Kolb, J. M. 395
Kolbesen, B. O. 247
Komatsu, T. 272
Konaka, M. 261, 271
Kondo, Y. 198
Konno, H. 29
Korde, R. S. 284
Korotkina, O. 31
Kotz, R. 354
Kozuka, H. 241
Kravets, R. R. 451
Kreishman, G. P. 428
Krstajic, N. V. 401
Krutchen, S. L. 262
Kudo, T. 92
Kugimiya, K. 204
Kukimoto, H. 166
Kulkarni, C. L. 465
Kunimatsu, K. 371
Kunz, R. E. 368
Kurosawa, K. 270
Kwart, Y. 260

Lagowski, J. 62, 199, 265, 322
Lai, S. K. 214
Lamereaux, R. H. 276
Lanford, W. A. 294
Larkin, D. 486
Laslaz, G. 93
Lau, S. K. 334
Law, H. H. 87

Abstract No.

Lazzari, M. 88
Lee, C. H. 318
Lee, C. L. 283
Lee, J. Y. 320
Lee, K. C. 361
Lee, L. K. 506
Lee, M. K. 283
Lee, S. 288
Lee, S. H. 286
Lee, Y. K. 141
Lehmann, W. 156
Le Hoang, M. D. 483
Lehrer, W. I. 228
Leidheiser, H., Jr. 16, 36, 123
Leiva, E. P. M. 526
Lemme, R. 246
Leroy, B. 331
Levine, S. 383
Levy, P. F. 461
Li, W. L. 158
Liao, P.-k. 344, 345, 347, 348
Lin, L.-F. 72
Lin, W. 186
Lin, W. L. 213
Linga, H. 76
Linholm, L. W. 253
Lious, F. T. 383
Liu, B. D. 353
Liu, H. Y. 486
Liu, J. 153
Liu, M.-B. 4
Liu, S. D. 283
Llewelyn Leach, J. S. 28
Locke, M. C. 127
Lockwood, A. 379
Lodi, G. 398
Lombardi, J. R. 358
Longo, J. M. 520, 528
Lopez, G. A. 391
Lorenz, W. J. 69, 524
Lorimer, S. E. 492
Lozykowski, H. J. 175
Lu, S. H. 148
Lucchese, C. J. 227, 301
Luer, G. 433
Luksha, E. 48, 82
Luo, X. 173
Lyons, M. E. G. 47

Ma, T. P. 215
Macagno, V. A. 49
Macdonald, D. D. 72
MacDougall, B. 46
MacInnes, R. D. 64
MacKirdy, I. S. 430
MacLaurin, B. K. 52
Maeda, M. 297
Magee, T. J. 273
Magnea, N. 161
Magner, G. 534
Mahmood, M. N. 507A
Mahoney, M. 367
Mahuson, T. C. 103
Major, J. 335
Maki, M. 241
Malachesky, P. A. 388
Mallam, N. 258
Mallory, C. L. 250
Mamantov, G. 360
Man, M. C. M. 507A
Marassi, R. 360
Marcus, R. B. 278
Martin, E. P. 186
Martin, J. E. 274
Martinez-Duart, J. M. 91
Maru, H. C. 9
Masui, T. 188
Matsuda, I. 404

Abstract No.

Matsukawa, T. 264
Matsumoto, S. 273
Matsuoka, T. 167
Matsuo, S. 192
Matteson, S. 226, 319
Mattis, R. L. 253
McBreen, J. 5, 505
McColl, J. R. 150, 151, 178
McCreery, R. L. 427
McIntosh, L. 276
McIntyre, N. S. 70
McMahon, J. J. 364
Mei, L. 260
Melendres, C. A. 24, 506
Mendez, E. E. 149
Merz, C. J. 280
Meschter, P. J. 340
Metzger, M. 31, 33
Miles, M. H. 495
Miller, L. L. 441, 445, 446, 447
Miller, N. E. 285
Milligan, S. N. 423, 432
Mimura, S. 271
Miner, C. J. 52
Mitchell, W. C. 380
Mittal, K. L. 98, 129
Mitteldorf, J. 8
Miyoshi, K. 290
Mohnot, S. M. 12
Molinorolo, W. 362
Molva, E. 162
Monte, S. J. 139
Montero, I. 91
Mooney, J. B. 276
Moraczewski, J. 424
Morawski, A. 62
Moran, K. 464
Mori, F. 230
Morimoto, K. 166
Morin, J. 332
Morris, J. L. 22
Moulton, C. W. 275
Mozota, J. 396, 397
Mukai, K. 298
Muller, K. 44
Munoz, E. 533
Muraoka, H. 192
Muraoka, S. 187
Murarka, S. P. 225
Murgai, A. 191
Murphy, T. J. 391

Nagashima, H. 192
Nagayama, M. 29
Nagelberg, A. S. 355, 356
Naguib, H. M. 293
Nagy, Z. 484
Nakamura, S. 204
Nakamura, T. 229
Nakanishi, H. 190
Nakata, H. 264, 292
Nakayama, R. 270
Narita, K. 177
Natishan, P. 489
Nava, F. 230
Nazri, G. 354
Nee, H. H. 94
Nelsen, S. F. 422
Nelson, K. 276
Nesbit, L. A. 303
Nestleroth, J. B. 133
Netherton, S. W. 266
Newby, K. 388
Newman, J. 471
N'Guyen, V. T. 332
Ni, S. 137
Nidola, A. 418
Nishimura, T. 180

Abstract No.

Nitta, T. 167
Noble, B. 35
Norenberg, M. A. 15
Novak, D. M. 397
Nozaki, T. 302
Nozik, A. 464
Nuntnarumit, C. 429

O'Brien, T. J. 390
O'Clock, G. D., Jr. 262
O'Connor, R. 251
O'Dell, B. 413
Ogirima, M. 241
O'Grady, W. E. 475, 499, 516
Ohkawa, S. 313
Ohsawa, A. 313
Oi, R. 460
Okabayashi, H. 302
Okamoto, A. 322
Okubo, Y. 189
Oldfield, J. W. 6
Olender, H. 495, 505
Oleszek, G. M. 266
Oliver, M. R. 319
Onga, S. 261
Ono, S. 38
Oppolzer, H. 246
Orazem, M. E. 471
Ord, J. L. 50
Orent, T. W. 288
Ortega, C. 55
Osaka, J. 203
Osteryoung, J. 435
Osteryoung, R. A. 76
O'Sullivan, E. J. M. 47, 512
Ottaviani, G. 230
Owen, S. J. T. 170

Packham, D. E. 100
Paetsch, L. 9
Pallotta, C. 502
Panagopoulos, C. 28
Panousis, P. T. 254
Pappalardo, R. G. 176, 179
Parcells J. W. 442
Park, J. M. 110
Park, S.-M. 384, 385, 390, 439, 440
Parkinson, B. A. 386, 387, 488
Patel, D. 9
Patel, J. R. 196
Paunovic, M. 493
Pautrat, J. L. 161, 162
Pearce, C. W. 238
Pearson, B. R. 28
Pearson, L. 493
Pebler, A. 18
Pecile, D. 172
Pedroza, G. C. 131
Peek, R. C., Jr. 138
Pehl, M. A. 15
Perloff, D. S. 250
Perone, S. P. 436
Perriere, J. 53, 54
Peters, D. A. 116
Peters, T. E. 151, 176
Petersen, R. O. 147
Pethica, B. 452
Pettinger, B. 359
Pfeiffer, H.-P. 339
Philpott, M. R. 359, 368
Phillips, G. M. 15
Pieper, H. 207
Pierce, J. M. 228
Piersma, B. J. 66, 507
Pignatel, G. 230
Pinizzotto, R. F. 202, 226
Pitts, R. 374
Plattner, E. 416, 444

Abstract No.

Plieth, W. 370
Ploughonven, C. 331
Plueddemann, E. P. 136
Plummer, J. D. 216
Poate, J. M. 219
Pocius, A. V. 102
Popov, K. I. 401
Popovic, R. S. 249
Pouli, D. 402
Predel, B. 349
Pringle, J. P. S. 32
Prinke, G. 269

Raleigh, D. O. 466
Rao, G. M. 324
Rao, K. V. 206, 311
Rasiyah, P. 527, 529, 530
Ratcliff, M. 459, 464
Rava, P. 199
Ray, A. K. 234, 280
Raza, A. 276
Recktenwald, J. 276
Reedy, R. E. 308
Reeve, C. P. 253
Regis, A. 369
Reichman, B. 400
Reinisch, L. A. 222
Reisman, A. 234, 280
Resch, G. 77
Revesz, A. G. 281
Reynolds, G. 379
Rieke, L. I. 423
Rieke, R. D. 423, 432
Riley, T. J. 103
Rivier, M. 260
Robbins, D. J. 164
Robinson, J. 76
Robinson, R. 427
Rose, J. L. 133
Rosler, D. 294
Ross, P. N., Jr. 498
Rossi, P. 427
Roy, B. 370
Rozas, R. 533
Rozgonyi, G. A. 224, 315
Ruggeri, R. T. 124
Rusling, J. 431
Russell, J. W. 371
Ryssel, H. 269

Sabelli, N. 506
Sahami, S. 79
Sakai, H. 305
Salomon, M. 81
Saminadayar, K. 161
Sammells, A. F. 450
Sampathkumaran, P. S. 128
Sanders, F. H. M. 231
Sanderson, J. E. 461
Sanjurjo, A. 325
Saraswat, K. C. 282
Sartell, J. A. 288
Sathyanarayana, M. N. 128
Sato, T. 38
Savy, M. 534
Scarbeck, G. 534
Schaake, H. F. 202
Schachterle, S. D. 436
Scherer, G. G. 44
Scherson, D. 496
Schiavone, L. M. 511
Schiffman, R. A. 338
Schmalzl, P. W. 445
Schmickler, W. 39
Schmidt, L. D. 518
Schouler, E. J. L. 474, 476
Schreiber, H. P. 104
Schreiner, R. 168

Abstract No.

Schroeder, H. A. 454
Schultze, J. W. 61
Schulz, M. 218
Schwerzel, R. E. 463
Scrosati, B. 88
Sculfort, J.-L. 86
Seats, P. 144
Sefara, M. 107
Segretario, J. 431, 458
Seibert, K. 103
Seidel, T. E. 238
Seko, M. 417
Sellers, J. 299
Seraphin, B. O. 352
Series, R. W. 205, 221, 328
Seshan, K. 352, 479
Sethi, R. 5
Shabana, M. 267
Shelby, J. E. 357
Sheng, T. T. 278
Shi, C-S. 181, 182
Shibata, M. 305
Shibata, T. 270, 271
Shibatomi, S. 313
Shigyo, N. 270
Shilo, I. 338
Shimizu, K. 336
Shimizu, K. 30, 34
Shioya, Y. 297
Shirai, S. 187
Shoesmith, D. W. 70
Shohno, K. 272
Shousha, A. H. M. 59
Shyu, C. M. 212
Sickfeld, J. 134
Sides, P. J. 392
Sieka, J. 53, 54, 55, 62
Sigmon, T. W. 308
Silverman, H. P. 407
Silvestre, E. 67
Silvestri, V. J. 321
Simoliunas, S. 119
Simone, M. J. 428
Sinclair, J. D. 25
Singh, H. 282
Sirtl, E. 194
Sivasamban, M. A. 128
Skarstad, P. M. 85
Sleszynski, N. 458
Smirnov, L. S. 223
Smith, D. E. 434
Smith, D. H. 170
Smith, D. J. 51, 56
Smith, R. 452
So, Y.-H. 446, 447
Someno, M. 336
Sopher, D. W. 454
Sparrow, G. R. 101
Spasojevic, M. D. 401
Spitzer, D. P. 376
Splinter, M. 300
Spore, E. M. 405
Srinivasan, S. 383, 495, 505, 508, 516
Stacy, W. T. 208
Stadtherr, M. A. 406
Stallhofer, P. 242
Steckl, A. J. 296
Steffek, D. J. 422
Steinberg, M. P. 451
St. John, M. R. 450
Stimming, U. 61
Stojadinovic, N. D. 249
Stoner, G. E. 442, 489
Storck, A. 480
Streater, R. W. 52
Streckert, H. H. 168
Streetman, B. G. 222
Strunk, H. 243, 247

Abstract No.

Stucki, S. 44
Stupp, S. I. 113
Stutius, W. 160
Su, C-H. 344, 345, 347, 348
Su, Y. K. 353
Suetaka, W. 112
Sugawara, S. 290
Sugerman, G. 139
Sukegawa, K. 290
Sumino, K. 197
Sun, B-K. 201
Sun, T. S. 125, 126
Sundaram, S. 323
Sunder, S. 70
Sung, C. S. P. 137
Sung, C-Y. 201
Sung, N. H. 137
Sunu, W. G. 1
Suzuki, T. 95, 189, 211
Suzuki, Y. 292

Tadjeddine, A. 363
Tajima, M. 188
Takac, K. 107
Takagi, M. 297
Takahara, T. 180
Takahashi, H. 29
Takahashi, S. 298
Takai, H. 304
Takamatsu, A. 305
Takano, Y. 241
Takeishi, Y. 184
Takeshita, T. 378
Tanaka, K. 292
Tanemoto, K. 360
Taniguchi, K. 261
Tarui, Y. 184
Tempelhoff, K. 205A
Tennyson, M. R. 274
Tessier, D. 500
Theis, D. 169
Thevenin, J. 89
Thomas, J. 172
Thompson, G. E. 30, 34
Thompson, R. D. 289
Thompson, S. 317
Tilak, B. V. 402
Ting, C. Y. 306
Tobias, C. W. 87, 392, 478
Tohier, J. 421
Toki, H. 166
Topich, J. A. 268
Torii, S. 460
Toyokura, N. 229
Trasatti, S. 398, 501
Tremillon, B. 483
Trevisan, E. 331
Triebe, F. M. 429
Tripkovic, A. V. 516
Truesdell, J. W. 23
Truhan, J. 73
Tryk, D. A. 439, 440
Tsai, K. C. 22, 485
Tsai, M. Y. 227, 301

Abstract No.

Tsai, Y. L. 353
Tsaur, B. Y. 289
Tseung, A. C. C. 527, 529, 530
Tu, K. N. 289
Tucker, I. 423
Tuenge, R. T. 171
Tung, T. 344, 345, 347, 348
Tuomi, D. 377
Turner, A. K. 507A
Turner, J. 464
Turner, T. S. 6
Twardowski, Z. 412, 414
Tyagi, M. S. 284

Untereker, D. F. 15
Usami, T. 192
Ushio, S. 295

Van De Mark, M. R. 23
van der Wekken, C. J. 494
Van Effen, R. M. 457
Van Landuyt, J. 240
Van Overstraeten, R. 240
Varker, C. J. 206, 311
Varma, R. 362
Varsanyi, M. L. 16
Vaughan, D. J. 138
Venables, J. D. 125, 126
Venburg, G. D. 432
Verghaus, H. 169
Venkatasetty, H. V. 78
Venkatesh, S. 485
Verkuil, R. L. 263
Vertes, A. 16
Vielstich, W. 515
Vilche, J. R. 65
Viswanathan, K. 415
Vitko, J. 357
Vutetakis, D. G. 463

Wada, K. 203
Waite, M. S. 174
Wakatsuki, T. 180
Walker, G. W. 491
Wang, K. L. 226
Wang, K.-M. 294
Wang, W. 123
Wang, W-N. 201
Wang, Y-F. 63
Wang, Z. H. 148
Warren, J. 63
Warszawski, B. 407
Watanabe, M. 49, 180, 192
Watase, S. 92
Weaver, M. J. 79, 364, 486, 531, 532
Webber, A. 435
Webber, H. C. 221
Weber, K. 123
Weber, N. 375
Wei, C. C. 353
Wei, J. J. 148
Weininger, J. L. 13
Weisbrod, K. R. 19
Wells, M. A. 456

Abstract No.

Wengert, R. R. 165
West, C. 164
Westwood, W. 52
Wetterling, S. 252
Whelan, D. P. 47
White, R. E. 492
Whitfield, J. D. 206
Whyte, J. R., Jr. 479
Wilemski, G. 8
Will, F. G. 467
Willeford, B. 423
Willis, J. P. 465
Willoughby, A. F. W. 258
Wilson, J. R. 384, 385
Wolf, G. K. 499
Wolf, J. F. 40
Wolter, O. 515
Wood, C. 379
Wood, D. 507A
Wood, G. C. 30, 34
Wood, V. E. 463
Woodman, E. 456
Woods, R. 509
Wordeman, M. R. 227
Worrell, W. L. 334, 335
Wright, M. L. 469
Wright, W. 251
Wu, H. J. 320
Wu, T-C. 208
Wu, Y. 148

Xu, S. H. 148, 158

Yamaji, T. 295
Yamamoto, H. 183
Yamazaki, T. 292
Yang, C. Y. 383, 475, 497
Yang, K. W. 170
Yaniv, M. 472
Yankley, R. E. 319
Yao, N. P. 4, 362
Yasuda, H. 109
Yasuda, M. 411
Yeager, E. 354, 496
Yeager, H. L. 412, 413, 414
Yeh, L. S-R. 40
Yen, A. C. 318
Yoko, T. 490
Yoo, H. I. 195
Yoshimi, T. 305
Yoshimura, S. 525
Yoshizawa, S. 525
Young, L. 51, 56

Zagal, J. 533
Zahavi, J. 31, 33
Zahn, M. 408, 409
Zanzucchi, P. 193
Zhang, W-P. 181, 182
Zhang, Y.-X. 20
Zhang, Z.X. 158
Zhao, S. Y. 148
Zhou, L. 173
Zuman, P. 421, 431, 452, 456, 458

SOCIETY NEWS

Building Fund Update

The Electrochemical Society membership is proving to be generous and farsighted in its support of the recently established Building Fund. Many contributions have significantly exceeded the suggested minimum level, and the Society feels that this generosity should be appropriately and appreciatively recognized.

Toward this purpose, such exceptional gifts will be inscribed in a book to be displayed in the new building. Categories of contributions to be recognized in this book will include Society Friends for gifts of $100 to $299, Society Sponsors for gifts of $300 to $999, and Society Benefactors for gifts over $1000.

The Electrochemical Society is deeply appreciative of the contributions of all its contributors, who are numbering a major fraction of the membership. This degree of support reflects the healthy and essential involvement of our members in the affairs and aspirations of our Society.

GROUP NEWS

Energy Technology Group

Report of the Nominating Committee for the Election of Group Officers at the Spring Meeting in Minneapolis, Minnesota, May 10-15, 1981

The nominating committee (J. M. Woodall, Chairman, S. Srinivasan, and S. Wagner) proposes the following slate of candidates:

Chairman: James McBreen, Brookhaven National Laboratory

Vice-Chairman: Arthur J. Nozik, Solar Energy Research Institute

Secretary: A. John Appleby, Electric Power Research Institute

Treasurer: Harold J. Hovel, IBM Watson Research Center

In accordance with the bylaws of the Group, additional nominations for office may be made by a petition signed by five members of the Group. Such petitions must be in the hands of the chairman of the nominating committee at least ten days before the election, together with the assurance of the nominee's willingness to serve if elected.

DIVISION NEWS

Research Award of the Electrodeposition Division

Nominations are being sought for the Research Award of the Electrodeposition Division. The award which was given for the first time in Fall 1980 to Rolf Weil, consists of a cash prize of $200 and a plaque. It is given for recent outstanding research in electrodeposition. The award will be given to an author or co-authors of a paper or papers, at least one of which must have appeared in **This Journal** or other publications of The Electrochemical Society, reporting this new achievement.

The award committee is composed of T. C. Franklin, Chairman, A. H. Graham, J. Griffin, F. Ogburn, and R. Weil. Recommendations for the award in the form of a letter detailing the accomplishments of the nominee should be sent to the Committee Chairman at the Chemistry Department, Baylor University, Waco, Texas 76798. Recommendations received prior to the March 20, 1981 deadline will be considered for the award, to be given at the Fall 1981 meeting.

Organic and Biological Division

Report of the Nominating Committee

The Nominating Committee of the Organic and Biological Division has proposed the following slate of officers:

Chairman—John Wagenknecht, Monsanto Co.

Vice-Chairman—Martin Blank, Columbia University

Secretary-Treasurer—Peter Zuman, Clarkson College of Technology

Physical Electrochemistry Division

Report of the Nominating Committee

The Nominating Committee of the Physical Electrochemistry Division has proposed the following slate of officers:

Chairman—Elton J. Cairns

Vice-Chairman—Robert A. Osteryoung

Secretary-Treasurer—Larry R. Faulkner

Executive Committee—Jerry Braunstein and Jose Giner

SECTION NEWS

Ontario-Quebec Section

The Spring Symposium of the Ontario-Quebec section of The Electrochemical Society will be held at Concordia University on April 24, 1981. Ten papers will be presented dealing with Solid-State Materials and Devices including a contribution by Dr. W. Westwood of Bell Northern Research. In addition, the recipient of the 1981 W. Lash Miller Award in recognition of outstanding technical contributions to the field of electrochemistry will be announced.

For further information, contact Prof. B. A. Lombos, Concordia University, 1455 de Maisonneuve, Montreal, Que., Canada H3G 1M8.

Oregon Section

The first meeting of the Oregon Section was held December 3, 1980 at Portland State University. Dr. David Roe, Professor of Chemistry, called the meeting to order. A letter from Dr. Ted Beck, Past President of the Society, expressing his regrets that he could not attend the first meeting of the Oregon Section, was read.

A slate of officers for the local section was nominated. It was moved, seconded, and passed unanimously that the slate of officers be elected. They are:

Chairman—Dr. David Roe, Portland State University

Vice-Chairman—Dr. Larry Church, Tektronix

Councilors—Dr. Gary McGuire, Tektronix, and Dr. Robert Meredith, Oregon State University

Secretary-Treasurer—Dr. Drannan Hamby, Linfield College

Member-at-Large—Dr. Bill Harshbarger

The bylaws of the Oregon Section were presented by Dr. Roe. It was moved and seconded that the bylaws be accepted as presented. The approval was unanimous. Dr. Gary McGuire was then introduced and he spoke briefly about the need to promote membership in the local section and a need to establish local dues. Dr. McGuire then introduced Dr. Richard Kayoma, who gave an informative, well-prepared, and interesting presentation on "Gallium Arsenide Materials for High Speed Technology."

Drannon Hamby
Secretary-Treasurer

PEOPLE

Robert Baboian, head of the Electrochemical and Corrosion Laboratory, Texas Instruments, Inc., has been elected to a three-year term on the Board of Directors of the American Society for Testing and Materials (ASTM).

A native of Watertown, Massachusetts, Baboian received his B.S. degree in chemistry from Suffolk University in 1959 and his Ph.D. in the same from Rensselaer Polytechnic Institute in 1964. He began working for Texas Instruments in 1966. His early work in the company led to fused salt processes for the electrodeposition of titanium. He established the Corrosion Laboratory in 1969 and initiated work on design and evaluation of corrosion resistant materials. He has been engaged in the development of clad metals for corrosion resistance and the development of devices for corrosion monitoring and protection. He has developed principles of galvanic corrosion and established test methods and design criteria for dissimilar metal systems.

In 1976, Dr. Baboian was elected a TI Fellow, the company's highest award given for a scientific and technological achievement.

An Active Member of The Electrochemical Society, Dr. Baboian is also a member of the National Association of Corrosion Engineers, the American Chemical Society, the Society of Automotive Engineers, and the Honorary Society of Sigma Xi. He has authored over 45 papers and co-edited three books in the field of electrochemistry and corrosion. He is the holder of 12 U.S. patents on materials systems and electrochemical processes.

Metal Extraction Engineer

RMI Company, the leading producer of titanium mill products, is looking for a specialist to conduct research on the extraction of titanium metal from ores or from an intermediate product. Minimum requirements include a BS degree and an understanding of metal reduction technology, basic chemistry, electrochemistry and thermodynamics. Experience with reactive metals and background information on mechanical and chemical engineering would be desirable.

RMI Company, owned by U.S. Steel and National Distillers and Chemical Corporation, is an integrated producer of titanium mill products with plants and offices in Niles and Ashtabula, Ohio; Washington and Sullivan, Missouri; Los Angeles, California; London, England; and Hartford, Connecticut. We offer an excellent salary and benefits. Please send resume and salary requirements to Personnel Department.

RMI Company
Corporate Office
1000 Warren Avenue
Niles, Ohio 44446

RMI TITANIUM

Equal Opportunity Employer M/F/H

NEW MEMBERS

It is a pleasure to announce the following new members of The Electrochemical Society as recommended by the Admissions Committee and approved by the Board of Directors in January 1981.

Active Members

Adamczyk, M. E., Schaumburg, IL
Avigal, Y., Santa Clara, CA
Baumgartner, C. E., Schenectady, NY
Bennett, C. P., Towson, MD
Bennett, P. D., Cleveland, OH
Ben-Zvi, E., Los Angeles, CA
Bhamre, S. L., Los Altos, CA
Blaske, T. A., Garland, TX
Bonifield, T. D., Dallas, TX
Butler, M. R., Mesa, AZ
Chambers, S., Beaverton, OR
Chen, D.-B., San Diego, CA
Clayton, F., Chandler, AZ
Cotton, T. M., Chicago, IL
Coyne, R. D., Santa Clara, CA
Current, M., Sunnyvale, CA
Dasgupta, S. R., Milwaukee, WI
Dih, J.-J., Irvine, CA
Duane, M., Houston, TX
Duarte, M. Y., Corrientes, Argentina
Fouzder, N. B., London, England
Gobrecht, J., Golden, CO
Hafen, D. P., Redwood City, CA
Hamilton, F. G., North Andover, MA
Hartman, D. C., Dallas, TX
Hassan, J. K., Hopewell Junction, NY
Holmblad, C. M., Cambridge, MN
Hong, J. D., San Jose, CA
Hunsicker, R. L., Branford, CT
Isaac, R., Yorktown Heights, NY
Ishihara, T., Santa Clara, CA
Istone, W. K., Suffern, NY
Iwayanagi, T., Kokubunji, Tokyo, Japan
Lau, A., Vancouver, B.C., Canada
Lee, J. D., Seoul, Korea
Leon, S. A., Colorado Springs, CO
Levine, S., Setauket, NY
Lewernez, H. J., Berlin, West Germany
Mahmood, M. N., Middlesex, England
Maltiel, R., Santa Clara, CA
Mastroianni, S. T., Mesa, AZ
Matsumoto, Y., Utsunomiya, Japan
Middelhoek, J., Enschede, The Netherlands
Nishi, H., Nakaharaku, Kawasaki, Japan
Oye, H. A., Trondheim, Norway
Patel, B., Brooklyn Center, MN
Pe, F. S., Camp Springs, MD
Pelton, A., Montreal, Que., Canada
Pennington, C. E., Indianapolis, IN
Peters, D. T., Suffern, NY
Pilapil, R. O., Fullerton, CA
Pinsky, N., Troy, MI
Psioda, J. A., Tarrytown, NY
Raman, N., Wappingers Falls, NY
Rasmussen, J. J., Butte, MT
Rivas, I. V., Mesa, AZ
Sanderson, J. E., Cambridge, MA
Sattar, A., Rajshahi, Bangladesh
Schiavone, L. M., Holmdel, NJ
Secco D'Aragona, F., Scottsdale, AZ
Shihata, K., Kawasaki, Japan
Sidman, A. L., Malden, MA
Smith, H. G., Phoenix, AZ
Smith, S. M., Tempe, AZ
Steinbicker, R. N., Coopersburg, PA
Syllaios, A. J., Richardson, TX
Tam, G., Tempe, AZ
Tang, C.-W., Billerica, MA
Teschke, O., Campinas, Brazil
Thakar, G. V., Dallas, TX
Tierney, E. J., Poughkeepsie, NY
Tomaswick, K. M., New Kensington, PA
Travers, H.-C., Palo Alto, CA
Tsang, B. H., Tempe, AZ
Turchan, M. J., Sudbury, MA
Wallace, W. L., Golden, CO
Warszawski, B., Paris, France
Wood, J. M., Jr., Baton Rouge, LA
Wu, C. C., Cupertino, CA
Yim, Z., Nutley, NJ
Zebliskey, R. J., Melville, NY
Zoski, G. D., Waltham, MA

Corrosion Engineer

RMI Company, the leading producer of titanium mill products, seeks a corrosion specialist to plan and conduct corrosion test programs on titanium at the corporate research laboratory in Niles, Ohio. The work will support and enhance the wide and growing usage of titanium products in the chemical and allied process industries.

Minimum qualifications include a BS degree and an understanding of corrosion phenomena, corrosion testing, chemistry, metallurgy and electrochemistry. Experience with titanium and background information on the chemical process industries would be desirable.

RMI Company, owned by U.S. Steel and National Distillers and Chemical Corporation, is an integrated producer of titanium mill products with plants and offices in Niles and Ashtabula, Ohio; Washington and Sullivan, Missouri; Los Angeles, California; London, England; and Hartford, Connecticut. We offer an excellent salary and benefits. Please send resume and salary requirements to Personnel Department.

RMI Company
Corporate Office
1000 Warren Avenue
Niles, Ohio 44446

RMI TITANIUM

Equal Opportunity Employer M/F/H

Minneapolis, Minnesota, Meeting Program 51C
ECS Short Course Offered 718
Society News 138C
Group News 138C
Division News 138C
Section News 138C
People 139C
New Members 139C-140C
Notice to Members 140C
News Items 141C
Position Available 141C
New Books 142C-143C
Call for Papers—
Denver, Colorado, Meeting 149C-154C

Notice to Members

April 1 is Cut-Off Date

Your attention is called to Article III, Section 8 of the Society Constitution which states: "Any member delinquent in dues after April 1 of each year shall no longer receive the Society's publications, and will not be allowed to vote in any Society election until such dues are paid. All members in arrears for one year after the first of April shall lose their membership status and can be reinstated only by action of the Board of Directors." Members who have not sent in 1981 payments were mailed a second notice in February and are urged to make payment promptly in order to avoid delay in receipt of the JOURNAL.

Student Members

Ballinger, R. G., Cambridge, MA
Bancroft, E. E., Newark, DE
Bravman, J. C., Stanford, CA
Chen, A. S., La Jolla, CA
Chen, J. C., Ann Arbor, MI
Chen, S., Stanford, CA
Fang, Y. K., Taiwan, China
Flores, J., Davis, CA
Hanson, M. E., Cleveland, OH
Huang, Y.-H., Urbana, IL
Hung, C.-F., Cleveland, OH
Jacobson, N., Berkeley, CA
Kobrin, A., Stanford, CA
Leising, G., Graz, Austria
Lessner, P., Berkeley, CA
Liao, S. H., Cleveland, OH
Lu, H. E., Cincinnati, OH
Lyon, J. T., Houston, TX
Marsan, B., Montreal, Que., Canada
Martinez-Montes, G., Tucson, AZ
McGuire, J., Raleigh, NC
Mozaffari, M., San Jose, CA
Naftel, S., Berkeley, CA
Oberstar, J. D., Urbana, IL
Pendse, R. D., Berkeley, CA
Risch, T. K., Berkeley, CA
Salinas, J. G., Champaign, IL
Satyadharma, V., Delft, The Netherlands
Tuschel, D. D., Milwaukee, WI
Van Der Vaart, D. R., Raleigh, NC
Wang, Y.-H., Taiwan, China
Whitney, G. M., Berkeley, CA
Wu, L.-K., Albany, CA
Yilmaz, H., Ann Arbor, MI

Reinstatements

Blount, H. N. III, Newark, DE
Howard, F. L., Spokane, WA
Yeh, P. P., Solvay, NY

CHANGES OF ADDRESS SHOULD BE PROMPTLY REPORTED.

Mail to the Circulation Department, The Electrochemical Society, Inc., 10 South Main St., Pennington, N.J. 08534.

ATTACH LABEL HERE

Change of Address

To change your address, place address label here for proper identification. Print your NEW address below.

name

address

city **state** **zip code**

NEWS ITEMS

New Book Available

A new book entitled "Science and the Sons of Genius: Studies on Humphry Davy" is now available. The book is edited by Dr. Sophie Forgan, and is based on papers presented at the Royal Institution, London, at the Davy Bicentenary Symposium. For further information, contact Science Reviews Limited, 3/4 St. Andrews Hill, London EC4V 5BY, England. The cost of this book is $15.00.

Report on International Conference

The "Third International Meeting of Solid Electrolytes," a conference supported jointly by The Electrochemical Society and six Japanese societies, was held Sept. 15-19, 1980 in Tokyo, Japan. Professor T. Takahashi was Chairman of the Organizing Committee. The Department of Energy and the National Science Foundation provided some financial support. Eleven plenary lectures and 125 other presentations emphasized the areas of solid-state ionics and galvanic cells.

Future meetings will be called "International Conference on Solid-State Ionics." The fourth conference is scheduled for 1983 in France, with M. Kleitz, University of Grenoble, serving as Co-Chairman. The fifth conference will be held in the United States, with R. Huggins, Stanford University, as Co-Chairman.

POSITION AVAILABLE

Electrochemist-Metallurgical Engineer—Conduct fundamental research on failure processes in metal/alkali batteries using low frequency impedance techniques, ellipsometry, and numerical transformation of time-domain data into frequency domain. Master's degree in metallurgy or electrochemistry required, computer programming helpful. Send resume with references to Professor D. D. Macdonald, Fontana Corrosion Center, The Ohio State University, 116 West 19th Avenue, Columbus, Ohio 43210. OSU is an equal opportunity employer.

ADVERTISERS' INDEX

ECO	143C
Hooker Chemicals & Plastics Corp.	141C
Kerr-McGee Corp.	141C
Princeton Applied Research Corp.	144C
RMI Co.	139C
RMI Co.	140C

ELECTROCHEMICAL ENGINEER/ ELECTROCHEMIST

Newly formed section at corporate research facility in Oklahoma City has immediate openings for scientists with strong theoretical and experimental backgrounds for research and process development programs involving electrolytic anodes, cathodes and cells. An advanced degree and 5 years experience desired. These positions offer competitive salary and benefits and excellent opportunities for professional development and advancement. Interested, qualified candidates should submit resume', including salary history, in confidence to:

J. C. Hilburn
KERR-McGEE CORPORATION
P. O. Box 25861
Oklahoma City, Oklahoma 73125
405/270-3660

We Are An Equal Opportunity Employer M/F/H/V

KERR-McGEE CORPORATION

HOOKER CHEMICALS & PLASTICS CORP.

GRADUATE STUDENT SUMMER GRANTS

During the summer of 1980, HCPC awarded three grants for the support of graduate students doing research in electrochemistry or electrochemical engineering and will again offer a limited number of such grants during the summer of 1981. The intention of these awards is to encourage and assist outstanding student research in any area of electrochemical science and technology. Each award will be for $3,000 and may be utilized for stipend, purchase of materials or equipment, travel or any other approved purpose of direct benefit to the student; no university overhead charges will be paid.

Proposals should be made on application forms available from HCPC which will require a recommendation of the student's eligibility based on past performance and future promise; an outline of the student's research project and a budget showing how the award will be utilized. Only those proposals will be accepted which are made on application forms provided and no additional information will be required.

Requests for applications should be made to Dr. Russell L. K. Carr, Hooker Chemicals & Plastics Corp., Research Center, Long Road, Grand Island, NY 14072. Completed applications should be sent to his office by *April 30, 1981.*

Book Reviewers Needed

The Electrochemical Society needs competent individuals to review books for the Journal.

Any Society member who wishes to volunteer his services should send his name, address, and field of competence to the attention of the Book Review Editor, Dr. Julius Klerer, c/o The Electrochemical Society, 10 South Main Street, Pennington, N.J. 08534.

NEW BOOKS

Modern Polarographic Methods in Analytical Chemistry, by A. M. Bond.

1980, Marcel Dekker Inc., 270 Madison Ave., New York, NY 10016. 518 pages, bound. $65.00.

This is a book for the analytical chemist who is considering using polarography and wishes to ascertain which polarographic method to choose and how to use it. With the rebirth of interest in electroanalytical methods, and in polarography in particular, a vast number of polarographic methods have become available, some for the first time and others based on techniques recently revived. Each method has its subtle drawbacks and advantages, and it is difficult for the chemist—even with a broad knowledge of analytical techniques—to know how to make the best use of this recently elaborated methodology.

It provides an up-to-date discussion of modern polarographic methods, complete with examples, experimental details, and, most importantly, the author's insight into the relative merits of each method. For practicing analytical chemists and electroanalytical chemists, this is the best book to consult before venturing into new territory.

Metallurgical Coatings 1979, edited by J. N. Zemel.

1979, Elsevier Sequoia S.A., Avenue de la Gare 50, P.O. Box 851—1001 Lausanne, Switzerland. 882 pages, bound. $120.00.

This conference is an established forum for the dissemination of information on coatings for high technology applications. It demonstrates that coatings are an essential and indispensable feature of modern technology. The various sessions are: plenary session; developments and economics in physical vapor deposition technology; surface modification by ion bombardment; coatings for radiation environments: fission, fusion; integrated and guided wave optics; characterization of coatings; defects and internal stresses in coatings; metallurgical aspects of microelectronic materials; coatings for high temperature corrosion/erosion; coatings for corrosion and battery applications; coatings for erosion and wear; coatings for solar energy applications; refractory compound coatings; metal and alloy coatings.

Hydrogen as an Energy Vector: Its Production, Use and Transportation, by Commission of the European Communities.

1978, The Commission Ventre Louvigny, P.O. Box 130, Luxembourg. 592 pages, paper.

There were three sessions: thermochemical production of hydrogen; hydrogen production by water electrolysis; hydrogen use, storage, and transportation. Some specific topics discussed in the 38 papers: pulsed electrocatalytic dissociation of water vapor; problems concerning the electrochemical step of the sulfuric acid hybrid cycle; alkaline inorganic-membrane-electrolyte water electrolysis; anodic materials for the electrolysis of water; optimization of gas evolving Teflon-bonded electrodes; thermodynamical conditioning of gases produced by water electrolysis; gas bubble behavior during water electrolysis; hydrogen storage by means of reversible magnesium alloys; hydrogen storage by use of cryoadsorbents in comparison to alternatives; the use of nonfossil-derived hydrogen in coal conversion processes; and technico-economic study of the use of hydrogen and methanol for automobiles.

CALL FOR RECENT NEWS PAPERS AND EXTENDED RECENT NEWS PAPERS

Minneapolis, Minnesota, Meeting May 10-15, 1981

Triplicate copies of a 75-word abstract of a Recent News Paper, for a 10 minute presentation, must be received by the Symposium Chairman not later than March 24, 1981.
Triplicate copies of a 75-word abstract and, also, a 200-300 word abstract of an Extended Recent News Paper, for a 20 minute presentation, must be received by the Symposium Chairman not later than March 14, 1981.

ELECTRONICS DIVISION AND DIELECTRICS AND INSULATION DIVISION

Recent News Papers and Extended News Papers are invited for the sessions sponsored by the Electronics Division and Dielectrics and Insulation Division for the 1981 Spring Meeting in Minneapolis, Minnesota. The time allotted for the 75-word Recent News Paper will be 10 minutes, including 2 minutes for discussion. The time allotted for the Extended Recent News Paper will be 20 minutes, including the question/answer period.

The Extended Recent News Paper requires, in addition to the 75-word abstract, a 200-300 word abstract in triplicate and should be received significantly earlier than the normal deadline date because these papers will be reviewed for technical content, appropriateness of the paper, time limitations, duplication of material, etc. Topics for Recent News Papers and Extended Recent News Papers include:

1. Silicon materials science and technology.
2. Display technology and special purpose cathode-ray tubes.
3. Luminescence of II-VI compounds.
4. Chemical modification of grain boundaries in photovoltaic devices.
5. Electrolytic capacitor technology.
6. Adhesion aspects of polymeric coatings.
7. Anodic oxidation.
8. Transport under electrical and thermal gradients.
9. Papers of general interest in dielectrics, electronics, and insulation.

Copies of all abstracts, as outlined above, should be sent to the Recent News Papers Symposium Chairman: W. A. Pliskin, IBM Corporation, Department 108, Internal Zip 48A, Route 52, Hopewell Junction, New York 12533. Please note the deadlines are for receiving the papers and not for mailing them.

Ferroelectric Semiconductors, by V. M. Fridkin.

1980, Plenum Corp., 227 West 17th St., New York, NY 10011. 318 pages, bound. $69.50.

Electron processes in nonlinear crystals have been successfully studied in connection with quantum electronics, nonlinear optics, and electro-optics. In recent years, the study of ferroelectric semiconductors has evolved into an independent research direction. This volume, translated from Russian, contains extensive theoretical and experimental material and includes a bibliography. Topics covered include thermodynamics of ferroelectric semiconductors, screening of spontaneous polarization, photoferroelectric phenomena and photostimulated phase transitions, and ferroelectrics as nonlinear semiconductors.

Physical Chemistry of High Temperature Technology, by E. T. Turkogan.

1980, Academic Press, Inc., 111 Fifth Ave., New York, NY 10003. 447 pages, bound. $49.50.

Insulating Films on Semiconductors 1979 (Conference Series 50), by G. G. Roberts and M. J. Morant.

1980, Published by Heyden & Son, Inc., 247 S. 41st St., Philadelphia, PA 19104. 290 pages, bound. $75.00.

The nine invited and 24 contributed papers presented in this volume are concerned with both the basic physical processes of MIS structures and device applications, such as memory devices, microwave transistors, MIS solar cells, and electroluminescent and switching devices. Although more than half of the sessions were devoted to more "traditional" studies involving silicon oxide or silicon, Chap. 4 contains papers dealing with group III-V semiconducting materials. These are at present attracting considerable interest for high frequency, low noise applications.

Electrodeposition of Metal Powders Materials Science Monographs, 3, by A. Călușaru.

1979, Published by Elsevier North-Holland, 52 Vanderbilt Ave., New York, NY 10017. 544 pages, bound.

This book is concerned with a branch of electrochemistry defined by a specific topic: electrocrystallization of metallic dendrites due to processes occurring in the region of the limiting diffusion current. This topic is a part of electrocrystallization and is related to two distinct disciplines, those of crystallization and electrochemistry. This book covers a wide area including basic aspects of crystallization, electrocrystallization, and electrodeposition of whiskers and metal powders.

Liquid Chromatography of Polymers and Related Materials II (Chromatographic Science Series, Vol. 13), edited by J. Gazes and X. Delamare.

1980, Published by Marcel Dekker, Inc., 270 Madison Ave., New York, NY 10016. 1232 pages, paper.

Except where noted, these books have been prepared by the staff of The Engineering Societies Library, and were selected for inclusion in the **Journal** by Dr. Daniel Cubicciotti of Stanford Research Institute. The Electrochemical Society does not have copies available for sale or loan. Orders for the books should be forwarded directly to the publishers.

The ECO CMS-10 Combines Data Processing with the Advanced Corrosion Measurement System

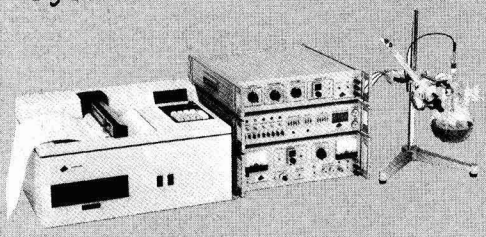

The new microprocessor based system from ECO INSTRUMENTS offers the corrosion researcher at least *seven* advantages . . .

- High speed digital plotter — produces a complete curve in less than 15 seconds.
- Standard corrosion calculations performed at the touch of a button.
- User programmable memory for special studies.
- Hi-speed and Hi-voltage potentiostats available.
- Wide choice of optional accessory instrumentation including: Differential Electrometers, Programmable Function Generators and Test Cells.
- Economical — you will be pleased with the value.

Write or call Dennis Crouse for complete information and prices on the unique new CMS-10 Digital Corrosion System.

ECO INSTRUMENTS
Division of KOR Incorporated
56 Rogers Street
Cambridge MA 02142
Tel: 617-661-8080

See the CMS-10 in Booth 95, 1981 Corrosion Show Toronto April 6-10.

Uncompromising Instrumentation For the Creative Electrochemist

Model 173 Potentiostat/Galvanostat

Accuracy. Reliability. Flexibility. Qualities which set the **Model 173 Potentiostat/ Galvanostat** apart from all others. A work horse for the creative electrochemist.

The 173 features current capability of 1 ampere with compliance voltages as high as 100 volts in either polarity, and a slew rate of 5 volts per microsecond.

It incorporates two independent potential/current sources, each continuously variable over a range of ±4.999 volts, with a control amplifier stability of better than 100 μV per day. The design allows for either manual or remote switching between these two sources. Two additional external potential/current signals can be added to those provided by the instrument. A wide variety of triggering and switchingwaveforms may be employed to control the overall potential or current application programs.

The Model 173 is designed to operate with any of several available current readout plug-in modules, including the Model 176 Current-to-Voltage Converter, the Model 179 Digital Coulometer, and the Model 376 Logarithmic Current Converter.

The Model 173D version provides digital display of either measured current or applied potential. Addition of a Model 176D, Model 179, or Model 376 plug-in provides BCD output of current or potential, including current range information.

For a discussion of how the Model 173 Potentiostat/ Galvanostat can fulfill your particular requirements, contact the Analytical Instrument Division Applications Group. EG&G PRINCETON APPLIED RESEARCH, P. O. Box 2565, Princeton, NJ 08540, USA; Phone: 609/452-2111.

EG&G PRINCETON APPLIED RESEARCH

APPLICATION FOR ADMISSION

TO

The Electrochemical Society, Inc.

Return completed application to:

Secretary
The Electrochemical Society, Inc.
10 South Main Street, Pennington, New Jersey 08534
609-737-1902

For office use only

Date Rec'd. _____ $ _____

Notice of Ackn. _____

Checked: _____

Approved: _____

To the Board of Directors of The Electrochemical Society, Inc:

Please print complete name and address as it should appear on mailings.

Name: _____

Address: _____

_____

_____

_____

_____

Business Telephone: (include area code) _____

I hereby make application for admission to The Electrochemical Society, Inc., as a _____ member, and enclose the amount of $_____ covering the first year's dues. (Please see reverse side for proper class of membership and dues applying thereto, noting the options with regard to the date of election and active life membership and the credit available for nonmember meeting registration.)

1. Date of Birth: _____ (month) _____ (day) _____ (year)

2. Please check LOCAL SECTION with which you wish to affiliate:

— Boston (05)	— European (27)	— Natl. Capital Area (45)	— Pacific Northwest (65)	— San Francisco (85)
— Chicago (10)	— Indianapolis (30)	— North Texas (55)	— Philadelphia (70)	— So. Calif.-Nevada (90)
— Cleveland (15)	— Metropolitan N.Y. (35)	— Ontario Quebec (60)	— Pittsburgh (75)	— Twin Cities (96)
— Columbus (20)	— Midland (Mich.) (40)	— Oregon (62)	— Rocky Mountain (80)	— None (99)
— Detroit (25)				

3. Please indicate your DIVISIONAL and GROUP interests, noting your primary interest(s) with the number 1 and secondary interest(s) with the number 2.

— Battery (AO)
— Corrosion (BO)
— Dielectrics and Insulation (CO)
— Electrodeposition (DO)
— Electronics (EO)
check specific interest(s) below
☐ General Materials and Processes (E1)
☐ Luminescence (E2)
☐ Semiconductors (E3)
— Electrothermics and Metallurgy (HO)
— Energy Technology Group (GO)
— Industrial Electrolytic (IO)
— Organic and Biological Electrochemistry (FO)
— Physical Electrochemistry (JO)

4. Education:

Institution	Dates Attended	Major Subject	Degree Earned

5. Work Experience:

Name of Employer (current, followed by previous)	Dates	Position

6. The Society's Constitution provides that two Active Members of the Society (who can substantiate the above record) must recommend you for admission to membership. It will facilitate the handling of your application if you are able to have your references sign this application form; if this is not convenient, please list their names and addresses. On a student application, only a single faculty member recommendation with signature (including title and and institution) is required.

Name (please print)	Signature	Address
Name (please print)	Signature	Address

The undersigned certifies that the above statements are correct and agrees, if elected to the Society, to be governed by its Constitution and Bylaws and to promote the objects of the Society as stated in its Constitution.

Date _____ 19 __

_____
(Signature)

Rev. 5/80

EXTRACTS FROM THE CONSTITUTION AND BYLAWS

CONSTITUTION—Article II

Membership

Section 1. The individual membership shall consist of Active, Honorary and Emeritus Members. The Board of Directors may from time to time authorize other classifications of membership as defined in the Bylaws of the Society.

(Active Member—Annual Dues $40.00)

Active Member

Section 2. An Active Member shall be interested in electrochemistry or allied subjects and possess a Bachelor's degree, or its equivalent, in engineering or natural science. In lieu of a Bachelor's degree, or its equivalent, any combination of years of undergraduate study and years of relevant work experience in electrochemistry or allied subjects adding to at least seven years shall be required. Election to Active Membership shall require the recommendation of two Active Members in good standing.

BYLAWS—Article II

Non-Voting Membership
(Student Member—Annual Dues $4.00)

Student Member

Section 1. Student Member. A Student Member shall be a full-time undergraduate or graduate student registered for a degree in natural science or engineering. The applicant for Student Membership shall be recommended by a member of the faculty of the school. Upon graduation with a Bachelor's degree or equivalent in natural science or engineering, the Student Member may apply for Active Membership. The application shall be approved by two Active Members of the Society in good standing. If the Student Member enters graduate school as a full-time student, the person may choose to apply for Active Membership or remain a Student Member.

BYLAWS—Article XXI

Dues and Fees

Dues

Section 1. The annual dues for Active Members shall be forty dollars. The annual dues for Student Members shall be four dollars. Each member shall receive the JOURNAL OF THE ELECTROCHEMICAL SOCIETY.

Date of Election

Section 2. When individuals are elected to membership, they must elect to initiate their membership as of January 1 or July 1 of the year of election; or, if elected during the last quarter, January 1 of the year following election. In the case of a July 1 election for starting membership, dues will be prorated.

Active Life Membership

Section 3. Any Active Member who shall pay in one lump sum the amount equivalent to two-thirds of the remaining dues to age sixty-five at the time of payment, but not less than an amount of 5 years of full dues, shall be exempt from payment of any further dues and shall be considered an Active Member during the remainder of his or her life.

Nonmember Meeting Registration Credit

BOARD OF DIRECTORS ACTION OF OCTOBER 9, 1960

If application for new membership is received within four months of the payment of nonmember registration at a Society Meeting by the applicant, the difference between the nonmember and member registration fees shall be credited toward the first year's dues.

CONSTITUTION—Article III

Admission and Dismissal of Members

Section 1. Application for individual membership shall be in writing on a form adopted by the Board of Directors.

Section 2. The Admissions Committee shall be a rotating committee consisting of three members. One member shall be appointed each year by the President with the approval of the Board of Directors for a term of three years to replace the outgoing member. This Committee shall receive from the Secretary all properly executed and properly recommended applications for admission which he has received from persons desirous of becoming members of the Society. It shall be the duty of this Committee, after examining the credentials of applicants, to make appropriate recommendation to the Board as to approval or rejection of the applications. Unanimous approval of an applicant by this Committee shall be required before the candidate's name may be submitted to the Board of Directors for election. The election to membership shall be by a mail vote of the Board of Directors. The candidate shall be considered elected two weeks after the date the proposed membership list is mailed to the Board if no negative votes have been received by the Secretary. If a candidate receives one negative vote, his application shall then be considered and voted upon at the next meeting of the Board of Directors. Two negative votes cast at this meeting shall exclude a candidate. The Board of Directors may refuse to elect a candidate who, in its opinion, is not qualified for membership. The names of those elected shall be announced to the Society. Duly elected candidates shall have all the rights and privileges of membership as soon as their entrance fee, if any, and dues for the current year have been paid.

Section 3. A member desiring to resign shall send a written resignation to the Office of the Society.

Section 4. Upon the written request of ten or more Active Members that, for cause stated therein, a member be dismissed, the Board of Directors shall consider the matter and, if there appears to be sufficient reason, shall advise the accused of the charges against him. He shall then have the right to present a written defense, and to appear in person before a meeting of the Board of Directors, of which meeting he shall receive notice at least twenty days in advance. Not less than two months after such meeting the Board of Directors shall finally consider the case and, if in the opinion of the majority of the Board of Directors a satisfactory defense has not been made and the accused member has not in the meantime tendered his resignation he shall be dismissed from the Society.

Section 7. The entrance fee, if any, annual dues and any other payments to be made by the members of the Society shall be paid in accordance with regulations set forth in the Bylaws.

Section 8. Any member delinquent in dues after April 1 shall not receive the Society's publications and will not be allowed to vote in any Society election until such dues are paid. All members in arrears for one year after April 1 shall lose their membership status and can be reinstated only by action of the Board of Directors.

The Electrochemical Society, Inc.
10 South Main Street, Pennington, New Jersey 08534 • Telephone: 609-737-1902

Instructions to Authors

The **JOURNAL OF THE ELECTROCHEMICAL SOCIETY** is the official monthly journal of the Society. It contains three sections: Electrochemical Science and Technology, Solid-State Science and Technology, and Reviews and News. Technical Papers, Technical Notes, and Accelerated Brief Communications are published in the first two sections and Review Papers in the third. All manuscripts submitted are considered for publication, with the understanding that they have not been submitted, accepted for publication, or published elsewhere. A wide range of subject matter is acceptable. Manuscripts can be handled promptly and efficiently if these instructions are followed.

TYPES OF PAPERS

Technical Papers describe fundamental or applied studies in depth. They contain new data and/or new interpretations of existing data. Abstracts summarizing the results are required.

Technical Notes report briefly on limited research or development that is not being pursued further. No abstracts are required.

Accelerated Brief Communications present, in camera-ready format of limited length, scientific or technological information warranting rapid dissemination. No abstracts are required.

Review Papers furnish critical analyses of topical subjects. Abstracts are required.

SUBMISSION

Submit three complete, clear copies of each manuscript and the originals of all figures and illustrations to:

Editorial Office
The Electrochemical Society, Inc.
10 South Main Street
Pennington, New Jersey 08534

A letter accompanying the manuscript should give (a) the name and mailing address of the author to whom correspondence should be sent, (b) reference to any presentation of the work at a meeting of The Electrochemical Society, (c) the Division or Group of the Society or the Divisional or Group Editor (both are listed in the front of each issue of the Journal) whose interests are most closely related to the work being discussed, (d) the section of the Journal in which the work should appear, and (e) the names and addresses of people able to act as reviewers.

EDITORIAL PRACTICES

Following receipt by the Editorial Office, each manuscript is sent to a Divisional or Group Editor with knowledge of the subject matter. This editor arranges for review of the manuscript and communicates with the author(s) regarding revisions. Final acceptance or rejection of a manuscript is determined by the Editor.

Accelerated Brief Communications are handled as rapidly as possible, ordinarily with a response to the author(s) from the Divisional Editor, the Group Editor, or the Editor within three weeks of their arrival at Pennington. Response to the authors of other manuscripts usually takes place within six weeks. Following acceptance, authors are notified of the Journal issue in which publication is scheduled; about one month before publication, page proofs and an order blank for reprints are provided. Proofs must be promptly corrected and returned. Extensive alterations by the author may delay publication; their cost will be billed to the author(s).

PUBLICATION CHARGE

To help meet publication costs, a payment of $65.00 per printed page is requested for the publication of technical material. If at least one author is a Society member or an employee of a Patron or Sustaining member, a 10% reduction is allowed. Acceptance of manuscripts for publication is, however, based on merit and is in no way dependent on such payment, which may be waived in individual cases upon request.

PRESENTATION

Organization and clarity are essential elements of successful written communication. Identify the subject matter in the title, using words useful in indexing. State the purpose of the work early in the text. Avoid introductory and explanatory material that is overly familiar to those in the field. Present the work and the arguments in an order that leads naturally to clearly specified conclusions. Provide enough information for the work to be reproduced and the logic behind it to be understood. Identify and justify any assumptions that are made; avoid tacit assumptions. Omit details that are generally known or that can be covered by reference to other publications. Give the magnitude and define the significance of experimental errors. Use headings and subheadings as appropriate. Avoid proprietary and trade names, but capitalize them where their use is necessary. Define unusual technical terms and abbreviations. Where symbols are used extensively, list them with their definitions at the end of the paper. Avoid repetition in the text and duplication of material in figures and tables. Be brief but clear.

Edit and proofread the manuscript carefully; these are not the responsibilities of the editors or reviewers.

KEY-DESCRIPTORS

To aid in indexing, authors must supply standard key-descriptors, preferably four of them, from a list with instructions published annually in the December issue of the Journal and available from the Editorial Office. These key-descriptors must appear at the bottom of the first page of the manuscript.

MANUSCRIPT PREPARATION

Accelerated Brief Communications must be typewritten or printed on standard forms obtained, with detailed instructions for their use, from the Pennington Editorial Office.

All other manuscripts must be typewritten or printed, double-spaced throughout, on one side only of white 21.6 x 27.0 cm paper, with 2.5-3.8 cm margins. Do not use single spacing anywhere, in title, abstract, text, references, tables, or figure captions.

For general matters of style and format, see papers in recent issues of the **Journal** and consult a style manual such as that of the American Chemical Society or that of the American Institute of Physics. These also provide lists of common abbreviations and units. The following specific items should be noted:

(a) Système Internationale (SI) units are to be used; a description may be found in NBS Special Publication 330 or ASTM Metric Practice Guide E-380-72.

(b) The signs of cell and electrode potentials are to follow the IUPAC conventions of 1953.

(c) **Mathematical equations** should be written on a single line, if possible, using parentheses, brackets, the solidus, negative exponents, etc.

(d) **References** are to be listed separately at the end of the paper in the order they are cited in the text, being sure that each listed reference is cited. Authors' initials must be given, and Chemical Abstracts abbreviations must be used. Citations of other than the generally available literature should be avoided if possible.

(e) **Tables** are to be presented on individual sheets, with both captions and body double-spaced.

(f) **Figure captions** and numbers are to be included on a separate sheet and must not appear in the body of any figure or illustration.

(g) **Drawings** and **graphs** will ordinarily be reduced to column width (8.3 cm) and after such reduction should have lettering at least 0.15 cm high. Lettering must be of letter-guide quality. Originals in India ink on tracing cloth or paper are preferred, but India ink on coordinate paper with blue ruling is acceptable. When several curves are shown, each may be lettered and identified in the caption. The Editorial Office will not make corrections or additions to figures.

(h) **Photographs** should be used sparingly. The originals supplied must be glossy prints and should be protected against bending. Micrographs must have a labeled unit length within the body of the picture; reduction for printing makes magnifications meaningless.

Revised December 1, 1980

Printed in the United States of America

THE ELECTROCHEMICAL SOCIETY, INC.

The Electrochemical Society is an international organization of individuals and companies concerned with or interested in materials sciences.

OBJECTIVES

1. The advancement of the theory and practice of electrochemistry, electrometallurgy, electrothermics, electronics, solid state, and allied subjects.
2. To encourage research and the reporting of such research for the dissemination of knowledge in the field of electrochemistry and solid state.
3. To insure the availability of adequate training in the field of electrochemistry for chemists, engineers, metallurgists, physicists, and solid-state investigators.

BENEFITS OF MEMBERSHIP

1. Assurance of keeping abreast of the latest scientific developments in your particular fields of interest.
2. Enjoyment of personal association with fellow scientists and engineers in the professions.
3. Opportunity to contribute to the advancement of the science and application of electrochemistry and solid state in your areas of interest.
4. Stimulation of interdisciplinary exchanges.

DIVISIONS

The activities of the Society are carried on by its nine Divisions and Group as follows:

Battery
Corrosion
Dielectrics and Insulation
Electrodeposition
Electronics
General Materials and Processes
Luminescence
Semiconductors
Electrothermics and Metallurgy
Energy Technology Group
Industrial Electrolytic
Organic and Biological Electrochemistry
Physical Electrochemistry

SECTIONS

Local Sections of the Society have been organized in the following cities and regions:

Boston
Chicago
Cleveland
Columbus
Detroit
European
Indianapolis
Metropolitan New York
Midland (Michigan)
National Capital Area
Niagara Falls
North Texas
Ontario-Quebec
Oregon
Pacific Northwest
Philadelphia
Pittsburgh
Rocky Mountain
San Francisco
Southern California-Nevada
South Texas
Twin Cities

Call for Papers
160th Meeting, Denver, Colorado, October 11-16, 1981

Divisions which have scheduled sessions are listed on the overleaf, along with symposium topics.

1. Symposium Papers.

Authors desiring to contribute papers to a symposium listed on the overleaf should check first with the symposium chairman to ascertain appropriateness of the topic.

2. General Session Papers.

Each of the Society Divisions or Group which will meet in Denver, Colorado, can plan a general session. If your paper does not fit readily into a planned symposium, you should specify "General Session."

3. To Submit a Meeting Paper.

Each author who submits a paper for presentation at a Society Meeting must do three things:

A—Submit one original 75-word abstract of the paper on the attached form or a facsimile thereof. **Deadline for receipt of 75-word abstract is May 1, 1981.**

B—Submit original and one copy of an Extended Abstract of the paper. **Deadline for receipt of Extended Abstract is June 1, 1981.** See (6) below for details.

C—Determine whether the meeting paper is to be submitted to the Society Journal for publication. See (7) below for details.

Send all material to The Electrochemical Society, Inc., 10 South Main Street, Pennington, NJ 08534.

Unless the 75-word and required Extended Abstracts are received at Society Headquarters by stated deadlines, the papers will not be considered for inclusion in the program.

4. To Submit a Recent News Paper.

Recent News Papers and Extended Recent News Papers are invited for this meeting. Each author must submit one of the following items to the Session Chairman:

A—Triplicate copies of a 75-word abstract of a Recent News Paper, for a 10-minute presentation. Deadline for receipt is August 25, 1981.

B—Triplicate copies of a 75-word abstract and, also, a 200-300 word abstract of an Extended Recent News Paper, for a 20-minute presentation. Deadline for receipt is August 15, 1981.

Send all material to the appropriate Session Chairman listed, for Recent News Papers only.

5. Meeting Paper Acceptance.

Notification of acceptance for meeting presentation, along with scheduled time, will be mailed to authors with general instructions no earlier than two months before the meeting. Those authors who require more prompt notification are requested to submit with their abstracts a self-addressed postal card with full author-title listing on the reverse.

6. Extended Abstract Volume Publication.

All scheduled papers will be published in the EXTENDED ABSTRACTS volume of the meeting. The volume is published by photo-offset directly from typewritten copy submitted by the author. Therefore, special care should be given to the following instructions to insure legibility.

A—Abstracts are to be from 500 to 1000 words in length and should not exceed two pages, single spaced. The abstract should contain to whatever extent practical all significant experimental data to be presented during oral delivery.

B—Abstracts should be typed single spaced on the typing guide forms which are sent to each author after the submission of a short abstract. If it is necessary to use white bond paper, it should be 8½ x 11 inches with 1¼ inch margins on all sides. Submit all copy in black ink. Do not use handwritten corrections.

C—Title of paper should be in capital letters. Author(s) name and affiliation and address should be typed immediately below in capital and lower case letters. Please include zip code in address. It is not necessary to designate paper as "Extended Abstract" or to quote the divisional symposium involved.

D—If figures, tables, or drawings are used, they should follow the body of the text and should not exceed one page. Submit only the important illustrations and avoid use of halftones. Lettering and symbols should be no smaller than ⅛ inch in size. Figure captions should be typed beneath the figure and be no wider than the figure. Table titles should be typed above and the same width as the table.

E—Mail original and one copy of the abstract to: The Electrochemical Society, Inc., 10 South Main Street, Pennington, NJ 08534, unfolded.

Abstracts exceeding the stipulated length will be returned to author for condensation and retyping.

7. Manuscript Publication in Society Journal.

All meeting papers upon presentation become the property of The Electrochemical Society, Inc. However, presentation incurs no obligation to publish. If publication in **Journal** is desired, papers should be submitted as promptly as possible in full manuscript form in order to be considered. If publication elsewhere after presentation is desired, written permission from Society Headquarters is required.

Denver, Colorado, Meeting Symposia Plans—Fall 1981
October 11-16, 1981

a.) For receipt no later than May 1, 1981, submit a 75-word abstract of the paper to be delivered on the attached form.
b.) For receipt no later than June 1, 1981, submit two copies of an extended abstract, 500-1000 words.
c.) Send all abstracts to The Electrochemical Society, Inc., 10 South Main Street, Pennington, NJ 08534, with the exception of Recent News Papers. For Recent News Papers see preceding page.

BATTERY

Accelerated Testing of Batteries

This symposium will focus on recent advances in methodology of accelerated testing for prediction of life and performance of primary and secondary batteries. Special emphasis will be given to testing of secondary batteries applicable to electric vehicles, utility load-leveling, and solar photovoltaic energy storage. Papers are solicited in areas which include: 1. methodology of accelerated testing; 2. practical experience with accelerated testing and data correlation with real-time results; 3. theoretical considerations and approaches to accelerated testing; 4. accelerated testing of battery components and its relation to battery system failures; and 5. diagnostic testing of battery failures.

The publication of a proceedings volume is being considered. Suggestions and inquiries should be sent to the Symposium Chairman: N. P. Yao, Argonne National Laboratory, Chemical Engineering Div., 9700 South Cass Ave., Argonne, IL 60439.

Environmental Safety and Recycling of Batteries

This symposium will solicit basic and applied papers dealing with the environmental safety and recycling of both primary and secondary batteries. Electrochemical systems of special interest will include lithium batteries using inorganic electrolytes, organic electrolytes, high temperature electrolytes, solid electrolytes, or novel types. Papers dealing with zinc chlorine batteries, mercury batteries, nickel-cadmium batteries, silver-zinc batteries, and lead-acid batteries will also be of interest. Suitable topics would include: 1. innovative methods of disposal; 2. toxicity and reactivity of by-products (manufacturing and disposal); 3. neutralization of waste products; 4. the economics of recovery/recycling of system materials; and 5. the stability/safety of batteries during storage, transportation, handling, and disposal.

Suggestions and inquiries should be sent to the Symposium Chairman: C. E. Mueller, Naval Surface Weapons Center, Electrochemistry Branch (R33), Silver Spring, MD 20910.

The Nickel Electrode

This symposium will include papers dealing with all fundamental and applied aspects of the nickel electrode. It is intended that this symposium will provide a forum not only for presentation of recent work in this field, but also for reviewing and putting into perspective results of nickel electrode work that has taken place over many years. New insights into fundamental problems will be of particular interest. Suitable topics will include: 1. fundamental electrochemistry and solid-state processes; 2. basic investigations of reaction mechanisms and electrode behavior; 3. effects of additives, such as Co and Cd; 4. colloidal and electrophoretic effects; 5. electrolyte pumping, concentration changes, and their effects; 6. development of microporosity; 7. Ni electrode characteristics as made by all methods; 8. Ni sinter characteristics and effects; 9. impregnation of active materials by various means, stressing physical and chemical effects; 10. corrosion during manufacture and operation; 11. variables affecting oxygen and hydrogen overpotential; 12. effects on Ni electrode of different negative electrodes (Cd, Zn, Ag, etc.); 13. wearout and cycling changes, their causes and effects; 14. physical and electrical changes from electrode expansion; and 15. computer modeling of electrode behavior.

Suggestions and inquiries should be sent to the Symposium Chairman: S. Gross, Boeing Aerospace Co., P.O. Box 3999, MS 8C-62, Seattle, WA 98124.

Thermal Analysis in Battery Design

This symposium will focus on the theoretical and practical considerations of thermal analysis in batteries and battery design. Papers are solicited which deal with thermal analysis in the development of aqueous (basic and acidic electrolytes) and nonaqueous (molten salts, solid, and organic electrolytes) battery systems. Topics of interest as they are related to batteries are: 1. theoretical and practical aspects of thermal modeling of battery systems; 2. effects of thermal phenomena on battery performance including physical and chemical properties of the electrodes, electrolyte, and components; 3. heat transfer studies; 4. model development and mathematical treatment including numerical solutions for engineering evaluation; and 5. thermal management in batteries including methods of heat removal during charge and/or discharge.

Suggestions and inquiries should be sent to the Symposium Chairman: R. A. Sutula, NSWC (WO), Metallic Materials Branch, Bldg. 24, White Oak, Silver Spring, MD 20910.

General Session

Papers are solicited which deal with practical and theoretical considerations on aqueous batteries of commercial interest (electric vehicle and load leveling), more specifically, lead-acid, nickel-zinc, nickel-iron, zinc-chlorine at a state of advanced development. Data on large cells and full batteries are desirable and reasons for improved performance should be presented.

Suggestions and inquiries should be sent to the Session Chairman: A. Himy, Dept. of the Navy, Code 5433, Naval Sea Systems Command, Washington, DC 20362.

BATTERY/CORROSION/ ELECTROTHERMICS AND METALLURGY/ ENERGY TECHNOLOGY

Corrosion in Batteries and Fuel Cells

This symposium will emphasize corrosion and materials degradation associated with all types of batteries and fuel cells. Included will be basic investigation of processes, evaluation of mechanisms, methodology of testing, and new materials and processes. Papers on high temperature batteries and fuel cells are especially appropriate. Papers are also solicited on interaction of battery and fuel cell components with internal and external environments of corrosive chemicals, industrial pollutants, and marine atmosphere. Of special interest are papers defining new and novel methods to minimize material degradation and corrosion reactions. Appropriate papers should focus on failure modes and reaction mechanisms which cause premature failure via reactions other than power-producing electrochemical reactions. Suitable topics would include: 1. corrosion problems and resistant cell and case materials for high temperature cells; 2. mechanisms and preventative methods to reduce corrosion of electrode and cell-case seals; 3. accelerated tests to evaluate cell corrosion; 4. prevention of parasitic corrosion reactions which degrade active electrode materials; and 5. effect of additives and inhibitor mechanisms for corrosion prevention.

Suggestions and inquiries should be sent to the Symposium Co-Chairmen: A. Himy, Dept. of the Navy, Code 5433, Naval Sea Systems Command, Washington, DC 20362; or C. J. Johnson, Boeing Aerospace Co., P.O. Box 3999, MS 8C-62, Seattle, WA 98124.

BATTERY/ENERGY TECHNOLOGY

Acid Fuel Cell Technology: An Update

The major near-term fuel cell effort in the U.S. is based on acid fuel cells. This symposium will feature recent developments in phosphoric acid and related fuel cell technology. Papers covering the following topics are solicited: 1. fuel cell electrode design, development, and performance; 2. corrosion studies on elements of the phosphoric acid fuel cell; 3. fuel cell stack design and scale-up; 4. performance in atmospheric and pressurized fuel cells; 5. new acid electrolytes; 6. phosphoric acid fuel cell systems; and 7. economic assessments and applications for phosphoric acid fuel cells.

Suggestions for papers outside the immediate scope of the above topics are welcome. *Suggestions and inquiries should* be sent to the Symposium Co-Chairmen: J. Huff, U.S. Army MERADCOM, Electrochemical Division (DRDME-EC), Fort Belvoir, VA 22060; or B. S. Baker, Energy Research Corp., 3 Great Pasture Rd., Danbury, CT 06810.

Metal-Air Batteries

This symposium will deal with all aspects of the technology of metal-air batteries of both primary and secondary type, together with that of primary and secondary type, together with that of primary refuelable systems (metal fuel cells).

Papers are solicited in the following areas: 1. primary metal-air cell design and construction; 2. primary cell air electrode design; 3. secondary cell air electrodes; 4. secondary cell systems design; 5. problems specific to zinc-based systems; 6. iron-air systems; 7. metal fuel cell systems and applications.

Suggestions and inquiries should be sent to the Symposium Co-Chairmen; J. E. Oxley, Gould Laboratories, 40 Gould Center, Rolling Meadows, IL 60008, or J. L. Cooper, L-51, Bldg. 2302, Lawrence Livermore Laboratory, P.O. Box 808, Livermore, CA 94550.

CORROSION

Impedance and Pulse Methods for Investigation of Corrosion Processes

Papers are invited which describe recent advances in investigation of corrosion processes. This might include the application of new electronic and computer technology and instrumentation, as well as their use in investigation of steady and transient corrosion reactions. The following subjects are of particular interest: 1. impedance and pulse measurements in corrosion; 2. instrumentation for Fourier transform and correlation measurements; 3. transient and oscillatory corrosion processes; 4. initiation of localized corrosion; and 5. new techniques for corrosion rate determinations.

Suggestions and inquiries should be sent to the Symposium Co-Chairmen: W. H. Smyrl, Sandia National Laboratories, Div. 5841, Albuquerque, NM 87185; or D. D. MacDonald, Dept. of Metallurgical Engineering, Ohio State University, Columbus, OH 43210.

Corrosion in Metal Matrix Composites

Papers are being solicited for a symposium dealing with all aspects of corrosion in metal matrix composites (MMC). Possible subjects of interest are: 1. the mechanisms of corrosion, in metal matrix composites; 2. the effect of corrosion on the mechanical properties of metal matrix composites; 3. corrosion kinetics; 4. electrochemical techniques, including cell design, etc.; 5. the formation of passive surfaces to inhibit corrosion; 6. galvanic effects due to MMC-metal couples; 7. corrosion in various environments; and 8. the effect of MMC processing on corrosion rates. Areas of interest should include both theoretical, as well as engineering or service aspects of the subject.

Suggestions and inquiries should be sent to the Symposium Chairman: S. G. Fishman, Naval Surface Weapons Center, Dept. of Research and Technology, White Oak, MD 20910.

H. H. Uhlig, Seventy-Fifth Birthday Symposium

Papers on all aspects of corrosion, especially passivity, localized corrosion, and

corrosion fatigue, are invited for this symposium honoring Professor Uhlig.

A proceedings volume is planned. Short and extended abstracts, as well as the completed manuscripts, must be submitted by May 1, 1981. The book will be distributed at the symposium in Denver.

Suggestions and inquiries should be sent to the Session Co-Chairmen: F. B. Mansfeld, Rockwell International Science Center, P.O. Box 1085, Thousand Oaks, CA 91360; or R. P. Frankenthal, Bell Laboratories, Rm. 1D-352, Murray Hill, NJ 07974.

General Session

Papers on all aspects of low and high temperature corrosion and associated phenomena will be considered. Experimental techniques for the study of corrosion processes and corrosion products are also of interest.

Suggestions and inquiries should be sent to the Session Chairman: R. P. Frankenthal, Bell Laboratories, Rm. 1D-352, Murray Hill, NJ 07974.

CORROSION/ENERGY TECHNOLOGY

Corrosion in Solar Energy Systems

This symposium will discuss material degradation problems related to solar energy systems. Solar energy includes energy production by solar thermal, photovoltaics, biomass, and wind and ocean conversion systems. Containment material corrosion and fluid degradation of solar thermal conversion systems which employ high temperature gas, liquid metal, molten salts, pressurized water, oil, silicones, water/glycol, or air as heat transfer fluid will be examined. The reliability of all components of reflector surface will be discussed. The durability of photovoltaic systems with respect to encapsulation, metallization, thin film reliability, and stability of interconnections will be explored. Material problems associated with all biomass conversion processes will be discussed. Material and reliability concerns of the various components of wind turbines will be addressed, and corrosion problems associated with ocean system development, in particular ocean thermal energy conversion (OTEC) devices will be examined. A number of invited papers will be presented, and other papers dealing with these energy technologies are solicited. The publication of a proceedings volume is being considered.

Suggestions and inquiries should be sent to the Symposium Co-Chairmen: S. L. Pohlman, Solar Energy Research Institute, 1617 Cole Blvd., Golden, CO 80401; or F. B. Mansfeld, Rockwell International Science Center, P.O. Box 1085, Thousand Oaks, CA 91360.

DIELECTRICS AND INSULATION/ ELECTRONICS

Cleaning Processes and Contamination Control in the Semiconductor Industry

This symposium will focus on advanced cleaning processes and contamination control operations, which are significant for obtaining high semiconductor yields and reliable electronic products.

Papers are solicited on cleaning and contamination control methods including studies on electronic devices, analytical methods and instrumentation for the detection of contamination, and equipment and installations for producing an electronic grade environment.

A proceedings volume is being considered. Papers for this volume must be provided, in camera-ready copy, at the time of presentation.

Suggestions and inquiries should be sent to the Symposium Co-Chairmen: K. D. Beyer, IBM Corp., Data Systems Div., Zip 53A, Hopewell Junction, NY 12533; or F. Schwettman, Hewlett-Packard Laboratories, 3500 Deer Creek Rd., Palo Alto, CA 94304.

Organic Insulators

This symposium will be held to discuss several aspects relevant to the use of organic materials as insulators in microelectronic devices. The purpose of the symposium is to promote communication between the materials specialists and the device application technologists. Of particular importance are the structural features of organic insulators which govern their functional and reliability properties in device structures. Special attention will be directed toward characterization techniques. Suggested topics include: 1. cleaning processes; 2. adhesion; 3. interfacial studies; 4. high temperature polymers; 5. electrical, mechanical, and environmental considerations; 6. surface and "bulk" characterization of thin films; and 7. processing considerations and limitations. Also of interest are application-oriented papers which address mechanical stress generation, electrical breakdown characteristics, failure analysis, process optimization, role of impurities, among others. A number of invited papers will be presented and contributed papers are solicited.

Suggestions and inquiries should be sent to the Symposium Chairman: H. R. Anderson, Jr., IBM Corp., Data Systems Div., Zip 40E, Hopewell Junction, NY 12533.

Third Symposium on Plasma Processing

Papers are solicited on all aspects of the science and technology of plasma processes. Of particular interest, though not exclusively, is the application of plasma techniques to semiconductors materials including semiconductors, metals, organic and inorganic dielectrics, as well as photosensitive materials. Some suggested topics are: 1. Plasma Science—identification and concentration of chemically active species in the plasma, energy distribution of ions, electrons, and neutrals in and near the plasma, mass and optical spectroscopy of plasma, other plasma diagnostics techniques; 2. Plasma Technology—plasma etch processes, plasma initiated deposition or reaction processes, plasma enhanced CVD deposition processes, topology and its control in plasma etching and deposition; 3. Plasma Reactor Design—design considerations, process end-point detection, novel reactor designs; and 4. Device Results—dimensional control of plasma processed components, influence of plasma operating parameters on device performance including radiation damage, and novel use of plasma etching and deposition in device structures.

Because of the extensive interest in plasma technology, a proceedings volume is being considered. In order for the volume to be available for the conference, typed camera-ready copies of the presented papers, including appropriate key words for the subject index, should be submitted by August 15, 1981.

Suggestions and inquiries should be sent to the Symposium Co-Chairmen: (America) J. L. Mauer, IBM Corp., Zip 48A, Route 52, Hopewell Junction, NY 12533 or R. G. Frieser, IBM Corp., Zip 41A, Route 52, Hopewell Junction, NY 12533; (Europe) J. Dieleman, Philips Research Laboratories, 5600 MD, Eindhoven, The Netherlands; or (Japan and Far East) H. Abe, Mitsubishi Electric Corp., LSI Development Laboratory, 4-1 Mizuhara, Itami, Hyogo, Japan.

ELECTRODEPOSITION

Engineering Topics in Electrodeposition

This symposium will address the following topics of current interest in the field of electrodeposition: New Materials and Processes for Electronics and Other Industrial Applications. Subtopics will include: 1. precious metals, alloys, and substitutes; 2. nonprecious metals and alloys; and 3. electroless processes. New trends in materials and processes that are driven by the need for cost reduction and tighter performance requirements will be included. The impact of environmental restrictions relative to new materials and processes are of special interest.

Suggestions and inquiries should be sent to the Symposium Chairman: R. Sard, Oxy Metal Industries, Warren, MI 48089.

General Session

Original papers dealing with theoretical and applied aspects of electrodeposition are invited for this session. Experimental techniques for the study of electrodeposition processes and the resulting deposits are also of interest.

Suggestions and inquiries should be sent to the Session Chairman: T. Franklin, Dept. of Chemistry, Baylor University, Waco, TX 76706.

ELECTRONICS

Semiconductors

Ion Implantation in Compound Semiconductors

This symposium will focus on recent advances in ion implantation and associated processing of compound semiconductors. Papers are invited in the areas of encapsulation and annealing, advanced processing techniques, and materials preparation, growth, and characterization for use with ion implantation. Contributions describing implantation and materials work utilizing characterization tools such as DLTS, SIMS, TEM, electrical measurements, and other techniques are sought. Studies of defects, layer and contact formation, and impurity redistribution, as well as applications to integrated circuit, microwave, optoelectronic CCD, and solar cell devices will be included.

Suggestions and inquiries should be sent to the Symposium Co-Chairmen: B. G. Streetman, Coordinated Science Laboratory, University of Illinois, Champaign, IL 61801; C. G. Kirkpatrick, Rockwell International, Electronics Research Center, Thousand Oaks, CA 91360.

Materials for Optical Recording

This symposium will be devoted to developments in materials and structures for optical data storage. The preparation and recording characteristics will be emphasized. Ablative, organic dye, magnetooptic, photographic, thermoplastic, erasable, and nonerasable materials are all considered to be appropriate for this symposium. Sensitivity, archival life, and storage density are parameters related to the recording materials which will be addressed. This symposium will include invited and contributed papers.

Suggestions and inquiries should be sent to the Symposium Co-Chairmen: A. Bell, RCA Laboratories, David Sarnoff Research Center, Princeton, NJ 08540; G. M. Blom, Philips Laboratories, 345 Scarborough Rd., Briarcliff Manor, NY 10510; or J. M. Eldridge, IBM Corp., Research Center, 5600 Cottle Rd., San Jose, CA 95193.

Surface and Thin Film Analysis of Semiconductor Materials

The symposium will deal with the application of modern methods for surface, thin film, and interface analysis to semiconductor material studies on the fields of basic research, technological development, materials processing, and failure investigations. Invited speakers will survey the more established techniques of Auger electron spectroscopy, x-ray photoelectron spectroscopy, secondary ion mass spectrometry, ion scattering spectroscopy, and Rutherford backscattering, together with an insight into depth profiling by sputter etching. Contributed papers are solicited for oral presentation. Although these will probably center around the above five techniques, applications utilizing other methods such as laser Raman spectroscopy, scanning acoustic microscopy, and sputter-induced photon spectroscopy are not excluded. However, all contributions should emphasize the application of existing techniques or novel developments in their application. Also, analyses involving new techniques would be particularly welcome.

The publication of a proceedings volume is being considered. Suggestions and inquiries should be sent to the Symposium Co-Chairmen: G. B. Larrabee, Texas Instruments, Inc., P.O. Box 225936, MS 147, Dallas, TX 75265; or A. E. Morgan, Signetics Corp., MS 065, 811 East Arques Ave., Sunnyvale, CA 94086.

ELECTRONICS/DIELECTRICS AND INSULATION

Dielectric Materials and Processing for Multilevel Metal Technology

This symposium will deal with all aspects of dielectric materials and processing for multilevel metal/insulator structures. Both organic and inorganic dielectric materials are of interest. Original work or substantial review papers are solicited on the following suggested topics: 1. properties of dielectric materials such as electrical characteristics, defect densities, and ability to planarize; 2. deposition processes such as evaporation, sputter deposition, plasma-enhanced CVD, spin, and spray coatings; 3. patterning techniques to include radiation and photosensitive dielectric materials; 4. etching processes such as solution, vapor phase, plasma, and ion-assisted techniques; 5. device fabrication and test results for multilevel structures; 6. reliability of multilevel metal/insulator structures; and 7. new circuit capabilities using multilevel metal/insulator technologies.

Suggestions and inquiries should be sent to the Symposium Co-Chairmen: L. Rothman, IBM Corp., Zip 48A, East Fishkill Facility, Hopewell Junction, NY 12533; or S. Wolf, Dept. of Electrical Engineering, California State University, Long Beach, CA 90840.

Silicon Dioxide and Other Insulators for VLSI

As device and circuit technologies move into the VLSI era, requiring lithographic dimensions of 2 μm or less, the demands placed on every aspect of semiconductor processing push hard on the existing capabilities for dimensional and properties control of the materials. Insulators pose perhaps the greatest problems since they are the thinnest films employed (<30 nm), and often require the highest processing temperatures, thereby influencing the ability to maintain desired junction concentration and junction depth. They are often the prime yield and reliability determining factors.

This symposium will focus on the special problems and requirements associated with insulators in VLSI applications. Specific areas will include: 1. methods of preparation (conventional thermal, high pressure, in situ plasma, CVD, etc.); 2. preoxidation cleaning of substrates and control of particulate size; 3. susceptibility to defect generation in the presence of process-related ionizing radiation (effects of E-beam lithography, E-beam metal evaporation, and ion etching, etc. on fixed positive charge, interface traps, and neutral trap densities); 4. barrier metallurgies compatible with annealing processes and nonconventional annealing approaches; 5. potential uses for high ϵ insulators (Si_3N_4, Ta_2O_5, etc.), and for organic insulators; 6. improved methods for characterizing thin insulator films (physical/chemical/electrical testing techniques); and 7. processes for optimizing topography (glass fusion tapering, contour etching, etc.).

Suggestions and inquiries should be sent to the Symposium Co-Chairmen: A. Reisman, IBM Corp., Thomas J. Watson Research Center, P.O. Box 218, Yorktown Heights, NY 10598; E. H. Nicollian, Bell Laboratories, Murray Hill, NJ 07974; or W. Kern, RCA Laboratories, David Sarnoff Research Center, Princeton, NJ 08540.

General Session

Papers which deal with all aspects of materials of interest for electronic devices including their preparation, characterization, interactions, and device applications and whose subject matter is not covered by the special symposia are invited to be submitted to this session. Also invited are papers on the basic chemistry and physics of materials processing, computer control of material processing, and computer modeling of the formation and of the characterization of materials and devices. Of particular interest are new materials and processes.

Suggestions and inquiries should be sent to the Session Co-Chairmen: D. W. Shaw, Texas Instruments Inc., P.O. Box 225936, MS 147, Dallas, TX 75265; R. E. Enstrom, RCA Laboratories, Princeton, NJ 08540; or G. C. Schwartz, IBM Corp., Zip 48A, East Fishkill Facility, Hopewell Junction, NY 12533.

Recent News Papers Session

Recent News Papers and Extended Recent News Papers consisting of topics covered by the symposia and sessions being sponsored or cosponsored by the above Divisions are invited for presentation.

Suggestions and inquiries should be sent to the Session Co-Chairmen: W. A. Pliskin, IBM Corp., Dept. 108, Zip 48A, Route 52, Hopewell Junction, NY 12533; or G. C. Schwartz, IBM Corp., Dept. 206, Zip 48A, Route 52, Hopewell Junction, NY 12533.

A special Call for Recent News Papers will appear in the June, July, and August 1981 issues of the JOURNAL.

ELECTROTHERMICS AND METALLURGY

Amorphous Materials, Processes, and Applications

This symposium solicits recent developments in metallic and nonmetallic amorphous materials in bulk, ribbon, powder, and thin film form: Transportation and Forming—Topics of special interest include chemical, metallurgical, and mechanical techniques for processing amorphous materials alone or in combination with other materials. This covers heat-treating and annealing, kinetics, recrystallization, environmental testing, and fabrication into commercially useful form, as well as significant new results of manufacturing the basic material. Structure and Properties—All areas of characterization and structure determination are encouraged, in particular those shedding new insight into transformation and forming and into application reliability. Applications—Topics of special interest include new applications or new information on the significance of transformation, forming, structure, and properties for commercial application. Application related to electrochemical behavior, corrosion, catalyses, and hydrogen storage are of particular interest.

Suggestions and inquiries should be sent to the Symposium Co-Chairmen: R. S. Carbonara, Battelle Columbus Laboratories, 505 King Ave., Columbus, OH 43201; J. P. Dismukes, Exxon Research and Engineering Co., P.O. Box 8, Linden, NJ 07036; or B. Liebert, Dept. of Mechanical Engineering, University of Hawaii, Honolulu, HI 96822.

High Temperature Materials Chemistry

This symposium addresses the chemical behavior of materials in systems related to high temperature technology. Pertinent topics include: thermodynamics and kinetics of high temperature reactions; chemical problems of materials used in high temperature energy conversion systems such as lamps, nuclear power systems, fossil fuel combustion including MHD, solar thermal receivers, etc.; and materials in high temperature metallurgical and chemical processes. Sessions on the following topics are contemplated: corrosion of refractories, vaporization of materials; coal ash fouling; vapor processes for silicon production; reactions of high temperature sulfur species, chemistry of and corrosion by high temperature water; chemical aspects of hot corrosion; and kinetics of gas-solid reactions, solid electrolytes for high temperatures.

Publication of a proceedings volume is being considered. Suggestions and inquiries should be sent to the Symposium Co-Chairmen: D. L. Hildenbrand, SRI International, 333 Ravenswood Ave., Menlo Park, CA 94025; or D. Cubicciotti, Electric Power Research Institute, P.O. Box 10412, Palo Alto, CA 94303.

ELECTROTHERMICS AND METALLURGY/ DIELECTRICS AND INSULATION/ ENERGY TECHNOLOGY

Silicon Purification

Successful development of inexpensive silicon solar cells depends critically on the availability of low cost, high purity silicon. This symposium addresses the issues, problems, and advances relating to silicon production/purification. Papers are solicited that are applicable to all aspects of solar silicon production/purification, whether they be from the solar silicon field specifically or from the closely related metallurgical silicon or semiconductor silicon fields. Invited and contributed overviews are planned.

Topics of particular emphasis include new processing methods, new or newly applied diagnostic tools, process-related effects on solar cell efficiencies, single and multi-component impurity effects, and schemes or methods that couple the purification/production process with the crystal growth step. The following purification techniques are suggested but not intended to limit the scope of the symposium: 1. metallurgical—use of high purity raw materials, use of unique raw materials in coreduction, slagging and crystallization from alloys; 2. chemical—acid leaching, gas blowing, electrochemical refining, and gettering; 3. physical—vaporization and/or segregation during crystal growth from molten silicon or its alloys. It is desired to have papers that discuss the mechanisms, advantages, and limitations of production/purification processes in addition to those giving only quantitative results.

The publication of a proceedings volume is planned. Papers for this volume must be provided, in camera-ready form, at the time of presentation.

Suggestions and inquiries should be sent to the Symposium Co-Chairmen: J. M. Olsen, Solar Energy Research Institute, 1536 Cole Blvd., Golden, CO 80401; or L. P. Hunt, Exxon Research and Engineering Co., P.O. Box 8, Linden, NJ 07036.

ENERGY TECHNOLOGY

Measurement Techniques for Photoelectrochemical Solar Cells

The symposium will concentrate on measurement techniques and procedures applied to efficiency, stability, and fundamental interface phenomena in photoelectrochemical cells and devices.

Papers are invited on: 1. electrochemical and optical techniques to explore the semiconductor-electrolyte interface, such as Mott-Schottky capacitance, photocapacitance, reflectance, and impedance measurements; 2. measurement techniques for probing interface kinetics, adsorption phenomena, fundamental semiconductor-electrolyte transport properties and surface state associated phenomena; 3. techniques for measuring semiconductor, electrolyte, and photoelectrochemical device stabilities and degradation mechanisms; 4. measurement techniques and issues for determining efficiencies for photoelectrochemical cells; and 5. procedures for standardization of tests and measurements in photoelectrochemistry.

Suggestions and inquiries should be sent to the Symposium Co-Chairmen: S. Deb, A. Nozik, or W. Wallace, Solar Energy Research Institute, 1617 Cole Blvd., Golden, CO 80401.

General Session

Papers are solicited in all areas of energy technology not covered by concurrent symposia. Of particular interest are electrochemical aspects of power sources and convertors, as well as of energy distribution, storage, and conservation. Power sources include fossil and biomass, nuclear, geo- and ocean-thermal, and solar. Contributions to specific applications, for instance power sources and fuels for individual transportation, or fuels for transmission in pipelines, are also solicited.

Suggestions and inquiries should be sent to the Session Co-Chairmen: J. McBreen, Brookhaven National Laboratories, Bldg. 815, Upton, NY 11973; or A. J. Nozik, Solar Energy Research Institute, Golden, CO 80401.

ENERGY TECHNOLOGY/ ALL DIVISIONS

Electrochemistry in Our Future: The Year 2000 Symposium

Electrochemistry and its technologies have acquired their present forms with two centuries of discoveries and developments. This symposium will focus on both applied and fundamental aspects of electrochemical technologies and sciences with the aim of identifying those technologies or areas of science that will make major contributions over the next two decades. A sound approach is required to judge if today's technologies or new developments in energy conversion and storage, industrial electrolytic processes, and biomedical applications can portend to become panaceas. Original papers that emphasize the interdisciplinary nature of electrochemistry, or venture to consider the potential of new and existing technologies in light of the changing economics, energy supply and materials demands; or consider radical, novel, and new technological developments will be included. A number of keynote lectures in electrochemical sciences and technologies will be presented. Contributed papers are solicited.

Suggestions and inquiries should be sent to the Symposium Co-Chairmen: A. R. Landgrebe, U.S. Department of Energy, 600 E St., NW, MS 404, Washington, DC 20585; E. J. Cairns, Energy and Environment Div., University of California, 90-3026, Lawrence Berkeley Laboratory, Berkeley, CA 94720; or F. M. McLarnon, Energy and Environment Div., University of California, 90-3026, Lawrence Berkeley Laboratory, Berkeley, CA 94720.

INDUSTRIAL ELECTROLYTIC

General Session

The session will include papers of general interest to the electrolytic industry. Papers are requested on theoretical and applied topics.

Suggestions and inquiries should be sent to the Session Chairman: L. Nanis, SRI International, Electrochemistry, Menlo Park, CA 94025.

INDUSTRIAL ELECTROLYTIC/ ELECTRODEPOSITION/ENERGY TECHNOLOGY/NEW TECHNOLOGY SUBCOMMITTEE

Chemical and Electrochemical Methods for Deposition of Semiconductors

The symposium will include all aspects of chemical and electrochemical deposition of elemental and compound semiconductor materials. Papers are invited which deal with both theoretical, experimental, and applied aspects. Deposits in thin film or bulk form will include single crystal, polycrystalline, or amorphous structures. Chem-

ical deposition techniques will include chemical vapor deposition, low pressure CVD, plasma methods, spray pyrolysis, molecular beam epitaxy, reactive sputtering, and liquid waste epitaxy. Electrochemical methods will include electrodeposition from molten salts, aqueous and nonaqueous electrolytes.

Authors are encouraged to relate theoretical and experimental observations to practical applications in materials preparation and device fabrication such as substrate influence on deposit morphology and control of deposit stoichiometry.

Suggestions and inquiries should be sent to the Symposium Co-Chairmen: A. Sanjurjo, SRI International, Materials Research Laboratory, Menlo Park, CA 94025; or D. Stevenson, Dept. of Materials Science, Stanford University, 554Q, Stanford, CA 94305.

PHYSICAL ELECTROCHEMISTRY

Photoelectrochemical Processes

The symposium will deal primarily with fundamental processes at the semiconductor-electrolyte interface. The objective will be to promote understanding of dominant mechanisms that lead to energy storing reactions at photoexcited semiconductor electrodes. Experimental and theoretical investigation of electron transfer and the associated chemical reactions will be emphasized. Surface treatments to modify those processes and techniques to measure interface state properties are also appropriate topics. Device-related work should focus on understanding interface properties as they influence device performance.

Suggestions and inquiries should be sent to the Symposium Chairman: R. H. Wilson, General Electric Corp., Research and Development, P.O. Box 8, Schenectady, NY 12301.

General Session

Papers concerning any aspect of physical electrochemistry not included in the topic areas of the symposia are welcome.

Suggestions and inquiries should be sent to the Session Chairman: E. J. Cairns, Energy and Environment Div., University of California, 90-3026, Lawrence Berkeley Laboratory, Berkeley, CA 94720.

PHYSICAL ELECTROCHEMISTRY/ BATTERY/CORROSION

New Techniques for the Study of Electrode Processes

The symposium will deal with advances in the techniques for studying reactions taking place at or near the electrode-solution interface and important in the overall mechanisms of electrode processes, including corrosion. Of concern will be techniques for the study of electrode surfaces, including various spectroscopic methods, ellipsometry, Raman, etc., employed under in situ conditions, and various techniques, such as Auger, ESCA, and other forms of electron spectroscopy, which require imposition of a high vacuum prior to making the measurement. The symposium will also explore methods which involve characterization of reactant intermediates by electrochemical methods, or a combination of electrochemical and other methods, including ESR or spectroscopic methods (spectroelectrochemistry) but where the interest is in intermediates or preceding or following chemical reactions, rather than characterization of the electrode surface. Techniques specific to the study of modified electrodes will be considered. Advances in electronics related to instrumentation and its implementation, and the theory thereof, will be a topic of interest.

Emphasis of talks to be presented during the symposium should be on techniques, with relevant chemistry presented primarily to illustrate technique applications. Practical aspects and problems should be stressed, and invited speakers should present sufficient introductory material to permit those not familiar with their approach to gain an appreciation of the particular method. Where appropriate, theoretical papers, dealing with elucidation of the technique would be welcomed.

Keynote lectures will be presented by invited speakers. Contributed papers are solicited in any of the relevant topical areas.

Suggestions and inquiries should be sent to the Symposium Co-Chairmen: B. D. Cahan, Dept. of Chemistry, Case Western Reserve University, Cleveland, OH 44106 or R. A. Osteryoung, Dept. of Chemistry, SUNY at Buffalo, Buffalo, NY 14214.

NEW TECHNOLOGY SUBCOMMITTEE/ BATTERY/DIELECTRICS AND INSULATION

Ion-Conducting Polymers

Papers are solicited on ionically conductive polymers with possible application as solid electrolytes for batteries and fuel cells. Ion conducting polymers include solvent-free polymer-salt complexes, gelled polymer electrolytes, and polymer membranes. Topics of interest include materials preparation, chemical and electrical properties, stability and interaction with other battery/fuel cell materials and applications.

Suggestions and inquiries should be sent to the Symposium Co-Chairmen: J. J. Auborn, Bell Laboratories, Murray Hill, NJ 07974; M. B. Armand, Laboratorie d'Energetique Electrochimique, ENSEE Grenoble, BP 44 Domaine Universitaire, 38401 St. Martin-d'Heres, France; or N. Margalit, INCO Research and Development Center, Inc., Sterling Forest, Suffern, NY 10901.

---

a.) For receipt no later than May 1, 1981, submit a 75-word abstract of the paper to be delivered on the attached form.
b.) For receipt no later than June 1, 1981, submit two copies of an extended abstract, 500-1000 words.
c.) Send all abstracts to The Electrochemical Society, Inc., 10 South Main Street, Pennington, NJ 08534, with the exception of Recent News Papers. For Recent News Papers see preceding pages.

Use overleaf in submitting your abstract for
The 1981 Fall Meeting
of
The Electrochemical Society, Inc.
to be held at the
Denver Hilton
Denver, Colorado
October 11-16, 1981

75-Word Abstract Form

(Deadline for receipt May 1, 1981)

DENVER, COLORADO, MEETING—OCTOBER 11-16, 1981

Submit to: The Electrochemical Society, Inc.
10 South Main Street, Pennington, N.J. 08534

Schedule for ..... of .....
Symposium ECS Division

Abstract No. .....
(do not write in this space)

(Title of paper) .....

.....

(Authors) (Underline name of author presenting paper) .....

.....

(Business Affiliation and Address) .....

.....

.....
(ZIP Code) (Tel. No.)

(Type abstract in this area—double spaced.)

Do you require any audiovisual equipment?
☐ 35 mm (2 x 2 in.) slide projector
☐ Vu-Graph
☐ other (specify)
Is a full length paper on this work to be submitted for Society Journal publication?
☐ Yes ☐ No

Papers presented before a Society technical meeting become the property of the Society and may not be published elsewhere without written permission of the Society. Papers presented at Society technical meetings must be authored by a member or sponsored by an active member.

.....
Insert name of Society member author or sponsor

THE ELECTROCHEMICAL SOCIETY PATRON MEMBERS

Bell Laboratories
Murray Hill, NJ

Dow Chemical Co.
Inorganic Chemicals Dept.
Midland, MI

Exxon Research and Engineering Co.
Corporate Research
Advanced Energy Systems Laboratory,
Solid State Sciences Laboratory,
Linden, NJ

Engineering Technology Div.
Florham Park, NJ

General Electric Co.
Battery Business Dept., Gainesville, FL

Chemical Laboratory, Knolls Atomic Power Laboratory,
Schenectady, NY

Lamp Div., Cleveland, OH

Materials & Process Laboratory, Large Steam
Turbine-Generator Dept., Schenectady, NY

General Electric Co. (continued)
Research and Development Center,
Chemical Systems & Technology
Laboratory & Physical Chemistry Laboratory,
Signal Processing & Communication Laboratory,
Schenectady, NY
Semiconductor Products Dept.,
Syracuse, NY

International Business Machines Corp.
New York, NY

INCO Research and Development Center
Suffern, NY

Olin Corp.
Chemicals Div.
Charleston Technology Center
Charleston, TN

Philips Research Laboratories
Eindhoven, The Netherlands

Westinghouse Electric Corp.
Electronic Tube Div., Elmira, NY
Lamp Div., Bloomfield, NJ
Semiconductor Div., Youngwood, PA
Research Laboratories, Pittsburgh, PA

THE ELECTROCHEMICAL SOCIETY SUSTAINING MEMBERS

The Aerospace Corp.
Los Angeles, CA

Airco Industrial Gases
Murray Hill, NJ

Airco Speer Carbon Graphite
St. Marys, PA

Allied Chemical Corp.
Industrial Chemicals Div.
Solvay, NY

Aluminum Co. of America
New Kensington, PA

Aluminum Co. of Canada, Ltd.
Montreal, Que., Canada

AMAX Inc.
Greenwich, CT

AMP Inc.
Harrisburg, PA

Analog Devices, Inc.
Norwood, MA

Applied Materials, Inc.
Santa Clara, CA

Asahi Chemical Industry Canada, Ltd.
Toronto, Ont., Canada

ASARCO, Inc.
South Plainfield, NJ

Battelle Memorial Institute
Columbus, OH

Battery Technology Co.
A Division of Duracell International
Tarrytown, NY (2 memberships)

Bell-Northern Research
Ottawa, Ont., Canada

Boeing Co.
Seattle, WA

The Borg-Warner Corp.
Roy C. Ingersoll Research Center
Des Plaines, IL

BP Research Centre
Middlesex, England

Brown, Boveri & Co., Ltd.
Research Center
Baden, Switzerland

Canadian Industries Ltd.
Montreal, Que., Canada

Cominco Ltd.
Trail, B.C., Canada

The Continental Group, Inc.
Energy Systems Laboratory
Cupertino, CA

Corning Glass Works
Corning, NY

Crawford & Russell Inc.
Stamford, CT

Diamond Shamrock Corp.
Painesville, OH

Duro-Test Corp.
North Bergen, NJ

Eagle-Picher Industries, Inc.
Electronics Div.
Joplin, MO

Eastman Kodak Co.
Rochester, NY

Electric Power Research Institute
Palo Alto, CA

Electrochemical Technology Corp.
Seattle, WA

Electrode Corp.
Chardon, OH

Eltra Corp.
Prestolite Div., Toledo, OH
C&D Batteries, Conshohocken, PA

Energy Development Associates
A Gulf and Western Co.
Madison Heights, MI

Energy Technology
A Division of Medtronic, Inc.
Minneapolis, MN

SUSTAINING MEMBERS (CONTINUED)

Ever Ready Co. (Holdings) Ltd.
Whetstone, London, England

Exmet Corp.
Bridgeport, CT

Fairchild Camera & Instrument Corp.
Research & Development Laboratory
Palo Alto, CA

FMC Corp.
Inorganic Chemicals Div.
Buffalo, NY

Ford Motor Co.
Dearborn, MI

The Gates Rubber Co.
Denver, CO

General Motors Corp.
Delco-Remy Div., Anderson, IN
Research Laboratories Div.
Warren, MI

Gould Inc.
Gould Laboratories—
Energy Research
Rolling Meadows, IL
Gould Information Center
Cleveland, OH

Great Lakes Carbon Corp.
New York, NY

GTE Laboratories
Waltham, MA

GTE Sylvania Inc.
Chemical & Metallurgical Div.
Towanda, PA

The Harshaw Chemical Co.
Cleveland, OH

Heliotronic GmbH
Burghausen, Germany

Hewlett Packard Co.
Loveland, CO

Hewlett Packard Laboratories
Palo Alto, CA

Hill Cross Co., Inc.
West New York, NJ

Hoechst-Uhde Corp.
Englewood Cliffs, NJ

Honeywell, Inc.
Power Sources Center
Horsham, PA

Hooker Chemical Corp.
Niagara Falls, NY (2 memberships)

Hughes Research Laboratories
Div. of Hughes Aircraft Co.
Malibu, CA

INCO ElectroEnergy Corp.
Engineering & Development Center
Ray-O-Vac Corp.
Madison, WI
Engineering & Development Center
Exide Corp.
Yardley, PA

International Lead Zinc Research Organization, Inc.
New York, NY

International Minerals and Chemical Corp.
Electrochemical Div.
Orrington, ME

Johnson Controls, Inc.
Milwaukee, WI

Kaiser Aluminum & Chemical Corp.
Pleasanton, CA

Kawecki Berylco Industries, Inc.
a subsidiary of Cabot Corp.
Boyertown, PA

KW Battery Co.
Skokie, IL

Arthur D. Little, Inc.
Cambridge, MA

Lockheed Missiles & Space Co., Inc.
Research Laboratory
Palo Alto, CA

Marathon Battery Co.
Waco, TX

Marston Bermuda
Hamilton, Bermuda

Matsushita Electric Industrial Co., Ltd.
Osaka, Japan

Mead Advanced Systems Research and Development Laboratories
Dayton, OH

Mepco/Electra, Inc.
Columbia, SC

Microwave Associates, Inc.
Burlington, MA

Molycorp, Inc.
New York, NY

Monsanto Co.
St. Louis, MO

Motorola Inc.
Phoenix, AZ

M&T Chemicals Inc.
Detroit, MI

NIFE Jungner AB
Oskarshamn, Sweden

Noranda Research Centre
Pointe Claire, Que., Canada

Occidental Research Corp.
La Verne, CA

Olin Corp.
Metals Research Laboratories
New Haven, CT

Owens-Illinois Inc.
Toledo, OH

Oxy Metal Industries Corp.
Warren, MI

Perkin-Elmer Corp.
Norwalk, CT

Phelps Dodge Refining Corp.
Maspeth, NY

Philips Laboratories, Inc.
Briarcliff Manor, NY

PPG Industries, Inc.
Chemical Div.
Pittsburgh, PA

Prototech Co.
Newton Highlands, MA

RCA Corp.
Color Picture Tube Div.
Lancaster, PA

Reynolds Metals Co.
Reduction Research Div.
Sheffield, AL

Rockwell International
El Segundo, CA

Sandia Laboratories
Albuquerque, NM

J. C. Schumacher Co.
Oceanside, CA

Shipley Company, Inc.
Newton, MA

Siemens Aktiengesellschaft
Munich, Germany

Signetics Corp.
Sunnyvale, CA

Siltec Corp.
Menlo Park, CA

Sperry Research Center
Sudbury, MA

Sprague Electric Co.
North Adams, MA

The Stackpole Corp.
St. Marys, PA

Standard Telecommunication Laboratories Ltd.
Essex, England

Stauffer Chemical Co.
Dobbs Ferry, NY

St. Joe Minerals Corp.
Monaca, PA

Tektronix, Inc.
Beaverton, OR

Teletype Corp.
Skokie, IL

Texas Instruments Inc.
Attleboro, MA
Dallas, TX

Tokyo Shibaura Electric Co., Ltd.
Toshiba Research and
Development Center
Kawasaki, Japan

Toyota Central Research and Development Labs, Inc.
Nagoya, Japan

Union Carbide Corp.
Battery Products Div.,
Corporate Research Dept.
New York, NY

United States Steel Corp.
Research Laboratory
Monroeville, PA

Varian Associates
Palo Alto, CA

Wacker Chemitronic
Burghausen, Germany

Western Electric
Princeton, NJ

Xerox Corp.
Webster Research Center
Rochester, NY

Yardney Electric Corp.
Pawcatuck, CT

Yuasa Battery Co., Ltd.
Osaka, Japan